Petrology

Gautam Sen

Petrology

Principles and Practice

Springer

Gautam Sen
American University of Sharjah
Sharjah, United Arab Emirates

Additional material to this book can be downloaded from http://extras.springer.com.

ISBN 978-3-662-51187-9 ISBN 978-3-642-38800-2 (eBook)
DOI 10.1007/978-3-642-38800-2
Springer Heidelberg New York Dordrecht London

Preface

It is always easier to write a textbook the second time around, or so I thought. Writing my first textbook entitled "Earth's Materials: Minerals and Rocks" (published in 2001 by Prentice-Hall) was difficult because I had to make some tough decisions about what materials to include and what to leave out. Based on my own thinking and input from colleagues and students since that time, I decided to write a textbook on petrology and leave out mineralogy altogether. The result is the present textbook. It was anything but easy to write this book.

Petrology is a dynamic subject. Many research papers have appeared in the literature since 2001. Some important NSF-funded workshops on pedagogic practices in petrology have since occurred. It is important for any textbook to capture all these new discoveries and changes while maintaining rigor and readability. I have tried to do this and hope that students and faculty will like the book. No reward is better than that. I do not expect anyone to cover every detail in all of the chapters of the book in a single semester. There is enough useful material in this book that will make it a useful reference beyond the classroom. The format I followed is more along the lines of classical treatment of the subject, with an emphasis on phase equilibrium controlled processes. I have added some exercises that will help the student in applying their knowledge to real-world problems.

I am grateful to my ex-students and colleagues at Florida International University and elsewhere for helping me through discussions and actual reading of the revised chapters. I am grateful to the following individuals for their help and discussions at different times over the last 10 years or so: Drs. Shantanu Keshav, Zachary Atlas, Sedelia Durand, Melroy Borges, Indra Sen, Kevin Chau, Massimilliano Tirone, Michael Bizimis, Mihai Ducea, Dean Presnall, Robert Stern, Frank Spera, William Leeman, Vic Camp, Bruce Marsh, Simon Peacock, Grenville Draper, Marc Hirschmann, Asish Basu, Jibamitra Ganguly, Surendra Saxena, Frederick Frey, John Wolff, Steve Reidel, Richard Naslund, Neptune Srimal, Florentin Maurrasse, Somnath Dasgupta, Pulak Sengupta, D. Chandrasekharam, Dalim Paul, Sanjib Biswas, Arijit Ray, Jyotisankar Ray, Keith Cox, John Mahoney, and Peter Hooper. I am thankful to Lewis Ashwal, Nick Arndt, and Vic Camp for sending me photographs and figures for use in the book. I am particularly grateful to the following individuals for reading various chapters and making very helpful suggestions: Drs. Robert Stern (University of Texas at Dallas), Jason Saleeby (California Institute of Technology), Asish Basu (University of Texas at Arlington), N. Chalapathi Rao (Benaras Hindu University), Shantanu Keshav (University of Montpellier), Sedelia Durand (Florida International University), and Indra Sen (Woods Hole Oceanographic Institution and Indian Institute of Technology Bhubaneswar). I also thank various authors and journals/organizations for their permission to reproduce some of the diagrams/figures. I thank the support and encouragement I received from Carlo Schneider (Springer) for his editorial help. This book would not be possible without the support and understanding of my wife, Sanjukta. She sacrificed many weekends and evenings so that I could finish this book. I dedicate this book to my former professors—Dean Presnall and James Carter (UT Dallas), Gary Ernst (Stanford University), Amal Dasgupta (Asutosh College, Kolkata, India), and the late Aniruddha De (Calcutta University).

American University of Sharjah, Sharjah, UAE Gautam Sen

Contents

Introduction

1

Abstract

This chapter provides an overview of the concepts about the *solid Earth* that are normally developed in a freshman Earth science or physical geology course. This level of understanding is necessary for relating petrology to global Earth processes. Perhaps the most important among them is the grand unification concept of *plate tectonics*, which proposes that the Earth's outer shell behaves like a composite system of *plates* that are constantly shifting positions in response to internal forces. Most or all observable phenomena on Earth, such as earthquakes and volcanism, are somehow tied to the movement of plates. Some basic and pertinent data on planet Earth are first presented, and then the concept of plate tectonics is briefly discussed.

Some Basic Facts About the Earth

Earth is one of the four *inner planets* (so-called because they are closer to the Sun) in our solar system, the others being Mercury, Venus, and Mars. The *outer planets* consist of Jupiter, Saturn, Uranus, Neptune, and Pluto. The outer planets are very cold and largely composed of gases (mostly hydrogen and helium); however, Pluto is an exception in that it is more like a satellite (such as the Moon) in terms of its size, and it is composed of a frozen mixture of ice, rock, and gas. An *asteroid belt*, composed of asteroids and gases, separates the inner planets from outer planets. Most meteorites that fall on Earth from the outer space are believed to originate from the asteroid belt. They provide important clues to how our solar system formed.

Earth has the shape of an *oblate spheroid* (i.e., it is not a perfect sphere but a sphere that is somewhat flattened at the poles), which accounts for its smaller polar radius relative to the equatorial radius (Table 1.1). Studies of earthquake-generated waves, or *seismic waves*, indicate that the Earth has a concentrically layered structure. When a major earthquake occurs, some seismic waves generated from it can travel through the entire interior of the Earth. Along their paths, such waves bend (refract) or reflect as they encounter different layers of different physical properties (e.g., differing densities). A boundary between any two such layers is referred to as a *seismic discontinuity*.

Based on the existence of seismic discontinuities, the following major layers within the Earth are recognized: a solid *inner core* at the center of the Earth, surrounded by a molten *outer core*; a rocky *mantle;* and a thin outer layer, called *crust* (Fig. 1.1). A diffuse layer of uneven thickness (200–400 km) occurs between the mantle and core. This layer is called the *D″ layer*. Laboratory studies of seismic wave velocities through different planet-forming materials, along with other types of studies, allow the scientist to evaluate the composition of the Earth's internal layers. Based on such evaluations, it appears that the inner core is made of metallic iron, whereas the outer core is likely composed of a mixture of iron and iron sulfide, iron oxide, and/or other compounds of iron. The mantle and crust are dominantly made of silicate minerals.

G. Sen, *Petrology*, DOI 10.1007/978-3-642-38800-2_1,

Table 1.1 Some basic parameters of the Earth (various sources)

Mean density	5.515 g cm^{-3}
Surface gravity	9.8202 m s^{-2}
Mass	5.9736×10^{24} kg
Mean radius	6,371.01 ± 0.02 km
Equatorial radius	6,378.136 km
Polar radius	6,356.752 km
Thickness of Earth's major layers	
Inner core	1,215 km
Outer core	2,159 km
D″ layer	200–400 km
Lower mantle	2,331 km
Transition zone	260 km
Upper mantle	392 km beneath mature ocean basins
	360 km beneath stable continental shields
Oceanic crust	6–8 km
Continental crust	35–45 km
Densities of common crustal rocks	
Sedimentary	2–2.8
Metamorphic	2.6–3.0
Igneous	2.5–3.1
Density of mantle peridotite	3.3–3.6 g cm^{-3}

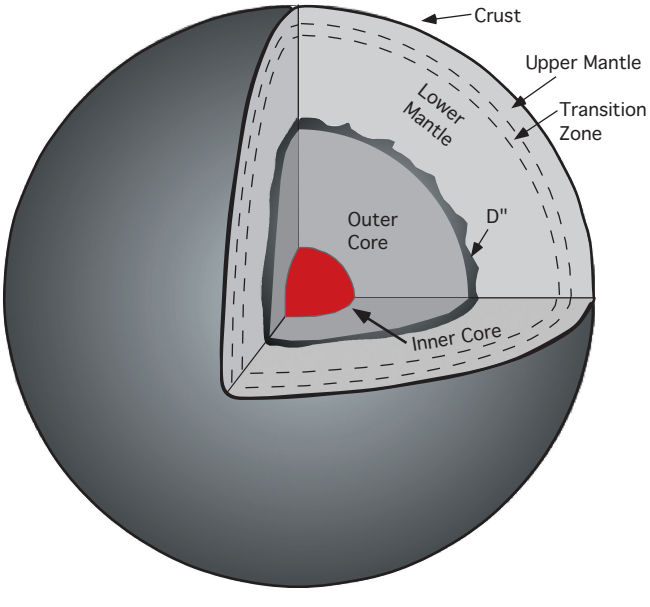

Fig. 1.1 Earth's internal layered structure. See Table 1.1 for thickness and text for composition of the individual layers

The mantle itself has several distinct layers within it. Of particular significance is the *transition zone* that occurs between 400 and 670 km discontinuities. The transition zone divides the Earth's mantle into a shallower *upper mantle* and a deeper *lower mantle*. It is generally believed that the upper and lower mantles have different compositions: The mineral *olivine* is the dominant constituent of the upper mantle, and another mineral, called *silicate perovskite*, is the principal component of the lower mantle. Up until the 1990s, most scientists accepted that the upper and lower mantles were convecting independently of each other, and the transition zone served as a boundary layer through which the two mantle layers episodically exchange heat and materials. Over the past decade, new types of seismic tomography have produced 3D images of the whole mantle, which shows that circulation in the mantle is incredibly complex (discussed later).

Finally, the Earth's *crust* is significantly richer in silica and lighter than the mantle. The crust that forms continents is considerably thicker, lighter, and richer in silica, soda, and potash than the oceanic crust. Rocks or minerals older than ~270 million years of age do not occur in the oceans, whereas much older rocks and minerals (3.6–4.2 billion years) have been found on continents.

Earth's Beginning

The Sun, Earth, and other planets of the *solar system* are all believed to have formed some 5 billion years ago from the *solar nebula*, a rotating, disk-shaped cloud of dust and gas. Much of the mass of the nebula quickly concentrated in the center due to gravitational attraction of the particles to each other, leading to the birth of the "baby" Sun, or *protosun* (Fig. 1.2). As the protosun grew, it began to compress under its own weight and became hot, which eventually led to the start of *nuclear fusion* at around 1,000,000 °C. The nuclear fusion that continues to occur today in the Sun to provide its energy is the same reaction that occurs in a hydrogen bomb explosion; it involves "fusion" of two atoms of hydrogen into forming an atom of helium. The heat and solar wind during the formation of the protosun drove away the bulk of the gases to the cooler, outer reaches of the solar system where they eventually formed *gaseous giant outer planets* such as Jupiter and Saturn and ice giants such as Uranus and Neptune. Pluto's origin is somewhat complicated: many scientists believe that it is a captured comet or a "leftover *planetesimal*" (defined in the next paragraph) that did not grow to sufficiently large size.

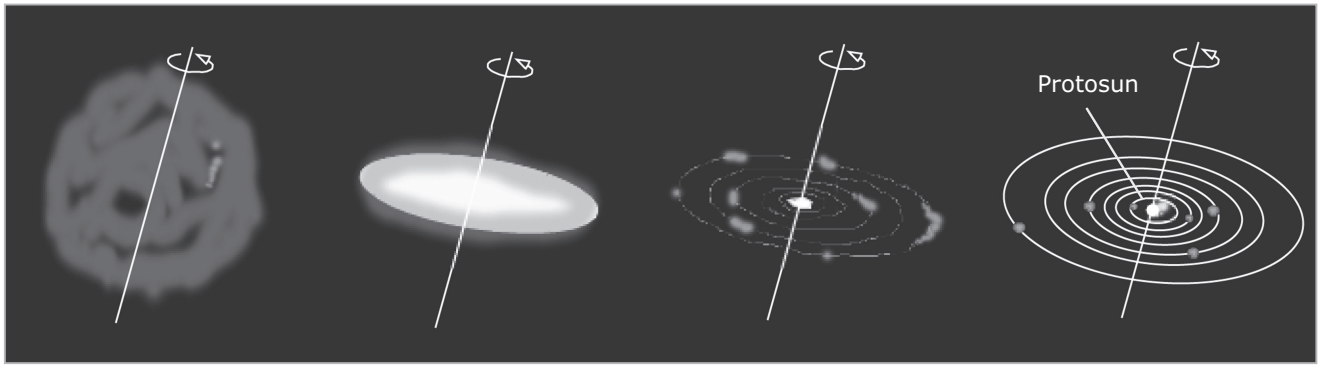

Fig. 1.2 Formation of the solar system from a nebula

Table 1.2 Approximate condensation temperatures of materials forming in the solar nebula at 10^{-4} bars pressure (after Grossman and Larimer 1974; Brown and Mussett 1993)

Mineral	Chemistry	Temperature (K)	Nature
Corundum	Al_2O_3	1,680	More refractory
Perovskite	$CaTiO_3$	1,560	
Melilite	$Ca_2Al_2SiO_7$–$CaMgSi_2O_7$	1,470	
Diopside	$CaMgSi_2O_6$	1,410	
Spinel	$MgAl_2O_4$	1,390	
Iron metal	Fe (Ni)	1,380	
Forsterite	Mg_2SiO_4	1,370	
Enstatite	$MgSiO_3$	1,360	Less refractory
Anorthite	$CaAl_2Si_2O_8$	1,230	
Alkali feldspars	$(Na, K)AlSi_3O_8$	1,060	
Troilite	FeS	650	More volatile
Magnetite	$FeO{\cdot}Fe_2O_3$	410	
Hydrous silicates		300	
Water ice	H_2O	240	
Ammonia ice	$NH_3{\cdot}H_2O$	130	
Methane ice	$CH_4{\cdot}6H_2O$	90	
Nitrogen ice	$N_2{\cdot}6H_2O$	90	Less volatile

Box 1.1: Origin of the Moon

Everyone knows that the moon started out
as a renegade fragment of the sun, a solar
flare that fled that hellish furnace
and congealed into a flat frozen pond suspended
between the planets. . .
(quoted from "On the Origins of Things" by Troy Jollimore (source: POETS.org, from the Academy of American Poets)

The Moon has appealed to the deep senses of the poet and the scientist alike. Its origin had remained a favorite subject of folklore and romantic poems, until NASA's Apollo program landed man in the late 1960s and 1970s on the Moon and returned large quantities of rock and soil samples from the Moon. Scientists

(continued)

Box 1.1 (continued)

across the world continue to examine these samples and discover new things concerned with the nature and origin of the Moon.

The Moon is 27 % of the size of the Earth and is much less dense (3.35 g/cm^3) than the Earth (5.515 g/cm^3). Its low density is attributed to the lack of a prominent dense core like that of the Earth. The surface of the Moon is very distinctive from that of the Earth, as it is covered by (a) large dark areas covered with basalt lava, called *lunar maria*, (b) many large and small craters created by meteorite and asteroid impacts, and (c) bright areas called lunar highlands which are composed of a rock called anorthosite (discussed in detail in other chapters). Isotopic dating of rocks from the lunar highlands gives the oldest ages of 4.45 billion years or, giga years, Ga. (Method of age calculation using isotope ratios is detailed in the Appendix.) On the other hand, most basalts from lunar maria yield much younger ages of around 3–3.5 Ga. Thus, lunar highlands are the areas where the ancient lunar crust is exposed. These are also the areas where the impact craters are significantly more abundant.

On Earth, plate tectonics has been operational for a long time and has managed to erase the ancient structures and rocks to a large extent by dragging surface rocks back to the mantle and by constantly altering the features of the Earth's surface. The thick atmosphere that envelops the Earth has been instrumental in altering and eroding ancient rocks. The Moon has a very thin atmosphere and has lacked plate tectonics for much of its existence, which has allowed the preservation of ancient structures and rocks on its surface in very pristine conditions. Interestingly, isotope ratios of oxygen of the Earth and Moon are very similar, which suggests that they had a common origin.

The low density of the Moon and its compositional similarity to the Earth have been taken to support the "giant impactor theory." This theory suggests that a Mars-sized asteroid, called Theia, impacted the early Earth soon after its core had segregated. The collision knocked off a large chunk of the Earth, which mixed with the disintegrated impactor and formed the early Moon. Later in Chap. 6, we will discuss the origin of the highland rocks, which formed by floating plagioclase crystals in a giant ocean of magma or molten rock.

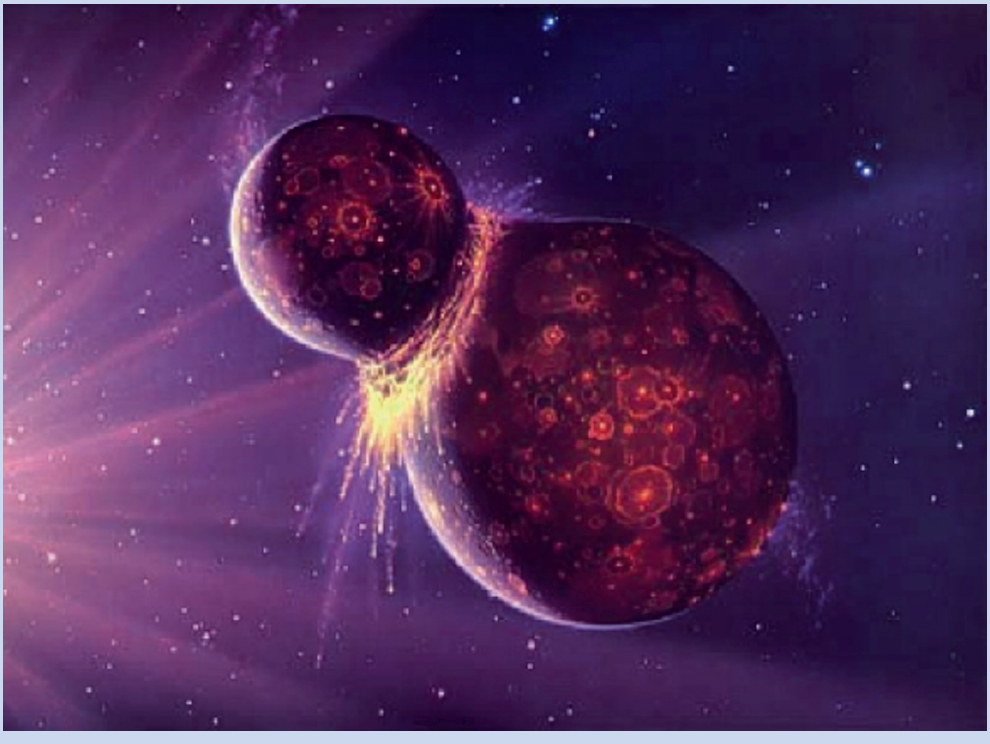

Joe Tucciarone (cited by: http://starchild.gsfc.nasa.gov/docs/StarChild/questions/question38.html)

As the inner parts of the solar nebula cooled, refractory elements (those that melt at very high temperatures) were formed by condensation of vapor at about 1,800 K and 10^{-4} bar pressure. Refractory metals, such as iridium and osmium, condensed first at ~1,800 K. Refractory oxides of Ca, Al, Mg, and Ti were next to form as condensates at ~1,700 K (Table 1.2). Metallic iron (Fe) and nickel (Ni) then condensed from the cooling nebula, followed later by silicates. Particles formed of these elements eventually clumped (or *accreted*) together to form meter-sized bodies, which further accreted to form asteroid- to Mars-sized bodies, called *planetesimals*. The larger planetesimals "swept up" the smaller ones by their gravitational pull and became planets. Thus, some 4.55 billion years ago, the earliest, rocky inner planets (also called *terrestrial planets*), including protoearth, were formed.

Origin of the Earth's Internal Layering

How and when the Earth developed its internal layering are questions that continue to intrigue the student of Earth sciences. It is commonly accepted that the Earth's internal layering developed very early—perhaps within the first 500 million years. However, the record of such early history is not preserved in terrestrial rocks and must be inferred from meteorites, because many meteorites contain the same materials that composed the protoearth. Broadly speaking, two classes of hypotheses commonly referred to as the homogeneous accretion and heterogeneous accretion hypotheses have been put forward about the origin of the Earth's internal layering. The majority of scientists appear to believe that the protoearth became very hot as it grew in size through continuous bombardment (and absorption) of asteroids and meteorites. The heating resulted mainly from conversion of mass as the planet became dense due to compression under its own weight and from the decay of short-lived radioactive isotopes. In the *homogeneous accretion model*, it is believed that the Earth started out as a homogeneous body composed of variously sized planetesimals and some trapped gases, and intense internal heating subsequently led to melting of iron metal which segregated to the Earth's center to form the core (Fig. 1.3). The term "*iron catastrophe*" has been used to describe the iron-melting event. The process of development of layering from an initially homogeneous body is called *planetary differentiation*.

The *heterogeneous accretion model* calls for the accretion of already differentiated planetesimals. The fact that individual meteorites consist of many different types of materials (e.g., minerals, chondrules, metal) has led some scientists to propose that the core formed by accretion of planetesimals in which metallic iron had already separated from silicates. The presence of strong isotopic compositional variations in meteorites has been used by some scientists to argue for the existence of strong heterogeneities even in the solar nebula (e.g., Taylor 1992). The existence of distinct reservoirs within the Earth, as required by a number of different radioactive isotopic systems, also supports the maintenance of strong vertical and lateral heterogeneities within the Earth since its beginning. Such heterogeneities may have had their origin in the accretion history. The heterogeneous accretion model does not rule out the former occurrence of an iron catastrophe; it only proposes that the materials accreted were already differentiated and, thus, the Earth had a heterogeneous beginning.

Many scientists believe that at some point (perhaps 4.4 billion years ago) the Earth's surface became largely molten and a 450-km-deep *magma ocean* formed (Fig. 1.4). Some authors have suggested that the mineral olivine floated in this magma ocean to ultimately form an olivine-rich upper mantle, whereas the silicate mineral perovskite sank and formed the lower mantle. Some authors have also sought a link (direct as well as indirect) between this "surficial" magma ocean and sinking of molten droplets of iron (Fe) and iron sulfide (FeS) from the bottom portion of this magma ocean to the core by percolation through the partially molten zone beneath the magma ocean. The magma ocean hypothesis has not gained universal acceptance, and therefore, many questions about it, which are beyond the scope of the text, remain unresolved.

Eventually the magma ocean cooled enough so that a solid, rigid "skin" (called the *lithosphere*) of igneous rocks formed on the surface. This early lithosphere may have had a thin crust composed of solidified ultramafic lavas, called *komatiite*. This idea is based on the fact that komatiite is almost *exclusively* found in the oldest terranes on continents. The lower part of the lithosphere was made of *peridotite*, an olivine-rich coarse-grained rock that is the dominant component

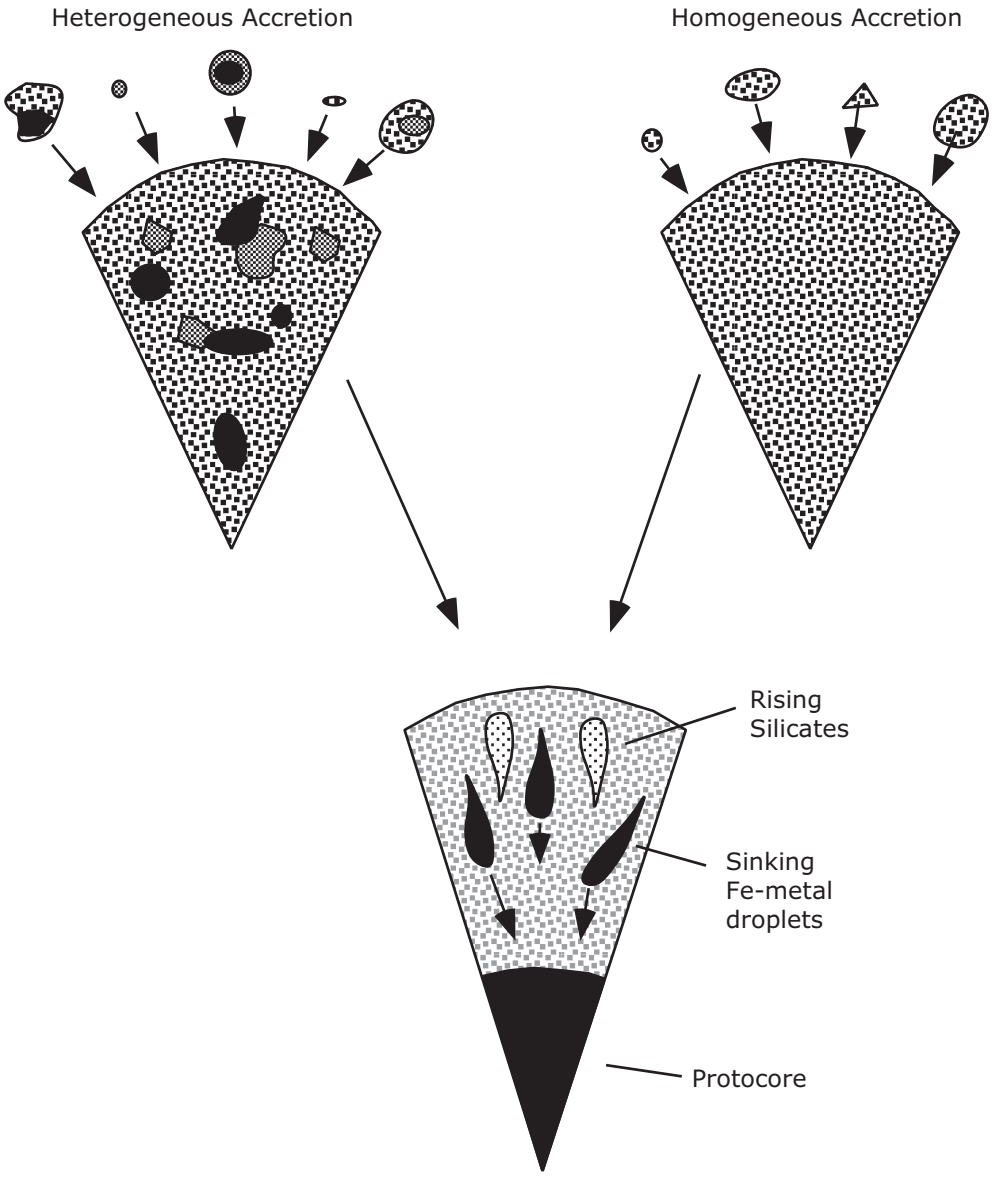

Fig. 1.3 Origin of the Earth by accretion of planet-forming materials. The heterogeneous accretion model calls for accretion of already differentiated asteroid-like bodies, whereas homogeneous accretion model suggests the formation of protoearth from undifferentiated planetesimals. The newly accreted protoearth was much smaller in size than the Earth we know today. Early in its history, the Earth underwent a major heating event when metallic iron melted and sank to form the core, whereas the lighter silicates were left behind at higher levels or moved up

of the Earth's upper mantle today. A highly uneven lithosphere, with very thick (~35 km) crust at some places but thin in others, may have developed around 4.3 billion years ago. Even today the world's oceanic crust is somewhat uneven. On the average it is about 8 km thick, but in the so-called oceanic plateaus (e.g., the Ontong-Java plateau in the Pacific Ocean) and in some seas (e.g., the Caribbean Sea), it is significantly thicker (about 12–30 km).

The history of continents is truly fascinating. The discovery of a 4.2-billion-year-old mineral zircon in some very old sedimentary rocks from Australia offers an interesting insight into early continent formation. This mineral is a common but minor constituent of *granitoid* rocks, and granitoids in turn are a fundamental component of continental crust. Therefore, the finding of such an old zircon suggests that at least some continental crust had already formed by 4.2 billion

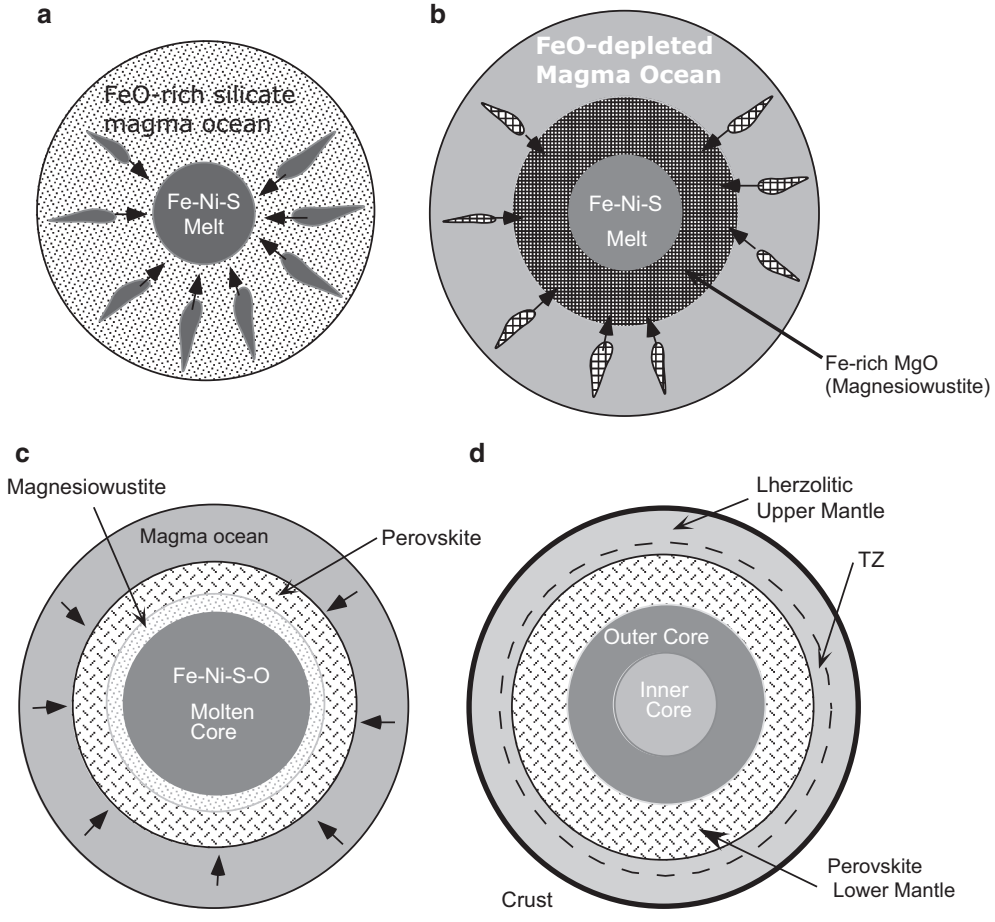

Fig. 1.4 Agee's hypothesis by (1990) (Nature *346*, pp. 834–837) calls for a complicated evolutionary history of the Earth (the diagrams here are somewhat simplified from his work). (**a**) Early formation of a FeO-rich silicate magma ocean and of the molten protocore. (**b**) At some point the mineral magnesiowustite (MgO with considerable amount of Fe in solution) formed and segregated to form a shell around the core. Separation of this mineral from the magma ocean caused a depletion in FeO in the magma ocean. (**c**) Then formed the silicate mineral perovskite (composition—$(Mg,Fe)SiO_3$), which is the dominant constituent of the lower mantle today. The magnesiowustite layer became smaller because it lost iron to the core. The core became enlarged. Note that the stages (**b**) and (**c**) may have happened sequentially or simultaneously. (**d**) The magma ocean solidified to form the mantle and crust. Inner core solidified as well. Note that subduction and other plate tectonic processes are not shown in these diagrams for brevity

years ago! In general, continents are much older than oceans: whereas the oldest continental rocks are generally 3.4–3.5 billion years old, oldest oceanic crustal rocks are only ~270 million years old. The theory of *plate tectonics* attributes this age difference to constant recycling of the older oceanic crust back into the mantle through a process known as "subduction," whereas the continental crust, being less dense, is unsubductible and collects on the surface of this dynamic planet like froth on milk. In summary, it is evident that continents were well in existence within the first billion year of the Earth's formation from solar nebula.

The mineral diamond has provided an additional critical clue to the puzzle of continental lithosphere thickness and temperature (Haggerty 1999). Diamond is found in an igneous rock, called *kimberlite*, in the oldest parts of continents where the rocks are generally older than 2.7 billion years. Silicate mineral inclusions in some diamonds date back to 3.5 billion years and appear to have been brought up from a depth of ~200 km where the temperature was ~950 °C. This temperature is not much higher than the temperatures estimated to exist within the present-day continental lithosphere. Thus, one is forced to conclude that cool, thick, continental lithosphere existed 1 billion years after the birth of the planet. The inclusions in diamonds further tell us that such primitive continental lithosphere was already 200 km thick.

Water molecules probably did not form around this time because temperatures at the surface of the Earth

were still much above the boiling point of water. However, it is likely that steam from primitive mantle escaped and formed a thin envelope of atmosphere around the planet. Many authors also believe that comets that crashed into the Earth during its early history may have provided some of the water.

Plate Tectonics

In the Beginning

It is commonly thought that the early lithosphere, however, unevenly thick, did not remain static: hot mantle jets or plumes beneath the lithosphere kept poking it until it cracked. Through these cracks, magma gushed out and solidified in the crack as the convection currents in the hot mantle below carried the cracked lithospheric "plates" away from each other. At the other ends, these plates collided with each other, one being pushed up over the other, thus began what we call *plate tectonics*.

It is likely that the earliest lithospheric plates were constantly breaking up and colliding with each other. Plate movements were quite vigorous and were driven by strong convection currents and hot spots in the mantle. Although true water-filled ocean basins probably had not yet developed, subduction of "proto-oceanic" lithosphere, similar to the present-day situation, was occurring where the lithosphere was relatively thin. By virtue of having an overall relatively lower density, the early continental lithosphere resisted subduction much like the way it has throughout Earth's history. About 4 billion years ago, the conditions became right, such that water was in sufficiently high atmospheric concentration to precipitate as rain and filled up the "basins" formed by the thinner lithospheric basins surrounded by the high continents. Thus, we finally had the beginning of ocean formation. At that point, Earth looked vaguely familiar: tiny but thick continental plates; giant, thin, oceanic plates; and abundant hot spot-generated volcanoes probably dotted this planet.

Modern Plate Tectonics

Plates and Plate Boundaries

Before proceeding further on the theory of plate tectonics, it is pertinent to examine the concept of the lithosphere, which plays a fundamental role in the theory. The term "lithosphere," as commonly used, has a mechanical connotation that stemmed from Barrell's (1914, cited in Anderson 1995) idea of a "strong outer layer (about 100 times stronger than the asthenosphere) overlying a weak asthenosphere that could flow to maintain isostatic compensation" (Anderson 1995, p. 125). Although there are thermal (as defined by the contrasting thermal behaviors of the lithosphere and asthenosphere) and chemical definitions of the lithosphere, in this chapter we follow the mechanical definition of the lithosphere in the most general sense. Because mechanical behavior of rocks, specifically their brittle versus ductile behavior, is related to their mineralogy, temperature, stress, and strain rate, the thickness of the lithosphere (as defined in a mechanical sense) must also vary throughout the globe. The average thickness of the modern oceanic lithosphere is about 100 km and that of continental lithosphere is about 150 km.

According to the plate tectonics theory, the lithosphere is not laterally continuous but is broken into eight large *plates* and many small plates (Fig. 1.5). Size and shape of plates change with geological time because some plates break up into smaller plates and other plates collide with each other and become a single plate. Earthquakes and volcanism mark boundaries of each of these plates. Three types of plate boundaries are recognized:

1. *Divergent plate boundary*. Along such a boundary, two plates move apart from each other as new lithospheric material is added by magmas generated at depth (Fig. 1.6a). The best example of divergent plate boundary is the 65,000-km-long global oceanic ridge system, e.g., the Mid-Atlantic Ridge (Fig. 1.5), where the lithosphere on the two sides of the ridge axis (also known as *spreading center*) "spreads" away from each other, forcing hot asthenosphere below to passively rise to shallower levels. Such rise causes the asthenospheric material to partially melt by decompression melting (this process is described in detail in a later chapter), and magma derived from the rising asthenosphere wells up at the ridge axis and solidifies to hard rock, creating new crust. The melt-depleted residue forms the mantle part of the lithosphere. The seafloor spreading rate, which is commonly referred to as the *half-spreading rate*, is the rate at which one side of the ridge spreads away from the spreading center. This rate can vary considerably from one ocean to another and even from one part to another along the same ridge axis! A really fast spreading rate is 11 cm per year, whereas 1 cm per year is considered very slow.
2. *Convergent plate boundary*. Such a boundary is characterized by the convergence of two plates, one of

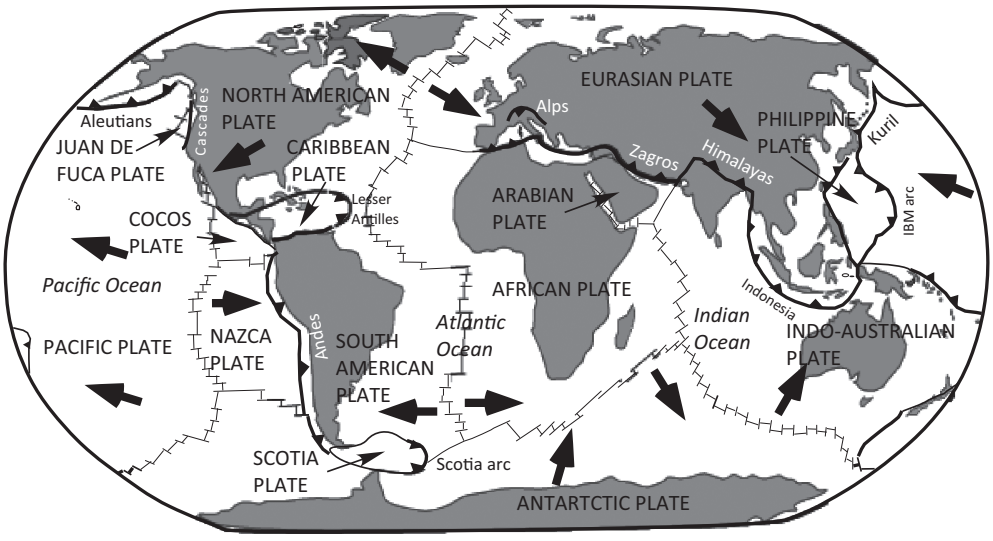

Fig. 1.5 Earth's surface showing only the major plates. Plates are continents that are shown in *gray*, and *colorless areas* are oceans. Divergent plate boundaries and transform faults that are short oblique offsets to the divergent boundaries are shown as *light gray lines*. Convergent plate boundaries are shown as *dark lines*. The *small dark triangles* on them point toward the direction of subduction. The *arrows* show the overall direction of plate movement

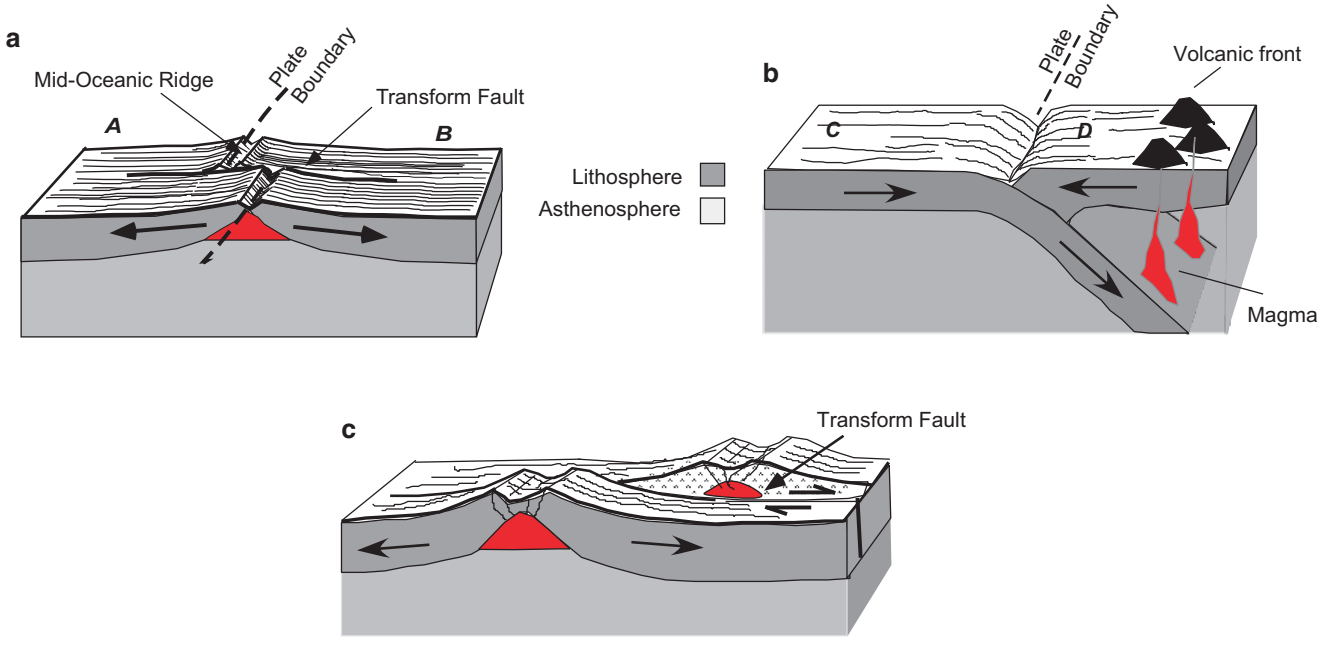

Fig. 1.6 Schematic 3D block diagrams illustrating the three types of plate boundary. (**a**) Divergent plate boundary. The schematic drawing shows the separation of two plates (plates A and B) at a mid-oceanic ridge axis, where magma formed in the asthenosphere ascends and makes new crust at the ridge axis. (**b**) Convergent plate boundary. This example shows convergence of two oceanic plates, C and D. C is being subducted underneath D. A trench zone marks the plate boundary. Magma production above the subduction zone generates a volcanic front on the overriding plate. (**c**) Transform fault. Along some plate boundaries, the plates may not separate from or converge toward each other but simply slide past one another. A transform fault is a special type of fault that offsets mid-oceanic ridge axis segments. The famous San Andreas fault, which runs through the state of California, is such a fault boundary along which the North American plate is sliding past the Pacific plate. San Francisco is located on the North American plate, whereas Los Angeles is located on the Pacific plate and is moving northward

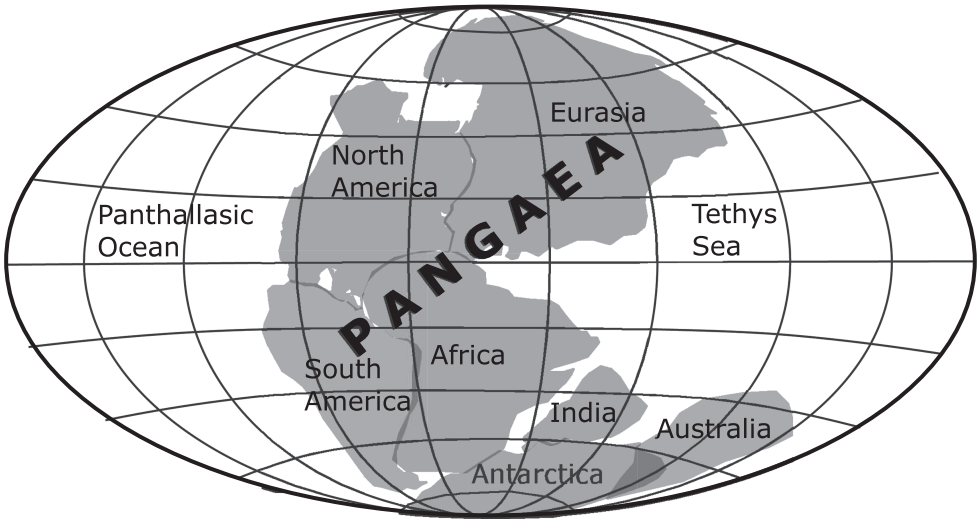

Fig. 1.7 Pangaea, the supercontinent that is believed to have split up about 200 million years ago

which gets "subducted" or consumed back into the mantle as the other overrides it (Fig. 1.6b). Plate convergence zones are typically associated with explosive volcanic activity. The most prominent zone is the "Pacific Ring of Fire," which marks the volcanic zone along the entire boundary of the Pacific plate. Deep focus (around 650 km) earthquakes are found only along such boundaries, whereas they are absent in plate divergent boundaries. In oceanic plate-continental plate convergence zones, it is the oceanic plate that always subducts into the mantle because the continental lithosphere is lighter than the oceanic lithosphere, e.g., subduction of the Nazca plate beneath the South American plate. In the case of continent–continent plate convergence, one of the plates slides under the other but because both are buoyant, enormously thickened continental mass results. The Himalayan Mountains formed this way during the collision of the Indian plate with the Eurasian plate.

3. *Transform fault boundary*. Along such a boundary, the adjacent plates do not converge or diverge but just simply move past each other along large faults (Fig. 1.6c). Transform fault boundaries are typically found in ocean basins where a mid-ocean ridge axis is not continuous but is offset by a series of transform faults (Fig. 1.6c). These faults develop due to the curvature of the Earth's surface and differential spreading rates along the ridge axis. An important transform fault on land is the San Andreas Fault in California, along which the Pacific plate is sliding past the North American plate along a northwesterly direction.

Plate boundaries can change over geologic time: for example, some 200 million years ago, all the continents formed a single, giant, landmass that was given the name *Pangaea* (Fig. 1.7). This single plate eventually broke into many continental plates, each of which has subsequently undergone modifications due to plate tectonic processes. Oceans can "close and open" as well, several times! For example, it is clear that the Atlantic Ocean closed at least once before, during which the North American, Eurasian, and African plates collided and created the Appalachian Mountains.

Hot Spots and Giant Mantle Plumes

There are many areas on Earth where active volcanism is occurring in the middle of a plate rather than at a plate boundary. An example of this is the "Big Island" of Hawaii in the middle of the Pacific plate, where two active volcanoes, Kilauea and Mauna Loa, have been spewing out large quantities of basaltic lava. It is generally accepted that there exists an anomalously hot area (or *hot spot*) in the mantle beneath Hawaii. This hot spot has remained essentially stationary at least for the last 90 million years and has been supplying magmas to the Hawaiian–Emperor island–seamount chain (Fig. 1.8a). The volcanic chain formed due to the passage of the oceanic lithosphere over a relatively fixed hot spot or plume (Fig. 1.8b). There are other hot spot tracks in the Pacific that parallel the Hawaiian–Emperor track, and all are believed to have resulted from hot spot volcanism. A prominent bend occurs in the Hawaiian–Emperor track, which corresponds to an abrupt change in the direction of movement of the Pacific plate that occurred 40 million years ago. Throughout the Earth's geologic past, there have been episodes of massive outpourings of basaltic lavas on the ocean floor and on continents. The large plateaus

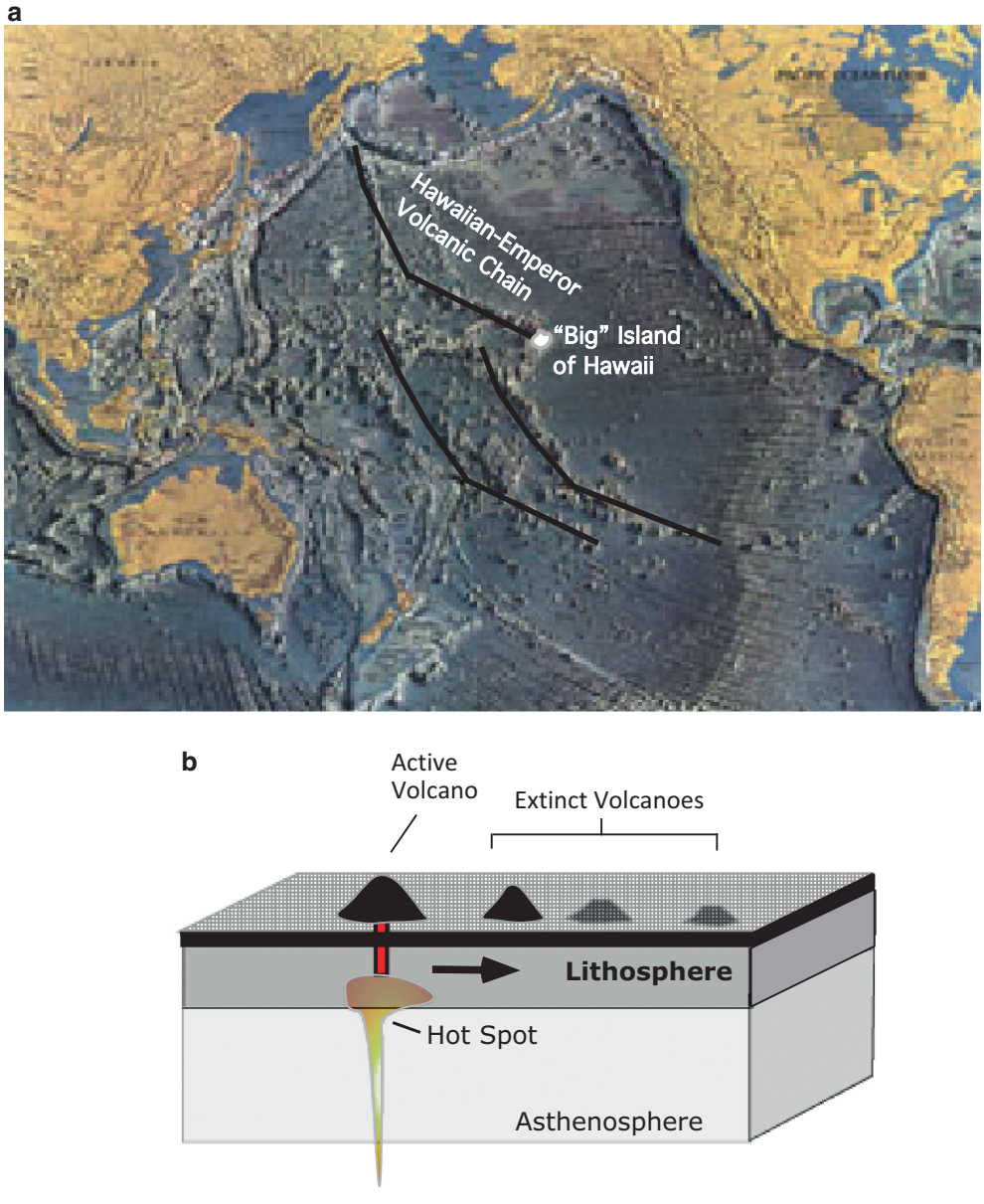

Fig. 1.8 (**a**) Intraplate volcanic chains in the Pacific Ocean. The Hawaiian–Emperor volcanic chain in the middle of the Pacific plate is highlighted. This chain is thought to be a hot spot track, with active volcanism occurring in the "Big Island" of Hawaii, where Kilauea and Mauna Loa, two of the world's largest volcanoes, remain active. (**b**) This block diagram shows how a volcanic chain develops as a plate moves over an active hot spot supplying magmas that form the volcanoes. The Hawaiian–Emperor volcanic chain is thought to have formed over at least 90 million years as the Pacific plate migrated over a relatively fixed hot spot, which now resides beneath the active volcanoes on the Big Island. As the Pacific plate migrates away, a new volcano begins to form atop the hot spot, whereas the old one becomes extinct and migrates away as a "piggyback" rider

that were formed by such volcanism have been variously called *flood basalt provinces* or *large igneous provinces* (Fig. 1.9). In some ways, they are anomalous because their estimated eruption rates were found to be very high relative to the rate at which basalt magma erupts at normal plate tectonic boundaries or at known hot spots today. Such provinces occur in the middle of a plate, and in many cases of continental eruptions, they appear to occur on the edge of the continent. Some notable examples of continental flood basalt provinces are the Deccan Traps (India), Parana basalts (South America), Karoo basalts (Southern Africa), and Columbia River basalts (western USA). Ontong-Java and Manihiki plateaus (Pacific Ocean) and the Caribbean Sea floor are thought to be oceanic examples of flood basalt provinces. In a large number

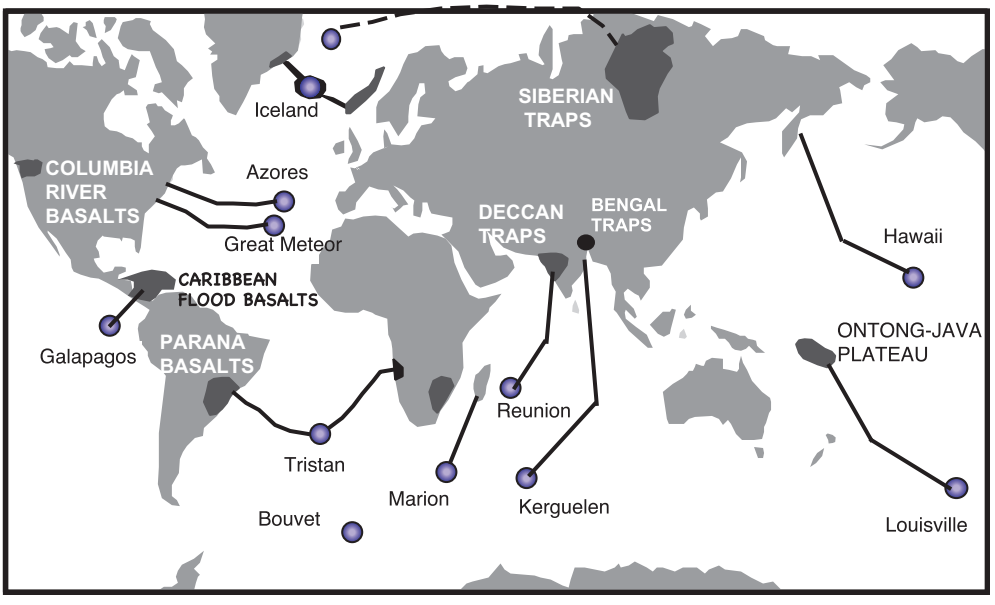

Fig. 1.9 Large igneous provinces and hot spot tracks that connect them to known hot spots. Origin of large igneous provinces. It is believed that episodically large plume "heads" rise from the deep mantle and melt when they reach the base of the lithosphere. Such melts or magmas give rise to large igneous provinces, such as the Deccan Traps of India. The "tail" of such a plume persists for many millions of years and creates volcanic chains (*source of the diagram*: Richards and Duncan 1989)

of cases, these large igneous provinces are commonly linked to volcanic tracks that terminate at known hot spots (Fig. 1.9).

Large igneous provinces are generally thought to develop from volcanic activities, which result from partial melting of giant plume "heads" that rise from the deep mantle (Fig. 1.10; e.g., Richards et al. 1989; Lay et al. 2004; Torsvik et al. 2006; Burke 2011). Some scientists believe that the narrow "tails" of such giant plumes continue to supply magmas for millions of years after the plume head had "melted" away (In a later chapter we will see that this hypothesis is in trouble because there are other hot spot chains in the mid-Pacific that bend at different times.), producing hot spot tracks (Duncan and Richards 1991).

Wilson Cycle

The theory of hot spots, plumes, plates, break up of single continents, ocean, and continent formation was largely developed in the 1960s, by such pioneers as H.H. Hess, F.J. Vine, D. Matthews, D.P. McKenzie, J.W. Morgan, J.T. Wilson, and others. J. Tuzo Wilson, a Canadian Geologist, provided a unifying hypothesis that relates plume activity, seafloor spreading, and subduction to continental break up, ocean formation, and growth of continents. This is known as the *Wilson Cycle*. The cycle begins with a plume or hot spot impinging upon the base of a continental plate. This causes the overlying lithosphere to "dome up" (Fig. 1.11a). Such uplift and heating of the lithosphere initiates cracking and rift valley formation in the shape of a three-armed star (like the Mercedes Benz logo: Fig. 1.11b). Volcanic activity and continued rifting result in two of the rift systems to spread away from each other, thus resulting in the formation of a new ocean basin (Fig. 1.11c, d). The third arm fails to grow further.

The formation of the Ethiopian rift system, Red Sea, and Gulf of Aden (Fig. 1.11e) is commonly cited as an excellent example of the early stage of the Wilson Cycle. The Red Sea and the Gulf of Aden represent early stages of ocean formation by separation of the Nubian–Arabian plates and Arabian–Somalian plates, respectively. The East African Rift system, which is associated with active normal faulting, earthquake activity, and volcanism, may be the failed arm of the Wilson model. The triangular region, where the three important rift systems meet, is known as the Afar triangle. Presumably, this is where the plume first impacted in starting the Wilson Cycle.

As the oceanic plates in the newly formed oceanic ridge system spread away from each other, they cool, thicken (the thickening of the lithosphere is roughly equal to the square root of its age), and become heavy. At some point, the oceanic lithosphere becomes heavy

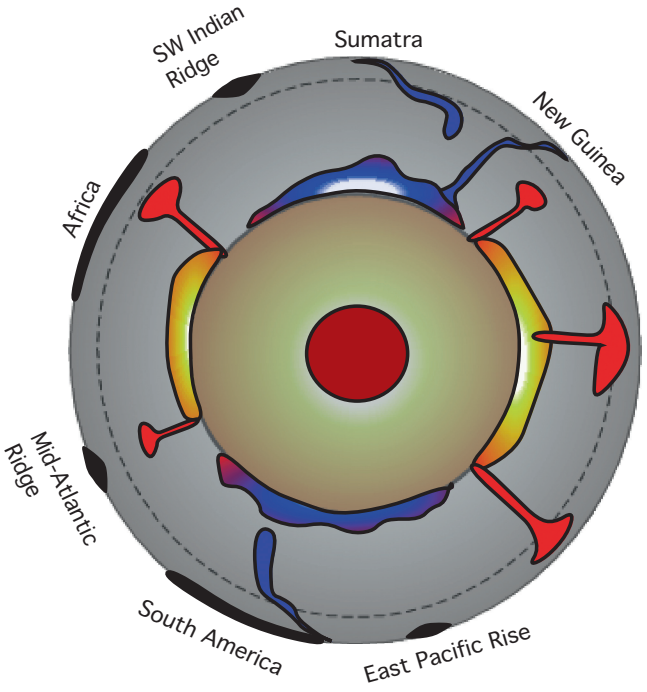

Fig. 1.10 An equatorial cross section of global mantle circulation, based on seismic tomography, is shown here [modified from Fig. 5 in Burke (2011)]. Subduction of lithosphere (*gray*) at Sumatra, New Guinea, and the western continental margin of South America are shown. These "downgoing" slabs bend sharply at the bottom of the transition zone at 660 km (*dashed*), which also marks a sharp discontinuity in material composition and properties. The old slabs accumulate at the core–mantle boundary. Two thick layers (shown as stippled) characterized by large negative shear wave velocity anomalies (presumably hotter) occur between these antipodal "slab-burial grounds" at the core–mantle boundary. It has been suggested that mantle plumes (*red*) rise from the boundary regions of such low-velocity layer at the core–mantle boundary (redrawn from Fig. 5 in K. Burke 2011)

enough to break and begin to subduct. Such subduction process may bring together two distant continents sitting on the two plates, ultimately resulting in collision of two continents, and the sediments accumulating at the leading edge of the two continents would deform and form a large folded mountain belt between the two continents (Fig. 1.11f, g). Such mountain building "bonds" the two previously separate continents into a single large continent (Fig. 1.11f). This continent may undergo the entire Wilson Cycle again at some point in its future.

Post-Wilson Hypotheses

Throughout the Earth's geologic past, there were at least three times when large supercontinents existed—Pangaea [which broke up around 200 million years ago (Ma)], Rodinia (split up around 800 Ma), and mid-Proterozoic supercontinent (split up around 1.3–1.4 billion years ago: Larson 1995; Condie and Sloan 1997). Roger Larson invoked a model that involves large "*superplumes*," which are broad mantle upwellings (imagine a plume that is the size of a continent 4,000 km wide and 2,000 km in height: Larson 1995), which rise from the deep mantle and break up supercontinents.

A commonly accepted model for plume impingement-continental separation is the one that was presented by White and McKenzie (1989; Fig. 1.12). In this model, the continental lithosphere is uplifted upon the impingement of a large plume. This uplift is accompanied by erosion, stretching, rifting, and thinning of the lithosphere. As the lithosphere is thinned to half of its original thickness, the plume starts melting, giving rise to large volumes of magmas. These magmas rise through the rift zones and produce flood basalts. Continued extension and magma production eventually leads to the splitting of the continent, and an ocean basin is formed between the separated continental plates.

Several authors have suggested that such plumes rise from the core–mantle boundary. Seismic shear wave velocity models of the deep mantle show that there are two large regions of anomalously (anomalous relative to a standard reference Earth model) low velocities that occur in the bottom 400–500 km of the lower mantle. These regions are centered beneath Africa and the Pacific Ocean (red-colored zones in Fig. 1.13). These "red" regions are separated by regions that have relatively high velocities (shown in blue in Fig. 1.13). A common interpretation of this velocity structure is that the red regions are hot and blue regions are cold: The blue regions are the "burial grounds" for old subducted slabs, and the red regions are the feeders of superplumes and long-active Hawaiian-type plumes (e.g., Romanowicz 2003; Burke et al. 2008). Some authors have further suggested that superplumes that produce large igneous provinces start at the boundaries of the red regions (e.g., Burke et al. 2008). Figure 1.10 schematically shows a cross section of the whole mantle, depicting the origin of plumes mainly from the boundaries of anomalous low-velocity regions. More recent numerical simulations show complex models of plume origin, impingement, and continent separation (Fig. 1.14).

In contrast to the plume or superplume models, Don Anderson suggested a different mechanism for

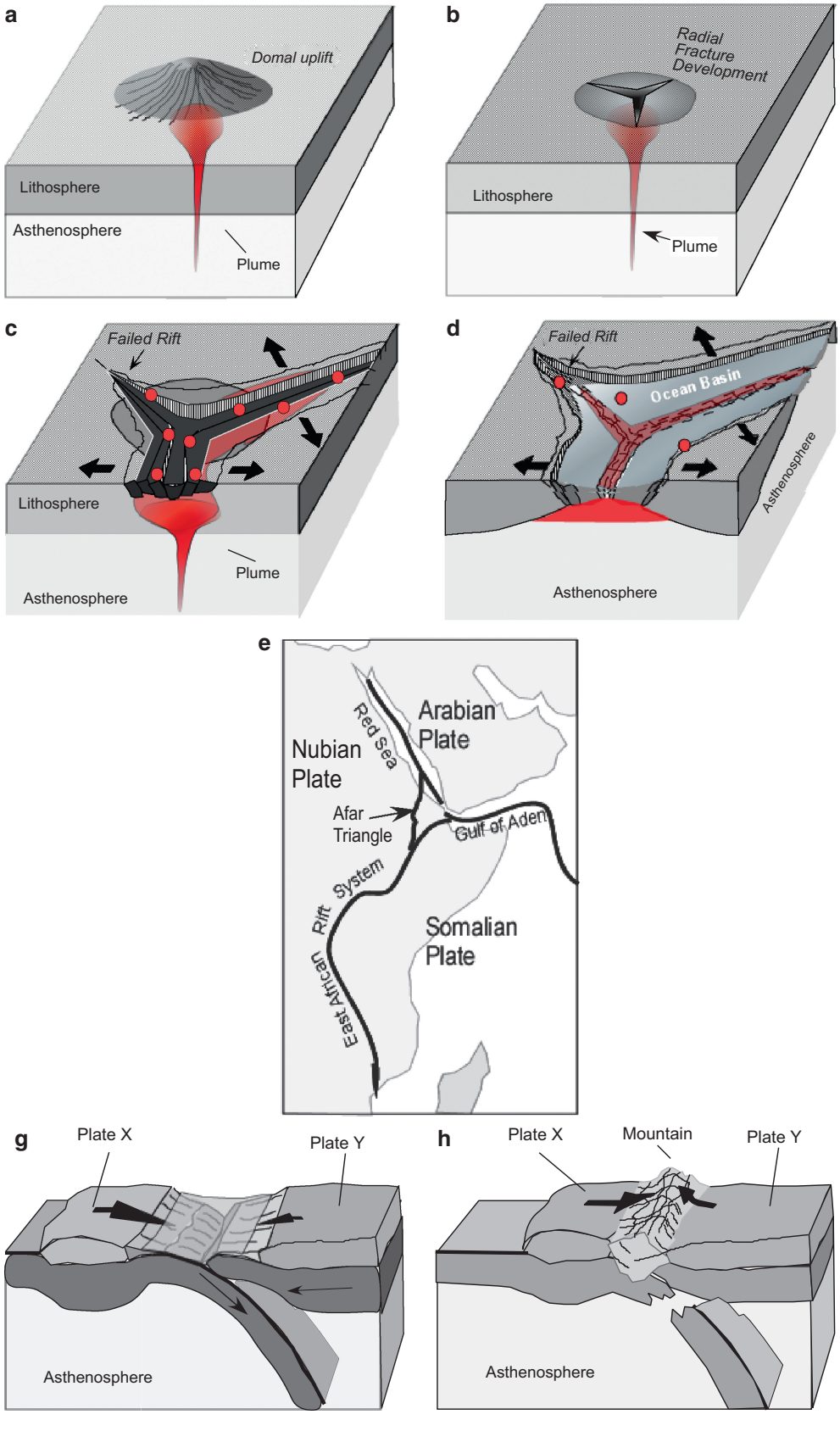

Fig. 1.11 The Wilson Cycle (see text for a detailed discussion of these diagrams). The various stages of the Wilson Cycle—from plume impingement, continental separation, and ocean formation to subduction and collision (amalgamation) of continents—are shown in block diagrams (**a**–**d**) and (**f**, **g**). (**e**) Shows the East African Rift zone and formation of new ocean basins (Red Sea and Gulf of Aden) as

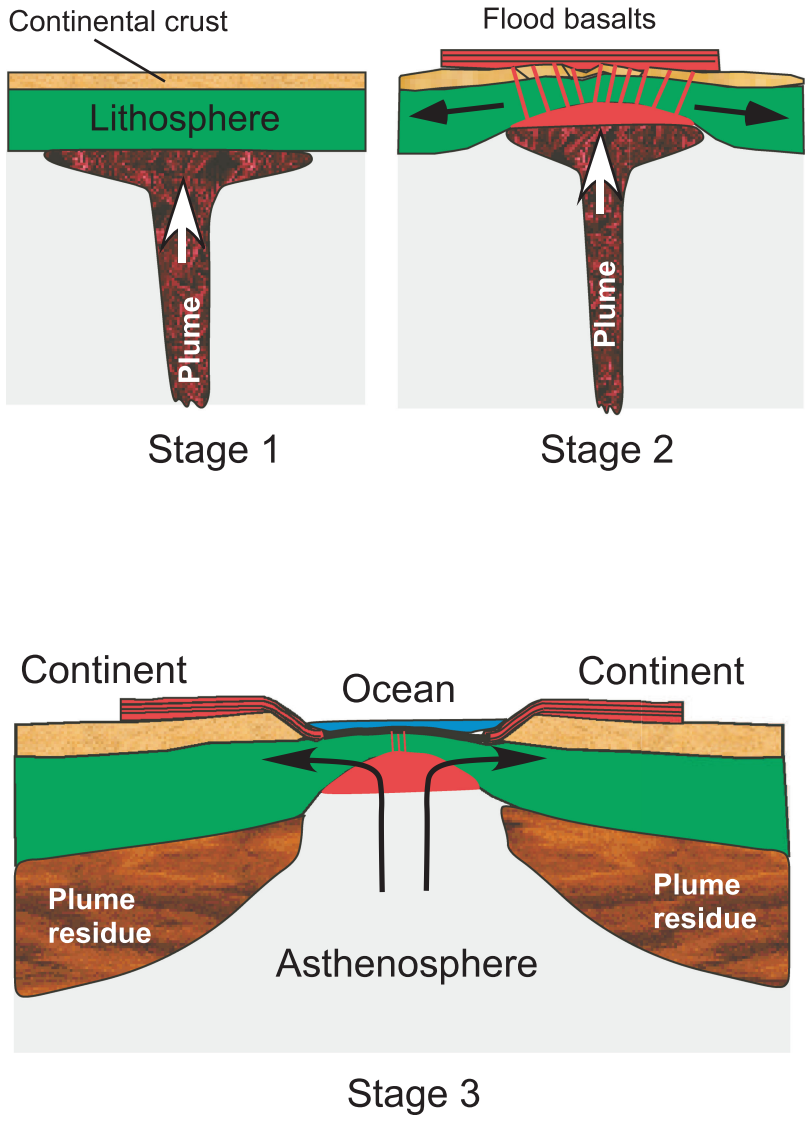

Fig. 1.12 The model of large plume initiated rifting, flood basalt formation, and separation of continents by White and McKenzie (1989) is schematically depicted here. Stage 1. Plume emplacement beneath the continental lithosphere. Stage 2. Uplift, erosion, and rifting of the lithosphere. Lithosphere thinning to 1/2 its thickness is required before partial melts (magma) forms in the plume. This melts then erupt through the rifts forming flood basalts. Stage 3. Continents eventually split, and the plume residues get attached to them and move laterally away as asthenosphere rises and melts to produce Mid-ocean ridge basalts. Along many passive continental margins, seaward dipping seismic reflectors have been found that have been interpreted to be dipping flood basalts interclated with shelf sediments

the initiation of the Wilson Cycle (Anderson 1994). Specifically, his model does not require the presence of a plume or hot spot to trigger the rift valley formation and continental splitting. Anderson pointed out that the continental crust is a good insulator. Therefore, large continental masses (called *supercontinents*), such as Pangaea (Fig. 1.7), can effectively trap heat in its underlying mantle over geologic time. Such heat buildup in the mantle eventually triggers melting, which leads to immense flood basalt-type volcanism, to rifting, and to the formation of new divergent plate boundaries (Fig. 1.15).

Fig. 1.11 (Continued) examples of early stages of continental rifting, separation, and ocean formation. (**a**) Plume impingement and domal uplift. (**b**) Development of radical fractures. (**c**) Continued rifting and failing of the third arm. (**d**) Oceanic lithosphere formation. (**e**) Triple junction between three plates. (**f**) Convergence of two continental plates X and Y. (**g**) Collision of continents and mountain building

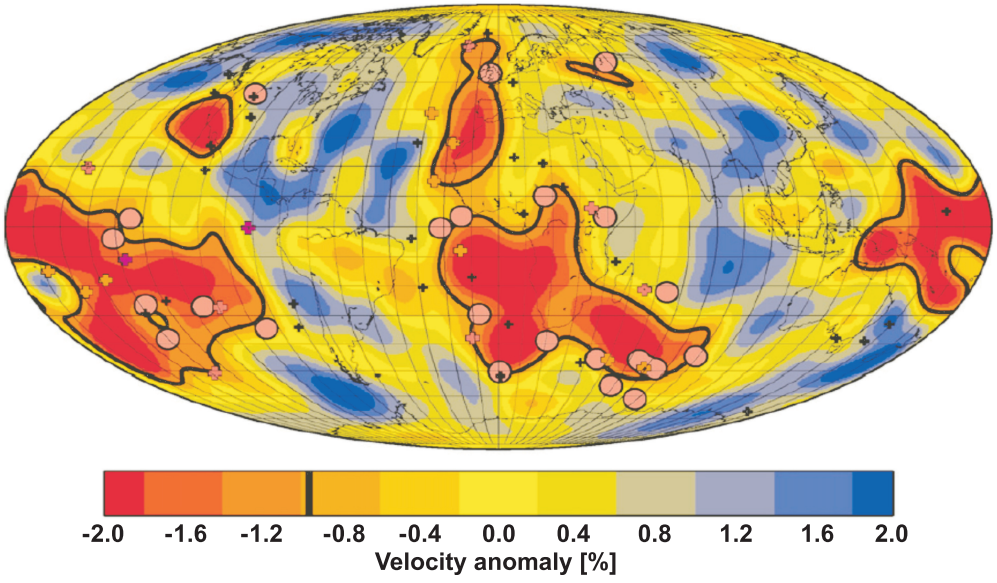

Fig. 1.13 Shear wave velocity anomalies relative to PREM at the core–mantle boundary are shown here (from Burke 2011). *Red zones* are lower velocity (hotter) and *blue* are colder zones

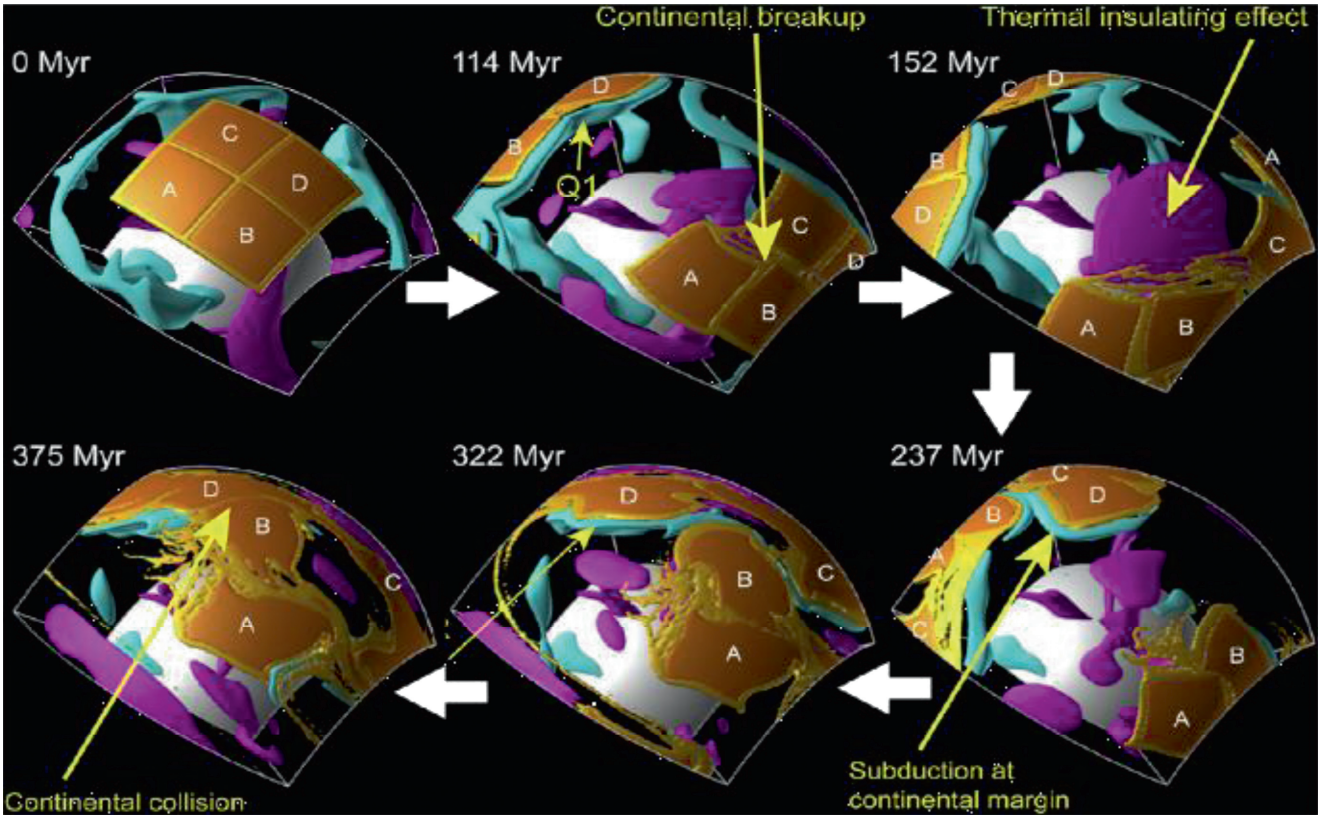

Fig. 1.14 A numerical simulation model of cycling of stages of "normal" mantle convection, supercontinent formation, and supercontinent breakup. White, core–mantle boundary; purple, rising mantle plumes; and blue, colder subducting slabs (from Fig. 9 in Yoshida and Santosh 2011)

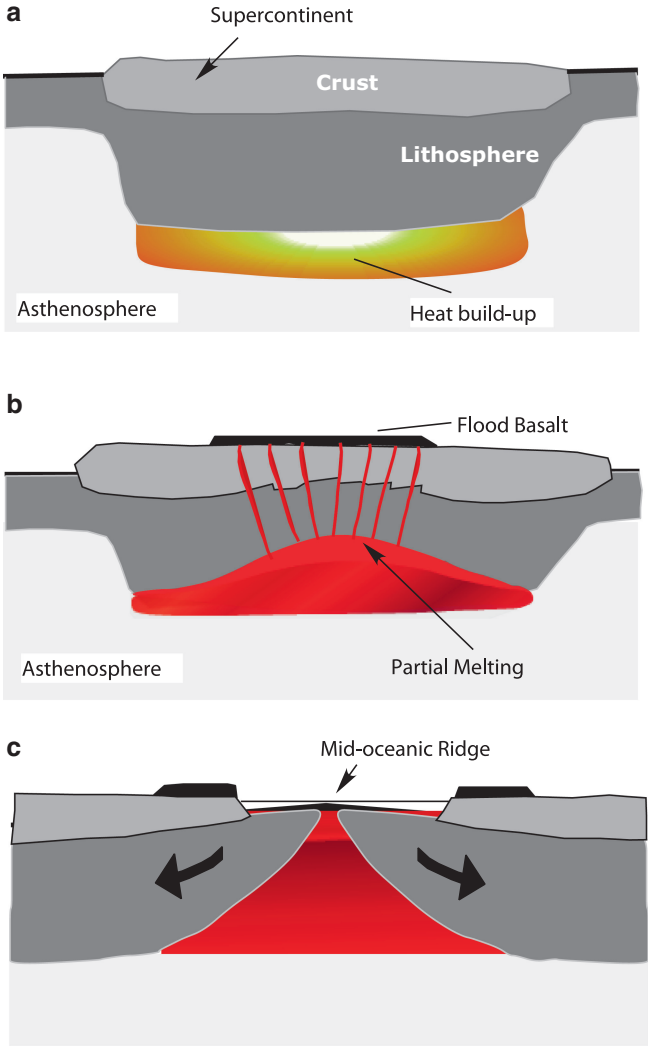

Fig. 1.15 Thermal insulation model of flood basalt volcanism, splitting of continents, and formation of ocean basins. Heat builds up in the mantle beneath large continental landmasses (like Pangaea), which leads to doming of the lithosphere and flood basalt volcanism. Finally, rifting and seafloor spreading take over, and ocean basin forms

Anderson's model is based on the theoretical models developed by Michael Gurnis who showed that single large continental mass can effectively trap heat, and such heat buildup eventually leads to the break up and dispersal of continental plates.

The superplume or plume model is clearly very different from Anderson's shallow melting model. There are many other models that are variations on the major ones described here; however, it is not within the scope of this text to discuss them at length.

Study of Petrology

Geologists study the Earth in a number of different ways: for example, the subject of *seismology* deals with earthquakes and allows us an unparalleled insight into the deeper Earth structure and processes. *Paleontology*, i.e., the study of fossils, is concerned with ancient life on Earth. Similarly, the study of minerals and rocks that comprise the solid Earth gives us fundamental information on the constitution of the Earth and on such diverse processes as volcanism, sedimentation, and the Earth's internal forces that are responsible for uplift and denudation of mountains. The subject of *petrology* deals with the study of rocks. This in subject is usually taught after courses physical geology (or introduction to Earth science) and mineralogy. I expect the student users of this book to be sufficiently familiar with mineralogy, crystallography, and physical geology. They should know that there are three types of rocks—igneous, sedimentary, and metamorphic rocks. Igneous rocks form by solidification of *magma* or molten rock. Sedimentary rocks form by *lithification* of sediments. Metamorphic rocks form by largely solid-state transformation (the process is called *metamorphism*) of other rocks into a new rock. This book is structured in a way that it provides a useful amount of coverage of igneous, sedimentary, and metamorphic petrology. It is not expected that all of the materials will be covered in one semester; however, one could take a modular approach and use sections/subsections from various chapters as modules in his/her lectures.

Summary

1. Earth is one of the inner planets, and like the other inner planets, it is rocky. It formed about 4.6 billion years ago.
2. The velocity of a seismic wave changes abruptly as it passes through layers of contrasting physical properties. Such boundary layers are called seismic discontinuities.
3. Seismic discontinuities require that the Earth is composed of several concentric layers or shells that are very different in density.
4. The principal layers are inner core, outer core, lower mantle, transition zone, upper mantle, and crust. The lower mantle is probably chemically stratified into two fairly distinct layers, and the boundary between the

upper and lower layers occurs at ~1,600 km. The Earth's core is dominantly composed of metallic iron, whereas mantle and crust are almost entirely composed of silicate minerals.

5. The core differentiated from the mantle and crust by an initial melting episode that occurs early in the Earth's history.
6. Further differentiation within the mantle and crust occurred during the formation of a global magma ocean.
7. Oldest continental rocks and minerals are significantly older than oceanic rocks. Such an observation is compatible with the idea that oceanic rocks are destroyed due to their recycling back into the mantle via plate tectonics, whereas unsubductible continental rocks collect on the surface.
8. Very old mineral inclusions in diamond indicate that some parts of the continental lithosphere had become ~200 km thick some 3.5 billion years ago.
9. Earth's seismic and volcanic activities are best explained in terms of the unifying hypothesis of plate tectonics. Plates include continental and oceanic masses. Plates are created at divergent plate boundaries and are destroyed via subduction at sites of plate convergence.
10. Continental plates grow by accretion and are broken up by plume activity. The Wilson Cycle explains the evolution of continents and oceans in terms of plate tectonics. The cycle begins with the impingement of a hot spot or plume onto the base of the continental lithosphere. Eventually the lithosphere breaks into three radial rift zones, two of which eventually become ocean basins. The collision of continents related to subduction is the end of the cycle. In Anderson's model, continental splitting results in flood basalt volcanism, which is due to long-term entrapment of heat in the subcontinental lithosphere and not due to plume impingement.

Introduction to Igneous Rocks

2

Abstract

Igneous rocks comprise the bulk of the Earth, Moon, and other terrestrial planets. They form by the solidification of magma or "molten rock." This chapter introduces the reader to magma and igneous rocks. It deals with the nature of magma and some of the fundamental descriptive aspects of igneous rocks, primarily their mineralogy and textures. And finally, the reader is introduced to the concepts of igneous rock classification.

Magma: Fundamentals

Magma may be thought of as a molten rock. Magma is not often a simple liquid but rather a complex mixture of liquid, solid materials (crystals and rocks), and dissolved vapor. Magma's chemical composition and physical properties, such as viscosity and density, are all important factors that control magma's overall behavior—how fast or slow it will move, how explosive it will be, what minerals will form in it, and their grain sizes and physical interrelationships (i.e., *texture*). Below we discuss some of these aspects of magma.

Chemical Composition of Magma

In terms of chemical composition, all magmas (except rare *carbonatites* that are rich in a carbonate component) are silicate magmas in which the dominant component is silica (SiO_2), which generally comprises 45 % or more by weight. Alumina (Al_2O_3), with its abundance in common igneous rocks somewhere between 13 and 18 %, is a distant second (Table 2.1). SiO_2, TiO_2, Al_2O_3, Fe_2O_3, CaO, MgO, MnO, FeO, Fe_2O_3, Na_2O, and K_2O are often referred to as *major* oxides because together they comprise 99 % of any igneous rock. (Actually, the term "major element" is generally used, which is a bad practice that has been perpetuated through decades of geochemical practice. This is rooted in the fact that these are analyzed as elements but expressed as oxides because the most abundant element, oxygen, is generally not analyzed.)

There are many other elements (e.g., V, Sr, Ni, La, Ce, Nd, Sm, Eu, Yb, Hf, etc.) whose abundances are generally much lower (parts per thousand or parts per million levels) and are hence referred to as *trace elements*. These elements are nonetheless important because they provide significant clues to the origin of igneous rocks.

Common Magma Types

As a starting point, it is useful to classify magmas into four broad groups, namely, *ultramafic*, *mafic*, *intermediate*, and *felsic* types (Table 2.2), based on relative abundances of SiO_2, MgO + FeO + Fe_2O_3 (called the *mafic* component), and total alkalis ($Na_2O + K_2O$). Equivalent terms for the above types are as follows: ultramafic magma = *komatiite magma*; mafic magma = *basaltic magma*; intermediate magma = *andesitic magma*; and felsic magma = *rhyolitic magma*.

It is apparent from Table 2.2 that the mafic component is minimal in felsic magmas and it increases toward ultramafic magmas. Alkalis and silica exhibit the opposite behavior. What minerals may form from a magma depend on the magma's chemical composition: for example, an ultramafic magma with its low SiO_2

G. Sen, *Petrology*, DOI 10.1007/978-3-642-38800-2_2,

Table 2.1 Major element composition of some igneous rocks

	Komatiite	Picrite	Basalt	Andesite	Rhyolite
SiO_2	45.26	43.68	49.20	57.94	72.82
TiO_2	0.33	2.19	1.84	0.87	0.28
Al_2O_3	6.74	9.83	15.74	17.02	13.27
Fe_2O_3	2.13	1.90	3.79	3.27	1.48
FeO	8.66	8.44	7.13	4.04	1.11
MnO	0.17	0.01	0.20	0.14	0.06
MgO	22.98	15.24	6.73	3.33	0.39
CaO	6.94	15.82	9.47	6.79	1.14
Na_2O	0.88	0.65	2.91	3.48	3.35
K_2O	0.05	0.38	1.10	1.62	4.30
P_2O_5	0.02		0.35	0.21	0.05
H_2O^+	3.41		0.95	0.83	1.10
H_2O^-	0.57	1.00	0.43	0.34	0.31
CO_2	0.84		0.11	0.05	0.08
Total	99.00	99.14	99.95	99.93	99.96

and very high MgO + FeO should be expected to crystallize minerals like olivine and pyroxenes, which have high MgO + FeO. Quartz (SiO_2) would *not* be expected to form in such a magma because formation of olivine and pyroxene crystals would use up all the available silica so that there will not remain any excess silica needed to form quartz. On the other hand, in a felsic magma, which is very high in silica and alkalis and poor in MgO + FeO, one should expect crystals of alkali feldspars [(K, Na)$AlSi_3O_8$] and quartz to form. Table 2.2 shows this direct correlation between magma's chemical composition and minerals that crystallize from it. This is the basis for *norm calculation*, which is further discussed in a later section.

Rock names are not only based on chemical composition but also on its grain size, which is determined by whether rock formed by quenching of lava (i.e., volcanic), by extremely slow cooling and solidification in a deep crustal pluton, or by relatively rapid crystallization in a shallow (hypabyssal) crustal intrusion, such as a dike or sill. The bottom part of Table 2.2 shows that different names are given to rocks that have identical chemical composition but very different mode of occurrence or texture. For example, basalt and gabbro have the same chemical composition, but basalt is fine grained relative to gabbro, which is a coarse-grained plutonic rock.

Solid Component in Magma

Magma rises from its place of origin primarily by buoyancy due to its lower density (although other factors, such as volatile pressure, also contribute to magma's ascent) than that of the surrounding wall rocks. Magma does not usually rise directly through a single conduit from its source region to eruption; instead it may stall in some *magma chambers* that may be located at various levels in the crust or upper mantle (Fig. 2.1). Magma generally cools in these magma chambers such that crystals form and separate from it. In erupted lavas, such crystals, often with well-developed faces (they are called *euhedral* crystals), may be recognized as *phenocrysts* by virtue of their larger grain size relative to the surrounding glass or fine crystals that form due to rapid quenching of the lava.

Magma may also carry rock and mineral fragments broken off the conduit wall as it rises violently from the deep. Such wall rock and mineral inclusions are called *xenoliths* and *xenocrysts*, respectively (Fig. 2.2). The study of xenoliths and xenocrysts has proved to be particularly valuable because many of them come from depths in the Earth's upper mantle that cannot otherwise be sampled by drilling. Xenoliths and xenocrysts are often identified on the basis of their chemical composition, mineral assemblages, and disequilibrium reaction textures (such as rounded or *resorbed boundaries*), which develop due to their being out of chemical equilibrium with the host magma.

Table 2.2 First-order classification of magma and igneous rocks

Magma type	Ultramafic	Mafic	Intermediate	Felsic
SiO_2	42–48	46–54	60–65	>70
MgO + FeO + MnO + Fe_2O_3	35–46	15–28	10–21	<3
$Na_2O + K_2O$	<1	2–3.5	3–6	5–10
Majo minerals	Olivine (generally dominant) + pyroxenes	Plagioclase + pyroxene	Pyroxene + plagioclase + amphibole	Alkali feldspar + quartz
Volcanic	Komatiite	Basalt	Andesite	Rhyolite
Hypabyssal	Komatiite	Diabase		
Plutonic	Peridotite	Gabbro	Diorite	Granite

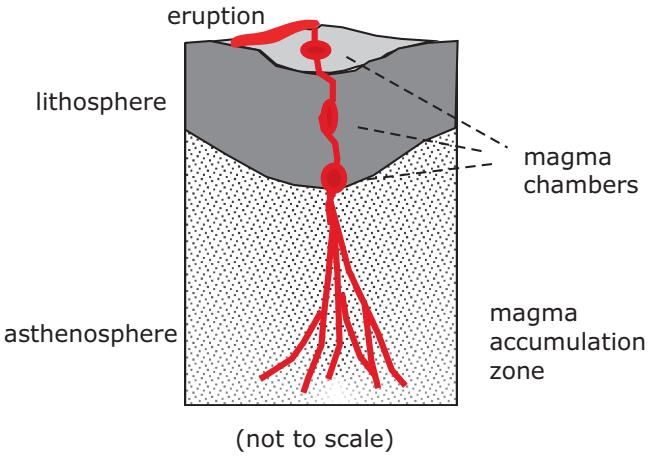

Fig. 2.1 Schematic diagram showing how magma collects to form larger veins and intrusions. On the way up the magma may reside in magma chambers at various depths, cool and crystallize, and then eventually erupt through a volcano

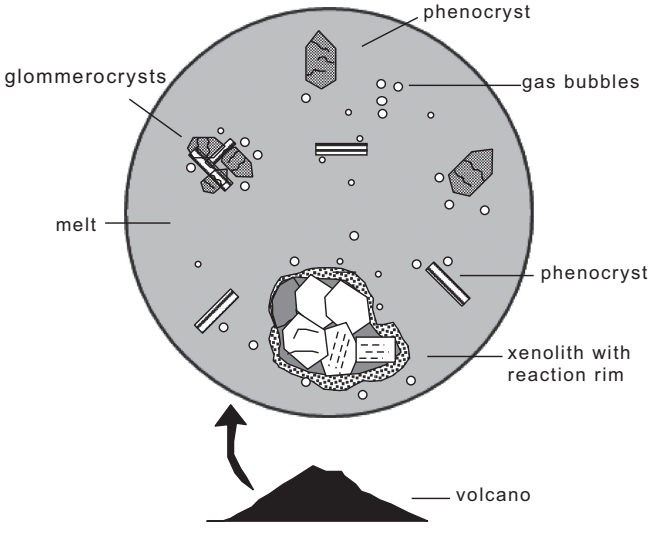

Fig. 2.2 Schematic drawing of a microscopic view (crossed polars) of a volcanic rock showing the presence of glass (isotropic), phenocrysts of two different minerals (olivine and plagioclase), cluster of phenocrysts (glomerocrysts), exsolved gas bubbles (preserved as vesicles), and a xenolith. Because the xenolith was not in equilibrium with the host lava, a reaction rim composed of different minerals developed between the host lava and the xenolith

Structure of Silicate Magma

Magma's viscosity and density are important factors that determine how fast it will rise. These physical properties of magma are fundamentally related to its internal arrangement of atoms and molecules (Fig. 2.3). Magma's atomic structure may be understood by referring to the atomic structures of silicate minerals. The fundamental structural unit of all silicate minerals is the $[SiO_4]^{4-}$ tetrahedron in which a small Si^{4+} cation at the tetrahedron's center is covalently bonded to four O^{2-} anions occupying its apices. In most silicate groups, for example, the chain silicates,

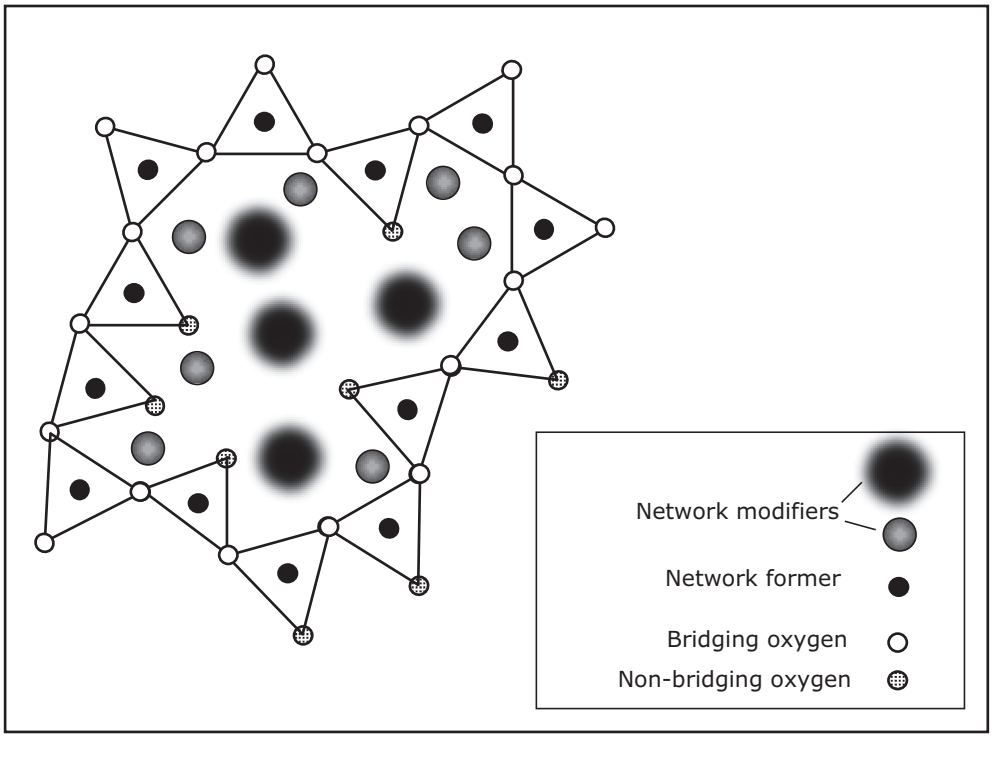

Fig. 2.3 Atomic structure of a silicate melt showing polymerized chains of silicate tetrahedra, network formers, and network modifiers

$[SiO_4]$-tetrahedral units share apical oxygen ions whereas the non-shared oxygen ions are bonded to other cations (Mg, Fe, Na, Ca, etc.) present in the mineral's structure. The shared versus non-shared oxygen ions are called *bridging* and *non-bridging* oxygen ions, respectively. Si and other fourfold coordinated cations (principally Al) that form the "backbone" of a tetrahedral network are called *network formers*. The cations (e.g., Mg, Ca, etc.) that usually occur in higher coordination and link the networks are called *network modifiers*. Silicate magmas, like silicate minerals, are composed of extensive networks of $[SiO_4]$-tetrahedral units with neighboring tetrahedra containing bridging and non-bridging oxygen ions. During melting of a silicate mineral or a rock, the covalent bonds between Si^{4+} and oxygen ions of each tetrahedron are generally too strong to break. On the other hand, the bonds between non-bridging oxygen ions and network modifiers do break, enabling these other cations to move around within the framework of polymerized $[SiO_4]$ chains in a molten silicate (Fig. 2.3). As one would expect, SiO_2 content of a magma exerts strong control over the extent of polymerization of a melt—the greater the SiO_2, the more polymerized the melt.

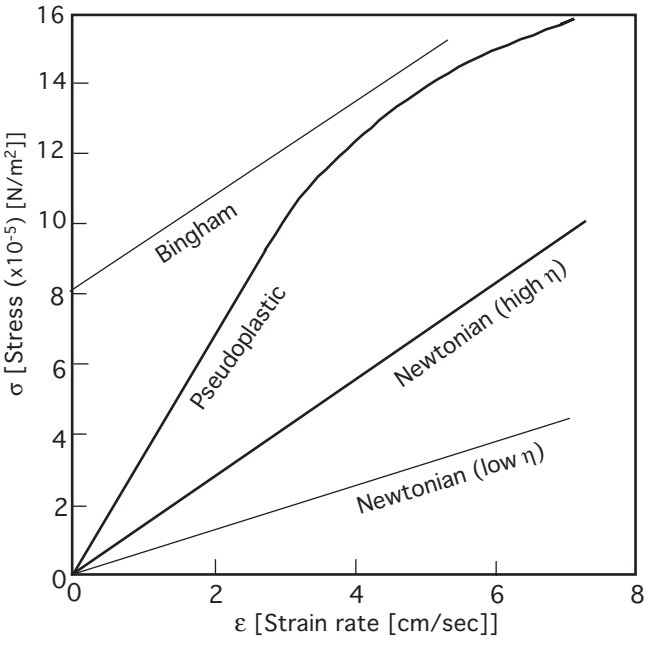

Fig. 2.4 Stress–strain relationships and types of magma viscosities

Viscosity

Viscosity (η) of a magma is simply defined as its internal resistance to flow and is given as:

$$\eta = \sigma/\varepsilon$$

where σ and ε are applied *shear stress* and *rate of shear strain*, respectively. A convenient way to understand what viscosity means is to compare how syrup and water flows: syrup is said to be more viscous than water because it flows more slowly than the latter. Magmas or fluids in general can show a range of viscosity characteristics: *Newtonian* fluids exhibit a linear relationship between σ and ε and pass through the origin in a stress versus strain rate plot (Fig. 2.4). Crystal-free basalt magmas show Newtonian behavior. On the other hand a basalt or andesitic magma containing abundant crystals may behave like a *Bingham plastic*, that is, they may possess some finite yield strength and thus flow only when a certain threshold value of stress has been exceeded. Rhyolitic magmas exhibit *pseudoplastic* behavior in that it shows a nonlinear relationship between stress and strain rate. As should be expected, the extent of polymerization (i.e., how many silicate chains occur in the magma, which is directly dependent on the abundance of SiO_2) exerts a strong control over viscosity: thus, rhyolite magma with its highest SiO_2 content is more viscous than andesite and basalt magma (Fig. 2.5).

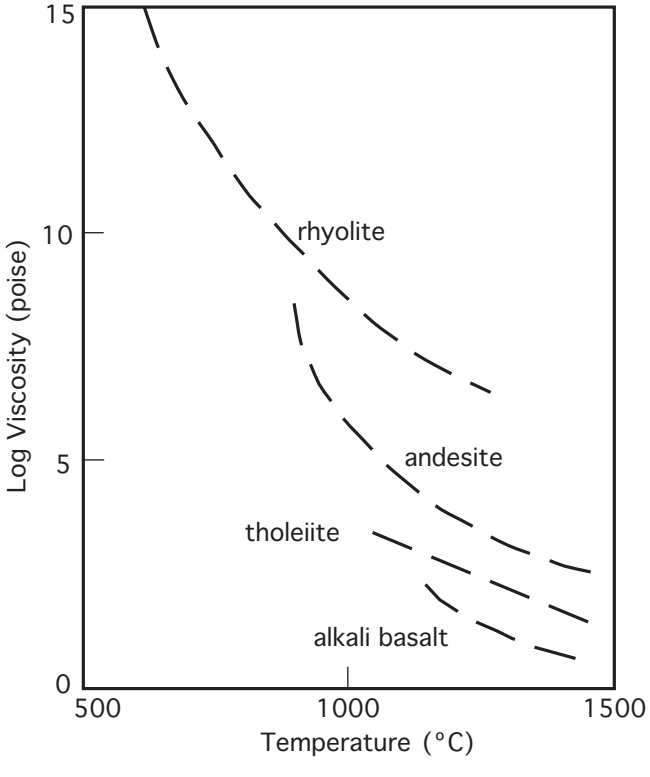

Fig. 2.5 Viscosities of four principal magma types at 1 atm pressure and as a function of temperature (McBirney 2007)

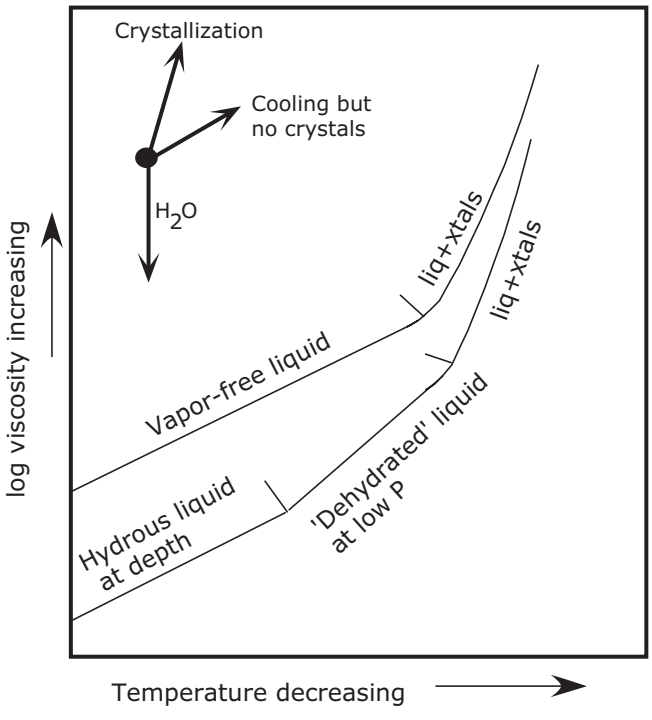

Fig. 2.6 Viscosities of hydrous versus anhydrous magmas as a function of devolatilization and partial crystallization (modified from Hess 1989). Hydrous magma has lower viscosity than anhydrous magma of broadly similar chemical composition. As a hydrous magma rises, it may expel ("exsolve") its dissolved volatiles (such as H_2O) due to lowering of pressure or temperature (discussed in a later chapter), and its viscosity may increase as a result. Appearance of crystals in great abundance may also sharply increase the viscosity of a magma

Temperature increase breaks down more silicate networks in the magma and thus lowers its viscosity. On the other hand, increase in crystal content in a cooling magma makes it progressively more viscous. Increase of dissolved H_2O, a network modifier, greatly lowers the viscosity of magma (Fig. 2.6).

Box 2.1: Viscosity, Density, and Velocity of Xenolith-Bearing Magma from Hawaii

The island of Oahu is composed of two large shield volcanoes and numerous small cinder cones. Lavas that erupted some 1–2 million years ago from the small cones contain mantle xenoliths. Using some simple viscosity-density values of the xenoliths and magma, it is possible to calculate a *minimum ascent velocity* of the magma. Note that these xenoliths are denser (density = 3.4 g/cm^3) than the magma (density = 2.8 g/cm^3) and therefore should have precipitated (or settled) out of the magma, but they were brought up because the magma was rising faster than the

(continued)

Box 2.1 (continued)

xenoliths could settle. Using a simple law, called Stoke's law (see below), and assuming that the magma behaved as a Newtonian fluid, one can calculate the minimum ascent velocity of the magma that prevented the xenoliths from settling.

Stoke's law is given as

$$\mathbf{V} = \frac{2gr^2\left(\rho_{\text{cryst}} - \rho_{\text{liq}}\right)}{9\eta}$$

where

$\mathbf{V}$ = settling velocity of the xenolith in magma

g = acceleration due to gravity (assumed to be constant; 980 cm/s^2)

r = radius of the xenolith (2.5–10 cm)

ρ_{cryst} = density of xenolith (assumed to be 3.4 g/cm^3)

ρ_{liq} = density of liquid (assumed to be 2.8 g/cm^3)

η = viscosity (varies between 20 and 50 Pa.s (1 Pa.s = 10 Poise) for basalt magmas ± crystals)

Plugging these values into the equation, minimum ascent velocities of the host magma were calculated and plotted in Fig. 2.7 for two different sizes of xenoliths and two different magma viscosities. It is clear that viscosity has no effect on ascent velocity for small xenoliths; however, for larger sizes the effect is quite strong. Note that these estimates will increase by twice as much if the magma behaved like a Bingham fluid. However, field observations (such as a thin glassy coat of the host lava around the xenolith) on some of these xenolith-bearing magmas of Hawaii suggest that they were extremely fluid and may have behaved like a Newtonian fluid. The interested reader is referred to Spera (1980).

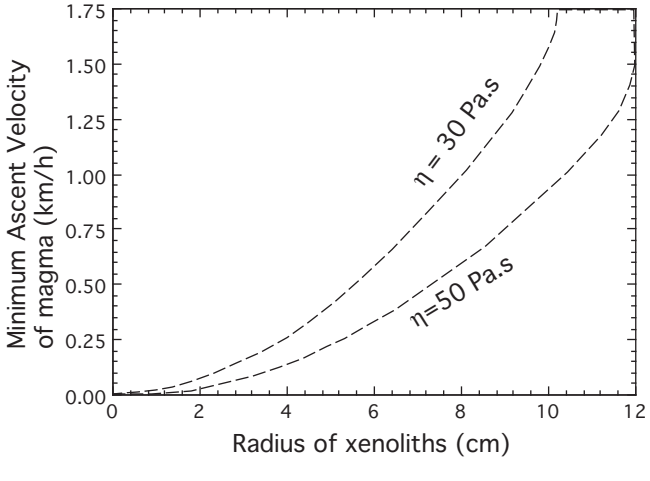

Fig. 2.7 Xenoliths and magma ascent rates

Density

Densities of different magmas have been measured in the laboratory, mostly at atmospheric pressure, and they vary between 2.2 and 3.1 g/cm^3 (Fig. 2.8). Density of magma is directly related to the abundance of the mafic (i.e., Mg + Fe) component in it. Thus, rhyolite magmas are less dense than andesites, and andesites are less dense than basalts. Magma rises from its point of origin by buoyancy, much like a helium-filled balloon rises through the atmosphere. This happens because the magma is lighter (i.e., less dense) than the surrounding wall rock.

Consider a simple example of buoyant rise of a basaltic magma from a depth of 60 km to the surface. We assume that the wall rock at ~60–40 km is peridotite with a density of 3.3 g/cm^3. The magma's density is assumed to be constant at 2.9 g/cm^3. The pressure on the magma and wall rock at any depth can be calculated from

$$P = \rho g h$$

where P is pressure (in GPa), ρ is density, and g is acceleration due to gravity (assumed to be constant with a value of 980 cm/s^2).

$$P_{\text{rock}} \text{at 60 km} = (6,000,000 \times 3.3 \times 980)/10^{10} = 1.94 \text{ GPa}$$

$$P_{\text{magma}} \text{at 60 km} = (6,000,000 \times 2.9 \times 980)/10^{10} = 1.70 \text{ GPa}$$

Therefore, the pressure difference (ΔP) of 0.24 GPa between the magma and wall rock makes the magma sufficiently buoyant to rise to the surface. In reality, however, this pressure difference may disappear when the magma reaches Moho, which is the seismic discontinuity that separates crust from the mantle. This is because crustal rocks, especially in continents, often have a lower density (~2.7 g/cm^3) than that of the magma; and therefore, the magma will not be buoyant when it reaches the Moho. Instead, it may be trapped at the Moho, where it would start cooling and crystallizing. After some amount of crystallization, the remaining differentiated magma may rise again when its density becomes less than that of its surrounding crust. Stolper and Walker (1980) showed that the vast majority of mid-oceanic ridge basalts (MORBs) undergo such density filtration and differentiation in magma chambers. Thus, they

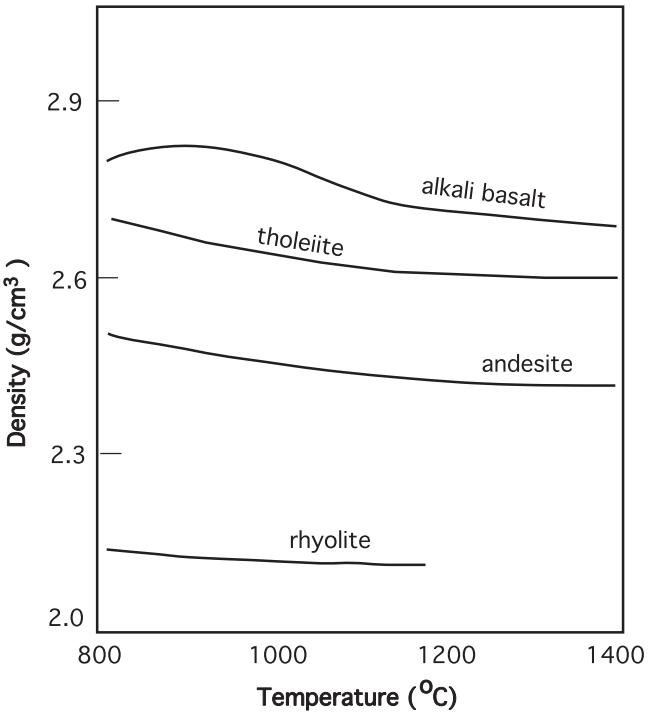

Fig. 2.8 Densities of magmas as a function of temperature and at atmospheric pressure

argued that erupted MORBs are not the *primary* magmas formed directly by partial melting of the mantle but are derived from them by crystallization differentiation. (The concept of primary magma will be discussed in a later chapter.)

Density of magma at atmospheric pressure can be calculated from its chemical composition and molar volume as follows:

$$\rho = \frac{\Sigma X_i M_i}{\Sigma X_i V_i}$$

where X_i, M_i, and V_i are mole fraction, gram molecular weight, and molar volume of an oxide. In a magma composed of many different oxide components SiO_2, Al_2O_3, TiO_2, etc., the mole fraction of any particular oxide, say, SiO_2, is calculated as follows: X_{SiO_2} = moles of SiO_2/(moles of SiO_2 + moles of TiO_2+ moles of Al_2O_3 + etc.).

Expressed in more general terms, in a magma or a crystal composed of chemical components $a, b, c, \ldots i$, mole fraction of the component "i" may be given as

$$X_i = (m_i)/(m_a + m_b + m_c + \ldots m_i), \quad \text{or}$$
$$X_i = m_i/\Sigma m_{a\ldots i}$$

where $m_{a\ldots i}$ are moles of $a, b, c, \ldots i$ components.

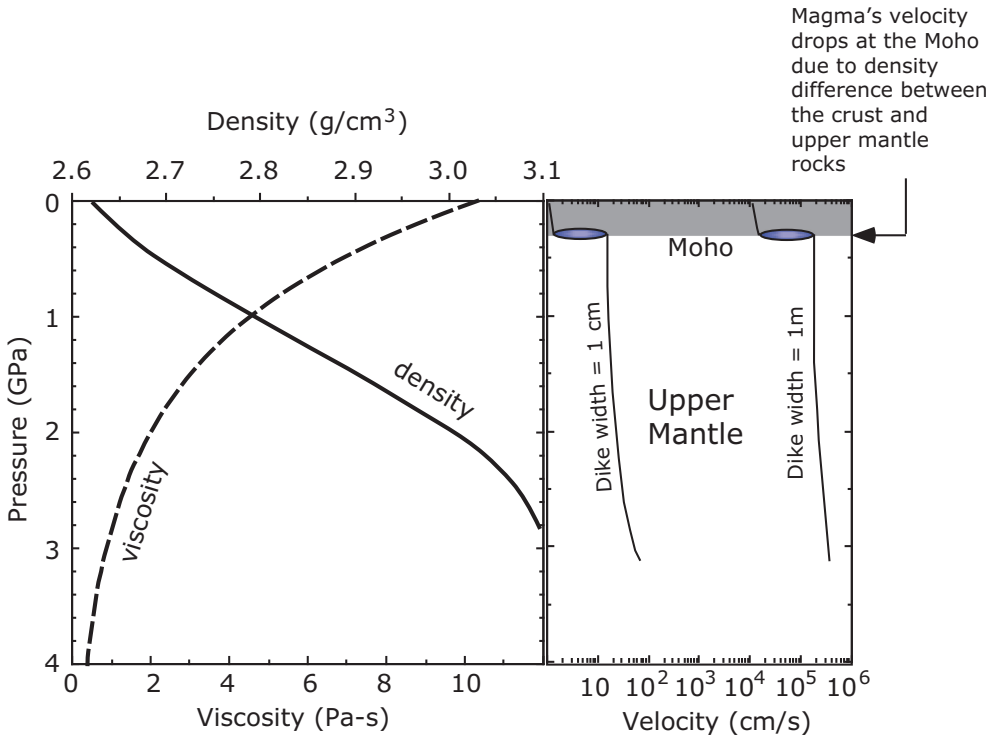

Fig. 2.9 Density and viscosity of tholeiitic basalt magma as a function of pressure (based on Kushiro 1980)

High-pressure measurements of density and viscosity have been very few (Fig. 2.9). Kushiro's (1980) experiments show that the density of a basaltic magma rises from 2.95 g/cm^3 at 1 atm pressure to about 3.5 g/cm^3 at a pressure of 3 GPa, whereas viscosity decreases drastically.

Earlier we noted that densities of magmas are generally less than those of mantle minerals. However, because magmas are more compressible than minerals, magma's density increases at a more rapid rate than minerals as pressure is increased. Some scientists have determined that ultramafic (komatiitic) magmas become denser than mantle minerals at 11–12 GPa (i.e., 330–360 km: Agee and Walker 1993; Ohtani et al. 1995). The occurrence of such a density crossover implies that magmas generated in the Earth's lower mantle will not leave its source area and instead will sink. The only way they could be buoyant is if some other component, such as dissolved volatiles, lowers their density.

Cooling of Magma and Textural Development

Magma formation and crystallization are in some ways different from how a pure metal, such as gold, melts or crystallizes. Pure metals have a fixed melting/freezing point, above which it is entirely molten and below which it is solid: for example, note that gold has a single melting/freezing point, which is 1,064.18 °C. In contrast, laboratory experiments have shown that magma solidifies over a temperature range: basaltic magma, 1,230–980 °C; andesitic magma, 1,050–850 °C; and rhyolitic magma, 800–650 °C. This is what is to be expected based on what we will learn from the simple system phase diagrams in Chap. 3.

Figure 2.10 shows the crystallization sequence of minerals from a basalt magma, as determined in a series of equilibrium experiments in a laboratory furnace at atmospheric pressure. The temperature above which a magma is completely molten is referred to as its *liquidus*, and *solidus* is the temperature below which the melt is fully crystalline. In Fig. 2.10, the liquidus and solidus temperatures are 1,250 °C and 980 °C, respectively.

Figure 2.10 shows that crystals and melt coexist within the temperature interval between solidus and liquidus. Crystals of different minerals form at different temperatures in the magma. Under equilibrium conditions of cooling, magma is slowly cooled such that crystals and melt can exchange chemical components as dictated by their crystal/melt equilibrium partition coefficients (explained later). This type of slow cooling can only occur in deep-seated magma chambers but not at Earth's surface, where erupted

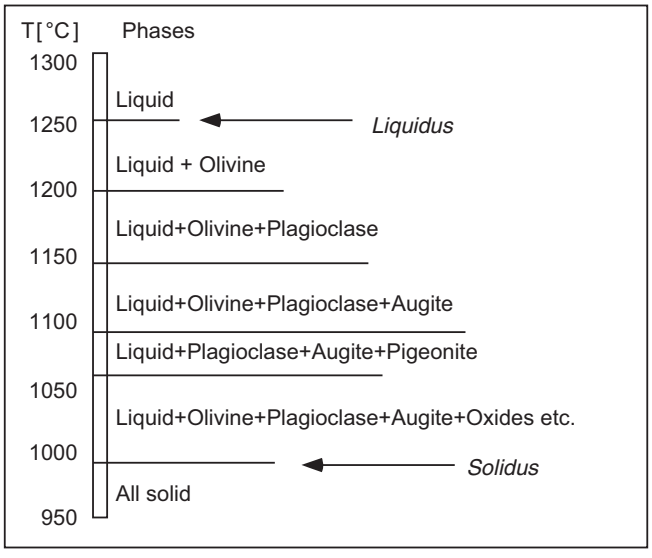

Fig. 2.10 Equilibrium crystallization of a basalt magma composition at atmospheric pressure as determined from laboratory experiments. This result is specific to the starting composition used, which includes the temperature at which the melt begins to crystallize (called the *liquidus* temperature), the temperature it is fully crystallized (called the *solidus* temperature), and the sequence in which different minerals appear at different temperatures. Other starting compositions will give different results

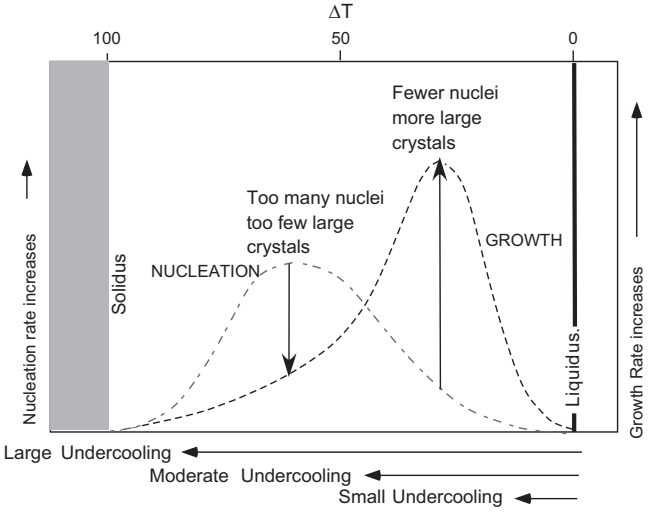

Fig. 2.11 Relationship between undercooling (ΔT = liquidus temperature–actual temperature), nucleation, and growth of crystals. Large undercooling (i.e., rapid "quenching") produces abundant nuclei, whereas small undercooling produces coarse crystals

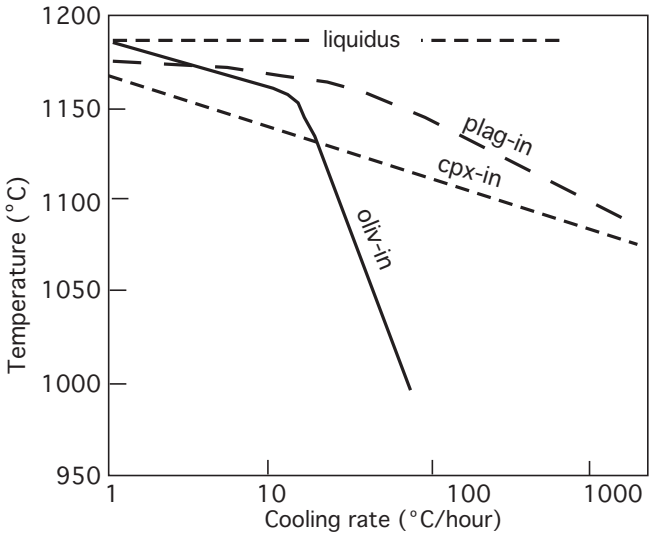

Fig. 2.12 Crystallization of minerals from a basalt magma at different cooling rates. This figure shows that the sequence in which minerals crystallize may depend on the rate of cooling (after C.E. Lesher, with permission)

lava cools much faster, i.e., it is *undercooled*, as it rapidly loses heat to the atmosphere and the ground. The rate at which magma is cooled below its liquidus, expressed as °C/s, is referred to as rate of undercooling. The rate of undercooling is an important factor that controls nucleation of mineral crystals, their chemical composition, and crystal morphology. An understanding of these relationships may be useful in interpreting cooling conditions of lava flows, for example.

Figure 2.11 shows the relationship between nucleation, crystal growth, and undercooling. When the degree of undercooling is great, large number of nuclei will form; however, none of these nuclei will grow to form large crystals (e.g., arrow pointing downward). At small degrees of undercooling, fewer nuclei will form, but they will most likely grow to form larger crystals (arrow pointing upward). Rapid undercooling to subsolidus conditions will result in the formation of glass. Basaltic lava can be glassy or very fine grained, reflecting rapid undercooling. Cooling in shallow dikes can result in moderate undercooling and therefore result in a coarser-grained texture. Plutons approximate equilibrium conditions and experience very little undercooling, and therefore, plutonic rocks are coarse grained.

Undercooling may delay the nucleation of mineral phases to a great extent and, particularly, suppress the appearance of a phase altogether, as illustrated with a series of experiments on a basaltic starting melt (Fig. 2.12). Note that under equilibrium or extremely slow rate of cooling (less than 4°/h), olivine appears at the liquidus, followed by plagioclase and then clinopyroxene. Olivine's appearance (i.e., nucleation) is significantly suppressed at a cooling rate between about 10 and 100 °C/h such that it appears last in the

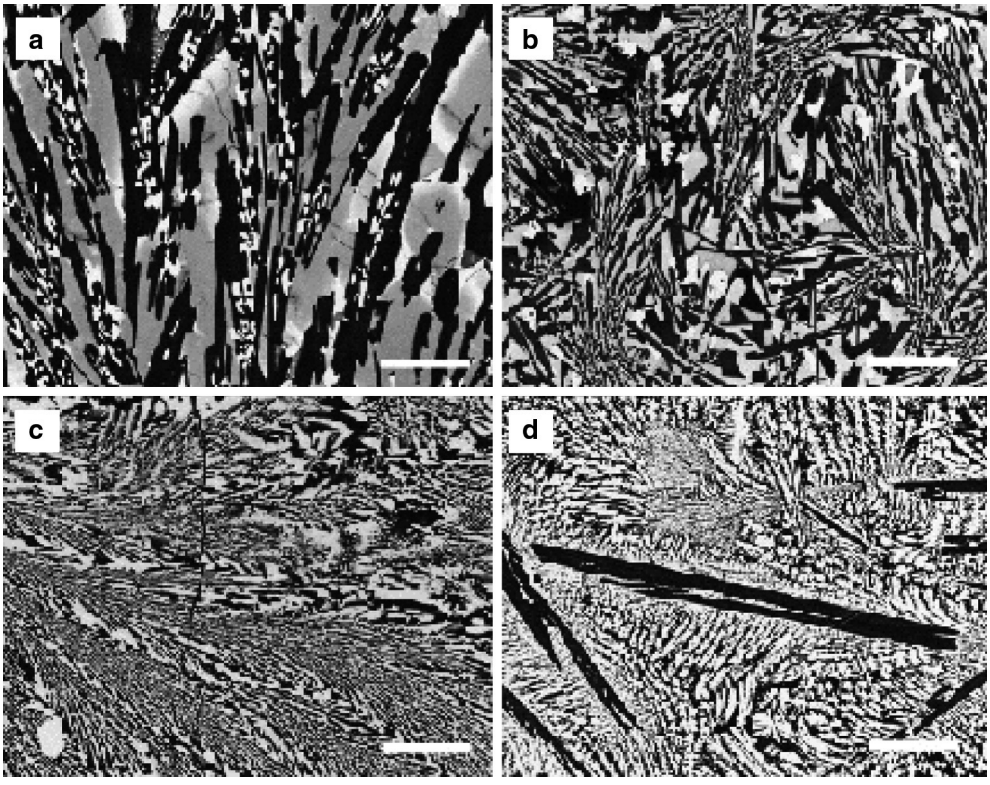

Fig. 2.13 Cooling rate versus run textures: cooling rate increases from (**a**) to (**d**). *Dark*, plagioclase, and *light*, pyroxene (back-scattered electron image: from Lesher et al. 1999)

crystallization sequence. Even more rapid cooling rate completely suppresses nucleation of olivine.

Morphology of crystals is also strongly affected by the rate of cooling. Crystals of olivine, pyroxene, and plagioclase are generally very skeletal or feathery at high cooling rates, whereas at slower cooling rates, these minerals assume their equilibrium shapes (i.e., lath to tabular shapes for plagioclase and euhedral-subequant shape for olivine and prismatic–subprismatic for pyroxene). Figure 2.13 shows the relationship between crystal size, morphology, and rate of cooling in four runs, in which (a) represents the slowest cooling rate (therefore, the coarsest grains) and (d) represents fastest undercooling, and plagioclase forms feathery dendritic growths here.

Undercooling is also related to compositional zoning (zoning refers to contrasting chemical compositions of different parts of the same crystal) in minerals, particularly in plagioclase (discussed in a later chapter). Slowly cooled plagioclase crystals in plutonic intrusions are generally unzoned, whereas plagioclase crystals in shallow intrusions and matrix of lava are strongly zoned. Pyroxenes also show strong chemical variation due to rapid, metastable crystallization due to rapid cooling.

Box 2.2: Experimental Petrology

Experimental petrology is a branch of petrology that attempts to simulate the deeper crustal and mantle environment in which magmas form and crystallize. The instrumental setup for experiments varies considerably based on whether one wishes to examine phase relationships at 1 atm or at higher pressures. Whereas one-atmosphere furnaces are useful for the purpose of simulating crystallization in lava lakes and shallow magma conduit, anyone trying to understand melting at upper mantle conditions or magma crystallization in the mantle or deep continental crust will need to use a piston-cylinder apparatus (0.3–4 GPa). Experiments at higher pressure (5–30 GPa) require a multi-anvil apparatus or a diamond-anvil apparatus for simulating the extreme pressures of the deep

(continued)

Box 2.2 (continued)
lower mantle or the outer core of the Earth. Pictures and descriptions of such instruments may be found in a number of websites; the "Magma Factory" website of Tokyo Institute of Technology (http://www.geo.titech.ac.jp/lab/takahashi/takahashilab.e.html) is an excellent place to look at some of these instruments and what they do.

To study magma crystallization at atmospheric pressure, the starting material (powdered mixture of oxides, rock, or minerals) is placed in a suitable capsule (graphite, iron, platinum, etc.) or is compressed into a pellet and hung from a platinum wire and then inserted in a furnace in which the partial pressure of oxygen can be controlled. It is important to control oxygen pressure for any system that contains iron, because oxygen influences the proportion of Fe^{2+}/Fe^{3+} ratio in the melt, which in turn controls phase equilibrium behavior (particularly that of the oxide phases) of the melt during crystallization. It is then held at a certain temperature for a long time (hours to days) and then quenched by dropping the capsule/pellet into water or other liquid. Such long times are used to ensure that the run products have reached equilibrium. The run products are then examined with a petrographic microscope, scanning electron microscope, or an electron microprobe to determine the phases (mineral types and/or glass), their proportions (mode), and their chemical composition. Undercooling experiments are done in a furnace where the temperature controller can control the rate in which a run can be cooled. Having said all this, I should note that there is a great deal of variability in the ways experiments are designed and the instruments are chosen.

Experimental petrology continues to play a very important role in our understanding of how the Earth works by providing fundamental information on magma behavior at deeper crustal and mantle pressures. The greatest difficulty lies in "scaling" up such information gathered from tiny capsules to a scale of thousands of cubic kilometers within Earth. We will see examples of these difficulties in various other chapters in this book.

Crystal Size Distributions

The study of distribution of sizes of plagioclase crystals in basaltic rocks can greatly contribute toward understanding crystallization processes in magma chambers (Marsh 1988a, b; Cashman and Marsh 1988). An important aspect of the study of crystal size distributions (CSD) is its simplicity in the data collection process. In modern times when petrology/geochemistry research seems totally dependent on expensive instruments that only the very rich institutions can afford, application of CSD in petrology is an important breakthrough. All it requires is the use of a standard petrographic microscope to measure the grain sizes and then plotting crystal size (L, crystal length in mm) against population density, which is expressed as $\ln(n(L))$ where $n(L)$ is the number of crystals per volume of rock per crystal size. The interested student is urged to visit Professor Mike Higgins' website (http://geologie.uqac.ca/~mhiggins/CSD.html) and textbook (Higgins 2006), which are excellent resources for CSD research methods.

Basaltic lavas generally show two extreme types of textures—(a) porphyritic texture with coarse phenocrysts of plagioclase ± olivine ± augite crystals set in a fine-grained groundmass of tiny plagioclase laths, granules of augite, and Fe–Ti oxide minerals (i.e., magnetite and ilmenite) or (b) aphyric or phenocryst-free texture, in which the groundmass may be all glass or a fine-grained mixture of crystals or crystallites (crystals too small and are barely visible under the microscope with 10× objective) and glass. CSDs of all such lavas have a negative slope in the log–linear plots (Fig. 2.14). The intercept of a CSD on the Y-axis (i.e., 0, y) represents the nuclei density, whereas the slope is a product of time for crystal growth and growth rate. The intercept and the slope of a CSD together reflect the histories of crystal population in a rock. A smooth CSD (Fig. 2.14a) reflects a common crystallization history ("single nucleation event" Marsh 1998) where the larger grains are simply older and plot further away from the (0,y) point. On the other hand, a CSD with two distinct linear segments with a break ("dog leg" CSD) reflects two distinct populations of crystals with two different nucleation histories (Fig. 2.14b). This may be a consequence of two mixed magma batches, for example. Other complications can occur that may change the form of the CSD: for example, in a study of Kiglapait intrusion, Labrador, Higgins (2006) noted that CSDs for plagioclase, olivine, and pyroxene look "humped" at the smallest grain size end and a sort of

"flattening" to "concave up" pattern of the CSD with increasing grain size (Fig. 2.14c). Higgins proposed that this is due to a textural coarsening process called Ostwald ripening in which smaller grains are dissolved and larger grains are enlarged due to growth from interstitial liquid between the larger grains.

Finally, we consider the CSDs of rocks in different parts of a magma chamber or a conduit in which a phenocryst-free magma enters and crystallizes *in situ* from walls inward (Fig. 2.15). If the textures of the rocks formed in different parts of such a chamber or conduit is not further complicated by crystal accumulation, wall rock assimilation, Ostwald ripening, and such, then the CSDs of rocks sampled from different parts of such intrusions may look like those schematically shown in Fig. 2.15.

Box 2.3: Magma Cooling, Crystal Percentage, and Size

Size and percentage of crystals of various minerals in an igneous rock depend upon several factors that include nutrient availability, nucleation rate, crystal growth rate, rate of cooling, crystallization energy, competition from other growing crystals of other phases, etc. Several of these factors are intimately dependent on one another, and therefore, one can use a simple formula, originally developed by Melvin Avrami in 1939–1941 and later modified by others, to understand how crystal percentage and size can vary as a magma body cools. Although the original equation was not developed to understand magma cooling and crystallization, Bruce Marsh of Johns Hopkins University first made use of the Johnson–Mehl–Avrami (JMA) equation to study magma crystallization. Here, we can use a simple exercise based on the JMA equation below and see how crystal size and percentage may occur in magmas (Marsh 1996):

$$\text{Crystal}\% = 100 \times \left[1 - \exp\left[-\frac{\pi}{3}\left(J_o (G_o)^3\ t^4\right)\right]\right]$$

In this equation J_o is the nucleation rate, G_o is the growth rate, and t is time.

Let us consider growth of plagioclase crystals in basalt magma. Following Marsh, we ignore complications that are embedded in the assumptions made in the application of the JMA equation and nonlinear variation in the nucleation and growth rates and use constant values of J_o of 10^3 cm^3/s and G_o of 10^{-10} cm/s for illustrative purpose.

As a side note, we explore how the above two values came about. They come from the examination of samples cored from a lava lake that formed in a small crater in Hawaii, called Kilauea Iki. In November 1959 Kilauea Iki erupted for 36 days, and the erupted lava formed a 120-m-thick lavas lake. This lake cooled slowly and became fully solidified in 2003 (source: Hawaii Volcano Observatory: http://hvo.wr.usgs.gov/volcanowatch/archive/2003/03_01_09.html). The lake was drilled multiple times from 1960 to 1988, temperatures were measured in situ, and drill core samples were examined for crystallization development. To many petrologists this lava lake represents a good natural analog of a near-surface magma chamber.

Returning to the application of the JMA equation, we need to add one more factor that can relate crystal percentage to crystal size and that is the simple relationship between crystal size (L, cm) and growth rate (G_o): $L = G_o \cdot t$. When we do this, we find that (1) crystallization should be complete at the end of 10 years; (2) maximum crystal size should be 0.32 mm; and (3) crystal% versus time follows a sigmoidal profile, i.e., crystal% changes very little with time at the beginning and at the end of the crystallization process, but the crystal% rapidly increases in the middle of the crystallization process (Fig. 2.16). This gives us some basic understanding of kinetics of crystallization in magmas even though cooling rate and convective overturns, and input of fresh batches of magma, and magma mixing in natural magma bodies may greatly complicate the supply of nutrients that the crystals need for growth.

An interesting observation is that largest crystal of plagioclase in Kilauea Iki is about 0.3 mm long. This compares favorably with the size we calculated earlier using the JMA equation; however, the problem is that the observed crystals attained that size in 53 years! There are several ways to explain this "age" discrepancy, one of which is that the largest plagioclase crystals did not grow much in the last 33 years.

(continued)

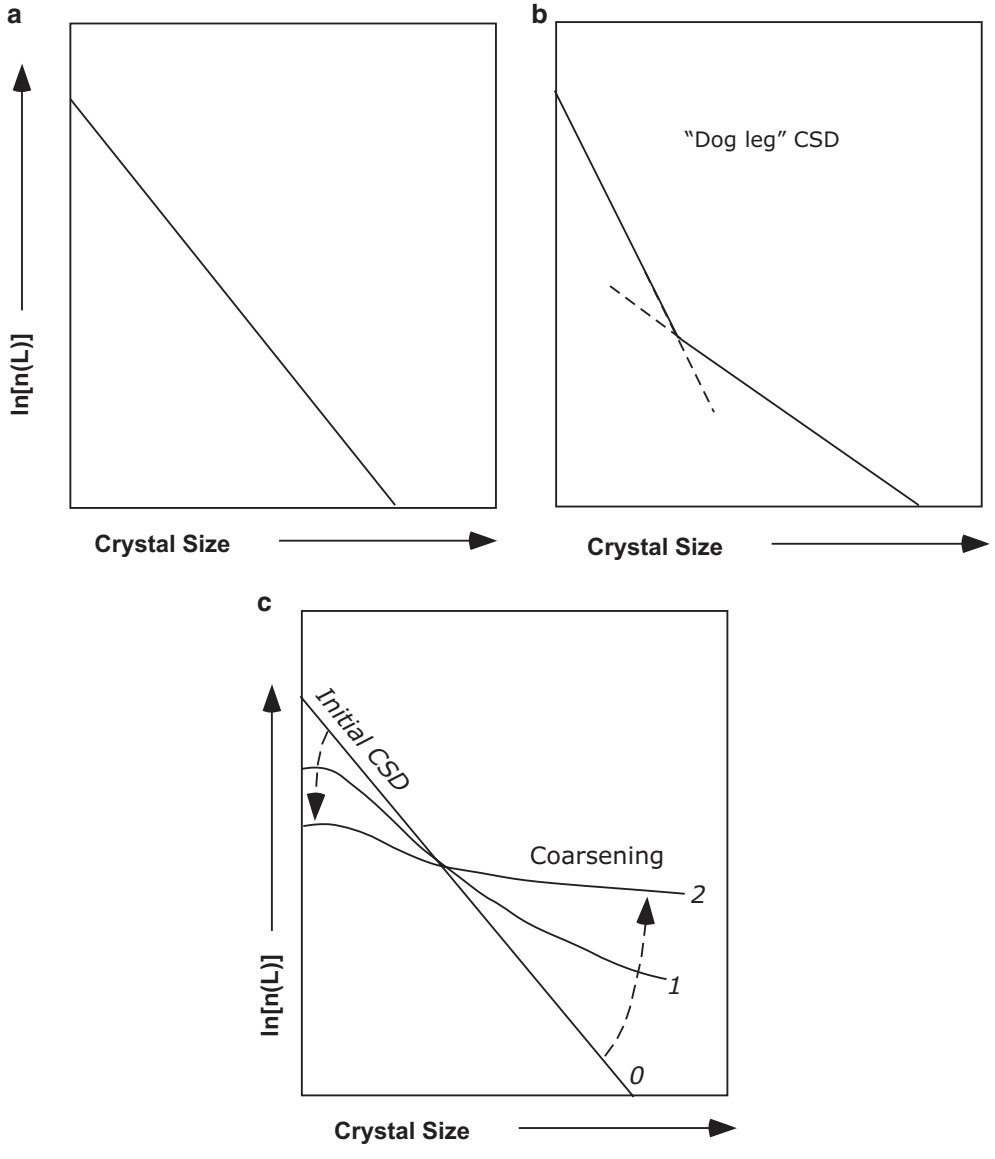

Fig. 2.14 Crystal size distribution (CSD) plots. (**a**) A simple CSD where all crystals in the rock are related by nucleation and growth history. (**b**) A kinked CSD with a "dog leg" expected of a mixed population of crystals with two distinct nucleation and growth histories. (**c**) "Flattening out" of CSD by coarsening ("Ostwald ripening") process in a large intrusive body

Igneous Rocks: Mode of Occurrence

Magma's transformation to an igneous rock via solidification can occur along many different pathways that depend primarily on the conditions of lithostatic pressure, volatile pressure, and rate of undercooling. Minerals that crystallize from it and the *texture* (which represents the physical relationship between the crystals or noncrystalline materials) provide significant clues to how an igneous rock may have formed from magma. As discussed in a later section, it is common for a batch of magma to go through several stages where they may be stored in magma chambers in the crust before eruption (Fig. 2.17). In some cases, the magma may completely solidify below the surface, and in other cases they may erupt to form lava. Thus, based on the depth of emplacement, igneous rocks can be divided into *intrusive*, meaning those that solidify below the surface, and *extrusive* types, which includes all the hardened eruptive products. To be sure, molten lava may not be the only product of an eruption, and extrusion of solid or solid plus gaseous products (called *pyroclastic materials* or *tephra*) is abundant in the case of intermediate and felsic eruptions. Mafic magmas generally erupt as lava and do not have such significant pyroclastic component. Below I describe some general features of volcanoes and intrusive igneous intrusions.

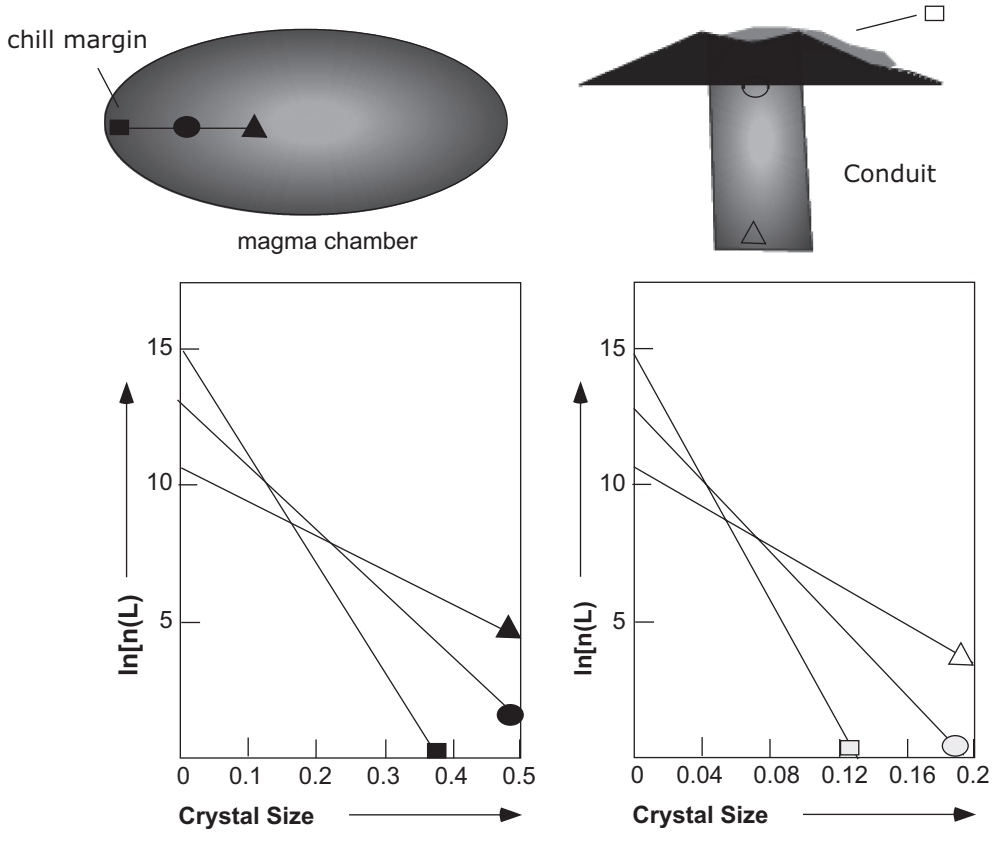

Fig. 2.15 *Left*: CSD of rocks in a large magma chamber. Magma closer to the margin would cool faster where as hotter interior would cool more slowly, resulting in different CSDs from margins to the interior of the intrusion. *Right*: lava quenches more rapidly, forming abundant finer crystals and fewer coarse crystals. In contrast, deep in the conduit magma cools more slowly and therefore forms larger crystals. This difference is reflected in distinct CSDs as well (redrawn from Zieg and Marsh 2002)

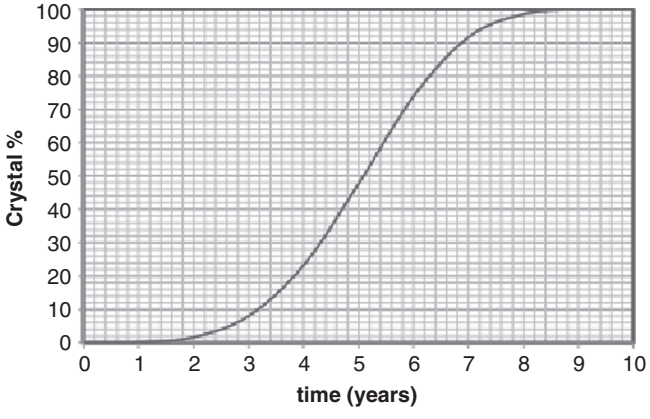

Fig. 2.16 Crystal% versus time as calculated from JMA equation

Volcanoes and Their Products

As discussed in Chap. 1, igneous activities predominantly occur along plate boundaries, and intraplate volcanism, such as the Hawaiian–Emperor chain in the middle of the Pacific plate, is rather rare on a global

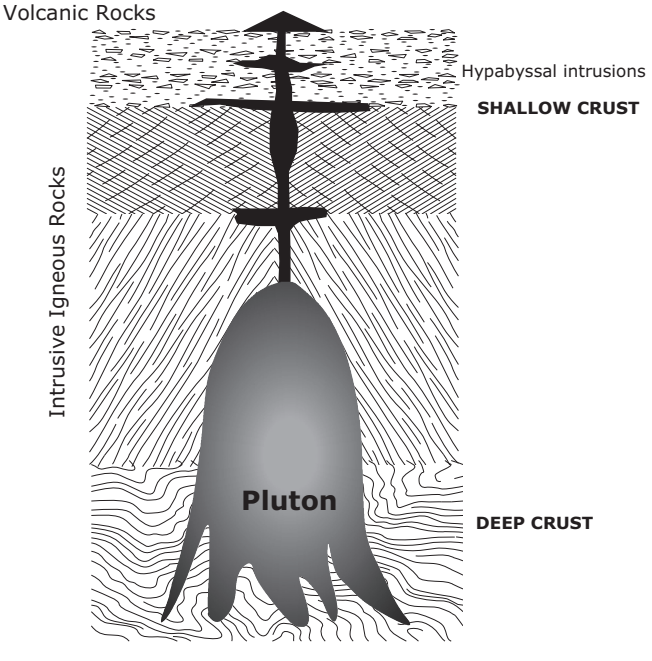

Fig. 2.17 Plutons, hypabyssal intrusions, and lava flow

Table 2.3 Volcano Explosivity Index (VEI)

VEI	Description	Ash plume height	Ejecta volume	Frequency	Example
0	Nonexplosive	<100 m	<10,000 m^3	Daily	Mauna Loa
1	Gentle	100–1,000 m	>10,000 m^3	Daily	Stromboli
2	Explosive	1–5 km	>1,000,000 m^3	Weekly	Galeras (1993)
3	Severe	3–15 km	>10,000,000 m^3	Yearly	Nevado del Ruiz (1985)
4	Cataclysmic	10–25 km	>0.1 km^3	≥10 years	Soufriere Hills (1995)
5	Paroxysmal	>25 km	>1 km^3	≥50 years	St. Helens (1980)
6	Colossal	>25 km	>10 km^3	≥100 years	Mt. Pinatubo (1991)
7	Super-colossal	>25 km	>100 km^3	≥1,000 years	Tambora (1815)
8	Mega-colossal	>25 km	>1,000 km^3	≥10,000 years	Toba (73,000 BP)

scale. Lava eruption can occur through volcanoes or through cracks (called *fissures*) in the crust or on the sides of a volcano. Some magmas erupt with great fury, spewing out large amounts of ash and other *pyroclastic materials*. Large pyroclastic eruptions can generate an ash column that can rise above 500 m in the atmosphere and circle the globe at more than 400 km per hour as part of the jet stream. For example, the June 1991 eruption of Mt. Pinatubo (Philippines) produced 5 km^3 of pyroclastics and a 400-km-wide ash cloud that rose 35 km and encircled the globe several times over a 2-year period, producing beautiful sunsets in the areas over which it passed and dropping Earth's annual mean temperature by 1 °F over a 2-year period.

Newhall and Self (1982) introduced the concept of a Volcano Explosivity Index (VEI) that is based on several factors, such as the volume of eruptive products, ash cloud height, and some qualitative observations, to categorize various volcanic eruptions (Table 2.3). A value of 0–8 is assigned to eruptions that range from "nonexplosive" to "mega-colossal" types.

The explosivity is directly related to how much gas (mainly steam) the magma carries when it nears the surface. Intermediate to felsic composition magmas generally contain a relatively greater amount of dissolved water that they inherit from their source region of melting. As these magmas ascend to shallow depths, they exsolve (i.e., they boil and release the vapor into the surroundings) the dissolved water—much like the release of pressurized CO_2 gas when a bottle of carbonated beverage is opened. This exsolved vapor blasts through the overlying column of rocks, producing a volume of tephra.

Explosive eruptions may also result from heating of groundwater (often referred to as *meteoric* water as opposed to *juvenile* water that comes from the magma itself) by a shallow magma body. The groundwater turns into steam, which has a much greater volume than water, and therefore, the steam pulverizes the ground above it into tephra. This type of eruption is called *phreatic* eruption.

Tephra and Lava

Based on the size of individual particles, the tephra is classified into *ash* (particle diameter <4 mm), *lapilli* (4–32 mm), and *blocks* or *bombs* (>32 mm). Bombs typically have an ellipsoidal shape with flanges at the two sharp ends because they usually have a molten lava coating on a core of a rock fragment as they are thrown up in the air. The lava quenches to a glass as it drops back on Earth. Blocks have sharp edges and lack the roundness of bombs. *Tuff* is a type of rock that represents hardened pyroclastic materials.

Whether or not magma would flow out of a volcano as lava or barely rise to fill or partially fill the volcanic crater as a *dome* (a simple domal structure) depends on the magma's viscosity, which is in turn linked to its composition and dissolved vapor content. Felsic lava is so viscous that it normally does not easily form a lava flow and instead form domes inside a volcano. Mafic magmas are less viscous and therefore form lava flows. The most common type of mafic magma (called *tholeiite*, discussed later) is the least explosive, and their corresponding lavas can flow over great distances. In fact, some lava flows of the 16-million-year-old Grande Ronde formation of the Columbia River Basalt Group in Pacific Northwest (covering much of Washington and Oregon) are nearly 100 m thick and appear to have traveled hundreds of km from their eruption sites located close to the Washington–Idaho border to the Oregon coast.

Volcano Types

Based on their geometrical form and relative size, volcanoes can be fundamentally of the following types*: shield volcano, stratovolcano, cinder or scoria cone, maar, tuff ring, and tuff cone* (Fig. 2.18). Shield

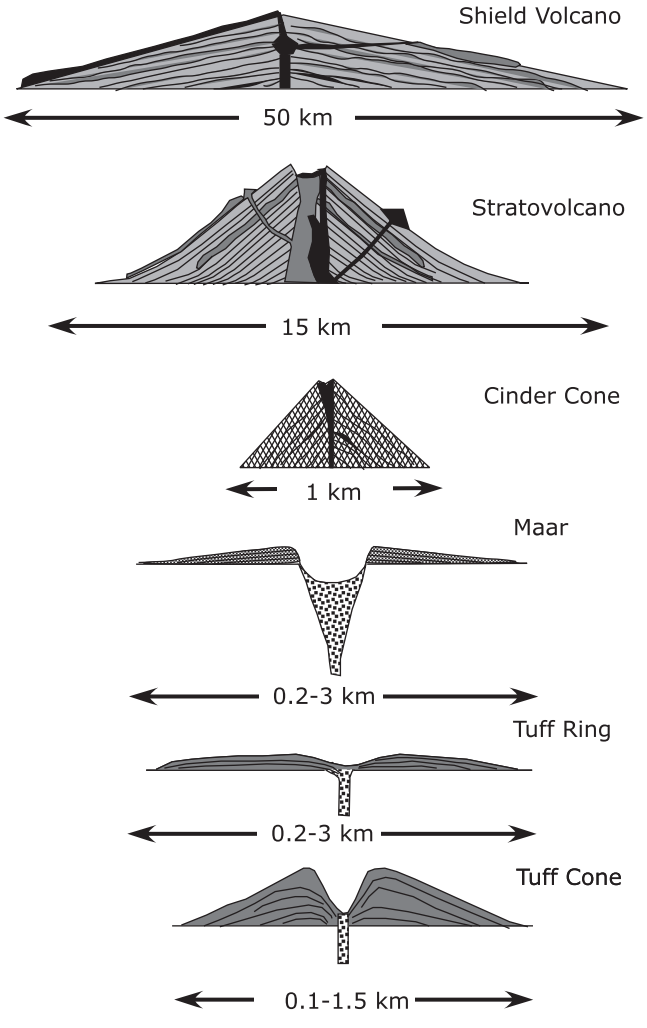

Fig. 2.18 Types of extrusive bodies

volcanoes are truly giant volcanoes with gently dipping flanks that take several tens of thousands of years to build with layers and layers of lava. They are best exemplified by the Earth's largest volcano—Mauna Loa (Hawaii)—which rises 4,100 m (13,444 ft) above sea level (Fig. 2.18). When its height is counted from the ocean floor to its peak, Mauna Loa stands 10,099 m (33,132 ft) tall, and by this measure, Mauna Loa is the tallest mountain on Earth—taller than Mt. Everest (8,850 m, 29,035 ft). The largest shield volcano in the terrestrial system is Olympus Mons on Mars (many pictures of Olympus Mons can be found on the web).

Shield volcanic eruptions are relatively "nonexplosive" because they erupt very fluid basaltic lava without emitting gases in any significant amount. Such lava flows can travel for several tens of kilometers. The lavas that come out of shield volcanoes are often so fluid that they can flow like a river, and as they harden, they develop structures that appear like folded cloth or entangled ropes. This type of lava is called *ropy* or *pahoehoe* lava (Fig. 2.19). The other type of lava that is associated with shield eruptions is *Aa lava*, which is also called *block lava* because they are composed of blocks and clinkers that travel at a very slow speed. The interior of block lava is generally partially molten and is pushed forward by the molten interior that gets replenished with magma supply from the volcano.

Stratovolcanoes (also called *composite cones*) are typically associated with subduction zones. They are highly explosive and are built of alternate layers of tephra and lava. Lavas are dominantly intermediate in composition, although basaltic and shoshonitic lavas may form a part of them as well (these names are discussed later). The tephra layers are usually associated with intermediate to felsic eruptions. Stratovolcanoes occur all along the continental margins around the Pacific Ocean, which is commonly referred to as the "Pacific Ring of Fire" (Fig. 2.20). Mt. St. Helens (NW USA), Pinatubo (Philippines), and Mt. Fuji (Japan) are all examples of stratovolcano (many spectacular pictures of these volcanoes may be found on the Web).

Cinder cones, maars, tuff cones, and tuff rings are much smaller than either shield or stratovolcanoes, and they can be found in all tectonic environments. They generally form by a single phase of explosive volcanism that can last a year to a few years. Cinder or scoria cones are so-called because they are generally composed of cinders or blocks of mafic lava, some ash, and other pyroclastics. Paricutin volcano in south-central Mexico is a famous example of a cinder cone. It erupted lava and tephra during 1943–1951.

The basalt *scoria* is full of vesicles that form in mafic lava due to escape of vapor bubbles. Sometimes these vesicles are refilled with minerals like zeolite, calcite, and quartz that form from hot water-rich fluids. Such refilled vesicles are called *amygdules*. Often these amygdular minerals grow to be very large (up to 1.3 m) and develop perfect crystal faces, and in such cases, they are called *geode*.

Pumice is similar to scoria in the sense that both are strongly vesicular; however, scoria is black and pumice is light colored because the glass in pumice is felsic in composition. Scoria sinks in water, but pumice floats because it contains many more vapor bubbles that make it less dense than water. Felsic magma is much more viscous than mafic magma, and therefore, it effectively traps the vapor bubbles, whereas in the latter they easily escape.

Fig. 2.19 Pahoehoe and Aa lava

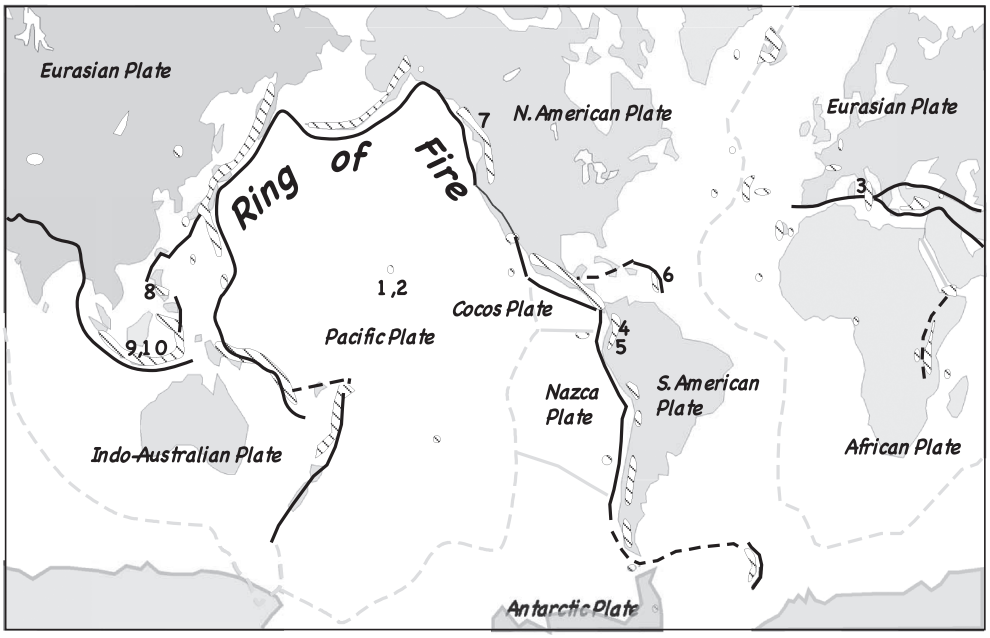

Fig. 2.20 Map of circum-Pacific ring of fire (reprinted with permission from US Geological Survey)

The term *tuff* is used to describe the rock that forms by compaction and recrystallization of pyroclastic materials. Maars, tuff rings, and tuff cones are all built of tephra and are often stratified (layered). They are usually created by phreatic eruptions. Maars have a much wider central depression than tuff cones and tuff rings (Fig. 2.18). The difference between a tuff cone and a tuff ring is in the height of the tuff rim.

Pyroclastic Deposits

Pyroclastic Fall Deposit. In an explosive eruption, pyroclastic materials of all sizes may rise up in a column, which is called a tephra column. The coarsest materials, such as blocks, bombs, and lapilli, along with ash fall back closer to the volcanic crater. As the ash column reaches the higher atmosphere, it spreads laterally to form a rapidly moving ash cloud. Some of the ash falls back to the Earth and forms a thick blanket on over a large area in the downwind direction from the volcano. Such deposits are collectively called *fall deposits* (Fig. 2.21).

Pyroclastic Flow Deposit. In some cases the tephra column may collapse and the tephra flows downslope at tremendous speeds (about 100–150 km per hour). Rapid pyroclastic flow downslope can also occur if the tephra blasts off the side of a volcano. This type of flow is called *nuée ardente* (glowing avalanche). Eventually the flow comes to rest at a distance away from the volcano.

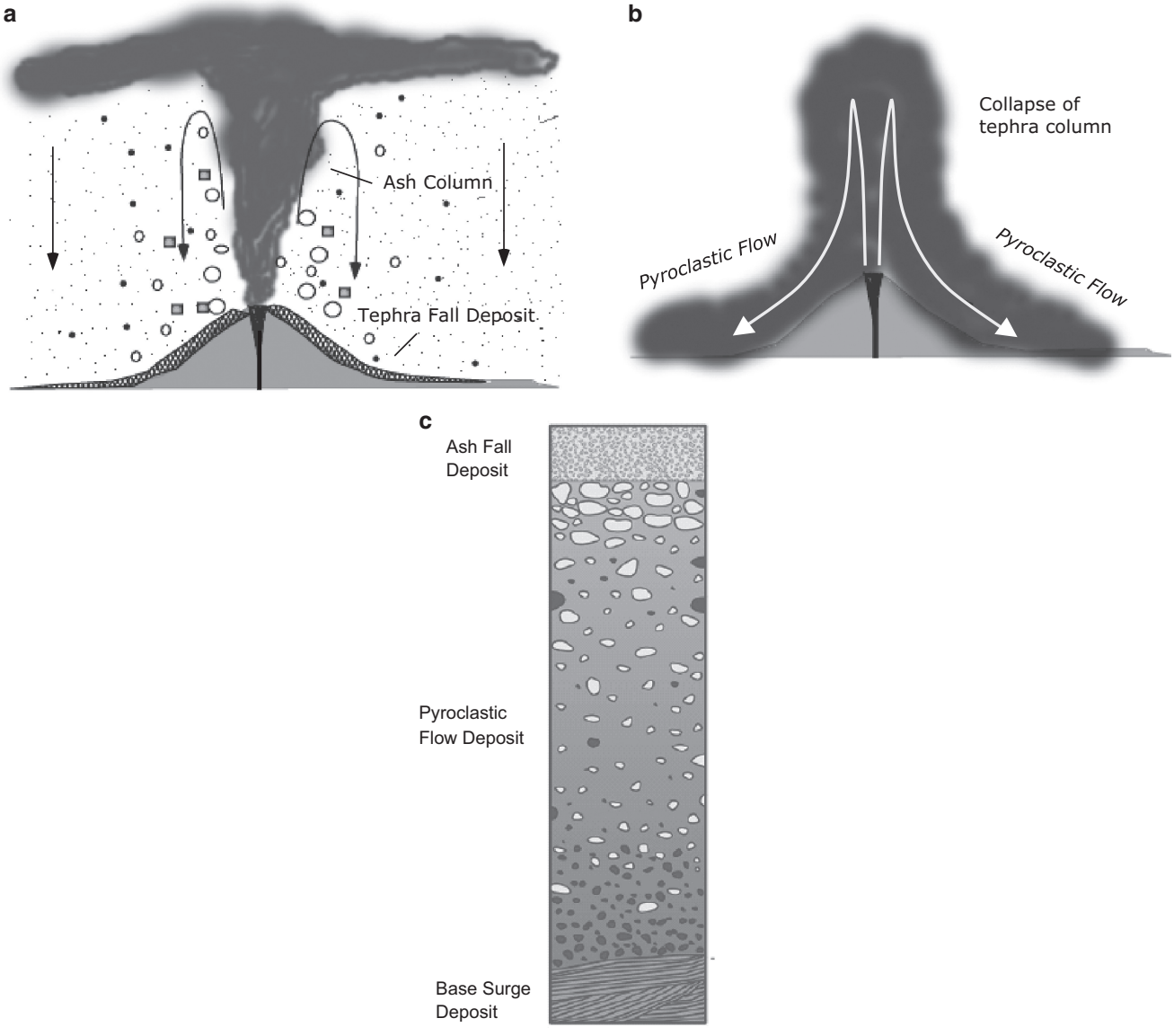

Fig. 2.21 Pyroclastic eruptions and their deposits. (**a**) Ash column and fall deposits. (**b**) Pyroclastic flow (nuee ardente). (**c**) Deposits from ash, base surge, and flow deposit

In recent US history, Mt. St. Helens produced a major pyroclastic flow via lateral blast. The deposit that forms from pyroclastic flow is called a pyroclastic flow deposit (Fig. 2.21c). *Ignimbrite* is a special class of pyroclastic flow deposit that is associated with silicic volcanism.

Base Surge Deposit. Some pyroclastic flows move at a tremendous speed while hugging the slope but cannot go too far from the volcano. Deposit formed from such flow is generally stratified with well-developed parallel and cross-stratification and is called a *base surge deposit*.

Lahar. It is an Indonesian term that refers to dangerous mudflows that are triggered by explosive eruption. Such mudflows are mixtures of volcanic ash, rain, or ice/snow melt water and can rapidly cover large areas.

Magma Emplacement in the Crust: Plutons and Hypabyssal Intrusions

Tectonic uplift and erosional processes sometimes expose magma's storage areas, called intrusions or intrusive bodies, in the crust. Study of these intrusive bodies tells us that they can be of various shapes and sizes. The term *pluton* is generally used to describe moderately large to really large intrusions that occur at depths greater than about 3 km (Fig. 2.22). At such deep levels, the crustal rocks are considerably hotter, and therefore, a magma emplaced in a pluton loses heat

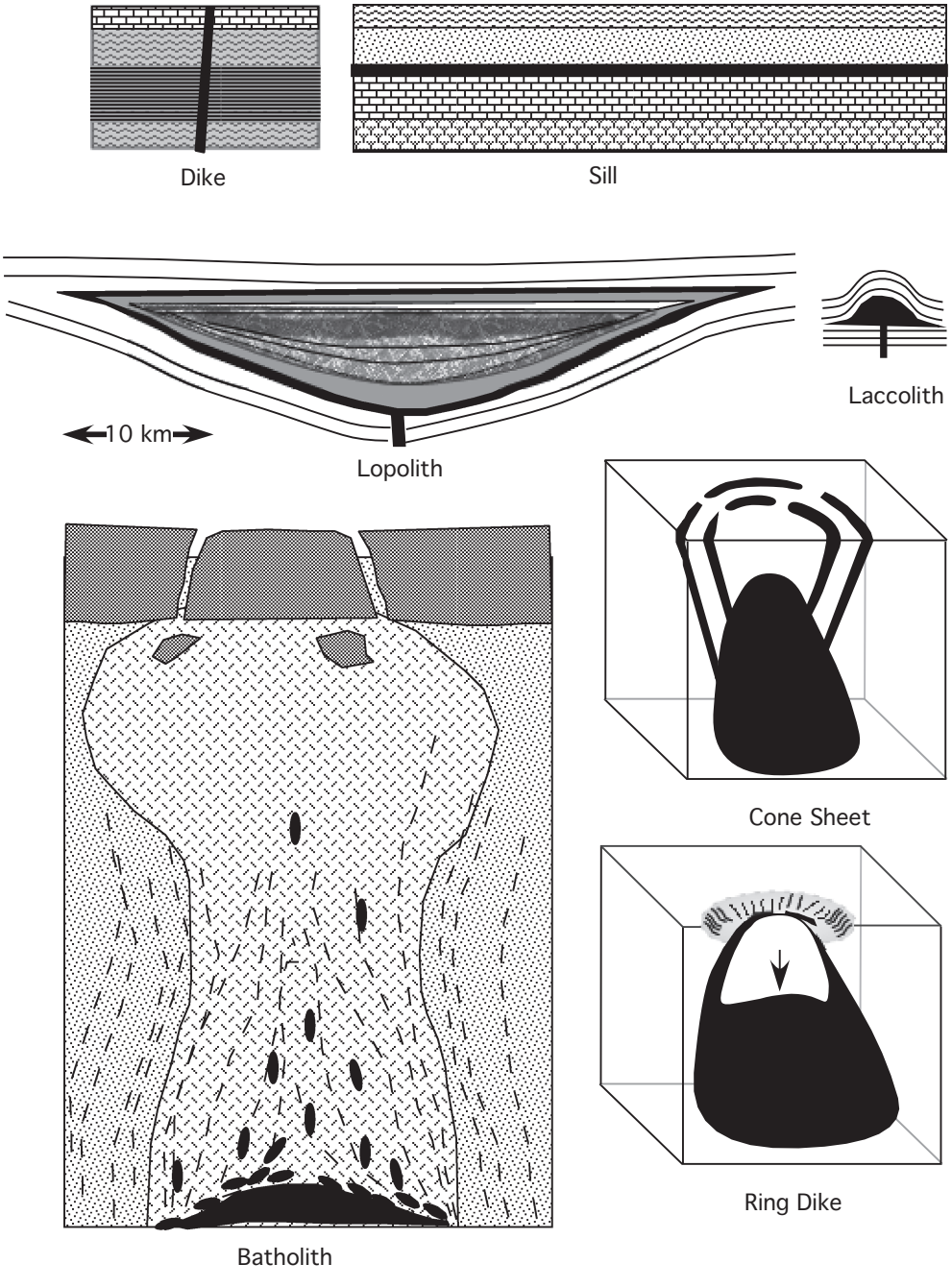

Fig. 2.22 Size and forms of igneous intrusions

very slowly to the surrounding crust. Really large plutons (hundreds of km in diameter) can take hundreds of thousands of years to completely solidify. Such slow cooling allows crystals to grow to large sizes while maintaining chemical equilibrium with the magma. Thus, plutonic rocks are coarse grained, free of glass, and the minerals in them are generally unzoned. Shallow level (0–3 km) intrusions are called *hypabyssal intrusions* and rocks in them have an intermediate grain size.

The terms *concordant* and *discordant* are used to describe the nature of contact between the intrusion and surrounding wall rocks (often called *country* rocks): an intrusion is said to be discordant when they cut through the wall rocks and concordant when they are parallel to the structures, such as the layers, in the country rock. Below is a list of names assigned to plutons and hypabyssal intrusions based on their size, shape, and relationships with the wall rocks.

Plutons (Fig. 2.22)

Laccoliths. Laccoliths are dome-shaped concordant plutonic intrusions. They acquire this form by pushing up the overlying rocks during magma emplacement.

Lopoliths. Plutons of mafic magmatic composition tend to have the form of a *lopolith*, which is a broad funnel- or keel-shaped intrusion whose exposed surface area could be as much as 64,000 km^2 (e.g., Bushveld intrusion of South Africa). Lopoliths generally have a gently "sinking" roof and a discordant, funnel-shaped bottom. Their large size allows magma to cool very slowly and developed layers of different rock types (discussed later).

Batholiths and Stocks. Felsic and intermediate magmas generally form batholiths, which are very large, discordant, and complex bodies of vast aerial extent. In terms of geometrical form, they can vary from large lenticular bodies to classic "bell jar" shapes. Their bottom is generally not exposed. Smaller batholiths are called *stocks*. Stocks are likely simple apophyses or "tongues" of larger batholiths below. A single batholith is generally not a single-phase intrusion but may grow in size over thousands of years by multiple phases of magma intrusion. *Mafic enclaves* or blobs and lens-like bodies of mafic rock are common in felsic batholiths. We will discuss more about batholiths in a later chapter.

Hypabyssal Intrusions

There is a large temperature contrast between the wall rocks and the magma when magma is emplaced at shallow depth. As a result, the magma forms a fine-grained or glassy margin along the contacts of a hypabyssal intrusion with the wall rock. Such a margin is called *chill* margin. Chill margin composition of an intrusion can give valuable clues to the nature of the original magma—its chemical composition, amount and composition of dissolved volatiles, and whether or not phenocrysts were present in the magma at the time of emplacement. The interior of hypabyssal intrusions is generally coarser grained, and the grain size may vary depending upon the rate of cooling of the intrusion. The coarsest grains tend to grow in the upper zone of an intrusion, where the grain size is not only due to slow cooling but also aided by concentration of volatiles. Occasionally, xenoliths of the wall rocks or larger crystals (megacrysts) or rocks (*cognate* xenoliths) formed from an earlier batch of magma may be found in an intrusion.

Dike. A dike is a tabular, discordant, intrusion. Dikes are commonly formed by basalt magmas and can vary from a few cm in width to tend of meters. The biggest dike on Earth is the Great Dyke of Zimbabwe. A system of parallel and cross-cutting dikes and sills, called a *dike swarm*, is often common in continental flood basalt provinces; for example, a dike swarm that fed many of the lava flows of the Columbia River Basalt Group is exposed close to the border of Washington and Idaho states in northwestern United States.

Sill. A sill is a tabular concordant intrusion. They can be several kilometers long and over a hundred meter thick. One of the best-known sills in the world is the *Palisades sill* whose outcrops are best exposed along New York–New Jersey State line on the New Jersey side of the Hudson River.

Ring Dikes and Cone Sheets. Ring dikes and cone sheets are a system of concentric dikes that form a ring-like structure on the surface (Fig. 2.23). The difference between the two is the dikes dip toward the center of the underlying pluton in a cone sheet, whereas they dip away from each other in a ring dike. Ring dikes form because of roof collapse when the magma pressure decreases in the underlying pluton. During such collapse, magma oozes out as dikes surrounding the collapse caldera. On the other hand, cone sheets form by magma pressure, which fractures the overlying roof rocks and magma then emplaces along such fractures.

Pegmatitic Intrusions. Pegmatites are extremely coarse-grained silicic rocks in which individual grains may grow to be several meters. They usually form lens-like intrusive bodies around a felsic batholith or stock. Such strong grain growth is attributed to crystallization in equilibrium with a vapor phase. Pegmatites are volumetrically almost insignificant when compared to basalts, andesites, and granites; however, they commonly host economically important ore minerals like gold and gemstones such as *emerald* (scientific name—Beryl).

Diatremes. These are essentially maars or tuff rings when viewed at the surface; however, their feeder dike is usually 1–2 m wide and reaches deep into the upper mantle. They are considered *a* special class of intrusion because they typically host diamond-bearing *kimberlite*s. Kimberlites are believed to be fluid-rich magma that rises from as deep as 300 km and carries the deepest mantle rocks found anywhere.

Elements of Petrography of Igneous Rocks

Physical description of the appearance of a rock is the very first step of any petrologic study. *Petrography* deals with such descriptive or observational aspects of a rock, and *petrogenesis* refers to processes that lead to the formation of an igneous rock. A good petrographic

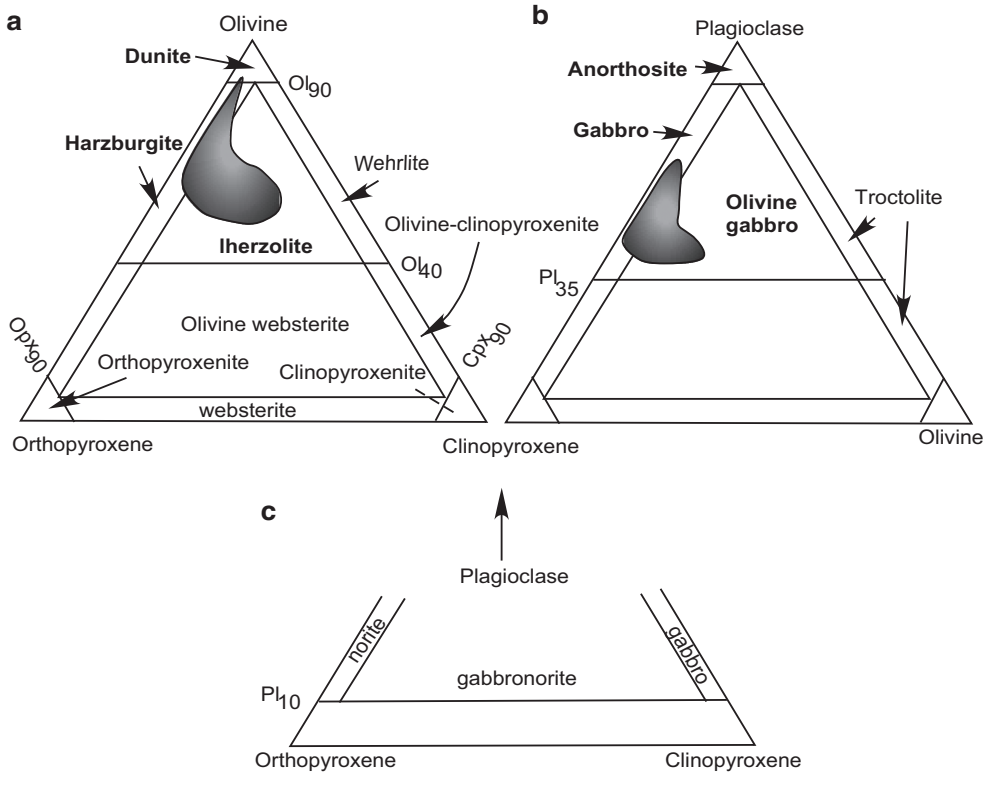

Fig. 2.23 Classification of mafic and ultramafic rocks

description of a rock should be such that it will afford the reader a clear mental picture of what the rock looks like without even looking at the actual specimen. It is also helpful to draw sketches of the rock or to take photomicrographs with a microscope.

There are two aspects of petrography—*mineralogy and texture*. A typical petrographic description must begin with the identification of the *essential minerals* (i.e., the dominant mineral components of the rock) and the *accessory minerals* (i.e., the minor mineral constituents). The next step is to provide a visual estimate of the *mode* (i.e., proportions of minerals). If necessary, one may wish to obtain quantitative modes by *point counting* under a microscope or image processing methods from back-scattered electron images of the rock obtained via a scanning electron microscope. Normally, a visual estimate is sufficient for routine descriptions.

In describing the texture of an igneous rock, the following aspects must be brought out:

Crystallinity

Crystallinity reflects the relative abundance and development of crystals in an igneous rock. When lava solidifies rapidly so much so that no mineral can nucleate, then the resultant volcanic rock is *glass*. The terms *glassy* and *holohyaline* are used to describe the texture of such glass. However, if the magma solidifies less rapidly, the resulting rock texture is called *aphanitic* if it is a mixture of glass and fine crystals called *crystallites* (which are so small that their individual grain outlines cannot be easily deciphered with a petrographic microscope) or *microlites* (the crystals are more visible but still extremely small). It refers to the extent to which a magma has crystallized. The terms *holocrystalline* (fully crystallized, generally medium to coarse crystals; somewhat analogous to the term *phaneritic*), *microcrystalline* (crystalline but crystals are very small (<1 mm) even under a microscope: also, *aphanitic*), *merocrystalline* (mixture of crystals and glass), and *holohyaline* (*glassy*) are generally used.

Sizes, Shapes, and Habits of Crystals of the Essential Minerals

In general, the terms *coarse* (>5 mm), *medium* (1–5 mm), and *fine* (<1 mm) are used to describe the overall grain size. In the case of very large (cm to m scale) crystals of pegmatites, the term "*pegmatitic*" is used to describe such crystals.

The terms *euhedral*, *subhedral*, and *anhedral* are used to describe, in a relative sense, how well-developed crystal faces are for each mineral phase. A mineral grain is said to be euhedral when all/most of its faces are smooth and well developed, and anhedral is just the opposite—none of the faces are well developed. A subhedral grain has some of its faces well developed. The shape of a grain is described by using such terms as *equant*, *subequant*, *prismatic*, *subprismatic*, *tabular*, *lath shaped*, etc.

In rapidly quenching lava, minerals often do not have the time to form well-developed crystals and instead form feathery, dendritic (i.e., like a tree), long, optically discontinuous crystals. This type of crystals is known as a *skeletal* crystal.

Specific Textural Terms for Description of Rocks in the Field

Texture or fabric of a rock is essentially a description of the geometrical relationships between individual mineral grains (and/or glass or other materials) of a rock. Below is a set of textural terms used in field description of a rock.

Glassy. Rapid quenching of liquid forms a glass. Therefore, the texture of a glass or a glass-rich rock is glassy. Obsidian is well known for its glassy appearance.

Spinifex. Ultramafic lavas of Archean age are characterized by this texture. In these lavas long (few cm), discontinuous, skeletal crystals of olivine rapidly grew toward the interior of the lava flow from the flow tops, giving the lava the appearance of inverted slabs of grass. The term spinifex is based on a type of grass found in southern Africa.

Aphanitic. The texture is called *aphanitic* if the rock is very fine grained so that individual grains are not discernible.

Phaneritic. This term refers to coarsely crystallized texture.

Porphyritic. Porphyritic texture is defined by the presence of conspicuously large crystals set in a groundmass of finer-grained minerals or glass or a mixture of glass and finer crystals. If the phenocrysts form clusters, then the texture is called *glommeroporphyritic texture*.

Aphyric. When a rock lacks any distinct phenocrysts, its texture is described as aphyric. This texture has held special significance in igneous petrology because aphyric textured rocks are generally thought to represent actual liquids.

Vesicular. This texture is common in basalt lavas, which contain numerous holes that were once filled with vapor bubbles that left during the eruption and solidification of the lava. It is also common for the vesicles to be subsequently filled with secondary minerals or mineraloids, such as quartz, amethyst, and calcite, when the texture is called *amygdular* and the fill-in materials are referred to as *amygdules*. Some of these amygdules can be basketball sized (or even bigger) and have well-formed crystals projecting toward the interior of the hole. They are called *geodes*.

Pumiceous. This type of texture usually forms in felsic lavas where vesicles comprise more than 50 % of the rock (light colored) and such a rock, called *pumice*, floats in water. Basalt lava can also have more than 50 % vesicles, but it would not float in water because the rock is denser. Such a texture is called *scoriaceous* and the rock is called *scoria.*

Flow Banding or Trachytic. In flowing viscous lava, lath-like crystals of plagioclase (and other minerals) may orient themselves parallel to the flow direction, giving rise to what is known as flow banding. This texture is typical of trachytes but is also found in other volcanic rocks.

Spherulitic. This type of texture is formed by intergrowth of fine, radiating, needlelike crystals. It is common in some glassy rocks where the centers of individual spherules serve as nucleation centers for spherulitic crystallization. In obsidian, spherulites of quartz and feldspar can develop during devitrification (i.e., loss of water during cooling) of glass.

Ocellar. This is a texture found typically in lamprophyre dikes: individual *ocelli* consists of concentrically banded spheres wherein the bands consist of alternating light-colored and dark-colored minerals. They are unlike spherulites and may form liquid immiscibility or by late-stage melt emplacement into gas cavities.

Graphic/Granphyric/Eutectoid Intergrowth. This texture is defined by a hieroglyphic type intergrowth of quartz and alkali feldspar, usually formed during eutectic crystallization of these two minerals. The rock that has this distinctive texture is commonly called a *graphic granite*.

Microtextures

Textures, as viewed under the microscope, may be broadly divided into two groups—*inequigranular*, in which two or more distinct size groups of crystals occur, and *equigranular* (all grains are roughly equal in size) textures. If distinct size groups do not occur, and instead the grain size variation is a continuum between large and small sizes, then the term *seriate texture* is used. The terms used in field descriptions are also applicable to microscopic descriptions. As needed, additional expressions are used to describe the texture of a rock under the microscope.

Inequigranular Textures

Porphyritic Texture. As described above, in a porphyritic textured rock, phenocrysts are embedded in a finer

groundmass. It is a common texture among volcanic rocks. Some volcanic rocks may be aphyric, i.e., devoid of phenocrysts. Sometimes authors distinguish between megacrysts, phenocrysts, and microphenocrysts, based on whether it is visible in hand specimen (megacrysts and phenocrysts, the former being much larger) or only under the microscope (microphenocrysts). Some authors feel that the term megacryst is simply a phenocryst that grew to much larger size but essentially in the same magma (or related) in which it is found. The same authors would use the term *xenocryst* to refer to crystals that clearly was an accidental inclusion (such as wall rock fragment) in the magma in which it is found.

Poikilitic Texture. It refers to a texture in which small crystals are entirely enclosed by larger crystals, and the term *subpoikilitic* is used when such enclosure is only partial. The terms *subophitic* and *ophitic textures* are used to describe the textures of diabase (dolerite in European and Asian countries), a hypabyssal rock in which coarse crystals of augite partially (subophitic) to completely (ophitic) enclose lath shaped to tabular crystals of plagioclase. An oikocryst is an especially large type of crystal that grows late from the magma and encloses a large number of crystals.

Intergranular and Intersertal Textures. Cooling of mafic magma is such that earlier-formed crystals in a rock may trap melt between them. Such melt may rapidly quench later to glass, giving rise to what is called *intersertal* texture. The glass is often not preserved and may become *devitrified* (i.e., alter to clay minerals or mineraloids). On the other hand, the trapped liquid may have enough time to form smaller crystals of plagioclase, pyroxene, magnetite, ilmenite, apatite, and sulfides. Such a texture is called intergranular texture.

Equigranular Textures

Equigranular textures are more common in plutonic rocks. Such overall textural terms as *panidiomorphic granular*, *hypidiomorphic granular*, and *allotriomorphic granular* are used when the bulk of the constituent grains are euhedral, subhedral, or anhedral, respectively. In large mafic (defined later) plutonic intrusions, layered structure on field to microscopic scales is common. Such rocks are called *cumulates*, and a whole range of textural terms are used to describe such rocks (described in a later chapter).

Other Textural Terms Used in Petrographic Description

Micropegmatitic or Microgranophyric. These terms refer to blebby to hieroglyphic intergrowths of quartz and alkali feldspar in the interstitial areas between coarse grains of mafic plutonic–hypabyssal rocks (gabbro and diabase).

Myrmekitic. Myrmekitic texture refers to an irregular intergrowth of quartz and oligoclase that "intrude" into an alkali feldspar grain. It is thought to be an igneous replacement texture.

Sieve Texture. Sieve texture specifically refers to plagioclase crystals with numerous glass (melt) inclusions giving the appearance of a plagioclase "sieve." They are found in volcanic or hypabyssal mafic rocks.

Mineral Zoning. Zoning in individual crystals is an important feature that is easily visible between crossed polars under a petrographic microscope. We have discussed normal, reverse, and oscillatory zoning in plagioclase in a later chapter. Pyroxenes are also known to show zoning of various types, in particular, sector zoning, patchy zoning, and hourglass zoning. In sector zoning different sectors of a grain go extinct at a time when the microscope stage is turned and with the polars crossed. In hourglass zoning, the sectors go extinct forming an hourglass pattern. In patchy zoning or wavy extinction, a mineral grain goes extinct in patches or in a continuous "wave" as the stage is turned.

Exsolution. Exsolution texture, defined by exsolved blebs or lamellae of one mineral in another, occurs in slowly cooled plutons of varied compositions. In felsic plutons, exsolution features are common—formed by exsolved plagioclase blebs or streaks in potash-rich feldspar (called *perthite*) and vice versa (*antiperthite*). In mafic plutons, exsolution of pigeonite and orthopyroxene lamellae in augite and exsolution of augite in crystals of orthopyroxene and pigeonite are relatively common.

Reaction Texture. Reaction texture develops when a mineral crystal becomes unstable in magma for whatever reason and starts reacting with the melt, and the products of the reaction form a mantle surrounding the crystals of the first mineral. Most commonly, reaction corona develops around a xenolith, i.e., a wall rock fragment, in magma. Formation of pyroxene rim around an olivine crystal in basalt magma is also well known.

Classifications of Igneous Rocks

A Simple "Field" Classification

Chemical composition of magma dictates what minerals may crystallize from it. The rate at which the magma cools, which is related to its depth and mode of emplacement, controls the sizes and shapes of crystals and its texture. Therefore, it is only natural that naming an igneous rock must take into account its

chemical composition, mineralogy, and texture (mode of emplacement). Table 2.2 shows such a general classification. A classification of this type is particularly useful in the field, where usually a pocket lens is the only tool one can use to identify a rock. There is a direct correlation between the hand specimen color of a rock and its content of *mafic minerals* (minerals with relatively high content of Mg and Fe—such as olivine and pyroxene): the greater the mafic mineral content, the darker the rock. Based on color of the hand specimen, igneous rocks are classified into *melanocratic (mafic minerals >60 %), mesocratic (mafic minerals 30–60 %), and leucocratic (mafic minerals <30 %) types*.

Brief Petrography of Some Common Igneous Rocks

Komatiites, Peridotites, and Pyroxenites

Komatiites are ultramafic lavas that erupted in the Archean (with only one exception in the Phanerozoic in Gorgona Island). The most distinctive feature of komaitiites is the presence of long skeletal crystals of olivine and/or pyroxene. As discussed earlier, its texture is called *spinifex*.

Peridotites are generally coarse-grained rocks, and their mode may vary a great deal. They are generally composed of $\geq$60 % olivine (Fo_{88}–Fo_{92}), $\leq$25 % aluminous (>5 wt% Al_2O_3) orthopyroxene, $\leq$15 % diopsidic clinopyroxene (with 4–8 wt% Al_2O_3 and 0.5–1.2 % Cr_2O_3), and an aluminous mineral (either plagioclase, spinel, or garnet). Textures of peridotites may vary tremendously from metamorphic types (foliated, cataclastic, etc.) to more hypidiomorphic granular. In a protoclastic texture, large deformed crystals (protoclasts) show granulation along grain boundary and are set in a groundmass composed of sheared, much smaller, grains. Exsolution in pyroxenes, triple-point junctions between grains, and subgrain boundaries (deformation lamellae) in olivine are generally common in these rocks. Most commonly, these rocks thus display metamorphic textures, which will become apparent upon comparison with metamorphic rock textures.

Pyroxenites are very coarse-grained rocks (i.e., individual mineral grains are visible with the naked eye) that are generally composed of $\geq$90 % pyroxene. Clinopyroxenites (i.e., pyroxenites in which clinopyroxene is dominant) are generally much more common than orthopyroxenites. Their grain size can vary from pegmatitic (extremely coarse) to coarse/medium. The very coarse-grained pyroxenites often have pyroxenes with spectacular exsolution structures. The exsolved phase may form lamellae to highly irregular, blebby shapes. The exsolved phases may be a pyroxene or an aluminous phase (garnet, spinel, or plagioclase). An aluminous phase, commonly a green-colored spinel, plagioclase, or garnet, is generally present in pyroxenites. Olivine is rare to absent. Phlogopite and a brown amphibole are generally present in minor amounts. The textures of these rocks are commonly igneous types, mostly hypidiomorphic granular; however, strongly recrystallized metamorphic textures with triple-point junctions are more common among the smaller-grained pyroxenites.

Basalt, Gabbro, and Diabase

These mafic igneous rocks are all dominantly composed of lath shaped to tabular crystals of plagioclase (commonly of An_{70}–An_{55} composition) and subprismatic to prismatic crystals of augitic clinopyroxene. These two minerals occur in roughly equal proportions in the rock. Pigeonite, and sometimes orthopyroxene, may also occur only in the tholeiitic/olivine–tholeiitic variety of these mafic rocks. Olivine's abundance usually varies between 0 and 15 %. Olivine may often be altered (partially or wholly to an iddingsite (an orange-colored clay or serpentine) but can be recognized by its relict shape. Magnetite and ilmenite are generally present, although their abundance is generally less than 5 %. Besides these, small globular forms of sulfides (usually chalcopyrite, pyrite–pyrrhotite, and pentlandite), formed due to sulfide–silicate liquid immiscibility, are also ubiquitous (<1 %). Tiny (generally <25 μm) euhedral crystals of apatite may also be found in the interstitial spaces.

The difference between the basalt, diabase, and gabbro is principally one of texture. Basalt is a fine-grained or glass-rich rock and is often porphyritic in nature. They may contain vesicles or amygdules. The most common phenocryst assemblages are olivine or olivine + plagioclase or olivine + plagioclase + augite. Intergranular and intersertal textures are common in the groundmass of porphyritic basalt. Diabase is medium grained and has a characteristic ophitic–subophitic texture. Gabbros are coarse grained, and the plagioclase and pyroxene crystals generally form coarse hypidiomorphic granular-type textures. Intergranular texture, defined by the occurrence of pyroxene, magnetite, and ilmenite crystals or microlites in the

interstitial spaces between plagioclase crystals, is also a common feature.

Andesite and Diorite

Andesites vary greatly in their modal composition. They generally exhibit porphyritic texture, dominated by strongly zoned plagioclase phenocrysts, euhedral-to-subhedral red-brown amphibole phenocrysts, and/or pyroxene phenocrysts. The plagioclase composition varies tremendously due to zoning, but the mean composition is ~An_{40}. Cores of individual plagioclase crystals may be as calcic as An_{85}. Amphibole phenocrysts are often rimmed by pyroxene and opaque oxide mineral grains. One interpretation of these rims is that they formed due to dehydration breakdown reaction of the amphiboles as the lavas rose toward the surface. Zoned pyroxene phenocrysts of subcalcic augite, pigeonite, or orthopyroxene are often found. Olivine, biotite, and glass are generally uncommon.

Diorites (broadly used here to include diorite, monzodiorite, quartz diorite, and quartz monzodiorite as defined by the International Union of Geological Sciences, discussed later) are composed of plagioclase, amphibole, and pyroxenes ± quartz. They exhibit more equigranular, hypidiomorphic granular, texture. Plagioclase generally tends to dominate the mode. Granodiorites and other somewhat quartz-rich rocks have similar textures.

Granite and Rhyolite

By definition, the two minerals that dominate the compositions of these rocks are quartz and alkali feldspar. In hypabyssal intrusions and volcanic rhyolites, sanidine, a high-temperature polymorph of K-feldspar, is usually the dominant feldspar. The quartz phenocrysts in lavas are sometimes euhedral, but quartz grains in the groundmass are always anhedral and small. Extremely glassy dark-appearing (in hand specimen) equivalent of rhyolite is recognized as *obsidian*. *Rhyolites* are generally vesicle free. *Flow texture*, defined by curvilinear arrangement of alkali feldspar and quartz crystals, sometimes occurs in hypabyssal intrusions or crystal-laden lavas.

Granite and granodiorite typically form batholiths. Their texture is generally coarse-grained hypidiomorphic granular. They are composed of an alkali feldspar and quartz. Subhedral to euhedral albitic plagioclase crystals may also occur. Whether one or two types of feldspars occur in granite has significance in understanding their depths of origin (discussed further later). Perthites and antiperthites can be found in some granite group of rocks. Biotite and hornblende may occur, and their proportion may vary greatly between different granitic rocks. Granophyric or micropegmatite intergrowth is common in the interstices. Minor euhedral crystals of zircon, apatite, and sphene may also occur in the interstitial spaces.

Syenite and trachyte are similar to granite and rhyolite, respectively, except that they have lesser amounts of normative and modal quartz (note that nepheline syenite and phonolite are alkalic rocks and therefore have normative and modal nepheline). In general, syenites form small plutons and ring-dike complexes.

Rigorous Classifications

Many different classification schemes have been proposed in the literature. Among them, the one proposed by the *I*nternational *U*nion of *G*eological *S*ciences (more popularly known as the *IUGS Classification*, given in LeMaitre et al. 1989) for plutonic rocks is commonly used today. This classification is based on the observed proportion of mineral constituents (i.e., *mode*). The IUGS classification of volcanic rocks is not widely used because in such rock minerals are often not discernible. In the case of volcanic rocks, classification schemes based on chemical or normative (discussed later) compositions are generally used. In this book, we will adopt the IUGS classification of plutonic rocks and LeMaitre's chemical classification of volcanic rocks.

Classification of Plutonic Rocks

The IUGS classification is based on the modal abundance of quartz [Q], alkali feldspar [A], plagioclase [P], feldspathoids [F], and mafic minerals [M]. If the proportion of M, also known as the *color index*, exceeds 90 %, then it is an *ultramafic rock*. Rocks with color index less than 90 are classified in terms of their proportions of Q, P, A, and F contents (discussed later).

Classification of Ultramafic Rocks

Ultramafic rocks are dominantly composed of three minerals—olivine, orthopyroxene, and clinopyroxene. Figure 2.23a shows IUGS classification of ultramafic rocks in terms of *the olivine–orthopyroxene–clinopyroxene triangle*. *Dunite* is a rock with >90 % olivine.

Harzburgites are dominantly composed of olivine and orthopyroxene, with little or no clinopyroxene. *Lherzolites* contain more pyroxenes than a dunite and more clinopyroxene than a harzburgite. Because an aluminous phase (plagioclase, spinel, or garnet) is usually present in a lherzolite, an additional qualifier is added as a prefix to indicate what type of aluminous phase is present: if the aluminous phase is a spinel, then the rock is called a *spinel lherzolite*. Similarly, the names *garnet lherzolite* and *plagioclase lherzolite* are used when garnet or plagioclase, respectively, occurs. It is important to note that lherzolite is the predominant constituent of the Earth's upper mantle. The gray area in Fig. 2.23a shows where the bulk of the ultramafic rocks worldwide plot (gray-shaded area). Other ultramafic rocks, such as wehrlites, websterites, and clinopyroxenites, are much less abundant and are generally of igneous origin.

The majority of upper mantle lherzolites and harzburgites exhibit distinct *metamorphic textures*. It is therefore ironic to consider these important rock types as igneous rocks! Presumably, this tradition has continued because lherzolite is commonly accepted to be the source rock for basalt magmas, which form all of the oceanic crust and much of the continental crust! In such a case, *eclogite*, clearly a metamorphic rock composed of pyrope-rich garnet and an omphacitic clinopyroxene, must also be considered here since it too likely plays some role as a source rock for magmas.

In the literature, the terms peridotite and pyroxenite are loosely used to refer to olivine-rich versus pyroxene-rich ultramafic rocks. Peridotite thus broadly includes lherzolite, dunite, harzburgite, olivine websterite and wehrlite, whereas pyroxenites include mainly clinopyroxenite, orthopyroxenite, and websterite.

Mafic Plutonic Rocks

In this book a slightly modified version of the IUGS scheme of classification of mafic and felsic rocks is used. In this version many of the "nomenclature details" (which are essentially descriptive jargon) have been skipped because the focus of this book is on only those rocks that are most common.

Mafic plutonic rocks are classified on the basis of modal contents of olivine, plagioclase, and pyroxenes (Fig. 2.23b, c). Rocks containing >90 % plagioclase are called *anorthosite*. Anorthosite occurs as layers in plutonic layered intrusions and as massive, km-scale bodies of Precambrian age. Note that the "highlands" on the Moon are largely composed of anorthosite. *Gabbros* (plagioclase + clinopyroxene) and olivine gabbros (gabbros commonly with 5–15 % olivine) are most abundant mafic plutonic rocks (Fig. 2.23b). *Troctolite* (olivine + plagioclase rocks) occurs as layers in layered intrusions. Figure 2.23c shows that if the dominant pyroxene is an orthopyroxene (instead of clinopyroxene), then the orthopyroxene-bearing equivalent of a gabbro is called *norite*. Norites, *olivine gabbronorites*, generally occur in layered intrusions and also may be found associated with anorthosite massifs.

Felsic Plutonic Rocks

The modal proportions of quartz (Q), alkali feldspar (A), plagioclase (P), and feldspathoids ("foid," F) are used to name various rock types (Fig. 2.24). IUGS classification recognized a fundamental distinction between rocks that contain quartz and those containing feldspathoids. We will see in a later chapter that feldspathoids and quartz are not compatible, that is, they cannot occur in the same rock. Thus, IUGS classification has two triangles—QAP and FAP—which are shown to share the PA edge. In the field, more general terms are often used—for example, a rock containing more than about 20 % quartz is referred to as *granitoid*. An exact mode allows a more precise naming of the rock—for example, a rock will be called granite if it has 40 % Q, 40 % A, and 20 % P, because it will plot within the "granite" field. The IUGS classification recommends the use of a complex system of prefixes based on detailed modes; however, such detailed naming is often unnecessary.

The distinction between gabbro and diorite can only be made based on the proportion and nature of mafic minerals (gabbro being generally pyroxene rich and diorite being amphibole rich) and plagioclase composition (gabbro, $>An_{55}$; diorite, $<An_{50}$).

Classification of Volcanic Rocks

There are a number of classifications of volcanic rocks available in the literature. Among these, IUGS's TAS (stands for total alkalis, i.e., $Na_2O + K_2O$, and silica) classification and LeMaitre's classification (1989, Fig. 2.25) are commonly used. Both are based on total alkalis versus silica contents of volcanic rocks and have been shown to be quite useful (Cox et al. 1979). I have used the TAS classification throughout this book.

As far as mafic volcanic rocks are concerned, the most useful classification is a genetic classification that

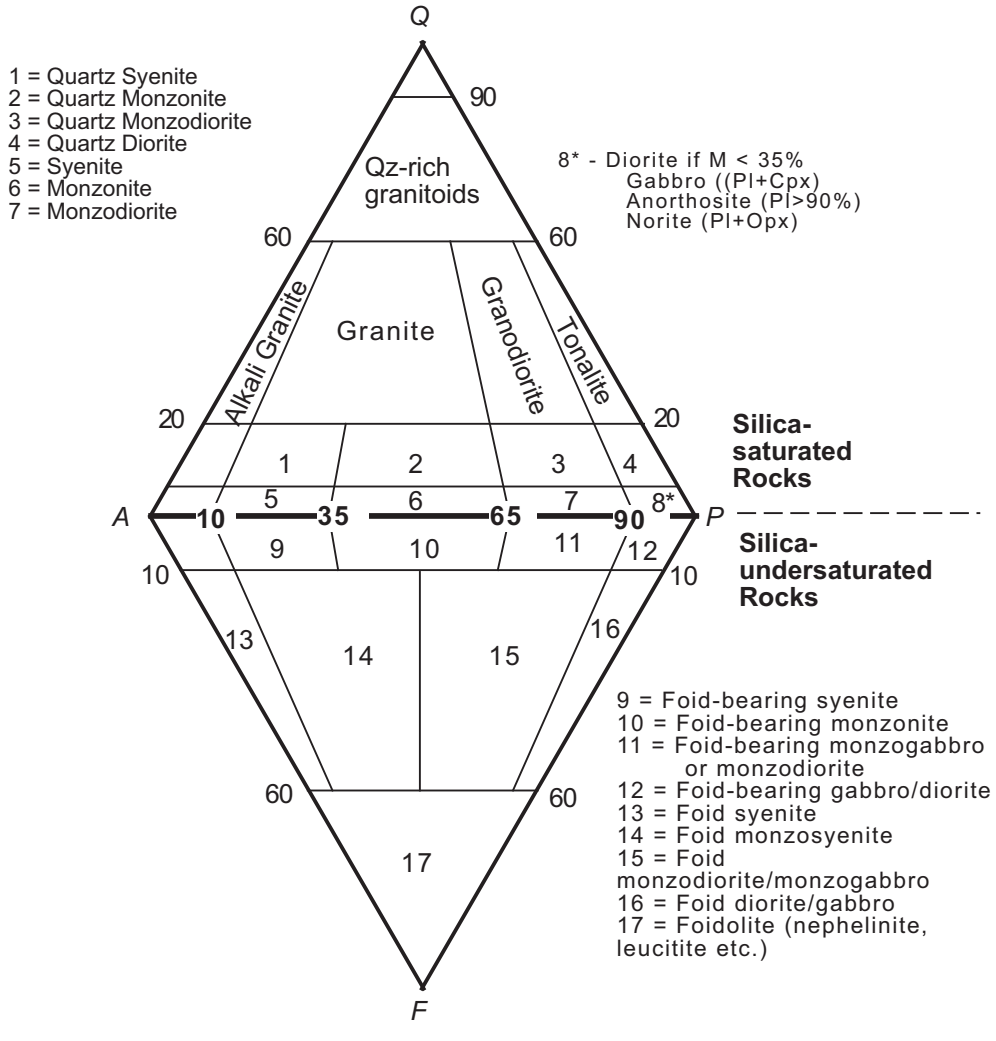

Fig. 2.24 QAPF classification of felsic plutonic rocks. The *upper triangle* (*gray*) is applicable to rocks with modal quartz (i.e., SiO_2 saturated). All silica-undersaturated rocks containing feldspathoids plot in the *lower triangle* (SiO_2 undersaturated)

was proposed by Yoder and Tilley (1962). This classification (popularly known as the "*basalt tetrahedron*"; discussed in a later chapter) is based on calculated mineral molecules (or *norm*) and has been known to be most useful in understanding the petrogenesis of basalt magmas.

Three ultramafic volcanic rocks, namely, kimberlites, lamproites, and komatiites, have not been discussed in terms of the above classification and are briefly discussed here. *Kimberlites* are a class of rare potassic volcanic ultramafic rocks that contain phenocrysts of phlogopite, altered olivine, abundant xenoliths, and xenocrysts of the mantle, mixed with a very fine-grained material. Kimberlites have been a popular subject because many contain deep mantle xenoliths and are diamond bearing.

Lamproites are a rare group of volcanic to hypabyssal rocks that are unusually rich in K_2O and vary from ultramafic compositions through mafic to more evolved compositions. Leucite and sanidine are generally

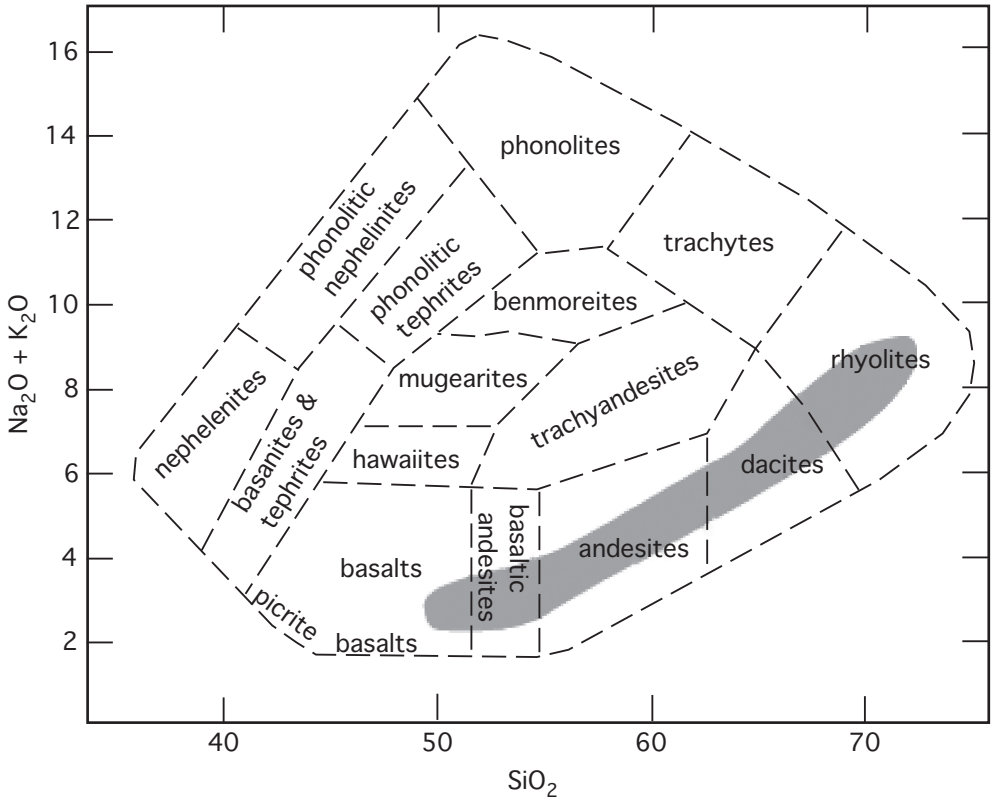

Fig. 2.25 LeMaitre's et al. (1989) classification of volcanic rocks

present in the highly evolved lamproites. Olivine lamproites are ultramafic and contain phenocrysts of olivine ($Fo_{91–94}$), diopside, phlogopite, and potassic amphibole in a fine-grained groundmass dominantly composed of diopside, phlogopite, and phlogopite.

Komatiites have been discussed earlier and are ultramafic lavas with spinifex structure. The presence of komatiites in the Archean attests to very high temperatures within the Earth's shallow upper mantle.

CIPW Norm Calculation

Plutonic and hypabyssal rocks are medium to coarse grained, and so one can easily identify their constituent minerals and count their mode. On the other hand, volcanic rocks are generally too fine grained or glassy so that visual inspection does not allow a comparison of such rocks with their plutonic equivalent. In 1903, Cross, Iddings, Pirsson, and Washington realized that a way to put volcanic rocks on a more "equal footing" with plutonic rocks would be to calculate the proportions of a set of standard minerals (called *normative minerals*) from the chemical composition of the rock (detailed procedure given in appendix). This procedure, which may seem daunting, has almost become a standard practice over several decades, and there are websites that one can visit to perform the calculations. The mineral percentages so calculated from a chemical analysis are referred to as CIPW norm, as opposed to the *mode*, which refers to actually counted mineral percentages from a thin section of the rock specimen using various microscopic techniques. Also, it should be noted that CIPW method calculates normative minerals in terms of weight percent; however, if molecular percent of such normative minerals is calculated, then it is called a *Niggli norm*.

Commonly, a relatively smaller number of normative minerals are used, which generally are apatite (*ap*), ilmenite (*il*), magnetite (*mt*), feldspar (composition given in terms of orthoclase (*or*), albite (*ab*) and anorthite (*an*) components), diopside (*di*—composition is further broken down in terms of wollastonite (*wo*), enstatite (*en*), and ferrosilite (*fs*) components), hypersthene (*hy*—composition may be further broken down into *en* and *fs* components), olivine (*ol*—composition

A Few Examples That Illustrate the Basic Principle of CIPW Norm.

The underlying premise in developing the CIPW scheme of norm calculation is as follows: (1) A magma, if cooled slowly in a crustal environment, would form a rock containing proportions of crystals of certain chemical compositions; and (2) because minerals contribute to the chemical composition of a rock, one could "invert" its chemical composition to determine the proportion of mineral molecules (with ideal chemical formulae). This logic of norm calculation may be illustrated with a few examples as follows:

Example 1

Consider a "rock" that is composed only of CaO, MgO, Al_2O_3, and SiO_2 (table below). Its chemical composition is given in Column (2).

1	2	3	4	5	6	7	8	9	10	11	12
	Wt%	Mol. Wt.	Mole prop.	An	Di	Remaining			Moles	Mol. Wt.	CIPW
SiO_2	49.09	60.0843	0.817	0.395	0.153	0.270		An	0.197	278.208	54.81
Al_2O_3	18.12	101.96	0.178	0.197	0.000	0.000		Di	0.076	216.552	16.54
MgO	15.45	40.304	0.383	0.000	0.076	0.307		Hy	0.233	100.388	23.39
CaO	15.33	56.079	0.273	0.197	0.076	0.000		Ol	0.037	140.692	5.21
										Total	99.94

Column (3) simply gives the molecular weights of each oxide. Column (4) lists the mole proportions of each oxide in the "rock" (Column 4) obtained by dividing Column (2) by Column (3). At this stage we are in a position to distribute the appropriate moles of each oxide to form the possible mineral moles.

We first distribute all of Al_2O_3, an equal amount of CaO, and twice as much SiO_2 to make anorthite ($CaO{\cdot}Al_2O_3{\cdot}2SiO_2$) moles (Column 5). We then assign the remaining CaO, an equal amount of MgO, and twice as much SiO_2 to make diopside ($CaO{\cdot}MgO{\cdot}2SiO_2$; Column 6). At this stage we check for whether the remaining SiO_2 (S) is less than, equal to, or greater than the remaining MgO (M). There are three possibilities to consider:

If $S = M$, then one can only make enstatite ($MgO{\cdot}SiO_2$).

If $S > M$, then one has to make enstatite and the excess SiO_2 will form quartz.

If $S < M$, i.e., silica is deficient, then the result has to be a mixture of enstatite and forsterite ($2MgO{\cdot}SiO_2$) because forsterite requires much less silica than enstatite.

According to Column 7, $S = 0.270$ and $M = 0.307$. That is, $S < M$. Now the question is how we divide M and S among forsterite and enstatite moles?

Let us suppose SiO_2 in enstatite $(SiO_2)^{en} = x$. Then $(MgO^{en}) = x$.

If we assume SiO_2 in forsterite $(SiO_2{}^{fo}) = y$, then $MgO^{fo} = 2y$.

$S = x + y = 0.270$ and $M = x + 2y = 0.307$. From these equations, we obtain x (i.e., enstatite moles) $= 0.233$ and y (forsterite moles) $= 0.037$. We convert all the moles to wt% norm by multiplying them with their respective molecular weights (see below). These are the same columns as columns (9) through (12) in the table above.

	Moles	Mol. wt.	CIPW NORM
an	0.197	278.208	54.81
di	0.076	216.552	16.54
hy	0.233	100.388	23.39
ol	0.037	140.692	5.21
			99.94

Example 2

Consider a second example (below) of slightly greater complexity. This is a rock composed only of normative olivine and hypersthene. The table below shows the wt% contents of FeO, MgO, and SiO_2 in the rock. As before, we first obtain mole proportions of each oxide.

	Wt%	÷	Mol. wt.	=	Mole prop.
SiO_2	43.62		60.3		0.723
FeO	11.40		71.85		0.159
MgO	44.82		40.3		1.112

(continued)

A Few Examples That Illustrate the Basic Principle of CIPW Norm (continued)
After calculating the moles, we are at a loss as to how to distribute them between normative olivine [2(MgO, FeO). SiO_2] and hypersthene [(MgO, FeO)·SiO_2], since both are composed of MgO, FeO, and SiO_2! We add FeO to MgO and treat it as *M*. Following our previous example,

$$\text{For hypersthene, } (SiO_2)^{hy} = x = (MgO + FeO)^{hy}$$

$$\text{For olivine, } (SiO_2)^{ol} = y \text{ and } (MgO + FeO)^{ol} = 2y$$

Therefore, in the present example,

$$\text{hy moles} = x = 0.175$$

$$\text{ol moles} = y = 0.548$$

At this stage of calculations, we know that in hypersthene MgO + FeO = 0.175; however, we do not know MgO and FeO values individually, and we need to know those values if we are to obtain CIPW norms, which require multiplication by appropriate molecular weights. Here we make the assumption, as required by the CIPW calculation procedure, that the MgO/(MgO + FeO) ratios of both minerals are equal to that available:

$$[MgO/(MgO + FeO)]^{hy} = [MgO/(MgO + FeO)]^{ol} = [MgO/(MgO + FeO)]^{available}$$

We know from above calculations that

$$[MgO/(MgO + FeO)]^{available} = 1.112/1.271 = 0.875$$

Therefore,

$$[MgO/(MgO + FeO)]^{hy} = [MgO/(MgO + FeO)]^{ol} = 0.875$$

We already know $(MgO + FeO)^{hy} = 0.175$ and therefore easily calculate $(MgO)^{hy} = 0.875 \times 0.175 = 0.153$ and $(FeO)^{hy} = 0.175 - 0.153 = 0.022$. These numbers can now be used to obtain CIPW norm of enstatite and ferrosilite components in normative hypersthene in the same manner as in our first example:

	Mole prop.	En	Fs
SiO_2	0.175	0.153	0.022
FeO	0.022		0.022
MgO	0.153	0.153	

CIPW normative en = 0.153 × 100.38 (mol. wt. of enstatite) = 15.36
CIPW normative fs = 0.022 × 132.15 (mol. wt. of ferrosilite) = 2.91

Similarly, olivine has 0.548 SiO_2 and total MgO + FeO = 1.096.

	Mol. #	Fo	Fa
SiO_2	0.548	0.4795	0.0685
FeO	0.137		0.137
MgO	0.959	0.959	

CIPW normative fo = 0.4795 × 140 (mol. wt. of fo) = 67.13
CIPW normative fa = 0.0685 × 204 (mol. wt. of fa) = 13.97

Adding up all the normative components, en + fs + fo + fa, we get a total of 99.37.

may be further broken down into forsterite (*fo*) and fayalite (*fa*) components), nepheline (*ne*), and quartz (*q*). There are websites available that perform norm calculations, and here I will not carry out the series of steps needed to perform a complete norm calculation. Instead, I will use a couple of examples to illustrate the principle of norm calculation.

The following important assumptions are made in norm calculation:

1. Hydrous phases are ignored and the magmas are assumed to be "dry."
2. Mafic minerals are assumed to be free of Al_2O_3. Alumina content is used to calculate the feldspars or feldspathoids.
3. Mg/Fe ratio of all Mg- and Fe-containing minerals is assumed to be the same.
4. The procedure recognizes the incompatibility of quartz and feldspathoids (e.g., nepheline, leucite) based on the well-founded observation that quartz and feldspathoids can never occur in the same rock under equilibrium conditions. Thus, quartz and nepheline never appear together in the norm of any rock.

None of these assumptions are particularly "way off base." However, like any simplifying procedures, the norm calculation procedure also has its limitations, for example, ignoring hydrous phases renders this method to be of limited application to andesitic rocks. Perhaps the greatest value of norm calculation is in the classification of basaltic rocks, as will be seen in a later chapter.

Utility of Norm Calculation: The Bottom Line

In this modern world of high-tech instruments and high-precision trace element and isotopic analyses, the student may wonder if there is any value to calculating norm. I believe that the real advantage of calculating norm is that it allows a way to compare volcanic rock compositions, specifically basaltic rocks, to phase diagrams. Such information is useful in deducing melting, crystallization, and mixing histories of individual magmatic suites, as we will see in a later chapter.

O'Hara (1965) was one of the pioneers who demonstrated the power of plotting normative compositions of basaltic rocks on phase diagrams in making petrogenetic inferences. Noting that the components CaO, MgO, Al_2O_3, and SiO_2 comprise more than 90 % of mafic and ultramafic rocks and contain all the major minerals that form upper mantle peridotites and those that crystallize in a basalt magma, he reasoned that converting normative compositions of natural basalts to these four components would allow a direct comparison of the phase relationships in this system with natural mafic and ultramafic rocks. This comparison can then lead to a more quantitative understanding of basalt magma generation and crystallization at various pressures. The utility of plotting normative compositions of basalts in various phase diagrams will become clearer as we delve into the issues of basalt magma formation and crystallization in later chapters.

Summary

1. Magma can be classified into ultramafic, mafic, intermediate, and felsic types based on their chemical composition. Mg and Fe decrease from ultramafic to felsic while Si and (Na + K) increase.
2. In terms of atomic structure, silicate magma is principally composed of polymerized SiO_4 chains and network modifier cations.
3. Density increases from felsic to ultramafic magma, whereas viscosity decreases. Dissolved volatiles dramatically decrease viscosity of magma. Increasing presence of crystals increases viscosity.
4. Undercooling of the magma controls crystal size, morphology, and sequence in which different phases appear.
5. Crystal size distribution or CSD is a powerful way to understand the magma's cooling history.
6. Volcanoes can be of many different types—ranging from large shield volcanoes to tuff cones and scoria cones. Mafic lavas are in general the least viscous and form the largest volcanoes with long flowing lava flows. Felsic volcanoes form smaller volcanoes.
7. Intrusions are of two fundamental types—plutons and hypabyssal intrusions. Batholiths, stocks, and lopoliths are various types of plutons, whereas dikes, sills, laccoliths, ring dikes, and cone sheets are all various types of hypabyssal intrusions.
8. Plutonic rocks are classified on the basis of mineralogy and texture. Volcanic rocks are classified on the basis of their major element chemistry.
9. CIPW norm classification is a useful way to convert chemistry into potential mineral proportions.

Exercises

1. In the following sketch, a magma chamber has formed a 100-m-thick boundary layer of troctolite, i.e., a rock composed of olivine and plagioclase crystals. There is no layering in the rocks that comprise the boundary layer.

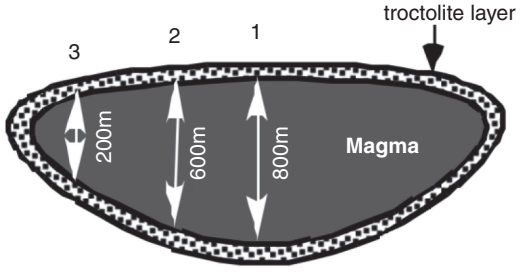

If a spherical block of 150 cm diameter breaks off from the roof at each of the sites 1, 2, and 3, then how long will it take for the blocks to reach the bottom at each site? Assume that the densities of troctolite and magma are 3.0 and 2.8 g/cm^3, respectively. Newtonian viscosity of the magma = 50 Pa.s. [*Answer*: *site 1*: *2.72 h*, *site 2*: *2 h*, *site 3*: *0.7 h*]

2. An experimental study by I. Kushiro has given the following data on relationship between pressure (P), density, and viscosity of crystal-free basalt magma.

P (GPa)	Viscosity (Pa-s)	Density (g/cm^3)
0	9.8	2.62
1	4.7	2.79
2	2	3.02
3	1	3.1

Plot these data on two separate graphs and obtain mathematical relationships between (a) pressure and viscosity and (b) pressure and density. (c) Calculate the viscosity of crystal-free basalt magma at 4 GPa. [Answer to (c): 0.45 Pa-s]

3. Assuming that the basalt magma rises from 120 to 50 km through a dike of 1 m diameter (d), calculate its velocity (v in cm/s) at the following depths: 100, 80, 70, and 50 km using the following equation (discussed later in Chap. 5): velocity $(v) = [d^2 \cdot \Delta\rho \cdot g]/64\eta]$ where $\Delta\rho$ = density of wall rock (density of magma), g = acceleration due to gravity, and η = magma viscosity.
[Assume 1 GPa = 30 km]. Calculate density and viscosity of magma using the equations below. Densities of wall rocks are given in the table below.

Viscosity (Pa-s) $= 0.8356e^{(-0.77P)}$	
Density(g/cm^3) $= -0.035P^3 + 0.135P^2 + 0.07P + 2.62$	
Depth (km)	Density of wall rock (g/cm^3)
0–50	2.0
51–70	3.04
71–80	3.30
81–100	3.30

Plot the calculated velocities (cm/s) on X-axis and depth on Y-axis. At what depth will the magma stop rising?

4. Calculate how long (in days) it will take for a fully molten magma body to completely crystallize, assuming a constant nucleation rate of 10^{-3} cm^3/s and growth rate of 10^{-10}cm/s. Keep the calculation range within 1 and 120 days and 20 day intervals. Plot the curve that describes crystal% versus time (days). Within what range of days is the solidification rate the highest? (Refer to Box 2.3 to solve this problem.)

Phase Relations in Simple Systems: Key to Magma Generation, Crystallization, and Mixing

3

Please note the Erratum to this chapter at the end of the book

Abstract

Minerals and rocks form in a variety of temperature and pressure conditions within the earth. An understanding of their origin requires elementary knowledge of thermodynamic principles. The objective of this chapter is to introduce the student to such concepts; however, a rigorous thermodynamic treatment of mineral phase equilibrium is beyond the scope of this book. In this chapter the student will be exposed to geometrical techniques that can be used to understand the conditions of melting and crystallization in simplified mineral–melt systems that serve as analogs of magma formation and crystallization. The phase diagrams discussed in this chapter refer almost exclusively to igneous systems, i.e., crystallization of minerals from melts.

Elementary Thermodynamics

The subject of thermodynamics deals with stability of minerals and other materials in a variety of pressure and temperature conditions. Phase diagrams are a graphic means of portraying the stability of phases in pressure–temperature–composition space. Where thermodynamic stability of minerals/materials is concerned, adequate descriptions require an understanding of such terms as system, phases, degrees of freedom, and components. These terms are first explained in the following paragraphs.

System. The definition of a *system* depends on how one defines its boundaries! While this statement may seem very abstract, it is nonetheless the most appropriate definition. If our problem is to examine the behavior of atoms within a mineral, then that mineral can be "isolated," in an abstract sense, from the rock and be considered as a system that is contained within it. Consideration of all other minerals in that rock may be totally irrelevant to the mineral's internal atomic behavior; in such a situation, the mineral, rather than the rock, is the system. On the other hand, if our interest is in the crystallization or melting behavior of this mineral, then the entire rock must be considered as the system because in such a case, this mineral's crystallization and melting behavior is tied to that of the other minerals in the rock.

In a *closed system,* the system does not exchange materials with its surroundings, whereas in an *open system,* such exchange occurs. In both cases, however, the system can exchange energy with the surroundings. Note that in our discussion in this chapter, closed systems are most commonly discussed.

Phase. A phase is a physically distinct and mechanically separable part of a system. Consider, for example, the rock *gabbro*. Gabbro is principally composed of only two minerals—pyroxene and plagioclase. Each of these two minerals (but not each grain of these minerals) is distinct by virtue of its compositional characteristics and therefore is a *phase*. A phase may exist in solid, melt, or gaseous states. If we are dealing with an immiscible mixture of oil and water, then the two are distinct phases although both are in a melt state because they are "physically distinct and mechanically separable."

Components. Each phase in a system is composed of chemical components. The number of chemical components in a system is the *minimum number of chemical constituents* required to define the compositions of all phases in the system. For example, consider the system forsterite–quartz.

G. Sen, *Petrology*, DOI 10.1007/978-3-642-38800-2_3,

The chemical composition of forsterite may be written as Mg_2SiO_4 or $2MgO{\cdot}SiO_2$, and quartz is SiO_2. Although three elements occur in this system—Mg, Si, and O—compositions of the phases in this system can be entirely described with just two (i.e., Mg_2SiO_4 and SiO_2 *or* MgO and SiO_2) rather than three (i.e., Mg–Si–O) components. Therefore, the system forsterite–quartz is considered to be a two-component and not a three-component system.

One-, two-, three-, and four-component systems are called *unary, binary, ternary, and quaternary systems*. It turns out that although rocks contain a large number of components, much of their phase relationships can often be adequately described with systems containing as few as three components. Therefore, in a later section of this book, a rigorous geometrical analysis of phase relationships in some important but simple one-, two-, and three-component systems is carried out.

Chemical Potential and Gibbs Energy

The chemical potential (μ) may be viewed as an inherent tendency of a material to react. A chemical reaction within a system may occur when reactants have higher chemical potential than the products. For example, consider the polymorphic transformation reaction between diamond (chemical potential—μ_d) and graphite (chemical potential—μ_g).

Figure 3.1 shows that at a temperature of 1,000 °C and pressure of 6 GPa (=60 kbar, which is roughly equivalent to a depth of 200 km in the earth), diamond is the stable mineral, and that is because $\mu_d < \mu_g$ at such a pressure (P)- temperature (T) condition. By similar reasoning, at ~1,000 °C and 2 GPa, graphite is stable (i.e., $\mu_g < \mu_d$). At equilibrium $\mu_g = \mu_d$, or, the chemical potential difference, $\Delta\mu = \mu_d - \mu_g = 0$.

When a phase is composed of more than one component, it is necessary to consider the *Gibbs energy*, or G, which is the sum of the chemical potential of each component times the number of moles of each components in the phase. Thus, Gibbs energy, or simply the *free energy*, may be expressed as

$$G = \sum_i \mu_i n_i$$

where μ_i and n_i are the chemical potential and number of moles of component "*i*." For a pure phase in a one-component system, $G = \mu$. When individual phases are not pure but are solid solutions, one has to calculate G by considering free energy contributions made by each end-member in the solid solution series. An important thing to note is that the free energy of the solid solution will always be lower than the value one would obtain by simply mixing the two end-members. This may be illustrated using the mineral olivine. Olivine forms a complete two-component solid solution between forsterite (Mg_2SiO_4) and fayalite (Fe_2SiO_4) end-members. Consider an olivine crystal that has 80 mol % forsterite component and 20 mol% fayalite in solid solution. Its composition is written as Fo_{80}. In terms of mole fractions, the same olivine crystal has 0.8 mol fraction of forsterite and 0.2 mol fraction of fayalite. In a general sense, in any binary system, if a solid solution has X moles of one of the components, then it must also contain $1-X$ moles of the other component. The free energy $(G_{ol})^{mix}$ of the mixture made up of 0.8 mol fraction of forsterite and 0.2 mol fraction of fayalite will simply be

$$(G_{ol})^{mix} = 0.8(\mu_{fo})^{ol} + 0.2(\mu_{fa})^{ol}$$

Using $\mu_{fo} = -2{,}202.4$ kJ/mol and $\mu_{Fa} = -1{,}523.17$ kJ/mol, we get a G value of $-2{,}066.55$ kJ/mol for the mixture. However, the free energy of the olivine solid solution at any temperature will be calculated from the following equation:

$$(G_{ol})^{\text{solid solution}} = X_{Fo}\mu_{fo} + RT \cdot X_{Fo} \ln X_{Fo} \qquad (3.1)$$

Using Eq. (3.1) above, we calculate $(G_{ol})^{\text{solid solution}}$ of the olivine crystal (Fo_{80}) to be $-4{,}507.31$ kJ/mol at a temperature of 1,923 K. ($R = 8.314$ J/K-mol and using the above chemical potential.) Thus, the olivine solid solution has a lower free energy than the mechanical mixture of the two end-members, which makes the solid solution stable. Figure 3.2 shows free

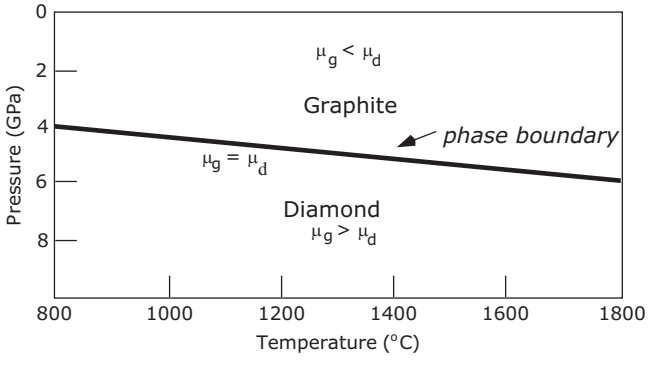

Fig. 3.1 Stability fields of diamond and graphite in pressure–temperature space

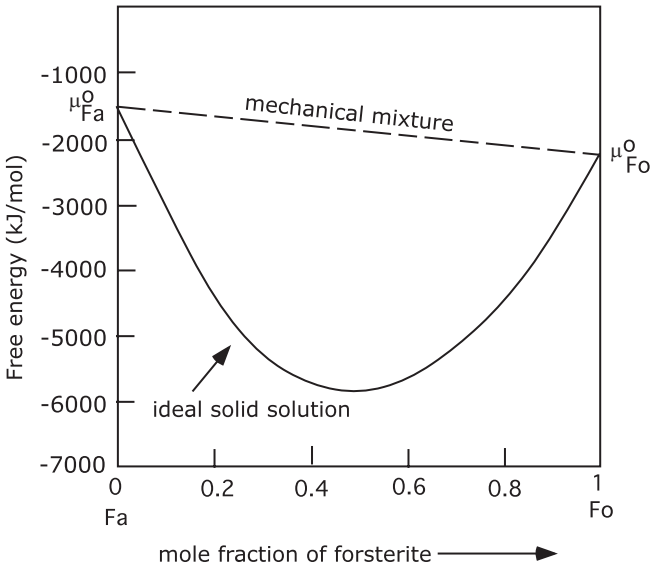

Fig. 3.2 Free energy (G)–composition (X) diagram for olivine

energy–composition (G–X) diagram for olivines calculated from Eq. (3.1).

In general, the total free energies of the reactants and of the products are equal when they are in chemical equilibrium, that is, $\Delta G = G_{\text{products}} - G_{\text{reactants}} = 0$ at equilibrium. A reaction may proceed only when $G_{\text{reactants}} > G_{\text{products}}$ (i.e., $\Delta G < 0$).

Free Energy, Enthalpy, and Entropy

The Gibbs energy or free energy of a substance or system is also given as

$$G = H - TS$$

where H is the heat content, or *enthalpy*, and S is its *entropy*, which is a measure of the degree of disorder. H is mathematically defined as

$$H = E + PV$$

where E is the *internal energy* of a system and P and V are pressure and volume, respectively.

Heat capacity at constant pressure (C_p) is defined as the heat required to increase the temperature of 1 mol of a substance by 1 °C at constant pressure. The temperature of a substance increases roughly proportionally as it is heated at a constant pressure. C_p is generally expressed as a proportionality constant as follows:

$$dH = C_p dT \text{ or } C_p = dH/dT$$

Tables of data on enthalpy, heat capacity, volume, and other thermodynamic parameters of minerals can be found in many publications or on the Internet (listed in references). Generally, these values are experimentally measured or calculated at a reference temperature of 298.15 K and 1 bar pressure. This reference state is generally expressed as a superscript "o" on the property in consideration, e.g., G^o and H^o, unless stated otherwise elsewhere in the text.

Determination of the values of these parameters at temperature and pressure other than the reference state requires additional calculations. For example, H at a particular temperature T can be integrated from H^o (i.e., H at 1 bar pressure and 298 K temperature) as follows:

$$_{298}\int^{T} dH = {}_{298}\int^{T} C_p dT$$

$$H_T - H^o = {}_{298}\int^{T} C_p dT$$

C_p of a mineral or glass is generally a polynomial function of temperature and may be given as

$$C_p = a + bT - c/T^2$$

where a, b, and c are experimentally determined constants for the mineral or material of interest. Thus, H_T can now be obtained by combining the last two equations above:

$$H_T = H^o + {}_{298}\int^{T} [a + bT - c/T^2] dT \text{ or } H_T$$
$$= H^o + [(a + bT^2/2 + c/T) dT]^{T}_{298}$$

Entropy may be thought of as a degree of disorder. The molecules of a substance are much more dispersed (i.e., greater disorder) in a gaseous state than in a melt state. Thus,

$$S_{\text{gas}} > S_{\text{melt}} > S_{\text{solid}}$$

The entropy of a mineral can be calculated from relations between heat capacity and entropy, as laid down by the laws of thermodynamics (discussed in the next section):

$$dS = dH/T$$

$$dS = [C_p dT]/T$$

The entropy of any phase at a temperature T may be calculated from S^o and C_p as follows:

$$_{298}\int^{T} dS = {}_{298}\int^{T} (a/T + b - c/T^3)dT$$

$$S_T = S^o + [a \ln T + bT + (c/2T^2)]^{T}_{298}$$

$$S_T = S^o + a \ln (T/298) + b(T - 298) + (c/2)(1/T^2 - 1/298^2)$$

Similarly, the free energy of any substance can be calculated at a high P, T from the above equations. In a reversible reaction,

$$\Delta G^{P,T} = \Delta G^o + {}_1\int^{P} V^o dP, Z$$

which is the same as

$$\Delta G^{P,T} = \Delta H^o - T\Delta S^o + (P - 1)\Delta V^o Z$$

Therefore, from equations above, we get

$$\Delta G^{P,T} = [H^o + {}_{298}\int^{T} C_p dT] - T[S^o + {}_{298}\int^{T} (Cp/T)dT] + {}_1\int^{P} V^o dPZ$$

The Clausius–Clapeyron Equation

The *first law* of thermodynamics states that the internal energy (E) of an *isolated system* is constant. The first law is best understood by the mathematical representation:

$$dE = dQ - dW$$

where dQ represents the amount of heat added to the system. The system expends this heat by performing a certain amount of work (dW). The usual example used in thermodynamics textbooks to explain the first law is that of heating a gas in a cylinder fitted with a frictionless piston. When this gas is heated, its volume expands and displaces the piston, i.e., the system performs work. Normally, work is defined as force multiplied by the distance. In the example given, the work done is pressure–volume work or

$$dW = PdV$$

where P is pressure that causes the volume to change by dV and the first law can be rewritten as

$$dE = dQ - PdV$$

In a reversible reaction, the second law of thermodynamics is expressed as

$$dS = dQ/T$$

Combining the above equations, we get

$$dE = TdS - PdV$$

Recall that

$$G = H - TS \text{ or } G = E + PV - TS$$

Differentiating and rearranging,

$$dG = (dE + PdV - TdS) + VdP - SdT$$

However, $dE + PdV - TdS = 0$, therefore

$$dG = VdP - SdT$$

In order to understand the utility of the above relationship, consider the equilibrium transition between diamond and graphite as an example, where diamond is a high-pressure polymorph of carbon:

$$\text{Graphite} = \text{Diamond}$$

At equilibrium, the free energies (chemical potentials) of diamond and graphite must be equal. Therefore, we get

$$V_g dP - S_g dT = V_d dP - S_d dT \text{ or } V_d dP - V_g dP = S_d dT - S_g dT$$

where the subscripts "d" and "g" stand for diamond and graphite, respectively.

The above equation can be rewritten below as

$$\Delta V dP = \Delta S dT \text{ or } dP/dT = \Delta S/\Delta VZ \qquad (3.2)$$

Table 3.1 Thermodynamic data for the aluminosilicate phase diagram

Mineral	V (cm^3/mol)	S (J/mol/K)	H (kJ/mol)
Kyanite	44.69	236	−2,519.31
Sillimanite	50.23	246.9	−2,512.78
Andalusite	52.29	245.1	−2,515.15

where ΔV and ΔS are volume and entropy differences, respectively, for the graphite = diamond reaction.

Equation (3.2) is known as the *Clausius–Clapeyron equation*. This equation is useful in that the slope of any equilibrium reaction boundary between any numbers of minerals can simply be calculated if their entropy and volume data are known. Such data on minerals are easily available (see references). Below is a worked-out example in which the aluminosilicate (Al_2SiO_5) phase diagram has been calculated from entropy–volume data.

Table 3.1 gives a set of thermodynamic data at 500 °C and 1 bar for the aluminosilicate phases. The Clapeyron slope (dP/dT) for each of the reactions may be calculated as follows:

$$\text{Reaction}: \textit{Kyanite} \leftrightarrow \textit{Andalusite}$$

$$dP/dT = \Delta S/\Delta V = (245.1 - 236)/(52.29 - 44.69) = 1.197 \text{ MPa/K} = 11.97 \text{ bar/K}$$

Similarly, we get the following dP/dT's for the following reactions: *Kyanite* ↔ *Sillimanite* = 19.8 bar/K and *Andalusite* ↔ *Sillimanite* = −8.7 bar/K.

We now need to calculate at least one point in P, T space for each of the three reactions above in order to completely draw the phase diagram. We know that at equilibrium, $\Delta G = \Delta H - T\Delta S = 0$ for each one of the three reaction boundaries. Therefore, equilibrium temperature $(T_e) = \Delta H/\Delta S$. As an example, we calculate the T_e at 1 bar for the reaction:

$$\textit{Kyanite} \leftrightarrow \textit{Andalusite}: T_e = [\Delta H/\Delta S]_{ky=and} = (-2515150 + 2519310)/(245.1 - 236)] = 457\text{K}$$

Similarly, we obtain for *Kyanite* ↔ *Sillimanite*, T_e = 599 K, and for *Andalusite* ↔ *Sillimanite*, T_e = 1,317 K.

We know from published reports that *Kyanite* ↔ *Sillimanite* boundary does not extend to 1 bar pressure. Therefore, the T_e for this reaction at 1 bar cannot be correct. Without going into much additional detail, note that this temperature at 1 bar pressure is the location of the metastable extension of the equilibrium boundary. Based on the calculated values of T_e and slopes of the curves for the reactions *Kyanite* ↔ *Andalusite* and *Andalusite* ↔ *Sillimanite*, the two curves are drawn first in P, T space. Then, the *Kyanite* ↔ *Sillimanite* boundary is constructed with the calculated slope (19.8 bars/K) through the point (which is the invariant point on this diagram, discussed in the later section) where the other two curves meet (Fig. 3.3).

This phase diagram is extremely important in metamorphic petrology as a measure of P–T of metamorphic mineral assemblages. It is worth mentioning that even this apparently simple Al_2SiO_5 system is not so simple in the sense that large uncertainties exist in experimental and calculated data on each of the three reaction boundaries. Metastable persistence of these phases way beyond their stability field has also been demonstrated in many field studies of metamorphic rocks.

Phase Rule and Phase Diagrams

The phase rule, or the Gibbs phase rule, was perhaps one of the most outstanding contributions to science made in 1,876–1,878 by J. Willard Gibbs, an American chemist. The phase rule states that in a system of c components and ϕ phases, the variance (f) or degrees of freedom,

$$f = c - \phi + 2$$

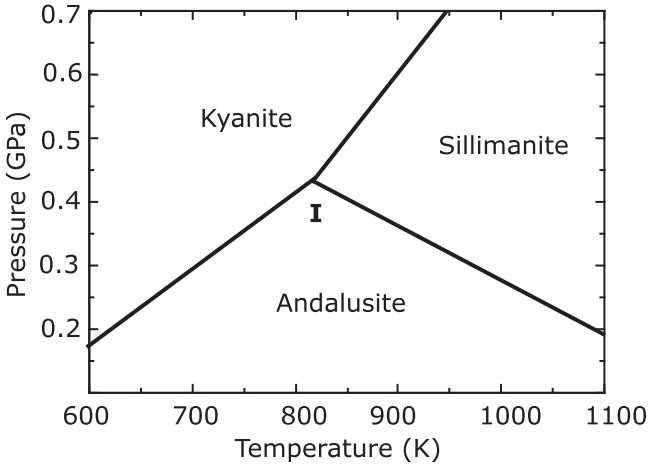

Fig. 3.3 The aluminosilicate phase diagram calculated here. Point "*I*" is the invariant point or "triple point" where all three minerals coexist

"*f*," or degrees of freedom, represents the number of intensive variables (temperature, pressure, and composition) that can be changed independently without the loss of a phase. The numerical "2" represents pressure and temperature; when one of these is held constant, then the numeral reduces to "1." At constant pressure (or temperature), the phase rule thus reduces to $f = c - \phi + 1$. The implications of the phase rule may be understood with the following example of the Al_2SiO_5 system (Fig. 3.3).

Unary Systems

The Al_2SiO_5 system is a good example of a unary system in which there is only one component (Al_2SiO_5) and three phases—kyanite, sillimanite, and andalusite. These three phases are polymorphs because they have the same chemical composition but different atomic structures. Following the phase rule, we know that in any one-component system, a maximum of three phases can coexist at a point, called the *invariant point,* because the variance or the degree of freedom (f) is zero. ($c = 1$, $\phi = 3$, so $f = 1 - 3 + 2 = 0$.) This is point "*I*" in Fig. 3.3. The phase rule also informs us that when two phases can coexist in a one-component system, $f = 1$. This means that two phases can occur only along a line where both phases are stable because only along a line can one simultaneously vary P and T (but not independently of each other) and still have both phases present. This line is called a *univariant line* because along it, $f = 1$. As we can see in Fig. 3.3, the three univariant lines are kyanite = sillimanite, andalusite = sillimanite, and kyanite = andalusite. In this diagram, there are three fields where the three phases are stable. Each of these is called a divariant field because $f = 2$ in each field.

It is important to understand that the phase rule does not say anything about the maximum number of phases that can occur in a system. For example, consider the unary system SiO_2. A large number of phases occur in this system, for example, melt SiO_2, α-quartz, β-quartz, tridymite, cristobalite, coesite, and stishovite (Fig. 3.4). Note that not all of these phases are stable around a single invariant point in this diagram, because the phase rule allows only a maximum of three phases at any single invariant point in unary systems.

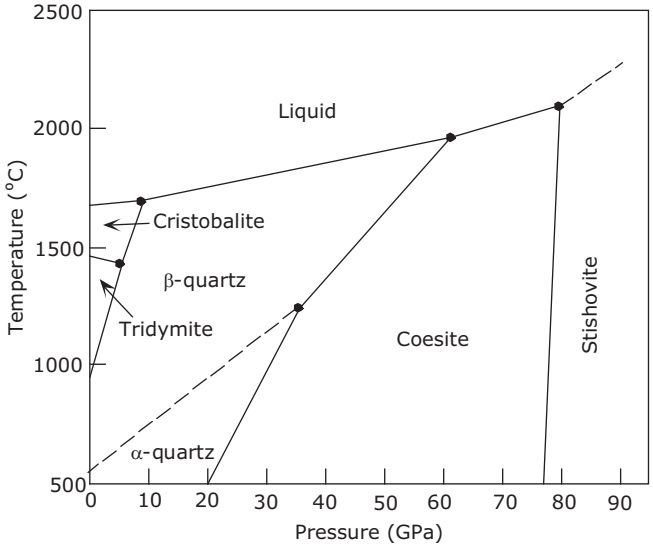

Fig. 3.4 Phase diagram for the unary system silica; invariant points are shown as *dots*

Binary Systems

Graphical Representation

Two-component systems at a constant pressure (*isobaric* phase diagram) are best viewed in terms of a temperature–composition (or *T–X*) graph, in which temperature is plotted on the *Y*-axis and composition is plotted on the *X*-axis. One has a choice of plotting *molar* or *weight percentages* of the two components on the composition axis. The choice of molar versus weight percent makes a big difference in the nature of the phase diagram; therefore, it is important to understand what is being plotted—weight or mole proportions.

Consider the examples of forsterite and enstatite, both of which are composed of MgO and SiO_2. Their formulae can be written as $2MgO{\cdot}SiO_2$ and $MgO{\cdot}SiO_2$, respectively; that is, the ratio of MgO to SiO_2 moles is 2:1 in forsterite and 1:1 in enstatite. In terms of mole percent, enstatite can be thought of a 50:50 combination of Mg_2SiO_4 and SiO_2 (i.e., MgSiO3 = 0.5 Mg_2SiO_4 + 0.5 SiO_2). Therefore, in a molar plot, enstatite plots in the middle between forsterite and SiO_2 (Fig. 3.5). The molecular weight of forsterite is 140.38, and its chemical composition is 57 wt% MgO and 43 wt% SiO_2. Enstatite has 40 wt% MgO and 60 wt % SiO_2. Therefore, in a weight percent plot between

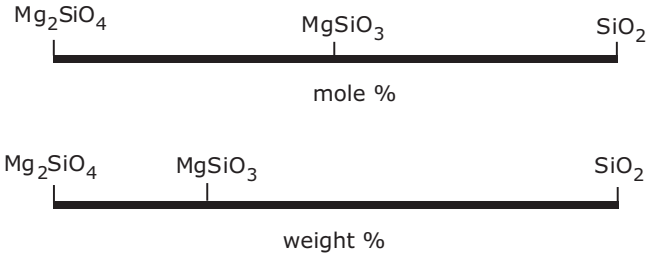

Fig. 3.5 Location of enstatite in mole versus weight percent diagrams

forsterite and silica, enstatite will plot at the 70.2 % forsterite and 29.8 % SiO_2 point. In this particular example, the differences between mole percent and weight percent plots are clearly large and demonstrate how important it is to note whether a particular phase diagram is a mole% or weight% diagram. All phase diagrams in this chapter are weight% diagrams unless otherwise specified.

Phase Relations

Binary systems exhibit a wide range of mineral–melt phase relationships—from eutectic crystallization (and melting) to solid solution to incongruent melting (peritectic reaction). We will explore these different types of phase behavior with a number of binary systems that are of relevance to petrology. In each system, we will consider two extreme conditions of crystallization from melts and melting of solids: in *equilibrium crystallization* (and *equilibrium melting*), chemical equilibrium is always maintained between coexisting phases, and in the other (*fractional crystallization* and *fractional melting*), rapid physical separation of melt and crystals results in complete disequilibrium between phases. In nature, crystallization of magmas and melting of rocks likely follow some intermediate paths between the two extremes mentioned.

Binary Solid Solutions

Plagioclase and olivine are two important and common minerals that exhibit extensive solid solution between two end-members. Natural olivine crystals are nearly perfect binary solutions between forsterite and fayalite and usually contain less than 1 wt% dissolved Ni and Ca. We use olivine as an example to illustrate the phase relationships in binary solid solutions.

At atmospheric pressure, the olivine phase diagram forms a "loop" in a temperature–composition (*T*–*X*) diagram, with the melting points of forsterite and fayalite defining the two ends of the loop (Fig. 3.6). The higher temperature and the lower temperature curves of the loop are known as the *liquidus* and *solidus*, respectively. Above the liquidus, only a melt phase is stable, and below the solidus, a solid phase is stable. Between the liquidus and solidus, a solid phase coexists with a melt phase. Note that the increase of pressure causes the melting points of both forsterite and fayalite end-members to increase, and therefore, the entire liquidus–solidus loop is also shifted to higher temperatures.

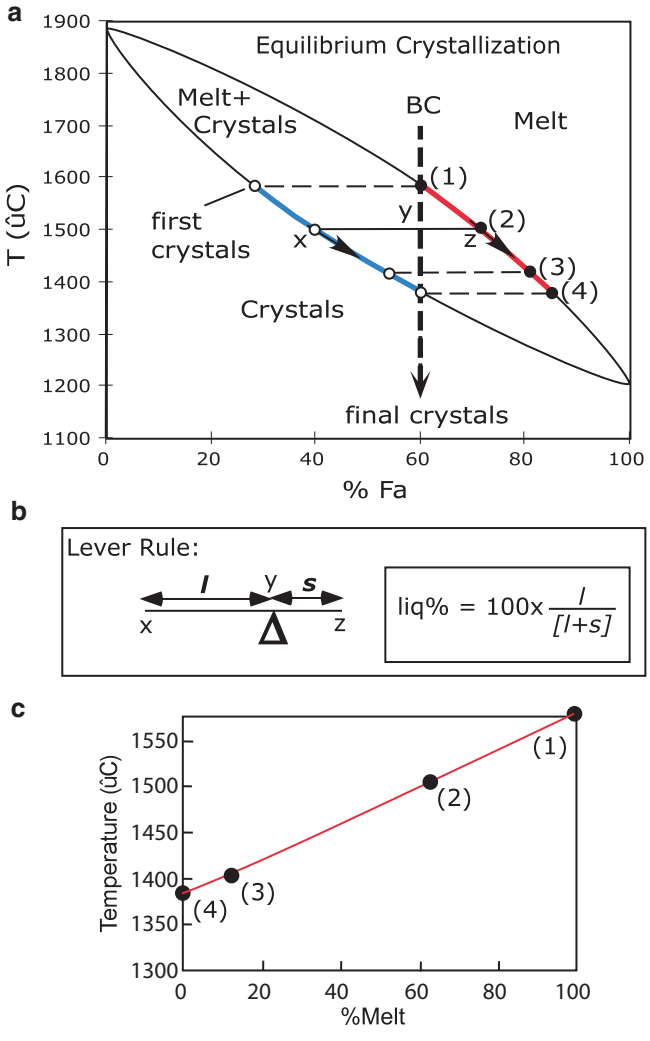

Fig. 3.6 Equilibrium crystallization of a liquid of composition "BC" in the system forsterite–fayalite at 1 atm pressure

Equilibrium Crystallization and Equilibrium Melting in the Olivine System

Consider the case of a melt of bulk composition "BC" (i.e., 60 % fayalite, 40 % forsterite, or $Fo_{40}Fa_{60}$) (Fig. 3.6a). This melt will begin to crystallize when it

is cooled to its liquidus temperature of 1,590 °C [stage (1)]. The composition of the first crystal that will form in equilibrium with this melt can be determined by drawing a line, called a *tie-line*, from the liquidus intersection point to the solidus at 1,590 °C. In this example, the coexisting solid phase will have a composition $Fo_{75}Fa_{25}$. As the melt + crystal assemblage is cooled, the crystals and melt will continuously exchange components and thus gradually change their compositions along the solidus and liquidus, respectively. The final solid must have the same composition as the initial melt [i.e., the bulk composition, stage (4)]. The compositional change in the melt (*melt path*) is shown as (1) through (4), as the corresponding olivine changes (*solid path*, Fig. 3.6a).

At any given temperature, the compositions of the coexisting solid and melt phases are given by the solidus and liquidus, respectively; for example, at 1,400 °C the coexisting solid and melt compositions are $Fo_{45}Fa_{55}$ and $Fo_{20}Fa_{80}$, respectively. One can also calculate the melt and solid proportions at any temperature using the *lever rule*. The *lever* is a tie-line connecting the coexisting phases at a given temperature, and the bulk composition is the "fulcrum" of the lever. The lever rule makes use of the constraint that no matter how many crystals have formed in the melt, the bulk composition (i.e., crystals + melt) at all times must remain constant (because crystals and melt are not taken out). At 1,525 °C [stage (2) in Fig. 3.6a, b], a "lever" x–z is drawn, where x and z are coexisting solid and melt compositions, respectively. Since BC is the bulk composition, it follows that it can be defined by the sum of the proportions of the solid x and melt z. In our example, we can calculate the percentage of melt using the lever rule as

$$\text{liq}\% = 100 \times \frac{l}{[l+s]}$$

where l is the distance between x and y and s is the distance between y and z (Fig. 3.6b). Since this is a binary system, %crystals = 100 − %melt. Thus, using the lever rule, one can calculate %melt (or solid) as a function of temperature for a given bulk composition. Figure 3.6c shows such a plot for the bulk composition we selected.

In *equilibrium melting*, the solid and melt paths are exactly reversed; for example, an olivine of composition $Fo_{40}Fa_{60}$ will not melt until the temperature reaches ~1,380 °C (Fig. 3.6). As the temperature is raised further, more melting will occur at the expense of crystals. At each temperature, the proportion of melt and solid phases can once again be calculated from the lever rule. Complete melting will take place at 1,590 °C, i.e., the liquidus temperature of the $Fo_{40}Fa_{60}$ olivine.

Fractional Crystallization

In fractional crystallization, crystals are removed from the melt as soon as they form; thus, with every infinitesimal cooling step, a new bulk melt composition is created that is more fayalite-rich than the melt that would form by equilibrium crystallization. Such perfect removal of crystals makes it theoretically possible for the melt path to be extended to pure fayalite composition (Fig. 3.7). Two types of solid paths are recognized in fractional crystallization: *instantaneous solid path* (*ISP*), one that tracks the compositions of solids that are in equilibrium with melt at each *instant* of crystallization, and total solid path (TSP), which tracks the *integrated* compositions of all solid fractions. In fractional crystallization the ISP falls on the solidus and can reach pure fayalite composition, but the TSP follows a curved path (which can be calculated but is somewhat complex) below the solidus and reaches the bulk composition when the last drop of melt runs out (Fig. 3.7). Qualitatively, one can see why the TSP curve is of this form by examining the vectors (the short arrows) at each temperature of crystallization. In fractional crystallization, the system cools rapidly so that the solid and liquid phases cannot maintain chemical equilibrium, and hence the cooling vector is longer than the compositional vector. When the liquid path (LP) reaches close to the end point of crystallization, the TSP must curve more slowly toward the bulk composition of the system.

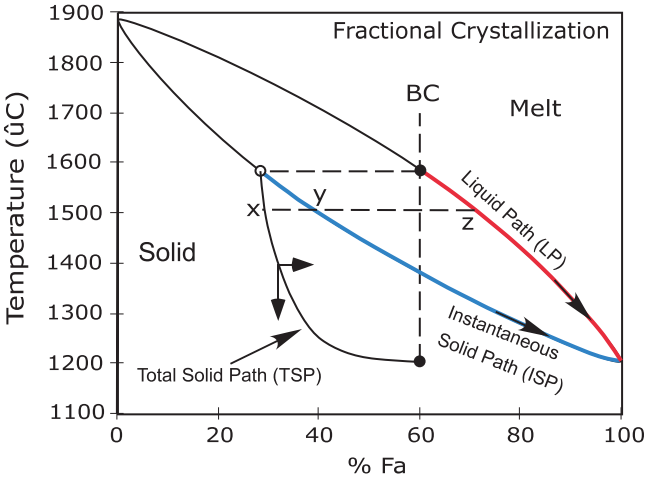

Fig. 3.7 Fractional crystallization of a liquid in the system forsterite–fayalite

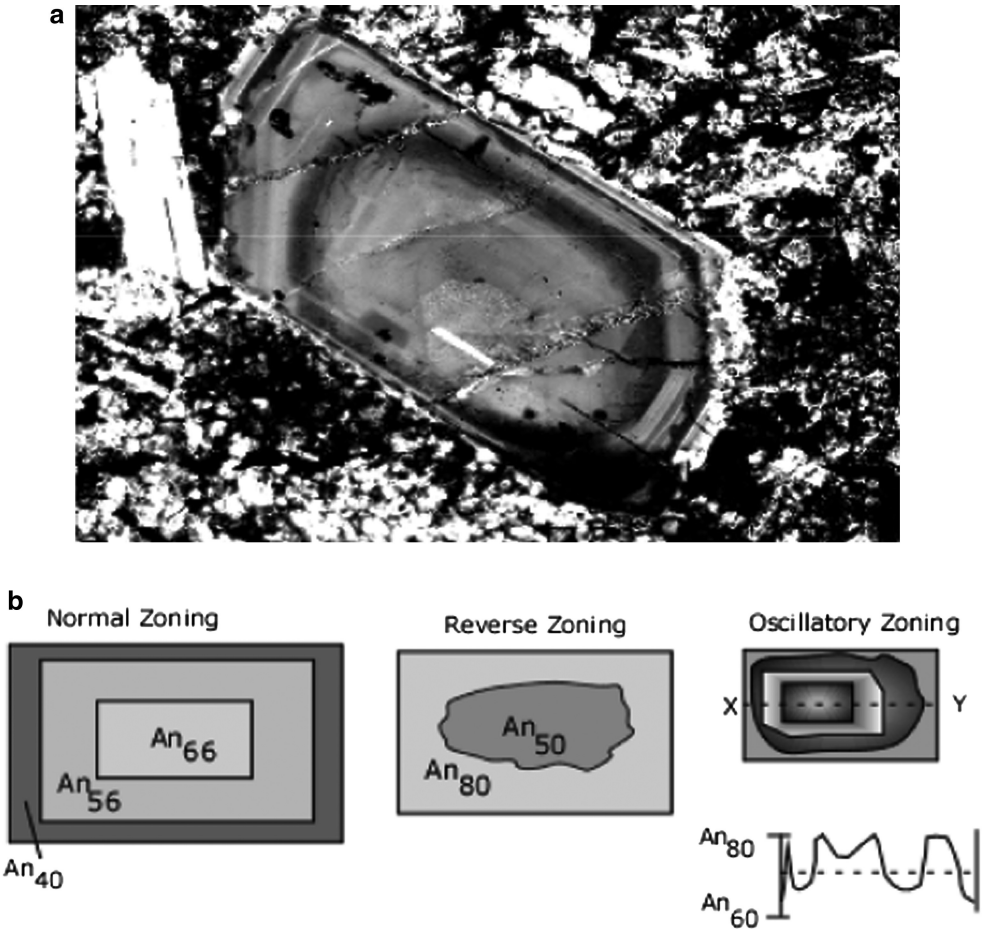

Fig. 3.8 (**a**) Photomicrograph of a plagioclase with oscillatory zoning (magnification: ×80). (**b**) Three basic types of zoning illustrated

Fractional crystallization can produce zoned olivine crystals that are common in alkali olivine basalts. Strong compositional zoning in plagioclase crystals is more common in basaltic lavas and intrusions (Fig. 3.8a). Because a growing plagioclase crystal cannot keep pace with the rapid change in melt composition, the crystal often grows in layers or zones with distinct compositions. Three basic types of zoning have been recognized: normal, reverse, and oscillatory (Fig. 3.8b). *Normal zoning* means a core to rim decrease in anorthite (An) content. In a *reverse zoned* crystal, the rim has higher An than the core. However, the most common type of zoning is *oscillatory* or more complex types of zoning where the An content oscillates considerably from core to rim. Whereas normal zoning is generally a result of crystal growth from a progressively differentiating magma, reverse and oscillatory zoning may result from a number of different processes, such as magma mixing, crystallization interrupted by magma degassing. Many times certain zone boundaries within the crystal may appear *resorbed* or uneven (Fig. 3.8b) from reaction with the surrounding melt that may have come from elsewhere (via melt mixing) and has hence temporarily thrown the crystal zone into disequilibrium.

Fractional Melting

In fractional melting, melting begins at the same temperature as in equilibrium melting, but the big difference is that the melt is removed as soon as it forms. Thus, in fractional melting, the solid residue from which melt fraction has been removed becomes a new bulk solid source composition for the next melt to be formed and extracted. Such efficient melt extraction could lead to a final solid residue composed of pure forsterite or anorthite in our olivine and plagioclase examples, respectively.

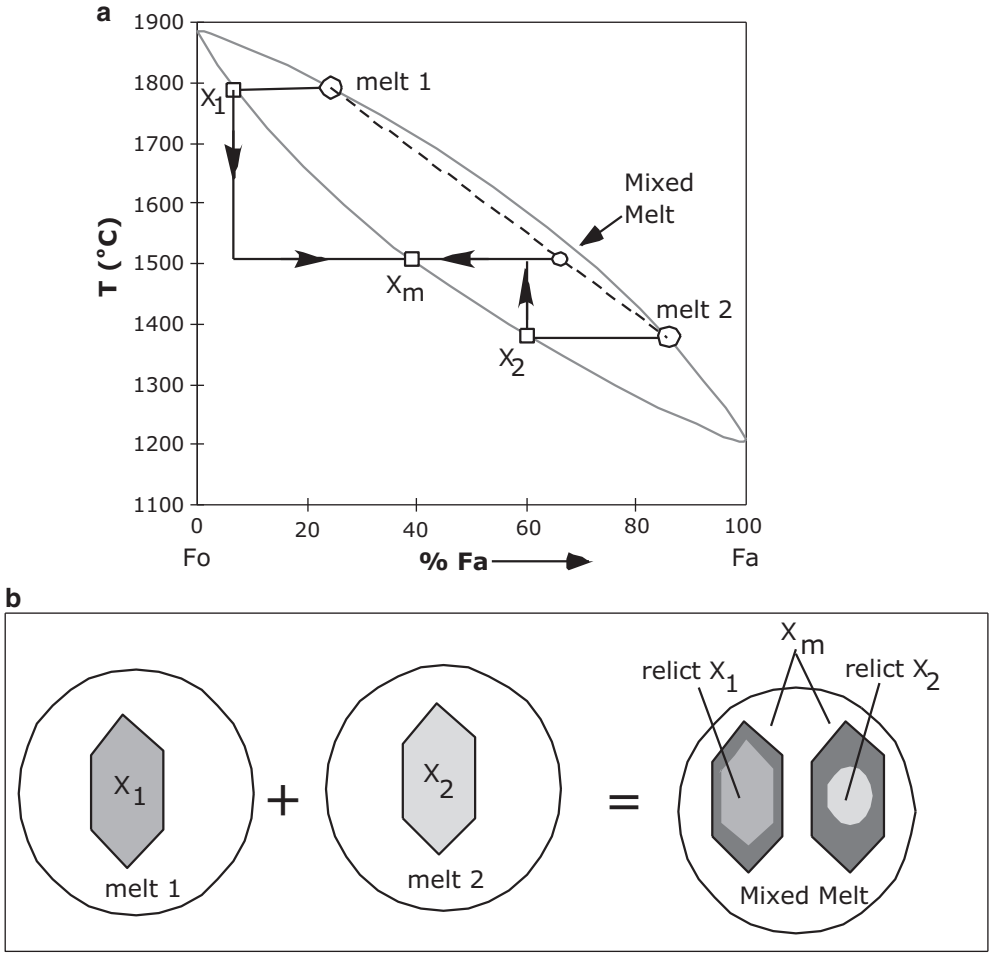

Fig. 3.9 (**a**) Mixing of melts 1 and 2 in the olivine system. X_1 and X_2 are olivine crystals in equilibrium with melts 1 and 2, respectively. X_m is the equilibrium olivine for the mixed melt. (**b**) Textural development of olivine crystals in the mixed melt

Melt Mixing

Consider a case where two melts, melts 1 and 2 (Fig. 3.9a), carrying olivine crystals (phenocrysts) of composition X_1 and X_2, respectively, are mixed (say in a magma chamber) in 25:75 proportion (for example) such that the new melt falls on a mixing line between the two melts. As Fig. 3.9a shows, the new mixed melt is situated below the liquidus, i.e., it is supersaturated. Therefore, it will be forced to crystallize crystals of composition X_m and reach the liquidus at that temperature (1,500 °C). This mixing makes both X_1 and X_2 crystals unstable in the new mixed melt, since the only solid phase that can coexist with this melt is of composition X_m. X_1 in the hotter melt will be supercooled to 1,500 °C and a euhedral rim of olivine composition X_m will grow on it (Fig. 3.9b). On the other hand, the crystal X_2 in the cooler melt 2 will be superheated and partially dissolved (resorbed) until 1,500 °C is reached, and then a rim of X_m composition will grow on it (Fig. 3.9b). In igneous rocks, mixed and differently zoned (both normal and reversed zoning) olivine, pyroxene, and especially plagioclase crystals occur. The presence of both types of zoning in a single rock is a good indicator of magma mixing.

Box 3.1: The Olivine Phase Diagram and Composition of the Earth's Upper Mantle

Rocks and minerals from the Earth's upper mantle are sometimes ripped off and brought to the surface by violent magmas. Such rocks and minerals are called xenoliths and xenocrysts, respectively. A familiar example of a xenocryst is the mineral diamond. We know that diamond can only be stable at a minimum depth of about 140 km in the upper mantle (Fig. 3.1), and

(continued)

Box 3.1 (continued)

therefore, it follows that all the world's diamonds must have been transported to the Earth's surface by magmas. Some of the deepest xenoliths and xenocrysts come from as deep as 400 km!

Scientists have long been fascinated with xenoliths and xenocrysts because they provide the only direct window into the Earth's mantle. Here, we consider an example of how a simple binary phase diagram can give us a fundamental piece of information about the composition of the Earth's upper mantle based on a study of mantle xenoliths. In 1970, James L. Carter of the University of Texas at Dallas published a research paper on a very large number of xenoliths from an area in New Mexico, called Kilbourne Hole. Using textural and chemical criteria, he could identify two classes of xenoliths—one of them being principally lherzolites (a rock generally composed of 60 % or more olivine, orthopyroxene, and clinopyroxene and with 5 % or less spinel) and the other pyroxenites (90 % or more of clinopyroxene) and wehrlites (composed largely of clinopyroxene; olivine and spinel are minor phases). (These rock names are better defined in a later chapter.) Carter plotted the compositions of olivines in the two xenoliths suites (as shown in Fig. 3.10a) and noted a fundamental difference between the two: 90 % of olivines in lherzolites are more forsteritic than Fo_{88}; whereas those in the other suite (Carter interpreted this group to have had an igneous origin, i.e., they formed by magma crystallization) are $<Fo_{86}$.

The olivine phase diagram (Fig. 3.10b) tells us that during partial fusion of an olivine, the residues of melting will be more forsteritic than the source, and the olivines that crystallize from the melts will *generally* be less forsteritic than the source. For example, when a source olivine "*Y*" (Fo_{87}) is melted, the residual olivine becomes progressively forsteritic (as shown by the arrows and the example "*X*"). Carter used this reasoning to conclude that the majority of lherzolites are residues of melt extraction and that the "*undepleted source*" lherzolite (undepleted means magma has not at all been extracted from the source) of the Earth's upper mantle must have an olivine composition of Fo_{87}, where there is a paucity of residual and magmatic olivine compositions.

(continued)

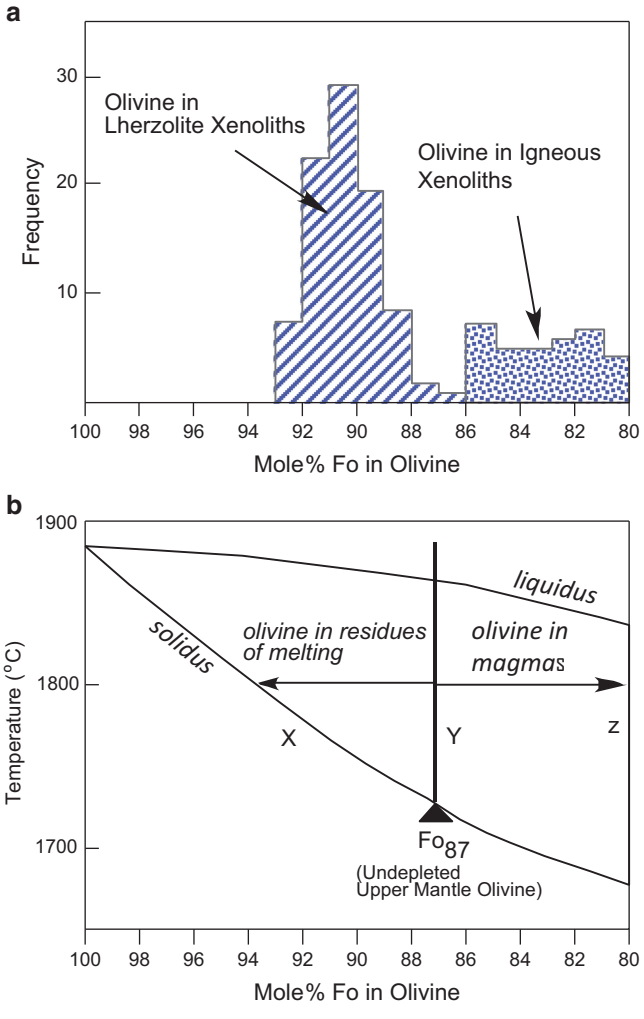

Fig. 3.10 (**a**) Frequency distribution of olivine composition (mole% forsterite content) in two classes of mantle xenoliths from Kilbourne Hole, New Mexico, USA (Redrawn from Carter 1970, Geol Soc Am Bull. 81, 2021–2034). Olivines in what seem to be from pieces (xenoliths) of the upper mantle (spinel lherzolite) are inherently more forsteritic than the other xenolith olivines, which Carter thought to be of magmatic origin. Carter proposed that the upper mantle olivines are residues of partial melting that produced the magmas and that the Earth's undepleted (i.e., without any depletion via magma extraction) mantle olivine had a composition of Fo_{87}, where olivine compositions are very rare in the sampled xenoliths. (**b**) Carter's inference of the undepleted mantle olivine composition is explained with a part of the binary phase diagram forsterite–fayalite. Typically, olivine phenocrysts in primitive tholeiitic basalts (the most voluminous basalts on earth) are usually no more magnesian than Fo_{84}. Using Carter's definition, the undepleted mantle lherzolite had Fo_{87} olivine. If such an olivine is melted, the phase diagram tells us that the residues will be more Fo- rich than the original starting olivine (Fo_{87}) and the magmas generated will presumably crystallize to some extent before erupting on the surface. Thus, their olivine phenocrysts will tend to be much less magnesian

Box 3.1 (continued)

The latter conclusion allowed him to provide an overall estimate of the abundances of other elements in the upper mantle as well.

(continued)

Box 3.1 (continued)

Similar studies from other areas by different authors (including those on Hawaiian xenoliths by the present author) have noted a very similar frequency distribution of olivine compositions. However, it is generally believed that the upper mantle lherzolite is not often simply a residue but a residue that has been metasomatized or re-enriched (particularly in lighter elements) by passing melts. In a general sense, however, Carter's conclusion regarding the composition of the Earth's undepleted upper mantle remains valid today. Several other authors (particularly, the late Professor A.E. Ringwood of Australian National University) used different approaches to obtain constraints on the undepleted upper mantle composition.

Note that although the binary system Fo–Fa was used to reach such an important conclusion, it is highly unlikely that the temperature of melting in the shallow mantle ever reaches ~1,700 °C! The presence of other components in a lherzolitic source rock drops the melting temperature by hundreds of degrees. However, the compositional effects on olivine, as described above, remain valid.

Binary Eutectic Systems: Diopside–Anorthite at One Atmosphere

In a binary eutectic system, a new melting point (called the *eutectic point, E* in Fig. 3.11a) occurs where melt of a fixed composition (called *eutectic composition*) forms when mixtures of two minerals are heated at a fixed pressure. The temperature at which eutectic melting occurs is called the *eutectic temperature*. It is important to note that regardless of the proportion of the two minerals in the mixture, melting of all mixtures of the two minerals must always begin at the eutectic point.

At a fixed pressure (isobar), the phase rule becomes $f = c - \phi + 1$, and therefore, point E is an invariant point because $c = 2$ and $\phi = 3$ (two crystalline phases and a melt phase). When both pressure and temperature variation is considered, the phase rule becomes $f = c - \phi + 2$, and the eutectic point at a single pressure now becomes part of a univariant line along which all three phases can occur in P, T space (not shown here).

One familiar (though incorrect in detail, we will ignore such details here for brevity) example is the *diopside– anorthite* system at 1 atm pressure (Fig. 3.11a). When crystals of anorthite are heated to anorthite's melting point, a melt of anorthite composition will form. This is not strictly true for diopside because diopside does not have a definite melting point but has a small melting range (Kushiro 1973). To keep things simple in our discussion of the diopside– anorthite system, here we will assume that diopside has a definite melting point and not a range of melting temperatures.

When crystals of anorthite and diopside are mixed together, no matter in what proportion, melting will always begin at the eutectic point E when the mixture is heated. We continue our discussion of crystallization and melting in this system in the following sections.

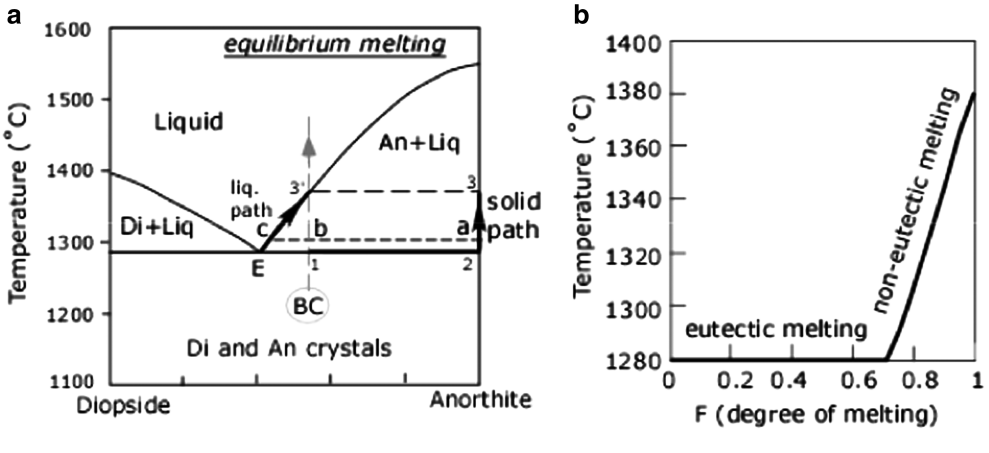

Fig. 3.11 (**a**) The "system" diopside–anorthite at 0.0001 GPa pressure. Equilibrium melting of a solid mixture BC of composition $Di_{48}An_{52}$ is illustrated here. Its solid path and liquid path are shown as *dark lines with arrows*. The *dashed line c–b–a* is an example of a lever that can be used to calculated met and solid percentages at 1,300 °C. (**b**) Degree of melting versus temperature for equilibrium melting of BC. Because BC lies close to the eutectic point *E*, as much as 73 % melt can be generated at the eutectic temperature (1,280 °C)

Box 3.2: Calculation of Eutectic Systems

It is possible to calculate a binary eutectic diagram from thermodynamic data using what is called a *cryoscopic equation*. As an example, let us calculate the diopside liquidus in the Di–An system. At any temperature T on the liquidus, the melt and solid diopside are in equilibrium, i.e., the chemical potential of diopside in the solid is equal to that of diopside in melt:

$$\mu_{\mathrm{Di}}{}^{\mathrm{s}} = \mu_{\mathrm{Di}}{}^{\mathrm{L}}$$

$$\mu_{\mathrm{Di}}{}^{\mathrm{s}} = \mu_{\mathrm{Di}}{}^{\mathrm{o,s}} + RT\mathrm{In}\mathbf{a}_{\mathrm{Di}}{}^{\mathrm{S}}$$

and

$$\mu_{\mathrm{Di}}{}^{\mathrm{L}} = \mu_{\mathrm{Di}}{}^{\mathrm{o,L}} + RT\mathrm{In}\mathbf{a}_{\mathrm{Di}}{}^{\mathrm{L}}$$

where $\mu_{\mathrm{Di}}{}^{\mathrm{s}}$ and $\mu_{\mathrm{Di}}{}^{\mathrm{L}}$ are chemical potentials of diopside in solid and melt phases and $\mathbf{a}_{\mathrm{Di}}{}^{\mathrm{S}}$ and $\mathbf{a}_{\mathrm{Di}}{}^{\mathrm{L}}$ are activities of diopside in solid and melt, respectively (Note: activity = mole fraction in ideal solutions; however they are not the same in more complicated real solutions. Read on). $\mu_{\mathrm{Di}}{}^{\mathrm{o,s}}$ and $\mu_{\mathrm{Di}}{}^{\mathrm{o,L}}$ is chemical potential of pure solid and molten diopside, respectively. R is the universal gas constant.

At T, then,

$$\mu_{\mathrm{Di}}{}^{\mathrm{o,s}} + RT\ \ln \mathbf{a}_{\mathrm{Di}}{}^{\mathrm{S}} = \mu_{\mathrm{Di}}{}^{\mathrm{o,L}} + RT\ \ln \mathbf{a}_{\mathrm{Di}}{}^{\mathrm{L}}$$

or $\quad \mu_{\mathrm{Di}}{}^{\mathrm{o,s}} - \mu_{\mathrm{Di}}{}^{\mathrm{o,L}} = RT \ln \mathbf{a}_{\mathrm{Di}}{}^{\mathrm{L}} - RT \ln \mathbf{a}_{\mathrm{Di}}{}^{\mathrm{S}}$

The left side is ΔG of melting of pure diopside, and therefore the above equation can be rewritten:

$$\Delta G^{\mathrm{m}} = RT \ln \mathbf{a}_{\mathrm{Di}}{}^{\mathrm{L}} - RT \ln \mathbf{a}_{\mathrm{Di}}{}^{\mathrm{S}}$$

$$\Delta H^{\mathrm{m}} + T\Delta S^{\mathrm{m}} = RT \ln \mathbf{a}_{\mathrm{Di}}{}^{\mathrm{L}} - RT \ln \mathbf{a}_{\mathrm{Di}}{}^{\mathrm{S}}$$

ΔH^{m} and ΔS^{m} are enthalpy and entropy of fusion of pure diopside:

$$\Delta H^{\mathrm{m}} + T\Delta S^{\mathrm{m}} = RT \ln \mathbf{a}_{\mathrm{Di}}{}^{\mathrm{L}}$$

or

$$\Delta H^{\mathrm{m}}/RT + \Delta S^{\mathrm{m}}/R = \ln \mathbf{a}_{\mathrm{Di}}{}^{\mathrm{L}}$$

(continued)

Box 3.2 (continued)

Above, note that we ignored the second term (i.e., $RT \ln \mathbf{a}_{\mathrm{Di}}{}^{\mathrm{S}}$) on the right-hand side of the equation since activity of pure diopside crystal is 1. In melting of pure diopside, $\Delta S^{\mathrm{m}} = \Delta H^{\mathrm{m}}/T^{\mathrm{m}}$, where T^{m} is the melting point of pure diopside. Therefore, the above equation becomes

$$\Delta H^{\mathrm{m}}/RT + \Delta H^{\mathrm{m}}/RT^{\mathrm{m}} = \ln \mathbf{a}_{\mathrm{Di}}{}^{\mathrm{L}}$$

or

$$\ln \mathbf{a}_{\mathrm{Di}}{}^{\mathrm{L}} = \Delta H^{\mathrm{m}}/R\ [1/T^{\mathrm{m}} - 1/T]$$

$\mathbf{a}_{\mathrm{Di}}{}^{\mathrm{L}}$ is generally written as $X_{\mathrm{Di}}{}^{\mathrm{L}} \cdot \gamma_{\mathrm{Di}}{}^{\mathrm{L}}$, where X is mole fraction (=Moles of Di/(moles of Di + An) in the case of Di–An system) and γ is a parameter known as *activity coefficient*, which is 1 when the solution behaves ideally. In the present example, the melt's activity coefficient may be assumed to be 1, and therefore activity = mole fraction.

Therefore, the above equation can be written as

$$\ln\ X_{\mathrm{Di}}{}^{\mathrm{L}} = \Delta H^{\mathrm{m}}/R\ [1/T^{\mathrm{m}} - 1/T]$$

This equation is known as the *cryoscopic equation*. Since ΔH^{m}, T^{m}, and R are known, T can be determined at any given $X_{\mathrm{Di}}{}^{\mathrm{L}}$ or vice versa. From several different T and $X_{\mathrm{Di}}{}^{\mathrm{L}}$, the liquidus curve may be drawn.

Here, we will construct the Di–An system at 0.0001 GPa (i.e., atmospheric pressure) using the cryoscopic equation. We use the following values (using thermodynamic data available in the literature) for our purpose: R = 8.3144 J/mol/K, ΔH^{m} of diopside = 142.6 kJ/mol, and T^{m} of diopside = 1,668 K. We calculate the liquidus temperature T corresponding to different values of mole fraction of diopside from 0.9 to 0.1 and calculate the following data:

X (input mole fraction)	T [K]
1	1,668
0.9	1,651
0.8	1,633
0.7	1,612
0.6	1,589
0.5	1,563
0.4	1,532
0.3	1,493

(continued)

Box 3.2 (continued)

Now we do the same for anorthite using the following values: $T^m = 1{,}830$ K, $\Delta H^m = 136$ kJ/mol:

X (input mole fraction)	T [K]
1	1,830
0.9	1,809
0.8	1,785
0.7	1,760
0.6	1,731
0.5	1,698
0.4	1,660
0.3	1,613
0.2	1,551

Plotting these values, we obtain a calculated liquidus diagram for the Di–An system at 1 atm (Fig. 3.12a). This figure shows that although there is an overall similarity between the calculated liquidi and experimental liquidi, the location of the eutectic point and the liquidus surfaces are considerably different. One among several interpretation of this discrepancy may be that the assumption of activity = mole fraction is probably incorrect. One could then use the mismatch to determine activity coefficient or γ. Figure 3.12b shows relationship between calculated γ and X of anorthite in melt. The curve is a power law fit to the calculated data with an excellent correlation coefficient (0.99).

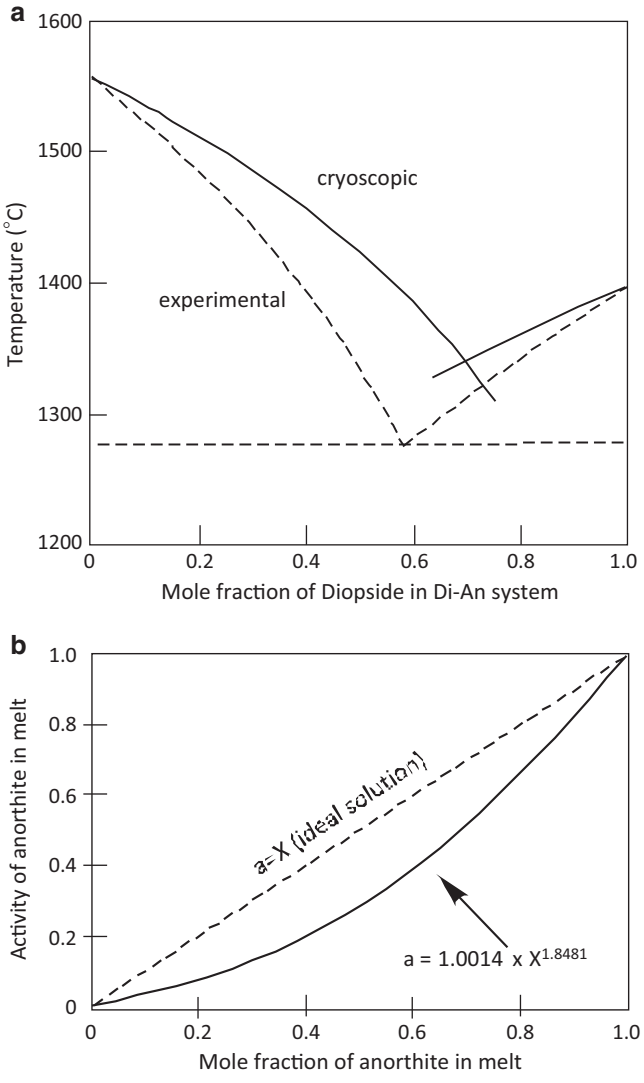

Fig. 3.12 (**a**) Comparison between the liquidus curves calculated using the cryoscopic equation and those drawn from actual experimental data. (**b**) Activity versus mole fraction of anorthite component in melt estimated from the difference between experimental and cryoscopic data. The activity is clearly not equal to mole fraction (if the solution were ideal)

Equilibrium Melting in Diopside–Anorthite "System"

Equilibrium melting is illustrated with the example of melting of a mixture containing 55 % anorthite and 45 % diopside crystals (i.e., $An_{55}Di_{45}$). Heating this mixture will lead to the initiation of melting at E (Fig. 3.11a). Further heating will not raise the temperature of the melt + crystals assemblage, and the melt composition will stay at E until *all* crystals of diopside have been melted. When all diopside crystals are dissolved in the melt phase, the solid path would have reached the anorthite composition axis (line 1 → 2 in Fig. 3.11a), and as the temperature is raised further, the melt will move up the liquidus of anorthite from E to 3′ while the corresponding solid composition will move from 2 to 3. When the melt reaches 3′, the starting mixture will be fully molten.

The lever rule shows us how this happens. At any temperature, a tie-line or lever can be drawn by connecting the coexisting phases, and such a line must go through the bulk composition. Figure 3.11a shows a lever *a–b–c* for a selected mixture BC (also called, *bulk composition*) at 1,300 °C. We calculate melt percentage to be 80 % using the lever rule as follows:

$$\%\text{melt} = 100 \times \text{distance } a - b/(\text{distance } a - c)$$

Similar levers can be constructed at different temperatures to see how the melt proportion increases

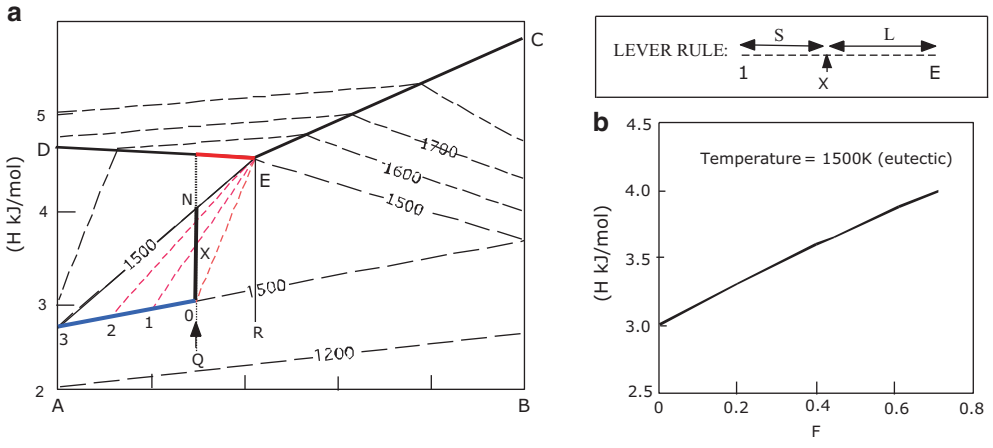

Fig. 3.13 (**a**) Enthalpy (*H*)-composition diagram for a hypothetical binary eutectic system *A–B*. *Long-dashed lines* are isotherms with temperatures marked on them. *Short-dashed lines* are tie-lines for application of the lever rule (shown in the panel below). (**b**) Changing melt fraction with enthalpy for bulk composition *Q* in (**a**)

as temperature is raised. When we plot melt% against temperature (Fig. 3.11b), we see that the bulk composition BC can generate up to 75 % melt at the eutectic point without any increase of temperature.

How does this happen? Eutectic melting shows us the importance of the latent heat of fusion (ΔH^{fusion}). Here, we explore this melting behavior using an enthalpy–composition (*H–X*) diagram for a hypothetical system *A–B* (Fig. 3.13a). In this diagram, the curve *C–E–D* is the liquidus, and the dashed lines are the isotherms (temperature is in Kelvin). Note that a triangular isotherm emanates from the eutectic point *E*. In this system, a eutectic solid *R* will begin to melt at the 1,500 K isotherm and then continue to melt toward *E* as it is heated. At *E* it will be completely molten. The *Y*-axis tells us that this melting interval corresponds to a latent heat or enthalpy of fusion (ΔH of fusion) of 1.35 kJ/mol for this eutectic solid.

Using the lever rule, we can calculate *F* (degree of melting) versus enthalpy (*H*) for non-eutectic starting solid compositions as well. Consider the bulk composition *Q* (Fig. 3.13a). It will begin to melt as it is heated to the 1,500 K isotherm and will continue to melt as heat is added to the system; however, the temperature will not rise as long as the bulk composition path (the thick line 0 → *N*) remains within the 1,500 K triangular isotherm. We can now draw tie-lines at various points as the starting material is heated from *Q* to *N* at the eutectic temperature. These are the short-dashed lines that emanate from *E*, cut through the bulk composition line, and reach the base of the 1,500 K isotherm (Fig. 3.13a). Thus, in this diagram, the solid path at the eutectic temperature is 0 → 1 → 2 → 3, while the melt composition remains fixed at *E*. The inset in Fig. 3.13a shows an example of a lever when the solid path reaches 1. Calculation of the melt fraction *F* as a function of enthalpy (*H*) at the eutectic using successive levers (*E*–2, *E*–3, etc.) results in an *F–H* plot (Fig. 3.13b). In this example, 1 kJ/mol of heat is consumed at the eutectic temperature.

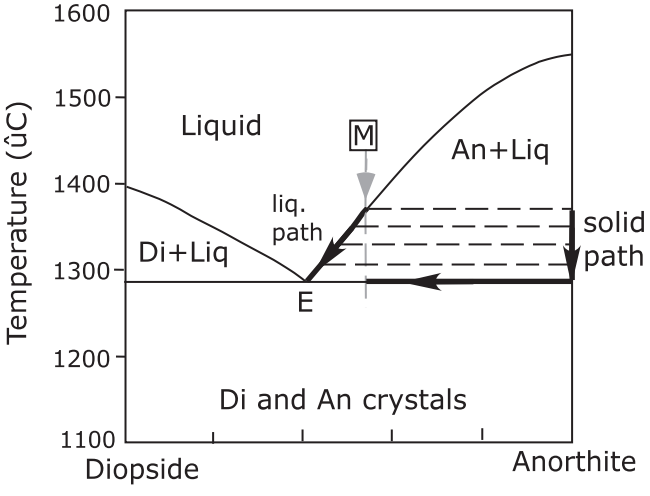

Fig. 3.14 Equilibrium crystallization of liquid M. *Dashed lines* are tie-lines; Solid and liquid paths are shown as *bold lines*

Equilibrium Crystallization in Diopside–Anorthite system

Equilibrium crystallization can be thought of as exactly the reverse of equilibrium melting. Melt and solid paths are the same as in equilibrium melting except that the directions (arrows in Fig. 3.11a) are reversed (Fig. 3.14).

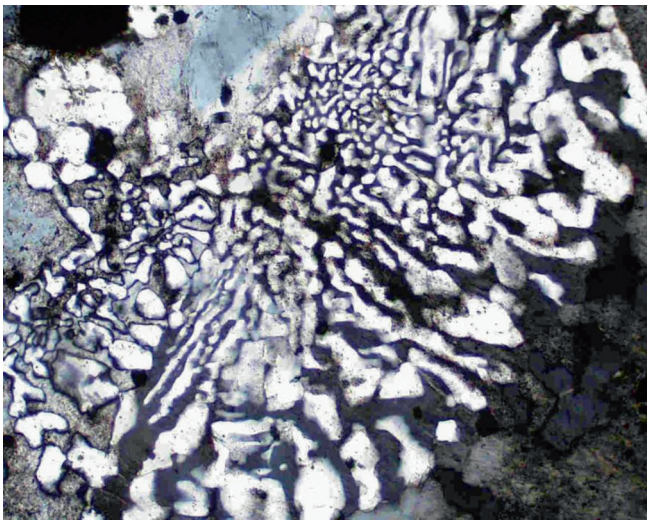

Fig. 3.15 A photomicrograph showing granophyric texture (also called eutectic or eutectoid texture) in a granophyre

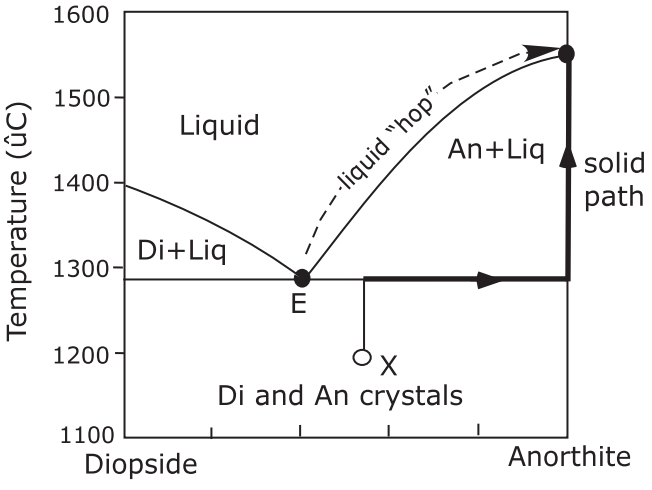

Fig. 3.16 Fractional melting of a starting solid *X* in the system Di–An. Note the liquid "hops" while the solid path is continuous

Consider equilibrium crystallization of the starting melt *M* in Fig. 3.14. This melt will crystallize anorthite when it is cooled to its liquidus temperature (1,375 °C), and a tie-line (dashed line at 1,375 °C) can be drawn to depict, through the lever rule, the fact that there will be hardly any crystals. With further cooling, more anorthite crystals will form, as can be seen by studying the various tie-lines (the other dashed lines) at various temperatures, as the residual melt will move toward *E*. At *E*, diopside and anorthite crystallize together in eutectic proportion until all of the melt disappears. This happens when the solid path reaches the starting bulk composition.

Crystallization at the eutectic point often produces a blebby or hieroglyphic-type intergrowth texture called *eutectoid* texture**.** This texture is most commonly formed by quartz and alkali feldspar intergrowth in a type of igneous rock called *granophyre* (Fig. 3.15). In this rock type, such texture develops due to simultaneous crystallization of quartz and alkali feldspar at their binary eutectic point.

Fractional Crystallization in Diopside–Anorthite System

In binary eutectic systems, melt and solid paths for any particular melt composition are the same for fractional and equilibrium crystallization; however, a much greater amount of residual melt remains when the eutectic point is reached during fractional crystallization.

Fractional Melting

The only thing that fractional melting has in common with equilibrium melting is that melting begins and continues at the eutectic point until one of the solid phases is exhausted from the residue. For example, a "rock" composed of $An_{55}Di_{45}$ will begin to melt at the eutectic point. Progressive melting at *E* and rapid extraction of the melt from the source (which is fractional melting) will ultimately yield a solid residue composed only of anorthite, i.e., the solid path will reach the anorthite axis. Further melting will not occur until the crystals are heated to the melting point of anorthite. Therefore, in fractional melting, the solid path is still a continuous path whereas the melt composition "hops" from the eutectic point to the congruent melting point of anorthite (Fig. 3.16).

Some Additional Comments

Eutectic melting has always been a subject of great interest to igneous petrologists. In the 1950s and 1960s, before significant modern analytical tools were developed and great many details of compositional variations in basalts were discovered, voluminous basalt lavas on continents and on the ocean floor were thought to be compositionally uniform. Because eutectic melting provides a convenient way to generate compositionally uniform magmas from diverse variety of source rocks, early authors thought that these magmas were generated in the upper mantle by an eutectic-type melting process.

In the late 1980s and early 1990s, some authors noted that the rock *lherzolite*, which is the most abundant rock in the Earth's upper mantle, melts directly to

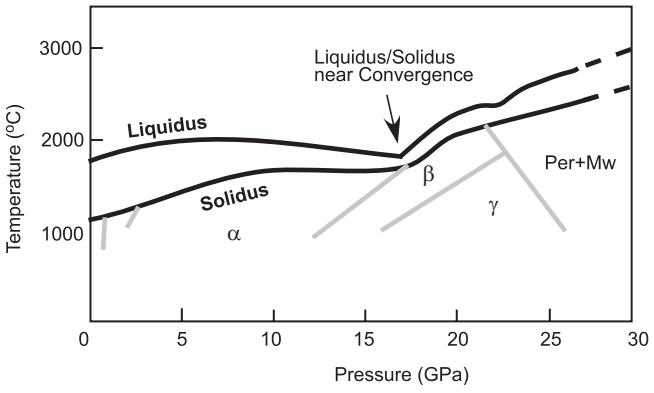

Fig. 3.17 Experimentally determined phase relations of an upper mantle rock (from Ito and Takahashi 1987, Nature). α, olivine; β, modified spinel phase; γ, silicate spinel; Per, silicate perovskite; and Mw, magnesiowustite. The near convergence between liquidus and solidus for this mantle composition suggests that this rock could have been molten and multisaturated with multiple mineral phases (similar to a eutectic). However, there have been alternate interpretations of this data

its own composition at a high pressure, much like a eutectic mixture melts to its own composition (i.e., eutectic composition). Based on this eutectic or near-eutectic behavior of the mantle peridotite, they hypothesized that the Earth's upper mantle may have once been molten like a giant *magma ocean* that formed by eutectic melting (Fig. 3.17). Examples like these show how simple observations on phase diagrams can trigger one's imagination in proposing global scale phenomena. I should note that later studies have found major gaps in the magma ocean hypothesis as applied to Earth; however, in the case of the Moon, there is little debate that it was covered by magma ocean(s). Such magma ocean was formed due to large-scale impacts of meteorites and asteroids.

Box 3.3: Magma Ocean on Primitive Earth: Clues from Phase Diagrams

Evolution of the earth since its birth 4.5 billion years ago is an exciting area of study. Unfortunately, the virtual absence of the record of Earth's earliest few million years in rocks has made it a rather difficult problem to unravel. Many fundamental questions continue to haunt scientists. For example, when and how did the Earth's mantle differentiate into three layers—lower mantle, transition zone, and the upper mantle! Was there ever a time when the Earth's outer part was molten like a giant magma ocean?

(continued)

Box 3.3 (continued)

In the mid-1980s, some scientists (most notably, Claude Herzberg of Rutgers University and David Walker of Lamont–Doherty Earth Observatory, Columbia University) noted that the solidus and liquidus of Earth's upper mantle rock seem to converge at a pressure of about 15 GPa (about 450 km) in pressure–temperature space. (Recall that the solidus of a particular rock is the curve at which the rock begins to melt and liquidus is the curve above which it is entirely molten: Fig. 3.17). These scientists pointed out that the only way this convergence could happen is if the Earth's upper mantle rock itself formed by eutectic-type crystallization from a giant magma ocean at that pressure. Verification of this idea came when Eiji Ito and Eichi Takahashi of Okayama University carried out melting experiments on an upper mantle xenolith up to a pressure of 25 GPa. They noted that indeed the solidus and liquidus come to a near convergence at about 16 GPa. What is also interesting is that the liquids near the convergence zone are compositionally almost identical to the starting mantle rock. As discussed elsewhere in this chapter, this is exactly what would be expected when the starting rock composition coincides with the eutectic composition at a given pressure! Some authors have doubted the magma ocean hypothesis on the basis of other chemical arguments; however, Ito and Takahashi indicated that many/all of those chemical differences are explained by fractionation of silicate perovskite in the lower mantle. On the other hand, based on some simple oxide–oxide plots (discussed in a later chapter), Carl Agee and David Walker of Columbia University noted that simple fractionation of perovskite from a chondritic magma ocean (with iron taken out to form the Earth's core) cannot form the peridotitic material that is supposed to be the dominant constituent of the Earth's upper mantle. These authors noted that addition of olivine (by flotation in the magma ocean) would be necessary to form the upper mantle.

The debate about the existence of a primordial magma ocean on earth is far from over. For our purpose, however, the important thing is to realize how far a simple observation on a phase diagram can go in deciphering earth history.

The System Nepheline–Silica at 1 atm Pressure: A Complex Double Eutectic System with a Thermal Divide

The system nepheline–silica diagram (Fig. 3.18a) looks quite complex because it shows (a) silica polymorphs tridymite and cristobalite, (b) polymorphism between carnegieite and nepheline, (c) limited solid solution between albite and carnegieite/nepheline, and (d) two eutectic points—*E*1 and *E*2. We ignore much of this complexity and focus on the eutectic points *E*1, where albite and quartz crystallize, and *E*2, where nepheline (solid solution) crystallizes with albite. Note that albite forms in this system because of the reaction:

$$NaAlSiO_4 + SiO_2 = NaAlSi_3O_8$$

Here the melting point of albite serves as a *thermal divide* (like a watershed) or a thermal maximum between melts (such as *M*1 in Fig. 3.18b) that proceed to *E*1 versus those melts that fall on the other side of the divide (such as *M*2), which move toward *E*2 upon cooling and crystallization. Thus, this diagram tells us that nepheline and quartz cannot crystallize together from any melt, i.e., there should not be any igneous rock that contains both nepheline and tridymite (or quartz, which is a low-temperature polymorph of tridymite).

Long before this phase diagram was determined experimentally, S.J. Shand noted from his field studies of igneous rocks that nepheline and quartz/tridymite do not occur in the same rock. This led to the recognition of two genetically distinct classes of magmas—(a) alkalic magmas, which are SiO_2-deficient magmas that can potentially crystallize nepheline, and (b) subalkalic magmas (magmas that can potentially crystallize quartz or tridymite or any other silica polymorph). Not surprisingly, this fundamental division between two major chemical classes of igneous rocks is still valid today!

As an aside, one can carry out an interesting exercise of mixing two melts *L*1 with and *L*2, both carrying albite crystals, such that a new bulk melt composition (L_m) falls precisely on the albite composition line (Fig. 3.18b). In this peculiar example, the new melt will quickly quench to form an all-albite crystalline assemblage, and there will be no record of the prior existence of two separate melts. Of course, that would be an unusual situation. There can be other mixing scenarios in which the mixed melt composition will

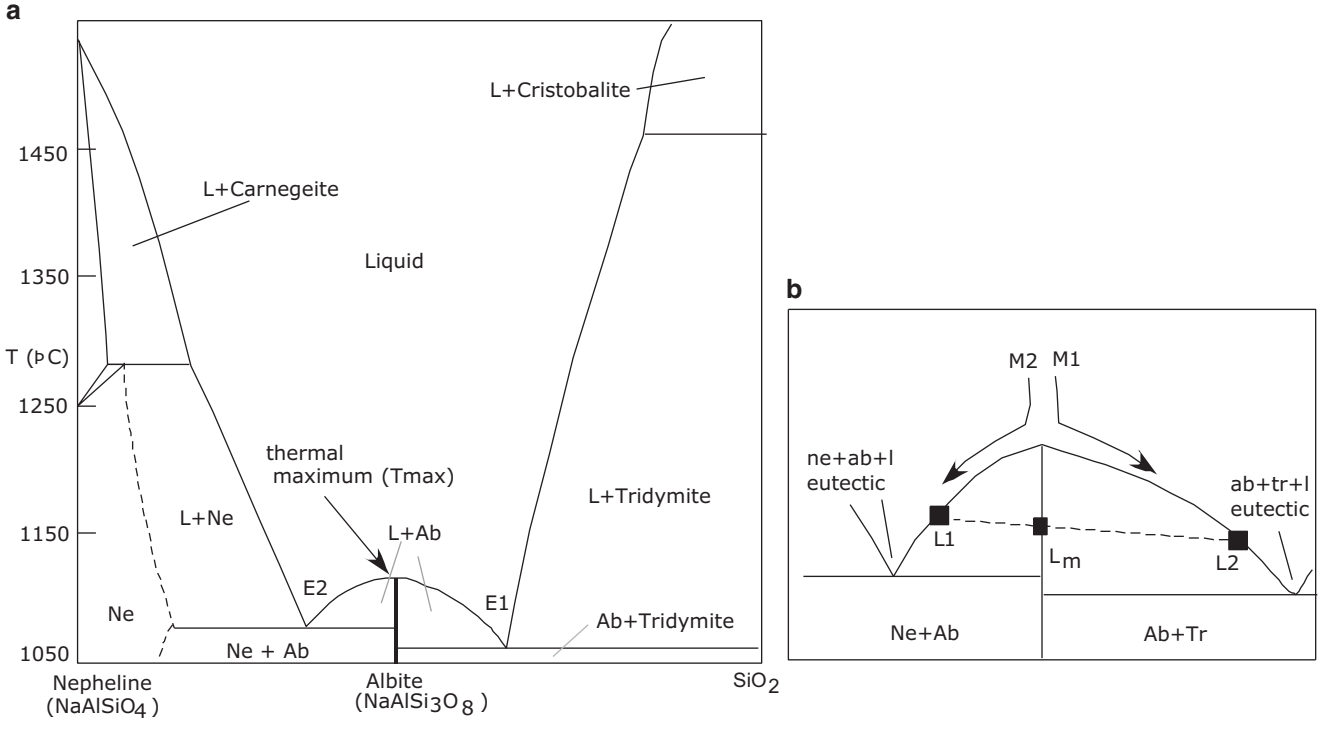

Fig. 3.18 (**a**) Nepheline–silica system. This system is complicated by two phase transformations (cristobalite/tridymite and nepheline/carnegeite) and solid solution between nepheline and albite. We will ignore these complications and focus on the thermal maximum (also known as thermal divide) created by albite, which forms by reaction between nepheline and silica. There are two eutectic points *E*1 and *E*2 on either side of the albite maximum. (**b**) The effect of the thermal maximum on melt paths is shown. *M*1 and *M*2 melts, falling on either side of the thermal maximum, can only proceed to their respective eutectic points upon crystallization. A peculiar case of mixing between melts *L*1 and *L*2, forming a new bulk composition of L_m, is shown. The new composition is that of albite, and therefore it will quickly solidify to pure albite

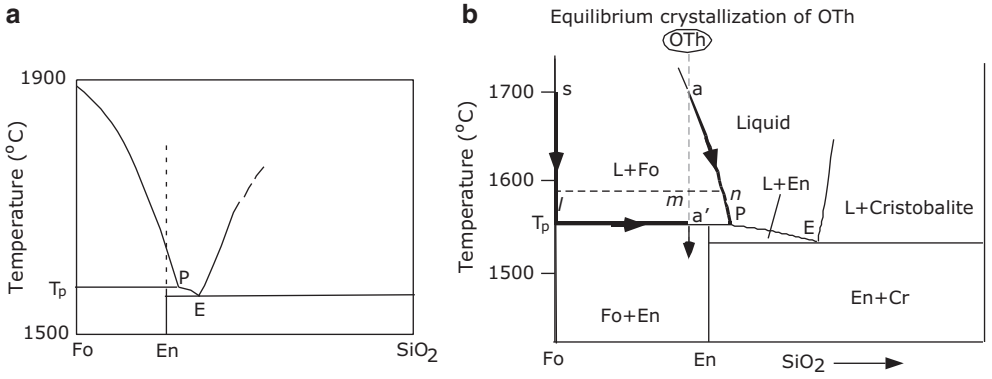

Fig. 3.19 (**a**) The system forsterite–silica showing the peritectic point at *p* and *a* eutectic point at *E*. Enstatite shows incongruent melting behavior: En = Fo + L. (**b**) Equilibrium crystallization of a liquid "OTh" is illustrated. Forsterite crystals start forming when OTh reaches its liquidus at a. The liquidus temperature of OTh is s (i.e., 1,700 °C). With progressive cooling, the liquid follows the path $a \rightarrow n \rightarrow p$, and the crystals follow the path $s \rightarrow T_p \rightarrow a'$. Once a' is reached, the crystalline assemblage, consisting of enstatite and forsterite crystals, will have the same bulk composition as the starting liquid OTh. Therefore, under equilibrium conditions, the liquid cannot go beyond *P* because the peritectic reaction Fo + L = En will use up all the liquid when point a' is reached

fall on the left or right side of the albite divide. It is up to the student to figure out what sorts of textures may develop from such mixing.

Incongruent Melting Behavior and Binary Peritectic Systems: The System Forsterite: Silica at 1 atm Pressure

In contrast to the systems, we have considered, so far, some binary systems contain an additional mineral that cannot melt to its own composition (i.e., *congruent melting*) but breaks down to another mineral + melt when heated to a certain temperature. Such melting behavior is called *incongruent melting*. There are multiple examples of such behavior in natural magmas, and a particularly good one is that between olivine, pyroxene, and melt:

$$MgSiO_3 = Mg_2SiO_4 + \text{Melt}$$

In the above reaction, enstatite ($MgSiO_3$) cannot melt to its own composition but breaks down to forsterite (Mg_2SiO_4) and melt when heated. Figure 3.19 shows how this incongruent melting behavior works.

In passing, note that protoenstatite is one of three polymorphs with a $MgSiO_3$ composition; the others are orthorhombic enstatite and clinoenstatite. The actual pyroxene that forms is a protoenstatite, but for the sake of brevity, we will call the pyroxene enstatite.

When enstatite crystals are heated to 1,557 °C (T_p in Fig. 3.19), they will melt, yielding a melt at *P* and forsterite crystals. The point *P* is called the *peritectic point*. The temperature T_p is the incongruent melting point of enstatite. A eutectic point (*E*) also occurs between cristobalite (a polymorph of SiO_2) and enstatite in this system (Fig. 3.19).

The Fo–SiO_2 system is of considerable importance in igneous petrology because it contains two minerals, namely, an olivine and orthopyroxene, that comprise 75–85 % of the upper mantle rock, called peridotite. Peridotite serves as the source rock for basalt magmas, which make up all of the ocean floor, hot spot-generated crust, and a significant part of the continental crust. Fractional crystallization of olivine can play an important role in how basalt magma may evolve compositionally in crustal magma chambers. It is therefore important to discuss crystallization and melting behavior in this simple system as a possible analog of how natural basalt magma may form and crystallize.

Equilibrium Crystallization in Fo–SiO_2 System

For the purpose of brevity, we will ignore the SiO_2 side of the diagram and concentrate only on crystallization and melting relationships that involve forsterite and enstatite. In this system the enstatite composition line (dashed line in Fig. 3.19a) determines the final solid assemblage that would crystallize from a given melt: Starting melt compositions falling on the olivine side (left side) of the dashed line will end up crystallizing olivine + enstatite as a final assemblage, and bulk melt compositions falling on the right side of the dashed line will end up generating enstatite + cristobalite as a final assemblage. We will consider equilibrium crystallization of two starting melt compositions on either side of the enstatite line (Figs. 3.19b and 3.20).

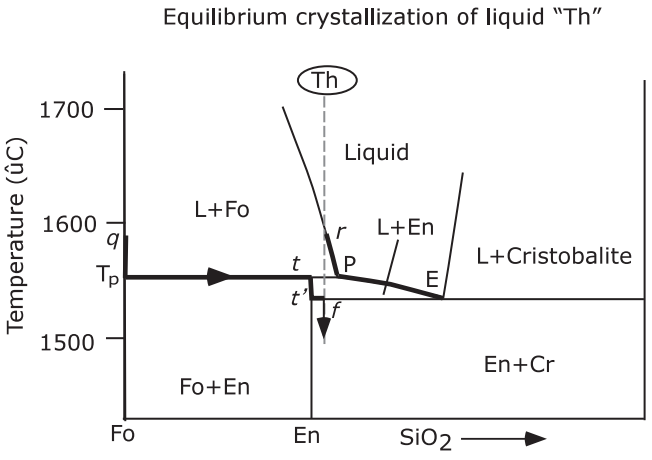

Fig. 3.20 Equilibrium crystallization of starting liquid "Th" is shown: It begins to crystallize forsterite crystals at a temperature of 1,580 °C, when the Th reaches its liquidus at *r*. The corresponding forterite crystals formed are at the point *q*. As the liquid is cooled, it follows the path $r \rightarrow p \rightarrow E$, and the corresponding solid path is $q \rightarrow T_p \rightarrow t \rightarrow t' \rightarrow f$. The final solid assemblage at *f* has the same starting composition (Th)

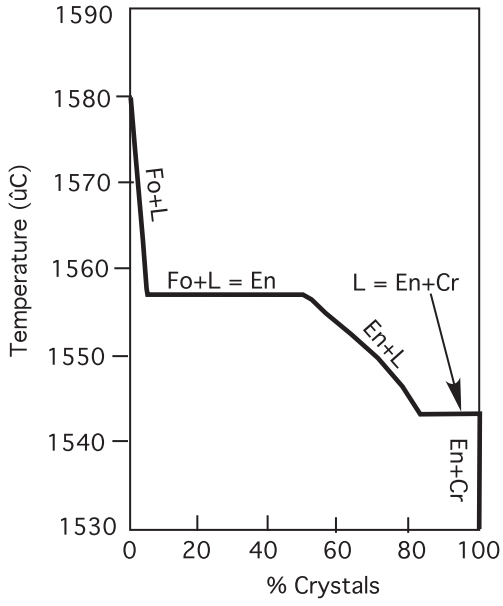

Fig. 3.21 Crystalline assemblages and total crystal percentage are plotted against temperature decrease as the melt "Th" is cooled. The crystal percentages were calculated using the lever rule

Melt OTh

In Fig. 3.19b, the melt OTh will start crystallizing forsterite crystals at 1,700 °C (i.e., its liquidus temperature). Further cooling will produce more forsterite (Fo) crystals as the melt moves down the liquidus toward *P* (Fig. 3.19b). Once again, at any given temperature, the lever rule may be used to calculate the proportions of crystals and melt, for example, when the melt composition reaches *n*,

$$\text{melt}\% = 100 \times \text{distance}\, lm/\text{dis tan ce}\, ln$$

$$\text{forsterite}\% = 100 \times \text{distance}\, mn/\text{distance}\, ln$$

With further cooling the melt will reach *P*, and at this point, forsterite crystals will react with the melt *P* and produce crystals of enstatite owing to the following reaction:

$$\text{forsterite} + \text{melt} = \text{enstatite}$$

Texturally, the forsterite crystals will appear resorbed with rounded grain boundaries. In igneous rocks evidence of such reaction may be seen as resorbed crystals of olivine surrounded by a rim of pyroxene. This reaction will continue until all of the melt is used up while the temperature remains constant. The solid path will progress from Tp to a', which is the bulk composition. When the solid path reaches a', all of the melt will be gone, and the solid assemblage will be composed of forsterite and enstatite crystals.

Note that as long as equilibrium is maintained throughout, the melt *cannot* move down to *E* because that would mean *all* forsterite crystals would be dissolved, which cannot happen since the bulk composition constraint forces the final crystalline assemblage to be composed of forsterite and enstatite.

The composition OTh chosen here is an excellent analog representation of natural olivine tholeiite, which is an important type of basalt in nature (discussed in a later chapter).

Melt Th

The melt Th falls on the right-hand side of the enstatite line and starts crystallizing forsterite at *r* (Fig. 3.20). From *r* to *P* it will crystallize forsterite, and as before, enstatite crystals will form due to reaction between forsterite crystals and melt. However, the lever rule tells us that there will be an excess of melt at this point than is needed to consume all of the forsterite crystals, and therefore, once all the forsterite crystals are dissolved, the melt will be free to move down to *E* while crystallizing enstatite only. At *E* the melt will crystallize enstatite and cristobalite. The corresponding solid path is shown in Fig. 3.20.

(*Question*: Can you tell how crystallization will proceed for a melt that falls exactly on the enstatite composition line?)

Figure 3.21 was constructed using the lever rule at various temperatures and shows how the %crystals and nature of the crystals will change during crystallization

of Th. Note how the slope of the liquidus controls crystal% during cooling—percentage of enstatite crystals increases rapidly over a very short temperature interval relative to how forsterite behaves. Also, at the first invariant point *P*, crystal% jumps quickly.

Fractional Crystallization and Fractional Melting

In perfect fractional crystallization, the bulk composition does not impose a control on the melt path because a new instantaneous starting solid composition is produced every time the crystals are quickly separated from the melt as soon as they form. Therefore, for all bulk melt compositions, including OTh, the final melt will end up at *E* (Fig. 3.22a).

Consider the case of OTh. It will start crystallizing forsterite at *a,* and the crystals will be extracted as soon as they form such that every new residual melt is a new starting melt composition. In sharp contrast to equilibrium crystallization, the melt path will not end at *P* because fractional crystallization would have removed all forsterite crystals from contact with the melt. Thus, the melt will be free to move down to *E* while fractionally crystallizing enstatite. The melt will crystallize enstatite and cristobalite in eutectic proportion when it reaches *E*.

As we noted earlier in the case of eutectic systems, fractional melting produces continuous solid residue paths but distinct melt compositions or "melt hops." In the present case, fractional melting behavior may be understood with reference to the bulk solid composition *X* (Fig. 3.22b). *X* will begin to melt at *E* (1,543 °C) and will continue until the residue becomes pure enstatite. Once the residue becomes pure enstatite, further melting will not occur (because all the melts would have been removed) until the temperature is raised to the peritectic temperature of 1,557 °C. At 1,557 °C, melting will occur at *P*. Melting will stop once all enstatite crystals are consumed and the residue is composed of pure forsterite. Melting will resume only when the temperature is raised to the melting point of forsterite. Thus, we see distinct melt compositions are generated at *E*, *P*, and at the melting point of forsterite while the instantaneous solid path is continuous.

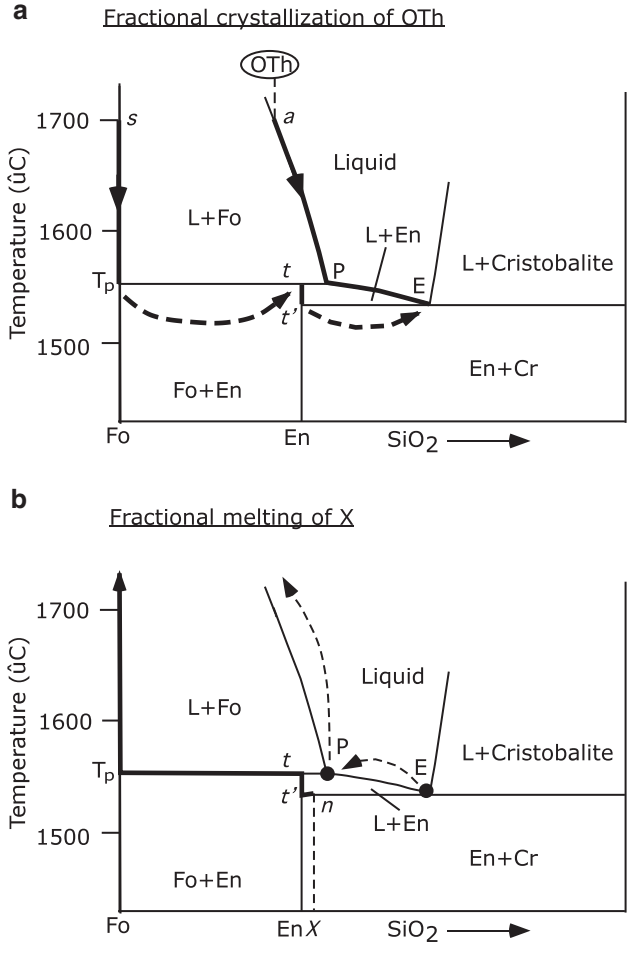

Fig. 3.22 (**a**) Fractional crystallization of starting melt composition "OTh." The melt will follow the path $a \rightarrow P \rightarrow E$ while solid path will be discontinuous: $s \rightarrow T_p$ (solid hop) $\rightarrow t \rightarrow t'$ (solid hop) $\rightarrow E$. (See text for further explanation.) (**b**) Fractional melting of a rock "*X*." The solid path is continuous: $n \rightarrow t' \rightarrow t \rightarrow T_p \rightarrow$ pure Forsterite melting point (not shown in the diagram). The melt path is discontinuous ("hops") $E \rightarrow$ (hop) $P \rightarrow$ (hop) melting point of forsterite

Melt Mixing

Mixing of melts, which is of paramount importance in igneous processes, may produce some interesting results in this system. Here we consider the case of mixing melts *m1* and *m2* to generate a new melt composition of *mx* (Fig. 3.23). Note that *mx* is well above its liquidus, i.e., it is *superheated*! Thus, if the parent

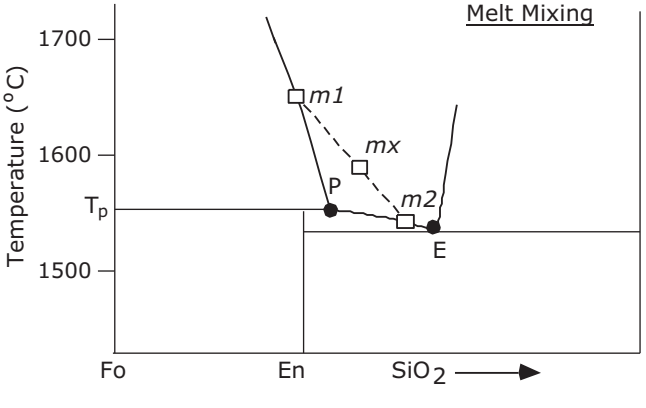

Fig. 3.23 Melt mixing in the system Fo–silica is shown here. Melts *m*1 and *m*2 are mixed to produce a new mixed melt *mx*. Although *m*1 and *m*2 may have contained some crystals of forsterite and enstatite, respectively, *mx* is a superliquidus melt, and thus, all the preexisting crystals must dissolve in it

melts *m1* and *m2* carried a few crystals of forsterite and enstatite, respectively, such superheating may result in the dissolution of both sets of crystals. Once *mx* is cooled to its liquidus temperature, it will only crystallize enstatite, and all evidence of the existence of a Fo-saturated parent melt would be lost. In nature mixing is often imperfect, and some key textural features are often preserved as relicts, which helps the petrologist deduce an igneous rock's evolutionary past.

Binary Systems with Limited Solid Solution and Exsolution: 2. Albite–Orthoclase

Some minerals show only limited solid solution between their end-members, e.g., alkali feldspars and pyroxenes. Alkali feldspars are a major mineral in granitoid rocks and are solid solutions of albite ($NaAlSi_3O_8$) and potassic feldspar ($KAlSi_3O_8$) with limited amount of anorthite component. The phase relationships in the "system" albite–orthoclase (Figs. 3.24 and 3.26) are thus relevant to the crystallization of granitoid magmas. Figures 3.24 and 3.26 show the phase relationships at two different pressures—1 atm and 0.5 GPa pressure under water-saturated conditions. Although this phase diagram is quite rich in its details, for the sake of brevity, we will focus on how crystallization occurs at the left half of the diagrams.

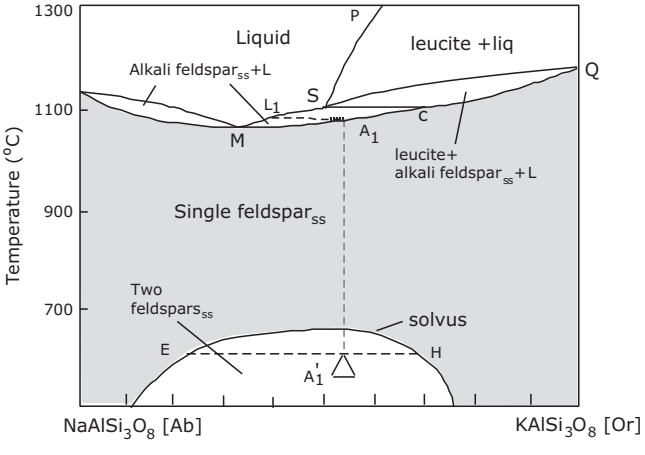

Fig. 3.24 The system albite–orthoclase at 0.0001 GPa. A single feldspar$_{solid\ solution}$ is stable in the gray field. When such feldspar is cooled below the solvus or immiscibility gap, it will unmix into two different feldspars (both solid solutions). As an example, note that a single feldspar (solid solution) of composition A_1 will crystallize from a liquid of composition L_1 at 1,100 °C. As this crystal is cooled, it will remain a single homogeneous solid solution until it reaches the solvus. It will then begin to unmix, i.e., one feldspar will begin to exsolve from the other: for example, at 600 °C, host feldspar *H* will form with the exsolved feldspar *E*. The proportion of the host:exsolved phases will be determined by lever rule (the fulcrum of the lever is shown as a *triangle*)

Let us first consider the albite–orthoclase "system" at 1 atm pressure (Fig. 3.24). (It is actually a join and not a system, but we will ignore that complexity.) The liquidus and solidus touch each other at a point (*M*) known as a *minimum*. A single alkali feldspar solid solution exists at the solidus. Point *M* has a variance of 1 (the student should use the phase rule to figure this out)—only a single feldspar$_{ss}$ (the subscript "ss" stands for solid solution) can crystallize at this point from a corresponding melt. A *minimum* is therefore *not* a binary eutectic (which is invariant at a constant pressure). In fact, Ab–Or is not a system but a join because some melts upon crystallization leave the binary and enter into a ternary system (not shown here). For our purpose of illustration, we will treat the Ab–Or join as a system and assume that the compositions of all melts made of the components Ab and Or always remain within the boundaries of this binary, i.e., none of the melts ever leave the binary. Note that because of the existence of the two solid solution loops in Fig. 3.24, starting melts higher up on the liquidus on either side of *M* do not have to reach *M* during equilibrium crystallization. They will, of course, reach *M* if the crystallization process is fractional.

An interesting complication is the existence of a *miscibility gap* or a *solvus* (Fig. 3.24). Within this gap, a single alkali feldspar$_{ss}$ cannot be stable and must decompose into two different feldspar$_{ss}$—one sodic (i.e., Na-rich with some dissolved K) and the other potassic (K-rich with some dissolved Na). For example, a feldspar crystal A_1 ($Or_{57}Ab_{43}$) will form at ~1,080 °C from a melt L_1. This crystal will begin decomposing to two feldspars as it cools extremely slowly (i.e., maintaining chemical equilibrium) through the miscibility gap (starting at about 660 °C): one of these will be emerged as blebs of a separate feldspar phase within the other (host) feldspar phase (Fig. 3.25). This phenomenon is called *exsolution*. The proportion of the host and exsolved feldspar phases at any temperature can be calculated using the lever rule; for example, the feldspar A_1 will decompose to feldspars *E* and *H* at a temperature of about 610 °C, and the percentage of *E* (exsolved phase) will be equal to$100*A_1'H/EH$, and the percentage of *H* (host phase) feldspar will be equal to $100*EA_1'/EH$.

Increase of pressure (under water-saturated conditions) depresses the solidus to lower temperature and elevates the solvus to higher temperature. The diagram at 0.5 GPa partial pressure of water (p_{H2O} =

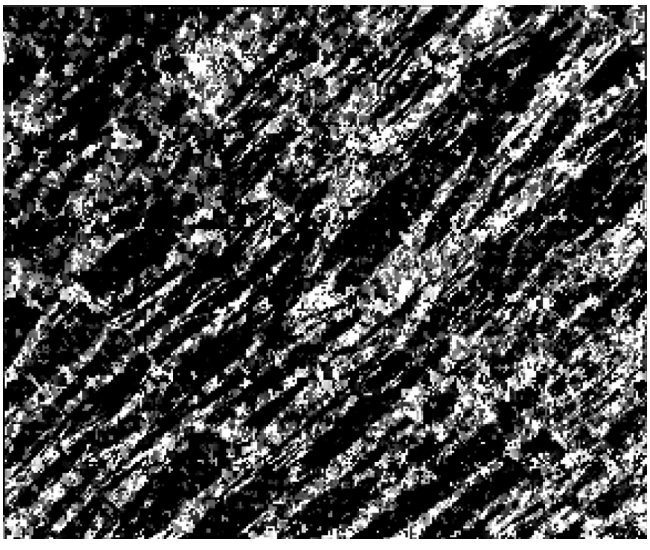

Fig. 3.25 Photomicrograph of perthite (×80 magnified, between crossed polars). The *dark (extinguished) part* is the host feldspar

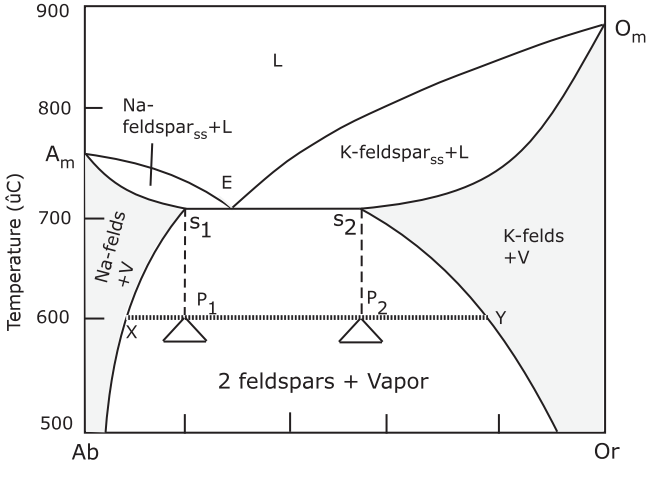

Fig. 3.26 The system albite–orthoclase at 5 kbar pressure under H_2O-saturated conditions. In contrast to the low-pressure phase relations (Fig. 4.23), a eutectic point *E* occurs in this system. The eutectic liquid *E* will crystallize two feldspars S_1 and S_2. These crystals will start exsolving upon cooling; for example, at 600 °C, S_1 will change its composition to *X* by exsolving feldspar of composition *Y*, and S_2 will become *Y* with exsolved feldspar of composition *X*

P_{total}; Fig. 3.26) shows that the solvus "penetrates" the solidus and liquidus so that the minimum is now replaced by a eutectic point (*E*). At the eutectic temperature, two feldspars—S_1 and S_2 (both solid solutions)—will crystallize from the eutectic melt. The existence and importance of one versus two feldspars in igneous rocks of granitic composition have been recognized for a long time. Large, tens-of-kilometer-sized, plutons of granite often occur in the core regions of folded mountain belts. Geologists classify them into two groups—*hypersolvus* and *subsolvus granites*—depending on whether they contain a single or two feldspars, respectively. In the context of the solvus versus pressure effects described above, it is clear that two-feldspar granites must solidify at a deeper level in the crust than one-feldspar granites.

At 0.5 GPa partial water pressure (i.e., $pH_2O = 0.5$ GPa), the two feldspars S_1 and S_2 will both exsolve as the temperature is lowered slowly enough so that equilibrium is maintained. A 600 °C we will have two feldspars *X* and *Y*, and both will have exsolved blebs of each other. The percentage of exsolved versus host phase in *X* and *Y* can be calculated using the lever rule: for example, *X* will contain $100*P_1X/XY$ or 12.5 % exsolved blebs of *Y*. The student is encouraged to calculate how much exsolved blebs will occur in *Y* crystals.

Effect of Pressure and Volatiles in Unary and Binary Systems

In the discussion of Ab–Or system above, we have seen that H_2O pressure can have profound effect on the phase relationships. In this section, we expand on the topic to other systems to have a clear understanding of the effect of pressure and volatiles.

The System Fo–H_2O

The effect of pressure and volatiles on forsterite is a good place to start (Fig. 3.27a, b). Figure 3.27a is a three-axis diagram that depicts the effects of both pressure and H_2O content. Figure 3.27b shows the same effects on a pressure– temperature, or *P*–*T*, diagram. As pressure increases, so does the melting point of forsterite: for example, *M*1 and *M*2 represent the melting points of forsterite at 1 and 2 GPa.

The presence of H_2O at high pressure lowers the melting point of forsterite: the shaded surface in Fig. 3.27a is the surface where forsterite coexists with a melt phase that is saturated with vapor. Any point on that surface represents a melt composition that has the maximum amount of H_2O dissolved in the melt phase. At a fixed high pressure, e.g., 1 GPa, and in presence of H_2O, a eutectic point exists (*E*1 at 1 GPa) where forsterite coexists with a melt (*E*1) and an aqueous fluid (*V*1 at 1 GPa). This fluid is not pure H_2O but one that has a small amount of forsterite dissolved in

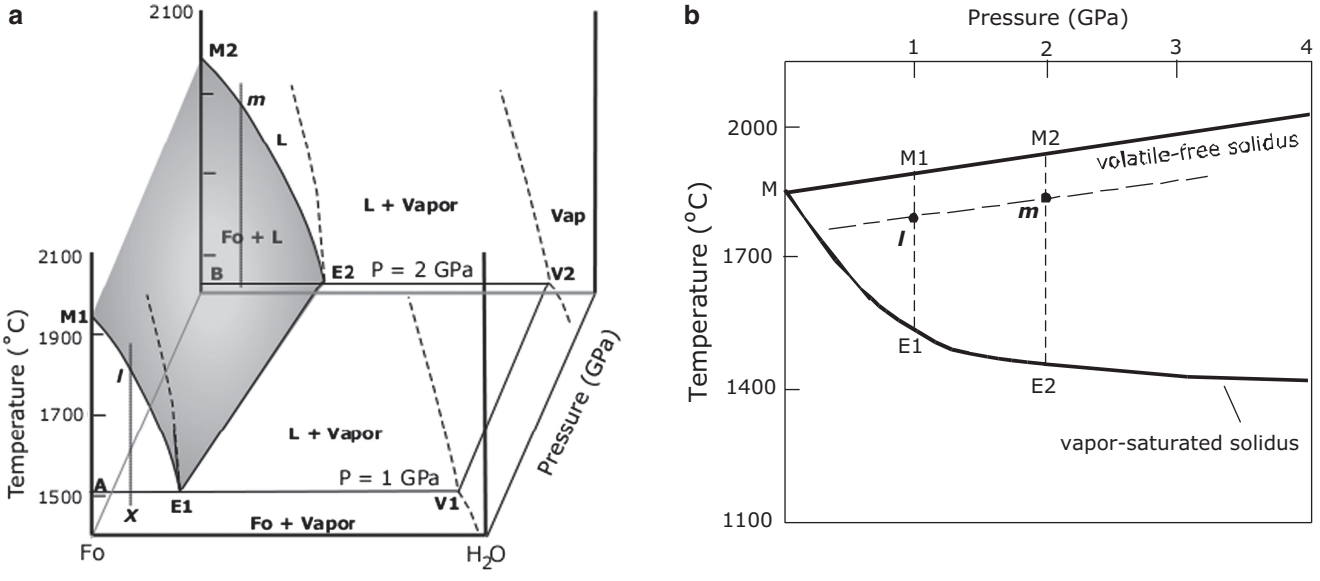

Fig. 3.27 (**a**) The system forsterite–H_2O over a pressure range of 1–2 GPa. At the 1 GPa isobar, the solidus is defined by the eutectic relationship *A* (forsterite)—*E*1 (eutectic point at 1 GPa)—*V*1 (a fluid phase with some dissolved silicate). *A*–*B*–*V*1–*V*2 is the solidus surface at 1–2 GPa. The *shaded surface* represents a polybaric surface where forsterite coexists with a H_2O-saturated fluid: at any temperature and at constant pressure (say, 1 GPa), the fluid composition would be determined by the point of intersection of the isotherm with the dashed line that represents the fluid composition. (**b**) Pressure–temperature diagram for the system Fo–H_2O based on Fig. 4.26. See text for further discussion

it. Thus, the solidus at 1 GPa is *A*–*E*1–*V*1. Similarly, *B*–*E*2–*V*2 is the solidus at 2 GPa (Fig. 3.27a).

Increase of pressure shifts the eutectic between forsterite and fluid away from forsterite composition: contrast the location of *E*1 with *E*2 in Fig. 3.27a. Figure 3.27b shows two curves—*M*–*M*1–*M*2 is the solidus of pure forsterite (i.e., loci of all melting points as a function of pressure), and *M*–*E*1–*E*2 is the vapor-saturated solidus (i.e., loci of all eutectic points). Based on what we discussed above, the maximum amount of dissolved H_2O (i.e., saturation) along *M*–*E*1–*E*2 increases with increasing pressure. At any pressure, say 1 GPa, a melt can have maximum amount (about 30 %) of dissolved vapor (which is not pure H_2O but *V*1) allowed by point *E*1.

As the shaded surface in Fig. 3.27a shows, even at 1 GPa, a melt carrying forsterite crystals can have much less dissolved H_2O at higher temperatures than the maximum allowed at its eutectic point *E*1 at that pressure. Consider the equilibrium fusion of a "rock" with a bulk composition *X* at 1 GPa (Fig. 3.27a). This rock will begin to melt at the solidus, and the first formed melt will have the composition at *E*1, in association with a vapor of composition *V*1. Thus, the melt *E*1 is vapor saturated. Temperature will rise only after the maximum amount of melt is produced at *E*1. The final melting will occur at *l* because that is where the bulk composition line intersects the liquidus. Note that *l* is not a vapor-saturated composition because there is no free vapor phase that coexists with this melt. The maximum H_2O content of the final melt will be the same as that of the bulk composition. Thus, for all bulk compositions falling between *A* and *E*1 at 1 GPa, the isobaric solidus temperature and the first melt composition will be the same; however, their liquidus temperatures will be very different.

Figure 3.27b is a more commonly used diagram where the volatile-free solidus is plotted along with the vapor-saturated solidus in *P*–*T* space. As discussed above, any melt at any point on the vapor-saturated solidus at any pressure will have the maximum dissolved H_2O at that pressure. In Fig. 3.27a, we saw that *l* and *m* are the liquidus temperatures for the bulk composition *X* at 1 and 2 GPa, respectively. One can draw a line, such as the dashed line in Fig. 3.27b, along which melts will have the same %dissolved H_2O.

Effect of Pressure on Binary Eutectic System: Isoplethal Diagrams

In the absence of volatiles, melting points of minerals and temperature of eutectic points increase as pressure is increased. The eutectic melt composition also changes with pressure. Thus, melting point and eutectic point at a single pressure become univariant lines in

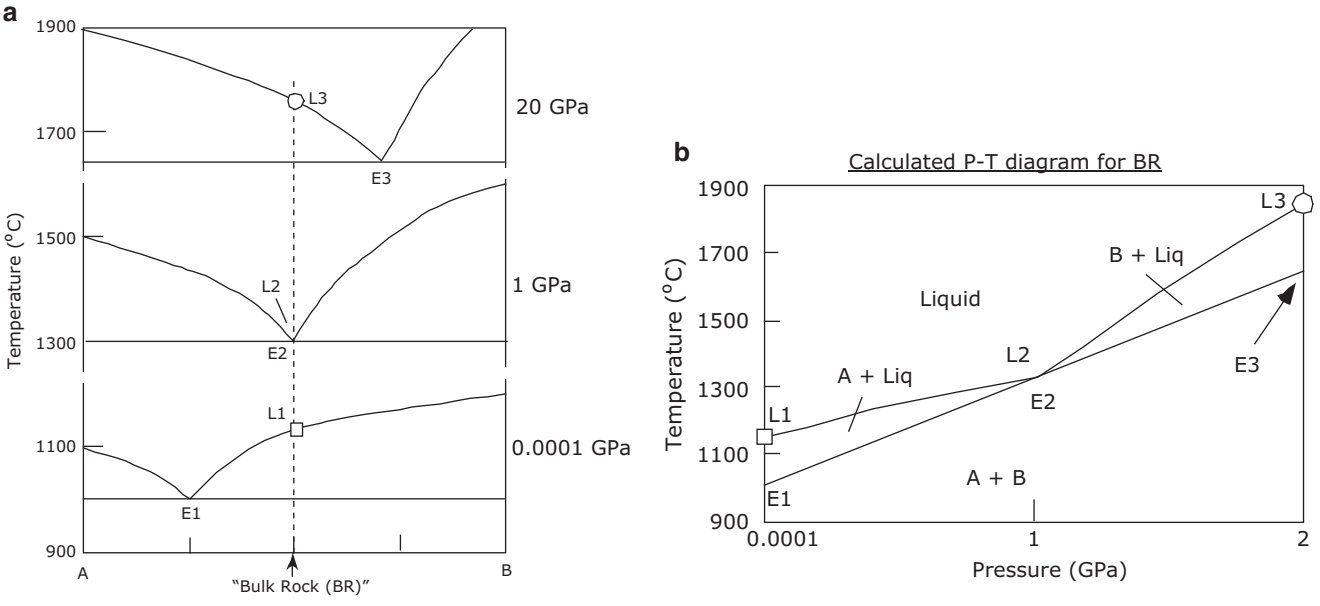

Fig. 3.28 Construction of isoplethal diagram and multisaturation point. (**a**) *T–X* diagrams for the hypothetical system *A–B* at three isobars (0.0001, 1, and 20 GPa). A "rock" of composition at "BR" will have isobaric liquidus composition same as the starting bulk composition. At the three pressures, BR will have the liquidus temperatures corresponding to *L*1, *L*2, and *L*3 and solidus temperatures corresponding to *E*1, *E*2, and *E*3, respectively. $L2 = E2$, i.e., there are the exactly same eutectic point. (**b**) Isoplethal pressure–temperature diagram for BR constructed from information on solidus and liquidus gathered from (**a**). The point where the liquidus and solidus meet (*L*2, *E*2) is referred to as a multiphase saturation or simply multisaturation point. It is clear that the rock we have chosen, BR, has a composition that is identical to the eutectic liquid *L*2, and thus, a straightforward interpretation of this rock would be that it is a solidified primary melt that was generated at 1 GPa by eutectic melting of a source "rock" containing A and B crystals. Although there are other interpretations possible, such coincidence especially in natural systems is extremely unusual. Therefore, multisaturation points are often used as an important criterion in determining how primary and primitive a magma is and hence its depth of origin

P–T space. Figure 3.28a shows a hypothetical eutectic system *A–B* to illustrate the effect of pressure in the absence of volatiles. Note that the melting points of *A* and *B* increase, as do the isobaric eutectic points between *A* and *B*, as pressure goes up from 0.0001 to 2 GPa.

One can also construct *P–T–X* (pressure–temperature–composition) diagrams to evaluate the melting and crystallization behavior of individual bulk "rock" compositions (Fig. 3.28b). Consider the starting "bulk rock" composition BR (Fig. 3.28a, b). This rock will start melting at different temperatures at different pressures: at *E*1 (1,000 °C) at 0.0001 GPa, *E*2 (1,300 °C) at 1 GPa, and *E*3 (1,650 °C) at 2 GPa. That is, *E*1, *E*2, and *E*3 are the solidus temperatures for BR at these pressures. Under equilibrium melting compositions, BR will be fully molten (i.e., liquidus temperatures) at *L*1 (1,140 °C) at 0.0001 GPa, at *L*2 at 1 GPa, and at *L*3 at 2 GPa pressures. Combining this information and interpolating between the three sets of solidus and liquidus temperatures, we can construct a *P–T* diagram for BR (Fig. 3.28b). This

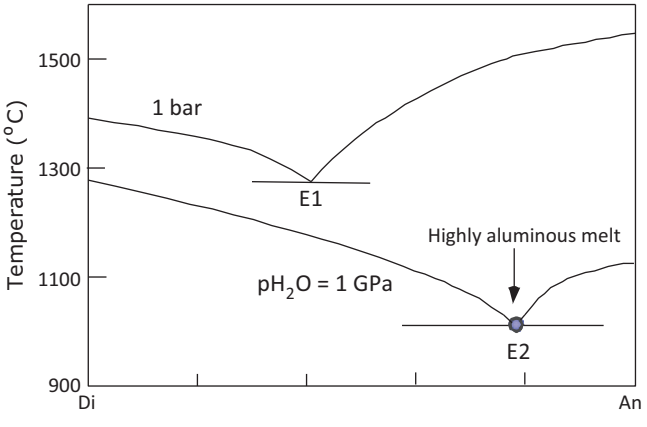

Fig. 3.29 Effect of water (pr [article pressure of water], P_{H2O}) on phase relationships in the system diopside–anorthite. P_{H2O} lowers the solidus and liquidus and significantly changes the eutectic melt composition

type of diagram is called an *isoplethal* diagram because it pertains to a single bulk composition. It should be apparent that one could draw many isoplethal diagrams for many individual compositions within this system.

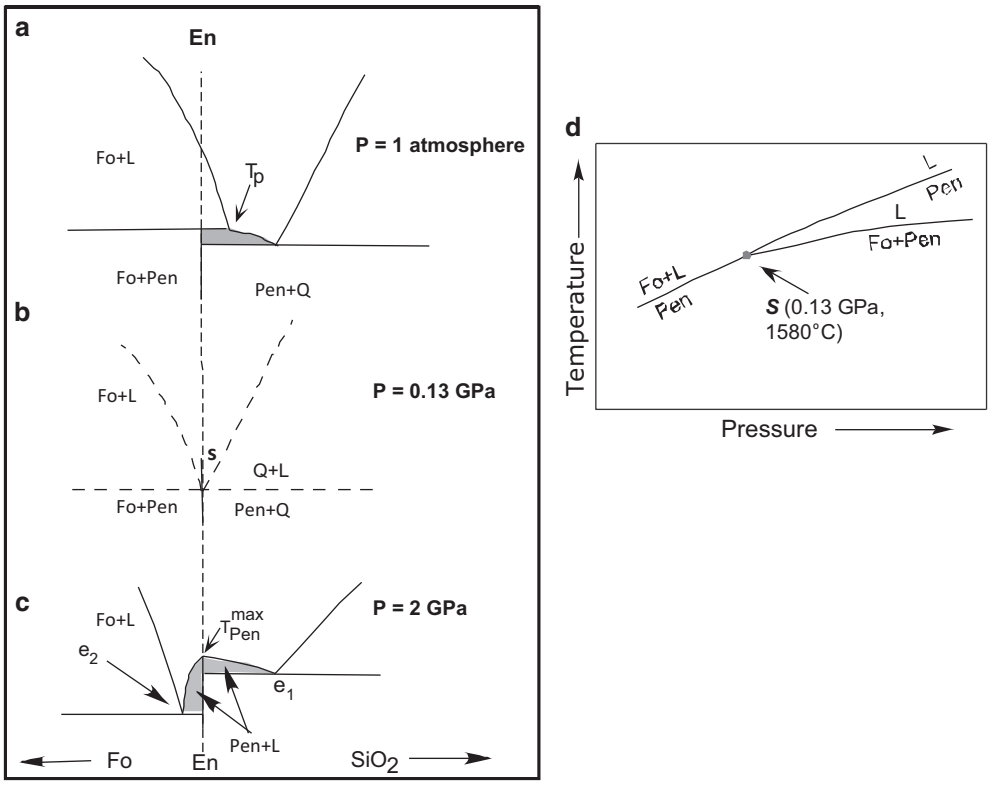

Fig. 3.30 Effect of pressure ("dry" or volatile free) on the system forsterite–silica. (**a**), (**b**), and (**c**) are phase diagrams at three different pressures. At low pressure (0.0001 GPa), the reaction relationship Fo + L = Pen occurs. At high pressure (say, 2 GPa), protoenstatite (Pen) has its own melting point, which creates a thermal maximum (T^{max}_{Pen}) and two separate eutectic points (e_1 and e_2). (**b**) is an estimated diagram representing a singular point "*s*" that probably occurs around 0.13 GPa 1,580 °C. (**d**) A schematic diagram showing the nature of the singular point in relationship to the peritectic Fo + L = Pen and the two cotectic curves (Fo + Pen = L and En + SiO2 = L (which is not shown here for brevity)) and the melting curve of Pen (*source*: Presnall et al. 1998)

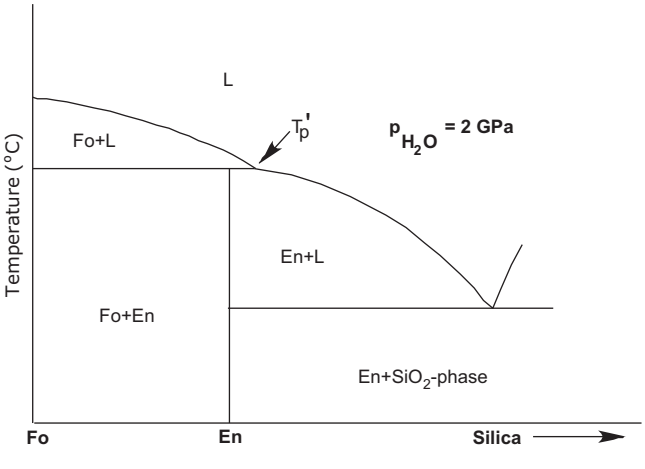

Fig. 3.31 Effect of H_2O on the system Fo–SiO_2 at high pressure

As we will see in later chapters, chemical composition of plausible source rocks of magmas can vary a lot, and so the liquidi in their corresponding isoplethal diagrams would be expected to vary considerably, but their solidi should be pretty close to each other as long as the same mineral phases are present. In fact, Hirschmann (2000) found that all experimentally determined solidi for different peridotite compositions in different laboratories hardly vary over a pressure range of 0–4 GPa and that the mean solidus can be fitted with the equation:

$$T\ (^{\circ}\mathrm{C}) = aP^2 + bP + c$$

where $a = -5.104$, $b = 132.9$, and $c = 1{,}120.66$, and P is in GPa.

The student is urged to use this equation to calculate the solidus of an average peridotite and contrast that to the "dry" forsterite solidus we discussed earlier in order to have an appreciation of the similarity and difference in melting behavior of a pure mineral (olivine in this case) and a natural rock (peridotite) that has about 60–65 % of that mineral.

Effect of P_{H2O} on Diopside–Anorthite System

H_2O plays an important role in the origin of a whole suite of magmas that characteristically form in subduction zones. As will be discussed in a later chapter, most arc magmas contain greater amounts of Al_2O_3 than those that form at rift zones and at hot spots. This increased Al_2O_3 content is commonly attributed to the effect of H_2O in magma production.

As we noticed in our discussion of Fo–H_2O system, one important effect of H_2O is to depress the solidus temperature at higher pressure. In the case of system diopside–anorthite, H_2O not only lowers the melting points of diopside and anorthite, but it also shifts the eutectic point closer to anorthite, such that the melts generated at the eutectic are significantly more Al-rich (Fig. 3.29). This diagram thus provides a reasonable explanation for the high Al content of subduction zone magmas as being due to high H_2O content in the magma source region.

System Fo–SiO_2

Perhaps the most significant pressure effect that is of relevance to magmas in this system is that the well-known low-pressure reaction relationship forsterite + liquid = orthopyroxene (protoenstatite, Pen) disappears as pressure is increased beyond a certain threshold (about 0.13 GPa; Fig. 3.30b). Instead, protoenstatite has its own melting point such that a new isobaric eutectic point between forsterite and protoenstatite (Fo + Pen = L) is created at higher pressure (Fig. 3.30c).

Chen and Presnall (1975) showed that the behavioral change from a reaction relationship to one of eutectic relationship between forsterite and enstatite at higher pressure is only possible when a *singular point* (s) occurs on the liquidus at which en, fo, and L coexist (Fig. 3.30b). The nature of the singular point is best understood in *P–T* space (Fig. 3.30d). Here three univariant curves come into grazing coincidence, and these curves are Pen = Fo + L (which represents incongruent melting of protoenstatite), Pen = L (congruent melting of protoenstatite), and Fo + Pen = L (a cotectic curve).

Addition of H_2O to this system at high pressure has the following effects: (1) It extends the reaction relation Fo + L = En, (2) the peritectic point is moved toward silica such that hydrous melting of olivine + enstatite rock will result in relatively SiO_2-rich melt, and (3) it lowers the eutectic point En + Q = L. (Fig. 3.31).

Summary

1. The concepts of phase rule, chemical potential, Gibbs' free energy, entropy, enthalpy, and volume are all fundamentally important in understanding phase relationships.
2. Many different types of phase behavior are shown by mineral/melt systems, such as eutectic, reaction relationship, complete solid solution, limited solid solution, and subsolidus unmixing. (Liquid immiscibility also occurs but will be discussed in a different chapter.)
3. Melting and crystallization processes in any system can be of two extreme types—equilibrium and fractional. In most systems, melt and solid paths during equilibrium versus fractional melting (crystallization) are very different. Melt paths in fractional melting are different from melt paths in fractional crystallization.
4. The lever rule is an important constraint on the proportion of crystals and melt at any given *P*, *T* condition.
5. Mixing of melts can result in extensive crystallization or partial or total resorption of crystals and crystallization.
6. Pressure has a strong effect on phase relations, as does H_2O. Overall, partial melting of peridotite in the presence of H_2O would result in silica and alumina-rich magmas.
7. Addition of volatiles substantially lowers the melting temperature (solidus) relative to the "dry" solidus.

Exercises

Problem 1.

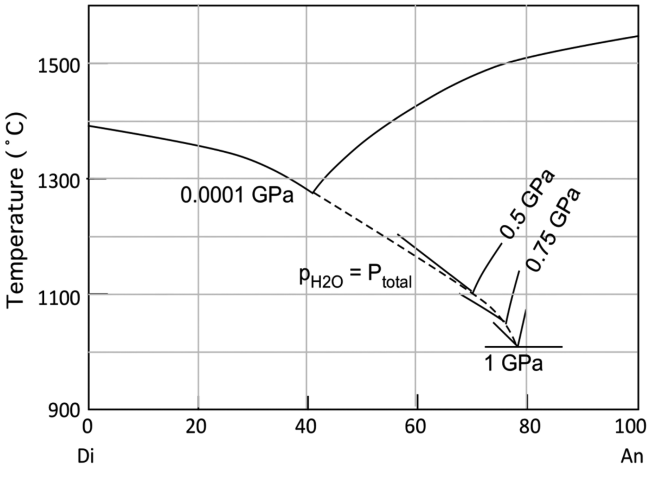

The above diagram shows how the eutectic point at 0.0001 GPa between diopside and anorthite changes with increasing P_{H2O}. The dashed line traces the solidus of this system with increasing pressure. (Note that the diagrams at 0.5 and 0.75 GPa are approximate.)

(a) Draw a *P–T* diagram showing the solidus in this system from 1 bar (0.0001 GPa) to 1 GPa.
(b) Calculate the compositions (on anhydrous basis) of the isobaric eutectic melts at 0.0001 and 1 GPa in terms of CaO, MgO, Al_2O_3, and SiO_2.
(c) Calculate the maximum percentage of melt that may be produced from the starting mixture $Di_{58}An_{42}$ at the isobaric eutectic points at 0.0001 and 1 GPa.

Problem 2.

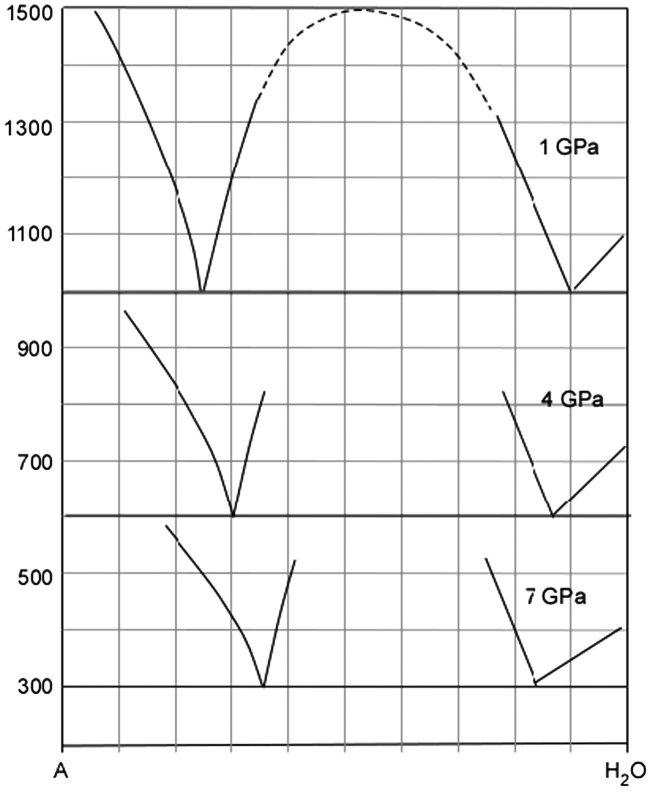

In the above diagram, slices of three isobaric phase diagrams at 1, 4, and 7 GPa are shown for the system A-H_2O. It is similar in appearance to the Fo–H_2O system discussed in the text.

(a) Draw the solidus and liquidus for the bulk starting composition $A_{80}(H_2O)_{20}$.
(b) What are the minimum and maximum dissolved H_2O contents of melts produced by equilibrium fusion of the above starting composition at each pressure?
(c) Plot the line in *P–T* space that represents melt with constant 20 % H_2O.

Phase Relationships in Ternary Systems

4

Abstract

This chapter builds on what we learned about mineral–melt relationships in simpler systems in the previous chapter. The five oxides, CaO, MgO, FeO, Al_2O_3, and SiO_2, make up 90 % or more of the common igneous rocks on Earth. In this chapter, we expand our understanding of phase relationships in three-component systems that are made of these oxides and as such are excellent analogs of natural melt–mineral relationships. We also consider the effect of pressure and H_2O and CO_2 on ternary phase equilibrium.

Introduction to Ternary Eutectic System

Consideration of three components and temperature requires the addition of a third dimension, as shown in Fig. 4.1a. Figure 4.1a is an example of a 3D perspective diagram of a hypothetical ternary system at a fixed pressure. In it A, B, and C are three hypothetical components plotted at the apices of the triangular base, and temperature is plotted along the vertical dimension. Each side of the triangular base represents a binary eutectic diagram such that there are three binary eutectic points here—E_1, E_2, and E_3. The three sloping surfaces (shaded) represent the liquidus surfaces for each of the three crystalline phases A, B, and C. Isotherms (i.e., constant temperature contours) are shown as dashed contours on the three liquidus surfaces.

A "thermal valley," called a cotectic boundary, occurs where two adjacent liquidus surfaces come into contact: for example, the liquidus surfaces of C and B merge at the cotectic E1 → E. There are three cotectic boundaries in this diagram: E1 → E, E2 → E, and E3 → E. E is the *ternary eutectic point*, which is the lowest temperature at which a melt can exist with A, B, and C crystals. Each of the cotectic boundary is also an isobaric univariant curve because three phases (two crystalline phases and a melt) coexist along it. The arrow on each cotectic curve in Fig. 4.1a points toward the "downslope" or lower-temperature direction. The ternary eutectic point E has a variance of zero, which can be shown as follows. Since pressure is fixed, the phase rule reduces to $f = c - \phi + 1$. At E, $c = 3$, and $\phi = 4$; therefore $f = 0$. Therefore, E can also be referred to as an isobaric invariant point.

The use of such 3D diagrams is clearly cumbersome in quantifying phase relationships. Therefore, it is more useful to project the liquidus surfaces and isotherms onto the triangular base ABC (Fig. 4.1b). Similar to topographic contours, spacing between adjacent isotherms indicates the steepness of the slope of the liquidus surface: the tighter the spacing the steeper the liquidus surface.

Plotting compositions on a triangular diagram requires the knowledge of the percentages of any two components because the third is then automatically fixed, i.e., if % of A and B are 15 and 25 in a starting melt composition, then C must be equal to 100 – (15 + 25) or 60 %. Figure 4.2 shows a triangular graph, on which the percentages along A–C are labeled to show how the percentage of A and C change. Also plotted is the composition $A_{40}B_{30}C_{30}$ in order to illustrate how the plotting inside the triangle is done. Horizontal lines represent % A, increasing in 10 % steps from 0 % along B–C boundary to 100 % at the apex A. Similarly, %B is 0 at the A–C boundary and increases in 10 % steps along the lines

G. Sen, *Petrology*, DOI 10.1007/978-3-642-38800-2_4,

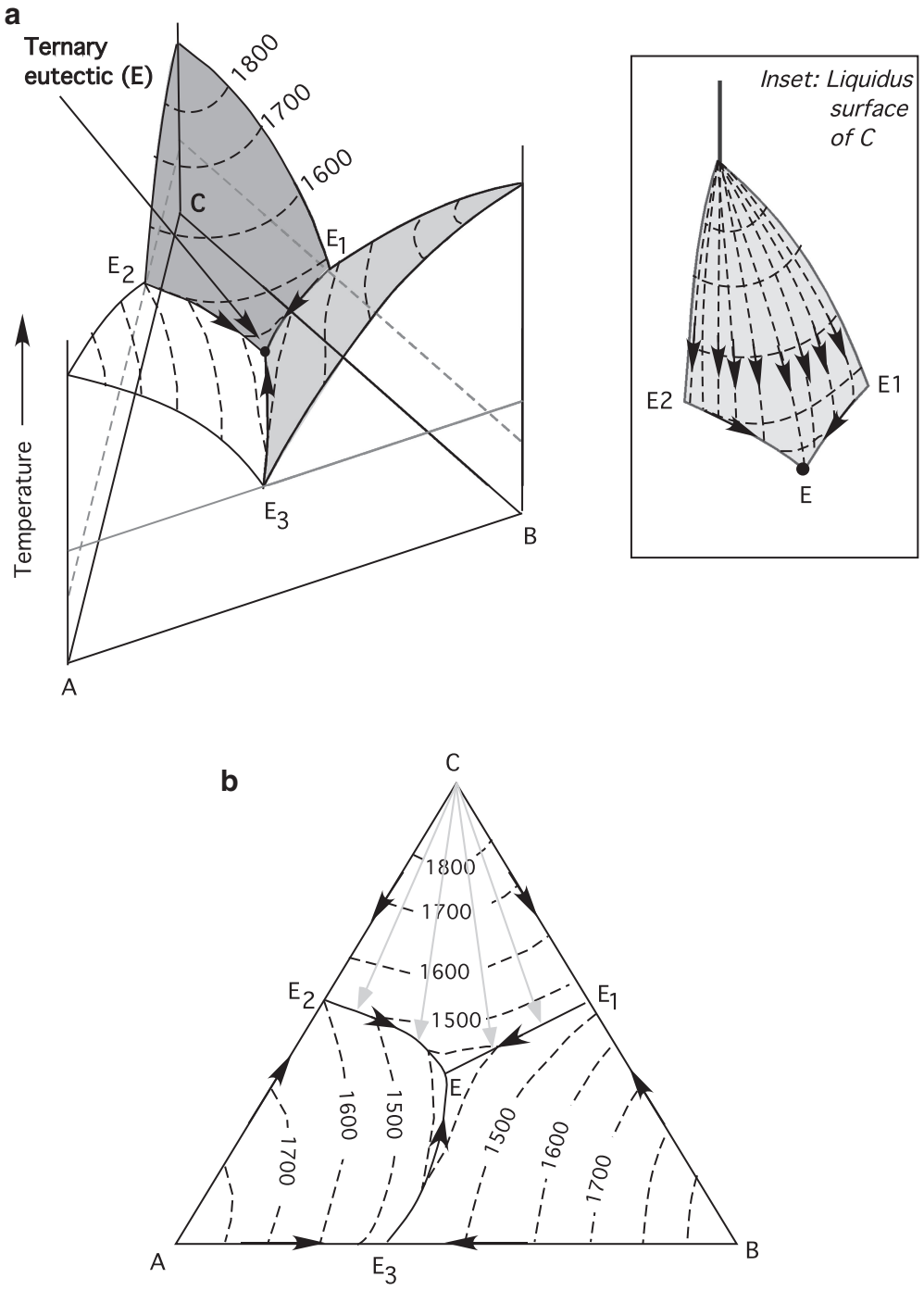

Fig. 4.1 (**a**) Perspective sketch of the nature of the liquidus surfaces (differently shaded) in temperature–composition space for the hypothetical ternary eutectic system A–B–C at a fixed pressure. The three bounding eutectic points are E_1, E_2, and E_3, and the ternary eutectic point is located at E. The *dashed curves* are isotherms. *Arrows* indicate down-temperature directions of the cotectic curves. The *inset* shows the liquidus surface of C, with *dashed arrows* indicating movement paths of various liquid compositions as they cool. (**b**) The temperature–composition diagram in (**a**) is projected onto the base of the triangle A–B–C

parallel to the A–C boundary, increasing to a maximum of 100 % B at the B apex. And, %C lines are parallel to the A–B boundary. So, $A_{40}B_{30}C_{30}$ plots where the three lines representing A_{40}, B_{30}, and C_{30} intersect.

Different authors have used different projections (i.e., wt% versus mole%) in discussing phase diagrams in the literature. In this chapter, the phase diagrams are wt% diagrams unless otherwise stated.

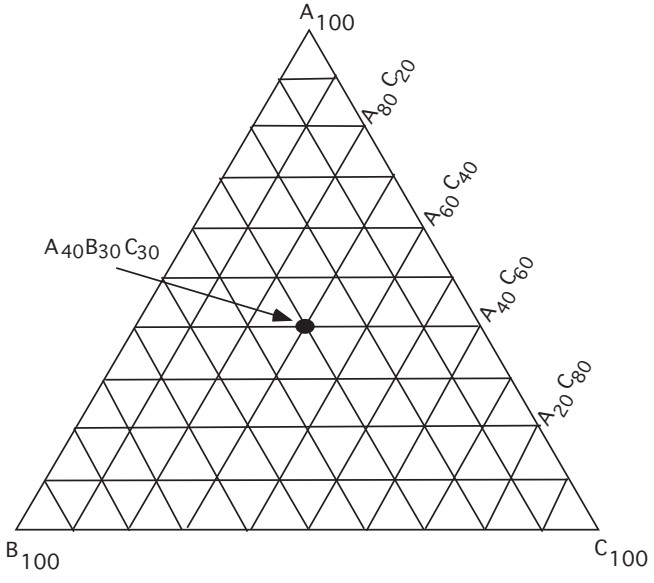

Fig. 4.2 Plotting a ternary composition in a triangular graph

Equilibrium Crystallization and Melting

Let us first consider the crystallization of a melt M in the hypothetical system A–B–C (Fig. 4.3a). M lies within the liquidus field of B and has a liquidus temperature of 1,600 °C (note that it plots on the 1,600 °C isotherm). Therefore, M will begin to crystallize B at 1,600 °C and change composition directly away from the B corner (since crystallization of B will deplete the melt in B component). The melt will move toward the cotectic E3–E as it crystallizes more and more of B, eventually reaching it at the point "1." Along the cotectic, crystals of A will join crystals of B as the melt moves toward E. At the ternary eutectic E, which is the lowest temperature point, A, B, and C crystals will crystallize, and the melt will eventually be all solidified. So, the melt path in this case is M–1–2–3–E.

The solid path can be constructed with the help of tie-lines (long-dashed lines, Fig. 4.3a). When the melt just reaches 1, the tie-line is 1–M–B, and one can use the lever rule to calculate melt and solid% (melt % = 100*Distance MB/Distance B1). When the melt reaches 2, one can draw a tie-line through the bulk composition M to the B–A line (since B and A are crystallizing). So, at this point, the solid path has reached 2′. When the melt reaches E, the last tie-line 4′–M–E can be drawn. While the melt remains at E, the solid path will move toward E (from 4′ to M) because A, B, and C are crystallizing and the final bulk solid must be the same as the starting melt (i.e., bulk) composition. Thus, the total solid path is B–2′–4′–M.

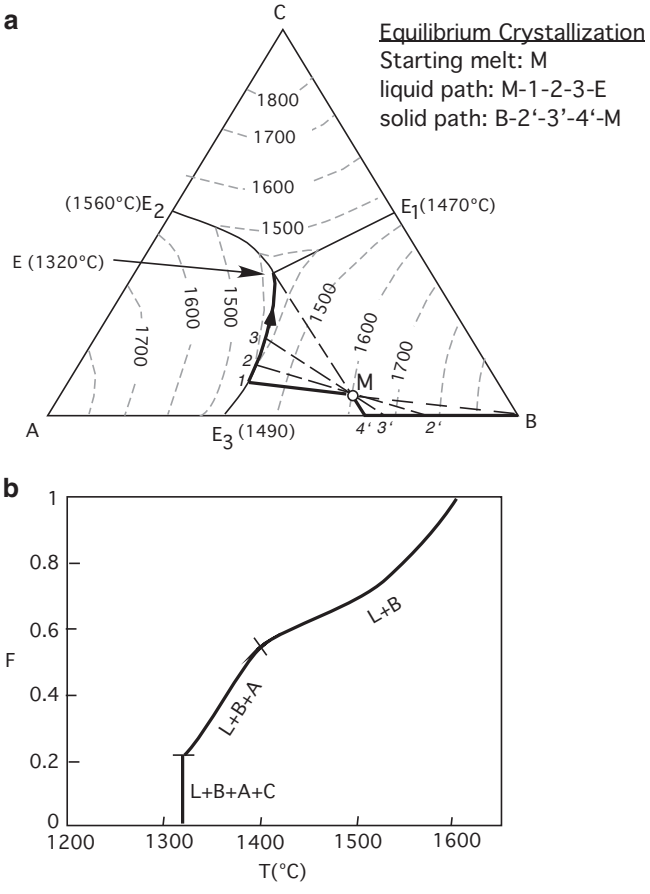

Fig. 4.3 (**a**) Equilibrium crystallization of a melt M in the hypothetical ternary eutectic system A–B–C. Solid and liquid paths are shown as *bold lines* and tie- lines are shown as *dashed lines*. (**b**) Temperature versus melt fraction (F) for starting melt M in (**a**)

Application of the lever rule at various temperatures leads us to a crystallization curve for M in temperature–melt fraction diagram, or *T*–*F* diagram (Fig. 4.3b). Note that B crystallizes over a fairly long temperature interval until about 60 % melt (i.e., $F = 0.6$). Then A joins B, as the slope of the crystallization curve also changes. Crystallization of both A and B continues until the melt reaches E, where 22 % melt is left. This melt slowly becomes fully crystalline at the eutectic point. During eutectic crystallization, the temperature remains fixed.

Equilibrium melting paths for solid residue and melt generated are exactly the reverse of equilibrium crystallization. This can be seen in the case of heating a starting "rock" composition X (Fig. 4.4). X will not melt until the temperature of the ternary eutectic (1,320 °C) is reached. Continued heating will not raise the temperature but produce more melt at E while the solid residue moves toward 4′ and reaches 4′. At this point all crystals of C would have been

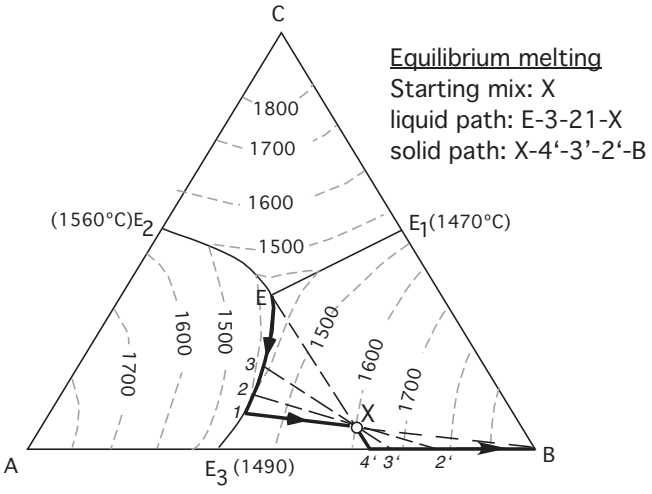

Fig. 4.4 Equilibrium melting of composition X in the system A–B–C

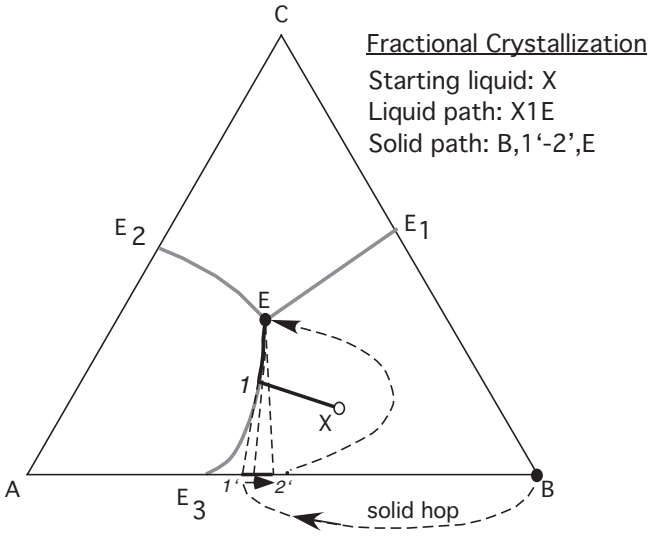

Fig. 4.5 Fractional crystallization of starting liquid X is shown

dissolved, and the melt will be free to move up along the cotectic to point 1, where the last tie-line can be drawn through the bulk composition to the B corner. When the melt reaches 1, it will have seen the last crystals of A and with further heating will move toward the starting composition X. When it reaches X, the entire rock will be molten.

Fractional Crystallization

Consider a melt of bulk composition X (Fig. 4.5). As with equilibrium crystallization, this melt will begin to crystallize B at the liquidus temperature of X. Prompt removal of B crystals from melt, as required by fractional crystallization, will drive the residual melt composition directly away from B toward point 1, and at any given instant, the melt composition is a new bulk composition.

Once the melt reaches 1, it will start crystallizing B and A. The *instantaneous* mixture of B and A crystals will have its composition at the point where a tangent (1–1′) to the cotectic E–E_3 at 1 meets the binary side A–B of the triangle. This is a "solid hop" where the solid path is not continuous but composed of jumps. The proportions of B and A in the crystalline precipitate can be determined by using the lever rule: a proportion in solid = B–1′/B–A.

The melt at 1 will continue to move down the cotectic toward E; and a series of tangents from melt on the cotectic on to the base A–B may be constructed in order to track the total solid path (1′ → 2′). When the melt reaches E, the total solid path will "hop" to E as well.

Fractional Melting

Perusal of phase relations in binary systems showed that during fractional melting, the residual solid composition changes continuously, whereas the melt composition path is a discontinuous one—"hopping" from invariant point to invariant point. This behavior persists in ternary systems as well, as illustrated by the example below.

Consider the example of a "rock" X in Fig. 4.6. It will begin to melt at the ternary eutectic point E, and the solid residue will move toward Y. Because fractional melting would have extracted all the melts, the residual

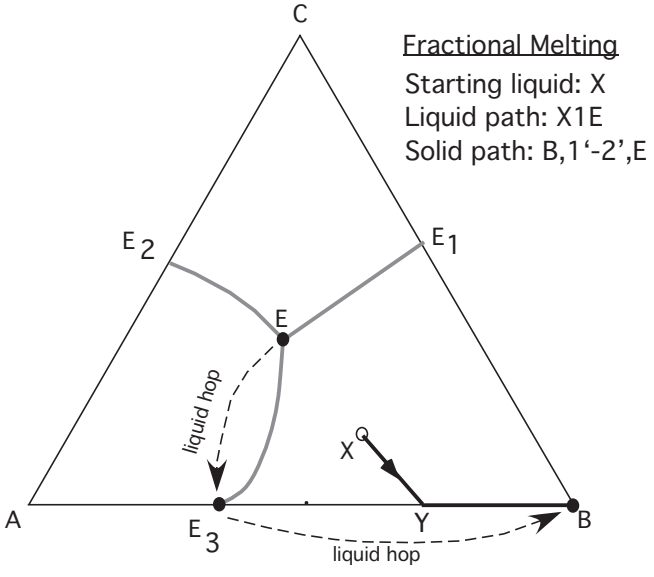

Fig. 4.6 Fractional melting of composition X is shown

solid at Y will simply be composed of B and A. Melt being absent, the solid Y will no longer behave like a ternary but as a binary A–B; and melting will resume only when the temperature is raised to the binary eutectic temperature of E_3. Prompt removal of melt of composition E_3 will drive the composition of the solid residue composition toward B corner. When the solid residue reaches B, it will behave like a unary system being composed entirely of B crystals, and thus it will not melt again until the melting temperature of B is reached. Thus, once again, the total solid path is continuous, and the melt path is discontinuous (melt hops) in fractional melting.

Box 4.1: Phase Relationships on a "Join" in a Ternary

Sometimes it is useful to examine phase relationships of various melt compositions along a line transect within a ternary system because they reveal things that may not be obvious from visual inspection of the ternary. An example of such a line transect, called a *join*, is the line X–Y that cuts through the ternary A–B–C in Fig. 4.7. The diagram depicting phase relationships on the join is called a *pseudobinary* diagram (Fig. 4.8) because the residual liquids from crystallization of any starting melt composition on the join do not remain confined to the join (as in the case of a true binary system) but moves into the ternary system.

Consider the phase relationships along the join X–Y with reference to Fig. 4.7. In constructing the pseudobinary, we need to track liquid paths for crystallization of several starting liquid compositions on the join, which are shown as dots and represented with symbols a–f. The above figure shows the arrows representing such liquid paths. These arrows for X, a, b, and c, radiate from the A corner, as they all fall within the liquidus field of A and therefore must move away from A upon crystallization. Similarly, arrows for d, e, f, and Y radiate from the B corner. Each liquid path will have somewhat different temperatures of appearance of different phases, and including this information on the temperature–composition space will result in the pseudobinary diagram as shown in Fig. 4.8.

For example, the starting liquid "a" will begin to crystallize A when it reaches its liquidus temperature (1,600 °C) and will crystallize only phase A until it reaches the A + C + L cotectic

(continued)

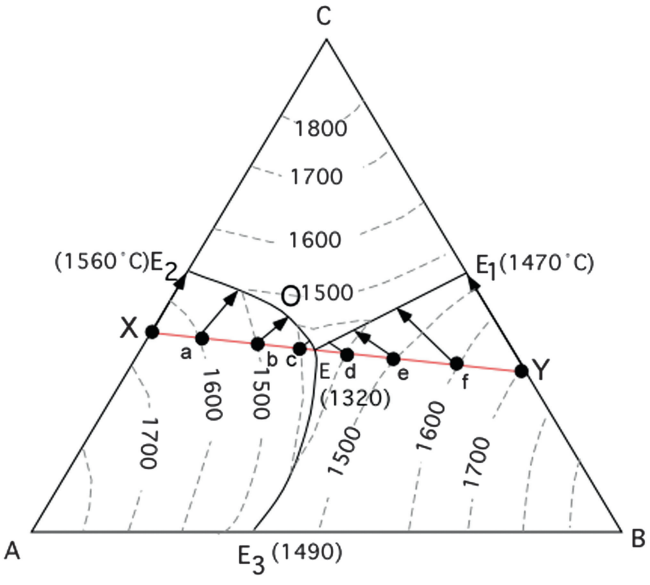

Fig. 4.7 Phase relationships on the join X–Y

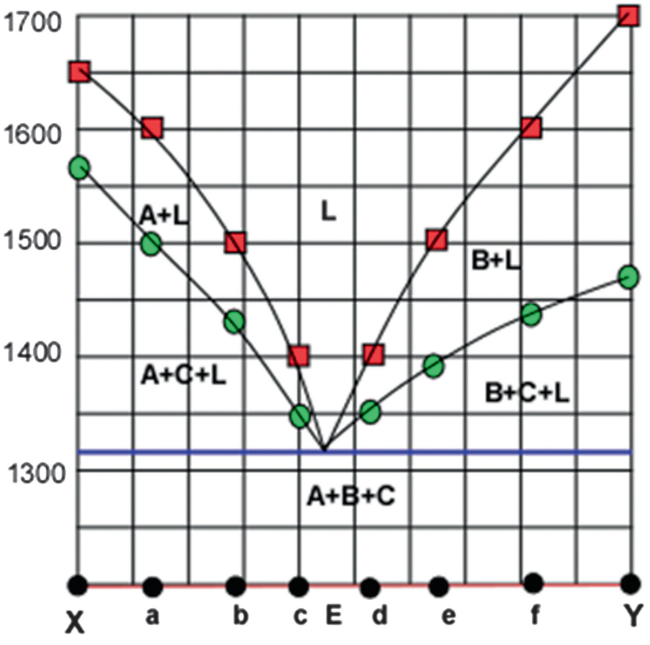

Fig. 4.8 Pseudobinary diagram for X–Y

Box 4.1 (continued)

at 1,500 °C. With further cooling, the residual liquid will move down the cotectic and will crystallize the eutectic assemblage A + B + C + L when it reaches the eutectic temperature (1,320 °C). The complete diagram is thus constructed by noting the temperatures of various phase appearances for each starting liquid composition.

Examples of Ternary Eutectic Systems

Anorthite–Forsterite–Diopside

The system anorthite–forsterite–diopside at atmospheric pressure shows ternary eutectic behavior between the three crystalline phases—anorthite, forsterite, and diopside (Fig. 4.9). However, the appearance of a spinel liquidus field introduces some complexities because crystallization of spinel, whose composition ($MgAl_2O_4$) does not plot within this triangle, drives the residual melt composition out of the ternary diagram. Thus, melts plotting inside the spinel liquidus field or its boundaries (shaded field) will crystallize spinel; and the resulting solid and liquid paths will fall outside the An-Fo-Di plane. In fact, this plane is not a system but part of a larger four-component system $CaO–MgO–Al_2O_3–SiO_2$ (Fig. 4.10). The univariant lines on the An–Fo–Di plane as shown in Fig. 4.9 are actually intercepts of liquidus boundary planes that extend into and out of the forsterite–diopside–anorthite–silica tetrahedron (Fig. 4.10). Also, the invariant points in Fig. 4.9 are locations where univariant curves in the tetrahedron pierce the An–Fo–Di plane. Therefore, in a true sense, An–Fo–Di plane is not a system but is called a *join*, and the points on it, such as *a* and *b* in Fig. 4.9, are called *piercing points*.

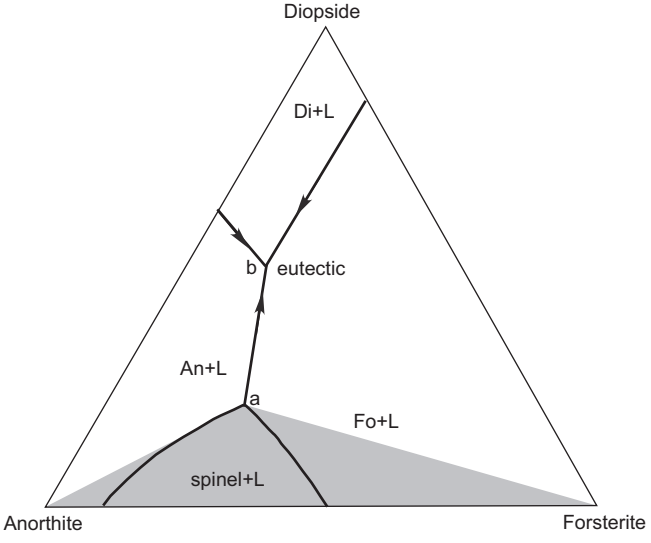

Fig. 4.9 The "system" diopside–anorthite–forsterite at 0.0001 GPa (1 atm). Any melt falling inside the *shaded area* will crystallize spinel upon cooling and leave the ternary. Also, diopside is aluminous in this "system"; therefore, any liquid crystallizing diopside will also leave this plane and go inside the $CaO–MgO–Al_2O_3–SiO_2$ (CMAS: see Fig. 4.10). Thus, the diopside–anorthite–forsterite is called a *join* and not a system

Ternary System with Solid Solution: Diopside–Albite–Anorthite at 0.0001 GPa (1 atm)

Basalts and gabbros are a group of igneous rocks that forms the oceanic crust. They are also a major component of the continental crust. The two abundant minerals in these rocks are clinopyroxene and plagioclase. The system diopside–albite–anorthite at 0.0001 GPa pressure (Fig. 4.11) serves as an analog of natural basalt magmas because crystallization behavior of clinopyroxene (diopside) and $plagioclase_{ss}$ from basaltic magmas may be illustrated in some detail with this system. The three binaries that comprise the boundaries of this system are a solid solution between albite and anorthite (i.e., $plagioclase_{ss}$) and two eutectic systems diopside–anorthite and diopside–albite. It should be noted that this often-used example is in reality not a system and has some complications, which we will ignore for our purpose here and treat diopside–albite–anorthite as a true ternary system.

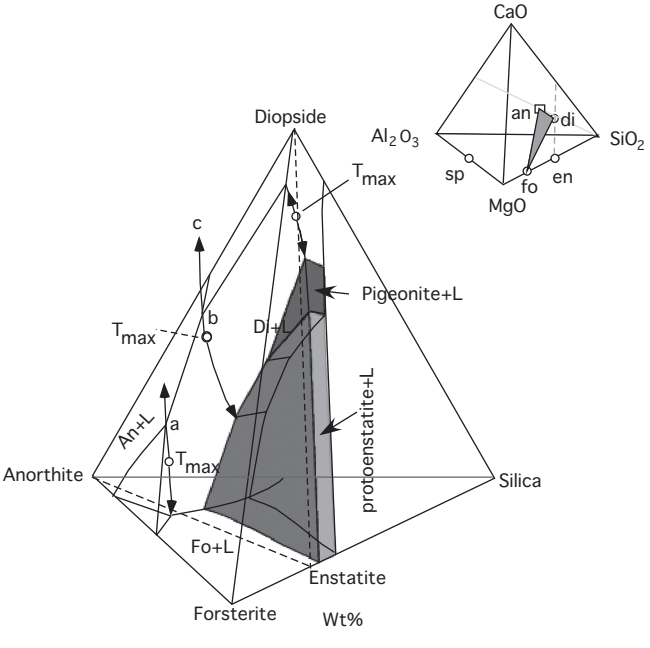

Fig. 4.10 Phase relations inside this four-component system at 0.0001 GPa are shown (based on Presnall et al. 1979). Comparison between this diagram and Fig. 4.9 shows that the "invariant points" *a* and *b* in Fig. 5.10 are simply the traces of two univariant curves in the CMAS system where they intersect the triangular plane diopside–anorthite–forsterite. By definition, therefore, diopside–anorthite–forsterite is not a ternary but a join (often called a *pseudoternary*); and *a* and *b* are called *pseudoinvariant* points. The *inset* shows that diopside–anorthite–forsterite is a part of the larger four-component system—CMAS

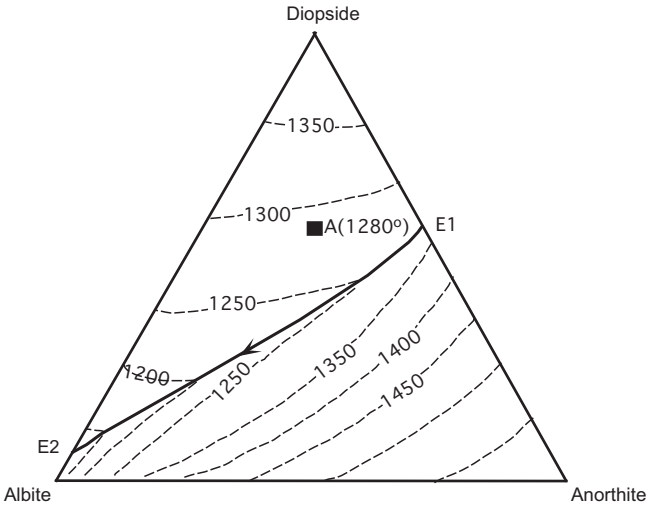

Fig. 4.11 The system diopside–albite–anorthite at 0.0001 GPa. Because diopside is aluminous in this system, melts crystallizing along the cotectic or in the diopsides field do not remain on this plane, and therefore, this is also a pseudoternary. However, one can ignore the complications and treat it as a ternary system for illustrative purposes only

The curve E1–E2 is the only cotectic boundary that occurs in this system, and it is like a thermal valley whose high temperature terminus is the eutectic point E1 between anorthite and diopside, and the lowest temperature point is the eutectic point E2 (Fig. 4.11). Melts on this curve will evolve by moving down toward E2 while crystallizing diopside and plagioclase$_{ss}$. An important handicap of this diagram is that the plagioclase composition coexisting with any melt on the cotectic cannot be directly read off the diagram but requires additional knowledge of the coexisting plagioclase. Detailed discussion of the paths taken by solid and melt phases during fractional crystallization in this system is beyond the scope of this book, except to note that the melt will reach E2 and the final solid will be a eutectic mixture of diopside and albite. Below we will only discuss equilibrium crystallization paths of melts and solids in the diopside and plagioclase$_{ss}$ liquidus fields in some detail. Fractional crystallization or melting paths are briefly discussed, mostly in the form of a passing reference.

Equilibrium Crystallization

Consider the melt A located in the Di + L. This melt will begin to crystallize diopside crystals at 1,280 °C, its liquidus temperature, which can be estimated from A's location between the 1,250 and 1,300 °C isotherms. Crystallization of diopside will drive the residual melt composition directly away from the diopside corner (Fig. 4.12a), and the residual melt will eventually reach point B on the cotectic. At this point, a plagioclase$_{ss}$ (An_{80}, based on plagioclase

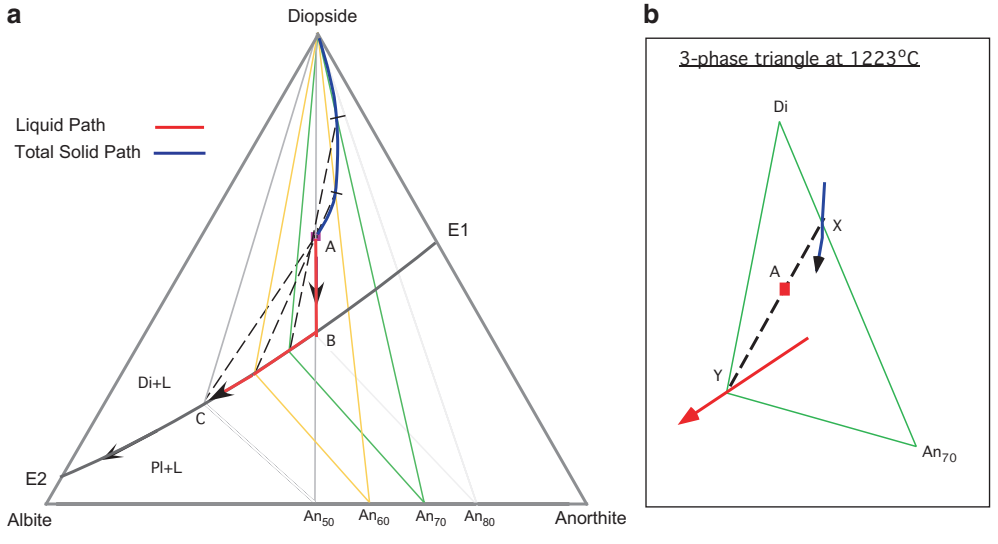

Fig. 4.12 (**a**) Crystallization of a melt A in the diopsides–albite–anorthite system. Note the *color*-coded three-phase triangles anchored at the diopside corner and sweeping across the diagram represent coexisting phases along the cotectic. *Dashed lines* are the tie-lines. Intersection of a tie-line with its corresponding three-phase triangle gives the location of a point on the solid path. Total solid path (*blue*) is obtained by connecting all such points for all possible three-phase triangles. (**b**) A three-phase triangle diopside–Y–An_{70} at 1,223 °C is used to illustrate the lever rule. The tie-line X (solid)–Y (liquid) can be used as a "lever" to calculate proportions of liquid and solid at 1,223 °C. The bulk composition "A" is the fulcrum. The *blue arrow* is the trace of the solid path and the purple arrow is the trace of the liquid path. The proportions of diopside and An_{70} crystals in the solid assemblage can also be calculated from the Di–An_{70} line using "X" as the fulcrum (see text for further discussion)

diagram—not shown here) will crystallize together with diopside. A triangle, called a *three-phase triangle*, connecting the three coexisting phases (melt B and crystals of diopside and An_{80} plagioclase) can now be constructed (Fig. 4.12a). Several such triangles are constructed to illustrate solid and melt paths as compositions of both melt and $plagioclase_{ss}$ change with cooling. Further cooling of melt B will move it down the cotectic as $plagioclase_{ss}$ composition continuously changes toward the albite corner. Because diopside composition does not change, *all* three-phase triangles will be anchored at the Di corner while "swinging" from right to left of the diagram. (In reality, note that diopside composition also changes somewhat because some Na and Al go into it as solid solution.)

At any instant, the coexisting solid composition can be determined by drawing a line from the melt composition through the bulk composition on to the base of the appropriate three-phase triangle. For example, note the three-phase triangle Di–An_{70}–Y at 1,223 °C (Fig. 4.12b). When a line is drawn from the melt composition Y through the bulk composition A to the base of this three-phase triangle, we obtain the solid composition X coexisting with melt Y. Thus, XY is a tie- line. When coexisting solid composition is located this way for each successive three-phase triangle, a curved TSP (total solid path) emerges that starts at the *Diopside* corner and terminates at A, i.e., the bulk composition (Fig. 4.12a). When TSP reaches A, the last melt will be at C and the coexisting plagioclase will be An_{50}. At this point, the right arm of the last three-phase triangle will pass through the bulk composition. It is clear that one cannot construct any more down-temperature three-phase triangles beyond this point because such triangles will not contain the bulk composition (which is an impossibility). The proportions of crystals and coexisting melt at any temperature can be determined using the appropriate tie-line and lever. For example, at 1,223 °C, the tie-line is X–A–Y; and

$$\%\text{solid} = 100 \times \text{AY}/\text{XY} \text{ and } \%\text{melt} = 100 - \text{solid}\%$$

$$\%\text{plagioclase}(\text{An}_{70}) = 100 \times \text{XDi}/\text{DiAn}_{70} \text{ and } \%\text{diopside} = 100 - \%\text{plagioclase}$$

Melts whose compositions fall within the $plagioclase_{ss}$ + L field take a curved path during crystallization because $plagioclase_{ss}$ continuously changes composition (Fig. 4.13a). Consider the crystallization of a melt P, for example. The first $plagioclase_{ss}$ to crystallize from it is S, which will drive the residual melt directly away from S. As the melt evolves slightly, the $plagioclase_{ss}$ will become more Ab-rich, and this will force the melt path to curve up. Several tie-lines, S–P, Q–P–q, T–P–t, and R–P–M, are constructed to show how the melt path curves up: each of these tie-lines

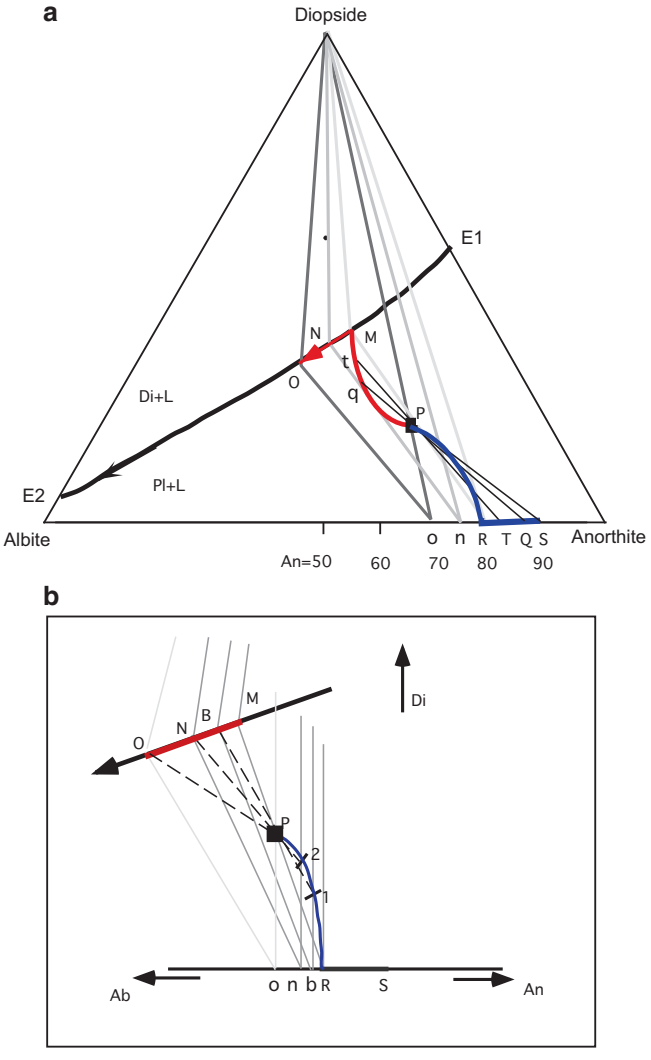

Fig. 4.13 (**a**) Equilibrium crystallization of a liquid "P" in the liquidus field of $plagioclase_{ss}$ (Pl + L). The liquid path is marked by the *red curve with an arrow*, P–M–O, and the solid path is the *blue curve* S–R–P. The tie-lines are P–S, q–P–Q, and *t–P–T*, and the three-phase triangles are M–R–diopside, N–n–diopside, and O–o–diopside. (**b**) Details of construction of a portion (R → P) of the solid path S–R–P shown in this figure. For example, when the liquid is at "B," a *dashed line* B–P is drawn and extended to meet the appropriate three-phase triangle. This line intersects the diopside-b arm of the three-phase triangle at "1," which is where the coexisting solid composition must exist. Similarly, a second coexisting solid composition "2" corresponding to liquid "N" is located. The last tie-line is the *dashed line* O–P, when the liquid is all used up as the solid reached the bulk composition. Joining R, 1, 2, P gives the curved portion of the solid path which results from cotectic crystallization of diopside and $plagioclase_{ss}$

connects coexisting solid and melt phases and goes through the bulk composition P. Once the melt reaches M, diopside will start crystallizing, and the residual melt will move down the cotectic E1–E2. Three 3-phase triangles, namely, diopside–R–M, diopside–N–n, and diopside–O–o, describe the melt path and coexisting solids. The melt will be completely crystallized at O. Once again, we see that when equilibrium is maintained, the melt solidifies long before it reaches the lowest temperature in the system.

The total solid path can be divided into two parts—from S to R when plagioclase$_{ss}$ is the only phase to crystallize, and the second part, R to P, is constructed by drawing appropriate tie-lines from melt through bulk composition to the three-phase triangle at each instant of melt movement (Fig. 4.13b). Several tie-lines (dashed lines) are constructed to demonstrate this: B–P–1 starts from melt composition B, goes through P (bulk composition), and cuts the three-phase triangle B–b–diopside at 1. The second tie-line N–P–2 cuts its appropriate three-phase triangle N–n–diopside at 2. The total solid compositions will be located at 1 and 2 when the melts are at B and N, respectively. The final tie-line connects the final melt O with the bulk composition P, where the TSP must end. Connecting R, 1, 2, and P thus gives the part of the TSP after diopside joins plagioclase in crystallization.

Once again, at any instant, an appropriate tie-line can be used to calculate the percentages of melt and solid: for example, consider the tie-line *B* (melt composition)—*P* (bulk composition)—1 (solid composition):

$$\text{Melt}\% = 100 \times [(\text{distance } P - 1)/\text{distance } B - 1];$$
$$\text{and solid}\% = 100 - \text{melt}\%$$

The proportions of diopside and plagioclase$_{ss}$ (composition at "*b*") are given as follows:

$$\text{Di}\% = 100 \times \text{distance } b - 1/\text{distance } b - \text{Di}$$

$$\text{Plagioclase}_{ss}\% = 100 - \text{Di}\%$$

During the *fractional crystallization* of melt P, the melt path will have less of a curvature than in equilibrium crystallization because of instantaneous separation of crystals from melt at each stage. The residual melt will not end at O but will ultimately reach E2.

The first melt generated by either equilibrium or fractional melting of any solid assemblage lying within the Di–Ab–An phase diagram will be located somewhere on the cotectic curve E1–E2 as required by the appropriate three-phase triangle. In equilibrium melting, the solid and melt paths will be exactly the reverse of the equilibrium crystallization paths. However, in fractional melting, the final solid will be either pure diopside or anorthite depending upon the location of the original staring composition.

Ternary System with Reaction Relationship: The System Forsterite–Diopside–Silica at One Atmosphere

The system forsterite–diopside–silica at 1 atm (i.e., 0.0001 GPa) serves as another (Di–An–Ab was the first) important analog for basalt magma crystallization at low pressure. Earlier in our discussion of the system forsterite–silica, we noted that enstatite, an orthopyroxene, forms as an intermediate mineral between forsterite and silica and exhibits the reaction relation: Fo + L = En. Later experimental studies have shown that there are three different polymorphs with the same $MgSiO_3$ composition—*protoenstatite*, *clinoenstatite*, and orthorhombic enstatite also called *orthoenstatite* or, simply, enstatite. In the system forsterite–diopside–silica at 1 atm pressure, protoenstatite and orthoenstatite have their individual liquidus fields (Fig. 4.14). The reaction relation between orthopyroxene, forsterite, and melt persists

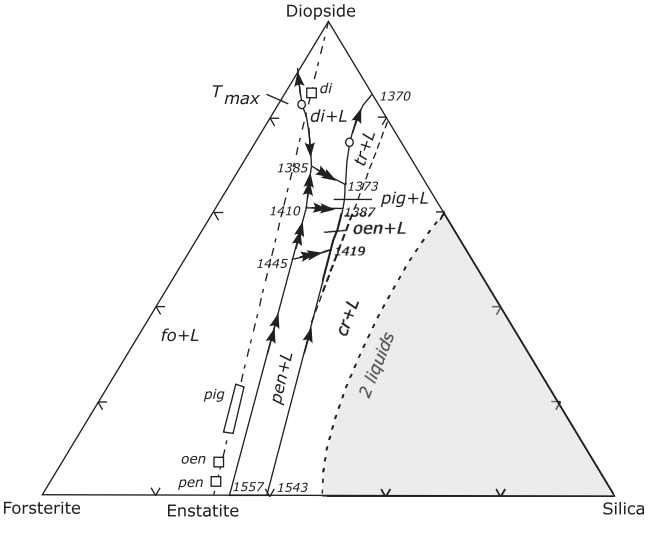

Fig. 4.14 The system diopside–forsterite–silica at 0.0001 GPa. There are four pyroxene phases—diopside$_{ss}$ (di), pigeonite$_{ss}$ (pig), orthoenstatite$_{ss}$ (oen), and protoenstatite$_{ss}$ (pen)—that crystallize in this system. Reaction curves are shown with double arrows, and cotectic curves are shown with single arrows (after Longhi and Boudreau 1980)

even when diopside is added to the system (Fig. 4.14). In addition, *pigeonite*, a Ca-poor pyroxene, appears in this diagram and has a very small liquidus field. We will ignore the protoenstatite + melt field for much of our discussion below for it should be similar to orthoenstatite + melt. The liquidus fields of silica polymorphs (tridymite and cristobalite) or of two immiscible silica melts are not of particular interest here and therefore shall not be discussed.

Equilibrium Crystallization

In Fig. 4.15, following conventional practice, reaction curves and cotectic curves are marked by double versus single arrows, respectively. In addition to the reaction curves between the Fo + L field and the Pen + L, Oen + L, and Pig + L fields, there is an important thermal maximum (T_{max}) that exists on the Di + Fo + L cotectic. This T_{max} exists because the diopside that actually crystallizes from melts in this system is not pure diopside but contains significant amount of enstatite component in solid solution. Thus, when a line is drawn from the forsterite corner to the liquidus

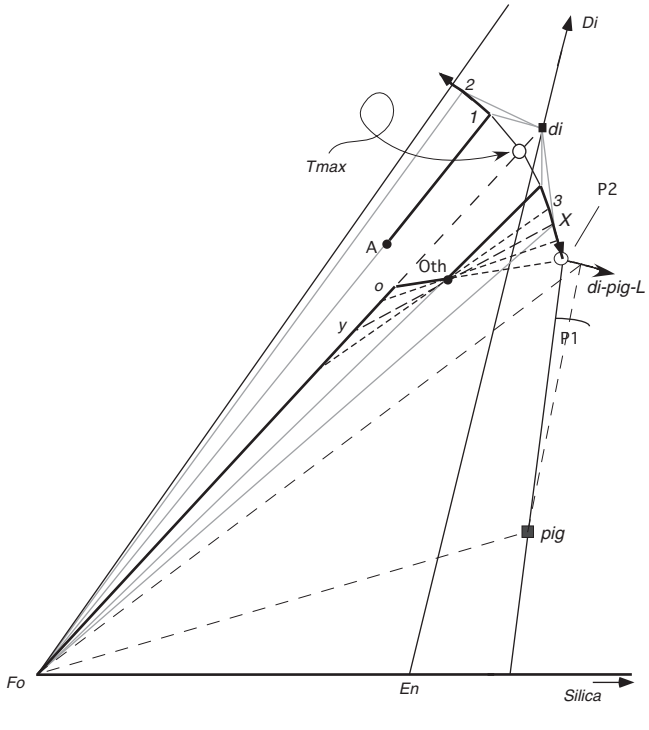

Fig. 4.15 Expanded view of a portion of the system diopside–forsterite–silica (some complexities with the Ca-poor pyroxenes are ignored here) showing equilibrium crystallization liquid paths for two starting liquid compositions—A (A → 1 → 2–) and *Oth* (Oth → 3 → P2). In the case of A, the residual liquid moves further away from silica and out of the diagram. Residual liquid for starting melt Oth ends up at P2. *Dashed lines* represent tie-lines that can be used to calculate liquid and solid proportions. The solid path is Fo → y → o → Oth

diopside solid solution (di in Fig. 4.15), it creates a T_{max} at the point of intersection with the Di–Fo–L curve. The existence of this T_{max} can be verified by drawing two 3-phase triangles (by connecting melt–forsterite–di) on either side of the T_{max} (Fig. 4.15). Note that di–2–Fo and di–3–Fo are two such three-phase triangles, which point in opposite directions of the melt movement. Thus, melt A will take a path A–1–2 upon equilibrium crystallization. Melt A will first move toward 1 as increasing amounts of forsterite crystallize. At 1, $\text{diopside}_{\text{solid solution}}$ (di) joins forsterite as an additional crystalline phase, and the residual melt is driven toward 2.

On the other hand, because of the thermal maximum, the melt path for the starting melt composition "Oth" will be very different: Oth–3–x–P2. It is reasonable to ask why the melt path should end at P2 when the curve di–pig–L allows for a lower-temperature direction for the residual melt to follow. The answer is simple: bulk composition. Suppose that the residual melt is allowed to go down the di–pig–L curve (Fig. 4.15), then one could take any arbitrary point on that curve and construct a three-phase triangle (such as the long-dashed three-phase triangle shown in Fig. 4.15) connecting the two solid phases (di and pig) with the melt composition. If you do that, you will see that no such three-phase triangles can be constructed that will include the bulk composition Oth. Of course, that cannot happen because some combination of melt and solids must always define the original starting composition. Therefore, the residual melt for Oth cannot travel further down than P2.

The corresponding solid path (*Fo–y–o–Oth* in Fig. 4.15) for the melt path that we just described can be constructed using the same geometrical methods we have used before. The solid path will be pinned at Fo until the residual melt reaches 3. At point 3, diopside joins forsterite as a crystallizing phase, and from that point until the melt reaches P2, only di and Fo will crystallize. Therefore, through this crystallization range, the coexisting total solid assemblage must be composed of di and Fo; that is, the solid path must move from Fo along the line connecting Fo–di. The solid composition can only move up to o because at o pigeonite becomes the third solid phase to join the other two. One can draw the very last tie-line P2–Oth–o; at this stage, the melt composition is pinned at P2 and the total solid composition moves from o to Oth. When the total solid composition reaches Oth, i.e., the original bulk composition, the melt will be completely crystallized.

The lever rule can be used to calculate the proportion of melt and solid at any instant through the crystallization interval. For example, when the melt reaches point 3,

$$\text{Melt}\% = 100 \times \text{distance Fo} - \text{Oth}/\text{distance Fo} - 3$$

As the melt travels toward P2, the appropriate tie-lines (i.e., levers) are the small-dashed lines that reach from melt to total solid composition through Oth. For example, when the melt reaches point X,

$$\text{Melt}\% = 100 \times \text{distance Y} - \text{Oth}/\text{distance X} - \text{Y}$$

Two fundamentally different basalt magma types occur in nature—alkali olivine basalts and olivine tholeiites. The compositions A and Oth in Fig. 4.15 represent these two magma types. From this diagram, we learn that (1) alkali olivine basalts cannot crystallize a Ca-poor pyroxene (pigeonite, protoenstatite, and orthoenstatite), whereas olivine tholeiites can; (2) olivine does not show reaction relation with the magma in the former, whereas olivine tholeiites do (i.e., Fo + L = Ca-poor pyroxene); and (3) residual melts from alkali olivine basalt crystallization become poorer in silica, whereas the opposite trend is shown by tholeiitic magmas.

Equilibrium Crystallization of Melt Th (Fig. 4.16)

The melt composition Th, representing some tholeiitic basalts, falls inside the Fo + L field and will therefore crystallize forsterite first once its liquidus temperature is reached. Crystallization of forsterite will drive the residual melt to the pen–fo–L reaction curve, where the reaction fo + l = pen occurs. *Note that we are ignoring the Oen liquidus field to keep the illustration simple*. When the melt reaches point O, a three-phase triangle can be constructed with apices at O (i.e., melt composition) and Fo and Pen (coexisting solids). Several such triangles can be constructed until the melt reaches P1, where pigeonite is also stable.

At this point, one has to wonder which way the melt will move—toward 4 or 1. This dilemma can be resolved by constructing three-phase triangles. Any three-phase triangle with apices at Fo, Pen, and any point on the curve P1–4 will exclude the bulk composition (Th), which cannot happen. On the other hand, many three-phase triangles between the triangles 1–Pig–Fo and P1–Pen–Fo can be constructed that will include the bulk composition. Thus, the melt can move up toward point 1. This also means that at P1, protoenstatite crystals must dissolve, leaving only forsterite (which has also been a reactant phase) and pigeonite crystals plus melt. At P1 two reactions occur: Fo + L = Pig and Pen + L = Pig. Any triangle (such as the small-dashed triangle shown in Fig. 4.16) beyond point 1 on the boundary curve Fo–Pig–L will not contain the bulk composition, and therefore the melt cannot move beyond 1 on that boundary. At this point all forsterite crystals would have been dissolved via reaction, and pigeonite will be the only stable phase such that the melt will be free to move into the pigeonite liquidus field, along a path (1 → 2) directly away from pigeonite (we have also ignored solid solution range for pigeonite in the figure for brevity). After that the melt will move along 2 → 3, ending up in the invariant point tridymite + pigeonite + diopside + melt, which is not shown in Fig. 4.16.

The solid path (thick gray line) for this bulk composition can also be constructed using the tie-line concept. As always, the lever rule at any instant can give the melt and solid compositions and proportions. One may also wish to construct a three-phase triangle for the melt path between points 2 and 3 to convince oneself that the melt will indeed move toward 3.

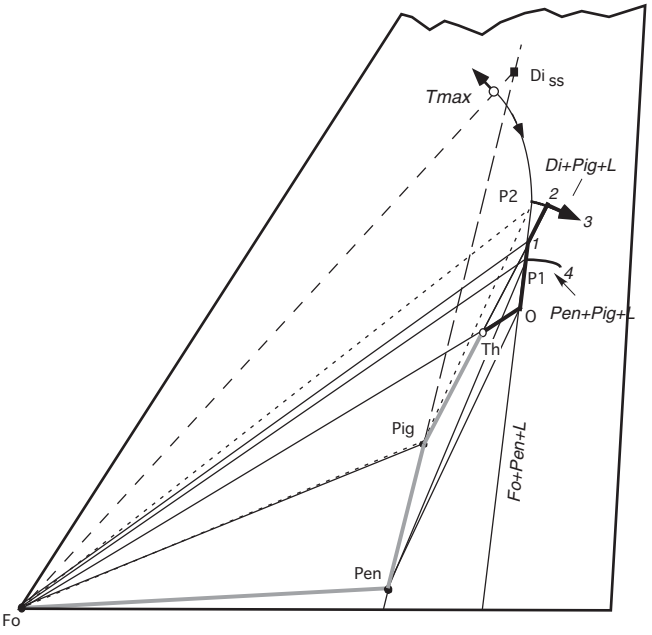

Fig. 4.16 Equilibrium crystallization of melt *Th*. The liquid path is Th → O → P1 → 1 → 2 → 3 (e2 in Fig. 4.17). The three 3-phase triangles, Fo–Pen–O, Fo–Pen–P1, and Fo–Pig–1, are shown to construct the liquid path (see text for further discussion)

Fractional Crystallization of X (Fig. 4.17)

Crystallization and immediate removal of Fo from the melt X will move the residual melt toward m (Fig. 4.17). At m, the melt will be free to leave the Fo + Pen +L boundary and into the Pen + L field because the boundary is a reaction boundary Fo + L = Pen and Fo crystals would have been removed (a requirement in fractional crystallization). Inside the Pen + L field the melt will move directly away from Pen composition because it is the only phase precipitating from the melt. The residual melt will eventually reach Pen + L = Pig reaction curve at *n*. At n the melt will be free to move across the Pig + L field, directly away from Pig composition, while precipitating pigeonite. The melt will eventually reach o and move down the Di_{ss} + Pig + L cotectic toward e2.

The solid path (1, 2, 3, 4, 5) is discontinuous and relatively simple to construct in this case: First, the solid is pinned at the Fo corner; then as the melt travels from m → n and then from n → o, the solid composition hops to Pen and then to Pig, respectively. Dropping tangents from each point on the melt path on the Di_{ss} + Pig + L curve to the Di_{ss}–En line gives the next portion of the solid path. Once the melt reaches e2, the solid hops to e2 and is entirely crystallized there.

Equilibrium and Fractional Melting of X (Figs. 4.18 and 4.19)

Again, we ignore the Oen liquidus field in the following discussion for brevity. As with other systems, equilibrium melting paths are the reverse of equilibrium crystallization paths (Fig. 4.18): because the solid "rock" X is composed of diopside, pigeonite, and forsterite crystals, its initial melting must occur at P2, where these three crystalline phases are stable with a melt. The melt composition will stay at P2 until all diopside crystals melt and the total solid composition moves from X to 1. The total solid composition will then move from 1 to 2 as the melt composition moves from P2 to P1. Further melting will not move the melt composition from P1 until the solid residue reaches 3 from 2. When the solid residue reaches 3, all pigeonite crystals would have been dissolved. The melt composition will then be free to leave P1 and move toward f, as the solid residue composition will move from 3 to the forsterite corner. Once all protoenstatite crystals melt, and the residue is only composed of forsterite, the melt composition will leave the reaction curve (Pen = Fo + L) and move toward X. At any instant, lever rule can be used to calculate proportions of phases. Several tie-lines are shown as small-dashed lines.

During fractional melting of any mixture of crystalline phases, the initial melt will be generated at the appropriate invariant point, and the solid residue will move directly away from that invariant

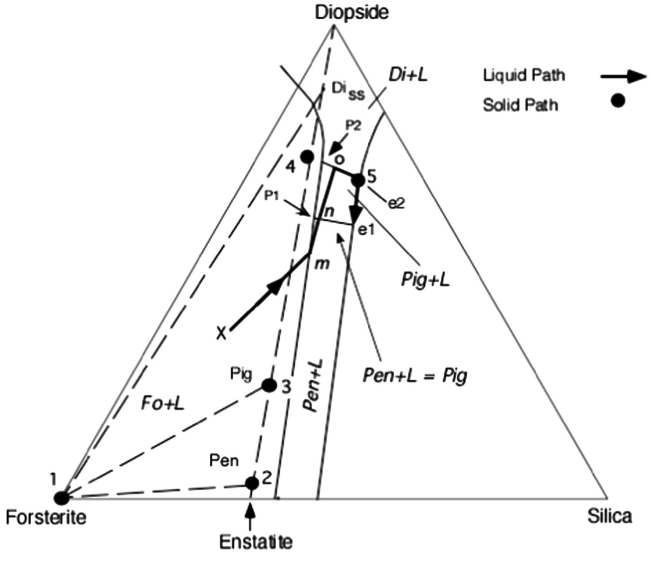

Fig. 4.17 Fractional crystallization of liquid X: The liquid path is the continuous path X → m → n → o → 5. The solid path is discontinuous: 1, 2, 3, 4, 5

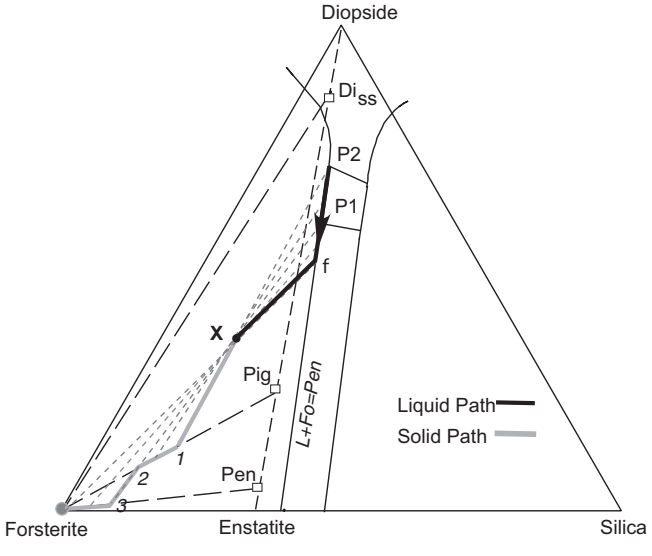

Fig. 4.18 Equilibrium melting of solid X. Short-dashed lines are the tie-lines. Long-dashed lines simply connect the solid phase compositions

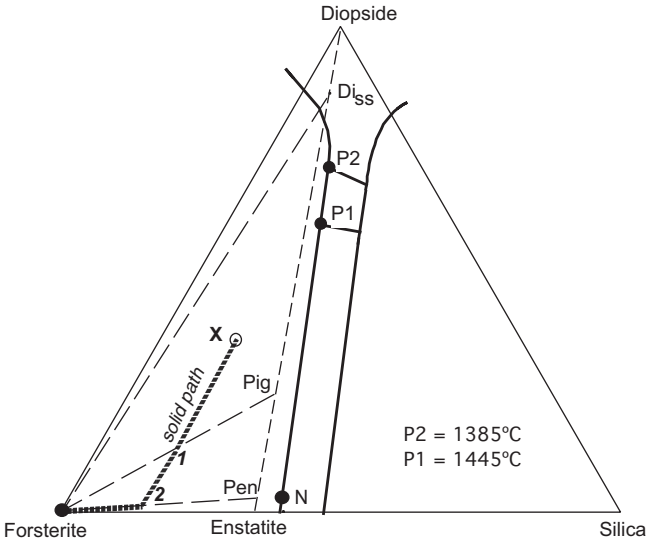

Fig. 4.19 Fractional melting of X: The liquid path is discontinuous, P2, P1, N, forsterite. The solid path is continuous: forsterite → 2 → 1 → X

point. Figure 4.19 considers two solidus surfaces—Fo–Di_{ss}–Pig and Fo–Pig–Pen. As a specific example, let us consider melting of X, a "rock" composed of Di_{ss}, Fo, and Pig crystals. The melt path is once again discontinuous (large dots), and the solid path is continuous (X–1–2–forsterite). The invariant point where these phases are first involved with a melt is P2. Therefore, melting will begin at P2 at 1,385 °C, and the solid residue will move from X to 1 (i.e., directly away from P2) while the temperature remains constant. When the solid residue reaches 1, all Di_{ss} crystals would have disappeared from the residue, and melting cannot continue until the temperature is raised to the invariant melting temperature (1,445 °C) at P1. Once the residual solid assemblage is heated to 1,445 °C, the solid residue would move from 1 to 2 (directly away from P1) as more and more melt is generated at P1 and immediately extracted (requirement of fractional melting). When the solid residue reaches 2, there would be no pigeonite crystals left. Once again the temperature will have to be raised so that melting can resume again at a point on the Pen–Fo–L curve where the extension of Fo–Pen line meet. Melt production at this point will drive the residue composition to the forsterite corner. Once the residue is composed entirely of forsterite crystals, melting must stop and cannot renew until forsterite's melting point is reached.

Effect of Pressure and P_{H2O} on Ternary Systems

Pressure has the following effects on a ternary diagram: (1) All the melting points are increased, (2) reaction relationship can sometimes be replaced with congruent melting behavior (as we saw in the Fo–silica example), (3) liquidus fields of participant minerals change size and shape considerably, and (4) some low-pressure invariant points may disappear and new ones may appear. The student should note that not all the changes stated above would occur in every system.

Anorthite–Forsterite–Silica

Figure 4.20 compares the phase relations in An–Fo–silica at 1 atm and at 1 GPa. Note that the liquidus boundary curve between the forsterite and enstatite liquidus fields shifts from the right to the left side of the En–An line, signaling the change from the reaction relationship Fo + L = En at 1 atm to a cotectic behavior (Fo + En = L) at 1 GPa. (For the sake of brevity, polymorphism in $MgSiO_3$ has been ignored in the following discussion and in Fig. 4.20, referring to all orthopyroxene in this diagram as enstatite.) The second noticeable change is the expansion of the spinel and enstatite liquidus fields with pressure so that the invariant points *a* and *b* are replaced with *c* and *d*. A starting rock *H* will generate a melt of composition at *a* in equilibrium with anorthite (+Fo + En) at atmospheric pressure, but at 1 GPa, anorthite cannot be a stable residual mineral for this starting composition because the initial melt will be at *d*, where the equilibrium phases are Fo, En, and *spinel*.

If a lava flow or an intrusive dike is found to contain euhedral phenocrysts of olivine and orthopyroxene, then one can conclude that such crystals grew in the magma along a cotectic such as the Fo + En = L at 1 GPa. Also, in order to preserve such texture, the magma must have ascended rapidly from great depth (~30 km). This will be the case for our hypothetical melt "M" in Fig. 4.20. On the other hand, and as is more likely, if M rises toward the surface but then stalls in a conduit within the shallow crust, then its composition will fall inside the Fo + L field, and forsterite crystals will form and drive the remaining melt composition toward l, where enstatite will dissolve or be rimmed by the growing forsterite crystals. In the shallow chamber, the reaction boundary Fo + L = En will destabilize forsterite crystals, and the likely resulting texture will be resorbed (rounded or partially rounded) forsterite crystals

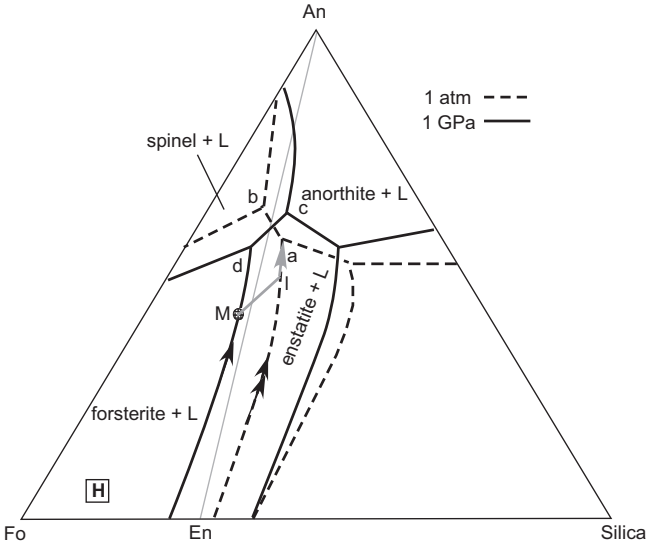

Fig. 4.20 The system anorthite (An)–forsterite (Fo)–silica at 0.0001 GPa (*dashed lines*) and at 1 GPa (*continuous lines*). The reaction curve Fo + L = En at atmospheric pressure is marked by *double arrow*. At 1 GPa this curve becomes a cotectic (shown as a *single arrow*) at 1 GPa because enstatite melts congruently at this pressure (Sen and Presnall 1984)

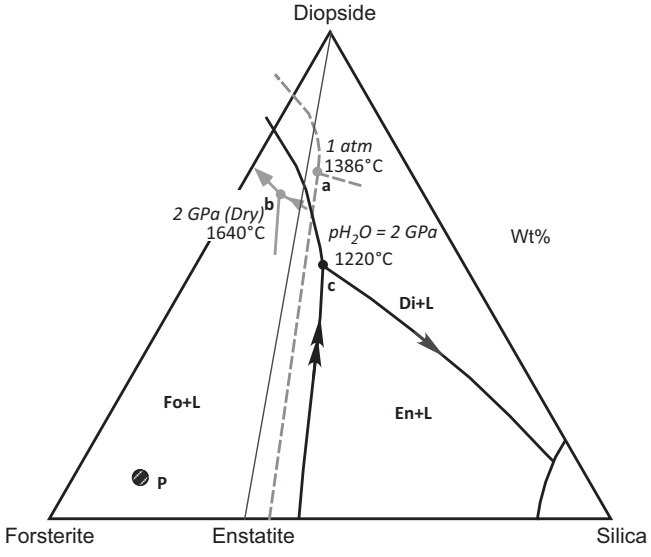

Fig. 4.21 Phase relationships under volatile-free conditions in the system diopside–forsterite–silica at 1 atm (0.0001 GPa) and at 2 GPa are compared with those at 2 GPa under H_2O-saturated condition

rimmed by enstatite. In the case of M, the residual melt will now move from l toward a.

Spinel crystals rimmed by plagioclase have sometimes been found in lavas. In fact, such spinel-rimmed-by-plagioclase textures have been described from a class of moon rocks (called lunar breccia) that were brought back by NASA's Apollo 14 mission. A plausible explanation for the formation of such texture is that spinel formed in the magma at greater depth; however, as the magma rose to shallow levels, spinel became unstable and plagioclase crystals grew on them, forming a rim. The inverse texture, i.e., plagioclase crystals rimmed by spinel, is uncommon in natural lavas. Reaction rims of orthopyroxene + magnetite (magnetite is a type of spinel) around olivine have also been found in lavas, which may be explained by this diagram. Figure 4.20 tells us that such textures can form at d at 1 GPa by the reaction: Fo + L = En + Sp.

Forsterite–Diopside–Silica at High Pressure (with and Without H_2O)

At the outset, it is important to point out that when H_2O is added as a component to the ternary forsterite–diopside–silica, it is no longer a ternary system but a four-component or quaternary system. Figure 4.21 shows the effects of "dry" (i.e., volatile-free) and "wet" (H_2O saturated) pressure on this phase diagram. a, b, and c are invariant points at which forsterite, diopside, and enstatite coexist with melt: Point "c" is the "wet" invariant point at 2 GPa, "b" is the "dry" invariant point at 2 GPa, and "a" is at atmospheric pressure (i.e., 0.0001 GPa).

First we consider the case of high-pressure phase relations under *volatile-free* (no H_2O) condition. Contrasting a with b shows that the increase of dry pressure shrinks the forsterite field and expands the diopside and enstatite liquidus fields. A hypothetical mantle peridotite P will begin to melt at the invariant point b at 2 GPa. The expansion of the diopside field with pressure means that magma produced from such peridotite will have greater amount of dissolved olivine component and lesser amount of dissolved clinopyroxene than a magma generated at the lower pressure invariant point. In other words, 2 GPa (dry) invariant melts will have relatively high MgO and less CaO than, say, 1 GPa (dry) invariant melts. Consequently, when magmas generated at such two different pressures are brought up to the Moho and allowed to sit and fractionate crystals, the 2 GPa melt will fractionate significantly more olivine crystals than the 1 GPa melt (phase diagram not shown) for their residual melts to reach the same degree of fractionation, e.g., silica value. Interestingly, if a peridotite-derived magma generated at a pressure greater than 2 GPa (dry conditions) is allowed to stagnate in a magma chamber and cool at 2 GPa, it will fractionate olivine and

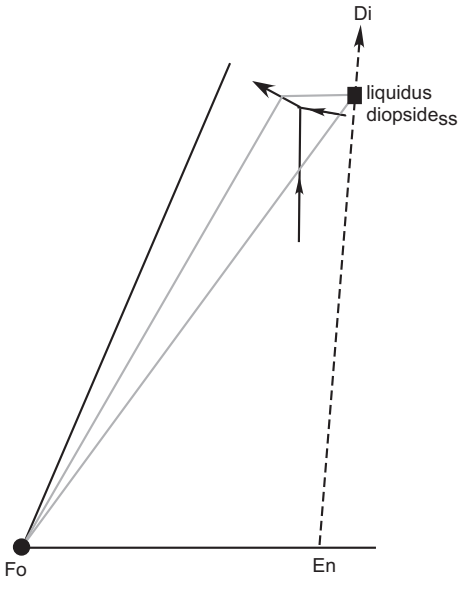

Fig. 4.22 A 3-ϕ triangle connecting coexisting liquid, forsterite, and clinopyroxene (diopside solid solution) is used to determine the direction of liquid movement upon cooling on the boundary curve Fo + Di = L

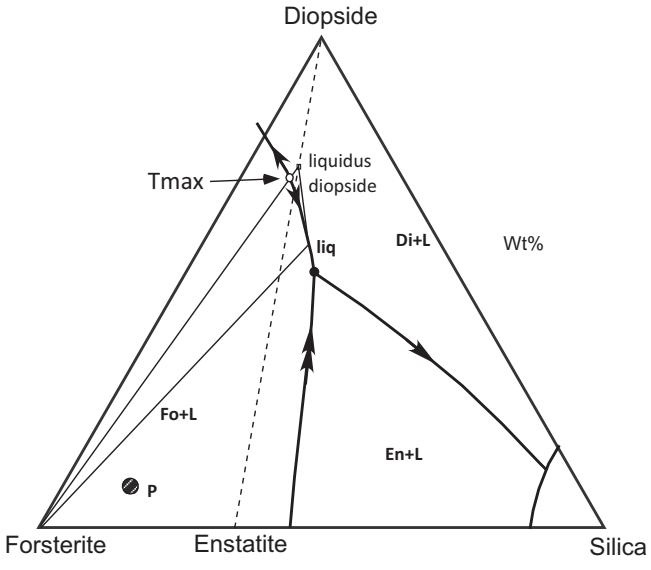

Fig. 4.23 The system Fo–Di–Silica at 2 GPa (H_2O saturated). The point of intersection between the line joining liquidus diopside and forsterite and the liquidus boundary Fo + Di = L is a thermal maximum (T_{max}). The 3-ϕ triangle (Forsterite-liq-liquidus diopside) is shown to indicate that the liquid on the right side of the T_{max} will move toward the point Fo–En–Di–L. Although not shown here, any 3-ϕ triangle on the other side of the T_{max} will point toward the diopside–-forsterite boundary, and therefore, any liquid on that side of the T_{max} will move toward that boundary

diopside and move away from silica (i.e., alkalic trend). This is because the composition of the liquidus diopside at such pressure contains considerable amount of enstatite in solid solution; and as a result, any three-phase triangle (such as the one shown in gray in Fig. 4.22) connecting melt, forsterite, and liquidus diopside$_{ss}$ crystals will point away from silica end, indicating that a liquid crystallizing forsterite and diopside crystals will become progressively less silicic (i.e., more alkalic). Note that the Fo + Di + L curve must be a cotectic because if a tangent is drawn anywhere on the boundary curve Fo + Di + L, it will always intersect the base connecting liquidus diopside$_{ss}$ and Fo, such that one could write a reaction L = Fo + Di$_{ss}$, which is a cotectic reaction.

H_2O has a strong effect on the melting relationships in the system Fo–Di–Silica (Fig. 4.23). It lowers the solidus temperature of a haploperidotite (i.e., a crystalline assemblage composed of forsterite, enstatite, and diopside) by 100–150°, and the melt compositions are considerably hydrous and richer in silica relative to volatile-free conditions. The pyroxene liquidus fields expand greatly while maintaining the reaction relation Fo + L = En, which is characteristic of low-pressure phase relationship. The liquidus diopside plots toward enstatite, creating a thermal maximum (T_{max}) that occurs where the Fo-liquidus diopside line intersects the liquidus boundary Fo + Di + L. In later chapters we shall see examples of fractionation of basalt magma at different pressures, and this discussion will then become more relevant.

Under hydrous condition, our hypothetical upper mantle peridotite P will begin melting at c (Fig. 4.21), and this melt will have about 12 % more silica and 15 % less diopside component than in the dry case at the same pressure. One interesting aspect of the H_2O-saturated phase relations is that hydrous melts can have a long history of crystallization of pyroxenes before quartz (or some other form of silica) ever appears in the residual magma. As we will see in a later chapter, understanding the effect of H_2O on melting and crystallization of magmas is particularly important in the case of igneous processes in plate converge boundaries.

Forsterite–Diopside–Silica–Carbon Dioxide

Carbon dioxide (CO_2) has an important effect on the system CaO–MgO–SiO_2 (CMS), which includes Fo–Di–Silica and the important haploperidotite minerals (as mentioned before, haploperidotite is the simpler analog of natural peridotite in that it contains Fo + En + Di minerals). The effect of CO_2 on the haploperidotite solidus in the CMS system is negligible until a pressure of about 2 GPa is reached. The

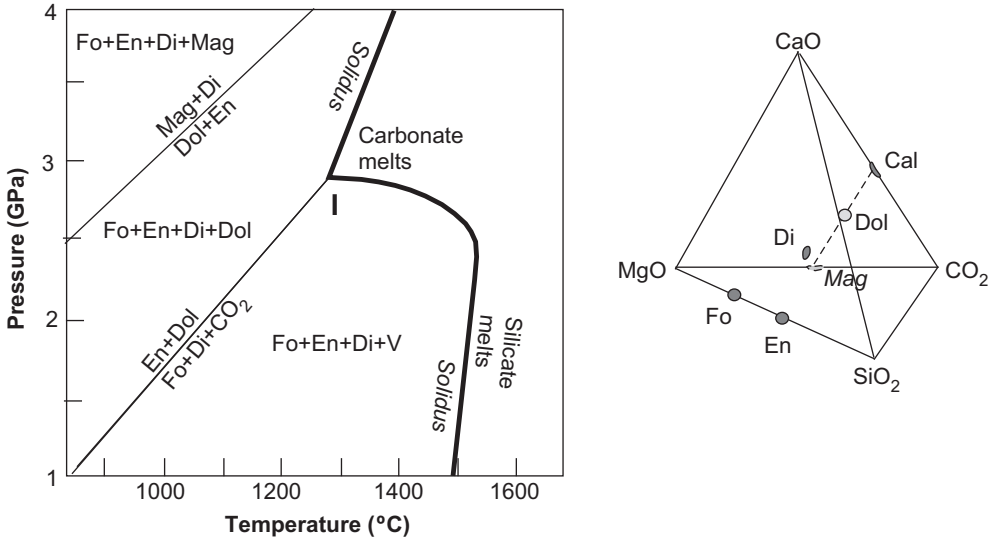

Fig. 4.24 *P–T* diagram for the system CaO–MgO–SiO_2–CO_2. The point I is the invariant point defined by the assemblage Fo + En + Di + Dol + L + V (see text for further discussion). The *inset* shows where various solid compositions plot inside the CMS–CO_2 tetrahedron

following important reaction occurs in the system CMS–CO_2 at about 2.8 GPa (Moore and Wood 1998, and references to the original experimental papers by Eggler, Wyllie and colleagues):

$$\underset{\text{Fo}}{2Mg_2SiO_4} + \underset{\text{Di}}{CaMgSi_2O_6} + 2CO_2 = \underset{\text{En}}{4MgSiO_3} + \underset{\text{Dol}}{CaMg(CO_3)_2}$$

This reaction curve intersects the CO_2-saturated Fo + En + Di + L solidus at about 2.8 GPa and creates a strong depression on the solidus (Fig. 4.24b). The near-solidus melts at this depression are carbonatitic (we will discuss this in detail in a later chapter). At pressures greater than this reaction curve, a free CO_2 vapor phase can no longer coexist with the haploperidotite, as it would react with the forsterite and diopside to form a carbonate mineral (most likely, dolomite) and enstatite. The sharp bend that occurs between 2 and 2.8 GPa on the haploperidotite solidus is commonly referred to as a "ledge." Carbonatitic melts containing 35–40 %-dissolved CO_2 formed at pressures greater than 2.8 GPa, upon attempting to cross the ledge, would react with the mantle lherzolite (ol + opx + cpx) and produce a wehrlite (ol + cpx) and a CO_2-rich vapor phase around 2–2.8 GPa.

The actual phase relationship between the silicate and carbonate minerals and the melt phase that coexist at various pressures can be better understood by studying two ternary isobaric diagrams at 2 and 3 GPa (Fig. 4.25a, b). Note that all lines and points on each of these ternaries are projected from the CO_2 apex of the CMS–CO_2 tetrahedron (inset in Fig. 4.24). The point "I_1" represents the isobaric invariant point where a melt is saturated with forsterite, diopside, and enstatite at 2 GPa (Fig. 4.25a): Fo + Di_{ss} = En_{ss} + L (with a small amount of dissolved CO_2). At 3 GPa (Fig. 4.25b), there is no such invariant point because there is a new invariant point "I_2" where a melt is saturated with forsterite, $enstatite_{ss}$, and $dolomite_{ss}$ (it is a dolomite [$CaMg(CO_3)_2$] with a small amount of dissolved calcite [$CaCO_3$]), but the $diopside_{ss}$ liquidus field is slightly removed from I_2. At 2.8 GPa, the liquidus fields of forsterite, $diopside_{ss}$, $enstatite_{ss}$, and $dolomite_{ss}$ all converge to create the polybaric invariant point "I" in Fig. 4.24.

We can use the phase rule to check the number of phases at isobaric invariant points I_1 and I_2 (Fig. 4.25) on the haploperidotite solidus and contrast that to that at the invariant point I (Fig. 4.24). At I, there are six phases (ϕ), i.e., forsterite, $enstatite_{ss}$, $diopside_{ss}$, $dolomite_{ss}$, CO_2 vapor, and a CO_2-saturated melt, and number of components (c) is 4. Then, according to the phase rule (i.e., $f = c - \phi + 2$), $f = 0$; that is, it is an invariant point in *P–T* space. In contrast, I_1 has five phases (Fo, En, Di, V, L), and therefore, it is a point on the univariant curve that is the haploperidotite solidus.

It is also important to understand the effect of projection of the points I_1 and I_2 from the CO_2 apex onto the CMS plane (Fig. 4.26). I_2 melt composition has as much as 44 % dissolved CO_2, and therefore, it plots well within and closer to the base of the tetrahedron.

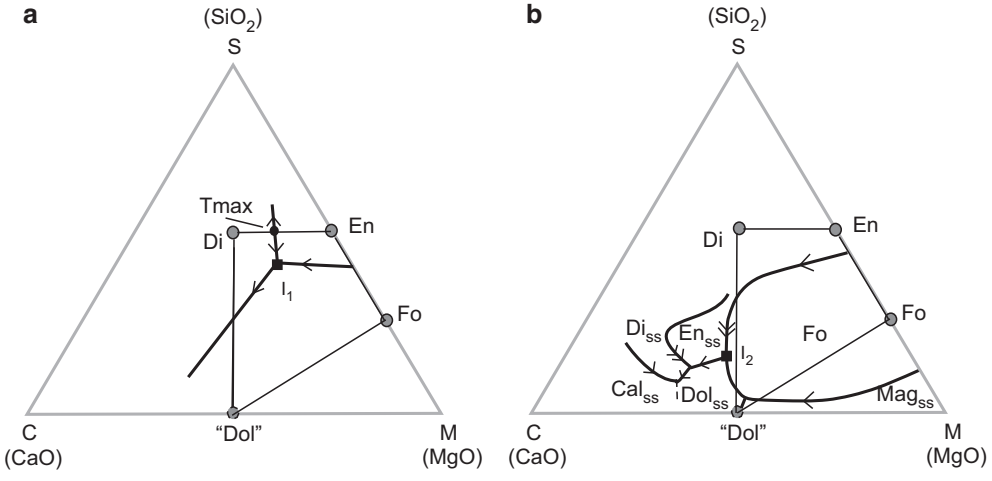

Fig. 4.25 (**a**) CMS ternary at 2 GPa, with all points and lines projected from the CO_2 corner of the CMS–CO_2 tetrahedron (modified from Moore and Wood 1998). I_1' is the isobaric invariant point. Note that although Moore and Wood (1998) show the *curve* Fo–En–L as a reaction curve, geometrical analysis of this phase diagram suggests that it is a cotectic. (**b**) CMS ternary at 3 GPa, projected from CO_2 (modified from Moore and Wood 1998). Again, the part of the Fo–En–L curve close to the point I_2' is shown here to be a reaction curve although the original authors indicated this to be a cotectic curve

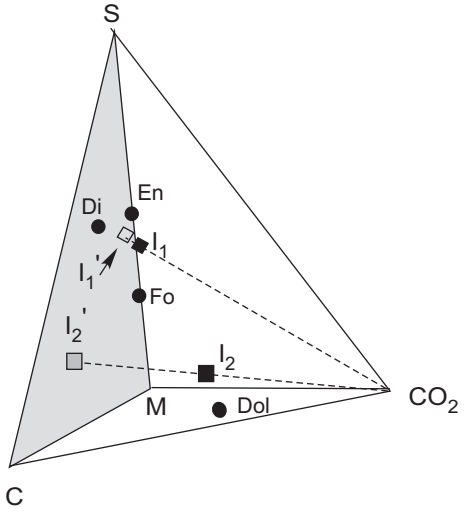

Fig. 4.26 The effect of projecting points plotting inside the CMS–CO_2 tetrahedron to its CMS base (*shaded*) from CO_2 is illustrated here (schematic) for points I_1 and I_2 (refer to Fig. 4.25). The projected points are I_1' and I_2', respectively

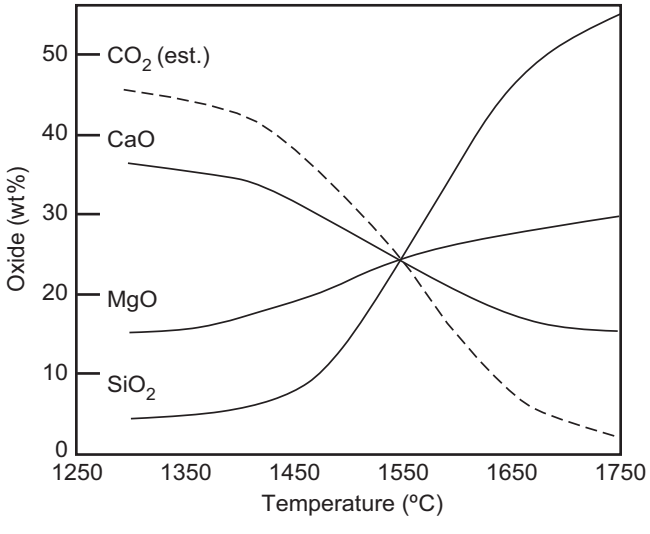

Fig. 4.27 Composition of melts from near solidus to near liquidus temperatures at 3 GPa in the system Fo–Di–En–CO_2

When projected from CO_2, the projection distance is considerable. On the other hand, I_1 melt has very nominal amount of CO_2 and plots very close to the plane of projection, i.e., the CMS plane.

The melt compositions in this system are complicated as they range from being carbonate-rich to a silicate melt at and above 2.8 GPa. For example, at 3 GPa, Moore and Wood (1998) showed that the silica content of the melt increases rapidly with temperature (Fig. 4.27). The melt is carbonatitic with about >35 % dissolved CO_2 and basaltic (broadly defined) with >45 % SiO_2. This diagram is useful in explaining the common carbonatite–nephelinite association (discussed in a later chapter).

Finally, at higher pressures, dolomite is replaced by magnesite as the carbonate phase. Magnesite forms as a result of the following reaction (Fig. 4.24):

$$\underset{\text{Dol}}{CaMg(CO_3)_2} + 2\underset{\text{En}}{MgSiO_3} = 2\underset{\text{Mag}}{MgCO_3} + \underset{\text{Di}}{CaMgSi_2O_6}$$

Because of this change in the composition of the carbonate, melts are of considerably different composition at pressures where magnesite is stable on the solidus (discussed in a later chapter).

Box 4.2: Relating Simple Systems to Complex Natural Systems

In order to understand how natural magmas form, crystallize, and mix by extending the knowledge gained from the studies of phase relationships of pure systems, whether binary or ternary, or more than three components, is far from straightforward. This is because natural magmas have many major/minor components (SiO_2, TiO_2, Al_2O_3, Fe_2O_3, FeO, MgO, CaO, MnO, Na_2O, K_2O, P_2O_5) that significantly increase the variance. In order to provide a link between the simple system experiments to natural magmas, rocks, and minerals, petrologists have used various schemes that combine the chemical components in some reasonable manner and make them resemble simple systems. We can take a look at some of these schemes.

The simplest projection used by some authors is simply to calculate the norms from compositions of rocks, minerals, and magmas (discussed in Chap. 2). A similar scheme has been in vogue since it was first proposed by O'Hara (1968a), in which the wt% of various chemical components in a magma/rock/mineral are combined and represented as a four-component system CaO–MgO–Al_2O_3–SiO_2. In this scheme, moles of each oxide of a magma/rock are first calculated, and then the "structurally similar" moles are added to give "simplified moles" of CaO, MgO, Al_2O_3, and SiO_2 components. These are then converted to wt% by multiplying the respective moles by the appropriate molecular weights:

$$C = (\mathrm{CaO} - 3.33\mathrm{P_2O_5} + 2\mathrm{Na_2O} + 2\mathrm{K_2O}) \times 56.08$$
$$M = (\mathrm{FeO} + \mathrm{MgO} + \mathrm{MnO} - \mathrm{TiO_2}) \times 40.31$$
$$A = (\mathrm{Al_2O_3} + \mathrm{Cr_2O_3} + \mathrm{Fe_2O_{3+}Na_2O} + \mathrm{K_2O} + \mathrm{TiO_2}) \times 101.96$$
$$S = (\mathrm{SiO_2} - 2\mathrm{Na_2O} - 2\mathrm{K_2O}) \times 60.084$$

Instead of using weight percentages, one could also plot mole percentages by converting the

(continued)

Box 4.2 (continued)

moles to mole percentages and ignoring the mole-to-weight conversion step above. The mole% or wt% of plagioclase, olivine, augite, and quartz can then be calculated using the following formulae, which are based on the formulae of the each of the pure mineral's chemical composition.

$$\text{Plagioclase} = A$$
$$\text{Augite} = C - A$$
$$\text{Olivine} = (M - C + A)/2$$
$$\text{Quartz} = S - (M + A + 3C)/2$$

Many other schemes have since been proposed because no scheme has been found to be entirely satisfactory. For example, Maaloe and Abbott (2005) suggested that the following simpler conversion formulae work better for the CMAS simulation:

$$C = \mathrm{CaO}$$
$$M = \mathrm{MgO} + \mathrm{FeO}$$
$$A = \mathrm{Al_2O_3} + \mathrm{Cr_2O_3}$$
$$S = \mathrm{SiO_2}$$

It is beyond the scope of this book to talk about relative merits and demerits of various projection types, but the usefulness of these projections will become apparent in later chapters where we extrapolate natural magmas and experimental data to simple ternary projections and discuss their phase relationships.

Summary

- Ternary systems discussed here include simple systems that include the major mineral components and melt compositions that are relevant to phase relationships in natural peridotite–basalt magma system.
- Ternary diagrams have invariant points, univariant lines, and divariant fields. Divariant fields are mapped with isotherms to indicate the slopes of the liquidus surfaces.
- The univariant curves can be cotectic or reaction curves; and invariant points can be eutectic or reaction points. Thermal minimum or maximum can occur on univariant curves.
- Equilibrium and fractional crystallization and melting processes are discussed for several ternary systems. In the system An–Fo–silica at 1 atm pressure is an

example of a ternary eutectic system. The system Di–Ab–An is an example of a system with a single univariant curve. In the system Di–Fo–Silica, important reaction relationship between forsterite, enstatite, and melt occurs at low pressure. This reaction relationship disappears at high pressure, and the boundary between forsterite and enstatite liquidus fields becomes cotectic.

- The liquidus fractionation paths are straight when no solid solution is involved and curved when there is solid solution.
- CO_2 and H_2O lower the haploperidotite solidus temperature in the system Di–Fo–Silica, but their effects are considerably different. The effect of H_2O on the haploperidotite solidus is much greater than CO_2 at pressures between 1 atm and 2 GPa. The melt compositions are also very different: H_2O tends to make melts more silicic, whereas CO_2 makes melts more alkalic at high pressures.

Exercises

Problem 1. The following diagram is a phase diagram (two copies provided for answering questions b and c separately) for a hypothetical ternary eutectic system A–B–C. M and N are two starting liquid compositions.

(a) What are the liquidus temperatures of M and N?
(b) In the top diagram, draw liquid path in red ink and solid path in blue for equilibrium crystallization of M.
(c) In the bottom diagram, draw the equilibrium liquid path in red and corresponding solid path in blue on this diagram for both M and N.
(d) Estimate (using lever rule) and plot *F* versus *T* for liquid M.
(e) On the second diagram, show the solid path in blue and liquid path in red for fractional crystallization of liquid M.

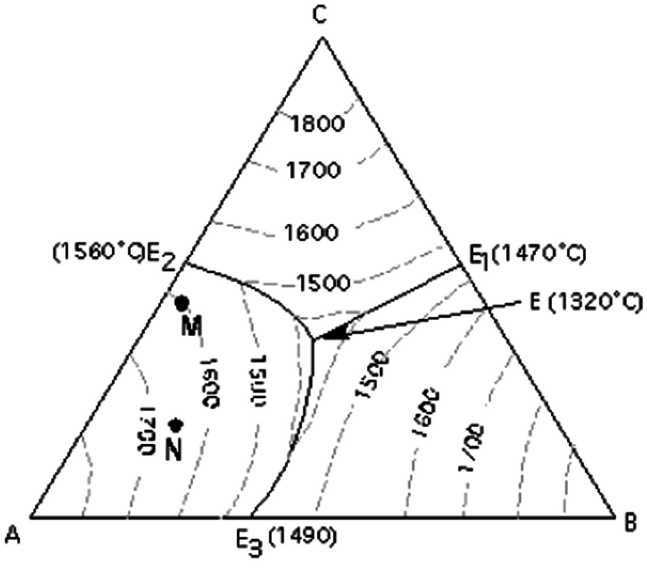

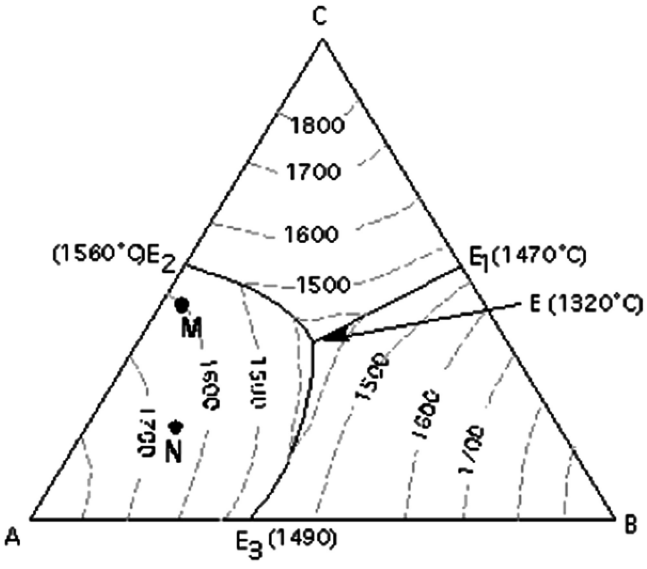

The two above diagrams are the same. One is for you to use for questions a–c and the other for answering d. In the above diagrams, the two black dots marked as M and N are bulk liquid compositions.

Problem 2.

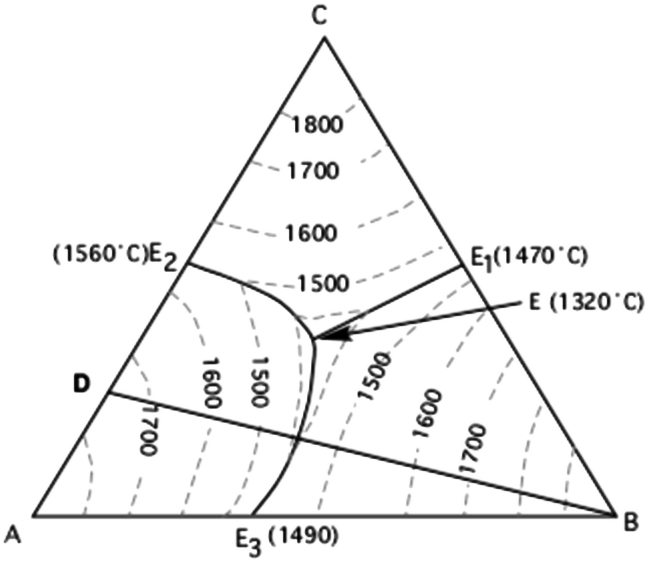

Construct a pseudobinary diagram for the join B–D.

Problem 3. Consider a case where a magma carrying 5 % crystals of A,B, and C leaves its magma chamber located at 10 km [see bottom figure, (b)] and rises through a conduit to erupt at the surface. On its way up the magma loses heat at the rate of 10 °C per km by adiabatic cooling. (Ignore any heat loss or gain from crystallization or melting.) Using the phase diagram (a) below, answer the following questions.

(a) What is the temperature of the magma at 10 km?
(b) What is the temperature of the magma at the surface?
(c) What crystalline phases will it carry upon arriving at the surface?

(d) At what temperature will the magma begin to crystallize once it reaches the surface?

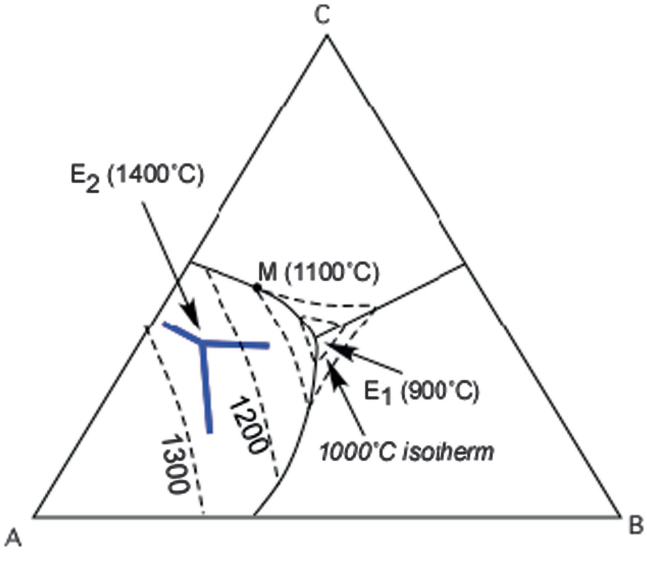

(**b**) Diagram above compares phase boundaries at 0.1 Gpa (~10 km, *blue*) with those at atmospheric pressure. The isotherms and the eutectic points are applicable to the atmospheric pressure diagram

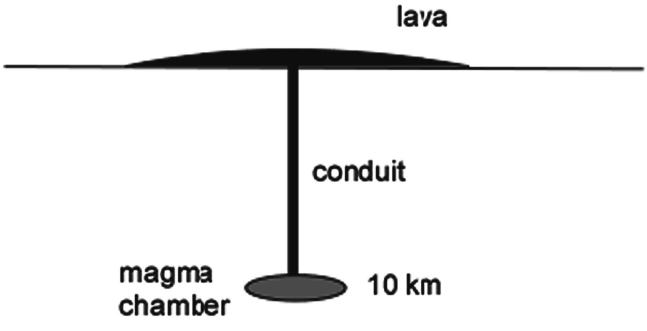

(**a**) Sketch showing magma erupting from a chamber located at 10 km

Magma Formation and Segregation

5

Abstract

This chapter builds on the previous chapters and deals with the physical and chemical aspects of melting, magma segregation, and magma's ascent toward the Earth's surface.

Magma Formation, Segregation, and Ascent

Under favorable thermal conditions, tiny fractions of magma may form in the crust or upper mantle. Once formed, such magma must somehow segregate from the source rock and form larger pools that will ascend toward the surface. Many magma bodies may only rise to a certain level and freeze, whereas others may erupt through volcanoes. Next we consider the processes that are responsible for the generation and delivery of magma to the crust.

Magma Formation: Interplay of the Solidus and Geotherm

Our understanding of phase equilibrium (Chaps. 3 and 4) tells us that any source rock composed of two or more minerals should normally begin to melt at its solidus and continue to melt over a range of temperature as it is heated. It will be fully molten only when it is heated above its liquidus temperature. One exception to this is if the starting material or source rock happens to have a eutectic-like composition in which case it will start and finish melting at the eutectic point.

Melting at any depth within the Earth can occur when the actual temperature is greater than that of the solidus of the rock that occurs at that particular depth. The *geothermal gradient* or *geotherm* is the curve that represents temperature change with depth (dT/dz) and gives us the needed information on temperature at any particular depth (Fig. 5.1). [*Figure 5.1 actually does not show depth (in kilometers) but pressure (in gigapascals). A simple rule of thumb for converting pressure (GPa) to depth (km) is to multiply it by 30. So, a pressure of 2 GPa will occur at an approximate depth of 60 km.*] Melting would occur only when the geothermal gradient crosses the solidus at a particular depth or over a depth range.

The geothermal gradients beneath an Archaean shield, continents, and old ocean basins have one common feature, and, that is, in both cases the temperature increases rapidly with depth down to a certain depth, beyond which (i.e., when they get into the asthenosphere) the dT/dP gradient is relatively flat, i.e., temperature change with pressure is much more gradual (Fig. 5.1). This is because within the continental and oceanic lithospheres, heat transfer occurs mainly by conductive transport, which is an extremely slow process. On the other hand, heat is transported by convection within the asthenosphere. Note that the geothermal gradients in the old oceanic and continental lithospheres do not cross the upper mantle solidus at any depth and therefore lithospheric melting would not be expected in such scenarios.

Temperature changes only a little (about 1 °C per km) beneath a mid-oceanic ridge axis because of rapid advective transport of mantle material; and the dT/dz gradient is essentially an adiabatic gradient (see Box 5.1). Any rising mantle parcel beneath a mid-oceanic ridge axis will start melting when it crosses the solidus and continue to melt as long as the dT/dP gradient stays above the solidus (Fig. 5.1).

G. Sen, *Petrology*, DOI 10.1007/978-3-642-38800-2_5,

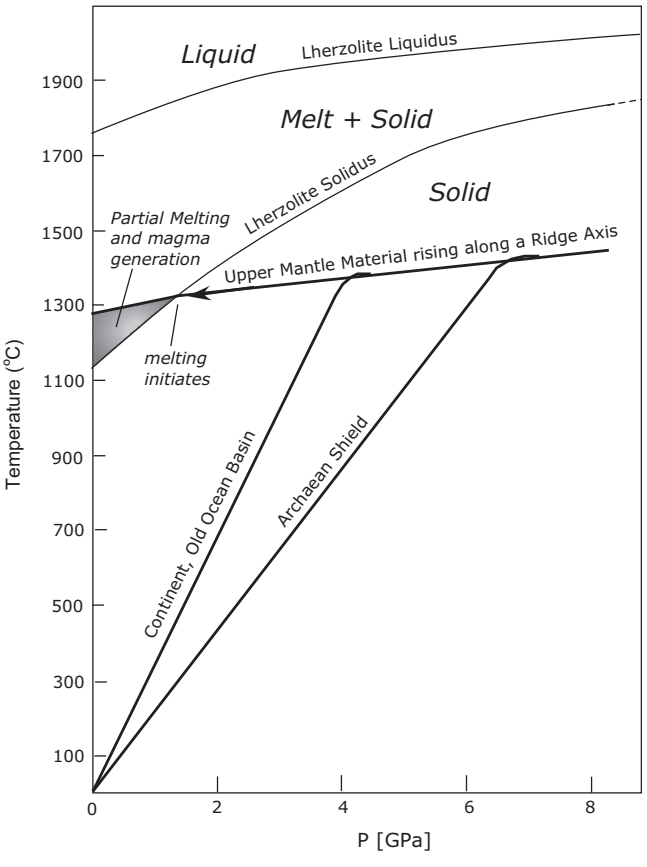

Fig. 5.1 This diagram shows the solidus and liquidus of upper mantle lherzolite, adiabatic ascent path of mantle rock beneath a mid-oceanic ridge (MOR), and geothermal gradients in Archaean shield areas, stable continental platform areas, and old (far away from ridge axis) ocean basin (redrawn after McKenzie and Bickle 1988). In this model, the mid-ocean ridge adiabat represents the path taken by a parcel of mantle rock (asthenosphere) that rises and crosses lherzolite solidus at about 1.8 GPa, at which point it begins to melt. It continues to melt all the way up to the base of the crust. This partially molten region is depicted as the *gray area* here

Box 5.1: Adiabatic Gradient and Melting

It is apparent from Figs. 5.1 and 5.2 that decompression melting can happen because the solidus has a positive slope (i.e., the melting point of a rock increases with pressure) and the path followed by the rising mantle parcel has a shallower slope. The rise of deep, hot, rock bodies is generally believed to follow an *adiabatic gradient*, i.e., they cool entirely due to expansion of volume as pressure decreases. The adiabatic gradient is expressed as

$$\frac{dT}{dz} = \frac{\alpha g T}{C_p}$$

where α is the volume coefficient of thermal expansion, T is temperature, z is depth, and C_p is heat capacity. The adiabatic gradient (dT/dz), or change of temperature as depth decreases, for the upper mantle lherzolite is ~0.3 K/km, which is a much smaller number than the dT/dz slope of the mantle solidus (~8 K/km) over the depth range of 60–20 km. Therefore, the adiabatic gradient of a rising mantle parcel will intersect the mantle solidus at a shallow angle, which will result in partial melting of such a parcel (Fig. 5.2). Once melting ensues, latent heat of fusion (~418 J/g) will be used up in the melting process and cool the mantle parcel, and the resulting dT/dz gradient will then have a steeper gradient ($dT/dz \sim 3$ K/km). Note in the above calculations the following numbers were used: $\alpha = 3 \times 10^{-5}$/K, $C_p = 1.25$ J/g.

Melting Mechanisms

Melting in the Earth's crust or mantle may happen in one of two ways: by bringing a hot, deep, rock to shallow level where its temperature is higher than its melting (solidus) temperature (referred to as *decompression melting*) or by lowering the solidus temperature through the introduction of a volatile phase (called *volatile-aided melting*). In *divergent plate margins* (e.g., mid-oceanic ridges), as plates are pulled apart, hot asthenosphere passively rises and begins to melt at a shallow level (called *passive melting*: Fig. 5.2). In places like Hawaii, it is commonly believed that a plume or "hot jet" brings up hot materials from the deep mantle. These hot materials decompress as they rise, eventually producing magma as they cross the solidus beneath the lithosphere (Fig. 5.2). This type of decompression melting is referred to as *plume melting*.

A likely place where volatile-aided melting dominates is above a subduction zone. The mid-ocean ridge crust and the shallowest mantle eventually get hydrated via reaction with ocean water, as a result of which hydrous minerals like zeolites, serpentine, and chlorite form. When such altered plate is subducted, the hydrous minerals start breaking down at different depths and new, less hydrous or anhydrous, minerals are produced and a H_2O-rich fluid is released into the overlying mantle wedge (Fig. 5.3). This H_2O-rich fluid lowers the solidus of the rocks comprising the mantle wedge and triggers melting. The magma that forms in the presence of volatiles is very different, usually richer in Al_2O_3 and SiO_2, than magma produced under

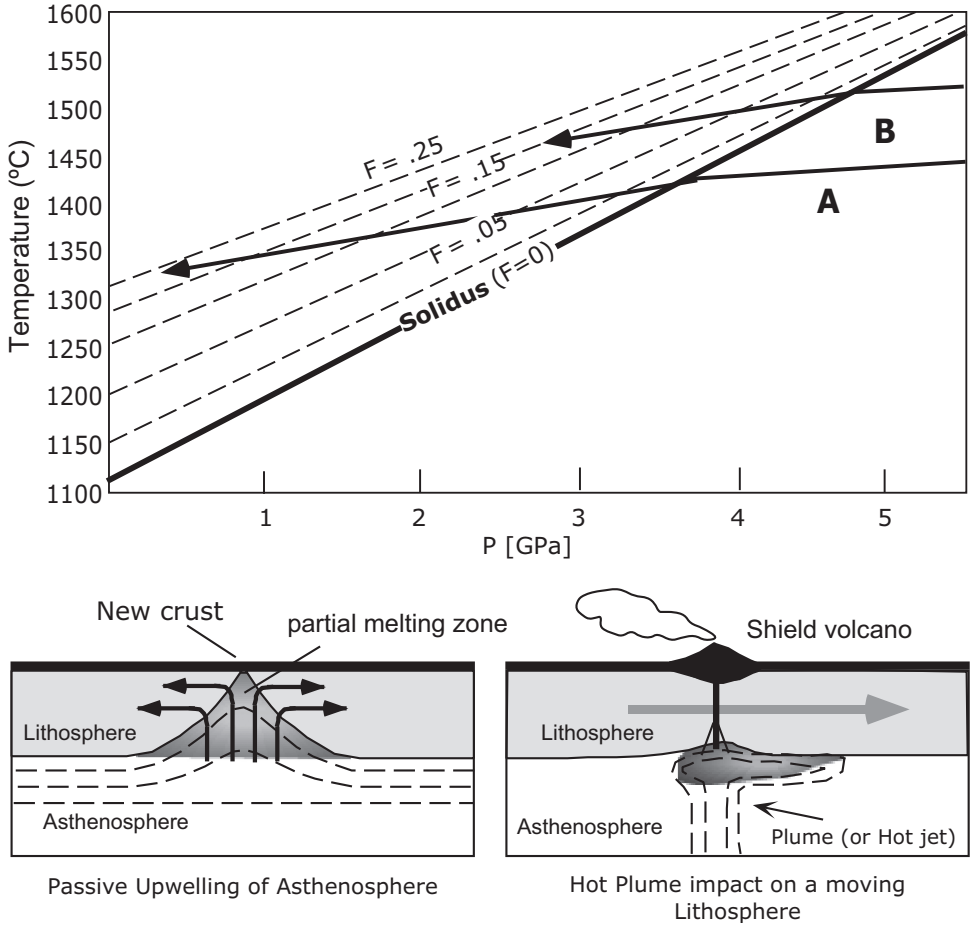

Fig. 5.2 *Bottom left*: partial melting and melt accumulation in passive melting regime beneath an extensional environment, such as a mid-oceanic ridge, MOR, where extension of two lithospheric plates causes the asthenosphere to passively rise to shallow depth and partially melt to generate MOR basalt magma. The magma generated within the *triangular* partial molten regime "focuses" to a form new crust (*black*) at the ridge axis, while the melt-depleted residue is transported laterally (as shown by the *arrows*) to form the lithosphere. *Bottom right*: Partial melting in a plume or hot jet environment in which a hot plume rises from the deep and partially melts near the lithosphere/asthenosphere boundary. The melt collects and ascends via cracks through the lithosphere to erupt at the surface. In the present example the lithosphere is moving from left to right, whereas the hot plume remains stationary. This arrangement results in a volcanic island chain like the Hawaiian–Emperor chain in central Pacific in which the volcanic islands get progressively older as they move away from the hot spot or plume. *Dashed contours*—isotherms. *Top panel*: paths of mantle parcels in the plume (path B) versus passive melting regimes (path A). F means melt fraction. $F = 0.01$ means 1 % melt and 99 % solid matrix or residue. Each *dashed contour* represents a fixed value of F [this diagram is principally based on data from Jaques and Green (1980), Hirose and Kushiro (1993), and Baker et al. (1995)]

volatile-absent condition from the same rock at the same pressure. As an example, note that olivine tholeiitic partial melt will form under anhydrous conditions from a lherzolite when it is heated to its solidus at a pressure of about 1.5 GPa; and the same lherzolite under hydrous conditions at 1.5 GPa will produce a high-alumina basalt or a magnesian andesite magma. Further discussion will follow in a later chapter.

Magma Segregation

Experimental petrology and seismology indicate that most magmas erupted within the Cenozoic era have been generated within the top 200 km of the Earth. Deep in the source region where melting begins, tiny pockets of magma are likely distributed along intergranular pore spaces of the source rock. Such partially molten rocks rise to shallower levels by diapirism, i.e., the entire mass of rock + melt flow upward by deforming the very hot rocks that surround the partially molten zone (e.g., Philpotts and Ague (2009)). During this process, magmas leave behind their matrix by porous flow, i.e., they migrate along intergranular pore spaces. Such porous flow may be accompanied by reaction and selective dissolution of some wall rock minerals, which enhances magma transport (e.g., Kelemen 1998). *Compaction* becomes a highly effective process: The matrix compacts, deforms, and flows downward and the melt is squeezed out to form a layer

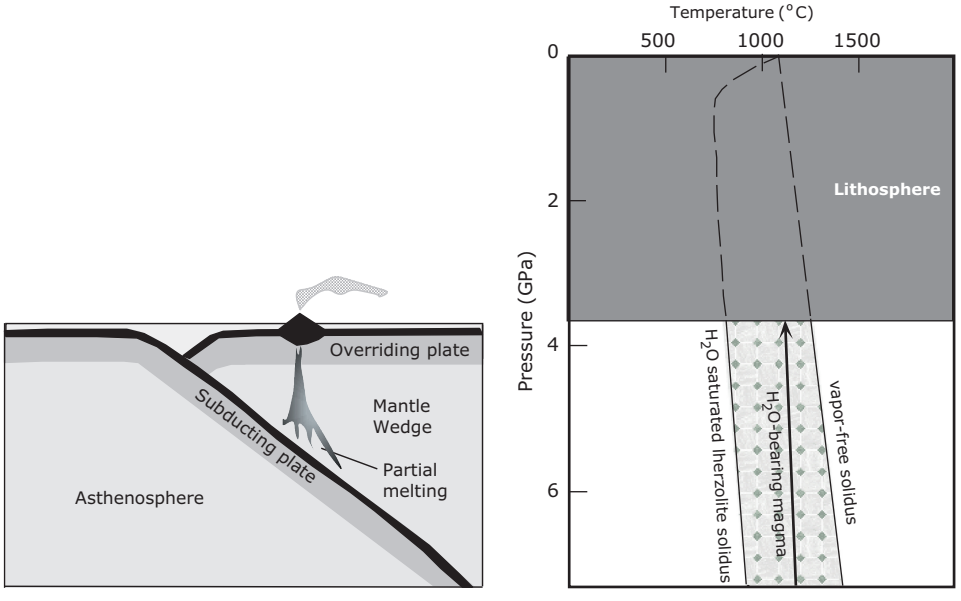

Fig. 5.3 Hydrous melting in a subduction zone. *Left*: schematic cross section of a subducting plate where H_2O-rich fluid is given off the subducting plate. This fluid lowers the melting temperature of the mantle wedge above the subducting plate, triggering melting. *Right*: this diagram illustrates the extent to which H_2O lowers the mantle lherzolite solidus. It also shows the vertical temperature gradient in the wedge (*arrow*). Note that this path is lower than the volatile-free solidus; therefore, melting would not occur in the asthenosphere if H_2O were not added to it

at the top (see Box 5.2). An excellent example of compaction is when one walks on sandy beach: The sand is compacted and pore water between sand grains is squeezed out to the surface. Returning to magma segregation, the accumulated magma from compaction eventually leads to *pipe flow*, in which magma pockets become sufficiently large that they are transported in well-defined conduits. Magma may create its own

Box 5.2: Compaction and Magma Segregation

To understand magma segregation via porous flow, one must know the geometry of pore spaces in the source rock. Significant progress has been made over the last decade toward quantifying the segregation of basaltic magmas from their upper mantle source rock—lherzolite. Melting appears to begin at the intersections ("triple-point junctions") of grains of three different phases. Melting along corners occurs in order to minimize the interfacial energy differences between the crystalline surfaces and melt. In this process, the *dihedral angle* (θ) between two adjacent solid grains and melt plays an important role in controlling melt distribution in the pore spaces of the rock (Fig. 5.4). If $\theta < 60°$, then melts in all corners will be interconnected, which allows the

(continued)

Box 5.2 (continued)

melt to escape along grain boundaries even when the melt fraction [i.e., mass of melt/(mass of melt + mass of rock)] is very small. Basaltic magmas and lherzolite matrix exhibit this behavior. When $\theta > 60°$, the melts at the pore spaces will not form an interconnected network and thus melt will escape from the matrix only when a certain porosity threshold (melt fraction) is crossed. Granitic melts generally show this type of behavior and therefore they do not escape from the source very easily.

Flow of magma through interconnected pores (i.e., porous flow) is governed by *D'Arcy's law*:

$$v = \frac{K}{\mu\phi}\frac{\mathrm{d}P}{\mathrm{d}z}$$

where v is magma velocity, K is permeability, ϕ is porosity, and μ is viscosity of the magma. $\mathrm{d}P/\mathrm{d}z$ is simply the pressure gradient caused largely by the density difference between a magma and the solid residue. Permeability is affected by grain size and porosity: coarser grains have greater permeability. The greater the viscosity, the slower will be melt velocity; therefore, basalt magma will travel

(continued)

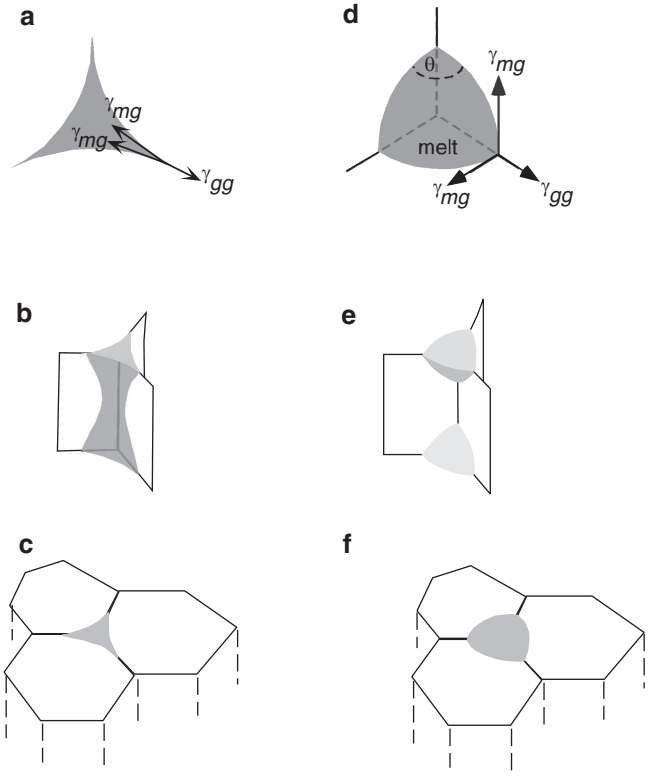

Fig. 5.4 Melt distribution in pore spaces between mineral grains in a rock. (**a**), (**b**), and (**c**) apply to mafic melts and (**d**–**f**) apply to felsic melts. Interfacial energy differences between two adjacent grains and between melt and grain are given as γ_{gg} and γ_{mg}, respectively. (**a**) Mafic melt occupancy at a triple-point junction in a peridotite due to small dihedral angles. (**b**) Mafic melt channel in 3D along the grain boundaries between three adjacent grains in a peridotite. (**c**) Perspective diagram of (**b**). (**d**) Felsic melt occupancy at a triple point junction. (**e**) 3D diagram showing distribution of melt along the vertical dimension. (**f**) Perspective drawing of (e) [After Watson (1982)]

Box 5.2 (continued)

faster than granitic magma because of its lower viscosity. D'Arcy's law indicates that melt velocity is inversely proportional to melt fraction (ϕ). Note that at higher ϕ, the dihedral angle may become greater than 60°, as a result of which the channels connecting the pores may get pinched off (Fig. 5.4).

In *compaction* two-phase flow occurs in which the melt flows (segregates) upward from the solid matrix (residue) as the latter deforms and flows downward (Fig. 5.5). This happens due to the sharp density contrast between melt and matrix. McKenzie (1984) provided a rigorous treatment of compaction and showed that in the case of basalt magmas, a maximum of about 3 % melt may occupy the pores in order to satisfy grain/melt

(continued)

Box 5.2 (continued)

interfacial energies; and once such a value is exceeded, the matrix will deform expelling the melt.

Consideration of a slightly modified version of D'Arcy's law tells us whether compaction would occur or not:

$$v_{\text{melt}} - V_{\text{matrix}} = -[K/\phi\mu][\mathrm{d}P/\mathrm{d}z + \rho_{\text{melt}}g]$$

where v_{melt} and V_{matrix} are velocities of melt and matrix, K = permeability, P = pressure, ρ_{melt} = density of melt, g = acceleration due to gravity, and z = vertical height which *becomes positive* upward. When the pressure is hydrostatic, melt movement will not occur:

$$\mathrm{d}P/\mathrm{d}z = -\rho_{\text{melt}}g \qquad (5.1)$$

or

$$\mathrm{d}P/\mathrm{d}z + \rho_{\text{melt}}g = 0$$

The mean density of matrix + magma assemblage is:

$$\rho_{\text{mean}} = (1-\phi)\rho_{\text{matrix}} + \phi\rho_{\text{melt}}$$

or

$$\rho_{\text{melt}} = [\rho_{\text{mean}} - (1-\phi)\rho_{\text{matrix}}]/\phi$$

Matrix will not expand or compact when the pressure gradient

$$\mathrm{d}P/\mathrm{d}z = -\rho_{\text{mean}}g$$

or

$$\mathrm{d}P/\mathrm{d}z = [(1-\phi)\rho_{\text{matrix}} + \phi\rho_{\text{melt}}]g \qquad (5.2)$$

To prevent deformation both Eqs. (5.1) and (5.2) need to be true, which can only happen if $\phi = 1$ (i.e., no matrix may be present). Since this is impossible, matrix must undergo compaction.

Compaction must be considered in terms of length and time scales (Fig. 5.5). Since melt must form and segregate upward, the melt velocity must be zero at some depth (the lower

(continued)

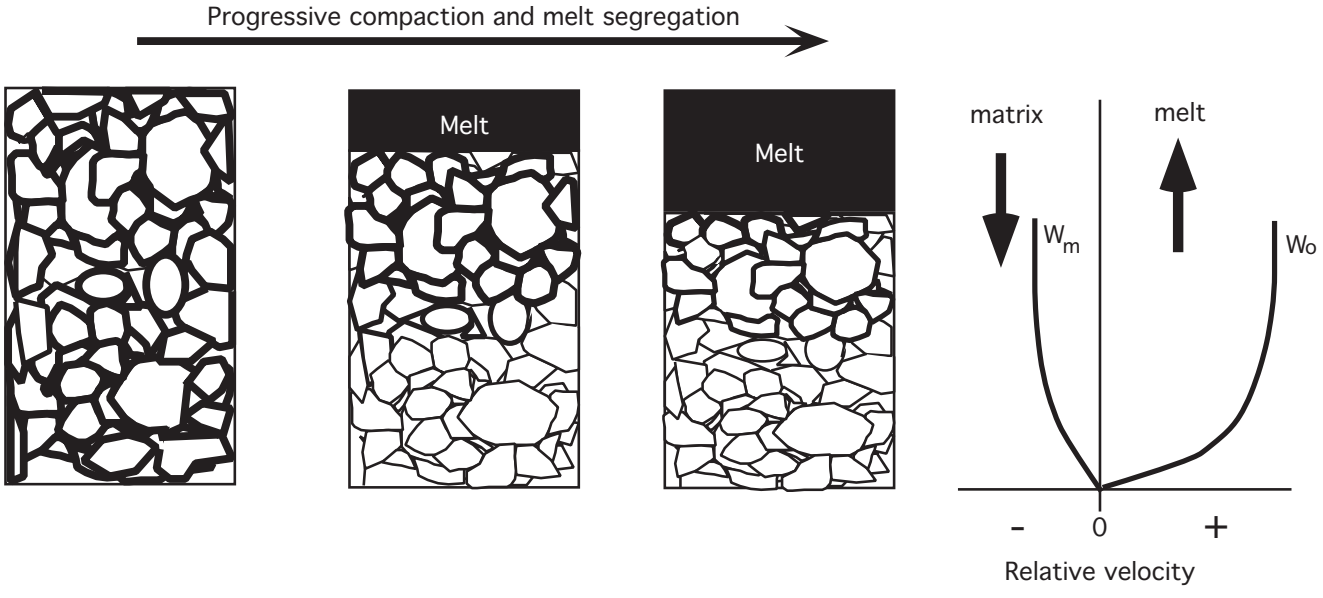

Fig. 5.5 *Left three panels* show schematic drawings of how compaction proceeds. In the beginning ("uncompacted") the melts are located along grain boundaries (*left*). With progressive compaction the solid matrix settles to the *bottom*, while the melt separates and collects at the *top*. The *right panel* shows relative velocities with which the melt (velocity = W_m) and matrix (W_o) segregate from one another. The velocity signs represent the direction along which material is flowing: (+) for upward flow and (−) for downward flow. The melt velocity is high in the lower part of the compacting column and becomes constant above a certain height. The matrix velocity is lower than the melt velocity at all heights

Box 5.2 (continued)

boundary of the length scale). The upper boundary of this system may be defined to have zero stress on the matrix. Melt velocity (W_m) increases from the lower boundary until at some height it reaches a constant value (w^0), at which it can balance the pressure gradient due to mean density. Compaction is therefore the greatest close to the lower boundary and diminishes exponentially upward, becoming zero at the upper boundary, which may be an impermeable layer or a permeable layer through which the melt may percolate (McKenzie 1984). McKenzie (1984) used a dimensionless parameter, called *expansion rate* ($1/\phi\partial\phi/\partial t'$), to show this behavior: it is zero at the lower boundary, remains negative up to the upper boundary, but its rate decreases exponentially from bottom to top (Fig. 5.5). The *compaction length* (δ_c) is defined as a dimensionless quantity:

$$\delta_c = \sqrt{\frac{\zeta + 1.33\eta}{\mu}K} \qquad (5.3)$$

(continued)

Box 5.2 (continued)

where η and ζ are shear and bulk viscosities of the matrix, μ is the viscosity of the melt, and K is permeability.

Permeability may be expressed, as a first-order approximation, as

$$K = a^2\phi^3/\left[\kappa(1-\phi)^2\right]$$

where a is the spherical radius of grains in the matrix, ϕ is porosity (or melt fraction), and κ is a constant whose value may be about 1,000 (McKenzie 1984).

As an example of a back-of-the-envelope calculation, consider the case of a basalt magma segregating from the upper mantle beneath a mid-oceanic ridge. We assume the values 10^{18} and 10 Pa.s for matrix viscosity (ζ+1.33η) and melt viscosity (μ), respectively. Table 5.1 shows permeability and compaction length values calculated for different melt fractions (f and two different sizes of grains (a = 0.2, 0.3 cm). Table 5.1 and Fig. 5.6 show that the compaction length (δ_c) is likely to be less than 600 m for melt percentage (Φ) of up to 3 % in the upper mantle where the

(continued)

Table 5.1 Calculation of compaction lengths

a (radius) (cm)	f porosity (cm^2)	κ	K permeability (cm^2)	Matrix viscosity (P)	Melt viscosity (P)	Compaction length (m)
0.2	0	1,000	0	1.00E+20	100	0.00
0.2	0.01	1,000	4.08122E−11	1.00E+20	100	63.88
0.2	0.02	1,000	3.33195E−10	1.00E+20	100	182.54
0.2	0.03	1,000	1.14784E−09	1.00E+20	100	338.80
0.2	0.04	1,000	2.77778E−09	1.00E+20	100	527.05
0.2	0.05	1,000	5.54017E−09	1.00E+20	100	744.32
0.2	0.06	1,000	9.77818E−09	1.00E+20	100	988.85
0.3	0.01	1,000	9.18274E−11	1.00E+20	100	95.83
0.3	0.02	1,000	7.49688E−10	1.00E+20	100	273.80
0.3	0.03	1,000	2.58263E−09	1.00E+20	100	508.20
0.3	0.04	1,000	6.25E−09	1.00E+20	100	790.57
0.3	0.05	1,000	1.24654E−08	1.00E+20	100	1,116.48

Box 5.2 (continued)
average grain radius (as estimated from xenoliths) is about 0.2–0.3 cm, and beyond this height the magma must move by percolation or in dikes. Note that this compaction length is much smaller than the average length over which magma is generated beneath a mid-oceanic ridge (tens of km). It thus seems likely that the magma segregates from the bottom to near the top of the melting zone through a series of compaction layers and not one single compacting "column." In the lowermost column, compaction forces magma to migrate upward via porous flow. The magma collects at the top of the column and eventually migrates further upward via porous flow in the column above. This new matrix + magma layer undergoes another compaction expelling the melt upward, and so on. Thus, the magma may reach the crust through a series of magma waves resulting from compaction.

conduit by *stoping*, i.e., by fracturing and incorporating wall rocks, or such pathways may be preexisting fractures.

Magma's flow through dikes (i.e., pipe flow) can be described with the following equation (Sparks 1993):

$$v = \frac{d^2}{64_\eta}(\Delta\rho)g \tag{5.4}$$

where v = magma velocity, d is the width of the dike, η is the viscosity of the magma, $\Delta\rho$ is the density difference between the rock and magma, and g is acceleration due to gravity. In the case of a tholeiitic basalt magma (η = 300 P or 30 Pa.s) moving along a dike (d = 10 cm) within the lherzolitic lithosphere, the $\Delta\rho$ = 0.6 g/cm^3; and the flow velocity may be calculated from the prior equation:

$$v = \left[10^2/64 \times 300\right] \times 0.6 \times 980$$

$$v = 3.06 \text{ cm/s}$$

Volatile-saturated magmas can ascend much faster and more explosively as the vapor exsolves from the magma during ascent. A classic example of this is kimberlite magma, which appears to have erupted at supersonic velocities.

Chemistry of the Melting Process

Phase Diagram Constraints on Major Elements

In Chaps. 3 and 4 we noted that phase diagrams are necessary to understand the relationship between temperature and composition of melts that may form by partial melting of any rock at any pressure. We noted that melting initiates at an invariant point in a system containing two or more components. Natural rock systems generally contain more components but their melting behavior in general approximates the simple systems we studied in Chaps. 3 and 4. As an example, we use the diagram Di–An–Fo and assume it to be a ternary system at all pressures (which is not true but does not do any harm for our purpose of illustration). Figure 5.7 shows the location of invariant points (*a*, *b*, *c*, *d*) at four different pressures—1 atm to 2 GPa. A source peridotite plotted in Fig. 5.7 will generate

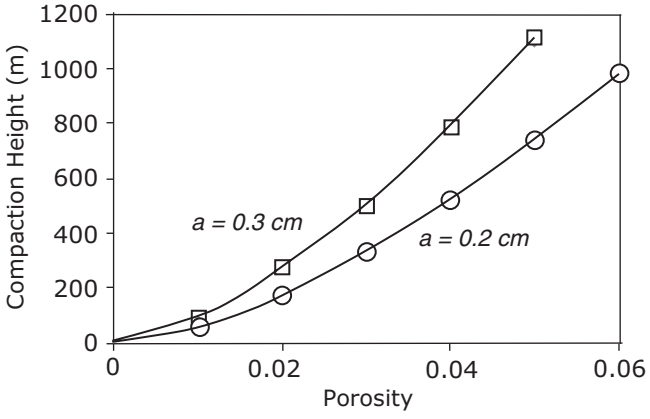

Fig. 5.6 Compaction length as a function of grain size (radius = a) and melt fraction (F)

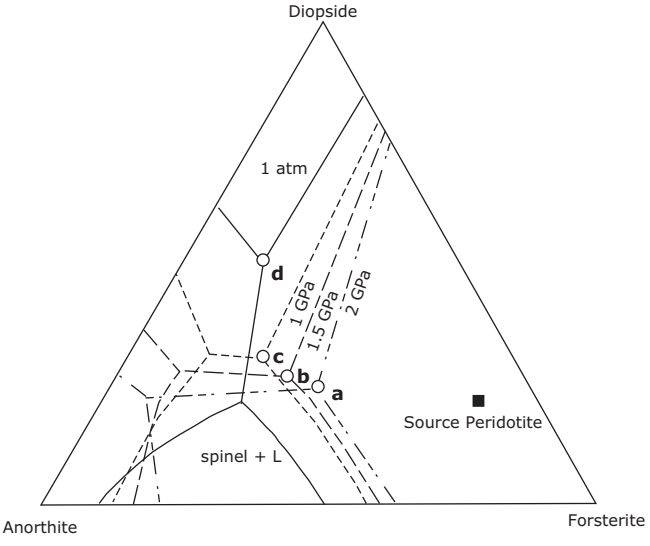

Fig. 5.7 Phase relations in the "system" Di–An–Fo at four different pressures (redrawn from Presnall et al. 1978). Points a, b, c, and d are invariant points that are of interest in our discussion in the text of partial melting of a peridotite source rock. As discussed in the text, Di–An–Fo is really a join and not a system at any pressure

considerable amount of partial melt at any of these invariant points at different pressures, which can be calculated with lever rule at each pressure. Since we know the compositions of a, b, c, d in terms of percentages of diopside ($CaO{\cdot}MgO{\cdot}2SiO_2$), anorthite ($CaO{\cdot}Al_2O_3{\cdot}2SiO_2$), and forsterite ($2MgO{\cdot}SiO_2$) components, and we know the chemical formulae of the components, it is a simple matter to calculate the composition of the invariant melts *in terms of oxide %*, as shown in the example in Table 5.2.

Table 5.3 shows calculated compositions of invariant melts at different pressures that can be produced from the peridotite source rock plotted in Fig. 5.7. Figure 5.8 shows how the composition of these melts change as pressure increases: CaO and SiO_2 decrease drastically and MgO increases. Are these trends reasonable if we were to melt a natural peridotite? The short answer is yes. Natural peridotites contain significant amounts of orthopyroxene, which is not considered in this diagram; and therefore, the comparison is not straightforward. Also, because of the presence of many other components in a natural peridotite, the melting is not exactly the type of invariant melting considered here. We will discuss melting of peridotite in a later chapter.

Trace Elements

Trace element abundance in magmas gives us considerable insight into magma formation and crystallization. Here we will consider a few fundamental equations that describe the chemical aspects of melting. During melting or crystallization, an element may prefer to remain in a particular mineral of the residue or it may prefer the melt phase. This selective behavior may be described in terms of *partition coefficient* or K_d, where

$$K_d = C_i^S / C_i^L$$

and C_i^S, C_i^L are concentrations of any element i in a mineral and coexisting liquid, respectively. As an example, consider the partition coefficient for the element Sr between olivine and liquid, $[K_d]_{Sr}^{ol/L} = 0.005$: this means that for the element strontium (Sr), the partition coefficient indicates that Sr prefers the melt 200 times more than olivine. On the other hand,

Table 5.2 Steps to calculate oxide wt% composition from ternary components

Comp. of components				Calculation of Di50An35Fo15	
Wt%	Di	An	Fo		Oxide Wt%
CaO	25.92	20.16		CaO = 0.5 × CaO(di) + 0.35 × CaO (an) =	20.01
MgO	18.62		57.29	MgO = 0.5 × MgO(di) + 0.14 × 57.29(*fo*) =	17.91
Al_2O_3		36.66		Al_2O_3 = 0.36 × 36.66 =	13.20
SiO_2	55.46	43.13	42.71	SiO_2 = calculate yourself =	49.23

Table 5.3 Calculated invariant melts for Fig. 5.7

Invariant pt.	Composition	P(GPa)	CaO	MgO	Al_2O_3	SiO_2	Total
a	Di22Fo38An40	2.00	13.764	25.869	14.664	45.681	99.977
b	Di25Fo31An44	1.50	15.348	22.417	16.13	46.08	99.975
c	Di30Fo25An45	1.00	16.845	19.911	16.497	46.722	99.974
d	Di50Fo15An35	0.00	20.013	17.906	12.831	49.23	99.98

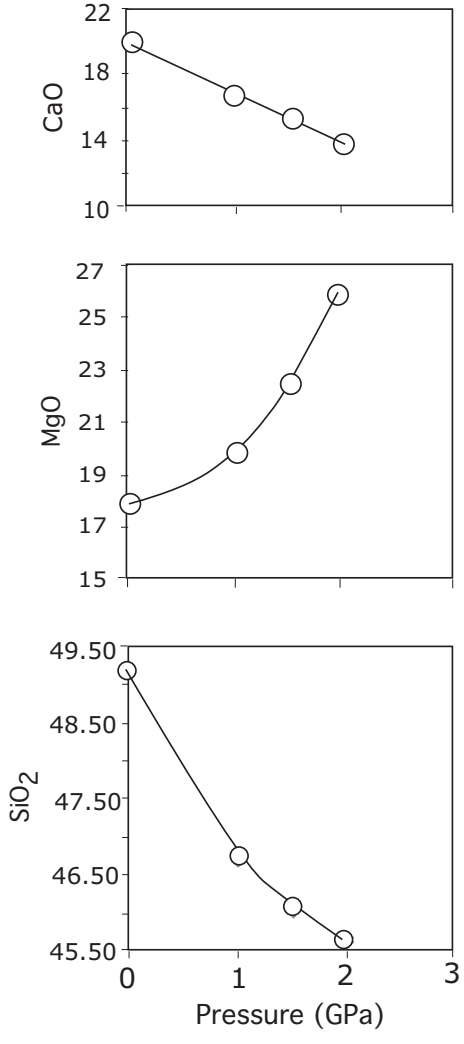

Fig. 5.8 Composition of melts at the invariant points in Fig. 5.7 plotted here in terms of pressure versus oxide wt%

$[K_d]_{Ni}^{ol/L} = 12$ means that nickel prefers to stay in olivine over melt. If K_d for a certain element is 1, it means that the element has no special preference toward either the melt or the mineral. K_d can vary as a function of pressure, temperature, and melt composition. An element is called *incompatible* if K_d is less than 1 and *compatible* if K_d is greater than 1. In the examples above, Ni is a compatible element in olivine but Sr is incompatible. Interestingly, Sr is a compatible element for plagioclase ($K_d = 2$). Mineral/melt partition coefficients for various elements have been measured in laboratory experiments and are listed in Table 5.4 and shown in Fig. 5.9.

In the case where an element is being partitioned between a melt and a rock consisting of several minerals, the term *bulk distribution coefficient* (D) is used to account for the total partitioning of an element between the bulk solid and melt. This is done by using the partition coefficients of each solid adjusted for their weighted abundances in the bulk rock: for example, for a rock composed of the minerals clinopyroxene (Cpx) and garnet (Gar), D can be calculated as follows:

$$D = X_{Cpx} K_d^{Cpx/L} + X_{Gar} K_d^{Gar/L}$$

where X_{Cpx} and X_{Gar} stand for weight fractions of the Cpx and Gar, respectively, in the bulk solid and K_d'*s* are partition coefficients for any element i between these phases and the melt. Weight fractions are calculated as the weight of the mineral divided by the total weight of all minerals combined; for example, X_{Cpx} = Cpx/(Gar + Cpx). (Note: *mode* of a mineral in a rock determined by various counting methods in the laboratory represents volume. Such volume percentage of that mineral will first have to be converted to weight fraction by multiplying it by the mineral's density.)

Let us consider an example in which we are trying to calculate the D for the element Samarium (Sm) for a rock containing only two minerals—clinopyroxene and garnet in modal percentages of 60 and 40, respectively. A little online search will tell you that these two minerals have densities around 3.5 and 3.65 g/cm^3, respectively. Thus, multiplying the modes by their respective densities, we get Cpx = 60 × 3.5 = 210, and Gar = 40 × 3.65 = 146. From these we calculate the weight fractions of each: Cpx wt. frac. = 210/(210 + 146) = 0.59; and Gar wt. frac. = 0.41. The partition coefficients for Sm between Cpx/L and Gar/L are 0.445 and 0.102, respectively. Thus, D = (0.59 × 0.445) + (0.41 × 0.102) = 0.304.

The method to calculate D for a simple bimineralic rock above can be expanded for the general case in which

Table 5.4 Partition coefficients for rare earth elements

Element	Plag/L	ol/L	Sp/L	Cpx/L	Opx/L	Amph/L	Gar/L
La	0.1500	0.0004	0.0030	0.0590	0.0003	0.1950	0.0020
Ce	0.0900	0.0100	0.0160	0.0860	0.0030	0.0990	0.0050
Nd	0.0740	0.0030	0.0100	0.1290	0.0030	0.4400	0.0520
Sm	0.0360	0.0060	0.0100	0.3860	0.0080	0.7600	0.4800
Eu	0.7300	0.0080	0.0100	0.7500	0.0200	1.0000	1.0000
Gd	0.0400	0.0070	0.0100	0.6800	0.0200	0.8600	1.8000
Dy	0.0400	0.0070	0.0100	0.4400	0.0540	0.7800	2.2000
Er	0.0300	0.0170	0.0100	0.6000	0.0690	0.6800	4.0000
Yb	0.0300	0.0150	0.0100	0.4300	0.1070	1.0000	4.0300
Lu	0.0300	0.0180	0.0100	0.4390	0.1100	1.0000	5.5000

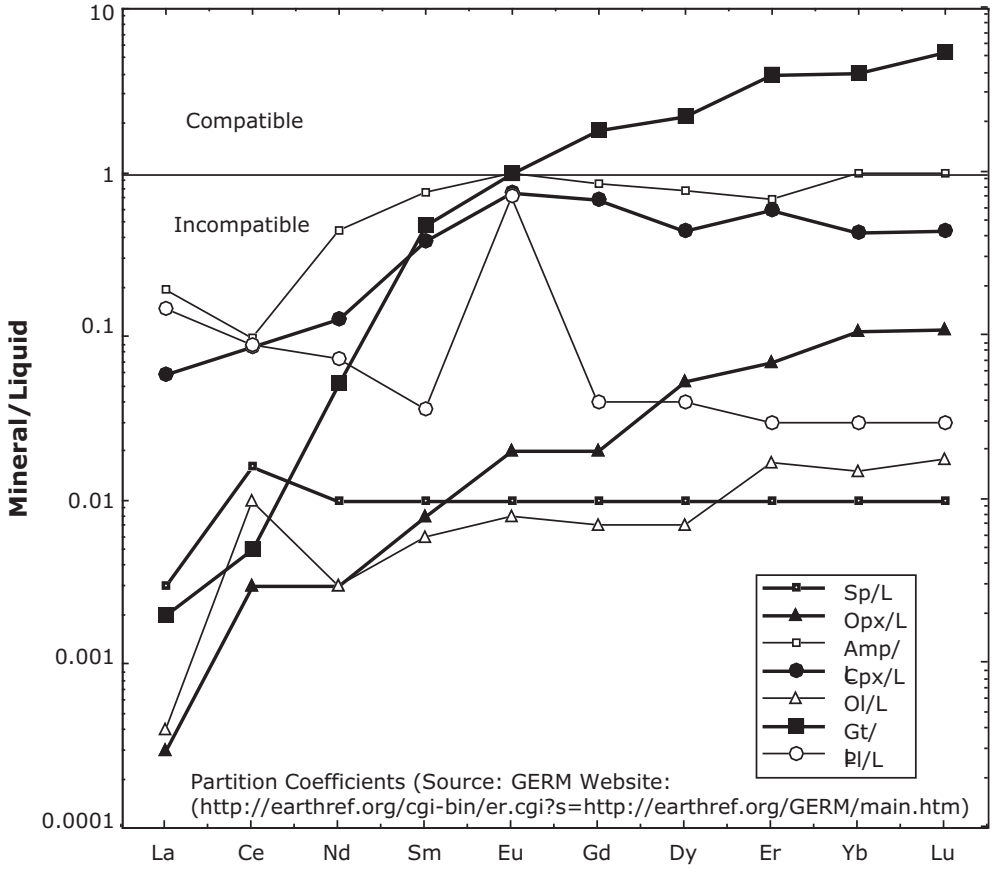

Fig. 5.9 Melt/mineral partition coefficients for some important minerals and mafic melts are shown here

the source rock has many more minerals using the following formula:

$$D_i = \Sigma X_j K_{\mathrm{d},i}{}^{j/L}$$

where j represents the mineral phases and i represents an element. As before, X and $K_{\mathrm{d},i}$ are weight fraction of a phase and mineral–melt partition coefficient for element i for that phase.

Although a number of different melting models are mathematically possible, two end-member melting processes are generally considered to cover all possible melting types. These two extreme models are the so-called batch melting and fractional melting processes. Batch melting is simply equilibrium melting. The simplest case of batch melting may be expressed with the following equation (called the *modal melting equation*):

$$\frac{C_i^{\mathrm{L}}}{C_i^{\mathrm{o}}} = \frac{1}{D(1-F)+F} \tag{5.5}$$

where C_i^{L} and C_i^{o} are concentration of the element i in liquid and in the original solid, respectively, D as defined above, and F represents melt fraction (goes from 0, i.e., no melt, to 1, i.e., 100 % melted). (Note that this same equation can be used for equilibrium crystallization.) This is called *modal batch melting* model because it assumes that the weight proportion in which minerals dissolve into the melt is the same as that in which these minerals occur of the starting rock. Similarly, *modal fractional melting* is the simplest possible fractional melting process one can think of. It is represented by the following equation:

$$\frac{C_i^{\mathrm{L}}}{C_i^{\mathrm{o}}} = \frac{1}{D}(1-F)^{\left[\frac{1}{D}-1\right]} \tag{5.6}$$

As we saw in Chap. 3, fractional melting is an extreme case where any incipient amount of melt is extracted from the source rock as soon as it forms. These tiny fractions of melt likely accumulate in the conduit system as they ascend upward. The following equation can be used to calculate the composition of such an aggregate melt $\left(\overline{C}_i^{\mathrm{L}}\right)$:

$$\frac{\overline{C}_i^{\mathrm{L}}}{C_i^{\mathrm{o}}} = \frac{1}{F}\left[1-(1-F)^{\frac{1}{D}}\right] \tag{5.7}$$

Nonmodal melting is a more realistic type of process in which an additional term, P, is introduced that represents the weight fraction contribution of the minerals to the melt: for example, it would be calculated from weight fraction of the minerals contributing to the melt at an invariant point. In our earlier example of melting of a rock containing garnet and clinopyroxene

$$P = Y_{\mathrm{Gar}} K_{\mathrm{d}}^{\mathrm{Gar/L}} + Y_{\mathrm{Cpx}} K_{\mathrm{d}}^{\mathrm{Cpx/L}}$$

where Y_{Gar} and Y_{Cpx} are the weight fractions in which garnet and clinopyroxene dissolve into melt. Let us say that at a particular pressure garnet and clinopyroxene dissolve in 70:30 weight proportions. Then $Y_{\mathrm{Gar}} = 0.7$ and $Y_{\mathrm{Cpx}} = 0.3$. So, for the element Samarium we calculate $P = 0.7 \times 0.102 + 0.3 \times 0.445 = 0.205$. This value is quite different from the D value we calculated earlier. The *nonmodal batch melting equation* is written as

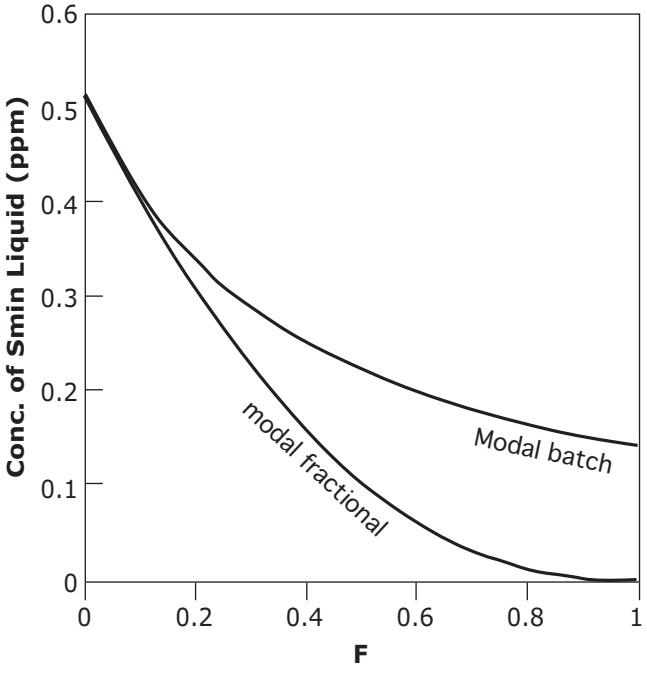

Fig. 5.10 Concentration of Sm in melt versus F is shown for two different melting models (see text for further discussion)

$$\frac{C_i^{\mathrm{L}}}{C_i^{\mathrm{o}}} = \frac{1}{F(1-P)+D} \tag{5.8}$$

In the case of *nonmodal fractional melting*, the appropriate equation is

$$\frac{C_i^{\mathrm{L}}}{C_i^{\mathrm{o}}} = \frac{\left[1-\frac{P.F}{D}\right]^{\left[\frac{1}{P}-1\right]}}{D} \tag{5.9}$$

Using an EXCEL®spreadsheet (or using other spreadsheet programs), one can easily calculate the concentration of Sm in the melt ($C_{\mathrm{Sm}}^{\mathrm{L}}$) for varying degrees ($F$) of melting if D, P, the original concentration ($C_{\mathrm{Sm}}^{\mathrm{o}}$) in the source rock are known. Figure 5.10 shows Sm variation in the liquid as a function of F for different melting models stated above. There is hardly any difference between modal and nonmodal melting models (not plotted) in the example chosen; but there is significant difference in Sm concentration in melt between equilibrium and fractional melting models. In passing, note that we kept the P constant in our calculations although P should be expected to vary as melting proceeds at a single pressure or at variable

pressures. The student may wonder which of these equations accurately portray how melting happens in rocks. The reality probably is probably closer to near-fractional melting followed by accumulation of the melt fractions.

Primary Magmas

The term *primary magma* is used to denote the magma droplets that form by direct partial melting of the source rock and the magma that forms by aggregation of such droplets. No chemical or mineral components must be lost from it or added to it subsequent to its formation (the student is encouraged to read Herzberg et al. 2007). The concept of primary magma versus derivative or evolved magma is particularly useful in any discussion of composition of basaltic lava, melt inclusions, and chill margin rocks of layered mafic intrusions vis-à-vis the experimentally produced melts from mantle peridotite. Lavas and other natural rocks are rarely (if ever) the *primary magmas* that form *by direct* partial melting in the Earth's upper mantle. This is because during its ascent from source to the Earth's surface, basaltic magma commonly undergoes partial crystallization, gets contaminated with the crustal melts, mixes with other melts in the conduit system, etc.; and therefore, composition of the erupted lava is considerably different from the magma that was generated in the mantle. The term *derivative* or *evolved* composition is used to refer to the changed nature of the erupted lava.

It is important to recognize what compositional characteristics primary magma must possess if we are to gain an understanding of the pressure–temperature conditions of its formation. The examples I have chosen below all pertain to peridotite source–basalt magma "system" because they illustrate the concept of primary magma very well.

Some General Tests of Primary Magmas

Presence of Mantle Xenoliths

Some specific types of mafic lavas (basanites, nephelinites, alkali basalts, etc.) and kimberlite intrusives commonly carry *xenoliths* (i.e., accidental inclusions of wall rock fragments) and *xenocrysts* (accidental inclusions of mineral crystals) from the upper mantle. The presence of the inclusions indicates that such magmas rise so fast to the surface that they do not get the chance to drop off their significantly denser inclusions; and therefore, these lavas and intrusives are the best candidates of primary or near-primary magma that come out of the upper mantle. Their chemical compositions also support this view. There are ways to calculate the depth (or depth range) of origin of these xenoliths (discussed in a later chapter). Such calculated depth would signify that the magmas that carried them must have come from even deeper levels. For example, kimberlites that carry diamonds must have originated deeper than at least 120 km because the minimum pressure in the mantle where diamond is stable is about 4–5 GPa, i.e., 120–160 km deep (see Fig. 3.1).

Chemical Test of Equilibrium with Source Rock

Peridotites sampled from the ocean floor, from ophiolites (discussed in a following chapter), and those that occur as xenoliths in alkalic lavas and kimberlites give us reasonable clue as to the chemical composition of the upper mantle peridotite. Such peridotites carry >60 % olivine with a fairly narrow olivine composition range with molar $Mg/(Mg + Fe^{2+})$ ratio of 88–90. Experimental studies have shown that one can easily calculate $Mg/(Mg + Fe^{2+})$ ratios of the primary liquids that can be in equilibrium with such olivine because the exchange coefficient (K_d) for the Mg, Fe exchange reaction between olivine and basalt magma is fairly constant, varying only little with pressure: it has a value of 0.3 at pressure less than about 0.5 GPa, 0.32 at 0.5 to 1.5 GPa, and about 0.35 at higher pressures (Putirka 2005).

The reaction in which olivine (ol) and coexisting liquid (L) exchange MgO and FeO is written as

$$[\mathrm{MgO}]^{\mathrm{ol}} + [\mathrm{FeO}]^{\mathrm{L}} = [\mathrm{FeO}]^{\mathrm{ol}} + [\mathrm{MgO}]^{\mathrm{L}}$$

$$K_{\mathrm{d}} = \frac{[\mathrm{FeO}]^{\mathrm{ol}}[\mathrm{MgO}]^{\mathrm{L}}}{[\mathrm{MgO}]^{\mathrm{ol}}[\mathrm{FeO}]^{\mathrm{L}}}$$

This can be also written as

$$K_{\mathrm{d}} = \left[\frac{[\mathrm{FeO}/(\mathrm{MgO}+\mathrm{FeO})]^{\mathrm{ol}}}{[\mathrm{MgO}/(\mathrm{MgO}+\mathrm{FeO})]^{\mathrm{ol}}}\right] \times \left[\frac{\mathrm{MgO}/(\mathrm{MgO}+\mathrm{FeO})^{\mathrm{L}}}{[\mathrm{FeO}/(\mathrm{MgO}+\mathrm{FeO})]^{\mathrm{L}}}\right]$$

or

$$K_{\mathrm{d}} = \left[\frac{[\mathrm{Fe}\#]^{\mathrm{ol}}}{[\mathrm{Mg}\#]^{\mathrm{ol}}}\right]\left[\frac{[\mathrm{Mg}\#]^{\mathrm{L}}}{[\mathrm{Fe}\#]^{\mathrm{L}}}\right]$$

where Mg# is molar MgO/(MgO + FeO) and Fe# is FeO/(FeO + MgO). Because we are considering binary solutions, Mg# + Fe# = 1, or Fe# = 1 − Mg#. Thus, we rewrite the above expression of K_d as follows:

$$K_d = \left[\frac{[1 - \text{Mg}\#]^{ol}}{[\text{Mg}\#]^{ol}}\right]\left[\frac{[\text{Mg}\#]^{L}}{[1 - \text{Mg}\#]^{L}}\right]$$

or

$$\left[\frac{\text{Mg}\#}{[1 - \text{Mg}\#]}\right]^{L} = K_d\left[\frac{\text{Mg}\#}{[1 - \text{Mg}\#]}\right]^{ol}$$

In the above expression we plug in the values of K_d (=0.32) and Mg# (=0.88) of mantle peridotite olivine:

$$\left[\frac{\text{Mg}\#}{[1 - \text{Mg}\#]}\right]^{L} = 0.32 \times \frac{0.88}{0.12}$$

From the above relationship we calculate the Mg# of the liquid to be 0.701. *So we conclude that mantle-equilibrated magmas should have a minimum Mg# of about 0.7*. More depleted mantle (with higher MgO) will equilibrate with magmas with higher Mg#.

This has been a powerful constraint that has been used in many studies; however, recent studies have recognized that basalt source regions may not be entirely peridotitic everywhere. Some magma generation sites may have pockets of eclogite (which are composed of garnet and clinopyroxene and are formed by high-grade metamorphism of basalt) that are recycled fragments of ancient subducted ocean crust. Because eclogites are much more Fe-rich than peridotite, one could generate relatively Fe-rich magma in the upper mantle. However, if such magma equilibrates with the peridotitic mantle on their way up, it should equilibrate with the upper mantle olivine and thus become more magnesian.

There have been varied uses of the Mg# test in the literature. Most highly magnesian, "primary-appearing" basalt lavas (or chill margins) are not glassy or entirely aphyric but they contain olivine phenocrysts. In such cases one must first do a test to see if the lava has accumulated olivine phenocrysts along the way so that its bulk rock composition is not that of a melt but melt + extra olivine crystals. If the phenocrysts percentage is not much (say, 5 %), then it is usually not a problem. The test is basically to check

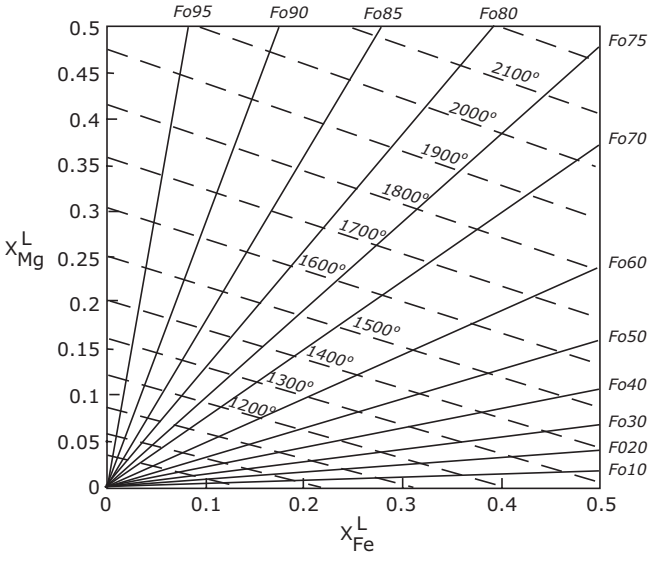

Fig. 5.11 Olivine–liquid equilibrium at 0.0001 GPa (1 atm) pressure (after Putirka 2005). The *dashed lines* are isotherms and temperatures are °C. $X_{Mg}{}^{L}$ and $X_{Fe}{}^{L}$ are cation fractions of Mg and Fe in liquid, respectively

if the olivine crystals are in equilibrium with the whole rock (i.e., liquid) because in such a case the olivine-whole rock K_d value should be close to 0.3 (±0.02) (Fig. 5.11).

It is not uncommon to have a glassy basalt (i.e., erupted as liquid) with Mg# (say, 0.60) that is too low to be in equilibrium with the upper mantle olivine. In such a case one can incrementally add olivine of appropriate composition while maintaining a constant K_d of 0.3 until the Mg# rises to 0.70. This is for the student to calculate as homework assignment.

In the above discussion I have assumed that our target primary magma should have Mg# = 0.7; however, it is quite possible that the magma last equilibrated with a more magnesian mantle olivine (Mg# = 0.91), in which case the Mg# of the equilibrated melt should also be higher (the student should calculate this). Which one of the two calculated primary magmas is more realistic? And what would such a primary magma signify in terms of their pressure–temperature conditions of origin? Answers to these questions may be found in the next section. In passing, note that Mg# is not the only major element ratio that we can count on. Equipped with the knowledge of partition coefficients and a pretty good idea of composition of the upper mantle minerals, one can construct a chemical "recipe" for primary-"looking" magmas: for example, in general mantle-derived primary basalt magmas should have at least ~300 ppm Ni.

Glassy or Aphyric Character (Not a Particularly Good Criterion)

Glass forms by rapid solidification or quenching of melt. Therefore, the best candidate for a primary magma must be a quenched melt or glass that has not undergone any loss or addition of crystals (via phenocrysts accumulation or addition of xenocrysts) or has not picked up any wall rock fragments (xenoliths). Glassy basalt lavas are indeed found in nature, but in most cases their chemical compositions seem to be evolved, i.e., they could not have equilibrated with their source rock (i.e., upper mantle peridotite). Thus, an additional test that the glass must also pass is a compositional one that would indicate whether or not it could be in chemical equilibrium with mantle peridotite.

Perhaps the best example of natural glass close to being a quenched primary magma was found by Clague et al. (1991) in submarine turbidite sands at Puna Ridge, which is a submarine extension of Kilauea volcano's (Hawaii) east rift zone. The Puna glass fragments are remarkable in that they have 15 wt% MgO and a Mg# [=molar ratio MgO/(MgO + FeO)] of 0.7. As pointed out in the previous section, magma with such chemical composition could be in equilibrium with a typical upper mantle olivine composition of Fo_{88} and therefore could potentially be a primary magma.

In general, such magnesian glasses are almost never found. In such an event, the next best thing is to choose is fine-grained lava (or chill margin of an intrusion) that is devoid of phenocrysts, i.e., aphyric, even though an aphyric rock is not glass but a quenched liquid that did not carry any phenocrysts. The only difference is that fine-grained, aphyric rock cooled slightly more slowly so that fine crystals had time to form. Once again, for an aphyric rock to represent primary or near-primary magma composition, it must pass the additional compositional filter discussed before. In general, being aphyric or glass by itself is not a good test of being primary.

Multiphase Saturation

If one could perform experiments on a starting rock powder or glass with the appropriate Mg# to be primary magma and show that such a liquid could be in equilibrium with the expected upper mantle minerals (and not just olivine) at a given pressure (or a small pressure range), then that would be a good argument for that starting material to have been a primary magma at that pressure. On a *P–T* diagram such a "point" is referred to as a multiphase saturation point. This concept of multisaturation and depth of equilibration of primary magma seems straightforward but read on!

The concept of multiphase saturation can be explained with an example we used in Chap. 3 in which we constructed an isoplethal diagram for a single bulk composition in a hypothetical binary system in *P–T* space (Fig. 5.12). Let us imagine that our source "rock" is composed of *A* and *B* crystalline phases. We see that melt *M* is saturated with both *A* and *B* crystals only at 1 GPa pressure. So, it is reasonable to state that melt *M* (our chosen primary magma) last equilibrated a source with both *A* and *B* at the 1 GPa eutectic point.

Does such logic hold up if we add more components? This time we draw isoplethal *P–T* diagrams for two melt compositions, *M* (represented as filled circles in Fig. 5.13a–c) and *N* (unfilled square), in a hypothetical ternary system *A–B–C* to illustrate that it does. Figure 5.13a–c shows three isobaric phase diagrams for the system *A–B–C* and at pressures of 0.5, 1, and 1.5 GPa, respectively. Figure 5.13d, e shows the isoplethal diagrams constructed for *M* and *N* starting melt compositions, respectively. The construction of each isoplethal diagram follows the principle outlined in Chap. 4. The ternary eutectic points at each of these pressures are the points on the solidus in *P–T* space at these respective pressures. No matter what the bulk composition, all melts must finally solidify at the solidus, and that is the only thing common between Fig. 5.13d, e. The rest of the curves in d and e are constructed based on the sequence in which each melt composition crystallizes different phases with cooling at each pressure. For example, let us consider the construction of the liquid-present curves in Fig. 5.13e. Each of the unfilled circles that line up along a constant pressure represents the point of entry of a crystalline phase or phases as the liquid is cooled. We gather such information by reading off the equilibrium crystallization paths of the starting melt from Fig. 5.13a–c. We then appropriately connect the dots in the *P–T* diagram to generate the isoplethal diagram that is internally consistent about the appearance of various phases at each *P*, *T*.

Melt *M* shows a multiphase saturation point at 1 GPa in *P–T* space in the sense that it directly solidifies to an assemblage of *A*, *B*, and *C* crystals at the same temperature. In other words, this would be the pressure where the melt would be in equilibrium with all the crystalline phases present in the source, i.e., this is the pressure (30 km depth) of last equilibration of the primary magma so chosen. I say "last equilibration" because it

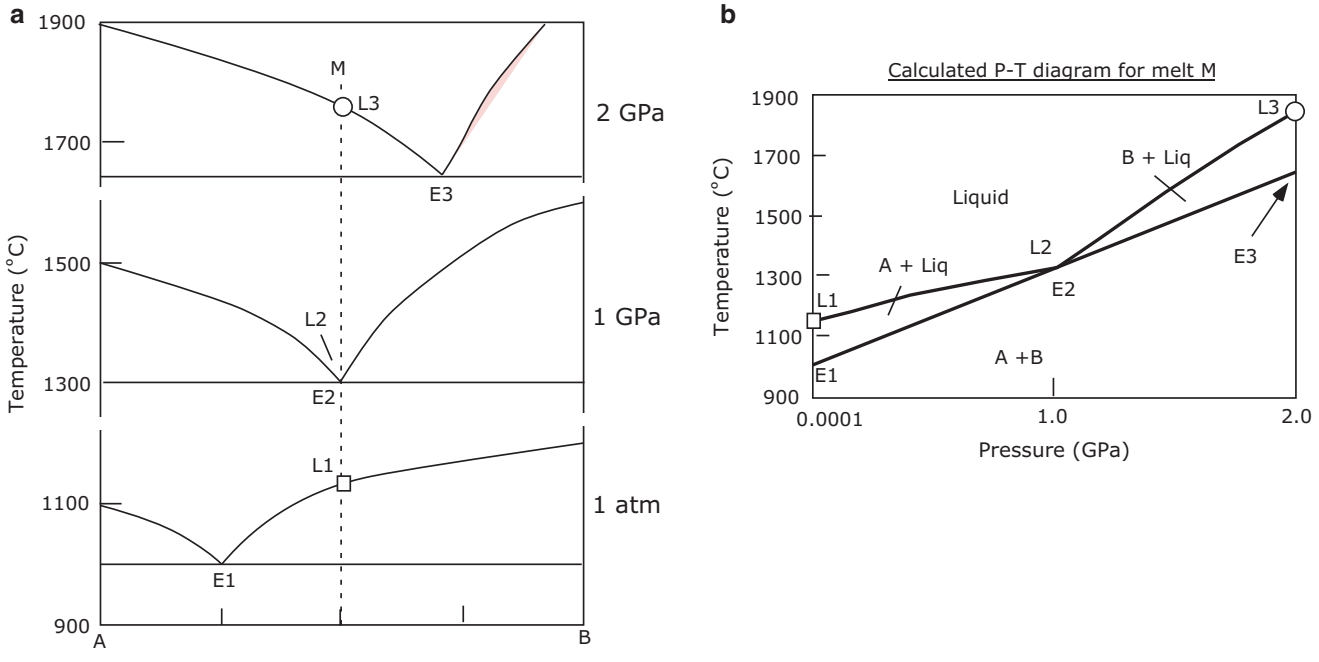

Fig. 5.12 (**a**) Isobaric phase diagrams for a hypothetical binary system at three different pressures. (**b**) An isoplethal section for the bulk melt composition *M* is constructed based on phase relations in the three isobaric diagrams in (**a**). Note that in this example, *M* is multiply saturated at 1 GPa, where it is also the polybaric invariant point (*E*2 = *L*2)

is possible that the melt *M* is an aggregate of melt droplets that have formed over a wider depth range, but the aggregate melt itself equilibrated with *A*, *B*, and *C* at the lowest possible pressure of 1 GPa.

Should any bulk composition show such a multiphase saturation? The isoplethal diagram for *N* demonstrates that the answer is negative (Fig. 5.13e). Note that at none of the pressures melt *N* will be saturated with all three crystalline phases and so it cannot be a primary magma.

Experimental petrologists have time and again performed experiments with the principal purpose of finding multiphase saturation points for specific "primary-appearing" basalt magmas in order to constrain their depths of origin. Fujii and Bougault (1983) conducted high-pressure crystallization experiments on a mid-ocean ridge basalt and found that this melt was saturated with plausible upper mantle peridotite phases (i.e., olivine + orthopyroxene + clinopyroxene + spinel) at 1 GPa (Fig. 5.14) and concluded that this basalt was a primary or near-primary magma. Stolper (1980) and later Takahashi and Kushiro (1983) ran a series of experiments in which they put basalt and upper mantle peridotite next to each other inside capsules and let the two equilibrate at different pressures in an effort to obtain the composition of mantle-equilibrated (i.e., multiphase saturated) liquid compositions in *P*–*T* space for natural basalt magmas. Stolper (1980) noted that the multiphase saturation points at 1–2 GPa do not plot anywhere close to mid-ocean ridge basalts and therefore concluded that none of these basalts could be primary magmas (Fig. 5.15). I use the above two examples just to show that using multisaturation concept to talk about the depth range of melting is not straightforward.

Extreme caution must be taken in how we interpret multiphase saturation points on isoplethal diagrams. Sometimes such multiphase saturation points may be completely at odds with other pieces of evidence that rule out the depth of magma equilibration as suggested by such points. For example, experiments have consistently shown that primary-appearing (MgO = 15–18 wt%) Hawaiian tholeiitic basalts show multiphase saturation at about 2 GPa, which would mean that these basalts come from the lithosphere (since the lithosphere is about 90 km thick beneath Hawaii). However, Nd, Sr isotope (and other radiogenic isotopes) compositions of these basalts are so different from that of lithospheric xenoliths from Hawaii that there is no way that Hawaiian tholeiites could have equilibrated with the lithosphere. Several ideas have been put forth to explain this discrepancy, that is, the meaning of multiphase saturation of Hawaiian tholeiites in terms of *P*, *T* of origin. Maaloe (2004) has argued that the primary magna for Hawaiian

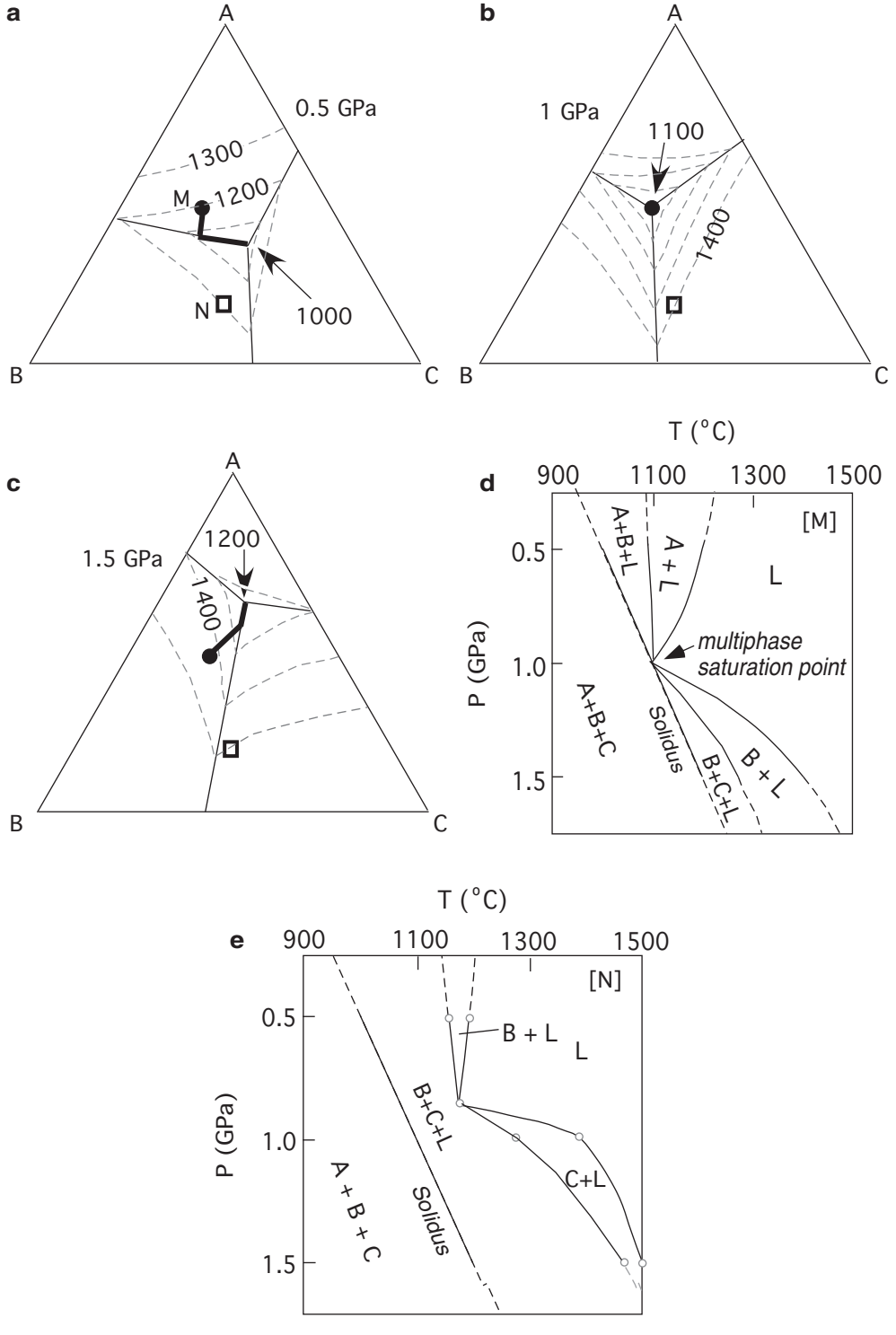

Fig. 5.13 Multisaturation in a hypothetical ternary system *A–B–C*. Isobaric phase diagrams at three different pressures are shown in (**a**), (**b**), and (**c**). Liquid path for melt composition *M* is shown as *dark line* and *point* at these pressures. From this information an isoplethal section for *M* is constructed in (**d**). Note that *M* is multiply saturated at 1 GPa. (**e**) Isoplethal section for melt composition *N* [as depicted as a square in (**a**), (**b**), and (**c**)] is similarly constructed here. *N* is not multiply saturated at any pressure

tholeiites is more magnesian (23 % MgO) and calculated its multisaturation at 3.6 (±0.5) GPa (i.e., 112 km) and 1,680 °C (±50°).

Asimow and Longhi (2004) have suggested that the depth implied by multiphase saturation point is simply an average depth of accumulation of an aggregate melt that is an accumulation of tiny melt fractions generated

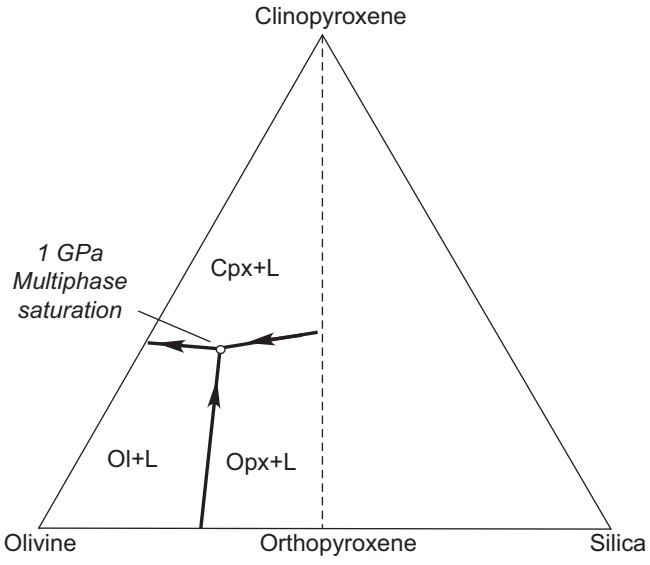

Fig. 5.14 Saturation of a MOR basalt with olivine, orthopyroxene, and clinopyroxene was experimentally determined at 1 GPa by Fuji and Bougault (1984)

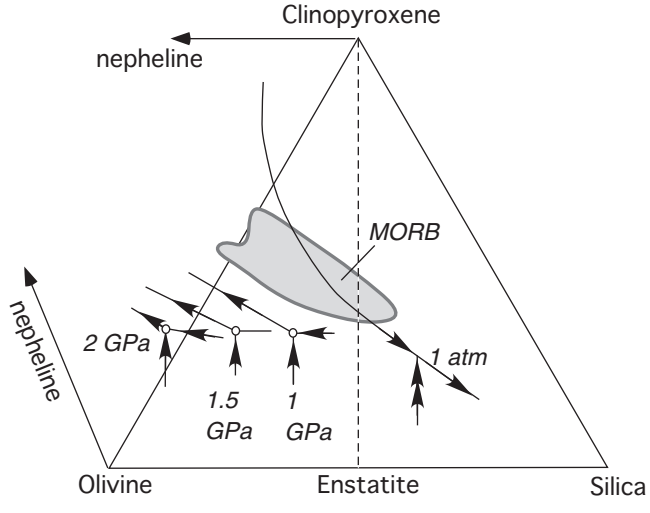

Fig. 5.15 Stolper (1980) experimentally determined multiply saturated (i.e., pseudoinvariant points) in natural basalt–peridotite system at several different pressures. He noted that MOR basalts do not touch any of these points at any pressure and therefore concluded that MORBs are not primary magmas

by small degrees of melting along an adiabat. In my view, the bottom line is that multiphase saturation by itself is not a trustworthy way to make inferences about the depth of equilibration of primary magmas. One must consider a wholesome approach that additionally includes trace element geochemistry and isotope composition of the erupted lavas.

Isotope and Rare Earth Element Geochemistry

In this section I briefly consider the expected nature of primary magmas based on peridotitic source rocks in different tectonic environments. Some background information on radiogenic isotopes may be found in the appendix. These days many different isotope systems are considered for petrogenetic inferences about sources and conditions of magma generation: $^{143}Nd/^{144}Nd$, $^{87}Sr/^{86}Sr$, $^{206}Pb/^{204}Pb$, $^{207}Pb/^{204}Pb$, $^{208}Pb/^{204}Pb$, $^{3}He/^{4}He$, $^{187}Os/^{188}Os$, $^{176}Hf/^{177}Hf$, etc. These are briefly considered below.

The basic premise of all geochemical synthesis is that the Earth's mantle started out as a "carbonaceous chondritic reservoir" in the sense that its trace element and isotopic composition is similar to that of carbonaceous chondrite-type meteorites. This mantle has irreversibly changed in composition since its humble beginnings, primarily through two processes—extraction of continental crust (and lithosphere) and recycling of altered oceanic lithosphere into the mantle via subduction. The mantle's geochemical nature remains a subject of much interest that is best suited for detailed discussion in a geochemistry course. I will simply highlight some of the points that are of significance in our petrological theme of the book. Geochemists point to three fundamental mantle reservoirs that serve as sources of basaltic primary magmas: (1) hot spot, plume, enriched, or so-called ocean island basalt (OIB) source (read Hawaiian source); (2) normal mid-ocean ridge (N-MORB) or depleted MORB mantle (DMM) source; and (3) arc basalt source. As we will see in Chap. 10, arc lavas are highly variable in chemistry, reflecting a highly variable source mantle composition and contamination problems.

Table 5.5 summarizes the characteristics of the mantle sources from which primary OIB and MORB magmas may be derived. N-MORB lavas from the global ocean ridge system are consistently more depleted (relative to chondrites) in incompatible trace elements (including REE) and radiogenic isotope compositions (such as Nd, Sr isotope ratios), as summarized in Fig. 5.16. It is generally thought that primary MORB magmas tap a shallow upper mantle source (asthenosphere) that has lost part of its incompatible element reserve to continental crust-building magmas over time. In contrast, Hawaii-type basalt is consistently enriched in LREE and significantly less depleted or enriched isotopic ratios. Therefore, it is commonly accepted that Hawaii or plume (OIB)-type primary magmas are derived from a deeper mantle

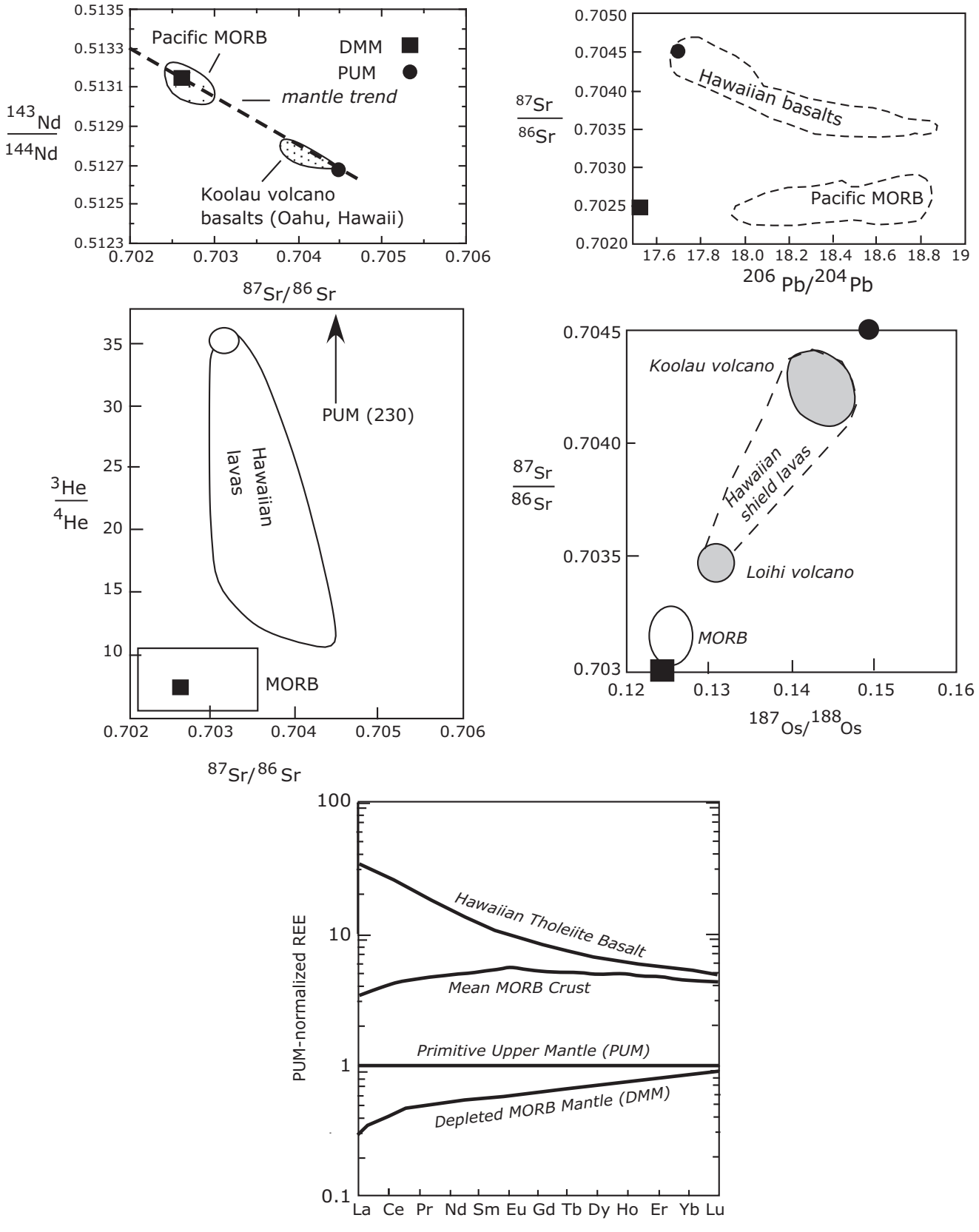

Fig. 5.16 Some isotopic ratios and REE patterns (normalized to PUM) are shown for "primitive upper mantle" (PUM), which is the major source component for ocean island basalts (e.g., Hawaii), and "depleted MORB mantle" (DMM). Sources for PUM are listed in GERM website, and the DMM are from Salters and Stracke (2004). In a simplistic way the two source components may be thought of lower and upper mantle

Table 5.5 Trace element and isotopic composition of mantle source for N-MORB and OIB. Chondritic abundances are also shown for comparison

Selected trace elements	DMM source	OIB source
REE (ppm)		
La	0.234	0.72
Ce	0.772	1.56
Pr	0.131	0.237
Nd	0.713	1.19
Sm	0.27	0.387
Eu	0.107	0.146
Gd	0.395	0.584
Tb	0.075	0.094
Dy	0.531	0.746
Ho	0.122	0.161
Er	0.371	0.473
Tm	0.06	0.063
Yb	0.401	0.489
Other important trace elements (ppm)		
Rb	0.088	0.31
Th	13.7	0.035
Nb	210	0.72
Pb	23.2	0.175
Ta	13.8	0.035
Sr	9.8	19.9
Y	4.07	4.37
Zr	7.94	10.81
Hf	0.199	0.31
Ni	1,960	
Isotope ratios		
143Nd/144Nd	0.51311	0.512634
87Sr/86Sr	0.7026	0.7045
176Hf/177Hf	0.2833	0.282843
208Pb/204Pb	37.92	17.7
187Os/188Os	0.123	0.15
3He/4He	7	Varies[a]

[a]The He isotope ratios [R] are given as relative to that of the atmosphere [R_A] and are therefore represented as R/R_A

source (lower mantle or transition zone) that rises as a plume and melts to produce such magmas. The geochemical data on lavas thus suggest that the lower and upper mantles do not mix very well over time and thus support a two-layer convection model in which the lower and upper mantles convect separately. This does not mean that there is no material and heat transfer across the two convecting layers: in fact the rise of plumes and recycling of subducted slabs into the lower mantle are two processes that breach the boundary layer (transition zone).

The simplistic interpretations about mantle source reservoirs and convection are by no means accepted by all, and in particular, there has been much discussion about how to interpret the $^3He/^4He$ isotope ratios. $^3He/^4He$ of depleted MORB mantle is generally thought to be about 8 (R/R_A, where R is the measured ratio and R_A is that of the atmosphere at present time). But OIBs show a great variety of $^3He/^4He$ values, and accordingly, scientists have argued for "high-He" plumes ($R/R_A > 15$), "moderate-He" plumes ($R/R_A = 9–15$), "low-He" plumes ($R/R_A < 7$), etc. Class and Goldstein (2005) suggest that He isotope ratio (relative to R_A) of the Earth's undifferentiated mantle reservoir was about 230. Mantle plumes come from reservoirs that have been isolated from the depleted (shallow) reservoir at different times in Earth history, and thus there are regions in the deeper mantle that may have different He isotope ratios.

The problem is that even within a single geographic location, $^3He/^4He$ of basalts often shows opposite behavior to that shown by all other radiogenic isotopes: for example, the basalts of Loihi volcano, the newest seamount off the island of Hawaii, shows the highest $^3He/^4He$ (maximum R/R_A of 36) but has the almost MORB-like (i.e., depleted) Sr, Nd, and Os isotope ratios (Fig. 5.16). In contrast, lavas from the Koolau volcano, an extinct shield volcano on Oahu, Hawaii, are characterized by the highest (i.e., least depleted mantle reservoir-like) Sr, Nd, and Os isotope ratios but the lowest $^3He/^4He$ ratio. Observations such as these have led to much speculation about the helium paradox and even the very existence of plumes has been questioned. Unfortunately, any extended discussion of this topic is beyond the scope of this book; however we will briefly review this issue again in a later chapter.

Summary

1. Magmas show large variation in terms of their mafic ($MgO + FeO + Fe_2O_3$) and alkali ($Na_2O + K_2O$) contents and can be fundamentally divided into ultramafic, mafic, intermediate, and felsic types. Examples of these magmas are as follows: ultramafic, komatiite; mafic, basaltic magmas; intermediate, andesitic magmas; and felsic, rhyolitic magmas.

Fig. 5.16 (Continued) reservoirs, respectively. Also shown are Hawaiian basalts and average oceanic crust (estimated by Niu and O'Hara (2003)) for comparison. The isotope data are based on Lassiter and Hauri (1998), Class and Goldstein (2005), Bizimis et al. (2005), and Salters and Stracke (2004)

2. In terms of its atomic structure, silicate magma is principally composed of polymerized SiO_4 chains and network modifier cations.
3. Density and viscosity of magmas are important properties that control their ascent. Both factors vary as a function of pressure and composition. Viscosity is also controlled by other factors, such as crystal content and volatile content.
4. Magma formation is controlled by the solidus of the source rock and the ambient temperature at any depth. At a given depth, a rock will melt at a lower temperature in presence of volatiles (commonly H_2O and CO_2) than in absence of volatiles. Magma may form due to decompression (at hot spots and mid-ocean ridges) or volatile-aided melting (at plate convergent boundaries).
5. Magma transportation occurs via porous flow (controlled by interfacial energies between magma and crystal grains in contact) and pipe flow. Porous flow is driven by compaction.
6. Composition of primary magma is controlled by phase relationships at high pressures. Abundance of a trace element in a primary magma is controlled by partitioning behavior of that element between the source rock and the melt and by the melting process.
7. Presence of mantle xenoliths, major and trace element composition, isotopic composition, and multiphase saturation of magma is used to identify primary or near-primary magmas. However, this exercise is far from being straightforward.
8. Most radiogenic isotope ratios reveal that there are at least two distinct mantle reservoirs—a shallow, depleted reservoir (asthenosphere), which supplies MOR basalts, and a much less depleted (almost bulk Earth-like) reservoir, which supplies the Hawaii-like OIBs. This reservoir is located in the lower mantle or perhaps at the core–mantle boundary.

Exercises

Problem 1

Calculate Mg# (=molar ratio MgO/[MgO + FeO]) of the melt composition (in oxide wt%) given in the table below. Assuming an equilibrium K_d value for olivine–liquid equilibrium of 0.3 (see text), calculate the composition of olivine that would be in equilibrium with this melt.

Problem 2

1. Calculate D_{Sm} and D_{Yb} for a peridotite and an eclogite from the data in the table given further below.
2. Calculate P_{Sm} and P_{Yb} for peridotite melting using the following melting reaction for peridotite at 3 GPa: 0.27Ol + 0.667Cpx + 0.44Gar = 0.33Opx.
3. Calculate P_{Sm} and P_{Yb} for eclogite melting using the following melting mode: $Cpx_{62.5}Gar_{37.5}$.

Oxide	Wt%
SiO_2	44.55
TiO_2	0.72
Al_2O_3	12.17
CaO	10.71
MgO	18.78
FeO*	10
Na_2O	2.23
K_2O	0.33
Total	99.49

*Refers to total iron oxide as FeO

4. Calculate the concentration of Sm and Yb in the melt with increasing values of F from 0 to 0.24 at steps of 0.02 during nonmodal melting of a garnet peridotite and eclogite, using D and P values you calculated in problems 2 and 3, and Sm and Yb concentrations in the starting peridotite and eclogite as follows:

	Wt. frac	Wt. frac.					
Mineral	Peridotite	Eclogite		K_d(Cpx/l)	K_d(gt/l)	K_d(ol/l)	K_d(opx/l)
Olivine	0.65						
Orthopyroxene	0.20						
Clinopyroxene	0.10	0.60	Sm	0.45	0.10	0.01	0.05
Garnet	0.05	0.40	Yb	0.54	6.17	0.05	0.34

Sm (ppm) in peridotite	0.27
Yb (ppm) in peridotite	0.4
Sm (ppm) in eclogite	0.153
Yb(ppm) in eclogite	0.17

5. Calculate Sm/Yb ratio for all the melts calculated in problem# 4 above and plot them against F. What can you surmise from the comparison between peridotite and eclogite-derived melts?

Igneous Rock Series: Basalt Magma Evolution

6

Abstract

In the previous chapter we learned that magmas can vary considerably in chemical composition and hence in their mineralogy. What are the causes for such diversity? Is it possible that all the major magma types are somehow genetically related? In this chapter we focus on the processes that modify composition of magmas.

Introduction

In the early 1900s, scientists began to explore the questions listed above. Norman L. Bowen, the "father of modern igneous petrology," and some of his notable colleagues at the Geophysical Laboratory of Washington, DC, developed a unique experimental approach to decipher magma's chemical evolution. This approach involved crystallization of magmas in laboratory furnaces and application of thermodynamic principles, such as the phase rule, to igneous rocks. These pioneering studies and many subsequent studies have shown that a number of processes besides crystallization can modify magma's composition: for example, partial melting, wall rock contamination, and magma mixing. Bowen himself believed that basalt magma is primary and rhyolitic and andesitic magmas are derived from it by fractional crystallization. Hawaiian lava lakes offer a natural laboratory to study how basalt magmas (of the type that Bowen believed to be the parent magma) can crystallize and evolve through time.

Detailed field and laboratory studies of igneous rocks from Hawaii and other places on earth since Bowen's time have made it clear that many different processes affect magma's chemistry and have yielded constraints on what is possible and what is not. Here we will examine examples of natural, deep-seated, fossilized magma chambers, called layered intrusions, to explore how natural systems may actually behave. Basalt magma takes a central role in this chapter because (1) basalts comprise the bulk of the earth's crust and (2) Bowen proposed that all magmas are derived through fractional crystallization of basalt magma.

Classification of Basaltic Magmas

Basalts and Basalts

Early practitioners of geology felt that basalt was not a very exciting rock type to study. To them basalt was a rather boringly uniform black rock that occurs everywhere. As time passed, however, analytical and experimental tools became more sophisticated and accessible to a much larger number of well-trained scientists and students. Vast amount of high-quality chemical data continues to accumulate at a fierce pace on basalts covering the entire globe—from the ocean bottom to the top of the tallest volcano. These new data have made it clear that basalts are anything but boringly uniform and that there are "basalts and basalts," i.e., there are distinct types of basaltic magmas that cannot be generated from each other by low-pressure (crustal) fractional crystallization or other processes. Even a single volcano can spew out lavas of different composition over time. On a global scale, chemically distinctive basaltic provinces appear to exist, whose differences are apparent especially in terms of isotopic ratios of lead, neodymium, and strontium. Such variations tell us a great deal about the internal

G. Sen, *Petrology*, DOI 10.1007/978-3-642-38800-2_6,

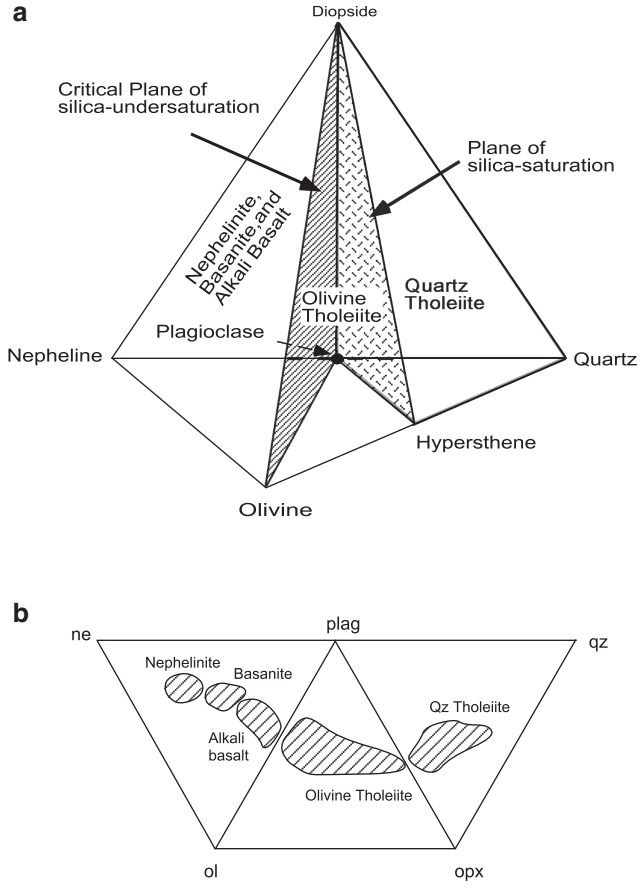

Fig. 6.1 (**a**) The "basalt tetrahedron" of Yoder and Tilley (1962). Composition volumes for three main basalt types—alkalic basalt, olivine tholeiite, and quartz tholeiite are shown. (**b**) "Exploded" view of the basalt tetrahedron showing where basaltic rocks plot

workings of the planet—from the small-scale processes within a magma conduit beneath a single volcano to global scale dynamic processes that drive plate tectonics and global mantle circulation.

In 1962, H.S. Yoder, Jr., and C.E. Tilley presented a systematic *normative* classification of basalts, known as the *basalt tetrahedron* (Fig. 6.1), based on experimental and laboratory studies of basaltic rocks. The four apices of the tetrahedron are clinopyroxene (Di; diopside in the simplified basalt system $CaO–MgO–Al_2O_3–Na_2O–SiO_2$), nepheline, olivine (Ol; forsterite in the simple system), and silica (quartz). Plagioclase (Pl; albite or ab in the simple system) plots in between nepheline (ne) and silica (because $NaAlSi_3O_8$ [ab] = $NaAlSiO_4$ [ne] + $2SiO_2$). Likewise, hypersthene (Hy) plots between olivine and quartz (since $2MgSiO_3 = Mg_2SiO_4 + SiO_2$). The reasons for selecting these minerals as apices of the tetrahedron are simply that (1) together these mineral components generally comprise 90 % of the normative composition of basalt and (2) low-pressure phase relationships of various basaltic magma types can be graphically depicted with reference to various "slices" through this tetrahedron (which will become more meaningful later on in this chapter).

The basalt tetrahedron makes a fundamental distinction between nepheline-normative magmas from those that lack nepheline. Based on the system nepheline–silica (Chap. 3), we know that at 0.0001 GPa albite acts as a divide between nepheline-normative magmas and hypersthene-normative magmas. In the basalt tetrahedron, the triangular plane *Ol–Pl–Di* is a low-pressure thermal divide that prevents magmas from one side to go across to the other by any low-pressure crystallization process. Yoder and Tilley called the plane Ol–Pl–Di *critical plane of silica undersaturation* because it separates silica-deficient nepheline-normative magmas from silica-saturated olivine tholeiites. [Recall that $NaAlSiO_4$ (*ne*) + $2SiO_2$ = $NaAlSi_3O_8$ (*ab*), i.e., nepheline has less silica than albite and is therefore silica-deficient relative to albite]. The volume *Di–Ne–Pl–Ol* (i.e., left portion of the tetrahedron in Fig. 6.1a) is called

the *alkali basalt volume*, named after the more dominant nepheline-normative magma type, i.e., alkali basalt. A second plane *Pl–Hy–Di* separates magmas that contain normative quartz (and hypersthene) from those that contain normative olivine (+hypersthene). Yoder and Tilley referred to the plane Pl–Hy–Di as *plane of silica saturation*. Note that this plane does not act as a thermal barrier and olivine tholeiite magmas can fractionate and evolve to quartz-normative tholeiites (see, e.g., the discussion of the system Di–Fo–SiO_2 in Chap. 4). Figure 6.1b shows the "blown out" version of the basalt tetrahedron in which common basaltic rocks are shown as shaded fields.

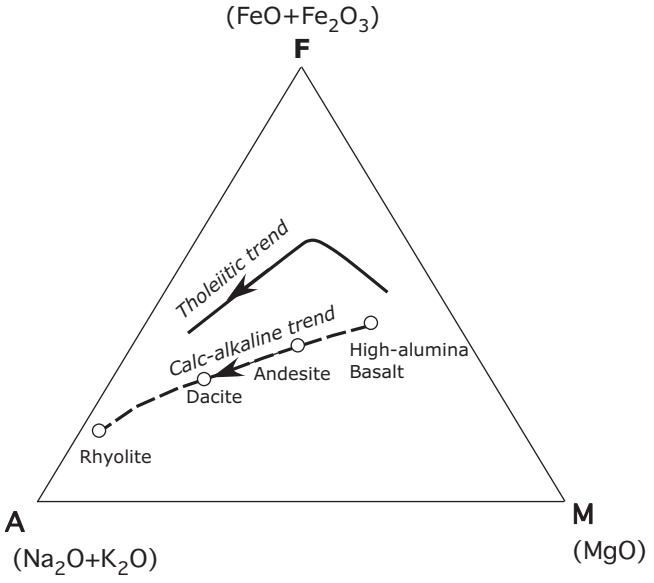

Fig. 6.2 AFM diagram showing tholeiitic and calc-alkaline series trends

The Concept of Igneous Rock Series

In the late 1800s, long before the concept of plate tectonics was established, petrologists had recognized the existence of *igneous rock series*—a term that was used to signify the genetic relationship between a group of chemically (and petrographically) different but regionally associated igneous rocks. In the 1890s Scottish geologists recognized the importance of *magma differentiation* processes, such as fractional crystallization, assimilation, and other processes, which force a *parent magma* to evolve chemically to a series of compositionally different *daughter magmas*. They recognized the distinction between *alkaline series* and *subalkaline* (i.e., tholeiitic) series rocks by the presence of normative feldspathoids (e.g., nepheline, leucite) in the first series or group. This key distinction served later as the basis for igneous rock classifications, as attested by Yoder and Tilley's classification. Aside from the alkaline and tholeiitic series, a major global igneous rock series, typically associated with subduction zones, is the *calc-alkaline series***.** The tholeiitic series, typically exemplified by the ocean floor basalts, continental flood basalts, and Hawaiian shield volcanoes, exhibits an initial trend of iron enrichment followed by silica and alkali enrichment (Fig. 6.2). Alkaline series lavas occur in all plate tectonic environments but are generally volumetrically insignificant relative to tholeiitic and calc-alkaline series.

Any discussion of magma evolution must begin with the nature of the starting magma that undergoes differentiation processes and evolves into other magma types. In this regard, petrologists often like to distinguish between *primary, primitive*, *and parental magmas*. Note that these terms are generally used to distinguish basaltic magmas that are in different stages of evolution—from a primary magma that is in equilibrium with upper mantle rocks to a residual magma that is evolved from a primary magma via crystallization, mixing, or other processes. It is likely that primary basaltic magmas rarely erupt and most lavas undergo modification during their rise through the crust, whether through crystallization, magma mixing, wall rock assimilation, or other differentiation processes.

Although the concept of primary magma is important in petrology, the concept of *parent magma* is often used in the literature to denote a magma that is generally the most Mg-rich lava among a suite of erupted lavas, with the inherent understanding that parent magma need not be a primary magma. The expression *primitive magma* is also used in referring to Mg-rich lava (or chill margins of intrusions) that may be compositionally close to putative primary magma. A parental magma is necessarily a primitive magma, but the two terms are not interchangeable since parental magma must refer to a genetically related magma series. It is common practice to use the term *liquid line of descent (LLD)* to refer to a series of liquids derived from single parent magma in oxide–oxide or other types of chemical plots; and we will see examples of such LLDs later in this chapter.

Mechanisms of Magma Differentiation

Fractional Crystallization

Crystal Settling and Crystal Flotation

As defined in Chap. 3, *fractional crystallization* is a process in which tiny fractions of crystals are physically removed from the magma as soon as they form. In general, natural processes probably never reach such extreme conditions and some amount of equilibrium is maintained for a brief period between crystals and magma. Bowen demonstrated that fractional crystallization of basalt magma might occur by settling of olivine crystals through magma because olivine is denser (generally higher than 3.3 g/cm^3) than basalt magma (around 2.7 g/cm^3). This process is called *crystal settling* (Fig. 6.3a). Crystal flotation is the opposite of crystal settling (Fig. 6.3b). The density of plagioclase (generally 2.68–2.73 g/cm^3) is very close to that of the basalt magma; and therefore, plagioclase crystals can float, sink, or remain neutrally buoyant in basalt magma depending upon whether it is lighter or heavier or has the same density as the basalt magma. Plagioclase flotation is particularly common in relatively Fe-rich and therefore denser, differentiated basalt magmas.

Many thick sills and lava flows show field and mineral chemical evidence of olivine settling to the bottom and plagioclase flotation toward the top. Figure 6.3c shows a hypothetical sill that has accumulated plagioclase crystals via flotation near its roof; and olivine and pyroxene crystals have settled to the bottom. Granophyric melts, rich in alkalis and silica, which are generally the last products of differentiation, also collect near the top. Figure 6.3d (left) schematically shows how settling of Mg, Fe-rich minerals (olivine, pyroxene) and flotation of felsic materials (plagioclase, granophyre) would be reflected in terms of modal variation of the mineral phases in the sill. Figure 6.3d (right) shows the chemical signature of such processes.

Palisades sill in New Jersey is particularly well known for a thick olivine-rich zone near its base although the rest of the intrusion is devoid of olivine (Fig. 6.4). Early studies argued for an origin of the olivine-rich zone by crystal settling in which crystals were already present in the magma and/or formed near the roof and settled to the floor of the sill. Later studies ruled out such an origin of the olivine-rich layer and suggested that there were two or more episodes of magma intrusion. The original sill magma was largely

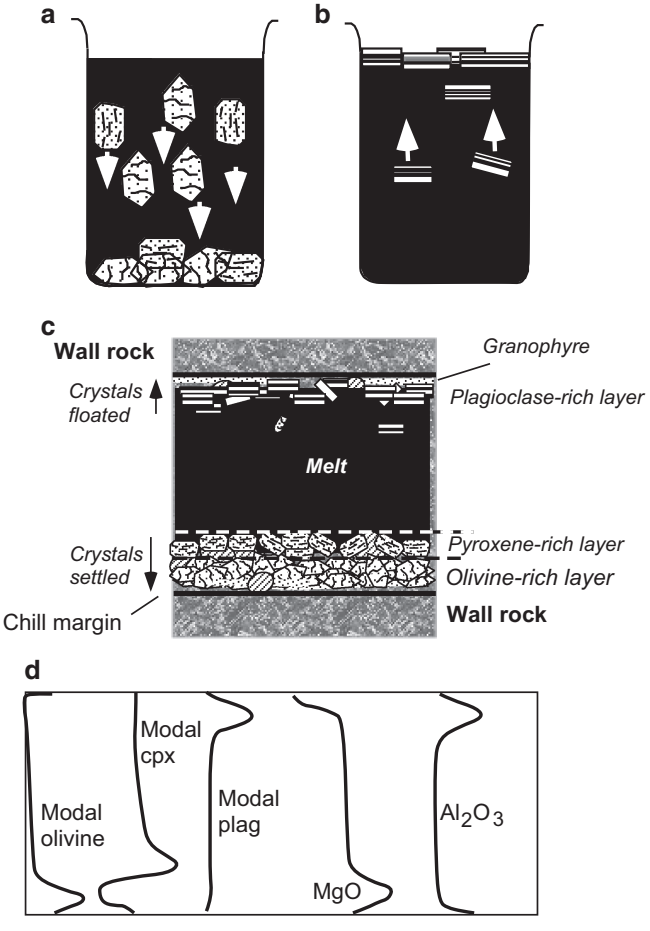

Fig. 6.3 (**a**) Schematic diagram showing settling of olivine (with curved fractures) and pyroxene (with cleavage) to the bottom of magma (*dark*). (**b**) Flotation of plagioclase crystals in magma. (**c**) A hypothetical case of crystallization in a large sill in which olivine and pyroxene layers at the *bottom* are formed due to early settling of olivine crystals followed by pyroxene settling. Plagioclase flotation forms a plagioclase-rich layer at the *top*. (**d**) Schematic variation in mode and chemical composition within the sill

olivine-free tholeiite. As this magma was cooling and solidifying, a new batch of olivine-rich magma intruded close to the base of the sill; and thus, the olivine-rich zone was fed by this second batch of magma. There is strong chemical evidence in support of this hypothesis, such as a complete mismatch between incompatible element ratio of the layer and the main sill.

Perhaps the most impressive example of crystal flotation is the *lunar highlands—the* brightly reflecting area on the moon that covers 83 % of its surface (discussed in Chap. 1). The lunar highlands are dominantly composed of a plagioclase-rich rock, called *anorthosite*. It is commonly believed that the lunar anorthosites formed by accumulation of floating

Fig. 6.4 A panoramic view of the Palisades sill, NJ, across the Hudson River from New York City

plagioclase crystals in a denser magma ocean that once covered the top 350 km of the moon about 4.4 billion years ago (Fig. 6.5). On earth, many large layered intrusions also show evidence of plagioclase flotation, as we will note in a later section of this chapter. Age determinations on the lunar anorthosite samples returned by the Apollo Lunar Missions (1963–1972) gave very old ages (4.4–4.3 billion years; Norman et al. 2003). In contrast, the oldest rocks on earth are usually no more than 3.2 billion years old. This difference is due to the fact that the earth's rocks have been recycled via plate tectonics, whereas the moon never had strong plate tectonics and thus very old rocks on the moon's surface have been preserved *as is*.

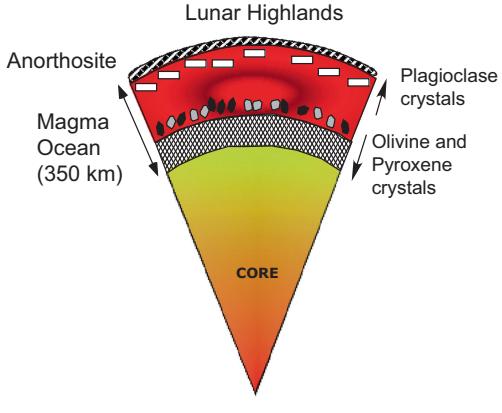

Fig. 6.5 Formation of the lunar highland anorthosite (a rock with more than 90 % plagioclase) on the moon is thought to be due to flotation of plagioclase crystals and settling of mafic minerals in a large magma ocean that covered the moon very early in its history

In Situ Crystallization and Convective Crystallization

Crystallization, without the aid of gravity, can lead to significant compositional changes in the residual magma. Growth of crystals in situ, and not by migration of crystals (such as settling or flotation), along the walls of the magma chamber is believed to be a very important way in which magmas fractionate (Fig. 6.6). Examination of several slowly cooling Hawaiian lava lakes (e.g., Kilauea Iki, Alae, Makaopuhi lava lakes) over the years by the United States Geological Survey (USGS) and studies of large plutonic intrusions and sills have given us some understanding of how in situ crystallization operates. The Hawaiian lava lakes are essentially ponded lava flows that quickly solidify to form a thin crust. Such ponding occurs when a lava flow finds a topographic depression in its way. The interior of a lava lake can remain molten for several years.

The USGS drilled through the crust and into the partially molten interior of a lava lake, clearly documenting how lava lakes solidify over time (e.g., Helz 2009). Heat is lost primarily from the top and/or

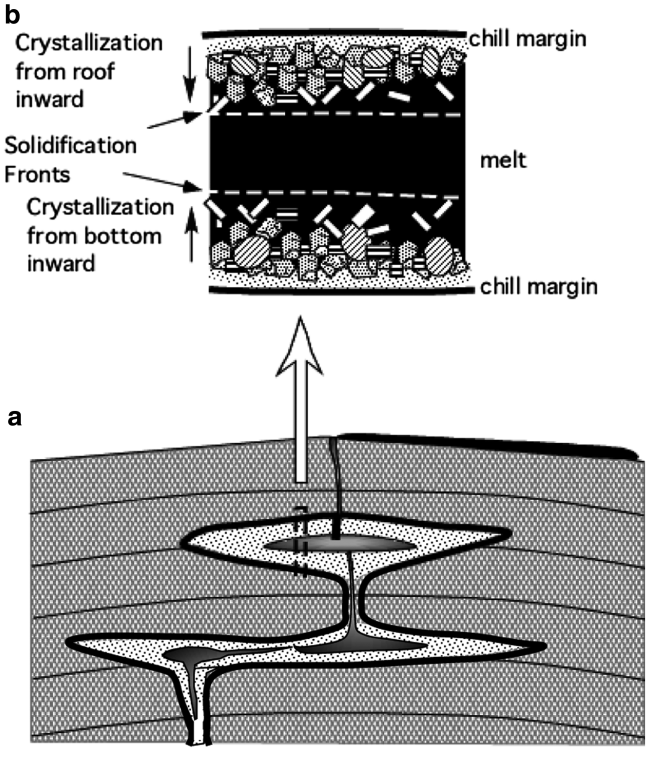

Fig. 6.6 (**a**) Sketch showing passage of basalt magma through a system of sills and dikes prior to eruption. (**b**) It is an expanded sketch of a sill to illustrate in situ crystallization of the sill magma from the roof and the base as a result if heat loss to the surrounding rocks (see text for detailed discussion)

along the sides to the surrounding wall rocks. In the case of a lava lake, rapid heat loss from the surface results in rapid solidification of the surface magma, giving rise to the development of a thin glassy chill zone at the top. Similar chill zones develop along the margins of a sill or dike or even a larger pluton, where the magma first comes into contact with the cooler wall rocks and is rapidly quenched. Chill zone rocks are useful in offering a glimpse into the nature of the parent magma—for example, whether it carried any phenocrysts prior to its emplacement or it was essentially a melt. However, one should be cautious about blindly equating chill margin composition to parent magma composition because wall rock fragments and other contaminants (e.g., alteration by groundwater, mixing with melts derived from partial melting of the wall rocks) can modify the original chill margin magma composition.

As time progresses, cooling of magma in a large intrusion results in the development of a *solidification front*, which is essentially a "solidus surface" that separates purely molten interior (assuming that the original input magma was crystal-free) from a boundary layer that consists of crystals and melt close to the margins of the intrusion (Fig. 6.6). In this boundary layer behind the front, the crystal–melt proportion increases toward the margins of the intrusion. Marsh (1989) subdivided the crystal ± melt bearing boundary layer into several sublayers consisting of (from margin to the interior) *all crystals* (close to the contact with wall rocks) → *rigid crust* (less than 50 % interstitial melt) → *mush or crystal–liquid mush* (50–75 %melt) → *suspension zone* (more than 75 % melt).

The sequence in which minerals crystallize in this boundary layer is determined by their phase relationships, nucleation, and crystal growth. With time the solidification front moves from the walls toward the central part of the intrusion. Ultimately, the entire intrusion solidifies in which layers with distinct mineralogy and grain size develop along the walls to the interior of the intrusion.

In a magma chamber that experiences periodic input of hot magma from the source region, melt mixing in the central part of the intrusion may force the solidification front to temporarily move back toward the intrusion's margins. Input of such extras magma from below may also lead to inflation of the magma chamber, magma chamber collapse, and/or volcanic eruption. The fact that basalt lava flows on earth generally contain less than 25 % phenocrysts suggests that such eruptions tap only the suspension zone of the magma chamber (Marsh 1989). The crystal–melt mush zone with more than 50 % crystals, located near the margins of an intrusion, is rarely tapped during lava eruption.

We can examine the phase relationships in the system anorthite–forsterite–silica at 1 GPa as a means to understand how mineral layers may form by in situ crystallization in a hypothetical magma chamber 30 km below the surface (Fig. 6.7a). Here we consider the example of crystallization of a forsterite-saturated liquid that fills the magma chamber. This magma will immediately form a fine-grained or glassy chill zone

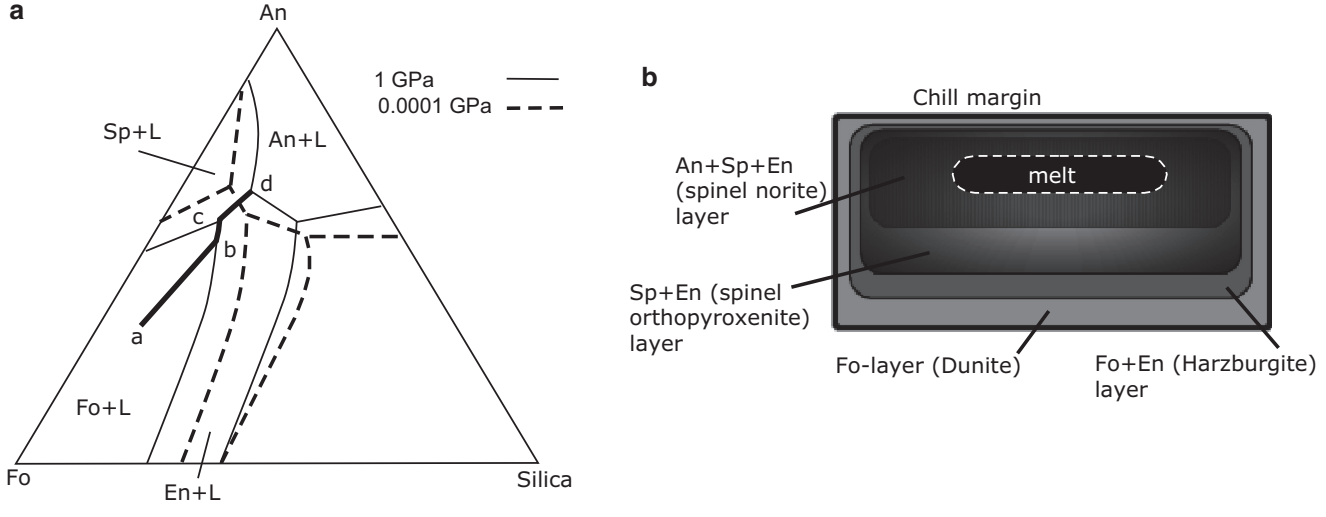

Fig. 6.7 (**a**) Crystallization of basalt magma is illustrated in the "system" forsterite–anorthite–silica. Liquidus phase boundaries at 1 atm and 1 GPa pressures are shown. We consider the crystallization of magma "*a*" in a large magma chamber at ~30 km (i.e., 1 GPa pressure) below the crust. As this magma cools under equilibrium conditions, the magma will evolve alone the path $a \rightarrow b \rightarrow c \rightarrow d$. (**b**) A schematic diagram showing how different mineral layers may form from such an evolving magma

due to rapid undercooling and nucleation along the margins of the intrusion. The interior of the magma will cool slowly from the chamber margins inward, forming crystals of different phases as the melt evolves along the path $a \rightarrow b \rightarrow c \rightarrow d$ (Fig. 6.7a). Crystallization of olivine (forsterite) from $a \rightarrow b$ will form a dunite layer first, followed by cotectic crystallization of olivine +orthopyroxene (Fo + En) assemblage along $b \rightarrow c$. c is a reaction point where forsterite dissolves and enstatite forms, allowing the residual liquid to move from c to d, during which spinel + enstatite will crystallize.

Thus, if crystallization proceeds from the margins to the interior of the intrusion and is not perturbed by crystal settling or input of new batches of magma from below, then the following sequence of layers would be expected to form: forsterite → forsterite + enstatite → enstatite + spinel and, finally, spinel + anorthite + enstatite (Fig. 6.7b). Studies of layered plutons show that such a simple pattern is usually complicated by nucleation and growth (even if we ignore all local physical disturbances, such as localized crystal–liquid dismemberment, crystal settling, or compaction). For example, Fig. 6.8a shows a hypothetical situation where the residual magma makes repeated excursions across the liquidus boundary between enstatite and forsterite fields while traveling from b to c. These excursions can result from different rates of nucleation and growth of crystals of enstatite and forsterite: When the liquid reaches the cotectic, it experiences a burst of enstatite nuclei formation and crystal growth while fewer forsterite nuclei form. This imbalance forces the surrounding melt, which is now depleted of enstatite component, to move into the forsterite liquidus field causing the crystallization of forsterite alone. Forsterite crystal formation would deplete the surrounding liquid in forsterite component and push it back across the cotectic into the enstatite liquidus field, and the process repeats itself many times—much like a ping-pong ball across the net! All of this may result in the development of finer scale, alternating layers of enstatite and spinel (Fig. 6.8b).

Crystallization is relatively rapid while chemical diffusion (i.e., movement of ions through melt and solid phases) is a very slow process. Thus, well behind the solidification front, the interstitial liquid that is trapped between growing crystals cannot maintain chemical equilibrium with the main body of the magma and develop highly differentiated compositions. Quartz and alkali feldspar-rich intergrowths often crystallize from such highly evolved trapped melts. Such intergrowths are referred to as *micropegmatite* or *microgranophyre (*if they are of microscopic dimensions), or *granophyre, melagranophyre, or pegmatite* (if they are large and visible in the field). Such felsic masses can also rise toward the roof, often aided by compaction, to form larger lenses beneath the roof of a large mafic intrusion.

So, what is more important—crystal settling or in situ crystallization in magma differentiation? This question is best answered by looking at large, plutonic, mafic, layered intrusions, which are essentially fossil magma chambers. Layers of contrasting textures, grain size, or modal proportions of different minerals are highly visible (and mappable) features of these intrusions (discussed later). The very occurrence of near-vertical or vertical layers of dense minerals near

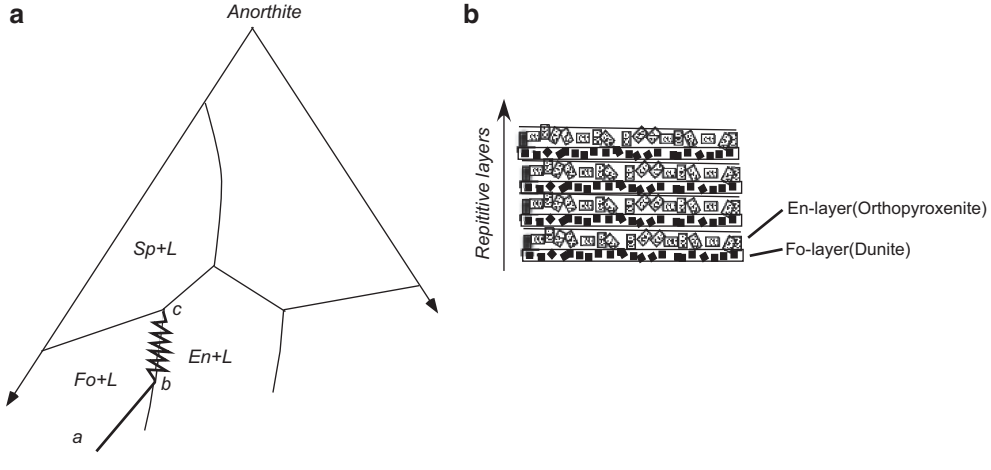

Fig. 6.8 (**a**) This diagram shows how competitive nucleation and growth rates of olivine versus enstatite force the evolving melt to "crisscross" the Fo–En liquidus boundary repeatedly. (**b**) This diagram shows how such back-and-forth movement of the evolving melts results in the repetitive development of alternate layers of dunite (>90 % olivine) and orthopyroxenite (>90 % orthopyroxene)

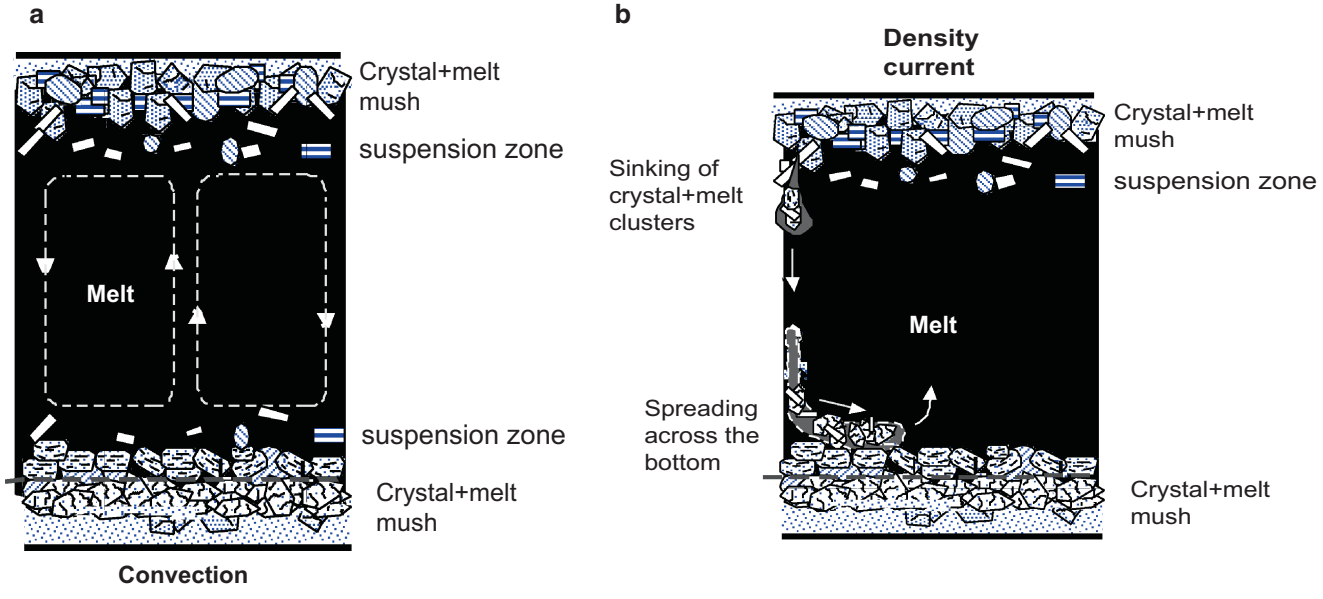

Fig. 6.9 A schematic diagram depicting how roof crystallization gives rise to crystal + melt mush. Chunks of such mush fall off owing to its greater density than the underlying melt. Crystals from such mushy material settle down on the floor, while compaction (due to accumulation of the crystals and pressure of the overlying melt) squeezes out the interstitial melt from the mush, and such melt moves upward and mixes with the overlying melt. Such movements are essentially localized convection currents

the sides of many layered intrusions indicates that gravity-induced crystal settling does not play a major role in magma differentiation in such chambers because gravity would have dragged down those crystals down toward the bottom of the chamber as soon as they form. Among other evidence that points to a greater role of in situ crystallization is the occurrence of dense layers of harzburgite (olivine + orthopyroxene) interlayered with much lighter anorthosite (>90 % plagioclase) layers in the lower parts of some layered intrusions (e.g., the Stillwater Intrusion of Montana; Wager and Brown 1968). Crystal settling cannot reasonably explain such repeated interlayering of low-density and higher-density layers. Therefore, it is generally believed today that some form of in situ crystallization must be more prevalent than crystal settling in these intrusions.

Crystal-rich melt layers well behind the solidification front, where melt% is 25–50 %, are generally too viscous (as discussed in Chap. 2) to mix easily with the rest of the magma chamber. Such a layer closer to the roof of the chamber may become gravitationally unstable and sink along the walls and eventually drop crystals off near the bottom of the magma chamber (Fig. 6.9). Once the crystals are released, the melt portion of the layer becomes lighter and it rises again only to mix with the melt in the interior. Evidence of such small-scale convection currents and crystal precipitation from convective layers has been seen as current bedding/layering in many large layered mafic intrusions. However, debate continues over whether or not chamber-wide convection occurs in large plutonic intrusions.

Assimilation ± Fractional Crystallization

Magma may react with wall rocks as it rises through the crust or upper mantle. Such reaction may result in:

1. Partial melting of the wall rock: For example, basalt magma with an inherent temperature of around 1,300 °C emplaced in the lower continental crust can partially melt the high-grade metamorphic wall rocks, whose solidus temperature is often around 1,000 °C at deeper levels. However, as pointed out in the Advanced Reading Box, heat and mass exchanges in this type of dissolution process significantly control how much assimilation of wall rocks would occur.
2. Selective dissolution of certain wall rock minerals accompanied by precipitation of other minerals: As pointed out by Kelemen and others (Grove et al. 1982; Kelemen 1990), this could be an important process in altering the composition of the lower continental crust and in controlling the composition of magmas at continental volcanic arcs. Pioneering work by Boyd (1989) showed that compared to the suboceanic lithosphere, the subcontinental lithosphere is richer in orthopyroxene.

Kelemen and others (1998) suggest that this is due to selective dissolution of forsterite and simultaneous precipitation of orthopyroxene from the moving magma due to the reaction:

$$\begin{aligned}&\text{Magma (Silica-rich, hydrous?)}+\\&\quad\text{Olivine (in the wall rock)} =\\&\quad\text{Orthopyroxene}\end{aligned}$$

Field studies of ophiolites, which are slices of the oceanic lithosphere (see Chap. 7), have shown the presence of dunite (a rock with >90 % olivine) dikes in a dominantly peridotitic volume. Kelemen and others have suggested that these dunites result from selective dissolution of pyroxene and precipitation of olivine from the passing magmas that are on the way to mid-ocean ridge. According to Kelemen, these dunite bodies serve as channels for magma transport and delivery to the crust at mid-ocean ridges.

The presence of veins of amphibole and or phlogopite in mantle xenoliths and other ultramafic bodies in the Alps has led to the concept of *mantle metasomatism*, in which hot H_2O-rich fluids circulating in the upper mantle replace pyroxenes with amphibole. Phlogopite results from direct precipitation from these fluids.

Another type of reaction involves the upper mantle where carbonate-rich fluids (melts) can dissolve orthopyroxene and precipitate clinopyroxene according to the following reaction (discussed in Chap. 4):

$$4MgSiO_3 + CaMg(CO_3)_2 \rightarrow 2Mg_2SiO_4 + CaMgSi_2O_6 + 2CO_2$$

This reaction explains the presence of wehrlite (a rock composed of olivine and clinopyroxene) xenoliths in alkalic basalts and wehrlite veins in peridotite massifs.

3. Xenolith digestion and contamination: Magma (particularly, volatile-rich magma) creates their own pathways by breaking up wall rocks in front of them and partially or wholly "digesting" them, which is a process known as "stoping." Large blocks and smaller xenoliths of wall rocks in different types of igneous intrusions and lava serve as evidence in favor of the operation of such a process.

Figure 6.10 shows the sketch of an embayed (reacted) quartz crystal surrounded by a rim of pyroxene crystals in basalt lava. Because quartz is not an expected to form phenocrysts in basalt magma, one can conclude that it is a xenocryst that had fallen into the ascending magma from some quartz-bearing country rock. The pyroxene crystals simply nucleated on the quartz as the magma was saturated with pyroxene.

Fig. 6.10 Sketch of a photomicrograph showing a quartz xenocryst surrounded by orthopyroxene needles in a tholeiite basalt lava (×160 magnified)

How important is assimilation (±fractional crystallization) process in igneous petrogenesis? Bowen thought it is not that important. However, more recent studies of isotope and trace element composition of large volcanic provinces and field studies of ophiolites and crustal intrusions suggest that this is an important process. How much wall rock assimilation can occur depends on a number of factors—ascent velocity and temperature of the magma, the enthalpy difference between magma and wall rock, solidus of the wall rock, physical nature of the contact between magma and wall rock (more fractured the contact more xenoliths are likely to fall off into the magma), etc. In a vigorously convecting magma chamber, magma may be able to break off xenoliths of wall rocks more efficiently, thereby exposing fresh surfaces on wall rocks and then assimilating them. On the other hand, a relatively stagnant body of magma may quickly quench to a thin selvage of "chill zone" at the contact between wall rock and magma, which may prevent further assimilation of wall rocks. Geochemical consequences of coupled assimilation–fractional crystallization process are discussed further in a later section.

Box 6.1: Advanced Reading: Enthalpy and Wall Rock Assimilation Capacity of Magma

The heat released by magma in assimilation of wall rocks may come from the latent heat of crystallization of its minerals or the magma may be "superheated" in the sense that its temperature may be above its liquidus temperature. Long ago, Bowen (1924) pointed out that it is unlikely for magma to carry significant superheat and too much superheat in a large mass of magma would be needed to melt a very small mass of rock. In melting a certain mass of wall rock ($=M_r$), a mass of magma ($=M_m$) must first heat

(continued)

Box 6.1 (continued)
up the wall rock to its melting point and then provide additional latent heat of fusion (H_f) to initiate melting at a constant temperature. If C_p^r and C_p^m are heat capacities of wall rock and magma, respectively, ΔT_1 = difference in ambient temperature and solidus temperature of the wall rock, ΔT_2 = cooling of the magma, then the heat lost by the magma and heat gained by the wall rock must balance:

$$M_m C_p^m \Delta T_2 = M_r \left(C_p^r \Delta T_1 + H_f \right)$$

$$M_m / M_r = \left(C_p^r \Delta T_1 + H_f \right) / C_p^m \Delta T_2 \qquad (6.1)$$

If the wall rock is close to its solidus temperature when the magma encounters it, then

$$M_m / M_r = H_f / C_p^m \Delta T_2 \qquad (6.2)$$

As an example, imagine a mass of magma assimilating 1 g of wall rock whose ambient temperature is 400 °C. Assuming that the wall rock's solidus temperature is 1,000 °C, the wall rock must be first heated by 600°, and then the magma must provide an additional latent heat of fusion (H_f), around 418 J, to melt 1 g of the rock. If we choose a reasonable value for C_p^r of 1.25 J/g degree for the wall rock, then to raise the temperature of 1 g of wall rock by 600 °C will require 600 × 1.25 or 750 J (based on $C_p = [dH/dT]_p$). Thus, a total of 1.17 kJ (752 J to heat up the wall rock and 418 J to melt it) would be needed to melt 1 g of wall rock. Assuming a reasonable value of 1.045 J/g/K for C_p^m, this heat may be provided by 7.73 g of magma assuming that it cools by 200° [Eq. (6.1)]. A larger mass of magma would be required if the temperature drop is less than 200° and vice versa.

Figure 6.11 shows that the M_m/M_r ratio is >1, i.e., magma mass will always be significantly greater than the mass assimilated. Also, the hotter wall rocks will require a lower M_m/M_r ratio than cooler wall rocks. Basalt magma at 1,200 °C may crystallize entirely if its temperature drops by as much as 300°. Given the fact that upper crustal rocks are much cooler than deep crustal rocks, assimilation of lower crustal rocks would require less energy from the assimilant basalt magma

(continued)

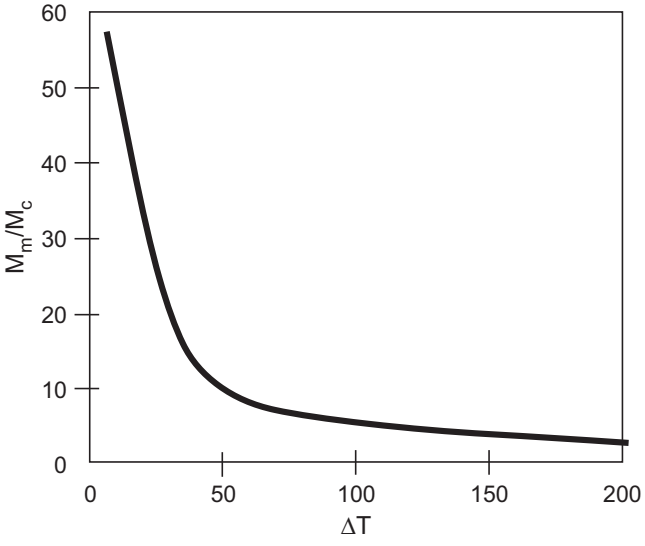

Fig. 6.11 Relationship between assimilation, crystallization, and ΔT

Box 6.1 (continued)
than upper crustal rocks. Also, there is a greater probability of a magma crystallizing entirely when it assimilates upper crustal rocks. In the event that the magma is not carrying superheat, the magma mass M_m would be the same as mass crystallized (or M_c) in the above equations. Thus, it is possible to calculate the extent of crystallization of magma during assimilation.

Flowage Differentiation

In some cases crystals may be concentrated in the center of a moving magma body as the magma flows through a dike or a sill, a process known as flowage differentiation (Fig. 6.12). This happens when the flow is laminar and magma develops a velocity gradient across the intrusion. The dispersive force that pushes phenocrysts apart increases from the center to the walls of the intrusion and thus concentrates the crystals in the center of the intrusion—much the same way dead leaves and trash gather toward the center of a flowing river.

Filter Pressing

This is a process of compaction that involves squeezing out of melt from a crystal–melt mush. Loading of crystals in a crystal–liquid mush (and hence, gravity),

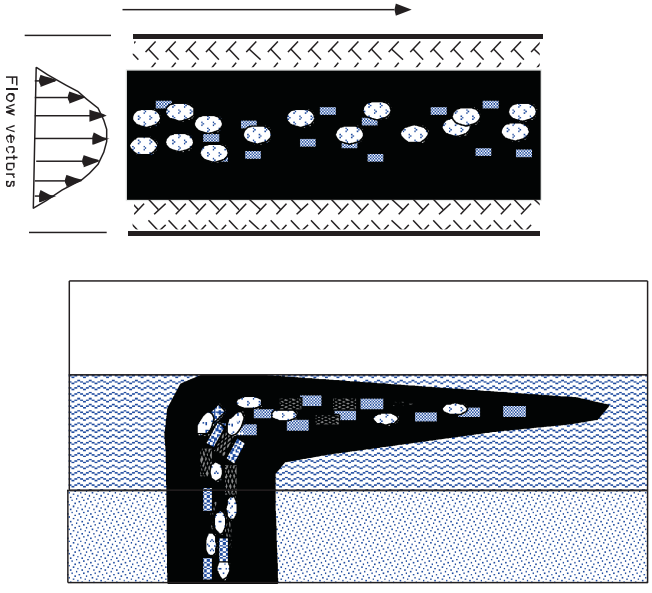

Fig. 6.12 Flowage differentiation in a dike. Magma flow through the dike focuses the suspended crystals to be concentrated in the center of the dike

a stress regime, or flow through constrictions may cause melts to be separated this way. This process is likely to be very important in separating a small melt fraction from its source rock during partial melting. It is also likely to be an important process in the separation of the residual liquid in the interstitial spaces between primocryst or cumulus crystals in large layered intrusions.

Magma Mixing and Mingling

I consider magma mixing and magma mingling as two fairly distinct processes: in mixing two magma batches are sufficiently well mixed to yield a new mixed magma in a conduit or magma chamber. However, if one magma batch does not really mix with the other and the two magmas more-or-less preserve their physical identities, then such a process is magma mingling. All magmatic systems are usually dynamic in the sense that multiple batches of magma may come from the source areas and travel through the same "plumbing system." In the end-member case, the incoming magma may thoroughly mix with whatever residual melt may already be present in the magma chamber or conduit system. At the other end, the viscosities of the residual magma and the incoming magma may be so different that they cannot mix thoroughly and instead mingle, maintaining their identities.

In Chap. 2 we considered specific cases of magma mixing in which two magmas may mix to produce undercooled magma, superheated magma, and partial to total crystallization. Evidence of magma mixing includes (1) the presence of disequilibrium phenocryst(s), (2) the presence of normal and reverse zoned crystals in the same rock, (3) unusual reaction rims on crystals (e.g., pigeonite rim around an embayed augite crystal even though there is no reaction relation between pigeonite and augite: Durand and Sen 2004; Fig. 6.13), (4) compositionally distinct melt inclusions in phenocrysts, and (5) linear trends projected on ternary diagrams and, in some cases, on binary oxide–oxide or oxide–trace element plots.

In recent years the advent of such sophisticated instruments as laser ablation inductively coupled plasma mass spectrometer (LA-ICPMS) and ion microprobe (also called secondary ion mass spectrometer, or SIMS) has allowed the scientist to study trace element and $^{87}Sr/^{86}Sr$ isotope zoning in individual mineral grains. Figure 6.14 shows an example of $^{87}Sr/^{86}Sr$ isotope zoning in two large plagioclase phenocrysts from the Deccan Traps. Distinct $^{87}Sr/^{86}Sr$ isotope zoning in these crystals is evidence that the core of the crystals initially grew from a melt whose $^{87}Sr/^{86}Sr$ isotope composition was less than 0.7102. The variation in the rim composition suggests that the rim grew from mixed magmas whose composition progressively changed toward 0.7106–0.7108. The narrow outermost zone grew from the final melt that crystallized the groundmass (i.e., the lava that carried it during eruption). An alternative interpretation

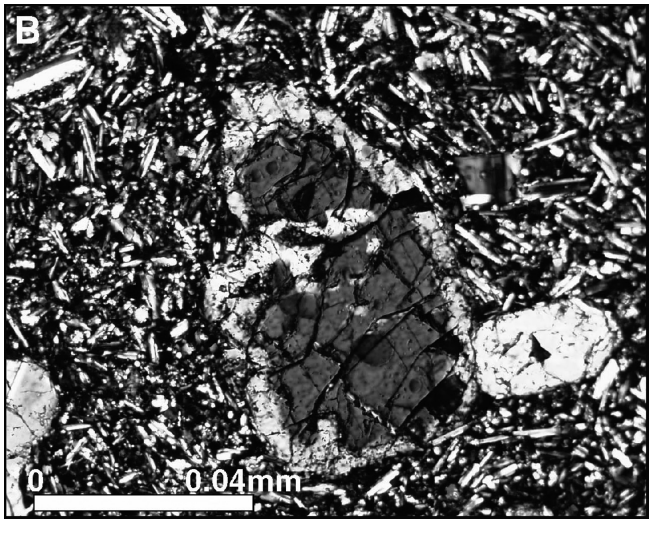

Fig. 6.13 Photomicrograph of pigeonite rim around augite in a Grande Ronde basalt (from Durand and Sen 2004)

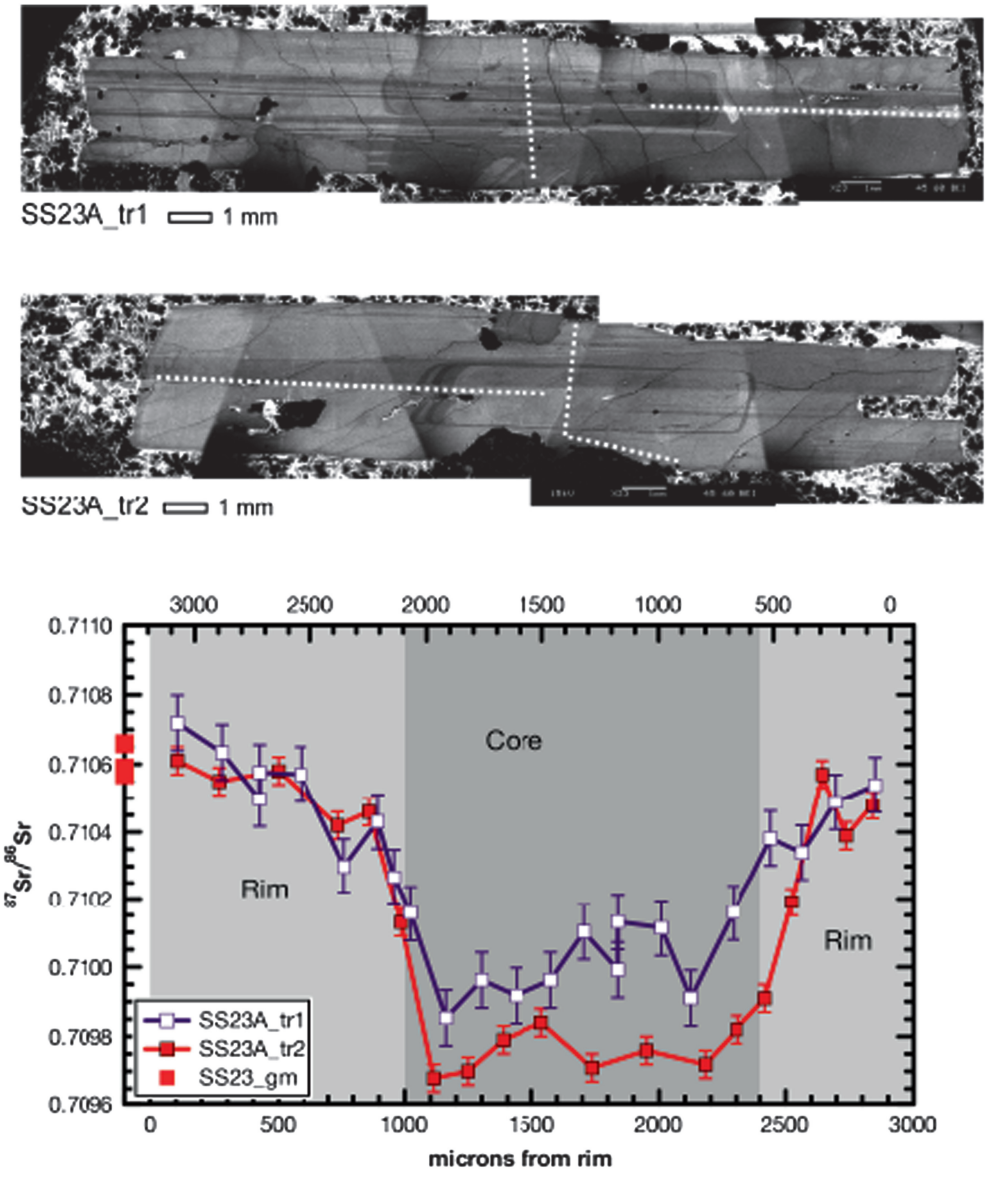

Fig. 6.14 $^{87}Sr/^{86}Sr$ zoning in a plagioclase crystal from a Deccan Trap lava (courtesy of Melroy Borges). The *top two panels* show cathodoluminescence images of two "giant plagioclase" crystals. The *white dotted lines* show the tracks along which $^{87}Sr/^{86}Sr$ ratio was determined. The *bottom panel shows* $^{87}Sr/^{86}Sr$ zoning in the two crystals. Groundmass plagioclase crystal composition is shown as *red squares* on the *Y*-axis on the *left*

(which cannot be discussed here at length) is that the crystals had a step zoning, with the initial $^{87}Sr/^{86}Sr$ compositions (steps) of core and rim being ~0.7097 and ~0.7097, respectively, and the zoning profiles in the rim region developed at magmatic temperatures due to diffusion resetting. As an aside, I would like to point out that several authors have used diffusive re-equilibration of such isotopes/trace elements across a zone boundary to calculate residence time and growth history of a crystal in the chamber. A simple equation to calculate time of residence of a crystal in magma can be obtained from $x = \sqrt{Dt}$, where x = thickness of the zone boundary (i.e., compositional gradient between adjacent zones), D = diffusion constant, and t is time. It is beyond the scope of this book to take this up any further but the interested reader will find voluminous literature on the subject on the Internet with little effort.

Liquid Immiscibility

Silicate-liquid immiscibility can occur in magmas, as has been demonstrated by laboratory experiments and petrographic observations of natural lavas, such as the globular form of the immiscible droplets in volcanic rocks. The most well known is the atmospheric pressure phase diagram for the system fayalite–leucite–silica, in which a prominent two-silicate-liquid immiscibility field occurs between Fe-rich silicate liquid and an alkali-rich silicate liquid (gray shaded in Fig. 6.15). In the 1970s there was considerable excitement in the petrology community when strong evidence of such immiscibility was found in the returned moon rocks. In a later chapter we will learn about immiscibility between silicate and carbonate magma.

In basaltic magmas liquid immiscibility between silicate magma and volumetrically minor sulfide-rich liquid occurs over a wide temperature range. Texturally, such sulfides occur as globules of pyrite, pyrrhotite, pentlandite, and chalcopyrite. This type of immiscible sulfide liquid separation has given rise to the formation of some layered ore deposits of PGE (platinum group of elements)-rich sulfides in the Bushveld intrusion (discussed later).

During the late stages of differentiation of tholeiitic basalt magma in slowly cooled layered basaltic intrusions, immiscibility commonly occurs in the late-stage differentiates, causing the separation of light alkali-rich silicate liquid and dense iron-rich silicate residual liquids. The flotation and accumulation of the lighter, immiscible felsic liquids toward the roof of the intrusion results in the formation of a distinctive Fe-granophyre zone near the roof of the intrusion. It is interesting that such granophyre is commonly associated with a Fe-rich olivine, which would be expected, based on Fig. 6.15.

Liquid immiscibility is commonly believed to have given rise to the *ocelli* structure, which are globular structures composed of feldspar and minor amounts of mafic minerals and are common in lamprophyre dikes worldwide (the student can find some nice pictures of ocelli on the web). These structures are thought to develop from liquid immiscibility, although Carstens (1982), based on his study of some lamprophyre dikes in Norway, concluded that these structures are formed by spherulitic growth from undercooled volatile-rich magmas. It is beyond the scope of this book to undertake an evaluation of origin of ocelli in detail.

There is no doubt that liquid immiscibility occurs in magmas. In a volumetric sense, it plays an insignificant role in basalt magma differentiation. Geochemical and petrographic evidence indicates that crystal sorting and magma mixing must be the two dominant processes in magma differentiation.

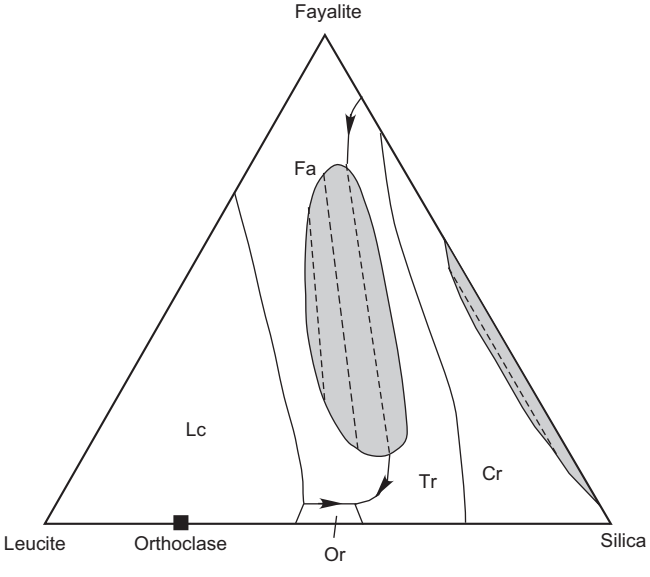

Fig. 6.15 The system fayalite–leucite–silica showing two liquid immiscibility fields (*gray*). The one in the middle is more relevant to late-stage immiscibility in basaltic magmas. The *dashed lines* are tie-lines that connect the conjugate liquids. *Lc* leucite, *Or* orthoclase, *Tr* tridymite, *Cr* cristobalite, *Fa* fayalite

Volatiles and Magma Differentiation

In Chaps. 3 and 4, we learned that the solubility of H_2O in magma increases with pressure, and therefore, deep-seated magma containing 4 % H_2O in solution will not be able to hold such an amount of H_2O in solution as it rises to shallow level (Fig. 6.16a). It will have to exsolve the excess H_2O, which will come out as bubbles, i.e., the magma will start to boil (Fig. 6.16b). This is known as "first boiling." In a magma chamber or conduit, crystallization can lead to vapor supersaturation in the melt, as a result of which a vapor phase is exsolved. This phenomenon is known as "second boiling."

Magma differentiation can occur in a conduit or magma chamber via transfer of vapor bubbles from deeper to shallow levels within a magma chamber, where the vapor bubbles may concentrate in the highly differentiated liquids near the roof of a magma chamber. These fluids may concentrate rare metals. Volatile transfer is of particular significance in the formation of rich ore-bearing pegmatites and hydrothermal veins

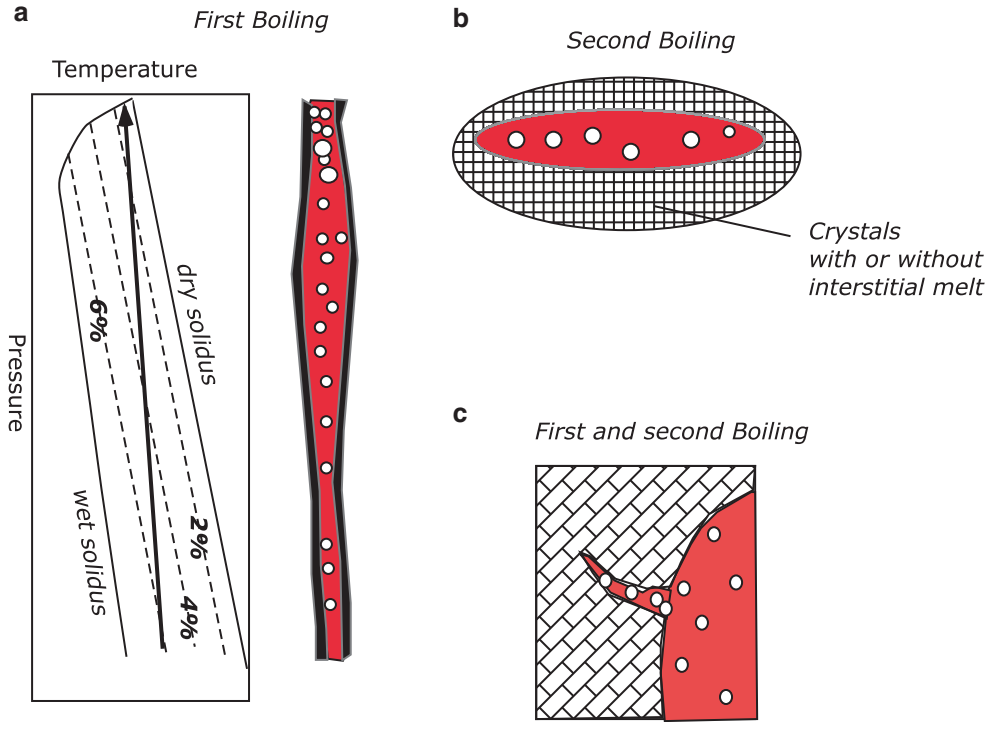

Fig. 6.16 Exsolution of vapor (i.e., "boiling") from magma. (**a**) A pressure–temperature diagram showing H_2O-free (i.e., "dry") and H_2O-saturated ("wet") solidi for a hypothetical granitoid magma. Each *dashed line* represents constant H_2O content (isopleth) in magma over P–T space. The *arrow* represents the path taken by a rising magma with a 6 % H_2O dissolved in it. This magma must exsolve H_2O ("first boiling"; the diagram on the right in Fig. 6.15a) as it rises to shallower depths because the solubility of H_2O decreases as pressure decreases. (**b**) As the magma crosses the solidus, it must entirely solidify while exsolving H_2O (in reality, it is a H_2O-rich fluid), and this is referred to as "second boiling." (**c**) This schematic diagram shows how magma may initially undergo first boiling and later undergo second boiling at a shallow depth

around large granitoid batholiths. The rocks that form from such H_2O fluids have distinctively large (often up to several meters) crystals and are called *pegmatites*. Hydrothermal veins are so-called because in the field they solidify from a hot, aqueous fluid and they form vein-like intrusions into the surrounding wall rocks. When a granitoid batholith solidifies, the very last fluid becomes a very H_2O-rich fluid that carries dissolved silicate materials and ions of tin, beryllium, copper, gold, and other metals and behaves like a viscous gel. These fluids then intrude the surrounding wall rocks and deposit their metals in large concentrations so that they become economically important ore deposits.

Chemical Signature of Differentiation: Variation Diagrams

A fundamental goal of the igneous petrologist is to determine which differentiation processes are responsible for generating a chemically diverse group of lavas from the same volcano or compositional diversity of a suite of rocks from a geographic area. This bit of detective work inevitably requires the petrologist to plot the compositions of such lavas or rocks on graphs of various kinds—from simple oxide versus oxide plots to ternary diagrams. Such diagrams are known as *variation diagrams*, examples of which will be seen later. A statistical best-fit line or curve through the data points on any such plot, often referred to as a *liquid line of descent,* offer clues to how the magma had chemically evolved over time.

We can now call upon the "system" diopside–anorthite–forsterite (Fig. 6.17a) to illustrate how the chemical composition of magma evolves as a result of crystallization of various minerals from it. Our starting primary magma is *a,* which is generated at the isobaric invariant point at 2 GPa. This magma rises rapidly to a shallow chamber where it just sits and undergoes fractional crystallization. Phase boundaries at 1 atm are most suitable to model such

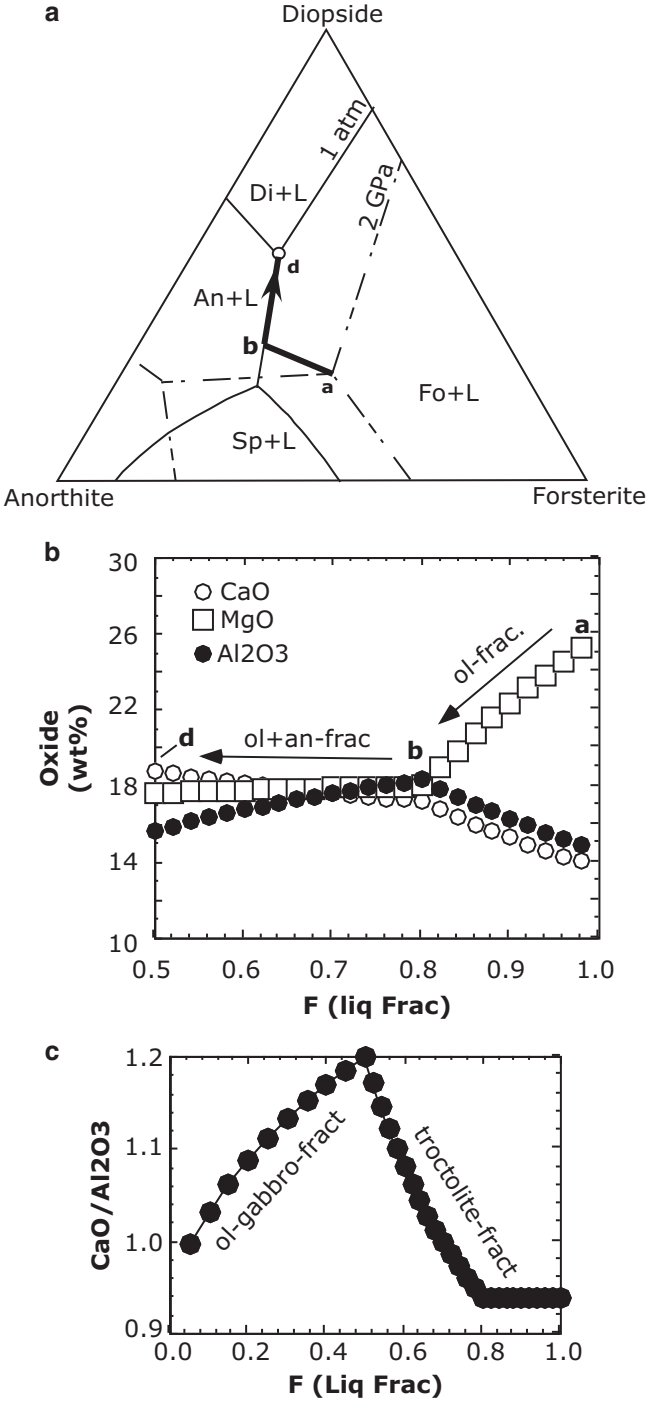

Fig. 6.17 (**a**) The concept of igneous rock series or liquid line of descent is illustrated in the "system" diopside–anorthite–forsterite. The liquidus boundaries are shown at two different pressures—2 GPa and 1 atm (from Presnall et al. 1978). Magma "*a*" is generated at an invariant point at 2 GPa. It then rapidly rises to a shallow magma chamber (~1 atm) where it fractionally crystallizes and evolves along the path $a \rightarrow b \rightarrow d$. If this magma chamber periodically erupts lavas whose composition falls on this path, then such lava compositions will describe a liquid line of descent or an igneous rock series. (**b**) The liquid path in the above phase diagram is converted to oxide wt% as a function of liquid fraction. (**c**) This diagram shows how CaO/Al_2O_3 ratio in an evolving magma can be a significant indicator of what minerals have fractionated from it at different stages

fractional crystallization. Figure 6.17a shows the path that would be followed by the parent magma: from *a* to *b* it will crystallize forsterite alone and olivine + anorthite (note: a rock composed only of olivine and plagioclase is called *troctolite*) from *b* to *d*. If di–an–fo were a true isobaric system at 1 atm, then the residual liquid would remain at *d* and crystallize as a ternary eutectic gabbroic assemblage. In reality, the residual liquid moves off the diagram as a gabbroic assemblage fractionates along a 4-phase cotectic (fo + an + di + l) in the four-component system CMAS. Figure 6.17b shows how MgO, Al_2O_3, and CaO will evolve in the residual magma. Olivine fractionation will result in a sharp decrease in MgO but increases in CaO and Al_2O_3 contents of the liquid, because forsterite needs MgO but rejects CaO and Al_2O_3. Because anorthite is composed of CaO and Al_2O_3 (and SiO_2), plagioclase's appearance marks a sharp change ("kink") in both CaO and Al_2O_3. Figure 6.17c shows that CaO/Al_2O_3 ratio is a sensitive indicator of troctolite (a rock composed of plagioclase and olivine) versus gabbro (clinopyroxene + plagioclase) fractionation from magma: The former causes an increase in CaO/Al_2O_3, whereas the opposite behavior is shown by gabbro-fractionation. Now imagine a series of lavas from a geographic area, whose chemical compositions fall on the trend between *a* and *d*. All those lavas would belong to the same liquid line of descent.

Alfred Harker was an early petrologist who plotted the abundances (weight%) of various oxides against SiO_2 and demonstrated that the rock compositions can be related to each other in some systematic manner. Such a diagram has since been called a *Harker diagram*, which is only one possible type of diagram among many others; and the general term *variation diagram* encompasses all such possibilities of X–Y type binary compositional plots. One must remember that plots like these only suggest what is mathematically possible but they are not a definitive way to identify a differentiation process. Ideally, one should use multiple criteria, such as isotope ratios and trace element geochemistry, and thermodynamic modeling.

Most current petrologists prefer the use of the Mg/(Mg + Fe) molar ratio (referred to as Mg#), Mg/Fe ratio or weight% MgO on the *X*-axis, instead of SiO_2 (Fig. 6.18a). This is because olivine is usually the first mineral to crystallize and its separation from the magma depletes the magma in MgO, Mg/Fe, and Mg#. Thus, one could use any of these three parameters as a marker or index of differentiation. Furthermore, pyroxenes have a different Mg# than olivine, and plagioclase has insignificant amount of MgO. Thus,

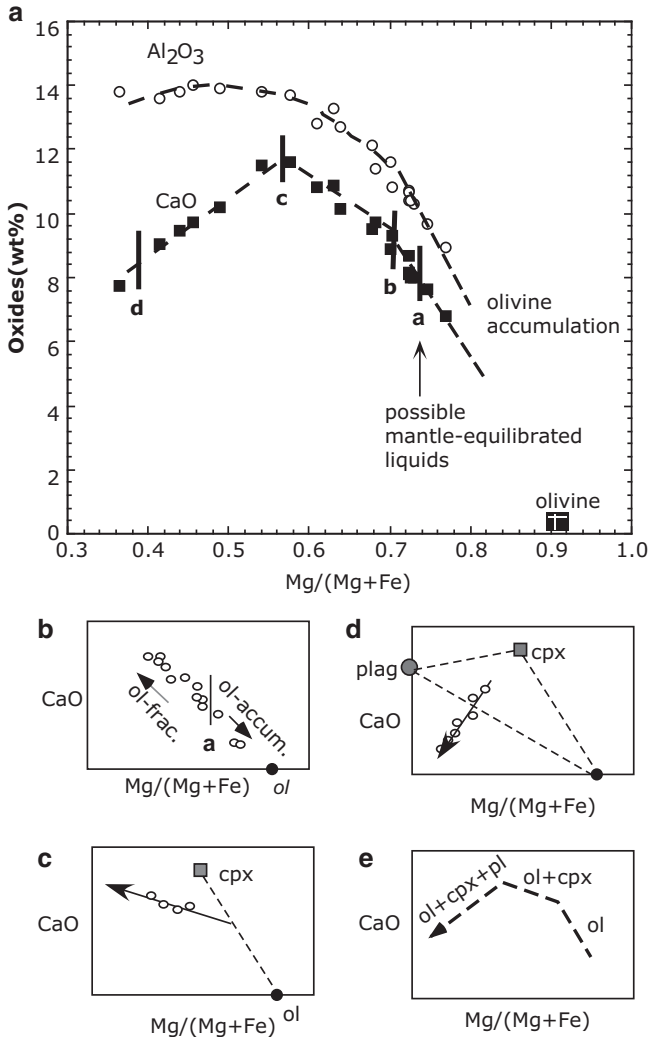

Fig. 6.18 (**a**–**d**) Selected compositions of lavas from Kilauea shield volcano (Hawaii) are plotted to illustrate olivine accumulation and fractionation of olivine, plagioclase, and augite at different stages of evolution of Kilauea volcano. (**b**–**d**) illustrate how different mineral fractionations have shaped the Kilauea liquid line of descent. (**e**) is a summary of the entire trend (explained in detail in the text)

during crystallization of magma, appearance of these phases at different stages of cooling produces a noticeable change in the residual liquid composition in terms of MgO, Mg/Fe, or Mg#. Thus, plotting any of these three in the *X*-axis is very useful.

Figure 6.18 illustrates the utility of Mg# quite well in the case of some lavas from the Kilauea volcano (Hawaii). For example, the CaO variation trend in Fig. 6.18a is divided into several segments *a–b–c–d*. Lava plotting at "*a*" has the appropriate composition that would be in equilibrium with a typical upper mantle peridotite with Fo_{90} olivine; and olivine with Fo_{90} composition also occurs as phenocrysts. Therefore lavas with composition around "*a*" could be potentially primary magmas, especially if they are glassy or aphyric (discussed in a later chapter). In the same vein, lavas with higher Mg/(Mg + Fe) ratio than "*a*" could either have equilibrated with more magnesian upper mantle rock or have accumulated extras olivine, i.e., they may have picked up fragments from earlier crystallized dunite layers in the conduit. Figure 6.18b schematically shows that such olivine accumulation would trend toward olivine composition. In fact, the extremely magnesian (picritic) Kilauea lavas have accumulations of Fo_{91} olivine and therefore point toward such a composition (Fig. 6.18a). On the other hand, olivine fractionation from lavas plotting at "*a*" in Fig. 6.18a will result in lowering of Mg/(Mg + Fe) and an increase of CaO in the melts because olivine is high in Mg/(Mg + Fe) and CaO is incompatible in olivine (Fig. 6.18b). The liquid line of descent shows sharp bends or kinks at "*b*" and "*c*" in Fig. 6.18a. The trend from "*b*" to "*c*" can be explained by the fractionation of an assemblage that has about 40 % olivine and 60 % clinopyroxene (cpx; Fig. 6.18c). Finally, the trend from "*c*" to "*d*" in Fig. 6.18a can be explained by the fractionation of an olivine–gabbro assemblage (i.e., plagioclase + clinopyroxene + olivine) as schematically shown in Fig. 6.18d. Figure 6.18e shows the kinks in Kilauea's liquid line of descent and summarizes how such a trend is explained by fractionation of different minerals in Kilauea's magma conduit system.

The Di–An–Fo and Kilauea examples serve to show that some general rules can be set about interpreting trends on variation diagrams. We saw that linear trends or linear segments of a trend can result from fractionation of one, two, or even a three mineral assemblage. Figure 6.19a, b shows a hypothetical example of variation diagrams in which %A and %B are plotted, where A and B could be two oxides or two elements. Figure 6.19a shows a single-phase fractionation case where a suite of lavas, namely, 1–2 to 1–6, has evolved from a parent magma by variable extents of fractionation of a mineral "*M*." The lever rule can be used to calculate how much fractionation of *M* is required to derive each of these lavas from the parent magma 1; for example, %fractionation of *M* to derive magma 1–6 from parent magma 1 may be given as 100 × [distance *M* to parent magma 1/distance *M* to 1–6]. Also, *M* fractionation may occur at a single pressure (i.e., isobaric) or over a range of pressures where the cotectic proportion does not change with pressure. One should

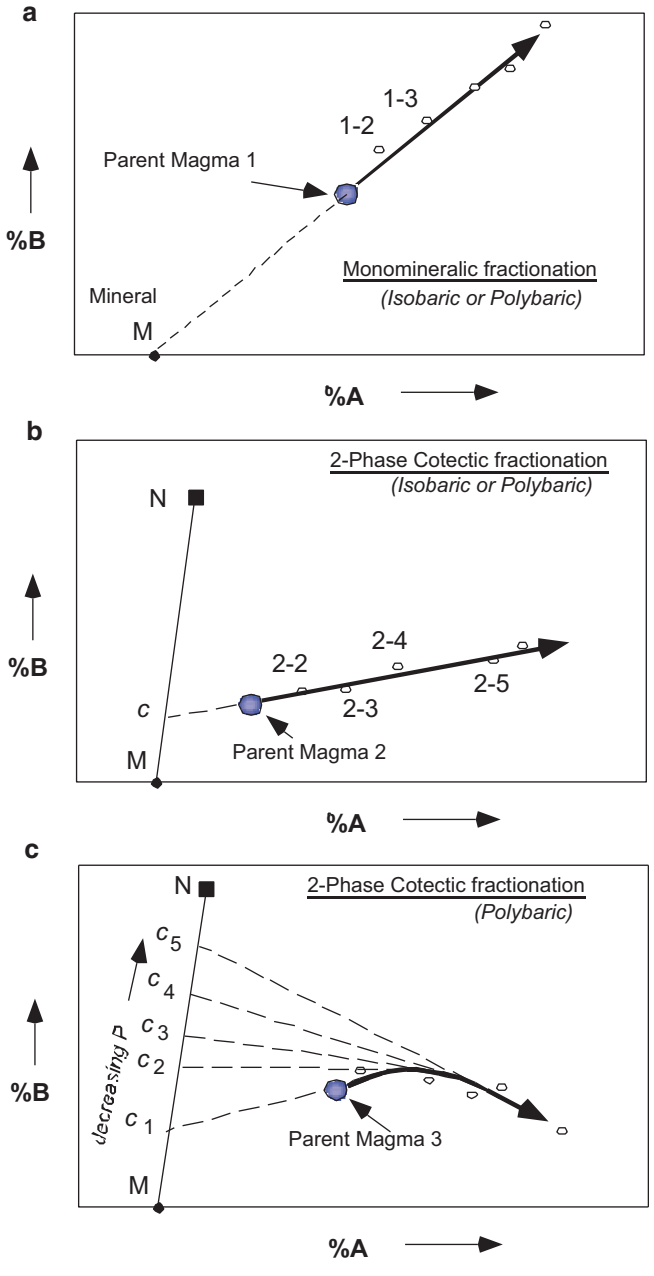

Fig. 6.19 Identification of the roles of single versus multiple fractionating minerals in liquid lines of descent as shown in oxide–oxide plots. 1–1, 1–2, etc. are rock compositions

exercise caution in making this type of interpretation because simple mixing between 1–2 and 1–6 melts could also lead to a linear trend like this. Thus, one diagram alone is unlikely to be sufficient to deduce which of the processes (or combination of processes) may have generated such a suite of rocks. Other pieces of evidence, such as petrographic evidence of magma mixing and other chemical criteria, may be used to decipher what actually happened.

In contrast to linear trends, curvilinear trends can be generated, for example, when the cotectic proportion changes in the case of polybaric fractionation of a two-mineral assemblage (Fig. 6.19c). Curvilinear trends also result when a mineral solid solution mineral fractionates, as we have seen in the system Di–Ab–An in Chap. 4.

The bottom line is that one should exercise caution in interpreting liquid lines of descent. There are several freely available software available on the web that can be used to model binary oxide or element plots. Among these, I have tried MELTS (Ghiorso and Sack 1995) and COMAGMAT (Ariskin et al. 1993) and have been generally satisfied with them even though neither one is completely free of problems.

Trace Element Behavior in Crystallization Processes

The behavior of trace elements in melting processes was discussed in Chap. 9. Here we consider how trace elements behave in magma chambers. The two simplest and extreme behaviors are of course equilibrium crystallization (EC) and fractional crystallization (FC). The equations for EC and FC are given as Eqs. (6.3) and (6.4), respectively:

$$C_i^{\mathrm{L}} = \frac{C_i^{\mathrm{o,L}}}{F + D(1-F)} \tag{6.3}$$

$$C_i^{\mathrm{L}} = C_i^{\mathrm{o,L}} \cdot F^{(D-1)} \tag{6.4}$$

where C_i^{L} and $C_i^{\mathrm{o,L}}$ are the concentration of an element 'i' in daughter magma and parent magma, respectively. F is fraction of liquid remaining (varies from 0 to 1), and D is bulk distribution coefficient (defined before).

As an example, consider how the abundances of two elements, namely, Sr and Ni, with different degrees of compatibility, will change in EC versus FC for the same example we chose in Fig. 6.17a (Di–Fo–An): that is, FC and EC of the 2 GPa melt at 1 atm. We assume that the parent magma has 300 ppm Sr and 300 ppm Ni. Using K_{d}'s for forsterite, diopside, and anorthite given in Fig. 6.20 caption, we calculate the residual liquid composition as a function of F using Eqs. (6.3) and (6.4) (Fig. 6.20). Note that appearance of a new phase forces adjustment of D and $C_i^{\mathrm{o,L}}$ (set to be the melt composition corresponding to the immediately previous melt fraction step). Figure 6.20 shows that Ni shows rapid decrease as melt% decreases while Sr dances around somewhat.

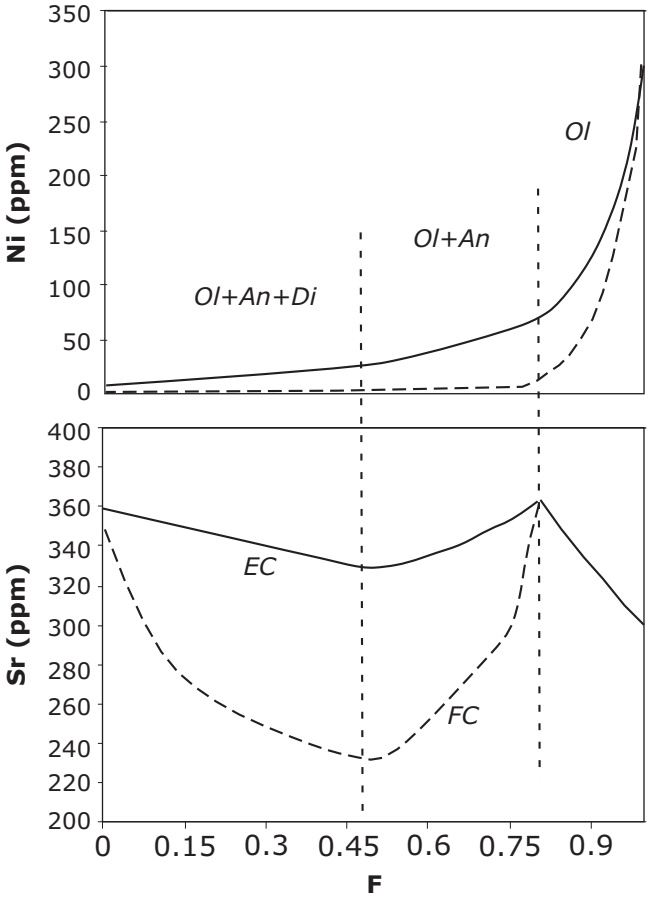

Fig. 6.20 Sr and Ni variation in evolving magma. F = residual melt fraction. EC = equilibrium crystallization. FC = fractional crystallization. Partition coefficients used for Sr: An/L = 2.5, Di/L = 0.1, Ol/L = 0.005. For Ni: Ol/L = 15, An/L = 0.001, Di/L = 0.005

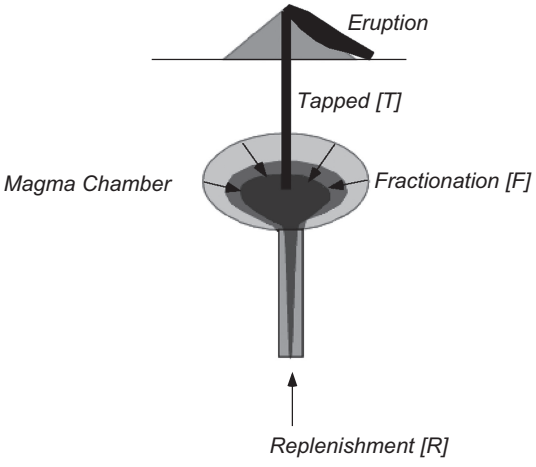

Fig. 6.21 Sketch showing how the RTF model works

Open System Crystallization and Steady-State Concentration

The above examples are somewhat idealistic, and in nature it is more likely that the magma chamber is an open system, where a differentiating magma chamber receives periodic influxes of primitive magma and also discharges magma through eruptions in order to maintain constant volume [the so-called RTF model (R = replenished, T = tapped, F = fractionating), Fig. 6.21]. O'Hara (1977) showed how effective this process can be in controlling the composition of the residual melt in a magma chamber. As a magma chamber goes through cycles of crystallization (crystal fraction = X), eruption (lava fraction = T), and replenishment of the same parent magma (concentration is given as C_i^{o}), concentration of individual elements tends to reach a steady-state concentration (i.e., nearly constant concentration) after several of these RTF cycles. The number of cycles required by individual elements to achieve steady-state concentration will be different as they are strongly dependent upon the element's relative compatibility as expressed through D, the bulk distribution coefficient.

Let us consider a RTF magma chamber that is undergoing equilibrium crystallization; and in each cycle a volume of erupted plus crystallized volume is replaced by a refilled volume of new magma. If C_i^{s} = concentration of an element i in the solid fraction, C_i^{ssl} = concentration of i in the steady-state liquid, and $D = C_i^{\mathrm{s}}/C_i^{\mathrm{ssl}}$, then:

$$C_i^{\mathrm{o}}(X+T) = T\,C_i^{\mathrm{ssl}} + XC_i^{\mathrm{s}}$$

Rearranging and substituting D in the above equation we get

$$C_i^{\mathrm{ssl}} = \frac{C_i^{\mathrm{o}}(X+T)}{T+XD}$$

A more complex derivation for the fractional crystallization in the chamber will lead to the following equation (O'Hara 1977):

$$C_i^{\mathrm{ssl}} = C_i^{\mathrm{o}}\left[\frac{(X+T)(1-X)^{D-1}}{1-(1-X-T)(1-X)^{D-1}}\right] \qquad (6.5)$$

As White (2013) has discussed, compatible versus incompatible elements behave very differently in a RTF magma chamber: compatible elements reach steady state after a few cycles, whereas incompatible elements may reach steady state after many cycles.

Trace Element and Isotope Behavior in Assimilation–Fractional Crystallization

Isotope and trace element geochemistry has contributed much toward our understanding of

a

Subgroup	Formation
WAI	Desur Panhala Mahabaleshwar Ambenali Poladpur
LONAVALA	Bushe Khandala
KALSUBAI	Bhimashankar Thankurvadi Neral Igapuri Jawhar

b

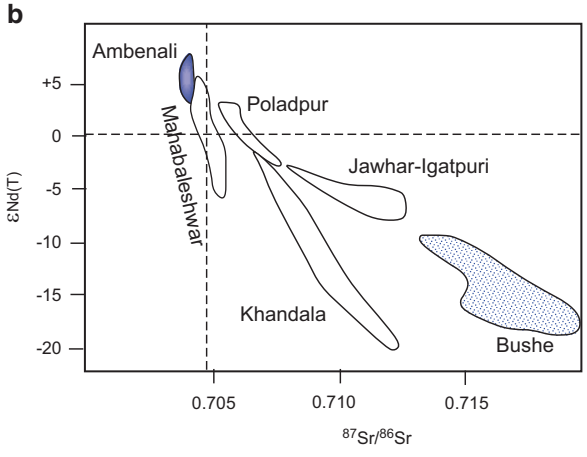

Fig. 6.22 (**a**) Stratigraphy of Deccan Trap lava flows from the Western Ghats. (**b**) Nd–Sr isotope composition of Deccan Trap basalts from the Western Ghats area

assimilation–fractional crystallization processes. Geochemists point to large volumes of basalt lava in continental provinces that have isotopic and trace element composition that is best explained by significant "contamination" of the mantle-derived magmas by continental crust. Figure 6.22 shows an example from the Deccan Trap flood basalt province from the Western Ghats near Mumbai, India, where the lavas are grouped into various formations based on their geochemistry. Among these, the Bushe Formation lavas have unusually high $^{87}Sr/^{86}Sr$ isotope ratios that may reflect significant contamination by old continental crust (Mahoney et al. 1982).

While discussing crustal contamination of basalt magma processes, geochemists often distinguish two end-member processes: (a) bulk assimilation (i.e., complete partial melting of wall rocks, which is going to be highly limited by heat and mass involved, as we saw earlier) and (b) assimilation accompanied by fractional crystallization, or AFC, which is favorable from the mass and heat considerations. In AFC, basalt magma loses heat in partially melting wall rocks; and this heat loss is balanced by the gain of heat released from simultaneous fractional crystallization of the magma. DePaolo's (1981) AFC equation illustrates how the concentration of a trace element will change during AFC process:

$$\frac{C_i^{\mathrm{L}}}{C_{\mathrm{o}}^{\mathrm{L}}} = F^{-z} + \left(\frac{R}{R-1}\right)\frac{C_{\mathrm{a}}}{zC_{\mathrm{o}}^{\mathrm{L}}}\left(1-F^{-z}\right) \qquad (6.6)$$

where C_i^{L} and $C_{\mathrm{o}}^{\mathrm{L}}$ represent concentrations of a trace element in the magma after and before assimilation, respectively, and C_{a} is its concentration in the assimilant (i.e., wall rock). R is the ratio of mass assimilated to mass crystallized. $z = (R + D - 1)/(R - 1)$; and F is the mass fraction of the original melt left. A similar equation is given for radiogenic isotope ratios (e.g., Sr, Nd, Pb isotope ratios), as given by White (2013):

$$\epsilon^{\mathrm{L}} = \frac{\left(\frac{R}{R-1}\right)\frac{C_{\mathrm{a}}}{z}\left(1-F^{-z}\right)\epsilon^{\mathrm{a}} + C_{\mathrm{o}}^{\mathrm{L}}F^{-z}\epsilon^{\mathrm{o}}}{\left(\frac{R}{R-1}\right)\frac{C_{\mathrm{o}}^{\mathrm{L}}}{z}\left(1-F^{-z}\right)\epsilon^{\mathrm{a}} + C_{\mathrm{o}}^{\mathrm{L}}F^{-z}} \qquad (6.7)$$

where ε^{L} and ε^{o} and are isotope ratio (such as $^{87}Sr/^{86}Sr$, $^{143}Nd/^{144}Nd$) of the magma after and before assimilation and ε^{a} is the isotope ratio of the assimilant.

Figure 6.23 shows how La ($D = 0.001$) and $^{87}Sr/^{86}Sr$ isotope ratio of basalt magma (5 ppm La, 200 ppm Sr, and $^{87}Sr/^{86}Sr$ of 0.703) will change as it is contaminated by old continental granulitic crust (36 ppm La; 700 ppm Sr; $^{87}Sr/^{86}Sr = 0.7140$). In the calculations for Fig. 6.23, I have assumed a constant D of 0.001 and a constant mass ratio of assimilant to crystal precipitate of 0.5. In this example, the melt gets strongly enriched in La and $^{87}Sr/^{86}Sr$ when melt % is 0–30 %; with further crystallization the $^{87}Sr/^{86}Sr$ ratio does not change as greatly as La abundance. One can of course use different values for R, D, and initial melt and contaminant compositions and obtain somewhat different plots that would be appropriate for their specific cases.

Although AFC is likely a common process, it is beyond the scope of this book to carry out a detailed discussion of this process. The student is well advised to read proper textbooks of geochemistry for that purpose.

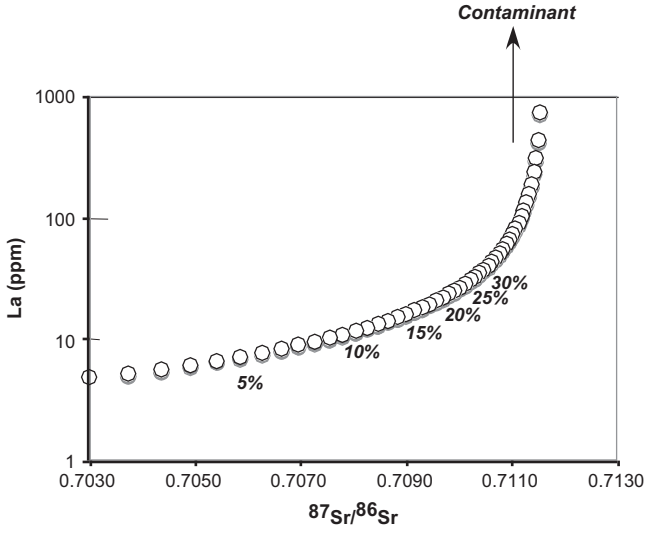

Fig. 6.23 Assimilation–fractional crystallization of magma

Basalt Magma Evolution: An Early Controversy Between Bowen Versus Fenner

The subject of petrology was largely treated in a descriptive manner in the 1800s. In the early 1900s N.L. Bowen revolutionized this field with his theoretical and experimental phase equilibrium studies. Driven by his desire to explore the origin of magma series and genetic relationships between different magma types of a magma series, Bowen and coworkers set out to perform numerous phase equilibrium experiments on simplified mineral systems that are relevant to the crystallization of such magmas. Combining these with theoretical considerations, field associations, and petrography of igneous rocks, Bowen proposed a unifying hypothesis, called *Bowen's reaction principle*, in which he proposed that tholeiite (subalkaline) basalt magmas are primary magmas, i.e., they are directly generated from the mantle, and that intermediate (i.e., andesitic) and felsic (i.e., rhyolitic) magmas are derived by fractional crystallization of various ferromagnesian (i.e., Fe, Mg containing) minerals and plagioclase from parent basalt magma (Fig. 6.24).

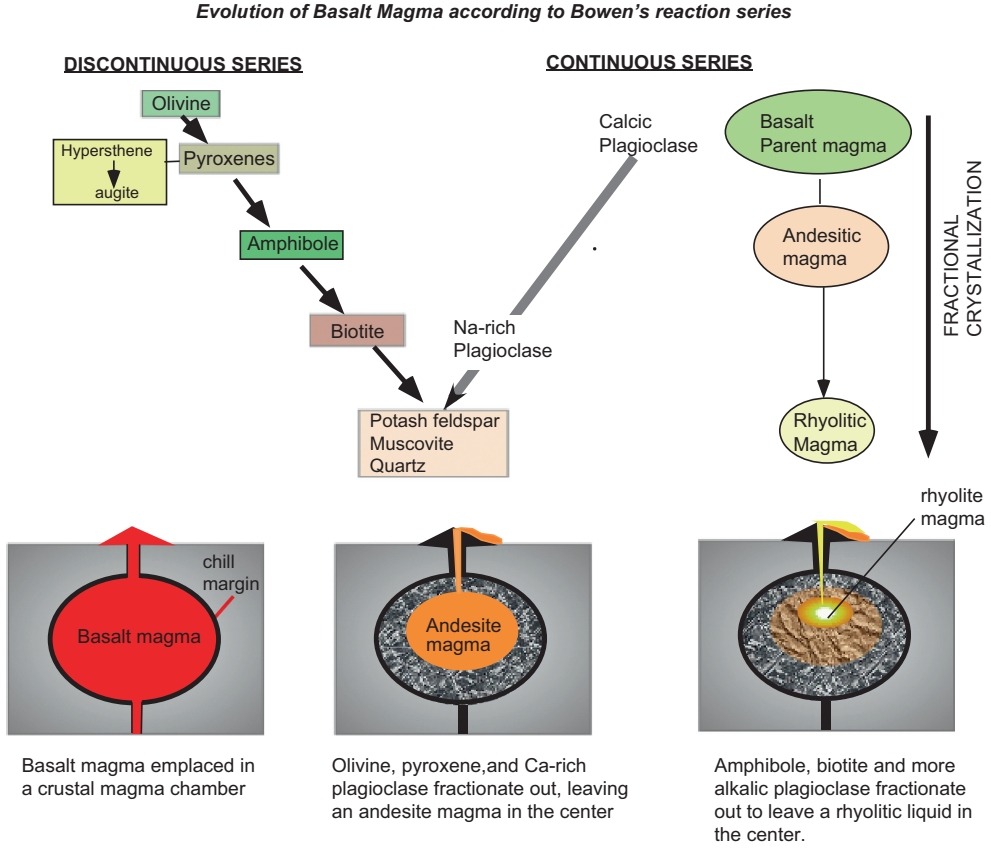

Fig. 6.24 Bowen's reaction series illustrated here. The *top panel* shows the discontinuous and continuous reaction series as postulated by N.L. Bowen. The *bottom panels* show how fractional crystallization of basalt magma (specifically, tholeiite basalt magma) may give rise to andesite magma and then rhyolite magma

Bowen recognized two *reaction series*: One of these simply represents continuous crystallization of plagioclase with progressive albite enrichment of the plagioclase with crystallization of the magma. Bowen called this the *continuous series*. He called his other series, formed by ferromagnesian minerals, the *discontinuous series,* because in his model individual mineral species crystallizes for a while and then a new one takes over (Fig. 6.24). In Bowen's scheme, plagioclase and olivine appear first during the cooling of basalt magma. After a while olivine crystals are replaced in the cooling sequence by pyroxene. Bowen proposed that an orthopyroxene forms first and a clinopyroxene (augite) later. Eventually amphibole, followed by biotite, replaces clinopyroxene as the crystallizing mineral, and so on. Note that olivine and pyroxenes individually exhibit solid solutions, and therefore their compositions also vary continuously during crystallization from Mg-rich toward Fe-rich compositions. The final residual liquid, which has evolved via fractional subtraction of the discontinuous series minerals and plagioclase, is essentially a granite magma that crystallizes alkali feldspar, muscovite, and quartz together.

Bowen was persuasive in his arguments, and his "reaction principle" convinced a large number of petrologists of his era. However, based mostly on field relations, some scientists found it hard to accept Bowen's proposal to account for the origin of *all* granites. Among many problems, two most notable are (1) the absence of appropriate volumes of associated mafic and intermediate rocks with granite batholiths and (2) field relations in some areas that showed transition from large batholiths to veins of partial melts (*migmatites*) of high-grade metamorphosed sedimentary rocks in deeply eroded orogenic belts. Subsequent studies have shown that most granites are not produced by fractional crystallization of basalt magma.

Returning to Bowen's time, however, it was C.N. Fenner, who was Bowen's colleague at the Geophysical Laboratory, who was not persuaded by the elegance of Bowen's proposal because he noted that the interstitial materials in coarsely crystallized diabase are mostly Fe-rich granophyre, characterized by their eutectoid or granophyric (wormy) intergrowth between alkali feldspar and quartz and abundance of Fe–Ti oxide minerals (magnetite and ilmenite). Therefore, Fenner argued that fractional crystallization of (tholeiitic) basalt magma does not lead to the formation of granite, which is poor in iron; instead, a Fe-rich residual felsic magma is generated. Fenner's contention was later substantiated by the classic study by L.R. Wager and W.A. Deer of the Skaergaard intrusion (Greenland), which is a mafic plutonic intrusion considered to be the best-known example of closed system differentiation of tholeiitic basalt magma. Several other major layered intrusions have been found since then, among which particularly notable is the Bushveld intrusion (South Africa). As we have also noted earlier, in the very late stages of differentiation, a basalt magma splits into two liquids—a felsic melt ("granite") and a Fe-rich granophyre.

Layered Intrusions: Basalt Magma Differentiation

Layered intrusions are enormous, mafic, intrusions that were emplaced within the shallow crust (1–15 km) and are characterized by centimeter- to kilometer-scale layered structure. Some of them have been alleged to be the feeders of continental flood basalts. Table 6.1 summarizes the general features of layered intrusions. In terms of size, they can exceed the dimensions of some small countries put together! The largest of them is the Bushveld intrusions of South Africa, which occupies an area of about 64,000 km^2. Most of them are of Precambrian age, although the Skaergaard intrusion of Greenland is 55 Ma old (i.e., tertiary). Simple heat loss calculations suggest that the smaller intrusions like the Skaergaard may have taken 130,000 years to solidify, whereas the really large ones, like the Bushveld intrusion, may have taken 1 million year to cool down to the surrounding wall rock (ambient) temperatures. In general, shapes of most layered intrusions are that of a lopolith; however, the Skaergaard intrusion is shaped like a funnel.

These intrusions generally have a *chill margin* or fine-grained zone along the contact with wall rocks. Such a zone forms by rapid quenching of the input magma against much cooler wall rock. As a general rule, petrologists have often used the whole rock composition of chill zone to be representative of the parent magma composition. Parent magma compositions, as estimated from the composition of chill zone rocks, are most commonly olivine tholeiite to tholeiite; however, alkaline and calc-alkaline layered intrusions do occur as well.

Mineral chemical variations from the least differentiated ultramafic rocks to maximum

Table 6.1 Layered igneous intrusions

What are they: Intermediate to deep crustal magma chambers that were exposed by tectonic uplift and subsequent erosion of the cap. Some are thought to have fed large continental flood basalt provinces
Size: Highly variable. Largest is the Bushveld intrusion of South Africa (64,000 km^2); and the Skaergaard intrusion of Greenland (170 km^2) is one of the smallest
Shape: Lopolith or funnel
Parent magma: Olivine tholeiite or tholeiite is common; but there are also alkalic ones
Structure and texture: Layering structure and cumulate texture
Layering
Principal types: Modal layering, rhythmic and cyclic layering, phase layering, cryptic layering
Additional curious types: Inch-scale layering, cross lamination
Attributes: The principal layering is always parallel to the margins of the intrusion from bottom up, inward from the sides, and roof downward. Thickest layers occur in the bottom upward sequence. Layering is generally poor in the central part of the intrusion
Origin of layering: Varies. The most common mechanisms are believed to be in situ crystallization, nucleation rate fluctuations versus growth of crystals; crystal settling; crystal flotation; compaction; melt mixing, convection; and appearance or disappearance of phases during normal crystallization of magma
Magma evolution
Chemical: Principally iron enrichment followed by alkali enrichment
Mineralogical: Normal cumulus sequence: Olivine → Opx → plagioclase → augite → pigeonite → magnetite → apatite
Olivine gap: Common in tholeiitic intrusions; olivine disappears and a more Fe-rich olivine reappears late in the crystallization sequence
Lithological zones (from least to maximum differentiated): Dunite and chromitite, orthopyroxenite, harzburgite, anorthosite, gabbro, ferrogabbro, granophyre
Important economic reserve: Important resource for chromite and platinum group elements

differentiated granophyric rocks in these layered intrusions suggest multiple magma intrusion and mixing in many cases, e.g., Bushveld intrusion (Wager and Brown 1968) and Muskox intrusion, Canada (Irvine 1980). The Skaergaard intrusion appears to be an exception in the sense that it seems to have experienced only one episode of magma intrusion followed by closed system differentiation. This intrusion shows the extreme development of differentiated liquids, and therefore this intrusion played an important role in Bowen–Fenner controversy. Briefly, Lawrence Wager, the famous British explorer and geologist, who first discovered the Skaergaard intrusion, calculated a liquid line of descent from the intercumulus materials (definition in the next section) and showed that the basalt magma differentiation resulted in the formation of Fe-rich granophyre, which ended the Bowen–Fenner debate in Fenner's favor. Later work by A.R. McBirney, J.D. Hoover, H. R. Naslund, T. Nielsen, C.K. Brooks, and others more-or-less verified Wager's Fe-enrichment trend. The only difference is that a few studies also showed that the very late-stage differentiates split into two liquids due to liquid immiscibility. This is particularly well shown in the AFM diagram (Fig. 6.25).

The Bowen–Fenner debate was briefly revived in 1987 when Hunter and Sparks suggested that Skaergaard rocks actually had volcanic counterparts that were mafic to silicic (i.e., Bowen trend) but such lavas have since been eroded away. However, McBirney and others pointed to the lack of such volcanic rocks, inappropriate parameters used in the modeling, experimental demonstration of silicate-liquid immiscibility, and other criteria to uphold Wager's original conclusion, that is, Fenner was right: fractional crystallization of basalt magma does not lead to the formation of granitic magma (which is poor in iron) of the kind that forms large continental batholiths but to an iron-rich granophyric differentiate.

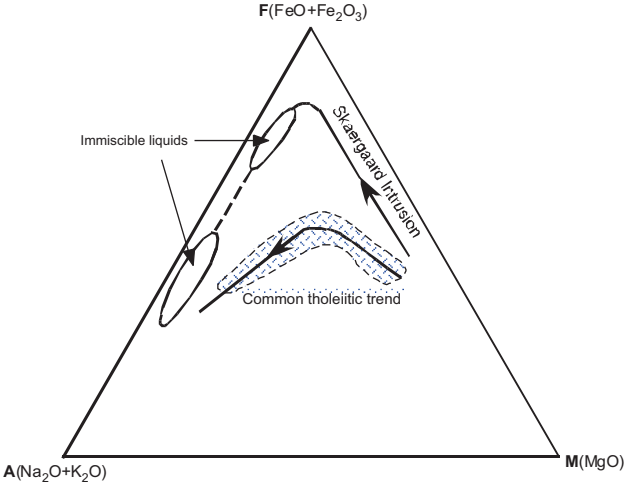

Fig. 6.25 AFM diagram showing the Skaergaard liquid line of descent

Cumulus, Intercumulus, Post-cumulus, and Cumulate

Lawrence Wager coined the above terms to explain the distinctive appearance of the minerals, rocks, and their textural features (Wager et al. 1960). Wager and coworkers used the term *cumulus* to describe the euhedral–subhedral mineral grains that they suggested to have formed in the liquid and later settled or floated to form the *cumulate* rocks in which they occur. By their definition, *intercumulus liquid* is any liquid trapped between the cumulus minerals; and *post-cumulus minerals* are those that later grow in the intercumulus liquid (Fig. 6.26).

Many authors have since debated the use of the term 'cumulus' because they argued that cumulus minerals commonly form by *in situ* crystallization and not necessarily by gravity-influenced crystal sorting processes. On the other hand, the uniqueness of the rocks of layered intrusions has forced the modern scientist to continue to use the term cumulus but with the important difference that these crystals are simply euhedral–subhedral and that they grow in an environment of large magma volume. In an effort to downplay the genetic aspect of the term cumulus, some authors prefer the use of the term "*primocryst*" to represent the euhedral–subhedral crystals that form earlier than the other crystals in the cumulate rock. The other terms, i.e., intercumulus and post-cumulus, are also used "as is."

A typical cumulate rock contains cumulus and intercumulus minerals. Wager et al. (1960) classified cumulate rocks into three types based on the proportion of intercumulus materials: a cumulate with 25–50 % intercumulus materials is called an *orthocumulate*. A cumulate with 7–25 % intercumulus materials is referred to as *mesocumulate*, and one with <7 % intercumulus materials is called an *adcumulate* (Fig. 6.26). An interesting feature of the adcumulate and mesocumulate rocks is the presence of cumulus crystals that show evidence of post-cumulus growth from the intercumulus liquid. Such growth is referred to as *adcumulus* growth. Excellent pictures of the various cumulate types can be found on the Internet, and therefore, I would urge the student to use those pictures along with this text.

Besides the three types of cumulate rocks mentioned above, an unusual type of cumulate, called *crescumulate*, also occurs. In it the crystals are obliquely oriented to the layering. This type of layering is inferred to originate by in situ growth of crystals from the base into the magma within the interior of the intrusion.

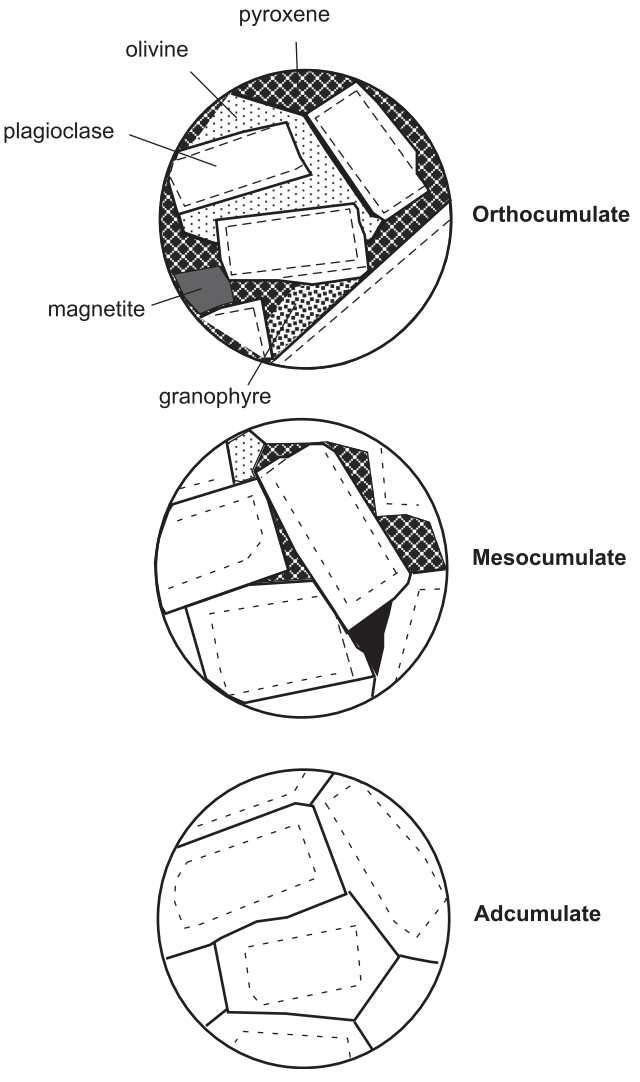

Fig. 6.26 Sketch showing plagioclase orthocumulate, mesocumulate, and extreme adcumulate. The dashed lines show the limit of original cumulus crystals with latter overgrowth falling outside the dashed lines. It is apparent that the overgrowth is the thickest in the adcumulate. Highest proportion of intercumulus minerals, pyroxene, olivine, magnetite, and granophyre, occurs in the orthocumulate. [Redrawn from Figure 1 in Wager et al. 1960), J. Petrol. 1, 73–85]

The volume and composition of the intercumulus liquid in a large layered intrusion are dictated by where such liquid is trapped: if it occurs deep in the mush zone and is overlain by a pile of cumulates, then it will undergo tremendous compaction (and thus the liquid will be squeezed out) and the remaining liquid will undergo strong fractionation by losing its components to the surrounding crystals. However, if it is trapped closer to the solidification front at the time of its entrapment, then it can be relatively free of compaction and also exchange components with the melt ahead of the solidification front and thus be less

differentiated. As magma in a layered intrusion cools and cumulus piles accumulate at the bottom (and at the sides and top), compaction becomes a major factor in that it squeezes out the intercumulus melt to higher levels, where such melt may mix with the less differentiated intercumulus melt. As a result, the post-cumulus minerals and rims of cumulus crystals develop complex zoning and reaction features.

An interesting aspect of layered intrusions is the *adcumulus* overgrowth of cumulus crystals. This overgrowth is believed to occur by precipitation from the intercumulus liquid. However, the details of such a process are sketchy. For example, consider the case of an anorthosite with ~95 % adcumulus crystals of plagioclase. For the adcumulus overgrowth of such crystals to occur, all non-plagioclase components (e.g., Mg, Fe, Ti) would have to be selectively taken out (i.e., diffused out) of the intercumulus liquid, and also, the Ca/Na and coupled Al/Si ratios have to be kept the same as that of the original cumulus crystal. Hess (1960) suggested that this happens via diffusion between the intercumulus melt and the main melt ahead of the solidification front. However, diffusion is a very slow process, and some authors suggest that cumulate pile up rate is a faster process, which would make it impossible for a deeply buried intercumulus liquid to effectively communicate with the main magma via diffusion. In contrast, some other authors have suggested that the intercumulus liquid may not have to go far and may exchange components with nearby intercumulus liquids or rocks (Irvine 1980).

The occurrence of poikilitic inclusions of many smaller cumulus crystals in a large (several cm) adcumulus crystal, called an *oikocryst*, is fairly common in layered intrusions. Sometimes they are hard to identify as such because of the grain sizes involved: however, between crossed polars of a petrographic microscope, such oikocrysts will appear optically continuous—meaning that the entire grain will go extinct (excluding the included minerals) at the same time. In the field, oikocrysts are visible when light reflects off mineral cleavage on freshly broken surfaces.

Layering

Many different varieties of layering occur within a single layered intrusion. It is impossible to cover all aspects of individual layered intrusions and I will try to cover some general aspects of these intrusions in this section. The student who is truly interested in understanding magma differentiation in large magma chambers should consult Wager and Brown (1968), Cawthorn (1996), and other more recent publications (see the website of the *Layered Intrusions Research Group:* http://www.earth.ox.ac.uk/~madeleih/Layered%20Intrusions%20Research%20Group/Welcome.html). Here I consider three principal types of layering—modal, phase, and cryptic layering (discussed below).

Modal layering is defined by conspicuous variations in abundances of dark and light minerals on a megascopic scale (Fig. 6.27). Cyclical or rhythmic repetition of the layers is fairly common, and hence terms such as *rhythmic layering* and *cyclic layering* have often been used to describe them. This type of layering often extends for tens to hundreds of meters. A most remarkable variation of modal layering, called *inch-scale layering*, was described by Hess (1960) from the Stillwater intrusion of Montana (USA). This layering is characterized by the repetition of alternate dark- (pyroxene, chromite) and light-colored (plagioclase) layers separated at the scale of inches with amazing regularity! Aside from these, *graded layering* is sometimes found, in which crystals are sorted in size such that individual layers are characterized by an gradual decrease in size of crystals from bottom to top. Density layering also occurs in some intrusions where an individual layer starts with the densest minerals at the bottom and grade upward into minerals of progressively lower densities. Grain size and mineral density layering often accompany each other. Cross-stratification structures, similar to those found in clastic sedimentary rocks, are also found near the

Fig. 6.27 Layers of chromite separated by plagioclase (from Eastern Bushveld Intrusion; *source*: http://web.uct.ac.za/depts/geolsci/dlr/301s/bushveld%20field%20photos.html)

margins of the intrusion, which suggests the presence of currents in the magma from which crystals are laid down by crystal settling. These types of convection currents are probably intermittent and local, initiated by destabilization of dense mineral clusters behind the upper solidification front of the intrusion.

As would be expected, chemical evolution of the magma is best reflected in the appearance (and disappearance) and compositions of mineral phases. Discontinuous reaction series, as professed by Bowen, is exemplified by the appearance and disappearance of phases. The "stratigraphy" of a layered intrusion is generally divided into a number of zones on the basis of such appearance and disappearance of mineral phases (see later discussion on the Skaergaard and Bushveld intrusions). Layering defined by the appearance or disappearance of phases is referred to as *phase layering*. For example, in the Bushveld intrusion the appearance of magnetite as a cumulus phase marks the boundary between the Main Zone and Upper Zone.

Cryptic layering represents slow gradual chemical compositional change in the solid solution of an individual phase, which is equivalent to Bowen's continuous reaction series. It is so-called because this type of layering is not visible in the field and is only discernible after determining compositions of the minerals. As an example of cryptic layering, note how the composition of plagioclase$_{\text{solid solution}}$ changes from An_{80} in the Lower Zone to An_{30} in Upper Zone of the Bushveld intrusion (Fig. 6.33).

Below we briefly consider the nature of two classic layered intrusions—the Skaergaard and Bushveld intrusions.

Box 6.2: Deep Magma Chamber(s) Beneath Hawaii

In 1989 I accidentally came upon a Hawaiian xenolith in the Dale Jackson Collection of the National Museum of Natural History (Smithsonian Institution) that was unlike anything I had ever seen before. Petrographic examination revealed the presence of distinct layering with olivine and Cr-poor spinel as cumulus phases. What made this rock different from cumulates in any layered intrusions around the world is the presence of *intercumulus garnet* (Figure 6.28).

Experimental petrology indicates that garnet can crystallize from a basalt magma only at very

(continued)

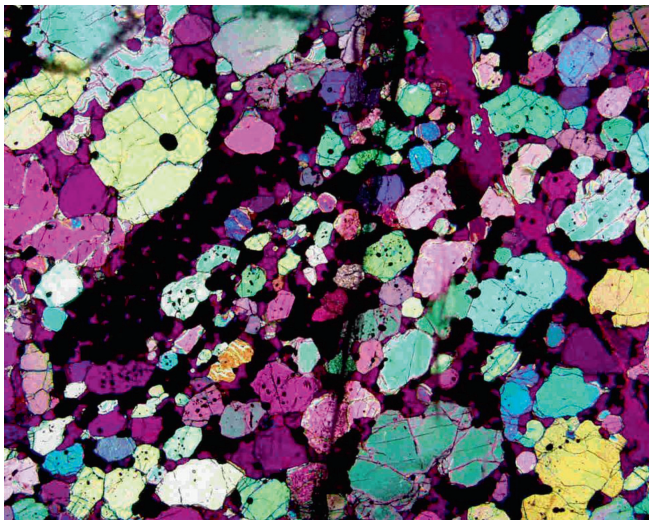

Fig. 6.28 Photomicrograph of an unusual mantle xenolith from Oahu, Hawaii, showing layered structure. The colored minerals are almost all olivine, and the opaque mineral is chrome–spinel. The picture was taken with polars crossed and gypsum plate inserted. The pink mineral (intercumulus) with high relief is garnet. Garnet is isotropic and therefore shows the same color as that of the gypsum plate

(continued)

high pressure, and thus garnet's presence suggested the formation of this cumulate in some deep-seated magma chamber, much deeper than any we have known. Comparison with high-pressure phase diagrams suggested that this cumulate formed from a melt at a pressure of ~3 GPa, which is at/near the base of the oceanic lithosphere beneath Oahu. To the author's knowledge, this was (and remains to be) the only report of the operation of cumulus processes in a magma chamber at such great depth.

Two Examples of Layered Intrusions

Skaergaard Intrusion, Greenland

The Skaergaard intrusion is 55 million year old, formed during the opening of the North Atlantic, and was the magma chamber for the 6 (±3) km thick East Greenland flood basalts (McBirney 1996; Larsen and Tegner 2006). It is generally accepted that the Skaergaard magma was a differentiated olivine tholeiite that was emplaced in a single, perhaps prolonged, episode; and this magma then solidified from its margins to the interior over a period of about 130,000 years. It is somewhat circular in map view (Fig. 6.29a)

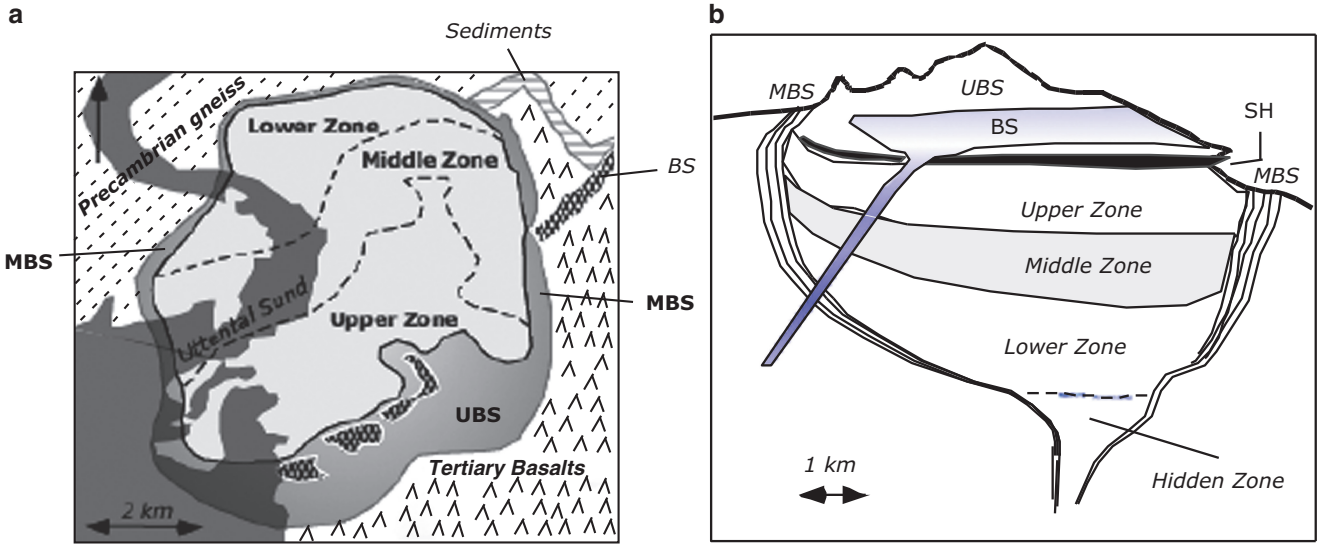

Fig. 6.29 (**a**) Map of the Skaergaard intrusion. *MBS* marginal border series, *UBS* upper border series. The Layered Series is composed of the lower, middle, and upper zones. *BS* Basistoppen sheet. (**b**) An east–west cross section of the Skaergaard intrusion. Abbreviation as in (**a**) *SH* Sandwich Horizon

and has an asymmetrical funnel-type shape in cross section (Fig. 6.29b). It intruded Precambrian gneisses and Mesozoic sediments. The intrusion has been tilted, eroded, and intruded by later granophyric dikes and sills, of which the Tinden sill and Basistoppen sheet are examples.

The Skaergaard intrusion is divided into three major units—the Layered Series (LS), Marginal Border Series (MBS), and the Upper Border Series (UBS) (Fig. 6.29a, b). Below the LS there is a small "Hidden Zone" that is believed to be composed of more primitive rocks. The MBS crystallized along the walls and grew inward; the UBS formed by roof crystallization and the LS formed on the floor of the intrusion. In terms of overall chemical variation, the three series parallel the chemical trends. The contact between the MBS and LS is sharply discordant on the western side; however, on the east side the layers in the LS curve up and become parallel with those of the MBS, making it difficult to recognize the contact between MBS and LS. The upper boundary of the LS meets with the lower boundary of the UBS at the *Sandwich Horizon*, which is generally a coarse granophyre-rich zone that marks the collection of the last remaining liquids from both roof crystallization and LS crystallization.

The Layered Series is subdivided into a Lower, Middle, and Upper Zones by the disappearance of abundant cumulus olivine crystals at the base of Middle Zone and its reappearance at the base of Upper Zone (Fig. 6.30). There are rare olivine grains in Middle Zone that are products of reaction between pyroxene and Fe–Ti oxides. Lower Zone is subdivided into smaller units—*a, b*, and *c*—based on the appearance of a distinctive poikilitic augite in LZa and the

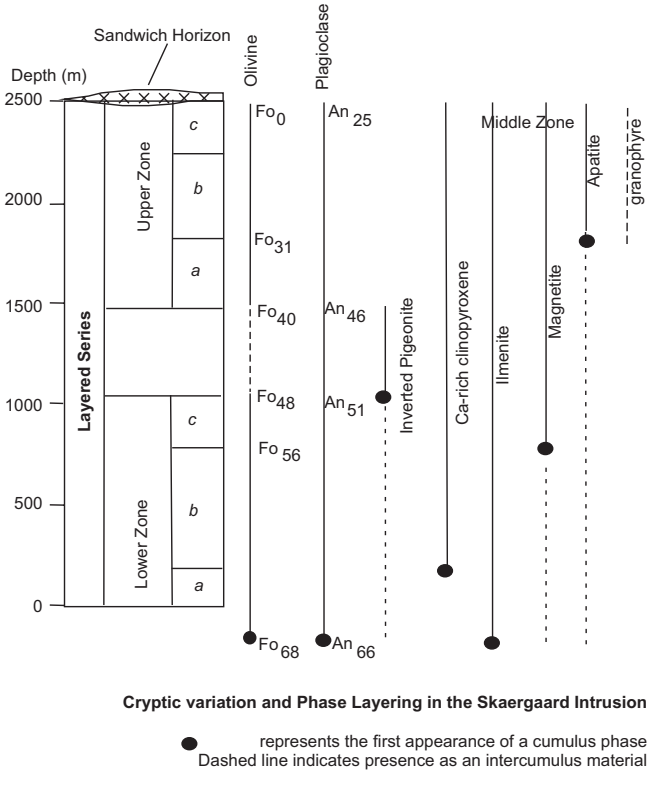

Fig. 6.30 Phase and cryptic layering in the Layered Series of the Skaergaard intrusion

appearance of abundant Fe–Ti oxide minerals at the base of LZc. Upper Zone is similarly divided into three subunits. Inverted pigeonite (see Box 6.4) is present in all rocks up to the middle of UZa. Layering is common all the way up to the middle of UZb (McBirney 1996). Local pegmatite and granophyre segregation veins, pods, and diapirs occur in LZ. Felsic dikes and sills also occur in the UZc (McBirney 1996). Modal and grain-size layering is common in much of the Layered Series. "Trough bands," which are synformal bands, cross stratification, and slump structures are also present.

As we have discussed earlier, magma differentiation seems to have followed a closed system fractionation path. LZc has played a prominent role in the debate between Hunter and Sparks (1987) and McBirney and others. Hunter and Sparks argued that the Skaergaard magma became more silica or iron depleted after magnetite started fractionating out of the magma at LZc. However, their opponents argued that the melt continued to become Fe-rich, while silica remained more-or-less constant. As indicated earlier, I believe that McBirney and others have won the debate.

As far as layering is concerned, there is no question that in situ crystallization was responsible for the development of layered structures of the MBS and UBS. However, the important question in how the Layered Series got to be so much thicker than the other two series. Many authors argue that convection played a central role in transporting cumulus minerals to the bottom from elsewhere in the intrusion (e.g., Wager et al. 1960; Hunter and Sparks 1987; Sparks 1990; Campbell 1996). At least three types of convection have been proposed—continuous convection, intermittent convection, and double-diffusive convection. It is beyond the scope of this book to discuss these in detail; therefore, I recommend the excellent review by Naslund and McBirney (1996) for further reading on the subject. Perhaps the best evidence of convection comes from the Duke Island intrusion (Canada), where Irvine (1980) described well-developed cross-bedding type structures that suggest strong currents in the magma. The parent magma of this intrusion was ultramafic, which has very low viscosity.

Based on "tank" experiments with paraffins, Marsh (1989, 1990) suggested that in basaltic intrusions, convection is likely to be weak to nonexistent and favored in situ crystallization instead. Sparks (1990) argued instead that strong, continuous convection can occur and perhaps is responsible for much large volume of

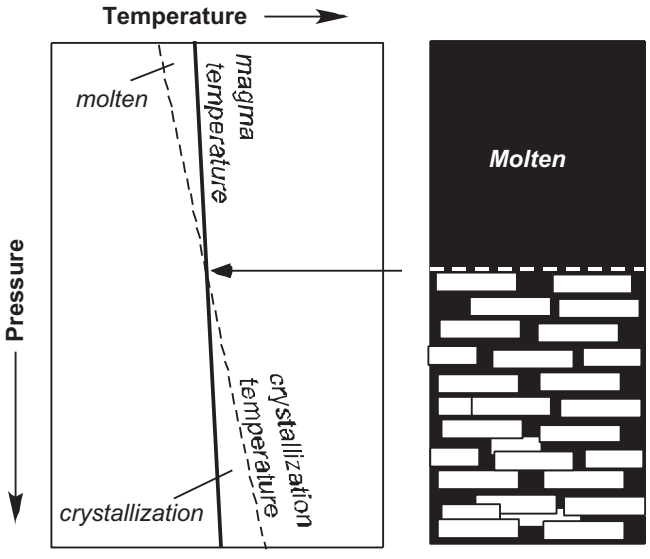

Fig. 6.31 The *left panel shows* how the d*T*/d*P* slope of the magma crystallization (liquidus) curve may intersect the magma adiabat (magma temperature) in a large intrusion. This will cause early start of crystallization and longer crystallization time for the bottom part of the intrusion

cumulates that accumulated in the lower part of the Skaergaard intrusion (and other intrusions) than at its top or sides, even though such a large intrusion cools mainly through the roof and sides. However, it is not within the scope of this book to further discuss whether or not continuous convection occurs in basaltic layered intrusions.

Finally, E.D. Jackson argued that cumulates are thicker in the lower part of a layered intrusion because of the intersection of the liquidus and the magma's adiabat (Fig. 6.31). The deeper magma in the intrusion, which falls below the intersection point of the two curves, will begin to crystallize much earlier than the upper part. This will allow a thicker lower zone.

Bushveld Intrusion, Southern Africa

The Bushveld intrusion is the world's largest layered intrusion located in South Africa (Fig. 6.32). The intrusion is not exposed in the middle; and there have been many discussions of what lies beneath the center. The intrusion is believed to have been a result of a massive impact by a large meteorite.

Figure 6.33 shows a schematic vertical lithological zonation of the Bushveld intrusion. The Marginal Zone rocks are somewhat finer grained than the rocks from the interior; and xenoliths of country rock are often found in this zone (Cameron 1978). This zone is commonly interpreted as the "chill zone" or where the

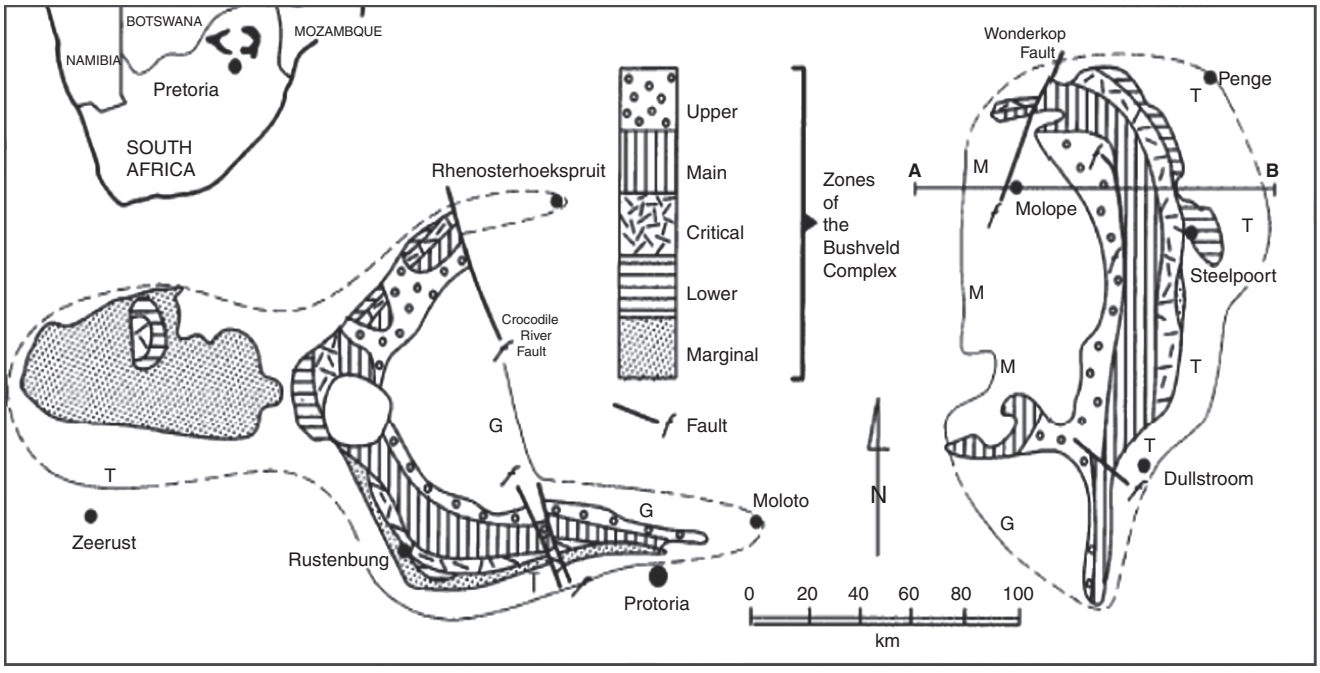

Fig. 6.32 Map showing location (*inset*) and distribution of the Bushveld intrusion (*source*: Cameron 1978)

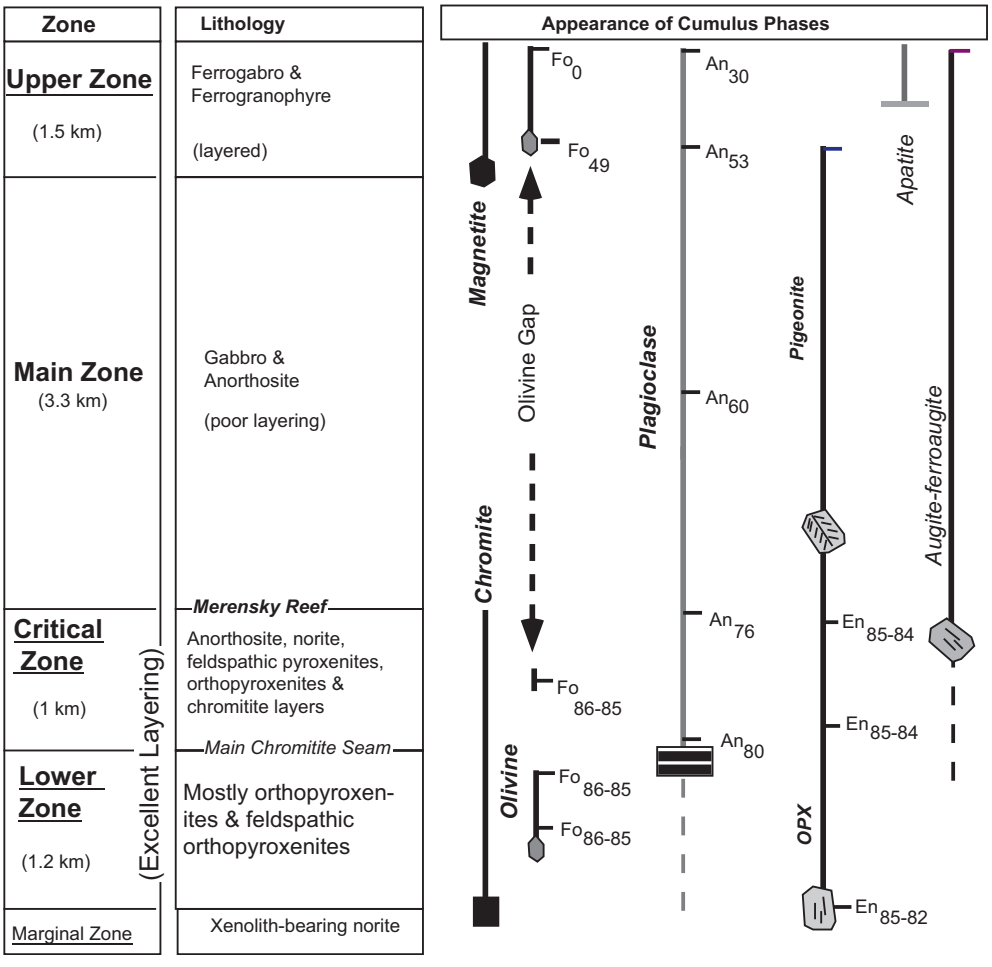

Fig. 6.33 Phase and cryptic layering in the Bushveld intrusion

Bushveld magmas first quenched against the wall rocks. In a sense Bushveld is not particularly a good example to use here because there is clear evidence that there were multiple episodes of magma intrusion and magma contamination by the crustal wall rocks. These multiple episodes of intrusion occurred when the Lower and Critical Zones were still forming. For at least two reasons, the study of Bushveld intrusion is appealing: (1) It is the largest intrusion that seems to have the least to most differentiated rocks and thus offers an opportunity to explore how magma evolves. (2) It has important economic mineral reserves of chromite and platinum.

The composition of the parental magma to the Lower Zone of the Bushveld intrusion has been better constrained by an examination of the core samples obtained by drilling through the eastern Bushveld Complex (Wilson 2012). The lowermost 1.2-m part of the core sampled wall rock quartzite and fine-grained chill rocks, rocks with spinifex structure (which are normally found in komatiites, Chap. 12), other quench-textured rocks, and olivine and orthopyroxene cumulates. The most magnesian olivine and orthopyroxene are Fo_{91} and En_{93}, respectively. Based on geochemical and mineral chemical considerations, Wilson proposed that the emplaced chill zone magmas had a maximum of 19 % MgO. Noting that the magmas had high Ni (which is usually high in ultramafic rocks) as well as high in K, Rb, and other elements that typically derived from continental crust, Wilson suggested that these magmas were variable, a mixture of komatiite (65–70 %) and continental crust (30–35 %).

Division of the differentiated rocks into various zones is based on the appearance or disappearance of a phase: for example, the base of the Upper Zone marks the first appearance of magnetite as a cumulus phase. Note that magnetite may be found in rocks from the zones below but only as an intercumulus phase.

The earliest cumulates are layers of chromitites and orthopyroxenites. Dunite layers are virtually absent near the bottom but become more abundant in the middle part of the Lower Zone (Cameron 1978). A highly forsteritic olivine appears as a cumulus phase in the Lower Zone but disappears even before it reaches the top of the Lower Zone. The origin of this "olivine gap" can be explained with reference to the system forsterite–fayalite–silica (see "Advanced Reading" below).

Advanced Reading: Olivine Gap.
Crystallization relationships of pyroxene and olivine in layered tholeiitic basalt intrusions are of much interest in petrology. The "olivine gap," i.e., olivine disappearance and reappearance in intrusions such as Bushveld and Skaergaard was originally thought by Lawrence Wager, the British explorer who discovered the Skaergaard intrusion, is a result of fractional crystallization. He used the system forsterite–fayalite–silica that may be used to explain this olivine gap (Fig. 6.34). Olivine and Ca-poor pyroxene (orthopyroxene in the forsterite–fayalite–silica system and orthopyroxene + pigeonite in the diopside–forsterite–fayalite–silica system (not shown here)) exhibit extensive solid solution. There are three liquidus fields in this system (Fig. 6.34a): the boundary between olivine and orthopyroxene liquidus fields is partly a reaction curve (1 to 2) and partly a cotectic (2–3). At 3 the Ca-poor pyroxene becomes unstable and gives way to a Fe-rich olivine. 3—*e* is the cotectic boundary between the liquidus fields of olivine and a silica polymorph.

Figure 6.34b shows the equilibrium crystallization behavior of a Skaergaard-like parent magma, *P*. Using the rules we learned in Chap. 4, we construct the liquid path ($P \rightarrow Q \rightarrow F$) and solid path ($O \rightarrow Q' \rightarrow P$) making use of appropriate three-phase triangles. Of course, we do not know the exact compositions of each phase during progressive crystallization but the topology of the diagram must be correct. We note that olivine never leaves the crystallization path, i.e., equilibrium crystallization cannot produce the "olivine gap."

Figure 6.34c shows the liquid and solid paths for *P* resulting from fractional crystallization of "*P*." *P* will fractionate olivine of continuously changing composition until the derivative liquid reaches 1, at which point olivine will be replaced by a Ca-poor pyroxene. Because the Ca-poor pyroxene will have a different Fe/Mg than the last olivine that crystallized, the liquid path will curve more strongly and follow $1 \rightarrow R$. From $R \rightarrow 3$, a Ca-poor pyroxene and a silica

(continued)

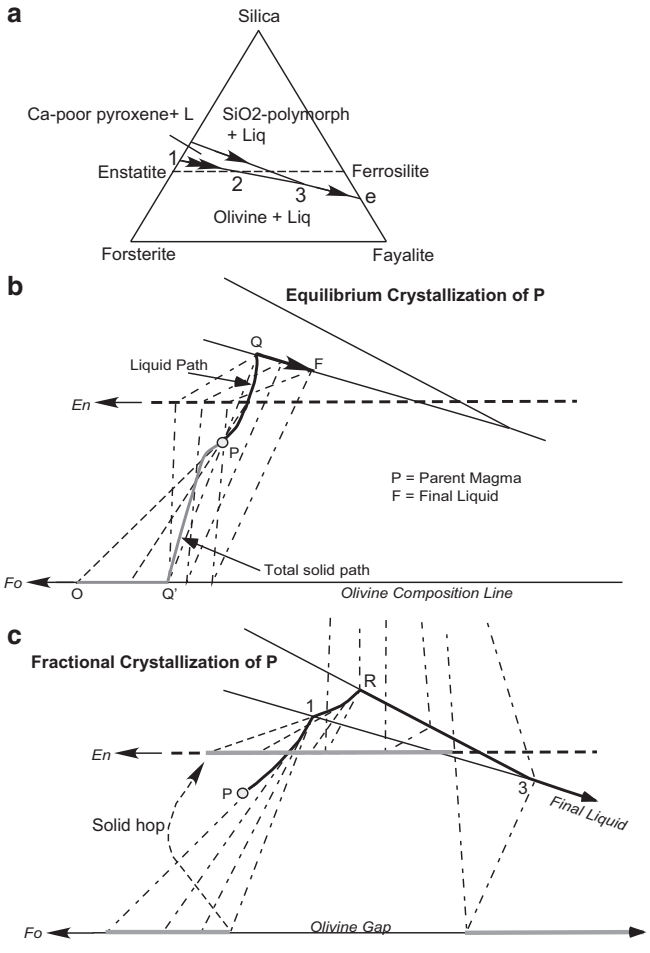

Fig. 6.34 Phase relations in the system Fo–Fa–silica illustrating olivine gap

Advanced Reading: Olivine Gap (continued)

polymorph will fractionate from the melt. When the derivative melt reaches 3, the liquid will once again be saturated with a Fe-rich olivine and silica polymorph. Thus, from 1 to 3 olivine could not form although it fractionated earlier and made a reappearance later.

Naslund and McBirney (1996) pointed out that in the Skaergaard intrusion, olivine does occur in the Middle Zone of the Layered Series as rare grains and as reaction products between pyroxene and magnetite. They also indicated that Ca-poor pyroxene (inverted pigeonite) does not stop when a Fe-rich olivine reappears but continues for a short time into the Upper Zone. Therefore, these authors suggest that the "olivine gap" may not be what Wager thought.

Cumulus plagioclase first appears at the base of the Critical Zone. A thick and laterally continuous chromitite layer (called "Main Chromitite Seam") separates the Critical Zone from Lower Zone. The Critical Zone rocks are dominantly composed of huge alternate layers of orthopyroxenites and anorthosites with fine interspersed layers of chromitite. The Main Zone rocks are anorthosites and gabbros and are characterized by the presence of cumulus augite, pigeonite (inverted: see Box 6.4), and plagioclase. These rocks lack good layering. The extremely differentiated rocks of the Upper Zone carry cumulus apatite, magnetite, and very Fe-rich olivine and Ca-rich pyroxene.

Box 6.3: Merensky Reef and Platinum Group of Elements

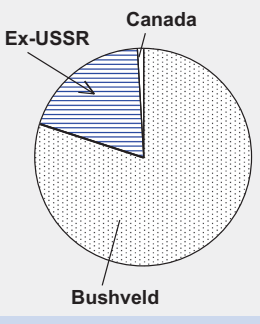

Merensky Reef of the Bushveld intrusion accounts for about 80% of the world's supply of platinum group of elements (PGE: platinum, palladium, iridium, ruthenium, rhodium, and osmium). The origin of the the Merensky Reef continues to be a matter of some debate.

Laterally the thickness of the reef varies from 30 to 90 cm. The average PGE content is about 10 g/t, although at places it may be as high as 40 g per ton. 60 % of PGE occur in solid solution in pyrrhotite, pentlandite, and pyrite. The other 40 % occurs as platinoid minerals, such as cooperite (PtS), laurite (RuS_2), Pt–Fe alloys, braggite (Pt,Pd,Ni)S, or their intergrowths (cf. Guilbert and Park 1986). Origin of the Merensky Reef is a matter of some debate. The hypotheses range from magmatic processes to late-stage hydrothermal concentration of PGE metals. Some sort of liquid immiscibility between PGE-rich sulfide melts and silicate magma likely had occurred at this level of the Bushveld intrusion. It has been suggested that chromite precipitation (forming chromitite layers) may have led to sulfur (and PGE) supersaturation in the melt in the immediate vicinity, which led to immiscible separation of PGE-sulfide melts.

Box 6.4: Pyroxene Crystallization in Tholeiitic Intrusions

Tholeiitic basalt magmas in layered intrusions generally crystallize all three pyroxene types—augite–ferroaugite, orthopyroxene, and pigeonite (Figure 6.35). With progressive differentiation all three pyroxene types show considerable Fe-enrichment. In the case of Bushveld intrusion, orthopyroxene crystallized early, and pigeonite made its appearance later. In the progressive differentiation sequence, the augite that coprecipitated with the Ca-poor pyroxenes (including orthopyroxene and pigeonite) became strongly Fe-rich as its Ca content dropped. At the base of the Upper Zone, pigeonite became unstable and the magma crystallized a more Fe-rich olivine (and silica polymorph) instead. Figure 6.35a shows tie-lines (dashed), each of which connects two coexisting pyroxenes. These tie-lines show that (a) augite–orthopyroxene coprecipitate first, followed by (b) all three phases, augite–orthopyroxene–pigeonite, crystallize for a short period (note the three-phase triangles), and then (c) ferroaugite crystallizes with pigeonite. During subsolidus cooling of pigeonite, it inverted to an orthopyroxene that has slightly more Ca than the primary orthopyroxenes which crystallized earlier in the sequence.

The presence of miscibility gaps limits the mutual miscibility between augite–ferroaugite and Ca-poor pyroxenes (i.e., orthopyroxene and pigeonite). Pyroxene phase diagram on the join $MgSiO_3$–$CaMgSi_2O_6$ (Carlson 1986) illustrates how pyroxene crystallization occurs in layered intrusions. The dashed lines in Figure 6.35a are also shown in this diagram to illustrate how such pyroxene may have formed. There are three pyroxenes in this diagram—protoenstatite (PEn), "rhombic" enstatite (REn), pigeonite (Pi), and diopside (Di). All of them form solid solutions. The colored fields are the stability fields of the various pyroxenes. There are three miscibility gaps in the subsolidus region, where two pyroxenes coexist (i.e., Di + Pi, Di + PEn, and Di + REn).

There are also inversion loops in this join, where one pyroxene breaks down into a diopside plus an orthopyroxene. Consider, for example, a

(continued)

Box 6.4 (continued)

pigeonite p_1 and a diopside d_1 forming from a liquid at the "eutectic" point *e*. After the melt has crystallized, both p_1 and d_1 will change composition toward p and d, respectively, upon slow cooling. This compositional change will be accomplished via exsolution. Below the line a–p–d, pigeonite is no longer stable, and further cooling will result in inversion of pigeonite to PEn. In fact, the line a–p–d represents a decomposition reaction: Pi = Di + PEn. Once all the pigeonite are gone via decomposition, the inverted pigeonite (PEn) and diopside crystals can cool further while exsolving each other. Inverted pigeonite crystals are recognized by the development of typical *herringbone exsolution* (Figure 6.36c). Exsolution of one mineral in another is controlled by atomic structure: the exsolved phase is expelled along what are called "common ion planes." Common ion plane for augite–orthopyroxene exsolution is the (100) plane (which is a prismatic direction), whereas that for augite–pigeonite exsolution is the (001) plane (which is the basal plane). In the case of a slowly cooling pigeonite crystal, augite blebs are exsolved parallel to the (001) face of the host crystal. When this pigeonite inverts to an orthopyroxene, two things happen: The exsolved augite blebs change direction and are expelled along (100) direction and, also, the crystal undergoes twinning. Thus, the inverted pigeonite (now orthopyroxene) crystal is a twinned crystal, and the original (001) exsolved blebs give it the herringbone appearance. Note that the second-generation prismatic exsolution of augite is also visible in Fig. 6.36.

Summary

1. A primary magma is one that is generated directly by melting a source rock. A primitive magma is a magma that has not undergone significant evolutionary change. A parental magma is simply a magma that is a suitable parent for a more derivative magma. The three definitions may or may not be mutually interchangeable.
2. The term differentiation is used as a general "umbrella" term that includes all types of processes that affect magma's composition following its generation. Crystal

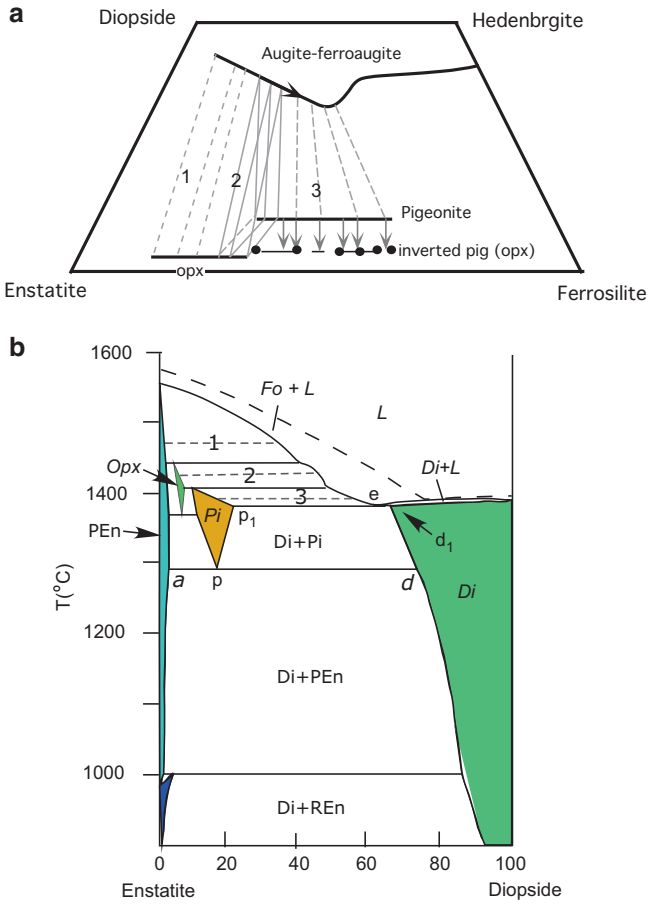

Fig. 6.35 Pyroxene crystallization, inversion, and exsolution in the Bushveld intrusion—(**a**) pyroxene crystallization and subsolidus cooling and inversion (explained in the text) and (**b**) phase equilibria in En–Di "system" (after Carlson 1986)

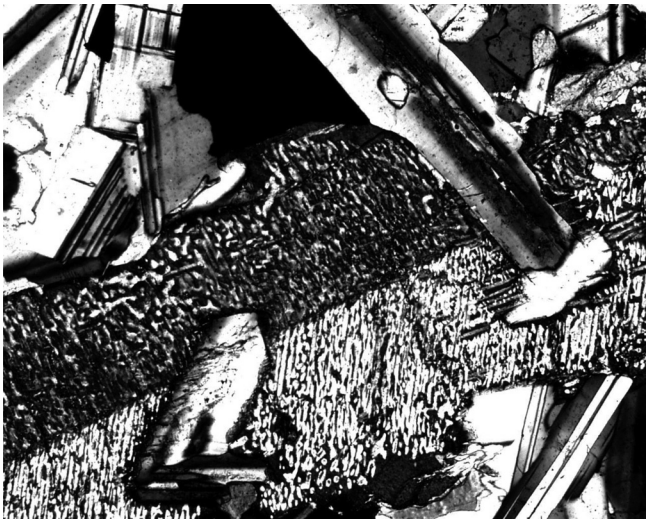

Fig. 6.36 Photomicrograph showing inverted pigeonite with herringbone exsolution structure

sorting, magma mixing, contamination, liquid immiscibility, etc. are examples of differentiation processes. Among them crystallization-related processes (e.g., in situ crystallization, crystal settling, crystal flotation) are considered to be most important.

3. Variation diagrams are types of diagrams in which oxides, elements, ratios of elements/oxides, and/or isotope compositions of a suite of lavas are plotted against each other. Such diagrams are used to draw inferences about the processes responsible for such variations.
4. Effects of equilibrium and fractional crystallization processes on magma chemistry can be easily modeled with appropriate equations. Incompatible and compatible elements behave very differently in such processes.
5. Layered intrusions are fossil magma chambers that are characterized by fascinating layered structure and mineral chemical variations. Their study was important in resolving the debate between Bowen and Fenner on the nature of the remaining melt during fractional crystallization of basalt magmas. Tholeiitic layered intrusions and lavas show prominent iron enrichment. Alkali and silica enrichment occurs in the very late stages of crystallization due to immiscibility of two liquids—one being an iron-rich silicate liquid and the other is an alkali-rich silicate liquid.

Basalt Magma Generation: Perspectives from Experimental Petrology

7

Abstract

The present chapter focuses on the pressure–temperature constraints derived from high-pressure melting experiments on the origin of basalt magmas.

Introduction

The recognition that alkali basalts and tholeiitic basalts are fundamentally different makes the dual problems of generation of different types of basalt magmas and the effects of high-pressure differentiation processes on these basalt magma types all the more interesting. Even as early as 1960, it became clear that basalt magmas are generated in the upper mantle. The questions that concerned the pioneers of high-pressure experimental petrology are as follows: (1) Is it possible to generate alkali basalt magma from tholeiite via differentiation processes (or vice versa), and if so, then how? (2) How do these different magma types occur in different tectonic regimes? (3) What is/are the appropriate source rock(s) that can melt and produce these different basalt magma types? (4) What sorts of pressure and temperature conditions are required to produce the different basalt magmas? (5) Do volatiles (and what are they) or some specific elements exert significant control over what type of basalt magma would be generated?

An era of experimental petrologic inquisition thus began with much vigor to resolve these issues. Two different experimental approaches were adopted—some scientists performed melting experiments on *natural rocks*, whereas others experimented with analog systems with fewer components. While the first approach allows a semiquantitative understanding of the natural system, the large variance (too many components) does not allow a quantitative evaluation. The advantage of the second approach is that it does allow a quantitative understanding of the phase relationships involved in magma generation and crystallization. The principal disadvantage is that the results must be extrapolated to the natural system for making "sense" of the natural system, which has its own shortcomings. In Chaps. 3 and 4, we have dealt with simple systems with few components. Here we will apply that knowledge and add new knowledge from melting natural rocks in deciphering the origins of basalt magmas. Below we begin with a discussion of the appropriate starting rocks that can melt to yield basalt magmas.

Source Rocks for Basalts

Table 7.1 summarizes the current thoughts on the source rocks that melt to produce basalt magmas. Prior to mid-1990s peridotite, or more appropriately lherzolite, was thought to be the only source rock for basalt magma because this rock is the dominant component of the upper mantle, and laboratory experiments have repeatedly shown that basalt magma forms by partial melting of such a source rock. The last decade has seen an explosion of ideas proposing eclogite as an additional viable source rock. Briefly, eclogite is a metamorphic rock composed of a pyrope-rich garnet and omphacitic (Na, Al-rich) clinopyroxene. In the upper mantle, this rock type may be distributed as blobs, blocks, or stringers in a largely lherzolite matrix. These are remnants of broken up old recycled subducted oceanic crust. Compositionally similar to eclogite is a rock called garnet clinopyroxenite, which also occurs in the upper mantle but is of igneous origin as it is found to occur as veins and dikes in lherzolite

G. Sen, *Petrology*, DOI 10.1007/978-3-642-38800-2_7,

Table 7.1 Some commonly used terms for basalt magma sources

Source rocks: Lherzolite, Eclogite, and Garnet Clinopyroxenite. Lherzolite is considered to be the predominant component of the upper mantle and the source of basalt magmas. Eclogite's role as a source is gaining acceptance. Eclogite source rocks are generally accepted to be a previously subducted oceanic crust. Eclogite is also likely an important constituent of the lower continental crust. Garnet clinopyroxenite commonly forms igneous veins in the deep oceanic lithosphere and could be a potential source rock as well
Useful definitions
Pyrolite—A.E. Ringwood (Australian National University) coined this term to mean a mantle source that has not lost any basalt magma-generating component. Ringwood simply numerically added a basalt component to a peridotite and called it a pyrolite
Undepleted mantle—J.L. Carter (University of Texas at Dallas) used this term to mean the same thing as a pyrolite except that he based his definition from observation on actual mantle xenoliths from Kilbourne Hole, New Mexico, USA. Both Ringwood's and Carter's model mantles have $Mg/(Mg + Fe^{2+})$ ratio of 0.87. Any mantle peridotite sample with greater $Mg/(Mg + Fe^{2+})$ ratio (i.e., >0.87) would be residuum of melting in which some basalt magma would have been lost
Geochemistry-based definitions
Depleted—geochemists usually define depleted source as one that has undergone long-term depletion via extraction of continental crust. Typically, such a source is depleted in incompatible elements, e.g., light rare earth elements, Ti and Na. They are also isotopically depleted (e.g., ε_{Nd} of ~+6 to +10 and $^{87}Sr/^{86}Sr$ of 0.7025–0.703). "Normal" mid-ocean ridge basalts (or N-MORB) source is depleted. Geochemists often equate the depleted mantle source reservoir to the upper mantle
Primitive—sometimes also referred to as chondritic mantle. The term is used to mean a mantle or a portion of the mantle that has not lost any magma since the formation of the Earth. For example, such a source should have a flat REE pattern when normalized to C1 chondrites; and its ε_{Nd} and ε_{Sr} should be 0. The existence of such reservoirs in the present-day mantle has been a topic of much controversy
Enriched—refers to a mantle source that had been first depleted via magma extraction, and then such a depleted source had been refertilized or enriched with respect to magmatic chemical components. Such a source should be high in LREE and incompatible elements; and its ε_{Nd} should be <-2 and $^{87}Sr/^{86}Sr$ should be >0.705
An *old enriched* source refers to a source in which both trace elements and long-lived isotopes are enriched. A *recently enriched* source refers to a source that may be depleted in terms of long half-life isotopes but enriched in incompatible elements

Table 7.2 Mineralogy of a Hawaiian spinel lherzolite xenolith (*source*: Sen 1988)

Spinel lherzolite from Kaau, Oahu, Hawaii	Olivine	Orthopyroxene	Clinopyroxene	Spinel
SiO_2	41.17	54.72	52.25	0.07
TiO_2	0.02	0.18	0.49	0.16
Al_2O_3		4.59	5.36	55.33
Cr_2O_3		0.18	0.49	9.07
FeO*	10.08	7.11	3.10	13.39
MgO	49.13	32.53	15.25	21.12
MnO	0.04	0.02	0.2	0.04
CaO	0.03	0.68	20.92	
Na_2O		0.11	1.32	
Total	100.47	100.12	99.20	99.76

xenoliths and large ultramafic massifs. As we will see later, eclogite's appeal as a source rock stems from the fact that it can produce a large amount of basalt magma at relatively low temperatures at upper mantle pressures. This has been proposed by some authors for the origin of the Columbia River Basalt Group in northwestern United States, which we will discuss in a later chapter. Nonetheless, peridotite is still considered to be the dominant source of basalt magma at most geological situations for many good reasons.

Lherzolite Sources

As pointed out in Chap. 2, a typical lherzolite is dominantly composed of 60 % olivine ($Fo_{88–93}$), 20 % orthopyroxene, 15 % clinopyroxene, and 5 % of an aluminous mineral—plagioclase, spinel, or garnet. The pyroxenes in lherzolites can be quite aluminous (3–8 % Al_2O_3). The clinopyroxene is typically green colored in hand specimen due to the presence of a significant amount of Cr_2O_3 (0.5–2 wt%). Plagioclase is extremely rare, but where found its composition is around $An_{90–84}$. Spinel is brown colored in plane-polarized light because it is a Cr-rich spinel. Table 7.2 gives the mineral compositions of a spinel lherzolite xenolith from Hawaii. This xenolith was brought up by basanite magma from the upper mantle.

Pressure is the dominant control in determining which of the three aluminous phases would be stable in a lherzolite: Plagioclase is the stable phase at pressure less than 1 GPa, a chrome–spinel is the stable phase at intermediate pressures, and garnet is the stable mineral at higher pressures (Fig. 7.1). Notice that the

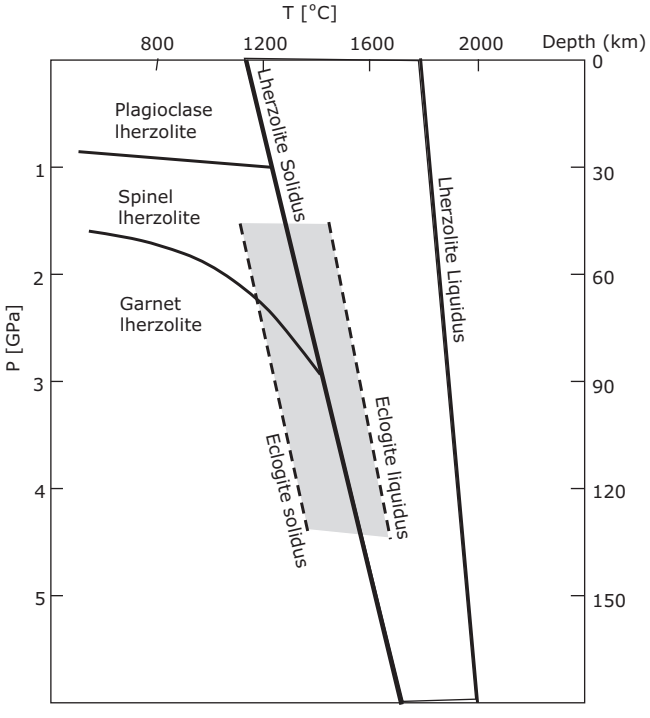

Fig. 7.1 Pressure–temperature diagram for upper mantle lherzolite showing the stability fields for three different types of lherzolites. The solidus and the liquidus for the common lherzolite are shown. Melting range of mantle eclogites generally fall within the *shaded region* (Hirschmann 2000; Kogiso et al. 2003)

spinel/garnet lherzolite boundary is at <2 GPa at moderate temperatures, but this boundary shifts to about 3 GPa close to the solidus (Fig. 7.1). Globally, plagioclase lherzolite is extremely rare. Garnet lherzolite is more abundant in kimberlites, and spinel lherzolite is more common in alkali basalts that are found in continents and ocean islands (e.g., Hawaii). (*Question: Why is plagioclase lherzolite uncommon in most continental settings? Under what circumstances could plagioclase lherzolite form beneath continents?*)

As stated in Table 7.1, geochemists use the terms *primitive, undepleted, depleted*, and *enriched* to refer to how much basalt magma can be potentially extracted from a given lherzolite source as can be ascertained from various geochemical indicators. In general, earth's original silicate mantle is thought to be chemically broadly similar to carbonaceous chondritic meteorites. The terms "primitive" and "undepleted" are used to indicate a mantle that has not lost any magma. Many authors equate such terms to a chondritic mantle or chondritic mantle reservoir. A "depleted source" refers to a source that has lost some amount of its magmatic components.

Experimental petrologists have in the past used such terms as "least depleted" or "undepleted" peridotite to describe a peridotite that has olivine of composition $Fo_{87–88}$ and about 15–20 % modal clinopyroxene. Thus, harzburgite, which has little or no clinopyroxene, is a depleted peridotite. In general, clinopyroxene–olivine modal ratio is an effective indicator of the degree of depletion of a peridotite. Figure 7.2 shows why this is so based on assumed invariant melting of lherzolite at 1.5 GPa. Although melting of a natural peridotite is not invariant at any pressure, however, this is a good simplistic assumption here because the residue mode is not significantly affected by the non-invariant behavior. As melt forming at the invariant point is extracted, the residue gets depleted in clinopyroxene, and the residue eventually turns into a harzburgite (i.e., ol + opx). Further melting will drive the melting path up the cotectic ol + opx + Liq, as the solid residue becomes depleted in orthopyroxene; and eventually the residue becomes a dunite (see Fig. 7.2 inset). (It is generally thought that melting in most cases inside the earth does not proceed beyond the lherzolite stage.) Therefore, as shown in Fig. 7.3a, the lower the clinopyroxene–olivine modal ratio, the *more* depleted is the source peridotite.

We learned in Chap. 3 that olivine becomes progressively more magnesian (i.e., greater Mg–Fe ratio) as the lherzolite becomes more depleted (Fig. 7.3a). Comparison between model OIB source mantle and DMM (depleted MORB mantle) in Table 5.5 shows that the abundance of incompatible trace elements, such as La, Ce, Rb, and Sr, is lower in the depleted mantle source that is calculated for the mid-ocean ridge basalts. Similarly, Na and Ti, two well-known incompatible minor elements, are also depleted in the depleted source.

In the 1980s, F.A. Frey and others noted that mantle-derived xenoliths do not always exhibit a strong correlation between major element depletion, isotopic depletion, and trace element depletion. Some exhibit long-term depletion in terms of long half-life isotopes of Sr, Nd, and yet they are enriched in incompatible elements, such as the LREE (Fig. 7.3b). This dichotomy can be best explained if the elemental enrichment happened a short time before the depleted mantle rocks were picked up by the host magmas so that their depleted isotope ratios were unaffected although the incompatible trace elements were reset. The term "*mantle metasomatism*" refers to such phenomenon.

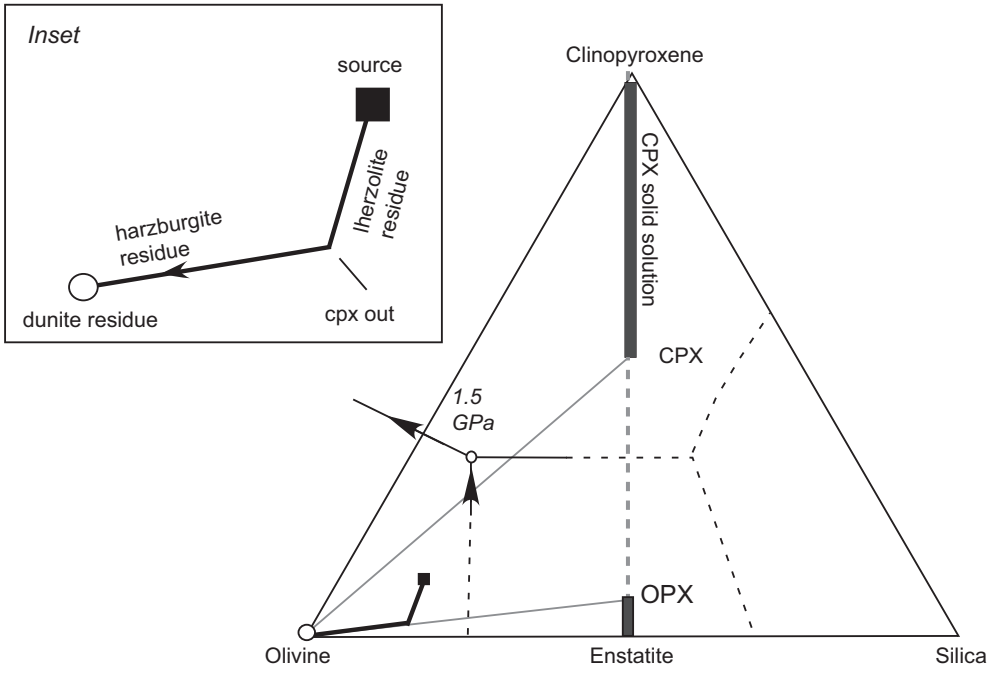

Fig. 7.2 This diagram illustrates the melting relationships of natural lherzolite at 1.5 GPa, as presented by Stolper (1980). The ol + cpx + opx saturated melt is located at the *dot where lines with arrows* (the three cotectic lines meet). The coexisting solid phases are shown by the three-phase triangle connecting olivine–OPX–CPX. It is important to note that the pyroxenes show extensive solid solution. The path described by the solid residue of melting a starting lherzolite, shown as *square*, is also shown. The *inset* is an expanded version of this solid path, schematically showing that progressive melting of lherzolite will first result in harzburgite (ol + opx) residue, and then, with even more melting, dunite (all olivine) will result

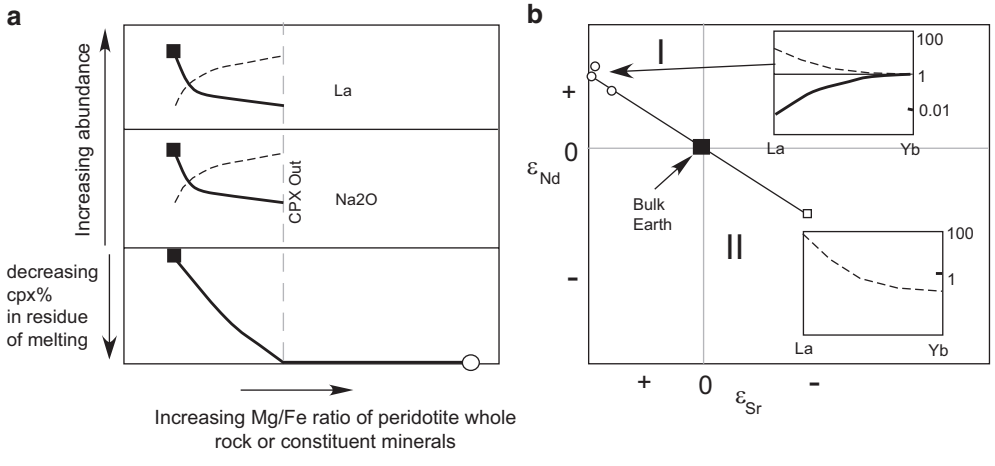

Fig. 7.3 (**a**) These schematic variation diagrams illustrate compositional and modal changes (*bold lines*) in lherzolite that result from melting and melt extraction. Metasomatism subsequent to melting results in enrichment (*dashed lines*) in incompatible elements, such as Na and La. (**b**) Nd–Sr diagram showing the isotopic effect of long-term depletion and enrichment. Quadrant I is where isotopically depleted (i.e., long-term depletion) mantle would plot. Real upper mantle rocks plotting in this field may show LREE depletion (*dark line*; *upper inset*) relative to a chondritic composition (*straight line*), reflecting that it is a truly depleted rock. Some upper mantle rocks plot in Quadrant I but show LREE-enriched pattern (*dashed line*). In this case, such a rock has been very recently enriched in LREE, thus preserving the old depletion record via Nd and Sr isotopes, which have very long half-lives. Quadrant II is where lherzolitic rocks that have been enriched over a long time would plot. The isotope ratios and REE pattern (*dashed line* in *lower right*) of such a rock should both record such depletion

The general belief is that deep-seated fluids passing through the mantle carry such elements and re-enrich the wall rock lithosphere in such elements through magma–wall rock reaction. In some cases such enrichment is accompanied by the crystallization of hydrous or carbonate phases, such as amphibole, phlogopite, and calcite, and in other cases such minerals do not occur. The term *modal metasomatism*

refers to the case where new mineral forms and *cryptic metasomatism* refers to the elemental enrichment process in which new minerals do not form.

Eclogite and Garnet Pyroxenite Sources

Eclogite and garnet clinopyroxenite are both composed of garnet and clinopyroxene. Kyanite, sillimanite, ilmenite, and other rare very high-pressure minerals, e.g., coesite and diamond, occur in eclogite; however, these minerals do not occur in garnet clinopyroxenite. In the case of Hawaii, garnet clinopyroxenite occurs as xenoliths in alkaline lavas and are found to contain, in addition to garnet and clinopyroxene, variable amounts of olivine, orthopyroxene, spinel, phlogopite, amphibole, ilmenite, magnetite, and sulfides.

Chemically, there is hardly any difference between eclogite and garnet clinopyroxenite; and in terms of magma generation, both rocks behave similarly in terms of magma composition and magma production rate. However, their melting behavior sharply contrasts that of lherzolite. For the purpose of our discussion that follows, we will consider both eclogite and garnet clinopyroxenite under the umbrella of the "eclogite source."

Below we consider how primary basalt magmas may form from lherzolite and eclogite sources in the mantle and then examine the results of experimental melting studies of such rocks. We already have a good idea of how the melt and residue compositions change in peridotitic systems with pressure and degree of melting from our examination of simple but relevant systems diopside–forsterite–silica and anorthite–forsterite–silica in Chap. 4. Broadly, these findings are consistent with the results from studies of natural rocks, which are described below.

Experimental Petrology: lherzolite Melting

Pioneering experimental studies in the 1960s by D.H. Green and A.E. Ringwood of the Australian National University on synthetic lherzolitic starting materials (which they called "pyrolite") showed that basalt magma forms by moderate degrees (<30 %) of melting of lherzolite in absence of volatiles such as CO_2 and H_2O. They also showed that magmas generated at low pressure (approx. <0.8 GPa) are quartz-normative tholeiites and with higher pressures magmas become increasingly olivine normative. Green and coworkers subsequently developed a "petrogenetic grid" for basalts, in which they delineated the pressure– temperature fields where various basaltic magmas are generated.

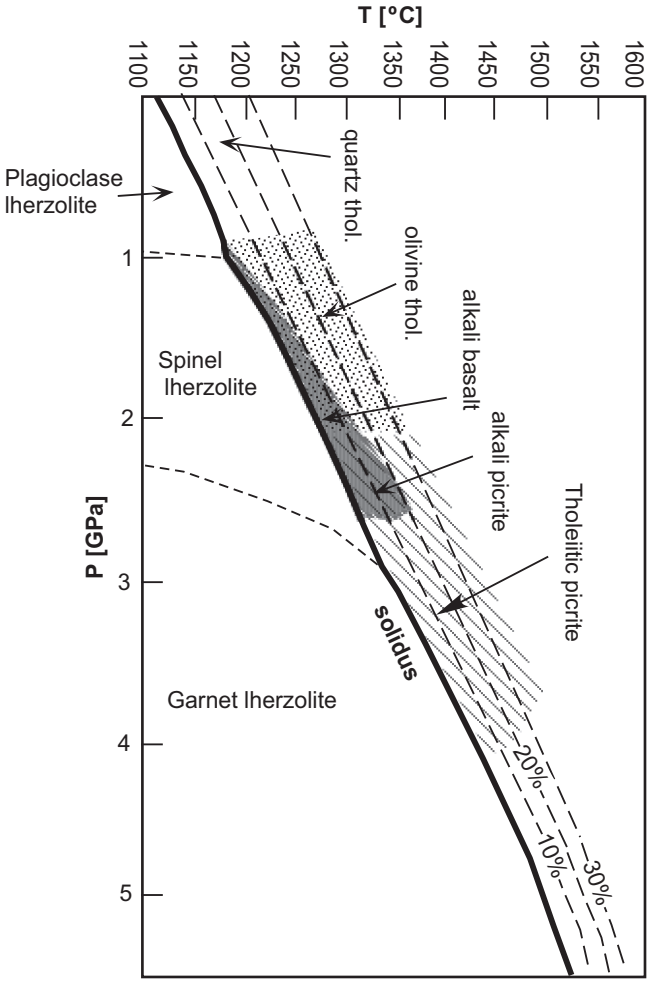

Fig. 7.4 Schematic phase diagram for lherzolites showing how composition of the liquid changes with pressure. The *dashed lines* exhibit % melting

Figure 7.4 shows a petrogenetic grid that is based on data from many older (up to early 1990s) experimental petrologic studies including those of Green and coworkers. It shows in an overall broad sense how magma composition changes as a function of both pressure (depth) and temperature (degrees of melting). For example, at a pressure of about 1.5 GPa (45 km deep), alkali basalt magmas will be produced by low degree of melting ($F < 10$ %) closer to the lherzolite solidus. Olivine tholeiite basalt magma will be generated at higher degrees of melting ($F > 10$ %) at the same pressure. Similarly, at pressures of less than 1 GPa (~30 km), the melts will be quartz normative, and at more than 1 GPa, the melts will have olivine in the norm.

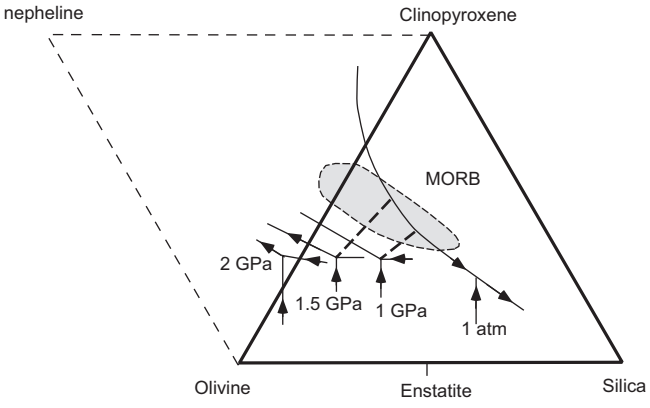

Fig. 7.5 This diagram shows how the composition of melt saturated with ol + opx + cpx becomes progressively olivine-normative tholeiite with increasing pressure from 1 atm to 1.5 GPa. At 2 GPa, the melt is nepheline normative (i.e., alkalic). The field for MORB is shown. The two *bold dashed lines* show fractionation paths followed by melts generated at 1 and 1.5 GPa and brought up to a near-surface magma chamber. Observing that the MORB field does not overlap lherzolite-saturated invariant points at any pressure, Stolper concluded that MORBs are not primary magmas but are all differentiated

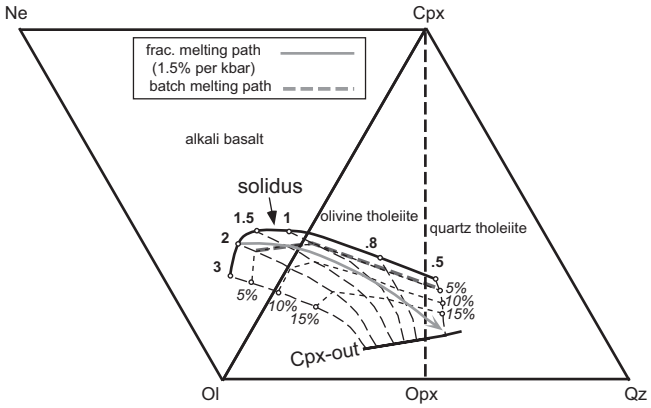

Fig. 7.6 Lherzolite phase diagram (redrawn from Takahashi and Kushiro 1983) showing that isobaric melting is not invariant over the pressure range of 0.5–3 GPa (see text for further discussion)

Magma Compositions as a Function of Pressure (*P*) and Degree of Melting (*F*) Under Volatile-Absent Conditions: Parameterization of Experimental Data

Subsequent experiments by many scientists have not altered two of the broad but nonetheless important conclusions reached by Green, Ringwood, and others: (1) Magmas become progressively more MgO-rich and SiO_2-poor (i.e., olivine-rich) with pressure, and (2) it is possible to generate alkalic and tholeiitic magmas from the same lherzolite by different degrees of melting.

Until about 1983, it was generally believed that lherzolite melts at a "pseudoinvariant point" (see, e. g., the 1, 1.5, and 2 GPa points in Fig. 7.5; Stolper 1980) defined by the confluence of liquidus fields of all the minerals present in the lherzolite, much like isobaric melting at an invariant point (eutectic or peritectic: Chaps. 3 and 4) in a simple two- or three-component system. We have seen earlier (Fig. 7.3) how invariant melting at 1 GPa produces harzburgite residue. Takahashi and Kushiro (1983) demonstrated that the liquid composition *does* change as melt% increases *even at a constant pressure*: for example, each long dashed curve for a particular pressure in Fig. 7.6 represents the four-phase melting curve (i.e., ol + opx + cpx + liq). According to this diagram, primary alkalic (i.e., nepheline-normative) magmas can be generated by low% melting of lherzolite at a pressure of $\geq$1 GPa. With increased amount of equilibrium melting, the melt composition changes to olivine tholeiite as soon as it crosses into olivine–clinopyroxene–orthopyroxene triangle.

An important problem is that all melting experiments on natural peridotites up to 1992 were equilibrium experiments in which large amounts of melts (~10–15 %) were made to equilibrate with the source rock; however, McKenzie (1984) pointed out that such melting process is inappropriate for the upper mantle because it is unlikely for basalt magmas to remain in the source region once they reach about 3 % of the mass of the original starting lherzolite. Johnson et al. (1990) and Yang et al. (1998) later verified McKenzie's hypothesis with trace element modeling of oceanic peridotites; however, the details of their arguments are beyond the scope of this book. It became clear that a quantitative understanding of the genesis of basalt magmas must rely on high-quality experimental data on the chemical composition of near-solidus (melt% <3) melts as a function of pressure (*P*), temperature (*T*), and degree of melting (*F*). As we discussed in Chap. 4, liquid paths for fractional melting and equilibrium melting are likely to be drastically different. To illustrate further the difference between near-fractional and batch melting process, we estimate the melt composition paths for both processes for a rising and decompressing mantle parcel that begins to melt at 2 GPa (Fig. 7.6). The two liquid paths are clearly distinct.

Experiments to reproduce near-fractional melting have been attempted in several laboratories with limited success. The available data are inadequate to

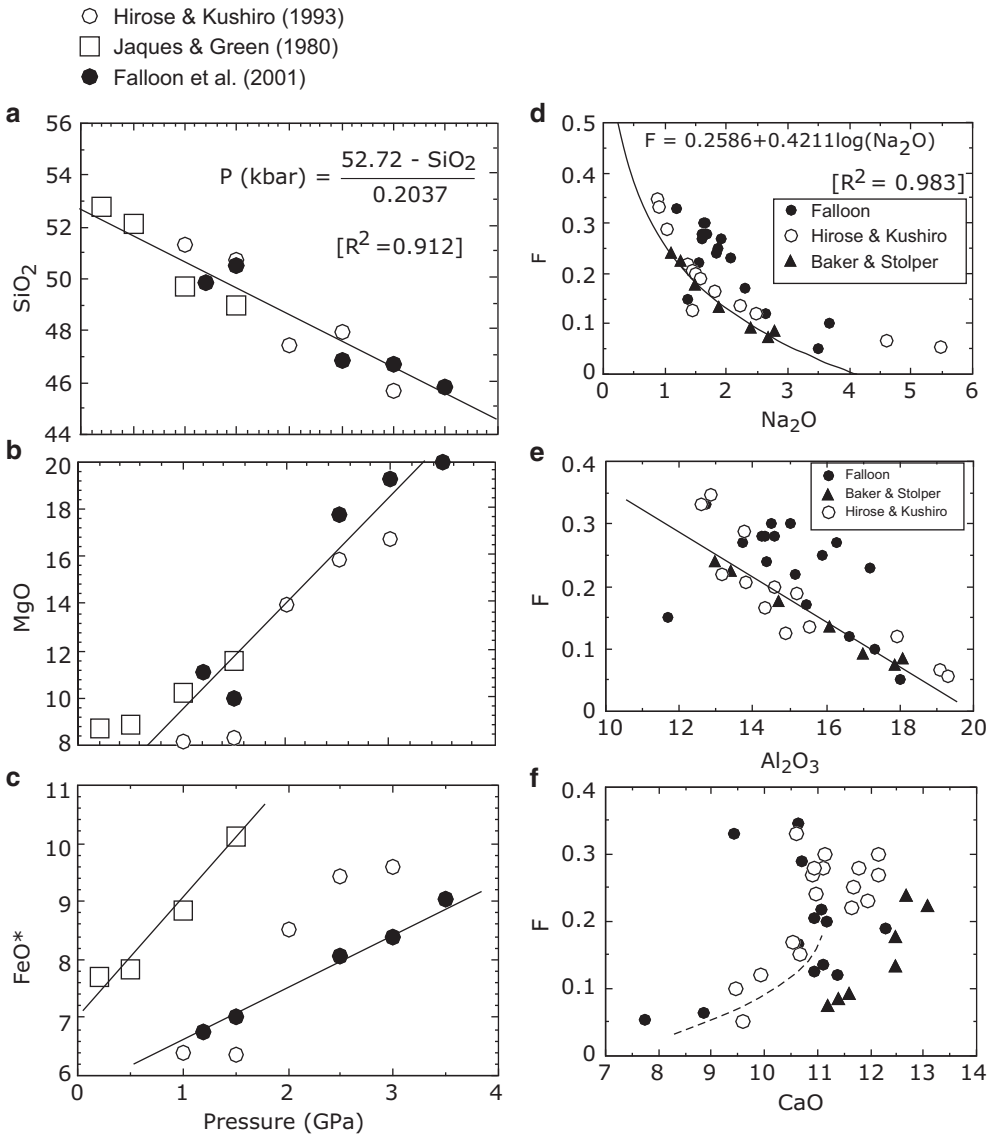

Fig. 7.7 Compositions of melts saturated with lherzolite in three different experimental studies (Jaques and Green 1980; Falloon et al. 2001; Hirose and Kushiro 1993) are shown. (**a**), (**b**), (**c**) Show how melt composition varies with pressure. (**d**), (**e**), and (**f**) Show how the compositions vary with degree of melting or *F*. The important point is that even though different lherzolite starting material was used in the three studies, some of the correlations are strong enough such that one can develop equations, which may in turn be used to calculate, for example, pressure or degree of melting from composition of primitive lavas or melt inclusions in phenocrysts. See text for further discussion

develop thermodynamically sound equations that can solve for any composition at any temperature and pressure range of interest. This has forced many researchers to seek alternative empirical and semiempirical methods to relate *P–T–F* of upper mantle lherzolites. Perhaps the best known among these is the thermodynamically based, MELTS software that is available on the web (http://melts.ofm-research.org/). The basic idea (as I understand it) is to relate *P*, *T*, and *F* of coexisting phases based on the available experimental data while requiring the Gibbs energy to be at a minimum for an appropriate reaction.

Results from some laboratory melting experiments on peridotite are plotted in Fig. 7.7 in order to illustrate how composition (i.e., wt% abundance of individual elements) of basalt magma changes with pressure and degree of melting of peridotite when the melt% does not exceed 15 % by mass of the source rock. Figure 7.7a shows that silica content of these melts is negatively correlated with pressure regardless of the starting

peridotite composition. This strong pressure dependence can be quantified with the following equation:

$$P(\text{GPa}) = [52.72 - \text{SiO}_2(\text{wt}\%)] \div 2.037$$

Thus, SiO_2 (wt%) of basalt magmas makes an excellent barometer. Similarly, MgO increases with pressure can be a potential barometer as well (Fig. 7.7b). Although FeO is also sensitive to pressure, its abundance is affected by bulk composition of the source peridotite (Fig. 7.7c). Wood and Turner (2009) recently evaluated some newer experimental data on lherzolite melting and showed that alkalis ($Na_2O + K_2O$) have a systematic effect on MgO and SiO_2 contents of the melts (Fig. 7.7). The alkali contents of common upper mantle lherzolite vary little such that the best-fit lines shown in Fig. 7.7 should be good enough for first-order melt composition barometry.

Na (and Ti) behaves as an incompatible element and prefers melt to the solid residue. Therefore, during partial melting of lherzolite, Na_2O content of the partial melts is the highest at extremely low % melting (i.e., near the solidus) and decreases as more melt is generated (Fig. 7.7d). In fractional melting, the Na_2O decrease in melt is more spectacular than in batch melting because the source gets rapidly depleted in Na_2O as melts are continuously extracted from the source. While this overall behavior of Na_2O is not disputed, the actual Na_2O contents of the lowest melt fractions at different pressure values remain controversial because of the difficulties in assessing the composition of experimental melts. The other problem is that it is significantly controlled by bulk composition of the source lherzolite: for example, a lherzolite with the greater Na_2O content will yield melt with higher Na_2O than one with lower Na_2O.

Al_2O_3 content of the melt appears to be mainly affected by the degree of melting: it decreases with increasing partial melting (Fig. 7.7e). CaO's behavior is little more complex (Fig. 7.7f). CaO of the melt increases with increasing degree of melting as long as clinopyroxene remains in the residue.

Several authors have used this type of approach but have added semiempirical thermodynamic parameters to come up with barometers and thermometers for natural basalts, that is, they have developed algorithms to calculate pressure– temperature of formation of basalt magmas from their chemical compositions. The following are examples of such thermobarometric equations developed by Lee et al. (2009):

$$T(\text{K}) = 916.45 + 13.68(\text{Mg}_4\text{Si}_2\text{O}_8) + [4580/(\text{Si}_4\text{O}_8)] - 0.509(\text{H}_{16}\text{O}_8)(\text{Mg}_4\text{Si}_2\text{O}_8)$$

$$P(\text{GPa}) = \frac{\ln(\text{Si}_4\text{O}_8) - 4.019 + 0.0165(\text{Fe}_4\text{Si}_2\text{O}_8) + 0.0005(\text{Ca}_4\text{Si}_2\text{O}_8)^2}{-770T^{-1} + 0.0058T^{1/2} - 0.003(\text{H}_{16}\text{O}_8)}$$

In the above equations Si_4O_8, $Fe_4Si_2O_8$, etc. are mol % of these various chemical "species" (the reader should read Lee et al. 2009 for additional information).

A note of caution seems appropriate here. If an erupted basalt lava has undergone differentiation, magma mixing, and contamination processes, then it is likely that such processes have altered its geochemistry sufficiently so that one cannot deduce its depth and temperature of origin in the mantle by using algorithms such as those above. Researchers working on basalts from a specific geographic area most commonly use an "inverse" method whereby they start with the most primitive (highest MgO), glassy or aphyric compositions, with a few or no olivine crystals; and then they numerically add appropriate equilibrium olivine compositions (i.e., while maintaining equilibrium K_d value for ol/liq (FeO/MgO) = 0.3) in small steps (say, 1 % olivine added at a time to the melt composition) until they obtain a melt composition that would be in equilibrium with the mantle-like olivine (e.g., Fo_{88}). Such researchers take the calculated composition to be the composition of the primary magma and then use appropriate algorithms and or software (such as MELTs) to calculate *P–T* of origin.

Effect of CO_2 and H_2O on Melting of Lherzolite

The function of CO_2 and H_2O, the two most abundant volatile components in the upper mantle, is to depress the solidus of the mantle lherzolite (Fig. 7.8a)—H_2O lowers the solidus a little more than CO_2, particularly at lower pressures. Their effects on composition of the melts generated near the solidus are also very different. Briefly, high relative abundance of H_2O tends to generate more silicic melts (andesitic to high-alumina basalt magmas of convergent plate margins: discussed in a later chapter). On the other hand, CO_2 tends to make magma compositions more alkalic. The presence of both CO_2 and H_2O can generate alkali basalts at relatively low to moderate pressure (~1.1–2.5 GPa), nephelinite and carbonatite magmas at moderate pressure (~2.5–3.5 GPa), and kimberlitic melts at much higher pressure (>4 GPa: Fig. 7.8b).

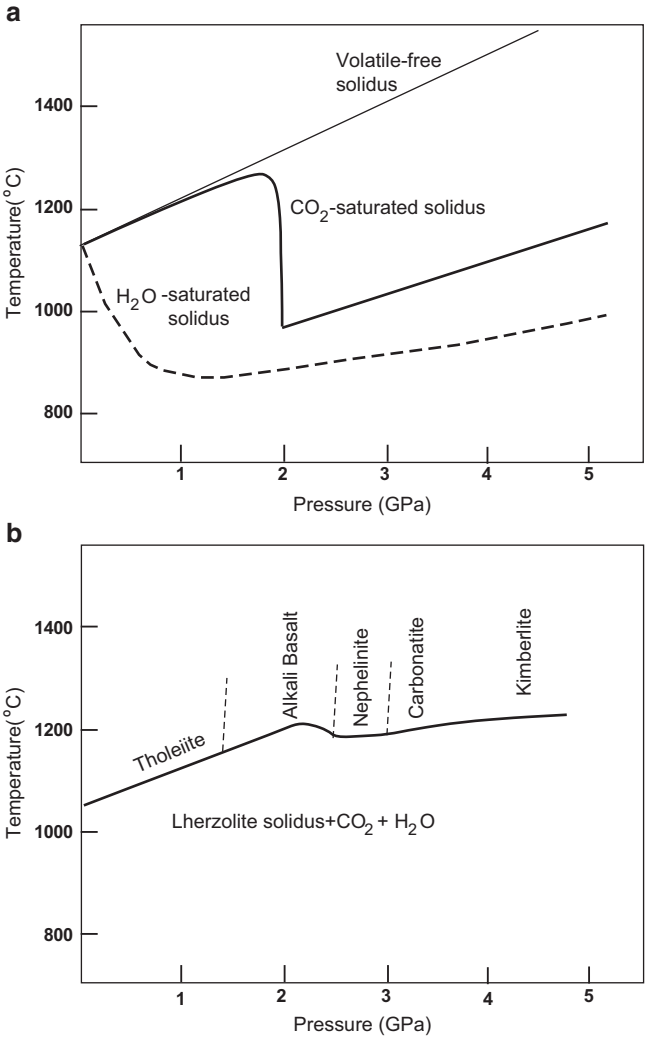

Fig. 7.8 (**a**) Volatile-free solidus of lherzolite is compared with CO_2- and H_2O-saturated solidi (based on Wyllie 1978). (**b**) Composition of magmas generated from lherzolite in presence of vapor (CO_2 + H_2O) at various pressures

garnet–clinopyroxene plane continues to play an important role in discussions of basalt magma generation or crystallization at high pressure (say, 3 GPa). O'Hara (1968b) and others more recently have suggested that at 3 GPa pressure, the garnet–clinopyroxene plane acts as a divide ("eclogite divide") between two invariant points (*p* and *e* in Fig. 7.9c)—one being silica-rich (*e*) and other alkalic (*p*). Therefore, relatively silica-rich eclogite that plots on the right-hand side of the divide would begin to melt at *e*, yielding silicic melts; and alkalic melts would form at *p* from silica-poor eclogites (rather, garnet clinopyroxenites).

The concept of an eclogite divide has been contested by Milholland and Presnall (1998) based on their experiments in the simplified basalt (called *haplobasalt* by N.L. Bowen) system CaO–MgO–Al_2O_3–SiO_2 (CMAS) system at 3 GPa (Figs. 7.10 and 7.11). In Figure 7.10, the eclogite + liquid plane is represented by the gt + cpx + L plane. The compositional plane gar–cpx–opx is also shown here in an effort to highlight the geometrical relationship between the two planes. In the four-component system the eclogite + liquid plane is divariant (the student can calculate the variance from the phase rule); and the important thing is, although not easily apparent in Fig. 7.10, that the gar + cpx + opx plane falls further to the left of the eclogite + liquid divariant surface such that upon crystallization of gar + cpx assemblage, the liquid will always evolve away from the gar + cpx plane; that is, the gar + cpx plane does not act like a divide. Figure 7.11 illustrates this a little better because here the gar–opx line (which is a trace of the gar–cpx–opx plane in Fig. 7.10) falls outside of the gar + cpx + liq (i.e., eclogite +liq) divariant surface. If the gar + px surface were a thermal divide, then it would have cut through the eclogite + liquid surface.

Eclogite Melting

Compositional Variation and the "Eclogite Divide"

Hirschmann et al. (2003) showed that mantle eclogites vary widely in composition in terms of a projection onto the plane CaTs (or Ca-Tschermaks, $CaAl_2SiO_6$)–Mg_2SiO_4–SiO_2 within the CaO–MgO–Al_2O_3–SiO_2 (CMAS) system (Fig. 7.9a, b). Figure 7.9b shows the actual tetrahedron and the location of the CaTs–Mg_2SiO_4–SiO_2 plane, and Fig. 7.9a shows the projected compositions in the plane. The

Melting Characteristics

Hirschmann and others have shown that solidus of an eclogite that is similar in chemistry to typical MORB is 100–200° lower than that of peridotite at 2–4 GPa (Fig. 7.12a). The partial melting contours in Fig. 7.12a also show that the eclogite could be almost 60 % melted by the time it reaches the solidus of lherzolite. Figure 7.12b compares the calculated degree of melting (*F*, expressed as a mass fraction of the source rock) of both peridotite and eclogite at a constant pressure of 3 GPa. It shows that the eclogite will be 60 % molten when the peridotite just starts to melt

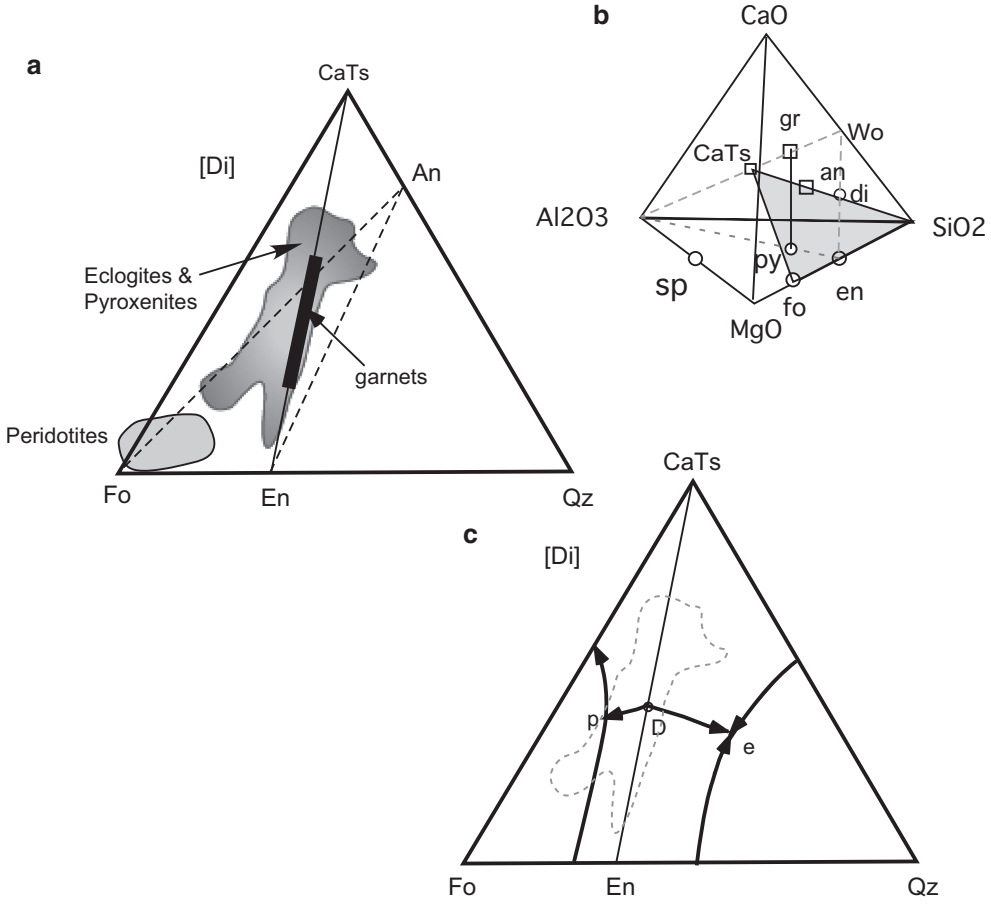

Fig. 7.9 Garnet pyroxenite and eclogite melting. (**a**) Compositions of global garnet pyroxenites, eclogite, and peridotites are shown (projected) in terms of normative Fo–Qz–CaTs (Ca-Tschermaks component, $CaAlAlSiO_6$). (**b**) The CaO–MgO–Al_2O_3–SiO_2 tetrahedron showing the actual nature of the triangular diagram in (**a**). (**c**) Phase diagram for garnet–pyroxene assemblages at 3 GPa showing that CaTs–pyroxene (En) line [which is the trace of the pyroxene plane—see (**b**)] is a divide that has an invariant point "*O*." Starting materials to the *left* will melt at the invariant point "*p*" and those on the *right* of CaTs–En will melt at "*e*"

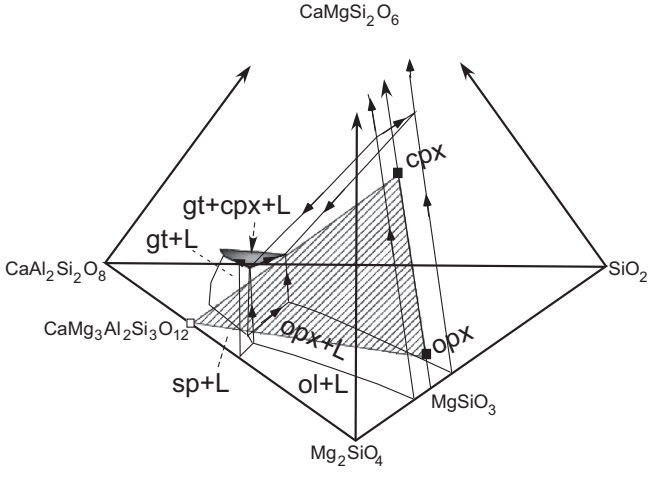

Fig. 7.10 Actual phase relationships of the four-component system. The eclogite + melt [plane is shaded (gt + cpx + L)]. The *arrows* show direction of melt movement upon cooling and crystallization. The "eclogite plane" in this four-component system as the ruled plane. Garnet composition is fixed at $CaMg_3Al_2Si_3O_{12}$. (From Milholland and Presnall 1998)

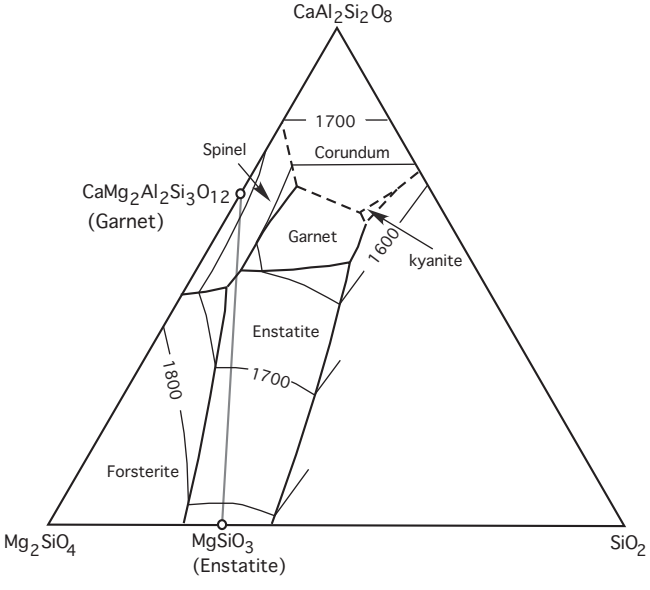

Fig. 7.11 The 3 GPa phase relations are highlighted here as a projection on to the plane $CaAl_2Si_2O8$–Mg_2SiO_4–SiO_2 plane. (From Milholland and Presnall 1998)

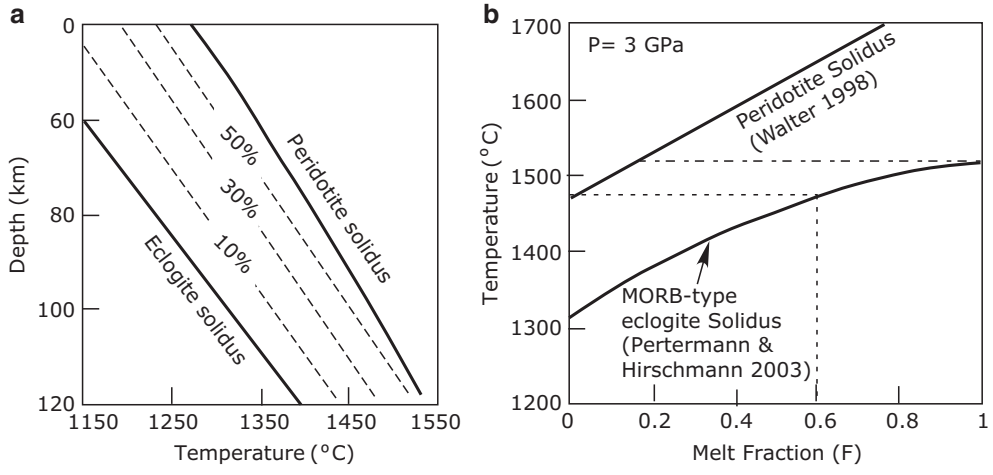

Fig. 7.12 (**a**) Solidi of eclogite and peridotite are compared. (**b**) Partial melt percentages in the supersolidus region of eclogite are shown along with peridotite solidus

and the peridotite will be about 17 % molten when the eclogite will be fully molten. This melting behavior of eclogite relative to peridotite has motivated some scientists to propose that eclogite is the dominant or even sole source for voluminous flood basalt provinces (Takahashi et al. 1998). This could be a plausible hypothesis in basaltic provinces where convincing arguments for a differentiation origin of the basalts cannot be made.

Summary

1. The source rock for basalt magma is lherzolite, the dominant upper mantle rock. Melting experiments on this rock in absence of volatiles show that low-degree melts are quartz tholeiite at <0.6 GPa and olivine tholeiite at 0.6–1 GPa. At 1–2 GPa, the near-solidus melts are likely to be *ne* normative changing to olivine tholeiitic or picritic at higher degrees of melting. At ~2 GPa, the near-solidus melts are picritic.
2. Recent laboratory experiments on lherzolite melting show that SiO_2 and Al_2O_3 contents of basalt magma can be good indicators of pressure and degree of melting, respectively. Because magmas are pooled over a range of pressures, it is possible to obtain a mean depth of magma formation and fraction of melting from the aggregate magma composition.
3. When lherzolite is partially melted in the presence of volatiles, CO_2 makes the initial magma composition more alkaline, whereas H_2O makes it more silica-rich.
4. Algorithms have been developed to calculate magma composition as a function of pressure and degree of melting. These are useful in modeling the petrogenesis of basalt magmas.

Basaltic Magmatism at Mid-Oceanic Ridges and Hawaiian Hot Spot

8

Abstract

Basalts occur everywhere—from divergent and convergent plate boundaries to hot spot volcanic chains and major flood basalt provinces. In this chapter, petrological characteristics of Mid-Oceanic Ridge Basalts (MORB) and Hawaiian basalts are discussed. We will explore what such characteristics tell us about their modes of origin.

Mid-Oceanic Ridge Basalts

Igneous activity beneath the entire length of the earth's 65,000-km mid-oceanic ridge system continuously adds new materials to the crust (Fig. 8.1). The ridge axis is not continuous and is offset by transform faults, or ridge segments along their length may overlap each other (Overlapping Spreading Center or OSC, Fig. 8.2). International Ocean-Drilling Program (and its predecessors, Deep-Sea Drilling Project and Ocean Drilling Program) has imaged, mapped, and sampled the ocean floor over several decades. Parallel studies of ophiolites, which are interpreted to be slices of the oceanic lithosphere obducted onto continents, have also been carried out (see Box 8.1). Studies of ophiolites and ocean floor basalts have together contributed much to our understanding of the igneous and tectonic processes that form the oceanic crust.

The oceanic crust is dominantly basaltic (in fact, tholeiitic). It has become a common practice to refer to them as *MORB* (acronym for Mid-Oceanic Ridge Basalts). MORB are chemically and isotopically heterogeneous along the entire length of the global ridge system, which appear to signify a complex set of magma generation and transportation processes and tectonic forces that shape the oceanic lithosphere.

The general petrologic characteristics of MORB are as follows:

1. Most MORB are *olivine- and hypersthene-normative* tholeiites and very few are quartz or nepheline normative. The most primitive, aphyric, or glassy (i.e., not enriched with xenocrysts) MORB contain ~9 % MgO. Extremely differentiated iron- and titanium-rich basalts (so-called Fe–Ti basalts) occur in some places, most particularly, the Galapagos rift.
2. Petrographically, these basalts may be glassy to phenocryst-bearing and moderately crystallized types. Phenocryst crystallization sequence is generally as follows: *olivine* (most primitive olivine ~Fo_{91}) ± *chrome-spinel* → *olivine* + *plagioclase* (most primitive ~An_{90}) ± *spinel* → *plagioclase* + *augite* (e.g., Hess 1989).
3. Trace element composition of MORB varies greatly, but the vast majority of *normal* MORB (*NMORB*) erupted at *normal* ridge axes (not influenced by hot spots or plumes) are characterized by LREE-depleted (chondrite-normalized) patterns (Fig. 8.3). There are MORB that are enriched in LREE and are called enriched MORB or *EMORB* (Fig. 8.3). EMORB are much less voluminous than NMORB and are chemically somewhat similar to basalts from hot spots, e.g., Hawaii.
4. NMORB are characterized by "depleted" $^{143}Nd/^{144}Nd$ isotopic compositions (and Sr, Pb, and He isotopic systems as well) relative to that of the *undifferentiated* or *bulk* earth (i.e., if the earth did not differentiate into crust, mantle, and core: Fig. 8.4). These REE and isotopic characteristics of N-MORB are generally interpreted to be due to their derivation from a source upper mantle layer (=convecting asthenosphere) that has been depleted in LREE and other strongly incompatible elements over the 4.6 billion year history of the earth. The extracted elements have been added to the continental crust.

G. Sen, *Petrology*, DOI 10.1007/978-3-642-38800-2_8,

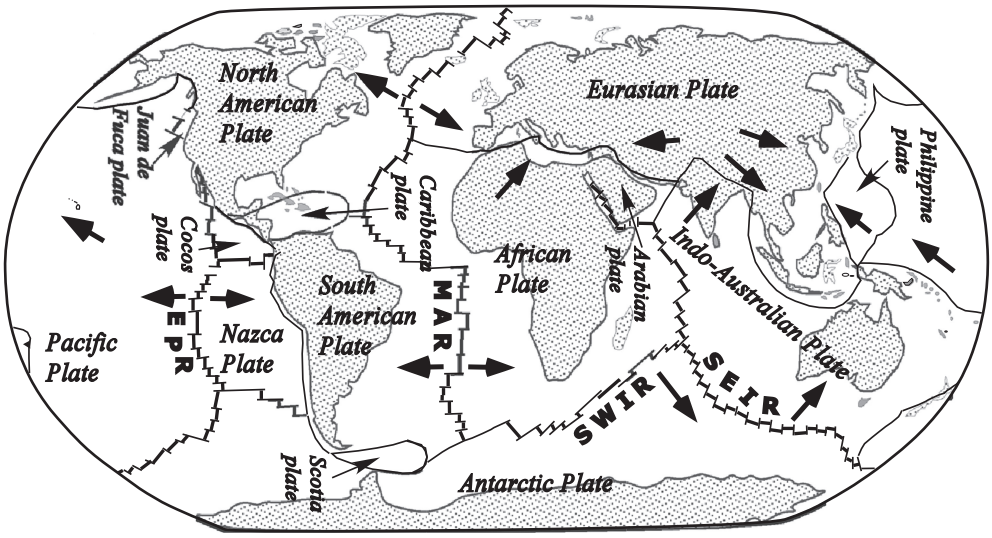

Fig. 8.1 Global oceanic ridge system

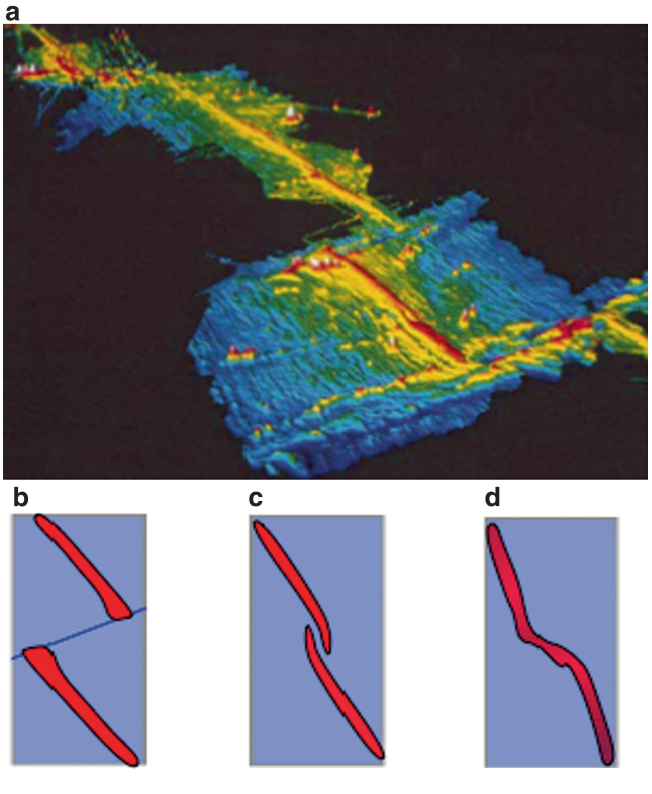

Fig. 8.2 (**a**) "Shaded relief map of a 1,000-km stretch of the East Pacific Rise extending from 83 to 173 N. Here, the East Pacific Rise is the boundary between the Pacific and Cocos plates, which separate at a 'fast' rate of 110 mm/year. The map reveals two kinds of discontinuities: large offsets, about 100 km long, known as transform faults and smaller offsets, about 10-km long, called overlapping spreading centers. Colors indicate depths of from 2,400 m (*pink*) to 3,500 m (*dark blue*)." [*Quoted verbatim from Fig. 2b in K.C. Macdonald (2001) Mid-ocean ridge tectonics, volcanism and geomorphology: in Encyclopedia of ocean sciences (eds. J. Steele, S. Thorpe, K. Turekian), Academic Press, pp. 1798–1813*] (**b**) Sketch showing a ridge axis offset by a large transform fault. (**c**) Overlapping spreading center. (**d**) Continuous ridge axis with a small bend

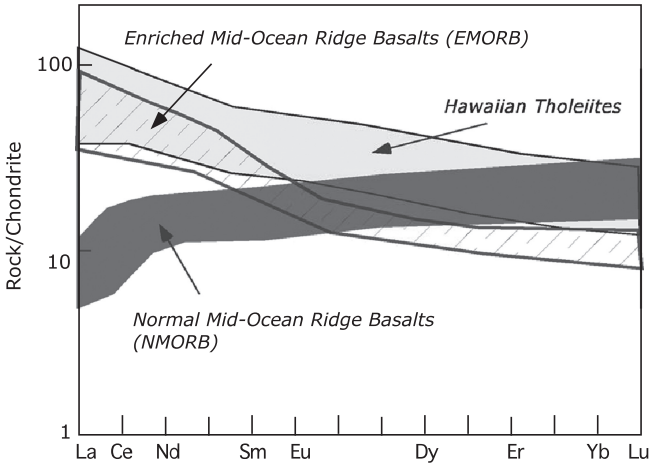

Fig. 8.3 Comparison of rare earth element patterns (chondrite-normalized) in Hawaiian tholeiites, NMORB, and EMORB

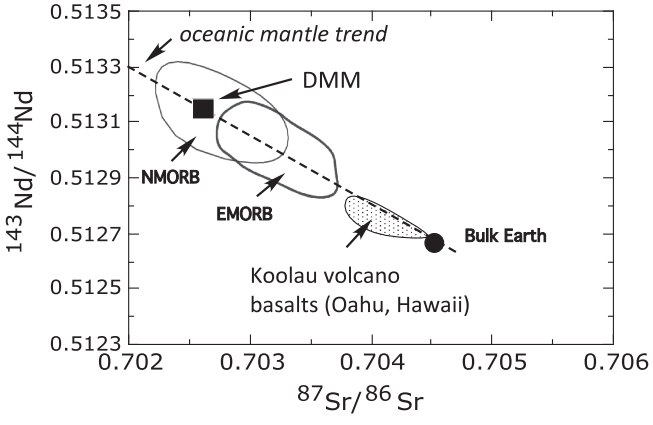

Fig. 8.4 Nd–Sr isotope ratio diagram showing the compositions of the depleted MORB mantle (DMM) and the bulk earth sources. It compares NMORB, EMORB, and tholeiitic basalts from the Koolau volcano (Oahu, Hawaii)

EMORB are somewhat less depleted than NMORB (Fig. 8.4) and are therefore generally considered to tap a deeper mantle that also serves as the source for mantle plumes, such as those that feed the Hawaiian basalts. There is considerable mixing of these magmas at shallow crustal and upper mantle levels, which explain the compositional range shown by MORB. The long half-life isotopes of Nd, Sr, and Hf thus lend considerable credence to the existence of a strongly depleted shallow upper mantle layer (i.e., asthenosphere) that feeds the global oceanic ridge system and to the existence of mantle reservoirs that may be more primitive (have not seen much loss of materials to continental crust) or more mixed—with sources coming from various levels in the mantle and perhaps from old, broken up subducted slabs.

Ridge Topography, Spreading Rate, and Magma Chamber

Seismic and gravity data indicate that the crust of the normal ocean floor is about 6–8 km thick. However, beneath Iceland, which is located on the mid-oceanic ridge axis in the North Atlantic and which continues to be volcanically quite active, the crust is unusually thick (14–25 km; Fig. 8.5). Based mainly on isotope and trace element geochemistry of the lavas, it is thought that the coincidence of a somewhat wet plume may be the cause of excess magma production and hence the anomalously thick crust. Seismic evidence shows that the mantle transition zone is 20 % thinner beneath Iceland, which has been interpreted to be due to a hot spot that is rooted at least in the transition zone (Shen et al. 1998).

The oceanic crust can also be 18–25 km thick beneath oceanic plateaus that are located far away from an active mid-oceanic ridge, e.g., Ontong-Java plateau in the Pacific Ocean. It is generally believed that such thick plateaus were created by excessive volcanism due to hot spot activity. Some basaltic plateaus in the oceans may have a more complex origin, such as the Kerguelen plateau in the Indian Ocean. Isotopic evidence shows that there are buried continental crust beneath Kerguelen Islands, which are interpreted to be left over fragments from Gondwana supercontinent breakup (Frey et al. 2002).

The topography of the mid-oceanic ridge varies considerably from place to place and correlates with spreading rate (Table 8.1). In slow-spreading (half-spreading rate <22 mm/year) areas of Mid-Atlantic Ridge (MAR), an axial graben or rift valley occurs at the ridge axis bounded on both sides by topographic highs formed by block faulting (Fig. 8.6a). In fast-spreading (half-spreading rate ~ 50–60 mm/year) areas, e.g., the East Pacific Rise (EPR), such axial rift valleys and highs are almost inconspicuous, and only a broad, gentle topographic swell is seen (Fig. 8.6b). Also, the water depth is shallower above a fast-spreading ridge relative to a slow-spreading ridge. Magma supply rate controls the topography of fast- vs. slow-spreading ridges (discussed in a later section).

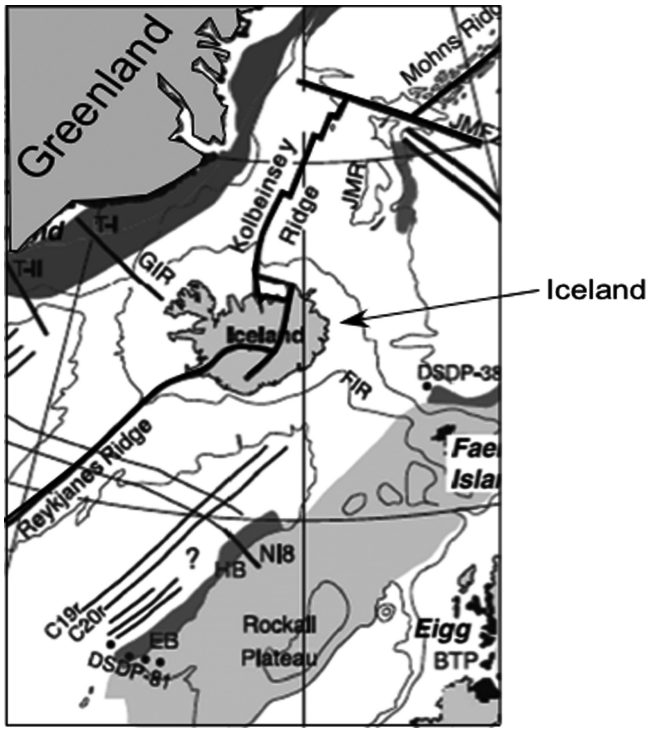

Fig. 8.5 Location of Iceland over the mid-oceanic ridge. The excessively thickened crust of Iceland is attributed to added magma supply from a hot spot or wet spot

Seismic studies indicate the presence of ten to hundreds of meters high and 1–2 km wide melt lens beneath the fast-spreading EPR. Such perennial melt lens does not occur beneath any slow-spreading ridge, where magma supply is believed to be intermittent.

Figure 8.7 compares the compositional fields of basalts from the EPR (fast spreading) and MAR (slow spreading) with liquid lines of descent (LLD) at different pressures. These curves were calculated from experimental data (Herzberg 2004). The critical difference to note between EPR and MAR basalts is that the EPR field is stretched out along the L + Ol + Pl + Aug portion of

Table 8.1 Comparison between fast-spreading and slow-spreading ridges

	Fast-spreading ridges	Slow-spreading ridges
Half-spreading rate	Fast spreading: >50 mm/year; intermediate spreading: 22–50 mm/year	Slow spreading: 10–22 mm/year; ultraslow spreading: <10 mm/year
Bathymetry	Water depth shallower (~2 km) relative to slow-spreading rate	Water depth ~2–3 km
Topography	Relatively smooth, broad arched topography	Well-defined axial valley and ridge structures
Associated transform faults	Longer transforms	Shorter transforms
Seismic velocity structure	Perennial melt sills/lenses present	Melt bodies not easily detectable
Chemical variability	Wider range in terms of MgO indicative of shallow mixing, homogenization, and fractionation	Shorter and more primitive range of MgO and greater scatter in CaO and other elements, suggesting melts erupting from a wider depth range without mixing with each other
Implication of chemical and seismic investigations	Magma "processing" in permanent or semipermanent shallow magma "lens"	No single perennial melt lens processes all the melts that erupt; thus melts from a wider depth range are represented
	The mantle electromagnetic and tomography (MELT) experiment over the equatorial EPR (fast spreading) inferred that the bottom of melt generation zone occurs around 150 km based on sharp drop in shear wave velocity at above this depth (Langmuir and Forsyth 2007)	

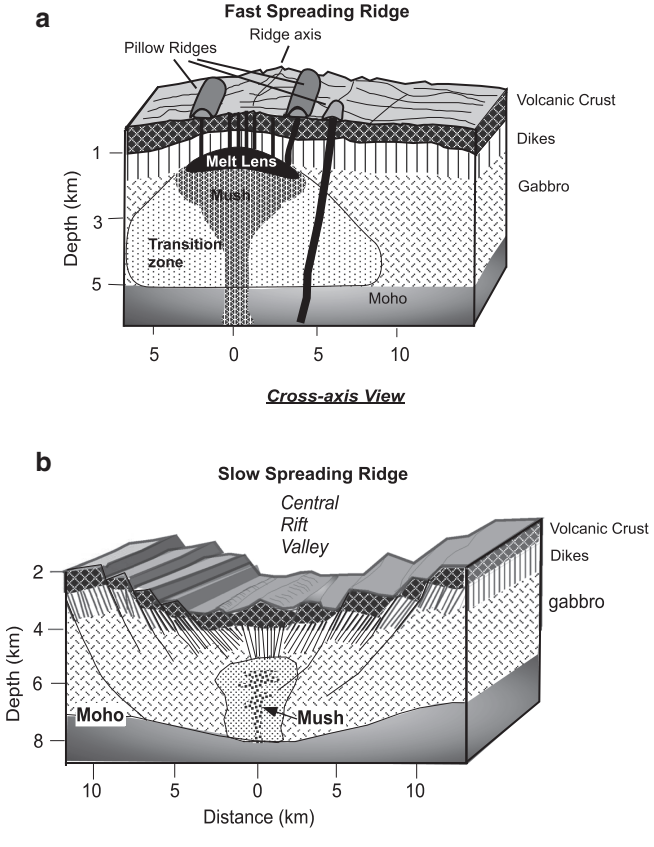

Fig. 8.6 Models of magma chamber and topography in (**a**) fast-spreading ridges (after MR Perfit (2001), "Midocean ridge geochemistry and petrology," Encyclopedia of Ocean Sci., Academic Press) and (**b**) slow-spreading ridges (after JM Sinton and RS Detrick (1992) "Mid-ocean ridge magma chambers," J. Geophys. Res. 97, 197–216)

the 1 atm LLD, whereas the MAR field cuts across LLDs over multiple pressures. These observations led Herzberg (2004) to conclude that erupted melts at EPR must be filtered through a very shallow magma chamber (like the "melt lens" in seismic models) where they undergo mixing and Ol + Pl + Aug or gabbroic fractionation. The MAR basalts do not consistently go through such a fractionation process and thus melts from many different depths are erupted directly on to the ocean floor.

Box 8.1: Ophiolites

An ophiolite is a large (several km^2), dominantly mafic–ultramafic, fault-bounded complex, which is found on continents and considered to be a slice of the oceanic crust and uppermost mantle. The process that is responsible for the emplacement of ophiolite on a continent is known as *obduction*. A complete ophiolite sequence starts with a highly deformed, discontinuous (max. thickness of ~12 km) layer of harzburgite or lherzolite layer at the bottom. This layer is often variably serpentinized and is intruded by large (tens of meters to km-sized) "pods" of dunite and by dunite and gabbroic dikes. This deformed ultramafic layer, often called the "tectonite" layer, is generally inferred to be the mantle portion of the ophiolite from which MORB magmas were extracted. This layer is followed above by layers

(continued)

Box 8.1 (continued)

of ultramafic and gabbroic rocks with cumulate texture. These cumulate ultramafic and gabbro layers are interpreted to have been formed by cumulus process in the bottom portion of a MORB magma chamber.

The cumulate layers are followed above by a large section of gabbro that lacks cumulate texture and is referred to as *isotropic gabbro*. Above the isotropic gabbro occurs the *sheeted dike complex*, which comprises a set of parallel, straight, vertical, or curved dikes. Such dikes are believed to have supplied magma to the overlying crust. Overlying the sheeted dike complex occur *pillow basalts*, which are basalts with a special type of bulbous structure that has the appearance of a pillow. Basaltic crust forming the ocean floor is also characterized by such pillow structure. Scientists have actually observed how pillow basalts form during underwater eruption. Finally, above the pillow basalt layer occurs a thin cherty layer with abundant remains of an organism known as *Radiolaria*. The cumulate layers, isotropic gabbro, sheeted dike complex, the pillow basalt layer, and the radiolarian chert layer together comprise the entire crustal section of an ophiolite. The maximum thickness of the crustal section of an ophiolite is about 9 km.

The Semail ophiolite (Figs. 8.8 and 8.9), located near the coast of Oman and the United Arab Emirates, is perhaps the best example of a well-preserved ophiolite. A series of thrusts have emplaced the ophiolite complex sometime around 92–95 Ma. The base of the ophiolite has a metamorphic sole composed of eclogites, amphibolites, blueschists, and greenschists. The upper mantle section of the ophiolite is 8–12 km thick and composed of deformed harzburgite and dunite with minor pyroxenite, wehrlite, and gabbro–noritic intrusions. The crustal section is 4–7 km thick and is composed of ultramafic and mafic cumulates, isotropic gabbros, trondjhemite, sheeted dikes, and pillow lavas. The uppermost crust is a thin pelagic layer composed mostly of radiolarian chert. Two different hypotheses have been put forth concerning the source of this complex: one is that this crust–mantle section came from a mid-oceanic ridge and the other suggests that the section came from a suprasubduction environment.

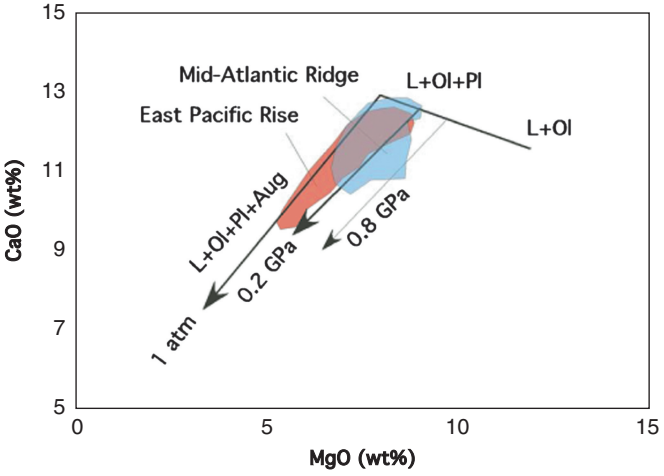

Fig. 8.7 Comparison between EPR (*blue*: fast spreading) and MAR (*orange*: fast spreading) basalts on a MgO·CaO diagram. It also shows LLDs at different pressures (redrawn from Fig. 5 in Herzberg 2004, J. Petrology, v. 45)

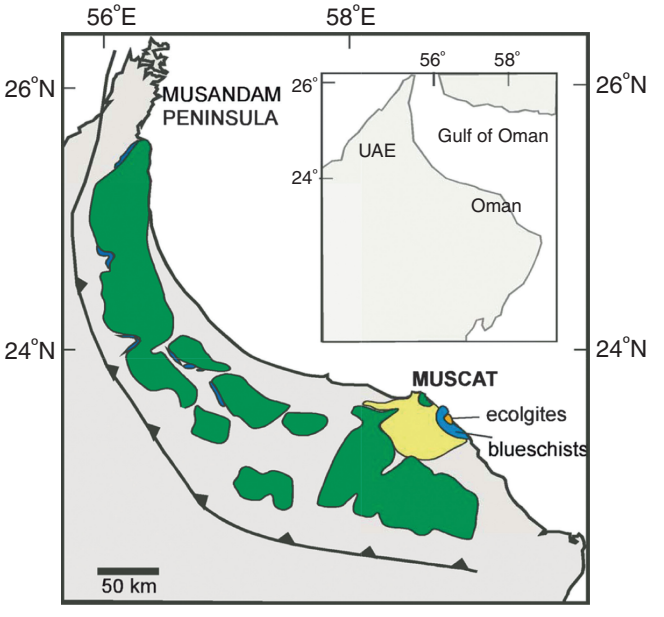

Fig. 8.8 Map of Semail ophiolite

The above observations, combined with lithologic characteristics of ophiolite complexes (see Box 8.1) and gabbroic rocks drilled/dredged from the ocean floor, offer a valuable insight into the nature of the magma "plumbing system" beneath fast- vs. slow-spreading ridges (Fig. 8.6: Perfit 2001; Sinton and Detrick 1992). Common to all spreading ridges is a 0.5-km thick volcanic crust, composed of basalts with pillow structures (Fig. 8.9). This layer is underlain by a *sheeted dike complex*, which serves as the conduit

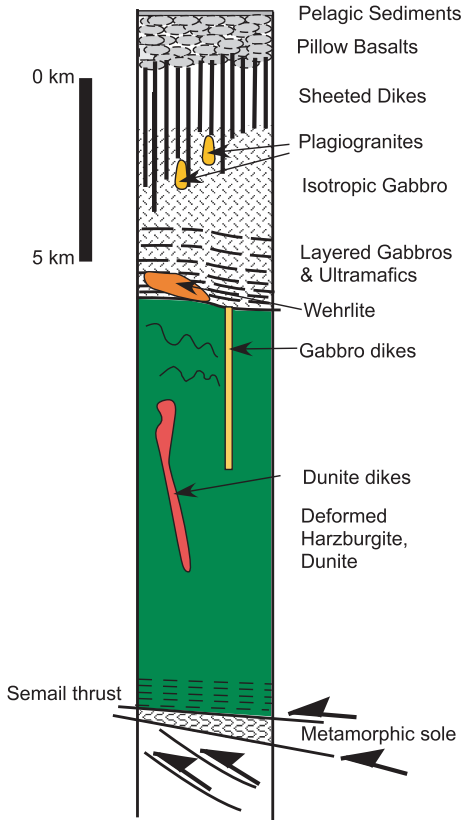

Fig. 8.9 Schematic cross section of the Semail ophiolite

for magma delivery to the shallow crust. In case of fast-spreading ridges, magmatic activity, high heat flow, the presence of a melt lens, and the occurrence of a broad seismic low velocity zone beneath the ridge axis indicate that (a) the melt lens is underlain by a broad region of crystal–liquid "*mush zone*" where some amount of interstitial melt is always present between mineral grains and (b) erupted lavas are processed (i.e., fractionation, mixing) in the melt lens prior to their eruption. The mush zone is surrounded by a "*transition zone*," which is a largely crystallized zone with even smaller amounts of interstitial melt. The transition zone then grades into surrounding, still hot, solidified gabbro. Similar mush and transition zones occur beneath slow-spreading ridges as well. The lack of a perennial melt lens beneath slow-spreading ridges suggests that the magmas that erupt at the ridge axis do not undergo significant fractionation and mixing in a shallow melt lens and therefore retain a stronger signal from their source mantle chemical characteristics. Such a hypothesis is compatible with the following observations from lavas erupted at the slow-spreading ridges (1) greater isotopic and trace element diversity, (2) generally less differentiated compositions of the lavas, and (3) the general lack of textural and compositional characteristics indicative of significant magma mixing. Note that in MORB terminology, the melt lens, mush, and transition zones are all considered to be parts of a complex magma chamber, which is never fully molten (cf. Sinton and Detrick 1992).

Contrasting topography of fast- vs. slow-spreading ridges is also related to their different styles of magma processing and eruption. A commonly accepted model is that the axial rift valley-and-ridge topography of a slow-spreading ridge is controlled by episodes of magma supply (the so-called "waxing" episodes) and of tectonic extension not accompanied by magma supply from below (the so-called "waning" episodes). Waxing of the magma supply system gives rise to axial highs and waning periods lead to magma chamber collapse, block faulting and rotation, and rift valley formation. This type of waxing and waning does not occur beneath a fast-spreading ridge, and the broad swell-type topography is perhaps due to magma chamber buoyancy pushing up broad regions beneath the spreading center. Carbotte et al. (2006) seismically imaged deep-seated melt lens (sill) to occur at 2.1–2.6 km beneath the axial volcanic ridge (AVR) along various segments of the Juan de Fuca ridge. Instead of the intermittent magma supply model controlling ridge topography as outlined above, they proposed a more complex model in which the ridge topography is controlled by magma-induced deformation of the crust by magma supplied from a deep-seated sill or lens via dikes and fault slippage along bounding faults (Fig. 8.10).

Magma Generation at Mid-Oceanic Ridges

Prior to 1987 the debate about the origin of MORBs was centered on whether or not any MORB was primary magma. O'Hara (1968b) championed the idea that MORBs are not primary magmas and are derived, via fractional crystallization and mixing, from MgO-rich (~17–20 % MgO) picritic magmas. On the other hand, Presnall et al. (1979) suggested that MORBs with about 10 % MgO are primary magmas and are generated by 25–30 % equilibrium (batch) melting of the upper mantle peridotite at a relatively shallow depth (~30 km). Strong arguments were made to support both ideas, and there was no middle ground.

McKenzie and coauthors clarified several aspects of MORB magma generation process in a series of publications in the 1980s that have guided completely new line of thinking about MORB magma generation

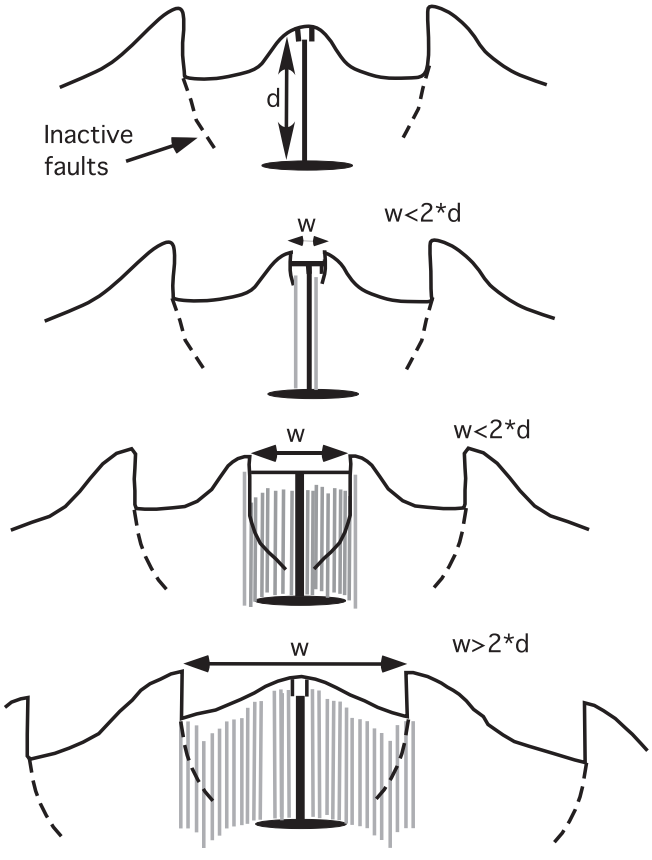

Fig. 8.10 Diking and spreading at the ridge axis (redrawn from Carbotte et al. 2006)

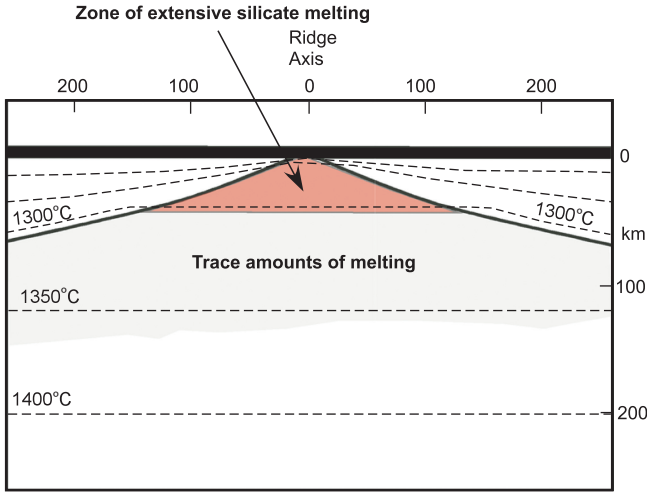

Fig. 8.11 MOR magma generation model as proposed by McKenzie and Bickle (1988)

(McKenzie 1984; McKenzie and Bickle 1988). First, he pointed out that batch melting in the upper mantle, as suggested by Presnall and others, is not possible because compaction would squeeze out small% grain boundary melts, and no more than 3 % melt can remain in the residue. Second, magma is generated beneath mid-oceanic ridges by passive upwelling of the asthenosphere as the lithospheric plates are pulled apart (Fig. 8.11, which is redrawn from Fig. 2b in McKenzie and Bickle 1988). Prior to this, the commonly accepted hypothesis was that ridges are areas of active mantle upwelling in which hot "jets" of mantle material rise to shallow levels and melt. Such a process likely occurs only in areas such as Iceland, where the ridge crust is too thick requiring excess magma production from a hot spot or plume. Third, magma ascends along an adiabatic gradient of about 1 °C/km. Thus, a magma with an initial temperature of 1,300 °C at a depth of 50 km will only lose 50 °C if it erupts without gaining or losing any heat from or to its surroundings. McKenzie and Bickle (1988) introduced the concept of potential temperature, rather than actual temperature at depth, of magma batches with respect to a common reference pressure (atmospheric pressure). It is beyond the scope of discussion here and the interested student is strongly recommended to read that classic paper. Fourth, the new crust that is added to the ridge is the sum of small amounts of melts that are extracted from a much larger volume at depth and not at a single depth, and the melt production zone is triangular in cross section (Fig. 8.11). Fifth, the pooled magma that generates the MOR crust has about 11 % MgO. Interestingly, in their model of ridge magma generation, McKenzie and Bickle (1988) suggested that bulk of the magma generation happens within the top 50 km or so, even though trace amounts of melts likely come from deeper levels due to volatile (H_2O, CO_2)-aided melting.

Using a somewhat different approach, Klein and Langmuir (1987) came up with conclusions that are similar to McKenzie's. They focused on whether chemical composition of the crust along the length of the global ridge system correlates with variation in crustal thickness. In a simple sense, thicker crust = more magma and thinner crust = less magma, because after all crust is created from magma. As we have seen in earlier chapters, magma composition is a result of one or more of the following three factors—composition of the source rock, degree of melting, and depth range of melting. Klein and Langmuir wanted to evaluate whether the composition of global ridge basalts says anything about the deeper processes that cause crustal thickness variation.

Klein and Langmuir (1987) realized that erupted basalts at the ridge crest probably undergo fractionation and mixing prior to eruption and, therefore,

devised a method of filtering out such effects so that the differences could only be attributed to magma generation processes. The data filtering method involved comparing rocks that have reached a comparable degree of fractionation, which they fixed at 8 % MgO (Fig. 8.12). They picked 8 % MgO because basalts with greater MgO only fractionate olivine until they reach 8 % MgO. Figure 8.12 illustrates this by plotting MORB crust compositions from three different ridges with very different crustal thicknesses on MgO vs. Na_2O diagram. Olivine fractionation causes MgO of the basalt magma to decrease and Na_2O to increase because Mg is compatible and Na is incompatible with olivine. Na_2O value at 8 % MgO is referred to as Na_8. Fe_8, which refers to FeO* at 8 % MgO, is computed the same way. Klein and Langmuir (1987) found these two parameters to be useful in unraveling the magma generation processes at mid-oceanic ridges.

In passing, note that each of the three trends shown in Fig. 8.12 is a fractionation trend. Clearly, they were derived from different primary magmas and the difference between the three trends at 8 % MgO should be attributable to differences in the melting processes that created their corresponding primary magmas in the first place.

Na behaves as an incompatible element during partial melting of mantle peridotite, and therefore, Na_2O content of the magma should show an inverse correlation with degree of melting (F): a melt produced by small F will have higher Na content than a high-F melt from the same source peridotite. Since mid-ocean ridge crust is produced from such partial melt accumulations, it follows that basalt at thick (i.e., greater amount of melt) MOR crust should have lower Na_8 than that from a thin crust. Measured values of Na_8 in global oceanic ridges were found to correlate well with the thickness of the crust—thicker the crust, lower the Na_8 value (Fig. 8.13a). Klein and Langmuir (1987) therefore proposed that the negative correlation between and crustal thickness is simply a result of melt production.

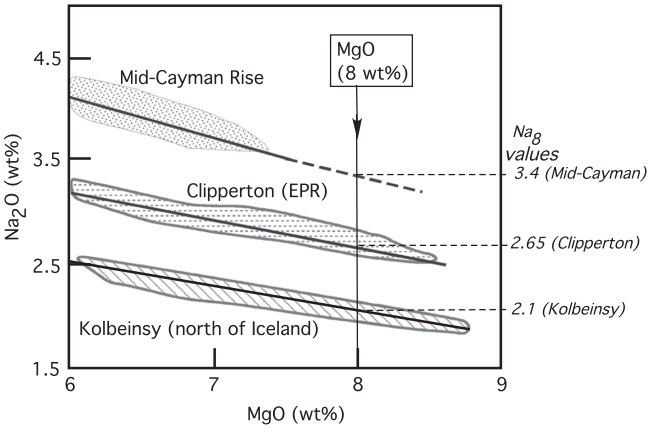

Fig. 8.12 Method of estimation of Na_8 (Klein and Langmuir 1987)

Similarly, Klein and Langmuir (1987) showed that Fe_8 increases with increasing depth of magma generation. Thus, the combination of Na_8 and Fe_8 yields information about the average depth and degree of melting. Figure 8.13b shows the field of global MORB in terms of the two parameters and compares it with partial melting trends at four different pressures (Kinzler and Grove 1992). The global trend is one of a broadly negative correlation between Na_8 and Fe_8, which suggests that the crust is thicker when the average depth of magma production is greater. However, the correlation between Na_8 and Fe_8 from an individual geographic site is at a sharp angle to the global correlation vector or global array for basalts (Fig. 8.13b). Klein and Langmuir and other authors have offered complicated explanations for the local trends, which is beyond the scope of our discussion here.

Klein and Langmuir (1987) pointed out that an initially hotter lherzolite will (1) begin to melt at a deeper level than a cooler lherzolite, as the former would intersect the solidus at a greater depth (Fig. 8.14a, b), and (2) melt over a longer depth range and therefore generate more melt (=more crust; Fig. 8.14b). For example, the model calculations performed by Langmuir et al. (1992) show that the Na_8–Fe_8 variation in the Reykjanes peninsula (thick crust) can be explained with a depth of onset of melting ~120 km (4 GPa), and in the case of Southwest Indian Ocean Ridge, it would be about 75 km. Bathymetry of the mid-ocean ridges is related to crustal thickness, e.g., thicker the crust, shallower the water depth. *Shallow water depth = thicker crust = more magma = hotter mantle adiabat* (*i.e., higher potential temperature*). In short, bathymetric variations along the ridge axis can be viewed as a reflection of variation in mantle potential temperature.

The success of the Klein and Langmuir (1987) model has been astounding notwithstanding its simplistic assumptions in which mantle chemical and modal heterogeneity and volatiles (H_2O and CO_2) are ignored. At face value, this success would suggest that (a) any lithological complexity (such as presence of pyroxenite veins) in the source region or volatiles is of little importance in controlling the volume of magma produced to make the crust, and (b) the magma extraction

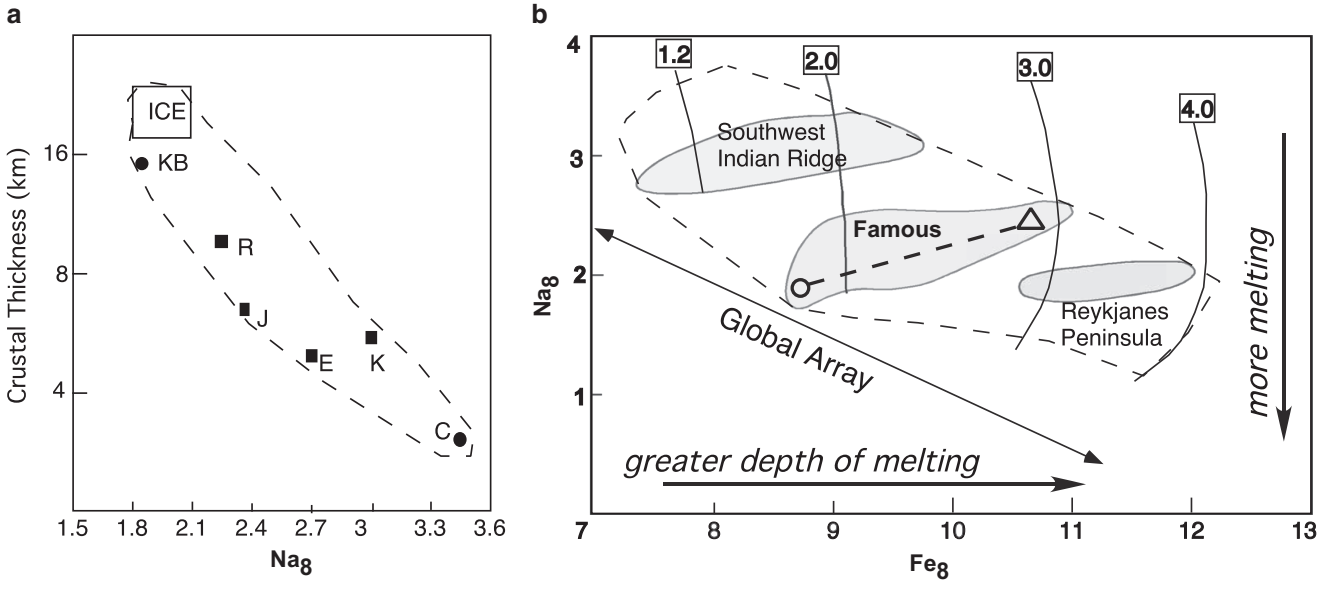

Fig. 8.13 (**a**) Na_8 vs. crustal thickness in global oceanic ridges (after Klein and Langmuir 1987). (**b**) Na_8 vs. Fe_8 in three selected oceanic ridges. Note that the local variation shown by each of these ridges is at an angle with the global trend. The *numbers in boxes* refer to pressure (GPa). At each pressure Na_8 is high at the solidus and decreases with increasing degree of melting (redrawn from Kinzler and Grove 1992)

and focusing process must be extremely efficient and one that preserves the depth signal in the pooled magma. Below we continue to explore these topics.

Langmuir and many other authors have since revisited the issue of primary MORB magma generation by taking into consideration the lithological complexities in the source region and volatiles (H_2O and CO_2). As an example, the upper mantle feeding the mid-oceanic ridges could be heterogeneous in its modal clinopyroxene content, perhaps introduced by streaks and veins of garnet pyroxenite or quartz eclogite, which have a lower solidus than peridotite. Figure 8.14c shows that pyroxenite and quartz eclogite will begin to melt at a deeper level than peridotite beneath a ridge (Dasgupta and Hirschmann 2006). Asimow and Langmuir (2003) examined the effect of H_2O on MORB magma generation in thick vs. thin crust ridges and found it could significantly influence magma generation. They estimated that melting of a peridotite with 750 ppm H_2O could explain the thick crust at Azores (which is considered by some to be a hot spot) relative to normal ridges with the temperature of melting differing only by 35 °C.

Dasgupta and Hirschmann (2006) showed that a carbonated peridotite can start melting at a depth of 300 km and contribute small% melts into MORB crust (Fig. 8.14c). The percentage contribution of melts derived from pyroxenitic lithologies and from volatile-bearing melting of peridotite is unlikely to be significant in controlling the major and minor element composition of the melts; otherwise the models presented by Klein and Langmuir (1987) or McKenzie and Bickle (1988) would not work as well as they do. Interestingly, McKenzie and Bickle (1988) had already anticipated this result, i.e., although trace amounts of deeper melts contribute to MORB, the bulk of MORB magmas are generated from dry peridotites over a shallow depth range (Fig. 8.11).

Magma Extraction

The efficiency of the magma segregation process was investigated in a series of papers by Kelemen and colleagues (e.g., Kelemen et al. 1995; Kelemen 1998; Fig. 8.15). By combining field observations on ophiolites (see Box 8.1), and theoretical studies and experimental simulations, Kelemen and colleagues have shown that the magma extraction process's efficiency and preservation of depth information arise from the fact that magmas travel through dunite channels in the mantle harzburgite (see Box 8.1). Olivine, which makes up more than 90 % of a dunite, has little or no effect on the magma's composition; for example, neither Na_8 nor Fe_8 would be modified through reaction with olivine. Such dunite channels (dikes) are created during porous flow of the melt through the deformed harzburgite. The initial batches

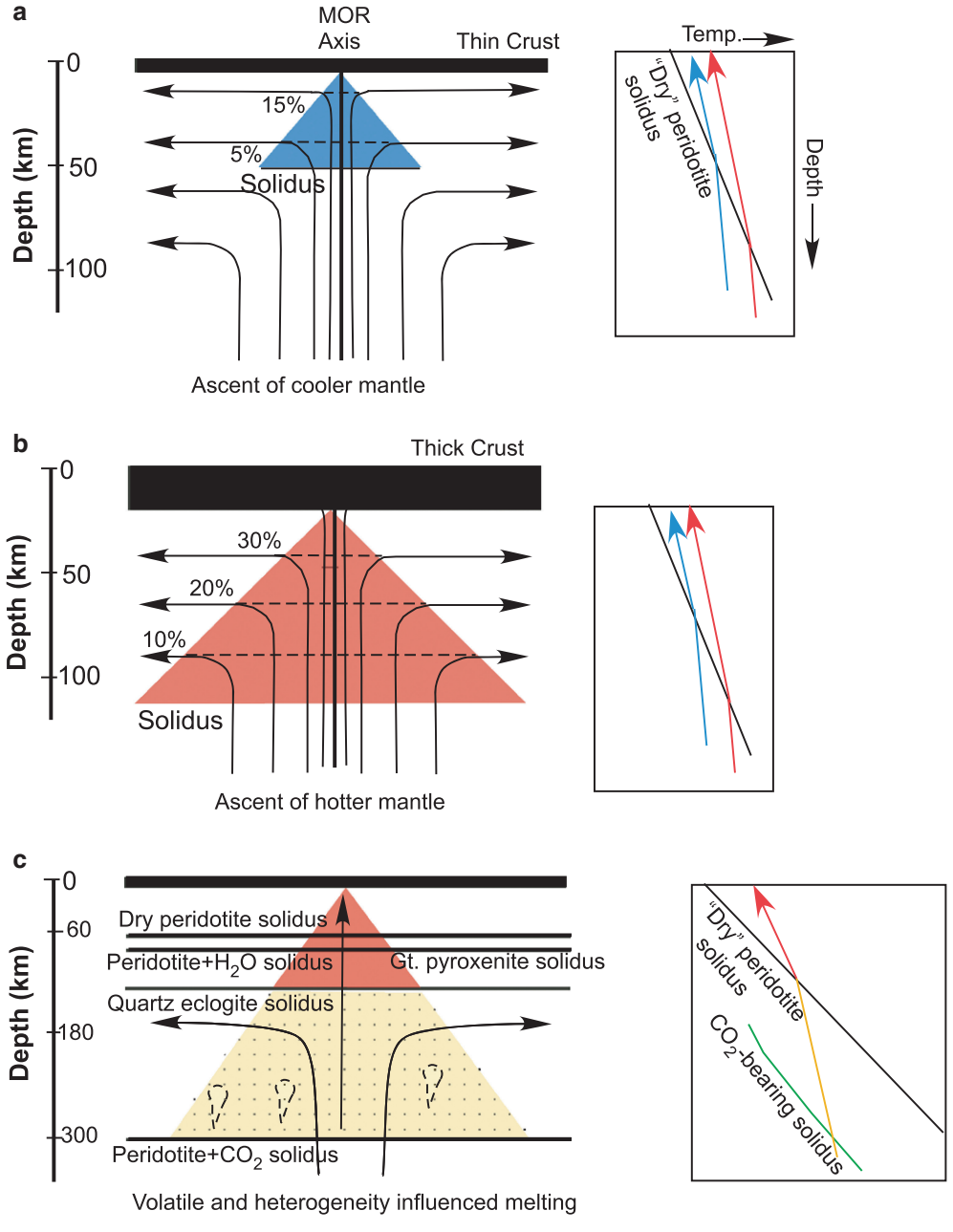

Fig. 8.14 Models of MORB generation. *Panels on the left* show schematically mantle flow lines (*curves with arrows*), partial melting zone (*colored*), the crust (*black*), and the upper mantle (*colorless*). *Panels on the right* depict the *P–T* paths followed in different scenarios presented in the *left panels*. (**a**) Melting in a "cold" ridge: melt volume is small relative to "hot" mantle melting in scenario (**b**). The melting paths of a mantle parcel at the ridge axis in the two cases are compared in the *P–T* diagram. These two diagrams are adopted from Langmuir and Forsyth (2007). (**c**) Melting in a carbonated mantle. *Red area* indicates voluminous melts at shallow depth and *yellow dotted zone* represents carbonate-bearing melts (after Dasgupta and Hirschmann 2006)

of melt created at depth would be unsaturated with the shallower level harzburgite, and as a result the melt batches would react with the wall rock and selectively dissolve orthopyroxene and leave behind only olivine, thus creating a dunite channel (dike). Later batches of melt will simply transit through such channels on the way to forming oceanic crust.

Seismology is the only direct way to detect the presence of partial melt in the mantle and therefore we would be remiss if we do not consider seismological constraints on the depth of MORB magma generation. In this regard, mention must be made of the MELT experiment (mantle electromagnetic and seismic tomography experiment) along a part of the equatorial

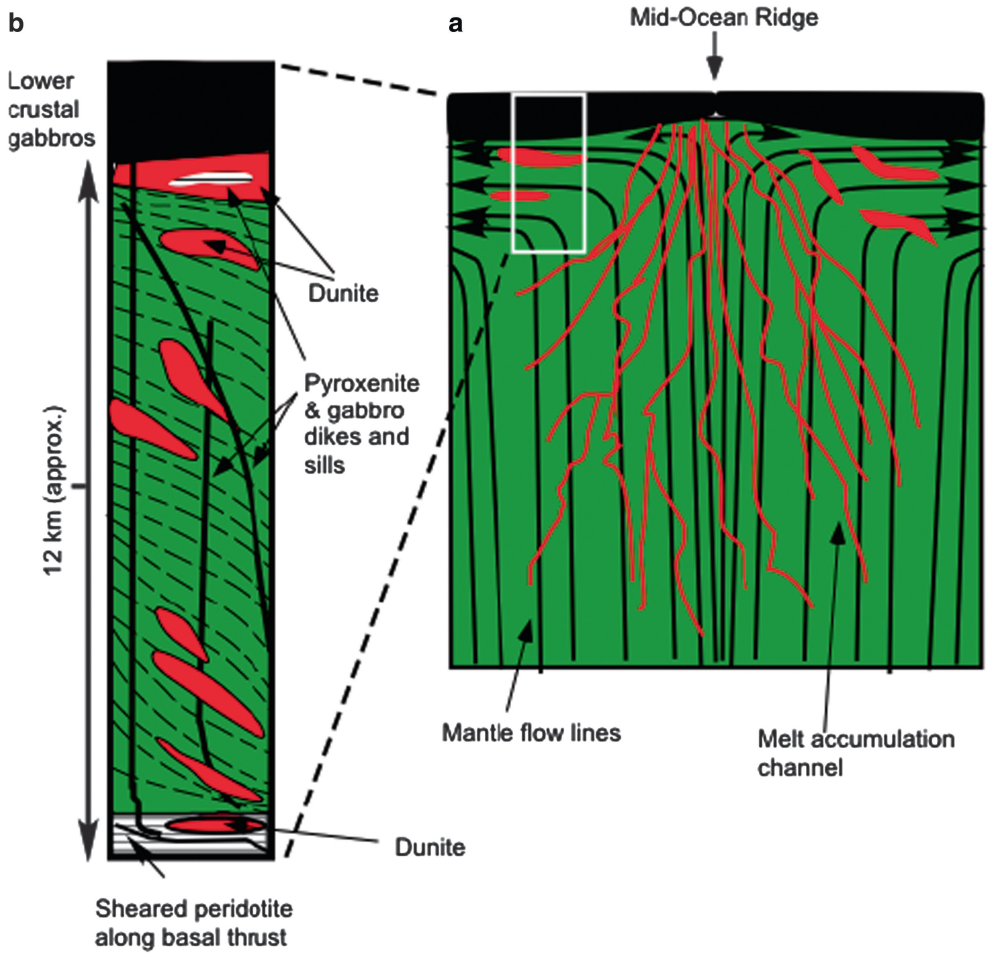

Fig. 8.15 (**a**) Accumulation and transport of magma (partial melts) in channels as they rise toward the mid-oceanic ridge. *Black lines with arrows* are mantle flow lines, which are paths taken by asthenospheric materials beneath a ridge axis (mainly after Kelemen 1998). (**b**) Details of the upper few kilometers are shown here

East Pacific Rise, where the spreading rate is high (i.e., high melt production rate) and transform faults are few (i.e., less complications: Langmuir and Forsyth 2007). The MELT experiment found that the shear wave velocity decreases sharply at a depth of 100–150 km (shear waves do not travel through melt and their velocities are lowered when they travel through partially molten rock), indicating the beginning of melting at such depths.

In sum, the model of magma generation at mid-oceanic ridges, as championed by Kelin and Langmuir (1987) and McKenzie and Bickle (1988), works quite well. They satisfy the constraints from experimental petrology, fluid dynamics, bathymetry, correlation between major element chemistry of the ridge crest basalts and melt production, and experimental petrology.

Based on the above presentation, it should be clear to the student that we have a good understanding of the magma generation and transport processes that lead to MOR crust and oceanic lithosphere formation. However, such processes do not occur in isolation from the physical, chemical, and thermal phenomena that are associated with movement of materials in the mantle. Some recent studies have tried to obtain this wholesome understanding of mantle dynamics, partial melt generation processes, and MORB geochemical variations (Tirone et al. 2012, Physics of the Earth and Planetary Interiors 190–191, 51–70). However, any discussion of Tirone et al.'s work is beyond the scope of this book and the interested student/practitioner is strongly encouraged to read their paper.

Mid-Ocean Ridge Basalts: A Summary

- MOR crust is generally 6–8 km thick. Unusually thickened crust (14–25 km) occurs at Iceland and other

ocean plateaus due to excess magma supply from plumes (hot plume) or wet plume (excess H_2O) activity.
- Slow-spreading ridges (half-spreading rate of <22 mm/year) have a well-defined axial rift valley; whereas such a conspicuous structure is not apparent in fast-spreading (half-spreading rates of 50–60 mm/year) ridges.
- MORB are predominantly olivine- and hypersthene-normative tholeiites.
- Common phenocrysts are olivine and plagioclase.
- N-MORBs are depleted and E-MORBs are enriched in incompatible elements.
- In general, MORB-primary magmas may be generated over a depth range of 120–10 km (which is the base of the crust). The cross section of the melting regime beneath much of the global oceanic ridge system is triangular due to passive upwelling of the mantle.
- A perennial melt lens occurs beneath fast-spreading ridge axes but not beneath the slow-spreading ridges.
- The degree of melting and the depth range of melting are generally related and they together perhaps exert the strongest control on crustal thickness.
- Melt extraction via dunite channels allows efficient delivery of melt to the ridge crest. It also allows preservation of deeper chemical signals in the crustal rocks.

Intraplate Basaltic Volcanism: Hot Spot or Plume Melting

Whereas igneous activities at plate margins are generally well explained by plate tectonics, origin of basaltic volcanism in the middle of a plate, which is often referred to as "intraplate volcanism," has been a subject of much interest. Such volcanism has also been referred to as "hot spot" and "plume" volcanism. Hawaiian volcanic Islands—Emperor Seamount Chain, which occurs in the middle of the Pacific plate, is the most commonly cited example of such igneous activity (Fig. 8.16). Aside from the Hawaiian chain, there are many oceanic islands that have formed by such volcanism (see Chap. 1). The term *Ocean Island Basalts* (*OIB*) has been used to describe the rocks that form such islands. Wilson (1963) first proposed that the Hawaiian chain formed due to "hot spot" volcanism on a migrating lithosphere (Fig. 8.17). Later, Morgan (1971) proposed that the Hawaiian volcanoes and many other intraplate volcanoes are a result of hot, buoyant mantle plumes that rise from the lower mantle. Since that time many researchers have tried to gain an understanding of the behavior of plumes using seismic tomography and laboratory and numerical simulation experiments (e.g., Lei and Zhao 2006; Wolfe et al. 2011).

Over the past few years, the plume theory has come under close scrutiny by a group of scientists whose arguments and references may be found in the Web site http://www.mantleplumes.org. They reject the Wilson–Morgan concept of hot, deep lower mantle plumes and propose instead an alternative model in which such anomalous magmatism is attributed to melting of fertile bodies due to minor temperature variations in the shallow mantle rather than thermal plumes rising from the deep mantle. It is safe to say that the non-plume ideas have not gained enough ground to dislodge the plume hypothesis, and therefore, we shall not consider such ideas any further.

Given the central importance of the Hawaiian volcanic chain in igneous petrology and plume theory, it is important to consider Hawaiian volcanism first. In the next chapter, we will delve into the origin of even more problematic "Flood Basalt Provinces" or "Large Igneous Provinces (LIP)," whose formation is attributed by most scientists to giant mantle plume heads that episodically rise from the core–mantle boundary.

The Hawaiian-Emperor Volcanic Chain

The Hawaiian-Emperor chain starts in the middle of the Pacific plate and extends across the Pacific plate with a sharp bend in the middle (Fig. 8.16). The ocean floor immediately surrounding the Hawaiian volcanoes is bathymetrically shallow due to uplift of the lithosphere and is referred to as the *Hawaiian Swell*. The Hawaiian Swell's maximum height is 1.4 km and full width is 1,500 km. The origin of the swell has been a topic of some debate (as is almost everything else related to Hawaiian plume), but generally speaking, it is believed to have formed due to bottom heating of the migrating lithosphere by the Hawaiian hot spot.

Hawaii, also known as the Big Island, is located at the eastern extreme of the Hawaiian-Emperor chain. This island is home to two major active shield volcanoes—Kilauea and Mauna Loa. These two volcanoes have served as a natural laboratory for the study of shield volcanism and the effect of such volcanism on global climate. Although much of the volcanism appears to occur in the central caldera in both volcanoes, some eruptions occur along long-running rift fractures that radiate out of the volcanoes. The tholeiitic lava flows that form the shield volcanoes are quite fluid and rapidly flow across to the ocean. Besides Kilauea and Mauna Loa, there are three other extinct shield volcanoes that compose Hawaii, namely, Kohala, Hualalai, and Mauna Kea (Fig. 8.16). Kilauea

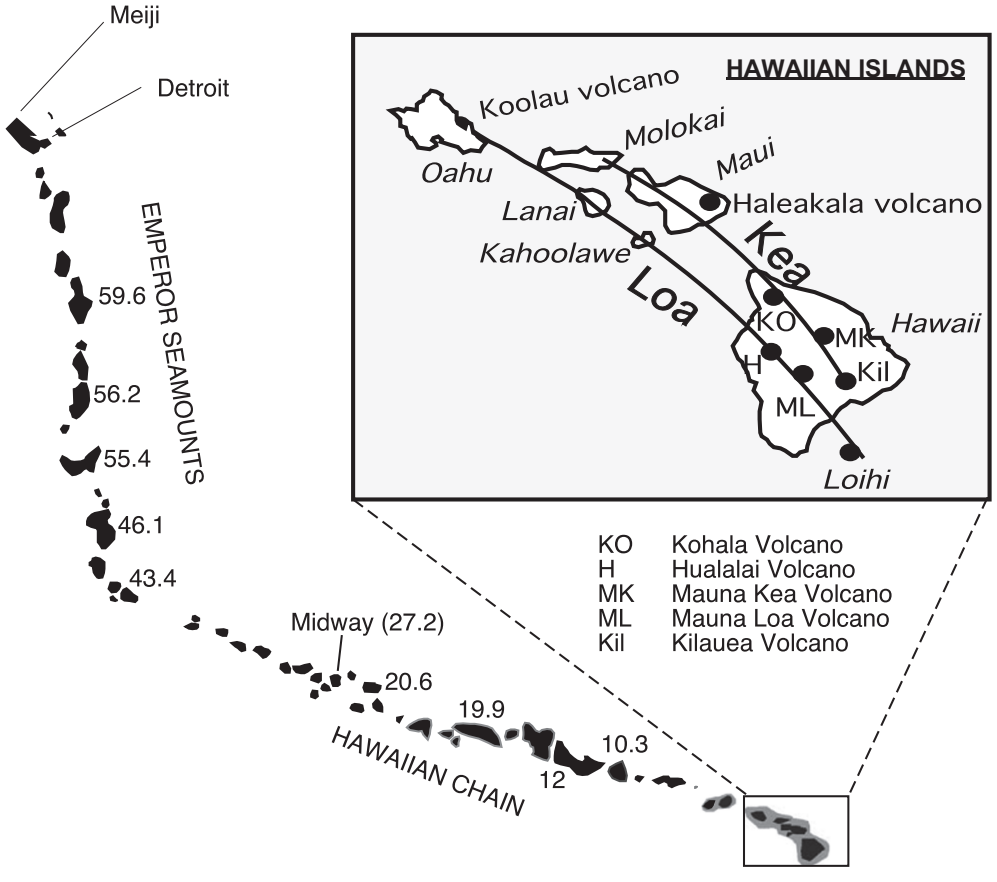

Fig. 8.16 Hawaii-Emperor volcanic chain. The *inset* shows the location of some of the volcanoes and the "Loa" and "Kea" compositional trends

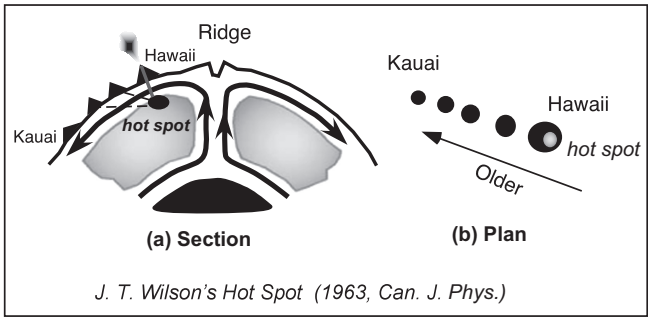

Fig. 8.17 Hot spot model presented by J.T. Wilson (1963) that started an entire new way of thinking about the origin of volcanic island chains in the Pacific

and Mauna Loa are presently erupting tholeiitic lava (i.e., shield stage, discussed later), whereas alkalic lavas (post-shield stage) were last to erupt on the other three extinct tholeiitic shield volcanoes.

Volcanoes of the Hawaiian-Emperor chain get older up the chain toward west–northwest (Fig. 8.16). Radioisotope dating shows a fairly linear age progression as one moves away from Kilauea to Detroit and Meiji seamounts—the two of the oldest members of the Emperor seamount chain. This age progression has been a cornerstone of the hot spot or plume hypothesis because it is exactly what would be expected of fixed hot spot volcanism over a migrating lithosphere. The sharp 60° bend that occurs at about 43 Ma (Fig. 8.16) is thought to be due to a sudden change in the direction of plate movement over a fixed hot spot. However, this fixed hot spot hypothesis has been doubted by a recent study that found two other volcanic chains (Gilbert Ridge and Tokelau seamounts) in the Pacific that show the bends at 67 and 57 Ma (Koppers and Staudigel 2005), indicating that either the hot spot moved or the origin of these bends is rooted in shallow melting processes.

The volcanoes of the Hawaiian-Emperor chain are some of the most extensively studied, and therefore, vast literature exists on this chain. Below is an attempt to summarize this knowledge. It ends with a discussion of plausible models of origin of the Hawaiian volcanoes.

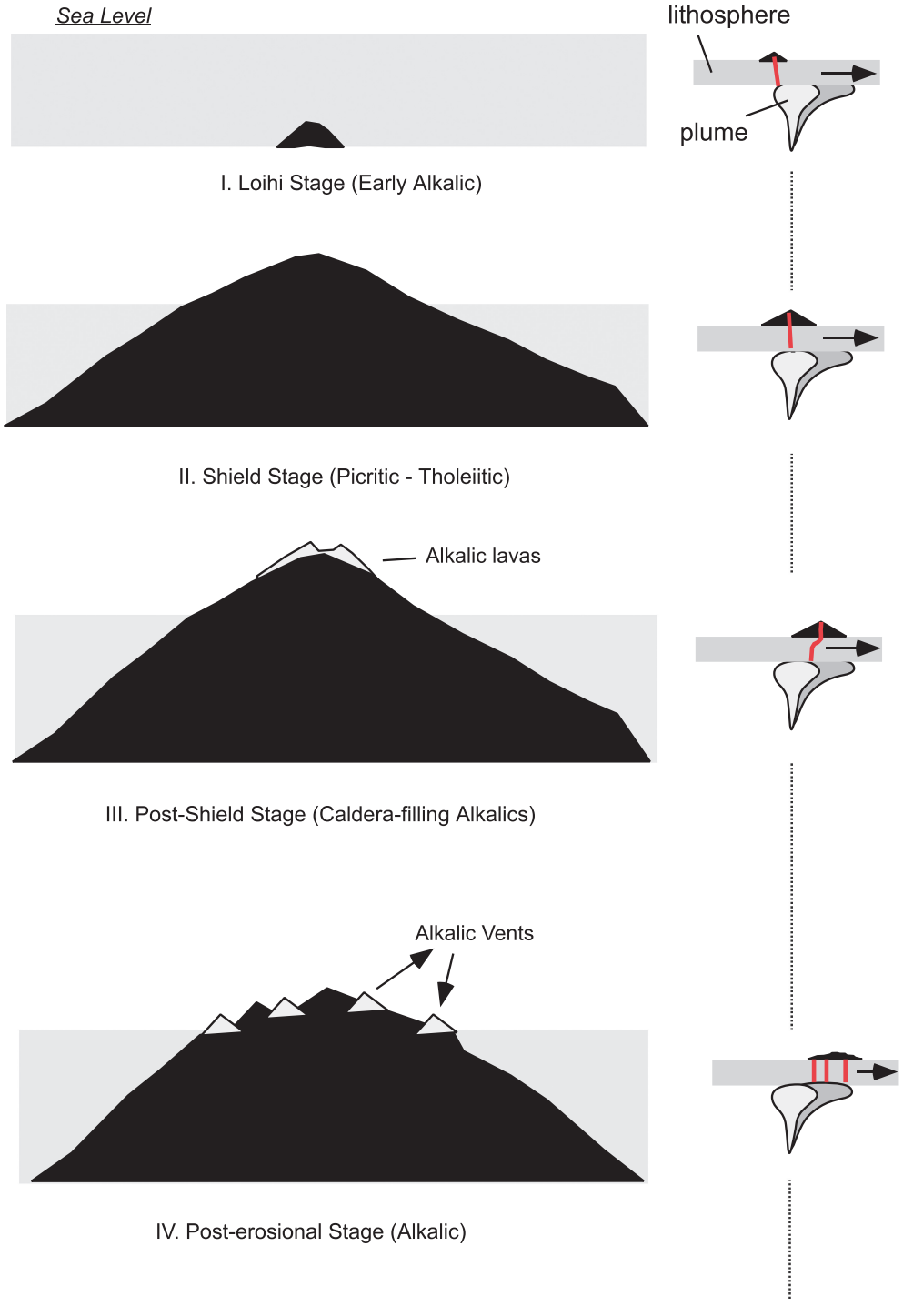

Fig. 8.18 Growth stages of a Hawaiian shield volcano. The stages are shown on the *left* and corresponding locations with reference to the Hawaiian plume are shown to the *right*. The plume is zoned with a hot, relatively dry core and a somewhat wet rim (Sen 1983)

Evolution of a Hawaiian Volcano

An individual volcano evolves through four stages in terms of chemical composition, volume, and eruption frequency, as the volcano (and the lithosphere on which it is located) passively migrates over the hot spot (Fig. 8.18). As the lithosphere approaches the hot spot or plume, small volumes of alkalic magmas formed at the edge of the plume erupt, forming a small volcano. This is the *pre-shield stage*. The submarine Loihi seamount located off the southeastern edge

of the Big Island of Hawaii exemplifies this volcanic stage. As the volcano gradually moves toward the center of the hot spot, the eruption frequency (magma supply) rapidly increases and the lavas become picritic (with ~15 % MgO) to tholeiitic (with ≤10 % MgO). This is the *shield stage*—so-called because rapidly erupting, fast flowing lavas form a giant shield volcano. The shield stage gradually gives way to *post-shield stage*, as the volcano moves away from the center of the hot spot, and the eruption frequency diminishes and the lavas become alkalic again. The volcano eventually stops erupting altogether as it migrates further away from the hot spot. However, following a ≤1 million year hiatus, during which the shield volcano undergoes heavy erosion, volcanism is renewed (*post-erosional or rejuvenated stage*). Much smaller volumes of strongly alkaline mafic lavas (basanite, nephelinite, alkali basalt) erupt, often carrying mantle xenoliths, through small vents scattered along fractures that are scattered across the shield volcano. Interestingly, lavas of similar characteristics are found on the ocean floor at North Arch and South Arch areas that are located on the Hawaiian Swell to the north and south of the older Hawaiian Islands (Maui, Oahu). Eventually, the heavily eroded Hawaiian shield volcano gets submerged as the cooling lithosphere itself gradually subsides, and the caldera rim of such a submerged volcano can be recognized today as an atoll—marked by the growth of coral reefs on them.

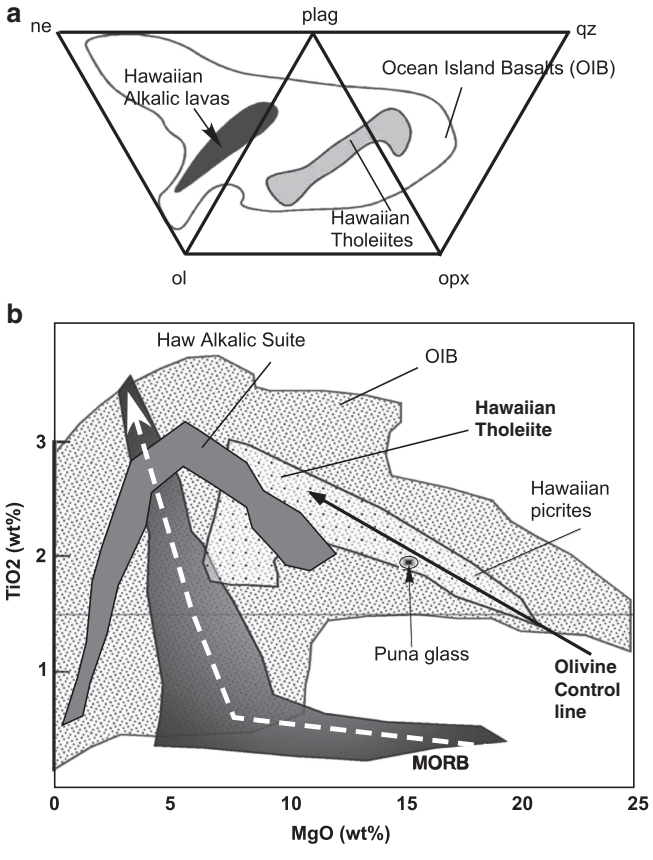

Fig. 8.19 (**a**) Hawaiian tholeiites, alkalic lavas, and the OIB fields are compared in this normative diagram. (**b**) Shows differences in TiO_2 between Hawaiian and MORB lavas, the olivine control exhibited by Hawaiian picrites and tholeiites, and very different compositional trends between MORB and Hawaiian tholeiites/picrites. Puna glass (Clague et al. 1995) found in a Hawaiian submarine landslide deposit has the highest MgO of all known naturally quenched liquid on earth

Petrology and Geochemistry of Hawaiian Lavas, Melt Inclusions, and Mantle Xenoliths

Lavas

Substantial geochemical differences exist between Hawaiian shield tholeiites and alkali basalts, between Hawaiian tholeiites and mid-ocean ridge tholeiites, and between tholeiites of different shield volcanoes even on the same island. Figure 8.19a compares Hawaiian tholeiites, alkali basalts, and Ocean Island basalts (OIB) in general in terms of their normative differences on a basalt tetrahedron. Hawaiian tholeiites form a field that trends toward the olivine corner, which is evidence of strong "olivine control" in generating the Hawaiian tholeiites. Figure 8.19b also shows the "olivine-control line" that points directly toward a highly magnesian olivine (Fo_{90}). This "olivine control" is a reflection of the compositional variation in Hawaiian picrites (10–23 wt% MgO) that contain variable amounts of olivine ($Fo_{76–90}$) phenocrysts. The very high MgO values of these picrites have drawn the attention of petrologists because of their potential to be primary magma.

In a general sense, the olivine-control line reflects lava compositions that have been affected by fractionation or accumulation of olivine. In the case of Hawaiian tholeiites and picrites, lavas with 15–17 % MgO appear to be the most primitive melts. Lavas with less than about 15 % MgO seem to have fractionated olivine crystals, and lavas with >15–17 % MgO have accumulated extras olivine crystals picked up from the magma chamber walls or conduit through which the magma passed. In this context, Clague et al.'s (1995) discovery of glasses from a submarine landslide at the Puna Ridge, off the southwest slope of Kilauea, drew much attention because of the high MgO (15–17 wt%) of the glasses (Fig. 8.19b). Because glass is quenched liquid, Clague et al.'s discovery

suggests that *primary Hawaiian tholeiite magma at Kilauea volcano must contain at least 15 % MgO*. The student should note that not all scientists accept the 15 % MgO threshold value for Hawaiian primary magma composition. As we will see later, some authors suggest that primary Hawaiian magmas contain even greater MgO.

The question is: how does one evaluate whether a lava (or melt inclusion) is primary magma or has accumulated extras crystals? There are tests to evaluate this. For example, a lava with fewer phenocrysts (i.e., the lava is close to being a liquid) and an olivine/liquid K_d (FeO, MgO) value of about 0.3, which is the equilibrium value (discussed in an earlier chapter), can be called "near primary" or "primary." On the other hand, an olivine-accumulated picrite lava is likely to show the following characteristics (a) a large modal percentage (>10 %) of olivine phenocrysts (i.e., the whole rock is not close to being quenched liquid but is an assemblage of liquid + crystals); (b) a range of olivine compositions (say, $Fo_{84–90}$) because some would be equilibrium and others nonequilibrium crystals in the host lava; (c) a variety of phenocryst morphologies—from euhedral single crystals (likely phenocrysts) to polycrystalline aggregates of olivine (likely fragments of wall rock dunite); and (d) disequilibrium olivine/lava K_d (i.e., very different from 0.3). One can use other criteria, such as Ni partitioning between olivine, whole rock, and Ni content of what would be a "reasonable" mantle partial melt.

Another interesting feature of Fig. 8.19b is the fact that at comparably high MgO values of 10–18 wt%, Hawaiian tholeiites and alkalic basalts contain higher TiO_2 than MORB. One cannot explain this fundamental difference between Hawaiian basalts and MORB in terms of different degrees of melting of a single source because in such a case one would see a complete overlap of the Hawaiian picrites and MORB. The TiO_2 difference therefore suggests that the Hawaiian mantle source had much greater TiO_2 than the MORB source. The difference between Hawaii and MORB sources also exists in terms of many other elemental and isotope plots as discussed in an earlier section. A final comment on MgO, FeO relationships here: note that MORB tholeiites lack the Hawaii-type olivine-control line. I believe this reflects that there is a fundamental difference in the composition of primary magmas of MORB and Hawaiian tholeiite/picrite and hence the way tholeiitic magmas accumulate and fractionate olivine between MOR and Hawaii.

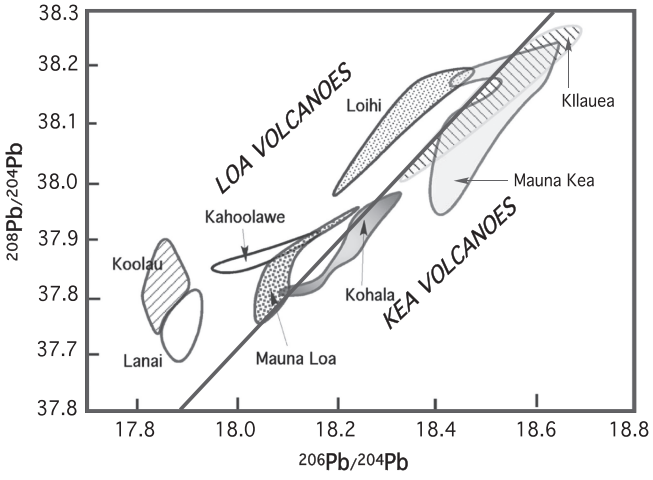

Fig. 8.20 The distinctive chemical nature of the Loa- and Kea-type volcanoes is shown in this Pb–Pb isotope ratio diagram (based on Fig. 2a in Abouchami et al. (2005) Nature 434, 851–856)

There are substantial elemental and isotopic differences even between tholeiites erupted from various shield volcanoes of the Hawaiian chain. Scientists have long noticed that the Hawaiian volcanoes line up along two lines of lithospheric weakness (Fig. 8.16): the volcanoes forming the southern group, the so-called Loa volcanoes, are chemically dissimilar to the volcanoes that form the "Kea" group to the north. Figure 8.20 shows this in terms of Pb isotope ratios—individual volcanoes within each group are distinct in their isotopic composition (Abouchami et al. 2005). The cause of these differences continues to puzzle scientists as they try to interpret them in terms of hypotheses of their origin by melting of some sort of heterogeneous plume (discussed later).

In terms of Sr, Nd isotope ratios, lavas from the Hawaiian-Emperor chain show an astonishingly large variation (Fig. 8.21). Lavas from the Koolau volcano really stand apart from the rest as they plot close to the "bulk earth" composition (i.e., this composition refers to the mantle composition that had not differentiated and remained chondritic). In general, the Emperor seamount lavas tend to be more depleted relative to the Hawaiian lavas, with the Detroit seamount lavas plotting squarely with the Pacific MORB. Individual volcanoes seem to be distinct in their isotopic compositions. These features are discussed further in a later section.

Rejuvenated stage alkalic lavas are generally more depleted than shield tholeiites. For example, the tholeiitic lavas that erupted from the 2–3 million years old

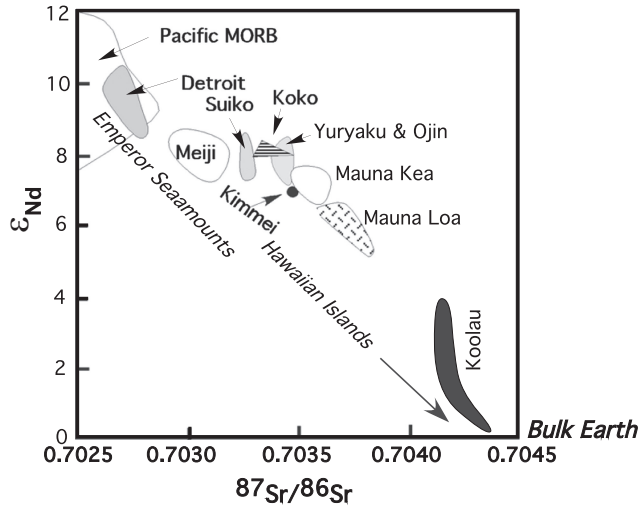

Fig. 8.21 Temporal variation shown by Hawaiian-Emperor chain (Keller et al. 2000)

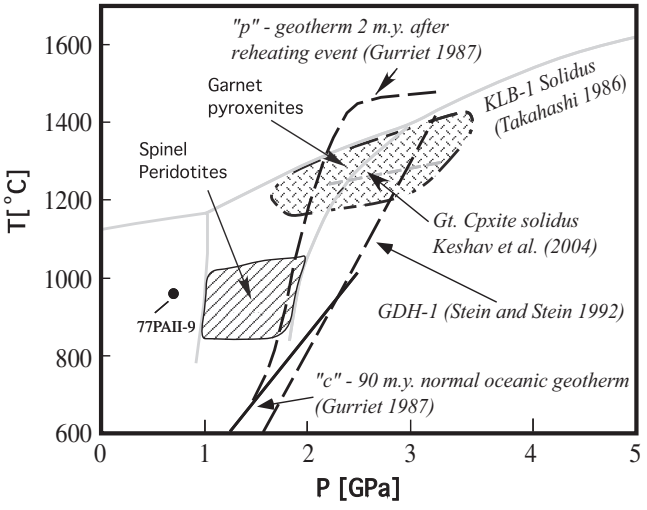

Fig. 8.22 *P–T* of spinel peridotite xenoliths from the Hawaiian lithosphere. Garnet pyroxenites form veins and cumulates in the lithosphere. The thermal conditions of these xenoliths are consistent with a lithosphere that was reheated by the Hawaiian plume (Sen et al. 2005)

Koolau shield volcano on the island of Oahu (Hawaii) have near "bulk earth" Figs. 8.4 and 8.23) isotope composition, whereas the rejuvenated stage Honolulu Series alkalic lavas, which erupted some 1 million year later through the Koolau volcano, have a much more depleted, lithospheric composition (Fig. 8.23). Clearly, shield lavas and rejuvenated stage lavas tap very different mantle sources, but how? We will seek answer to this question in a later section.

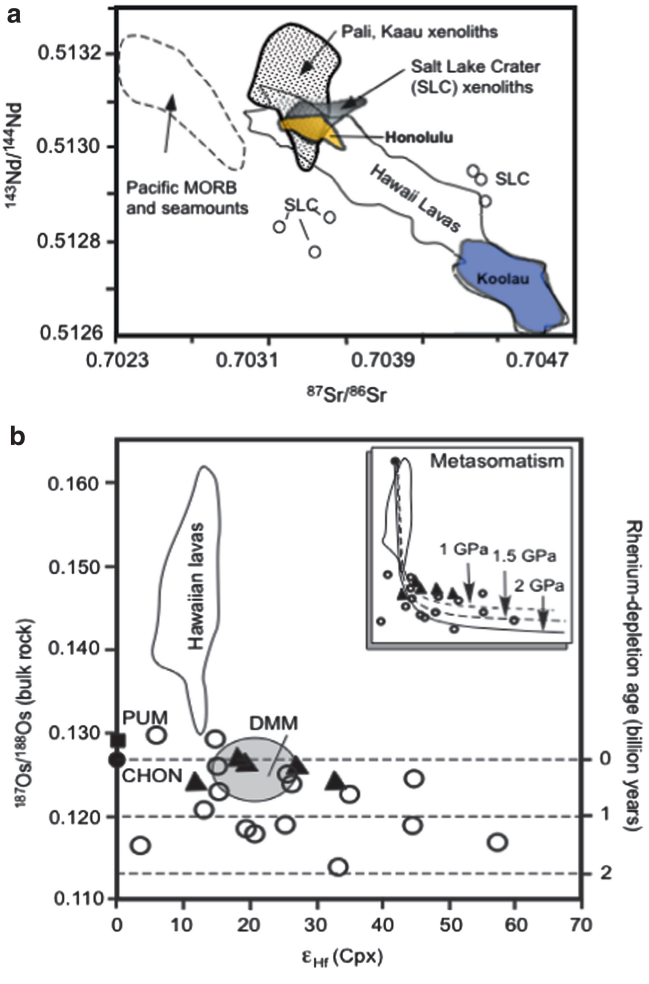

Fig. 8.23 Isotopic composition of Hawaiian mantle xenoliths compared with Hawaiian lavas and Pacific MORB and seamounts (source: Bizimis et al. 2007). (**a**) Nd–Sr isotopic composition of spinel peridotite xenoliths from Pali and Kaau vents (these are Honolulu vents located close to the caldera of the Koolau shield volcano) and from Salt Lake Crater (SLC). (**b**) Os–Hf isotopic composition of Hawaiian peridotite xenoliths (*triangles*—peridotites from Kaau and Pali; *circles*—peridotites from Salt Lake Crater) compared with Hawaiian lavas, DMM (depleted MORB mantle source), PUM (primitive upper mantle), and chondrites (CHON). The similarity between Pali and Kaau xenoliths and DMM suggests that they are from the lithosphere beneath Oahu. The SLC xenoliths have a more complicated origin. Bizimis et al. (2007) suggest that some of these may be as old as 2 Ga and were brought up from the deep mantle by the Hawaiian plume

Melt Inclusions

Ren et al.'s (2005) study of melt (glass) inclusions in olivine phenocrysts has an important bearing in the matter of origin of Loa and Kea trends. A melt inclusion forms when the host crystal (phenocryst) grows around and traps the melt that is at its growth front.

In general, melt inclusions often show much wider chemical variability relative to the erupted lavas from a single volcano. One simple interpretation of such difference between geochemistry of lavas and melt inclusions is that melt inclusions record small melt fractions from deeper (before any mixing) levels where they retain their primitive geochemical signals, and on the other hand, lavas are well-mixed melts that are supplied from shallow conduits. Ren et al. (2005) found that *both* Loa- and Kea-like melt inclusions occur in phenocrysts in individual volcanoes and even from single rocks. This suggested to them that the plume is a random mixture of Loa- and Kea-like components and it is the melting process that controls the mixing proportion of these components and hence the composition of the erupted shield lavas from different volcanoes.

Summary of Lava and Inclusion Geochemistry

The geochemical and temporal variation shown by various shield volcanoes is fascinating and is commonly interpreted as features of plume melting. Fundamental differences between MORB and all Hawaii shield lavas imply very different sources for the MOR vs. Hawaiian tholeiites.

We have talked much about the basalts but have not mentioned anything about the mantle xenoliths that are found in rejuvenated stage alkalic lavas of Honolulu Series on Oahu and on other islands as well. The following section focuses on the xenoliths.

Hawaiian Mantle Xenoliths: Nature of the Lithosphere

Hawaii is one of the rare places in the oceans where one also finds mantle xenoliths, which offers us an insight into the rock types and igneous processes that are operative in the mantle. The best-studied xenoliths are found in the rejuvenated stage Honolulu Series lavas (strongly alkaline) that erupted from many small volcanoes on Oahu, which is composed of two eroded shield volcanoes—Koolau and Waianae.

Oahu xenoliths are of three types—dunite, spinel peridotite (dominantly lherzolites), and garnet pyroxenite (including garnet clinopyroxenites, wehrlite, and websterite). Dunite xenoliths are relatively few and are found in the Honolulu volcanic vents that are proximal to the caldera of Koolau shield volcano. Sen and Presnall (1986) concluded that the dunites are shallow cumulates from both MOR and Hawaiian magmas. Spinel peridotite is the most common type of xenolith on Oahu and they have typical upper mantle compositional characteristics, such as high molar Mg/(Mg + Fe) of 0.88–0.92. Temperature calculation based on composition of coexisting pyroxenes in spinel peridotite xenoliths shows that the last equilibrated at 900–1,150 °C within the lithosphere (Fig. 8.22). These xenolith temperatures are higher than the calculated geotherms (e.g., c and GDH-1 in Fig. 8.22) for the sub-Oahu lithosphere, suggesting that the Oahu lithosphere was substantially heated up by passing Koolau/Honolulu magmas.

Garnet pyroxenite suite of xenoliths are only found in the Salt Lake area of Oahu; however, they have been found in other Hawaiian islands (M. Bizimis, personal communication). These xenoliths have received much attention in petrology as garnet-bearing xenoliths are rare or absent in other oceanic hot spots. The Hawaiian garnet-bearing xenoliths exhibit considerable variation in mode: although most are dominantly composed of garnet and clinopyroxene, olivine, orthopyroxene, phlogopite, and amphibole can occur in small (<1 %) to very high large amounts (30 %). There are also rare composite xenoliths in which garnet pyroxenite occurs as intrusive vein in spinel peridotite. This evidence alone indicates that these garnet pyroxenites are igneous veins in the Hawaiian lithosphere.

Bizimis et al. (2007) found that Hf, Os, Nd, Sr isotope composition of spinel peridotites from Pali and Kaau, two Honolulu vents situated close to the caldera of the Koolau volcano, is similar to that of the DMM source (Fig. 8.23a, b). Therefore, they concluded that the spinel peridotite xenoliths from Kaau and Pali are fragments of the 90 million years old oceanic lithosphere that lie beneath Oahu.

The peridotites from the Salt Lake Crater, which is a Honolulu volcano located some 50 km away from the Koolau caldera, may have a more complex origin. They are unusual in that they are significantly more depleted (high Mg/Fe and lower modal clinopyroxene) relative to the xenoliths from other vents (i.e., Pali and Kaau: Sen 1988). Most spinel peridotite xenoliths from Salt Lake overlap Honolulu lavas in Nd–Sr isotope ratios, although a few are quite distinctly enriched (Fig. 8.23a). The Hf–Os isotope diagram shows that most Salt Lake spinel peridotites are depleted in $^{187}Os/^{188}Os$ but enriched in ε_{Hf} (Fig. 8.23b). These isotopic features suggest that the Salt Lake peridotites are possibly fragments of old depleted (subducted fragments of about 1 billion year age) that were enriched at an ancient time (Bizimis et al. 2007). They were brought from great depths by the Hawaiian plume.

Garnet pyroxenites are isotopically identical to the host rejuvenated stage Honolulu lavas and are thus thought to be deep crystallization products of parental Honolulu magmas. Sm–Nd isotope geochronology of the constituent garnet and clinopyroxene of individual xenoliths suggest that they are of zero age, which would be essentially consistent with the interpretation that they formed from 0.9 Ma Honolulu magmas (Bizimis et al. 2005). Geothermobarometry shows that the garnet-bearing xenoliths equilibrated at 1,150–1,425 °C and 1.6–3.7 GPa (Fig. 8.22). Figure 8.22 shows that the field of garnet pyroxenites grazes the solidus of the peridotite KLB-1 (Takahashi 1986). The high temperature nature of the pyroxenite xenoliths supports their crystallization from magmas in the lower oceanic lithosphere.

Finally, mention should be made of two interesting discoveries in the garnet-bearing xenoliths of Hawaii. Keshav and Sen (2001) found some garnets that contain exsolved orthopyroxene blebs. They interpreted these garnets to be *majoritic* garnets that came from some 300–400 km depth. The second was the discovery of nanodiamonds (Wirth and Rocholl 2003). Keshav and Sen (2001) suggested that these unusual xenoliths are fragments of recycled, ancient oceanic crust.

The xenoliths and their inferred origins have led to a model of the post-Honolulu eruptive lithosphere beneath Oahu (Fig. 8.24; Sen et al. 2005). In this model, the lower part of the lithosphere is a mixture of garnet pyroxenite blobs, veins, and peridotites. The middle part of the lithosphere is composed of spinel peridotites. The upper part shows a thickened crust owing to the loading of the Koolau shield volcano on top of the preexisting oceanic crust. Koolau shield volcano's conduit is shown as a fairly well-defined pipe. Honolulu related volcanoes are scattered across the Koolau shield volcano.

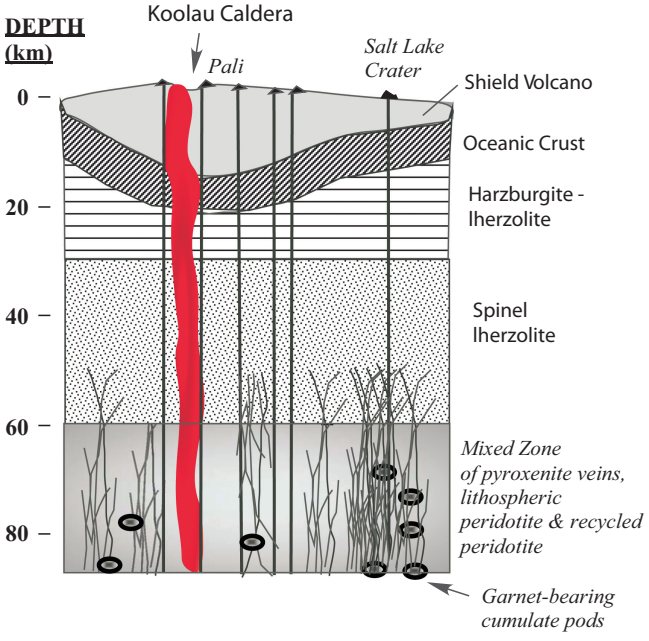

Fig. 8.24 Nature of the Hawaiian lithosphere beneath the ancient Koolau volcano on Oahu, Hawaii, inferred from the study of mantle xenoliths (Sen et al. 2005). The *red "pipe"* is depicted to have been the feeder of Koolau magmas (Sen et al. 2005)

Origin of Hawaiian Basalts

In summary, from the above presentation we learned that (a) xenolith-bearing Hawaiian post-erosional alkalic lavas are geochemically and isotopically distinct from the shield volcanic tholeiites; (b) Loa group of shield lavas are distinct from Kea lavas, but melt inclusions from a single volcano span the complete compositional Kea–Loa range; (c) shield lavas from individual volcanoes from even a single island are distinct from one another in their isotope composition; (d) the Emperor seamounts are generally more depleted than the younger Hawaiian volcanic chain with some (Detroit seamount) being as depleted as MORB; (e) xenoliths tell us that the lithosphere beneath Hawaii is isotopically depleted spinel peridotite; and (f) the Hawaiian plume has multiple isotopic components, the most distinctive of which is the primitive-appearing Koolau component. Based on this broad summary, we now explore what all of these things tell us about the Hawaiian plume and origin of magmas from a petrological perspective.

Non-plume Origin of the Rejuvenated or Post-erosional Stage Alkalic Lavas

Two important questions about the generation of Hawaiian magmas are (1) what are their source rocks and (2) what are pressure–temperature conditions at the site of magma generation? Based on the foregoing discussion we can surmise that shield magmas come from a source that is very different and isotopically more enriched than the source of the rejuvenated stage magmas. Based on the observation that the rejuvenated

stage Honolulu lavas on Oahu show large variation in K/Ce, Rb/La, and Ba/La ratios, Class and Goldstein (1997) suggested that residual phlogopite, which exerts significant control on K, Rb, Ba partitioning between residue and melt, must play an important role in their primary magma generation. They noted that phlogopite could only be stable in the lithosphere and therefore proposed that rejuvenated stage HV magmas are not produced from the Hawaiian plume but by melting of the lower lithosphere. Phlogopite does occur in garnet pyroxenite suite xenoliths in Oahu and therefore lend support to this hypothesis. The trace element composition and isotopically depleted character of the rejuvenated stage lavas are also consistent with the proposal that their parent magmas are of lithospheric/asthenospheric origin. Based on the fact that HV lavas bring up xenoliths from the deepest (90 km) lithosphere, Sen and Jones (1990) proposed that the rejuvenated stage magmas come from the asthenosphere. Finally, numerical modeling work by Ribe (cited by Sen et al. 2005) indicates that favorable thermal conditions can be created at the lithosphere/asthenosphere boundary for the generation of rejuvenated stage alkalic magmas.

On the basis of such evidence, we therefore accept the hypothesis that HV-type magmas are not generated from the plume itself but by melting of the asthenosphere±lithosphere, and move on to focus only on the generation of the shield-building magmas, which comprise more than 99 % of Hawaiian lavas and are generally accepted to be products of plume melting.

Origin of Shield Lavas

Source Rocks

Proposed source rocks for Hawaiian shield magmas have ranged from peridotite to eclogite and garnet pyroxenite. Whereas the bulk of the peridotite component is largely believed to come from the deep mantle, various authors have a second component that includes eclogite, garnet pyroxenite, and some depleted peridotites (represented by spinel peridotite xenoliths found at Salt Lake, Oahu) that are fragments of old, previously subducted "slab" (i.e., subducted oceanic lithosphere). Some authors have also suggested the presence of recycled sediments and even a chemical component from the outer core. Seismic tomography studies have "traced" the plume conduit all the way to the core–mantle boundary, which has bolstered the hypothesis that the Hawaiian plume has a deep mantle origin (Fig. 8.25).

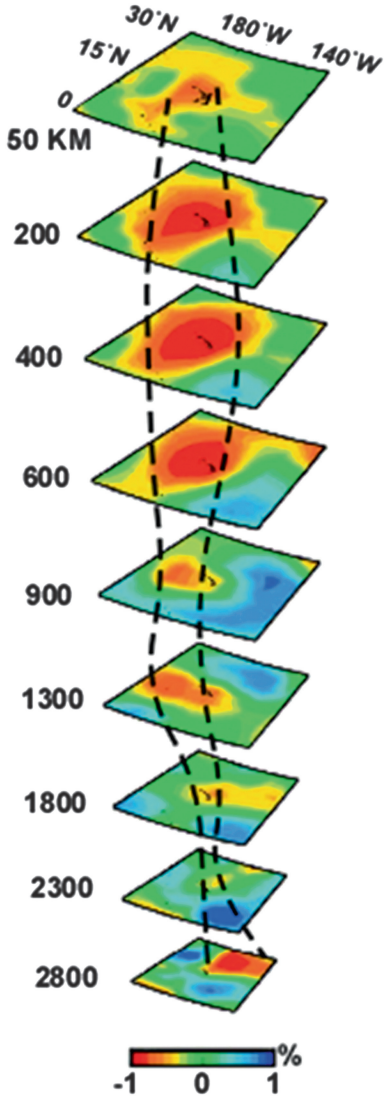

Fig. 8.25 Seismic tomography showing the trace of the Hawaiian hot spot (*red*) (Li et al. 2000)

Loa- Versus Kea-Type Shield Lavas: Indication of a Zoned Plume

Using olivine/liquid K_d concept that we have discussed elsewhere, Hauri (1996) computed plausible primary magma compositions for Loa- and Kea-type magmas that would be in chemical equilibrium with upper mantle peridotite having an $Mg/(Mg + Fe^{2+}) = 0.86–0.89$. He then compared these compositions with experimentally produced melts from similar peridotites at upper mantle pressures. Figure 8.26 is a modification of Hauri's original diagram. It shows the following (1) the experimental trend of peridotite-derived melts is at a sharp angle to the Hawaiian trend, crossing it at about

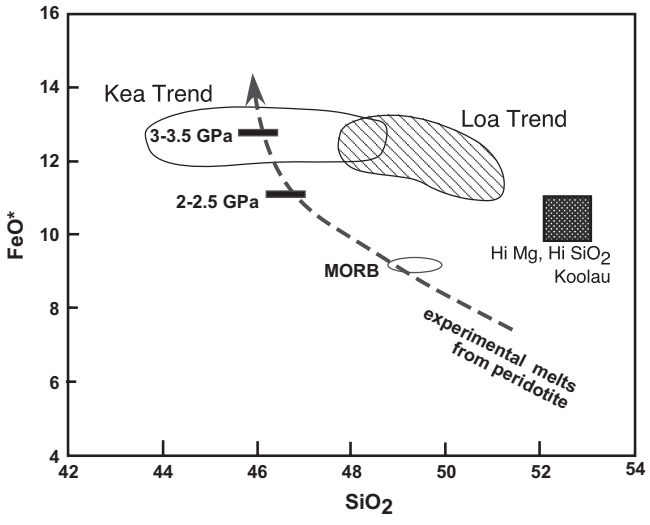

Fig. 8.26 SiO_2–FeO* relationship shown by Hawaiian lavas from Koolau volcano, and Loa and Kea group volcanoes are shown here, along with experimental melts formed by partial melting of peridotite (Hauri 1996)

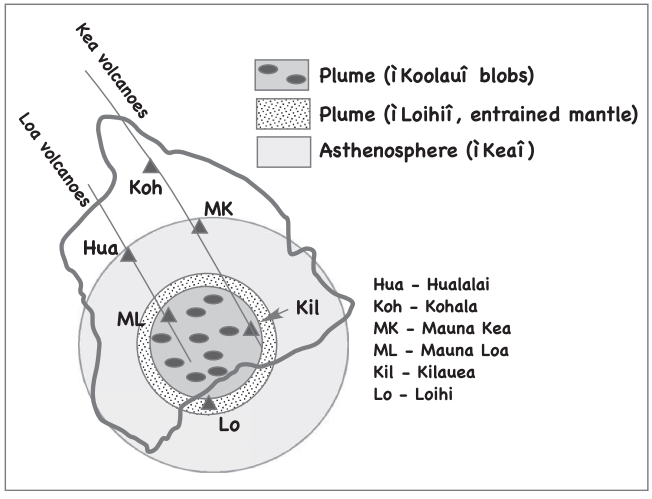

Fig. 8.27 Zoned plume model proposed by Hauri (1996)

3–3.5 GPa (i.e., about 90–100 km), which would be the pressure of equilibration of the Hawaiian magmas. (2) While the experimental melts overlap some of the Kea magmas, the Loa magmas and particularly those from Koolau volcano are too silica rich to be derived entirely from a peridotitic source. (3) The Hawaiian trend, most particularly Loa and Koolau magmas, requires contributions from a silica-rich "end-member" which Hauri (1996) considered to be dacitic melts produced by partial melting of recycled subducted crust (quartz eclogite).

Hauri (1996) proposed a radially zoned plume in which eclogite blobs (Koolau component) are surrounded by peridotite matrix in the hottest core of the plume, and this core is surrounded by a hot, narrow zone of peridotite that is entrained from the lower mantle (Loihi component), and then surrounding it is a broad rim of cool, passively upwelling asthenosphere (Kea component) (Fig. 8.27). Hauri proposed that the differences between Kea and Loa volcanoes could be explained by their relative location over this zoned plume because that would control the relative contributions of the three components to their respective primary magmas. Thus, according to this hypothesis, entrained lower mantle is a major magma source for the lavas erupting at Loihi, whereas Mauna Kea was located on the periphery of the plume and therefore asthenosphere was a major source for Mauna Kea lavas.

In spite of the many appealing aspects of Hauri's zoned plume model, its validity has been questioned by some: for example, Ren et al. (2005) noted that during the evolution of a single tholeiitic shield volcano, the eclogitic component, as reflected in greater silica content (for example) of the lavas, increases in the younger stages. They explained this by the passage of the volcano over a thermally zoned plume. These authors proposed that the eclogite component is *randomly* distributed through the plume, which itself is a heterogeneous aggregation of relatively Mg-poor to Mg-rich peridotitic materials. Thus, *all shield volcanoes* are composed of melts that come from both eclogite and peridotite sources regardless of their location relative to the hot spot. Because the solidus of eclogite is at a lower temperature than that of peridotite, the hot core of the plume would produce more of peridotite-derived melts whereas its cooler rim would produce more eclogite-derived melts. Therefore, as a shield volcano "ages" and passes over the downstream part of the plume, contribution from the eclogite source component becomes more dominant in its younger lavas.

Sobolev et al. (2005) pointed out that Hawaiian shield magmas have too much Ni and Si to be generated by melting of mantle peridotite or eclogite, although eclogite does play a fundamental role in their model (Fig. 8.28). Sobolev et al.'s plume contains suspended eclogite fragments in peridotite matrix. As the plume rises, the eclogites begin to melt first; such melts then react with peridotite to generate a pyroxenite. Larger proportion of pyroxenites and a smaller percentage of surrounding peridotite melt to produce Hawaiian magmas (Fig. 8.29). In this model Koolau and Mauna Loa primary magmas received as much as 80 % and 60 % melt, respectively, contributed from the secondary pyroxenite source.

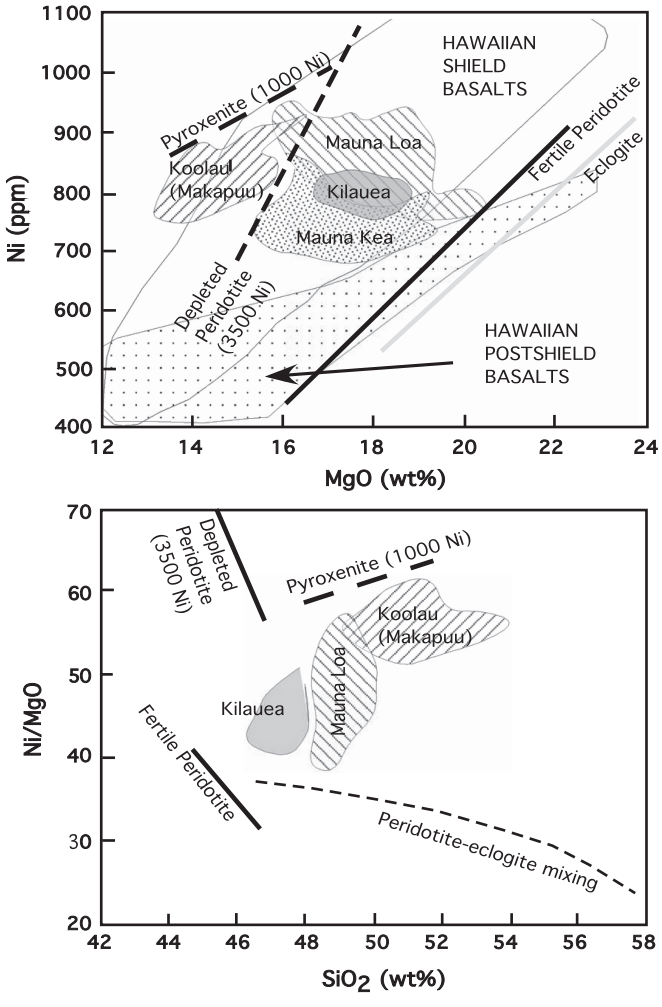

Fig. 8.28 MgO–Ni and SiO_2–Ni plots showing that Hawaiian lavas have too much Ni relative to peridotite-derived melts, suggesting an important role played by pyroxenite as a source rock (Sobolev et al. 2005)

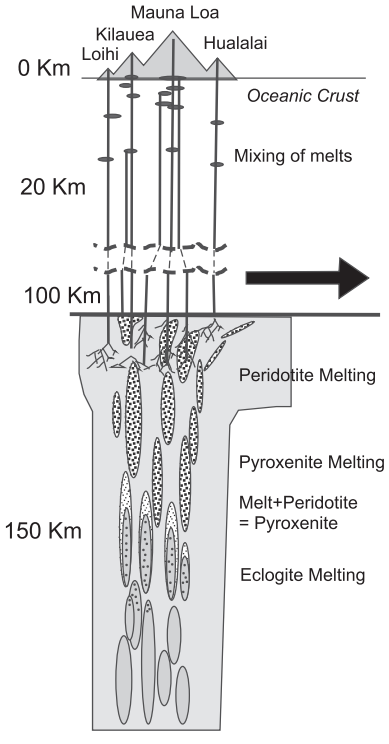

Fig. 8.29 Sobolev et al.'s (2005) model of Hawaiian plume melting

This is an interesting model; however, laboratory experiments have not yet substantiated whether such high-Ni secondary pyroxenites can form or if such high Ni, high Si melts can form by the melting process as suggested. Most recently, Wang and Gaetani (2008) performed experiments that showed that mixtures of peridotite-derived partial melts and eclogite-derived partial melts can have the high Si, Ni character if the silica content of the mixed melt is buffered to high levels due to equilibration with pyroxene in the peridotite. Their work thus negates the need for a derivation of Hawaiian shield magmas purely by melting of secondary pyroxenites, as was suggested by Sobolev et al. (2005).

Has the Hawaiian Plume Changed Over Time?

Amongst the many questions answered by geochemistry is whether the plume composition has changed over time. The foregoing discussion indicates that the plume is heterogeneous and the primary magmas forming the Hawaiian Islands have gone "back and forth" between the Koolau and a depleted end member, i.e., there has not been a unidirectional change with time for any of the chemical tracers. In this connection, mention should be made of a study by Keller et al. (2000), which showed that the magma composition was consistently more depleted in the Emperor seamounts than the Hawaiian Islands: one of the oldest Emperor seamounts, the Detroit seamount, plots squarely within the MORB field (Fig. 8.21; discussed earlier). This suggests that the Hawaiian plume may have started out as perhaps a thermal anomaly of largely asthenospheric origin. If, as suggested by Hauri and Sobolev et al., the high $^{87}Sr/^{86}Sr$ reflects greater contribution from recycled eclogites, then the consistently lower $^{87}Sr/^{86}Sr$ in the Emperor seamounts than the Hawaiian Islands may mean that the Emperor seamounts received more peridotite-derived melts, i.e., the plume was hotter.

How Hot Is the Hawaiian Plume?

There is a continuing debate about how hot the Hawaiian plume really is, i.e., whether it is a thermal plume or a chemical "anomaly." Ribe and Christensen (1999) suggested a maximum plume temperature of about 1,600 °C. On the other hand, petrologists have come up with potential temperatures (i.e., the temperature of the melt at the surface assuming it rose adiabatically from its mantle source) of 1,550–1,687 °C using olivine–liquid Mg/Fe exchange thermometer on olivine phenocrysts in Hawaiian lavas (e.g., Herzberg et al. 2007; Putirka 2008). Herzberg et al. noted that their calculated potential temperature of 1,550 °C for Hawaii is only 250 °C higher than ambient temperature of 1,300 °C of the asthenosphere beneath MOR. Putirka (2008) calculated a maximum temperature of 1,687 °C on the basis of maximum forsterite content of 91.7 (mole%) of olivine phenocrysts in Hawaiian lavas. A more recent study by Lee et al. (2009) found that while their estimated primitive MORB equilibrated at 0.7–1.7 GPa at 1,300–1,400 °C before rising toward the crust, Hawaiian primitive shield magmas equilibrated at 2–5 GPa and 1,450–1,600 °C, and that on average the Hawaiian tholeiitic basalts are 200 °C hotter than the average MORB. Any discussion of the methods employed by these different authors is beyond the scope of this book. My personal preference is to rely on any method that uses maximum Fo content of olivine phenocrysts as a boundary condition because that is a real constraint that one cannot ignore.

Clues to the Melting Conditions from Experimental Petrology

Results from experimental petrology on inferred primary Hawaiian tholeiite magmas have not been easy to interpret. Here we will mention two such studies. Wagner and Grove (1998) experimented on a starting melt with 17.3 % MgO, which is a glass discovered by Clague et al. (1995) at Puna ridge, off submarine slopes of Kilauea (discussed in an earlier section). They found the melt to be saturated with olivine + orthopyroxene at 1.4 GPa and 1,425 °C, which would imply that if this composition is a suitable primary magma for all Hawaiian shield magmas then these magmas equilibrate with a harzburgitic lithosphere at 45 km depth. However, other evidence rules out such an implication: for example, predominance of spinel lherzolite xenoliths in Hawaii implies that the lithosphere is lherzolitic and not harzburgitic. Geochemical evidence, such as high chondrite-normalized [La/Yb] ratios of Hawaiian tholeiites, indicates that Hawaiian magmas equilibrate with garnet lherzolite, which is stable at pressures greater than 2.8–3 GPa at the solidus, i.e., the magmas were most likely generated below the lithosphere. Wagner and Grove (1998) recognized this fundamental problem and accordingly, instead of calling for the origin of the magmas at ~45 km, the authors proposed a model where the primary magmas are generated much deeper in the garnet stability field, and these magmas then react heavily with harzburgitic wall rocks (lithosphere) at ~60–45 km. This is not a satisfactory solution either because isotope composition of these basalts rules out any significant contribution of the lithosphere to these melts. The student should note that this serves as a good example of testing the success or failure of a hypothesis using multiple constraints. We will see later a very different conclusion reached by Presnall and Gudfinnson (2011) than Wagner and Grove (1998).

Maaloe (2004) performed experiments on a Hawaiian tholeiite with 18.2 % MgO and found it to be saturated with olivine + orthoptroxene + clinopyroxene at 2 GPa and 1,550 °C (Fig. 8.30). He realized that the pressure is too low for any reasonable Hawaiian primary magma because (1) garnet is not stable at 2 GPa (garnet is a requirement based on trace element composition); (2) isotope studies tell us that the magmas must be generated below the lithosphere; and (3) seismic studies indicate that the lithosphere beneath Hawaii is about 90–120 km thick. Therefore, the primary magmas must originate at depth greater than about 100 km. Maaloe (2004) assumed that the Hawaiian primary magmas were saturated with a harzburgite residue, and estimated that only a magma with ~23.8 % MgO would equilibrate with a harzburgite of appropriate olivine composition (Fo_{91}) at ~3.6 (±0.05) GPa and 1,680 (±50) °C. Since garnet is unlikely to be a stable residue in his assumed harzburgite, this conclusion remains to be verified with further experiments. Maaloe's

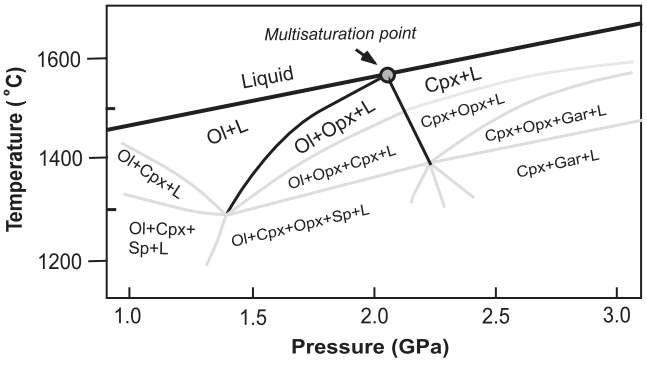

Fig. 8.30 Experimental determination of a multisaturation point for Hawaiian picrite (Maaloe 2004). See text for further discussion

estimated conditions fall within the pressure range estimated by Lee et al. (2009, discussed in the earlier section), but the temperature is about 80–100 °C too high.

Finally, Presnall and Gudfinnsson (2011) presented a study in which they compared normative compositions of a group of primitive Hawaiian glasses from the Puna Ridge, Hawaii (recall earlier discussion), with the solidus of simplified mantle lherzolite in the system $CaO–MgO–Al_2O_3–SiO_2$ over a pressure range of 0.9–6 GPa (Fig. 8.31). The glasses show olivine control, i.e., they can be related by olivine fractionation from a melt that would be normatively similar to a solidus (or near-solidus) melt generated at a pressure of 4–5 GPa. One interesting conclusion reached by Presnall and Gudfinnsson (2011) is that such melt would have the appropriately high SiO_2, MgO, and Ni, as required by Hauri (1996) and Sobolev et al. (2005, discussed earlier). Presnall and Gudfinnsson (2011) suggested that such mantle melt would have a temperature of 1,450–1,500 °C. Based on their estimated *P–T* condition (i.e., 4–4.5 GPa, 1,450–1,500 °C) of the Hawaiian tholeiite primary melt, Presnall and Gudfinnsson (2011) suggested that Hawaii is essentially tapping melts produced in the seismic low velocity zone. They opposed the idea of a plume and instead suggested that deep lithospheric "gashes" (fractures) probably tap such melts. It is beyond the scope of this book to discuss their model and the student is urged to read their paper.

In sum, there is a large volume of data on Hawaiian xenoliths and volcanism. The closest set of experiments that appears to constrain the depth of origin of Hawaiian tholeiites is that of Presnall and Gudfinnsson (2011). However, the highest temperature of the magmas, which has a strong bearing on the mantle plume model, is a subject of much debate.

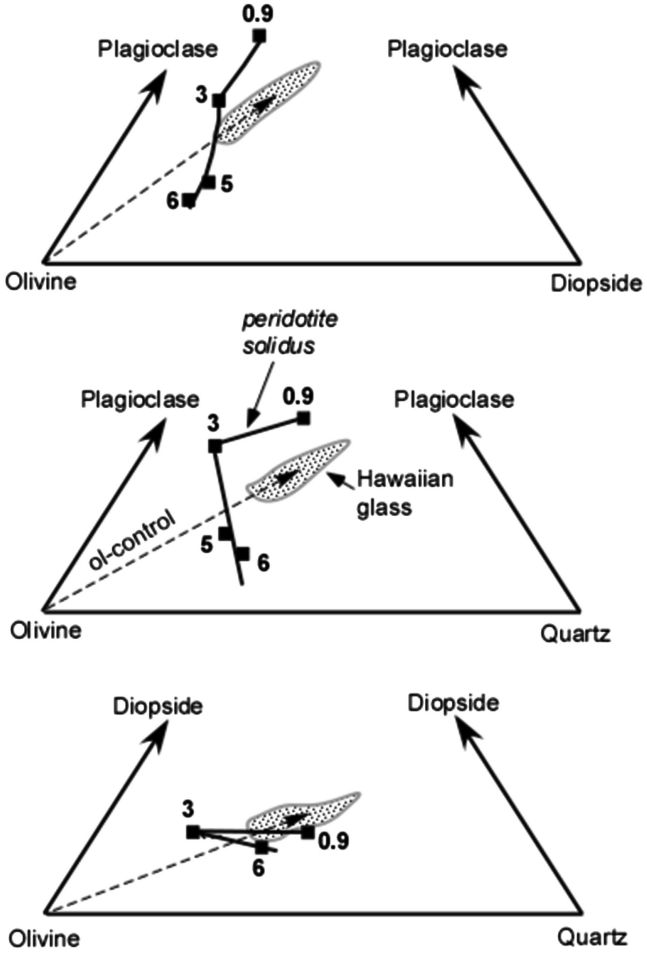

Fig. 8.31 Composition of primitive Hawaiian glasses from the Puna Ridge (*shaded*) is compared with synthetic peridotite solidus in the system $CaO–MgO–Al_2O_3–SiO_2$ in three different projections (redrawn from Presnall and Gudfinnsson 2011). The *numbers* refer to pressure in GPa. Olivine-control line (*dashed*) is also shown. Based on this comparison, the Hawaiian glasses (parents to tholeiites) seem to be derived by olivine fractionation from a peridotite-sourced melt at 4 GPa (120 km)

Summary

Hawaiian Volcanism

- Post-erosional alkalic magmas are generated by the melting of the oceanic lithosphere.
- Hawaiian primary shield magmas may be extremely magnesian with as much as 24 % MgO, although the most magnesian liquid (glass) recovered from the Puna ridge has 17.3 % MgO.
- Most erupted lavas have less than 10 % MgO; therefore, the erupted lavas must undergo significant olivine fractionation, which is borne out by the "olivine control" on Hawaiian lavas.
- The source rocks for the primary magmas may have a dominant "primordial" component (other names have been used by other authors, such as "near chondritic," "undifferentiated," "enriched"), and the other components include the recycled crust and recycled depleted slab peridotite.
- The plume is viewed as a zoned mixture of harzburgite (recycled lithospheric mantle) and eclogite lenses and filaments (recycled crust) dispersed in a peridotite matrix.
- Some experimental studies suggest that melting of the plume perhaps occurs at 3–5 GPa. Low-temperature components, such as eclogite or garnet pyroxenite, start melting at deeper levels and such melts go through reaction with surrounding peridotite and mix with melts

produced from the peridotite matrix as the plume rises, perhaps in a manner similar to the model presented by Hauri (1996).

- Presnall and Gudfinnsson's (2011) experiments suggest that the primary magmas, which feed the voluminous shield volcano-forming tholeiites, originate at about 4 GPa (120 km) from a peridotite source. These authors show that such melts would have the necessary high MgO, SiO_2, and Ni and would not require a pyroxenite component in the source mantle.
- The temperature of origin of the shield-building primary magmas is a controversial topic: Presnall and Gudfinnsson (2011) estimate the temperature to be 1,450–1,500 °C; Lee et al. (2009)—1,450–1,600 °C; Maaloe, Putirka, Herzberg et al. (refs. In text)—about 1,600–1,700 °C.

Large Igneous Provinces: Deccan Traps and Columbia River Basalts

9

Please note the Erratum to this chapter at the end of the book

Abstract

Earth has experienced episodic bursts of lava eruption that flooded large areas of continents and oceans in a relatively short time. Such volcanic provinces have been called flood basalt provinces or large igneous provinces (LIP). Continental flood basalts often occur on the tectonically passive edge of the continent; and therefore their origin is considered by some to be related to the continental separation process, as was discussed in Chap. 1 (Fig. 1.12). On the other hand, there are LIPs that have no link to continental separation. In this chapter we take a closer look at two of the well-studied LIP—one of which, the Deccan Traps (India), was involved in continental separation and the other (Columbia River Basalts, USA) was not.

Introduction

Large igneous provinces (LIPs) occur on continents as well on oceans (Fig. 9.1; Coffin and Eldholm 1994). Among them, the prominent ones are Ontong-Java Plateau (Western Pacific Ocean), Caribbean LIP (Caribbean Sea), Central American Magmatic Province (CAMP), Deccan Traps (India), Siberian Traps (Russia), Parana Traps (South America), and Columbia River Basalts (Northwestern USA). Ages of these various LIPs may be found in Fig. 9.4. Commonly, a "hot spot track" appears to provide a spatial link between an existing hot spot and a LIP (Fig. 9.1). A commonly accepted hypothesis, called the "plume heads and tails" hypothesis, suggests that large, bulbous, plumes occasionally rise from the deep mantle and melt as they impact the lithosphere. Melting of such a large plume head gives rise to the formation of flood basalts. The stable, narrow "tail" or conduit of such a plume remains relatively fixed in space and stays active for millions of years and generates volcanic chain on a lithosphere that migrates over it (Fig. 9.2).

Some continental LIPs have been linked to the separation of continents, as was discussed in Chap. 1; perhaps the biggest example of this is the Central American Magmatic Province (CAMP), which is a very large 200-Ma magmatic province whose remnants are preserved as lava flows and intrusives in North America, Africa, and South America (Fig. 9.3; Hames et al. 2000).

CAMP has been linked to the opening of the Central Atlantic Ocean (Hames et al. 2000). Like many other continental LIPs, CAMP volcanism produced tholeiitic magmas. A well-studied example of CAMP is the Palisades sill bordering the Hudson River between New York and New Jersey. Similarly, the Ferrar intrusives (Antarctica) and Tasmanian diabase intrusives are linked to the tectonic separation process of the Gondwana continents.

Many LIPs have been linked to global climate change and mass extinction events; for example, the Deccan Traps (India) and Siberian Traps (Russia) overlap with Cretaceous–Tertiary and Permo–Triassic mass extinction events (Fig. 9.4). There have been few studies that suggest a connection between LIP eruptions and global climate; but our understanding of this link is minimal at the moment (Wignall 2005). More recently, it has been shown that lavas from many LIPs, both continental (Deccan Traps, Karoo, West Greenland and Baffin Bay, Siberian Traps) and oceanic (Ontong-Java Plateau, Kerguelen), come from an old (4.4–4.5 Ga) and deep mantle reservoir that has non-chondritic isotopic and trace element composition

G. Sen, *Petrology*, DOI 10.1007/978-3-642-38800-2_9,

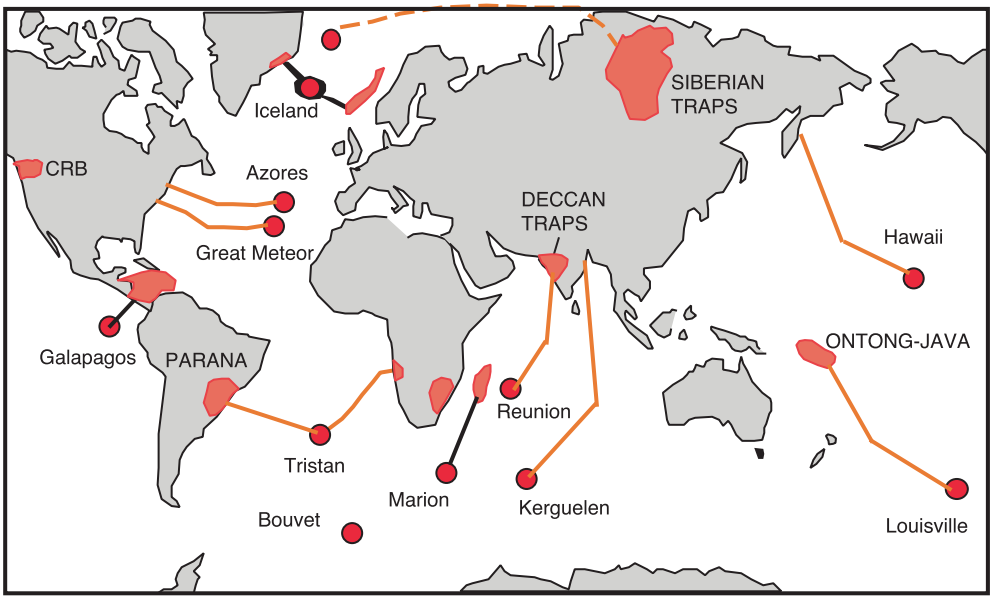

Fig. 9.1 LIPs linked to known hot spots on earth

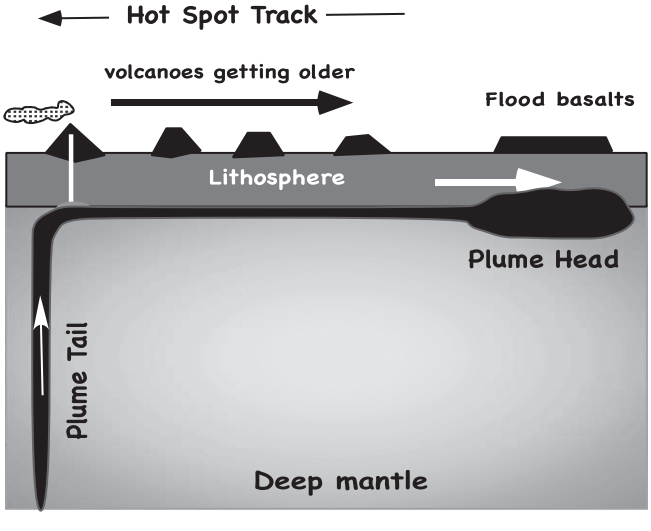

Fig. 9.2 Schematic diagram depicting the plume head and tail model (after Richards et al. 1989)

(Jackson and Carlson 2011). The apparent link between LIP activity and mass extinction events, their potential impact on climate, enormous volumes of LIPs, LIPs' link to ancient geochemical reservoirs in the deep mantle, connection between some LIPs, and the separation of continents are all great reasons to study LIPs. Our knowledge about them is still limited but what has been found so far makes them one of the most intriguing topics in the Earth sciences.

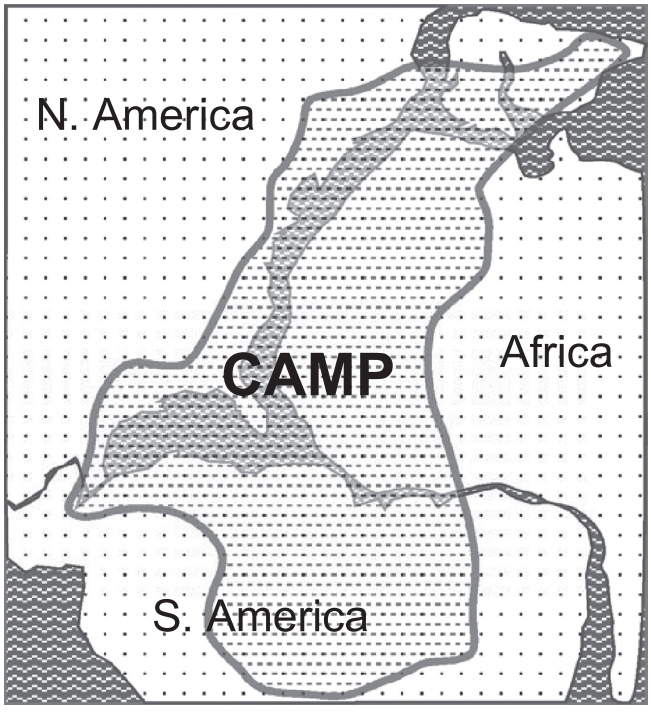

Fig. 9.3 Central Atlantic Magmatic Province (CAMP)

Characteristics of LIPs

Briefly, the following features characterize flood basalt provinces:

1. They cover as much as 500,000 km^2 in some cases (Deccan Traps).

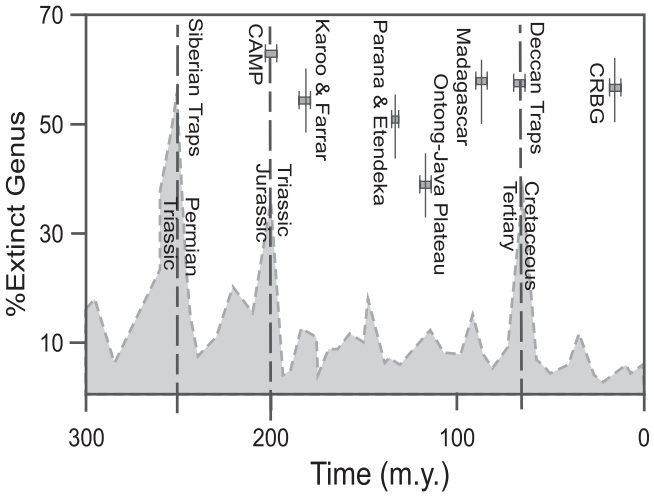

Fig. 9.4 Flood basalt eruptions and mass extinction events [after Fig. 1 in White and Saunders (2005)]

Fig. 9.5 A field picture of the Columbia River Basalts showing the horizontal lava flows toward the top and curved joints defining the entablature zone of a lava flow in the foreground (photo courtesy of Professor David Lee, Florida International University)

2. Individual lava flows can be very thick (as much as 70 m) and sometimes extend over distances of hundreds of km. Thicker flows generally are characterized by well-developed columnar joints in the upper and lower parts (called "Upper Colonnade" and "Lower Colonnade"). The central part of such a flow, called the "Entablature Zone," lacks such well-developed columns and instead is characterized by strong irregularly curved fractures (Fig. 9.5).
3. LIP lavas were erupted from *fissures/dikes* and not from well-defined volcanoes. Eruptions were largely nonexplosive, as indicated by the general rarity of pyroclastics (the Siberian Traps are an exception to this). Ernst and Buchan (1997) and other authors have identified major radiating dike "swarms" associated with LIPs, which have been linked to plume impact sites.
4. LIP lavas are *predominantly tholeiitic* basalts to andesitic basalts, and most (perhaps about 80 %) of them have 3–8 wt% MgO, pointing to their differentiated nature (Fig. 9.6). Picritic lavas with as much as 17 % MgO occur in most LIPs. An unusual type of ultramafic alkaline lava with as much as 30–40 % MgO occurs in the Siberian Traps. These are called *meimechites*. Some meimechites carry phenocrysts and xenocrysts of Fo_{93} composition and Fo_{91} olivine in the matrix (Arndt et al. 1995). Among other peculiarities, meimechite lavas and dikes contain biotite in the groundmass and have relatively high Ni (2,000+ ppm) and strongly LREE-enriched REE patterns (not shown here). Returning to the global LIPs, carbonatites, nephelinites, basanites, and alkali basalts occur in some provinces (e.g., the Deccan Traps, discussed later), albeit in minor volumes.
5. The tholeiites and tholeiitic picrites from various LIPs can be aphyric or carry 5–20 % phenocrysts of olivine (generally altered to iddingsite), plagioclase, and augite. Pigeonite and orthopyroxene phenocrysts are generally rare. In many LIPs the picrites are alkalic.

It is beyond the scope of this book to present a detailed analysis of all LIPs; therefore, we will focus on two best-studied examples instead—the Columbia River Basalts Group (CRBG) and the Deccan Traps.

The Deccan Trap Province, India

Deccan Trap lavas form an enormous plateau over about 500,000 km^2 of western and central India (Fig. 9.7). Differential erosion of individual lava flows has resulted in a staircase-like topography (Fig. 9.8).

The lavas erupted at a time when the Indian plate was situated over the current location of the Reunion hot spot (Fig. 9.9); and following its eruption, the Indian plate "raced" at 20 cm/year to collide with the Eurasian plate, which led to the formation of the Himalayas.

In the south, the lavas overlie Archaean rocks, whereas in the north and northeast areas, Deccan lava flows overlie Gondwana sedimentary rocks (Cretaceous). In some areas, sedimentary layers of variable thickness occur between lava flows. These layers are called "intertrappean beds" and they occasionally contain fossilized plants and dinosaur eggs.

The lava package is the thickest in the Western Ghats hills around Mumbai, where it reaches a thickness of 2.7 km. The lavas largely erupted through fissure eruptions, and small central-type eruptions (i.e., volcanoes) occur in a few places. Most authors

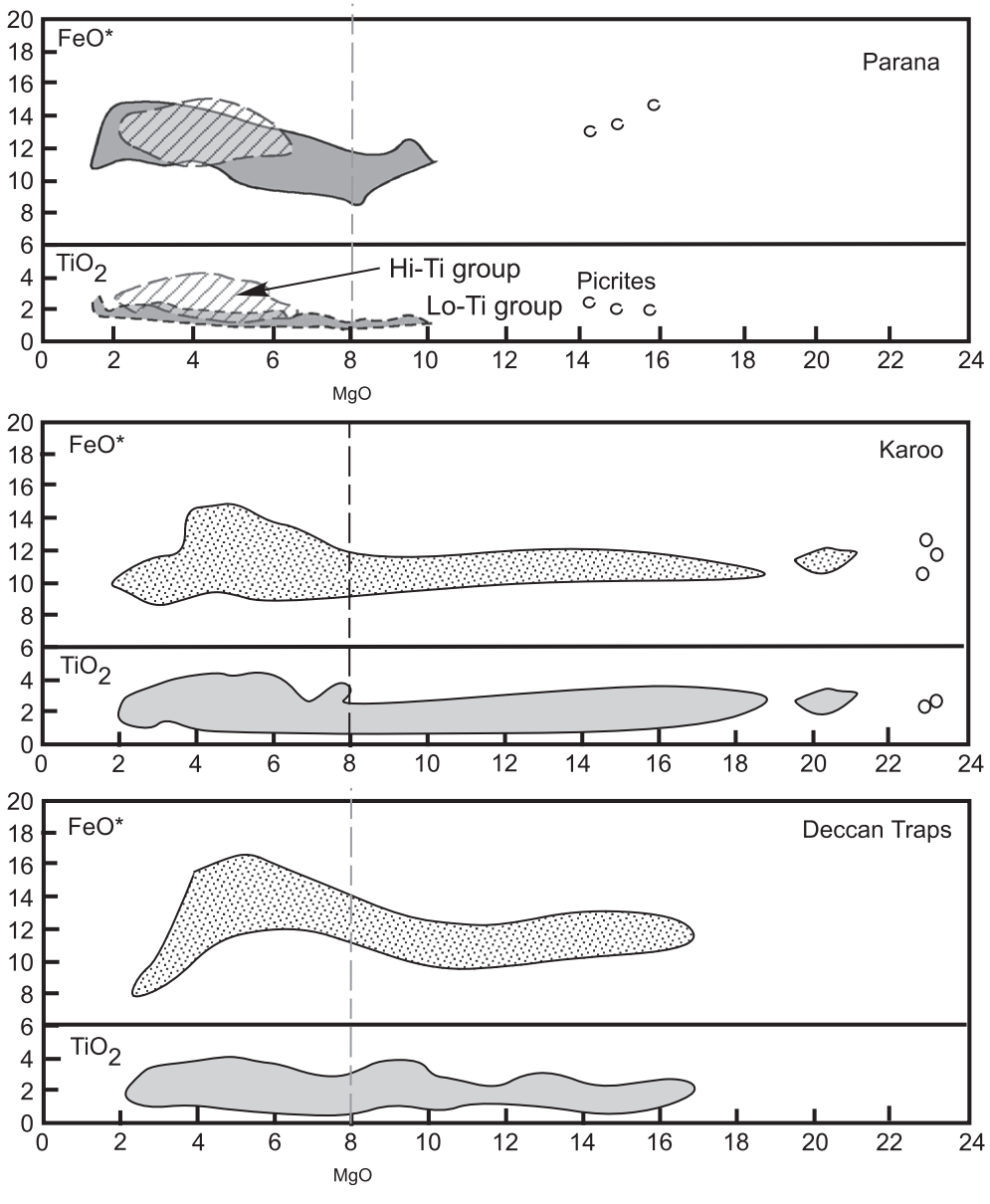

Fig. 9.6 (Continued)

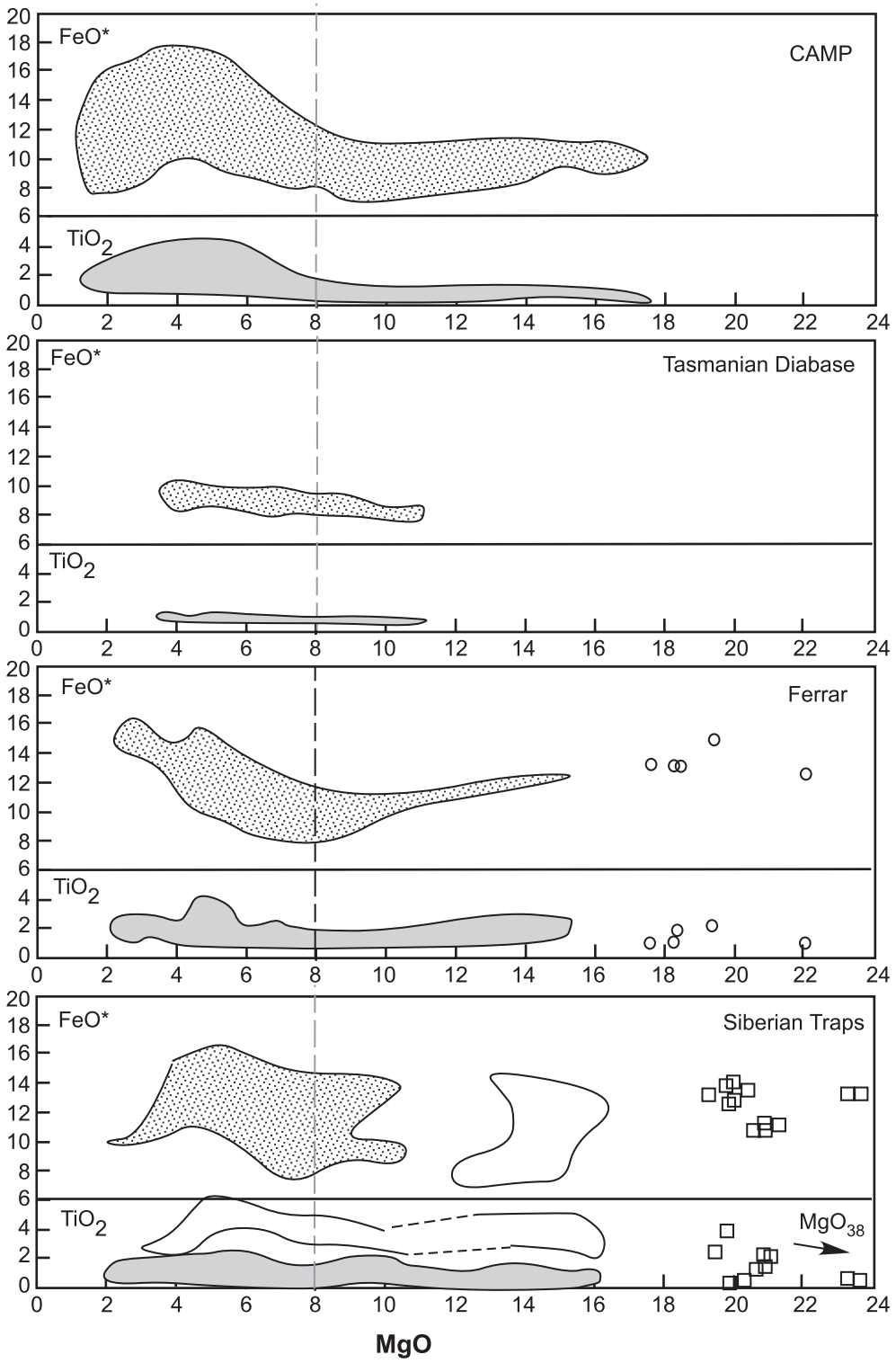

Fig. 9.6 MgO, FeO*, and TiO_2 variation in basaltic eruptives from several LIPs

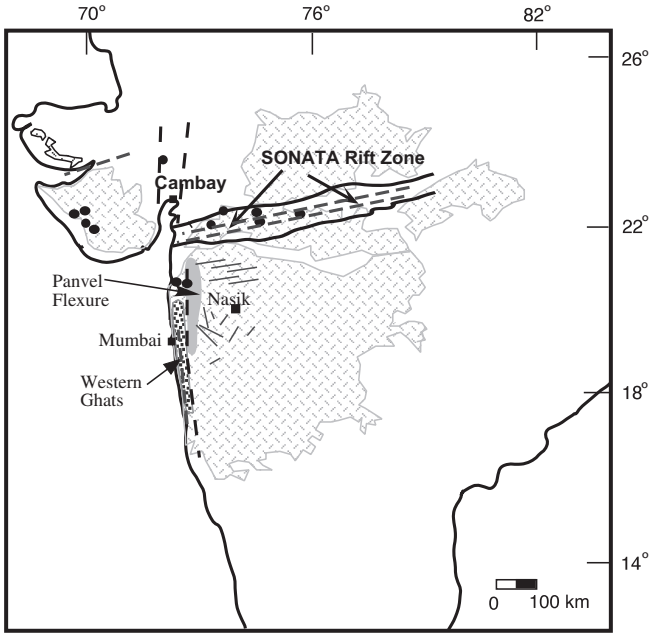

Fig. 9.7 Map showing the distribution of Deccan Traps LIP. Major rift systems, dikes (*short lines*), and the Western Ghats (*thickest section*) are all shown

Fig. 9.8 Field photograph of Deccan Trap lava flows

agree that the Deccan eruptions started in the northwest and rapidly moved south and along the east–west trending Narmada rift zone.

Age and Duration

Paleomagnetic measurements suggest that the eruptions occurred within three chrons: C30N, C29R, and C29N, with the bulk of it occurring in C29R, overlapping the K/T boundary (Courtillot et al. 2000;

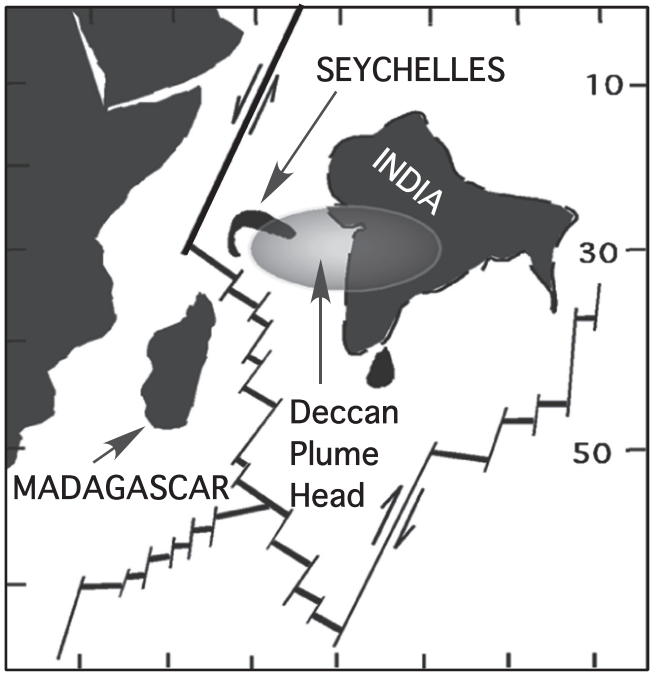

Fig. 9.9 Location of India over the Reunion hot spot at the time of Deccan Traps eruption

Fig. 9.10). K/Ar and $^{40}Ar/^{39}Ar$ dates obtained on rocks and mineral separates from lava flows in various parts of the Deccan suggest that the bulk of the volcanism occurred 65 ± 0.9 million years ago and that the earliest eruptions started around at 72 Ma. A recent study suggests that the 2-km-thick, 65-million year-old lava package at Western Ghats erupted within 30,000 years (Sen et al. 2006). Another recent study involving combined paleomagnetic and Ar dating has suggested that large volcanic pulses of very short duration (~1,000 years) formed the Western Ghats lavas (Chenet et al. 2007).

Lavas, Intrusions, and Mantle Xenoliths

The lavas are predominantly tholeiitic, although minor volumes of alkalic basalts, basanites, nephelinites, and carbonatites occur mainly in the peripheral regions and/or as intrusions in the rift zones. Rhyolites are relatively minor but have been found in northwestern and southwestern areas. Picritic lavas with 10–20 % MgO are also rare and are found in the lower parts of the lava sequence in the northwestern Deccan.

Dikes and sills related to the Deccan are well exposed around the peripheries of the Deccan. The intrusive system runs east–west in the Narmada rift zone (Sheth et al. 2009). North–south dikes are exposed along the west coast. Randomly oriented

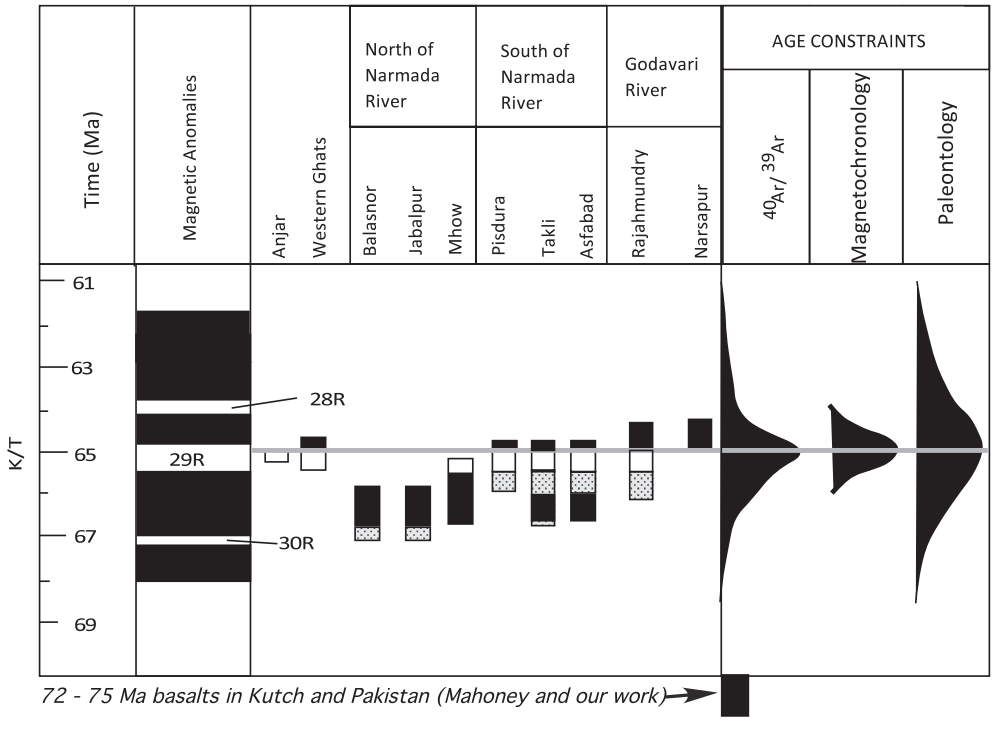

Fig. 9.10 Age of the Deccan Traps estimated by various methods (Sen and Chandrasekharam 2010)

dikes occur elsewhere (Fig. 9.7). Whereas some of these intrusions are feeders of lavas, others postdate eruption and cut through lava flows. Small cinder cones and "plugs" through which alkalic lavas erupted occur in the northwest, particularly in and around Kutch (Gujarat State).

Small (<3 cm) mantle xenoliths, composed of spinel lherzolite and wehrlite, occur in many of the alkalic intrusions/lavas in Kutch, and elsewhere. Garnet pyroxenite and granulite xenoliths have also been described from Mumbai area.

Petrology of Deccan Tholeiites

Phenocrysts

Most Deccan lavas are porphyritic and carry phenocrysts of olivine (usually altered to brownish iddingsite) and plagioclase. Augite phenocrysts also occur in many lava flows, particularly the younger ones. Pigeonite phenocrysts are rare even though it is a common groundmass mineral. Titanomagnetite and ilmenite microphenocrysts are rare but are common in the groundmass. Aphyric (or near-aphyric) textured lavas also occur but they are not as common.

Olivine is generally altered in the Deccan. Krishnamurthy et al. (2000) found that composition of unaltered olivine crystals shows a bimodal population: their Type 1 olivines ($Fo_{86–92}$) are significantly more magnesian than the Type 2 olivines ($<Fo_{86}$). Type 1 olivines occur in alkaline-to-transitional lavas in the northwestern Deccan Traps; and Type 2 occurs as phenocrysts in the more common tholeiitic lavas and dikes. Olivine crystals in mantle spinel peridotite xenoliths found in Kutch area (also northwestern Deccan) have $Fo_{88–92}$ composition. Lavas carrying Type 1 olivine phenocrysts therefore could be primary magmas (cf. Sen 2001).

Plagioclase phenocrysts commonly occur in tholeiitic lavas with MgO <7 %. They are conspicuously zoned with compositions ranging from $An_{76–61}$. The most calcic plagioclase ($An_{82–88}$) occurs in the primitive lavas of northwestern Deccan (the same ones that have the high-Fo olivine; see Sen 2001). Plagiolcase thermometry suggests that the lavas erupted at 1,125–1,200 °C (Sen 2001).

Phenocryst distribution in the type section of the Western Ghats is presented in Table 9.1 and Fig. 9.11. A special type of lava occurs in the Deccan that carries "giant" 5-cm-long plagioclase phenocrysts and is called "Giant Phenocryst Basalt (GPB)." GPB flows are not restricted to the Western Ghats and are

Table 9.1 Geochemical stratigraphy of Deccan Trap lavas at the Western Ghats type section near Mumbai

Subgroup	Formation	Thickness (m)	Phenocrysts	MgO range
Wai	Desur		Ol + Pl	5–6
	Panhala	>150	Ol + Pl	6.3–6.8
	Mahabaleshwar	280	Ol + Pl	5–6.7
	Ambenali	500	Ol + Pl	5–7
	Poladpur	370	Ol + Pl	6–9
Lonavala	Bushe	325	Ol + Pl + Aug	5–12
	Khandala	140	Ol + Pl + Aug	4.2–9.4
Kalsubai	Bhimashankar	140	Ol	5–6.5
	Thakurvadi	400	Ol + [Pl] + Aug	5–10
	Neral	100	Ol + Pl	5–11
	Igatpuri	150	Ol + Pl	5–10
	Jawahar	>200	Ol + Pl	5–10

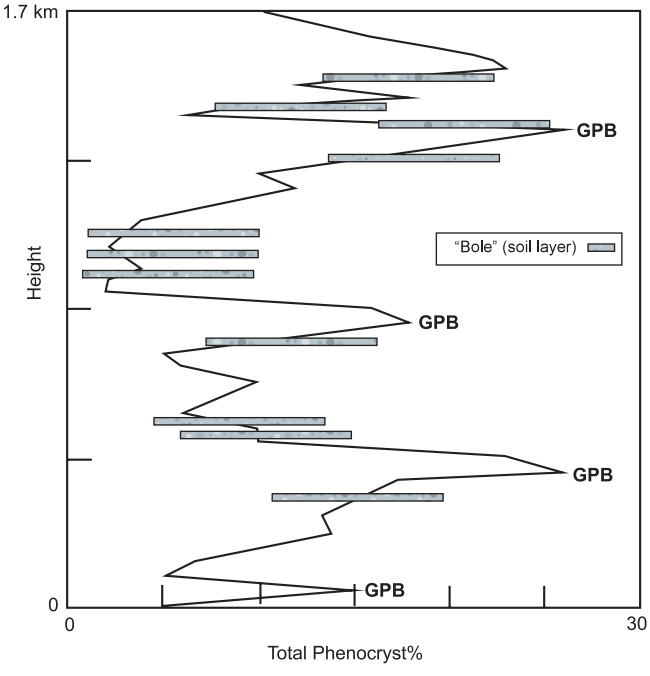

Fig. 9.11 Location of GPB lava flows and soil horizons (*gray with circles*) in the lower part of the Western Ghats type section (*source*: Sen 2001)

found sporadically throughout the Deccan. In the Western Ghats type section, GPB flows occur in the lower part, with each of them marking the end of a Formation (each of these formations are defined on the basis of geochemistry in the next section, and each formation is thought to have been fed by an individual magma chamber). In the Western Ghats, GPB lava erupted following a hiatus as marked by the occurrence of a

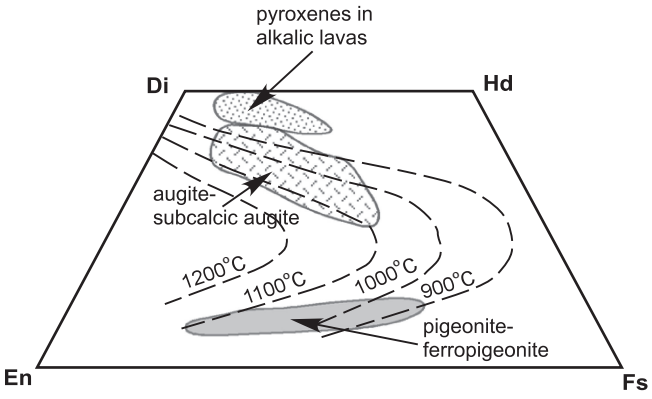

Fig. 9.12 Composition of Deccan Trap pyroxenes (after Sheth and Melluso 2008)

soil horizon, commonly referred to as a "Bole bed" (Fig. 9.11). Based on this observation, Sen (2001) suggested that the GPB lava eruptions marked the end phase of a dying magma chamber.

Deccan tholeiitic pyroxenes are dominantly augite; and pigeonite crystals are less common. Pyroxenes that occur in alkalic lavas are more diopsidic (Fig. 9.12). Augite appears later in the crystallization sequence than plagioclase and occurs as phenocrysts in tholeiites with less than about 6 % MgO. Pigeonite occurs largely as groundmass. Extremely Fe-rich pyroxenes occur in the most differentiated rocks in shallow intrusions. Orthopyroxene crystals have rarely been found in the groundmass. Figure 9.12 shows the compositional fields for augite–ferroaugite and pigeonite series pyroxenes that occur in the tholeiites. There are also sporadic quench (metastable) pyroxenes that plot between the two fields (not shown here). Pyroxene thermometry of tholeiites suggests that most of them erupted at about 1,100 °C. In the Deccan, Fe–Ti oxides are titanomagnetite and ilmenite. In the Western Ghats they give maximum temperature of 1,075 °C. Sulfides and native copper have been found to occur as a trace mineral. Their common globular form suggests an origin by liquid immiscibility (Sen 2001).

Geochemistry

Figure 9.13 shows Deccan Trap lavas from many different areas across the Deccan. The lavas from the type section of the Western Ghats are shown, where the lava package reaches a thickness of 2.7 km (Table 9.1). Although not shown here, the bulk of Deccan Trap tholeiites overlaps the Western Ghats.

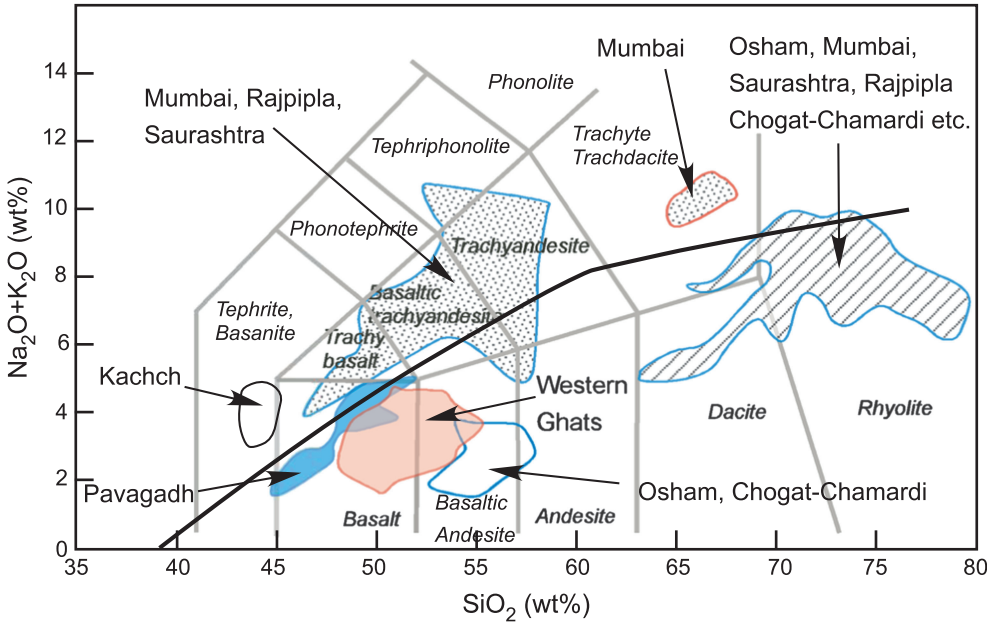

Fig. 9.13 Deccan Traps in alkali–silica diagram. Note that 90 % or more of the Deccan basalts plot overlap the Western Ghats field

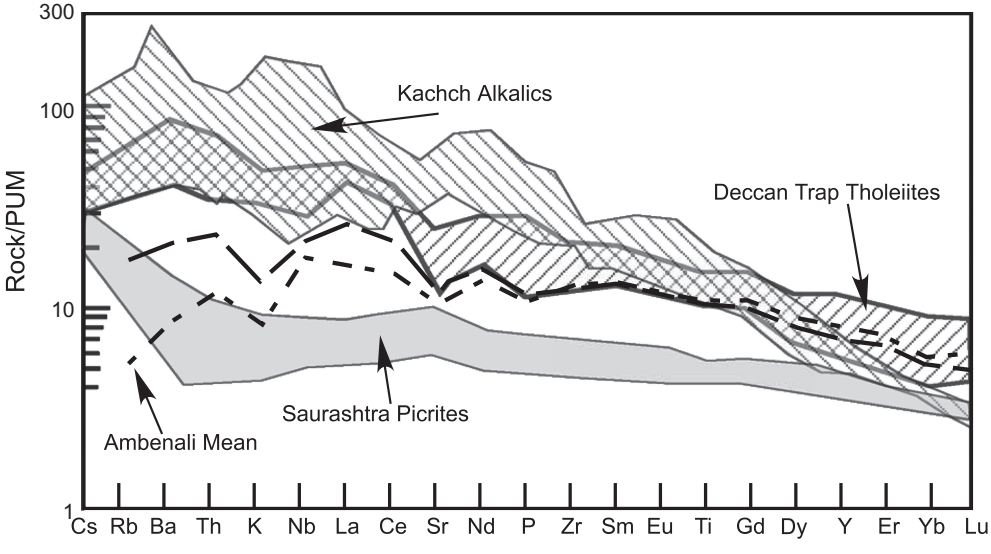

Fig. 9.14 Trace element diagram for the Deccan Traps

Xenolith-bearing alkalic lavas of Kutch (northwestern Deccan), rhyolites, and other differentiates from other parts of the Deccan are also shown in this figure.

In terms of trace elements, Deccan tholeiites, picrites, and alkalic basalts, nephelinites, and basanites all show strong incompatible element enrichment (Fig. 9.14). This enrichment is due both to crustal contamination of the magmas and to their derivation from an enriched source. Chondrite-normalized Sm/Yb ratios (i.e., $[Sm/Yb]_n$]) of the vast Deccan tholeiites vary from 1 to 3 over a range of $[Sm]_n$ = 15–80, from 1.2 to 2 in the tholeiitic picrites for $[Sm]_n$ range of 11–22. Alkalic picrites have $[Sm/Yb]_n$ of 3–4. Modeling of $[Sm/Yb]_n$ versus [Sm] suggests that these magmas were derived from spinel peridotite (Sen and Chandrasekharam 2011).

J. Mahoney, K. Cox, and others have carefully documented the extensive diversity in isotopic compositions shown by Deccan Trap lavas and intrusives (Fig. 9.15). Fields for Ambenali, Bushe, and some other lava formations from the Western

Ghats are identified in this diagram. Ambenali Fm. is uncontaminated or least contaminated by the continental crust. Its compositional similarity with lavas from the Reunion hot spot supports the hypothesis linking the latter with the Deccan plume. Mantle xenolith-bearing alkalic basalts from Kutch area from the northwestern Deccan, although not shown here, also seem to come straight from the depleted mantle, like Ambenali, without any contamination by the continental crust. On the other hand, Bushe Fm. tholeiites are isotopically the most contaminated by old continental crust (Fig. 9.15). The range of isotopic diversity has also been ascribed to contamination by old continental lithosphere through which the magmas passed. One perplexing aspect of the Bushe is that even though it is isotopically so much more contaminated than Ambenali, it is generally richer in MgO (i.e., less differentiated) than Ambenali. Normally, basaltic magmas that assimilate more crust also undergo greater cooling and loss of crystals; and from that perspective, Bushe should have been more differentiated than Ambenali, if they both came from similar parent magma. Why it is not more differentiated has perplexed many authors. Among the ideas that have been put forth to explain this discrepancy are as follows: (1) Bushe magmas formed by mixing of melts from the old continental crust and lithospheric mantle with some plume-derived melts, whereas Ambenali is almost entirely plume-derived; and (2) some other complicated process that involved mixing between magmas derived from crust-derived melts with hotter, more magnesian melts from the lithosphere (and not the plume itself) in producing Bushe.

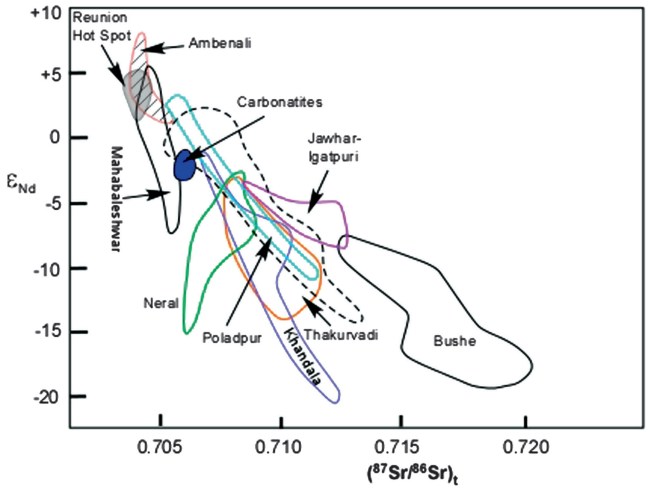

Fig. 9.15 Nd–Sr isotope ratio diagram showing great isotopic variability that characterizes the Deccan basalts (*source*: Sen et al. 2009)

Deccan Primary Magma(s)

Let us start with the issue of primary magmas of the Deccan. The highly magnesian, mantle xenolith-bearing, alkalic lavas of Kutch area have the right compositions to be primary magmas (Sen and Chandrasekharam 2011). However, their higher alkalis, TiO_2, and other characteristics indicate that they cannot be candidates for parent magmas to the significantly more voluminous tholeiites. So, what were the primary magmas of the tholeiites? K. Cox and coworkers suggested that picrite magmas, similar to those found in northwestern Deccan, were suitable primary magmas. There are both alkalic and tholeiitic picrites in the Deccan Traps; and tholeiitic picrites with about 13–17 % MgO could be potential primary magmas (Fig. 9.16). One could then use a "forward model" in which one starts with a selected primary magma (i.e., a Deccan picrite) and then "fractionate" it at various pressures using available software (such as MELTs: http://melts.ofm-research.org/; Ghiorso and Sack 1995) to evaluate the best fit(s) to the Deccan compositional field. A tighter constraint may be obtained by using an "inverse" model in which one uses the most magnesian, aphyric (i.e., crystal-free melt composition) Deccan lava(s) and then

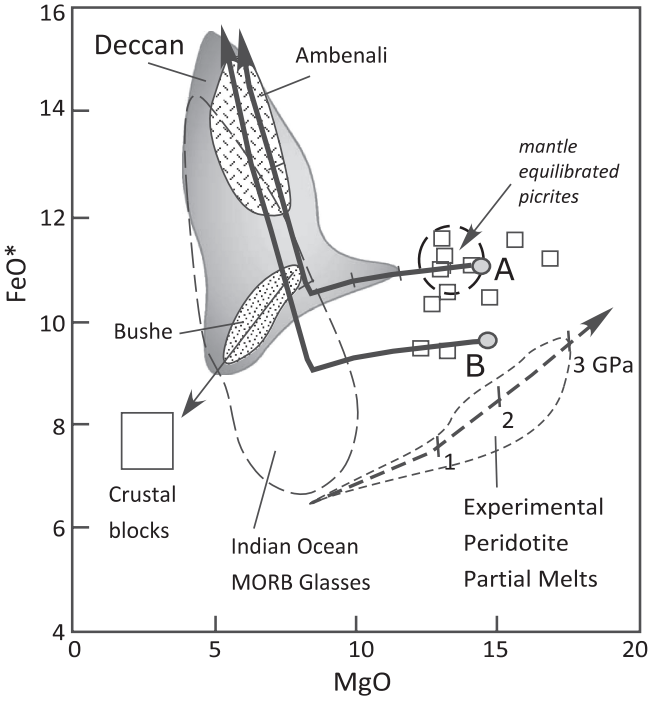

Fig. 9.16 MgO–FeO* diagram shows a comparison between Deccan picrites (*square*), Deccan tholeiites (*gray*), and experimental peridotite melts. Two modeled liquid lines of descent (*lines with arrows*) are from Sen and Chandrasekharam (2011)

incrementally add olivine crystals of appropriate composition (as constrained by $K_d = 0.3$) to it until a melt composition is obtained that would be in chemical equilibrium with a reasonable upper mantle peridotite with $Fo_{88–90}$ olivine. Sen and Chandrasekharam (2011) did this for the Deccan tholeiites using both approaches, as explained in the next section.

In spite of the complex isotopic trends that have been interpreted to reflect signatures of crustal contamination of plume-derived melts, mixing between lithospheric melts and plume-derived melts, the major element composition of the erupted lavas shows much less variability that can be mostly explained by fractional crystallization and magma mixing. For example, the bulk of the Deccan tholeiites, irrespective of their isotopic compositions, plots within the gray zone in Fig. 9.16. A large part of the gray zone, including Ambenali and Bushe, squarely overlaps with the Indian Ocean MORB glasses, which could not have been influenced by old continental crust. What this comparison shows is that low-pressure crystal fractionation, likely accompanied by magma mixing, was the principal factor in controlling compositions of Deccan tholeiites within the 5–9 % MgO range.

MELTS-based modeling of MgO, FeO contents of Deccan tholeiites shows two calculated liquid lines of descent (LLDs) at 0.2-GPa pressure fit the Deccan tholeiite data quite well and confirms a strong control exerted by low-pressure fractionation of most Deccan tholeiites. The two different starting melt compositions "A" and "B" for these LLDs were obtained by the inverse approach outlined above (Fig. 9.16). As we see, both A and B resemble Deccan picrites. B misses the critical "kink" toward higher MgO (>10 %) compositions of the Deccan field. Most interestingly, neither A nor B resemble the partial melts generated experimentally from mantle peridotite at 2–3 GPa because both A and B have higher FeO at comparable MgO values (15 %; Fig. 9.16). Sen and Chandrasekharam (2011) offered two hypotheses to explain this observation: (1) the picritic primary Deccan magmas were generated from a more Fe-rich source, such as a mixture of deep crustal eclogite and peridotitic plume; and (2) the actual primary magma was more MgO-rich (18–22 % MgO) than A or B and could have been generated at a much higher pressure (about 4.5 GPa). They preferred the first explanation.

Some possible primary magma compositions for Deccan tholeiites are presented in Table 9.3 (source: Sen and Chandrasekharam 2011). Potential temperatures for these compositions using four different thermometers are also given. Pressures were estimated from a barometer established by Lee et al. 2009 (given in Sen and Chandrasekharam 2011). According to this table, Deccan picrite magmas may have been generated at about 75 km depth and its potential temperature was somewhere around 1,550–1,590 °C. These high temperatures make the Deccan significantly hotter than MORB (1,270–1,400 °C), Iceland (1,450 °C), but as hot as Hawaiian hot spot (1,550 °C: Herzberg et al. 2007), which again supports a plume origin for the LIP.

Box 9.1: Inverse Modeling: Olivine-Addition Calculation

LIPs are dominantly composed of tholeiitic basalts, bulk of which have the chemical characteristics of differentiated magma, such as low MgO relative to the primary magma that can be in chemical equilibrium with upper mantle peridotite. A commonly used way to derive the primary magma composition for a suite of erupted LIP lavas is to incrementally add back the chemical components that were lost from the original magma. This is called "inverse modeling," and it is certainly a nontrivial task.

The first step in this type of inverse modeling is to select the lava composition that has the following characteristics:

- It has the maximum MgO (i.e., most primitive).
- It is olivine-saturated (i.e, contain only olivine phenocrysts) and not saturated with any other phenocryst phase.
- It does not have excess olivine, i.e., the magma has not picked up extras crystals of olivine from conduit walls (Note: this can be tested using olivine/liquid partitioning K_d, see Chap. 5).
- Phenocryst percentage is less than 5 % or so (i.e., the lava is nearly a melt).
- The chosen composition should have mantle-like isotope composition and exhibit no sign of crustal contamination.

The second step is to add back the olivine crystals at small fractional increments (I use 2 % increments as a rule of thumb) to the lava composition while adjusting the composition of the olivine at every step so that olivine/liquid equilibrium

(continued)

Table 9.2 Olivine-addition calculation

	1	2	3	4
Wt%	Parent	100 % normalized parent	Olivine to add: Fo86	2 % ol-added comp.
SiO_2	48.59	48.73	40.24	48.56
TiO_2	1.21	1.21		1.19
Al_2O_3	14.80	14.84		14.55
FeO*	10.56	10.59	13.44	10.65
MgO	10.72	10.75	46.32	11.46
CaO	11.03	11.06		10.84
Na_2O	2.16	2.17		2.12
K_2O	0.36	0.36		0.35
P_2O_5	0.28	0.28		0.28
Total	99.71	100.00	100.00	100.00

Box 9.1 (continued)

K_d value of 0.3 is maintained. This incremental addition calculation and recalculation needs to be continued until a calculated "magma" composition is reached that can be in equilibrium (to be tested using $K_d = 0.3$ criterion) with upper mantle olivine of composition $Fo_{88–90}$.

It is best to do these calculations using a spreadsheet such as EXCEL®. Table 9.2 gives an example of such olivine-addition calculation.

Column 1 gives the raw analysis of the olivine–phyric lava. Column 2 is the same analysis recalculated to give a total of 100 %. Using Ol/liq $K_d = 0.3$, it is determined that Fo_{86} olivine could be its equilibrium olivine composition. Column 3 shows composition of Fo_{86} olivine. In column 4, 2 % of Fo_{86} is added (i.e., 0.98*Column 2 + 0.02*Column 3).

Using the above method, it is calculated that primary magma in equilibrium with Fo_{88} olivine will have the following composition:

SiO_2	TiO_2	Al_2O_3	FeO*	MgO	CaO	Na_2O	KOP	P_2O_5	Total
48.07	1.10	13.45	10.77	14.30	10.02	1.96	0.33	0.27	100.27

Model for the Origin of Deccan Basalts

Two broad conclusions are reached from the above discussion: (1) primary Deccan magmas were picritic, hot, and somewhat Fe-rich; and (2) the bulk of the erupted tholeiites underwent extensive fractionation and mixing at about 0.2 GPa (about 6 km). Sen and Chandrasekharam (2011) presented an overall model for the generation of Deccan magmas based on their enormous volumes, rapid eruption rate, significant contamination by old crust, presence of a strong lithospheric component in the erupted lavas, and the *P–T* of origin (Fig. 9.17). The important features of this model are as follows:

- A large plume was the main source of both heat and magma.
- The bulk of the lithosphere prior to Deccan magmatism was thick in general except that it was then in places where it was thinned by prior rifting events.
- The lithospheric root was largely melted by the plume, thus providing the strong isotopic and trace element signal from old lithosphere that is preserved in bulk of the erupted basalts.
- Magmatism at the preexisting rift zones occurred at shallower depths and by smaller degrees of melting because such areas (e.g., Kutch) were far off the center of the Deccan plume and hence small degrees of volatile-rich magmas were produced.
- Plume impact thus thinned and eventually delaminated much of the lithospheric root, which perhaps contributed greatly in accelerating the speed with which the Indian plate moved after the melting event.

Table 9.3 Possible Deccan primary magmas and potential temperatures

		Picrite	Adjusted primary liquid (PMK)[a]	Sen (1995)	
		Pavagadh		Amb (A)	Amb
Wt%		K'2000		Melt2	Melt1
SiO_2		48.70	46.40	48	50.57
TiO_2		1.76	1.68	1.3	0.87
Al_2O_3		10.09	9.61	13	12.61
FeO*		10.29	9.91	11	10.88
MnO		0.18	0.17	0.1	0.1
MgO		14.78	18.96	15	13.96
CaO		11.76	11.20	10.25	9.13
Na_2O		1.49	1.42	1.7	1.96
K_2O		0.68	0.65	0.12	0.14
Total		99.73	100.00	100.47	100.22
Tp-H&G'09	°C	1,453	1,550	1,459	1,431
Tp-Put'08–15	°C	1,488	1,595	1,519	1,576
Tp-Alb'92	°C	1,435	1,549	1,445	1,402
Tp-Lee'09	°C	1,470	1,490	1,503	1,474
Mean Tp	°C	1,462	1,546	1,482	1,471
Pressure Lee'09	GPa	1.90	2.30	2.4	1.80

[a]Calculated from composition B

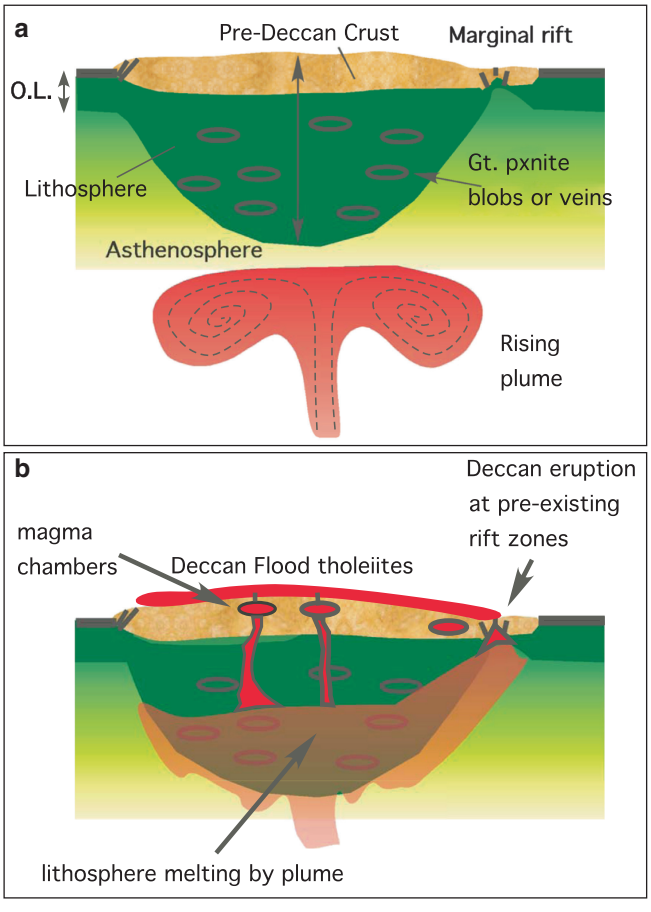

Fig. 9.17 Model of Deccan plume–lithosphere interaction (from Sen and Chandrasekharam 2011). (**a**) Pre-Deccan lithosphere had a thicker, heterogeneous, lithosphere. (**b**) Large-scale lithospheric melting was triggered by the Deccan plume

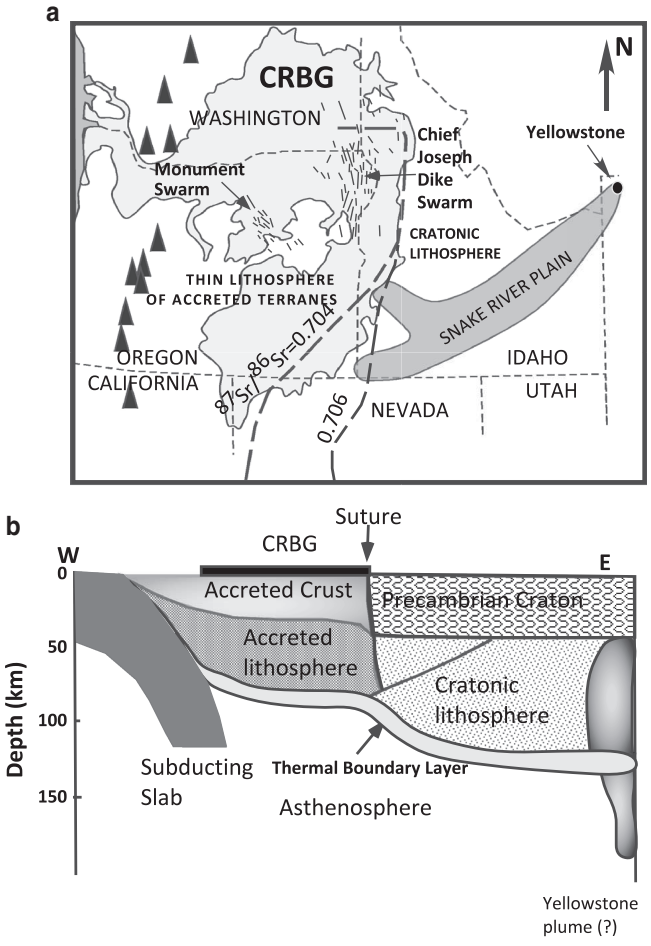

Fig. 9.18 (**a**) Map showing distribution of the CRBG (*light gray*), feeder dike swarms related to the CRBG, Cascades volcanoes (*Dark triangles*), the Snake River Plain, and the Yellowstone hot spot (simplified from Fig. 1 in Camp and Hanan 2008). (**b**) A schematic cross section (after Leeman et al. 2004) that depicts the complicated nature of the lithosphere at the present time: accreted and thinner lithosphere to the west and thicker, significantly older (Precambrian) lithosphere to the east of the suture zone. Cascades volcanoes are a product of subduction of the Farallon plate. At the eastern end, volcanic track of the Snake River Plain formed a result of the Yellowstone hot spot activity

Columbia River Basalt Group, Northwestern United States

The Columbia River Basalt Group (CRBG), with an estimated volume of 220,500 km^3, is the youngest (Miocene) of all flood basalt provinces. It forms a plateau of stacked lava flows covering a large area of Washington and Oregon states and a part of western Idaho (Hooper 1982; Hooper and Hawkesworth 1993; Camp and Hanan 2008; Fig. 9.18a). Its geological setting is complicated as the Columbia Plateau is situated between the Cascades range to the west and the Rocky Mountains to the east. The CRBG province edges up to the $^{87}Sr/^{86}Sr = 0.7060$ line, which is the surface expression of an important suture that glued the accreted lithosphere to the west with the cratonic lithosphere to the east (Fig. 9.18b). A further complication is the occurrence of the hot spot track of Snake River Plain that leads to the Yellowstone hot spot.

Dating indicates that although CRBG eruptions started at about 17.5 Ma, 94 % of the lava volume erupted between 16.6 and 15 Ma. Minor eruptions continued until 6 Ma (Camp and Hanan 2008). Some of the individual lava flows, such as the Roza flow, traveled more than 600 km to the Pacific Ocean being fed by N–S dikes that occur near the Washington–Idaho border (Fig. 9.18a; Hooper 1982). The bulk of the basalts (Grande Ronde Fm.) erupted through this dike swarm, known as the Chief Joseph dike swarm, and only a smaller volume of basalts (Picture Gorge basalts) erupted through the Monument dike swarm (Fig. 9.18a).

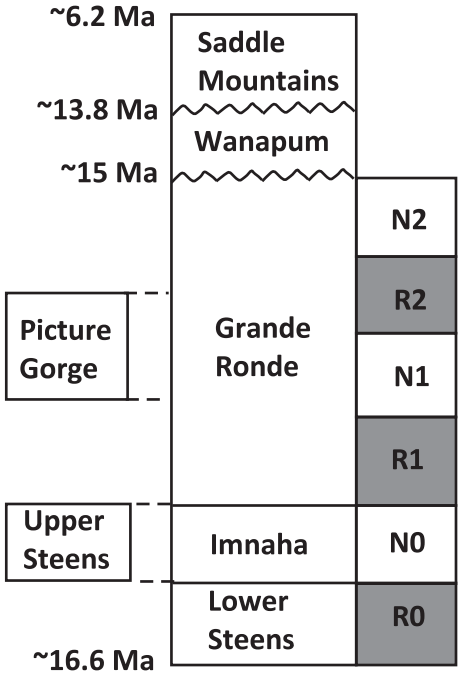

Fig. 9.19 Ages of individual CRBG formations

The CRBG is divided into several formations and members within each formation on the basis of geochemical criteria (e.g., Hooper and Hawkesworth 1993; Fig. 9.19). Among these formations, the lowermost Steens formation basalts erupted over southeastern Oregon (Camp and Hanan 2008; Wolff et al. 2008). The eruption center then moved north to Idaho–Washington border region where the Imnaha and the most voluminous Grande Ronde Formation lavas erupted from the Chief Joseph dike swarm (Fig. 9.18). Picture Gorge basalts, which are of the same age as the Grande Ronde, erupted from the Monument dike swarm. Contemporaneous with the culmination of the main eruptive phase ~15 Ma, rhyolites erupted on Snake River Plain and formed a volcanic track that ends in the currently active Yellowstone hot spot. Figure 9.20 shows relative volumes of the various formations of the CRBG (Hooper 1982; note that the timing of the eruptions as shown here on the *X*-axis has been improved since Hooper's pioneering work). Figure 9.21 shows spatial distribution of the various formations of the Columbia River Basalts.

Petrography and Geochemistry

The CRBG is generally tholeiitic. The Steens, Imnaha, and Picture Gorge basalts are olivine tholeiites with minor volumes of alkalic basalts. The Steens, Imnaha,

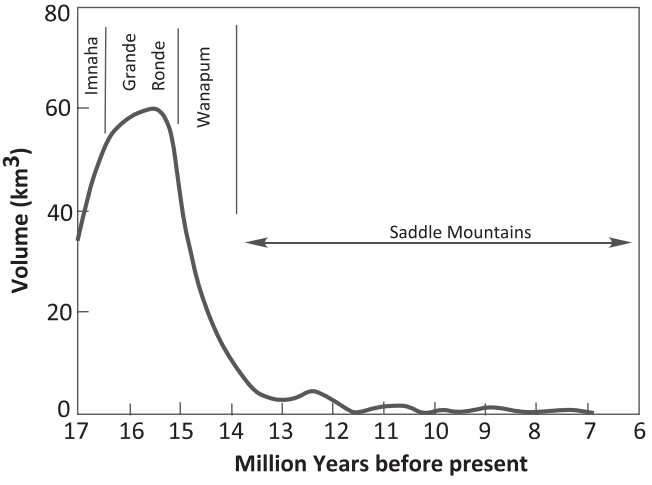

Fig. 9.20 Relative volumes of different formations in the CRBG (simplified from Hooper 1982)

and Picture Gorge basalts have olivine and plagioclase phenocrysts, whereas the voluminous Grande Ronde lavas are generally aphyric or contain <5 % microphenocrysts of plagioclase, pigeonite, and augite (Durand and Sen 2004; Caprarelli and Reidel 2005).

The earliest phase basalts of the Steens and Imnaha have lower SiO_2 than the voluminous Grande Ronde basalts, which are essentially basaltic andesite (Camp and Hanan 2008; Fig. 9.22a). Researchers have given special attention to the Grande Ronde lavas as they

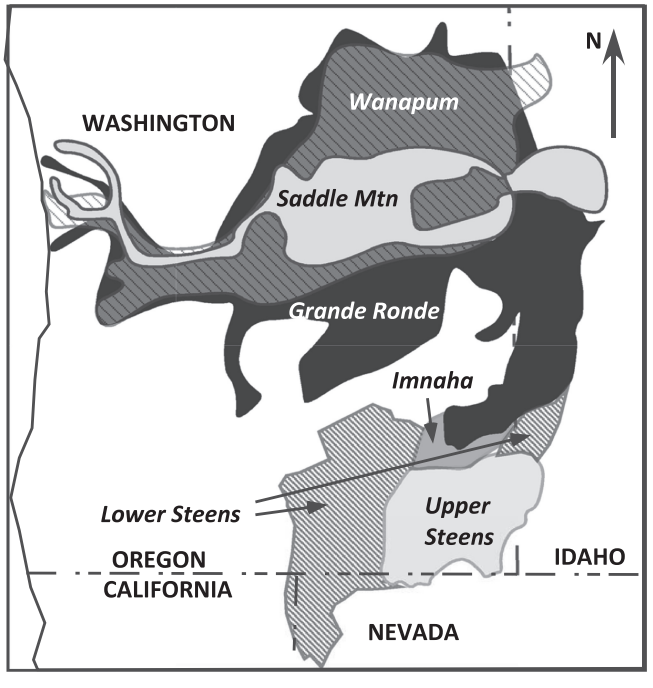

Fig. 9.21 Spatial distribution of individual formations of the CRBG (*source*: Fig. 5b in Camp and Hanan 2008)

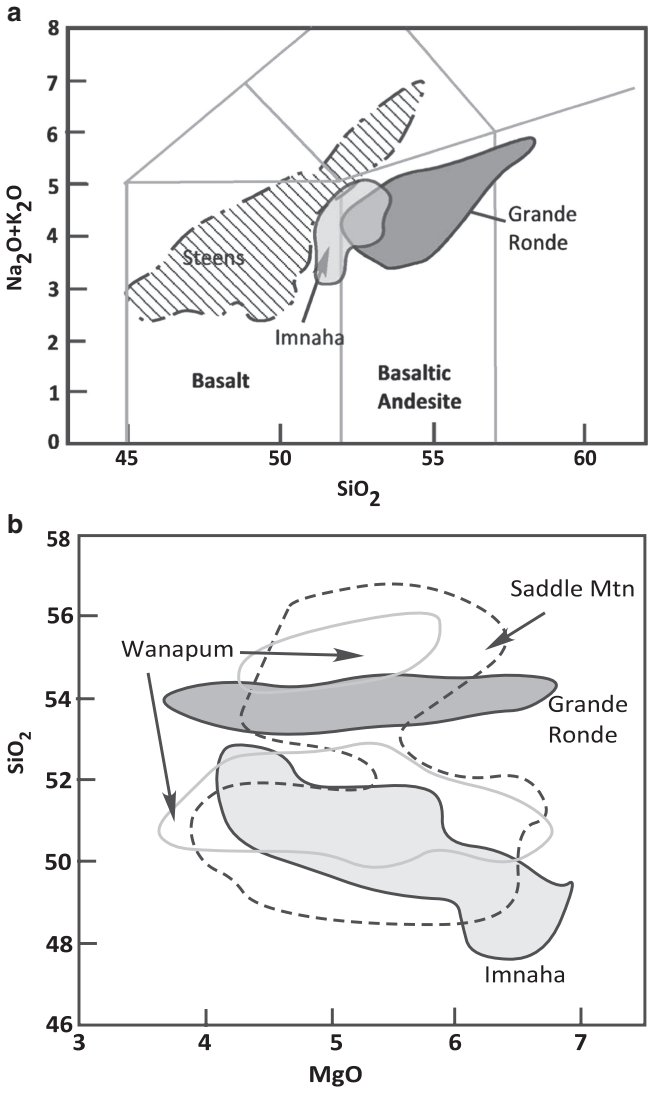

Fig. 9.22 (**a**) Silica–alkali variation in three major formations of the CRBG. (**b**) MgO–SiO_2 variation in the CRBG (*source*: Rodriguez and Sen 2013, in press)

compose about 90 % of the CRBG. Whereas the Imnaha basalts show a typical tholeiitic fractionation trend of increasing SiO_2 (~48–53 wt%) with decreasing MgO, SiO_2 of the Grande Ronde lavas remain essentially constant at a higher level (~54 %) over the same MgO range (Fig. 9.22b). This is an important geochemical characteristic of the Grande Ronde that cannot develop from fractional crystallization because such a process would have increased SiO_2 and correspondingly decreased MgO (as in the case of Imnaha). This feature is very likely a result extensive mixing of magma batches in subterranean conduits that kept the SiO_2 content at a constant level although MgO varied (Durand and Sen 2004). Durand and Sen (2004) presented strong petrographic and mineralogical evidence in favor of mixing in the Grande Ronde, such as the presence of both normal and reverse zoned plagioclase phenocrysts, both pigeonite-cored augite phenocrysts and pigeonite-free augite phenocrysts, and disequilibrium composition of many of the plagioclase and pyroxene phenocrysts.

Ramos et al. (2005) found plagioclase phenocrysts in various CRBG lavas to be zoned in terms of $^{87}Sr/^{86}Sr$ composition. If such crystals were held in their respective host magmas for a long time, then Sr diffusion across zone boundary in such crystals would have obliterated such zoning. The presence of zoning thus allowed these authors to calculate maximum time of residence of these zoned crystals in their respective magmas from the $^{87}Sr/^{86}Sr$ zoning profiles in each crystal. Such calculated residence times of these crystals turned out to be a few days to a few decades. This is important because it points to highly vigorous, shallow, magma chamber system where magmas were vigorously supplied and mixed and such chambers emptied rapidly via eruption so that there was little chance of crystal growth.

The low MgO and high SiO_2 of the volumetrically dominant Grande Ronde basalts indicate that they cannot be primary magmas from a typical upper mantle peridotite source because such magmas would typically have >10 wt% MgO and 48–50 % SiO_2. The aphyric to near-aphyric nature, extremely rapid eruption rate, and very large volume of erupted lavas of the Grande Ronde formation have prompted some authors to suggest that these lavas are essentially primary magmas generated by large-scale melting of eclogite source (e.g., Takahashi et al. 1998; Hooper et al. 2002; Camp and Hanan 2008). The younger Wanapum and Saddle Mountain formations show a large variation in SiO_2 and isotopic composition, which is generally accepted to be a result of crustal contamination (e.g., Wolff et al. 2008).

CRBG basalts show slightly enriched LREE-enriched patterns but almost flat Sm/Yb patterns (Fig. 9.23), indicating that their parent melts did not equilibrate with garnet as a residual phase, because in such case the basalts would have had strongly negative slopes between Sm and Yb. Therefore, if eclogite were involved in the melting process, melting degree must have been so high (perhaps >50 %) as to dissolve all garnet from the source rock. Alternatively, a straightforward explanation of the REEs is that their parent melts were derived from LREE-enriched spinel peridotite.

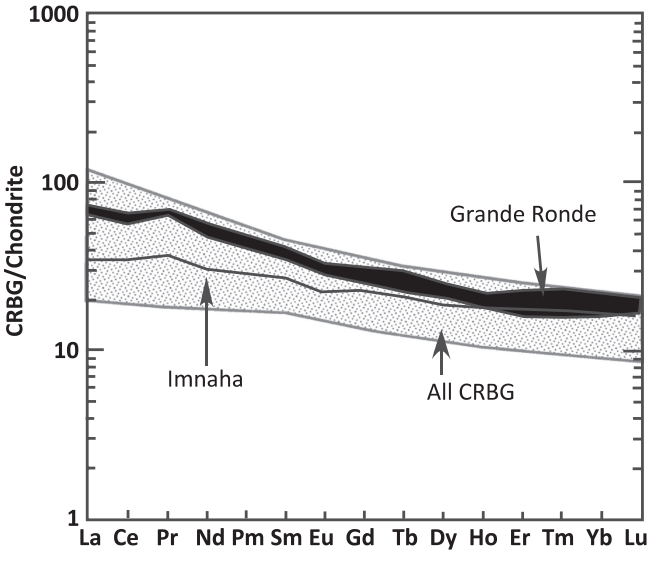

Fig. 9.23 REE patterns of the CRBG

He, Sr, Nd, Pb, and Os isotope data are available on the CRBG basalts. An extensive review of such data is not possible here. Instead, we focus on a recent interpretation of the Sr, Nd, and Pb isotopic variations in the CRBG (Fig. 9.24; Wolff et al. 2008). Although isotopically not as varied as the Deccan Traps, the CRBG lavas nonetheless show isotopic variations within individual formations and substantial differences between formations. Imnaha lavas exhibit the least variation and are thought to represent the composition of the mantle plume source for the CRBG (e.g., Hooper; Camp and Hanan 2008; Wolff et al. 2008). Imnaha also has moderately high (11.4 R/R_A) $^3He/^4He$ ratio, which supports a plume origin (Dodson et al. 1997). The isotopic composition of the other formations has been explained as resulting from crustal contamination for the Grande Ronde and Saddle Mountain formations and mixing with a depleted Pacific MORB-like source component for Steens and Picture Gorge basalts (Wolff et al. 2008). Saddle Mountain basalts are highly enriched due to extensive contamination with the old, enriched continental crust. Although some authors have argued for a subcontinental lithospheric component in some of the CRBG magmas, Os isotope composition (not shown here) appears to rule out any role of such a component (Chesley and Ruiz 1998).

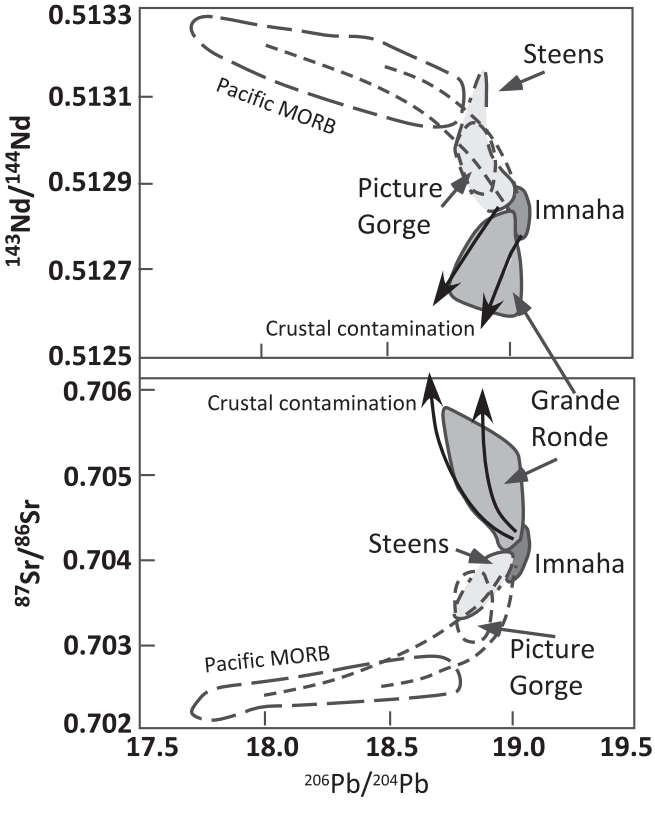

Fig. 9.24 Isotopic variations in selected formations of the CRBG compared with Pacific MORB. Wolff et al. (2008) used this diagram to argue for a centralized magma supply system for the CRBG

Petrogenesis of the Columbia River Basalts

Plume Versus Non-plume Models

Some early studies proposed the idea that CRBG primary magmas formed due to back-arc extension of the lithosphere while the Farallon plate (predecessor to the currently subducting Juan de Fuca plate) was subducting beneath Pacific Northwest during Miocene (Carlson and Hart 1988). There are other places on earth today where back-arc extension magmatism is actively occurring; however, the rates and volumes of eruption are nowhere close to those for the CRBG (Hooper et al. 2007). Therefore, the back-arc model has not gained much support. Plume proponents argue that only a large, short duration melting anomaly, such as a large plume head, is capable of achieving such rates. Accordingly, a popular idea is that a large plume head, whose tail is the nearby Yellowstone plume, was responsible for CRBG magmatic activity (e.g., Brandon and Goles 1988; Hooper and Hawkesworth 1993; Camp and Hanan 2008).

Briefly, the evidence used in supporting the Yellowstone plume origin of the CRBG is as follows:

- Eruption of a very large volume of lava (~207,270 km^3) in 1.6 million years.
- Moderately high, plume-like $^3He/^4He$ composition of the early eruptive CRBG basalts of the Imnaha formation.

- Seismological evidence for the existence of a ~100 km diameter plume conduit down to ~500 km beneath Yellowstone area (Yuan and Dueker 2005).
- There is little dispute that the Yellowstone magma source generated the Snake River Plain volcanic track. This track at 16 Ma was only 400 km south of the Chief Joseph dike swarm, which was actively producing CRBG lavas.

The problems with the Yellowstone plume idea are as follows:

- It has generated rhyolites over the past few 2.2 million years or so, whereas the CRBG are basaltic.
- The terminus of the Yellowstone–Snake River Plain track is still spatially off by 400 km from the site of CRBG volcanism.
- The occurrence of the CRBG magmatic source along a well-known structural plane of weakness, between a thick cratonic lithosphere and thin accreted terrane lithosphere (Christiansen et al. 2002). Accordingly, Christiansen et al. (2002) proposed that the magmatism instead was guided by lithospheric melting due to crack propagation.
- Thermobarometric calculations on the hottest magmas from the Snake River Plain led Leeman et al. (2009) to conclude that the maximum temperature of the Yellowstone source is only marginally higher (50° or less) than the ambient mantle. Since deep mantle plumes are supposed to be about 200° greater than normal upper mantle temperatures, a deep mantle origin of the Yellowstone plume becomes doubtful.

Some authors have offered solutions to some of the problems listed above: for example, to explain the 400 km N–S gap between the locus of the Yellowstone plume and the CRBG eruption site some 16 Ma (Fig. 9.25a), Geist and Richards (1993) presented a model called the "plume deflection model"

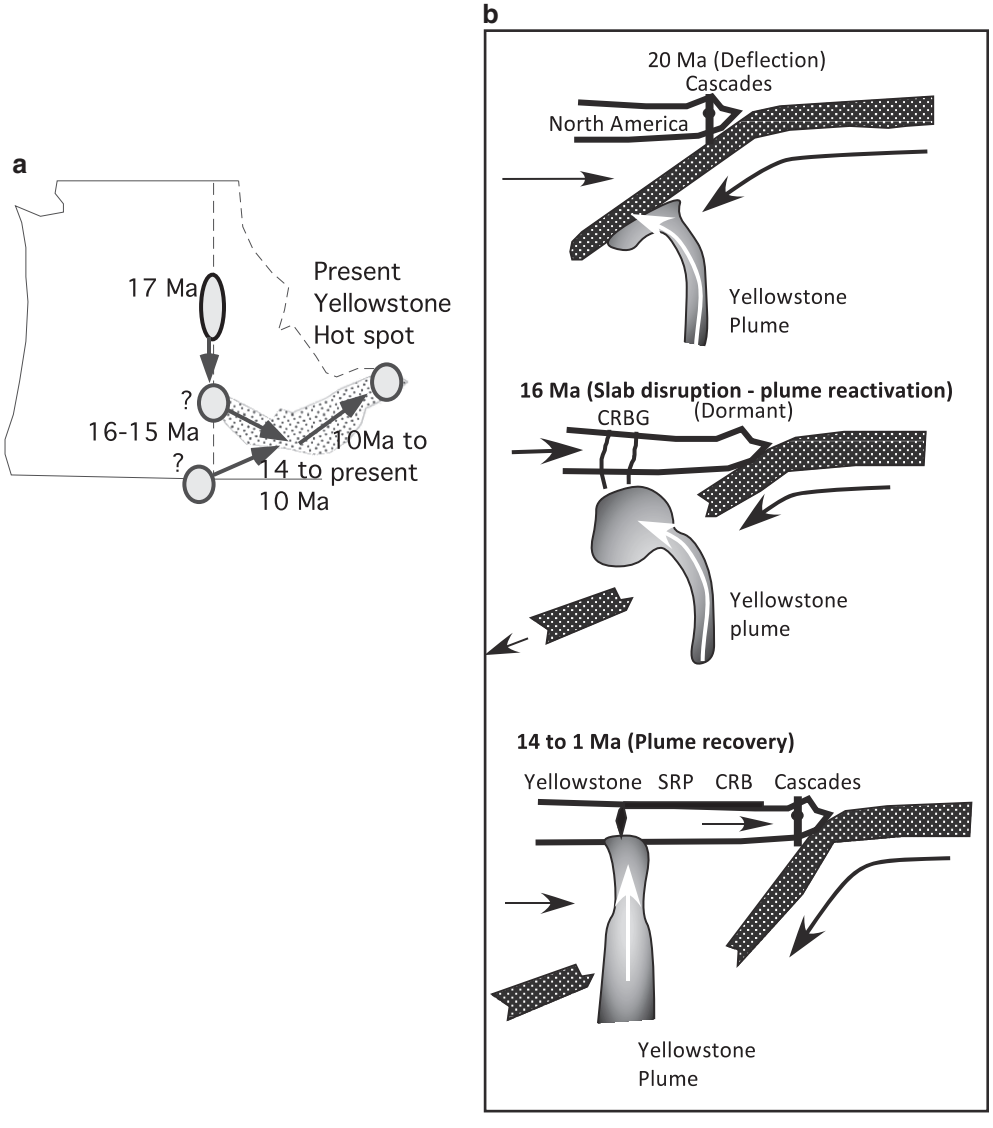

Fig. 9.25 Plume deflection model of CRBG magma formation (Geist and Richards 1993)

(Fig. 9.25b). In their model, the large bulbous head of the Yellowstone plume rose from the deep mantle some 20 Ma ago only to be blocked and dragged down by the subducting Farallon plate. However, by 16 Ma, the plume head had successfully broken through the Farallon plate and started to rise; and its decompression led to the formation of CRBG magmas. Between 14 and 1 Ma, the plume tail managed to "swing back" southward and create the Snake River Plains–Yellowstone hot spot track.

Camp and Hanan (2008) presented a complex plume-based model in which the plume goes through complex interaction with the lithosphere and crust to generate the CRBG (Fig. 9.26). In this model, the plume head initially melts to generate the older CRBG (i.e., Steens basalts) in southeast Oregon as it impinges upon the transitional and accreted lithospheres. During this time, the plume partially delaminates the lithospheric mantle, which becomes an added source of melting. The plume head rapidly spreads northward to northeast Oregon where it delaminates a substantial amount of the lithospheric mantle, producing the Imnaha basalts. Before Imnaha eruptions come to a close, the plume head had delaminated a substantial chunk of mafic crust-embedded lithosphere. Large-scale melting of the crust generates the Grande Ronde basalts. This is a "step function" change in the production of magma characteristics—from olivine-normative Imnaha basalts to more evolved "looking" Grande Ronde basaltic andesites. Continued migration of the plume head runs into the thicker cratonic lithosphere, isotopically enriched Grande Ronde and Wanapum and Saddle Mountain magmas formed.

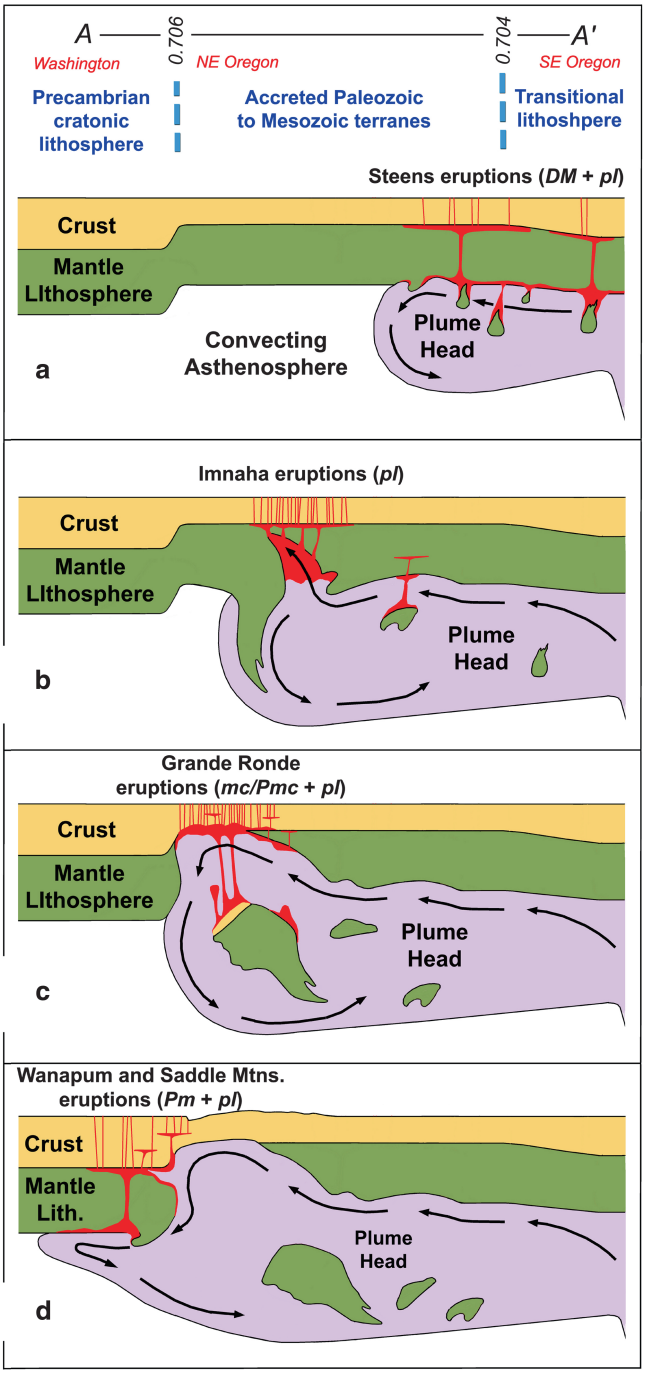

Fig. 9.26 Camp and Hanan's (2008) model for the generation of CRBG magmas by melting of a plume head and melts generated via lithosphere melting and erosion by the plume (courtesy of: Vic Camp)

Role of Eclogite and the Grande Ronde Formation in Petrogenetic Models

From the above discussion it should be clear that the Grande Ronde formation plays an important role in tectonic models of magma generation because of two reasons: (1) it is the most voluminous, comprising 90 % of the CRBG, and (2) the lavas are largely aphyric, which means they erupted as melts with 5 % or less crystals. Petrographic and mineral chemistry of the Grande Ronde lavas provide strong evidence for extensive magma mixing in shallow level chambers, obscuring the nature of their parent magmas. An added complication is crustal contamination of the Grande Ronde as evident from their isotopic composition (e.g., Wolff et al. 2008). Some recent authors find it easier to derive the Grande Ronde magmas by nearly whole-scale melting of eclogite because such a mechanism does not require enormously high temperatures and is also able to rapidly produce large volumes of what appear to chemically evolved melts. The derivation of Grande Ronde lavas from more primitive, peridotite-derived, partial

melts faces multiple problems—first, large amount of fractionation of the parent melts within the crust or Moho would be required. There is no geophysical evidence favoring the presence of large cumulate-filled fossil magma chambers. Second, there are also no large-scale collapse structures that may be expected to form as the chambers emptied out their lava. Finally, lava chemistries do not support large-scale fractionation from a primitive melt but do point to extensive magma mixing.

The question then becomes where was this eclogite source located? Takahashi et al. (1998) wanted such source to be ancient recycled oceanic crust embedded in the plume. However, the Os isotope composition of the Grande Ronde rules out their origin from an oceanic lithospheric source. Instead, the isotope composition points to an old continental mafic crust. Therefore, Camp and Hanan's (2008) model appears to provide a reasonable explanation for the origin of the Grande Ronde formation.

Summary

- LIPs are voluminous tholeiitic flood basalts that erupted through fissures in the crust. Many of them erupted at major stratigraphic boundaries; and the eruption rates were phenomenal. Most of them can be linked to their individual hot spot tracks. A currently popular model for their origin is that they are melts which form enormous plume "heads" whose long tails persist for another ~90 million years and produce hot spot tracks.
- Deccan Traps are predominantly tholeiitic, and smaller volumes of alkalic basalts, nephelinites, and carbonatites occur mostly in rift zones. The bulk of them erupted 65 ± 1 Ma.
- Tiny mantle xenoliths, mostly of spinel wehrlite and spinel lherzolite and fewer garnet pyroxenites, occur in alkalic lavas.
- Isotopic composition of Deccan Trap tholeiites suggests strong influence by crustal contamination. Ambenali formation lavas appear least or uncontaminated by the continental crust.
- Ambenali formation lavas are compositionally close to the Reunion hot spot lavas, which supports the causal link of this hot spot to the presumed plume head that was the source of Deccan lavas. The melting process involved large-scale melting of the subcontinental lithosphere as well.
- The bulk of the Columbia River Basalt Group in the Pacific Northwest erupted 15.5 ± 0.5 Ma from the Chief Joseph dike swarm located on the suture zone that connects the accreted lithosphere to the west with the cratonic lithosphere to the east.
- Grande Ronde formation forms some 70 % of the volume of the CRBG. They are largely aphyric, well mixed, and relatively evolved in their chemical composition. The Imnaha formation lavas, which underlie the Grande Ronde, are more magnesian.
- REE and isotope ratios suggest that some crustal/lithospheric contamination affected the composition of the lavas.
- Origin of the CRBG seems complicated, involving a plume that tore through the overlying subducted slab and melted the subcontinental lithosphere.

Subduction Zone Magmas

10

Abstract

The importance of subduction zones, which are major sites of earthquakes, mountain building, and basalt–andesite–rhyolite volcanism, was nicely presented by Stern (Rev Geophys 40:1012, 2002): "Subduction zones are also our planet's largest recycling system. They deliver raw materials to the subduction factory, where oceanic lithosphere, sediments, and seawater reequilibrate with ambient mantle, triggering melting and incidentally creating continental crust. What is not recycled in the upper few hundred kilometers of a subduction zone sinks to the core-mantle boundary, where this residue may be reheated for a billion years or so until it is resurrected as a mantle plume. . .".

This chapter's focus is on igneous processes associated with subduction zones (Fig. 10.1). Many of the world's most densely populated cities are located along volcanic arcs on convergent plate boundaries. Therefore, understanding the geologic processes and associated hazards associated with arcs is of critical importance. Such plate boundaries are also sites of major natural resources, such as gold, copper, and petroleum.

Intermediate composition magmas, which can be broadly referred to as andesitic magmas, are the most dominant magma type at convergent plate boundaries. Also, rhyolites and granitoid plutons are common in continental arcs, but such silica-rich igneous rocks are a minor component in mid-ocean ridges and oceanic hot spots.

It is difficult to present a comprehensive coverage of petrology of volcanic arcs because no two arcs are alike. With that caveat, I will proceed with my attempt to cover the most general aspects of convergent plate boundary igneous processes. Although the focus will be on volcanic arcs, rhyolitic volcanism in continental extension zones, in hot spots, and in mid-ocean ridge environments is also discussed.

Background on Plate Convergence and Subduction

In subduction zones, an oceanic trench and a dipping zone of active seismicity, called the Wadati–Benioff zone (after the Japanese and US scientists who independently identified these dipping zones), mark the location of the subducting lithosphere or the "downgoing slab." They are also sites of the deepest focus earthquakes (~700 km) and strongest earthquakes (Magnitude ~9). The dip of subducted slabs can vary greatly (Fig. 10.2). Even for a single subduction zone, the dip can vary with depth—sometimes starting out at a low dip angle at shallow depths and then steepening at greater depths. The cause(s) of such great variation in dips is controversial but the general idea is that "slab pull" (downward forces that pull the slab toward the core of the earth) must exert a strong overall control. At shallow depths the interaction forces with the overriding plate may be an important factor in controlling the initial dip of the subducting plate. The mean dip of global Wadati–Benioff zones is about 45°. Volcanism occurs only when the dip is greater than

G. Sen, *Petrology*, DOI 10.1007/978-3-642-38800-2_10,

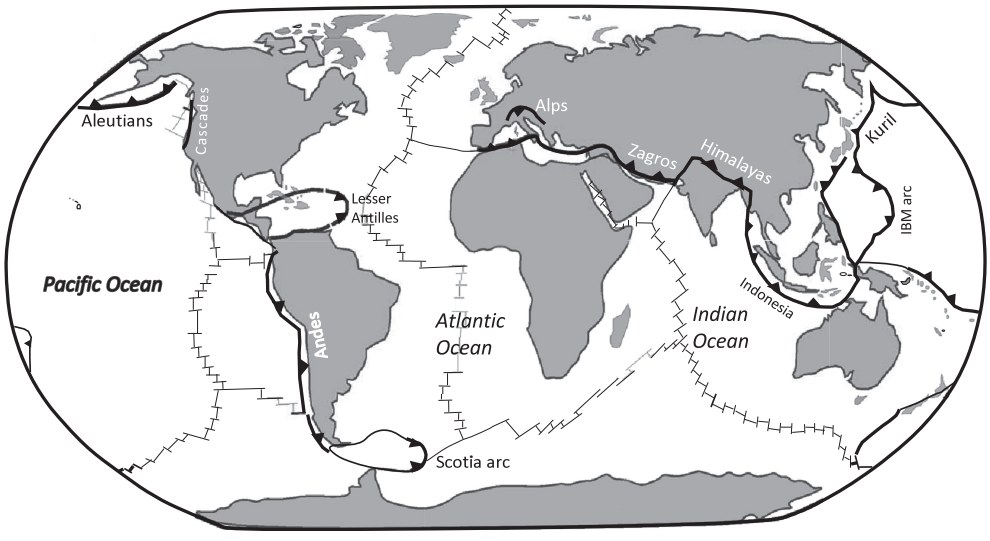

Fig. 10.1 Map showing mid-ocean ridges (*light lines*) and convergent plate boundaries (*dark lines*). The *short triangles* on the *dark lines* indicate the dip direction of the subduction zones

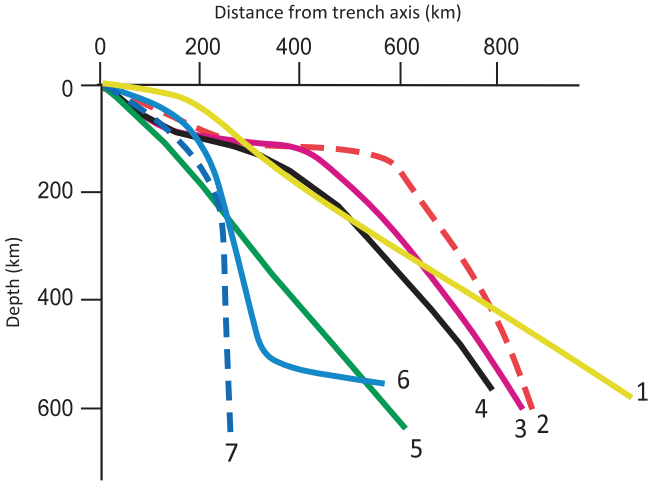

1 - Japan, 2- Peru, 3 - Central Chile, 4 - Northern Chile,
5 - Kermadec, 6 - Izu-Bonin, 7 - Central Marianas
[Source: Lallemand et al. 2005, G³ v. 6, 1-18]

Fig. 10.2 Dips of various subduction zones. *1* Japan, *2* Peru, *3* Central Chile, *4* Northern Chile, *5* Kermadec, *6* Izu–Bonin, *7* Central Marianas

about 25°. An interesting observation is that irrespective of the large variation in dips of the subducting plate, *the volcanic front seems to consistently occur at ~100–150 km above the Wadati–Benioff zone*, *which provides a strong constraint on the origin of arc magmas*.

What happens to the subducted slab once it enters the mantle continues to be a subject of much interest and intense seismic investigation. Some slabs appear to reach all the way to the bottom of the mantle; however, others are unable to penetrate the 670 km discontinuity (Fig. 10.3). In addition to changing dip angles on their way down, in some cases the slab may actually turn back ("slab roll back"; Fig. 10.3), forcing lateral migration of the trench and the subduction zone.

Notwithstanding the great variability of arc volcanism and seismicity associated with subduction zones, we can start with some general features of subduction-related igneous activities. A typical schematic cross section through an island arc is shown in Fig. 10.4 (after Stern 2002). A deep trench marks the area where the two oceanic plates come in contact. Most trenches associated with island arcs are "sediment starved," whereas trenches associated with continental arcs often have an abundance of sediments, which are a mix of marine sediments and sediments carried by rivers and glaciers to the sea. The fore-arc region of island arcs like the Marianas is draped by thin sediments, but its trench exposes fore-arc crust. In fore-arcs with high sediment flux, enormous packages of sediments are deformed and thrust in many continental and island arcs, forming an "*accretionary wedge*" or "*accretionary prism.*" The island of Barbados in the Caribbean Sea is an example of an accretionary wedge in which the sedimentary package is so thick that it has built up as an island. Fragments of the fore-arc crust and mantle may get sliced up and obducted to form ophiolites, and smaller fragments may get caught up in subduction zone sediments or serpentinites and come up to the surface as mélange (e.g., Draper 1986; Cloos and Shreve 1988; Stern et al. 2012).

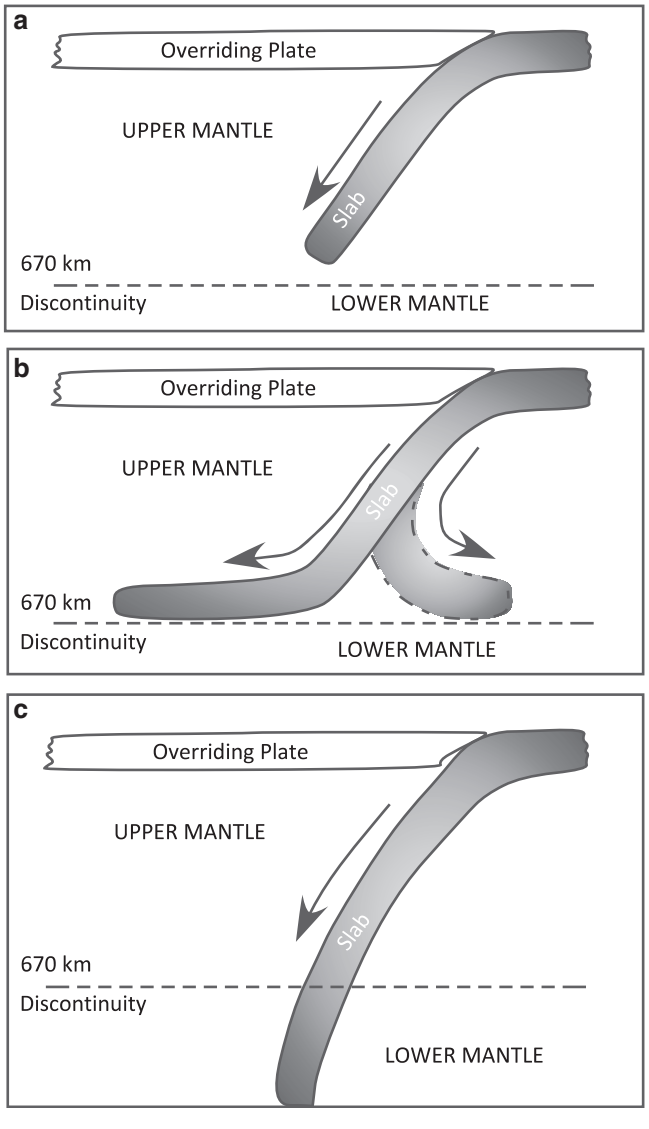

Fig. 10.3 Different behaviors of descending slabs (see text for further discussion)

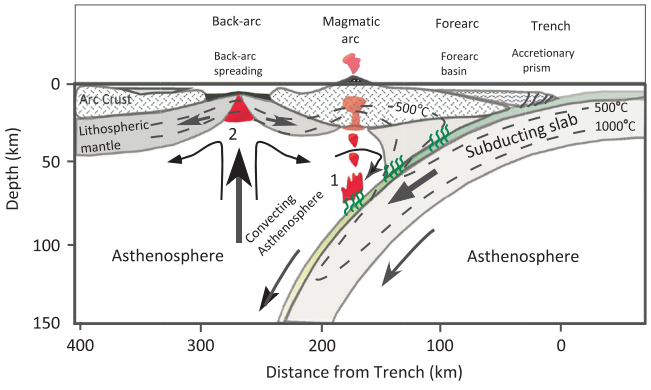

Fig. 10.4 Schematic cross section of an island arc highlighting its essential elements (from Stern 2002). The *green squeaky lines* mark fluids being released from the subducting slab. *Red* = magmas. Two isotherms are also shown to illustrate how the thermal conditions change from the arc to the subducting plate

Farther toward the volcanic front occurs a gently sloping area known as the *fore-arc*, which can be 100–200-km wide. Igneous activity has been noted in some fore-arc areas, but it generally lacks volcanism. The isotherms in Fig. 10.4 illustrate how cool lithosphere is gently warmed as it penetrates the asthenosphere. In the "basic scenario," ocean water enters through fractures in the crust and the shallow mantle close to the ridge axis where the ridge is still hot. The heated water reacts with the crustal and shallow mantle rocks and converts them into metamorphic rocks. Such metamorphism results in the formation of hydrous minerals like zeolites (e.g., natrolite—$Na_2Al_2Si_3O_{10}{\cdot}2H_2O$), chlorite (e.g., chamosite—$(Fe_5Al)(AlSi_3)O_{10}(OH)_8$), and serpentine (e.g., chrysotile—$Mg_3(Si_2O_5)(OH)_4$), which can contain significant amounts of water (commonly ~13–14 wt% H_2O) in their respective atomic structures. More water is carried in sediments deposited on the oceanic plate, and more water is introduced into the slab as a result of bending-related faulting just seaward of the trench. As this partially hydrated plate is subducted into the asthenosphere, temperature and pressure increase and cause destabilizing the hydrous minerals: they start breaking down at different depths depending on their *P–T* conditions of stability. Such breakdown reactions progressively lead to the formation of denser and less hydrous and/or anhydrous minerals, and the excess water is released into the *asthenospheric wedge* or *mantle wedge* above the subducting plate. This added fluid lowers the melting temperature of the hot peridotite of the asthenospheric wedge and thus magma is formed (Fig. 10.4). This phenomenon is known as *fluid-fluxed melting*. Melting of sediments on the top of the subducted slab also contributes to this flux, and this contains most of the incompatible trace elements that are carried up into convecting asthenosphere in the mantle wedge. A slight variation on this theme is a model that calls for the addition of slab-derived fluids and sediment melts that leads to generation of small amounts of hydrous melts closer to the slab, which then rise to and aid in the production of much larger volume of magma generated by melting in the wedge. The magma so formed rises due to buoyancy, and often after undergoing variable extents of crystallization and contamination by the overlying crust, it erupts through volcanoes forming the volcanic front. Deeper plutons also form beneath the volcanic front, so the trenchward limit of abundant igneous rocks in an arc is sometimes called the *magmatic front*.

Much of the global subduction occurs along the Pacific Rim and so that is a good place to start a

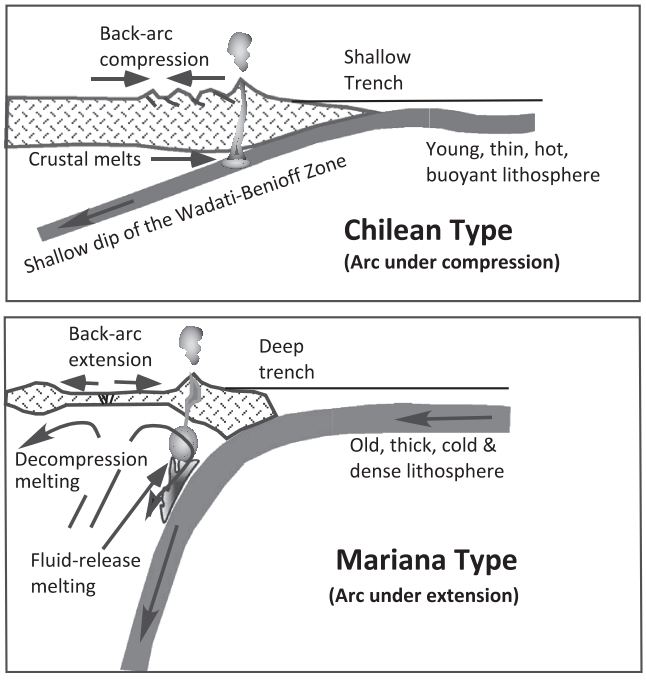

Fig. 10.5 Schematic cross sections of two very different types of subduction zones—Chilean and Marianas type (from Stern 2002)

conversation about subduction zone volcanism. Although the oldest parts of the Pacific crust are about 180 million years old, the Pacific Ocean has been in existence since Cambrian time (~500 Ma) and a large chunk of the Pacific plate has been recycled back into the mantle via subduction. The dip of the subduction zone and nature of volcanism vary greatly along the Pacific Rim—the western Pacific is dotted with island arcs formed by oceanic–oceanic convergence; in contrast, the eastern margin of the Pacific Ocean is marked by the subduction of oceanic plates beneath continental plates resulting in the formation of continental volcanic arcs.

Although the average subduction zone dips 45°, the shallowest dips are exemplified by the subduction of a young lithosphere beneath the Chilean Andes ("Chilean type"; Stern 2002); and the steepest dips occur beneath the Izu–Bonin–Marianas (IBM) arc in the western Pacific ("Marianas type"; Fig. 10.5). In the first case, subduction of 5–12-million year-old Nazca Plate (which is young, hot, and resists subduction) beneath South America occurs at a low angle and creates compression in the Andean back-arc region. In the second case, the Pacific Plate is old (~150 Ma), cold, and dense, and it subducts at a steep angle, causing extension in the back-arc. Such extension causes the asthenosphere to well up and generate MORB-like magmas by decompression melting; these are called *back-arc basin basalts* (*BABB*). It is interesting to point out that on the basis of a statistical study of many subduction zones, Lallemand et al. (2005) suggested that back-arc extension occurs only when the slab dips at greater than 50° and compression occurs when the dip is less than 30°.

Igneous Rock Series in Arcs

Many different types of lavas erupt from arc volcanoes—basalts, basaltic andesites, andesites, and rhyolites with andesites being generally more abundant. The basalts associated with arc volcanism are often very high in Al_2O_3 and are called *High-Alumina Basalts* (*HAB*). Some strongly alkaline lava also erupt, but they are relatively minor to rare in island arcs. Felsic magmas are common in island arcs but these generally do not build volcanoes that rise above sea level and their volumetric significance is often underappreciated. Rhyolites are more common in continental arcs. Granitoid and intermediate composition plutons form a major part of arcs, but these are only exposed on continents, where erosion has removed the volcanic carapace.

The term "igneous rock series" refers to the series of lavas, from basaltic to rhyolitic, from a single volcano, or from a series of volcanoes situated in a particular geographic area. Initially, there was an underlying assumption that the mafic–intermediate–felsic lavas of a series are all related by some sort of crystallization differentiation of a common parent magma (such as the Bowen's reaction series); however, many modern studies of volcanic arcs have shown that is often not the case and that complex processes, such as melting and assimilation of the crust, are involved in the derivation of different magma types.

Several classification schemes have been proposed for arc rocks among which two—based on FeO*/MgO versus SiO_2 and K_2O versus SiO_2—are commonly used (Fig. 10.6). The FeO*/MgO versus SiO_2 simply distinguishes between the tholeiitic series and calc-alkaline series (Fig. 10.6a) and is a simplified representation of the AFM diagram that was discussed in Chap. 6. Lava compositions, commonly ranging from basaltic andesite to rhyolite, from several Chilean are shown as trends in Fig. 10.6a—the *low-K series*, *the medium-K series*, *the high-K series*, *and the shoshonite series*. The low-K series is often referred to as the *island arc tholeiite series*, which is different from the tholeiites that erupt at mid-ocean ridges and other extensional plate boundaries or at ocean islands (e.g., Hawaii). The main difference is that the island arc tholeiites show mild Fe-enrichment accompanied by SiO_2-enrichment

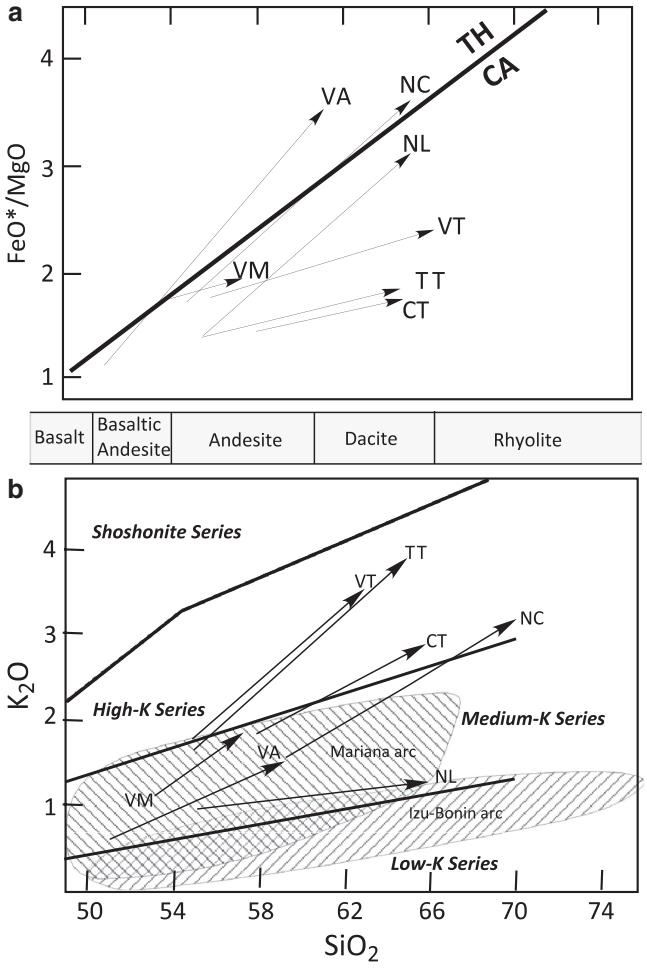

Fig. 10.6 Classification of volcanic rocks from convergent plate boundaries on the basis of (**a**) FeO*/MgO versus SiO_2 and (**b**) K_2O versus SiO_2. In (**a**) only two types are recognized—calc-alkaline (CA) and tholeiitic (TH). (**b**) Shows the fields for four major igneous series—low-K, medium-K, high-K, and Shoshonite series. The *middle bar* between (**a**) and (**b**) shows the corresponding names of volcanic rocks. Compositional trends in lavas erupted from several volcanoes in Chile are also plotted here: *CT* Cerro Tupungato, *TT* Volcan Tupungatito, *VM* Volcan Maipo, *VT* Volcan Tinguiririca, *SL* Cerro Sordo Lucas, *AZ* Cerro Azul, *NL* Nevado de Longavi, *NC* Nevados de Chillan, *VA* Volcan Antuco (*source*: Hildreth and Moorbath 1988)

(i.e., Bowen trend, Chap. 7), whereas "true" tholeiites (MORB, Hawaii, Deccan Traps types) show strong Fe-enrichment at a fairly constant SiO_2 (the Fenner trend, Chap. 7). The high-K and shoshonite series, by virtue of their high alkali contents, are special types of alkaline series. Within each series, the rocks may range from basalt through andesite to rhyolite. Also shown in Fig. 10.6 are compositional trends of lavas erupted from several volcanoes from the Chilean Andes and from the Izu–Bonin–Marianas (IBM) arcs (Hildreth and Moorbath 1988). The Marianas lavas exhibit calc-alkaline trend, whereas Izu–Bonin lavas follow an island arc tholeiitic trend (Fig. 10.6b). The Andean lavas tend to start out in the calc-alkaline field but then become much richer in K_2O. Such enrichment may result from crustal contamination and/or crystallization in a more oxidizing environment (discussed later).

The eruption behavior of arc volcanoes is highly variable and is related to the igneous series: tholeiite series volcanoes are generally nonexplosive and erupt basalts and basaltic andesites from small, youthful cones and shield volcanoes. These rocks are more aphyric than calc-alkaline series lavas. Calc-alkaline series volcanoes are generally explosive and commonly erupt pyroclastic materials. These volcanoes are stratovolcanoes that generally dominate mature island arcs. The lavas commonly contain abundant phenocrysts of plagioclase. Late-stage volcanic activity in an island arc is usually of shoshonite type. Shoshonite series volcanoes are minor relative to tholeiitic and calc-alkaline series. Like the calc-alkaline series, they are explosive as well. The lavas are predominantly alkali basalt.

Aside from the rock types mentioned above, a rather unusual type of lava, called *boninites*, with ~6–12 % MgO and 52–60 % SiO_2 occurs in some fore-arc regions of IBM arc. Boninite magmas are thought to form as a result of unusually high degrees of mantle melting, for example, when a subduction zone first forms (discussed later). They show strong enrichment in certain incompatible trace elements, such as light ion lithophile elements (LILE), and are generally believed to form when H_2O and LILE are added to previously depleted asthenospheric wedge. Boninites are of interest to petrologists because similar rocks have been found to occur in early Archaean "provinces" in the continents (discussed in Chap. 12). In 2009, boninite lavas were observed for the first time to erupt from a deeply submerged (1.1 km below sea level) volcano, called the West Mata volcano, located behind the Tonga arc in the Lau back-arc basin, about 200 km southwest of Samoa (http://www.nsf.gov/news/news_summ.jsp?cntn_id=116098). This is the deepest known volcano on earth.

There is another special type of arc lava called *adakite*, named after Adak Island from the Aleutian Islands. Adakites are found where the subducting plate is very young. They have >56 % SiO_2, >15 % Al_2O_3, about 3 % MgO; but what makes them distinctive is their relatively high Sr/Y and La/Yb ratio (Fig. 10.7). The high Sr/Y and La/Yb ratios are interpreted to be a result of melting of eclogitic crust in the subducted slab. Y and Yb are compatible elements in garnet, whereas Sr and La are incompatible elements during lherzolite or eclogite melting. Therefore, during melting of the

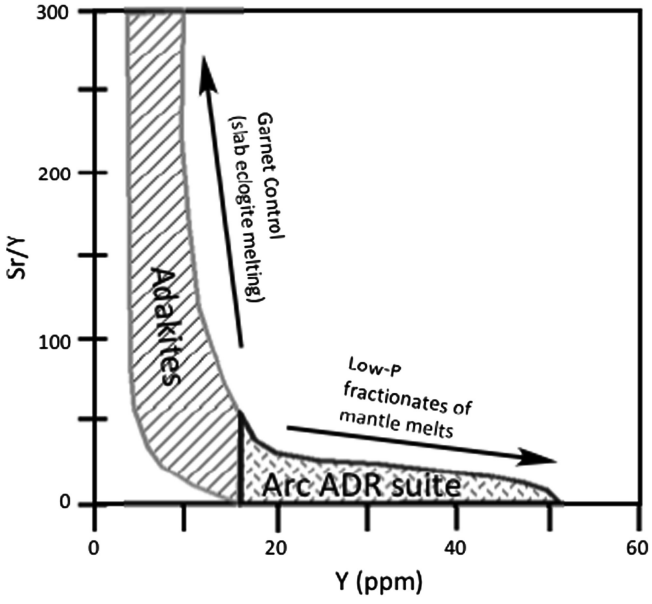

Fig. 10.7 This diagram shows a distinctive chemical characteristic of adakites, namely, strong variation in Sr/Y ratio over a very small range of Yb (ppm) (*source*: Stern 2002)

subducting eclogite crust, residual garnet sequester Y and Yb and increase La and Sr in the melt, which results in an increase in Sr/Y and La/Yb ratios in the melt.

Returning to the theme of calc-alkaline versus tholeiitic trend in arcs, there are many different hypotheses. Kennedy (1955, in Osborn 1979) and Osborn (1979) suggested that in the case of hydrous basalt magma, decomposition of water during magma ascent generates oxygen that oxidizes the magma and such oxidizing conditions stabilize magnetite early in the crystallization sequence at low pressure. Early fractionation of magnetite drives the residual liquid toward an early silica, alumina, and alkali enrichment, essentially forming the calc-alkaline differentiation trend. Other fractionation schemes have also been proposed, such as garnet fractionation, at moderate pressure (>1.6 GPa). Again, garnet fractionation would drive the residual liquid toward silica and alkali enrichment but deplete it in alumina. Moderate pressure amphibole fractionation has also been proposed as the driving force behind calc-alkaline trend generation.

Phenocryst Mineralogy

The mineralogy of island arc lavas varies as a function of silica content and series type: olivine ($Fo_{70–85}$), augite, and a highly anorthitic plagioclase ($\geq An_{90}$) are common phenocrysts in basalt and basaltic andesites (Table 10.1). Brown hornblende and biotite are common phenocrysts in andesites, dacites, and rhyolites of calc-alkaline and high-K series. These hydrous mineral assemblages suggest relatively high H_2O contents of the lavas. In contrast, the low-K series contains phenocrysts of orthopyroxene or pigeonite. Crystallization of pigeonite requires temperatures that are substantially higher than the temperatures at which hydrous mafic–intermediate magmas may crystallize at a moderate-to-low pressure. Therefore, the occurrence of orthopyroxene and pigeonite in the low-K series suggests that the low-K series (i.e., island arc tholeiitic series) magmas have relatively less H_2O compared to the other series. Plagioclase, which is a dominant phenocryst phase in calc-alkaline and low-K basalt and andesite, is not nearly as common in high-K and shoshonite series basalts. Pigeonite is a common groundmass mineral in the low-K or tholeiitic series, whereas orthopyroxene is the common groundmass Ca-poor pyroxene in andesites. Sanidine (±fayalitic olivine) may also occur as a phenocryst phase in rhyolites.

Trace Element Composition

Trace element characteristics are commonly displayed in terms of the so-called spidergrams in which elemental concentrations, normalized to primitive upper mantle or MORB compositions, are plotted (Fig. 10.8a, b). How elements are sequentially organized from left to right have varies somewhat from author to author, but the general idea is to arrange them in terms of increasing compatibility (recall that incompatible elements prefer melt or fluid and compatible elements prefer minerals). In general, the incompatible large ion lithophile elements (LILE) are more incompatible and plot toward the left and less (mostly) incompatible elements plot to the right side of the diagram. Figure 10.8a shows a comparison between basalts found in volcanic arcs (arc tholeiites and HABs) and those from Hawaii (tholeiites and alkali basalts), and a typical N-MORB. This comparison shows that arc basalts are generated from a source that must be significantly more enriched than either the OIB (plume) or MORB (asthenosphere) sources. This enrichment is attributed to elements added to the asthenosphere by fluids released from the subducted slab.

Arc basalts are distinct from N-MORB and hot spot or ocean island basalts (e.g., Hawaii) by their conspicuous spiky patterns, characteristic enrichments in some strongly incompatible elements (e.g., Cesium and Barium), and depletion in niobium (Nb) content relative to

Table 10.1 Phenocrysts in island arc igneous series (after Hess 1989)

Rock	Low-K	Calc-alkaline	High-K	Shoshonite
Basalt	Ol + Aug + Pl	Ol + Aug + Pl	Ol + Aug	Ol + Aug + Oxide
	±Tmgt		±Pl	±Pl, Hbl, Bi
	$Fo_{70–85}$			
	Max. ~ An_{90}			
Andesite	Pl + Aug + Pig	Pl + Aug + Opx		Pl + Aug + Oxide + Bi + Hbl
	±Ol, Tmgt	±Hbl, Tmgt, Bi		
	$An_{50–70}$			
	Some An_{90}			
Dacite, rhyolite	Pl + Aug + Opx	Pl + Hbl + Bi + Opx	Pl + Hbl + Bi	
	+Qz+Tmgt	+Qz	+San+Qz	
	±Fa, San	±Aug, Fa, San	±Fa	

the surrounding elements (Fig. 10.8a). Arc lavas have a flat MREE–HREE (chondrite-normalized) pattern, which indicates that garnet is not a residual phase in the magma generation process. An exception to this is adakite magma, which has a high MREE–HREE ratio and hence is likely to have been generated with residual garnet.

Weathering can reset the abundances of highly incompatible trace elements in exposed rocks because they are susceptible to dissolution and transportation by fluids (Fig. 10.8b). Such fluid-mobile elements are dissolved from the subducted crust and transported by fluids or fluid-saturated melts to the hotter parts in the asthenospheric wedge where these elements are added to magma. This process is primarily responsible for the jaggedy pattern and LILE enrichment in the N-MORB-normalized spidergram in Fig. 10.8b. This diagram shows that concentration of fluid-mobile elements, particularly from Cesium to Thorium, is significantly greater in arc tholeiites, back-arc basin basalts, and even in boninites, which supports the idea that these elements have been added by fluids to the asthenospheric wedge where such magmas are generated.

The strong depletion in REE in boninites is suggestive of their derivation from a strongly depleted peridotite source relative to MORB. The combination of relatively high fluid-mobile elements and depleted REE indicates that boninite magmas are generated from a harzburgite (depleted)-type source to which fluids from the subducted slab have been added.

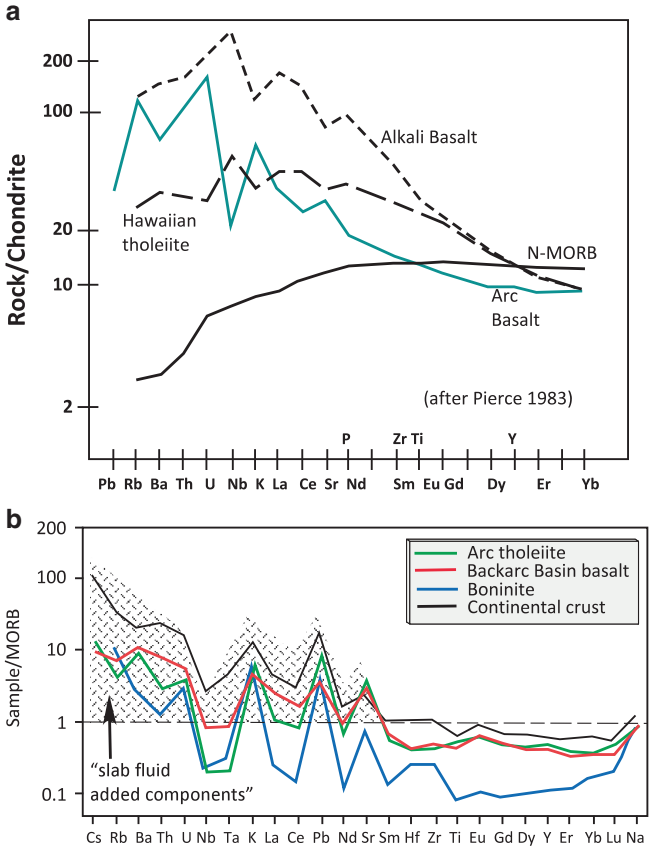

Fig. 10.8 "Spider diagrams" showing trace element composition of (**a**) basalts from various hot spots (e.g., alkali basalt and Hawaiian tholeiite), mid-ocean ridges (N-MORB), and island arc (arc basalt) (after Pearce 1983); and (**b**) of arc volcanics (after Stern 2002). Note that the rock compositions are normalized to the composition of a chondrite in (**a**) and to N-MORB in (**b**). Estimated compositional range of fluids coming off subducted slab is also shown in (**b**)

Isotope Composition

In terms of Pb, Nd, and Sr isotopic compositions, igneous rocks from several island and continental arcs define a rather wide field that overlaps the fields of N-MORB, hot spot basalt, oceanic sediments, and continental crust (Fig. 10.9a, b). The location of these arcs is shown in Fig. 10.1. Such great isotopic diversity signifies two things: (a) materials to arc magmas are contributed

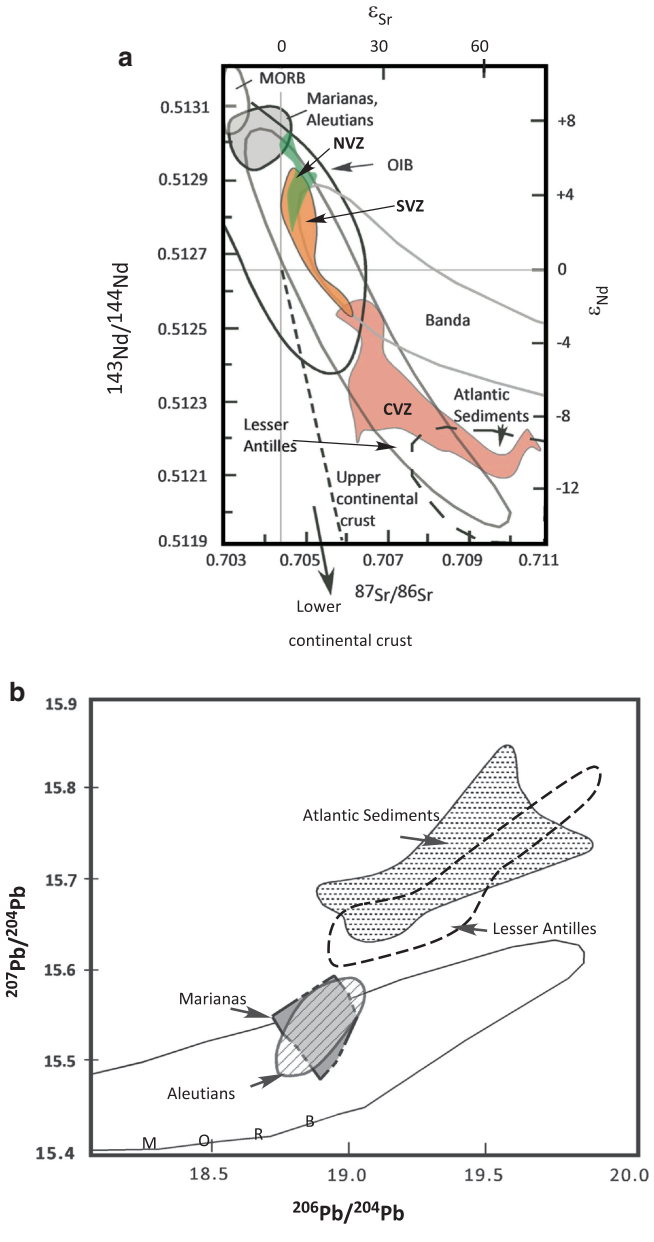

Fig. 10.9 (**a**) Nd–Sr isotopic compositions of arc volcanics from different convergent margins are compared with those of MORB, continental crust, Atlantic ocean bottom sediments, and ocean island basalts (OIB). Arc lavas from three volcanic zones from the Andes are shown as NVZ (Northern Volcanic Zone), SVZ (Southern Volcanic Zone), and CVZ (Central Volcanic Zone). Whereas Marianas and Aleutian volcanics appear to have not been affected by continental crust derived sediments, those from the CVZ, Lesser Antilles, and Banda arc (Indonesia) appear to have a strong continental crustal signature (after Wilson 1989). (**b**) Pb-isotope compositions of selected arc volcanics (Wilson 1989)

from a variety of sources—asthenosphere (i.e., N-MORB source), mantle plumes (OIB source), oceanic sediments, and continental crust (in the case of continental arc volcanics); and (b) different arcs can have very different isotopic compositions (Fig. 10.9a, b), indicating that the relative material contributions from these different sources can vary from arc to arc. For example, Fig. 10.9b shows magmas erupted at the Marianas and Aleutian arcs receive relatively little contributions from oceanic sediments; on the other hand, volcanoes from the Lesser Antilles clearly show a significant isotopic contribution from sediments. The physical means by which such "contributions" are made, for example, whether during melting in the subduction zone or through contamination of transient melts by the crust, is not often easy to discern.

Examples of Some Arcs

Izu–Bonin–Marianas Arc–Back-Arc System

This summary is largely based on Stern (2002) and Stern et al. (2003); and the interested student is well advised to read these papers for a more extensive knowledge about IBM arc tectonics and magmatism. The IBM arc–back-arc system occurs to the south of Tokyo and extends south to Guam and beyond (Fig. 10.10). Active subduction is going on to the east of the volcanic arc at the rate of about 2 cm/year to the south and 6 cm/year to the north of the Ogasawara plateau. The IBM system has the deepest trench in the world at the Challenger Deep in the Marianas trench. The Pacific plate that is being subducted is about 170-million year-old to the south of Ogasawara plateau and ~130–140-million year-old to the north of it.

Initiation of subduction of the Jurassic-age Pacific plate beneath the Philippine Sea Plate occurred about 52 Ma due to the fact that the dense, thick, and cold Pacific lithosphere juxtaposed against a much younger and thinner lithosphere began to sink (Fig. 10.11; redrawn from Stern et al. 2003). According to Stern et al. (2012), as the dense lithosphere "plunged" into the asthenosphere, it forced the lherzolitic asthenosphere in front of it to rise, decompress, and partially melt, generating tholeiitic magmas that are geochemically akin to MORB. Extension and emplacement of such MORB-like magmas (called fore-arc basalts or FAB) ensued, forming a sort of mid-ocean ridge situation in a fore-arc region, however, without the start of proper arc volcanism. Interestingly, 44–48-million year-old boninites have been found along the walls of Marianas trench, and such rocks are also exposed on the Ogasawara (Bonin) Islands. Clearly, such magmas formed early in the history of the IBM arc system before any proper arc volcanism occurred. Since

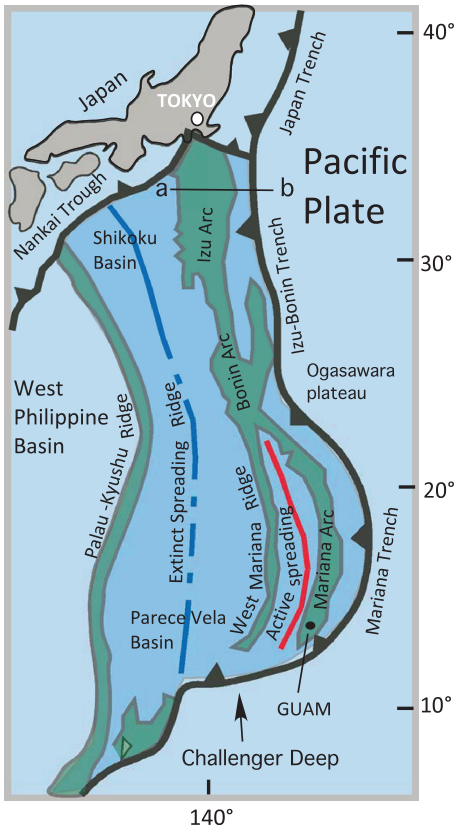

Fig. 10.10 Map of the Izu–Bonin–Marianas arc–back-arc system (modified from Stern et al. 2003)

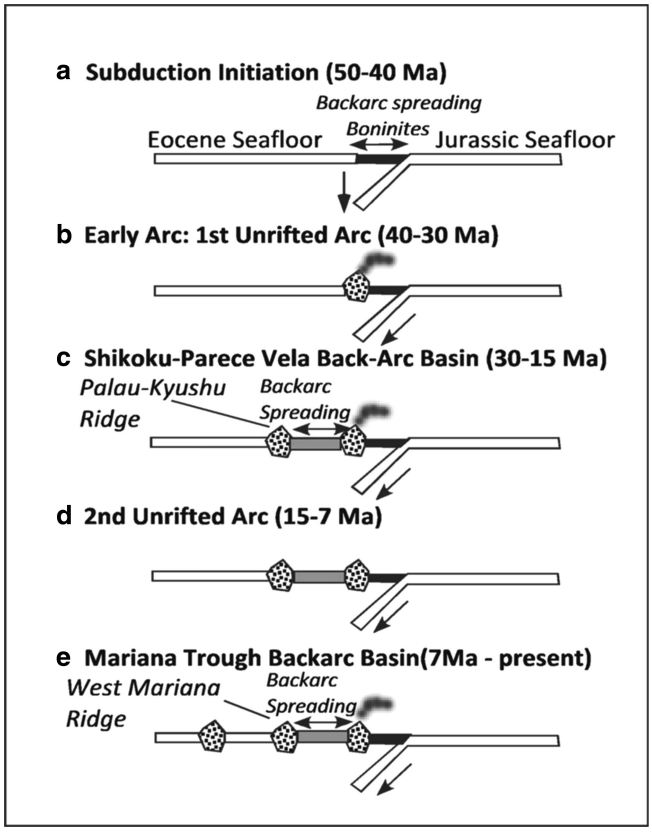

Fig. 10.11 Temporal and spatial evolution of the IBM arc–back-arc system (from Stern et al. 2003)

generation of boninites seems to require the assistance of subduction zone fluids and a depleted harzburgitic source, it appears that the FAB-depleted source was being affected by fluid coming off the subducting lithosphere. This was possible because of trench roll back (Stern et al. 2012). The added fluids lowered the solidus of the shallow, depleted, harzburgite and generated boninite magmas.

At 40 Ma, as the lithosphere reached more than 100 km depth, fluid-assisted melting in the asthenospheric wedge generated true arc magmas. Thus, about 40–30 Ma, arc volcanism created the Palau–Kyushu Ridge about 200 km away from the trench (Fig. 10.11). This was followed by a period of rifting and sea-floor spreading at 30–25 Ma, forming the Parece Vela Basin in the south and Shikoku Basin to the north. The two spreading basins met about 20 Ma. The combined Parece Vela–Shikoku back-arc basin spreading continued until about 15 Ma. The back-arc spreading stopped and volcanism continued to form the West Marianas Ridge from 15 to 7 Ma. Then a new episode of back-arc spreading at 3–4 Ma formed the Marianas Trough back-arc basin, and new volcanism formed the Marianas arc. According to Stern et al. (2003), volcanoes forming the Marianas arc are less than about 3–4-million year-old, whereas the Izu–Bonin volcanoes could be as old as 25 Ma.

Andean Volcanic Arc

Tectonic and magmatic processes associated with the subduction of the Nazca plate beneath South America have built much of the Andean mountain chain for the past 200 Ma (Stern 2004). The Chile–Peru trench, which marks the plate convergence boundary, occurs 80–100 km offshore. The Andean mountain chain can be divided into several N–S belts: for example, in northern Chile (Fig. 10.12a; Giese et al. 1999), the fore-arc region forms the western belt comprised of the Coastal Cordillera, the Longitudinal Valley, the Precordillera, and Preandean Depression (Fig. 10.12a). The magmatic arc forms the Western Cordillera, which has a large number of active volcanoes of Miocene to Quaternary age. The back-arc is formed by Altiplano and Puna, Eastern Cordillera, Subandean belt, and Chaco Foreland (Fig. 10.12b). The Coastal Cordillera is composed of

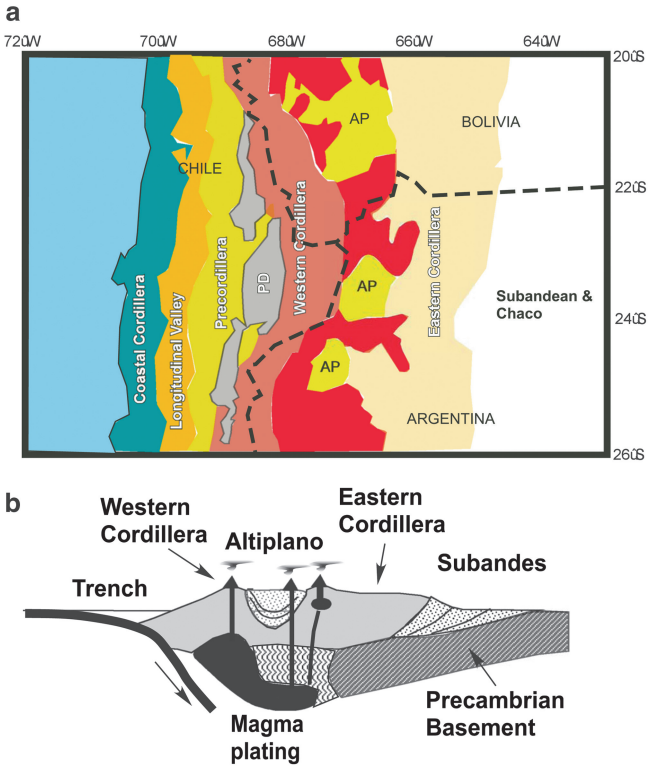

Fig. 10.12 (**a**) Map of Central Andean arc–back-arc system (after Schmitz et al. 1999). *PD* Preandean depression, *AP* Altiplano and Puna. (**b**) Schematic cross section in Central Chile (modified from Lamb et al. 1997)

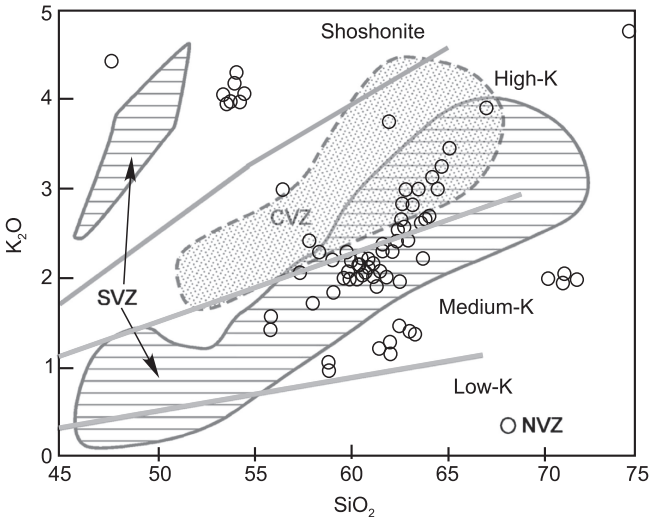

Fig. 10.13 SiO_2–K_2O variation in CVZ, NVZ, and SVZ (*data source*: GEOROC Database)

Mesozoic basaltic–andesitic plutonic and volcanic rocks. The Precordillera is situated on Mesozoic–Tertiary sediments and volcanic rocks and some Paleogene plutons underlain by a late Paleozoic basement. The Altiplano and Puna are sedimentary basins filled with Mesozoic–Cenozoic sediments that reach a maximum thickness of about 10 km (Fig. 10.12b; cross section drawn after Hoke et al. 1994). The Eastern Cordillera is built of Cretaceous–Cenozoic sediments sitting on a basement comprised of Precambrian–Paleozoic rocks (Giese et al. 1999). The Subandean zone is a 150–200-km-wide thin-skinned fold and thrust belt.

In the Quaternary, the subduction of the Nazca plate beneath South America has resulted in the generation of magmas that have formed plutons and some 200 active or potentially active volcanoes along much of Andes mountain chain in western South America. The Andean Quaternary volcanic belt is discontinuous and forms four segments (from north to south): Northern Volcanic Zone (NVZ, 5°N to 2°S), Central Volcanic Zone (CVZ, 16°S to 26°S), Southern Volcanic Zone (SVZ, 34°S to 46°30′), and Austral Volcanic Zone (AVZ, south of 46°30′) (Fig. 10.13, AVZ is not shown here separately). The Nazca plate dips 30° beneath the volcanic zones and less than 15° beneath the gaps that separate the active volcanic zones. Beneath the gap areas magmas are not produced perhaps because the asthenospheric wedge is either nonexistent or too narrow and not hot enough to generate magmas in large volumes.

The crustal structure is very different between NVZ, CVZ, and SVZ: the crust is more than 70 km thick beneath the CVZ, whereas it is 40–60 km thick beneath the NVZ, and 30–40 km beneath the SVZ. The NVZ lies over accreted oceanic crustal fragments that were emplaced during Jurassic, late Cretaceous, and Paleogene (Ramos 1999). In contrast, the CVZ and SVZ sit on thickened crust that largely formed by subduction-related tectonic and magmatic processes. There may also be slices of Precambrian shield fragments present.

There are significant differences in the types of volcanic products that occur in CVZ versus NVZ and SVZ (Fig. 10.13): for example, CVZ lavas are mostly high-K andesites, whereas NVZ lavas are mostly medium-K type and include basalts, basaltic andesites, andesites, dacites, and rhyolites. There are also shoshonites and dacites in the NVZ. The SVZ lavas cut across medium-K and high-K series. In terms of isotopic ratios, there are significant differences between SVZ, CVZ, and NVZ lavas (Fig. 10.9). The CVZ lavas have the lowest Nd and highest Sr isotope ratios, which reflects significant contamination by old enriched continental crust. The NVZ lavas reflect isotopically depleted sources and the SVZ lavas partly overlap NVZ but show very little overlap with the CVZ lavas. These highly contaminated

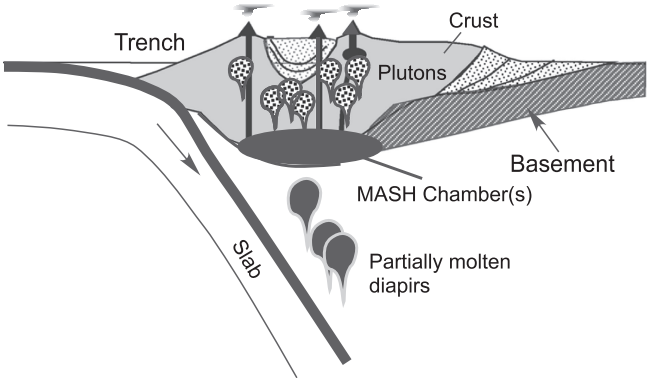

Fig. 10.14 Schematic cross section of a continental arc with considerably thickened crust. It shows how partial melts from the asthenospheric wedge may rise up to the arc lithosphere, pond at the Moho, where it may assimilate the crust, mix, and homogenize (see text for further discussion)

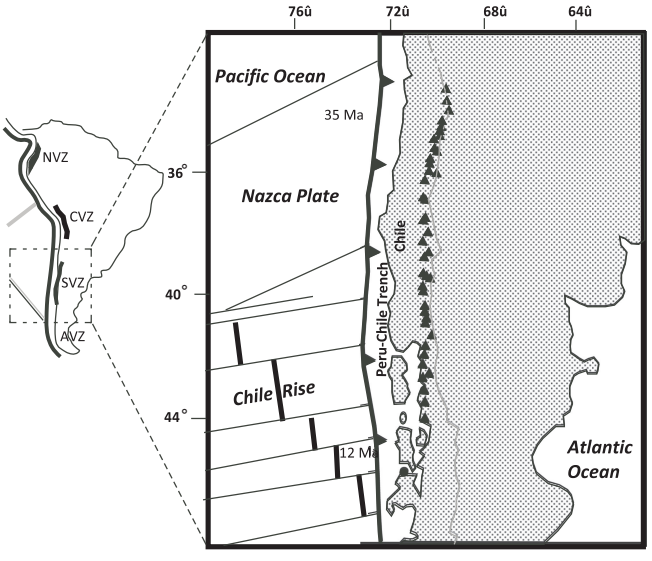

Fig. 10.15 Andean volcanic zones and Chilean volcanoes

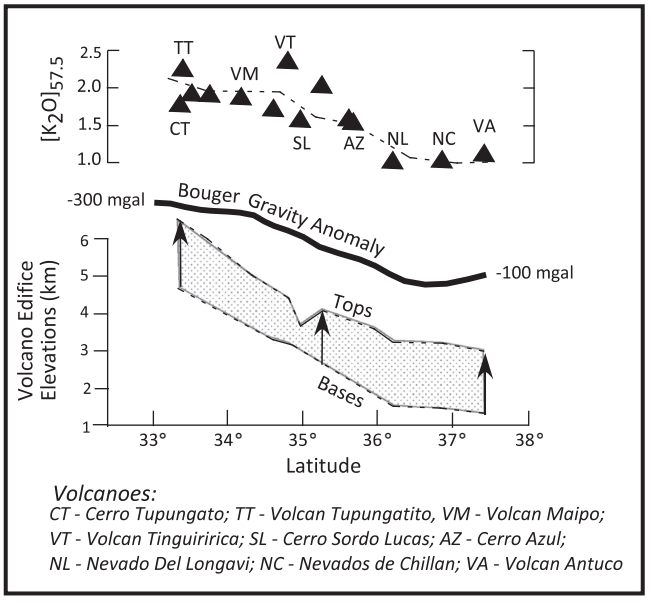

Fig. 10.16 Change in gravity, K_2O, and volcano heights of Chilean volcanoes shown in Fig. 10.15 (after Hildreth and Moorbath 1988)

isotope characteristics of the CVZ lavas, relative to NVZ and SVZ lavas, could have happened due to their long interaction with much thicker crust.

It is generally believed that the large volume calc-alkaline andesites or intermediate composition plutonic rocks found in continental arc settings are not primary magmas generated in the asthenospheric wedge. In areas of exceptionally thick continental crust with a long and complex history of tectonic and magmatic evolution, such as the Central Andes, this is to be expected. A common hypothesis is that primitive magma ascending from the asthenospheric wedge stagnates at the Moho because it is much denser than the crust above and is therefore no longer buoyant. Such ponded magma assimilates crust, and gives off heat and fluids to the crust above and as a result, it cools, and undergoes fractional crystallization. Eventually the magma becomes sufficiently evolved, both thermally and chemically, such that it becomes buoyant again and starts rising again (Fig. 10.14). This hypothesis of magma evolution is popularly known as the MASH, which stands for Melting, Assimilation, Storage, and Homogenization.

It is difficult to pinpoint the processes that alters magma composition from its origin to eruption because there are too many variables—subducted slab (age, temperature, composition), rate and geometry of subduction, composition and temperature of the wedge, nature of the lithospheric column (its thickness, thermal condition), and physical/chemical (chemistry, age, and lithology of rocks that comprise it). The goal of good science is to be able to navigate through such difficulties, peel off implausible scenarios on scientific merit, and thus pinpoint the plausible phenomenon. In this context, Hildreth and Moorbath (1988) carried out an interesting geochemical study of the SVZ with the goal of "peeling off" shallow crustal geochemical signature of the erupted lavas and thus identify the compositional features the magmas inherited from depth. They selected volcanoes between latitudes 33° and about 38° (Fig. 10.15) that are roughly equidistant from the trench and situated about 90 km above the Wadati–Benioff zone. The rate of subduction, geometry of the subduction zone, age of the seafloor, and age of the sediments on the seafloor are all essentially the

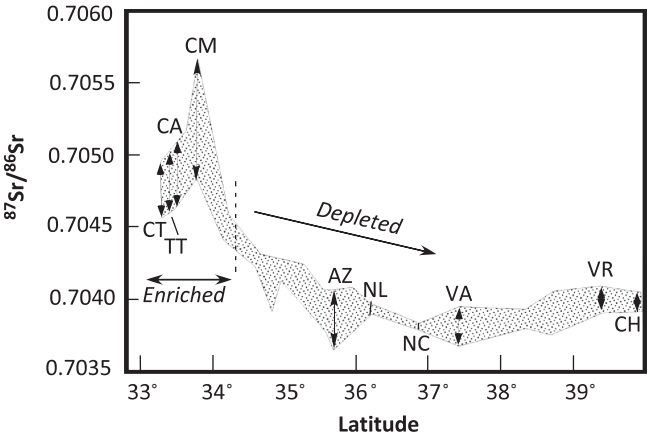

Fig. 10.17 Sr isotopic variation of the Chilean volcanoes (from Hildreth and Moorbath 1988)

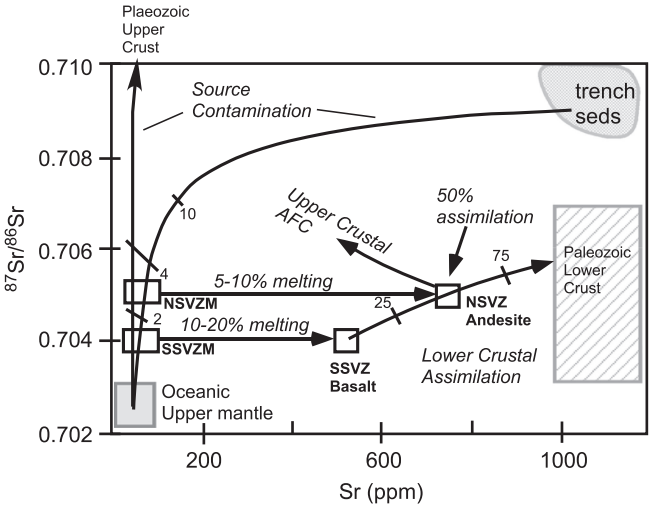

Fig. 10.18 C.R. Stren's alternative explanation of the Sr isotopic variations of the same Chilean volcanoes (see text for details)

same. There are, however, two things that change—first, the continental crust thickens from 30 to 35 km in the south to about 60 km in the north, as reflected in an increase in the Bouguer gravity anomaly (Fig. 10.16). Second, composition of the crustal material changes from south to north: Paleozoic–Triassic rocks are abundant in the crust beneath the northern volcanoes, whereas the southern volcanoes lie on younger crust.

Hildreth and Moorbath (1988) noted that some chemical parameters change from south to north in the SVZ: for example, Ba increases from 300 to 600 ppm, K_2O (at constant SiO_2) increases (Fig. 10.16), and $^{87}Sr/^{86}Sr$ increases from ~0.7036 to 0.7040 in the south to values as high as 0.7057 (Fig. 10.17). Hildreth and Moorbath (1988) did this comparison with two first-order goals: one was to identify the composition of the deeper magma feeding the MASH zone, which feeds all the volcanoes; and the second goal was to identify whether the upper or lower continental crust has stronger influence in altering their composition of the erupted lavas. For example, based on Fig. 10.17, Hildreth and Moorbath (1988) concluded that the baseline $^{87}Sr/^{86}Sr$ composition of the magma coming out of MASH magma chamber was 0.7036–0.7040 and that the higher Sr isotope ratios of the northern volcanoes of the study area were obtained by assimilating thickened lower crust.

Stern (1991) pointed out several difficulties with the model proposed by Hildreth and Moorbath (1988). Stern doubted their assumption of constant subduction geometry and indicated that seismic evidence showed that the subducted slab's dip decreases northward; and thus the asthenospheric wedge narrows northward, i.e., magma source volume diminished, and therefore neither the composition nor the volume of the magma supplied from the mantle wedge is similar in the north versus southern segments. Stern further pointed out, based on other studies, that even sediment supply into the wedge zone from the subducted slab cannot be the same from south to north, as assumed by Hildreth and Moorbath (1988); instead, more sediments are subducted in the north. A process called "tectonic erosion" of continental material along the trench wall produces such sediments. Stern calculated that a reasonable mixture of tectonically eroded continental sediments with $^{87}Sr/^{86}Sr$ of 0.709, for example, and oceanic mantle, when partially melted, better explained Sr-isotopes and other geochemical signals. On the other hand, it would require 50 % assimilation of the lower crust via MASH to explain the composition of lavas erupted in the northern SVZ (Fig. 10.18). That much assimilation is almost impossible as it would require extraction of a lot of magmatic heat, which in turn could force the magma to crystallize completely. Stern's preferred hypothesis was that the observed geochemical differences from south to north resulted from differences rooted in the amount of tectonically eroded continental sediments present in the magma production zone.

The above difference in interpreting the same data shows how science works. The study by Hildreth and Moorbath (1988) may have seemed at the time to be a well-conceived controlled experiment with reasonable interpretation of the observations; however, the alternative interpretation by Stern of the same dataset is just as reasonable. We have seen this same type of debate between Bowen and Fenner many years earlier. That is how "science marches on!"

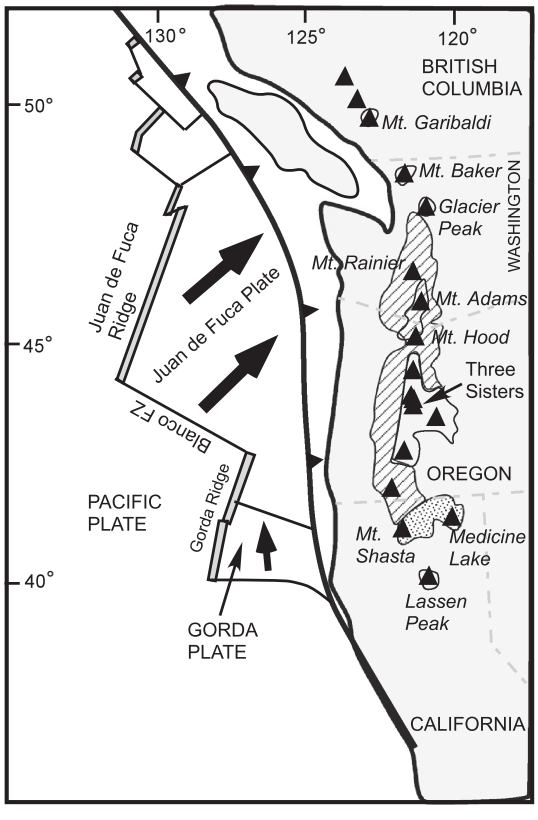

Fig. 10.19 Volcanoes of the Cascades arc, northwestern United States

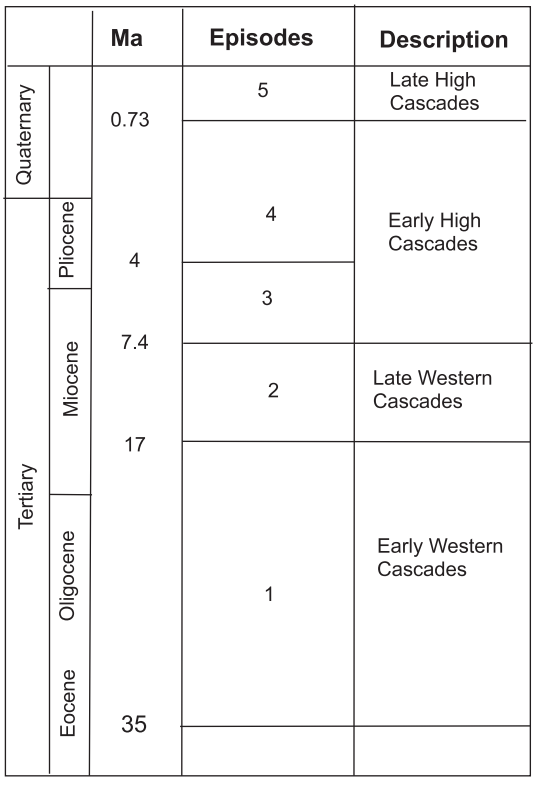

Fig. 10.20 Episodic evolution of the Cascades arc (Priest 1990)

Cascades Volcanic Arc

The Cascades volcanic arc in the northwestern United States and western Canada results from the subduction of the Juan de Fuca (JdF) and Gorda plates beneath the North American plate (Fig. 10.19). The JdF plate is young (12–14 Ma) and therefore warm; and it is presently subducting slowly (4 cm/year). This slow subduction has resulted in several interesting features—lack of a recognizable trench, rather infrequent earthquakes relative to other subduction zones, and a warm, largely dehydrated, crust that provides low fluid flux. This slow supply of fluids to the asthenospheric wedge has resulted in fewer volcanoes.

The velocity of subduction was not always so slow, and it appears that before 7 Ma the rate was 7–10 cm/year. The variation in slab subduction rate, dip, slab position, and stress regime in the upper plate over time has resulted in a complicated volcanic history of the Cascades. The narrow long chain of volcanoes that runs from northern California through Oregon, Washington, and to British Columbia in the High Cascades has developed only within the last 0.73 million years (Fig. 10.20).

According to Priest (1990), Cascade volcanism has been episodic (Fig. 10.20). The earliest major episode (Episode 1) of volcanism lasted from 35 to 17 Ma. In the Eocene (35 Ma), tholeiitic basalts mostly erupted on the coastal ranges of Oregon and Washington. Andesites were produced further west. There was a period of deformation around 25 Ma, which was followed by the eruption of voluminous siliceous pyroclastics around 18–17 Ma. This early Western Cascades volcanism ended about 14 Ma. Recall that overlapping this period, Columbia River flood basalts were literally pouring out of the crust further east about 16 Ma (Chap. 9); and yet there does not appear to be any relationship between the Cascades and Columbia River magma generation.

Episode 2 began at about 14 Ma with the eruption of dacitic pyroclastics in the Western Cascades; and voluminous andesites and minor basaltic and dacitic volcanism occurred from 13 to 8.8 Ma. Episode 3 (7.4–4 Ma) is characterized by the eruption of basalts and basaltic andesites and of some siliceous pyroclastics. This eruption occurred on the present location of High Cascades. Around 5–6 Ma (?), the Western Cascades were uplifted, while the High Cascades were forming tectonic grabens. Radiometric ages for volcanic rocks on

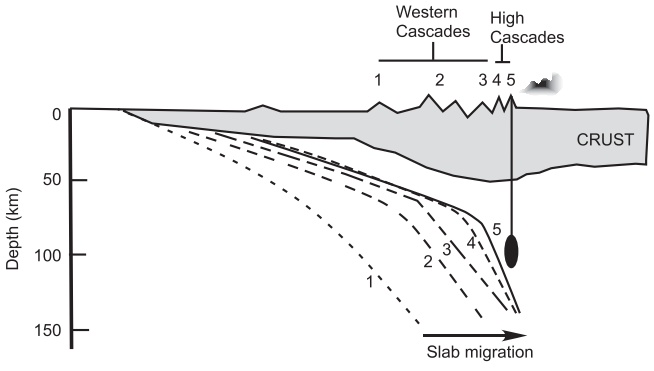

Fig. 10.21 Migrating slab and evolution of the Cascades arc (based on Priest 1990)

the uplifted Western Cascades are 4.5–5.13 Ma (Priest 1990). From 3.9 Ma to present, the High Cascades developed. In the final episode (Episode 5), 0.73 Ma to present, the volcanic arc has really narrowed into the currently dormant volcanic chain.

In sum, early Cascade arc volcanism occurred over a wider area and further to the east of the current volcanic arc (the High Cascades). The position of the arc has shifted westward, and the width of the volcanic chain has also narrowed over time. Both the locus of the volcanic arc and narrowing of the arc may be related to the slowly decreasing dip of the subducted plate at 100-km depth (Fig. 10.21). This figure shows that the slab has migrated eastward during the five episodes of volcanic activity. The early lavas were basalts and later andesites became dominant. Siliceous pyroclastics have erupted throughout but more erupted in the later episodes.

Cascades volcanic compositions stretch from tholeiitic basalts to rhyolites and encompass a much wider compositional range than Andean volcanics (Fig. 10.22a). McBirney (2007) indicated that andesites are the dominant lavas in the High Cascades. He pointed out that different volcanoes behave differently—for example, while Mt. Rainier and Mt. Baker have been spewing out andesites, Three Sisters volcanoes started erupting andesite and dacite but then switched to contemporaneous eruptions of basalt and rhyolite.

Focusing on the more primitive lavas of the Higher Cascades, Leeman et al. (2005) identified two major chemical groups (Figs. 10.22b and 10.23). These primitive lavas have Mg# (=100* Mg/[Mg + Fe^{2+}] as high as 75 for Group II and 68 for Group I; and both groups are also high in Ni, Cr and are sparsely porphyritic. These lavas have the appearance of primary mantle-derived magma that did not suffer much crustal assimilation or fractional crystallization. Group I has chemical

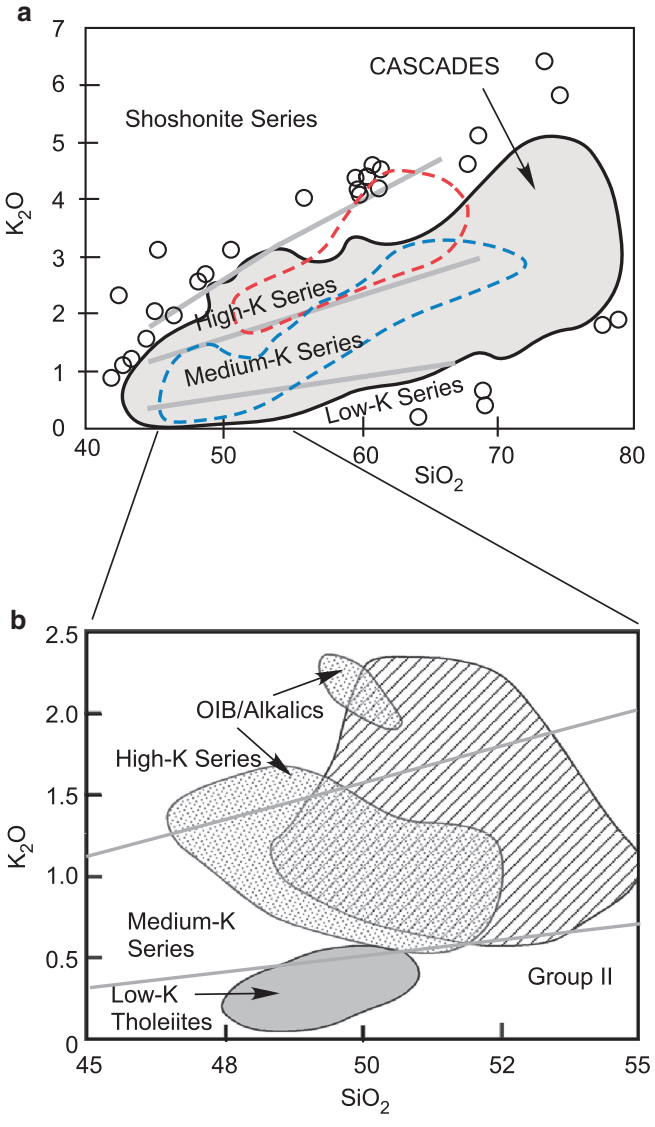

Fig. 10.22 (**a**) Bulk of Cascades lava compositions plot within the *gray field*, and the remaining are shown as *small circles* (>1,000 data points, *source*: GEOROC database). The *red* and *blue* fields CVZ and SVZ of the Andean volcanic arc. (**b**) Primitive arc lavas are plotted separately here (*source*: Leeman et al. 2005) (see text for further discussion)

characteristics that are similar to MORB and/or OIB (Fig. 10.23). Group II is enriched in Ba and depleted in Nb and thus resembles calc-alkaline lavas. Leeman et al. (2005) obtained primary magma compositions after correcting the lava compositions for possible fractionation so that they would be in equilibrium with the mantle olivine. Leeman et al. (2005) calculated the depth and temperature of equilibration of such primary magmas in the mantle to be as follows: Group I, 50–70 km, 1,180–1,280 °C, and Group II, 30–50 km, 1,160–1,300 °C. Leeman et al. noted that the bulk of both groups fall in temperature range 1,200–1,250 °C.

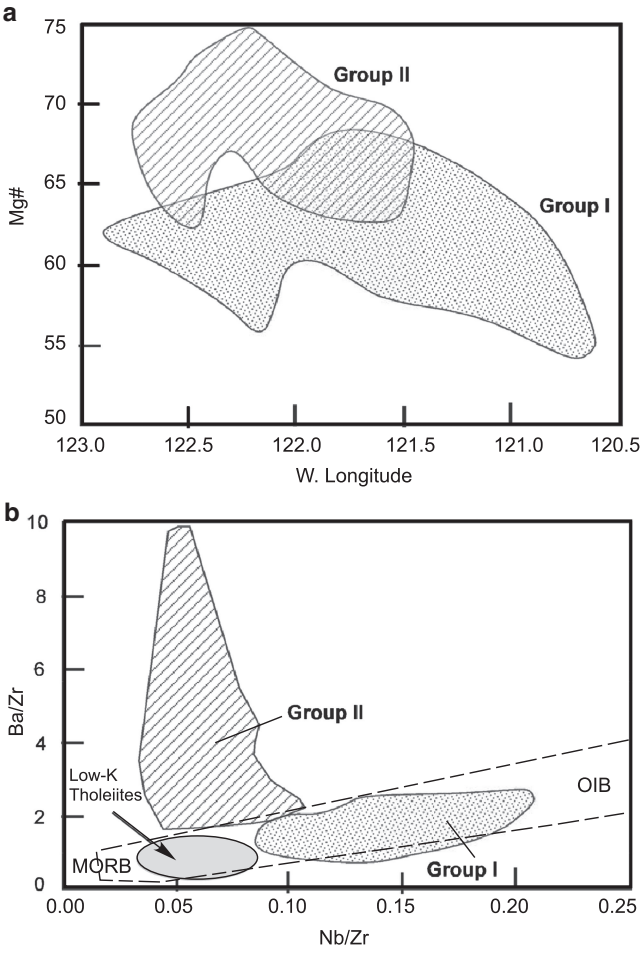

Fig. 10.23 Compositional groups of primitive Cascades lavas. (**a**) Mg# variations as a function of latitude and (**b**) Ba/Zr versus Nb/Zr variation (from Leeman et al. 2005)

From this Leeman et al. (2005) drew two important conclusions: (1) Group I formed by decompression melting of the asthenosphere (and not by fluid-fluxed melting as is normally expected beneath volcanic arcs), whereas Group II formed by fluid-fluxed melting. (2) Group I formed deeper in the mantle wedge and may have been the heat source for generating Group II magmas, which of course required fluid from the descending slab as well. Leeman et al.'s first conclusion is particularly significant for warm subduction zones like the Cascades, where advection may be an important process in generating magmas in the narrow slivers of the asthenospheric wedge (cf. Kelemen et al. 2003). The decompression melting can happen in two different ways—by oblique upwelling accompanying return flow in the wedge due to the viscous coupling with the descending slab or by diapiric rise of mantle + melt mixtures (review by Kelemen et al. 2003).

Primary Magmas, Daly Gap, and Experimental Petrologic Insights into Arc Magma Generation

Leeman et al.'s (2005) finding, as discussed above, has important implications for the nature of primary arc magmas and their generation. While their model is applicable to the Cascades, one needs to remember that slow subduction of a young and warm plate, and a laterally migrating slab over time, make this volcanic arc different from other areas, such as the IBM arc and Andean volcanic arcs. Primitive lavas of the Cascades are unusual among arc lavas in being virtually aphyric and highly magnesian (MgO $>$ 9 %), because arc lavas from elsewhere are generally quite porphyritic and have lower MgO (2–5 %).

If magmas coming off the asthenospheric wedge are severely contaminated by the subcontinental lithosphere and crust while going through MASH processes, then erupted lavas are not the original primary magmas from which they were once derived. There are exceptions to this statement: for example, in many arcs alkali basaltic lavas (e.g., Japanese volcanic arc) erupt carrying deep crustal and mantle xenoliths to the surface and this requires rapid magma rise that does not allow time for cooling and fractionation; such lavas should be pretty close to being primary. These rear-arc volcanoes are located away from the volcanic front and the trench. Nevertheless, xenolith-bearing alkaline lavas comprise relatively insignificant fraction of arc lavas. Similarly, primitive boninites (with 54 % SiO_2, MgO $>$ 10 %) or their parents may form by hydrous melting of depleted lithosphere during early arc development (as discussed before), and although boninites occur in some ophiolites, it is likely that boninite magmas are volumetrically minor relative to the andesites and basalts. The bulk of arc lavas form the calc-alkaline or medium-K series, and generation of their parent magmas is of greatest interest here.

Scientists have approached this problem in several ways—by studies of melt inclusions in phenocrysts, mantle and crustal xenoliths, geochemistry of lavas, numerical simulations, and via experimental petrology of mantle melting under hydrous conditions. Here I will discuss a single melt inclusion study and some experimental petrologic studies, as they are more germane to our interest in the generation of most voluminous magmas in arcs.

Reubi and Blundy (2009) constructed a SiO_2-frequency plot of a large number of melt inclusions in different phenocryst phases and of whole rock samples

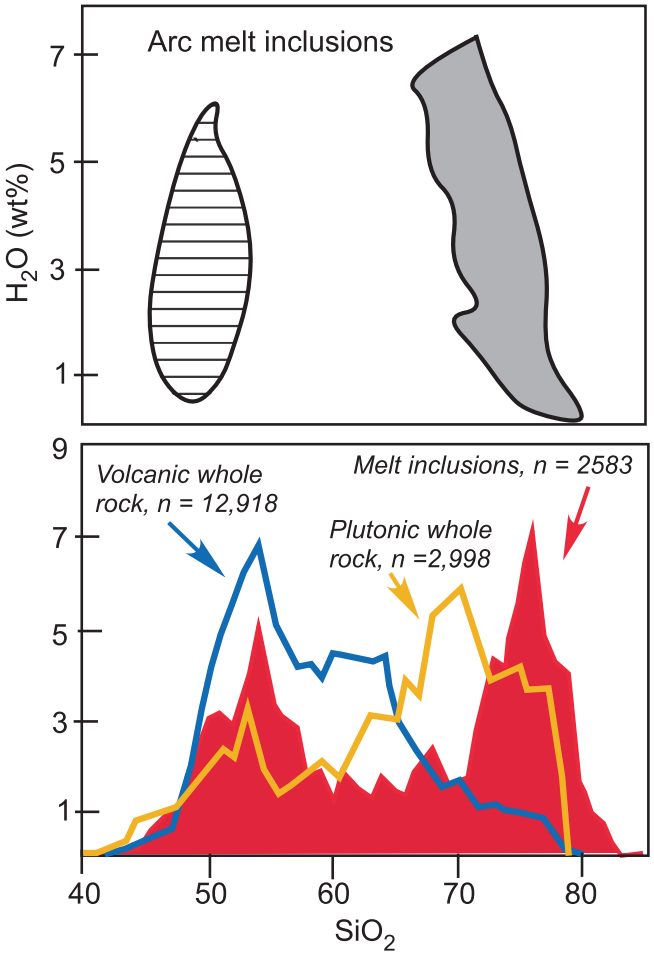

Fig. 10.24 Composition of melt inclusions in phenocrysts in arc volcanics worldwide (modified from Reubi and Blundy 2009). *Top diagram* shows two distinct groups of melt inclusions with very different SiO_2 contents. *Bottom diagram* compares whole rocks with melt inclusions

from volcanic arcs worldwide using the GEOROC database (Fig. 10.24a). The result was a clear bimodal distribution with two peaks corresponding to basalts and rhyolites; andesitic compositions are much less common. Whole rock analyses of volcanic rocks do not exhibit such bimodal distribution, and instead, we see a basaltic peak with a broader, smaller peak of andesitic composition. Reubi and Blundy (2009) hypothesized that the primary magmas produced at arcs are basalts and rhyolites and that andesites are produced by mixing between the two magma types. Other evidence presented in support of this hypothesis includes the following: (1) thermodynamically modeled or experimentally derived liquid lines of descent (LLD) from parent basaltic magma do not go through andesite compositions, (2) linear trends exhibited by arc lavas on oxide–oxide or elemental plots are better explained by magma mixing, and (3) the common presence of disequilibrium phenocrysts and magma mingling/mixing texture in intermediate composition lavas. The melt inclusions contained a maximum of 6 wt% dissolved H_2O, regardless of whether the host vapor-saturated inclusion was basaltic or rhyolitic. Their calculated minimum (minimum because they probably lost some vapor due to exsolution during ascent) entrapment pressure for such inclusions was about 0.5 GPa (18 km), indicating that the diverse melt inclusion compositions were acquired from greater depth—perhaps in the middle crust.

The gap or low frequency in andesitic composition is also known as the "*Daly gap*," after Reginald Daly who in 1925 noticed the dearth of igneous rocks between about 57 and 70 % SiO_2. As a passing note, the student is encouraged to check out Wikipedia (and the references therein) on Daly's other geological discoveries.

The Daly gap is not unique to arcs but also occurs in volcanic rocks associated with ocean islands (hot spots) and continental extensional ones (described in a different chapter). So, how does one explain the Daly gap in natural rock compositions, particularly with reference to volcanic arcs? Many proposals have been put forth, and some have been recycled over time with newer and better-quality geochemical data from volcanoes and experimental studies. We discuss a few here.

Grove and Donnelly-Nolan (1986) provided an interesting explanation, which followed an earlier suggestion by Peter Wyllie (reference in Grove and Donnelly-Nolan 1986), for the Daly gap at the Medicine Lake volcano (Cascades). They attributed the gap to arising from thermodynamics of fractional crystallization of basalt magma. Experimental crystallization of hydrated basalt magma at mid-lower crustal depth showed that the liquidus surface (i.e., $\Delta T/\Delta X$) flattens out sharply in T–X space as the liquidus surface Liq + Ol + Pl + Aug gives way to Liq + Pl + Hbl + Opx + Oxide (magnetite, ilmenite), and the slope steepens again when the melt composition becomes rhyolitic (Fig. 10.25). What this means is that andesitic melts can only form over a very limited temperature interval during which large amounts of crystals (in this case, hornblende norite cumulate) must fractionate from parent basalt magma. Thus, one would see fewer andesites erupting from a fractionating basaltic magma chamber. Rhyolite volume should also be small as the residual liquid percentage at that stage is going to be small. [*The student is encouraged to treat this diagram as a*

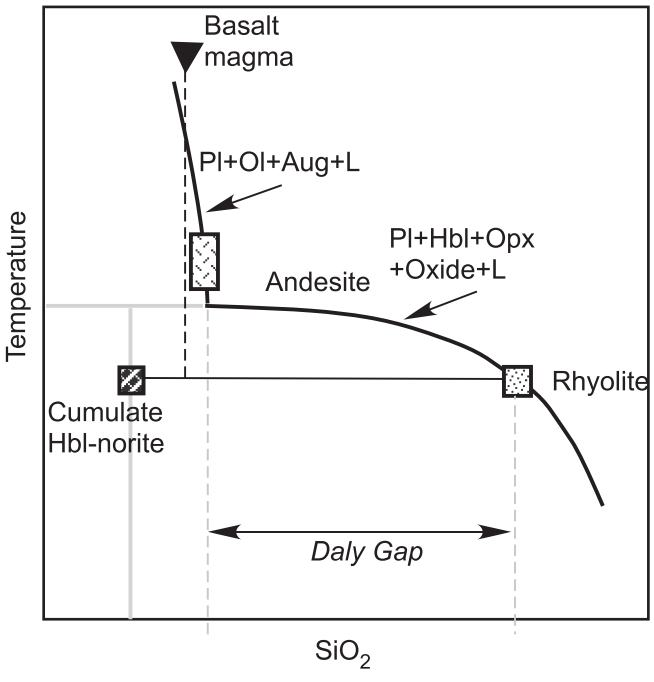

Fig. 10.25 Liquidus surface of a hydrous basalt (redrawn from Grove and Donnelly-Nolan)

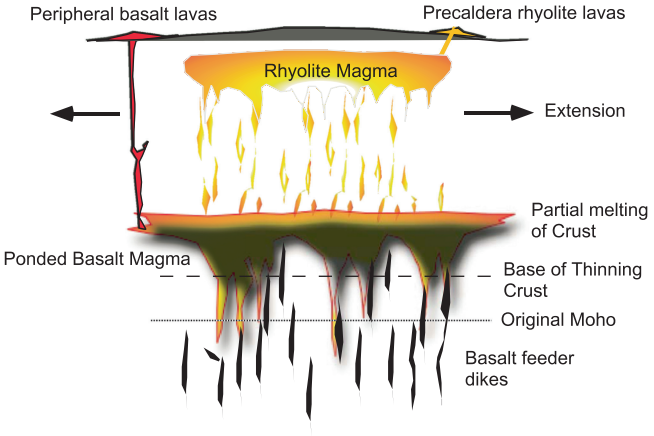

Fig. 10.26 Melting of the crust by heat released from basalt magma ponded at depth

peritectic phase diagram and calculate how melt fraction% (F) changes for the equilibrium crystallization of the given bulk composition (shown as a triangle). Assume that the temperature-axis goes from 800 to 1,400 °C, and silica% (X-axis) goes from 45 to 80.]

A more commonly accepted explanation for the Daly gap is the production of granitoid magma by melting of the continental crust due to basalt magma pooled and stagnated (basaltic "underplate") in the lower crust (Fig. 10.26). The heat is supplied from the ponded basalt magma in two ways—from the loss of its ambient heat (inherited from the mantle) and latent heat released by crystallization of mineral phases. This model works particularly well for continental extensional regimes where bimodal volcanism is a characteristic feature. Mixing between the fractionating basalt magma and granitoid magma can generate andesitic magma; however, the mixing has to be vigorous because, for reasons of high viscosity related to highly polymerized silicate chains, granitoid magma does not readily mix, as shown by the common presence of mafic "blobs" in granitoid plutons (discussed later), sometimes called "enclaves."

Granitoid magma can also form by other processes, such as hydrous melting of the basaltic (eclogitic/amphibolitic) underplate in a convergent margin (e.g., Rapp and Watson 1995), fractional crystallization, and silicate liquid immiscibility (as we have seen in the case of layered intrusions). Granitoids and rhyolite do occur on ocean islands and island arcs, where continental crust does not exist and such magma must be generated by some mechanism involving fractionation of basalt or andesitic magma or by remelting of the basaltic underplate. Andesite magma is unlikely to be primary and its origin is more complicated, as we have seen here. High-Mg andesite primitive magmas (Mg# $>$ 65) with aphyric texture found in some island arcs are likely produced as primary magma in the asthenospheric wedge.

Finally, in seeking primary arc magma compositions, one should remember that all magmas must pass through the mantle wedge, and therefore, they must equilibrate with $Fo_{89–90}$ olivine. One could thus determine the plausible primary compositions by applying equilibrium [Fe/Mg] olivine/liquid criterion (as was done by Leeman et al. 2005). Often the selection is nontrivial and one must filter out obvious olivine or olivine + pyroxene crystal-enriched compositions and calculate potential primary compositions from slightly olivine-fractionated lava compositions. Many authors have used this approach, but here we refer to the exhaustive review of such fractionation-corrected data for worldwide arcs by Kelemen et al. (2003).

Interestingly, Kelemen et al. (2003) found that basalts are significantly more abundant than andesites in the global arc database. In addition to examining the origin of primitive (Mg# $>$ 0.6, as defined by Kelemen et al. 2003) andesite magmas by mixing between basalt and rhyolite (or granitoid) melts, they also examined two other hypotheses: (1) whether both primitive basalts and andesites are primary magmas formed in the wedge, but the latter simply has greater

contribution from subducted sediments ± mafic crust ± harzburgite; and (2) whether basalts are formed by greater extent of melting and thus have less slab-derived fluid components. They concluded (and the interested student is encouraged to read their review paper) that both primary basalt and andesite magmas are produced in the wedge; high-Mg#, primitive andesites are likely derived from primary andesite magmas. This is consistent with the more recent findings of Leeman et al. (2005, discussed before). The classic calc-alkaline trend is generated from primary andesite magmas.

There are other authors who postulate that andesites are derived from high-alumina basalt (HAB) magmas and that HABs are primary magmas generated from the mantle in the presence of H_2O. However, some other authors contend that HABs are nothing but andesite magmas that have accumulated an excess of plagioclase phenocrysts perhaps by flotation in magma chambers.

Two important elements of the "arc conversation" that are missing in the above discussion are the physical (i.e., dynamics of flow of materials in the wedge) and chemical (i.e., phase equilibrium thermodynamics and chemical kinetics at the slab/wedge interface and within the wedge) processes involved in arc magma generation. These are complex issues. Kimura et al.'s (2009) recent work is an important attempt at bridging this gap. However, we do not understand the physical transport of materials in the wedge zone, whether by melt percolation or by diapiric upwelling of slab-top materials and subducted sediment melts and fluids. It is useless to talk about these things at length here, and instead I return to experimental petrologic constraints below that are more appropriate for the student.

Fluid-Fluxed Melting in the Asthenospheric Wedge: Insights from Experimental Petrology

Fluid-fluxed melting of the mantle wedge can be triggered in two ways—fluids coming off the descending slab, inducing melting in the wedge above by lowering the solidus; or fluid-rich low-degree melts (from the slab itself or produced closer to the slab) that rise and inflict large-scale melting in the hotter wedge above (e.g., Kelemen et al. 2003). Here we will not distinguish between the two mechanisms and instead simply examine whether primary high-Mg andesite magma, which would be suitable parents to the global calc-alkaline trends, can be generated from hydrous mantle peridotite.

It is well beyond the scope of this book to provide an exhaustive review of the experimental literature as it relates to primary arc magma generation. Instead, I will focus on a few experiments that provide an insight into how fluids are generated from the descending slab and to the composition of magmas generated by fluid-fluxed melting from the asthenospheric wedge at about 3–4 GPa, i.e., over a depth of 90–120 km, above subduction zones.

Fluid Production

Hydrated subducted slab is the principal provider of fluids to the asthenospheric wedge, and therefore, it is useful to have an understanding of the dehydration reactions that occur at 90 km or deeper. Many different groups have examined the *P–T* conditions where different hydrous minerals in the subducted basaltic (hydrated and altered) crust, sediments, and lithosphere may breakdown and release fluids. Briefly, these experiments suggest that Mg-rich chlorite, amphibole (in altered basalt), and serpentine (in altered basaltic crust and peridotite in the slab) are the likely hydrous minerals that breakdown to yield fluids.

Figure 10.27 shows the results of three different studies (Kawamoto and Holloway 1997; Ulmer 2001; Till et al. 2012) for the peridotite + H_2O system. Also shown is a range of possible d*T*/d*P* (i.e., rate of change in temperature as a function of changing pressure) gradients at the slab–wedge interface (from Grove et al. 2012). The agreement between the experimental studies is good for the stability limits of chlorite and serpentine but not good for amphibole. Till et al. (2012) put the maximum pressure of amphibole stability at less than 2 GPa, whereas Kawamoto and Holloway (1997) put it at about 3.3 GPa. The Australian group led by David Green, who has done many studies on H_2O in peridotite system, also puts it at about 3.2 GPa (e.g., Green et al. 2010). Therefore, whether or not amphibole breakdown would produce the needed fluid to the wedge is debatable, given the d*T*/d*P* gradients at the slab–wedge interface shown. On the other hand, it is very likely that chlorite and serpentine breakdown reactions in the slab provide the fluids to the zone of magma generation.

What kind of fluids these might be? Mibe et al. (2007) found that the fluid at about 3.8 GPa to be a supercritical fluid in the peridotite-H_2O system. In an isobaric phase diagram, such a supercritical fluid occurs above the second critical point, i.e., the peak temperature on a

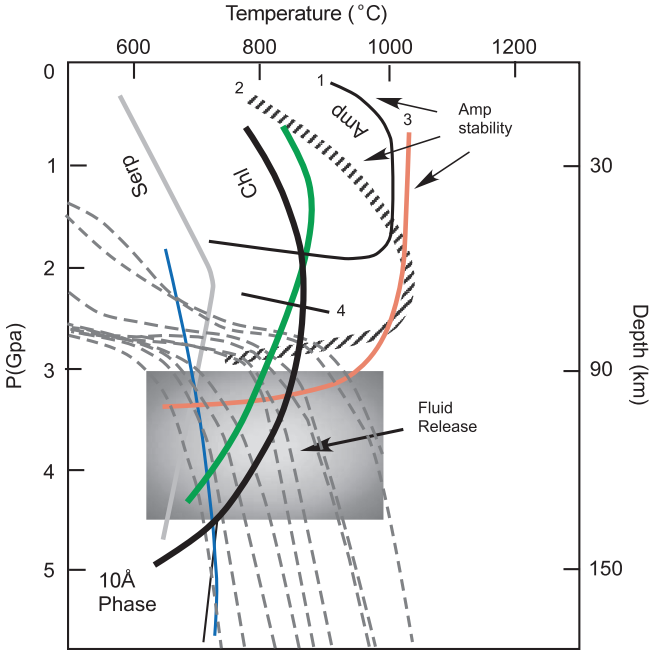

Fig. 10.27 Comparison of stabilities of hydrous phases. Chlorite (Chl), serpentine (Serp) are from Till et al. (2012). Amphibole stability: *1* Till et al. (2012), *2* Ulmer (2001), *3* Kawamoto and Holloway (1997), *4* Fumagalli and Poli (2005). The *dashed curves* are $\Delta T/\Delta P$ curves at slab–wedge interface (from Grove et al. 2012)

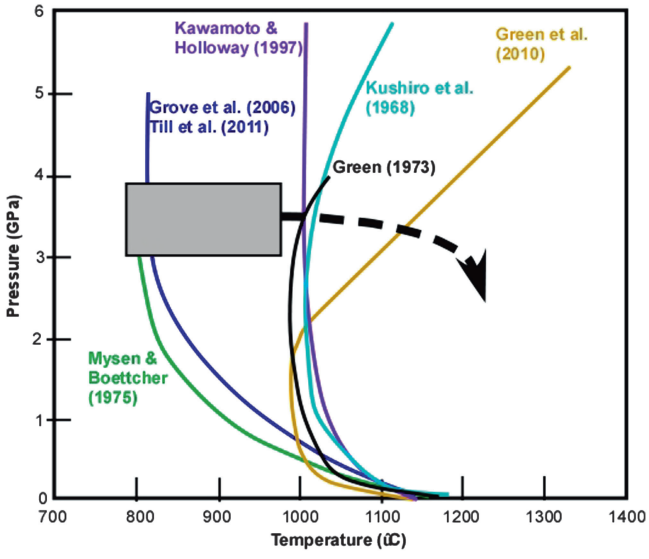

Fig. 10.28 Various solidi of H_2O-saturated lherzolite (from Grove et al. 2012). The *gray box* represents possible *P–T* range of fluid generation from the slab; and *black curve* represents migration path of the fluids into the hotter part of the wedge

liquid–vapor immiscibility curve. In the case of subduction, it is likely that supercritical fluid produced from the slab splits into melt and hydrous fluid phases as it rises into the hotter part of the wedge.

Melting and Melt Composition

Melting can only occur when the solidus temperature is exceeded; therefore, it is important to determine the solidi of both hydrous mantle wedge and subducted sediments and altered oceanic crust, preferably at about 3–5 GPa, the pressure of the slab beneath where the bulk of the melting in the wedge occurs. Figure 10.28 shows that there is a large discrepancy between different experimental studies about the location of H_2O-saturated lherzolite solidus. For cooler to average dT/dP of slab–wedge interface, the top of the chlorite-bearing slab will begin to melt if Till et al.'s (2012) solidus is correct; and on the other hand, excluding very warm slabs, "normal" slabs will not generally melt if the higher solidi are correct. In this diagram a possible trajectory of fluid path is shown: the fluid "parcel" will move into hotter region and thus eventually cross the hydrous wedge peridotite solidus and thus produce fluid-fluxed magma.

What kinds of melts are generated by fluid-fluxed melting at 3–4 GPa? This is a very difficult task in experimental petrology. The studies by Kawamoto and Holloway (1997), Green and others (cited by Tenner et al. 2012) suggest that in the presence of H_2O, magmas are alkalic (depleted in silica and therefore, ne-normative) when it forms from a garnet peridotite, which is stable at >2.8 GPa. On the other hand, the magmas are more high-Mg andesitic when they are generated from low to moderate degrees of partial melting of spinel peridotite (e.g., Tenner et al. 2012). Grove et al. (2012) produced a diagram in their attempt to explain the composition of hydrous magmas produced in the wedge (Fig. 10.29). They suggested that a variety of magmas are generated within the wedge with a fairly constant FeO*–MgO ratio of 0.5–0.8; and the higher-silica versus lower-silica melts are extracted from harzburgite versus lherzolite residues, respectively. Hydrous fractional crystallization produces the calc-alkaline trends (Bowen trend). On the other hand, "dry" fractionation of basalt magma generates the Fe-enrichment trend at similar silica content (Fenner trend).

Johnson and Plank (1999) performed experiments on a pelagic red clay (similar to subducted sediment) at 2–4 GPa in the presence of H_2O. The melts were peraluminous to peralkaline granites (look into the next section on granitoids and you will know what they are). It is possible that hydrous sediment-derived melts

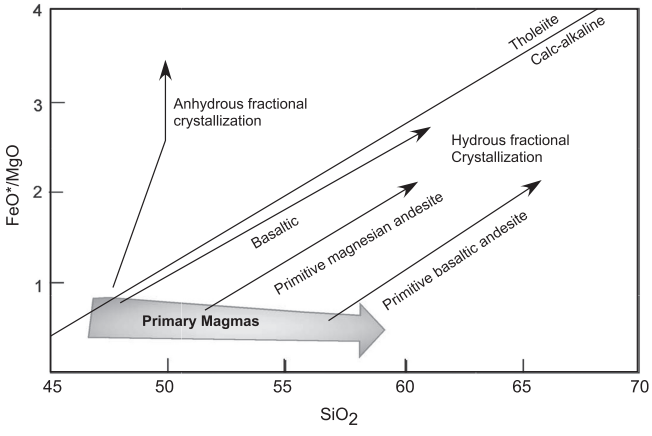

Fig. 10.29 Primary magmas and fractionation trends in subduction zones (from Grove et al. 2012)

migrate upward to the hottest part of the wedge and induce large-scale melting; and this latter (second stage but volumetrically more abundant) melt may be high-Mg andesite magma.

Summary

Magma generation in the asthenospheric wedge may result from both anhydrous decompression melting as well as by fluid-fluxed melting. While the former process produces tholeiitic basalt magma, the latter process produces a variety of magmas—from basalt to high-Mg andesite. The fluids are generated mostly from chlorite breakdown reaction. Serpentine breakdown may be involved in cooler slabs, but amphibole breakdown as a source of fluid is still debatable. The fluid released may be a supercritical fluid or a fluid + melt composite that rises up to the hotter part of the asthenospheric wedge, where it triggers more voluminous magma generation. Hydrous melting of silicic sedimentary and basaltic rocks in the subducted oceanic crust can also generate small volume granitic melts.

Granitoids

Nomenclature

It is a common practice to use the broad term "granitic" or "granitoid" (instead of granite) to refer to plutonic, coarse-grained igneous rocks that are composed dominantly of some mixtures of quartz, alkali feldspar, and plagioclase feldspar, with minor amounts of other minerals. In reality, however, based on the IUGS classification, the rock names may vary from tonalite, quartz diorite, and granodiorite to quartz monzonite and granite (see Chap. 8).

Although the IUGS classification of granitoids is used throughout this book, two other classifications have also been commonly used in the literature, one of which is based on major element chemical composition (Shand 1947; Clarke 1992), and the other is more of a genetic classification based on rock chemistry (Chappell and White 1974, and their subsequent papers). Shand's classification uses the concept of "alumina-saturation," i.e., whether the magma has more or less Al_2O_3 than what is required to make feldspar. Thus, it recognizes three major classes of granitoids—*peraluminous*, *metaluminous*, *and peralkaline* granitoids on the basis of Al_2O_3 content *vis-à-vis* alkali contents (Table 10.2). Table 10.2 lists average major element and isotopic composition of the three classes (from Clarke 1992). Clarke (1992) significantly updated Shand's classification and showed that granitoids belonging to the three classes also have distinctive minor minerals (i.e., minerals other than quartz and feldspar, Table 10.2). Interestingly, Shand's granitoid classes also correlate with plate tectonic environments.

Feldspar-Based Nomenclature

Granitoids are often divided into hypersolvus and subsolvus granitoids on the basis of whether they contain single feldspar (e.g., alkali feldspar) or two feldspars (alkali feldspar and plagioclase). At low pressure, the binary "system" albite–orthoclase is characterized by a minimum and the presence of a miscibility gap in the subsolidus region (see Chap. 4). As a result of this phase relationship, granitoid plutons emplaced at shallow levels in the crust crystallize a single $feldspar_{ss}$, and such granitoids are called *hypersolvus granitoids*. Upon very slow cooling, the single $feldspar_{ss}$ crystals decompose into two different $feldspar_{ss}$, one of which is exsolved in the other. Depending upon the composition of the $feldspar_{ss}$ that crystallized from the liquid, the exsolved (subsolvus) phase may be Or-rich and the host Ab-rich, or vice versa. An Or-rich crystal with exsolved plagioclase is called *perthite*; and when the host is Ab-rich and exsolved phase is Or-rich, it is called *antiperthite*. Cooling kinetics dictate the nature of the resultant texture exhibited by such $feldspar_{ss}$ grains—the slower

Table 10.2 Shand's classification of granitoid rocks (after Clarke 1992)

QAP			
60 % > Quartz > 20 %			
Alkali feldspar/(Alkali feldspar + Plagioclase) = 0–1			
	Peraluminuous	Metaluminous	Peralkaline
Major oxides	$Al_2O_3 > CaO + Na_2O + K_2O$	$CaO + Na_2O + K_2O > Al_2O_3 > Na_2O + K_2O$	$Al_2O_3 < Na_2O + K_2O$
Characteristic minerals	Al_2SiO_5-polymorphs, cordierite, garnet, topaz, tourmaline, corundum	Opx, Cpx, amphibole	Fa-rich olivine, alkali amphiboles aegirine
Other common minerals	Biotite, muscovite	Biotite, minor muscovite	Minior biotite
$^{87}Sr/^{86}Sr$ isotopic comp.	0.705–0.720	0.703–0.708	0.703–0.712
Plate tectonic association	Continent–continent collision	Continental and Island arcs	Post-tectonic extension
Average compositions			
SiO_2	75.45	67.43	74.01
Al_2O_3	14.76	14.67	11.59
FeO*	2.49	4.13	3.08
MgO	0.78	1.64	0.55
CaO	2.01	3.53	0.48
Na_2O	3.72	3.72	4.33
K_2O	3.52	3.2	5.09

the cooling rate, the larger the exsolved blebs. Various textural terms such as *macroperthite* (exsolution visible with naked eye), *microperthite* (microscope required), etc. are used to describe the relative size of the exsolved phase.

At higher pressures and at water-saturated conditions, the solvus (or miscibility gap) touches the solidus in the Ab–Or join, creating a eutectic point between two $feldspar_{ss}$ phases (see Chap. 4). Under such conditions, granitoid magma at the eutectic crystallizes two different feldspars. Therefore, the presence of two feldspars in a granitoid indicates a high water pressure and therefore a deep (about 12 km or deeper) crustal emplacement. Because the composition of $feldspar_{ss}$ is sensitive to temperature changes, its Ab/(Or + Ab) or Or/(Ab + Or) ratio may be used as a thermometer to estimate the final cooling temperature of the granitoid at the depth where it solidified. Even though later erosion may expose the granitoid at the surface, the feldspar compositions will not change because of extremely slow reaction kinetics. Thus, one can have a good understanding of past thermal conditions in the crust using feldspars from different depths and ages.

Alphabet Granitoids and the Fe–MALI–ASI Classification Scheme

Based on Sr isotope composition and other geochemical criteria, B.W. Chappell and coworkers used letters to classify granitoids—S, I, A, and M types (the so-called SIAM classification). Table 10.3 summarizes the characteristics of the four types. I-type is so named because it is believed to have an igneous protolith; and this type of magma was believed by partial melting of metamorphosed igneous (e.g., eclogite, granulite, amphibolite) rocks or perhaps fractional crystallization of mafic magmas. S-type stands for an origin by partial melting of sedimentary or metasedimentary rocks. S-type granitoids have higher $^{87}Sr/^{86}Sr$ ratios and relatively high Al_2O_3 content, reflected in minerals such as muscovite or garnet. On the other hand, I-type granitoids have low $^{87}Sr/^{86}Sr$ ratios and relatively high Na_2O contents. In general, I-type granitoids include most diorites, quartz diorites, and tonalites. S-type granitoids include granodiorites and granites. I- and S-type granitoids are generally subsolvus granitoids. A distinctive feature of the two types of granitoids is the nature of "restites" or enclaves they each carry. These encaves may be residues of the partially molten source rock or early fractionated cumulates, and these often occur as lenticular enclaves within granitoids. Enclaves in I-type granitoids include amphibole, pyroxene, and plagioclase, while those in S-type granitoids are biotite, garnet, sillimanite, cordierite, and plagioclase.

M- and A-type granitoids were later added to the alphabet soup! M stands for a supposed mantle origin; and M-type granites can be demonstrated to have formed via fractional crystallization of basalt magma and have mantle-like isotope compositions, such as $^{87}Sr/^{86}Sr$ ratio of about 0.7032. Plagiogranites (granitoids in which plagioclase is the dominant feldspar) found in ophiolites

Table 10.3 Comparison of alphabet granites

	S	I	A	M
$[^{87}Sr/^{86}Sr]_{initial}$	≥0.710	<0.705	Variable	<0.705
SiO_2 (wt%)	64–77	56–77	>74	54–73
Al_2O_3	High (peraluminous)	Moderate (metaluminous)	Moderate to high (peralkaline)	Moderate (metaluminous)
Na_2O	Relatively low	High	Variable	High
K_2O	Moderate	Low	High	Very low
Rock types	Granodiorite	Diorite	Alkali granite	Plagiogranite
(Plutonic)	Granite	Quartz diorite	Anorthosite	
		Tonalite		
		Plagiogranites		
(Volcanic)	Rhyolitic tuffs and lavas	Rhyolite tuffs and lavas, dacite	Peralkaline to alkali rhyolites	
Important modal minerals (other than quartz, K-feldspar)	Biotite	Amphibole	Alkali pyroxene	
	Garnet	Pyroxene	Plagioclase	
	Sillimanite	Plagioclase	Alkali amphibole	
	Cordierite		Biotite	
	Plagioclase		Quartz	
Enclaves	*Metasediments*	*Amphibolite*, *Diorite*		
Common association	Continental arcs, collisional zones	Mid-ocean ridges, island and continental arcs	Continental extensional rift zones	Mid-ocean ridges, intraplate, island arcs

are M-type. M-type granitoids in ophiolites are often called plagiogranites because they are poor in Or. In the IUGS classification, these are tonalities and trondhjemites. M-type is insignificant in relative to the abundant S, I, and A types. Also, M-type is virtually indistinguishable from the I-type for most practical purpose and is therefore ignored here.

Interestingly, the name of A-type granitoids (including both plutonic granites and volcanic rhyolites) does not refer to its petrogenesis but to its anorogenic tectonic association because this type occurs in post-tectonic arc environment or in continental extensional regimes (e.g., East African Rift, discussed in Chap. 11). A-type granitoids are commonly metaluminous or peralkaline and form shallow plutons beneath volcanoes. Their typical occurrence includes bimodal granite/rhyolite–basalt associations in continental rifts. A-type granitoids include all or most hypersolvus granites. They are rich in alkalis and are characterized by only one type of perthitic feldspar. Fluorite and biotite are common. Topaz-rhyolites and obsidians are volcanic examples of A-type granitoid magma. These magmas are believed to originate by melting of a source that has already been depleted of an I-type magma. A-type magmas have about 2–4 % dissolved H_2O and their near-surface liquidus temperature is about 900 °C.

Subsequent authors, including Chappell and White, have discovered that there are many exceptions to the major types just described above. Nonetheless, as far as source rocks are concerned, the above discussion is useful as it offers a glimpse into the many possible ways different granitoid magmas can form in different plate tectonic environments.

The various classifications presented above have not been entirely satisfactory to some scientists, and there has been a desire to keep the nomenclature simple, objective, and yet meaningful in a genetic sense for granitoids and rhyolites. As far as I am aware, the latest proposed classification scheme in this regard is that by Frost et al. (2001), which may be called the *Fe–MALI–ASI classification*. This classification scheme tries to embrace such diverse granitoid types as the Fe-rich siliceous differentiates found in layered mafic intrusions to those comprising huge granitoid batholiths. The classification is geochemical and uses a combination of FeO/(MgO + FeO) ratio, a "modified alkali-lime index" (or MALI, $Na_2O + K_2O - CaO$), and an Al-saturation index [or ASI, Al/(Ca-1.76P + Na + K)]. The rocks are first classified into a "ferroan" and "magnesian" categories based on their FeO/(FeO + MgO) ratio, and then they are further grouped according to their MALI and subgrouped based on ASI (Fig. 10.30; redrawn from Fig. 7 in Frost et al. 2001). In total, Frost et al. (2001) obtained 16 types of granitoids based on their scheme. Figure 10.30 shows how the nomenclature adopted in this classification compares with the standard alphabet classification.

As the student would have gathered by now, granitoid rocks (and their volcanic equivalent—rhyolite) occur in all types of plate tectonic environments—mid-ocean ridges, island arcs, continental arcs, and in hot spot

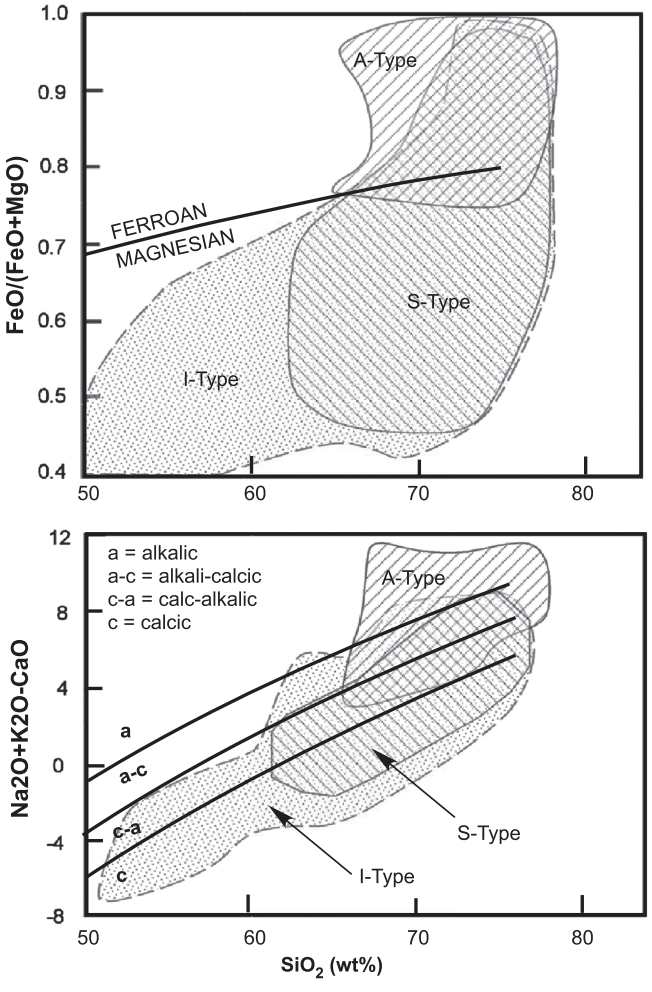

Fig. 10.30 Forst et al.'s (2001) classification of granitoids based on geochemical composition. (**a**) First-order classification based on FeO/(FeO + MgO) ratio. (**b**) Further classification into multiple subgroups. A-, S-, and I-type granitoids are compared with their classes. (See text for further discussion)

areas (Fig. 10.31). Granitoid batholiths that form the plutonic core of continental arcs and their associated large silicic ignimbrite (and lava) eruptions are volumetrically most important. The next few paragraphs are therefore dedicated to an understanding of granitoid batholiths and rhyolitic eruptions.

Granitoid Batholiths

Granitoid batholiths cover areas of ~hundreds of square kilometers in continental arcs and continent–continent collision zones. The name *Stock* is given to similar intrusions but that are smaller than 100 km^2. In terms of size and areal extent, batholiths that are found in continental arcs, such as the Sierra Nevada batholith of the United States (Fig. 10.32) and the coastal batholiths of Peru and Chile, literally dwarf collisional batholiths, of which the Himalayan batholiths are an example (Fig. 10.33a). The Himalayan batholiths formed by magmas generated due to collision between the Indian Plate and the Eurasian Plate (Fig. 10.33b).

In the following discussion we will only refer to arc batholiths, which are not homogeneous but are composed of many smaller (commonly 2–5 km^2) plutons that are emplaced over millions of years. The magma composition with each phase of intrusion changes as well. The coastal batholith of Peru consists of a chain of 800 plutons that were gradually emplaced over a period between 110 and 30 million years ago. The Tuolumne Intrusive Series, a relatively small pluton that occurs within the Sierra Nevada batholith, witnessed at least four distinct episodes of magma emplacement (Fig. 10.34; Bateman and Chappell 1979). A hornblende + biotite-bearing quartz diorite occurs at the peripheral region and was the first batch of magma to be emplaced. The intermediate region is composed of granodiorite and porphyritic granite occurs at the core of the pluton. Bateman and Chappell (1979) showed that these distinct episodes of magma intrusion occurred in the core region of the pluton while the pluton was still not fully solid. Intrusion of younger magma batches resulted in episodic breaching of the solid margins of the intrusion.

The exposed surface area of a granitoid pluton is related to the shape, volume, and extent of erosion. The plan view of granitoid plutons can vary from circular to elliptical to almost linear (cf. Clarke 1992). Their three-dimensional structure is often difficult to determine; however, geophysical studies and analogue model experiments indicate that they vary from dome, tabular, mushroom to inverted teardrop shapes (Clarke 1992; Pitcher 1993).

Buddington (1959) recognized three classes of plutons on the basis of field relations and inferred depths of emplacement: *epizonal* (depth of emplacement—0–5 km), *mesozonal* (~5–15 km deep), and *catazonal* (>~10 km). Epizonal plutons are characterized by sharp discordant contacts with wall rocks, intense hydrothermal alteration (and ore mineralization) of the wall rocks, and generally weak contact metamorphism of wall rocks. Catazonal batholiths are surrounded by high-grade, lower crustal, metamorphic rocks. Their contacts with the wall rocks are generally diffuse, and *migmatite* veins are common. Migmatites are generally believed to be low degrees of melt that are sweated out of the wall rocks. Mesozonal batholiths have intermediate characteristics, whose contacts with wall rocks may vary from sharp to gradational. Wall rocks often show

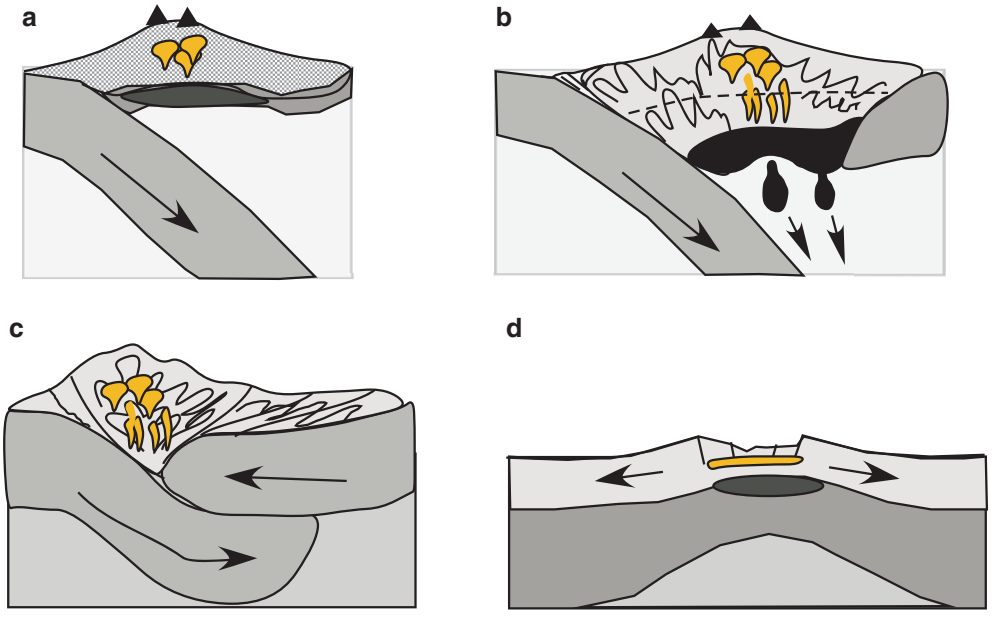

Fig. 10.31 Schematic diagrams to illustrate granitoid magma production in convergent boundaries (**a**, **b**, and **c**) and continental extension zone (**d**). *Yellow*—granitoid magma. *Black*—basalt magma underplate. (**a**) Island arc. (**b**) Continental arc. The *arrows* indicate detachment of root materials from the arc. (**c**) Continental collision

metamorphism of a previously weakly metamorphosed rock. Most exposed batholiths are mesozonal.

Armed with some general knowledge about continental arc batholiths, we can now examine a very well-studied example, the Sierra Nevada Batholith (SNB) of California in some detail next. The hope is that the student will have a better understanding of how continental crust forms, evolves, and how the crust couples with the mantle in these processes.

Sierra Nevada Batholith

The Sierra Nevada Batholith occupies much of California and part of Nevada (Fig. 10.32a). It is generally accepted that the western half of the SNB resides on an accreted lithosphere that was not part of the original North American plate but was "slammed" into place by plate tectonic movements. On the other hand, the eastern part of the SNB sits on the lithosphere of the North American craton. The $^{87}Sr/^{86}Sr = 0.706$ line divides the two sides of the SNB in Fig. 10.32b.

The SNB formed as a result of igneous activity related to the subduction of the Farallon Plate beneath the North American Plate some 220–80 Ma. The main exposure of the batholith is in central and southern part, where the bulk of the studies have been done. Deeper parts of the batholith are exposed in the southern SNB, where the batholith has been tilted. Figure 10.32b shows a schematic southeast–northwest cross section through the crust. To the west of the SNB is the Great Valley, which is a thick sedimentary fore-arc basin; and to the east is the Basin and Range Province, which has formed by roughly E–W extension of the crust.

The plutons comprising the SNB are composed of tonalites, granodiorite, and granite. Gabbro, diorite, and leucogranite plutons are small and probably comprise no more than 2 % of the outcrop (Lee et al. 2006, and references therein). Even though gabbroic and dioritic plutons and enclaves are minor, they are ubiquitous. Geobarometry indicates that this granitoid batholith was originally about 35 km thick. The top 5-6 km of the batholith resulted from magmatic activity that occurred in two episodes: the first episode occurred 160-150 Ma and the second occurred 100–85 Ma (Ducea 2001). According to Ducea (2001), most of the shallow crustal second episode, which formed 78 % of the batholith, occurred 100–85 Ma. Ducea (2001) called such events "magmatic flare-ups."

There is a significant body of information on the deeper parts of the batholith from sections exposed in the southern SNB, seismology, and from xenoliths that were brought up by much more recent volcanism from great depths through the SNB. Two suites of deep crustal and mantle xenoliths were brought up by Mid-Miocene volcanics in central and southern SNB and by Pliocene–Quaternary volcanics in southern SNB. Mid-Miocene volcanics-hosted xenoliths are the most intriguing and include garnet pyroxenites, garnet peridotites, spinel peridotites, garnet granulites, and some metasedimentary rocks. Pliocene–Quaternary volcanics-hosted xenoliths include plagioclase and

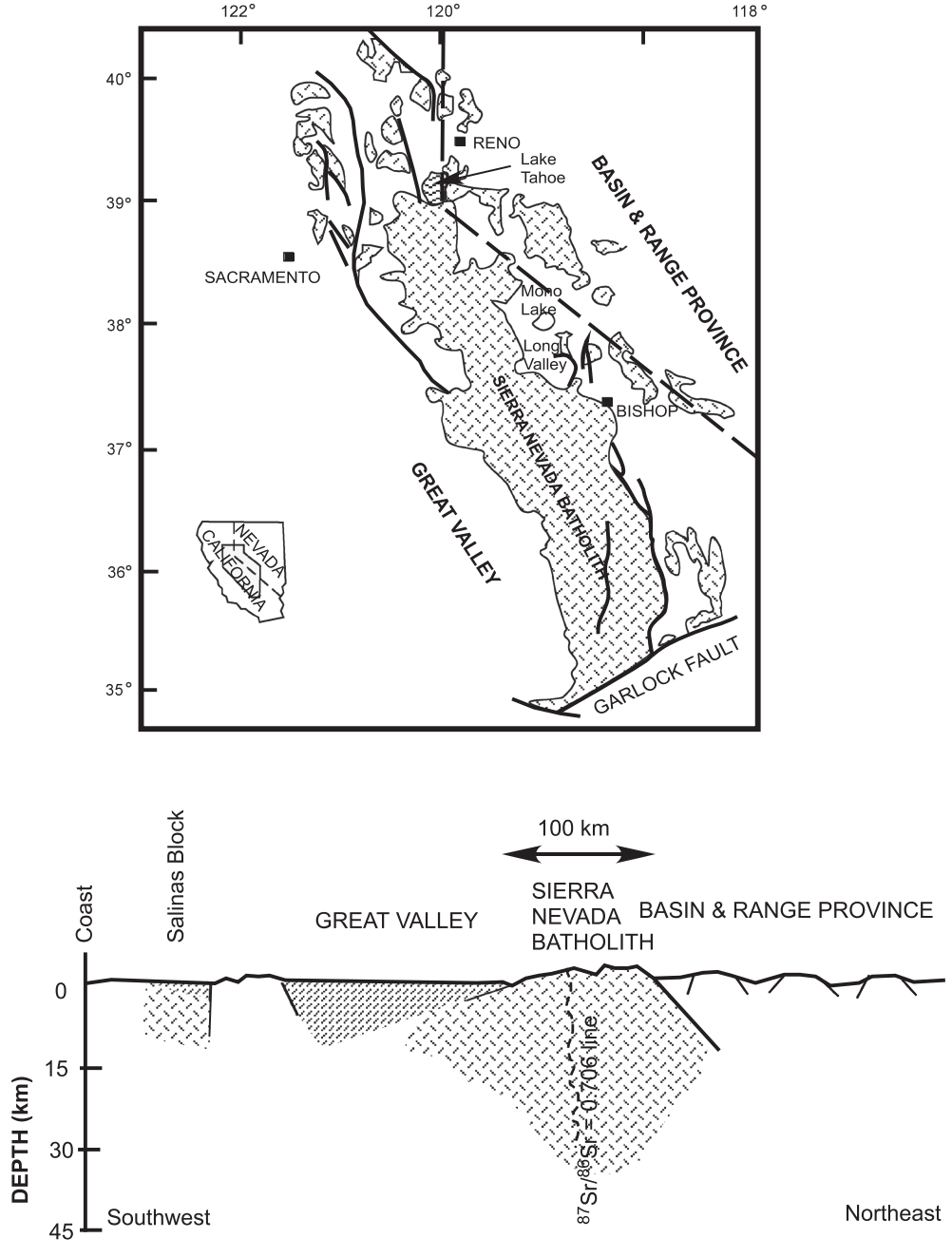

Fig. 10.32 (**a**) Somewhat simplified map of the Sierra Nevada Batholith. (**b**) A schematic cross section through the batholith and surrounding areas. The approximate position of the $^{87}Sr/^{86}Sr = 0.706$ line is also shown. To the east of this line, the basement is made of North American cratonic lithosphere, and to the west of it is accreted terrane

spinel peridotites. Significance of these xenoliths were summarized and discussed by Ducea (2001), Saleeby et al. (2003), and Lee et al. (2006).

The following is a summary of information on the xenoliths as they are relevant to the petrogenesis of the SNB.

- The Mid-Miocene garnet pyroxenites are the most abundant type of xenolith and are of two types (Fig. 10.35)—high-MgO pyroxenites (MgO < 15 %, SiO_2 45–52 %, Al_2O_3 < 10 %) and low-MgO pyroxenites (MgO > 15 %, SiO_2 < 45 %, Al_2O_3 > 10 %). These xenoliths are not eclogites because the clinopyroxene is not omphacitic (Lee et al. 2006).
- The high-MgO and low-MgO groups do not show continuous variation between them. The high-MgO pyroxenites have more clinopyroxene (>50 %) than garnet and some orthopyroxene. The low-MgO pyroxenites lack orthopyroxene and have more garnet (>50 %) and some amphibole and occasional plagioclase (Lee et al. 2006). Lee et al. (2006) suggested that the high-MgO xenoliths are

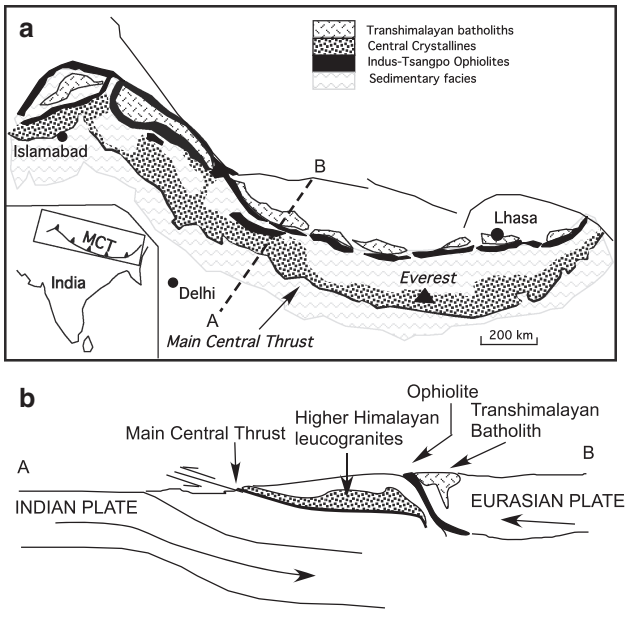

Fig. 10.33 (**a**) Map showing the location of large Transhimalayan granitoid batholiths. The smaller Higher Himalayan leucogranites are not shown. (**b**) A schematic cross section showing India–Eurasian collision and granitoid batholiths (redrawn after Le Fort 1981)

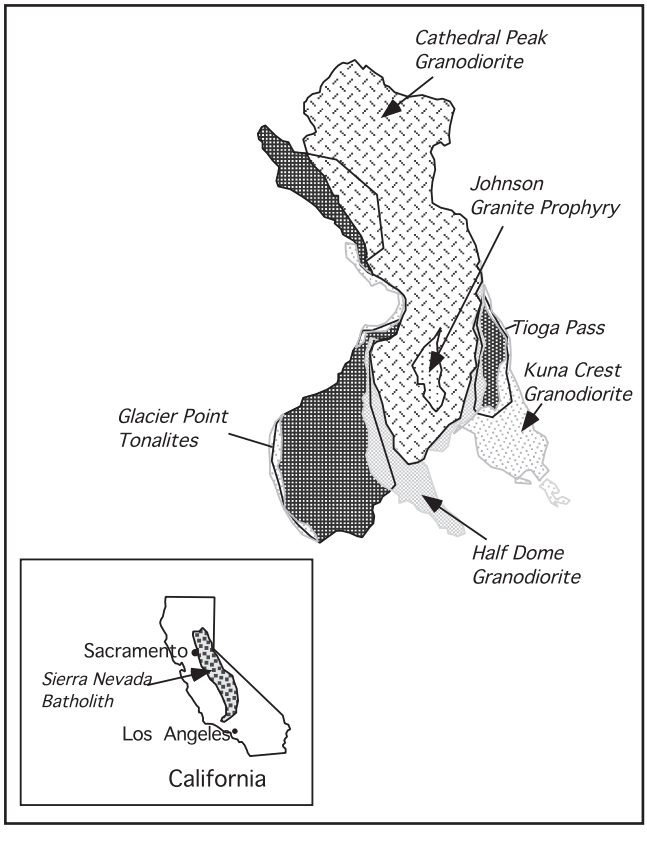

Fig. 10.34 Granitoid plutons of the Tuolumne complex, Sierra Nevada Batholith. (See text for further discussion)

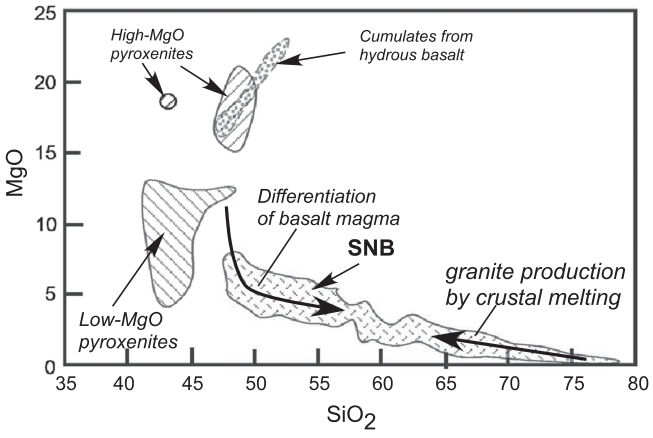

Fig. 10.35 Compositions of the two types of garnet pyroxenite xenoliths and the Sierra Nevada Batholith (SNB). Composition of cumulates in experimental crystallization of hydrous basalts is also shown. The *arrows* suggest that the high-silica granitoids in the SNB may have largely formed by fractional crystallization of basalt magma and the high-silica granitoids have formed by melting of the crust (after Lee et al. 2006)

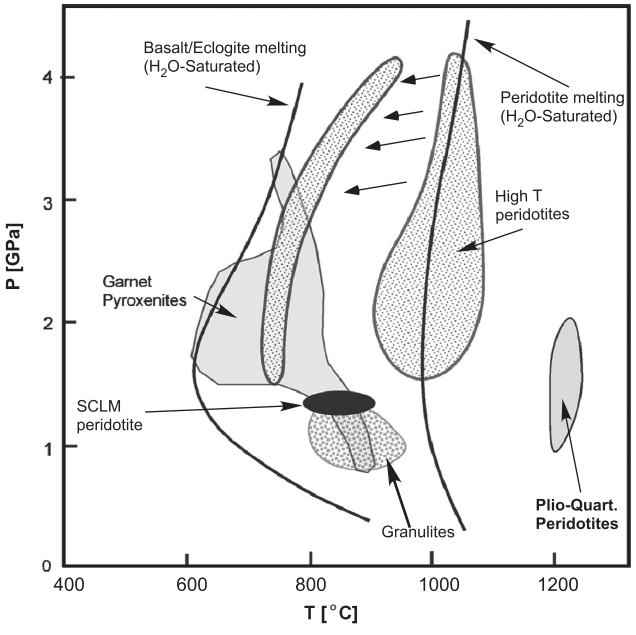

Fig. 10.36 Pressure–temperature of equilibration of the different xenolith types from the SNB. Except for the small group of peridotites that occur in the Pliocene–Quaternary volcanics, all of the xenoliths are Mid-Miocene volcanics (*source*: Saleeby et al. 2003). The two wet solidi shown here are also from Saleeby et al. (See text for a detailed explanation)

cumulates from hydrous basaltic magmas, because their compositions are similar to experimentally produced crystals from hydrous basalt/basaltic andesite magmas (Fig. 10.35). The low-MgO xenoliths were postulated to be cumulates or residues of melting. The REE data on such xenoliths indicate, however, that they are complementary residues of the felsic melts that comprise the SNB (Ducea 2001; Saleeby et al. 2003).

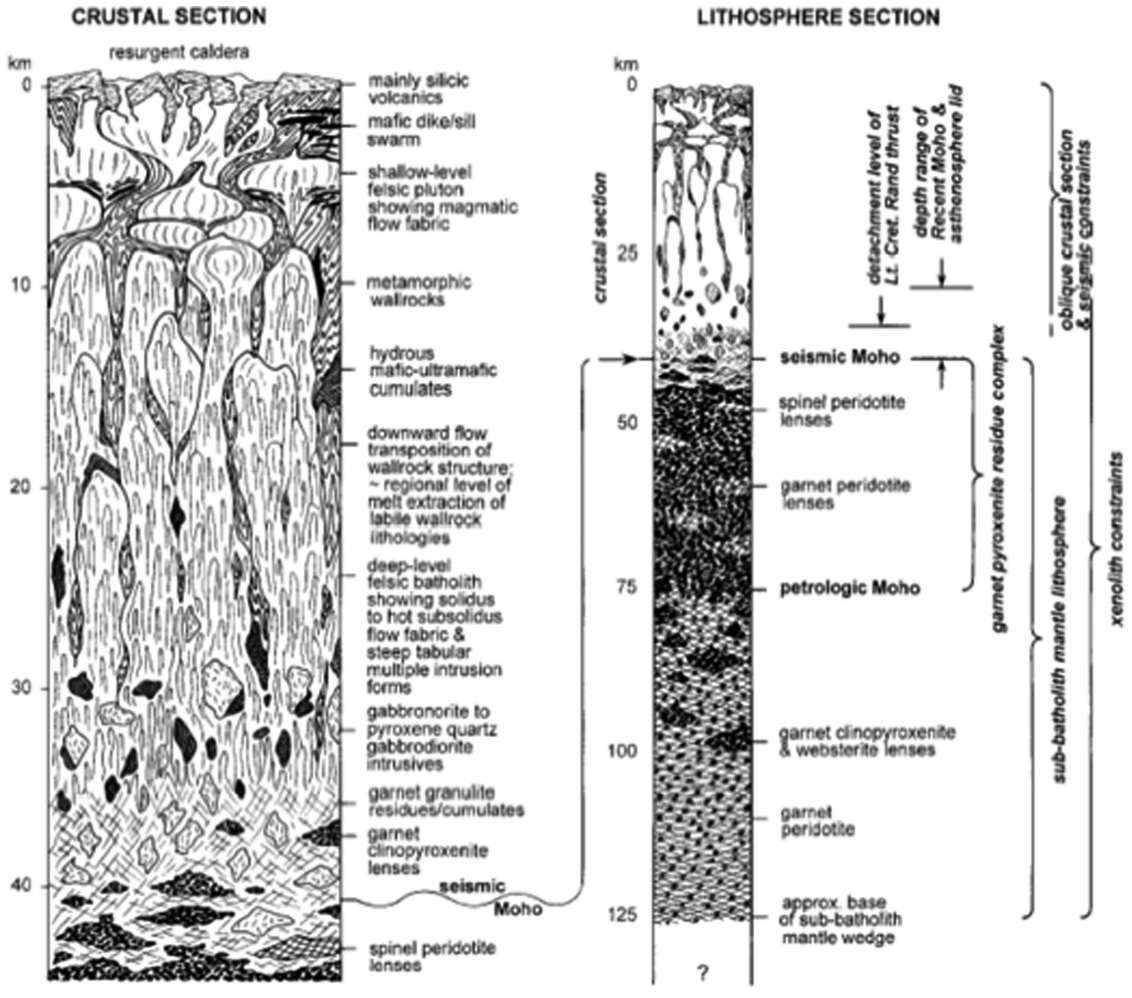

Fig. 10.37 Schematic cross section through the Sierra Nevada Batholith based on xenoliths (reproduced from Saleeby et al. 2003)

- *P–T* estimates from pyroxene thermobarometry of the xenoliths indicate that they cover a depth range of about 30–125 km depth: granulites and some metasedimentary xenoliths = 0.8–1.3 GPa; garnet pyroxenites = 1.5–3 GPa; garnet and garnet + spinel peridotites = 1.3–4.2 GPa; garnet-free peridotites = 0.9–1.2 GPa (Fig. 10.36). The temperatures of the garnet pyroxenite xenoliths are higher than the solidus temperature of hydrous basalt/eclogite, which provide indirect evidence that these xenoliths could have been involved in partial melting or could have crystallized from hydrous magmas. The *P–T* information on the xenoliths has led to the conclusion that a deep (~130 km) mafic–ultramafic root, composed mainly of garnet pyroxenites and garnet peridotites, had existed at least until Mid-Miocene (Fig. 10.37; cf. Saleeby et al. 2003). This root presumably developed during the extraction process of SNB magmas.
- It is most interesting that the xenolith suite brought up from great depths by the Miocene volcanics is completely missing in the younger Pliocene–Quaternary suite; and instead what is found are xenoliths of high-temperature spinel peridotite and spinel–plagioclase peridotites that came from 30 km (~1 GPa). This observation has led to the conclusion that the high-density root that existed during Mid-Miocene became had detached from the base of the SNB sometime between Mid-Miocene (~10 Ma) and Pliocene (~3 Ma). The Plio–Quaternary volcanics are thought to be from the mantle materials that had replaced the garnet pyroxenite-rich root.
- The root detachment model has found support in the isotopic studies of SNB and the xenoliths. For example, Nd–Sr isotopic composition of the garnet pyroxenites, garnet peridotites, and some garnet granulites overlaps that of the SNB and especially Cretaceous SNB, indicating a genetic relationship between these xenolith types and the SNB magmas [Fig. 10.38; data and fields from Ducea (2001) and Barth et al. (2011)]. The isotopic compositional span of the SNB is well explained as having derived from essentially two sources—depleted upper mantle and old continental crust.

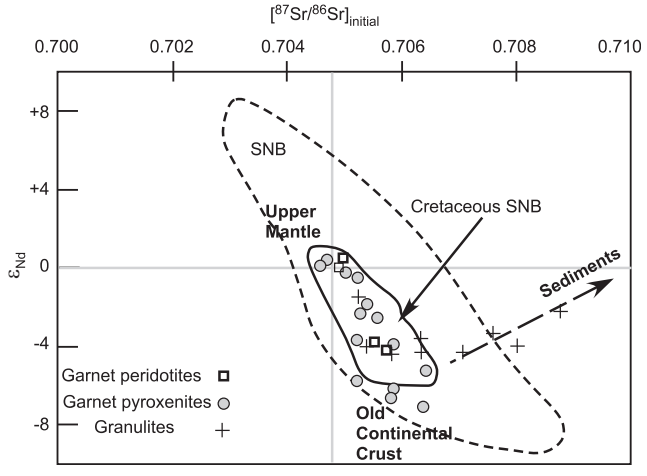

Fig. 10.38 Isotope compositions of xenoliths of various types are compared with the SNB and, especially, Cretaceous SNB (redrawn from Ducea 2001)

Interestingly, several seismological and magnetotelluric investigations have found evidence of the existence of a detached high-density root, likely related to the southern SNB, further to the west beneath the Great Valley (Fig. 10.39; from Zandt et al. 2004).

Large Ignimbrite Eruptions

An important feature of continental arc volcanism is giant ignimbrite eruptions that can cover thousands of km^2. Large silicic magma chambers within the shallow crust cool and crystallize along the walls, creating a mush of crystals and melt, with proportion of melt and vapor increasing toward a melt-rich "lens" near the roof of the chamber. Compaction contributes more melt to the lens by squeezing out the interstitial melt from the mush zone. Such processes can operate over hundreds of thousand year timescales. The result is a giant vapor-saturated melt lens near the roof. Exsolution of vapor bubbles from the melt leads to accumulation of vapor-rich, melt (and crystal)-poor layer near the roof. Eventual collapse of the roof leads to explosive eruption of an ignimbrite, which is a mixture of ash, glass shards, and solid particles (crystals in the chamber and overlying roof materials). The bulk of the material erupted this way comes from the shallowest part of the magma chamber; and with time deeper materials (lava and pyroclastics) are erupted.

Just as batholiths reveal the deeper plutonic processes related to granitoid magmatism, giant ignimbrite deposits tell us the processes and temporal changes in composition of the magma in the shallow chamber. Giant ignimbrites can be of two types (Bachmann and Bergantz 2008):

Group 1: this is the most common type of giant eruption. It shows gradational temporal change in the composition of the materials that are erupted out of the magma chamber. The eruption generally starts with crystal-free rhyolitic eruption. The proportion of crystals increases upward in the ignimbrite deposit. A well-studied example of this group is the Bishop Tuff, which will be addressed in the next section.

Group 2: this group does not show the compositional gradation with time; and crystal-poor rhyolites and crystal-rich (up to 45 % crystals) dacite are erupted. Because of the high crystal content of the dacite, Bachmann and Bergantz (2008) suggest that they are erupted mush material.

Bachmann and Bergantz (2008) identified a third type of ignimbrite deposit, which is of much smaller volume. This group shows abrupt change from early crystal-poor rhyolites to crystal-rich compositions.

In the following section, I briefly describe the Long Valley Caldera (California, USA) as a very well studied example of rhyolitic volcanism associated with a continental arc.

Long Valley Caldera

The Long Valley Caldera (LVC) is located at the boundary between the Sierra Nevada and the Basin and Range Province (Fig. 10.40a). About 760,000 years ago the volcano blew out its roof, formed the caldera, and poured out rhyolitic lava, pyroclastic flows, and ash. The ash spread as far as Nebraska (Fig. 10.40b). The thick welded pyroclastic deposit that formed due to this cataclysmic event is known as the Bishop Tuff. The s States Geological Survey (USGS) has recorded significant seismic activities beneath the LVC since 1978 that suggest active magma movement beneath this area, and therefore, it closely monitors the volcano for any possible signs of another catastrophic eruption.

The LVC is part of a larger volcanic system whose activities started about 4 Ma and continues today (Fig. 10.41; Bailey 2004; US Geological Survey Professional Paper 1692). Much of what is described here comes from the Bailey's summary of this volcanic system. Figure 10.41 shows the timing, volume, and type of eruptions that occurred over the last 4 million years over an area within 10 km of the LVC.

The early precaldera volcanism led to laterally extensive basalt–trachyandesite lava flows. On the rim and within the caldera, the volcanism turned to forming dacite domes, flows, and tuffs. The volcanism became rhyolitic and produced the Glass Mountain on the northern rim of the LVC.

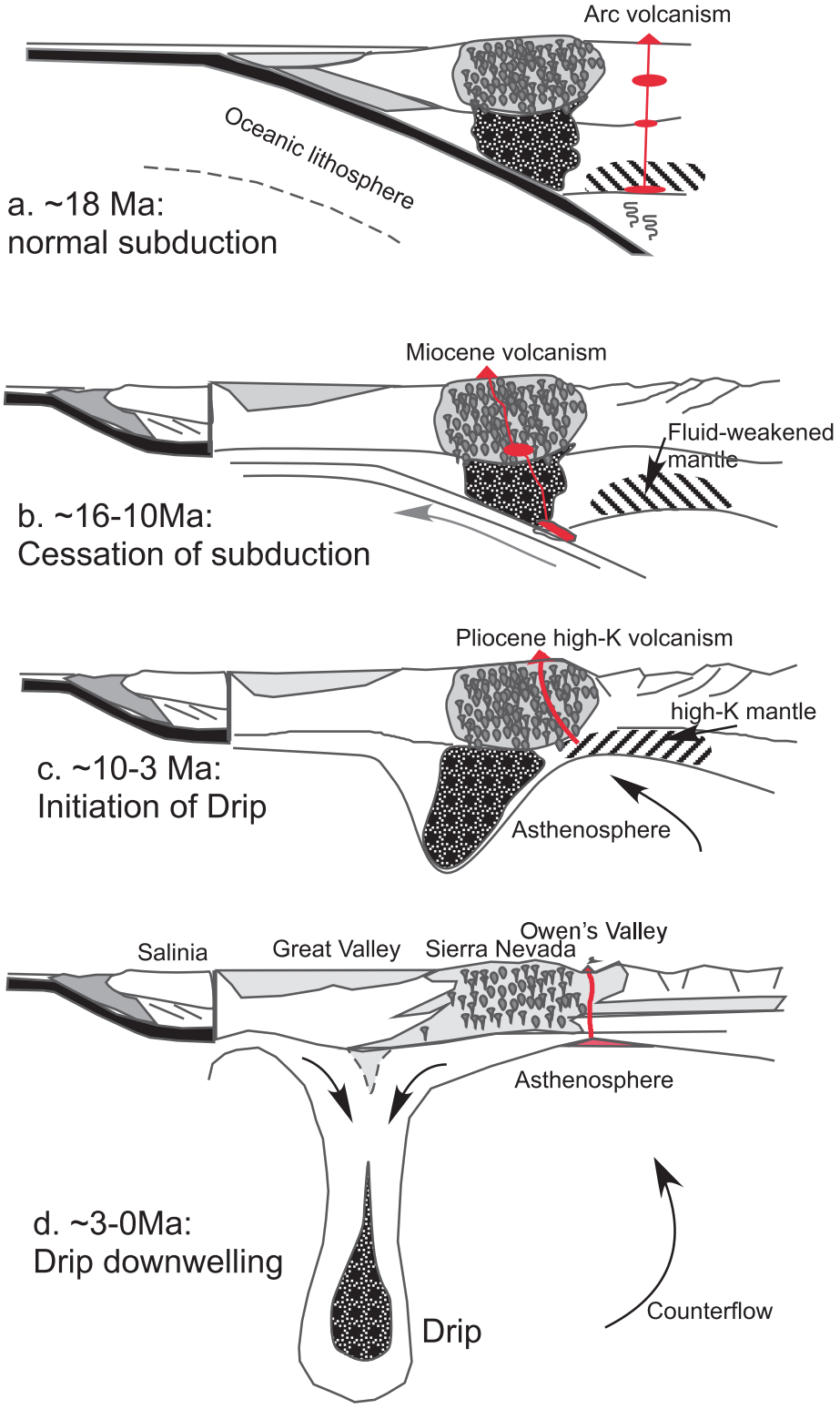

Fig. 10.39 Lithosphere delamination model presented by Zandt et al. (2004). The schematic cross sections show how the lithospheric root develops over time as a result of magma formation and extraction while thinning the surrounding lithosphere. Some 3–0 Ma the root or "drip" detached and is now buried under the Great Valley

After the roof collapsed, the magma chamber received new magma and inflated, forming the resurgent dome within the caldera. Rhyolite continued to erupt as lava flows, domes, and tuffs on the floor of the caldera. Basalt enclaves were found in the rhyolite. Basalt–dacite lava flows erupted from the rim of the

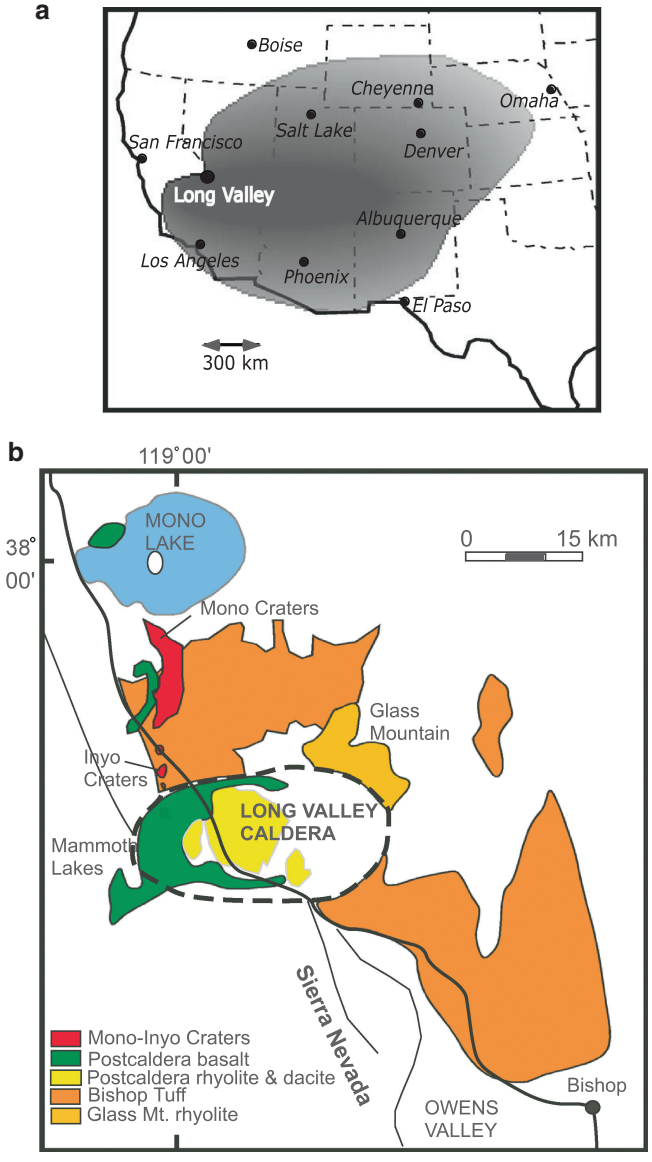

Fig. 10.40 (**a**) The spread of ash (in *gray*) derived from the Bishop Tuff eruptive event from the Long Valley Caldera. (**b**) Simplified map of the Long Valley Caldera system

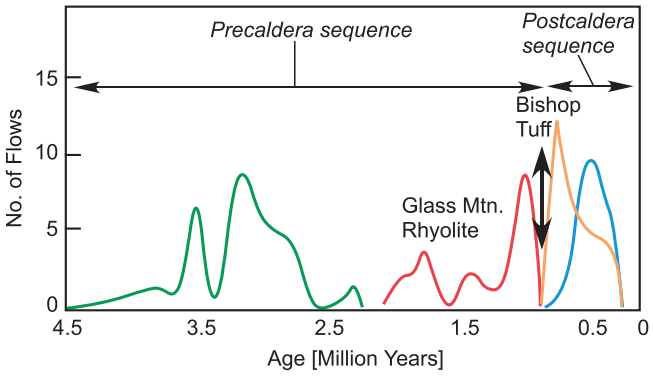

Fig. 10.41 Age and frequency of flows from the LVC system (*source*: Bailey 2004)

caldera and from the neighboring Inyo–Mono craters associated with a fissure system (Fig. 10.40a).

Composition of Precaldera, Bishop Tuff, and Postcaldera Lavas

Bailey (2004) noted significant differences between the precaldera lavas that erupted from Central Sierra, East Sierra, and the Basin and Range area (Fig. 10.42). The basalts from the three areas are alkalic in character and are high in K_2O; and they form subparallel trends in the TAS diagram, indicating the presence of at least two different parent magmas in each case. The East Sierra suite of lavas exhibits distinct compositional gaps between basalts, trachyandesites, and dacites. The postcaldera lavas, from basalts to rhyolites/alkali rhyolites, overlap the precaldera lava suites from Basin and Range and East Sierra. The precaldera basalts are distinctly more magnesian than the postcaldera basalts, although the more evolved pre- and postcaldera lavas overlap in composition (Fig. 10.42b). In terms of REE, precaldera basalts show steeper LREE enrichment and lower HREEs (Fig. 10.42c).

Detailed studies of the Bishop Tuff have been carried out by many different groups (references in Hildreth and Wilson 2007). It was determined that the Bishop Tuff eruption event lasted only 6 days. The Bishop Tuff has the composition of a high-silica rhyolite (SiO_2 = 74–78 %) and is composed of ash and pumice clasts of biotite–plagioclase–sanidine–quartz (Hildreth and Wilson 2007). Early works on the layers within the Bishop Tuff by Hildreth suggested that the LVC magma chamber was zoned in terms of its chemistry, temperature, and crystal content and such zoning is recorded in the vertical layering of the tuff. A vast body of literature exists debating the processes that might have contributed to the formation of such a zoned rhyolitic magma chamber. More recent studies have found, however, that such a simplistic picture needs rethinking. Hildreth and Wilson (2007) found that the proportion of crystals increased and so did the temperature (714–818 °C) with time. Their new study suggested that shortly before the Bishop Tuff eruption, the crystal-rich melt lens at the roof of the LVC was intruded by fresh, hotter, crystal-poor batches of low-silica rhyolite.

A simplified model magma chamber for the LVC is shown in Fig. 10.43 (source: Bachmann and Bergantz 2008), which summarizes the observations presented above. The model is based on Marsh's pioneering "solidification front" model of magma chamber, as has been

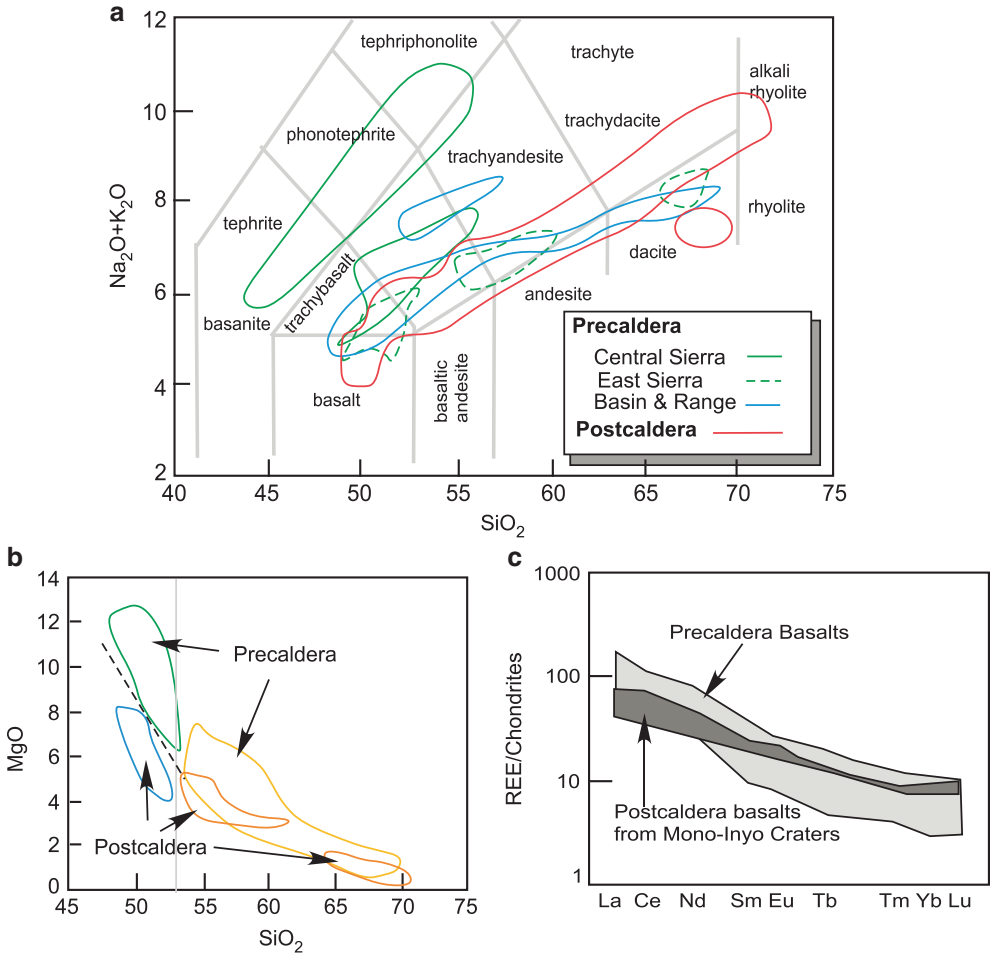

Fig. 10.42 (**a**) Composition of lavas erupted from the Long Valley Caldera (**b**) MgO–SiO_2 variation shown by precaldera and postcaldera lavas erupted from the Long Valley Caldera. (**c**) Comparison of REE patterns of precaldera and postcaldera basalts (*source*: Bailey 2004)

discussed before. Crystallization has led to the formation of a melt lens with less than 50 % crystals near the roof of the chamber. This is the only "eruptible" part of the chamber. The rest of the magma chamber has less than 50 % melt, which means that the crystals are interlocked with melt occurring between the crystals. What triggered the Bishop Tuff eruption is possibly the overpressure created by exsolved gases from the melt, augmented by new supply of heat and gases brought in by fresh batches of hotter magma (basaltic, dacitic, as well as rhyolitic). Further detailed analysis of this system is not possible here except to say that the various recent studies seem to suggest that another Bishop Tuff like eruption is unlikely.

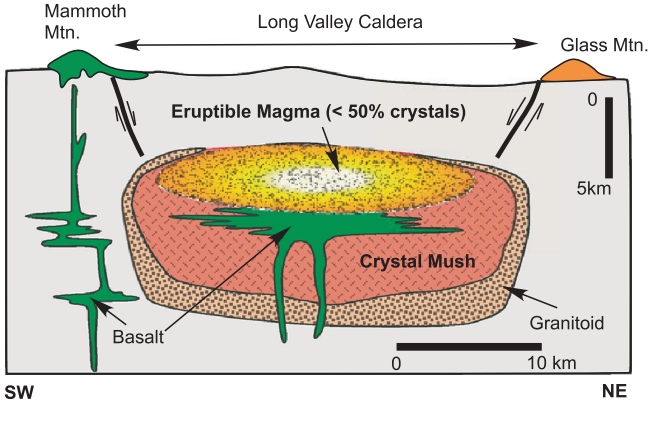

Fig. 10.43 Schematic cross section showing the physical nature of the magma chamber beneath the Long Valley Caldera (redrawn from Bachmann and Bergantz 2008)

The "Granite System" and Its Significance

We have said much about granitoid plutons and rhyolitic volcanoes. Here we will try to understand the phase equilibrium relationships that will help us gain a better understanding of silicic magma formation and crystallization. Quartz and feldspar, the two dominant minerals in granitoids, crystallize in the ternary system SiO_2(Q)–$NaAlSi_3O_8$(Ab)– $KAlSi_3O_8$(Or); and therefore this system is referred to as the "granite system"

(Fig. 10.44; Tuttle and Bowen 1958). In this system, a *ternary minimum* ("*m*") occurs at low pressures on the cotectic between quartz and feldspar liquidus fields (Fig. 10.44a). Two 3-phase triangles are schematically shown to indicate the direction of liquid movement upon crystallization and the coexisting phase compositions. As we saw in Chaps. 4 and 5, the minimum point is not a eutectic because in such a case 3 solid phases and a liquid should coexist in a 3-component system (recall phase rule). At pressures above 0.5 GPa (Fig. 10.44b), a ternary eutectic exists where quartz and two different feldspar solid solutions can simultaneously crystallize.

Figure 10.44c shows how the trajectory (dashed line) of the low-pressure minimum becomes a ternary eutectic point with increasing pressure. It also shows that 75 % of batholiths worldwide fall on this minimum/eutectic trajectory or the low-pressure "trough." This observation was used by Bowen to conclude that granites are of igneous origin. Bowen called it "petrogeny's residua system" because he argued that all liquids derived from parent basalt magma would end up here and form granite. Tuttle and Bowen (1958) also noted that the "invariant" melts generated at crustal pressure from silicic sedimentary or metamorphic rocks (e.g., arkose, graywacke, metapelitic rock) will also plot in this trough and suggested that granite magma could form directly as a crustal melt and not necessarily by fractional crystallization of basalt magma. This view still stands, and as discussed in an earlier section, it provides an excellent explanation of bimodal volcanism of basalts and rhyolites and for the occurrence of a large number of granitoid batholiths worldwide even though complementary fractionates, i.e., voluminous mafic or intermediate cumulates (which would be required if all granitoids were derived from basalt magma), do not occur.

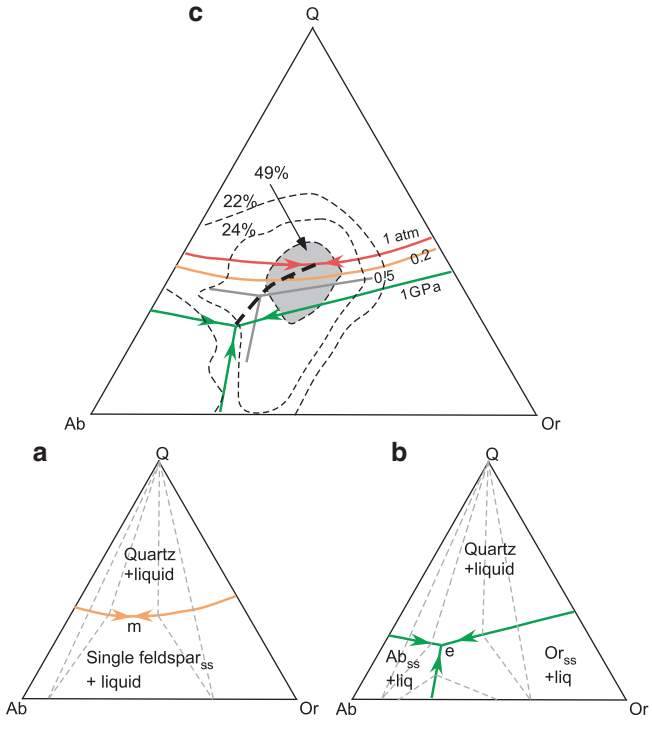

Fig. 10.44 (**a**) Liquidus phase relationships in the system $NaAlSi_3O_8$ (Ab)–$KalSi_3O_8$ (Or)–SiO_2 (Q) at 1 atm pressure. The cotectic between quartz and feldspar (solid solution), shown in *light brown*, has a ternary minimum "*m*," which is the lowest temperature point on the diagram. Each of the two *dashed triangles* is a 3-phase triangle, connecting liquid composition with the two coexisting solid phase compositions (i.e., quartz and a feldspar$_{ss}$). (**b**) At pressures greater than 0.5 GPa, the low-pressure minimum is replaced by a ternary eutectic point "e"; and the single cotectic is replaced by three cotectic curves (*green*). Three 3-phase triangles are also shown. (**c**) This diagram compares the phase relationships in the ternary system at different pressures (the various cotectics are shown in color with pressures marked on them). The contours show the normative compositions of batholiths worldwide. The *gray-shaded region* represents more than 49 % of the batholiths worldwide. The *thick dashed curve* traces the path of the low-pressure minima converting to 3-phase isobaric invariant points at higher pressure

Formation of Pluton-Forming Granitoid Magmas: Insight from Experimental Petrology

Studies of field relationships between high-grade metamorphic rocks, migmatites, and granitoids in deeply eroded orogenic belts have led to an excellent understanding of the typical environment in which large granitoid plutons form. Since migmatites are felsic veins that appear to be low% melts "sweated out" of the metamorphic rocks (generally of amphibolite or higher grade, in a later chapter), one could imagine coalescence of such melts on the way up into forming large granitoid batholiths, which were mobilized by compaction and buoyancy through surrounding, and occasionally melting, deforming wall rocks.

As with any melting process, there are two things that must be known: the source rock that provides the magma and the conditions of melting, i.e., effect of temperature, pressure, and H_2O.

Source Rocks

The plausible source rocks for the granitoid batholith magma could be (1) the middle or lower crust, particularly, sediments (or metasediments) that accumulate to form great thickness in arcs and mafic (or intermediate) metamorphic rocks (granulites and amphibolites), (2) subducted crust (amphibolite or eclogitic material, as

we discussed earlier), (3) "old" (≥3 billion years) subcontinental mantle that may have been reprocessed by basaltic and andesitic magma passing through it, or (4) pyroxenites or amphibole-rich veins in the mantle "wedge." Whatever the source rock, some involvement of water in the melting process is almost guaranteed because (a) hydrous minerals commonly occur in major granitoids and (b) temperatures in the melting region (generally the lower crust) are not high enough for the dry solidus to be reached (as we will see later).

Source of H_2O and Magma Generation

It is likely that granitoid magma generation does *not* commonly occur in a water-saturated environment because free aqueous fluids do not exist in the pore spaces in the continental crust except for the upper few kilometers (Patiño-Douce 1999). Free fluid may be involved in shear zones, where water may be dragged into the hot crust to trigger water-fluxed melting. Fluid may also come off a basaltic/andesitic magma underplate ponded at the Moho beneath an arc.

The three important hydrous minerals, muscovite, biotite, and amphibole, produce a granitoid melt when they break down. Melting resulting from dehydration reactions of these minerals is incongruent (see Chap. 4) of the type:

$$A = B + C + \text{hydrous melt}$$

in which A is a hydrous mineral and B and C may be some anhydrous minerals. The products of these reactions are granitoid melts and more refractory residue minerals (i.e., minerals with greater MgO, FeO, and CaO than the reactant minerals). The following reaction is an example in which amphibolite, a metamorphic rock with hornblende and plagioclase, decomposes producing a granitoid melt and an eclogite residue:

$$\text{Hornblende} + \text{Plagioclase} = \text{Garnet} + \text{Clinopyroxene} + \text{Felsic Melt}$$

Similarly, more aluminous metamorphosed sedimentary rock, such as muscovite schist and muscovite–biotite schist, can also produce melt upon dehydration breakdown reaction of muscovite and/or biotite. The breakdown reaction of biotite is shown in Fig. 10.45a (cited in Whittington and Treloar 2002):

$$\text{Quartz} + \text{Biotite} + \text{Plagioclase} = \text{K-feldspar} + \text{Orthopyroxene} + \text{Garnet} + \text{Melt}$$

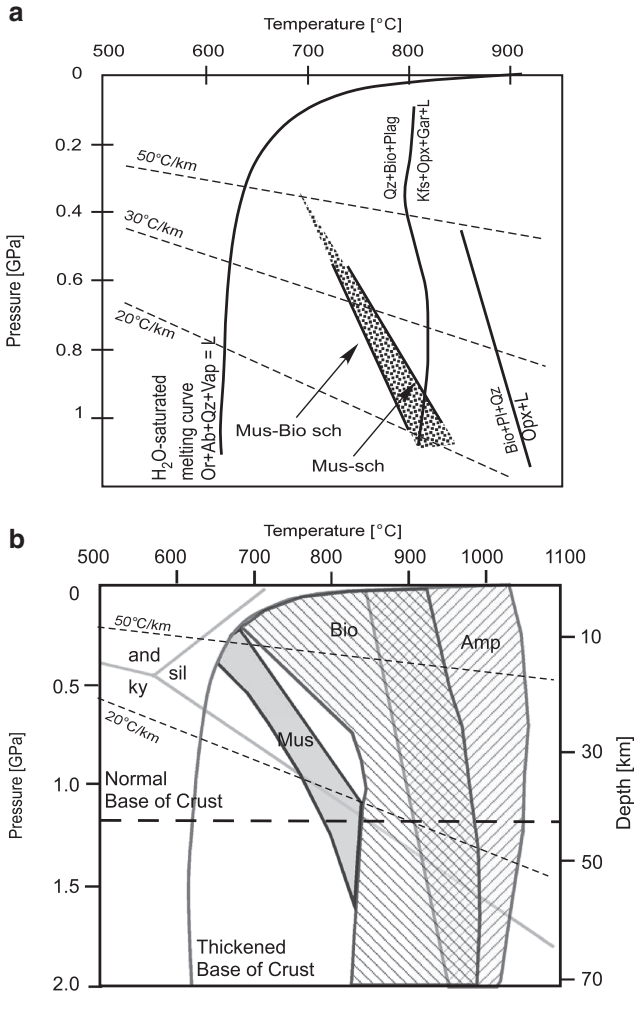

Fig. 10.45 H_2O-saturated granite melting curve and melt production by devolatilization reactions. *Mus* muscovite, *Bio* biotite, *Kfs* K-feldspar, *Gar* garnet, *L* liquid, *Pl* plagioclase, *Ab* albite, *Qz* quartz, *Opx* orthopyroxene, *Sch* schist. (**a**) *Dashed lines* are geothermal gradients. The dehydration curves and their sources are given in Whittington and Treloar (2002). (**b**) Stabilities of muscovite, biotite, and amphibole. *Dashed curves* are two possible geotherms (from Sawyer et al. 2011)

Figure 10.45a also shows the felsic melt-producing breakdown reactions of a muscovite schist and a muscovite–biotite schist from the Higher Himalayas studied by Patiño-Douce and Harris (1998, cited in Whittington and Treloar 2002). Patiño-Douce and Harris thought that these rocks could be sources for the Himalayan leucogranites. As shown in this figure, these rocks will start melting at about 0.6–1 GPa (15–35 km, i.e., intermediate to lower continental crust) and typically over a temperature range of about 750–850 °C along a normal geothermal gradient. A very hot geothermal gradient could see the beginning of melting at a temperature as low as 700 °C and about 10 km. All these melts are going to be granitic.

Figure 10.45b is a summary diagram that shows the *P–T* ranges where muscovite, biotite, and amphibole breakdown, generating magma in the process (Sawyer et al. 2011). The micas produce granitic melts, whereas amphibole breakdown generates tonalitic melt (review by Sawyer et al. 2011).

There are significant differences in composition of the melts generated from mica-rich sources (e.g., metamorphosed shale, graywacke) versus those that are produced from amphibole-rich sources (Patiño-Douce 1999): (1) The melts from mica-rich sources tend to have distinctively lower MgO + FeO than those from amphibole-rich sources. (2) The melts from mica-rich sources have distinctly higher $Na_2O + K_2O$ but lower CaO than amphibole-rich sources. (3) The melts generated from metamorphosed mica-rich sources are also more silicic than those from amphibole-rich sources. Thus, bulk source composition has a strong effect on the nature of magma produced.

Aside from bulk composition and H_2O content of the source rock, pressure and degree of melting can also affect the composition of the melt generated from a given source rock. For example, in their melting study of four amphibolites (metamorphosed basalts), Rapp and Watson (1995) observed that at 0.8–1.6 GPa, a high-K_2O granitic melt forms when melting degree is ~5 %, whereas the melts produced by 20–40 % melting have compositions of tonalite, granodiorite, quartz diorite, and diorite.

Based on the above discussion, one may come to a broad general conclusion that plagioclase-rich granitoids (i.e., tonalite, quartz diorites) form by partial melting of metamorphosed rocks of mafic–intermediate bulk compositions (basalts–andesites), whereas peraluminous granitoids are derived by melting of mica-rich aluminous source rocks. However, scientists who have extensively mapped granitoid plutons through the years have often proposed a *hybrid* (*mixed*) *origin* of many of the granitoid magmas (e.g., Reid and Hamilton 1987). In the field, these authors often noted large modal (and therefore chemical) variation occurring within individual batholiths due to mixing between variably disintegrated mafic–intermediate "enclaves" (could be melts, cumulates, or restites) and the host felsic intrusive. Such a hybrid origin in many batholiths is also supported by chemical and isotopic mixing arrays.

Patiño-Douce (1999) compared the SiO_2 contents of experimental melts with those of calc-alkaline (metaluminous, I-type) granitoids (CAGS), peraluminous S-type granitoids (PSGS), metaluminous A-type granitoids (MAGS), peraluminous leucogranites (PLGS, as found in the Himalayan continent–continent collision zone, generally S-types), and some other types of granitoids (an explanation of this nomenclature may be found in Patiño-Douce 1999). Patiño-Douce noted that the experimental melts have $SiO_2 \geq 70$ wt% and that only the PLGS magmas have such high SiO_2, whereas all other granitoid types have lower silica. Patiño-Douce (1999) therefore concluded that only PLGS are true crustal melts and that the other groups must have different origins, including a mixed origin (whether melt–melt mixing or crystal-rich melt–melt mixing).

Summary

- Granitoid magmatism occurs in a variety of plate tectonic settings. Batholiths and rhyolitic volcanism associated with continental arcs and continent–continent collision are volumetrically much more common.
- Granitoids have been classified in many different ways—some based on mode and others based on chemical composition and tectonic association.
- Granitoid magma may form by diverse processes—from fractional crystallization of basalt magma to melting of the lower continental crust. Large batholiths are products of crustal melting or crustal melts mixed with some mafic melts.
- Granitoid magma generation most commonly happens due to the breakdown of hydrous minerals. Fluid-saturated melting does occur but is not likely to be common.
- Amphibole breakdown produces tonalitic magma, whereas breakdown of muscovite and biotite generates more granitic magma.
- During batholith production the residues of melting are likely to be rich in garnet and pyroxenes, forming granulite to eclogitic rocks.

Alkaline and Ultra-Alkaline Rocks, Carbonatites, and Kimberlites

11

Abstract

The petrology and origin of some rare rock types that have high to very high alkalis, including kimberlites to phonolites, are discussed in this chapter. Carbonatites are also included here because they are commonly associated with alkaline igneous rocks. In previous chapters we have discussed alkaline igneous activities in intraplate and subduction environments. Here, we focus on alkaline and ultra-alkaline igneous activities in cratonic and continental rift environments.

Introduction

Alkaline igneous rocks are *silica-undersaturated* and have more alkalis ($Na_2O + K_2O$) than silica that is needed to form feldspars; and hence they contain modal and/or normative feldspathoids such as nepheline, leucite, and kalsilite (discussed in Chap. 3). Plutonic alkalic rocks, such as nepheline syenite or nepheline monzosyenite, are characterized by the presence of modal feldspathoids (Fig. 11.1a). Ultra-alkaline lavas have extremely high alkalis and less than about 41 % SiO_2 (Fig. 11.1b). In order to understand how alkali–silica ratio controls "alkalinity" of a magma, let us again consider the system nepheline ($NaAlSiO_4$)–silica (discussed in Chap. 4), in which albite ($NaAlSi_3O_8$) forms due to the reaction: $NaAlSiO_4 + 2SiO_2 = NaAlSi_3O_8$. Albite, whose composition can also be written as $Na_2O{\cdot}Al_2O_3{\cdot}6SiO_2$, requires Na_2O:Al_2O_3:SiO_2 in 1:1:6 molar proportion. An alkaline magma must have Na_2O–SiO_2 ratio greater than the above 1:6 proportion so that it will have nepheline in the norm (in this example). Similarly, K-feldspar ($KAlSi_3O_8$) forms by the following reaction: $K_2O{\cdot}Al_2O_3{\cdot}6SiO_2$ (orthoclase) $= K_2O{\cdot}Al_2O_3{\cdot}4SiO_2$ (leucite) + SiO_2. An alkaline magma will have less silica than the required K_2O:Al_2O_3:SiO_2 proportion of 1:1:6 and thus will have normative leucite, which requires 1:1:4 proportion.

Alkaline and ultra-alkaline rocks comprise perhaps no more than 1 % of all igneous rocks, and yet they have drawn great attention over the years because of a variety of reasons: many of them have a very appealing appearance because of their content of alkalic pyroxenes and other colorful rare minerals; some are source of important elements such as uranium, thorium, niobium, and the rare-Earth elements; and some other alkaline rocks, such as alkali basalts, nephelinites, and kimberlites, carry mantle xenoliths which offer important information on the composition and thermal characteristics of the lithosphere. In this group of unusual igneous rocks, kimberlites certainly stand out the most because they serve as the most important source for diamonds and deep xenoliths from the continental lithosphere.

It is also important to consider *peralkaline* rocks, which are commonly associated with alkaline rocks in the field. Peralkaline rocks have greater molar $Na_2O + K_2O$ than Al_2O_3. In such alumina-deficient magma, the excess (i.e., above that required to form feldspars) alkalis form *acmite* in the norm, and in natural rocks, the excess Na is accommodated in alkalic pyroxenes (e.g., aegirine) or amphiboles (e.g., riebeckite) or other phases. Note that peralkaline rocks may be silica-oversaturated (i.e., quartz in the norm), and examples include peralkaline rhyolite, aegirine–riebeckite granite, or they may be silica-undersaturated and have nepheline, leucite, and other feldspathoids in the norm, e.g., nepheline syenite.

G. Sen, *Petrology*, DOI 10.1007/978-3-642-38800-2_11,

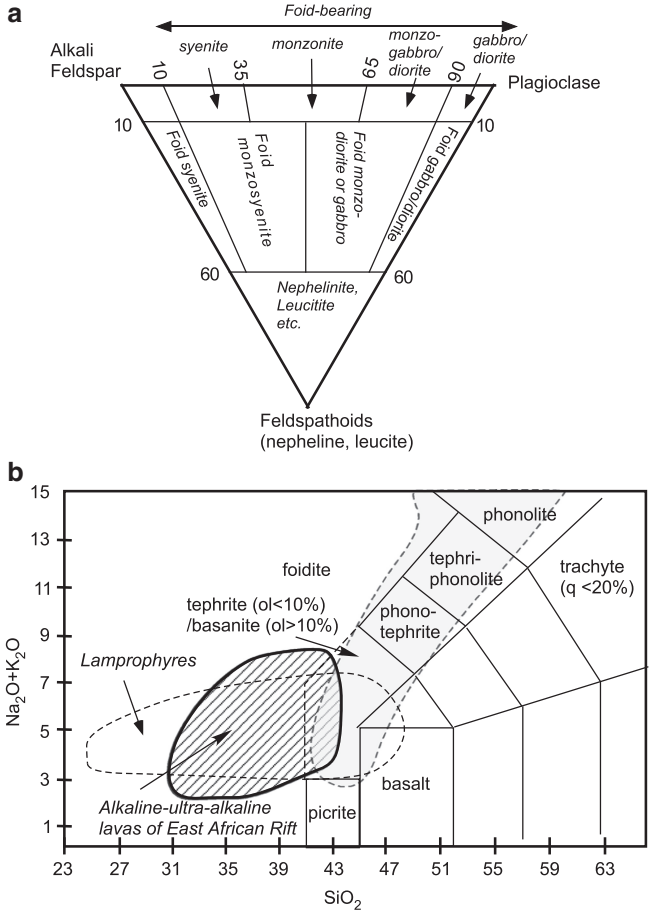

Fig. 11.1 (**a**) Classification of alkaline rocks in the A (alkali feldspar) P (plagioclase) F (feldspathoids) diagram. (**b**) TAS (total alkalis—silica) classification of volcanic alkaline rocks. Also shown are the fields where lamprophyres and East African alkaline and ultra-alkaline lavas plot

Before proceeding further on field associations and origin of continental alkaline igneous rock, it is useful for the student to remember the nomenclature of alkaline plutonic and volcanic rocks (from Chap. 2; Fig. 11.1). Figure 11.1b is the TAS (total alkalis versus silica) classification of volcanic rocks. It shows a broad field of alkaline volcanics that occur in continental areas—from basalts to phonolites. It also shows the field of alkaline-to-ultra-alkaline lavas that occur in the East African Rift System, which is discussed later. A useful summary of characteristics of the rock types discussed in this chapter is given below.

Nephelinite. It is the most common type of ultra-alkaline lava with dominant-normative nepheline and clinopyroxene. Other minor normative or modal components may be olivine, leucite, or melilite. Nephelinites have greater than 90 % of the total nepheline + plagioclase. They occur in a variety of tectonic environments—from oceanic hot spots, such as Hawaii (discussed earlier), to continental rifts. They often carry xenoliths from the crust and mantle. The plutonic variety is generally called ijolite (see below).

Foid Syenite. The commonly occurring varieties are nepheline syenite and nepheline monzosyenite. These plutonic rocks have two feldspars and nepheline. Perthitic and antiperthitic exsolution intergrowths are common. Alkalic pyroxenes (e.g., aegirine–augite, aegirine), amphiboles (riebeckite, arfvedsonite), and mica can occur. The rock name *essexite* refers to a type of foid monzodiorite in which plagioclase is more abundant than alkali feldspar and the mafic mineral may be hornblende, biotite, and titanaugite.

Theralite. It is essentially a nepheline gabbro in which zoned alkalic pyroxenes (aegirine) comprise 40 % of the rock.

Ijolite. These plutonic rocks generally have more nepheline (about 60 %) than clinopyroxene, which is usually a diopsidic pyroxene or aegirine–augite. Many interesting accessory minerals occur in these rocks, including sphene, apatite, sodalite, melanite, and carbonate minerals. The name *urtite* is used to describe a type of ijolite with more than 70 % nepheline and mafic minerals (dominantly clinopyroxene) making up the rest. *Melteigites* have more clinopyroxene than nepheline. It is useful to refer to the series of plutonic rocks consisting largely of nepheline and clinopyroxene as *ijolite series*, including urtites, ijolites, and melteigites. Ijolite series rocks are intimately associated with carbonatites, and at least in some cases, a strong case may be made in favor of an origin by liquid immiscibility causing the split of ijolite magma from carbonatite magma.

The potassic equivalent of ijolite is called *fergusite*. Fergusite is characterized by pseudoleucite—an aggregate of orthoclase, nepheline, and zeolites that forms pseudomorph after the original leucite crystals. Fergusites occur as ejecta blocks from volcanoes.

Phonolite. It is the volcanic equivalent of foid syenite and could be nepheline phonolite or leucite phonolite, depending on the norm. They are commonly porphyritic, and their groundmass often shows flow or trachytic texture. Phenocrysts of sanidine and anorthoclase are common. Phenocrysts of sodic pyroxene, titanaugite, and Fe-rich olivine also occur.

The name *Tinguite* is given to soda phonolites that occur as minor intrusions or chill margins of nepheline syenite plutons and are characterized by acicular aegirine–augite microlites.

Some other really unusual types of strongly alkaline rocks occur in nature, especially those with very high K_2O (K_2O: $Na_2O > 2{:}1$), and it is good to have some familiarity with their nomenclature should the student have a chance encounter with them—whether in Uganda, or at Leucite Hills in Wyoming (US), or at Umbria in central Italy, or some other parts of the world.

Kamafugite. Kamafugites are volcanic potassic ultramafic rocks with modal or normative kalsilite. Their unusually high K_2O (2.0–8.5 wt%) is characteristic, as are high MgO and low SiO_2 (8–18 wt% MgO, 33–44 wt% SiO_2). The name comes from a combination of *katungite* (which is a volcanic rock, a pyroxene-free melilitite, composed chiefly of melilite, with subordinate olivine and magnetite and minor leucite and perovskite), *mafurite* (olivine–clinopyroxene foidite with kalsilite as the principal feldspathoid mineral), and *ugandite* (clinopyroxene–olivine leucitite). Kamafugites contain either clinopyroxene or olivine as their dominant mafic mineral and kalsilite or leucite as felsic mineral. They may also contain melilite.

Orendite. It is a volcanic rock containing phlogopite and diopside as phenocrysts or microphenocrysts in a groundmass of olivine (~Fo_{90}), leucite, sanidine, phlogopite, richterite, and diopside. It has no nepheline. Orendite occurs in Leucite Hills, Wyoming (USA) (Definition sources: Kuehner et al. 1981, Am.Min; http://www.answers.com/topic/orendite#ixzz2A2Bit7s4).

Madupite. It is an aphyric volcanic rock with phlogopite and diopside as rare phenocrysts set in a glassy alkalic groundmass containing phlogopite, perovskite, and occasionally leucite. Madupite occurs in Leucite Hills, Wyoming (USA).

Lamproites. Lamproites comprise a group of peralkaline ultrapotassic rocks with 34–58 % SiO_2 (rarely up to 68 %) and 5–25 % MgO. They are thought to be related to kimberlites. Olivine is a common phenocryst. K-rich minerals such as phlogopite and leucite are characteristic minerals, and Ca, Na minerals (e.g., plagioclase, nepheline, and melilite) are absent. Lamproites are further classified on the basis of their mineralogy and textural characteristics, a discussion of which is beyond the scope of this book, but the interested reader may refer to the books by Rock (1991) and Mitchell and Bergman (1991).

Lamprophyre. Lamprophyres are porphyritic, dark colored, mafic to ultramafic rocks that contain phenocrysts of biotite, olivine, amphibole, and sometimes clinopyroxene set in a panidiomorphic granular matrix consisting of potassium feldspar, plagioclase, feldspathoids, calcite, Fe–Ti oxides, and various ferromagnesian silicates. They typically form shallow intrusions in continental settings in a variety of tectonic environments. They have a high H_2O content. Their extreme compositional variability and genetic/tectonic diversity has been a real problem for generations of geologists who have tried to classify them in some sort of meaningful way (Rock 1991).

Carbonatite. Carbonatites are intrusive or extrusive rocks that have >50 % modal carbonate (usually calcite, dolomite, or ankerite) and various ferromagnesian silicate minerals (olivine, monticellite, clinopyroxenes, calcic amphiboles, or biotite). More commonly, the carbonate percentage is about 75 % in these rocks. Characteristic minor minerals (but may be locally abundant) are magnetite, fluorapatite, pyrochlore, ilmenite, perovskite, titanite, and rare-Earth carbonates. In some cases, magnetite and apatite may occur in sufficient quantities to become commercially viable ore deposits. Carbonatites are further classified on the basis of their modal mineralogy or major-element chemical composition (Fig. 11.2).

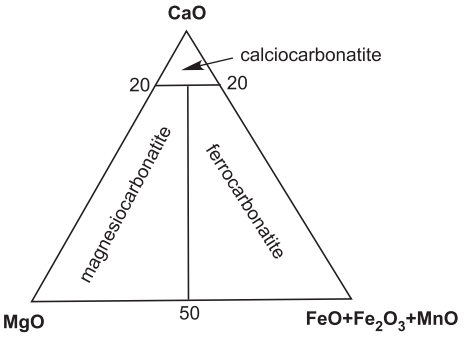

Fig. 11.2 Classification of carbonatites. Na-rich carbonatite (natrocarbonatite) is not shown

Missing in Fig. 11.2 is natrocarbonatite—which is a rare sodic carbonatite that erupts at a low temperature (~575 °C) from the only known active carbonatite volcano—Ol Doniyo Lengai in Tanzania. All natrocarbonatites are young, which have led some authors to believe that many older carbonatites may have originally been sodic, whose soda was later leached out by groundwater. Also, it has not been possible to generate natrocarbonatite melt in experimental melting studies of Na-bearing systems (Shantanu Keshav, personal communication 2012). The generation of these magmas remains an interesting problem.

Carbonatites can occur as individual intrusions or lavas without any obviously associated silicate intrusion or lava; however, more commonly, they are associated with alkaline and ultra-alkaline bodies (see Box 11.1). Association of carbonatites with rare mineral deposits and with alkaline and ultra-alkaline rocks and commonly in continental rift zones has given them a much greater significance to geologists.

Alkaline Magma Differentiation: Petrogeny's Residua System

The system nepheline–kalsilite–silica (Fig. 11.3) has played an important role in our understanding of differentiation of silica-saturated and silica-unsaturated (alkaline) magmas. In this system, the feldspar ($NaAlSi_3O_8$–$KAlSi_3O_8$ or Ab–Or) join acts as a divide

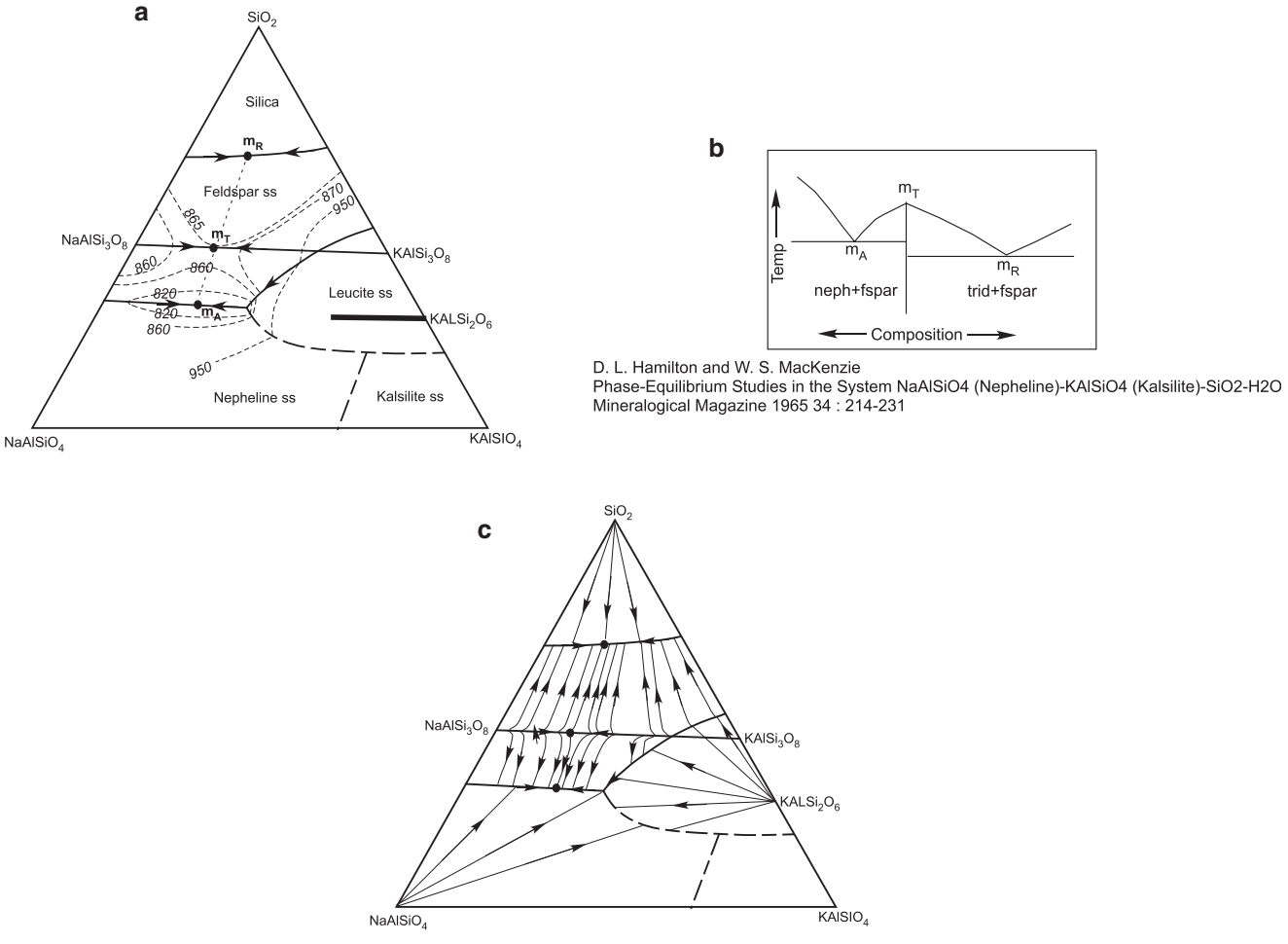

Fig. 11.3 (**a**) The system nepheline ($NaAlSiO_4$)–kalsilite ($KAlSiO_4$)–SiO_2 at $p_{H2O} = 0.1$ GPa (Hamilton and MacKenzie 1965). *Dashed curves*—isotherms. Composition of leucite solid solution is shown as the *thick straight line*. There are three minima in this diagram—m_R, m_T, and m_A. The *dotted straight line* connects them. (**b**) The relationship between the three minima along the dashed line is shown. (**c**) Liquidus fractionation lines in this diagram. They show how individual liquid compositions in much of the diagram will evolve with fractionation

such that silica-saturated melts cannot cross over this divide into the alkaline (nepheline–kalsilite) side or vice versa. Hamilton and McKenzie (1965) studied this system by adding water to it at 0.1 GPa pressure. These authors reasoned that along with alkalis and silica, H_2O also accumulates in the residual melt, as evident from the occurrence of hydrous minerals like biotite and hornblende and from the formation of pegmatite veins around granitoid bodies, and therefore the role of H_2O must also be taken into account if we were to understand what happens in the final stages of crystallization of a silicate magma.

Three important minima occur in the system nepheline–kalsilite–silica system: m_A, m_T, and m_R (Fig. 11.3a). Fractional crystallization of ne-normative silicate melts will result in a residual melt of composition at m_A (i.e., minimum for phonolite/nepheline–syenite magmas). Similarly silica-saturated (or qz-normative) melts will reach m_R (i.e., minimum for rhyolitic/granitic magmas) upon fractionation. Transitional melts of trachytic composition falling exactly on the feldspar join would end up at its relevant minimum—m_T. m_T is significant because it acts as a thermal maximum between the rhyolitic minimum and the phonolitic minimum (Fig. 11.3b). Figure 11.3c schematically shows the liquidus fractionation lines, i.e., lines along which liquid composition will move upon fractionation. In the liquidus field of $feldspar_{solid\ solution}$, the fractionation lines are curved—radiating away from feldspar join. As these lines show, silica-saturated versus silica-undersaturated liquids end up at m_R and m_A, respectively. Global data on silica-undersaturated plutonic and volcanic rocks with 80 % or more normative nepheline + alkali feldspar plot in the "trough" between m_A and m_T, supporting the view

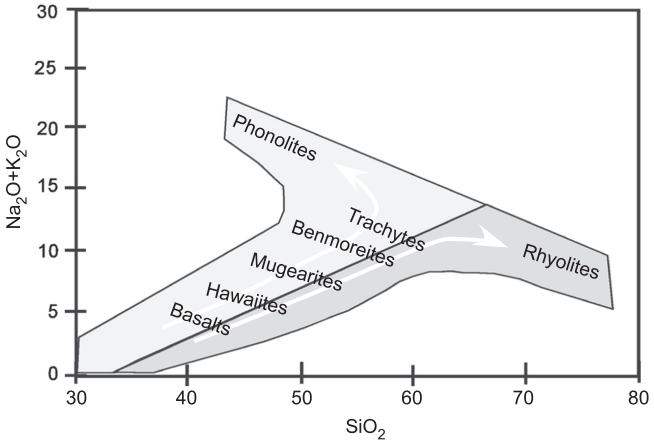

Fig. 11.4 Dual fractionation trends—alkaline and rhyolitic differentiation

that fractional crystallization of trachytic (syenite) melts results in phonolitic/nepheline syenite magmas. The "take away" lesson is that differentiation of an alkali basaltic magma results first in intermediate composition trachytic magma, and with further differentiation, a phonolitic residual magma form at m_A. On the other hand, differentiation of tholeiitic basalt magma will drive the residual liquid to rhyolitic magma at m_R (as Bowen pointed out). Natural magmas do not always reach m_A or m_R but instead erupt with compositions intermediate between these two minima.

There are many natural examples of differentiation of alkali basaltic to phonolitic magmas. For example, in the Gardar Province of southwestern Greenland, glacial erosion has exposed felsic and alkaline plutons, dikes, and volcanic remnants. When their compositions are plotted on an alkali–silica plot, they form on two distinct differentiation trends—one producing phonolitic final liquid and the other resulting in rhyolitic liquid (Fig. 11.4). Similar dual trends exist in the East African Rift System. In some cases, crustal contamination seems to have forced an initially alkaline melts to cross over the feldspar divide toward silicic differentiates.

Continental Rifts and Associated Alkaline Magmatic Activities

Rift zones within continents are often the loci of important igneous activity, where magmas display an astounding diversity—from tholeiites to alkali basalts, nephelinites, carbonatites, lamprophyres, lamproites, and various alkaline and ultra-alkaline lavas and intrusives. Tholeiites erupt late in the sequence,

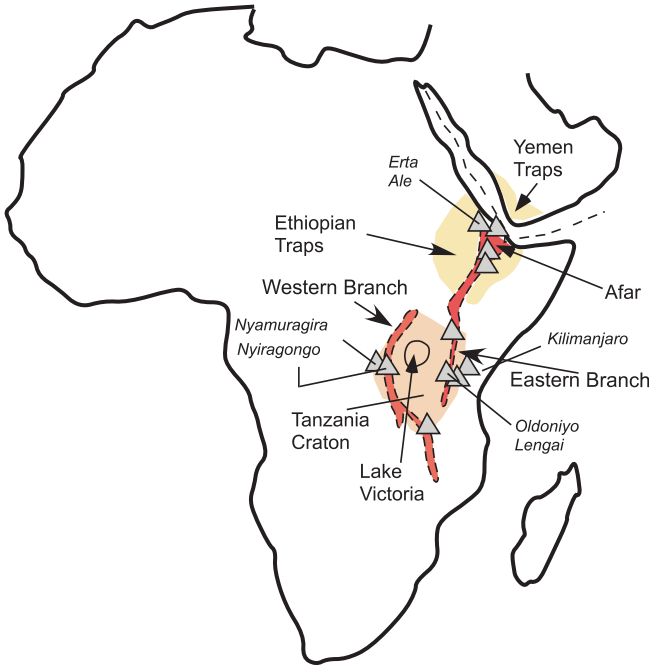

Fig. 11.5 The East African Rift System (*red*). Active volcanoes are shown as *triangles*

which is dominated by alkaline lava eruptions. Some prominent examples of continental rifts are the East African Rift System (EARS), Rio Grande Rift (USA), Baikal Rift (Russia), Oslo Graben (Norway), Narmada–Son Rift Zone (India), and the Gardar Province (Greenland). Here we will focus on the East African Rift System, which is a currently active and one that has played an important role in our conceptual understanding of the processes involved in continental breakup to ocean formation.

East African Rift System

The East African Rift System forms an extensional boundary between the Somalian and Nubian plates and stretches for about 3,500 km from the Afar Depression in the north to Turkana Depression and Kenya Rift to the south (Fig. 11.5). The rift system bifurcates into western and eastern branches around the Tanzania Craton. It cuts through two large domal structures—the Ethiopian and Kenyan domes. The Ethiopian dome was uplifted slowly but steadily from about 29 to 10 Ma. The rate of uplift increased somewhat at about 10 Ma, and at about 6 Ma, the dome experienced a sudden and sharp increase, which may have been largely responsible for the 2 km uplift of the Ethiopian dome (Corti 2009).

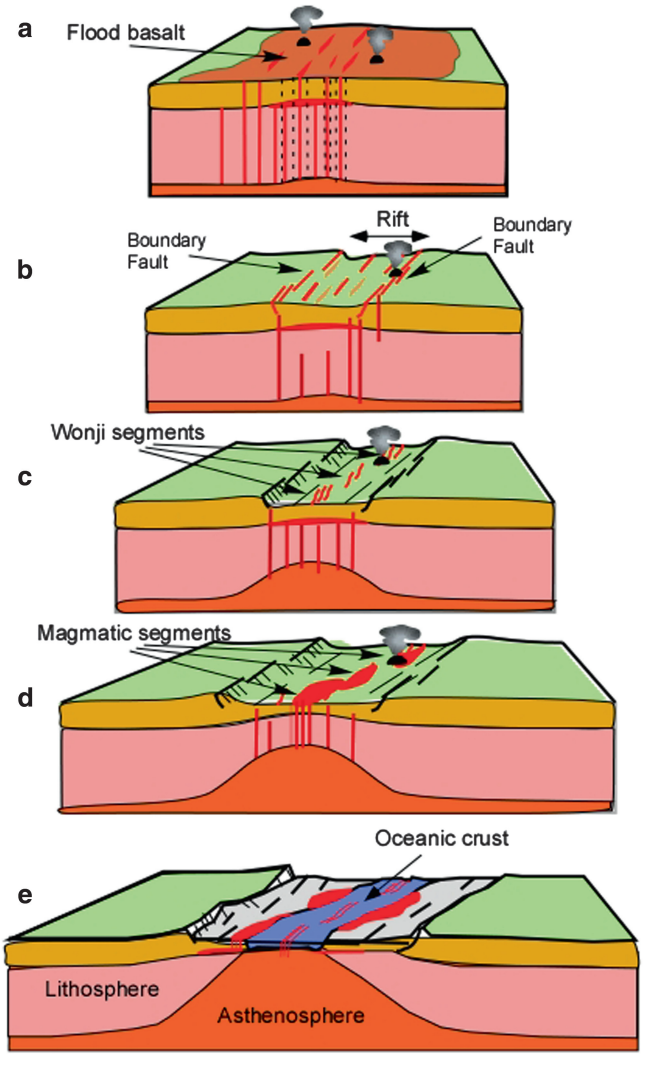

Fig. 11.6 A schematic model of the evolution of the Main Ethiopian Rift (from a to e; redrawn from Corti 2009). Stage e, which involves creation of oceanic crust has not occurred

Whether the Ethiopian and Kenyan domes formed due to the impact of a single plume or two separate plumes continues to be a matter of some debate. Large-scale magmatic activities began 30 million years ago with the fissure eruption of basaltic lavas and ignimbrites that formed the Ethiopian and Yemen Traps. Several studies have traced the plume into the deep mantle using shear wave velocity anomalies (e.g., Ritsema et al. 1999; Huerta et al. 2009). The plume is related to the so-called African superswell—a fairly broad low-velocity zone rooted in the deeper mantle (see Chap. 1). It has been suggested that the magmas formed in the plume have come up through preexisting lithospheric fractures that were active during the separation of East Gondwana from West Gondwana supercontinents.

Large boundary faults, rift basin subsidence, and diffuse volcanism were active from 11 to 2 Ma (Fig. 11.6a, b; Corti 2009). The large boundary faults were abandoned around 2 Ma, and the locus of deformation shifted to the rift valley, where oblique en echelon faults (Wonji Fault Belt) developed (Fig. 11.6c). At this stage, magmatic activity also shifted to the Wonji Fault on the rift valley floor (Fig. 11.6d). The Wonji Fault Belt is best developed in the Main Ethiopian Rift (MER).

The EARS rift system bifurcates into western and eastern branches around the Tanzania Craton. Lavas in these branches are alkaline to ultra-alkaline: the western branch lavas are potassic, whereas the eastern branch lavas are more sodic. Carbonatites occur in both branches. Figure 11.5 shows the loci of some of the historically active volcanoes along this rift system (after Fig. 12 in Hall 1987). The better known of these volcanoes are Erta Ale (Ethiopia), Kilimanjaro and Ol Doniyo Lengai (Tanzania), and Nyamuragira and Nyiragongo (Democratic Republic of the Congo). Nyamuragira and Nyiragongo are two of the most active volcanoes of Africa that are located in the western branch. They are stratovolcanoes. Nyiragongo is very unusual because of its ultra-alkaline lavas that travelled unusually rapidly. Ol Doniyo Lengai is the world's only active carbonatite volcano that is located in the eastern branch. It erupts natrocarbonatite lava. Erta Ale is a basaltic shield volcano that is also the most active volcano in Ethiopia.

Ethiopian Traps

The Ethiopian Traps form a broad plateau covering an area of about 500,000 km^2. The Traps consist of mainly basaltic lava flows intercalated with thinner rhyolitic ignimbrites. Lavas of intermediate composition are conspicuously absent. Employing careful dating techniques, Hofmann et al. (1997) showed that the entire Traps, including basalts and ignimbrites, erupted at 30 ± 1 Ma. In a later study of the ignimbrites, Ayalew et al. (2002) showed that although the bulk of the ignimbrites did erupt at 30 ± 2 Ma, two of them erupted at 15 and 8 Ma.

Immediately following the formation of the Ethiopian Traps, several large shield volcanoes formed over 30–10 Ma over the plateau, erupting alkali basalts, phonolites, and rhyolites. Note that in some literature, the entire Traps are referred to as "pre-rift" lavas because they appear to have formed by plume impact and prior to any rift formation.

The Ethiopian flood basalts are mostly transitional basalts (Fig. 11.7). Pik et al. (1998) identified three magma types on the basis of Mg#–TiO_2 relationship (Fig. 11.7)—two of them have relatively different high TiO_2 (HT1 and HT2) and the other has low TiO_2 (LT).

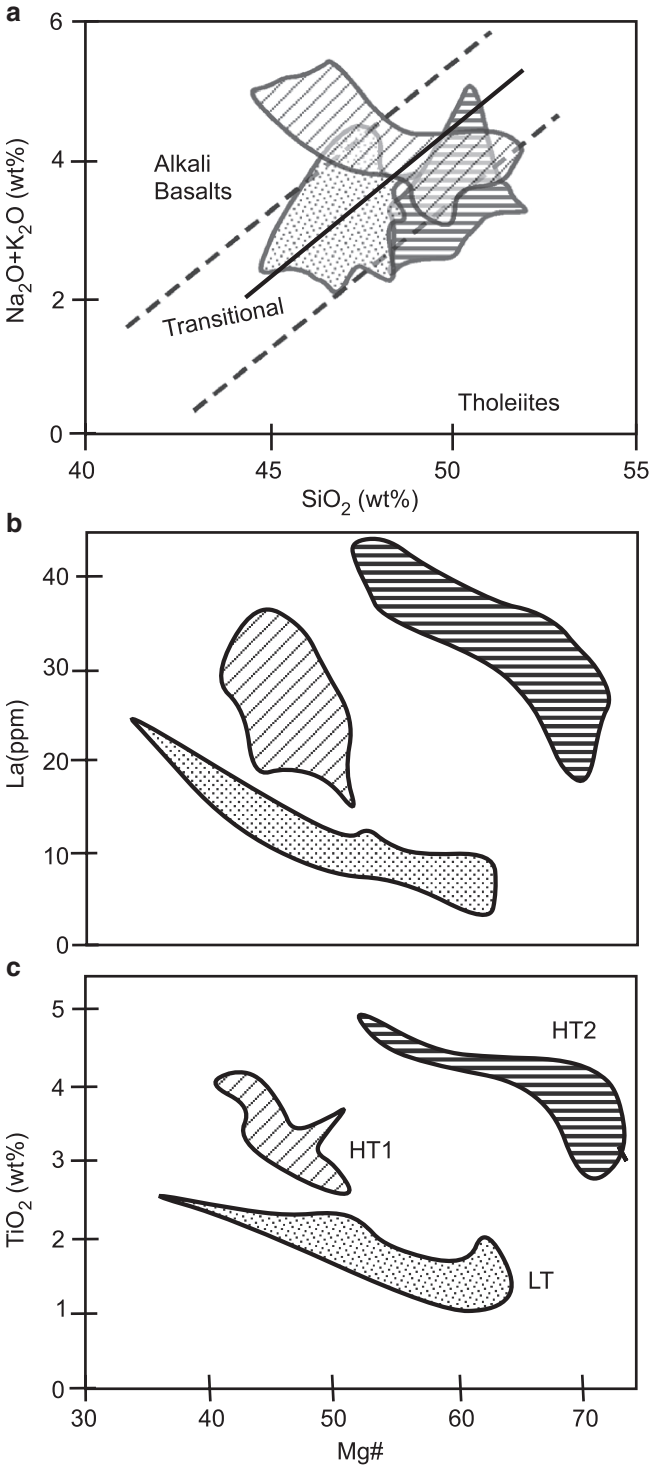

Fig. 11.7 Ethiopian flood basalts are plotted on three different binary plots to show the differences between the three basalt groups that comprise them (source: Pik et al. 1998). Note that the X-axis in is Mg# in (**b**) and (**c**)

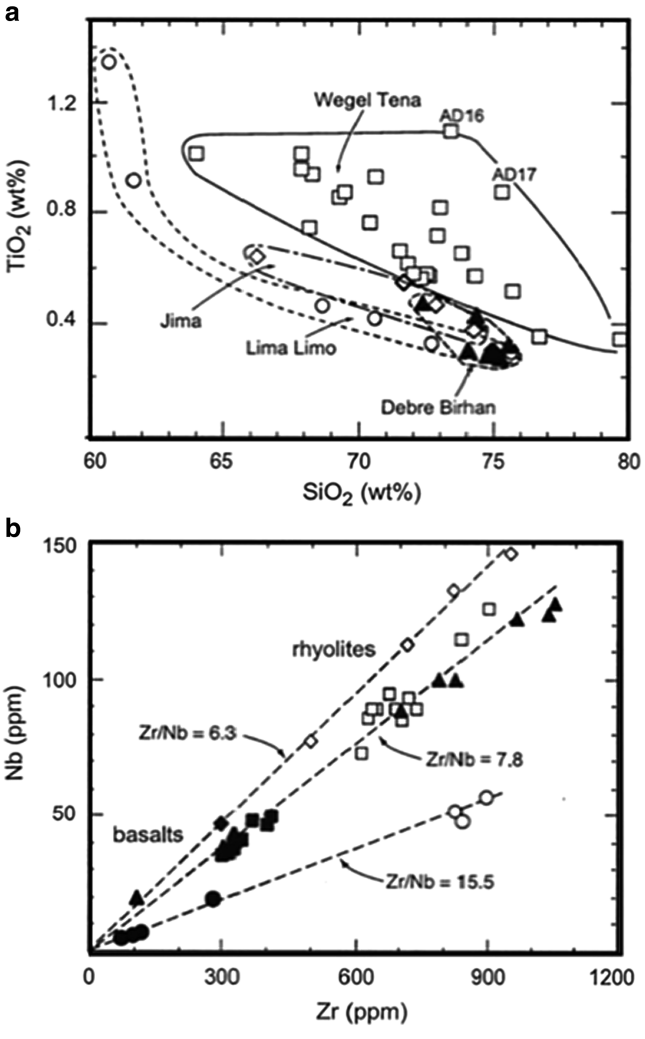

Fig. 11.8 Chemical groupings of the ignimbrite units from Ethiopian Traps. (See text for further discussion)

They are also distinct from each other in other chemical characteristics, e.g., La content, which indicates that the three types must have been derived from different parent magmas. According to Pik et al. (1998), there is also a strong spatial control on the distribution of these lava types—LT occurs only in the northern part of the Ethiopian plateau, and HT2 and HT1 basalts are found in the eastern and southern parts, respectively. The lavas vary from aphyric to porphyritic, with olivine-, plagioclase-, and augite-forming phenocrysts. HT2 shows a strong olivine control, whereas LT and HT1 basalts show Ol + Pl fractionation control at shallow crustal-level pressure (Pik et al. 1998).

Ayalew et al. (2002) presented a detailed study of the giant ignimbrites of the Ethiopean plateau from four different units (Jima, Lima Limo, Debre Birhan, and Wegel Tena). They showed that the ignimbrites are largely rhyolites, but some are trachytes in terms of their silica contents. These felsic rocks also show similar diversity in TiO_2 and exhibit the same Zr/Nb ratio as the corresponding basalts in the same geographic location (Fig. 11.8). REE (chondrite normalized) patterns

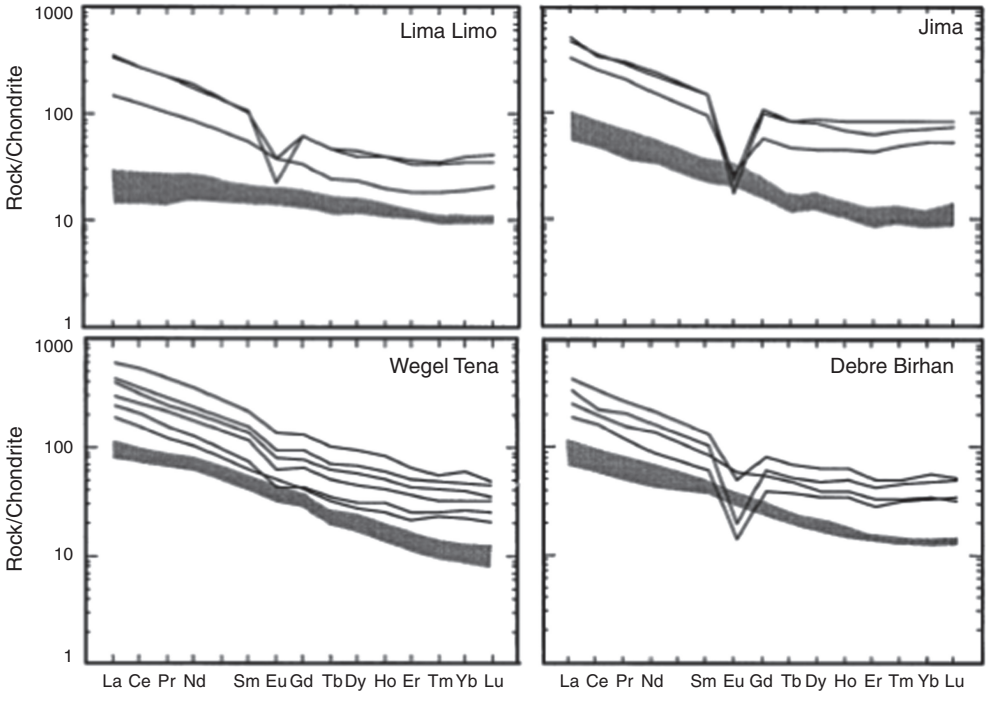

Fig. 11.9 Chondrite-normalized rare-Earth element compositions of the rhyolitic ignimbrites (*lines*) and basalts (*shaded*) in the Ethiopian Traps (from Ayalew et al. 2002)

of the basalts and rhyolites are similarly enriched in LREE, but the latter show prominent negative Eu-anomaly (Fig. 11.9). In terms of Nd–Sr isotope ratios, Ayalew et al. (2002) showed that the $^{143}Nd/^{144}Nd$ ratios of ignimbrites overlap those of the flood basalts, but the former have slightly greater $^{87}Sr/^{86}Sr$ ratios (Fig. 11.10). Based on these observations and trace element modeling, these authors proposed that the rhyolites were derived by fractional crystallization of corresponding basalt magmas with limited role by crustal contamination of the magmas, which only affected the $^{87}Sr/^{86}Sr$ but did not alter the $^{143}Nd/^{144}Nd$ of the rhyolites. Trace element modeling suggests the involvement of fractionation of olivine, augite, plagioclase, and Fe–Ti oxides.

It appears to me that even though trace elements and isotope composition of the rhyolites relative to the basalts support the fractional crystallization model, a serious problem is the absence of intermediate lavas or intrusives. It is hard to understand that the fractional crystallization process would be so perfect that only the beginning magmas and the final residual magmas would be erupted. Appealing to a thicker crust acting as a filter to only allow basalts and rhyolites to erupt is not acceptable since basalts are denser than intermediate magmas. In fact, intermediate magmas would have lower density and viscosity because of their likely greater concentration of H_2O. Alternative models call for hydrous melting of a basaltic "underplate." Such an underplate may form at the Moho as ascending basalt magma loses its buoyancy as it meets the lower density crust. The magma would mostly crystallize forming the underplate, and only a small volume of intermediate and felsic differentiates form and rise through the crust. One could speculate that further melting (for other reasons—hydration, extension of the crust) of such an underplate would form rhyolitic magmas. Intermediate composition melts would not form in such a case.

Rifting and Volcanism

Rift-related volcanic activities became widespread from 10 Ma to recent times. Basaltic lavas erupted from fissures and stratovolcanoes in the Afar Depression, and diverse types of alkalic and carbonatitic lavas extruded from volcanoes located along the rift-axis and rift-shoulder volcanoes throughout the EARS. The alkaline and ultrapotassic lavas (kamafugite) erupted in the western branch of the EARS, whereas more nephelinitic and other more sodic lavas effused through volcanoes in the eastern branch.

Figure 11.11 shows the compositions of silicate lavas that have been found in the entire EARS. The classic basalt-to-rhyolite trend is shown by the Main Ethiopian Rift (MER) lavas, whereas alkali basalt-/basanite-to-phonolite trend is exhibited by the lavas issued from the western branch volcanoes. Lavas

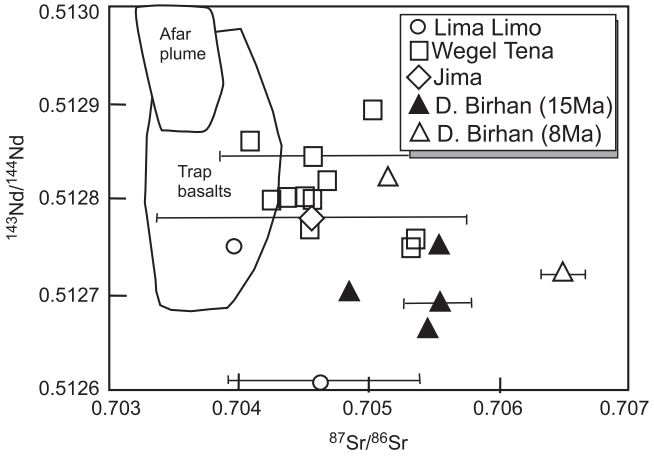

Fig. 11.10 Isotope compositions of Ethiopian traps (From Ayalew et al. 2012)

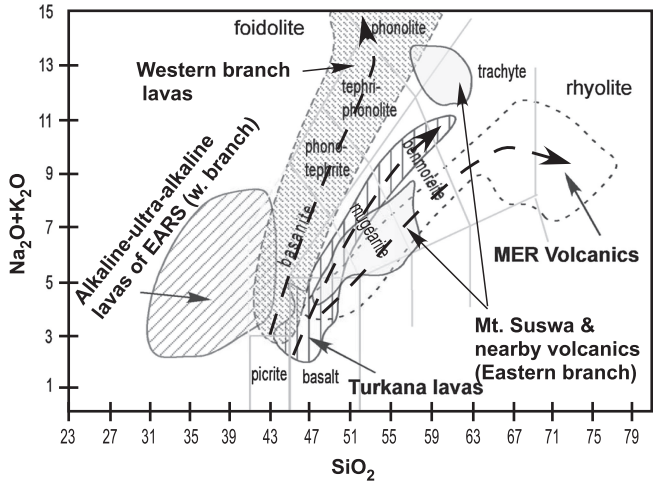

Fig. 11.11 Composition of the rift-related volcanics from the East African Rift System

from the volcanic centers in Turkana rift in northern Kenya, which fall between the Ethiopian and Kenyan domes, define a trend between the MER and western branch trends (Furman et al. 2006). Thus, there appears to be both a temporal and spatially controlled diversity in the trends exhibited by EARS volcanic products.

An interesting aspect is that an individual small volcano is fairly consistent in the composition of the lava it erupts; however, the next volcano may erupt a very different lava: for example, consider the lavas that poured out of Mt. Suswa and its nearby volcanoes from the Central Kenyan Peralkaline Province (CKPP, White et al. 2012). Mt. Suswa is a collapsed shield volcano that erupted two distinct suites of trachyte

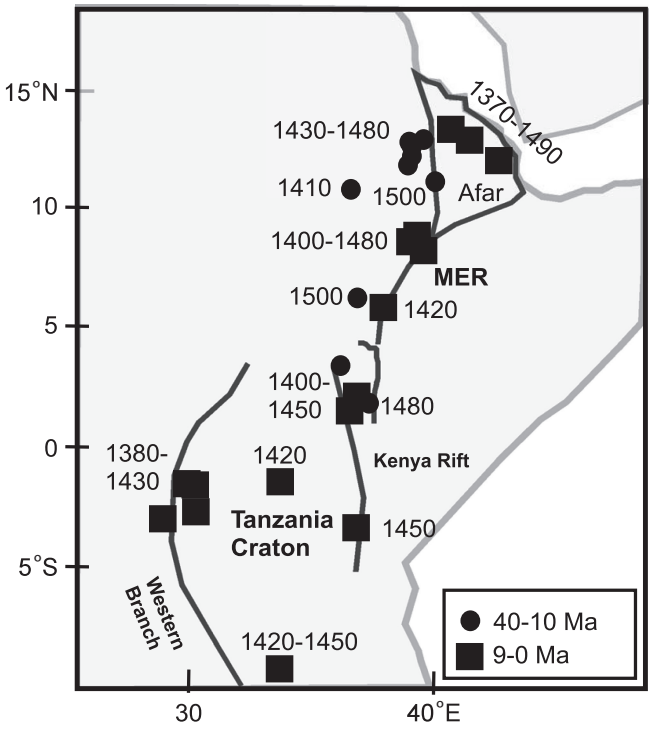

Fig. 11.12 Maximum potentail temperature (in C) of magnesian lavas along the East African Rift System (source of data: Rooney etal. 2012)

and phonolite lava and tuff: silica-saturated to mildly undersaturated trachytes erupted during shield eruptions and first caldera collapse, and later it erupted more silica-undersaturated phonolite during post-caldera collapse phase (Fig. 11.11). In contrast, Mt. Longonot, only 30 km away from Mt. Suswa, erupted only trachytes. Other volcanoes within 160 km of Suswa erupted basaltic-to-benmoreite lavas.

Finally, in an attempt to estimate how hot the EAR plume really is, Rooney et al. (2012) compiled a dataset of maximum Mg-rich basalt lavas of different ages from the EARS and calculated their mantle potential temperatures (Fig. 11.12). They discovered that the calculated temperatures were about 100°–140° higher than the ambient mantle (1,300–1,400 °C). This makes the EARS hot spot a much cooler hot spot (warm spot) than other known hot spots or plumes (e.g., Hawaii: 1,600 °C). Based on these cooler temperatures, Rooney et al. (2012) suggested that the seismic low-velocity zone observed beneath East Africa is due to the presence of partial melts that have formed due to CO_2-present melting. This is a good example of application of petrological knowledge to geodynamics.

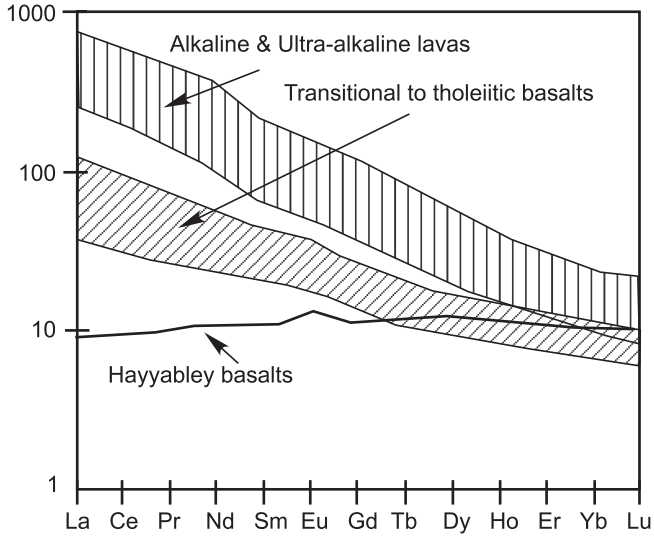

Fig. 11.13 REE patterns of lavas from the East African Rift System

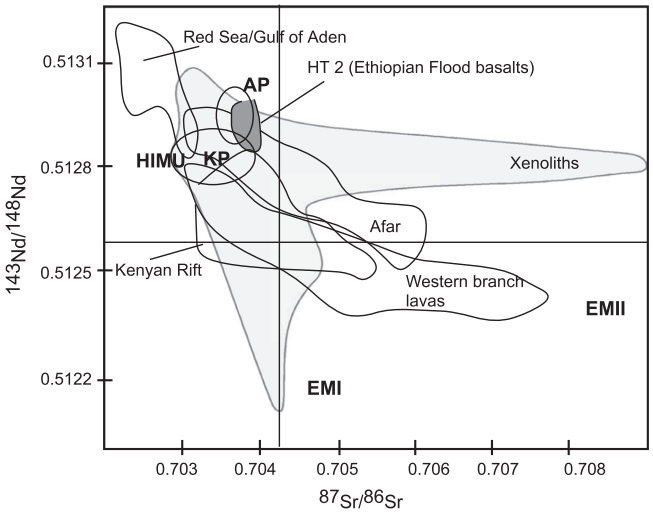

Fig. 11.14 Isotope compositions of lavas and mantle xenoliths from the EARS compared with depleted mantle component (Red Sea/Gulf of Aden) and enriched mantle components HIMU, EMI, and EMII. Also shown are the fields for the Afar plume (AP) and Kenyan plume (KP)

There is extensive literature on trace element and isotope geochemistry of the lavas from EARS, and it is beyond the scope of this book to discuss the many findings that appear in previous studies. The lavas are all LREE enriched, regardless of whether they are alkaline or tholeiitic, and LREE-depleted lavas are rare (Fig. 11.13). The LREE-depleted basalts shown in Fig. 11.13 are from the Hayyabley volcano in Djibouti (Daoud et al. 2010). The ultra-alkaline lavas exhibit maximum LREE (nearly 1,000× chondritic) enrichment and HREE depletion. These may have formed by metasomatized lithospheric mantle. Such mantle source is exemplified by the Tanzanian garnet lherzolite, spinel lherzolite, and pyroxenite xenoliths that contain phlogopite and/or amphibole (Aulbach et al. 2011).

In terms of Nd–Sr isotope geochemistry (Fig. 11.14), Kenyan rift lavas, western branch lavas, and Afar Depression lavas exhibit significant variation and suggest strong interaction between four isotopic source components (the Afar plume and Kenya plume) like depleted components, a HIMU component, and two enriched mantle components (EMI and EMII). Study of lherzolite and pyroxenite xenoliths, many of which contain phlogopite, suggests that the lithosphere has undergone several episodes of metasomatic enrichment—from ancient to very young (Aulbach et al. 2011).

It is difficult to summarize the great diversity exhibited by the igneous processes and products of the East African Rift System, but nonetheless, an attempt is made here. The magmatic and tectonic activities started with the formation of Ethiopian and Kenyan domal structures some 45 million years ago, which are attributed to the impact of a single or two separate plumes. Most recent thoughts appear to converge on a single plume that impacted near Afar Depression, and an "arm" of it migrated down the axis of the EARS, reactivating old lithospheric fractures that have been in existence since the splitting of Gondwana supercontinent. Application of petrological thermometers suggests that the plume was significantly cooler than the Hawaiian and other plumes. The Ethiopian Traps that form the Ethiopian dome are comprised of flood basalts separated by rhyolitic ignimbrite layers. The bulk of the Traps erupted within 1 million year, and this eruption occurred 30 Ma. Since that time, both magmatic and tectonic activities have been episodic—with strong activities at 15 Ma and 6 (±1) Ma. The rift system has produced a great variety of magmas—from carbonatites to alkaline phonolites, basanites, nephelinites, ultra-alkaline kamafugites, alkali basalts, trachytes, and silica-saturated rhyolites. The rift splits into western and eastern branches around the Tanzania Craton.

The eastern branch has produced more sodic magmas, whereas western branch has produced more potassic magmas. Lithospheric lherzolite and pyroxenite xenoliths occur in Tanzania, and they contain phlogopite and amphibole. Such materials are likely source of many of the lavas found in the EARS. The other sources involve a plume (Afar/Kenyan plume), and isotopically defined mantle sources, HIMU, and enriched mantle components—EMI and EMII.

Box 11.1: Carbonatite–Ijolite Association

Carbonatites and ijolite series rocks commonly occur as small plutonic ring complexes. The core of the complex is usually made of carbonatite, pyroxenite, ijolite, melteigite, melilitite (composed dominantly of melilite and titanaugite), jacupirangite (a very pretty rock composed of aegirine-augite and nepheline), and nepheline syenite. Such complexes are often intrusive into granitoid gneisses in Precambrian shield. A sodium-metasomatic reaction zone develops in the wall rock around the complex in which quartz is replaced by feldspar and feldspar by nepheline. This type of wall rock metasomatism is known as *fenitization*, and the rocks are called *fenite*, named after the Fen Complex in Norway. Figure 11.15 shows an example of carbonatite–ijolite series–fenite complex called the Spitskop complex, which was emplaced into the Kaapvaal Craton (South Africa) 1.4–1.2 billion years ago (Harmer 1999). Ijolite, nepheline syenite, and pyroxenite comprise the silicate magmas and carbonatites are calico–carbonatite (sövite) and dolomite–calcite carbonatite.

The origin of ijolite–carbonatite association has been attributed to three hypotheses (e.g., Bailey 1993): (1) carbonatites and the alkaline silicate magmas are all mantle-derived primary magmas formed by partial melting of carbonate-bearing peridotite in the presence of CO_2 and H_2O, (2) carbonatite and alkali silicate magmas have a common silicate parent from which they split by liquid immiscibility, and (3) carbonatite formed as a residual liquid from extreme fractional crystallization of a CO_2-saturated (or undersaturated) nephelinite-type magma.

Experimental peridotite and eclogite melting studies have shown that carbonatite primary

(continued)

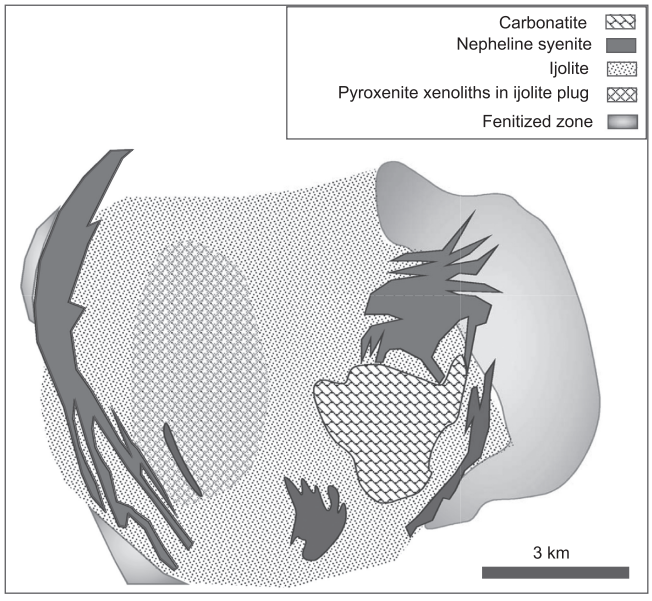

Fig. 11.15 Map of Spitskop Complex, South Africa (Harmer 1999)

Box 11.1 (continued)

magma can form in the mantle (discussed later). A strong case can also be made for liquid immiscibility based on experiments and naturally occurring melt inclusions in some cases. For example, Mitchell and Dawson (2012) discovered immiscible melt inclusions of carbonate and silicate compositions in nepheline, garnet, and pyroxene phenocrysts from Ol Doniyo Lengai. As shown in Fig. 11.16, these melt inclusions form conjugate pairs that define the boundary of a two-liquid field. For the purpose of comparison, an experimentally determined two-liquid curve at 1,250 °C, 0.5 GPa (Brooker and Kjasgaard 2011) is also shown. One could visualize a scenario where the conjugate melt inclusions would have formed at a lower temperature and at about the same pressure perhaps. The experimentally derived tie-lines are interesting.

In the case of Spitskop Complex, Harmer (1999) showed that the silicate rocks and the carbonatites have distinct isotopic compositions (Fig. 11.17), which rules out any possibility that the two magma types were conjugate immiscible liquids or be linked via fractional crystallization of a common parent magma. Harmer (1999) attributed the enriched isotopic composition of

(continued)

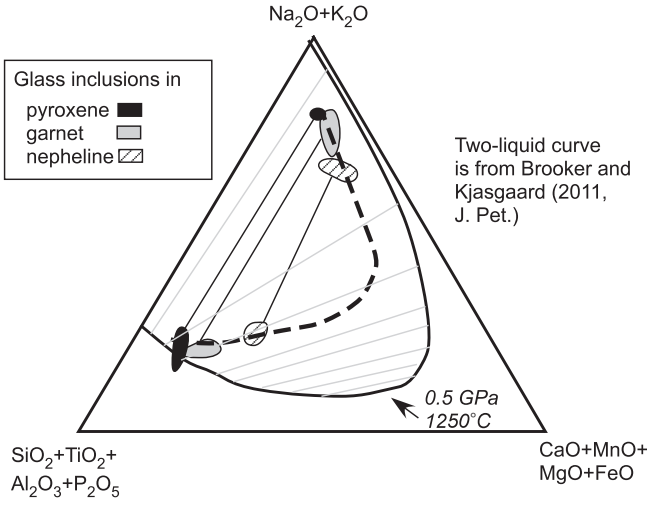

Fig. 11.16 Glass (melt) inclusions in minerals from Ol Doniyo Lengai form conjugate pairs that define the boundary of a two-liquid field (*dashed*). The tie-lines (*gray*) show conjugate pairs. An experimentally determined two-liquid field is also shown for illustrative purpose

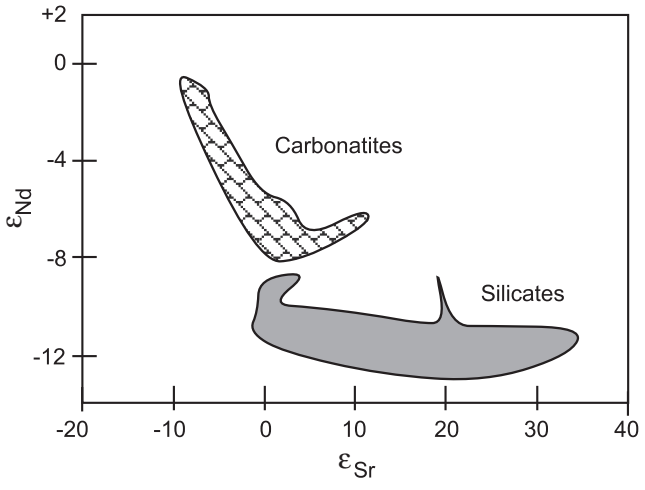

Fig. 11.17 Isotopic composition of carbonatites and silicate rocks in Spitskop Complex

Box 11.1 (continued)
the silicate "magmas" to their formation by melting of the lithosphere induced by carbonatite melts brought in from greater depths.

Kimberlites

Kimberlites are potassic, volatile (CO_2, H_2O)-rich ultramafic rocks with very high contents of both compatible (e.g., Ni, Cr) and incompatible (Ti, P, LREE) elements, and they characteristically contain some of the deepest mantle fragments (xenoliths and xenocrysts), including diamond. Wagner (1914, cited by Field et al. 2008) recognized two classes of diamond-bearing kimberlites, which he called "basaltic" and "lamprophyric" kimberlites. These have now become known as Group 1 and Group 2 kimberlites, which have also been called *orangeites*. There are substantial differences between the two groups (Table 11.1). Diamonds occur in both types and also in lamproites. Chemical composition of kimberlites is generally suggestive of their formation by very low degrees of melting of peridotite at high pressure.

Petrographically, kimberlites have a strong brecciated inequigranular texture, composed of large xenocrysts, xenoliths, megacrysts, set in a fine-grained groundmass (often highly altered) composed largely of olivine and lesser amounts of phlogopite, carbonate (commonly calcite), serpentine (altered olivine), diopsidic pyroxene, monticellite, apatite, spinels, perovskite, and ilmenite. Xenoliths can make up as much as 50 % of the rock. The larger crystals are largely olivine, with much less abundant crystals of phlogopite, ilmenite, chromian spinel, pyropic garnet, chrome diopside, and enstatite. Kimberlites are often strongly altered by deuteric processes leading to serpentinization and carbonation (Field et al. 2008).

Because of extensive alteration and hybrid nature of kimberlites, it is hard to estimate the composition of primary kimberlite magma. In rare cases, it has been possible to obtain reasonably constrained primary kimberlite melt composition, free of wall-rock materials (i.e., xenoliths or xenocrysts). For example, Price et al. (2000) found four aphanitic chilled margin samples from Jericho kimberlite dike (Group 1 type) pipe (Canada), which, on the basis of compositional and textural arguments, were thought to be the closest to primary melt compositions. These compositions are listed in Table 11.2.

In the case of 65-Ma-old Behradih and Kodomali kimberlite pipes in India, fairly unaltered Group 2 type kimberlite was sampled via drilling (Lehman et al. 2010). Interestingly, these kimberlites are of same age as the Deccan Traps, which suggest that the two eruptive events are related with the kimberlites erupting from the peripheral regions of the Deccan plume (Lehman et al. 2010).

Kimberlites commonly occur as carrot-shaped intrusions, referred to as pipes or diatremes, and less commonly as sills and dikes, tuffs (Fig. 11.18). These magmas rise at supersonic speed from great depths in

Table 11.1 Groups 1 and 2 kimberlites

	Group 1	Group 2
Mode of occurrence	Pipes	Many occur as dikes
Mineralogy	Olivine, monticellite, calcite, phlogopite, spinel, perovskite	Phlogopite dominates the groundmass
		Olivine, diopside, spinel, perovskite, apatite and melilite common
		Some Group 2 kimberlites contain sanidine, K-richterite, and leucite
Spinel, perovskite grain size	Coarse	Fine
Xenoliths	Peridotites, metasomatized peridotites, sheared peridotites, MARID suite	Generally devoid of metasomatized xenoliths and sheared peridotites
Chemistry	CO_2-rich	H_2O-rich; enriched in SiO_2, K_2O, Pb, Rb, Ba, and light rare-Earth elements and depleted in Cr and Nb relative to Group 1 kimberlites
Isotope geochemistry	Slightly depleted Sr–Nd isotopic signatures	Enriched Sr–Nd isotopes

Table 11.2 Jericho aphanitic kimberlite samples

Sample#	JD51	JD69	JD82
SiO_2	20.77	29.06	30.31
TiO_2	0.89	0.49	0.77
Al_2O_3	1.82	1.38	1.75
FeO*	6.39	5.71	7.30
MnO	0.19	0.13	0.15
MgO	16.65	23.69	25.14
CaO	25.45	16.69	13.32
Na_2O	0.10	0.13	0.24
K_2O	0.17	0.45	0.42
P_2O_5	0.85	0.56	0.75
CO_2	18.82	12.97	9.80
H_2O^+	5.30	6.40	7.50
H_2O^-	1.02	0.76	1.05
Sum	98.42	98.42	98.50
Mg#	0.82	0.88	0.86

From Table 2 in Price et al. 2010, J. Petrology, vol. 41, pp. 789–808

the mantle, breaking off surrounding wall rocks in the mantle and crust along the way. There has been considerable debate about how they rose with such ferocity and formed the typical pipe-shaped conduits. While it is realized that vapor was a key to such violent eruptions, the role of magma's juvenile vapor versus the vapor coming off boiling groundwater and the physical mechanism of diatreme formation has been debated. The various hypotheses can be grouped into two classes— magmatic versus phreatomagmatic origin of kimberlite pipes: the magmatic idea suggests that the juvenile volatiles (i.e., the vapor that was dissolved in the magma at high pressure) were the driving force, whereas the phreatomagmatic idea appeals to boiling groundwater as it came in contact with kimberlite magma. Representing the magmatic school, Wilson and Head (2007) suggested that kimberlite magma rose as a dike, with exsolved CO_2-forming foam behind

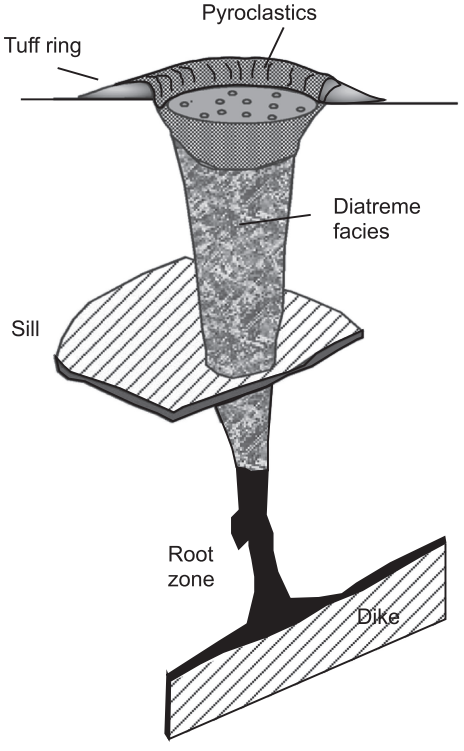

Fig. 11.18 Schematic representation of a kimberlite pipe

the dike tip. As the dike tip breached the surface, CO_2 blew out the top, and the sudden depressurization sent a shock wave further below causing implosion of the dike walls and fragmenting the magma, forming the diatreme. The whole process would have taken less than an hour.

Ages of Kimberlite and Diamond Inclusions

Kimberlites exclusively occur in continental cratons, which are the oldest and tectonically most stable parts

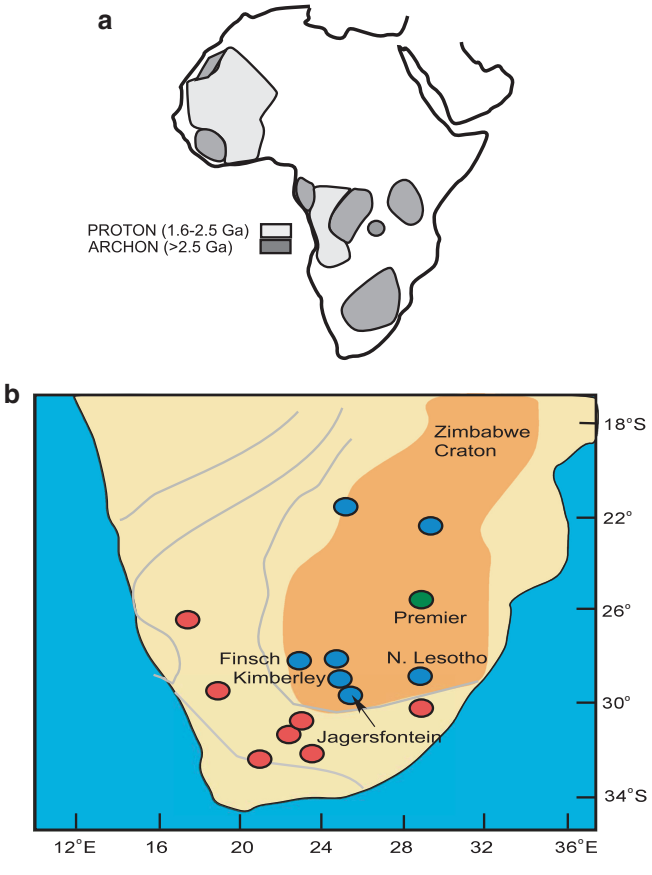

Fig. 11.19 (**a**) Proton and Archon provinces in Africa. (**b**) Kimberlite pipes in South Africa: *blue*—pipes that fall inside the Zimbabwe Craton; *red*—pipes that fall in mobile belt. The Premier pipe is shown separately as *green* (Begg et al. 2009)

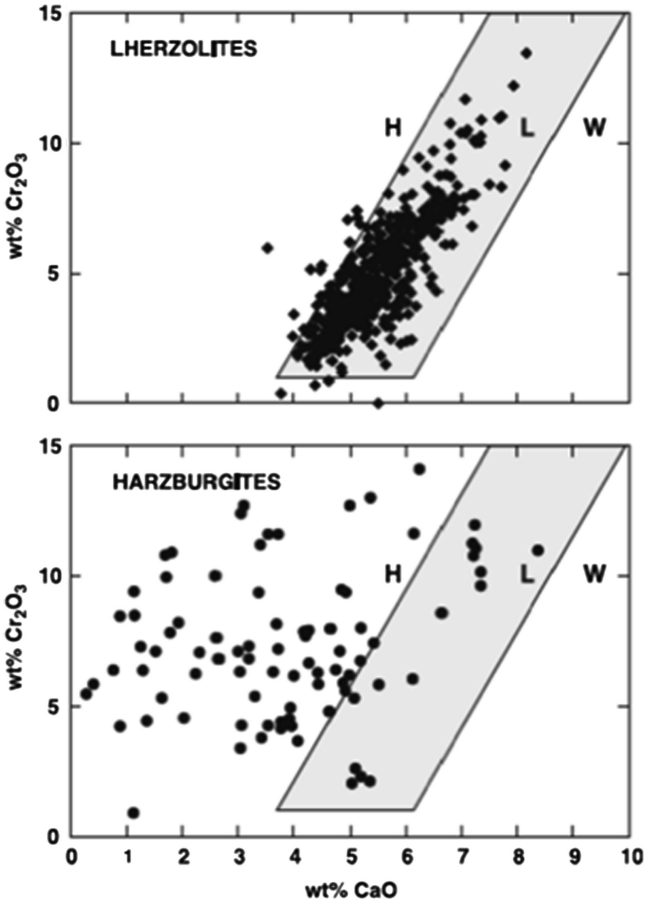

Fig. 11.20 Chemical discrimination of garnets of harzburgitic (H), lherzolitic (L), and wehrlitic (W) affinity (from Schulze 2003)

of the continents. Oldest cratons that are greater than 2.5 Ga old are called *Archon* (i.e., Achaean Craton), and those that are 1.6–2.5 Ga old are called *Proton* (i.e., Proterozoic Craton; Fig. 11.19a). These cratons were "glued" together by greenstone belts of Archaean–Proterozoic age that are either high-grade metamorphic belts or folded sedimentary basins during the early history of continent formation. Kimberlites have erupted over a broad period of geologic time—the oldest is the Premier pipe (now called Cullinan; Fig. 11.19b) in southern Africa, which is about 1.2 Ga old, and the youngest pipes are 45 Ma old. Globally, most kimberlites erupted between 70 and 120 Ma (e.g., Torsvik et al. 2010).

Mineral inclusions in diamonds have been dated and are usually much older than the host kimberlites. Both silicate and sulfide inclusions occur (Shirey et al. 2003). The silicate inclusions can be grouped into P-type, which has peridotitic affinity, and E-type or eclogitic. Such affinities can be determined by using mineral chemistry. P-type mineral inclusions include chromian pyropic garnet, diopside, enstatite, chromite, and olivine. P-type can be subdivided into harzburgitic type and lherzolitic type based on the Cr and Ca content of the garnet (Fig. 11.20; Schulze 2003) and/or orthopyroxene (+olivine, if present). E-type inclusions contain eclogitic mineralogy—pyrope–almandine garnet, omphacitic pyroxene, coesite, or kyanite. Sulfide inclusions are pyrrhotite–-pentlandite intergrowths with minor chalcopyrite. Sulfide inclusions also have P- or E-type affinities and are subdivided according to their chemical composition.

Silicate inclusions have been dated using Rb–Sr and/or Sm–Nd isotopic methods, whereas the Re–Os isotope system is used to date sulfide inclusions in diamond (Shirey et al. 2003). Table 11.3 shows the ages of the inclusions and the host kimberlites. With the exception of Premier kimberlite, there is a significant time gap between the inclusion age and kimberlite age. In the case of Premier pipe, E-type inclusions have essentially the same age as the kimberlite, meaning that the

Table 11.3 Southern African kimberlite and dimond inclusion ages (*sources: Shirey et al.* 2003, *Lithos, p. 248, Table 1, and Field et al.* 2008, *Ore Geology Reviews*)

Kimberlite age	Sulfide inclusion Re–Os age	Type	Silicate inclusion	Type
Premier				
1,202 ± 72 Ma (U–Pb on perovskite)			1,150–1,930 Ma (Rb–Sr)	E, P
De Beers Pool				
92 Ma (U–Pb on Zircon)	2,900 Ma	E	3,200 Ma (Rb–Sr)	P
Jwaneng				
235 ± 2 Ma (U–Pb on zircon)	1,500–2,900 Ma	E	1,540 Ma (Rb–Sr)	E
Orapa				
93.1 Ma (U–Pb)	1,000–2,900 Ma	E	990 Ma	E
Koffiefontein				
90.4 Ma (U–Pb)	990–2,900 Ma	E		
Finsch				
11 ± 2.8 Ma (U–Pb)			3,300 Ma	P
			1,580 ± 40 Ma	E

diamond formed very close to the formation of the kimberlite magma. In general, the ages of inclusions, and hence their host diamonds, fall into Archaean and Proterozoic groups, although some younger diamonds have also been discovered from Southern Africa that are not shown in Table 11.3. In general, these diamonds are very old (Precambrian) and come from a deep root or "keel" of the lithosphere that has been very stable for a long time.

Xenoliths in Kimberlites

The kimberlite literature is rich on the topics of its xenoliths and xenocrysts. Kimberlitic xenoliths come from both crust and mantle. Like the silicate inclusions in diamond, mantle xenoliths in kimberlites are of harzburgite, lherzolite, and eclogite types, with generally subordinate amounts of wehrlites and dunite. An unusually hydrous suite of rocks, called MARID (mica, amphibole, rutile, ilmenite, diopside) suite, also occur as minor xenoliths. The modal distribution of major peridotite- versus eclogite-type xenoltihs can vary considerably between various Southern African kimberlite pipes. Peridotite xenoliths are more abundant in kimberlites that fall in the craton. Texturally, the P-types can be fundamentally divided into those with a granular texture and others that have a sheared or foliated texture (Boyd 1976). Boyd suggested that the granular xenoliths come from the lithosphere, and the sheared ones originate from the asthenosphere.

Experimental petrology has shown that Al_2O_3 in solid solution in pyroxenes in lherzolites is a good geobarometer, and CaO content of pyroxenes is a good geothermometer (this is discussed in another chapter). Therefore, composition of coexisting pyroxenes in peridotite xenoliths gives us direct information on pressure (depth) and temperature of their origin: for example, Fig. 11.21 shows the *P–T* calculations for xenoliths from kimberlites located on the Kaapvaal Craton in South Africa (Stachel et al. 2003). Most of the xenoliths define a geothermal gradient with a surface heat flow of 42 mW/m^2. There are two groups of xenoliths that carry diamonds and fall within the diamond stability field: one of them falls more or less on the estimated geotherm as shown, and the other group is clearly hotter. Stachel et al. (2003)

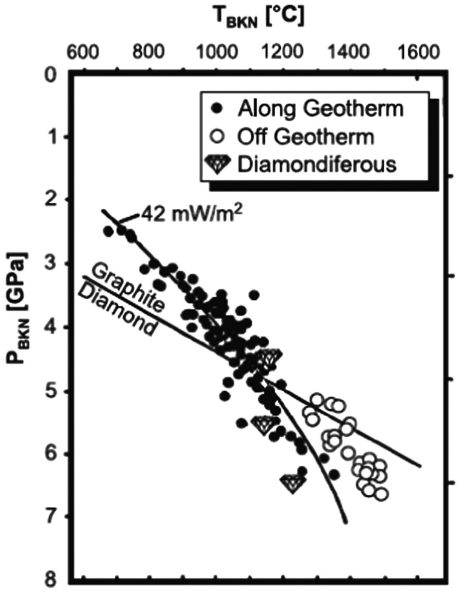

Fig. 11.21 Pyroxene-based geotherm from kimberlitic xenoliths from South Africa (from Stachel et al. 2003)

suggested that this heating occurred by intrusion of asthenospheric melts.

In general, application of the pyroxene thermobarometers to kimberlite xenoliths indicates that most kimberlitic mantle xenoliths come from no deeper than about 200 km. Rare xenoliths, for example, those which contain majoritic garnets (garnets rich in pyroxene solid solution), must have come from the transition zone of the Earth (Haggerty and Sautter 1990). As discussed in a later chapter, garnet dissolves pyroxene in solid solution as pressure is increased beyond 5 GPa pressure such that a garnet + pyroxene rock (eclogite or garnet pyroxenite) becomes garnetite (i.e., rock composed entirely of garnet) at a very high pressure. This is likely to happen in a subducting slab. If such garnetite is brought back up to a lower pressure by mantle upwelling or carried up by some magmas, and is made to sit there for a long time, then the dissolved pyroxene component would be exsolved out of the garnet. Thus, exsolved pyroxene in garnet indicates a very high initial pressure (depth) of origin of such a rock.

Nature of the Subcontinental Lithosphere

Much has been learned from kimberlite xenoliths and inclusions in diamond. These findings can be summarized as follows:

- There appears to be a general agreement that the xenoliths and diamond inclusions represent a deep lithospheric "keel" that is at least as deep as 200 km beneath cratonic areas.
- Some inclusions likely come from much deeper levels, such as the transition zone of the Earth.
- The cratons are generally underlain by depleted harzburgite. Harzburgite is less dense than lherzolite or eclogite. Thus, cratons are buoyant owing to their lithospheric composition. There are many ideas about how the craton got to be so depleted, but the two commonly accepted hypotheses are that they are residues of extraction that formed the early crust and/or they are products of reactive dissolution of clinopyroxene by passing magmas.
- The temperature distribution within the lithosphere is adequately represented by geotherms calculated from thermobarometry of xenoliths in kimberlites or in other alkaline intrusions. The base of the continental lithosphere around 250 km is around 1,400 ± 50 °C.
- MARID-suite xenoliths represent metasomatic veins resulting from fluids/magmas interacting with the lithosphere.
- Eclogite xenoliths represent ancient subducted slab materials or basaltic magmas plated onto the base of the lithosphere or as deep veins in the lithosphere.

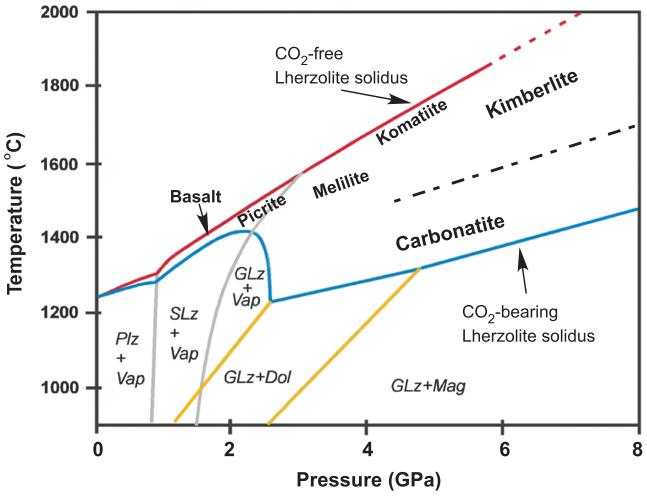

Fig. 11.22 Volatile-free lherzolite solidus (*red*) is compared with CO_2-saturated lherzolite solidus (*blue*). Compositions of various magmas produced between the two solidi are shown (from Gudfinnsson and Presnall 2005). Plz, SLz, and Glz are abbreviations for plagioclase-, spinel-, and garnet-lherzolites. *Dol* dolomite, *Mag* magnesite, *Vap* vapor

Kimberlite Petrogenesis

Strong constraints on the origin of kimberlite magma have come from experimental petrologic studies on melting and in CO_2-bearing peridotitic systems. As shown below, we can see that a variety of magmas—from carbonatite, nephelinitie, melilitite to kimberlite—can be generated from mantle peridotite in the presence of CO_2. On the other hand, K_2O- and H_2O-bearing melting studies have given us important constraints on conditions of phlogopite and amphibole stabilities in the lithosphere, potassic metasomatism, and origin of some potassic magmas. There is considerable published literature on this subject, and here we will discuss only a few that I consider relevant to the topic.

In Chap. 4 we briefly discussed a continuous relationship between carbonatite and silicate magma by increasing degree of melting in the system CMS–CO_2: carbonatite forms close to the vapor-saturated solidus and silicate magmas form at higher temperatures closer to the vapor-free solidus of peridotite (it is worth looking a second look at Figs. 4.24, 4.25, 4.26, and 4.27 and relevant discussion). Recently, Gudfinnsson and Presnall (2005) presented a similar study on the system CaO–MgO–Al_2O_3–SiO_2–CO_2 over a pressure range of 3–8 GPa.

Gudfinnsson and Presnall (2005) mapped out the composition of melts in the field between the CO_2-free and CO_2-bearing lherzolite solidi (Fig. 11.22). Similar to the findings of Moore and Wood (1998) in

CMS–CO_2, Gudfinnsson and Presnall (2005) found that progressive heating of CO_2-bearing peridotite generates carbonatites at low temperature (low F), and the melt composition grades into more mafic or ultramafic compositions at higher temperatures. They showed that near the vapor-free solidus, the melt composition changes from basalt at <2 GPa to melilite at 3–4 GPa to komatiite at 4–5 GPa and kimberlitic above 6 GPa. Closer to the CO_2-bearing solidus, the melt composition is similar to that of a magnesium carbontatite. Interestingly, they did not find a liquid immiscibility field between the silicate and carbonate compositions. However, as pointed out in an earlier section, other experiments have found silicate–carbonate liquid immiscibility to occur between nephelinite and carbonatite melts at low pressure, limiting such immiscibility to occur only at crustal depths.

Gudfinnsson and Presnall (2005) found similarities between the various Group 1 kimberlite compositions and experimental melts, which led them to conclude that one class (Group 1a) of Group 1 magmas formed at 5–6 GPa (~150–180 km), whereas another class (Group 1b) came from much greater depth—300 km or even deeper (≥10 GPa). This is consistent with the constraints provided by some of the deepest xenoliths, as discussed earlier. Gudfinnsson and Presnall did not include K_2O in their study, and we need to consider experimental results on phlogopite melting in the mantle to understand the origin of ultrapotassic magmas, Group 2 kimberlites, and lamproites that also carry diamonds and other deep-seated xenoliths.

Phlogopite Stability in the Mantle and Origin of Lamproites and Ultrapotassic Magmas

We start with a relevant experimental study by Edgar and Mitchell (1997) in which they carried out melting experiments on two lamproites. These authors found that phlogopite can be a stable phase in association with liquid, K-bearing clinopyroxene, and other minor phases. Figure 11.23 shows two cratonic geotherms (marked as 1 and 2), which shows that at 5–7 GPa, i.e., within the continental lithospheric keel, a phlogopite-saturated melt can occur. However, according to Edgar and Mitchell, this melt has a more fractionated composition relative to that of a lamproite. If lamproite were to partially crystallize in the deep lithosphere, then it would generate fractionated potassic residual liquids. If high-silica lamproites are generated as primary magmas from the asthenosphere,

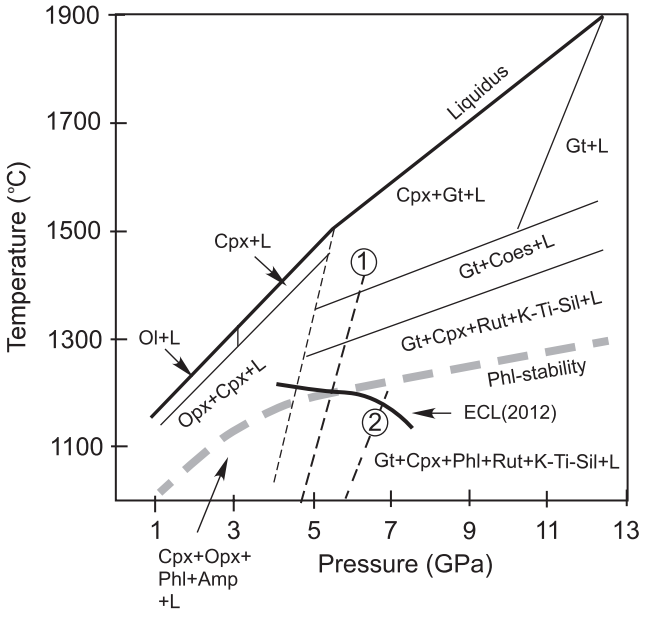

Fig. 11.23 Phase diagram of two lamproites (redrawn from: Edgar and Mitchell 1997)

then they will require a high-K_2O source and/or extremely low degree of melting of a high-K_2O peridotitic source. Also, based on where the geotherms could potentially intersect the liquidus, one could surmise that the melting would have to occur at about 1,550 °C and 7.25 GPa, i.e., close to the base of a 220-km-thick lithospheric keel. Interestingly, Edgar and Mitchell (1997) noted that the garnet and clinopyroxene near the liquidus are compositionally very different from those of eclogites, and thus, it is unlikely that eclogites could have served as a source rock for these magmas.

Enggist et al. (2012) performed melting experiments on the system K_2O–MgO–Al_2O_3–SiO_2–H_2O–CO_2 at 4–8 GPa; the results of which are relevant to our understanding of K-rich magma genesis. Figure 11.23 shows the curve that defines the stability limit of magnesite + phlogopite in their experiments. At temperatures lower than the phlogopite stability curve, a hydrous K-rich fluid coexists with crystals of phlogopite, garnet (pyrope), and magnesite. Above this curve, and over a temperature range of about 150 °C, phlogopite is stable with a melt, olivine, enstatite, and garnet. Phlogopite + magnesite may therefore be stable in the deep (180–200 km) subcontinental lithospheric keel. Such potassic, hydrated, and carbonated lithosphere can be a reasonable source of ultrapotassic to kimberlitic magmas. Thinning of the lithospheric keel by uplift and/or erosion, perhaps aided by a plume, could generate a variety of magmas from

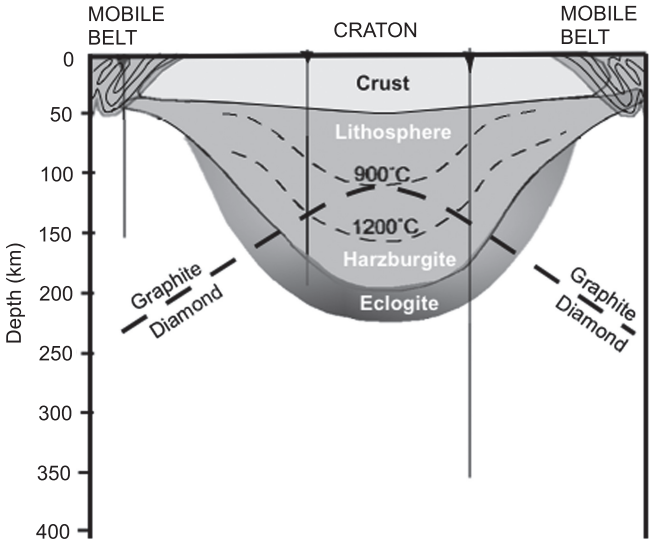

Fig. 11.24 Kimberlite xenolith-based model of the continental lithosphere (simplified from Haggerty 1986)

kimberlites to lamproites to perhaps ultrapotassic (kamafugite)-type magmas. However, the actual melt compositions in experiments have proved to be extremely difficult to obtain, and therefore, we lack stronger *P–T* constraints on the origin of these interesting magma types.

Nature of the Subcontinental Lithosphere

Combining knowledge acquired from experimental studies, depth–temperature information from xenoliths and diamond inclusions, and geological distribution of the kimberlite pipes, a clearer picture of the continental lithosphere has begun to emerge. Figure 11.24 is a schematic model of the continental lithosphere (significantly simplified and modified from Haggerty 1986), which is consistent with the findings from experiments and xenoliths. It shows that the cratonic lithosphere has a 200 (±50) km thick dominantly harzburgitic root or keel that is surrounded by mobile belts. The isotherms are based on xenolith-derived *P–T* estimates. Kimberlite melts can form at 150–180 km to more than 300 km. Diamond versus graphite formation in the lithosphere is tied to the depth of origin of a xenolith—whether or not it comes from a depth where diamond versus graphite is stable. Haggerty (1986) and others have suggested that eclogite xenoliths, sometimes carrying diamonds, come from eclogite "pods" at various levels in the lithosphere (from magmatic crystallization) and from an eclogite layer plated on the base of the peridotitic keel. Metasomatism, which obviously occurs in the lithosphere, is not shown in Fig. 11.24 for the sake of brevity.

Summary

- Alkaline and ultra-alkaline magmas are rare relative to basaltic, andesitic, and rhyolitic magmas. They are characterized by an excess of alkalis relative to silica than what would be required to form feldspars. Their characteristic minerals are Na, K-rich, such as feldspathoids, aegirine–augite type pyroxene, and alkalic amphiboles. The rocks discussed here represent a wide variety—from nephelinites to carbonatite to lamproites and kimberlites.
- Alkaline rocks are more commonly found continental rift environment, although they can occur in almost all types of plate-tectonic environment and hot spots. Kimberlites are found over cratonic areas. Carbonatites are more common in rift zones, where they are associated with alkaline and ultra-alkaline rocks.
- The system nepheline–kalsilite–silica adequately describes how fractionation of magmas in continental rift zones can develop distinctive differentiation trends—one leading to rhyolitic residual liquid and the other resulting in phonolitic liquids.
- The East African Rift System is composed of a variety of tholeiitic, alkaline, ultra-alkaline, and carbonatite volcanics that are spatially related to the rift system. The rifting and magmatism are related to mantle plume(s) from the seismically defined African Superswell, which reaches down to the D″ zone. These various magmas form by melting of plume as well as lithosphere.
- Kimberlites are potassic, volatile-rich ultramafic rocks with very high contents of both compatible (e.g., Ni, Cr) and incompatible (Ti, P, LREE) elements, and they characteristically contain some of the deepest mantle fragments (xenoliths and xenocrysts), including diamond. There are two types of kimberlites—Type 1 and Type 2. Kimberlite magmas, carbonatites, and alkaline silicate magmas all form from CO_2-bearing lherzolite over a wide range of pressures—from about 3 to >8 GPa—with kimberlites coming from the greatest depths.
- Lamproites and ultrapotassic magmas can form by melting of phlogopite-bearing continental lithosphere at about 5–7 GPa.

Anorthosites and Komatiites

12

Abstract

This chapter covers some unusual rock types that are volumetrically negligible relative to basaltic, andesitic, and granitoid rocks, and yet they are very significant in terms of our understanding of the Earth's igneous history and constitution and thermal structure of the deep continental lithosphere. It is difficult to present many levels of the detailed observations and inferences that have been made by many authors about each of these rock types, and in this chapter, I present a brief summary of what I consider that an undergraduate student needs to know.

Anorthosites

We read in Chap. 2 that anorthosite is a plagioclase-rich rock in which plagioclase makes up more than 90 % by volume of the rock. Although it is generally considered to have an igneous origin, many of the Proterozoic and Archean anorthosites show evidence of deformation and metamorphism, such as curved twin lamellae, curved crystal boundaries, neocrystallization, recrystallization, and development of metamorphic minerals. In Chap. 6, we also saw examples of layered mafic intrusions, specifically, the Bushveld intrusion, which has thick layers of anorthosite. We also learned that the topographically higher, "white" regions of the moon are largely composed of anorthosite. In general, lunar anorthosites are much older (close to the age of the Earth and Moon: Fig. 12.1) and a major constituent of the crust. Terrestrial anorthosites are volumetrically insignificant and are considerably younger (Fig. 12.1).

Here we expand our knowledge about anorthosite by learning more about the petrography, mineralogy, and chemical composition of this rock, and about the differences between the Archean and Proterozoic anorthosites. Below is an attempt at summarizing our current understanding of anorthosites.

Terrestrial Anorthosites

Ashwal (1993) classified terrestrial anorthosites into five different types as follows: (1) Archean megacrystic anorthosites; (2) Proterozoic massif-type anorthosites; (3) layered anorthosites of layered intrusions such as the Bushveld and Stillwater intrusions (discussed in Chap. 7); (4) anorthosites in mid-oceanic ridges and transform faults; and (5) xenoliths of anorthosites that occur in diverse varieties as granites, kimberlites, and basalts. It is not possible to cover all these types in any detail. Since we have discussed layered intrusion anorthosites before, here I will focus only on the two dominant classes of terrestrial anorthosites below. Much of what is written below is based on the reviews by Ashwal (1993, 2010).

Archean Megacrystic Anorthosites

They are mostly 2.7–3.7 billion years (Ga) old, commonly found in association with basaltic lavas and intrusions of many Archean Greenstone belts, and are characterized by large (up to 30 cm), abundant, equant (rather than the usual tabular or lath shapes that characterize layered gabbros and anorthosites), euhedral—subhedral megacrysts of anorthitic (commonly $An_{80–90}$) plagioclase set in a basaltic (or

G. Sen, *Petrology*, DOI 10.1007/978-3-642-38800-2_12,

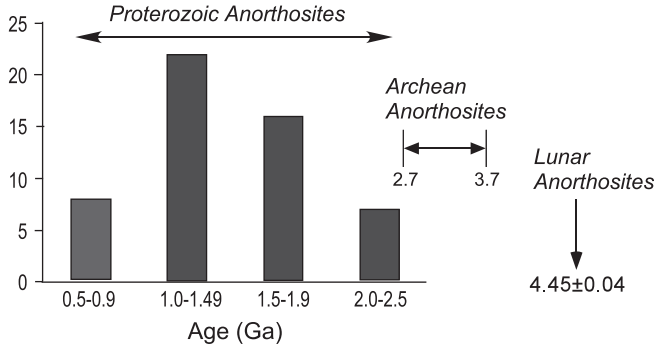

Fig. 12.1 Comparison of ages of terrestrial and lunar anorthosites

Fig. 12.2 Field picture of Archean anorthosite (Courtesy of Lewis D. Ashwal)

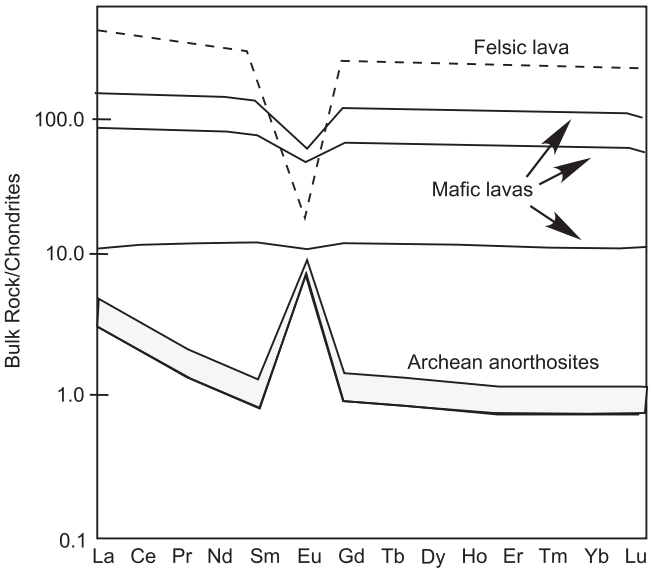

Fig. 12.3 REE pattern of Archean anorthosite compared with associated mafic and felsic rocks

metamorphosed) groundmass (Fig. 12.2). Leucogabbros with 75–90 % plagioclase are more common than actual anorthosites. In terms of spatial extent, these bodies are much smaller (15–560 km^2) than Protero massif anorthosites. They are commonly metamorphosed and range from less deformed, sub-greenschist facies to highly deformed, granulite facies. Their original magmatic texture is preserved to a varying degree. Some large Archean anorthosite inclusions occur as lenticular bodies in gabbros, giving the appearance of ocellar structure (e.g., Polat et al. 2008). Large megacrysts or megacryst assemblages also occur in sills and dikes.

The Archean anorthosites are dominantly composed of high-An plagioclase crystals and have very high Al_2O_3 (~30 wt%) and CaO (14–15 %). Their bulk REE compositions typically show a strong positive europium anomaly and a flat MREE–HREE slope (Fig. 12.3). The complimentary REE patterns with stronger negative europium anomaly in associated mafic and felsic lavas are commonly observed and suggest that anorthosites formed by plagioclase accumulation from such magmas. Interestingly, Bowen (1917) pointed out a long time ago that anorthosites could not be pure melts because their melting temperature would be too high. In sum, Archean anorthosites can be safely interpreted to have formed by some special mechanism of accumulation of plagioclase crystals, likely by crystal flotation near the roofs of magma chambers.

There has been much debate about (1) the tectonic setup in which the anorthosite bodies may have formed and (2) the type of parent magma from which the plagioclase crystals separated. It is not easy to track back the total bulk composition of the parent magma from which these plagioclase crystals separated.

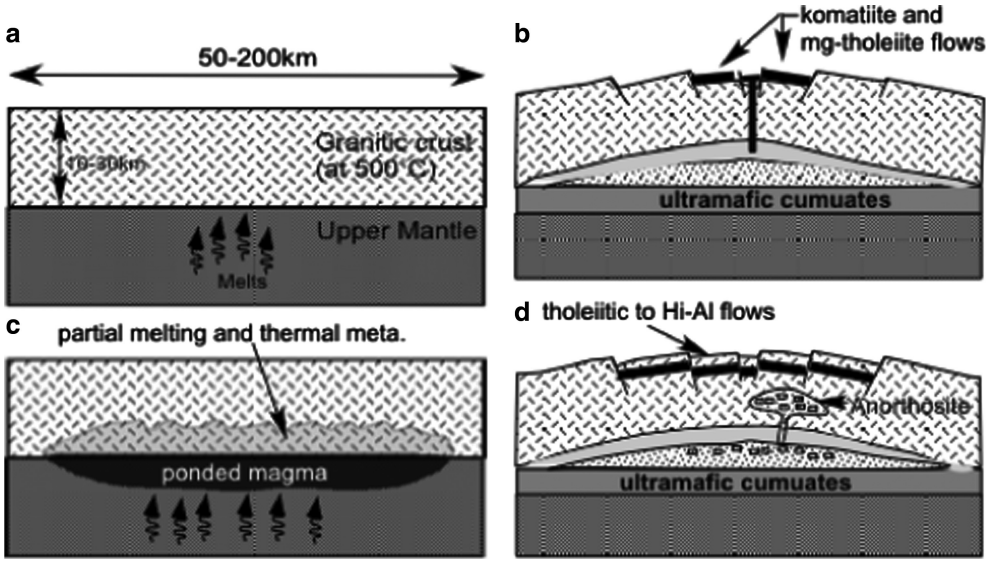

Fig. 12.4 An early model for the origin of Archean anorthosites (Phinney et al. 1988). Stage (**a**) simply shows the crust underlain by the mantle through which partial melt percolates and collects at the crust–mantle boundary. In stage (**b**), this melt melts the crust. In stage (**c**), the crust is domed up and rifted, and komatiite and Mg–tholeiite magmas erupt. Stage (**d**) shows accumulation of plagioclase crystals by flotation in the large magma body, and this body, enriched with cumulate crystals of plagioclase, separates from the main magma and rise diapirically into the crust

The three suggestions are high-alumina basalt magmas (such as those found in arcs), ferrobasaltic magmas, and komatiites.

An early model presented by Phinney et al. (1988) is given in Fig. 12.4. The model assumes a 10–30 km thick granitic continental crust, which acts as a density barrier for primitive melts, such as komatiite or high-Mg basalts. These hot magmas therefore stagnate at the base of the crust and fractionate, generating ultramafic cumulates and more Fe-rich tholeiite residual liquid. The emplacement of such magma causes the crust to dome up and undergo extension and rifting. Plagioclase crystals float in the differentiated magma, collecting in large volumes toward the roof of the magma chambers. The heat coming off the magma metamorphoses the lower crust and eventually melts it partially, producing felsic melts. These melts mix with the residual melts in the magma chambers. The plagioclase-rich roof melts rise via fractures or by diapirism by deforming the surrounding rocks to form intrusives in the shallow crust. Variety of magmas generated from the crust in this process may also come up in individual batches.

Other authors have hypothesized that the high-An content of plagioclase in Archean anorthosites indicates that these crystals formed in hydrous, highly aluminous magmas in ancient subduction environments. Additionally, some authors have also suggested that Archean subduction was hotter than Phanerozoic subduction and that Archean primary magmas may have been komatiitic or picrite (with more than 20 % MgO) basalt magmas.

Studies of well-preserved Archean crustal ophiolites in southwest Greenland are relevant here (Polat et al. 2008, 2011). In the 3.07 Ga old Ivaisaartoq intrusion in the greenstone belt in SW Greenland, for example, rocks are metamorphosed to amphibolite facies, and yet the primary magmatic structures are well preserved. Here leucogabbro and anorthosite occur as intrusions and xenoliths in the lower part of the ophiolite complex, with pillow basalts, layered, and cumulate gabbros occurring near the top of the section (Fig. 12.5; Polat et al. 2008). It also has metamorphosed (serpentine) ultramafic layers. Combining field geology, geochemistry, and isotopic study of the Ivaisaartoq complex, Polat et al. (2008) concluded that the anorthosite-pillow basalt–gabbro–ultramafic complex formed in an oceanic fore-arc extension environment where the extension was created by a slab roll back and magmas were formed by hydrous melting of the subducted crust (Fig. 12.6). The depth of emplacement of these anorthosite bodies was inferred to be around 6–9 km.

Finally, while it is possible that not all Archean anorthosite bodies formed the same way; however, it is very tempting to come up with some singular Archean-specific petrogenetic model. Such a model

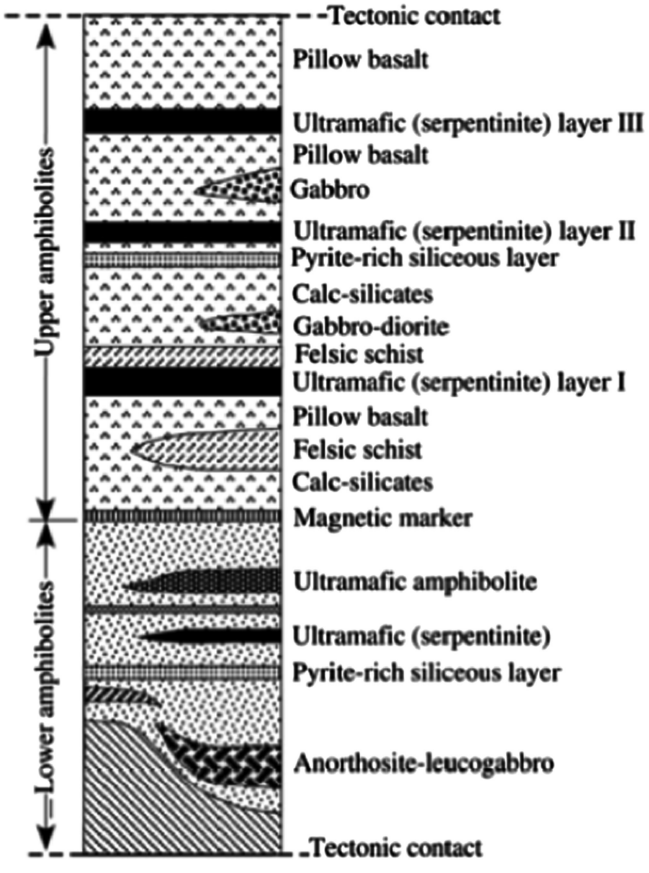

Fig. 12.5 A lithologic cross section of the Ivaisaartoq intrusion in southwestern Greenland (Polat et al. 2008)

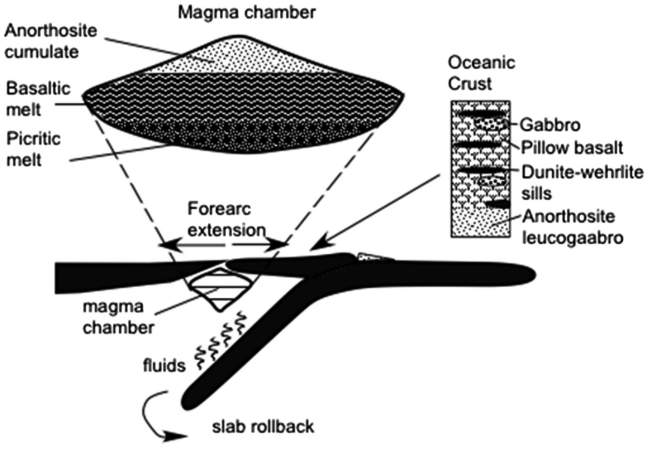

Fig. 12.6 A schematic model for the origin of the Ivaisaartoq anorthosite as a part of an ophiolite complex that was created in a fore-arc rift (Polat et al. 2008)

must be able to explain the overall similarities in field appearance, association with greenstone belts, and presence of high-An plagioclase crystals in different parts of the world. As far as I am aware, no such model yet exists.

Proterozoic Massif-Type Anorthosites

The French term "massif" broadly refers to mountain peaks, and because this type of anorthosite forms topographically distinctive highs, it is called *massif anorthosite*. Most Proterozoic massif anorthosites fall in the age range of 1–2 Ga. They commonly occur as stocks and batholiths, reaching spatial extent of 10,000–17,000 km^2. Many of them are not a single intrusion but are an intrusive complex formed by the coalescence of multiple smaller intrusions over time. In general, these bodies seem to be wide on the surface but not nearly as thick. These anorthosites are nearly pure with 90 % or more plagioclase. Plagioclase crystals in massif anorthosites can be as much as 1.8 m long. Plagioclase in massif anorthosites ($An_{40–60}$) is much less anorthitic than that in Archean anorthosites ($An_{>80}$).

Massif anorthosites occur in close field association with mangerite, charnockite, and granite, and this association is commonly referred to as AMCG (anorthosite–mangerite–charnockite–granitoid) suite. Mangerite is a hypersthene-bearing monzonite, and charnockite is hypersthene-bearing granite. The granite that occurs in AMCG suite is hornblende–biotite granite containing rapakivi texture, which is defined by oligoclase rims around round orthoclase crystals. The association is interesting; however, note that (a) relative abundances of these other rock types can vary considerably and (b) these various magmatic bodies were not all emplaced at the same time, but their emplacement often overlapped over thousands to a few millions (at best) of years. In AMCG complexes, anorthosite and granitoids form the bulk or the complex, and mafic intrusives are usually less. Typically, mafic intrusives intrude anorthosites, and granitoids intrude both.

Another interesting feature of Proterozoic anorthosites is that they are often deformed and are surrounded by "dry" granulites. This is taken as an evidence to suggest that most of them were emplaced in the deep crust and that the parent magmas were very dry, i.e., essentially anhydrous.

Gravity studies commonly show the lack of any significant buried volumes of corresponding mafic or ultramafic cumulates at depth. Unlike the layered anorthosites of layered mafic intrusions, such as the Bushveld intrusion, massif anorthosites do not have nearly as much interlayered mafic rocks. Some of these anorthosites lack layering and are concordant with the country rocks. These features pose a problem

for hypotheses that suggest the formation of these anorthosites by simple flotation in a basaltic magma chamber and necessitates a special mechanism by which cumulate anorthosite-bearing mush would be completely or largely isolated from the denser mafic/ultramafic fractionates.

A commonly accepted model (Ashwal 1993) that simultaneously explains the absence of voluminous mafic–ultramafic cumulates and the origin of the AMCG suites is one in which basaltic magma ponds and differentiates at the Moho, and within such magma chambers, olivine and pyroxene settle to the bottom and intermediate-composition plagioclase float and collect at the roofs of the magma bodies. Eventually, such plagioclase-rich mush (predominantly plagioclase crystals and some interstitial mafic melt) rises diapirically from the Moho and crystallizes in the mid-upper crust. The granitoids (i.e., MCG) form by melting of the lower crust and may be emplaced over a time period during which the anorthositic bodies are also emplaced (e.g., Fig. 12.7; Ashwal 1993). These plutons perhaps move very slowly by ductile deformation of the surrounding crust because of their high crystal content and viscosity. They stopped at the level where the brittle–ductile transition occurs in the crust because they could no longer move by ductile deformation or simply because they solidified. Doming associated with magma emplacement and eventual erosion and unroofing of the shallow crust exposes the AMCG plutonic suites.

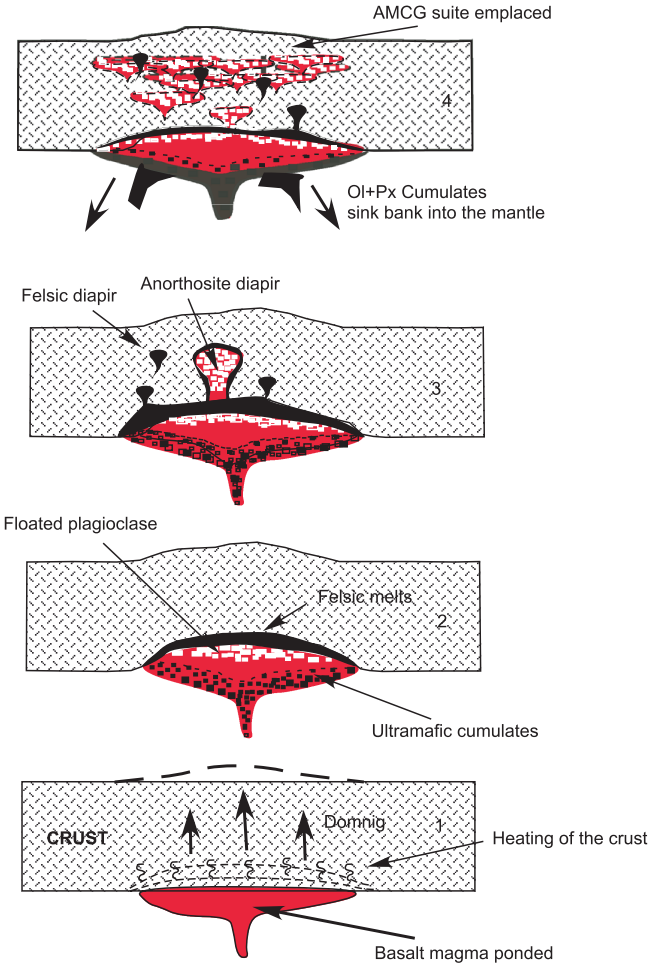

Fig. 12.7 Ashwal's (1993) model for the origin of Proterozoic anorthosite massifs. First, basaltic magma ponds at the Moho (Stage *1*) and undergoes settling of mafic minerals and flotation of plagioclase (Stage *2*). In stage (*2*), the ponded magma melts the overlying crust, producing felsic melts (MCG suite). In stage (*3*), felsic melts and cumulate bodies of anorthosite begin to rise diapirically into the crust. In stage (*4*), anorthosite and felsic melts are emplaced and solidified in the crust. The ultramafic cumulates that form at the bottom of the mafic magma chamber drop off and get recycled into the mantle

Global and Regional Anorthosite Bodies

Herz (1969) drew attention to the fact that Proterozoic anorthosites form two belts—one in the northern continents and the other in the southern continents—once the continents are reconstructed back to the Proterozoic (Fig. 12.8). There may even be two northern belts. Such anorthosite belt has not formed in any other geological time, which left Herz wondering about special scenarios in the Proterozoic that would have produced the global belt of anorthosites in the present-day cratons that were once attached to each other.

McLelland et al. (2010) considered the relationship between tectonics and ages of emplacement of the various rock types in the AMCG belt that stretches from the Adirondack Mountains to Labrador in the northeast (Fig. 12.9). They discovered that the entire AMCG suite was emplaced during the late- to post-orogenic phase, and intrusion of granitoid and anorthosite bodies occurred more or less simultaneously over a 20-milion year period. These authors presented a model that involves initial thickening of the continental crust due to collisional orogen. AMCG magma formation occurs when the thickened lithospheric root breaks off, initiating passive upwelling of the asthenosphere, and such decompression causes the asthenosphere to melt and produce basaltic magma. This magma then ponds and cools at the base of the crust. Anorthosite cumulates form by flotation and granitoids form by melting of the surrounding crust (this part of the model is the same as we have discussed in the previous paragraph). The denser olivine and

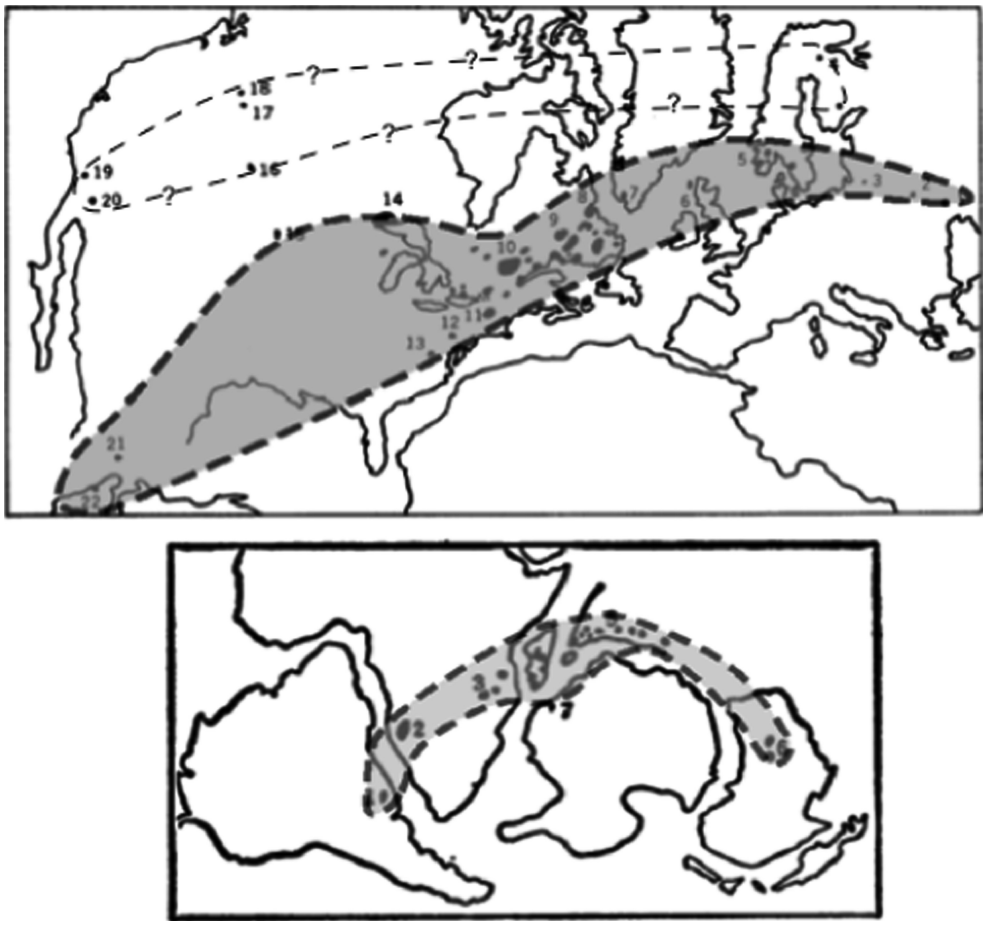

Fig. 12.8 Herz's (1969) reconstruction of Proterozoic anorthosite belts in the northern continents (*top diagram*) and southern continents (*bottom diagram*)

pyroxene cumulates delaminate from the crust and sink back into the mantle.

In this context, a recent study by Chakrabarti et al. (2011) of the 855 Ma anorthosites from the Chilka Lake area (Eastern Ghats, India) is worth mentioning. These authors noted that the Chilka anorthosites were emplaced at the boundary of India and Antarctica just prior to their separation at the time when the supercontinent Rodinia, which included Antarctica and India, was breaking up into several smaller continents. Below we will consider a few examples here in order to have a better idea about the composition and origin of individual complexes from the Proterozoic anorthosite belts.

AMCG Suite in Nain, Labrador

The AMCG suite in Nain is a 1.3 Ga igneous complex that has intruded the Nain Province (mid–late Archean) to the east and Churchill Province (Late Archean–Early Proterozoic) to the west. Figure 12.10 is a map from Emslie et al. (1994) that shows the detailed intrusive units within the Nain Massif. Emslie and colleagues (1994) grouped the plutonic rocks into the following lithologic groups:

- Mafic rocks and anorthosites—the rocks include anorthosites, leuconorite, leucogaabro, norite, troctolite, and subordinate volumes of gabbronorite. Both coarse and fine-grained varieties occur, and the coarser rocks show well-preserved cumulate textures. The anorthosites often have well-preserved cumulate texture and layering as well. A gabbroic or noritic material fills the interstices between the plagioclase crystals. Although gabbros, norites, leuconorites, etc., were grouped together by Emslie et al. (1994), it is probably better to consider the anorthosites and anorthositic rocks as a group separate from the more mafic rocks (discussed later).
- Ferrodiorites—these are the least abundant rocks. Both fine-grained and coarser cumulates occur in this group. A specific rock type, called *jotunite*, has received considerable attention as they form dikes that are only slightly younger than the anorthosite bodies that they intrude.

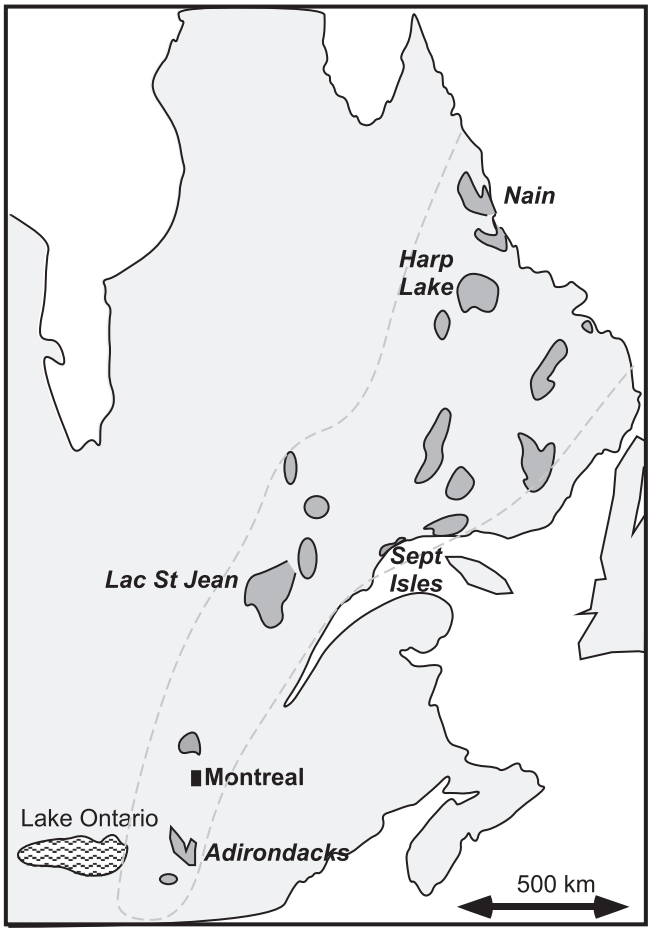

Fig. 12.9 Proterozoic anorthosite belt of northeastern Canada and the United States

Jotunite is a hypersthene-bearing monzodiorite, and its related varieties include monzonite and Fe–Ti–P-rich rocks. The more evolved varieties in this group include mangerites and charnockites. The Fe–Ti oxide minerals indicate that these rocks have crystallized under high fO_2 conditions and such fO_2 is attributed to crustal contamination.

- Granitoid rocks—these are rich in K_2O and hence in potassic feldspar. The rocks include monzonite, quartz monzonite, mangerite, charnockite, and granite.

In the field, granitoids appear to be generally younger than the anorthosites as the latter are intruded by the former. More recent U–Pb dating of zircon crystals from 13 anorthosite suite samples gave an average age of 1,154 ± 6 Ma, and 13 granitoid samples gave 1,158 ± 5 Ma, indicating that these rock suites are more or less coeval and that the emplacement of the bulk of such a large complex happened in a relatively short time (McLelland et al. 2004).

Emslie et al. (1994) presented geochemical data and subsolidus pyroxene compositions of the various groups (Figs. 12.11 and 12.12). The pyroxenes show extreme Fe enrichment. In grantioids, fayalitic olivine and quartz have formed by pyroxene breakdown reaction (e.g., $2FeSiO_3$ (ferrosilite) = Fe_2SiO_4 (fayalite) + SiO_2). Aluminous orthpyroxene megacrysts are also found that have prominent exsolution lamellae (indicative of slow subsolidus cooling) and are inferred to have formed around 0.6–1.1 GPa (18–30 km; Emslie et al. 1994). Citing that these orthopyroxene crystals have slight negative Eu anomaly, matching the positive Eu anomaly of the anorthositic plagioclase, Emslie et al. (1994) suggested that these two minerals may have formed along a cotectic (i.e., Ol + Opx = L) at depth. This is important because this would suggest that the original parent magma in which the plagioclase crystals accumulated was a noritic magma.

Although Emslie et al. (1994) included basaltic rocks in their anorthosite group, these rocks are plotted separately in Fig. 12.12 as they have distinctly different isotopic compositions. Based on chemical and isotopic compositions of the granitoids, such as the high $^{87}Sr/^{86}Sr$- initial ratio (called I_{Sr} by Emslie et al. 1994), negative values of ε_{Nd}, and very high Ba and K_2O, these authors concluded that the granitoids were generated by crustal anatexis (melting) and are not at all related to the magmas that produced the other groups. The mafic rocks and one highly magnesian sample (21.7 % MgO) all have elemental and isotopic composition of melts that are closest to that of the upper mantle; anorthosites appear to be somewhat contaminated by the continental crust. There is a broad overlap in isotopic composition of all three groups, which led Emslie et al. (1994) to believe that all three groups received melting components from the crust and mantle; however, this was not a case of simple mixing, and they presented a model that we discussed before.

Some Notes on Two Other AMCG Massifs

Laramie Anorthosites (USA)

The topic of AMCG complexes is vast, and there are similarities and differences between them. Although we have discussed the Nain complex, there are others that are very interesting. Consider, for example, the 1.43-million-year-old Laramie anorthosite complex in Wyoming (USA) that was emplaced in Archean rocks at perhaps mid-crustal levels (Lindsley et al. 2010). This complex has very well-preserved layered cumulate structure, scour

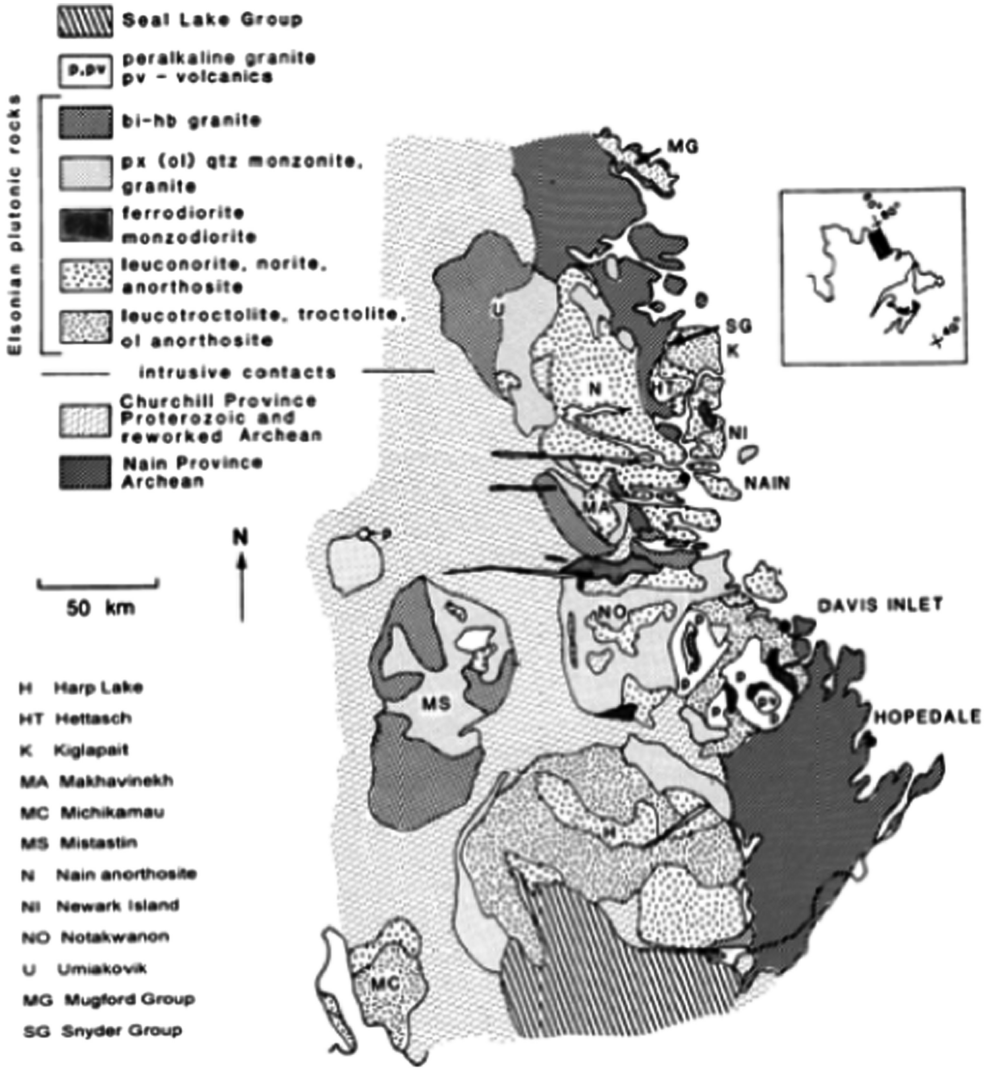

Fig. 12.10 Map of the Nain anorthosite complex (Labrador) (Emslie et al. 1994)

structures, settled blocks, and other primary magmatic structures, which have been superbly documented by Scoates et al. (2010). As the cross section in Fig. 12.13 shows, the northern Poe Mountain complex (part of the Laramie complex) is dominantly composed of layered anorthosites and has a thick layer of recrystallized anorthosite, which is stratigraphically followed upward by a layered zone composed of leucogabbros. Troctolite, olivine leucogabbro, granite, and ferrogabbro dikes cut through the lower anorthosite. Large Fe–Ti oxide mineral deposits occur in Sybille intrusion (see location in Fig. 12.13). There are also Fe–Ti–oxide mineral rich dikes that intrude the anorthosite.

The Poe Mountain complex resembles layered intrusions that we have discussed in Chap. 6. The only difference is the huge volumes of anorthosite that occur here. Commenting on the strongly dipping layers of anorthosites and missing mafic interstices, Scoates et al. also found large plagioclase megacrysts, which were brought up from depth. This would indicate

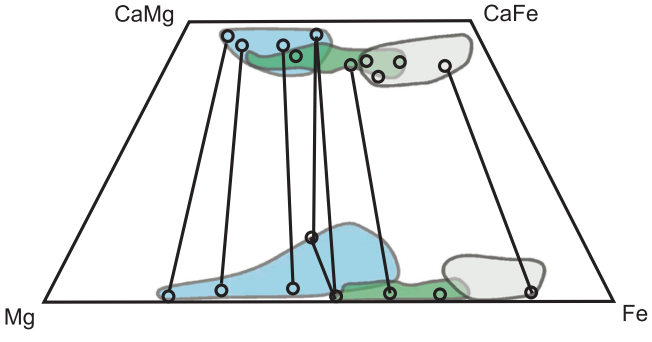

Fig. 12.11 Pyroxenes in the Nain complex (Emslie et al. 1994). *Blue*—anorthosites; *gray*—granitoids; *green*—ferrodiorites. Tie-lines of coexisting pyroxenes are also shown

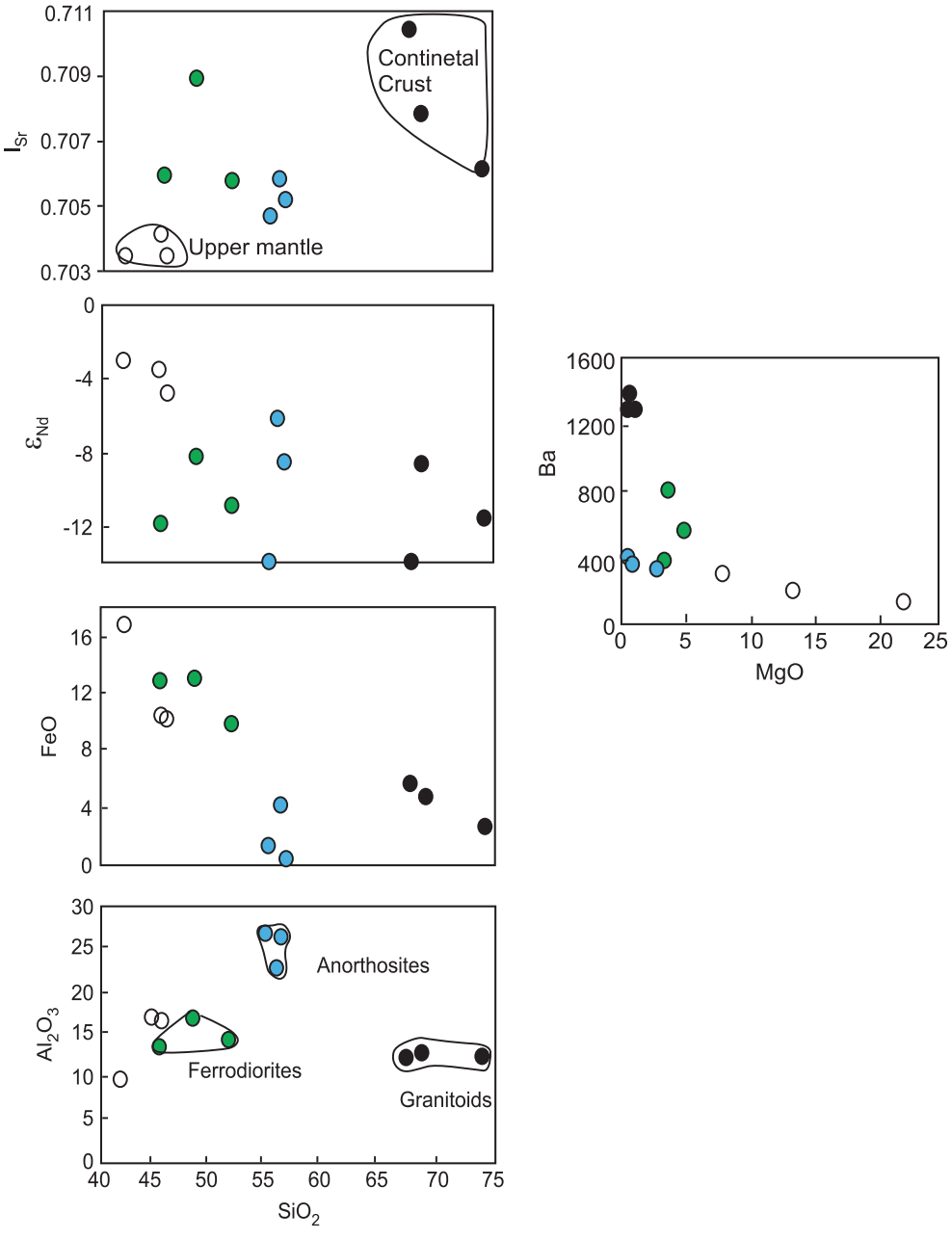

Fig. 12.12 Chemical composition of the various rock groups from the Nain complex are plotted in these diagrams (Emslie et al. 1994)

that the magma was saturated with plagioclase during emplacement. Scoates et al. (2010) suggested that the missing mafic melts were drained out of the anorthosite layers, which grew in situ.

Eastern Ghats Anorthosites (India)

Textures shown by aluminous orthopyroxene megacrysts in the metamorphosed AMCG complex of the Bolangir Massif in the Eastern Ghats, India, are noteworthy as they relate to the original magma composition of the magma from which the anorthosite cumulate separated and to the depth of magma segregation. The orthopyroxene megacrysts are mantled by a symplectite intergrowth of less aluminous orthopyroxene and $An_{77–90}$ plagioclase. These anorthosites also contain inclusion-free garnet (almandine with 20 % pyrope in solution) crystals (Bhattacharya et al. 1998). These garnets possibly formed during metamorphism at mid-to-lower crustal levels (0.7–0.8 GPa, 25 km), at the depth where the anorthosite was emplaced.

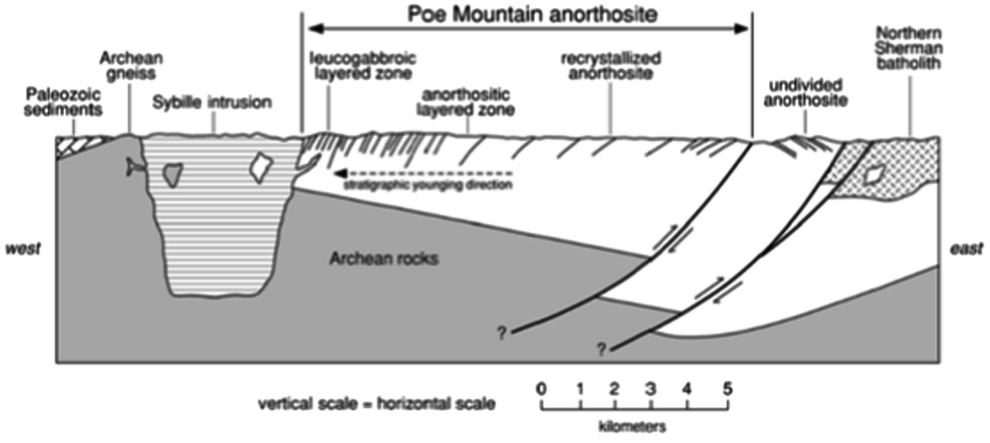

Fig. 12.13 Cross section of the Poe Mountain anorthosite complex (Scoates et al. 2010)

A detailed study of the trace element and Pb–Nd–Sr isotopic composition of the Eastern Ghats anorthosites from the Chilka Lake area by Chakrabarti et al. (2011) suggests that these anorthosites were derived from depleted mantle source and was contaminated by lower continental crust. These authors suggested that the source mantle was shallow (i.e., depleted asthenosphere). They suggested a model in which the anorthosites were emplaced between Antarctica and India during the separation of Rodinia supercontinent.

Some Final Comments

There are many interesting aspects of the Proterozoic AMCG complexes that are worth repeating:

- Their emplacement globally seems to have occurred over a short time and along at least two or three belts—two in the northern hemisphere and one in the southern hemisphere. This restricted occurrence in the Proterozoic suggests that their emplacement requires some special explanation. Among the various hypotheses proposed, the one that appeals to me is the one in which these belts represent collisional plate boundaries between two continents, where initial lithosphere thickening was followed by delamination of the mantle keel and passive upwelling of the asthenosphere, which generated the source magmas.
- The dominance of the anorthosites and preservation of igneous layering and textures is a telling sign that these plagioclase crystals separated from magma by some special mechanism. We have seen the case of in situ crystallization of plagioclase in Bushveld-layered intrusion. AMCG anorthosites are very different from Bushveld in lacking the voluminous interlayers of dense minerals (e.g., chromite). Thus, it is difficult to appeal to an in situ crystallization mechanism to generate such vast accumulations of plagioclase crystals. Therefore, crystal flotation offers the best explanation.
- The evolved and restricted range of composition ($An_{40–60}$) of plagioclase is important. It suggests that the crystals separated from a considerably evolved magma. The restricted composition is best explained by their flotation from an appropriate composition magma in which the plagioclase crystals were significantly less dense and easily floated to the top of such magma bodies. Figure 12.14 shows Scoates et al.'s (2010) calculation of density of basaltic magma at 0.3 GPa (9 km). This figure shows that $An_{40–60}$ plagioclase crystals can be slightly less dense than basalt magmas and thus float in basalt magmas at this pressure.

There are two additional factors that can increase the density contrast: pressure and Fe content of the magma. As liquids are more compressible than solids, the density of magma rapidly increases with pressure; Fe content

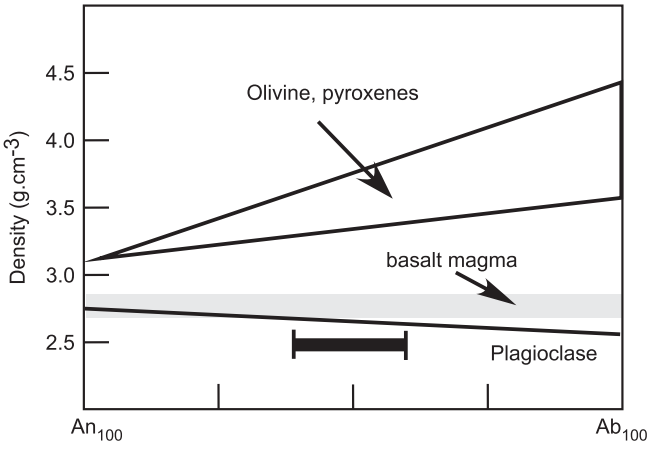

Fig. 12.14 Densities of plagioclase, olivine, and pyroxene compared with that of basalt magma at 0.3 GPa (Scoates et al. 2010)

has the same effect. Therefore, $An_{40–60}$ plagioclase will easily float in a more evolved basaltic magma at higher pressure. Most AMCG complexes seem to have been emplaced at 0.6–0.8 GPa. At such pressures, the "package density" of the mush carrying largely plagioclase crystals and very little interstitial melt will be buoyant, which will allow the mush to separate from the original magma chamber and rise as diapirs, finally emplacing at mid-crustal levels.

- The occurrence of high-Al megacrysts and more anorthitic plagioclase megacrysts in some AMCG complexes indicate that the anorthosite parent magma was a plagioclase + orthopyroxene-saturated magma, i.e., noritic magma at higher pressure. Also, it was high in CaO and Al_2O_3 so that so much plagioclase crystals could form. Its orthopyroxene saturation gives it a resemblance to some modern boninites, as has been pointed out by some authors. Longhi et al.'s (1999) experiments on evolved high-alumina basalt are quite relevant in this regard: Al–orthopyroxene crystallized at 1–1.3 GPa from such magma close to plagioclase saturation (Fig. 12.15a). Longhi et al. (1999) also noted that suitable anorthosite parent magmas lies along the plag + opx + aug pseudocotectic and also overlaps the thermal maximum that occurs around 1 GPa (Fig. 12.15b). These liquids lead to nepheline-normative compositions with further crystallization and cannot produce the noritic/troctolitic magmas seen in the massifs. Longhi et al. (1999) therefore surmised that mafic source is required for magmas parental to anorthosites and related mafic rocks and suggested that they could be in the lower continental crust or foundered mafic plutons. [However, the contribution from the crust is restricted by the isotope ratios (see further below)].
- The presence of very little interstitial melt in anorthosite mush suggests that the separation of mafic magma and mafic cumulates from the plagioclase cumulates was extremely efficient. The commonly accepted model that the mafic cumulates simply sank and mixed back into the mantle makes sense in this regard.
- Isotopic studies have shown that the granitoids associated with the anorthosites are largely derived from crustal melting, whereas anorthosites formed from mantle-derived basalt magma that underwent crustal contamination. Their overlap in age supports the idea that the melting regimes (one in the shallowest upper mantle and the other in the deepest crust) were in close proximity, and this in turn suggests that the heat of melting of the crust was provided by the basalt magma that ponded at the Moho.
- As an aside, I should mention that the origin of Fe-rich diorities has been a subject of some debate. Some authors suggest that these melts form as residual liquid from the melt that is parent to the anorthosites, and other authors suggest that they form by liquid immiscibility with the K-rich granitoids. In the latter case, the most evolved Fe-rich magma, residual from the anorthosite parent magma, would split into two conjugate liquids—granitoids and Fe-rich diorites.
- A general "flow chart" for the petrogenesis of various magmas in Proterozoic AMCG complexes, based on previous discussion, is shown in Fig. 12.16 (modified from Fig. 10 in Bhattacharya et al. 1998).
- Finally, it would seem that Proterozoic AMCG belts mark ancient collisional sutures or sites of continental separation.

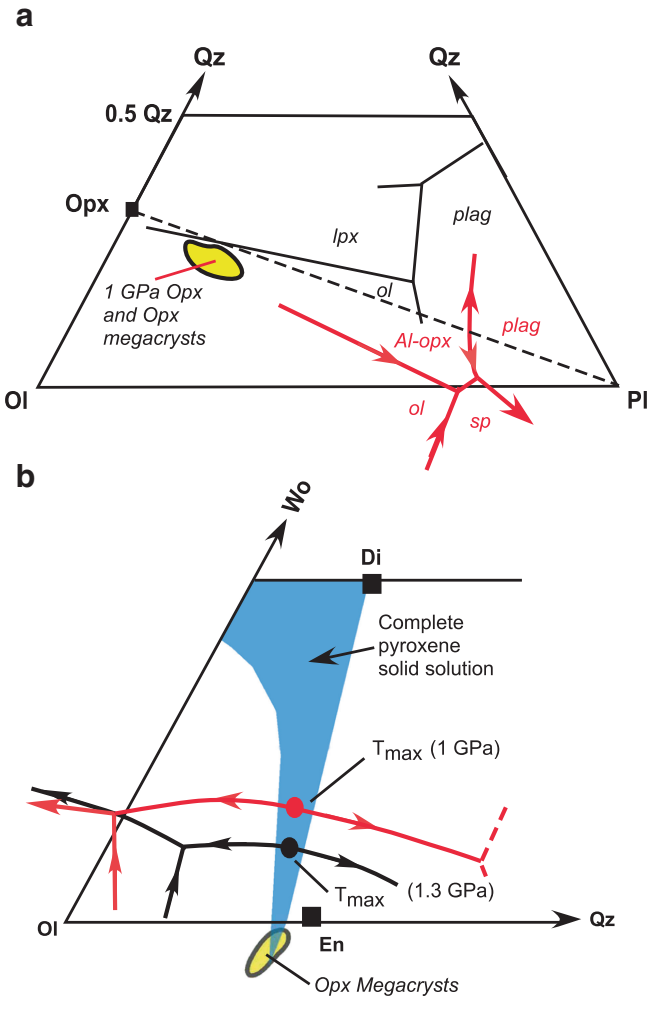

Fig. 12.15 1 GPa phase relations for a high-alumina basalt studied by Longhi et al. (1999) are shown in two different projections. (**a**) Olivine–plagioclase–quartz projection, which also shows that the Al–Opx crystals in the experiments plot close to the Pl–Opx line. (See text for further discussion.) (**b**) Wollastonite–olivine–quartz projection showing that at 1 and 1.3 GPa a pyroxene divide occurs on the liquidus between Cpx + L and Opx + L. The Al–opx plots on the divide. In all, both diagrams show that the experimental Al–opx crystals plot on or close to the divide Opx–Cpx–Pl

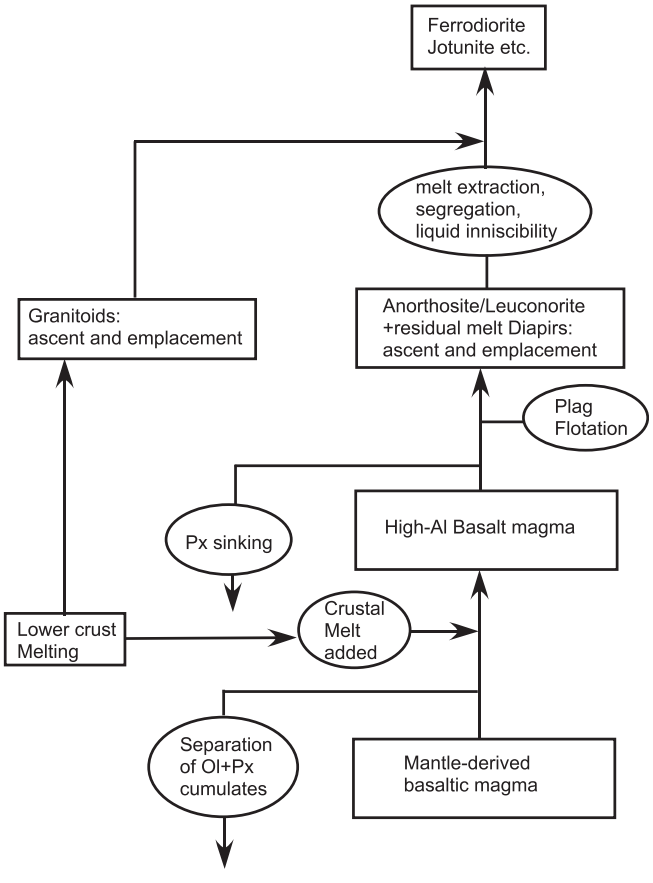

Fig. 12.16 A flow chart for the genesis of the AMCG suite (slightly modified from Bhattacharya et al. 1998)

Komatiites

Komatiites are 0.2–150 m thick ultramafic lavas and sills that are predominantly of Archaean age (Arndt et al. 2008). Some of the most famous occurrences are in the 3.5-Ga-old komatiites in the Barbarton Mountainland (South Africa), 2.7-Ga-old komatiites of Munro Township (Ontario, Canada), and Kambalda komatiites, Western Australia. The only Phanerozoic age (~89 Ma) komatiite has been found on Gorgona Island, off Colombia, South America (Serrano et al. 2011). Komatiites have 18–30 % MgO. All komatiites have been metamorphosed to some degree, and therefore, the extremely high MgO values (>25 %) have been suspected by a few authors to be a result of metamorphism. However, the composition of relict olivine crystals (>Fo_{90}) leaves no doubt that these magmas were ultramafic. Komatiite magmas had unusually high liquidus temperatures of ~1,600 °C at atmospheric pressure. For comparison, note that modern basalts erupt at about 1,100 – 1,200 °C.

Komatiites are recognized in the field on the basis of their "spinifex" texture (Fig. 12.17), which is defined by the presence of long (mm to dm) feathery or plate-like crystals of olivine or clinopyroxene set in a fine-grained matrix of skeletal crystals of clinopyroxene, chromite, and altered glass. In spite of having been

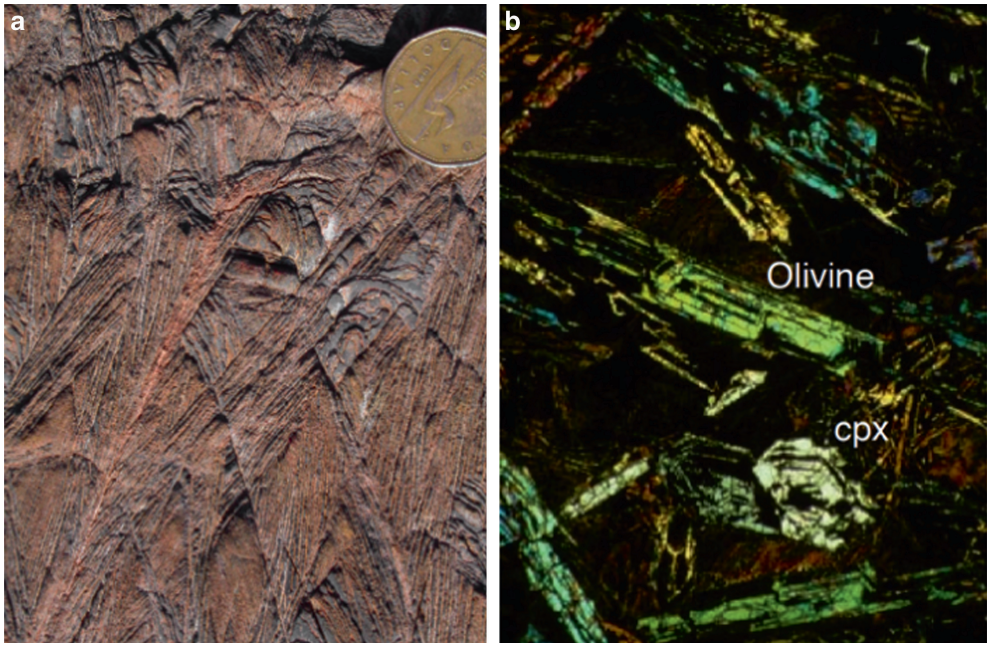

Fig. 12.17 (**a**) Spinifex structure in the field. (**b**) Spinifex olivine in thin section (crossed polars) (courtesy of N.T. Arndt)

metamorphosed, their texture is generally well preserved. Based on the chill margin rocks, it appears that komatiite magmas carried olivine phenocrysts at the time of eruption. The occurrence of spinifex texture in the interior of the lava flows and sills suggests that this texture developed during post-eruption cooling.

Figure 12.18 shows a schematic section of a komatiite flow that has an upper chill zone and a lower chill zone, a cumulate zone with highly forsteritic olivine crystals (up to Fo_{93}) at the bottom, an intermediate zone containing long platy olivine crystals where the spinifex structure is well developed, and an upper zone where the spinifex texture is more transient and the platy olivine crystals are shorter in length (after Faure et al. 2006). Faure et al.'s (2006) experimental study shows that such platy spinifex olivine forms under relatively slow cooling rate (1–5 °C/h) and a strong thermal gradient (7–35 °C/cm). The crystals grow perpendicular to the cooling front because the nutrients required for their growth is supplied from the magma in the interior of the lava flow.

Komatiites were extremely hot and dense (density of about 2.8 g/cm^3) magmas with extremely low viscosity (1–2 Pa.s). Normal basalt magmas are much more viscous (500–1,000 Pa.s). This combination of properties makes ascent and eruption of komatiite magmas through the lithosphere, and particularly lower density crust, a very interesting problem. It is believed that most komatiites were relatively dry (Arndt et al. 2008), and therefore volatiles played virtually no role either.

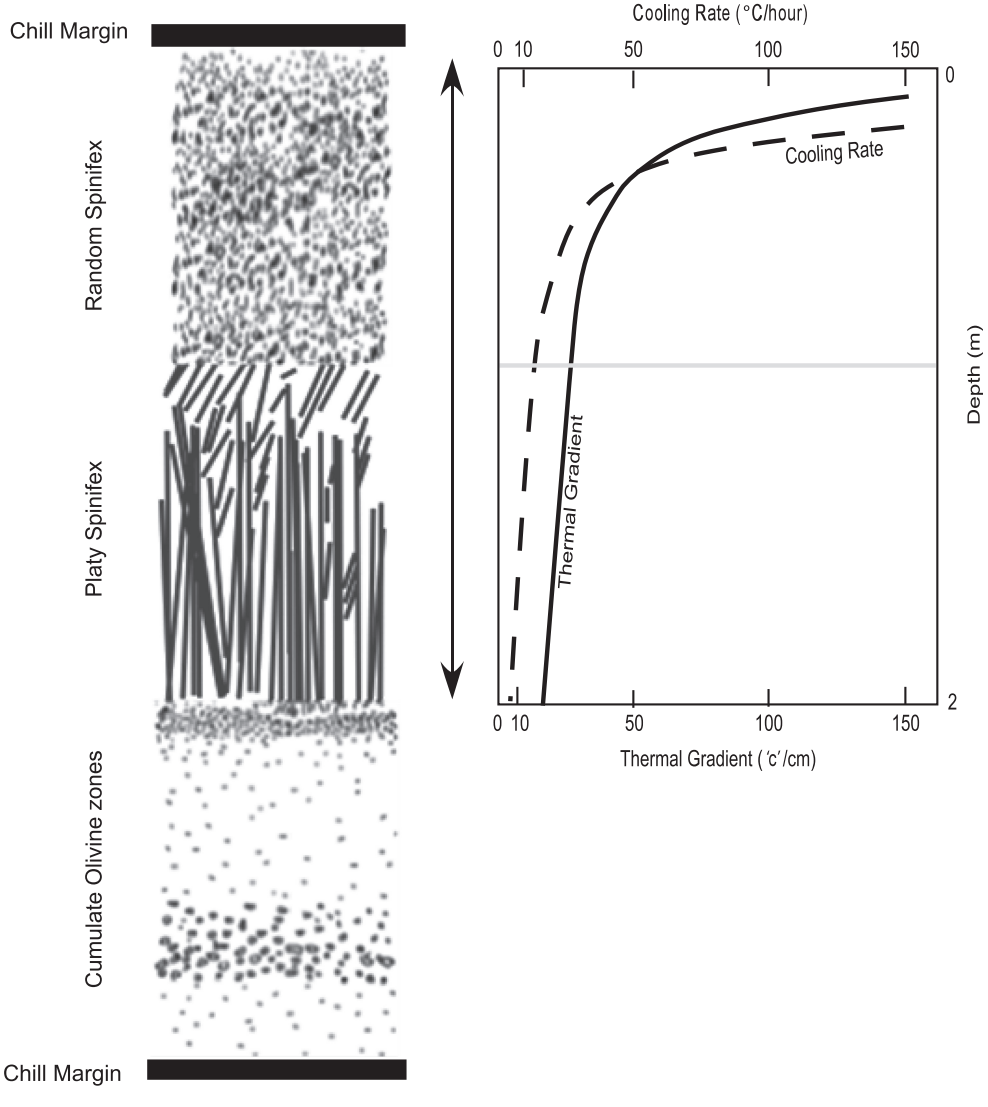

Fig. 12.18 Schematic cross section of a komatiite flow on the *left*. Cooling rate variation and thermal gradient in the flow are shown in the diagram to the *right* (Faure et al. 2006)

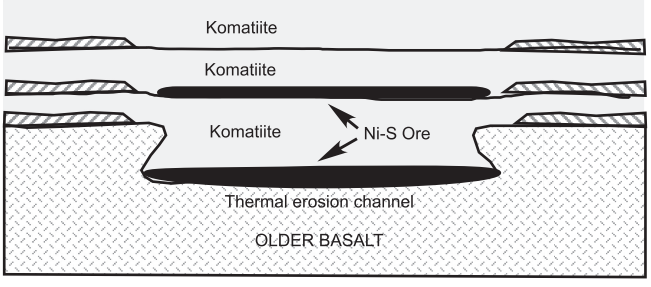

Fig. 12.19 Thermal erosion channels made by komatiite lava flows (Huppert and Sparks 1985)

Komatiites are known for their association with massive nickel–copper–PGE (platinum group elements) sulfide ore deposits; in fact, they comprise 14 % of the worldwide nickel production. Ni–S deposits in Kambalda (Western Australia) komatiites are very well known. At Kambalda, the erupting komatiite flows were hot and had high Ni contents, and they obtained the sulfur by thermal erosion of the S-rich sediments over which they flowed. The lavas then reached nickel sulfide saturation, at which time the latter separated as a liquid phase from the lavas and formed immiscible masses. Such immiscible liquid masses were heavy and settled at the bottom of the thermal erosion channels or at the base of the still-molten lava flow (Fig. 12.19; Huppert and Sparks 1985).

In general, three major chemical types of komatiites are recognized (Fig. 12.20)—the Al-depleted or Barbarton type, Al-undepleted or Munro type, and Al-enriched type. The 89-million year-old Gorgona Island komatiites seem to fall into two compositional types in terms of TiO_2 (Fig. 12.20a) and Al_2O_3/TiO_2 ratio and chondrite-normalized (Gd/Yb) ratio (Fig. 12.20b).

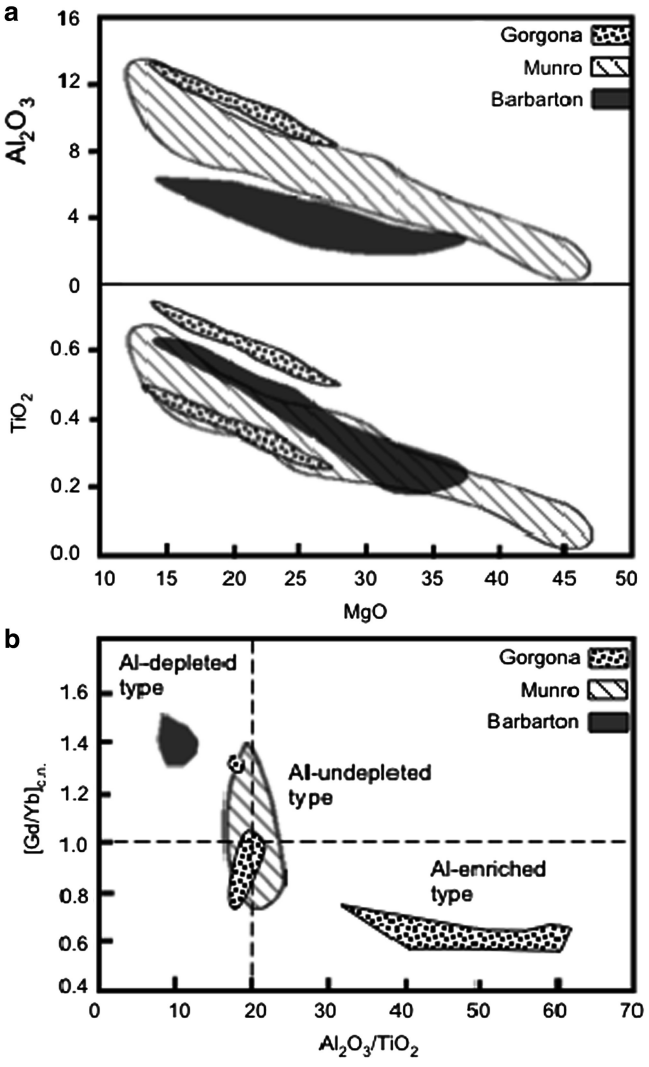

Fig. 12.20 Different Komatiite types are plotted on these diagrams (see text for details)

Significance of Komatiites

There has been much controversy about almost every aspect of komatiites—the environment in which they formed—plume, mid-oceanic ridge, or subduction, the *P–T* conditions in which the magmas formed, and how the magmas ascended to the surface. As stated in the above section, most authors believe that the magmas were dry (volatile free) and formed by large degree (50 % or more) melting of upper mantle peridotite at a very high temperature in the mantle.

Herzberg (1992) proposed a model in which different parts of a mantle plume supply all three komatiite magma types, with Barbarton type being the hottest (Fig. 12.21a). More recently, Robin-Popieul et al. (2012) have suggested an even higher *P–T* condition for the formation of Barbarton-type magmas. Their suggestion is based on two factors—(1) that the magmas would have last equilibrated with garnet + olivine + orthopyroxene (i.e., garnet–harzburgite) assemblage, which is required by their trace element chemistry and (2) the magmas formed by 50 % melting of the source peridotite (Fig.12.21b).

In contrast, Parman et al. (1997) proposed that Barbarton-type magmas were wet, containing as much as 4–6 wt% dissolved H_2O. Their proposal is based on H_2O-bearing experiments they conducted at relatively low pressure, in which they managed to reproduce the chemistry of spinifex clinopyroxenes. There are many reasons to doubt their conclusion: for example, relict vesicles have not been found in the erupted komatiites.

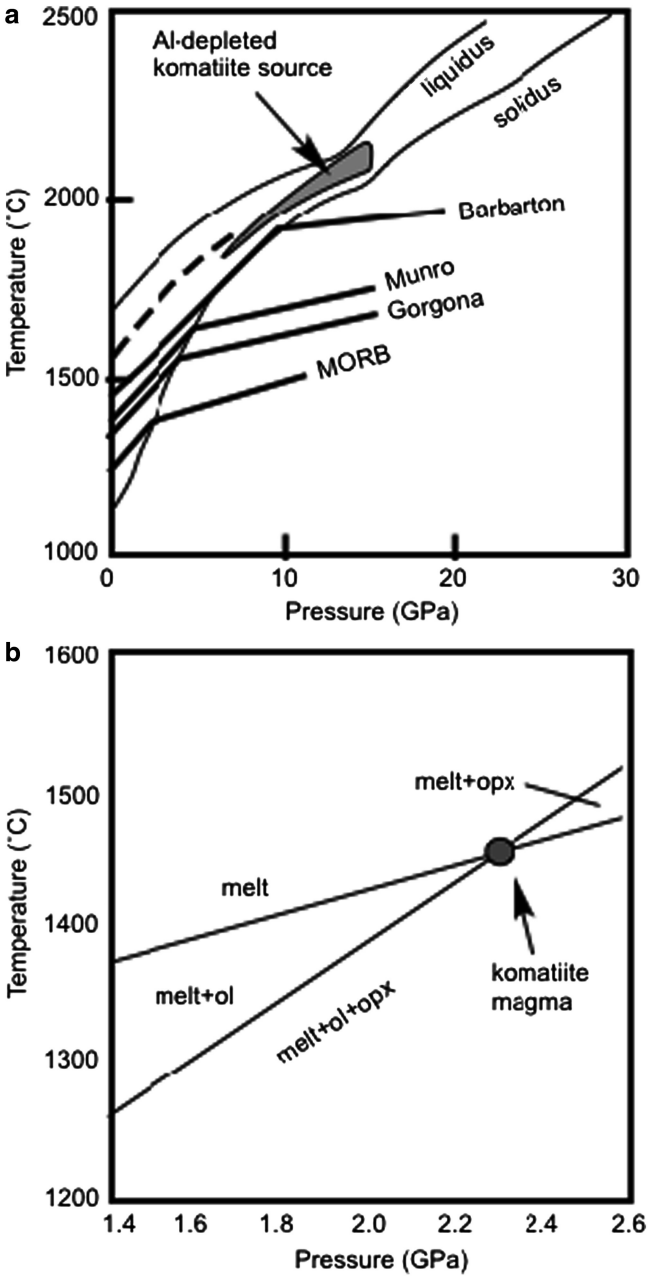

Fig. 12.21 (**a**) Ascent paths of various komatiite magma types are compared with the solidus and liquidus of upper mantle peridotite (redrawn from Herzberg 1992). (**b**) Phase diagram for Barbarton komatiite (Robin-Popieul et al. 2012)

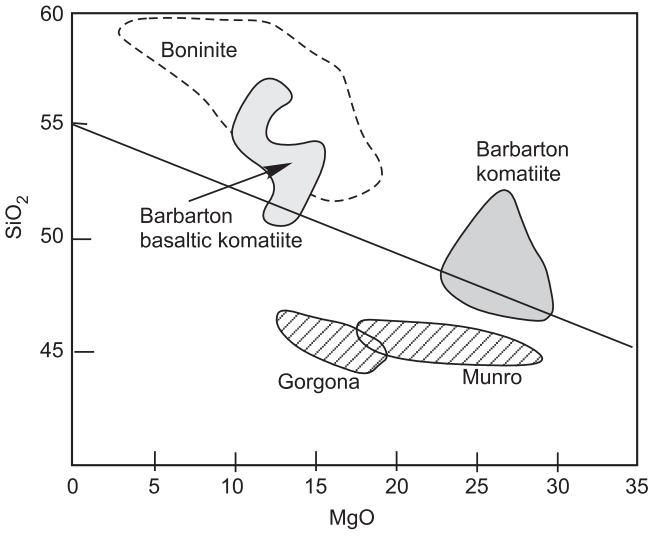

Fig. 12.22 MgO–SiO_2 variation among various komatiite types, compared with modern boninites (*source*: Grove and Parman 2004)

Also, their experimental melts did not have olivine on the liquidus—a requirement. Furthermore, Berry et al. (2008) found vapor-free glass (melt) inclusions in olivine in 27-Ga-old komatiite from Beligwe, Zimbabwe, that contain only −0.2 to 0.3 % H_2O. These authors also noted that Fe in the glass had not been oxidized, which would have happened if hydrogen were lost from the melt inclusion. On the other hand, Grove and Parman (2004) pointed to the relatively high silica content of Barbarton komatiites and associated komatiitic basalts (Fig. 12.22). Noting that the komatiitic basalts have similar silica to that of boninites found in modern island arcs, Grove and Parman (2004) proposed a subduction origin for them and invoked a hydrous melting model for the origin of Barbarton komatiites.

It is reasonable to conclude that komatiite magmas, especially the Barbarton-type, were extremely hot and dry magmas that erupted at 1,600–1,700 °C. They left behind a garnet–harzburgite residue. This gives an excellent constraint on the minimum pressure, which is about 4 GPa, based on Walter's (1998) experimental study. It should be noted that komatiite melt is denser than solid peridotite at a pressure greater than 13 GPa (Suzuki and Ohtani 2003), which means that komatiite magma would not have erupted if they formed from peridotite at or higher than 13 GPa. So, that can be taken as the maximum pressure where Barbarton-type magma started forming from its source. Walter (1998) proposed a pressure range of about 4–10 GPa for the beginning of komatiite magma formation. Such partially melted bodies would have ascended while continuing to melt. Somehow such melts segregated and formed larger pools that would eventually erupt. Finally, the high temperatures at which komatiite lavas erupted (1,600 ± 50 °C) were much higher than present-day MORB eruption temperatures (~1,200–1,250 °C). This is a reflection of secular cooling of the Earth's mantle.

In sum, the following general points can be made about komatiites:

- Komatiites are ultramafic lavas that mostly erupted during Archean times.
- They are characterized by spinifex texture, which results from skeletal crystallization of olivine and pyroxene.
- Komatiites were very hot (1,600 °C) and dry, and they formed by high degrees of melting of upper mantle peridotite.
- Three major chemical types of komatiites are recognized—the Al-depleted or Barbarton type, Al-undepleted or Munro type, and Al-enriched type.
- Komatiite magmas equilibrated with garnet harzburgite residue and indicate a deep origin (120–300 km) and large degrees (>50 %) of melting of the source.

Sediments

13

Abstract

Sediments include all loose (unlithified) solid materials that accumulate at or near the surface of the Earth. This chapter is about sediments from which sedimentary rocks are derived.

Introduction

Sediments and sedimentary rocks together comprise about 66 % of the exposed crust. These particles are either derived from preexisting rocks through weathering processes, direct chemical precipitation (e.g., from seawater), or skeletal remains of organisms (Fig. 13.1). Transportation processes are diverse and depend on the environment of origin and various factors on the Earth's surface such as climate and tectonic forces. Sediments can be deposited in a variety of subaerial and subaqueous environments. Following deposition, sediments are ultimately converted to sedimentary rocks by transformation processes known as diagenesis, with lithification (i.e., transformation into rock) as one of the most obvious changes. Temperature during diagenesis does not exceed a temperature of ~200 °C, beyond which it is metamorphic regime.

Sediment Production: Weathering Processes

Prolonged exposure of rocks to the atmosphere causes them to gradually breakdown into smaller pieces either by mechanical action (*mechanical weathering*) and/or by chemical reactions (*chemical weathering*). Both are irreversible processes. Chemical weathering produces new minerals, such as clays. The rate of weathering processes varies depending upon the nature of the source rock and the environment in which it is taking place (discussed further below). The term *erosion* is generally used to include mobilization processes that move the particles generated by weathering from the source area to a different site. Glaciers, rivers, and wind are all important vehicles for transporting sediments from one location to another.

How important is weathering? Weathering breaks down rocks and produces the residual particles, called *regolith*, which may accumulate as sediments, which eventually become sedimentary rocks. Sediments (soil included) play the most important role for the development of a vegetative cover on Earth, the production of oxygen in the atmosphere, and the carbon and nitrogen cycles—all of which are vital for sustaining life. Weathering is a slow process that, together with erosion, has the power to bring down the highest mountains in the world to nearly sea level. In a long range, by affecting mountains in such a way, weathering indirectly acts as the Earth's thermostat, because mountains are an important factor in controlling climatic patterns on Earth.

How Weathering Takes Place

Chemical weathering occurs because many rocks are unstable at the surface—a situation accelerated by rain water which, particularly with CO_2 of the atmosphere and from plants, launches a fierce attack on rocks to destabilize them further and eventually disintegrating

G. Sen, *Petrology*, DOI 10.1007/978-3-642-38800-2_13,

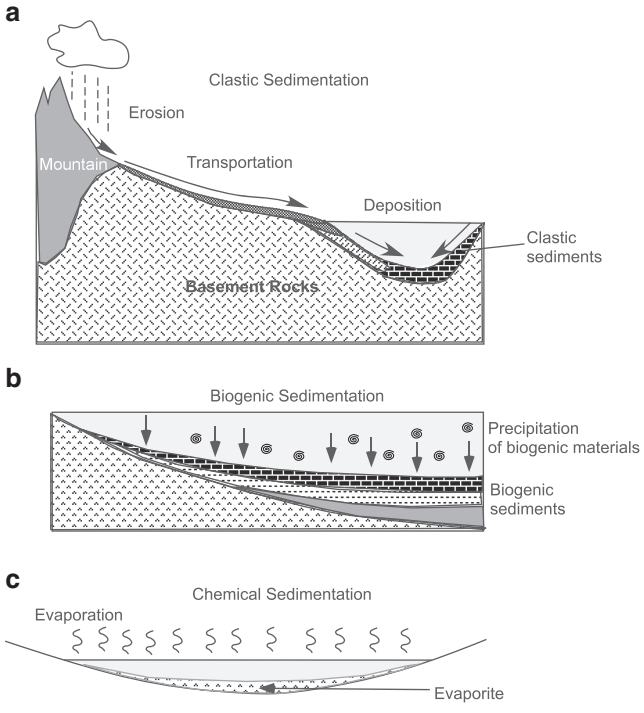

Fig. 13.1 Schematic representation of three types of sedimentation

them completely. Mechanical weathering (also called *physical weathering*) processes reduce the rock into smaller fragments without altering its chemical composition. Biological processes can also lead to weathering of rocks, but their effects are less significant as compared to mechanical and chemical weathering processes. Mechanical and chemical weathering generally operate together, because the former process increases the surface area in the rocks through cracks where reactive solutions can then penetrate and chemically alter the rocks more efficiently.

Examples of Mechanical Weathering

Mechanical weathering can occur in a number of ways. For example, in colder climates, water may seep into cracks in rocks and freeze. Ice has a 9 % greater volume than water, and therefore, when the water inside a crack turns into ice, it expands and breaks the rock apart. This process is called *frost wedging*. Many freezing and thawing cycles like that can turn a large boulder of rock into a pile of rubble. Frost wedging is also responsible for damaging freeways and water pipes of houses in cold regions.

Another example of mechanical weathering is *exfoliation*, which occurs when a plutonic rock (mostly granitoids) is exposed at the surface via erosion and removal of overlying rocks. Such exposed rocks develop parallel sheets of curved fractures along which the rock eventually peels off like onion skin. This happens because when the pressure on the rock from the overburden is removed, the rock naturally attempts to expand in volume, which then results in the development of concentric fractures. This type of weathering is also called *spheroidal weathering* because they generally result in spheroidal boulders.

Examples of Chemical Weathering

Chemical weathering processes are highly variable; they include *oxidation*, *hydrolysis*, *dissolution*, and other types of chemical reactions. *Oxidation* is a type of chemical reaction in which oxygen combines with a metal and makes a metallic oxide. Rusting of iron is an example of oxidation in which iron reacts with oxygen and forms hematite:

$$4Fe + 3O_2 = 2Fe_2O_3$$

Hydrolysis requires the presence of water. It involves a chemical reaction in which H^+ and $(OH)^-$ ions replace various cations in a mineral, thereby transforming it into a different mineral. Hydrolysis is responsible for converting feldspars, a dominant mineral in the Earth's crust, into clay minerals. One such reaction is shown in the example below, in which the white clay, called *kaolinite* (used in making pottery and china), is formed at the expense of K-feldspars by hydrolysis:

$$\underset{\text{K-feldspar}}{2KAlSi_3O_8} + 2H^+ + 9H_2O = \underset{\text{Kaolinite (clay)}}{Al_2SiO_5(OH)_4} + \underset{\text{silicic acid}}{4H_4SiO_4} + \underset{\text{K ion (in solution)}}{2K^{2+}}$$

Thus, granite, composed dominantly of quartz and feldspar, will eventually decay into loose quartz-rich residues as feldspars are all altered into clays and removed by, say, rain and wind; and other dissolved ions are removed by meteoric water.

Formation of acids by reaction between rainwater and atmospheric carbon dioxide, sulfur or nitrogen gases are particularly effective in accelerating weathering. The following reaction shows how carbonic acid (in acid rain) is formed:

$$CO_2 + H_2O = H_2CO_3 = H^+ \cdot CO_3H^-$$

An interesting example of weathering by carbonic acid may be observed by dropping a fingernail into a bottle of carbonated drink. Watch how long it takes for the fingernail to get totally dissolved!

Factors that Affect the Rates of Weathering Processes

1. *Nature of rocks and minerals*. Rock composition plays an important part in weathering because the mineralogy of some rocks is more amenable than others to certain types of breakdown mechanism. Goldich presented a flow chart that indicates how susceptible common rock-forming silicate minerals of the crust are to chemical weathering (Fig. 13.2). The sequence in which minerals are arranged is essentially a reversed order of Bowen's reaction series, with quartz being the most stable mineral (i.e., least susceptible to weathering) and olivine and calcic plagioclase being least stable (i.e., most susceptible to weathering).

   This concept is generally correct, but one should bear in mind that the stability of a mineral depends on dissolution rates, which vary from one environment to the other. For example, while quartz may be extremely stable in most sedimentary environments, it may rapidly dissolve in strongly alkaline waters, because silica is unstable at pH $\geq$ 9.

   During chemical weathering, feldspar alters to clay minerals, commonly smectite or illite, silica is released in solution, and the alkali ions are carried away in solution. Granite, for instance, may get completely altered to sediments rich in clay and quartz. Similarly, olivine alters to serpentine and iddingsite. An ultramafic rock, such as a dunite, composed largely of olivine, may become serpentinite. *Thus, the source rock exerts the primary control on the composition of the sediments*.
2. *Climate*. A rock usually weathers much faster in wet tropical climates than in dry arid areas. This is related to the facts that (a) the chemical and biological reactions associated with weathering are faster at higher temperature and (b) the bipolar structure of a water molecule makes it an effective agent for chemical weathering. In cold or arid areas, physical weathering may be active, but chemical weathering is minimal. For instance, century-old tombstones made of same types of rock in cold regions may be cracked, but the inscriptions are generally readable. In contrast, in humid areas, tombstones of similar ages would be smoothed and worn down by chemical weathering to the extent that the inscriptions would be illegible or totally erased.
3. *Structural weaknesses*. Rocks with well-developed joints or fractures are more amenable to weathering as they offer greater exposed surface area to the weathering agent. Thus, slate, a fine-grained, low-grade, metamorphic rock with extremely well-developed rock cleavage will break off along those planes of weakness during weathering. Under the same conditions, massive granite with little or no fractures may suffer minimal weathering compared to the slate.
4. *Topography*. The topography of the source rock area (generally defined *provenance*) dictates to a great extent the effectiveness of weathering and transportation processes. For example, in extremely rough terrains, where the topography is composed of steep hills and deep valleys, mass movement processes, such as landslides or rockfalls, are very effective in uncovering subsurface rocks and exposing them to weathering agents.
5. *Soil cover*. Regolith and soil cover may create an environment that is rich in reactive chemical solutions. In addition, the vegetative cover and associated bacteria and burrowing organisms further sustain an environment that is highly conducive to weathering. Thus, a rock with a soil cover may weather faster than a bare rock. In regions of steep topography, soil cannot remain stable on the slopes and is easily removed by erosional processes, and thus chemical weathering is slower.
6. *Time*. The longer a rock is exposed to the atmosphere, the more altered it becomes. A case in point is the fact that the highest peaks of older mountains (e.g., the Appalachian Mountains) are much lower than the peaks of younger mountains (e.g., the Rockies and the Himalayas). Using sophisticated dating and experimental techniques, geologists have been successful in measuring weathering and erosion rates of mountains of all ages. Similarly, by measuring the rate at which rivers carry loads of sediment from mountain peaks to lower grounds, scientists have been able to provide some estimate of the rates at which these mountains are eroding. On average, it seems that beveled-down continents are eroding at rates of about 0.03 mm per year. Mountains may erode at a much faster rate (0.2 mm per year).

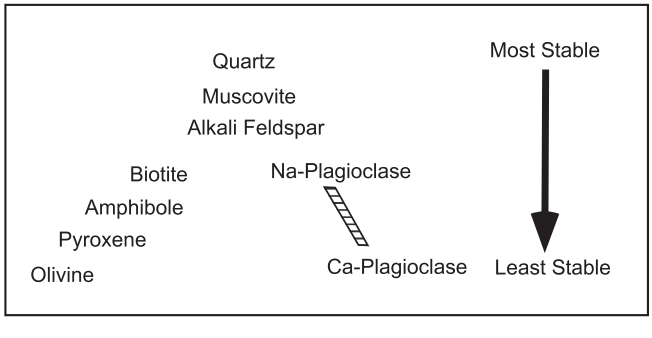

Fig. 13.2 Goldich's flow chart indicating general stability of minerals in sedimentary environments: a mineral lower in the series is less stable than a mineral higher in the series. Quartz is the most stable mineral, whereas olivine is least stable

Products of Weathering

Weathering produces essentially two kinds of products—*dissolved ions* and *solid particles* (*regolith*). Dissolved ions include Na^+, K^+, Ca^{2+}, and Cl^-. Solid particles include fragments of the bedrock, stable minerals like quartz, or new minerals produced by weathering, e.g., clay minerals.

Soil is simply a type of regolith that has been processed by water and near-surface chemical biological reactions. Soil forms in situ at the highest rate in wet humid regions under topographic conditions where erosion may be minimal. The names *residual soil* versus *transported soil* are given to those that remain in situ versus those that have been transported from elsewhere. Under most suitable wet tropical climatic conditions, thick accumulations of residual soil can take about 400–500 years to form.

The color, composition, and texture of a soil cover may change from the surface down to its contact with the bedrock. Vertical sections (called *Soil Profile*: Fig. 13.3) through soil covers are often best exposed in roadcuts. In humid areas with thick soil cover, five distinctive soil zones, called *soil horizons*, can be identified. These horizons develop through time, depending on local climatic and physiographic

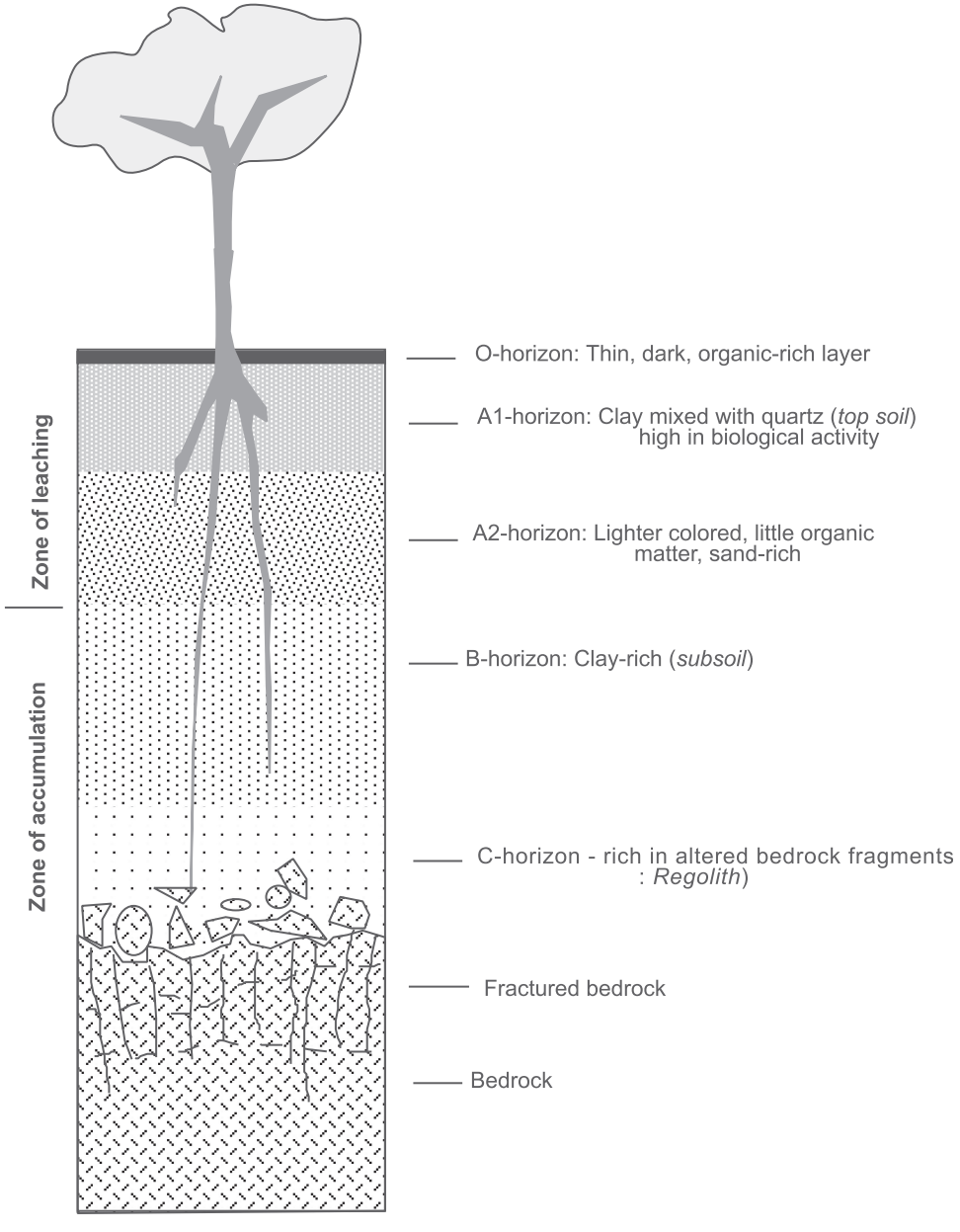

Fig. 13.3 A well-developed soil profile

conditions. At the top is the *O-horizon*, which is essentially the organic-rich topsoil where bacteria, algae, insects, and dead leaves are abundant. Below the O-horizon is the *A-horizon*, which is composed of inorganic residues and *humus* (a black, carbon-rich organic substance). The A-horizon downgrades into a lighter-colored *B-horizon*. Its lighter color owes to the general absence of dark organic matter. Water percolating downward through this zone also carries away ions and finer particles into the lower zones. B-, A-, and O-horizons are together called the *zone of leaching* because groundwater leaches out ions and inorganic materials from these zones and transports them to lower horizons, where clay particles removed from the overlying horizons are deposited. This horizon is also enriched in iron and aluminum. B-horizon is underlain by the *C-horizon*, which is composed of partially altered and fragmented bedrock. Part of the B-horizon and all of C-horizon together represent the *zone of accumulation* because all the leached materials from the overlying horizons accumulate at these levels.

Box 13.1: Paleosol and Evolution of Oxygen in the Atmosphere

Old soil dating back to some 3.5 Ga has been preserved in the rock record and is known as *paleosol*. Because climate and vegetation is closely tied to the chemical weathering processes that produce soil, paleosols have proved to be extremely useful as recorder of evolution of oxygen in the Earth's atmosphere. Red-colored soil gets its color from oxidation of iron to ferric oxide. One interesting discovery was that all red paleosol and red sedimentary beds are younger than about 2.2–2.4 Ga. Paleosols older than 2.4 Ga show evidence that iron was leached out of the soil as dissolved Fe^{2+} ions by surface waters. Fe^{3+} ions are not soluble in rainwater. The leaching of iron from >2.4 Ga paleosol and occurrence of younger red Fe^{3+}-bearing paleosol suggest atmospheric pO_2 jumped sharply at about 2.2–2.4 Ga (Fig. 13.4).

Paleosols are also useful indicators of locating past locations of continents and can be used for determining past atmospheric flow patterns. For example, we know that lateritic soil typically forms under relatively uniform maritime conditions on the windward side of continents

(continued)

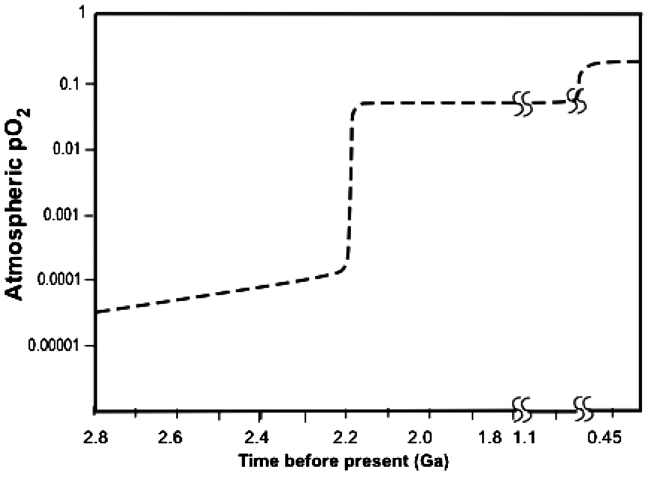

Fig. 13.4 Evolution of atmospheric oxygen (simplified from Rye and Holland 1998, American Journal of Science, Yale University)

Box 13.1 (continued)

under warm, humid conditions. Based on the occurrence of 80 Ma laterites in various continents and reconstructing paleogeographic positions of such continents, scientists have been able to reconstruct global wind flow patterns some 80 Ma.

Transportation and Deposition

The modes in which sediment is transported from source to the site of deposition may be *mechanical* (e.g., by a moving fluid), *chemical* (i.e., as dissolved ions), or *biochemical*.

Mechanical transportation includes processes by which loosened solid particles (called *detritus or clastic particles*, *or* "*clastics*") are physically picked up and transported by water, wind, or glaciers. It is by far the most important process in terrestrial environments and generally accounts for more than 90 % of the sediments transported by major river systems from continents to continental shelves. Gravity-induced mass wasting processes, such as landslides, rockfall, and submarine landslides (referred to as *olistostromal flows*) (Fig. 13.5), are also important mechanical transportation processes.

Transportation often induces two kinds of textural changes in the nature of the sediments, depending on the dynamics of the transport mechanism, travel distance, nature of the source rocks and minerals, and

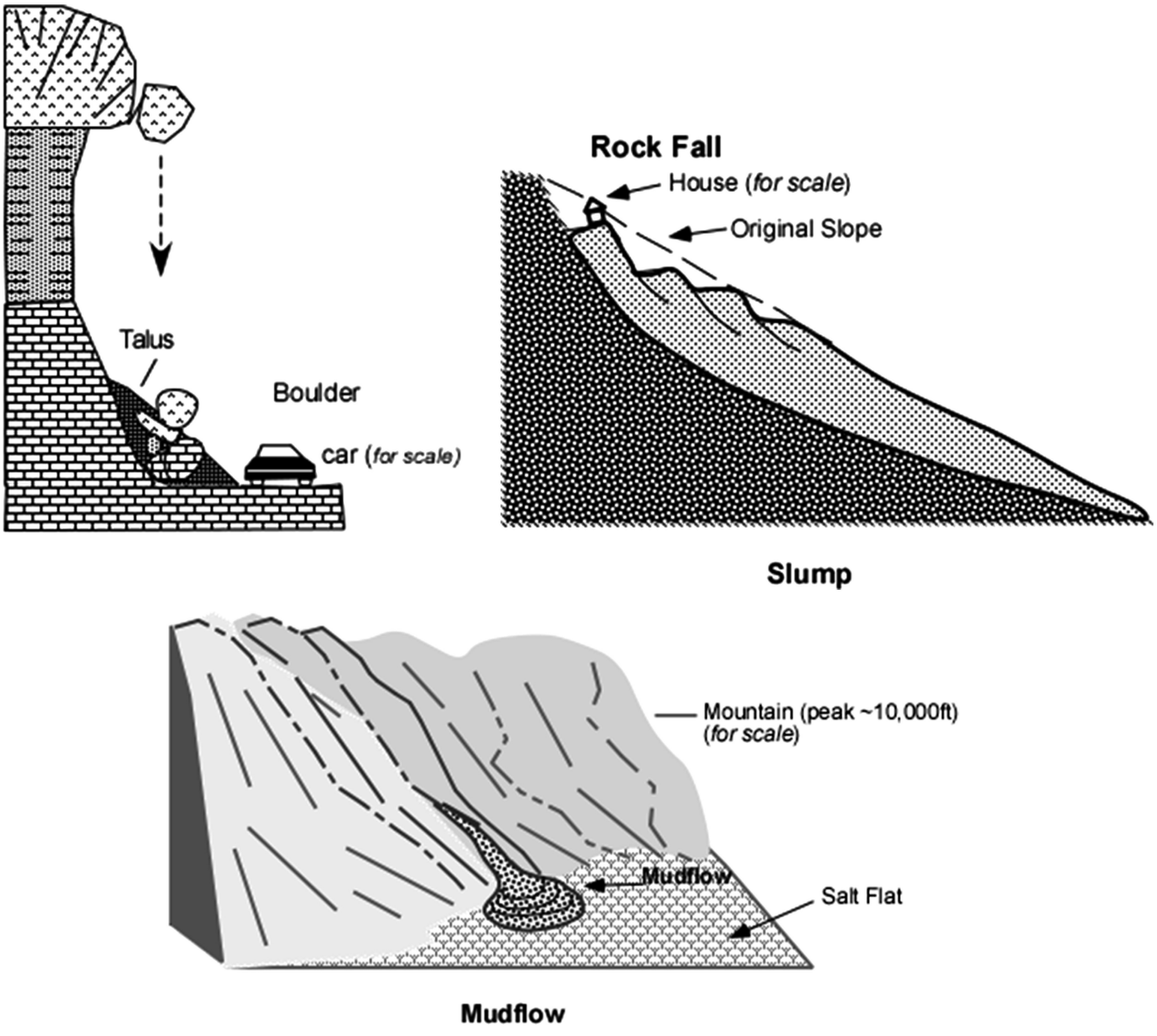

Fig. 13.5 Examples of mass wasting processes

initial grain size. The first change involves *grain size reduction and rounding of grains*: continuous knocking and grinding action due to collision of grains results in diminution of grain size and rounding of sharp edges and corners of detrital fragments. The second type of change is *sorting*, whereby the kinetic conditions of the transporting medium sort out grains according to size, shape, and composition (density), such that when these sediments are deposited, they may be distributed spatially according to these characteristics.

Figure 13.6 shows the relationship between nature (i.e., texture and composition) of transported detrital sediments and energy of the transporting medium. The term *maturity* is used to describe the sediments in terms of their sorting characteristics, roundness of grains, and percentage of clays present in the matrix. Long transportation of detritus and/or a dynamic transporting medium causes clays to be quickly removed from the larger framework grains, and the framework grains become well rounded and sorted through constant knocking and grinding processes. As a result, the sediments that have been transported in a dynamic environment (such as the beaches) are well sorted with rounded grains with very little intergranular clay. Such terms as "immature" to "supermature" are used to describe the degree of maturity of the sediment, where a supermature detritus

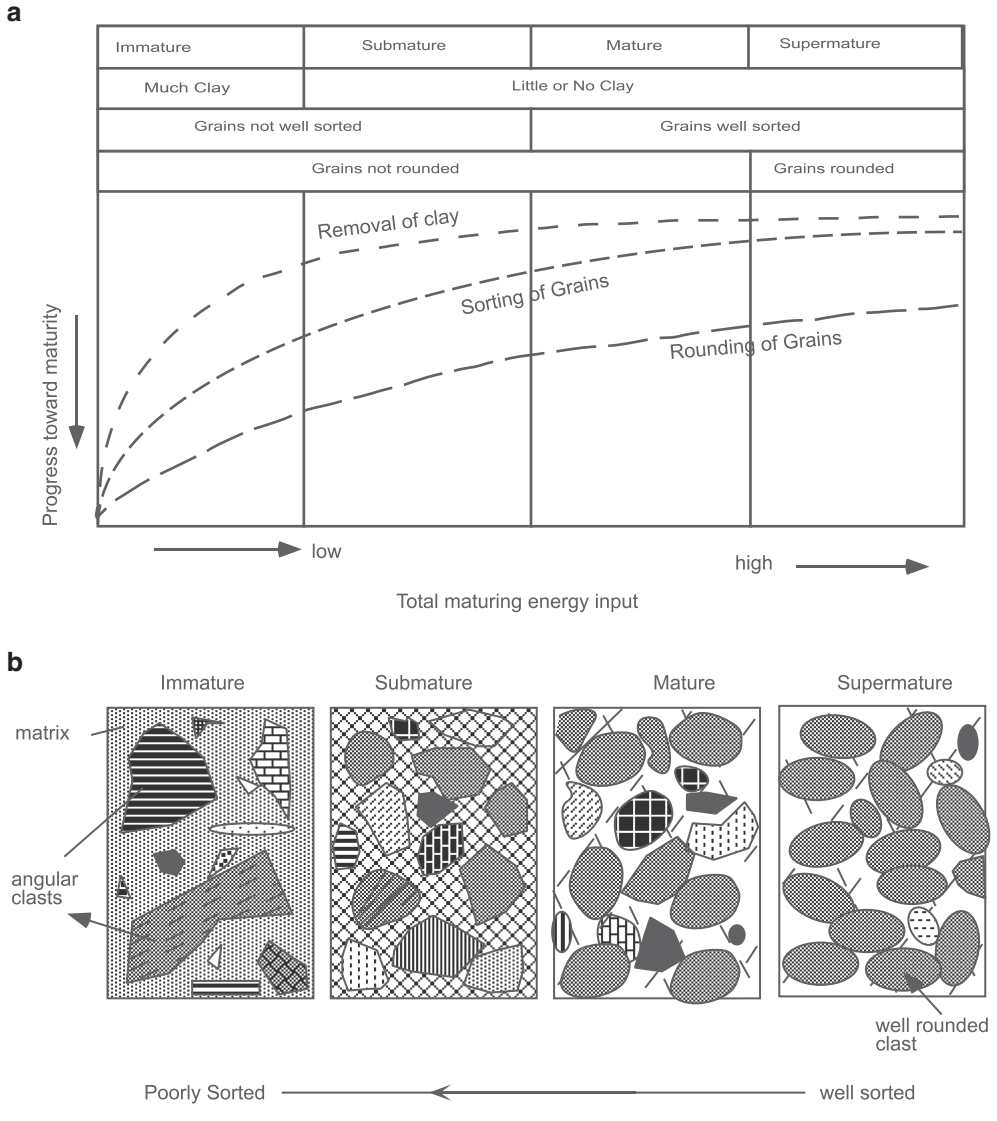

Fig. 13.6 The *upper panel* shows relationship between mineralogy, sorting, and other textural features of sediments and the kinetic energy of the transportation process. The *lower panel* is a schematic graphic representation of the nature of textures in sediments with varying degree of maturity

refers to well-sorted and well-rounded detrital grains (i.e., framework) with very little clay in the matrix, and an immature detritus is composed of poorly sorted, angular framework grains and an abundance of clays.

Because quartz is generally the most stable product of all weathering processes, a sand deposit composed of well-rounded quartz grains of nearly similar sizes (i.e., well sorted) points to its long transportation history during which the grains have gone through enough attrition and abrasion. In general, sand bars at the mouths of rivers carrying sediments over thousands of kilometers of distance are typically characterized by such well-rounded, well-sorted, quartz sands. Thus, the physical nature of a clastic sedimentary deposit can provide clues to its transportation history.

In *chemical transportation*, the transporting medium carries the sediment as a dissolved ion. A familiar example of this is the transportation of Na^+ and Cl^-, i.e., ions that form common salt, in seawater. Chemical transportation and depositional processes are affected by two factors—alkalinity (pH) and oxidation/reduction (or Eh). In nature, pH generally varies between 4 and 9, with 7 = neutral, <7 = acidic, and >7 = alkaline (Box 13.2). Ocean water normally has a pH of 8.1–8.3; water in desert playas (which are small lakes) has a pH $\geq$ 9. Rivers and streams in humid areas normally have pH between 5 and 6.5.

Eh is a measure of the oxidizing or reducing ability of a solution. Positive values of Eh mean oxidizing environment and negative values mean reducing

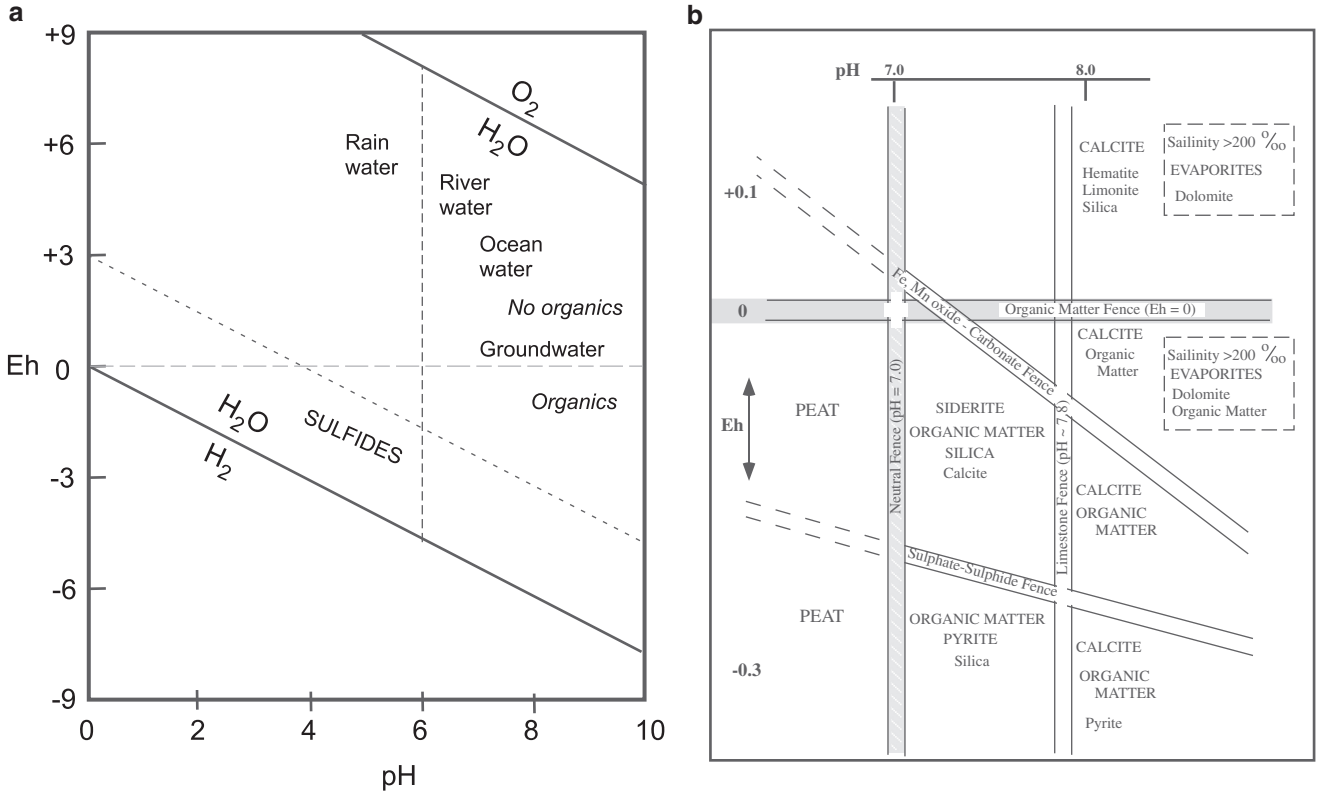

Fig. 13.7 (**a**) Eh–pH conditions of natural environments. (**b**) Eh–pH "fence diagram" showing stabilities of minerals in various sedimentary environments

conditions. Eh–pH variations in the natural system are shown in Fig. 13.7a. When this diagram is used with the Eh–pH "fence diagram" (Fig. 13.7b) of Krumbein and Garrels (1952), it becomes clear whether a specific type of material will be dissolved as an ionic solution or precipitated as a chemical precipitate. Let us consider the following example to see how this works: near the bottom of coastal estuaries or lakes, the water is strongly reduced with Eh <-0.2, and pH between ~7 and 8. The "fence diagram" indicates that in such an environment, pyrite and organic matter are stable and will be deposited. In fact, mud that accumulates in such environments is black (organic rich) and contains pyrite crystals.

Deposition of sediments occurs when the conditions are appropriate such that dissolved ions and transported particles can no longer be transported. Like transportation processes, deposition processes may be of three kinds: *mechanical*, *chemical/inorganic*, and *biological* (*organic*). Mechanical deposition of detritus is a very important process, which generally happens when the velocity of the transporting medium (river, wind, glaciers) drops, and its kinetic energy is no longer able to induce movement of the particles. Globally, the most voluminous sites of modern clastic sediment accumulation are at the mouths of about five rivers; and the thickest sediment accumulation is at the mouth of Ganga and Brahmaputra Rivers (India) in the Bay of Bengal (Fig. 13.8). These rivers have been transporting vast quantities of sediments derived from the Himalayas.

In *chemical* or *inorganic deposition*, dissolved ions are no longer able to stay in solution due to supersaturation caused by evaporation, temperature, or some other changes (say, Eh and/or pH) and are deposited as some mineral phase. For example, evaporation of water in a *playa* (i.e., desert pond or lake) results in supersaturation and deposition of salt (evaporite) on the playa floor, which is an inorganic deposition process.

Biochemical or organic depositional processes include those in which certain organisms (e.g., foraminifera, corals, and molluscs in the marine environment) secrete skeletons from dissolved ions, and when they die, their skeletal debris may accumulate on the bottom of oceans or lakes. Such deposits may be called *biogenic accumulates*.

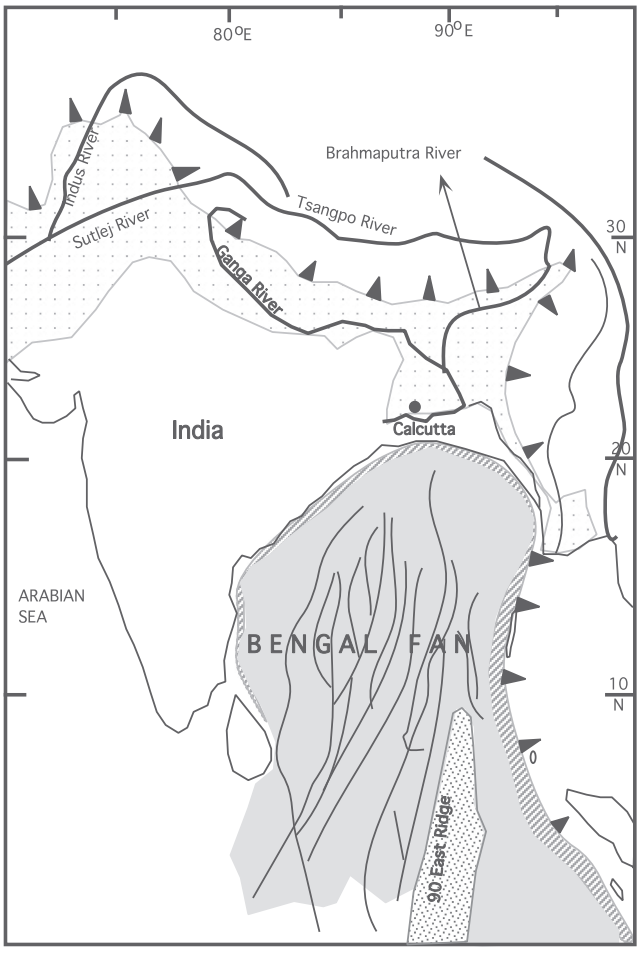

Fig. 13.8 Accumulation of sediments in the Bengal Fan at the mouth of the Ganga and Brahmaputra rivers in the Bay of Bengal

Box 13.2

pH can be explicitly understood in terms of the reaction:

$$OH^- + H^+ = H_2O$$

In a neutral solution, by definition, the concentrations of both H^+ and OH^- are equal to 10^{-7} *moles/liter* (*M*). The ionic product $[H^+] \cdot [OH^-] = 10^{-14}$ is constant at room temperature (25 °C) for all aqueous solutions, be it neutral, acidic, or alkaline. A 1N solution (N = "normal," meaning equivalents of acid or base per liter of solution) of a strong acid has 1 *M* H^+, a neutral solution has 10^{-7} *M* of H^+, and a strongly alkaline 1N solution has 10^{-14} H^+. Negative logarithm (base 10) of the neutral solution is 7, whereas that of the alkaline solution is 14, and

(continued)

Box 13.2 (continued)

so on. Therefore, the formal definition of pH is that *it is the negative logarithm of the hydrogen ion concentration in a solution*.

Eh:

Oxidation number or Eh represents the tendency of an element to oxidize or reduce in an aqueous environment and is expressed in terms of volts of electricity. The reduction of H^+ to H_2 is assigned to have a standard Eh value of 0 V. Eh increases in oxidation and decreases in reduction.

Nature of Accumulated Sediments

Composition

Sediments collecting at a depositional site may include clastic particles, inorganically or biogenically precipitated minerals, organically produced materials, and pyroclastic materials from volcanic eruptions. Clastic particles are easy to recognize, as they include fragments of preexisting rocks or mineral grains. Pyroclastic materials include volcanic ashes, blocks, or bombs that accumulate at a depositional site. However, when such materials are *reworked*, i.e., transported from the original site of deposition, then they become part of the clastic category. An example of chemically (inorganically) precipitated minerals is evaporite minerals (such as gypsum and halite) that form via evaporation of, say, waters in a desert playa.

Clastic or detrital sediments are classified according to their size (Table 13.1). Although the term *sand* is commonly (but erroneously) used to mean quartz grains, note that in geology, the name *sand is based on a specific size*. Similarly, the use of the term *clay* also *refers* to a particular size of sediments in engineering and causes a problem in geology because clays are a type of sheet silicate minerals.

We noted earlier that the texture and composition of a deposit of detrital sediments offers clues to its

Table 13.1 Classification of sediments based on size

Particle diameter (mm)	Name
>256	Boulder
256–64	Cobble
64–2	Pebble
2–1/16	Sand
1/16–1/256	Silt
1/256–1/4,096	Clay

transportation and deposition histories. For example, rapid transportation followed by quick deposition would result in a body of sediment that composed of poorly sorted mixture of all sorts of grain sizes and shapes. Sedimentary deposits of such character are in fact found in glacial environments and in landslide deposits. At the other extreme, long transportation followed by deposition of detritus by a river may result in a sedimentary deposit composed of mature sediments.

Sedimentary Structures

Internal Structures

Sedimentary deposits may develop structures that are indicative of the dynamics of transportation and deposition processes as well as biological and physical (mechanical)–chemical conditions within the depositional site. *Layering or stratification* is a first-order depositional structure that is common to almost all sediments. *Bedding* refers to a type of layering in which individual layers are more than 1 cm thick; and if each layer is less than 1 cm thick, then it is called *lamination*. Using a $\sqrt{10}$ scale (i.e., each smaller unit is $\sqrt{10}$ thinner than the next bigger unit), Ingram (1956) further classified beds and laminae into several types, as shown in Table 13.2.

Regardless of the thickness, layers are discrete units separated by individual planes. *Bedding planes* (i.e., planes between adjacent beds) may represent short changes in sedimentation rate, composition, or texture in an otherwise continuous sequence of sediments that produce the layers. Practically each unit is produced by a single episode of sedimentation. As Table 13.2 shows, the thickness of beds varies greatly and depends on sedimentation rate, duration of the depositional episode, and subsequent compaction. Rapid sedimentation produces thick beds, and compaction makes them thinner.

Table 13.2 Ingram's (1956) $\sqrt{10}$ scale of nomenclature of beds/laminae

Size of individual unit (cm)	Name
≥100	Very thick bed
31.6–100	Thick bed
10–31.6	Medium bed
3.2–10	Thin bed
1–3.2	Very thin bed
0.3–1	Thick lamina
<0.3	Thin lamina

Bedding (or lamination, depending on the size of individual layers, as discussed above) may be of several types, of which the fundamental ones are *parallel bedding* (*lamination*), *cross-bedding* (*lamination*), and *graded bedding* (*lamination*) (Fig. 13.9). In *parallel bedding*, bedding planes are *parallel* to each other. Parallel beds may be deposited from a fluid in a lower flow regime or in absence of currents. The term *varve* is used to describe a type of deposit with contrasting laminated couplets: for example, in glacial varves, light layers are silt, which are derived from the melting of the glacier during summer months; and the dark layers are organic-rich winter layers. Thus, the relative thickness of the two laminae in such couplets accumulated in a glacial lake is an indicator of the seasonal cycle: longer summer and short winter would result in thin dark laminae and thick light laminae and vice versa.

In *cross-bedding* (or current bedding), layers within an individual bed are inclined in the down-current direction. Cross-bedding is a characteristic feature of small grains of loose sediments deposited by a moving fluid. The slope and thickness of the inclined layers are controlled by the grain size of the sediments and the velocity of the current: in a fast flowing regime, coarse sediments will be deposited at a steeper angle.

Graded bedding is a general term used for any layer in which the grain size decreases progressively from the bottom to top of a single unit. A graded bed (or laminae) is a subaqueous deposit formed when a moving mix of detrital grains of various sizes carried by a density or turbidity current (these terms are explained later) loses momentum and the particles settle differentially by mass (coarse grains first) on the bottom obeying Stoke's law (which was discussed in an earlier chapter). Graded beds are often repeated in a vertical sequence, with each representing a different turbiditic event (see the next section on turbidity currents).

As we noted earlier, continental shelf–slope region at the mouth of a major river system is a prime depositional site for the detritus transported by such a system. Such sites undergo significant subsidence as more and more sediments accumulate and apply load pressure on the lithosphere. Sometimes an excessive supply of sediments (which may be due to heavy rainfall or excessive melting of the mountain glaciers that feed the river) or an earthquake may trigger subaqueous landslide (i.e., the slope fails). In such a case, a fast

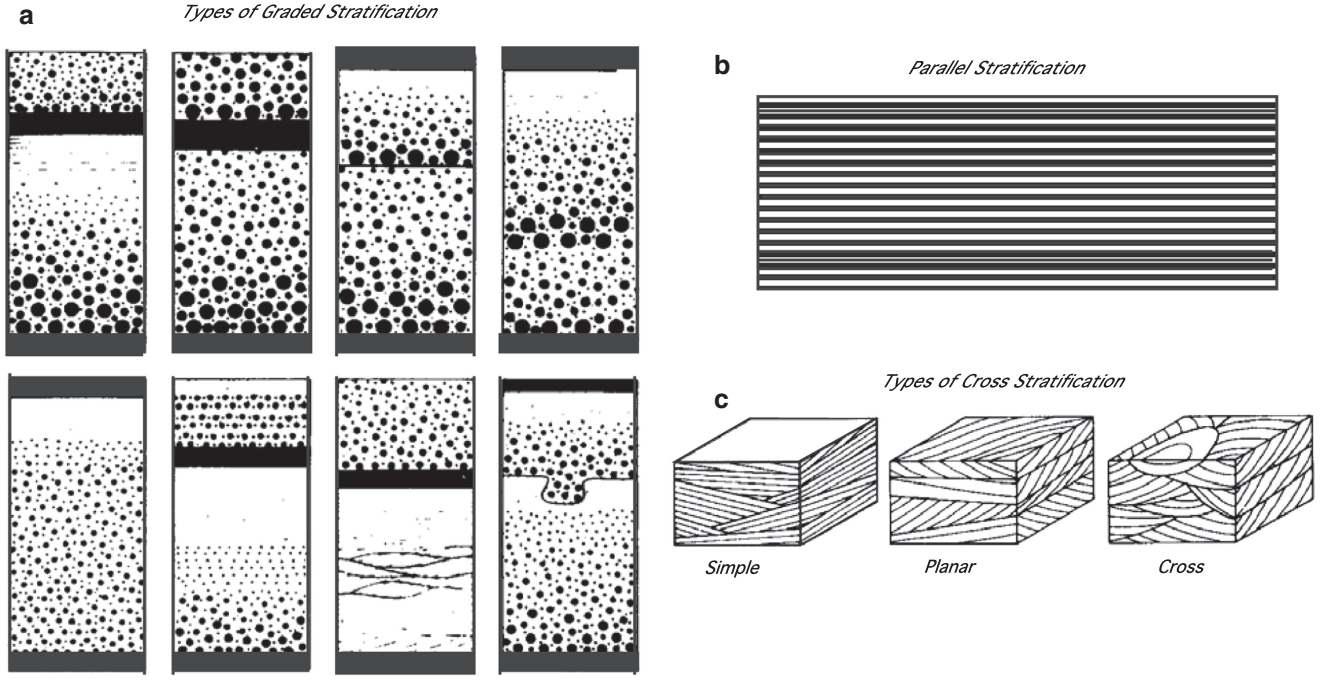

Fig. 13.9 Sedimentary strata. (**a**) Parallel laminae in a varve. (**b**) Cross-bedding in a sandstone. (**c**) Graded bedding

current, called *turbidity current*, driven by the water + detritus mixture moves down the continental slope. When such a current comes to rest, the sediments deposited from it may form a five-layer sequence, called the *Bouma sequence* (Fig. 13.10).

At the bottom of the Bouma sequence is a graded bed that has the coarsest particles at its base, and may also contain clasts ripped off the bottom. Within this unit, grains become finer upward and grades into a subunit of parallel laminated silt or sand. Above this unit is a cross-laminated silt or sand unit, which is successively followed upward by parallel laminated silt and clay. The Bouma sequence is typically found in submarine fans, which are enormous, fan-shaped submarine deposits off continental shelf and slope: a good example is the *Bengal fan* that occurs in the Bay of Bengal off the southern coast of eastern Indian and Bangladesh (Fig. 13.8).

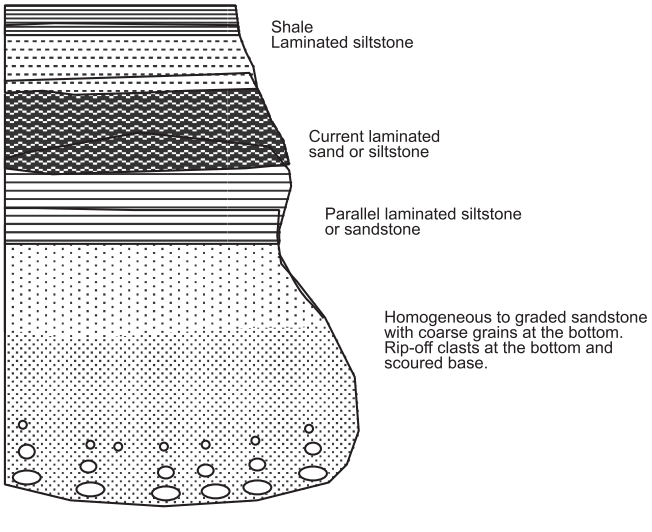

Fig. 13.10 Bouma sequence

In carbonate sediments, the following internal structures may be found: stromatolites and reefs. *Stromatolites* are much larger, internally laminated structures that can have a variety of forms—domal, conical, or irregular mounds (Fig. 13.11). These features developed due to trapping of sediments by algae growing as individual laminae. *Reefs* are domal to elongate structures built in situ by corals or other organisms. *Bioturbation* is a process caused by organisms burrowing into unconsolidated sediment. Burrowing organisms, like crabs and shrimps, often dig tubular structures (called *burrows*; Fig. 13.12) into the soft sediments, which may be so extensive that they may completely disrupt the original depositional layering. The term *bioturbated structure* is used to describe such disruption of primary depositional structure by burrowing.

Concretions (Fig. 13.13) are masses of mineral matter with spherical to subspherical or irregular shapes

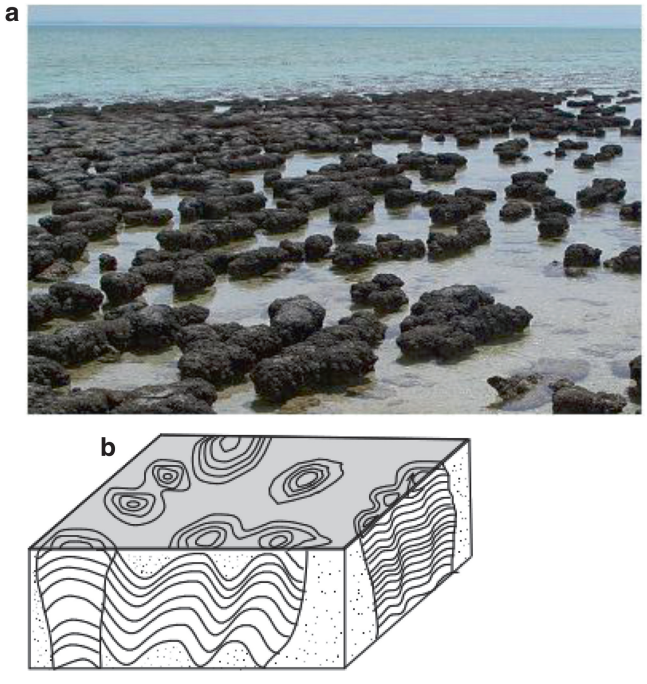

Fig. 13.11 Stromatolites

Fig. 13.12 Picture of fossilized burrows used as wall plaque on a house in a village near Salamanca, Spain

that are commonly characterized by a composition different from the surrounding rock. Fossils of plants and organic remains often make up the nucleus of concretions. Colored rings, called *liesegang rings*, develop different bands of colors due to oxidation and reduction and ion diffusion through a porous rock.

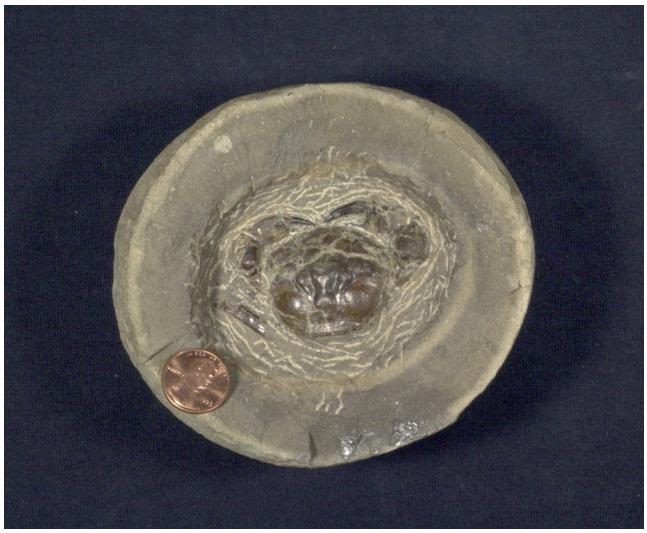

Fig. 13.13 Concretions

Surface Structures

Ripple marks are centimeter-scale undulations on the surface of a sedimentary deposit (Fig. 13.14). They may be formed by oscillating water waves and are called *oscillation ripple marks* or by unidirectional currents and are called *current ripple marks*. In highly deformed, folded sedimentary rocks, the pointed crests of oscillation ripple marks on bedding planes may help in deciphering the tops of beds. *Mudcracks or dessication cracks* are polygonal cracks developed in fine-grained sediments (clay to silt; Fig. 13.15). They form due to drying and shrinking from the surface. They can also be helpful as a top-determining criterion in highly deformed sedimentary rocks.

Oolites are small (<2 mm) egg-shaped grains with internal, onion-like, concentric laminae (Fig. 13.16). These typically form in shallow water and involve rolling of individual grains accompanied by chemical precipitation of calcium carbonates. Ooids can be deposited in a variety of environments (Fig. 13.17). Other similarly rounded structures include *fecal pellets*, which are essentially mud excreted by burrowing organisms.

Environments of Deposition

An important reason for studying modern sedimentary environments and their deposits is to be able to use that knowledge to reconstruct the paleo-environmental history recorded in sedimentary *rocks* now exposed on land. Such knowledge is vital (1) in understanding the

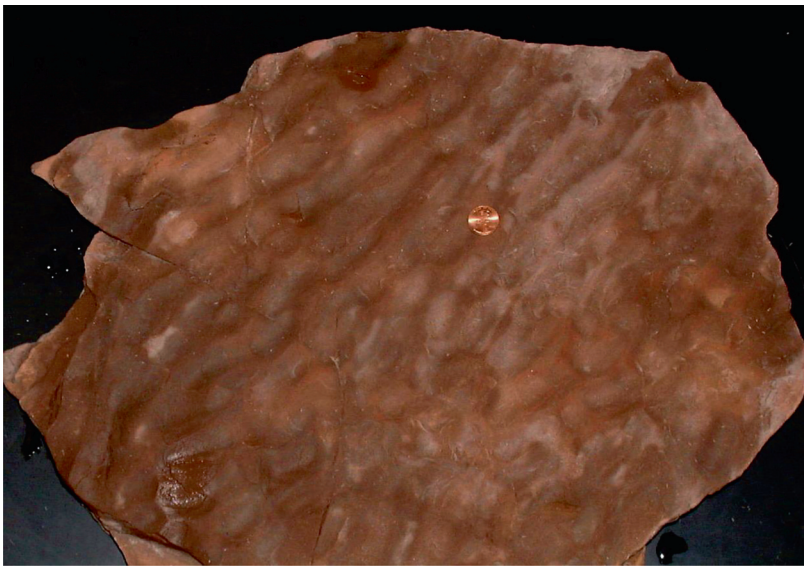

Fig. 13.14 Ripple marks

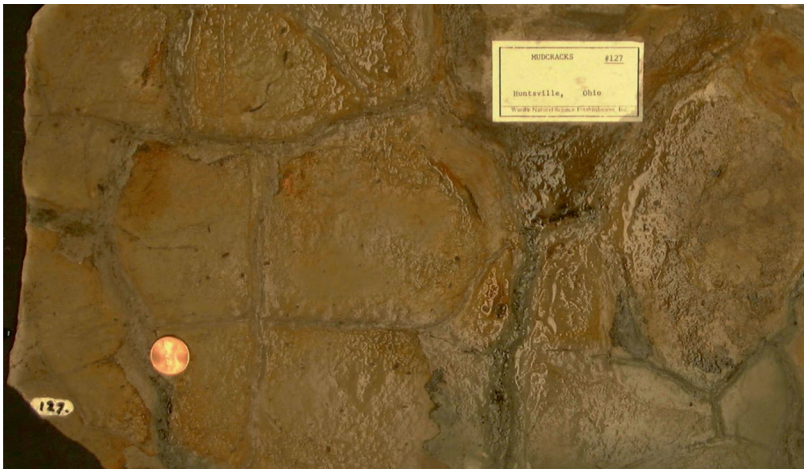

Fig. 13.15 Mudcracks

tectonic evolution of continents and oceans, (2) in deciphering global climate and air/ocean circulation patterns through time, and (3) in exploration for economic deposits (oil, coal, uranium, etc.) that occur in sediments deposited in particular environments.

Environments in which sediments are deposited may be grouped into three kinds—continental, marine, and transitional environments (Fig. 13.18). Continental environments include river, desert, glacial, and lacustrine (i.e., lake) systems on land. Transitional environments include deltas, offshore barrier islands, and lagoons along the coastal regions where marine environment comes in contact with continental environment. The transitional environment is of particular importance as two important natural resources, oil and coal, come from sedimentary rocks that are most frequently deposited in such environment. Marine environments include continental shelf, slope and rise, and abyssal plains.

Marine Environment

Table 13.3 gives a general summary of the various marine depositional environments and the nature of the deposits associated with them. In *marine environments*, the controlling factors, such as temperature, salinity, wave activity, and sunlight availability, are subject to a great deal of variability which is reflected in the types of sediments that characterize

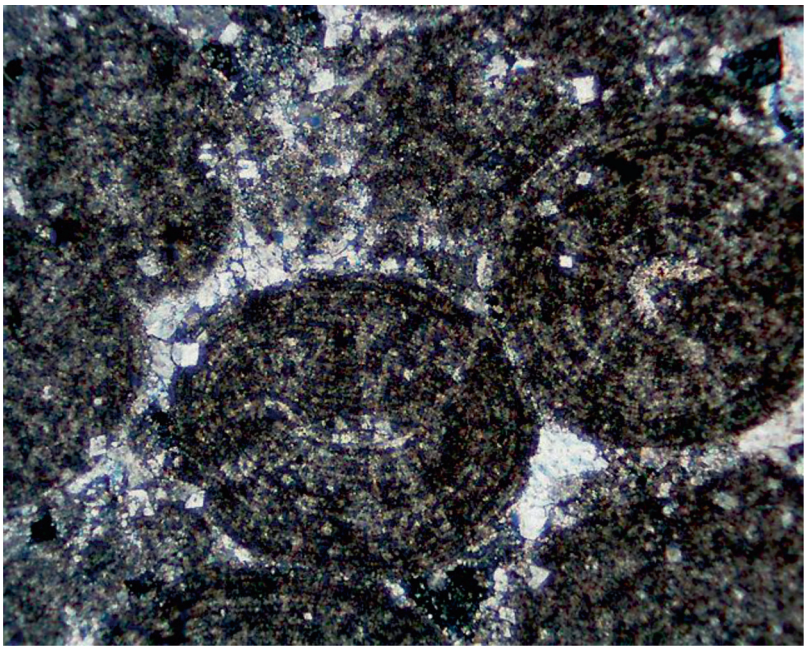

Fig. 13.16 Photomicrograph of ooids

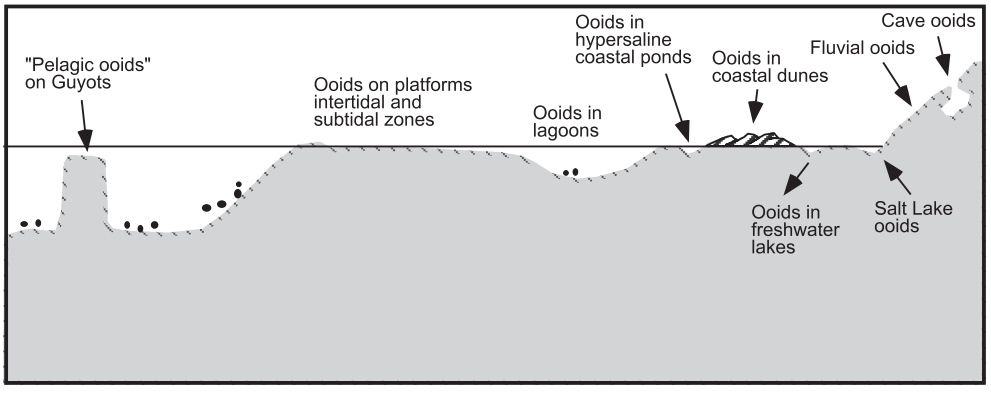

Fig. 13.17 Depositional environments of ooids (from Flugel 1982)

various marine environments. On the continental shelf, the water depth is generally less than 200 m, and this area receives both continentally derived sediments as well as carbonate biogenic particles generated in the ocean. A large variety of animals and plants generally thrive in these environments. In warm, equatorial regions, coral reefs commonly grow on continental shelves.

In the open-ocean basins, both terrigenous (i.e., continentally derived) clay and skeletal remains of carbonate-secreting organisms (foraminifera, pteropods, and coccolithophores) and silica-secreting organisms (diatoms and radiolaria) dominate the sediments in the hemipelagic environment, whereas only skeletal remains dominate in the pelagic environment. The *calcite compensation depth* (*or CCD*) is the depth (~3,500–4,500 m, depending upon latitude and the ocean) below which the ocean water is undersaturated with calcite because of dissolved CO_2 (Fig. 13.19). Therefore, calcareous tests of all organisms are totally dissolved below the CCD. Similarly, the *aragonite compensation depth* (*ACD*) occurs at a shallower depth (~2,000 m). Aragonite is used as a secreting material by the pteropods, which are pelagic molluscs.

Note that while foraminifera occur in all latitudes, the siliceous organisms such as the diatoms and radiolaria thrive only in upwelling areas of the oceans. Siliceous tests are preserved at all depths in the deep *radiolarian* or *diatomaceous oozes*

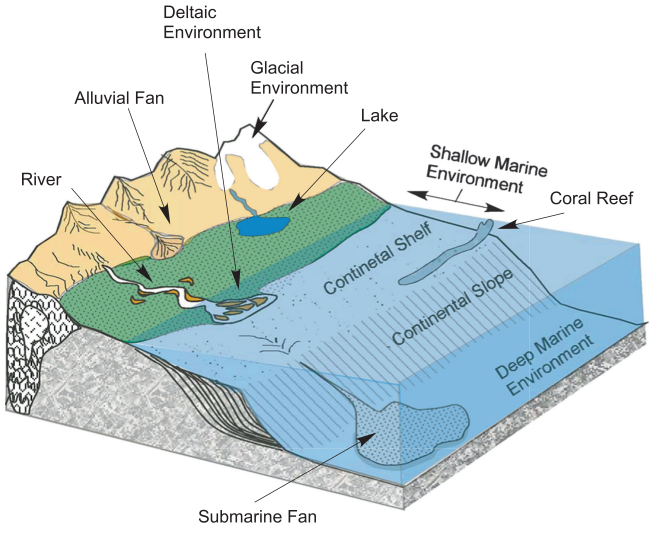

Fig. 13.18 A schematic diagram showing various continental, transitional, and marine environments of deposition

(which are sediments on abyssal plain rich in radiolaria and diatom, respectively). They become particularly prevalent below the CCD due to dissolution of calcareous skeletons. Siliceous oozes also predominate in high-latitude upwelling regions near the poles, where $CaCO_3$ productivity is minimum (Fig. 13.20).

Deltaic Environment

The physiography of an "average" delta may be divided into three parts: the *delta plain* (i.e., the flat, landward, platform area), *delta front* (i.e., the steeper sloping frontal area that dips into the prodelta region), and *prodelta* (i.e., the deeper water, flatter area in front of the delta). The prodelta is composed of fine suspension load of fluvial sediments. Deltafront is composed of coarser fluvial sediments. The delta plain is composed of braided stream channel (cross-bedded sand) and interchannel (laminated silt and clay) deposits (Fig. 13.21). Delta plain, delta front, and prodelta deposits are often equated to topset, foreset, and bottomset beds. Subsidence, due to sediment compaction and/or sediment loading, is a key factor in the sediment thickness and other depositional characteristics in large deltas. Deltas composed dominantly of mud can go through rapid subsidence because of great compaction.

Estuarine Environment

An estuary occurs at the mouth of a river where it receives both fluvial and marine sediments, and thus, estuarine sediments develop mixed characteristics,

Table 13.3 Sedimentary environments and sedimentary deposits

Type	Subtype	Site	Sediment composition and structure
Continental	*Aeolian*	Desert	Wind-blown deposit made entirely of Frosted sand with dune cross-bedding. Sand grains may be frosted indicative of long transport by wind
			Bahamites are wind-transported oolitic limestones
	Loess	Adjacent to major rivers and draining glaciers	Wind-blown angular silt, rock flour produced by glacial grinding of bedrock and later blown away by wind
	Fluvial	Alluvial Fans formed at fault mountain base	Wedge-shaped deposit in cross section
			Very poorly sorted mix of mud and sizes up to boulders
		Meandering river	Point bar deposit of cross-bedded sand; thinly laminated mud in floodplain
		Braided river	Braided pattern in a plan view. Generally gravel bars, lenticular, or sheet-like
	Lacustrine	Lakes	Lake margins have sandy beaches and deltas; centers are black mud, often parallel laminated
	Glacial	Alpine glacial valleys	*Till* (very poorly sorted mix of boulders to clays)
Transitional	*Deltaic*	Mouth of a river	Complex subenvironments and sedimentary *facies*
			Coal and oil deposits are often associated with Delatic environments
	Peritidal	Coastal swamps	Mangrove swamps and tidal flats. Cross-beds, oolites, bioturbation. Well-rounded quartz sand
	Barrier complexes		Elongated cross-bedded sand deposits with lagoon (mud deposits) on one side and open ocean on the other
Marine	*Continental shelf/slope*		Turbidites, lime mud, coral, or algal reefs
	Abyssal plain		Carbonate and or siliceous ooze, continentally derived fine detritus, extraterrestrial fine debris

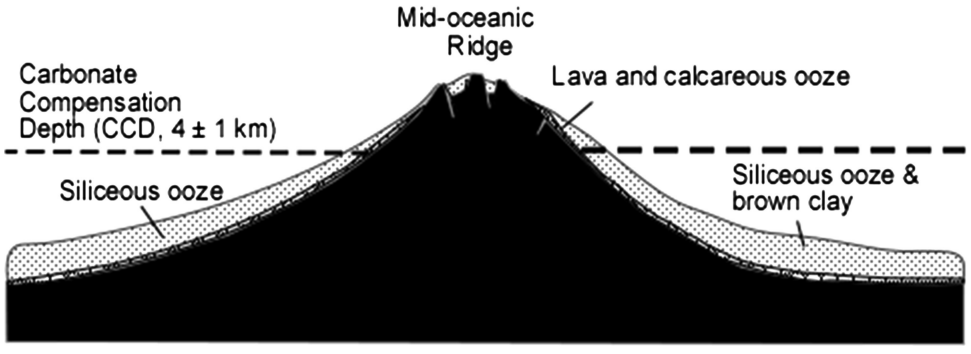

Fig. 13.19 The calcite compensation depth

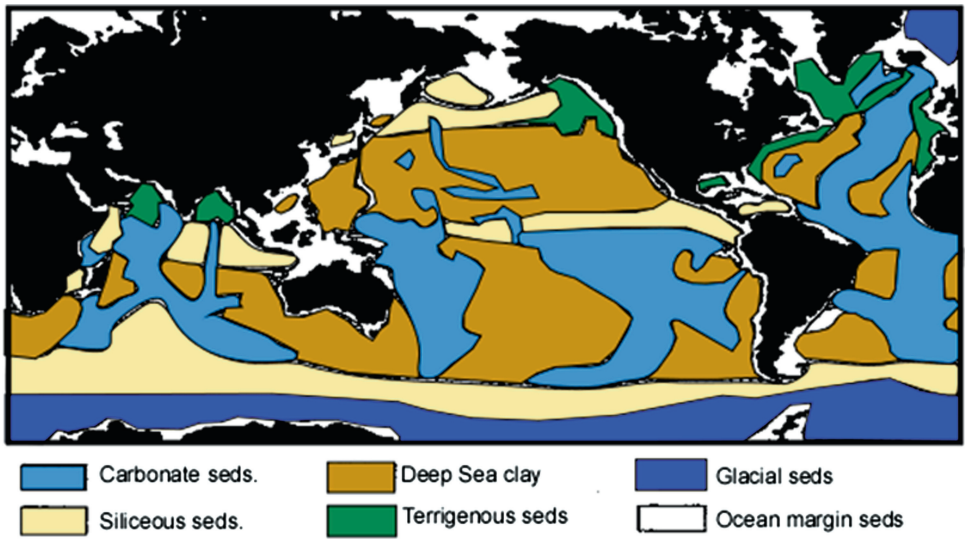

Fig. 13.20 Distribution of siliceous and carbonate sediments on the ocean floor

depending upon whether it is tide dominated or wave dominated (Fig. 13.22). Estuaries are typically associated with marine transgressions, which turn them into a delta if sediment supply is abundant. Similarly, a wave-dominated estuary, bar, barrier island, or spit develops, being composed of sand and gravel. Such a sand bar may stop ocean waves from reaching the shore, thus creating a lagoon in between the barrier island and the delta. The lagoon may become a hypersaline marsh with stagnant bottom waters from which mud may be deposited.

Terrestrial Environment

Terrestrial environment encompasses diverse types—from desert to streams/rivers to glacial environments. Discussion of the characteristics of each type of terrestrial environment is beyond the scope of this book, and only some overall observations are made here.

Mass movements in *the desert environment* are typically dominated by wind and supplemented by occasional flash flooding. *Alluvial fans* are enormous fan-shaped deposits (Fig. 13.23) that are commonly found in fault-bounded regions, such as the Death Valley region in western USA. Episodic flash flooding causes enormous debris flows and mudflows that are responsible for rapid sedimentation in such environment. The sedimentary deposit is characteristically a very poorly sorted mix of boulders to clay-sized particles. Sand dunes of several different types, salt flats, playas, etc., are all characteristics of a desert.

The environment of streams/rivers is referred to as *fluvial environment*. Streams/rivers can have a wide variety of channel patterns—*straight*, *meandering*, *or braided* (Fig. 13.24). A typical cross section of a mature braided stream shows that the water in a stream is restricted to the *channel*, which is bounded on both banks by ridges made of sand and gravel,

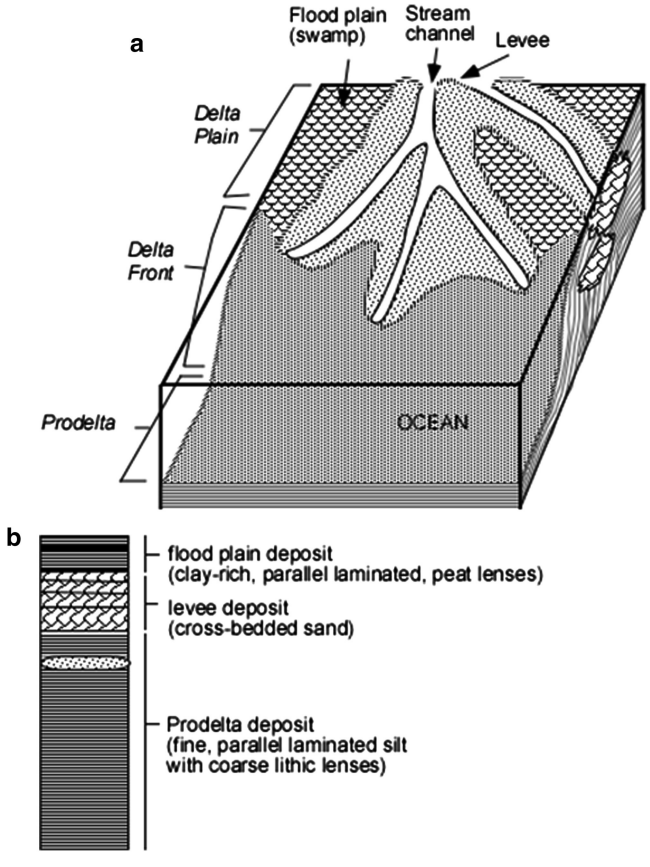

Fig. 13.21 Parts of a delta showing typical deltaic deposits

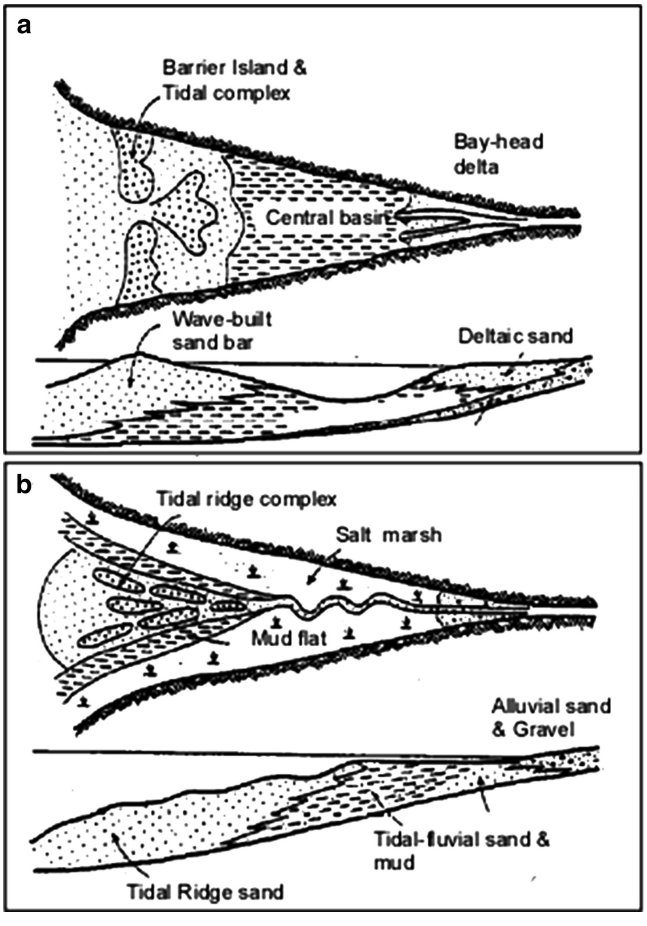

Fig. 13.22 Estuarine environments and their deposits. (**a**) Wave-influenced estuary. (**b**) Tide-influenced estuary. In both the *top panel* is a plan view and the *bottom* is a cross section

called *natural levees* (Fig. 13.25). Occasional flooding may occur when water may break the levees and fill the surrounding *flood plains*. Certain floodplains are essentially marshy land with mud and organic materials (peat) deposited from floodwaters. In meandering streams, sand deposition takes place on the convex curve of the channel (*point bar*) where water velocity is lower, while the concave curve gets eroded because of faster flow of water on that side of the river (Fig. 13.26). Through geologic time, erosion of the outer, concave, channel wall and simultaneous deposition on the convex inner wall causes the stream channel to migrate laterally.

The environment of a glacier is of considerable interest because a glacier is a very effective agent that

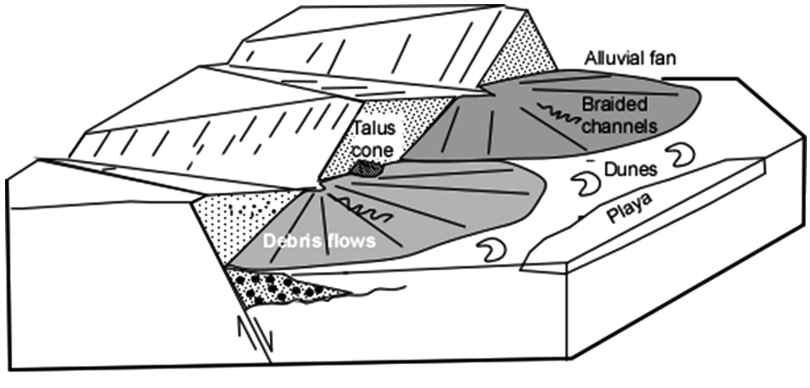

Fig. 13.23 (**a**) Alluvial fans. (**b**) Cross section through and alluvial fan

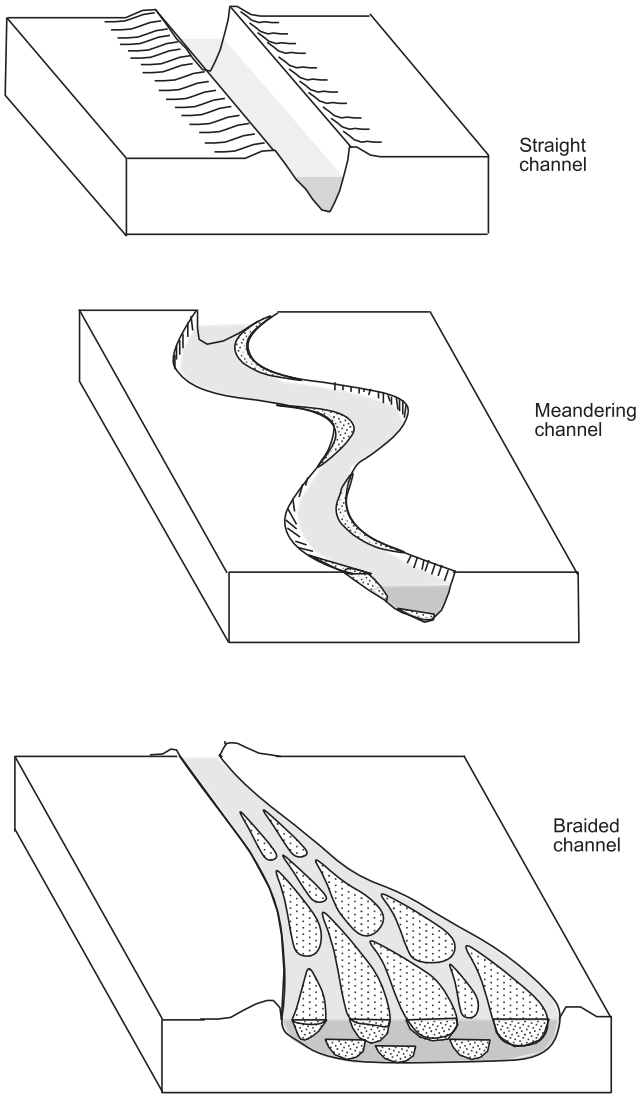

Fig. 13.24 Stream channel patterns

is capable of carrying house-sized boulders over great distances (Fig. 13.27). *Till* is a typical sedimentary deposit form glaciers, being composed of unsorted mix of mostly angular gravel to silt-sized sediments. Glacial meltwater streams generally form braided networks that lead to the accumulation of cross-bedded channel sand and gravel. The coarser grains in such a deposit are often striated due to grinding action of the glacier against bedrock. Another typical glacial meltwater deposit is *varve* (described in an earlier section). Glacial grinding of bedrock produces rock powder of silt to clay-sized particles, known as *rockflour*. Rockflour deposited by glacial meltwater streams in the front of a glacier may be picked up by strong winds and deposited *en masse* downstream as a *loess*, which is a structure-less light-colored deposit composed dominantly of silt.

Lithification or Diagenesis

Deposition of sediments is followed by lithification, which is the process of conversion of sediments into a sedimentary rock. In detail, this process includes the following:
Compaction
Dissolution
Recrystallization
Cementation
Replacement

Although diagenesis occurs mainly at depth, in some cases, it has been "observed" to operate at the surface (e.g., beach rocks). Three stages of diagenesis are commonly recognized—(1) *eogenesis* is a geologically brief period of diagenesis at near-surface conditions, (2) *mesogenesis* is long-term diagenesis that occurs during deep burial, and (3) *teleogenesis* is a late-stage diagenesis of an already lithified sedimentary body.

The nature of the pore fluids is an important factor in diagenesis, which is caused by chemical reactions such as dissolution of old minerals and precipitation of new minerals. These fluids may be primarily of three types—(1) modified meteoric waters that seep through the pore spaces, (2) compaction waters that migrate upward or laterally from sites of greatest compaction, and (3) thermobaric waters, which are structurally bound waters released from clay minerals in the deeper parts of a sedimentary basin. Meteoric waters are most important in diagenesis because they are constantly replenished at the site of diagenesis.

Compaction, Pressure Solution, and Recrystallization

Accumulation of large amount of sediments in a depositional basin leads to the compaction of the lower layers due the load (lithostatic) pressure of the overburden. Such compaction reorganizes the framework and squeezes out the pore fluid, resulting in a net reduction of *primary porosity* [Fig. 13.28; porosity = (100 × volumes of pores) ÷ total volume (i. e., grains + pores)]. The extent to which compaction can reduce porosity (and thus volume) of a sedimentary body depends upon the following factors:

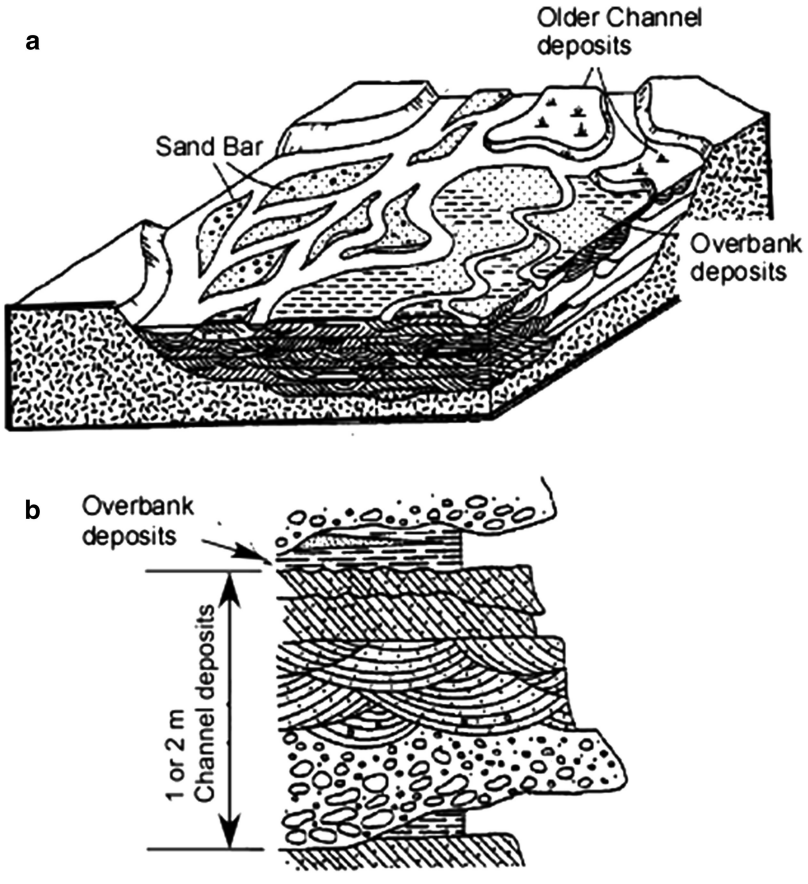

Fig. 13.25 Sedimentary deposits in braided streams

1. Texture of the sediment—the greater the clay percentage, the more the pore water, and thus more compacted it will be.
2. Sorting—for instance, well-sorted quartz sand will compact much less than poorly sorted glacial till.
3. Shape—well-rounded grains will compact less than irregular grains.
4. Competing processes—such as precipitation of matrix or cement in pore space. In this context, mention should be made of the phenomenon of *pressure solution*, which forms as a result of intense pressure along contacts between grains. The solution, containing dissolved ions of the minerals being squeezed, migrates to a more favorable site where it precipitates a mineral (*cement*) in pore spaces, thereby reducing porosity. Grains affected by pressure solution would recrystallize jointly, and the only clue as to them originally being different grains is usually the presence of a dusty suture-type boundary that may be visible under the microscope.

An easy experiment involving two ice cubes will help illustrate the recrystallization process: if two ice cubes are squeezed against each other for about 30 s and then released, the two cubes will recrystallize along their contact and become one. This effect is also seen in picnic-size bags of ice: if a bag is picked up from the bottom of the ice machine, the ice cubes would have to be broken apart!

Cementation

The process by which new minerals precipitate from migrating solutions in the pore spaces and bind the larger framework grains into a rock is called *cementation*. Composition of cements and the effectiveness of the cementation process depend on solute concentration, Eh, pH, and temperature of the pore fluid. Cements are generally made of a select variety of carbonates (dolomite, calcite, aragonite, and Mg calcite), silicates (chalcedony), and iron oxides (hematite, goethite). Several "generations" of dissolution (thus, development of secondary porosity) and cementation may occur through time within a sedimentary rock (Fig. 13.29).

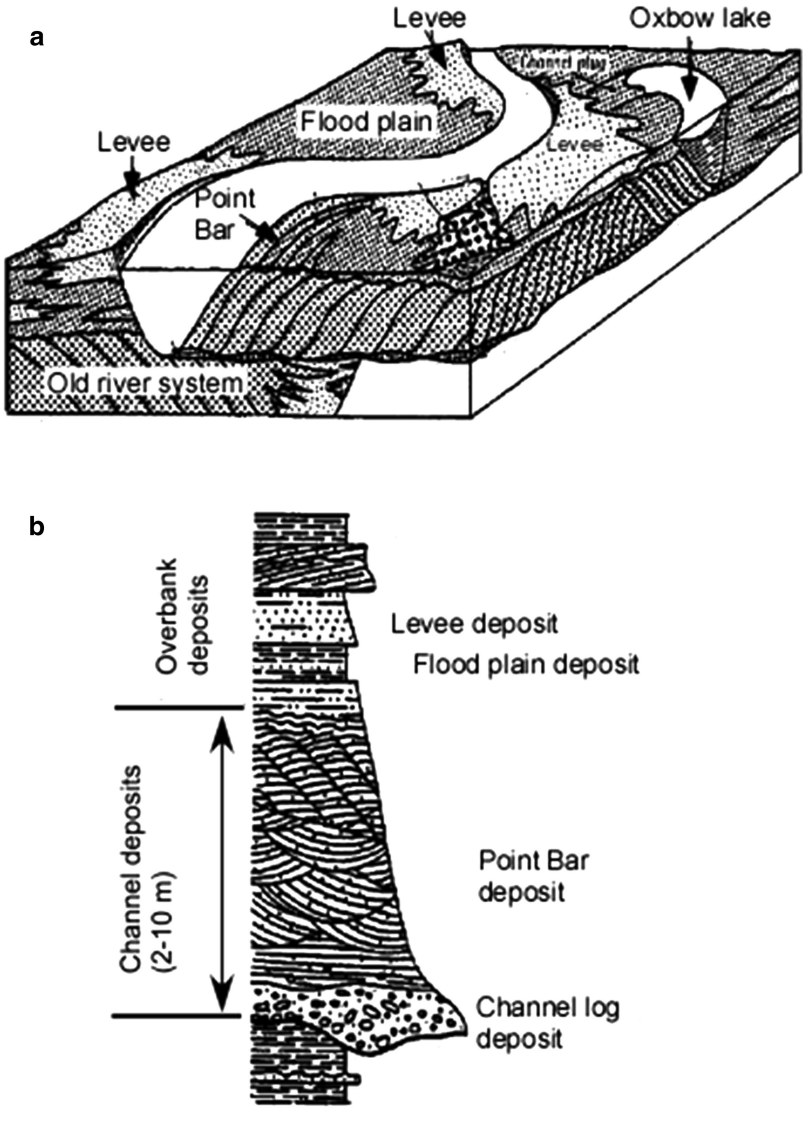

Fig. 13.26 Sedimentary deposits in meandering streams

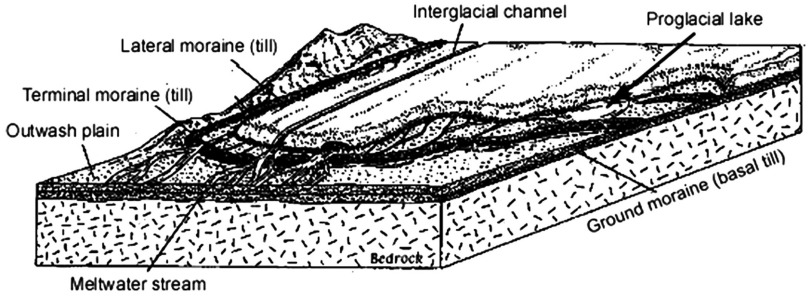

Fig. 13.27 (**a**) Glacial environment. (**b**) Glacial till. (**c**) Varve

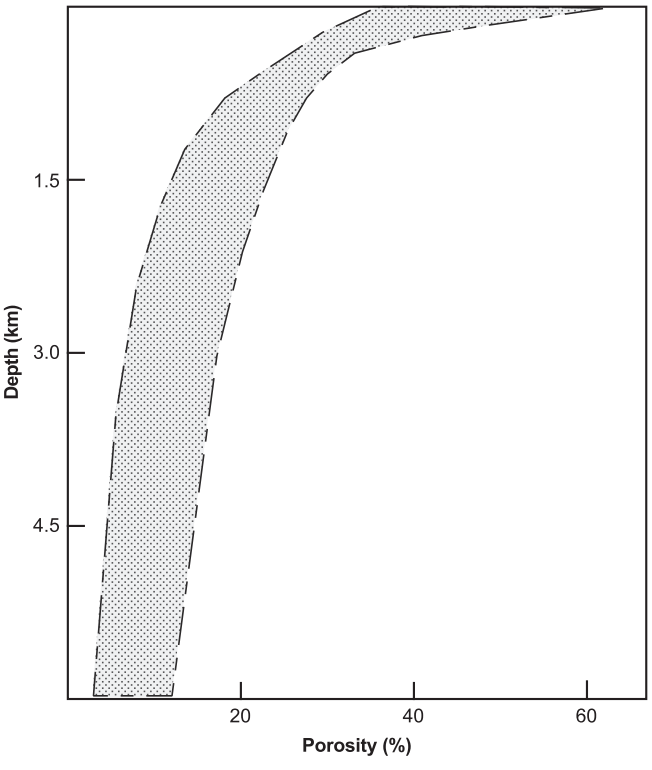

Fig. 13.28 Reduction of primary porosity as a function of burial depth in shales and sandstones (Dzevanshir et al. 1986)

Replacement

New minerals may precipitate from a fluid migrating through sediments/sedimentary rock and replace existing coarser mineral grains. Often the replacing mineral maintains the form of the originally deposited mineral; and in such a case, the replacing mineral is said to be a *pseudomorph* after the original mineral.

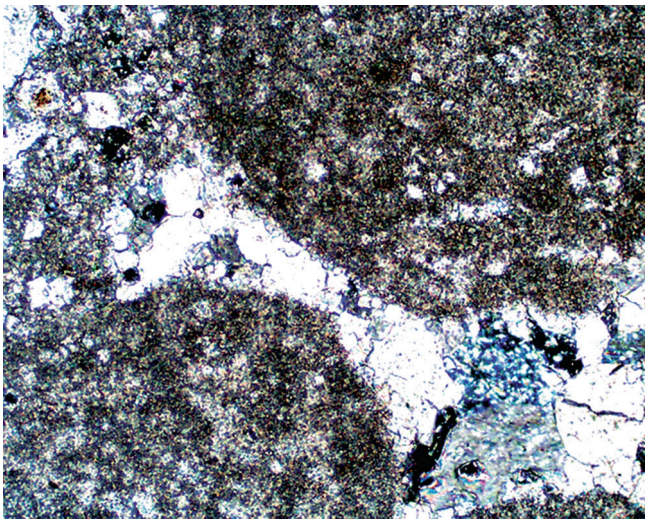

Fig. 13.29 Photomicrograph of a cement

Summary

Derivation, transportation, and depositional processes of sediments may be mechanical, chemical, or biogenic. Postdepositional change that transforms sediment to a sedimentary rock is called diagenesis. Mineralogy and texture of sediments reflect the compositions of the original source rocks and sedimentary processes. Depositional environments can fundamentally be grouped into continental, oceanic, and transitional types. Sediment composition and structure are tied to the conditions of deposition in these various environments. Two first-order postdepositional changes to sediments are porosity reduction due to burial and cementation. Cementation and all chemical sedimentation processes are largely controlled by Eh/pH conditions.

Sedimentary Rocks

14

Abstract

In the previous chapter we considered how sediments, the precursor to sedimentary rocks, form and ultimately become lithified. Sedimentary rocks are important to the geologist for two principal reasons: (1) They host petroleum, natural gas, coal, uranium, and many other economically significant deposits. (2) Their composition, structure, texture, and fossils provide clues to paleogeography, paleoclimate, and past life on Earth. It is clearly a vast topic and not every aspect, however important, can be covered here in sufficient detail. Instead, in this chapter we consider largely the broad petrogenetic aspects of some major types of sedimentary rocks.

Classification of Sedimentary Rocks

Sediments are primarily composed of three types of materials (Folk 1959): *terrigenous/Siliciclastic materials, orthochemical/authigenic materials, and allochemical materials*. *Terrigenous materials* are derived through weathering of rocks. These materials may also be called siliciclastics because they are predominantly siliceous (quartz-rich) clastic sediments transported by detrital processes. *Orthochemical (or authigenic) materials* are chemical or biogenic precipitates that are generated in situ. These would include all evaporites and cements. *Allochemical materials* are mechanically broken fragments of original chemical or biogenic materials. These may or may not be derived from within the depositional site.

Sedimentary rocks may be classified on the basis of modal contents of the three types of materials listed above (Fig. 14.1). Rocks that are composed of >50 % terrigenous materials are called *terrigenous rocks*. Sandstones, mudstones, and conglomerates are all examples of this class of rocks. *Allochemical rocks* must have >10 % of allochemical materials and <10 % terrigenous materials. The adjective "impure" is added if the terrigenous materials exceed 10 % of the volume of the rock. *Orthochemical rocks* contain >90 % orthochemical materials.

Terrigenous Rocks

Terrigenous rocks dominate the sedimentary rocks of the continental crust. They show a wide range of compositions and texture. Terrigenous rocks typically consist of clasts (framework), fine-grained detritus (matrix), or chemically precipitated cement that bind the clasts together (Fig. 14.2). Table 14.1 shows the classification of sediments according to the size of their clasts, using the Wentworth scale.

Breccias, Conglomerates, and Diamictites

Breccias, conglomerates, and diamictites are composed of >25 % gravel. Gravel is an unsorted mixture of particles of all sizes – from boulders to silt. If the framework grains (e.g., pebbles) are rounded, then the rock is called a *conglomerate* and a *breccia* if they are angular. *Diamictite* refers to unsorted, matrix-supported siliciclastics that are generally deposited as

G. Sen, *Petrology*, DOI 10.1007/978-3-642-38800-2_14,

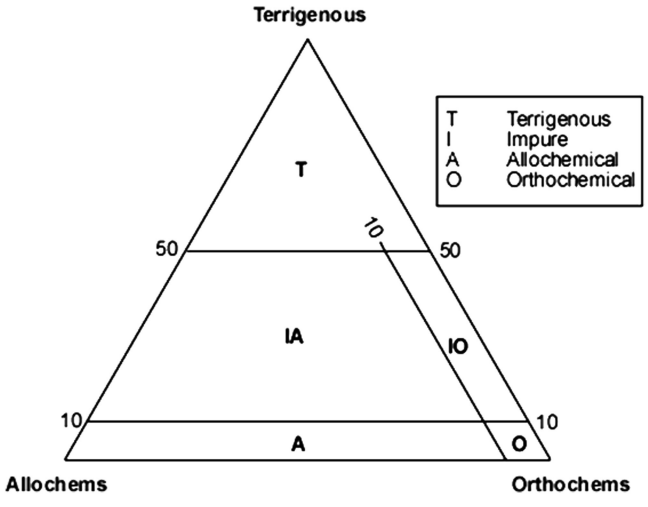

Fig. 14.1 A simple classification of sedimentary rocks (Folk 1959)

glacial tills, ice rafted, landslides, mudflows, etc. Conglomerates are composed of pebbles that have been rounded during transportation. Certain conglomerate horizons serve as excellent indicators of an erosional *unconformity*, which is a discontinuous surface that represents gaps in the depositional history of the sedimentary basin where the conglomerate occurs. Conglomerates may form in many ways, but the most common are actually depositional (e.g., fluvial gravel) in origin.

Breccias may have a number of origins—they may form from talus at the bottom of steep slopes or cliff (*talus breccia*), along fault planes during fault movement (*fault breccia*), from the collapse of reefs due to repeated pounding by ocean waves (*reef talus*), from meteorite impact (*impact breccia*), etc. (Fig. 14.3).

In describing a breccia or a conglomerate, it is important to recognize whether the clasts are of a single lithic type (termed a *monomict breccia* or *conglomerate*) or multiple types (*polymict breccia or conglomerate*). Also, the clasts in a conglomerate may all have some sort of a crude orientation, in which the conglomerate would be called an *organized conglomerate*, and if not, then it would be called a *disorganized conglomerate*. The framework clasts may also be graded in some cases. Each of these characteristics is helpful in unraveling the geological history of a conglomerate.

Sandstones

Sandstones are an abundant and important class of sedimentary rocks. The three principal framework components of sandstones are quartz, feldspar (which may become partially or entirely altered to clay minerals), and lithic (rock) fragments. The minerals are bound together by a fine-grained matrix or chemically precipitated cement. The matrix may be composed of clay, silt, and/or iron oxide. Carbonate and silica cements are common. In some cases *glauconite*, a chemically precipitated green claylike mineral, and iron oxide form the cement.

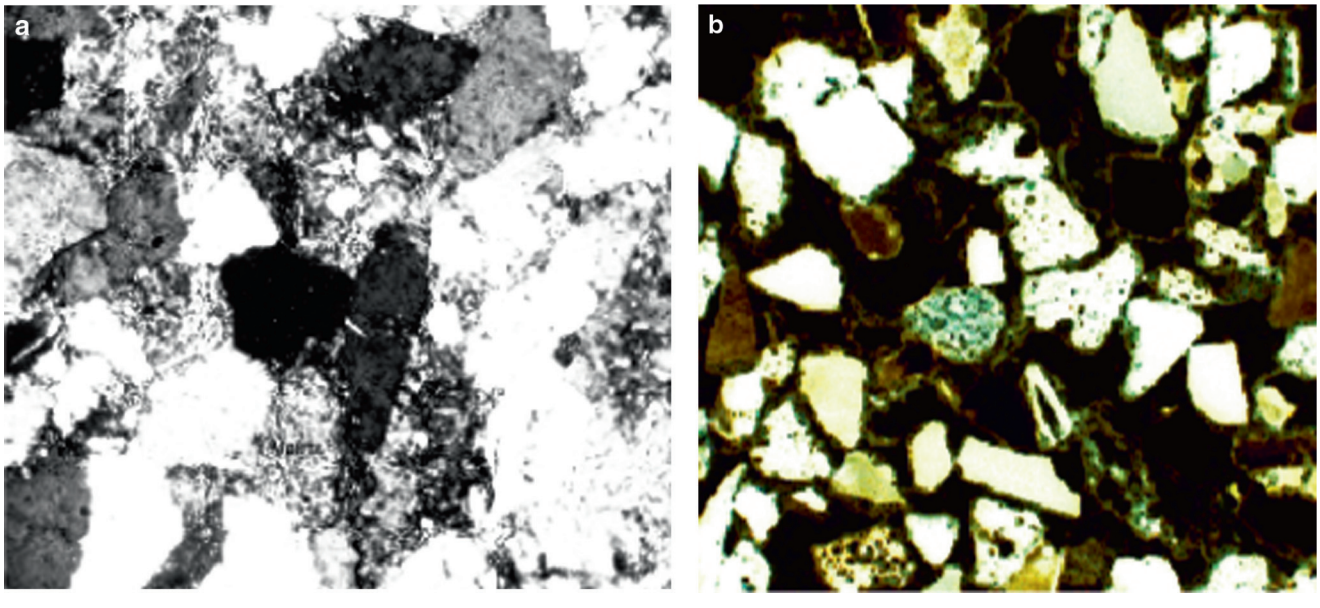

Fig. 14.2 (**a**) Photomicrograph of clay-rich matrix in an immature sandstone. (**b**) Photomicrograph of cement in a different immature sandstone. (Magnification in these and all subsequent photomicrographs is ×80, unless otherwise mentioned)

Table 14.1 Classification of terrigenous rocks

Clast size (mm)	Sediment	Sedimentary rock
>2	Gravel	Breccia (if angular), conglomerate (if rounded) or diamictite (if mixed)
0.063–2	Sand	Sandstone
0.004–0.063	Silt	Shale or mudrock
<0.004	Clay	Claystone or mudrock

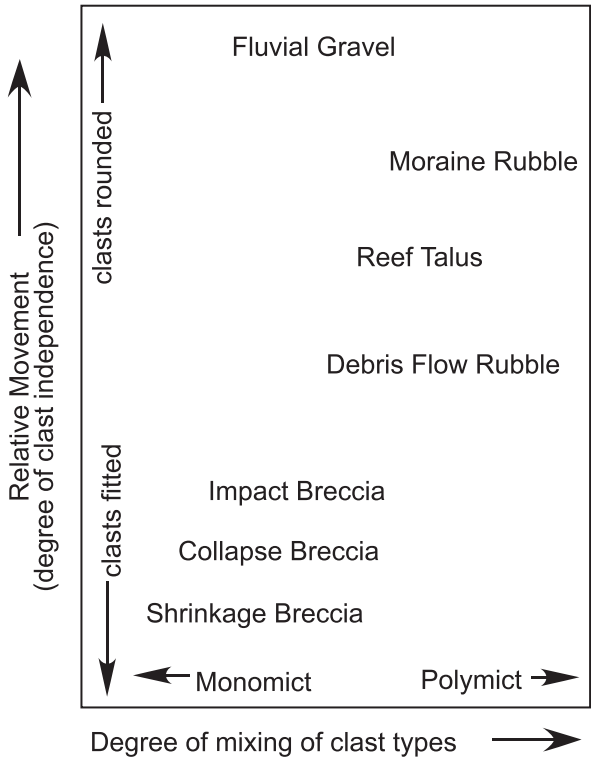

Fig. 14.3 Breccia types and their origins

Quartz grains may be single crystals or polycrystalline aggregates, which are easily observable under the microscope. The nature of quartz clasts may offer clues as to the type of the source rock they are derived from: for example, polycrystalline quartz grains are generally derived from metamorphic rocks. Another important (but obscure) example is the texture of quartz grains deformed by meteorite impacts: these are typically characterized by three sets of twin planes that cut across each other at acute angles. Such shocked quartz grains have been found in the cretaceous–tertiary boundary layers from around the world and have been used as evidence in favor of meteorite impact that ushered in a series of events that culminated in a major mass extinction event.

The abundance, variability, shape, and size of lithic fragments offer clues to the provenance (i.e., source area), transportation history, and tectonic settings. The *maturity* of the clasts indicates the kinetics of the transportation process (see Chap. 13). Extremely long transportation removes all of the clay particles and makes a deposit of well-rounded sand grains. A poorly sorted mixture of mud and angular sand grains would thus be clearly texturally *immature*. In a mineralogical sense, mature rocks may be expected to be dominantly composed of quartz because this is the most stable mineral in all sedimentary processes.

Feldspar composition and its degree and nature of clay alteration often provide important genetic clues: for example, in arid climatic regions, detrital feldspar may not alter at all at near-surface conditions nor during diagesis. The percentage of plagioclase over K-feldspar can be a source indicator: for example, a sandstone whose feldspar is dominantly a K-feldspar has likely had a granitic source.

A number of different schemes to classify sandstones exist in the published literature. These are generally based on the character of the clasts. A convenient and widely used classification is that put forth by Dott (1964; Fig. 14.4), which is based on clast composition as well as matrix percentage. In Dott's classification a first-order division is recognized between *arenites* and *wackes*, based on the proportion of matrix present. Each of these groups is further classified according to their modes with the use of a triangular diagram whose apices are quartz, feldspar (partially or wholly altered to clay), and lithic fragments. Thus, based on these diagrams, a sandstone with <5 % matrix and 50 % quartz, 40 % feldspars, and ~10 % rock fragments should be called a *feldspathic arenite*. If the same rock had >5 % matrix, it would be called a *feldspathic wacke*.

Another popular classification is that by Folk (1974; Fig. 14.5). Folk's classification makes a fundamental subdivision between rocks with >15 % matrix, which he called *graywackes*, and those with <15 % matrix. The latter group is further subdivided into various *arkoses* and *arenites* with the general sense that arkoses are feldspar rich and arenites are poor in feldspar content.

Although Dott or Folk may not have intended this classification to have any tectonic significance, Dickinson and Suczec (1979) found that the proportions of quartz, feldspar, and rock fragments can be a good indicator of plate tectonic regimes (Fig. 14.6): for example, sandstones rich in K-feldspar and lithic fragments are considered to form in continental arc settings. However, later authors pointed out various problems with this approach, citing complications due to multiple provenance, transportation, and diagenesis processes, as well as climatic influence (cited in Raymond 2007).

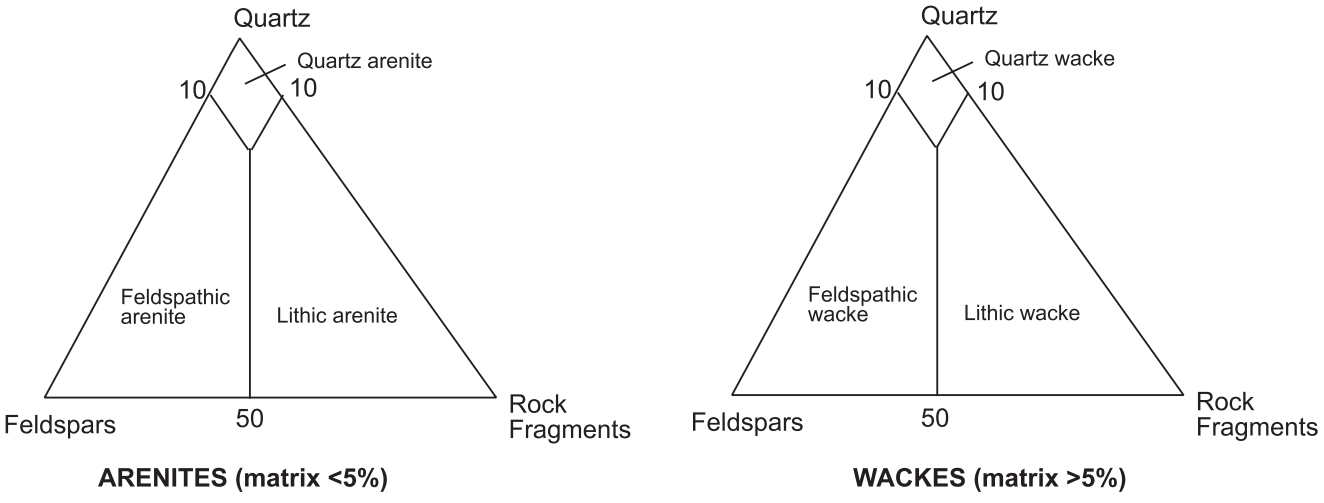

Fig. 14.4 Dott's (1964) classification of sandstones

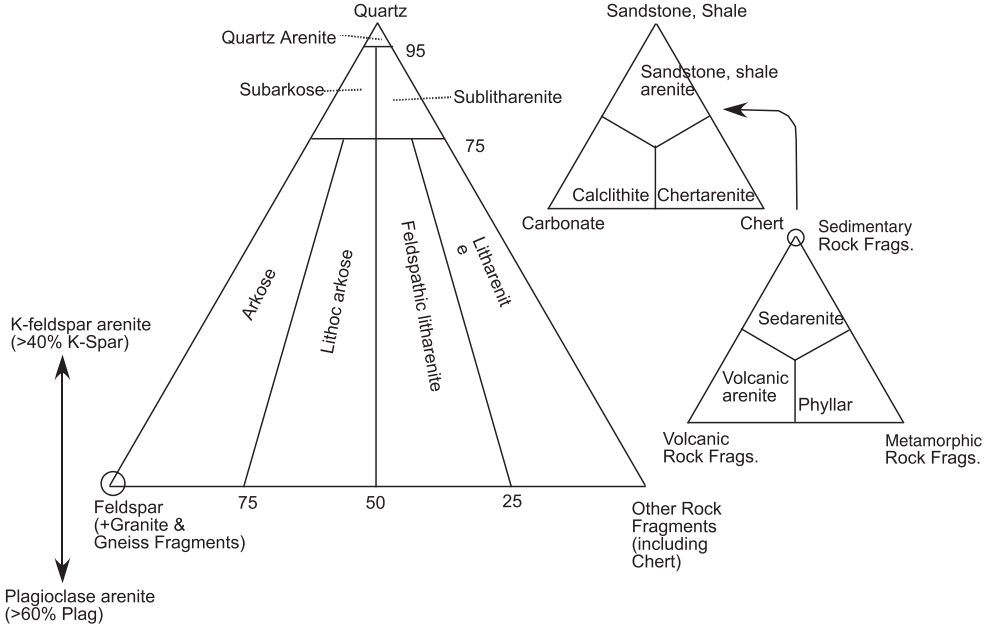

Fig. 14.5 Folk's (1974) classification of sandstones

In general, clastic fragments in sandstones are indicative of provenance; and their textures are indicative of transportation and depositional histories. Their structures (e.g., cross-bedding), nature of fossils, and association with other lithic types (e.g., peat, evaporite) must be considered together in order to decipher the depositional environment and paleogeography. In order to understand how this may be accomplished, let us consider an example in which a geologist maps the lithological units of an area and reconstructs a cross section such as in Fig. 14.7. These units are composed of a coarse conglomerate at the bottom followed successively above by a parallel-bedded sandstone, a thick sequence of cross-bedded sandstone, thin layers of mudstone with peat, and massive lenses of medium-grained sandstone. Based on what we learned about depositional environments in Chap. 13, this sequence can develop in a fluvial environment (meandering stream).

Mudrocks

Mudrocks are composed of silt-sized, angular, quartz grains, and clay minerals in variable proportions. The four most common clay minerals in mudrocks are illite, smectite, mixed illite–smectite, and kaolinite. Because the grain size is so fine, it is impossible to discern the proportion of quartz to clay with a pocket lens.

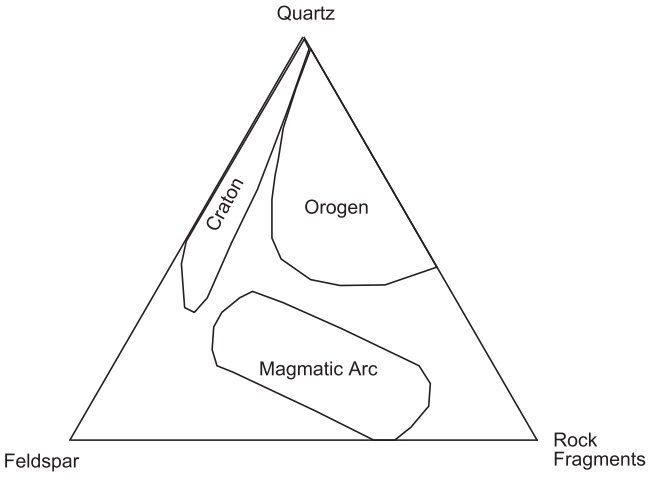

Fig. 14.6 Sandstone composition and plate tectonic environments (Dickinson and Suczec 1979)

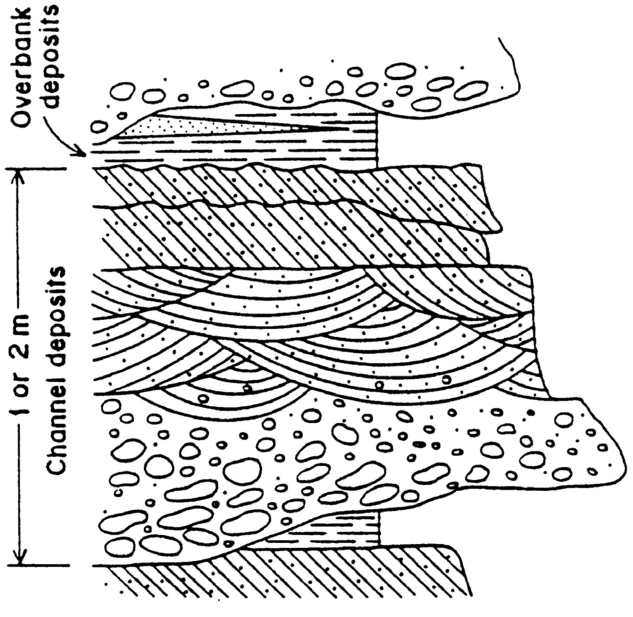

Fig. 14.7 A geological cross-section

Blatt et al (2006) outlined an alternative method of roughly estimating silt to clay proportion based on whether the rock tastes "gritty" (more quartz than clay) or "slimy" (more clay than quartz) when nibbled on. Mudrock is the general name given to all rocks that consist of silt and clay particles. The term *shale* is used to denote a mudrock with excellent fine lamination, which often causes splitting along parallel planes, a property referred to as *fissility*. Fissility is a result of parallel stacking of the sheets of clay minerals. Fissility may not develop in *siltstone or claystone*, which is defined on the basis of whether silt or clay, respectively, dominates the mode. Although mudrocks are generally associated with aqueous environments, there are two classes of mudrocks that have different modes of origin: *Bentonite* is a special type of mudrock that has its origin as a volcanic ash deposit. *Loess* is the other type which is essentially windblown rock flour derived by powdering of bedrock by a glacier.

As a group, mudrocks are a very important class of sedimentary rocks, comprising 60 % of the stratigraphic record. Because mudrocks occur in a wide range of depositional environments and they are distributed throughout much of the geological column (from Precambrian to present), mudrocks have proved to be very useful in unraveling Earth's paleogeography and environmental conditions. Mudrocks may form as floodplain deposits, as alluvial fan deposits, in transitional environments and in the marine environments.

The color of mudrocks can be an indicator of the depositional environment: for example, *black shales*, which occur at different levels throughout the phanerozoic rock record, are generally believed to have formed in dysoxic–anoxic, stagnant waters of lagoonal environments. They commonly contain pyrite as an indicator of anaerobic reducing conditions that exists in the basin. 85–150 million-year-old black shales occur extensively as laterally and vertically discontinuous bodies in the Atlantic Ocean crust, suggesting that during this period there were large areas of the Atlantic Ocean floor that suffered large-scale anoxia. Such anoxia was likely caused by the lack of open circulation within the early Atlantic. Paleozoic black shales are well exposed in the northern Appalachians (Fig. 14.8).

Black shales owe their color to their content of minor amounts of organic materials, which remain undecomposed by virtue of lack of oxygen availability. Commonly, a mudrock may be gray–black or red–yellow–green. The green color is due to the presence of green clay minerals, *chlorite* and *illite*. Red to yellow colors may be due to other minerals such as hematite (red) and limonite (yellow).

Mud readily undergoes compaction following deposition and burial. The initial porosity of water-saturated mud is about 80 %, but it can be reduced to almost zero in the first 8 km of burial. During such a process, hydrocarbons (formed in the pore spaces from breakdown of organic matter) may be squeezed out to a more suitable rock, e.g., sandstone, which is less compressible and whose open pore spaces can serve as a reservoir for oil by virtue of its greater porosity. Clay minerals are particularly sensitive to burial pressure and temperature causing their diagenesis. Smectite

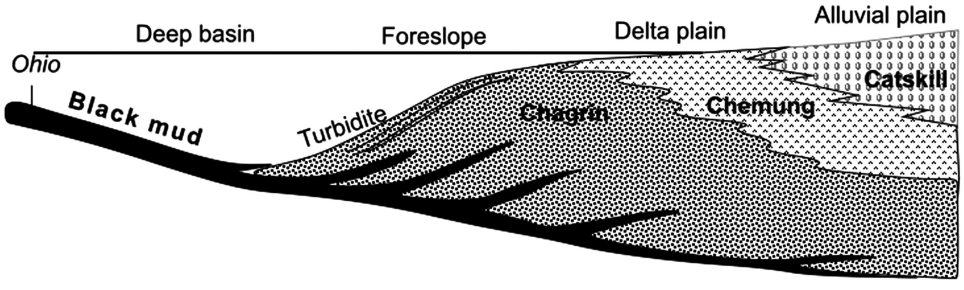

Fig. 14.8 Paleozoic black shales from the northern Appalachian mountains

and mixed-layer (illite–smectite) clays are dominant in muds and young mudstones but are not nearly as abundant in older and deeply buried clastic rocks. During diagenesis smectite alters to illite or chlorite. The percentage of illite in mixed-layer clays gradually increases with increasing degree of diagenesis. With further increases in pressure and temperature, illite coarsens and becomes chlorite/mica. In summary, clay minerals are particularly useful in recording the diagenesis of mudrocks.

Allochemical Rocks

Carbonate Rocks

Carbonate rocks contain >50 % carbonate minerals and comprise ~10 % of all sedimentary rocks. Carbonate rocks, their depositional environments, and diagenesis of carbonate rocks are subjects of great interest to the petroleum exploration industry, because many oil deposits occur in carbonate rocks. The two minerals that are the dominant constituents of carbonate rocks are *calcite* and *dolomite*, and carbonate sedimentary rocks are broadly grouped into *limestones* and *dolostones* based on whether they are dominantly composed of calcite or dolomite, respectively.

The common calcite crystallizes in the rhombohedral class and is sometimes referred to as *low-Mg calcite*. It forms the shells of most planktonic organisms and has little or no magnesium in solid solution (<8–10 mol% $MgCO_3$). Low-Mg calcite can also form during diagnesis. Chemically precipitated low-Mg calcite is *not common* in limestones. In contrast to the low-Mg calcite of planktic organisms, calcite of benthic organisms can have as much as 30 % Mg and is commonly referred to as *Mg calcite* or *high-Mg calcite*. High-Mg calcite can also form as a cement-forming, chemically precipitated, mineral. *Aragonite* is a polymorph of calcite that occurs in abundance in shallow marine deposits. Aragonite crystals may be chemically precipitated from ocean water and also form the shells of many organisms. The crystals are typically needlelike. Aragonite converts to calcite or is dissolved in interstitial fluids during diagenesis; and hence, aragonite is relatively rare in pre-Pleistocene rocks. Wilkinson (1979) noted that skeleton composition of marine organisms as a whole has changed through geological history: Paleozoic organisms were composed of high-Mg as well as low-Mg calcite, Mesozoic organisms were made of high-Mg calcite, and Cenozoic organisms are dominantly composed of aragonite.

Primary precipitates of dolomite form only in exceptional cases in present-day environments, and yet dolostones are an abundant component throughout the stratigraphic record. *This suggests that in such dolostones dolomite likely formed by diagenetic processes.*

Carbonate sediments form in a wide variety of environments, but they are most common in tropical shallow marine waters and lakes. As discussed in Chap. 13, calcite and aragonite form the skeletons of many organisms in shallow marine environments; and when these organisms die, their skeletal debris may accumulate on the ocean bottom and form a carbonate deposit. However, all carbonates dissolve below the carbonate compensation depth (CCD: see Chap. 13).

Carbonate rocks in general are composed of allochemical particles (or *allochems*) and a matrix or cement. Allochems are grains that form the framework in limestones and dolomitic limestones. They can be of several types—fossils–
skeletals, ooids, peloids, and intraclasts. It is generally possible for the petrographer to identify a few fossils, but a more detailed identification must be left to a professional paleontologist.

Ooids are nearly spherical, sand-sized grains with radial and concentric internal structure (Fig. 14.9). Modern carbonate ooids are composed of aragonite

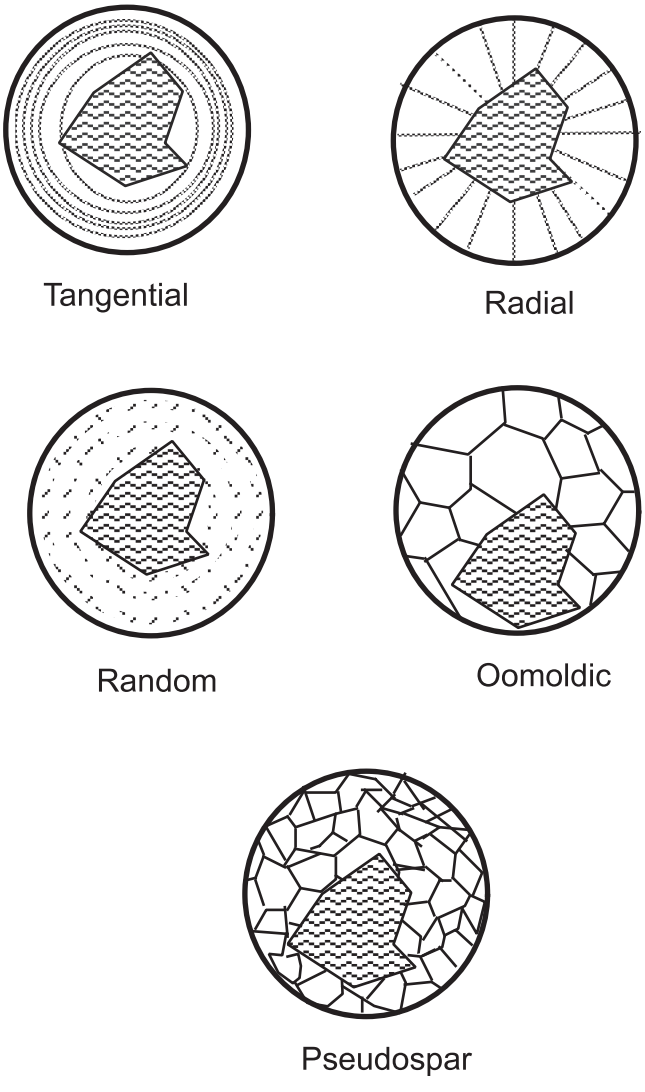

Fig. 14.9 Ooids types

needles organized in a radial fashion and tangentially in concentric spherical layers around a nucleus composed of any preexisting solid in the environment of deposition—such as a quartz grain, peloid, or some skeletal material. Ancient ooids are often which formed during diagenesis. Oolitic limestones are commonly cross-bedded, indicating their deposition from currents after precipitation in water. Oolitic limestones exposed on the Bahama Islands are called *Bahamites* and are actually eolianite or windblown deposits. In such a case the ooids became exposed under dry conditions and were reworked by winds to form oolitic dunes that later became lithified.

Based on laboratory experiments, Davies et al. (1978) concluded that ooids growing in calm waters develop radial internal structure and tangential lamination in agitated waters. In a study of the ooids in hypersaline waters of Baffin Bay (Texas Gulf coast), Land et al. (1979) noted that *tangential aragonite* crystals grow in agitated conditions and *radial structure*, *composed of high-Mg calcite*, grow in calmer waters.

Peloids are the most abundant type of allochems and originate from fecal pellets. Peloids are often crushed during burial to form the matrix of lime mud. However, many may survive but deform under pressure. *Intraclasts*, another common type of allochem, are fragments of previously formed limestones or partially lithified carbonate sediments.

The *matrix or cement* of carbonate rocks is generally composed of calcite or aragonite. The cement may also originate by chemical precipitation from pore waters. The matrix may originate as finely crushed fecal pellets, intraclasts, or skeletal debris. When originally deposited, the grain size of the fine matrix is ~1–5 mm and is called *micrite*. Diagenesis leads to recrystallization and coarsening of grain size whereby micrite turns into *spar*, which is a textural term to denote coarse, blocky, carbonate crystals (Fig. 14.10). Note that if a micrite were originally composed of aragonite, diagenesis would convert the micrite into spar of calcite or dolomite.

Carbonate rocks are *classified* in several different ways. One that is popular with the oil industry is Dunham's (1962) classification (Table 14.2). A first-order distinction is made between *mud-supported* rocks *and grain (allochem)-supported rocks*. In the former, mud separates the allochems, and in the latter, grains touch each other. Limestones lacking mud are called *grainstones*. Limestones made of rigid, organically bound, frameworks of skeletons are called *boundstones* and are normally formed in reefs. When mud is

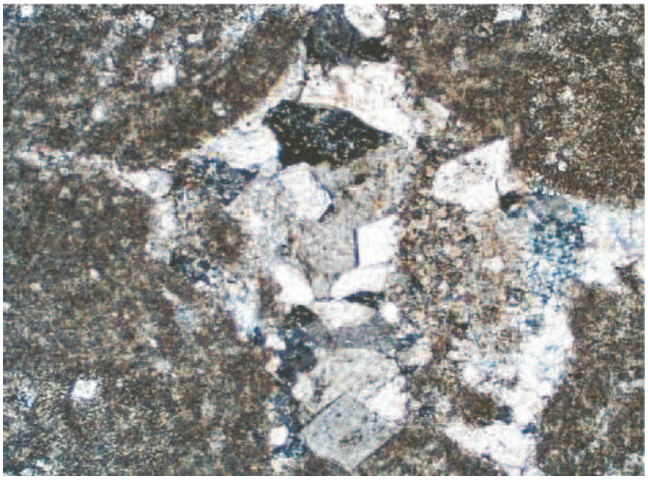

Fig. 14.10 Photomicrograph showing coarse dolomitic cement between ooids

Table 14.2 Classification of carbonate rocks

Components not organically bound during deposition				Organically bound sediments
Carbonate mud present		Mud absent		
Mud supported		Grain supported		
<10% allochems	>10% allochems			
Mudstone	**Wackestone**	**Packstone**	**Grainstone**	**Boundstone**

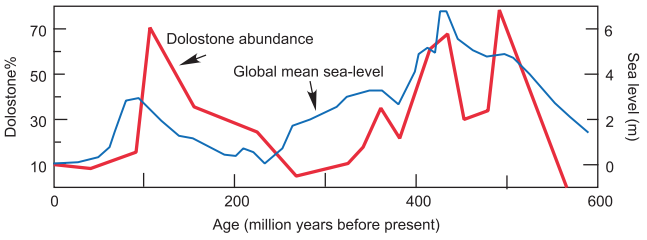

Fig. 14.11 Correlation of dolomite abundance and sea-level stand through time

<~25–30 %, the grains touch each other and mud fills the pore spaces. Such a rock is called a *packstone*. *Mudstone* and *wackestone* are both mud supported, but the difference is that the latter has >10 % allochems and mudstone has <10 % allochems. It is a common practice to use a forename based on a distinctive character of the rock: for example, a grainstone composed almost entirely of ooids would be named an *oolitic grainstone* or an *ooidal grainstone*.

Dolomitization

Dolomite may form in one of two ways: as a primary precipitate (Eq. 14.1 below) or as a diagenetic replacement of calcite or aragonite (Eq. 14.2):

$$Ca^{2+}[\text{soln.}] + Mg^{2+}[\text{soln.}] + 2(CO_3)^{2-}[\text{soln.}] = CaMg(CO_3)_2[\text{dol. cryst.}] \quad (14.1)$$

$$2CaCO_3[\text{calc/arag.}] + Mg^{2+}[\text{soln.}] = CaMg(CO_3)_2[\text{dol. cryst.}] + Ca^{2+}[\text{soln.}] \quad (14.2)$$

As discussed earlier, dolomite has not been found to precipitate in any modern "normal" environments nor has it been successfully made in the laboratory under "normal conditions." Thus, those dolostones containing structurally well-ordered dolomites that are common in the geological record must have formed by diagenesis.

In terms of physical evidence, there are many field examples of dolomite replacing limestone or evaporite and microscopic replacement of calcite by dolomite rhombs. Therefore, the majority of scientists believe that dolomite in stratigraphic sequences is entirely produced through diagnetic replacement of preexisting carbonate deposits—a process known as *dolomitization*. An overall correlation seems to exist between the abundance of dolostones and periods of high stands of sea level through geological time (Fig. 14.11). Also, dolostones are commonly associated with limestones and sometimes with evaporites (principally gypsum and anhydrite) or pseudomorphs of gypsum. These features have led scientists to propose different models of origin of dolostones via diagenetic replacement of calcium carbonate by dolomite. There are several dolomitization that can happen, as discussed below.

In the *evaporative reflux* model (Fig. 14.12a), the two required conditions are (1) stagnant pools of ocean water in supratidal regions and (2) carbonate deposits underneath such pools (Patterson and Kinsman 1982). In this model, evaporation of hypersaline waters in these pools leads to supersaturation and precipitation of gypsum ($CaSO_4{\cdot}2H_2O$), an evaporite. Formation of gypsum depletes the water in Ca^{2+} but enriches it in Mg^{2+} and increases its density, making it a Mg-rich brine solution. The brine sinks into the substratum because it is heavier than the accumulated layers of gypsum. The Mg-rich brine dissolves the calcite or high-Mg calcite as it seeps into the underlying carbonate substratum, thus converting the limestone into a dolostone. This model of dolomitization requires enormous masses of evaporite (or at least, pseudomorph or other structures reminiscent of previous existence of evaporite minerals, such as gypsum or anhydrite) to be associated with dolostones. In reality, however, many dolostone occurrences are not associated with evaporite (or former evaporite) beds.

A second model of dolomitization involves mixing between marine waters and freshwaters and is known as *dorag dolomitization* (Fig. 14.12b; Badiozamani 1973). In the subsurface of coastal areas, the lighter freshwater floats above denser saline (marine) waters in the pore spaces of the bedrock–regolith. The contact surface between the two pore waters crops out near the coastline and dips landward. In a detailed study of the formation of dolostone in Pleistocene reefs of Jamaica,

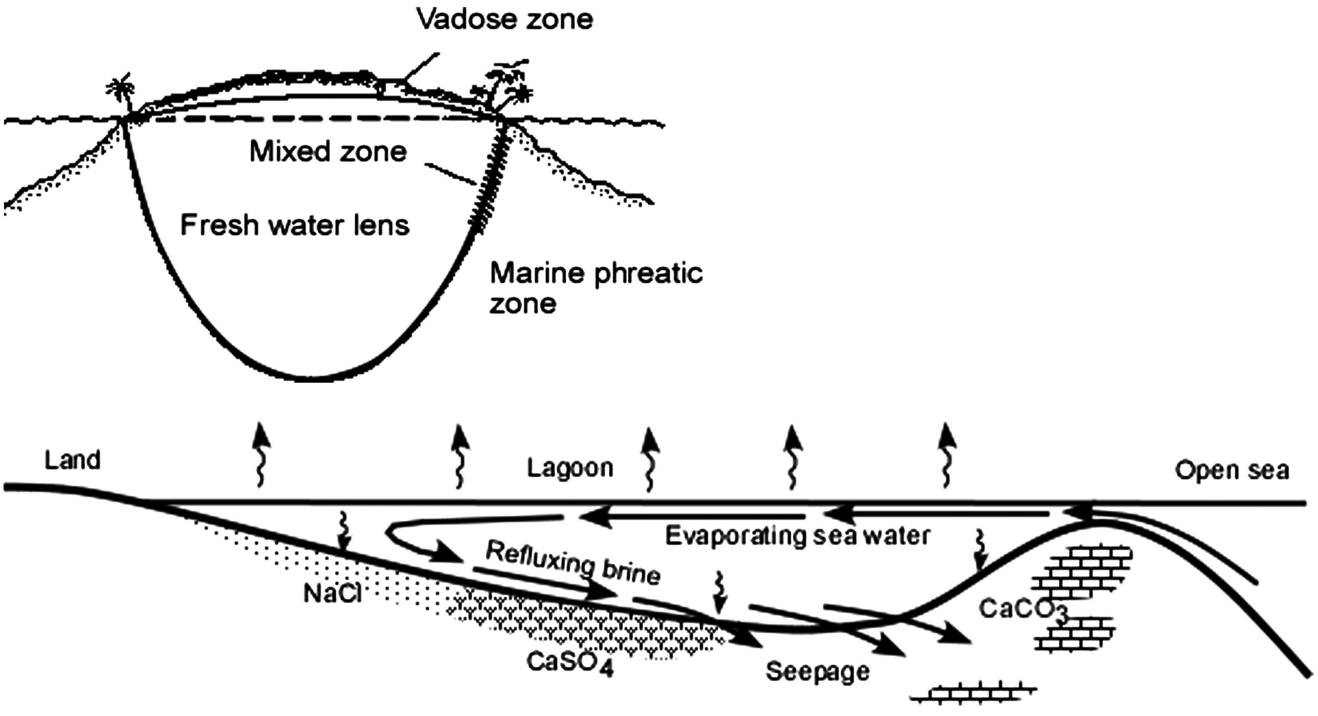

Fig. 14.12 Models of dolomitization

Land (1973) noted that the dolostone replaces limestone along such a dipping zone marking mixing between marine with fresh pore waters. The way this works is as follows. The curvature of the solubility curves of calcite is such that when the two different waters, both saturated with calcite, are mixed, the mixed water is likely to be undersaturated in calcite; and therefore, it will dissolve calcite of the limestone (Fig. 14.13). At the same time it will be superaturated with dolomite and therefore will precipitate dolomite. Whereas a wider range of mixing between seawater and freshwater is permitted for *ordered dolomite* precipitation (Fig. 14.13), the composition of the mixed water is rather limited [~30–40 % seawater and the rest meteoric (fresh) water] for the case of precipitation of *disordered dolomites*. Given this fact, it is truly

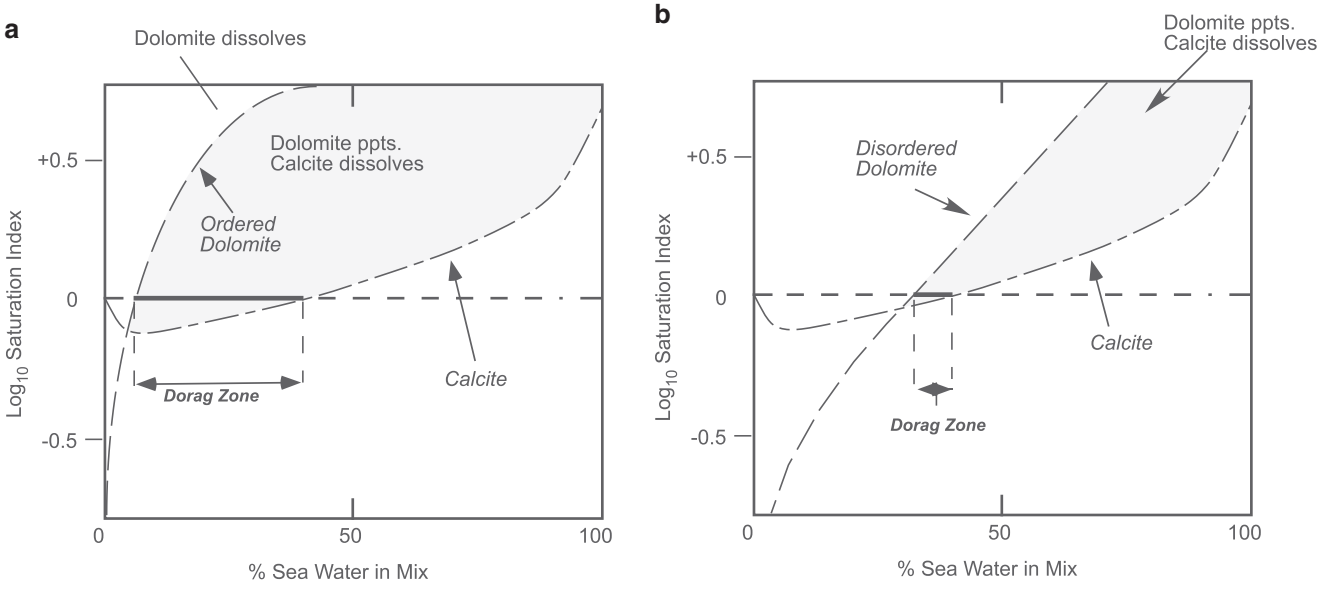

Fig. 14.13 Calcite and dolomite saturation conditions. The *shaded area* marks the area where dolomite precipitates and calcite dissolves. (**a**) Conditions for ordered dolomite precipitation. (**b**) Conditions for disordered dolomite formation

surprising why ordered dolomite does not precipitate in natural environments and must be due to some kinetically inhibiting factor (s).

Some authors believe that mixing between freshwater and seawater is unnecessary and dolomite may precipitate from normal seawater as long as enough unmodified seawater is continuously "flushed" through a limestone or lime mud, because such flushing would provide a constant source of Mg^{2+} and remove Ca^{2+}. Carballo et al. (1987) proposed such a model for dolomitization of lime mud at Sugarloaf Key, Florida, where they noted flushing by normal seawater through lime mud has been happening through tidal rise and fall of sea level. As a result, the pore fluids are constantly replenished in Mg^{2+} while Ca^{2+} is being removed, forming dolomite in the process. This process has been called *tidal pumping*.

The models discussed above are all concerned with shallow dolomitization, which most authors believe to be the most common mode of dolomitization. It seems plausible that such *early dolomitization* can happen in a wide variety of environments. *Late dolomitization* during deep burial is considered by other authors to be an important process. In such a process, the source of Mg in the dolomitizing fluids is often a problem. Some authors believe the Mg^{2+} comes from the breakdown of clay minerals (smectite). Others believe that seawater can continuously percolate through to deep levels obeying Darcy's law of fluid movement and replace calcite with dolomite. The "dolomite problem" is far from being over; however, it is beyond the scope of this text to discuss the merits and demerits of every published model.

In passing, it should be noted that dolomite may dissolve in fluids under certain conditions and calcite may be precipitated in its place. Such a process is referred to as *dedolomitization*. In such a case, it is generally possible to recognize a calcite pseudomorph after dolomite rhomb. Figure 14.13 shows that dedolomitization will likely occur if dolomite is exposed to open marine or restricted hypersaline (lagoonal) environments.

Orthochemical Rocks

Evaporites

Evaporites are rocks composed of minerals that precipitate directly from saline waters as a result of evaporation. The three most common classes of evaporite minerals are sulfates, halides, and carbonates. Carbonates have already been discussed in the preceding sections. Among the sulfates and halide minerals, the most abundant evaporite minerals are *gypsum* ($CaSO_4 \cdot 2H_2O$), *anhydrite* ($CaSO_4$), and *halite* or *rock salt* (NaCl). In general, evaporites are found in two types of environment—*continental deposits* generally formed in desert playas (ephemeral lakes) and *warm shallow marine environment* (salinas or sabkhas: Fig. 14.14). In both cases, the rate of evaporation is much greater than the rate of influx of water. In the shallow marine, salinas-type environment, deposition of evaporite occurs in a restricted basin largely isolated from open sea such that the basin receives only episodic influxes of seawater interrupting strong, long-term, evaporation. In this type of environment,

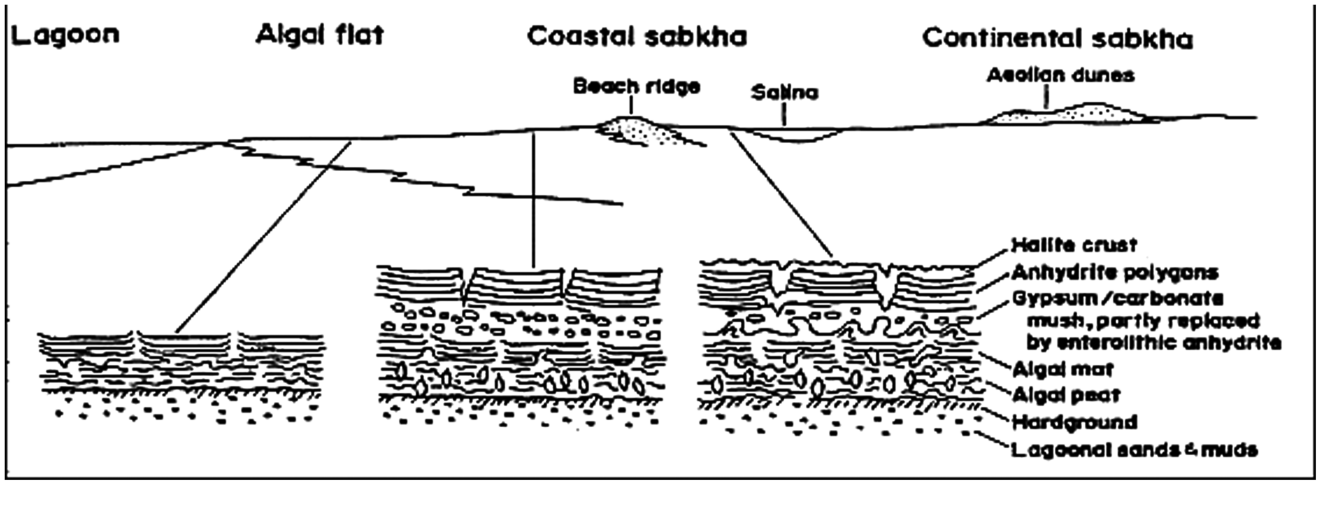

Fig. 14.14 Warm, shallow marine (sabkha) environment

evaporites are often associated with limestones and dolostones. In desert mudflats and playas, evaporite deposits are often associated with poorly sorted siliciclastic talus deposits.

Field occurrence of evaporite deposits and laboratory experiments indicate a definite sequence in which different evaporite minerals precipitate during evaporation of seawater (Fig. 14.15). Carbonates appear when the volume of water is reduced by half via evaporation. The next precipitate is gypsum when the original water volume is reduced to ~20 %, followed by halite. Sylvite (KCl) is last as water volume is further reduced to less than 2 %. Anhydrite forms either as a primary precipitate or by dewatering of gypsum during diagenesis.

Lamination, composed of alternate layers of white gypsum–anhydrite and gray calcite or aragonite ± organic carbon, is common in evaporite deposits. Mudcracks, slump structures, and ripple marks may also be found. Many other diagenetic structures are also found in evaporites.

Evaporite deposits have been found in sedimentary sequences dating from the late Cambrian to the Miocene in various parts of the world. Two notable examples are the >2-km-thick evaporites of the Messinian (Miocene) of the Mediterranean basin and the >600-m-thick Upper Silurian evaporites of the Michigan Basin. Interpretative models for the origin of such gigantic evaporite deposits have all been based on modern analogs and are thus not all satisfactory. One proposal for producing such ancient deposits of enormous thickness is a subsiding basin with occasional influx of seawater.

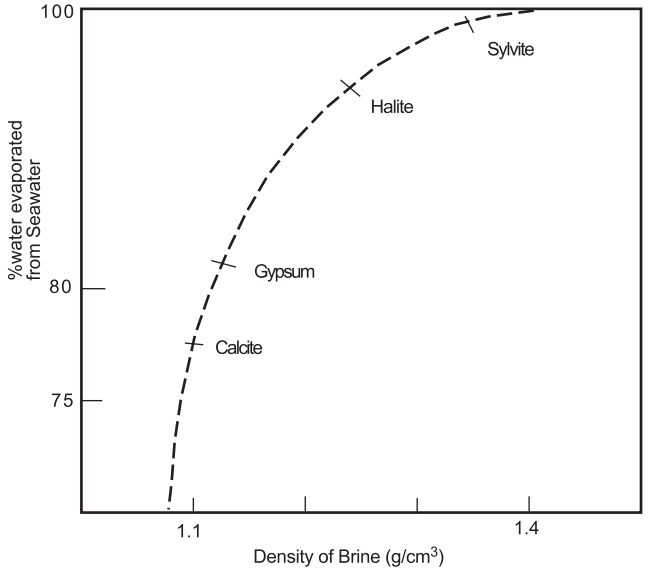

Fig. 14.15 Sequence of crystallization of evaporite minerals as a function of evaporation and density of brine

Chert

The name *chert* (syn. *Flint*) is used to broadly include all siliceous, generally biogenic, sedimentary rocks. They comprise <1 % of all sedimentary rocks but are found in stratigraphic sequences of all ages and from different facies, including the deep oceanic (pelagic) environments. Many different morphological and mineralogical types of cherts have been recognized. The silica minerals in cherts include *chalcedonic quartz*, *opal-A* (amorphous silica), and *opal-CT* (disordered cristobalite and tridymite). Many different types of cherts have been recognized in geological record: *Jasper* is a red-colored chert that is often associated with Precambrian banded iron formations. *Novaculite* is a particular fine-grained, very dense, variety of chert that is found in the mid-Paleozoic of Arkansas. *Porcelanite* is a type of chert that takes its name from porcelain because it fractures like porcelain.

It appears that a great number of cherts are *biogenic in origin* and they form by remobilization of silica from the accumulation of skeletal debris of siliceous *Protista*. Seawater is seriously undersaturated in SiO_2, and therefore, it is unlikely that SiO_2 can precipitate directly from seawater unless the pH is locally increased by some "special situation" to >10. In a sense it is surprising that radiolaria and diatoms can survive in seawater, which is so undersaturated in silica. Protection against dissolution may be provided when they are alive by an organic coating that prevents physical contact with seawater. Upon their death, the organic coating decomposes and the siliceous skeletal matter gets dissolved in seawater unless their deposition is faster than the rate of dissolution and productivity is high.

Opal-CT and quartz in ancient cherts probably all formed by diagenetic alteration of opal-A. The origin of *bedded cherts* or *ribbon cherts*, typically characterized by rhythmic bedding, is somewhat difficult to determine. These are common in old sedimentary rocks where they appear to be associated with shallow marine deposits.

Iron-Rich Sedimentary Rocks: Iron Stones and Banded Iron Formations

All sedimentary rocks contain some amount of iron, but those containing >15 % iron are generally referred

to as iron-rich sedimentary rocks. Volumetrically, these rocks are really a minor component of the Earth's sedimentary rocks; however, they are extremely important for a number of reasons. Among others, perhaps their economic significance is the most important because 90 % of the world's iron ore comes from Precambrian iron-rich sedimentary rocks.

Significantly, global deposits of iron-rich sedimentary rocks formed at three distinct time intervals—Precambrian/Archean (3,400–2,900 Ma), Early Proterozoic (2,500–2,000 Ma), and Jurassic–Cretaceous (200–65 Ma). These deposits can be broadly grouped into two types—*iron stones and iron formations* (also, *banded iron formations or BIFs*). The most abundant and economically important of these two are the *iron formations*. These are Precambrian in age and are generally alternately banded with jasper. Individual deposits are enormously thick (50–600 m), are widespread (hundreds of km), and are predominantly composed of magnetite and hematite. In contrast, ironstones are Phanerozoic in age, not as thick (few tens of m), and are poorly or non-banded. They are typically oolitic, are associated with carbonates, and appear to have been deposited in shallow marine or lacustrine conditions. The iron mineral is goethite or limonite forming the oolitic coatings on a nucleus of quartz, carbonate, or other allochems.

The origin of BIFs is very important. Most authors believe that the source of iron was continental crust. Lepp and Goldich (1964) first suggested that the oxygen level in Precambrian atmosphere was extremely low, allowing transportation of dissolved iron in Fe^{2+} state in rivers to shallow seas. Many authors believe that it is here somehow oxygen-rich environment was locally created by bacterial and/or photosynthetic algal activities, so that iron oxide was precipitated. There are many variations to these postulations, including groundwater transport and/or colloidal transport of iron. However, none of these explanations has been entirely satisfactory. Also, these models cannot explain the easily observed differences between BIFs and iron stones.

Box 14.1: How to Describe Sedimentary Rocks

Color, mineralogical composition, texture, and megascopic ("field"-scale) structures are all important parameters in deciphering the provenance, transportation, and depositional histories of sedimentary rocks. Accordingly, these

(continued)

Box 14.1 (continued)

elements must be present, if appropriate, in the *routine* description of a rock. The description must also be sufficiently detailed such that anyone can have a fairly good idea of what the rock may look like without actually seeing it!

Below is a list of items that should be included in the description of a rock.

Field Appearance (i.e., Megascopic/Hand Specimen Characteristics)

1. *Lithology*. Thickness, color, mineral–organic constituents, grain size (range as well as mean), roundness, shape, and sorting of clasts.
2. *Structure*. Large-scale structures, such as the nature of bedding (e.g., cross-bedding, how thick are foreset beds, the slope angle of foreset beds, etc.), and small-scale structures, e.g., mudcracks, must be described in as much detail as possible.
3. *Associated lithic types and their spatial relationships*. Similar descriptions for all other rock types present and how they are related to the sedimentary bed of interest should be made.

Microscopic Characteristics

The description must start out by identifying the overall textural elements (e.g., matrix supported or clast supported, porosity, fossiliferous) and separate the nature of allochemicals from matrix or cement.

Allochemicals

1. Modal composition (i.e., relative abundance of minerals, rock fragments, fossils, ooids, peloids, etc.)
2. Grain-size distribution (range, mode, etc.)
3. Grain shapes and roundness (spherical, well rounded, angular, etc.)
4. Sorting (well sorted, medium sorted, poorly sorted)

Cement/Matrix

Compositions and generations of cement and matrix and the physical relationships: It may be possible to identify different generations of cement in which one may replace (cut across) another and so on. Cathodoluminescence and SEM (back-scattered electron) imaging of cements often provide strong clues to zoning and replacement features in cement.

Metamorphism and Metamorphic Rocks

15

Abstract

In the previous chapters, we learned about igneous and sedimentary rocks. This chapter presents some general concepts concerned with the process of metamorphism and the formation of metamorphic rocks. How pressure, temperature, and fluids control metamorphic processes and resulting metamorphic changes are discussed.

Metamorphism

Metamorphism is the sum of all processes that involve mineralogical, textural, and chemical transformation of an igneous, sedimentary, or metamorphic rock into a different rock, called a *metamorphic rock*. Metamorphic reactions occur largely in solid state with only limited changes in chemical composition of the original rock or *protolith*. They occur in response to changes in the environmental conditions, e.g., changes in pressure, temperature, and fluids migrating through them, related to such diverse geological phenomena as mountain building to emplacement of igneous intrusions. Geological time is a significant factor in metamorphism, and it is generally believed that large, regional scale, metamorphic processes (i.e., orogenic metamorphism) operate over a timescale of about 10–50 million years (Bucher and Frey 1994).

The boundary between sedimentary diagenesis and the lower limit of metamorphism is commonly placed at ~150 ± 50 °C, which is roughly the temperature at which certain metamorphic minerals, including glaucophane, lawsonite, prehnite, pumpellyite, or stilpnomelane, begin to form in the rock undergoing increasing intensity of metamorphism. The high temperature limit of metamorphism is constrained by melting of the rock itself (Fig. 15.1). In Fig. 15.1, the solidi of "wet" (water saturated; $p_{H2O} = p_{total}$) and "dry" (volatile-free) granite are shown. Because crustal rocks are generally expected to form granitic melts upon melting, the two solidi simply show the minimum temperatures under wet versus dry conditions at which metamorphism gives way to igneous processes. The upper temperature "limit" of metamorphism (i.e., melting) will vary from place to place depending on the bulk composition of the protolith and abundance and composition of the fluid species. In terms of pressure limits, metamorphism can occur at fairly shallow levels in the crust, such as at the mid-ocean ridges, to as deep as the entire depth of the mantle and the inner core.

Until recently, there was not much knowledge available about the types of metamorphosed rocks of crustal origin (excluding peridotitic compositions) that may exist deep within the Earth. Experimental studies at high pressure and discoveries of metamorphic rocks with minerals like coesite and microdiamonds (altered) from a number of localities around the world (such as, Dabie Shan, Eastern China: Coleman and Wang 1995) have led to the recognition of a new class of metamorphism—metamorphism occurring at pressures of greater than 2.8 GPa is referred to as *ultrahigh-pressure* metamorphism (Coleman and Wang 1995).

G. Sen, *Petrology*, DOI 10.1007/978-3-642-38800-2_15,

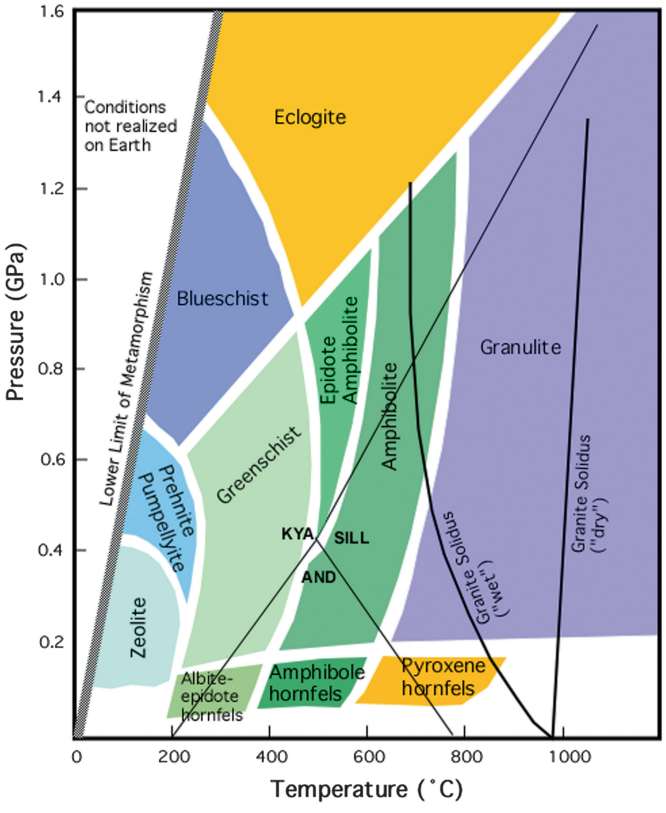

Fig. 15.1 Pressure–temperature regime of metamorphism. The Al_2SiO_5 phase diagram and metamorphic facies (discussed in Chap. 16) are shown for reference

Agents of Metamorphism

Temperature

The heat required for metamorphism may be supplied by (a) the heat released by igneous intrusions to the surrounding country rocks, (b) the geothermal gradient, (c) radioactive decay, (d) latent heat of crystallization given off by a crystallizing magma, (e) exothermic metamorphic reactions, and (f) shear heating (Spear 1993). Among them, magmatic heating and geothermal heat are by far the two most important mechanisms. Large (hundreds of cubic kilometers) sections of continental crust buried deeply beneath fold-thrust belts over a subduction zone are likely to be metamorphosed due to pressure and heat provided by the geothermal gradient as well as by granitic batholiths or other deep-seated igneous intrusions. At the other extreme, on a much smaller scale, contact metamorphism takes place: shallow crustal wall rocks around an igneous intrusion may be metamorphosed principally by the heat transferred from the intrusion to the wall rocks.

Box 15.1

In the event of an igneous intrusion, the wall rocks surrounding the intrusion are heated by the intrusion. Such heat transfer may result in nucleation and growth of new minerals or coarsening of mineral grains (or both) in the wall rocks, which is metamorphism. The mechanism by which heat is transferred to the wall rocks is largely conduction, although advective (i.e., "one way", irreversible) transport by fluids percolating through the wall rocks is also likely to be important.

Here we examine cases where igneous intrusions of different dimensions heat up the surrounding wall rocks and determine how long it takes for the wall rocks to heat up via conductive transport as a function of time and distance from the intrusion. Consider the case of transfer of heat by conduction from an intrusion along a specific direction "x" into the wall rock. *Fourier's law* indicates that the rate of heat flow across a unit area (i.e., $dQ/[dt\,A]$, where Q is heat, A is area, and t is time), known as the *heat flux* (J_x), is proportional to the temperature difference (dT) between the transmitter (magma) and the receiver (wall rock) and inversely proportional to the distance (dx) between them:

$$J_x \propto [dT/dx]$$

$$\text{or,} \quad J_x = k[dT/dx] \qquad (15.1)$$

where "k" is a proportionality constant known as *thermal conductivity*. The unit for thermal conductivity is $J\ s^{-1}\ m^{-1}\ C^{-1}$ (joules per sec per meter per degree Celsius). The unit for heat flux is $mW\ m^{-2}$ (milliwatts per square meter; 1 W = 1 J s^{-1}). Fourier's law indicates that the heat flux from a deep-seated pluton into the surrounding rocks will occur much more slowly than from a shallow-level intrusion (with same initial emplacement temperature) to the surrounding wall rocks, because "dT" (which is the temperature difference between magma and wall rock) will be greater at shallow levels than at deep levels.

Heat capacity of a rock at a constant pressure, C_p, is the amount of heat necessary to raise its

(continued)

Box 15.1 (continued)

temperature by 1°. Assuming that this rock has a density of r, then the amount of heat required to raise the temperature of unit volume of the rock by 1° is $C_p r$. *Thermal diffusivity*, k, is an important property of any material which tells us the rate at which the temperature of that material may increase and is given as

$$k = k/[C_p r] \tag{15.2}$$

k is roughly equal to 10^{-6} m^2 s^{-1} for most magmas and rocks.

In the one-dimensional case of heat flow from an intrusion into the wall rock, the rate of temperature rise (i.e., dT/dt) is given as follows (Fourier's equation):

$$dT/dt = k(\partial^2 T/\partial x^2) \tag{15.3}$$

The temperature "T" at a distance "x" within the wall rock away from an intrusion can be determined by a solution to the above equation. A simple solution was given by Carslaw and Jaeger (1959):

$$[T - T_o]/[T_s - T_o] = 1/2[\mathrm{erf}[(h - x)/(2 \times \sqrt{(kt)})] + \mathrm{erf}[(h + x)/(2\sqrt{(kt)})]] \tag{15.4}$$

where "T_o" is the initial magma temperature, "T_s" is the solidus temperature of the magma, and "h" is the half-thickness of the intrusion (in meters). "erf" is something called an "error function" and may be found in tables of some textbooks (such as Tables 4–5 in Turcotte and Schubert 1982). Equation (15.4) suggests that the initial thermal perturbation due to the emplacement of an igneous intrusion will decay exponentially with time.

A reasonable, straightforward, estimate of how long it may take for an igneous intrusion to cool to ambient temperature can be obtained from the equation

$$t = h^2/k \tag{15.5}$$

(continued)

Box 15.1 (continued)

Using Eq. (15.5), and assuming a $k = 1 \times 10^{-6}$ m^2 s^{-1}, we calculate that a 0.2-km-thick ($h = 100$ m) dike will take ~317 years to cool back to the ambient temperature, whereas a 20-km ($h = 10$ km)-thick pluton will take 3.17 million years to do the same. Therefore, all other factors being equal, a thick pluton will be more likely to have an extensive metamorphic aureole (i.e., zone of metamorphism surrounding the pluton) compared to a narrow dike.

Spear (1993) pointed out that Fourier's law of heat conduction is similar to Fick's law of chemical diffusion: $\partial C/dt = D(\partial^2 C/\partial x^2)$, where $\partial C/\partial t$ is the change of concentration of a chemical species as a function of time and D is chemical diffusivity (equivalent to thermal diffusivity). While k is around 10^{-6} m^2 s^{-1} (10^{-2} cm^2 s^{-1}), D is orders of magnitude smaller (e.g., 10^{-16} to 10^{-20} cm^2 s^{-1} for cation diffusion in garnet at 500–700 °C, Spear 1993). What this comparison means is that thermal equilibrium will be achieved much faster than chemical equilibrium in a volume of rock undergoing metamorphism.

Pressure

The pressure within the Earth's lithosphere is fundamentally of two kinds (Fig. 15.2): (1) *Confining pressure* (*syn. lithostatic pressure or load pressure*), which is the pressure applied on a deeply buried rock by surrounding rocks. It is like hydrostatic pressure (which is the pressure applied by water on an immersed object) in the sense that magnitude of this pressure is equal from all sides. The two examples—a square and a circle—in Fig. 15.2a exemplify the first-order effect of confining pressure: it mainly reduces the volume and increases the density of the rock. Confining pressure is important in deep, hot, crustal roots of mountains in orogenic belts. (2) *Deviatoric stress* (*syn. shear stress*, *directed pressure*) is one in which the pressure applied is strongly directional: Fig. 15.2b shows two examples in which the pressure, stress, is being applied only on the top and bottom. In each case, the top and bottom are being "dragged" in opposite directions so that both the square and the circle deform such that they assume more elongated geometrical forms.

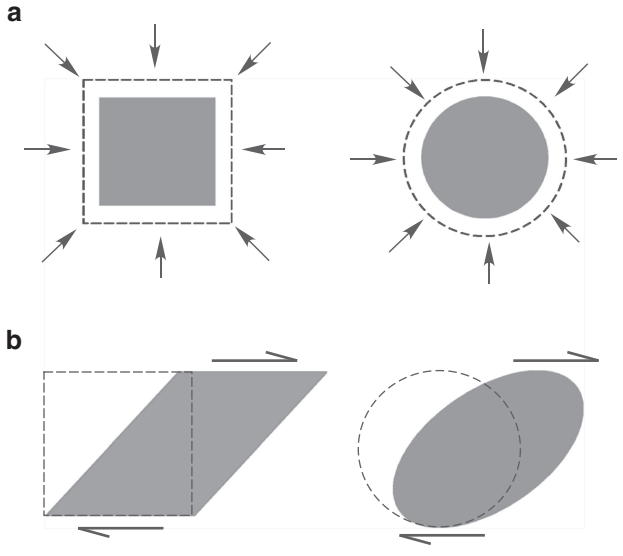

Fig. 15.2 Types of pressure responsible for metamorphism. (**a**) Confining pressure (also called hydrostatic pressure or lithostatic pressure) and its effect on a cube and sphere (shown in two dimensions). (**b**) Deviatoric stress and its effect on a cube and a sphere (in two dimensions)

How a rock will respond to deviatoric stress depends on confining pressure, temperature, and the strain rate: At low confining pressure, a rock may fracture due to brittle deformation, whereas the same rock may "flow" (ductile behavior) at very high confining pressure. Strain rate is the rate of deformation, of a mineral grain, i.e., change of the mineral's geometrical attributes such as shape and volume in response to pressure applied on it. As an example, consider the rock peridotite. At low crustal pressures and relatively "cooler" conditions, peridotite behaves as a brittle material. The same rock "flows," i.e., exhibits ductile behavior, in the asthenosphere due to high temperature and very low strain rate.

Aside from confining pressure and deviatoric stress, shock waves may be sent through a rock due to the impact of a meteorite. Such *shock pressure* may induce metamorphism in the impacted rock. Finding shock metamorphic minerals at/near the Earth's surface is sometimes the only way to positively identify the site of an ancient meteorite impact, because weathering, erosion, and sedimentation erase much of the telltale topographic signatures of an impact crater in most cases.

Fluids

The role of fluids in metamorphism is of great interest to metamorphic petrologists. Although metamorphism is largely a solid-state process, highly reactive intergranular *fluids* commonly participate in metamorphic reactions as a reactant or product and/or as a facilitator that accelerates reactions between solid reactants. Without any involvement of fluids, metamorphic reactions would be tremendously slow because diffusion of chemical components is orders of magnitude slower in solids than in fluids. The intergranular fluid is generally a mixture of H_2O and CO_2 and may simply be groundwater heated by geothermal gradient or by an igneous intrusion, or the fluid may be derived directly from the igneous intrusion.

Most petrologists distinguish between *isochemical metamorphism* (which is commonly accepted as metamorphism) and *metasomatism* depending on the extent to which fluids alter the bulk chemical composition of the original rock: If the bulk chemical composition is significantly modified, then the process is called *metasomatism*; if not, then it is called *isochemical metamorphism*. Some common, but limited, bulk chemical changes of the protolith occur—mainly by hydration or dehydration and change in Na and K contents in metamorphism.

Metamorphic Changes

Metamorphism results in the following changes in the mineralogy and texture of rocks:

1. *Recrystallization*. Change in grain size in response to temperature change and/or deviatoric stress is the simplest type of change. *Coarsening* of grains is an example of recrystallization. Grain-size reduction (*pulverization*) due to shearing along fault zones is another.
2. *Neomineralization*. Growth of new minerals is the most common type of metamorphic change. For example, in Chap. 3, we noted that when a kyanite-bearing metamorphic rock is heated to very high temperature and pressure, kyanite will transform into sillimanite. Thus, formation of sillimanite is due to a polymorphic transformation reaction. There are other ways for new minerals to form, for example, by hydration (e.g., formation of serpentine at the expense of olivine) or dehydration reactions (e.g., formation of K-feldspar at the expense of mica).
3. *Development of oriented fabric*. Metamorphism often results in the development of oriented fabric, such as foliation (a pervasive (i.e., present throughout the rock) planar structure defined by parallel structural planes in the rock, defined below) and lineation [pervasive alignment of linear elements (e.g., prismatic mineral grains) in a rock].

Types of Metamorphism

Metamorphic rocks can form in a variety of geological environments—from mid-ocean ridge to island arcs and continental arcs and orogenic belts (i.e., fold-thrust belts) to continent–continent collision zones (Fig. 15.3). *P–T* conditions are very different in each of these environments. Beneath the mid-ocean ridges, hydrothermal solutions (hot water solutions rich in dissolved chemical species) percolate into the crustal rocks and trigger metamorphic reactions. The water may have an igneous origin, or it may simply be ocean water filling up cracks in the crust and heated by shallow magma bodies. In this type of environment, pressure has virtually no role in initiating metamorphic reactions, and therefore the *P–T* path taken by the rocks undergoing metamorphism is one of very low pressure but low-to-high temperatures (Fig. 15.1). In contrast, in subduction zone environments and in areas where rapid overthrusting of continental slices is a characteristic feature, pressure generated by the convergence of two plates is the dominant control and temperature is a relatively minor factor. Metamorphic rocks produced in such an environment are characterized by a high *P*–low *T* path (Fig. 15.1). Orogenic belts located along active continental margins are hundreds to thousands of kilometers long and are characterized by extreme deformation and recrystallization. In this type of environment, both pressure and temperature increase (Fig. 15.1).

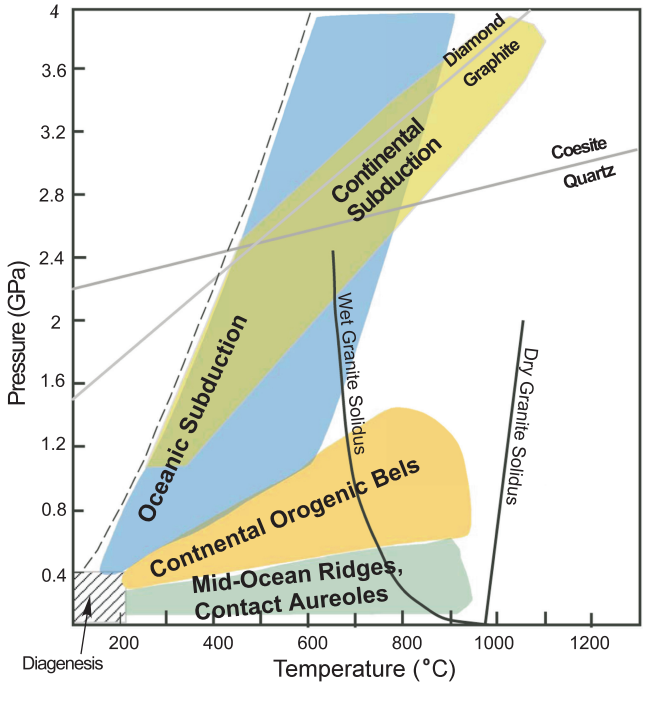

Fig. 15.3 *P–T* conditions in various plate tectonic regimes

Many different classes of metamorphism have been recognized. These classifications are based on the principal agent of metamorphism (i.e., *P* and/or *T*), geological setting (i.e., local or regional), or plate tectonic environment. Excellent accounts of classification schemes of metamorphism may be found in books by Spear (1993) and Bucher and Frey (1994), and the interested reader is advised to peruse these books for this purpose. In this book I will focus on the principal characteristics of the various types of metamorphism.

Following Bucher and Frey (1994), a first-order distinction is made between the types of metamorphism that are of local extent (less than "a few" kilometer) and those that are of regional extent (cover hundreds to thousands of square kilometers; Fig. 15.4). Further classification is based on the geological affinity. Note that, as with any classification, the boundaries between the divisions are gradational.

Regional Types

Regional Contact Metamorphism

Although contact metamorphism is a localized phenomenon, in orogenic areas, many intrusions may be emplaced fairly close to each other in space and time. And as a result, their contact metamorphic aureoles may overlap and form a broad region of metamorphism. In these areas, the conditions are mainly low pressure and high temperatures.

Burial Metamorphism

This type of metamorphism is typical of sedimentary basins where deeply buried sediments undergo compaction and metamorphism due to load pressure of the overlying sediments. In this case, temperature increases with pressure and closely follows the geothermal gradient. In burial metamorphism, the boundary between diagenesis and the beginning of metamorphism is not at all distinct. An excellent example of burial metamorphism comes from southern New Zealand (Boles and Coombs 1977).

Ocean-Ridge Metamorphism

Basalts, gabbros, and ultramafic rocks are often exposed along fracture zones that cut across mid-ocean ridges. Dredged and drilled samples of fracture zone rocks frequently show the presence of three types of

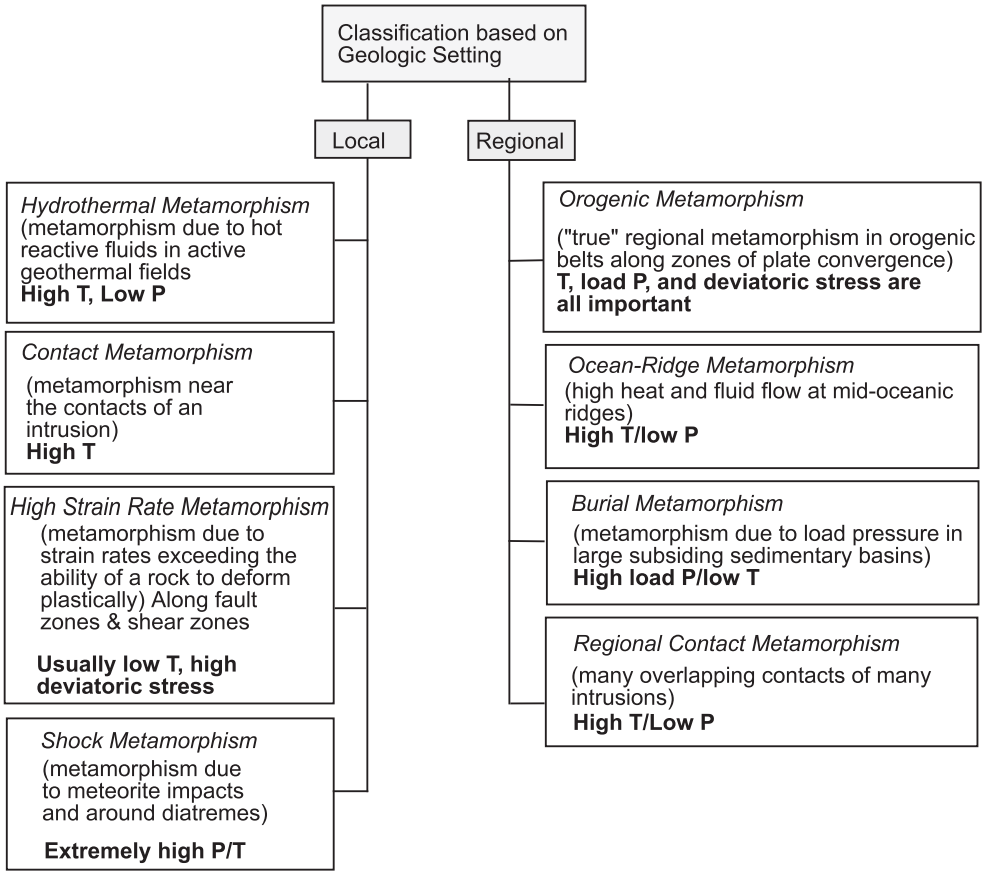

Fig. 15.4 Types of metamorphism

metamorphic rocks—serpentinite, amphibolite, and greenstone. Serpentinites are metamorphosed ultramafic rocks, whereas greenstones and amphibolites are metamorphosed basalts and gabbros. This type of metamorphism results from high heat flow along the ridge axis and hot circulating fluids running through pore spaces and fractures in the rocks and was called "ocean-ridge metamorphism" by Miyashiro et al. (1977).

Orogenic Metamorphism

This type of metamorphism is typical of orogenic belts along active continental margins (i.e., margins where subduction is active: continent–continent collision and continent–ocean collisional areas) and island arcs. The term "regional metamorphism," often used by many authors, is generally synonymous with orogenic metamorphism. Sometimes the term "dynamothermal metamorphism" is also used to mean the same thing because both pressure and temperature are important factors in this type of metamorphism. Orogenic metamorphic rocks form the most extensive belts among all types of metamorphic rocks. Most of the research on metamorphic rocks, present and past, has been focused on them because they provide valuable information on burial, uplift, and erosional histories of orogenic belts.

Local Types

Contact Metamorphism

This type of metamorphism occurs in the wall rocks of shallow crustal intrusions and is mainly caused by the heat provided by the intrusion. Pore water in the wall rocks and/or fluids released by magma (intrusion) often play a role in the metamorphism of the wall rocks. The metamorphosed contact zone is referred to as a *contact aureole*. Pressure is limited to a maximum of about 0.3 GPa in contact metamorphism. Contact aureoles are generally thin, ranging only up to a few kilometer. The thickness of the aureole depends upon the thickness of the intrusive and temperature difference between the magma and the wall rock. Because the temperature difference between a magma and wall rock is likely to be the highest at shallow crustal levels,

contact aureoles are generally most spectacular around shallow-level intrusions.

Contact metamorphic rocks typically lack any directional textures, such as *foliation* (*a penetrative planar texture*), and develop *hornfelsic* texture (a fine-grained texture lacking any directional features). Note that these textural terms are further illustrated in a later section. *Skarn* is a type of contact metamorphic rock formed due to reaction between limestone and fluids released by the igneous intrusion. Skarns are composed of calc–silicate minerals (such as wollastonite, diopside, grossular) and often serve as loci for ore deposits. Other contact metamorphic rock types include marble and hornfels.

Shock Metamorphism

This type of metamorphism results from shock waves created by the impact of a meteorite. Typical minerals produced by meteorite impact are some very high-pressure polymorphs of crustal minerals—such as coesite, stishovite, and, rarely, microdiamonds.

High-Strain Metamorphism

In areas such as along fault boundaries or shear zones, strain rates (and deviatoric stress) are very high, exceeding the ability of the rocks to deform plastically. In such an environment the rocks undergo crushing and grinding (*cataclasis*) without much temperature change. Such mechanical action pulverizes the rock into a fine-grained rock with fine foliation (called a *cataclasite*). Another typical rock that develops under such conditions is a *fault breccia*, which is a type of cataclasite with visible angular fragments.

In shear zones, however, ductile flow occurs which results in bending of grains, internal slip within grains, and some recrystallization (i.e., grain growth). In this case, the rock that develops is called a *mylonite*. Best (1982, pp. 350–365) provided an excellent explanation of the differences between fault zones and shear zones and illustrated how different textures may develop in high-strain metamorphic rocks, and the reader may wish to consult his book.

Hydrothermal Metamorphism

This type of metamorphism is typically found to occur in geothermally active areas where hot reactive fluids react with the wall rocks and form new minerals. Hydrothermal metamorphism may be studied by drilling into the rocks in such geothermal areas. The source of the fluids may be igneous intrusions or groundwater heated by deep-seated magmatic intrusions or hot groundwater heated by the geothermal gradient.

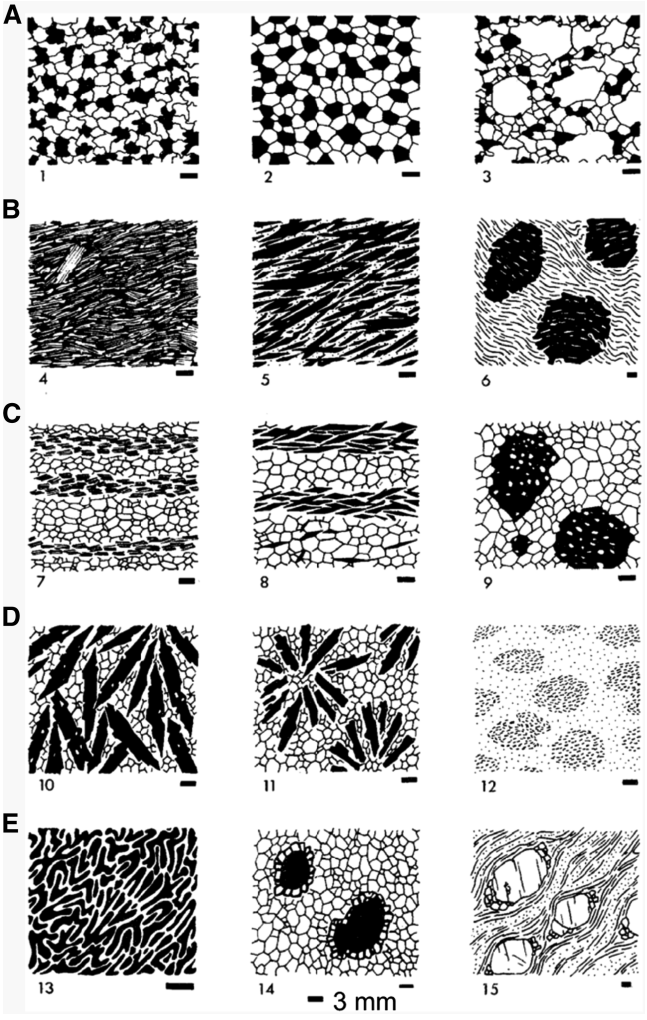

Fig. 15.5 Principal metamorphic textural types (After Bard 1986) *A. Granoblastic types*. *1* Isogranular texture (equal size xenomorphic/xenoblastic crystals). *2* Mosaic texture (with more triple junctions). *3* Heterogranular texture (different grain sizes). *B. Rock textures dependant on the habit of constituent minerals*. *4* Lepidoblastic texture (foliation defined by mica-type platy minerals). *5* Nematoblastic texture [foliation defined by needlelike or prismatic (e.g., amphiboles) minerals]. *6* Porphyroblastic texture. *10* Sheaf texture. *11* Rosette texture. *12* Vermicular texture *C. Combinations of A and B*—7, 8, 9—are combinations of textural types *A* and *B*. *D. Rocks with spheroidal-type minerals or groups of minerals*. *13* Nodular texture. *14* Reaction corona (explained in Chap. 7). *15* Augen (lens-like) texture. *E. Tectonite textures*

Metamorphic Textures and Their Origins

Many types of textures develop during metamorphism, depending upon the nature of the protolith and the relative intensities of various metamorphic agents (Fig. 15.5). The terms "blast" and "blastic" are used in describing metamorphic minerals and texture, respectively. The terms *idioblastic*, *subidioblastic*, and

xenoblastic are used to describe grain shapes in metamorphic rocks, and these are equivalents of euhedral, subhedral, and anhedral, respectively, we used in earlier chapters while discussing igneous rocks. Similarly, the terms *porphyroblast and porphyroblastic texture* are equivalents of *phenocryst* and *porphyritic* texture of igneous rocks, and *poikiloblastic texture* is metamorphic equivalent of poikilitic texture. Note that the prefix "blasto-" is used to refer to the original texture (i.e., relict texture in the metamorphic rock) of the protolith; for example, *blastoporphyritic* texture in a metamorphic rock means the original porphyritic texture of the igneous protolith that may be seen in the metamorphic rock.

Subsolidus or fluid-aided reaction between mineral grains in a metamorphic rock often results in the development of a *corona* or rim of grains of the product phases around the unstable reactant phase. Such corona structures provide important clues to the pressure–temperature paths followed by the rock. Decomposition of a homogeneous solid solution into two or multiple phases during subsolidus cooling results in *exsolution* structures in metamorphic minerals. It is particularly common in alkali feldspars that have re-equilibrated at lower temperatures. Exsolution structures are most common in metaigneous rocks, especially granulites.

In terms of overall texture of the rock on a microscopic to hand-specimen scale, metamorphic textures can be fundamentally divided into two classes based on whether or not foliation or some other preferred orientation (e.g., lineation) is present. The term *foliation* is a form of penetrative texture and refers to pervasive (i.e., "penetrative") parallel to subparallel planar structure present in a metamorphic rock. These planes are usually defined by subparallel alignment of platy or prismatic minerals like micas and amphiboles, which have a strong preference to grow along the direction of least compressive stress (Fig. 15.6). *Slaty cleavage*, *schistosity*, and *gneissose* texture are all different types of foliation. *Slaty cleavage* is typically developed in a low-grade (i.e., low *P–T*) metamorphic, fine-grained, rock called *slate*. It is characterized by fine subparallel-to-parallel sheets, i.e., rock cleavage. Individual minerals in the matrix are extremely fine grained in a slate. *Schistosity* is typically characterized by subparallel alignment of sheets of mica. The individual layers in a schist are relatively easy to peel off by hand. *Gneissose* texture refers to alternate bands of dark- (frequently amphibole or biotite) and light-colored (quartz and feldspar) minerals.

Lineation is a penetrative linear structure in a metamorphic rock. Lineation in a rock may be defined by the alignment of needlelike or prismatic minerals (such as sillimanite, amphiboles, and pyroxenes), intersection of two crosscutting sets of foliation, alignment of fold axes in a folded set of foliation planes, intersection of foliation, and bedding (in the case of a metasedimentary rock in which bedding is preserved through metamorphism) (Fig. 15.5).

The term *granoblastic texture* may be used to describe the texture of a metamorphic rock that lacks any preferred orientation and contains equant grains of one or more minerals. Triple-point junctions formed by the merger of three polygonal grains at a point are common. Contact metamorphic rocks typically develop a texture, known as *hornfelsic texture*, in which the grains are randomly oriented and well-developed polygonal aggregates are absent. Rocks possessing this texture are called *hornfels*. Hornfelses are called pyroxene—hornfels, amphibole–hornfels, or albite–epidote hornfels depending upon the type of minerals that characterize them. Note that *porphyroblastic* (or poikiloblastic) texture, which is defined by the presence of porphyroblasts (or poikiloblasts), can occur in any rock—whether or not it has a preferred orientation.

A special class of textures is exhibited by high-strain metamorphic rocks developed along fault boundaries and shear zones (discussed before). *Cataclastic texture* refers to fine-grained texture with strong foliation developed in fault zone rocks. *Porphyroclasts* are like porphyroblasts except that their grain boundaries show evidence of cataclasis and granulation. If the presence of porphyroclasts is the single most distinctive feature of a rock, then its overall texture would be best described as *porphyroclastic texture* (Fig. 15.5).

Processes and Textures

Table 15.1 provides a summary of the common types of textural changes that may be generated as a result of metamorphic conditions. *Coarsening* of grains is a common change that happens due to a process commonly known as *Ostwald ripening* in material sciences. As we have learned in a previous chapter, all systems work toward minimizing its Gibbs free energy; and in the case of a metamorphic rock, new mineral assemblages can develop at the expense of preexisting minerals because of their lower free energies. However, even when a mineral assemblage is stable because of their free energies, individual grains of each mineral may continue to grow in order to minimize grain boundary energies resulting from disordered

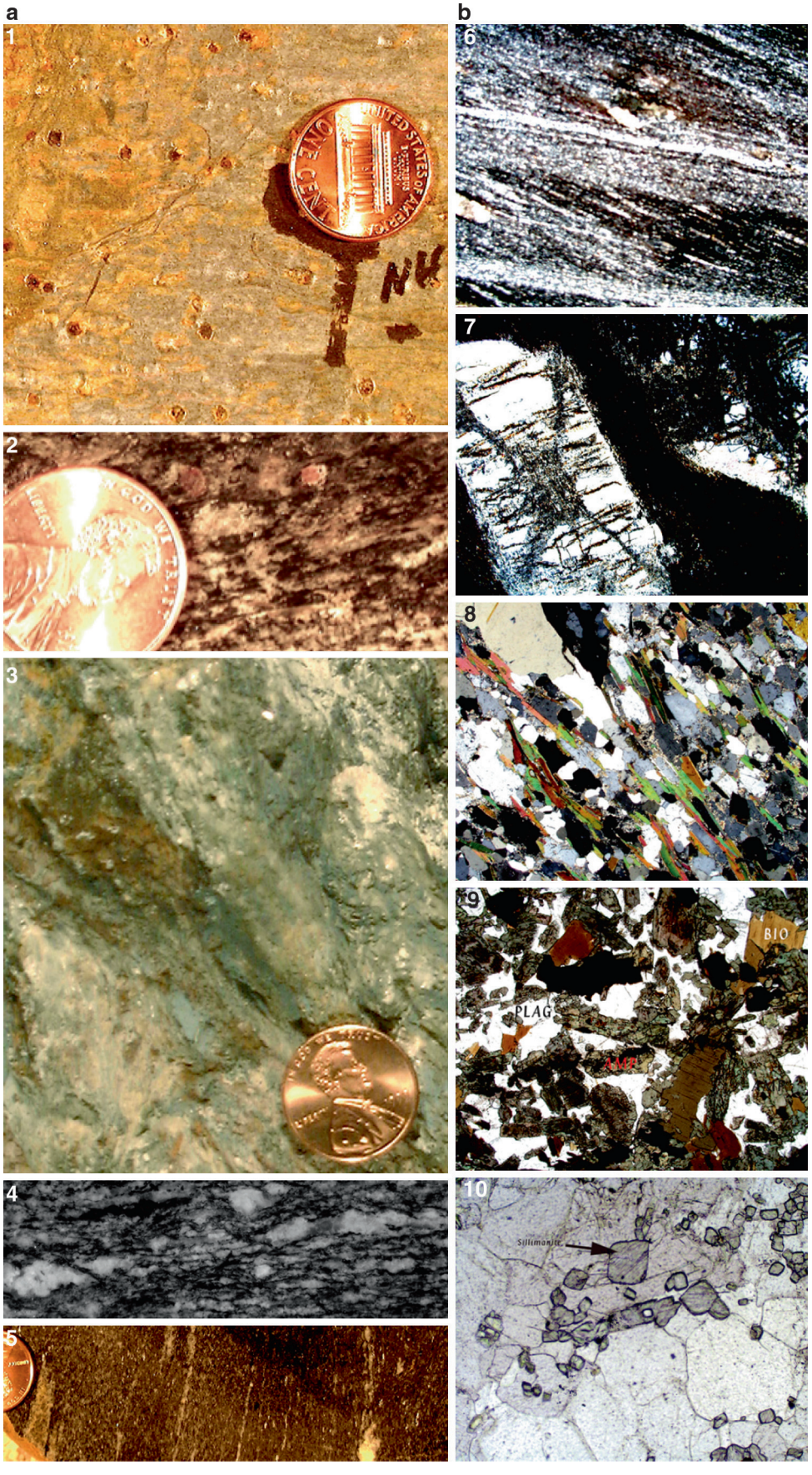
a
b
1
2
3
4
5
6
7
8
9
BIO
PLAG
AMP
10
Sillimanite

Table 15.1 Summary of common textural changes

Nature	Description	Causes
Coarsening	Increase of grain size, triple-point junctions	Minimization of contribution from grain boundary energies
Lineation	Pervasive development of linear alignment of mineral grains	Growth of elongated minerals along a direction least compressive stress; or by intersection of two sets of foliation planes
Foliation	Pervasive development of parallel to subparallel set of planes, defined by alignment of micas, amphiboles, etc.	Coarsening and alignment of micaceous and other minerals parallel to the least compressive stress
Slaty cleavage	A type of foliation, or rock cleavage, shown by slate, a low-grade metamorphic rock	
Schistorsity	Another type of foliation, defined by close, parallel–subparallel alignment of micaceous minerals. Rocks with such texture are called schists	
Gneissonsity	A third type of foliation, define by alternate, parallel bands of colored minerals (e.g., hornblende) and colorless minerals (e.g., feldspar). A rock that possesses such texture is called a *Gneiss*	
Cataclasis or Granulation	Development of finer grains at the expense of partially "ground down" coarse crystals (porphyroclast)	Brittle deformation at shallow depths
Mylontic	Commonly lenticular or eye-shaped coarse grains surrounded by fine grained materials	Brittle-to-ductile (grinding) deformation generates fine grains and rounding of coarse ones
Growth of porphyroblasts	Coarse crystals (called prophyroblasts) set in smaller grain—metamorphic equivalent of igneous phenocrysts	Inherent tendency of some minerals to grow faster than others, coupled with fewer nuclei of the coarse minerals per square area
Exsolution	Exsolved blebs, rods, or lamellae of one mineral in another. Common in pyroxenes	Limit or solid miscibility of one mineral phase in another under subsolidus conditions
Corona	Reaction rims of newly grown grains of one or more minerals around another, unstable, mineral grain	Reaction breakdown of one or minerals and growth of new minerals

distribution of atoms along grain boundaries. *Interfacial energy is high for small grains and for irregularly shaped grains*. If Ostwald ripening were allowed to go to completion in a rock, then all grains of each mineral phase should fuse to form only one grain of each phase in a metamorphic rock. However, that does not happen because diffusion of components from one grain to another is extremely slow; instead, different stable grain geometries or textures develop depending upon the mineral phases that constitute the rock. These geometries minimize the interfacial energies.

Shapes of mineral grains are often controlled by their *surface energy anisotropy* (*SEA*): Minerals with a natural tendency to grow equant grains have very low SEA, and those that prefer growth along specific crystallographic directions have high SEA. This degree of SEA is shown in by Table 15.2. The SEA series is not to be confused with the "*crystalloblastic series*," which shows a hierarchy of minerals that naturally tend to be idioblastic to those that have a tendency to be xenoblastic (Table 15.3). A comparison of Tables 15.2 and 15.3 shows that while some minerals, e.g., sillimanite, have both high SEA and sits high on the crystalloblastic series, others, particularly garnet, have low SEA, and yet it is high on the crystalloblastic series because it has a tendency to form well-formed crystals.

Metamorphic rocks, such as a quartzite (>90 % quartz), that are dominantly composed of a single phase with relatively low SEA tend to develop "soap-bubble"- or "honeycomb"-type texture with well-developed triple-point junctions and ~120° interfacial angles (Fig. 15.7), because that is the stable configuration for a low-SEA phase in which interfacial energies are minimized. Prismatic minerals, like amphiboles, pyroxenes, sillimanite, and kyanite, have a natural tendency to grow along the c-crystallographic direction. Thus, in a two-phase rock, such as a sillimanite-bearing quartzite, elongated or fibrous sillimanite crystals may

Fig. 15.6 (**a**) Hand specimen photographs of some metamorphic rocks (US penny for scale). (**b**) Photomicrographs (80x magnification). *1*. Garnet phyllite. Brown arnet porphyroblasts are protruding from the surface. *2*. Mica schist. *3*. Kyanite schist. *4*. Flaser texture. *5*. Gneissose texture. *6*. Cleavage in a phyllite. *7*. Andalusite porphyroblast in a slate. *8*. Folitaion in a mica schist. *9*. Amphibolite. *10*. Sillimanite grains in a sillimanite gneiss.

Table 15.2 Surface energy anisotropy in minerals

High SEA (least equant)	
↕	Sillimanite, actinolite, serpentine, riebeckite
	Biotite, muscovite, hornblende, tourmaline, andalusite
	Chlorite
	Sphene
	Rutile, ilmenite, kyanite
	Quartz, calcite
	Feldspars, epidote, pyroxene
	Garnet, pyrite, magnetite
Low SEA (most equant)	

Table 15.3 The crystalloblastic series

Minerals	*Grain habit*
Sphene, rutile, pyrite	Most idioblastic
Garnet, sillimanite, staurolite, tourmaline	↕
Epidote, magnetite, ilmenite	
Andalusite, pyroxenes, amphibole	
Micas, chlorite, dolomite, kyanite	
Quartz, alkali feldspar	
Plagioclase, cordierite, calcite	Least idioblastic

disrupt the smooth triple-point junctions between quartz grains, resulting in somewhat lesser number of interfacial angles of ~120°. Rocks with a higher abundance of grains of high-SEA phase tend to develop decussate-type texture (Fig. 15.7), although polygonal aggregates still dominate the texture.

Porphyroblasts in metamorphic rocks may grow over an extended period or may grow late during a metamorphic event. A number of factors contribute to the growth of porphyroblasts, particularly, relative growth rate and relative abundance. In an earlier discussion of nucleation, we noted that for a nucleus to become a crystal, it must exceed a certain critical radius. The critical radius is larger for some minerals, such as garnet, and thus, these minerals have a natural tendency to form large crystals or porphyroblasts. Also, in a rock containing a number of different minerals, some of the minerals may grow faster than others and thus forming porphyroblasts. In particular, when such a mineral forms relatively few nuclei, some of the nuclei may grow to large sizes while absorbing the rest of them. Porphyroblasts grow by pushing aside grains surrounding them or by simply including them as they grow (Fig. 15.8). The evidence of shear stress and resulting rotation of porphyroblasts is often preserved as subparallel S-shaped groups of inclusions in porphyroblasts. In a foliated rock, foliation may wrap around a porphyroblast, and slightly coarser crystals in the matrix may form in the so-called pressure shadows

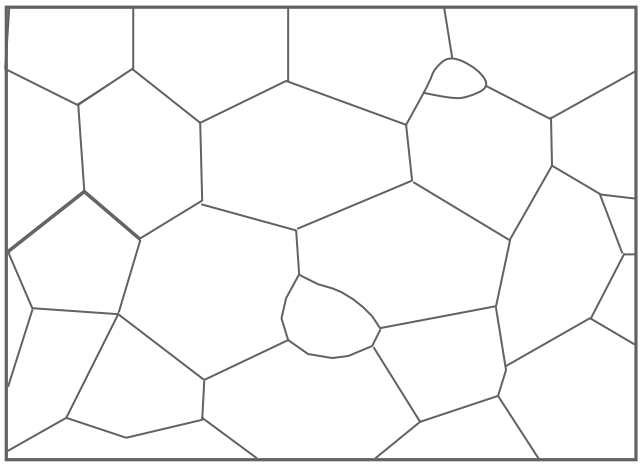

Fig. 15.7 "Soap-bubble" texture with prominent triple junctions

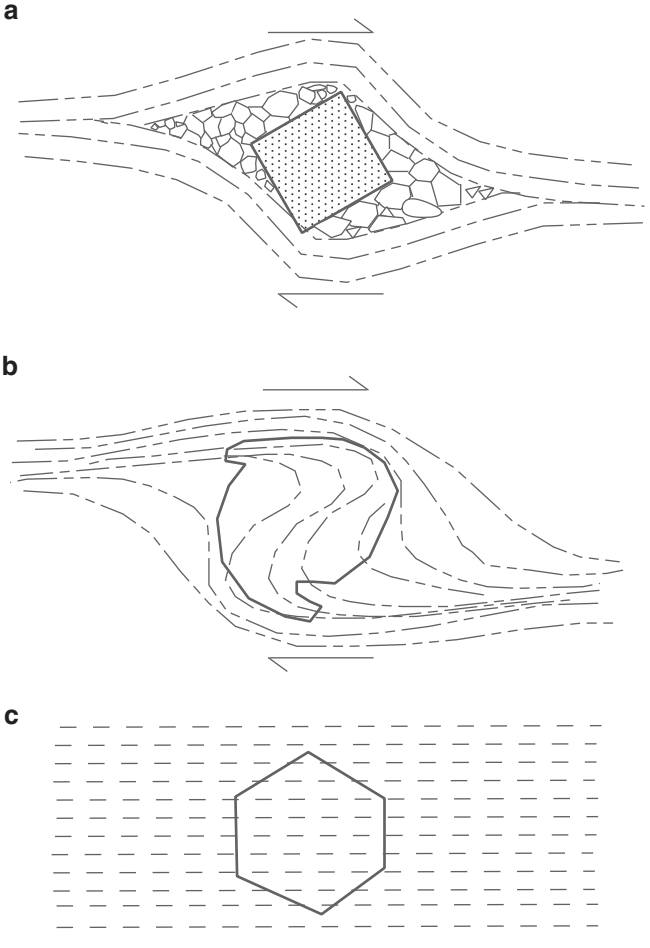

Fig. 15.8 Porphyroblasts in a mica schist. (**a**) Resistant porphyroblast pushing aside surrounding groundmass while rotating and growing under shear stress. Note the coarser groundmass grains growing in the strain shadow areas. (**b**) Rotating porphyroblast that has incorporated S-shaped inclusions that are continuous with the surrounding groundmass foliation. (**c**) Porphyroblasts growing without pushing aside surrounding groundmass

in front of and behind the porphyroblast. Porphyroblasts are sometimes compositionally zoned because of very slow diffusion rates of components through solids, and therefore they record a long history of the pressure, temperature, tectonic, and compositional environment in which they grew. Study of porphyroblasts is therefore a very important endeavor for metamorphic geologists.

Foliation may develop in a number of ways (Fig. 15.9): (1) maximum crystal growth of minerals along the direction of the least compressive stress or of maximum extension, (2) pressure solution, and (3) reorientation of glide planes in individual minerals. The development of foliation by the first mechanism has been confirmed by numerous studies of deformed and flattened ooids and fossils elongated along the foliation planes in a slate. Ooids (and other features) serve as a passive strain marker because their originally spherical shapes are modified by deformation. By noting the extent of shape modification, one can calculate the amount of strain. Strongly anisotropic (in a crystallographic sense) minerals, such as the micas, grow faster in specific crystallographic directions. In mica schists, for example, mica forms blades and flakes that grow in the direction of least compressive stress and define its schistosity.

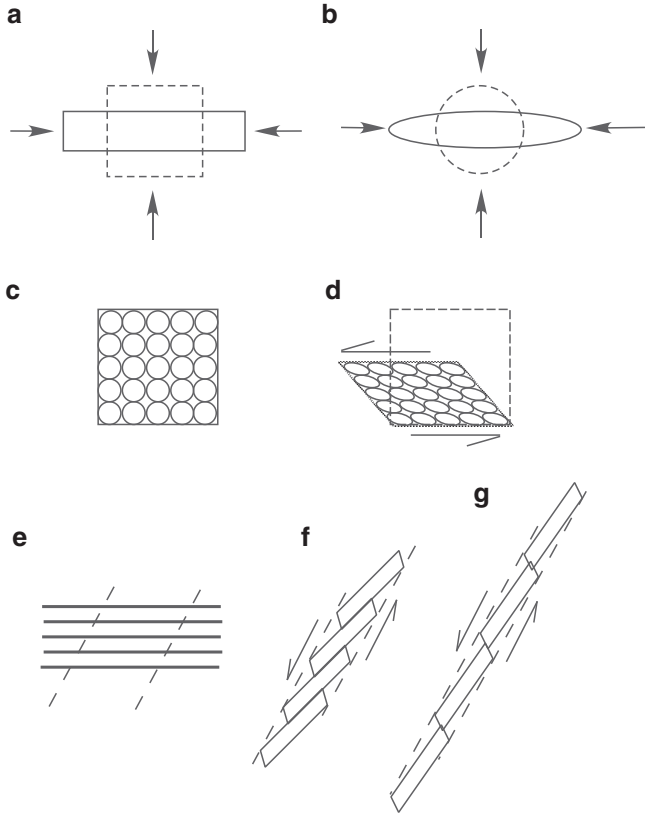

Fig. 15.9 Some schemes of development of foliation. (**a**) and (**b**)—Growth of crystals in a direction perpendicular to the maximum compressive stress (*arrows* pointing toward the grain). Pressure solution causes dissolution of the grain surfaces facing the maximum compressive stress directions; and reprecipitation along the surfaces where the compressive stress is minimum causes grain growth. Thus, square and spherical grains will become elongated. (**c**) and (**d**)—Flattening of grains due to shear stress. (**c**) and (**d**) show before and after scenarios. (**e**), (**f**), (**g**)—Foliation due to transposition of original glide planes in a mineral. (**e**) shows the original glide planes. (**f**) and (**g**) represent progressive deformation and transposition

Pressure solution of quartz grains can result in preferred orientation defined by elongated quartz grains in a foliated quartzite. Basically, in an environment of unequal stress distribution, the faces of a quartz crystal oriented perpendicular to the maximum compressive stress will dissolve, and the faces aligned along the least compressive stress will grow by reprecipitation.

Rotation of glide planes in some mineral grains may also result in an overall alignment of the grains in the direction of foliation. Olivine and quartz are well-known examples of this process.

Finally, deviatoric stress and accompanying brittle-to-ductile deformation can produce a series of textures such as mylonitic and cataclastic. In a fault zone environment, a layered rock consisting of bands of hard, brittle minerals in a matrix of softer, clay-rich materials can develop lenses of the brittle mineral (often called *Boudins*)—the rounding off the rough edges of such lenses being a result of rotation and grinding during translation and rotation imposed upon the brittle band by shear stress. Such textures are often described as *flaser texture or augen texture*.

Common Metamorphic Rock Names

In contrast to the nomenclature of igneous rocks, naming metamorphic rocks is a relatively simple effort and is generally based on modal mineralogy and texture (or structure at a mesoscopic scale). A metamorphic rock name usually has a root name and one or more prefixes. The root name may indicate dominant mineralogy (e.g., *amphibolite*—rock composed of amphibole and plagioclase) and/or structure/texture (e.g., *slate*, a fine-grained, very low-grade metamorphic rock with distinctive slaty cleavage; *greenschist*, a chlorite (therefore the green color)-bearing rock with schistose texture). The prefix (s) may include some specific textural/structural or mineralogical attribute: for example, garnet amphibolite, pyroxene granulite, etc. Sometimes the name may have a built-in reference to the protolith from which the

metamorphic was derived: for example, *metabasalt* is a metamorphosed rock that was originally a basalt. Sometimes the prefixes "ortho-" and "para-" are also used to identify the protolith: "ortho-" means that the rock was derived from an igneous rock, whereas "para-" means that the rock had a sedimentary protolith, e.g., orthogneiss, and paragneiss.

Below is a summary list of some commonly used metamorphic rock names (somewhat modified from Bucher and Frey 1994, pp. 21–24).

Gneiss—A metamorphic rock with gneissose texture. One can add a prefix to describe the rock more adequately, e.g., sillimanite gneiss and garnet–biotite gneiss.

Schist—A rock that has schistose texture, such as mica schist.

Slate—A fine-grained, low-grade, metamorphic rock with slaty cleavage.

Phyllite—Another fine-grained, low-grade, metamorphic rock with strong foliation in which the grains are slightly coarser and imparting a shininess to the cleavage surface.

Blueschist—A bluish-colored schist whose blue color is due to the abundance of the bluish, pleochroic, and amphibole crossite. This rock is typical of high-*P*/low-*T* environment of a subduction zone. It is often erroneously equated to *glaucophane schist*, whose amphibole is in fact glaucophane and not crossite!

Greenschist—A green-colored rock with schistose texture. The green color is due to the green-colored minerals like chlorite, actinolite, epidote, and pumpellyite.

Greenstone—Also a fine-grained green-colored rock, but lacks any foliation.

Hornfels—It is a fine-grained rock that lacks any foliation and generally retains relict features (minerals, texture) of the original protolith. A hornfels is produced via contact metamorphism.

Amphibolite—A rock dominated by amphibole and plagioclase. It is a metamorphosed basalt (or diabase or gabbro).

Eclogite—A high-pressure metamorphic rock with dark green color (due to omphacitic clinopyroxene) and roundish brown "patches" (due to brown garnet) and is composed essentially of garnet and an omphacitic clinopyroxene. This rock occurs at outcrop scale and is believed to be an important component of subducted lithosphere. Eclogites have also been to known to occur as xenoliths in kimberlites.

Granulite—It is typical of granulite facies (discussed in the next chapter) and displays characteristic granulitic texture with well-formed triple junctions. They generally contain an ortho- and clinopyroxenes and plagioclase or garnet and have a granoblastic texture. The lower continental crust is believed to be dominantly granulitic.

Serpentinite—A rock composed almost entirely of serpentine group of minerals. Serpentinites have an ultramafic protolith.

Marble—A metamorphosed limestone or dolostone composed of calcite and/or dolomite.

Calc–silicate rock—As the name suggests, this rock has Ca–silicate minerals, including epidote, zoisite, diopside, wollastonite, anorthite, scapolite, Ca–amphibole, and Ca–garnet (e.g., grossular).

Skarn—A contact metasomatized rock that exhibits compositional bands formed due to interaction between fluids released by an igneous intrusion and a calcareous wall rock. The minerals typically are wollastonite, forsterite, grossular, zoisite, anorthite, etc.

Quartzite—A quartz-dominated rock (>90 % quartz) with a distinct metamorphic texture.

Migmatite—These are complex stringers or lens-like rocks with felsic and mafic parts found near batholiths in exposed, deep to moderately deep, crustal sections of orogenic belts. They represent partial melts (felsic) and their mobilized residues (mafic).

Summary

Metamorphism includes all solid-state processes that transform one rock into another. The two dominant changes are in mineralogy and texture. Bulk chemical composition changes only little, mostly due to hydration or dehydration reactions. Extensive chemical change of the protolith, a process known as metasomatism, is not volumetrically important. The three agents of metamorphism are pressure (both load pressure and deviatoric stress), temperature (sources: magmatic heat, geothermal gradient, shear heating, crustal thickening), and intergranular fluid (sources: heated groundwater, magmatic water). Two most important textural changes are the development of foliation and the growth of porphyroblasts. Two fundamental classes of metamorphism, local versus regional, are recognized. Metamorphic rock names are relatively simple and are based on texture or mineralogy.

Metamorphic Facies, Reactions, and *P–T–t* Paths 16

Abstract

This chapter is concerned with metamorphic reactions that produce new minerals at the expense of reactant minerals in the protolith. Many of these reactions are useful thermometers and barometers. It is possible for the metamorphic petrologist to deduce the evolutionary history of a metamorphic complex in terms of pressure–temperature–time (or *P–T–t*) path. These topics and a brief presentation on metamorphic rocks are made in this chapter.

Mineralogical Changes: Zones, Isograds, and Facies

George Barrow's (1893) study of the Dalradian rocks from the Scottish Highlands (Fig. 16.1) was the first field-based documentation of mineralogical changes in a mudrock (commonly called a *pelite* in metamorphic petrology) as a function of increasing metamorphic intensity. Barrow and many later workers have shown that distinct *zones* can be mapped on the outcrop not only in Scottish Highlands but also throughout the world. The boundaries of such zones are marked by the appearance/disappearance of a specific mineral, called an *index mineral*. Barrow's zones and their typical minerals (index minerals are in *italics*) are as follows (arranged in the order of increasing metamorphic intensity or *grade*):

1. *Chlorite zone*: *Chlorite* + Muscovite + Quartz + Albite
2. *Biotite zone*: *Biotite* + Chlorite + Muscovite + Albite + Quartz
3. *Garnet zone*: *Almandine* + Quartz + Biotite + Muscovite + Albite-rich Plagioclase
4. *Staurolite zone*: *Staurolite* + Almandine + Quartz + Muscovite + Biotite + Plagioclase
5. *Kyanite zone: Kyanite* + Almandine + Quartz + Muscovite + Biotite + Plagioclase
6. *Sillimanite zone*: *Sillimanite* + Almandine + Muscovite + Biotite + Quartz + Plagioclase + K-feldspar

Barrow's interpretation that the metamorphic grade or intensity increased from the chlorite zone to the sillimanite zone was based on his observation that *grain size also increased*. These zones became known as *Barrovian Zones*. Barrovian Zones are now recognized as an intermediate *P–T* metamorphism (orogenic metamorphism). C.E. Tilley (cited in Spear 1993) later extended Barrow's study and introduced the concept of an *isograd*. An *isograd* is the surface expression of a three-dimensional surface that marks the first appearance or disappearance of an index mineral.

Following Barrow's work, many other studies have found similar as well as different types of metamorphic zonation in rocks of pelitic composition throughout the world. Not too far from Barrow's study area, in the Buchan region of eastern Dalradian, a very different sequence of metamorphic zones occurs in a pelitic protolith: here the index mineral sequence goes from *staurolite* → *cordierite* → *andalusite* → *sillimanite*. These zones, called *Buchan Zones*, represent much lower-pressure conditions than the Barrovian Zones (low *P–T*: Fig. 16.2).

While mapping of zones is a useful practice because of its simplicity and in developing a sense of "overall *P–T* conditions" for the field geologist, in detail many problems may occur in the interpretation stage: for example, one can get cross-cutting isograds as has been shown by Carmichael (1969) from the Whetstone

G. Sen, *Petrology*, DOI 10.1007/978-3-642-38800-2_16,

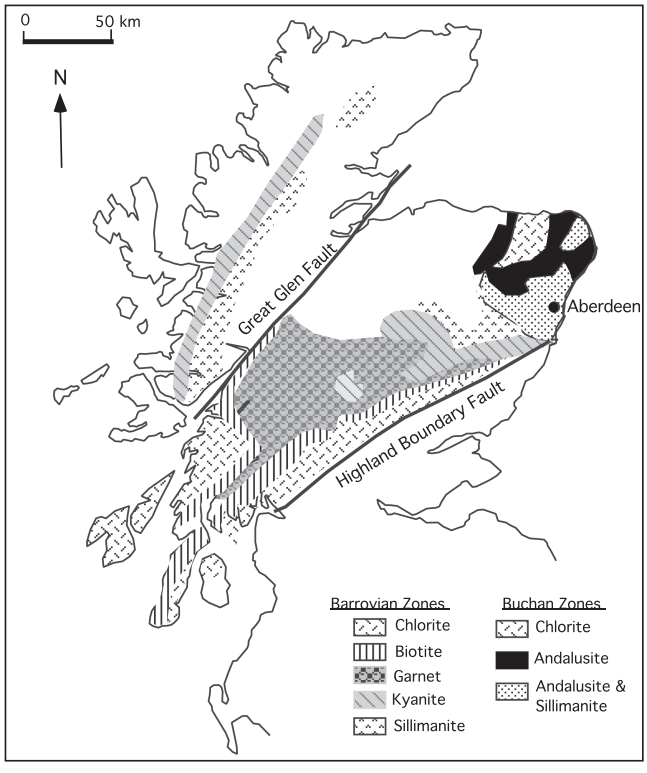

Fig. 16.1 Map showing Barrovian and Buchan metamorphic zones from Scottish Highlands

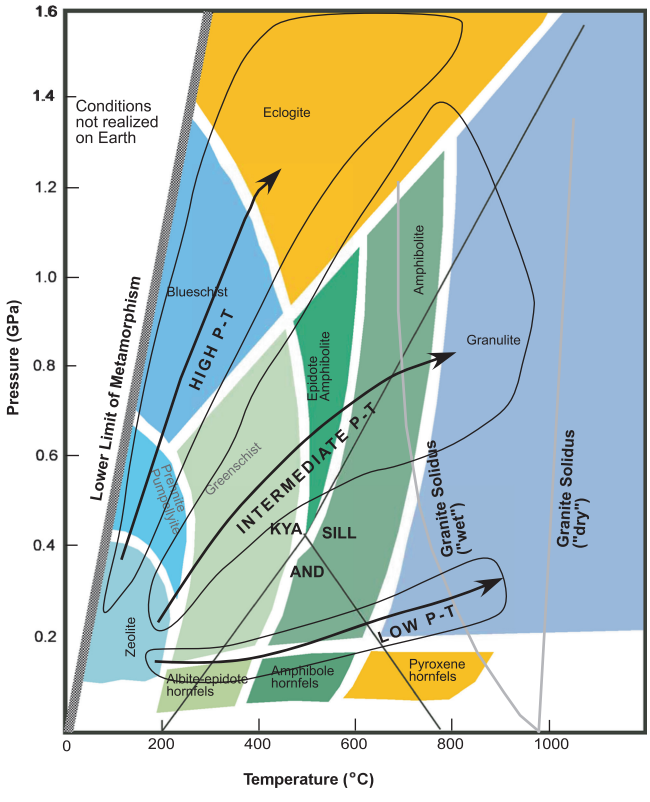

Fig. 16.2 Metamorphic facies series, facies, and tectonic associations

Lake area of Ontario. Carmichael and many other studies have shown that the bulk composition (including fluid composition) exerts an important control on the types of mineral reactions that can occur in a particular protolith and thus the single index mineral-based isograds. Many modern authors use two index minerals, instead of one, in mapping out zones.

Bulk composition is particularly important because it dictates what minerals may form at any given *P*, *T* and fluid composition. Broadly speaking, in an area of regional metamorphism, different starting rocks would end up becoming very different metamorphic rocks at a similar metamorphic intensity because of their bulk compositional differences. Below is an example of how very different rock types may result from different protoliths under very similar *P*, *T* conditions:

Protolith	Metamorphic rock
Sandstone	Quartzite
Limestone	Marble
Basalt	Amphibolite
Granite	Granitic gneiss
Shale	Sillimanite gneiss
Peridotite	Olivine–tremolite schist

An obviously important factor in the study of metamorphism is to decipher what reactions occurred because only then is there any hope of figuring out the *P–T* history of a series of metamorphic rocks in any given geographic area. This is not always easy, and one must consider many different observations: for example, one may find *reaction corona*-type structures (in such a structure the product minerals form a reaction rim around the reactant mineral). The reactants may also be preserved as *relict inclusions* in the product minerals.

It is important to recall that metamorphic reactions do not instantaneously go to completion but happen over geological time. While metamorphism itself is driven by chemical equilibrium, how far a reaction would progress is determined by kinetic processes, such as diffusion of ions from one mineral to the other. Thus, the stages of metamorphic reaction progress may be preserved in the form of *mineral zoning*, in which the core of a mineral grain may retain the reactant composition while its rim may be in chemical equilibrium with the surrounding groundmass minerals. For any given protolith composition, the modal proportions of the product minerals increase as the reactant mineral proportions decrease with the

progression of a reaction. Thus, the metamorphic geologist may be able to determine what reaction has occurred in a particular metamorphic terrane from changing modal proportions of minerals.

Facies

Recognition of problems that are inherent in the isograd concept encouraged metamorphic petrologists to think of other ways to represent variations in metamorphic intensities, which ultimately led to the development of the concept of *metamorphic facies*. The foundation of this concept was laid by Goldschmidt, VM (1911, cited in Turner 1968) in an outstanding study of a wide range of sedimentary rocks including mudrocks, sandstones, and limestones that were all metamorphosed by a pluton. He noticed that despite the wide variation in bulk composition of the starting, unmetamorphosed, parent rocks, these rocks developed metamorphic assemblages whose mineralogies were relatively simple; each lithology consists of four or five of the following minerals—quartz, K-feldspar, plagioclase, cordierite, wollastonite, diopside, hypersthene, and grossular garnet. He also noted that for a particular bulk composition, the mineral assemblage is the same: thus, a mudrock has quartz–K-feldspar–andalusite–cordierite and the equivalent calcareous metamorphosed rock has a diopside–grossular–calcite assemblage (cited in Turner 1968, p. 51). More or less at the same time, in a study of some hornfelses from Finland, Eskola, P (1915, cited by Turner 1968) made a similar observation, i.e., metamorphic mineral assemblages are simple in terms of number of minerals and are specific to a certain bulk composition. *More importantly, Eskola noted that the mineral assemblages in the Finlandian example were very different from those in Norway even though the chemical compositions of the rocks from the two areas were more or less identical*. Eskola concluded that these differences must be due to different *P, T* conditions of metamorphism at the two places, thus was born the concept of metamorphic facies, which was perhaps best defined by Fyfe and Turner (cited in Turner 1968) as:

> set of mineral assemblages, repeatedly associated in space and time, such that there is a constant and therefore predictable relation between mineral composition and chemical composition.

It is important to recognize that a metamorphic facies does not represent a single rock type but includes a wide range of rock types that form under the same (or very similar) conditions of *P, T* and fluid composition. Although Eskola recognized that rocks belonging to different facies must have formed at different *P, T* conditions, appropriate experimental data that are available today did not exist then, and therefore, he was unable to quantify the *P, T* differences between different metamorphic facies in terms of absolute ranges in *P, T* space. Subsequent studies by many workers have led to the development of a general facies diagram (Fig. 16.2, after Spear 1993). Note that the names given to the various facies are based on mineral assemblages that would develop in a *mafic bulk composition* at various *P, T* conditions; and the minerals that define each of these facies are as follows (Spear 1993):

Zeolite facies: zeolites

Prehnite–pumpellyite facies: prehnite and pumpellyite

Blueschist facies: glaucophane + lawsonite or epidote (+albite ± chlorite)

Greenschist facies: chlorite + albite + epidote (or zoisite) ± actinolite

Epidote–amphibolite facies: plagioclase (albite–oligoclase) + hornblende + epidote ± garnet

Amphibolite facies: plagioclase (oligoclase–andesine) + hornblende ± garnet

Granulite facies: orthopyroxene (+clinopyroxene + plagioclase ± hornblende ± garnet)

Eclogite facies: omphacitic pyroxene + garnet

The boundary between any two facies is *gradational*. These boundaries are generally based on discontinuous reactions (discussed in an earlier chapter and in a later section) in which a new mineral assemblage appears or another one disappears. Continuous reactions, involving solid solutions, and exchange reactions, involving exchange of components between different minerals, occur within each facies and across facies boundaries (these are also discussed further in a later section). Because many of the reactions that mark the facies boundaries involve loss or gain of volatile species, their temperature can vary somewhat depending on the pressure.

It is important to note that although rocks undergo metamorphism over an increasing (or *prograde*) as well as decreasing (or *retrograde*, during the exhumation period) set of *P–T* conditions, the assignment of a metamorphic rock to a particular facies is almost always based on the *peak metamorphic conditions* it reached. For example, before basalt becomes an amphibolite, it must go through several other facies conditions (such as the greenschist facies), and it must undergo retrograde *P–T* conditions as well during its exhumation to the Earth's surface. However, the

retrograde conditions are generally incapable of obliterating the peak *P–T* conditions reached by the rock, and hence the rock gets assigned to the amphibolite facies although it may be apparent that it has gone through a lot more complex metamorphic history.

Metamorphic Facies Series and Plate Tectonics

Miyashiro (1961) noticed the consistent differences between the Barrovian- and Buchan-type sequences in his studies of Japanese metamorphic belts. In fact, he recognized three types of sequences or *barric types* (because main difference between them is pressure) *or metamorphic facies series*:

1. Zeolite → prehnite → pumpellyite → blueschist → eclogite (high *P–T* or Sanbagawa type)
2. Greenschist → epidote–amphibolite → amphibolite → granulite (intermediate *P–T*, Barrovian type: shows kyanite → sillimanite conversion)
3. Greenschist → amphibolite → granulite (low *P–T*, Buchan or Abukuma type: shows andalusite → sillimanite conversion)

Even before the concept of plate tectonics was presented, Miyashiro had recognized the existence of subparallel belts of high *P–T* and low *P–T* metamorphic rocks in the Japanese islands parallel to the trench zone, called *paired metamorphic belts* (Fig. 16.3). The low *P–T* belt, composed of andalusite–sillimanite-bearing facies assemblages, occurs to the northwest of a major tectonic discontinuity ("Median Tectonic Line"), and the high *P–T* belt occurs to the southeast of it. The high *P–T* belt goes from zeolite facies rocks to blueschist–greenschist facies rocks (+some amphibolite) from southeast to northwest. Miyashiro noted the existence of similar high *P–T*–low *P–T* paired belts throughout the Mesozoic–Cenozoic rocks of entire Pacific rim.

Paired metamorphic belts have since been found in many other parts of the world, and their origin is clearly related to plate tectonics (Miyashiro 1973; Ernst 1976; Fig. 16.4). In the case of Japan, the high *P–T* belt marks the polarity of the subduction zone in that the higher-grade rocks are further to the northwest (which is the direction of movement of the subducting plate), and the low *P–T* belt is an ancient island arc that has been thrust against the high *P–T* belt. Such thrusting is common in subduction zones. The schematic diagram in Fig. 16.4 shows that the collision and subduction of the cold lithospheric plate creates a situation where high *P–T* facies series rocks are juxtaposed against a high *P–T* series.

At a *mid-oceanic ridge*, the isotherms are closest to each other above the active zone of magmatism (Fig. 16.4). The gap between the isotherms increases as the crust ages as it moves away from the ridge axis. Rocks dredged from oceanic fracture zones, where the middle and lower crustal rocks are often exposed, indicate that the oceanic crust probably does not get metamorphosed beyond amphibolite facies conditions under most circumstances.

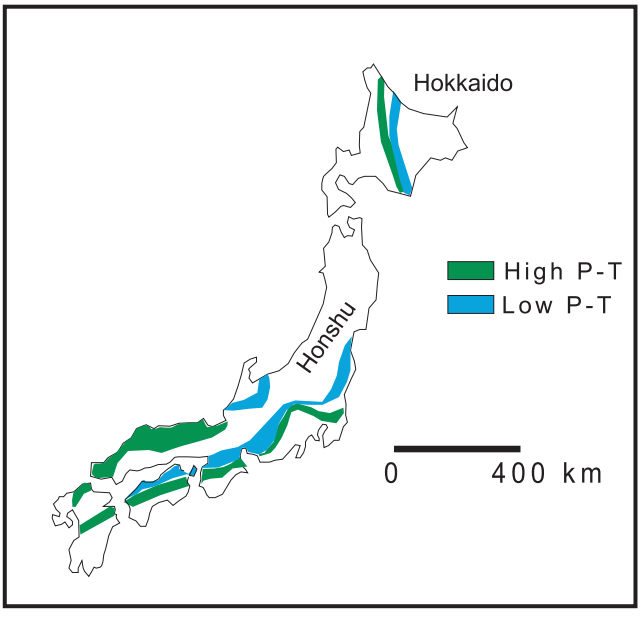

Fig. 16.3 Paired metamorphic belts of the Japanese islands (From Best 1982)

Metamorphic Reaction Equilibria, Graphical Representation, and Petrogenetic Grid

Reactions

The realization that different mineral assemblages can form in two different rock types although they both belong to the same facies led to the obvious need for the study of many different reaction equlibria involving minerals and volatiles. In a basic sense, one can classify metamorphic reactions into three fundamental types for the convenience of treatment:

1. Discontinuous reactions. In this type of reaction a phase breaks down and/or another appears at a univariant curve. Discontinuous reactions may be fundamentally of two types—*polymorphic reactions*, e.g., kyanite = sillimanite, and *net-transfer reactions* in which the components of reactant minerals are transferred to the product mineral(s). An example of a net-transfer reaction is as follows:

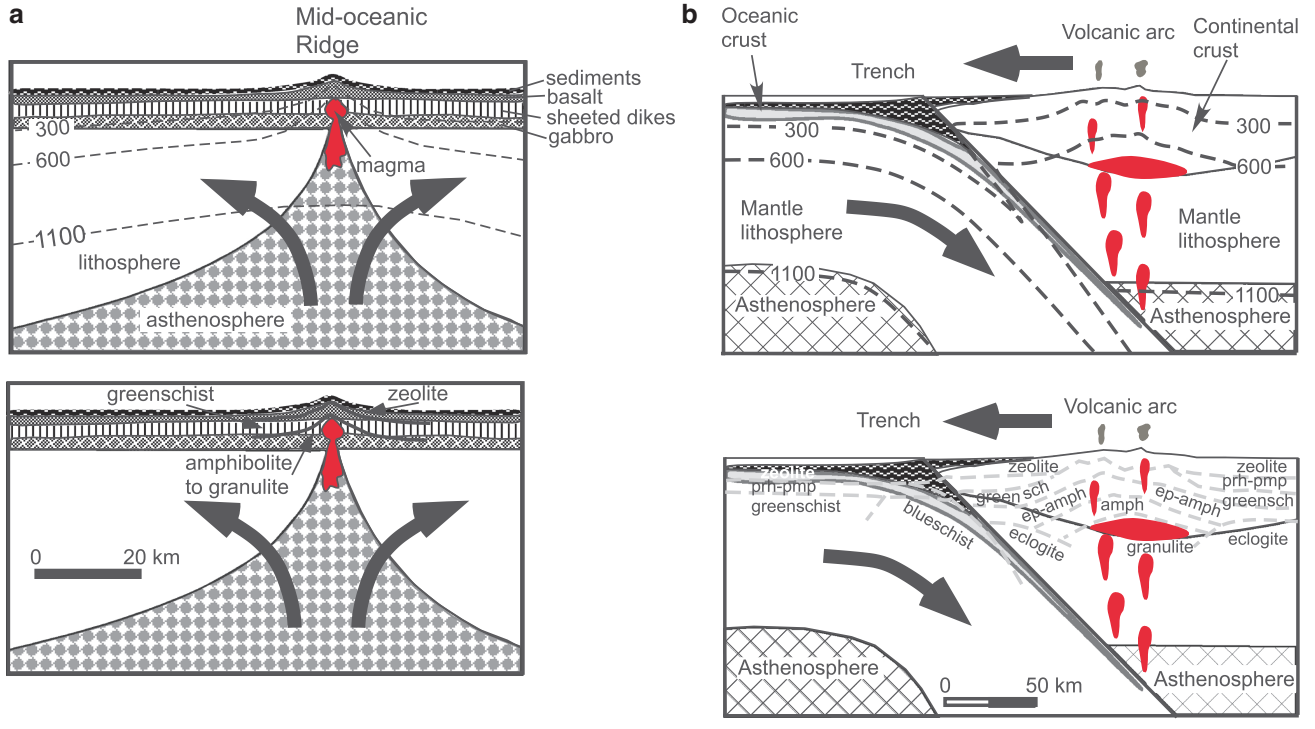

Fig. 16.4 These schematic diagrams show the close relationship between plate tectonics and metamorphism (From Ernst 1976). (**a**) Ocean ridge metamorphism. The *upper panel* shows the nature of the crust at a mid-oceanic ridge and the isotherms (*dashed with numbers*) in the lithosphere. The *lower panel* shows the location of various metamorphic facies. (**b**) Metamorphism associated with a subduction zone environment. The *upper panel* shows a typical cross-section of an island arc and the isotherms. The *lower panel* shows the location of various metamorphic facies

$$\text{jadeite}[NaAlSi_2O_6] + \text{quartz}[SiO_2] = \text{albite}[NaAlSi_3O_8]$$

2. Continuous reactions. In this type of reactions, the product and reactant minerals do not disappear but continuously change composition by exchanging components as *P, T* are varied. A good example of this is the following *exchange reaction* between garnet and biotite (Fig. 16.5):

$$Mg[gar] + Fe^{2+}[bio] = Fe^{2+}[gar] + Mg[bio]$$

Figure 16.5 resembles the types of solid solution diagrams we encountered in Chap. 3; the only difference here is that we are not dealing with liquidus and solidus, but both curves represent compositional variation in coexisting garnet and biotite as a function of temperature. For the bulk composition chosen as an example, garnet and biotite exchange Mg and Fe^{2+}, and both become progressively more magnesian with increasing temperature (i.e., prograde metamorphism) as the proportion of garnet in the rock also increases. The sensitivity of this exchange reaction to temperature makes it a very good *geothermometer* that can be used to determine the temperature of equilibration of metamorphosed rocks that contain the two phases.

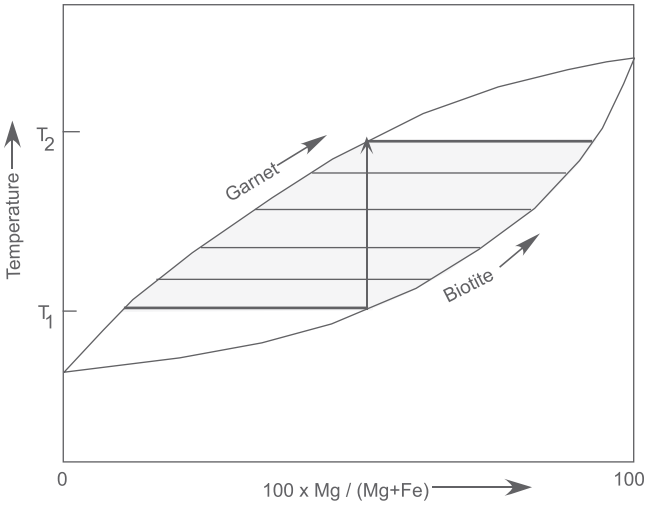

Fig. 16.5 Continuous reaction between garnet and biotite

3. Exsolution–Solvus reaction. In this type of reaction a single phase breaks down into two or more phases via

exsolution (or decomposition) during retrograde cooling of a rock. An example of this is the following reaction:

$$\underset{\text{[High Temp.]}}{Al_2O_3\text{-rich orthopyroxene}} = \underset{\text{[Low Temp.]}}{Al_2O_3\text{-poor opx}} + \text{garnet}$$

4. Reactions in which volatiles (primarily CO_2 and H_2O) are involved. Examples involving volatiles are given below:

$$CaCO_3[\text{calcite}] + SiO_2[\text{quartz}] = CaSiO_3[\text{wollastonite}] + CO_2[\text{gas}] \Uparrow$$
(decarbonation reaction)

$$\text{staurolite} + \text{chlorite} + \text{muscovite} = \text{biotite} + \text{kyanite} + \text{quartz} + H_2O \Uparrow$$
(dehydration reaction)

$$\text{margarite} + 2\ \text{quartz} + \text{calcite} = 2\ \text{anorthite} + 1\ CO_2 \Uparrow + 1H_2O \Uparrow$$
(mixed volatile reaction)

In Chap. 3, thermodynamic methods have been presented that allow calculation of univariant curves in *P–T* space. The method employs calculation of the slope of a given reaction using the Clapeyron equation, i.e., $dP/dT = \Delta S/\Delta V$, where ΔS and ΔV are entropy and volume changes, respectively. Because volatile-free solids are not very compressible (i.e., ΔV is constant), discontinuous and exchange reactions involving solids (volatile-free) are generally linear in *P–T* space. On the other hand, volatiles are very compressible, i.e., ΔV varies as a function of *P* and *T*, and hence volatile-bearing reactions always possess a curvature in *P–T* space.

Graphical Representation

Visual display of compositions and equilibrium assemblages is generally preferable over writing lengthy metamorphic reactions. Therefore, the goal of early to modern practitioners of metamorphic petrology has been to develop *graphical means* to illustrate what mineral assemblages would be stable at a given *P–T* regime in a particular protolith. Binary and ternary diagrams were originally developed by Eskola (1920) to include effect of bulk composition on metamorphic reactions. Because a rock is composed of multiple components, its bulk composition, mineral composition, and mineral (± volatile) reactions need to be treated in some manner so that they may be plotted on a ternary (in reality, they are all pseudo-ternary) diagram. This is done either as *projections* (i.e., when they are projected from an end-member mineral component) or as *condensations* (i.e., when the components are combined in some way and projected from some exchange component; that is, say, solid solution rather than an end-member). In reality, any plot of a natural rock in a pseudoternary diagram is a condensed plot. For example, consider plotting a protolith consisting of nine or more major and minor chemical components [SiO_2, TiO_2, Al_2O_3, Fe_2O_3, Cr_2O_3, FeO, MnO, MgO, CaO, Na_2O, K_2O ($\pm CO_2$, H_2O, OH etc.)] on an Al_2O_3–CaO–FeO (or ACF) diagram. Eskola suggested that in so doing one must combine the components in this way:

$$A = Al_2O_3 + Fe_2O_3 - (K_2O + Na_2O + CaO)$$

$$C = CaO$$

$$F = FeO + MnO + MgO$$

Clearly, any composition plotted in a pseudoternary ACF diagram this way is a condensed plot (Fig. 16.6a). Note that SiO_2, the most abundant component of all silicate minerals and rocks, is not a part of the combination process. What this means is that all compositions plotted on an ACF diagram are projected from SiO_2, and thus the underlying assumption is that the plotted rocks have excess SiO_2 (either as free quartz or other SiO_2 polymorphs). Note also that solid solutions are shown as extended fields in this diagram.

The ACF diagram was initially proved to be of value in portraying changing facies assemblages in mafic (i.e., basaltic) protoliths (Fig. 16.6a). Unfortunately, many important reactions involve minerals that are (Fe, Mg) solid solutions. The Fe, Mg variation in such minerals resulting from metamorphic reaction cannot be shown in an ACF diagram. One faces the same problem in using AKF diagrams (Fig. 16.6b). Later studies pioneered by Thompson (1982a, b) showed that reactions in mafic and pelitic rocks are best represented in an AFM diagram (discussed later).

It is instructive to see how the ACF diagram may be utilized in demonstrating changes in mineral assemblages in mafic rocks in response to metamorphism (Fig. 16.7). Because some mineral compositions

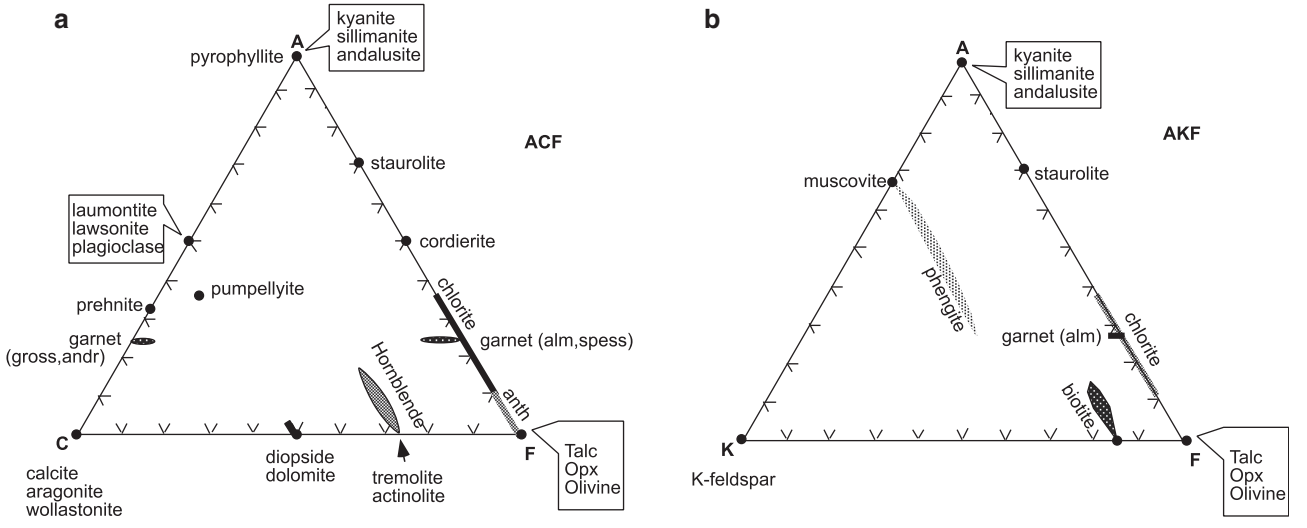

Fig. 16.6 (**a**) ACF diagram. (**b**) AKF diagram

plot as points and others plot as elongated areas (due to solid solution), each of the ACF triangles shown in Fig. 16.7 contains three-phase triangles (shown as lightly shaded areas). Recall from Chap. 4 that the apices of a three-phase triangle represent the three minerals in equilibrium and a tie-line connects two coexisting minerals. The field of basaltic rocks and three specific basalt compositions are shown in Fig. 16.7 in order to illustrate how different mineral assemblages may develop in each of these bulk compositions:

Protolith 1 (*basalt*)	
Facies	Assemblage
Zeolite facies	Heulandite (a zeolite) + chlorite + calcite
Prehnite–pumpellyite facies	Pumpellyite + actinolite + chlorite
Blueschist facies	Lawsonite + glaucophane + aragonite
Greenschist facies	Epidote + chlorite + actinolite
Amphibolite facies	Plagioclase + hornblende + garnet
Granulite facies	Clinopyroxene + garnet + plagioclase

The student may wish to determine what mineral assemblages will form in the other two bulk compositions.

The AFM diagram is the most powerful of them all in depicting reaction equilibria and facies assemblages because it is the only one that depicts the Fe ⇔ Mg exchange reactions between ferromagnesian minerals and it closely depicts thermodynamically valid-phase relations (Thompson 1957). It is important to recognize that compositions of minerals and rocks plotted in an AFM diagram (mole fraction) are actually located within the tetrahedron AKFM (and H_2O) and that they are projected from muscovite (and quartz) onto the plane AFM, which extends beyond the base of the AKFM tetrahedron (Fig. 16.8a). Naturally, the assumption is that the plotted rocks contain modal muscovite and quartz, which is valid for low and medium grade. At high grades, muscovite breaks down and K-feldspar forms in a metapelite, and the projection is made from K-feldspar instead of muscovite (Fig. 16.8b). Because most of the minerals plot on the AFM plane, the change from muscovite to K-feldspar as a projection point does not affect their relative position in the AFM diagram, with the exception of biotite, which plots inside the tetrahedron AKFM (Fig. 16.8b).

Recalculation of a multicomponent rock into AFM components is done the following way:

$$A = Al_2O_3 - 3K_2O$$

$$F = FeO$$

$$M = MgO$$

Because these are mole percent plots, one must first *convert* the weight percent analyses of rocks and minerals by the appropriate molecular weights and then add A (i.e., Al_2O_3–$3K_2O$) + F (FeO) + M (MgO) and normalize each component so that the total is 100 %. In other words, in the plane AFM, the calculated components of A, F, and M in a rock or a mineral should be as follows (note that the oxides below are mole fractions):

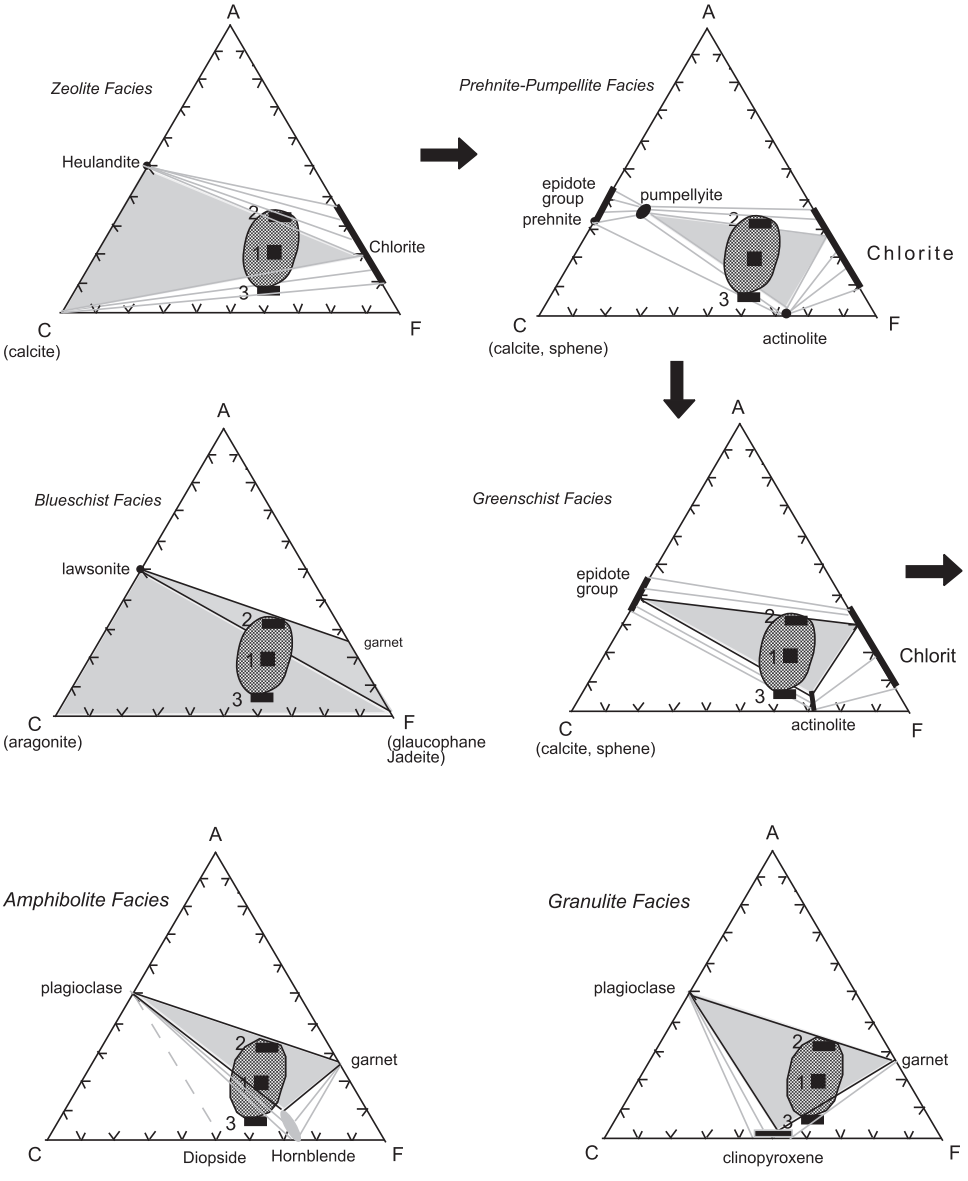

Fig. 16.7 Metamorphism of mafic rocks portrayed in a series of ACF diagrams representing various facies (discussed in text). The *arrows* indicate prograde metamorphism

$$A = 100 \times [Al_2O_3 - 3K_2O]/[(Al_2O_3 - 3K_2O) + FeO + MgO]$$

$$F = 100 \times FeO/[(Al_2O_3 - 3K_2O) + FeO + MgO]$$

$$M = 100 \times MgO/[(Al_2O_3 - 3K_2O) + FeO + MgO]$$

Note that the expression Al_2O_3–$3K_2O$ above derives from the formula of muscovite, which has three times as much Al_2O_3 as K_2O. K-free minerals plot inside the AFM plane, and therefore, there are no complications in plotting them. In the case of biotite [$K_2O{\cdot}6(FeO, MgO){\cdot}Al_2O_3$], the projection is made from muscovite onto the AFM plane because its solid solution composition lies within the AKFM tetrahedron. Note that the "*A*" component in biotite should be (based on the above formula): 100 × [1–3]/[(1–3) + 6] or 100 × (−0.5) = −50. The negative "*A*" number suggests that biotite must plot outside of the AFM triangle at a distance of −50 % away from the FM line (Fig. 16.8).

If compositions are to be plotted from K-feldspar, the "*A*" component must be redefined (=Al_2O_3–K_2O based on K-feldspar formula ($K_2O{\cdot}Al_2O_3{\cdot}6SiO_2$). Thus, biotite will now have the following "*A*" component (in terms of mole percent): 100 × [1–1]/

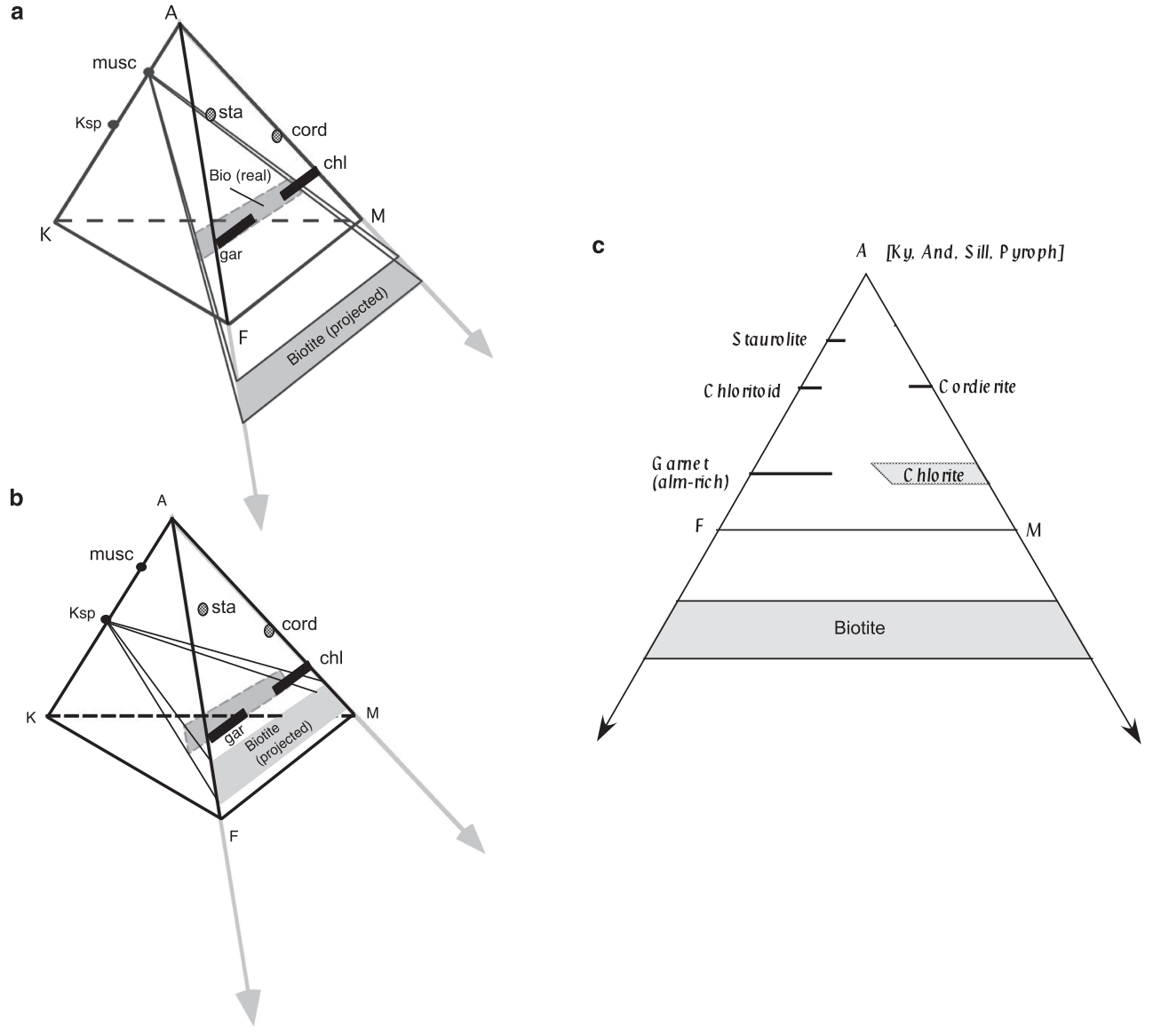

Fig. 16.8 The AKFM tetrahedron. The minerals lying within the tetrahedron are projected from (**a**) muscovite, and (**b**) K-feldspar. (**c**) AFM diagram (projected from muscovite)

[(1–1) + 6] = 0. That is, the projected biotite composition would plot right on the FM line! In reality, however, because of solid solutions, biotite compositional field plots within the AFM triangle (Fig. 16.9j, k).

AFM Diagram, Reactions, and Petrogenetic Grid: Metamorphism of a Pelitic Protolith as an Example

Figure 16.9 shows how the AFM diagram allows us to graphically portray metamorphic assemblages and reactions in a protolith of pelitic composition. In the example shown, the protolith experienced progressive intermediate *P–T*-type (or regional) metamorphism, and Fig. 16.10a–k represent various *P, T* points on such a trajectory (Spear 1993; Bucher and Frey 1994). In the lowest grade of metamorphism, the assemblages pyrophyllite + chlorite + muscovite or chlorite + K-feldspar + muscovite may be stable in high-Al versus low-Al pelites. Note that the arrows in Fig. 16.9 point toward K-feldspar.

Although for the specific bulk composition chosen in Fig. 16.9, biotite does *not* form until at a higher grade, one usually encounters the *biotite isograd* first because of the reaction:

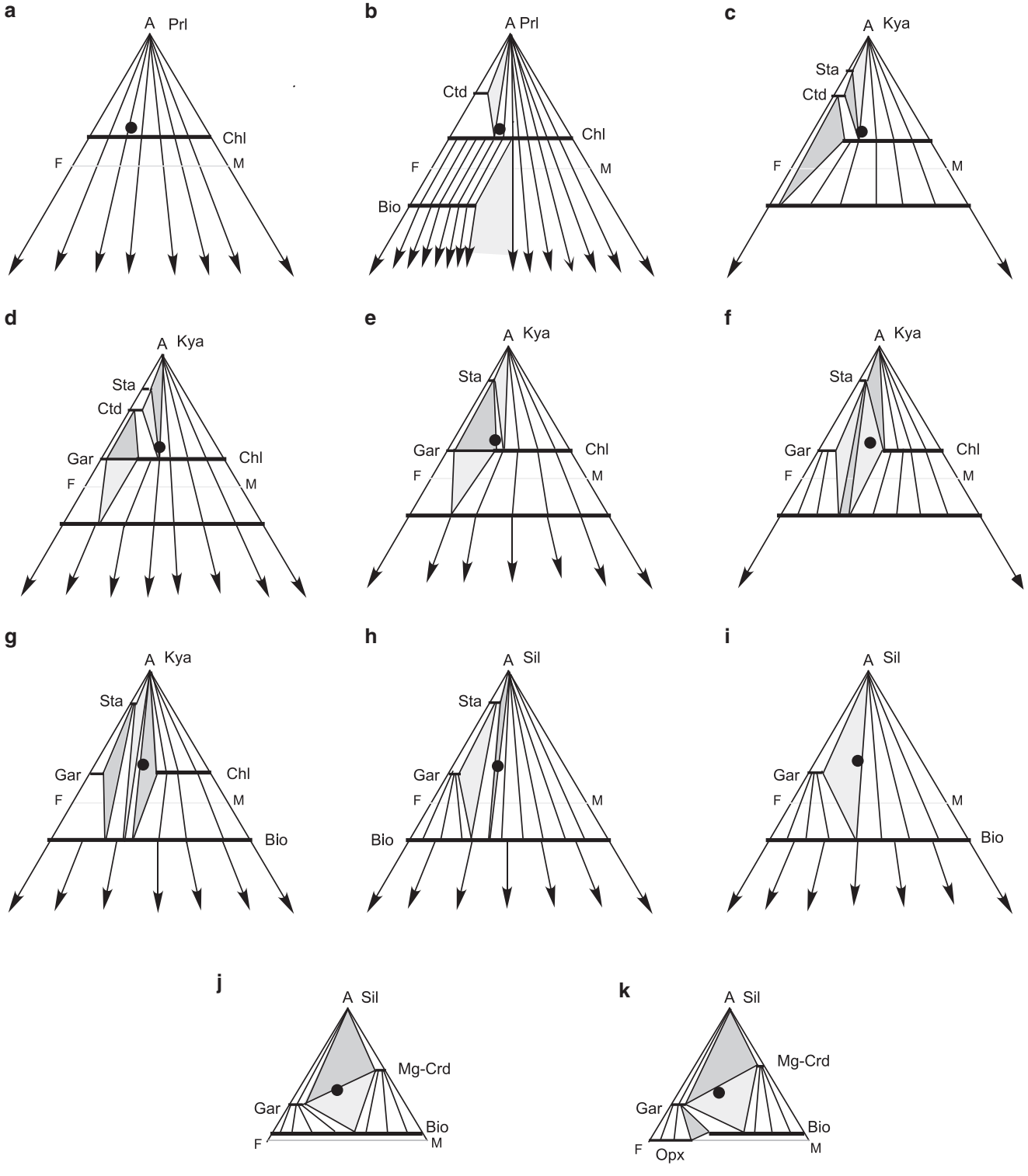

Fig. 16.9 A sequence of AFM diagrams (**a** through **k**) representing prograde metamorphism of pelitic rocks. The *dot* represents a selected bulk compositions that is discussed in the text. Note that (**a**–**i**) are projected from muscovite and the others from K-feldspar

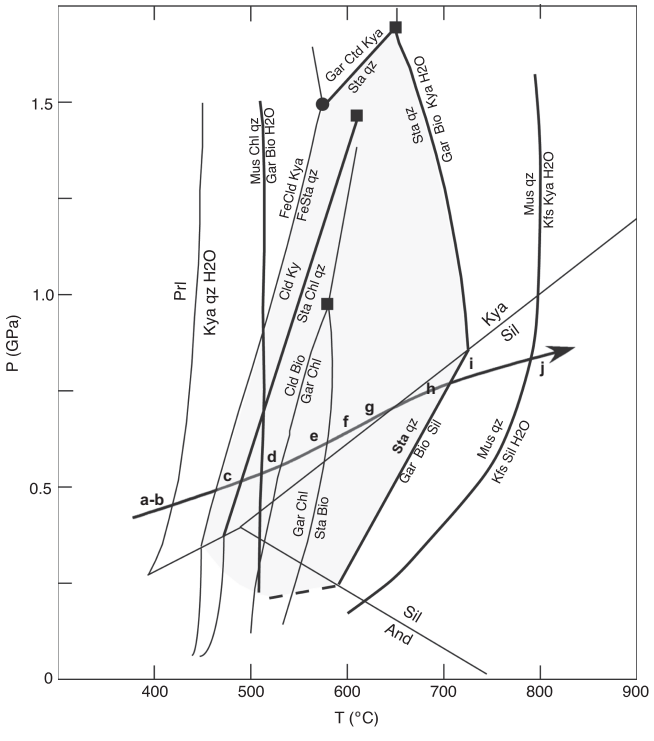

Fig. 16.10 Various reaction *curves* that are appropriate for metamorphism of pelitic rocks are shown. The *P–T* path (*dark broad arrow*) represents the prograde metamorphic sequence shown in Fig. 16.9. (**a–i**) correspond to Fig. 16.9a–i. The *shaded area* marks the stability field of staurolite

$$\text{Chlorite} + \text{K-feldspar} = \text{Muscovite} + \text{Biotite} + \text{Quartz} + \text{H}_2\text{O}$$

The above reaction is likely a pseudo-divariant reaction, and hence, the assemblage chlorite + biotite ± K-feldspar ±muscovite may persist in the rock, and the Mg–Fe ratio of biotite and chlorite will increase with increasing grade of metamorphism (i.e., the shaded region connecting biotite, chlorite, and K-feldspar slide from *F* to *M* side in Fig. 16.9b).

In a more Al-rich bulk composition, such as the example used in Fig. 16.9b, instead of biotite, Fe-rich chloritoid will form (*Fe-chloritoid isograd*) by a reaction between chlorite and pyrophyllite:

$$\text{Fe-chlorite} + \text{Pyrophyllite} = \text{Fe-chloritoid} + \text{Quartz} + \text{H}_2\text{O}$$

Chloritoid is an interesting mineral, because at intermediate *P–T*, it is generally very Fe-rich (Mg/(Mg + Fe) generally less than 0.15); however, a very Mg-rich chloritoid (Mg/(Mg + Fe) > 0.5) does form in the high *P–T* eclogite facies conditions.

Again, in Al-rich bulk compositions, the next isograd that would be expected to appear is the *kyanite or andalusite isograd* depending upon the pressure. For our chosen Al-rich bulk composition, *kyanite* will form from breakdown of pyrophyllite at about 400 °C and 0.5 GPa (AFM diagram not drawn but should be analogous to Fig. 16.9b but replacing "Prl" with "Kya"):

$$\text{Pyrophyllite} = \text{Kyanite} + \text{Quartz} + \text{H}_2\text{O}$$

One may encounter the *Fe–staurolite isograd* next due to either of the following reactions (Fig. 16.9c):

$$\text{Fe-chloritoid} + \text{Kyanite} = \text{Fe-staurolite} + \text{Quartz} + \text{H}_2\text{O}$$

or

$$\text{Chloritoid} + \text{Kyanite} = \text{Staurolite} + \text{Chlorite} + \text{H}_2\text{O}$$

Although the Fe-staurolite forming reaction marks the staurolite isograd on this diagram, staurolite may not necessarily appear in the rocks (due to inappropriate bulk composition). The second one is most important because it is usually the reaction that forms the staurolite isograd in high-Al pelitic rocks. This type of reaction is known as a "tie-line flip" where the tie-line between chloritoid and kyanite is broken, and a new tie-line forms between staurolite and chlorite. Tie-line flips affect different types of rocks (whose bulk compositions fall in the A–Sta–Chl or Sta–Ctd–Chl triangles in Fig. 16.9b) at once, and therefore, they make better isograds. Note that any of the following assemblages may form depending upon the exact bulk composition: staurolite + chlorite + kyanite, kyanite + chlorite, or staurolite + Fe-chloritoid + chlorite. It is obvious from Fig. 16.9c that in Fe-rich pelites (uncommon, but whose bulk composition would fall inside the Chl–Ctd–Bio triangle), the assemblage Fe-chloritoid + biotite + Fe-rich chlorite may form.

Figure 16.9d shows that *garnet isograd* would be expected to come next:

$$\text{Chloritoid} + \text{biotite} + \text{H}_2\text{O} = \text{Garnet} + \text{Chlorite}$$

This reaction is seen as a "tie-line flip" from chloritoid–biotite tie-line to garnet–chlorite tie-line (note Fig. 16.9c, d). The garnet isograd reaction shown above is an important one because the *P, T* range over which garnet + chlorite assemblage can occur is very small: $T = 520$–540 °C at ~0.5–0.75 GPa. However, note that dissolved

spessartine (Mn-garnet) component in garnet can expand the stability field over which garnet + chlorite can occur.

Next comes the *Chloritoid-disappearance-isograd*:

$$\text{chloritoid} = \text{staurolite} + \text{garnet} + \text{chlorite}$$

(compare Fig. 16.9d, e).

Figure 16.9f shows that the Gar–Chl tie-line breaks down with increasing grade in favor of a Sta–Bio 2-phase field, such that garnet will disappear from our selected rock and staurolite–chlorite–biotite assemblage will form. However, for more Fe-rich bulk compositions, the stable assemblage is staurolite–garnet–biotite, forming the *biotite isograd*.

Staurolite–chlorite assemblage breaks down with increasing metamorphic grade and kyanite + biotite assemblage becomes stable (compare Fig. 16.9f, g):

$$\text{staurolite} + \text{chlorite} = \text{biotite} + \text{kyanite} + H_2O$$

This usually marks the appearance of the *kyanite isograd* in low-Al pelitic rocks.

In our example, as the grade is increased from **g** → **h** (Fig. 16.10), sillimanite replaces kyanite as the stable Al_2SiO_5 polymorph (i.e., the appearance of the *sillimanite-isograd*). Sillimanite typically nucleates as fine fibrous masses in the rocks within muscovite or biotite as kyanite gets replaced by muscovite. At higher grade of metamorphism (granulite facies), sillimanite forms clusters of long prismatic crystals.

As the metamorphic intensity is increased from **h** → **i** (Fig. 16.10), staurolite breaks down due to the following reaction (*staurolite-out isograd*):

$$\text{staurolite} = \text{garnet} + \text{biotite} + \text{sillimanite} + H_2O$$

The shaded region in Fig. 16.10 thus represents the overall *P, T* field within which staurolite may occur.

The next important reaction that would be expected to occur in a pelitic rock (like the one in our example) is the breakdown of muscovite and the formation of the *K-feldspar isograd* as the metamorphic intensity is increased from **i** to **j**:

$$\text{muscovite} + \text{quartz} = \text{K-feldspar} + \text{sillimanite} + H_2O$$

Note that the phases representing this reaction cannot really be shown in an AFM diagram.

At even higher grades (but usually lower pressure), reactions in the granulite facies conditions may occur that may give rise to the formation of Mg–cordierite and pyroxenes in the rock, with the resulting assemblages depicted in the appropriate AFM diagrams (Fig. 16.10j, k).

Diagrams like Fig. 16.10 that depict possible reactions in various metamorphic rocks are generally based on experimental studies of simplified systems with fewer components backed up by laboratory and field studies. For example, most of the reactions shown in Fig. 16.10 are based on some of the key reactions in the system KFMASH, which is an abbreviation for K_2O–FeO–MgO–Al_2O_3–SiO_2–H_2O. The reactions form a type of "grid" of pseudo-univariant curves, which is commonly referred to as the *petrogenetic grid* because such grids, if applied to rocks of appropriate bulk composition, provide *P–T* history of the rock.

Petrogenetic Grid for Mafic Protoliths

The reader has already been briefly exposed to what mineralogical changes occur in a mafic (basaltic) rock during metamorphism in an earlier section (discussion on facies, facies series, and the ACF diagram). The purpose of this section is to highlight some of the important reactions that occur in rocks of mafic composition.

In the beginning stage of metamorphism of mafic (more appropriately, basaltic-to-andesitic rocks), the most important reaction that occurs is one of hydration, in which hydrous minerals begin to replace the anhydrous assemblage plg + cpx. In the lowest-grade rocks, relict phases and/or relict texture is often preserved. The water may be supplied in a hydrothermal environment near a mid-oceanic ridge or by groundwater in a plate convergent margin. The availability of water is of key importance in the metamorphism of mafic volcanic rocks. The lowest-grade assemblages are albite (from albitization of plagioclase) + chlorite (hydration of cpx) + carbonates and zeolites. *Laumontite* is a zeolite that forms at extremely low grade, bordering diagenesis (Fig. 16.11a), followed by another zeolite—*wairakite*—at a slightly higher temperature. Zeolite → prehnite–pumpellyite facies transition is not particularly clear-cut, but is thought to take place around 300 °C, 3–4 kb (Liou 1971). The breakdown of wairakite to prehnite-bearing assemblages marks the facies transition (Fig. 16.11b).

At *P, T* conditions higher than the prehnite–pumpellyite facies, several different reactions occur,

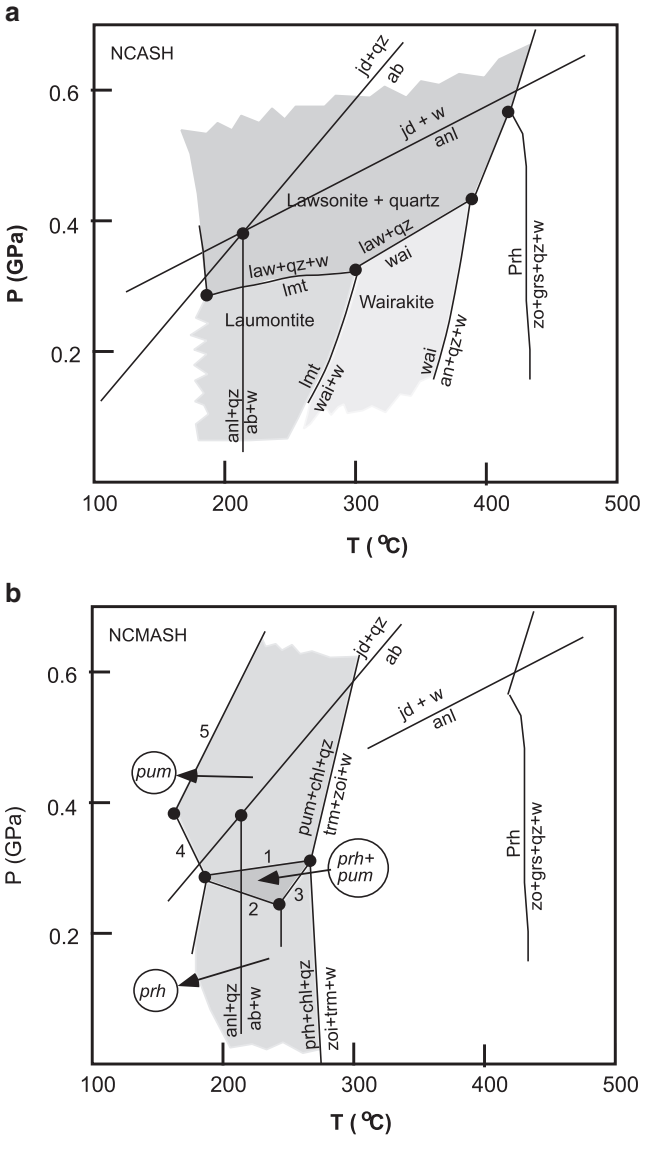

Fig. 16.11 (**a**) Petrogenetic grid for zeolite facies metamorphism of mafic rocks in the system Na_2O–CaO–Al_2O_3–SiO_2–H_2O (NCASH). The laumontite and wairakite *shaded areas* are two subfacies of the zeolite facies. (**b**) Petrogenetic grid relevant to the formation of prehnite and pumpellyite in the system Na_2O–CaO–MgO–Al_2O_3–SiO_2–H_2O (NCMASH)

resulting in very different *P*, *T* series assemblages. In a *high P–T series*, the progression is from zeolite-bearing assemblages → prehnite–pumpellyite bearing rocks → blueschist facies → eclogite facies. A key feature for *blueschists* is the development of a sodic amphibole (with high proportion of the glaucophane end-member component) that appears bluish under plane-polarized light. The sodic amphibole first begins to form due to the breakdown of chlorite- + albite-+ actinolitic amphibole-bearing assemblages and the formation of riebeckite and glaucophane-rich amphibole-± epidote-bearing assemblages due to the following reactions (Bucher and Frey 1994):

$$\mathrm{Trm + Alb + Chl = Law + Amp}$$
$$\mathrm{Trm + Alb + Chl = Amp + Zoi + Qtz + H_2O}$$
$$\mathrm{Alb + Chl + Qtz = Amp + Par + H_2O}$$

Garnet would form within the blueschist facies rocks due to the breakdown of paragonite and lawsonite:

$$\mathrm{Law + Amp = Par + Pyr + Zoi + Qtz + H_2O}$$
$$\mathrm{Par + Chl + Qtz = Amp + Pyr + H_2O}$$

Note that within the blueschist facies, the amphibole composition changes from Fe-rich (riebeckite component) to Na-rich (glaucophane component) amphibole with increasing grade. As pressure and temperature are raised further, the glaucophane-rich amphibole + paragonite will eventually breakdown, and typical *eclogite facies* rocks, composed of garnet + sodic pyroxene (omphacite, jadeite), will form due to the reactions:

$$\mathrm{Alb = Jad + Qtz}$$
$$\mathrm{Gln + Par = Pyr + Jad + Qtz + H_2O}$$

The approximate locations of the above reactions are shown in Figs. 16.11 and 16.12.

In an *intermediate P–T facies series*, the sequence of reactions at facies boundaries and within each facies is quite different. *Prehnite–pumpellyite* facies is followed by *greenschist facies*. The minerals chlorite, actinolite, and epidote, all of them green, are responsible for the green color of greenschists. The transition from prehnite–pumpellyite to greenschist facies is marked by the breakdown of pumpellyite and stabilization of chlorite + albite + actinolite + epidote +quartz assemblages (Figs. 16.11b and 16.12):

$$\mathrm{Prh + Chl + Qtz = Epi + Act + H_2O}$$
$$\mathrm{Pum + Chl + Qtz = Act + Epi + H_2O}$$
$$\mathrm{Law + Pum = Epi + Chl + Qtz + H_2O}$$

Actinolite forms at a lower temperature in Fe-rich bulk protoliths relative to Mg-rich rocks.

Greenschist facies is followed by *amphibolite facies*, which is characterized by hornblende + plagioclase

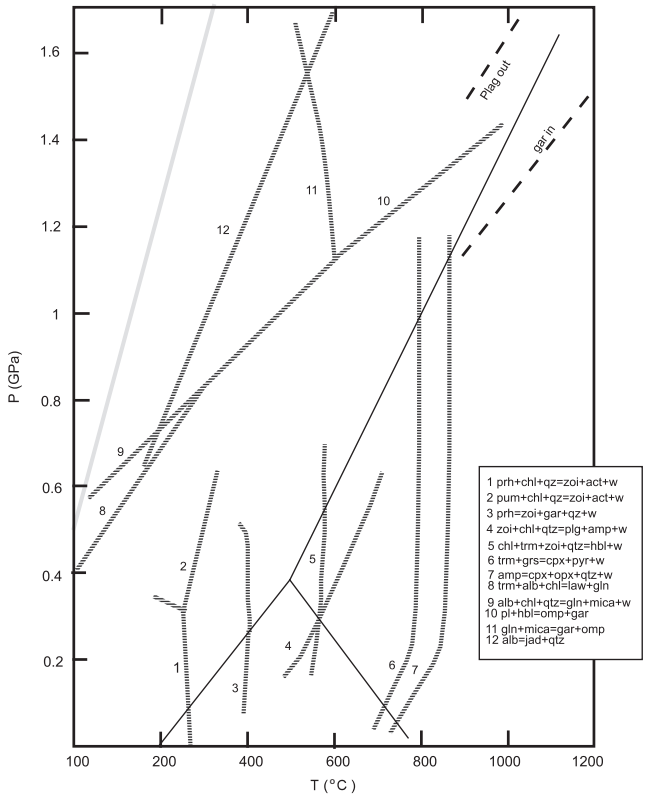

Fig. 16.12 A simplified petrogenetic grid for mafic rocks

assemblages (e.g., see reaction 4 in Fig. 16.12), due to some broad reaction as

$$\text{Epidote(zoisite)} + \text{Chlorite} + \text{Quartz} = \text{Amphibole} + \text{Plagioclase} + H_2O$$

An important change occurs in the plagioclase composition: it jumps from An_3 (albite) to $An_{17–18}$ (oligoclase) due to an immiscibility gap on the An-Ab solvus. The first appearance of oligoclase (*oligoclase isograd*) is generally taken as the beginning of the amphibolite facies. The other important change is in amphibole composition from actinolite to hornblende, which results from a series of complex reactions. The minerals epidote and chlorite decrease in abundance and eventually disappears at ~550–600 °C within the amphibolite facies. Chlorite breakdown reactions produce garnet, which become modally more abundant with increasing grade. Therefore, the amphibolite facies rocks above ~600 °C contain hornblende + plagioclase ($An_{30–50}$) + garnet ± biotite. At temperatures close to the amphibolite–granulite facies transition, clinopyroxene appears, and a typical assemblage is hornblende + plagioclase + clinopyroxene + garnet (see reaction 6 in Fig. 16.12):

$$\text{Amphibole} + \text{Zoisite} + \text{Quartz} = \text{Plagioclase} + \text{Clinopyroxene} + H_2O$$

The transition from amphibolite to granulite facies is gradual and takes place over ~200 °C interval and is marked by the first appearance of orthopyroxene. During the transition, the modal abundance of amphibole decreases and ultimately is replaced by pyroxenes. The general reaction that marks the incoming of orthopyroxene is (reaction 7 in Fig. 16.12):

$$\text{Amphibole} = \text{Cpx} + \text{Opx} + \text{Plagioclase} + H_2O$$

The transition from granulite facies to *eclogite facies* for a variety of basaltic rock types has been experimentally investigated by the Ringwood–Green group at Australian National University and Ito and Kennedy at University of California, Los Angeles (reviewed by Ringwood 1975: reaction 10 in Fig. 16.12). The general reaction for this transition may be written as:

$$\text{Opx} + \text{Plagioclase} = \text{Garnet} + \text{Cpx} + \text{Quartz}$$

However, this transformation from plagioclase-bearing to plagioclase-free assemblage occurs through a transition from *pyroxene granulite* (*Pl* + *Cpx* + *Opx* ± *Ol* ± *Sp*) *to garnet granulite* (*Gar* + *Pl* + *Cpx* ± *Opx* ± *Qtz*) *to eclogite* (*Gar* ± *Omp*). The pressure range over which this transition occurs at a given temperature is strongly dependent on bulk composition (Fig. 16.12).

Eclogites form in areas of oceanic plate subduction from blueschist facies assemblages (low *P–T* facies series). This type of eclogites registers high *P* but low *T* and, therefore, is referred to as *Low-T or LT-eclogites* (Bucher and Frey 1994). In areas of continental collision, such as the one between the Indian and Eurasian plates that formed the Himalayas, significant crustal thickening occurs. The crust may achieve thickness of >80 km. In such situations, eclogite is very likely to constitute the deep crust, followed above by amphibolites and may be granulites. This eclogite type may be expected to record intermediate temperatures and are called MT (medium T)-eclogites. Eclogites may also record high temperatures and may form from granulites in a collisional or extensional environment. The high temperature may be due to their direct crystallization from deep magmas or to heat supplied to granulitic lower crust by magmas. This type of eclogites is called HT (high T)-eclogites.

Ultrahigh Pressure Metamorphism

According to Coleman and Wang (1995, p. 2), "the term ultrahigh pressure metamorphism refers to a metamorphic process that occurs at pressure greater than ~28 kbar (2.8 GPa, the minimum pressure required for the formation of coesite at ~700 °C)." Until about 1984, no one could have imagined that continental crustal rocks could be metamorphosed at $P > 2.8$ GPa and be exhumed to the surface. An outstanding finding by Chopin (1984) of inclusions of coesite, a very high-pressure (>2.8 GPa) polymorph of SiO_2, in garnets of a quartzite from the Dora Maira area of Western Alps of Italy generated a new area of study in metamorphism—*ultrahigh pressure metamorphism (UHPM)*. Since that time coesite- and microdiamond (or graphite pseudomorphs after diamond)-bearing UHPM rocks have been discovered in many new sites in Europe and Asia where continent–continent collision has occurred. These new discoveries are giving new insights into how continental crust may be subducted deep into upper mantle depths and exhumed back to the surface. It is beyond the scope of this book to include a comprehensive review of all the recent work that has been done on UHPM, and the interested reader is encouraged to read the edited books by Coleman and Wang (1995) and Hacker and Liou (1998).

Significant attention has been given in recent years to the discoveries of coesite- and/or microdiamond-bearing eclogites from Norway, the *Dabie Mountains* of central China, Jiangsu and Shandong (*Su-Lu*) area of eastern China, and diamond-bearing gneiss from the *Kokchatev massif* of Russia. The peak metamorphic conditions, in terms of depth (pressure) and temperature, attained by the UHPM rocks of these three areas can be seen in Fig. 16.13 (largely based on Fig. 10.7 of Wang et al. 1995 in Coleman and Wang 1995). This figure shows the location of the polymorphic transformation boundaries quartz = coesite (Bohlen and Boettcher 1981) and graphite = diamond (Kennedy and Kennedy 1976). These curves provide minimum pressure estimates (by virtue of the presence of coesite or microdiamond) for the peak metamorphic conditions in Dora Maira, Su-Lu, and Dabie mountain areas. Whereas the occurrence of coesite and/or microdiamonds in such rocks is clearly indicative of ultrahigh pressure conditions, the temperatures of such peak metamorphism have largely been estimated from the garnet–clinopyroxene thermometer.

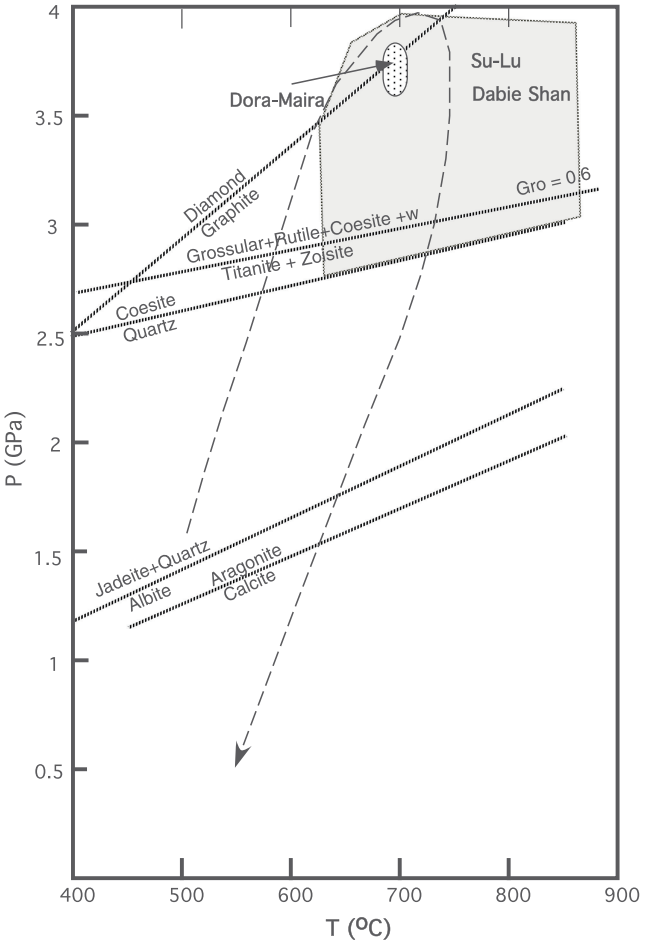

Fig. 16.13 Mineral reactions relevant to the ultra-high pressure metamorphism (UHPM). The two *shaded areas* mark the peak metamorphic conditions for the Dora Maira and Su-Lu areas. The *dashed curve* with *arrow* represents an inferred *P–T* path followed in UHPM

Garnet–clinopyroxene thermometer is based on the temperature-sensitive reaction involving the exchange of Fe^{2+} and Mg between garnet and clinopyroxene (see below).

The rocks in which such UHP minerals have been found are considerably varied:

Region	UHP minerals	Host rock
Dora Maira (Italy)	Coesite	Pyrope-quartzite
Dabie Shan (China)	Coesite, microdiamonds	Eclogite
Su-Lu (China)	Coesite	Eclogite
Western Gneiss Region (Norway)	Coesite	Eclogite
Fjorloft Island (Norway)	Microdiamonds	Kya–bio–gar gneiss
Kokchetav (Russia)	Coesite, microdiamonds	Eclogite (retrograded to gar–bio gneiss)

In most cases, the high-P assemblages have been retrograded to lower *P, T* assemblages during exhumation, and the UHP minerals are only found as rare relics or inclusions within resistant minerals such as garnet, pyroxene, epidote, or zircon. The protolith is most commonly an eclogite that occurs as isolated boudins within strongly deformed gneisses.

Several different models exist regarding the exhumation of these UHPM bodies to shallow levels; however, it is commonly accepted that:

1. They are associated with "cold" subduction areas because the peak temperature recorded by the high-P assemblages is generally very low relative to the normal continental geotherm.
2. The UHP minerals were preserved in these rocks because fluids could not access them during exhumation, such that they were not retrograded to some lower-grade assemblages.
3. The UHP assemblages are cooled during exhumation with the temperature of the blocks rarely reaching greater than about 800 °C (Hacker and Peacock 1995).

Figure 16.13 shows a likely path (dashed: schematic) that may be taken by one of these UHPM blocks during continental collision and subsequent exhumation. The fact that these rocks consistently record unusually "cool" temperatures (relative to what would be expected at such great depths) is a clear indication of their development through "cold" subduction conditions, which is to be expected in a continent–-continent collision.

From the foregoing discussion, it is perhaps apparent that an important task of the metamorphic petrologist is to estimate the pressure and temperature conditions at various times in the path of a metamorphic rock as it is buried, metamorphosed, and subsequently exhumed. How this is done is briefly reviewed in the next section.

Geothermobarometry, Reaction Kinetics, and Pressure–Temperature–Time (*P–T–t*) Paths

In his attempt to determine *P, T* conditions of metamorphism, the petrologist must use reactions that are sensitive to pressure and temperature, respectively. Such reactions may be univariant (or pseudo-univariant) or divariant (or pseudo-divariant). A quick example of a pressure-sensitive univariant reaction is the quartz–coesite reaction (Fig. 16.13), because over a large *T* range (500–800 °C), the pressure range at which quartz may transform to coesite is very narrow (2.7–3 GPa). Relative to the quartz–coesite curve, the graphite–diamond univariant curve is less *P* sensitive (Fig. 16.13). The sensitivity of mineral–mineral reactions to pressure versus temperature is the basis for *geothermobarometry, which is the subject that deals with P, T determination of rocks*.

Metamorphism is a continuous process in the sense that a rock may undergo progressive metamorphism during burial or subduction, attain peak *P, T* conditions at some depth, and subsequently be exhumed during which it must undergo retrograde metamorphism. Any reaction that occurs during this process may or may not reach equilibrium depending on kinetic factors that determine the rate at which such a reaction may progress. For example, geological time and fluid activity play an important role in metamorphism because both of these factors determine how much progress individual reactions may make at any particular *P, T* conditions. It follows that *reaction progress* will determine whether relict (i.e., unreacted) phases would remain in a rock or not, and preservation of such phases is a key to elucidating the complete *P–T–*time (*t*) history of the rock. What follows below is a brief discussion of geothermobarometry, reaction kinetics, and *P–T–t* paths taken by metamorphic rocks.

Geothermobarometry

As indicated above, the subject of geothermobarometry deals with estimation of temperature and pressure of equilibration of rocks using *T*- and *P*-sensitive reactions. Based on our discussion in Chap. 3 on Clapeyron equation, we know that a *P*-sensitive reaction should have a *large* ΔV and small ΔH and ΔS, and a *T*-sensitive reaction should have *large* ΔH and ΔS and small ΔV. Based on experimentally obtained datasets or from published thermodynamic values for various reactions, one can calculate "Clapeyron slopes" for such reactions and thus formulate geothermometers and geobarometers.

Figure 16.14a shows a hypothetical example of two univariant curves 1 and 2, reactions 1 and 2 being *P*-sensitive (geobarometer) and *T*-sensitive (geothermometer) reactions, respectively. A rock containing all of the phases (A, B, C, D, and E) in equilibrium would have formed at the *P, T* point where the two curves intersect. However, experimental or thermodynamic determination of any such curve is associated with some uncertainty of its precise location, which is shown as the shaded *error envelope* around each of the two curves. As a result, the *P, T* point will

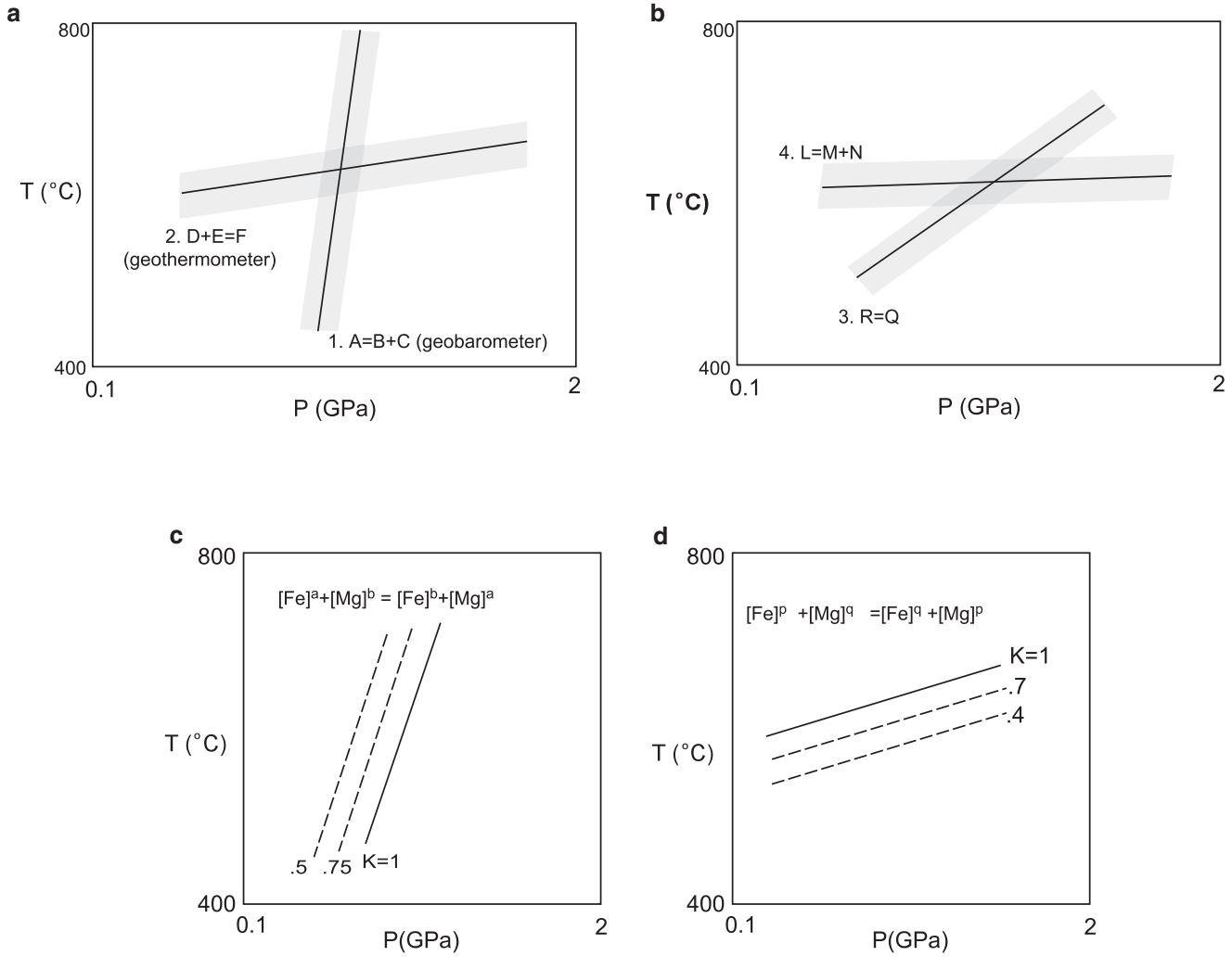

Fig. 16.14 Geothermobarometry. (**a**) and (**b**) are for discontinuous reactions; and (**c**) and (**d**) are for exchange reactions (see text for details)

have an error envelope (dark shaded area) around it. Figure 16.14b shows two different sets of reactions (3 and 4), one of which is a somewhat less *P*-sensitive polymorphic transformation $R = Q$. Because the angle at which the 3 and 4 intersect is smaller than that between 1 and 2 (compare Fig. 16.14a with b), the error envelope around the point of intersection is significantly larger.

Figure 16.14c, d shows two hypothetical exchange reactions, one of which is sensitive to *T* and the other to *P*. As noted earlier, in an exchange reaction between reactant and product minerals, the minerals exchange chemical components as the pressure or temperature (or both) are modified. Such exchange between reactants and products must occur in order to keep DG of the reaction equal to zero (i.e., equilibrium condition). Consider the case of an exchange reaction in which two chemical components Fe^{2+} and Mg are being exchanged between two phases "a" and "b" and a and b both being (Fe^{2+}, Mg) solid solutions:

$$\left[Fe^{2+}\right]^{a} + [Mg]^{b} = \left[Fe^{2+}\right]^{b} + [Mg]^{a}$$

The *equilibrium constant*, **K**, for this reaction can be written as:

$$\mathbf{K} = \left[\mathbf{a}_{Fe}{}^{b} \cdot \mathbf{a}_{Mg}{}^{a}\right] / \left[\mathbf{a}_{Fe}{}^{a} \cdot \mathbf{a}_{Mg}{}^{b}\right]$$

where "**a**" means *activity* of some component in a particular phase: for example, $\mathbf{a}_{Fe}{}^{a}$ means activity of component Fe in phase "a" (see earlier discussion in Chap. 7). How the activity of a particular component in a multicomponent solid solution may be calculated is somewhat of a complicated subject, and there are several excellent books that the reader may wish to consult

(e.g., Saxena 1973; Wood and Fraser 1976; Anderson 1996).

Briefly, the activity of a component in a multicomponent solid depends upon the composition of the solid solution and whether the solid solution in question behaves ideally or nonideally. $\mathbf{a}_A{}^p = \mathbf{X}_A{}^p \cdot g_A{}^p$, where $\mathbf{X}_A{}^p$ is mole fraction [=moles of A/(moles of A + moles of B)] of component *A* in phase *p* and g, is called the *activity coefficient*. In an ideal solid solution g is equal to 1, and therefore, activity = mole fraction. For a nonideal solution, *g* is not equal to 1, but such cases will not be dealt with here, and the reader is referred to the important textbooks listed in "Bibliography." For pure end-member compositions, such as pure forsterite, activity is always equal to 1. Olivine solid solutions, to a first approximation, show ideal behavior. Therefore, in the case of an olivine of composition $Fo_{80}Fa_{20}$, if ideal behavior may be assumed, then mole fraction and activity of pure forsterite may be related: $\mathbf{a}_{Fo}{}^{ol} = X_{Fo}{}^{ol} = 0.8$.

Now, returning to thermobarometry, let us consider two hypothetical Fe = Mg exchange reactions: reaction between the phases a and b is pressure sensitive (Fig. 16.14c) and that between c and d is temperature sensitive (Fig. 16.14d). Figure 16.14c, d shows the variation of equilibrium constant, **K**, for each of these reactions as a function of *P* and *T*. Each dashed curve represents a constant value of **K**. Although not shown in these figures, one can map the divariant region in each case over which both phases may be stable and **K** varying between 0 and 1. Determination of an exact value of **K**, which is possible through analysis of the minerals by an electron microprobe, will pinpoint the *P* (Fig. 16.14c) or *T* (Fig. 16.14d).

Below we use some actual examples to illustrate how *P, T* estimation may be done on a rock. A detailed review of all geothermobarometers applicable to metamorphic rocks is well beyond the scope of this book. The focus here is on mineral–mineral reactions (such as exchange reactions, solvus reactions) and other methods, such as isotopic and fluid inclusion thermobarometry (which are nonetheless important), will not be discussed. The interested reader may wish to consult the text by Bucher and Frey (1994, ***Sect. 4.7) and references therein.

Garnet–Clinopyroxene and Garnet–Biotite Thermometers

In the case of garnet–clinopyroxene thermometer, which is very important for eclogites, garnet pyroxenites, etc., the reaction of concern is the one in which the coexisting garnet and clinopyroxene grains exchange Mg and Fe^{2+} cations:

$$[\mathrm{Mg}]^{\mathrm{gt}} + \left[\mathrm{Fe}^{2+}\right]^{\mathrm{cpx}} = [\mathrm{Mg}]^{\mathrm{cpx}} + \left[\mathrm{Fe}^{2+}\right]^{\mathrm{gt}}$$

A relatively simple thermometer by *Ellis and Green* (1979) that is based on experimental calibration of **K** for this reaction is still quite popular:

$$T(^{\circ}\mathrm{C}) = \left[3030 + 10.86 * \mathrm{P\ (kbar)} + 3104 * [\mathrm{X_{ca}}]^{\mathrm{gt}}\right] / \left[\ln \mathrm{K_D} + 1.9034\right] - 273$$

$\mathbf{K_D} = \left(\mathrm{X_{fe^{2+}}}/\mathrm{X_{Mg}}\right)^{\mathrm{gt}} / \left(\mathrm{X_{Fe^{2+}}}/\mathrm{X_{Mg}}\right)^{\mathrm{cpx}}$, and $\mathrm{X_{Fe^{2+}}}$ and $\mathrm{X_{Mg}}$ are mole fractions ($\mathrm{X_{Mg}} = \mathrm{Mg}/(\mathrm{Mg} + \mathrm{Fe}^{2+}$, etc.). Note that this thermometer assumes ideal exchange of Fe^{2+} and Mg between garnet and clinopyroxene, i.e., $\mathbf{K_D} = \mathbf{K}$, such that the activities are assumed to be equal to the mole fractions. Figure 16.15 shows ln $\mathbf{K_D}$ versus *T* plot for a range of garnet–cpx $\mathbf{K_D}$ values at two different input values of pressure (3 versus 4 GPa). From this figure it is clear that even if one errs in using a pressure value by about 1 GPa, the temperature estimate is affected by no more than 50°. Thus, the garnet–clinopyroxene thermometer is an excellent thermometer. Note that more recent studies indicate that this thermometer overestimates the temperature of granulites and garnet–clinopyroxenites by 50–150 °C (Sen 1988). It is therefore not surprising that several newer calibrations of this reaction have appeared in the literature: for example, Krogh (1988) presented the expression:

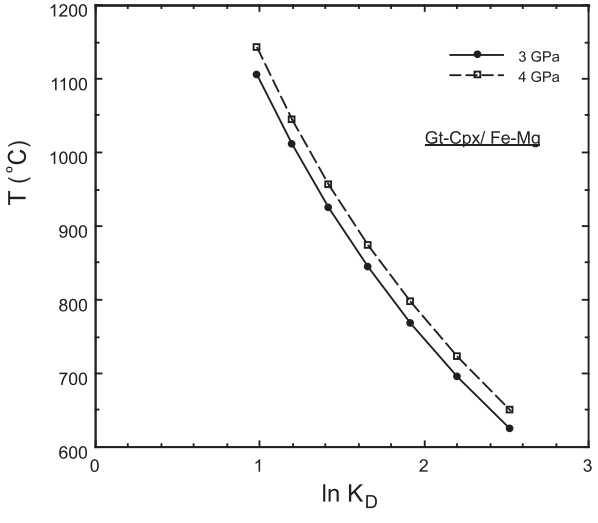

Fig. 16.15 Garnet-clinopyroxene thermometry

$$T(^{\circ}\mathrm{C}) = \Big[1879 + 10 * P(\mathrm{kbar}) - 6137 * \left[[\mathrm{X_{ca}}]^{\mathrm{gt}}\right]^2 + 6731 * [\mathrm{X_{ca}}]^{\mathrm{gt}} / [\ln \mathrm{K_D} + 1.393]\Big] - 273$$

According to Bucher and Frey, Krogh's thermometer apparently gives more reasonable estimates for LT and MT eclogites.

Garnet–Biotite Thermobarometry

In *garnet–biotite thermometry* the exchange reaction is once again Mg, Fe^{2+} exchange:

$$\left[\mathrm{Fe}^{2+}\right]^{\mathrm{gar}} + [\mathrm{Mg}]^{\mathrm{bio}} = [\mathrm{Mg}]^{\mathrm{gar}} + \left[\mathrm{Fe}^{2+}\right]^{\mathrm{bio}}$$

Many thermometers based on garnet–biotite Fe = Mg exchange have been presented, of which a commonly used one is that of Ferry and Spear (1978):

$$T(^{\circ}\mathrm{C}) = [[2089 + 9.56 * P(\mathrm{kbar})] / [0.782 - \ln K_{\mathrm{d}}]] - 273$$

where $K_{\mathrm{d}} = (\mathrm{Fe}^{2+}/\mathrm{Mg})^{\mathrm{bio}}/(\mathrm{Fe}^{2+}/\mathrm{Mg})^{\mathrm{gar}}$.

Although the garnet–biotite exchange reaction is largely *T* dependent, Spear and Selverstone (1983) developed an interesting petrogenetic grid for pelitic bulk compositions that allows determination of both P and T based on composition of biotite and garnet (Fig. 16.16). In this method, ideal mixing is assumed in both phases, and the compositional variation of garnet in *P, T* space is mapped in terms of $[\mathrm{X_{alm}}]^{\mathrm{gar}}$-*isopleths* (i.e., lines of constant mole fraction of almandine component in garnet$_{\text{solid solution}}$). Biotite compositional variation is expressed in terms of $[\mathrm{X_{ann}}]^{\mathrm{bio}}$-*isopleths* (i.e., lines of constant mole fraction of annite component in biotite$_{\text{solid solution}}$). Figure 16.16 shows that although both $[\mathrm{X_{alm}}]^{\mathrm{gar}}$ and $[\mathrm{X_{ann}}]^{\mathrm{bio}}$ isopleths vary as a function of both *P* and *T*, their slopes are sufficiently different such that their intersections can be used as a geothermobarometer.

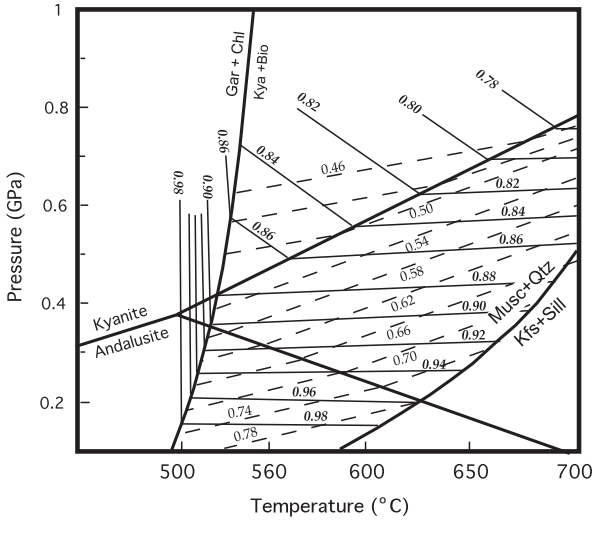

Fig. 16.16 $\mathrm{X_{alm}}^{\mathrm{Gar}}$ -isopleths (*thin lines*) and $\mathrm{X_{ann}}^{\mathrm{Bio}}$-isopleths (*dashed*) in coexisting biotite and garnet in meta-pelitic rocks

Two-Pyroxene Thermometry

In Chap. 3 the reader was first exposed to the concept of solid–solid immiscibility between two phases. Basically, two minerals may show complete miscibility (i.e., solid solution) at high temperature, but at a lower temperature (during retrograde metamorphism), such phases may exsolve each other due to the presence of an immiscibility gap or solvus. Figure 16.17 illustrates solid–solid immiscibility between diopside and enstatite over a pressure range 10–20 kbar (from Lindsley and Dixon 1976). The sensitivity of the diopside limb to temperature and relative insensitivity to pressure makes it a useful thermometer for rocks like lherzolites and two-pyroxene (*ortho-* and clinopyroxene) granulites. As the two-pyroxene phases in a metamorphic rock equilibrate with each other at any given temperature, their compositions are fixed on the two limbs of the miscibility gap (or solvus *sensu lato*) by the particular isotherm in question. Their compositions can only change, according to the temperature—composition diagram shown in Fig. 16.17, when the temperature is changed. This compositional exchange of the two coexisting pyroxenes can be expressed as follows:

$$[\mathrm{Mg_2Si_2O_6}]^{\mathrm{opx}} = [\mathrm{Mg_2Si_2O_6}]^{\mathrm{cpx}}$$

where $[\mathrm{Mg_2Si_2O_6}]^{\mathrm{cpx}}$ and $[\mathrm{Mg_2Si_2O_6}]^{\mathrm{opx}}$ signify enstatite components in coexisting clinopyroxene and orthopyroxene phases, respectively. **K** for the above reaction may be written:

$$\mathbf{K} = [\mathbf{a}_{\mathrm{En}}{}^{\mathrm{cpx}}] / [\mathbf{a}_{\mathrm{En}}{}^{\mathrm{opx}}]$$

where $\mathbf{a}_{\mathrm{En}}{}^{\mathrm{opx}}$ and $\mathbf{a}_{\mathrm{En}}{}^{\mathrm{cpx}}$ represent activities of the enstatite component in coexisting *ortho-* and clinopyroxenes. Because pyroxene solid solutions do not behave ideally, a number of pyroxene activity models exist in the literature, and a good starting point is the reference book entitled *pyroxenes* (see ref.

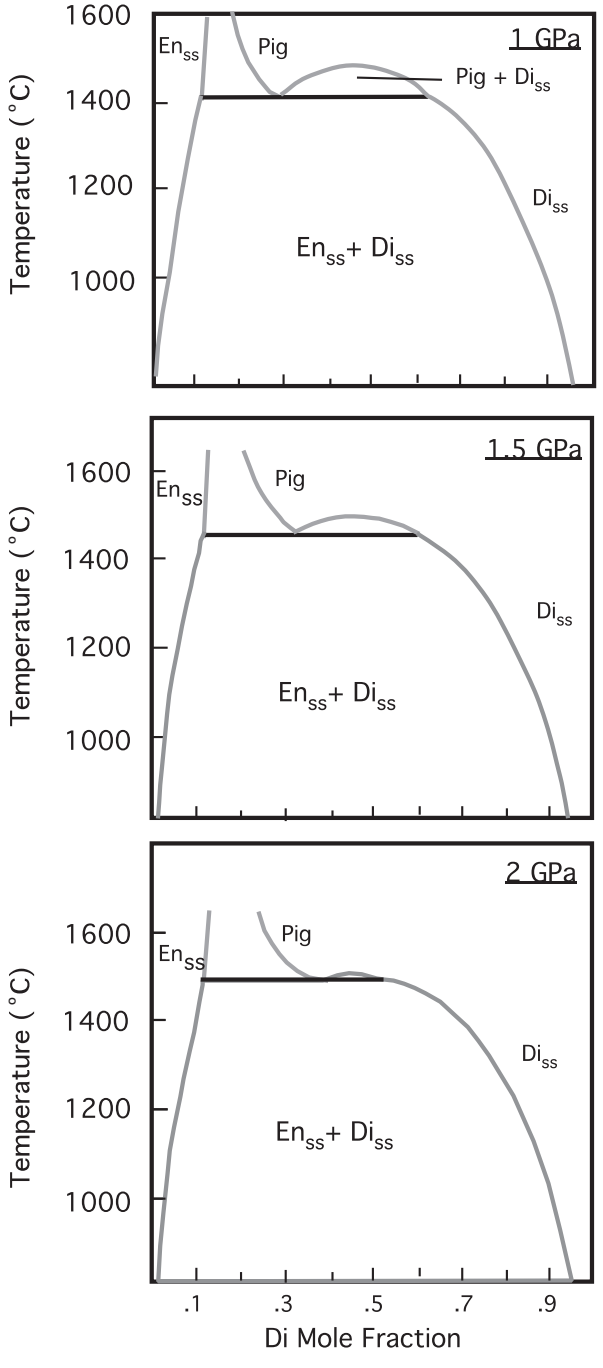

Fig. 16.17 Pyroxene immiscibility gap at three different pressures

list). Since the intention here is only to demonstrate how a thermometer is formulated, ideal solubility is assumed such that **K** can be related to mole fraction (**X**) (a parameter that can be determined from microprobe analysis of the coexisting pyroxenes in a rock):

$$\mathbf{K} \approx [\mathbf{X}_{\mathrm{En}}{}^{\mathrm{cpx}}]/[\mathbf{X}_{\mathrm{En}}{}^{\mathrm{opx}}]$$

The procedure to calculate these mole fractions is based on cation site occupancies in the atomic structure of pyroxenes as laid out in Wood and Banno (1973):

1. From formula cations (i.e., cations per six oxygens) allocate Ca and Na in M2 octahedral site and all of Si in the *T* (tetrahedral) site.
2. Allocate a portion of Al to the *T* site to make the *T* site total = 2.
3. Allocate the rest of Al and all of Cr and Ti to the smaller M1 site.
4. Distribute Mg and Fe cations to M1 and M2 sites according to their proportion in the mineral formula. After stages 1–3, M2 site will need 1-Ca–Na cations of Mg + Fe to fill it up. Similarly, M1 site will need 1-Ti–Cr–Al (in M1 site) cations of Mg + Fe to fill that site. Now, Mg/(Mg + Fe) of the pyroxene in question needs to be calculated, and then, amounts of Mg and Fe in M1 and M2 sites can individually be calculated assuming that the ratio Mg/(Mg + Fe) is the same in both sites, i.e.,

$$[\mathrm{Mg}/(\mathrm{Mg}+\mathrm{Fe})]^{\mathrm{mineral}} = [\mathrm{Mg}/(\mathrm{Mg}+\mathrm{Fe})]^{\mathrm{M1}} = [\mathrm{Mg}/(\mathrm{Mg}+\mathrm{Fe})]^{\mathrm{M2}}$$

5. Since Mg of the enstatite component occurs only in the M2 and M1 sites of the pyroxene in question, the mole fraction of enstatite in that pyroxene may be written as: $X_{en}{}^{pyroxene} = [X_{Mg}{}^{M1} \cdot X_{Mg}{}^{M2}]$. $X_{Mg}{}^{M1}$ is mole fraction of Mg in M1 site, which is the same as Mg cations present in the M1 site. The same logic holds for the M2 site.
   Mole fractions of enstatite in coexisting *ortho-* and clinopyroxene may thus be calculated: $X_{en}{}^{opx} = [X_{Mg}{}^{M1} \cdot X_{Mg}{}^{M2}]^{opx}$ and $X_{en}{}^{cpx} = [X_{Mg}{}^{M1} \cdot X_{Mg}{}^{M2}]^{cpx}$, and **K** can in turn be calculated from them ($\mathbf{K} \approx [\mathbf{X}_{\mathrm{En}}{}^{\mathrm{cpx}}]/[\mathbf{X}_{\mathrm{En}}{}^{\mathrm{opx}}]$)

In **K** for this reaction is very sensitive to temperature but is much less sensitive to pressure variations. Thus, this reaction is a good geothermometer for lherzolites (Sen and Jones 1989):

$$T(^{\circ}\mathrm{C}) = [4900/[1.807 - \ln\ \mathbf{K}]] - 273$$

In the spinel lherzolite stability field, Al_2O_3 content of pyroxene varies almost entirely as a function of temperature, and therefore, it is an excellent

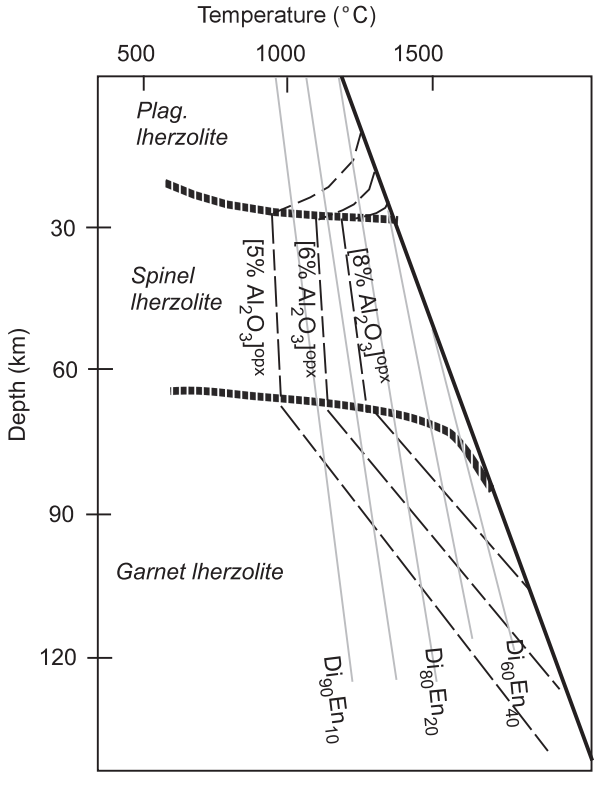

Fig. 16.18 Al_2O_3 (wt%)-in-orthopyroxene isopleths and En (mol%)-in-clinopyroxene isopleths for ultramafic rocks

geothermometer for spinel lherzolites. However, in garnet lherzolites and plagioclase lherzolites, the Al_2O_3 content of pyroxenes varies both as a function of *P* and *T* (Fig. 16.18). Combination of the two-pyroxene thermometer (which is shown as constant *mole%* En-in-cpx lines) with Al_2O_3 *isopleths* (i.e., lines of constant *weight%* Al_2O_3 in opx) creates a petrogenetic grid in the plagioclase lherzolite and garnet lherzolite fields. Thus, knowledge of these components in coexisting *ortho-* and clinopyroxene in a plagioclase or garnet lherzolite xenolith can be plotted on the grid shown in Fig. 16.18 in order to obtain an estimate depth (pressure) and temperature of the region from where the xenolith was picked. A number of scientists, led by two pioneers—Ian Macgregor (presently at the National Science Foundation) and F.R. (Joe) Boyd (Geophysical Laboratory)—have successfully used this concept to obtain "fossil geotherms" from garnet lherzolite xenoliths in kimberlite pipes.

The GASP Geobarometer

The G (garnet)—A (aluminosilicate)—S (silica)—P (plagioclase) geobarometer is widely used and is based on the net-transfer reaction:

$$\underset{\text{(anorthite)}}{CaAl_2Si_2O_8} = \underset{\text{(grossular)}}{Ca_3Al_2Si_3O_{12}} + \underset{\text{(ky/and/sill)}}{2Al_2SiO_5} + \underset{\text{(quartz)}}{2SiO_2}$$

The equilibrium constant, **K**, for this reaction can be written as:

$$\mathbf{K} = \left[\left(\mathbf{a}_{kya}\right)^{kya}\right]^2 \cdot \mathbf{a}_{qz} \cdot \left[\left(\mathbf{a}_{gro}\right)^{\mathbf{gar}}\right] / \left[\left(\mathbf{a}_{an}\right)^{\mathbf{pl}}\right]^3$$

Because quartz and Al_2SiO_5 polymorphs are essentially pure phases, their activities are equal to 1. On the other hand, the composition of natural plagioclase and garnet can vary considerably due to solid solutions. Assuming ideal solution, the following simplifications may be made: $(a_{gro})^{gar} = (X_{gro}{}^{gar})^3$ *and* $(\mathbf{a_{an}})^{\mathbf{pl}} = (\mathbf{X_{an}}^{\mathbf{pl}})$ in applying the GASP barometer (follows below) to natural rocks. However, because these minerals do not actually exhibit ideal solution behavior, many alternate barometers have appeared in the literature that takes into account departure of these solutions from ideal behavior.

Figure 16.19 shows a plot of **K** as a function of *P, T* (from Spear 1993, Fig. 15–8). Using the experimental data of Koziol and Newton (1978) and assuming $\Delta C_p = 0$ and using a constant $\Delta V = -6.608$ J/bar, Spear (1993, Eqs. 15–48) proposed the following equation for GASP:

$$-48,357 + 150.66\,T(K) + (P-1)(-6.608) + RT\ln K = 0$$

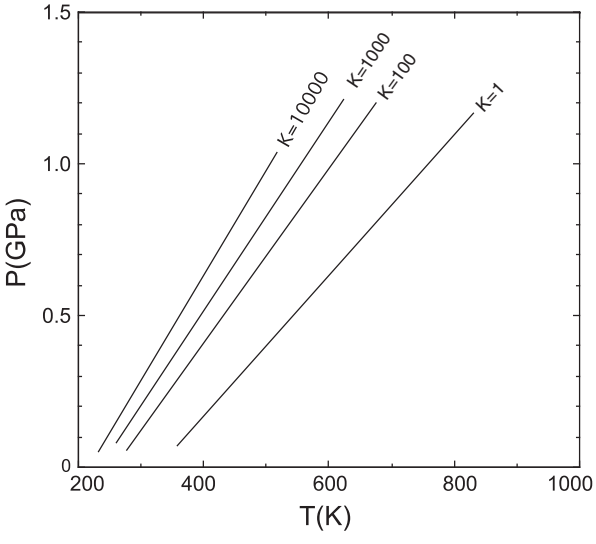

Fig. 16.19 The GASP geothermobarometer (see text for details)

Rearranging, the above equation becomes:

$$P(\text{bars}) = 1 + [[48{,}357 - \text{RT ln } K - 150.66T(K)]/(-6.608)]$$

This is the simplest form of the GASP geobarometer.

Practice of Geothermobarometry

In practice, the most reliable *P, T* estimates of the peak equilibrium conditions of a metamorphic rock would be the one that is constrained by one or more of the following:

1. Two reactions whose lines of constant **K**'s intersect at a large angle in *P–T* space can provide strong constraints on *P, T* of formation of a rock, even though both of the **K**'s may vary with respect to both *P* and *T*.
2. An invariant assemblage, such as the kyanite–andalusite–sillimanite triple point, provides an excellent control on *P, T* of formation of a rock, if such an assemblage is actually found (rare).
3. Intersection of two discontinuous reaction curves, one of which may be sensitive to *P* and the other to *T*, may provide valuable *P, T* information.
4. One may also use several sets of geothermometers and geobarometers for one or more rock types that are spatially and temporally related by the same metamorphic event.

When it comes to applying the mineral geothermobarometers to estimate the *P, T* of equilibration of metamorphic rocks, many complexities may arise: (1) a large part of which has to do with the difficulty of obtaining equilibrium in laboratory experiments, on which the geobarometer or geothermometer must be based. (2) Often, the activity models for individual phases may be inaccurate, which would render significant inaccuracy in the thermometer or barometer. (3) Different reactions may have different "closure" temperatures, e.g., an exchange reaction between two minerals may stop equilibrating after cooling to some temperature following the peak metamorphic temperature reached by a rock, whereas a second exchange reaction between two other minerals in the same rock or an adjacent rock may continue to much lower temperatures. Thus, the two different reactions may give different final *P, T* conditions of equilibration of the rock.

Reaction Kinetics

All of the above discussion was based on classical thermodynamics in which achievement of chemical equilibrium plays the central role irrespective of the actual processes. We learned that a reaction must proceed if the reactants have a higher free energy (G) than the product(s) and at equilibrium DG must be zero. In reality, however, different chemical reactions proceed at different rates, and in a metamorphic rock, reactions between two minerals may not go to full completion, as a result of which compositional zoning may persist within individual mineral grains (discussed earlier).

This section focuses on *reaction kinetics*, which include all rate processes that dictate how fast or slow a reaction may proceed. Even though the reactants may have higher free energy than the products, a reaction may not proceed spontaneously because the reactants must cross over an "energy hump" known as the *activation energy barrier* (Fig. 16.20a). Where several

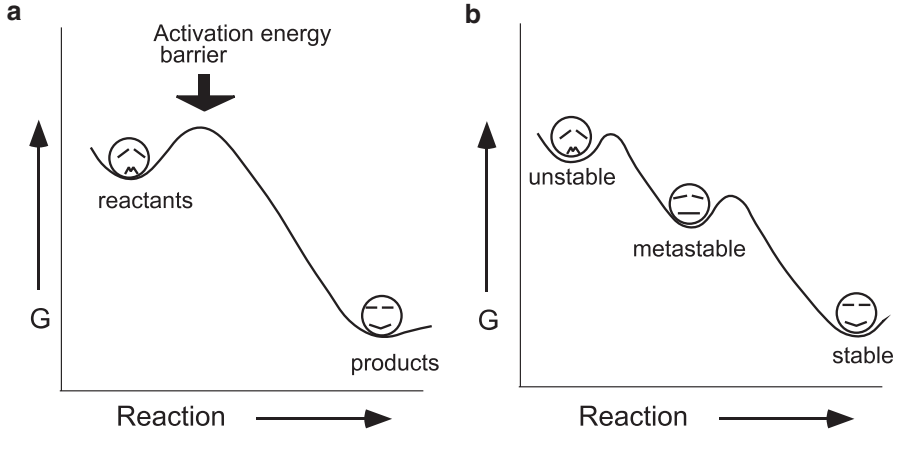

Fig. 16.20 (**a**) Schematic diagram showing free energy relations between reactants and products. (**b**) Free energies of unstable reactants, metastable products, and stable products

different reaction paths are possible, the one that has the minimum activation energy barrier will be followed. A step-wise process, in which the reaction may proceed via several steps in which *metastable* phases are produced, is commonly favored (Fig. 16.20b).

Reaction rate ($\mathbf{R_r}$) is expressed in terms of the so-called Arrhenius relation:

$$R_r = K \cdot e^{-E/RT}$$

where K is a constant (called "rate constant"), E = activation energy (J/mole), R = gas constant (8.3144 J/mol/K), and T is temperature (K). The above equation can be rewritten as:

$$\log_{10} R_r = \log_{10} K - [(E/RT)]$$

The above equation has the form of the equation of a straight line. Plotting experimentally obtained reaction rate versus temperature data for any experiment allows one to calculate the activation energy barrier, E, and the rate constant K from the slope and intercept, respectively (Fig. 16.21). Figure 16.21 shows such lines for three different reactions—"a," "b," and "c." Note that "a" and "c" are parallel, i.e., their E's are the same, but their intercepts (i.e., K) are different. The steeper the slope (**E**), the more temperature dependent will be the reaction rate. Thus, the reaction rate for "a" is the most temperature dependent and that for "b" is the least temperature dependent. The reaction rate for "c" is substantially lower than that for "a" because of a lower rate constant. Thus, both rate constant and temperature control how fast or slow a reaction may proceed.

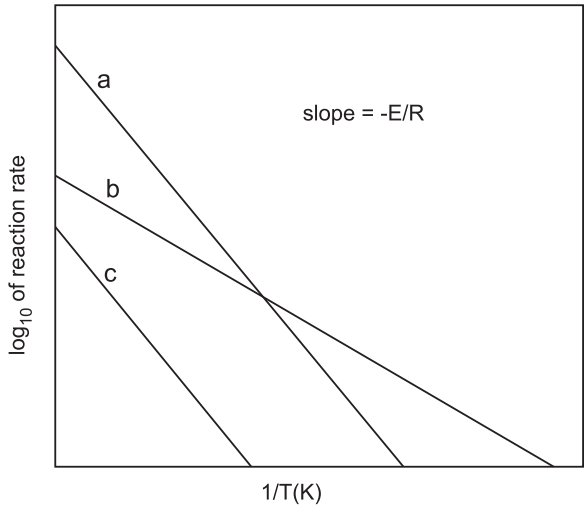

Fig. 16.21 Relationship between reaction rate and inverse temperature (in Kelvin) for three hypothetical reactions a, b, and c. E = activation energy. R = gas constant

Chemical components (ions) must diffuse in and out of mineral grains in any chemical reaction. This process of diffusion can be of different types, among which diffusion through the volume of a mineral grain (*volume diffusion*) is of interest in this section. Diffusion of components between reacting phases is controlled by *Fick's law*:

$$J_z = -D_i[\partial c/\partial z]$$

where J_z is the flux of a component "i" along a direction "z." $\partial c/\partial z$ is the concentration gradient of component "i" along "z" direction, and D_i is its diffusion coefficient. Values of D_i range between 10^{-10}–10^{-14} m^2/s in magmas and 10^{-15}–10^{-21} at 600–1,200 °C in common silicate minerals. These values indicate that *volume diffusion in solids is much slower than through silicate melt or any other fluid*. Fick's second law describes diffusion down a concentration gradient along the "z" direction:

$$dc/dt = D_i\left(d^2c/dz^2\right)$$

The above equation assumes D_i is constant; however, in most cases D_i is a function of composition, and this equation is rewritten as:

$$dc/dt = d/dz[D_i(dc/dz)]$$

The above equation can be used to calculate concentration gradients as a function of time. In terms of application, a concentration gradient in a zoned crystal can be determined with an electron microprobe, and if, by some other means, the time over which such zonation developed can be determined, then the diffusion coefficient may be calculated.

Pressure–Temperature–Time (*P–T–t*) Paths

The two fundamental controls for metamorphic reactions are free energy and reaction rate. Arrhenius relation (discussed above) indicates that reaction rate is exponentially related to temperature: at high temperatures a reaction will proceed at an exponentially faster rate than at a low temperature. Therefore, when a rock is increasingly metamorphosed (*prograde*

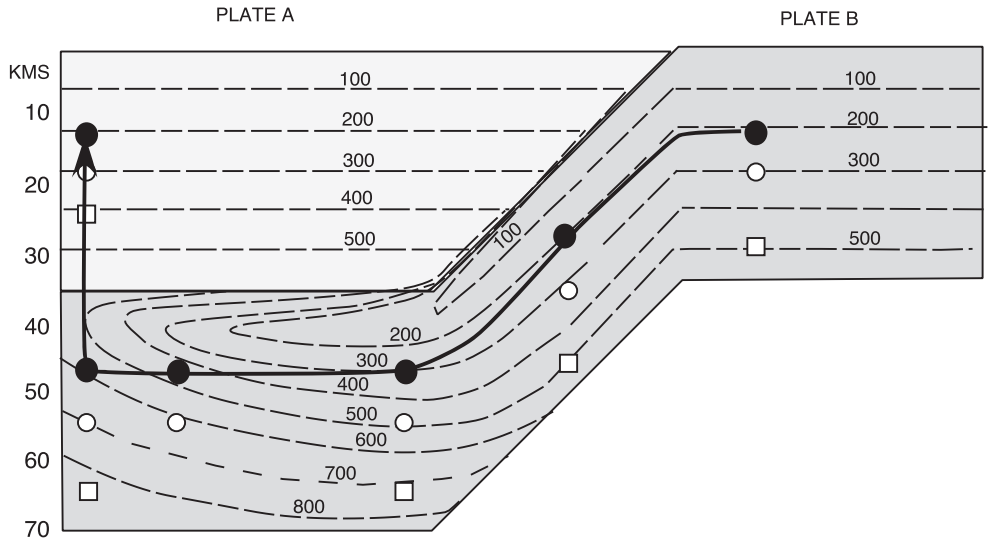

Fig. 16.22 A schematic model showing collision between two plates. *Dashed lines*—isotherms. *Solid circle*, *unfilled circle*, and *square* represent three reference points in the downgoing slab that track the changing *P, T* conditions as the underthrust slab moves forward and eventually is uplifted; and the *arrows* track the progress of the subducted lithosphere

metamorphism), reactions between its constituent minerals will proceed at the fastest speed when maximum (peak) temperature is attained (all other factors being equal, particularly fluid activity). The various stages of prograde metamorphism may be recorded in terms of zoning in minerals. When this rock is brought back up to shallower levels due to uplift and erosion of the overburden (which is related to isostatic adjustment), it should continue to undergo *retrograde* metamorphism, i.e., reactions should continue and minerals that are stable at decreasing *P, T* conditions should form, erasing any evidence of it once being metamorphosed at a much greater *P, T*. In reality, however, high-grade metamorphic rocks are quite commonly exposed at the Earth's surface with little evidence of any retrograde metamorphism except for minor alterations along grain boundaries. Obviously, these assemblages are only metastable at the surface. This happens because the retrograde reactions essentially come to a halt at lower temperatures, and also fluids, which help in keeping reactions going, do not penetrate the rocks as much.

The *P, T* conditions during the retrograde evolution of a metamorphic rock may be deciphered by using a fluid inclusion thermobarometric method, which is well beyond the scope of discussion here. The complete *P–T* path followed by such a rock—from the beginning to end of its metamorphic history—as a function of time, is commonly referred to as a *P–T–t* path. The *P–T–t* paths of metamorphic rocks can provide important clues about rates of burial, uplift, and erosional processes along plate convergent boundaries and are discussed in this section.

In an effort to show how actual *P–T–t* paths may develop in metamorphic rocks, a schematic model is presented in Fig. 16.22 (based on Bucher and Frey 1994). This figure shows how crustal thickening (via continent–continent collision) and subsequent exhumation (owing to isostasy and erosion) may result in three different *P–T–t* paths for three rocks that are initially located at three different depths within the underthrusting plate. The isotherms in the underlying slab are purely schematic, and their nature would be controlled by several factors, the most important of which are the initial geotherms, the speed of convergence, and radioactive (or magmatic) heating in the base of the crust.

Figure 16.23 shows the *P–T–t* paths for the three rocks, while ignoring the fact that these rocks are brought all the way up to the surface but, for brevity, are returned to the same levels where they originally started. It is important to note that all of the paths record a "cold–hot–cold" sequence, i.e., they are buried "cold" relative to a steady-state geotherm, and then they are heated at a maximum temperature, and finally uplifted and cooled. These paths do not define a steady-state geothermal gradient. Note that the thick line obtained by connecting the T_{max} (Temperature maximum) recorded by each of the three rocks does not coincide with the geotherm. This thick line is called a "metamorphic field gradient (MFG)." Long ago, Miyashiro (1961) recognized such *P, T* gradients defined by metamorphic terranes and called them *metamorphic facies series (discussed in a previous section)*, which are the equivalents of MFG's. *P-T-t* paths from metamorphic terranes from all over the world are

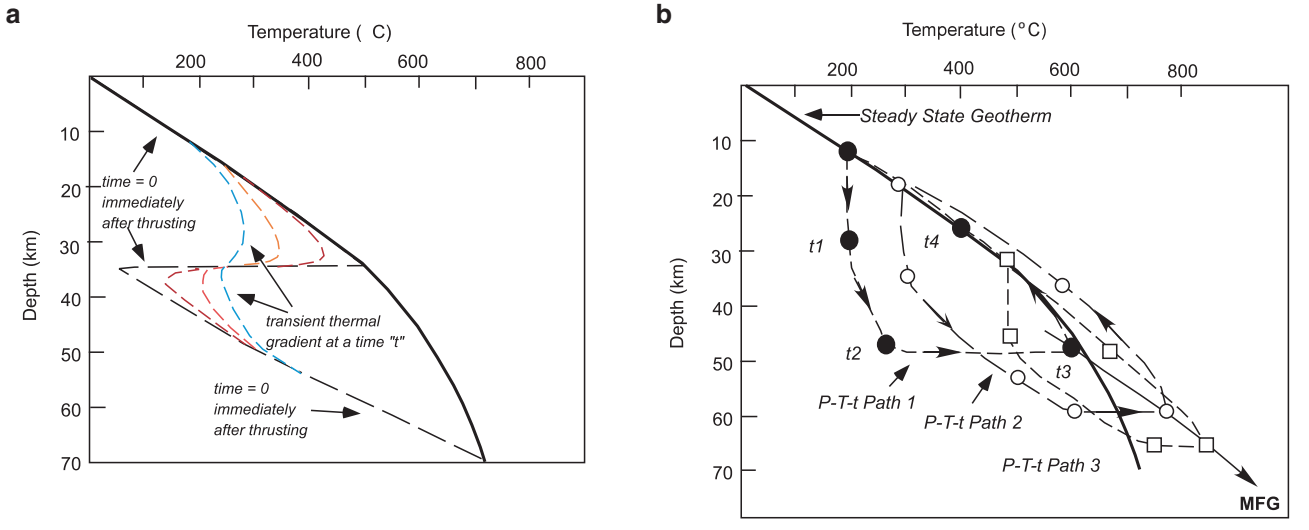

Fig. 16.23 (**a**) Changing thermal gradient as a function of time within the upper and lower plates of Fig. 16.22. *Dark line*—normal conductive geothermal gradient in a single lithosphere. (**b**) Schematic diagram showing *P–T–t* paths recorded by the rocks at three different depths (*circle*, *unfilled circle*, *square* in Fig. 16.22). *t*1, *t*2, etc., mark a time sequence from the oldest to youngest. *MFG* metamorphic field gradient (discussed in text)

plotted in Figure 16.24 (Ernst 1988). Two general observations may be made from this figure: (1) most paths are anti-clockwise and, as indicated above, they are probably results of crustal thickening. (2) There are clockwise paths as well and these occur mostly in the higher T part of the diagram, and it is likely that they result from initial magmatic heating. There are several important aspects of these *P-T-t* paths: (1) Because T_{max} generally coincides with P_{max} in crustal thickening models, P_{max},T_{max} conditions probably record the maximum amount of crustal thickening. (2) Time and amount of thickening together give the thickening rate. (3) The uplift rates may be modeled from *P–T–t* paths as well. Rapid convergence of cold crust leads to the formation of blueschists. If such blueschists are kept at depth for a long time, then radioactive heat production would eventually increase their temperature and convert these rocks to a higher *P, T* rock. Therefore, the only way a blueschist can occur at the surface is through rapid uplift to the surface. *P–T–t* paths and MFG's are clearly an important direction in metamorphic petrology, and the interested reader is strongly recommended to read the important reference work by Spear (1993).

Seismometamorphism

In most tectonic settings, earthquakes occur at relatively shallow depths (<30 km), but in subduction zones, earthquakes occur as deep as 670 km below the Earth's surface! Earthquakes are triggered by the sudden rupture of a fault which releases vast amounts of energy. At depths greater than about 40 km, "normal" brittle failure should be inhibited by the high normal stresses across a fault; in other words, at great depths the weight of the overlying rocks should create too much friction for fault slip to occur. Earthquakes that occur at depths >40 km, therefore, must be triggered by some other mechanism. In recent years, some scientists have focused their research on possible connections between metamorphism and earthquakes in subduction zones (cf. Green and Burnley, 1989; Kirby et al. 1991, 1996a, b; Peacock and Wang 1999). These studies suggest that both intermediate-depth earthquakes (50–300-km depth) and deep earthquakes (300–670-km depth) might be triggered by metamorphic reactions.

Intermediate-depth earthquakes appear to be triggered by devolatilization reactions within the subducting oceanic crust associated with the transformation of metabasalt and metagabbro to eclogite (Kirby et al. 1996a, Peacock and Wang 1999). As we have seen earlier, many devolatilization reactions would be expected to occur in a subducting oceanic crust, beginning with clay- and zeolite-breakdown reactions at shallow depths and culminating in eclogite-forming reactions at deeper levels. Fluids released by these devolatilization reactions increase local pore pressure and decrease effective stresses thereby promoting slip along preexisting faults (Kirby et al. 1996a).

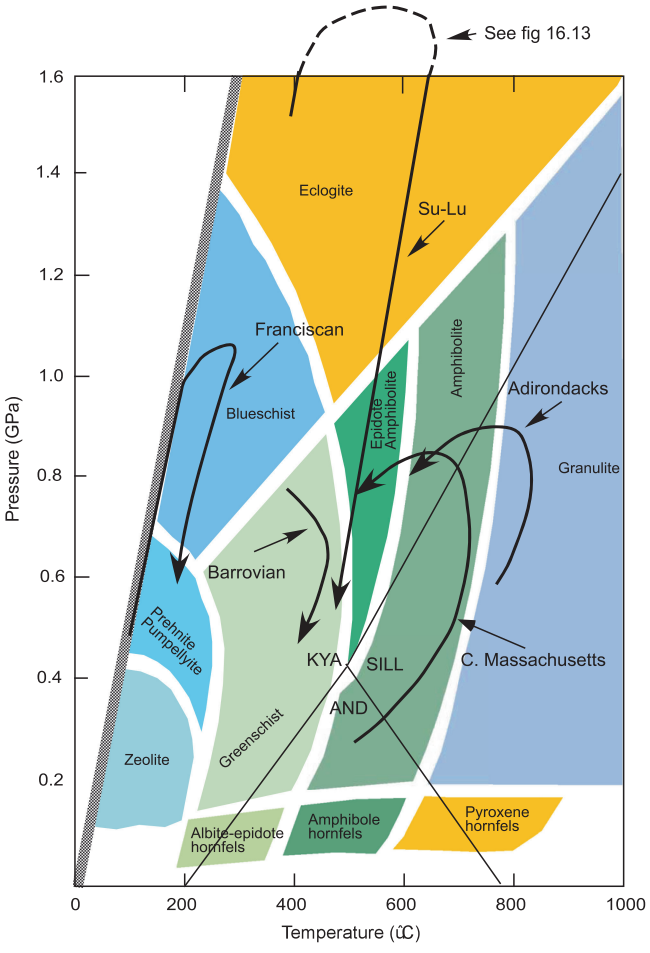

Fig. 16.24 Some representative *P–T–t* paths from the US and elsewhere (*sources*: Ernst 1988; Coleman and Wang 1995)

Deep earthquakes occur within the subducting oceanic lithosphere, the coolest part of the subducting slab. Experimental observations suggest deep earthquakes are triggered a shear instability associated with the metastable transformation of olivine to spinel (Green and Burnley 1989; Kirby et al. 1991, 1996b). Because the interior of the subducting lithosphere is relatively cold (500–700 °C), the kinetics of metamorphic solid–solid reactions may be quite sluggish, and olivine may persist metastably to depths greater than 400 km.

In SW Japan, arc volcanism is sparse (and highly silicic), and subduction-zone earthquakes do not extend beyond 65-km depth. In NE Japan, arc volcanism is more robust and intraslab earthquakes extend down to ~200-km depth. Peacock and Wang (1999) constructed detailed thermal-petrologic models of the SW and NE Japan subduction zones, concluding that:

1. The subducting oceanic crust beneath NE Japan is ~300 °C cooler than the crust subducting beneath SW Japan.
2. Eclogite-forming reactions and dehydration reactions occur much deeper beneath NE Japan than beneath SW Japan, thereby explaining the difference in observed earthquake depths.
3. The warm subducting oceanic crust beneath SW Japan dehydrates at a relatively shallow level and may partially melt. In contrast, dehydration reactions occur at deeper levels beneath NE Japan where released fluids infiltrate the hot overlying asthenosphere triggering arc volcanism.

The relationship between metamorphism and earthquakes is an exciting new area of research. Progress has been relatively slow in this area because it requires the collaborative effort of scientists from several different subdisciplines—mineralogy, petrology, rheology, seismology, and thermal modeling. Detailed studies like that of Peacock and Wang (1999) are needed in well-studied areas where vast amount of different types of information (thermal, seismological, etc.) are available to be integrated.

Summary

The basic purpose of the concepts of zones, grades, and facies is to distinguish rocks based on metamorphic intensity. Facies is a particularly powerful concept and uses mineral assemblages to distinguish between assemblages belonging to different facies. The concept of metamorphic facies series is very important in that it is part of a "big picture" that related plate tectonics to metamorphism: the three fundamental facies series are: high *P–T* series, intermediate *P–T* series, and low *P–T* series. These facies series may be juxtaposed due to plate convergence.

Graphical representation of metamorphic reactions is an important way to depict such reactions. Certain key reactions give us information on *P, T* conditions of metamorphism. Mineral thermobarometry gives *P–T* information on metamorphic rocks. Metamorphic rocks generally retain the peak *P–T* conditions. However, a detailed probing into them can reveal the history of evolution of metamorphic belts (i.e., their *P–T–t* paths).

Seismometamorphism is an interesting development that relates subduction zone earthquakes to metamorphic reactions.

Erratum to: Petrology

Gautam Sen

G. Sen, *Petrology*, DOI 10.1007/978-3-642-38800-2,

Chapter 3 p.54: the Z's in the 4 equations (3 in left column, 1 in right column bottom) are redundant.

Chapter 9 p.200, second last line in Box 9.1: KOP is incorrect. It should read K_2O.

The online version of the original chapters can be found under DOI 10.1007/978-3-642-38800-2

G. Sen (✉)
American University of Sharjah, Housing Unit E-16 Sharjah, United Arab Emirates
e-mail: sengorama@gmail.com

G. Sen, *Petrology*, DOI 10.1007/978-3-642-38800-2_17,

Appendix A: A Brief Introduction to Isotope Geochemistry

Radioactive isotope systems are used to determine ages of minerals and rocks and as tracers of magmatic processes and evolution of the earth. We have seen many examples of the use of Nd, Sr, and Pb isotopes and, in a few cases, He isotopes, throughout the book. It is anticipated that the student will have a proper geochemistry course in which isotope systems are discussed in great detail. Therefore, what follows below is a brief overview of the theoretical underpinnings of these isotopic systems.

In any isotope system that involves the breakdown of radioactive parent atoms into daughter atoms (which may or may not be radioactive), the number of atoms of the parent isotope (N_o) at time (t) = 0 and the number of atoms of the parent isotope (N) remaining after time t are related by the following relation:

$$N/N_o = e^{-\lambda t} \tag{A.1}$$

λ is a constant for any particular isotopic system and is known as the *decay constant*. The decay constant is known experimentally for each individual isotopic system.

Assuming that all of the atoms of a daughter isotope present in a rock were generated via radioactive decay, then at any time t, the number of atoms of daughter isotope (D^*) in that rock is $D^* = N_o - N$. Substituting this relationship to Eq. (A.1), we get

$$N/(D^* + N) = e^{-\lambda t}$$

By rearranging terms we obtain

$$D^*/N = e^{\lambda t} - 1 \tag{A.2}$$

In reality, however, some atoms of the daughter isotope (D_o) may be originally present in the rock at $t = 0$, so that $D = D^* + D_o$, and substituting this into Eq. (A.2), we get

$$(D - D_o)/N = e^{\lambda t} - 1$$

or

$$D = D_o + N(e^{\lambda t} - 1) \tag{A.3}$$

Equation (A.3) is the basis for *geochronology*, which is the science of determining ages of minerals and rocks.

Radioactive decay reactions are generally expressed in terms of half-lives, i.e., when $t = t_{1/2}$, $N = 1/2N_o$. Substituting this expression into Eq. (A.1) and rearranging terms we get

$$1/2 = e^{-\lambda t_{1/2}}$$

or

$$\ln 2 = \lambda t_{1/2}$$

Rearranging terms, we obtain

$$t_{1/2} = \ln 2/\lambda, \quad \text{i.e.,} \; t_{1/2} = 0.693/\lambda \tag{A.4}$$

Below we examine some isotopic systems that are useful in petrology. Table A.1 provides a list of these isotopes and their half-lives and decay constants.

Rb–Sr System

In this system, atoms of the radioactive parent isotope ^{87}Rb break down into the atoms of the daughter isotope ^{87}Sr and release a β-particle in the process. Based on Eq. (A.3) above, one may write

$$^{87}Sr = {}^{87}Sr_o + {}^{87}Rb(e^{\lambda t} - 1) \tag{A.5}$$

Scientists are able to determine isotope ratios with much greater precision than absolute values of individual isotopes; therefore, Eq. (A.5) is modified into the following equation by converting the above into ratios

G. Sen, *Petrology*, DOI 10.1007/978-3-642-38800-2,

by dividing each isotope by a non-radiogenic isotope of Sr, ^{86}Sr. ^{86}Sr value should be constant in a rock and in its constituent minerals because ^{86}Sr is not produced by radioactive breakdown reaction. We then get

$$^{87}Sr/^{86}Sr = [^{87}Sr/^{86}Sr]_o + ^{87}Rb/^{86}Sr\ (e^{\lambda t} - 1) \quad (A.6)$$

This equation has the form of a straight line: $y = mx + c$, *where* $m = \text{slope} = (e^{\lambda t} - 1)$, *and* $c\ (= [^{87}Sr/^{86}Sr]_o)$ is the intercept on *y-axis*. One can measure $^{87}Sr/^{86}Sr$ and $^{87}Rb/^{86}Sr$ ratios of a rock and its constituent minerals with an instrument called the *mass spectrometer*. Note that individual mineral phases in a rock will have different $^{87}Rb/^{86}Sr$ ratios because some minerals can hold more Rb relative to Sr in their atomic structure than others; for example, biotite can have more Rb substituting for K atoms in its atomic structure than any K-poor mineral, such as, say, pyroxene. So, $^{87}Rb/^{86}Sr$ will be higher in biotite than pyroxene in a rock containing both phases. Over time, ^{87}Sr will be generated by breakdown of ^{87}Rb, and $^{87}Sr/^{86}Sr$ in biotite will be higher than in pyroxene. Even though the constituent minerals of a rock will have different $^{87}Rb/^{86}Sr$ they should all have the same initial ratio $[^{87}Sr/^{86}Sr]_o$. Armed with the values of three unknowns, one can now calculate the age of the rock. The straight line that gives the age of the rock is called an *isochron*.

Figure A.1 illustrates the above statements. Let us imagine a rock that gives the following analyses of its mineral components and whole rock:

Rock/mineral	$^{87}Rb/^{86}Sr$	$^{87}Sr/^{86}Sr$
Mineral 1	0.05	0.7040
Mineral 2	0.10	0.7050
Whole rock	0.15	0.7060
Mineral 3	0.20	0.7070

Plotting these data and fitting a line through the data points give us Fig. A.1a. The straight line intercepts *y*-axis at 0.7030, which is the initial ratio, $[^{87}Sr/^{86}Sr]_o$. Applying the values of $[^{87}Sr/^{86}Sr]_o$, $^{87}Sr/^{86}Sr$, and $^{87}Rb/^{86}Sr$ and using the lambda value in Table A.1 in Eq. (A.6) give an age of 1,394 million years. Figure A.1b schematically shows how three minerals with different initial Rb/Sr evolve with time while maintaining a constant initial ratio $[^{87}Sr/^{86}Sr]_o$. Time increases from $t = 0$ to t_1 and t_2 as the slope of the isochron also increases.

Sr isotope system is extremely useful as a tracer of geological processes and earth evolution. Following is an example of how it can be used to trace back the evolution of continental crust–upper mantle system.

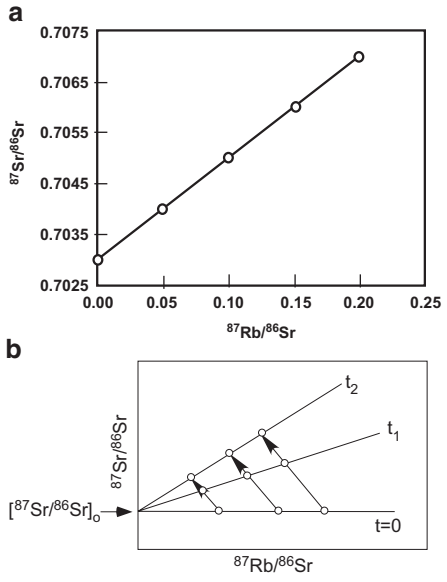

Fig. A.1 (**a**) Rb–Sr isochron diagram. The *dots* on the isochron represent minerals and whole rock analyses from the same rock. (**b**) This diagram schematically illustrates how the initial ratio stays constant while the isochrons develop steeper slopes with age

Before the separation of the continental crust from the mantle, it is commonly accepted that the bulk earth had an $^{87}Sr/^{86}Sr$ initial ratio of 0.69897, which is the so-called "BABI" (*B*asaltic *A*chondrite *B*est *I*nitial ratio). For a constant Rb/Sr ratio of 0.027, the present day $^{87}Sr/^{86}Sr$ ratio of the bulk earth should be 0.704 via production of ^{87}Sr via breakdown of ^{87}Rb over the past 4.55 Ga (Wilson 1989). Rb is preferentially transferred via magmas from the mantle to the continental crust. So, when a certain amount of continental crust with a much higher Rb/Sr ratio is extracted out of the mantle, the mantle is depleted by that much Rb/Sr. The extracted crust with a high $^{87}Rb/^{86}Sr$ will generate much more $^{87}Sr/^{86}Sr$ via decay than the upper mantle (with significantly lower $^{87}Rb/^{86}Sr$) over the same amount of time passed since the separation.

If a certain mass of continental crust with Rb/Sr = 0.18 had been extracted some 2.5 billion years ago out of the bulk earth reservoir (i.e., a portion of the mantle), then its $^{87}Sr/^{86}Sr$ would have evolved to a present day ratio of 0.718 (can be extrapolated in Fig. A.2). The "depleted" (i.e., depleted of continental crustal components) portion of the mantle, having a lower Rb/Sr (0.024), would then have a lower present day $^{87}Sr/^{86}Sr$ ratio than the calculated present day bulk earth ratio. Because the timing of extraction of the crust influences the degree of enrichment of the crust and depletion of the mantle relative to the bulk earth

Table A.1 Isotope ratios, decay constants, and half-lives (from W. White's lecture notes: http://www.geo.cornell.edu/geology/classes/Geo656/656notes09/656_09Lecture03.pdf)

Parent isotope	Daughter isotope	Isotope ratio	λ	Half-life (years)
^{87}Rb	^{87}Sr	$^{87}Sr/^{86}Sr$	1.42×10^{-11}/year	48.8×10^{9}
^{147}Sm	^{143}Nd	$^{143}Nd/^{144}Nd$	6.54×10^{-12}/year	1.06×10^{11}
^{187}Re	^{187}Os	$^{187}Os/^{188}Os$	1.64×10^{-11}/year	4.23×10^{10}
^{190}Pt	^{186}Os	$^{186}Os/^{188}Os$	1.54×10^{-12}/year	4.50×10^{11}
^{232}Th	^{208}Pb, ^{4}He	$^{208}Pb/^{204}Pb$, $^{3}He/^{4}He$	4.948×10^{-11}/year	1.4×10^{10}
^{235}U	^{208}Pb, ^{4}He	$^{207}Pb/^{204}Pb$, $^{3}He/^{4}He$	9.849×10^{-10}/year	7.07×10^{8}
^{238}U	^{206}Pb, ^{4}He	$^{206}Pb/^{204}Pb$, $^{3}He/^{4}He$	1.551×10^{-10}/year	4.47×10^{9}

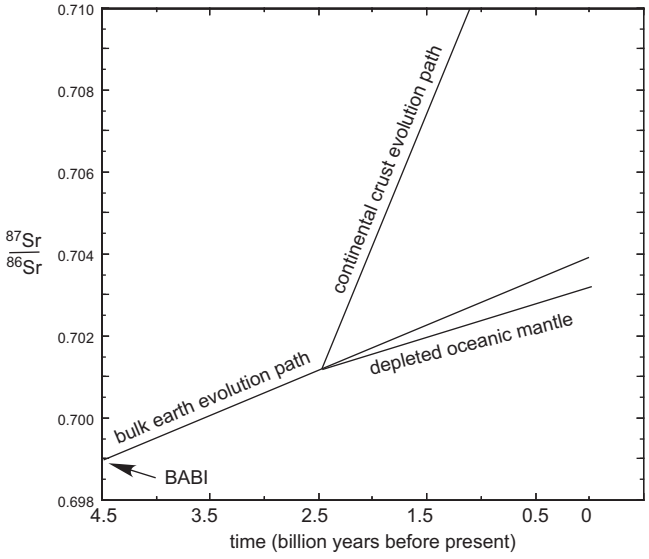

Fig. A.2 This diagram shows how the $^{87}Sr/^{86}Sr$ of BABI (representing the bulk earth) would evolve with time since the earth's formation 4.5 billion years ago. Also shown are *two lines*, one of which traces the evolution of $^{87}Sr/^{86}Sr$ of the continental crust (with a higher $^{87}Rb/^{86}Sr$ than the bulk earth) separated from the bulk earth some 2.5 billion years ago. The mantle reservoir that lost such continental crust would evolve along a very different path, which is perhaps recorded by the depleted oceanic mantle rocks

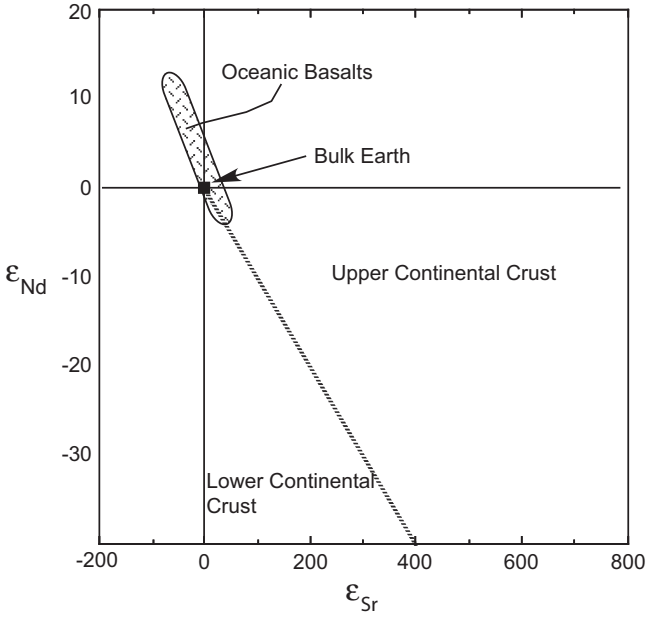

Fig. A.3 Fields of various oceanic basalts, lower and upper continental crustal reservoir rocks are shown in an ε_{Nd}–ε_{Sr} diagram

evolution curve, one can use the Sr isotope system to decipher how earth's various mantle reservoirs and crust have changed over time. Epsilon Sr (ε_{Sr}) is a useful quantity that expresses this degree of change (depletion or enrichment) with respect to the bulk earth $^{87}Sr/^{86}Sr$ value at present time.

$$\varepsilon_{Sr} = \left[\frac{(^{87}Sr/^{86}Sr)_{measured}}{(^{87}Sr/^{86}Sr)_{Bulk\ Earth}} - 1 \right] \times 10,000$$

DePaolo and Wasserburg (1979) presented a similar expression for ε_{Nd} for the Nd isotopic system. Combining ε_{Sr} and ε_{Nd}, as seen in Fig. A.3, has proved to be a powerful tool in understanding earth's evolution. Because close system magma differentiation processes do not alter the isotopic composition of magmas, isotopic compositions of intrusions and lavas can be used to trace contributions made by various sources, i.e., lithosphere, asthenosphere, plume etc., to the magma.

Sm–Nd System

Samarium (Sm) and Neodymium (Nd) are light rare earth elements and they generally behave as incompatible elements, i.e., they prefer magma over crystalline phases during crystal–liquid separation—be it partial melting or crystallization. Nd is slightly more incompatible than Sm. ^{143}Nd is a daughter isotope produced by α-decay of the radioactive isotope ^{147}Sm. Similar to the Sr system, Nd isotopic ratios are expressed in terms of $^{147}Sm/^{144}Nd$ (parent) and $^{143}Nd/^{144}Nd$ (daughter).

As stated above, partial melting results in a greater Sm/Nd ratio of the residuum because Nd is more incompatible than Sm. It follows that as time

progresses rocks crystallizing from such partial melts will evolve to lower $^{143}Nd/^{144}Nd$ than the residue because the residue will have a greater amount of $^{147}Sm/^{144}Nd$ ratio acquired during the partial melting event. Because of the differential change in Sm/Nd relative to Rb/Sr during partial melting, the sign of the epsilon values for the Sm–Nd versus Rb–Sr systems means the opposite: positive ε_{Nd} value means depleted whereas positive ε_{Sr} value means enriched composition.

The Sm–Nd isotopic system has a particular advantage over other isotopic systems in deciphering the evolution of continents through studies of detrital sediments. It turns out that fine-grained clastic sediments record the Sm/Nd ratios of their source rocks and these ratios are virtually unmodified by sedimentary processes, which is not true of Rb/Sr or U/Pb systems (O'Nions 1992). Continental crust with some reasonable Sm/Nd ratio extracted from the depleted mantle some 3 billion years ago will evolve to strongly negative ε_{Nd} values. Sediments derived from them will have the same characteristic ε_{Nd} as the source rocks. Using a Sm/Nd and $^{143}Nd/^{144}Nd$ ratio, a model age of such sediments may be calculated, which would essentially indicate the separation age of the continent from the depleted mantle. This model age is referred to as *crustal residence age* because it represents the time spent by such sediments in the continental environment. Remarkably, clastic particles from the entire globe seem to give a rather tight range of crustal residence ages with a mean of 1.7 billion years, which may be taken as the mean age of the continental crust (i.e., a weighted mean of crustal materials of all ages: O'Nions 1992).

U–Th–Pb Systems

Unlike the Rb/Sr and Sm/Nd isotopic systems, the U–Th–Pb systems go through a chain of radioactive decay reactions in which several intermediate radioactive isotopes are produced, which in turn decay into other ones and so on. This topic is rather complex and cannot be covered in any detail.

Uranium (U) has three naturally occurring radioactive isotopes—^{238}U, ^{235}U, and ^{234}U. Th occurs mainly as a radioactive isotope—^{232}Th, and as a few other short-lived isotopes that are produced as U series decay products. Lead (Pb) has several naturally occurring isotopes—^{204}Pb, ^{206}Pb, ^{207}Pb, and ^{208}Pb, of which ^{204}Pb is non-radiogenic. The end products of three

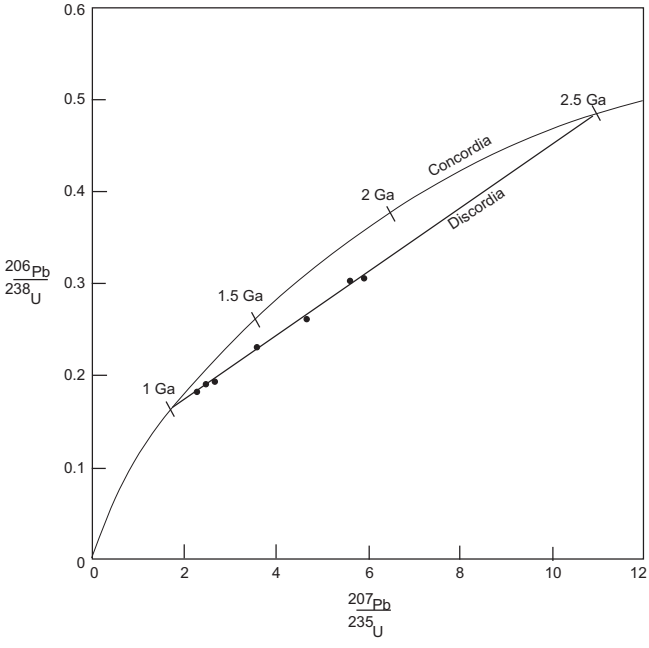

Fig. A.4 U–Pb concordia diagram

important chain reactions involving the formation of lead isotopes are as follows:

$$^{238}U \rightarrow ^{234}U \rightarrow ^{206}Pb$$

$$^{235}U \rightarrow ^{207}Pb$$

$$^{232}Th \rightarrow ^{208}Pb$$

Common lead, i.e., lead found in the earth, is a mixture of (a) lead that is present from the beginning of earth history ("primeval lead") and (b) radiogenic lead that is produced via decay of radioactive isotopes of U and Th. The measured isotopic compositions of primeval lead, as estimated from a mineral called troilite (Fe_2S) in Cañon Diablo meteorite, are as follows (Chen and Wasserburg 1983):

$$^{206}Pb/^{204}Pb = 9.3066$$

$$^{207}Pb/^{204}Pb = 10.293$$

$$^{208}Pb/^{204}Pb = 29.475$$

Age determination using U/Pb isotopes is not as straightforward as in the Rb/Sr and Sm/Nd systems, because uranium and lead are easily removed during weathering and metamorphic processes, and smooth, straight line isochrons are rarely obtained. It is

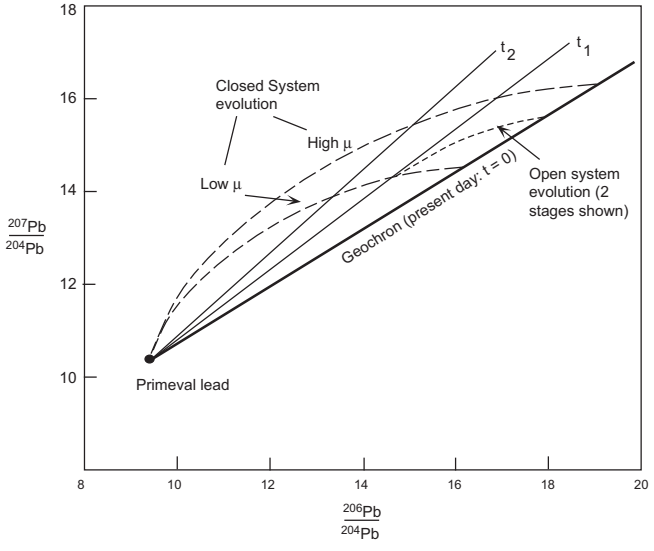

Fig. A.5 Evolution of lead isotope ratios (explained in the text)

somewhat less of a problem in $^{208}Pb/^{204}Pb$ dating because Th is less mobile than U. Normally, the same rock is dated with the three isotopic systems listed above, and generally one obtains discordant ages determined by the three methods due to variable loss of U and Pb. Typically, a plot of $^{206}Pb/^{238}U$ versus $^{207}Pb/^{235}U$, known as a *concordia diagram*, is made (Fig. A.4). ^{238}U and ^{235}U have half-lives of 4.47 and 0.7 billion years, respectively, i.e., the former decays at a much slower rate than the latter, and this differential decay rates result in the curvature of the concordia diagram. Rock and mineral samples from a petrogenetically related suite generally plot on a straight line, such as the one shown extending from 2.5 to 1 Ga. One interpretation may be that the suite was formed 2.5 billion years ago but was affected by metamorphic processes some 1 billion year ago. However, it is also possible that Pb was lost continuously during the metamorphic evolution of these rocks, in which case the lower age has no particular significance. The strength of age interpretation is dependent on how closely the rock samples plot toward the concordia curve. In passing, it is worthwhile to note that core-to-rim of individual zoned zircon crystals in clastic sediments and granitoid rocks can often be dated with U–Pb dating method to reveal their evolutionary history.

U–Th–Pb system can also be used to reveal petrogenic processes operating within the crust and mantle. A plot of $^{207}Pb/^{204}Pb$ versus $^{206}Pb/^{204}Pb$ has been found to be particularly useful in this context (Fig. A.5). The ratio $^{238}U/^{204}Pb$ is known as μ in Fig. A.5; the two curves show the closed system evolution of Pb isotopic ratios for two cases—one with a high μ and the other with a low μ Isochrons on this diagram are straight lines radiating from the primeval lead composition. Stony meteorites containing variable amounts of U and Th plot along such an isochron of 4.52–4.57 billion years. The isochron for present day (time $t = 0$) is called the *geochron*. Note that the two closed system cases shown in Fig. A.5 are examples of what is often called single-stage evolution. However, lead may not often evolve in a closed system and the U/Pb ratio may get reset by metamorphic or other processes, which may result in multistage lead evolution (Fig. A.5 shows an example of a two-stage lead evolution). Interpretation of stages of lead evolution is often not straightforward.

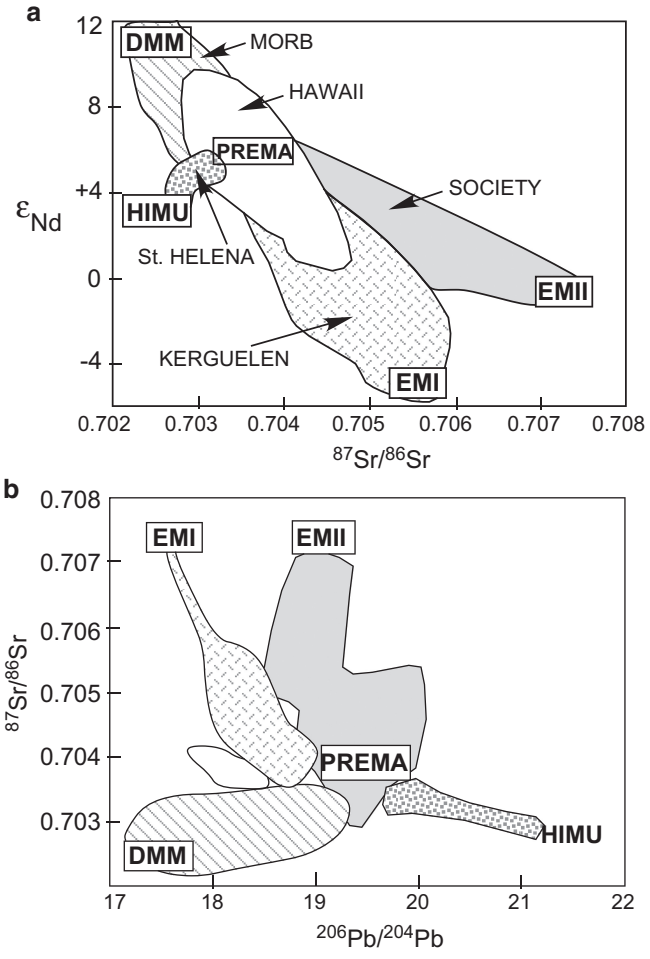

Fig. A.6 Various mantle reservoirs (DMM, EMI, EMII, PREMA, HIMU) are shown in these figures

Mantle Isotope Reservoirs

Pb, Sr, and Nd isotopic analysis of basalt lavas from various locations around the globe has resulted in a substantial database, which has shown that basalts from

different plate tectonic and geographic regions have distinct isotopic compositions. These differences reflect the isotope compositional differences of their source mantle rocks. Because these isotope systems have long half-lives, such isotopic differences in the mantle can only develop over many millions of years (Fig. A.6; White 1985; Zindler and Hart 1986).

The main mantle isotopic components identified by various authors over time are as follows: Depleted MORB Mantle (DMM), Enriched Mantle I (EMI), Enriched Mantle II (EMII), PREMA (Prevalent Mantle), and HIMU (High μ). Noting that the bulk of oceanic basalts plot in the broad area marked as PREMA, Zindler and Hart (1986) thought that the prevalent mantle composition falls here. More recently, PREMA appears to have been replaced by something called FOZO (abbreviation for Focused Zone: Hart et al. 1992). N-MORBs are principally derived from a DMM source with some input from EMI source. Hawaiian magmas appear to tap a significant fraction from EMI (enriched plume). There are other ocean hot spot islands that derive from a different type of enriched mantle—EMII. Given the mantle is increasingly being seen as a dynamic body, what these isotopic reservoirs signify is not well understood—for example, how these reservoirs form and evolve and how some magmas selectively tap certain reservoirs are all questions that are not entirely clear to me.

Aside from Pb, Sr, and Nd isotopes, new insight into the earth processes is being sought through studies of isotopic ratios of He, Os, and Hf. A discussion of these new advances is well beyond the scope of this book. The student is encouraged to get all that from a geochemistry class.

Appendix B: Simplified CIPW Norm Calculation

The guidelines given below are simplified from the original CIPW procedures in that not all the normative minerals are calculated. Instead, only norms that are useful for common volcanic rocks are considered. Minerals that are extremely rare in most rock norms (e.g., acmite, chromite, etc.) are ignored. Norms are rarely used today, and therefore, as far as I am concerned it is only useful for the student to understand the guiding principle of norm procedure. There are many websites that calculate norms, and the student working on rare rocks may use such a website to carry out norm calculation. The website that I found useful is http://minerva.union.edu/hollochk/c_petrology/norms.htm by Professor Kurt Hollocher of Union College.

Normative mineral	Composition	Molecular weight
Apatite (*ap*)	$3(3CaO{\cdot}P_2O_5){\cdot}CaF_2$	336.2
Ilmenite (*il*)	$FeO{\cdot}TiO_2$	151.7
Magnetite (mt)	$FeO{\cdot}Fe_2O_3$	231.5
Orthoclase (*or*)	$K_2O{\cdot}Al_2O_3{\cdot}6SiO_2$	556.7
Albite (*ab*)	$Na_2O{\cdot}Al_2O_3{\cdot}6SiO_2$	524.5
Anorthite (*an*)	$CaO{\cdot}Al_2O_3{\cdot}2SiO_2$	278.2
Diopside (di) components		
Wollastonite (*wo*)	$CaO{\cdot}SiO_2$	116.2
Enstatite (*en*)	$MgO{\cdot}SiO_2$	100.4
Ferrosilite (*fs*)	$FeO{\cdot}SiO_2$	132
Hypersthene (hy) components		
Enstatite (*en*)	As above	
Ferrosilite (*fs*)	As above	
Olivine (ol) components		
Forsterite (fo)	$2MgO{\cdot}SiO_2$	140
Fayalite (fa)	$2FeO{\cdot}SiO_2$	204
Quartz (*q*)	SiO_2	60.1
Nepheline (*ne*)	$Na_2O{\cdot}Al_2O_3{\cdot}2SiO_2$	284.1

Calculation Procedure

Step 1 (calculate molar prop.). Divide wt% abundance of various oxides by their respective molecular weights (column B). These are molar proportion of each oxide. Add MnO to FeO and treat MnO + FeO as FeO in the remaining steps. You will need these molar proportions for the following calculations.

Step 2 (calculate apatite). If P_2O_5 is reported in the rock analysis, then allocate all of P_2O_5 to apatite. Allocate CaO ($CaO = 3.33 \times P_2O_5$) under the apatite column. (*Running tab: remaining CaO = CaO − CaO used to make apatite. There is no residual P_2O_5 after this step.*)

Step 3 (calculate ilmenite). Allocate all of TiO_2 and an equal amount of FeO to make ilmenite. (*Running tab: TiO_2 available after this step—TiO_2 used = 0. FeO remaining = FeO—FeO used to make ilmenite.*)

Step 4 (calculate magnetite). Allocate all of Fe_2O_3 and an equal amount of FeO to form magnetite. (*Running tab: available $Fe_2O_3 = 0$, $FeO = FeO$ (remaining after Step 3)—FeO used to make magnetite.*)

Step 5 (calculate provisional orthoclase: or′). Allocate all of K_2O, an equal amount of Al_2O_3, and six times as much SiO_2 to make provisional orthoclase. (*Are you keeping a running tab?*)

Step 6 (calculate provisional albite: ab′). Allocate all of Na_2O, an equal amount of Al_2O_3, and six times as much SiO_2 to form provisional albite. (*Possible complication: If you have more Na_2O than Al_2O_3 then you have normative acmite. In that case go to one of the websites to do your calculation.*)

Step 7 (calculate anorthite: an). If there is any excess of Al_2O_3 after step 6, then it is used to make anorthite. Allocate available Al_2O_3, an equal amount of CaO, and twice as much SiO_2 to make anorthite.

The steps that follow involve (Mg, Fe) solid solutions of pyroxenes and olivine. At this stage you should be left with Na_2O, CaO, MgO, FeO, and SiO_2.

$$M = \mathrm{MgO} + \mathrm{FeO} \text{ and } S = \mathrm{SiO_2MR} = \mathrm{MgO/M},$$
$$\mathrm{FR} = \mathrm{FeO/M}$$

Step 8: Calculate the following:

$$M = \mathrm{MgO} + \mathrm{FeO};$$

$$S = \mathrm{SiO_2};$$

$$MR = \mathrm{MgO/M}; FR = \mathrm{FeO/M}$$

G. Sen, *Petrology*, DOI 10.1007/978-3-642-38800-2,

Step 9 (calculate diopside). Allocate CaO remaining after Step 7 and an equal amount of (MgO + FeO) and twice as much SiO_2 to make diopside. In order to assign the right amount of MgO and FeO to diopside, use the ratio relationship (recall example 2 in Chap. 2): MR in diopside = MR rock. $(MgO + FeO)^{di} = M$. So, you can calculate actual MgO and FeO in diopside.

Step 10 (calculate hypersthene and olivine). If available (after step 9) $SiO_2 >$ remaining (MgO + FeO), then allocate all of (MgO + FeO) and an equal amount of SiO_2 to form hypersthene. Any remaining SiO_2 may be calculated as quartz (q).

However, if (MgO + FeO) $> SiO_2$, then the rock is olivine-normative, and therefore, a different set of steps needs to be followed to calculate olivine and hypersthene. Use example 2 as guideline to calculate ol and hy.

Step 11 (calculation of nepheline and recalculation of albite). From the provisional albite calculated in Step 6, add the Na_2O, Al_2O_3, and SiO_2 back to their respective columns. See whether available $SiO_2 \geq 2 \times Na_2O$; if so, then divide the available Na_2O, Al_2O_3, and SiO_2 into nepheline and albite as follows:

Let $\mathbf{p}$ = nepheline moles and $\mathbf{q}$ = albite moles. $\mathbf{N}$ = available Na_2O. $\mathbf{S}$ = available SiO_2.

$$\mathbf{p} = (\mathbf{S} - \mathbf{2N})/4$$

$$\mathbf{q} = \mathbf{N} - \mathbf{p}$$

Allocate p amount of Na_2O, an equal amount of Al_2O_3, and twice as much SiO_2 to make nepheline. Allocate $\mathbf{q}$ amount of Na_2O, same amount of Al_2O_3, and six times as much SiO_2 to make albite.

(*Note that similar steps may be added to calculate normative leucite (lc, $K_2O{\cdot}Al_2O_3{\cdot}4SiO_2$) and orthoclase from provisional orthoclase. However, such calculation is generally not necessary for most common rock types.*)

Step 12. Convert mineral mole proportions so calculated into weight percentages by multiplying them by their respective molecular weights and then normalizing the values to 100 %. You have the norm.

References

Abouchami W et al (2005) Lead isotopes reveal bilateral asymmetry and vertical continuity in the Hawaiian mantle plume. Nature 434:851–856

Agee CB (1990) A new look at differentiation of the Earth from melting experiments on the Allende meteorite. Nature 346:834–837

Agee C, Walker D (1993) Olivine flotation in mantle melt. Earth Planet Sci Lett 114:315–324

Ague JJ, Brimhall GH (1988) Regional variations in bulk chemictry, mineralogy, and the compositions of mafic and accessory minerals in the batholiths of California. Geol Soc Am Bull 100:891–911

Anderson DL (1995) Lithosphere, asthenosphere, and perisphere. Rev Geophys 33:125–149

Anderson DL (1996) Enriched asthenosphere and depleted plumes. Int Geol Rev 38:1–21

Ariskin AA, Frenkel MY, Barmina GS, Nielsen RL (1993) COMAGMAT: a Fortran program to model magma differentiation processes. Comput Geosci 19:1155–1170

Arndt NT (1994) Archean komatiites. In: Condie KC (ed) Archean crustal evolution. Elsevier, Amsterdam, pp 11–44

Arndt NT, Lehnert K, Vasil'ev Y (1995) Meimechites: highly magnesian alkaline magmas from the subcontinental lithosphere? Lithos 34:41–59

Arndt NT, Barnes SJ, Lesher CM (2008) Komatiite. Cambridge University Press, Cambridge, 487 pp

Ashwal LD (1993) Anorthosites. Springer, Berlin

Ashwal LD (2010) The temporality of anorthosites. Can Mineral 48:711–728

Asimov PD, Longhi J (2004) The significance of multiple saturation points in the context of polybaric near-fractional melting. J Petrol 45:2349–2367

Asimow P, Langmuir CH (2003) The importance of water to oceanic mantle melting regimes. Nature 421:815–820

Aulbach S, Rudnick, RL, McDonough, WF (2011) Evolution of the lithospheric mantle beneath the East African Rift in Tanzania and its signatures in rift magmas: In: Beccaluva L, Bianchini G, Wilson M (eds) Volcanism and evolution of the African lithosphere, Geological Society of America Special Paper 478, pp 105–127

Ayalew D et al (2002) Source, genesis, and timing of giant ignimbrite deposits associated with Ethiopian continental flood basalts. Geochim Cosmochim Acta 66:1429–1448

Bachmann O, Bergantz G (2003) The magma reservoirs that feed supereruptions. Elements 4:17–21

Bachmann O, Bergantz G (2008) The magma reservoirs that feed supereruptions. Elements 4:17–21

Badiozamani K (1973) The Dorag dolomitization model-application to the Middle Ordovician of Wisconsin. J Sediment Petrol 43:965–984

Bailey DK (1993) Carbonate magmas. J Geol Soc Lond 150:637–651

Bailey RA (2004) Eruptive history and chemical evolution of the precaldera and postcaldera basalt-dacite sequences, Long Valley, California: implications for magma sources, current seismic unrest, and future volcanism, USGS Professional Paper 1692

Bard JP (1986) Microtextures of igneous and metamorphic rocks. Kluwer, Boston, MA

Barker DS (1983) Igneous rocks. Prentice-Hall, Englewood Cliffs, NJ

Baker MB, Hirschmann MM, Ghiorso MS, Stolper EM (1995) Compositions of near-solidus peridotite melts from experiments and thermodynamic calculations. Nature 375:308–311

Barrow G (1893) On an intrusion of muscovite-biotite gneiss in the south-eastern Highlands of Scotland, and its accompanying metamorphism. Q J Geol Soc 49:30–358, available from Lyell collection: http://jgslegacy.lyellcollection.org

Barth AP, Walker JD, Wooden JL, Riggs NR, Schweickert RA (2011) Birth of the Sierra Nevada magmatic arc: early Mesozoic plutonism and volcanism in the east-central Sierra Nevada of California. Geosphere 7:877–897

Basaltic Volcanism Study Project (1981) Basaltic volcanism on the terrestrial planets. Pergamon, New York, NY

Bateman PC, Chappell BW (1979) Crystallization, fractionation, and solidification of the Tuolumne intrusive series, Yosemite national park, California. Geol Soc Am Bull 90:465–482

Begg GC et al (2009) The lithospheric architecture of Africa: seismic tomography, mantle petrology, and tectonic evolution. Geosphere 5:23–50

Berman RG (2007) winTWQ (version 2.3): a software package for performing internally-consistent thermobarometric calculations. Geological survey of Canada open file 5462 (ed. 2.32), 41 p

Berry AJ, Danyushevsky LV, O'Neill HS, Newville M, Sutton SR (2008) Oxidation state of iron in komatiitic melt inclusions indicates hot Archaean mantle. Nature 455:960–963

Best MG (1982) Igneous and metamorphic petrology. Wiley, New York, NY

Best MG (2002) Igneous and metamorphic petrology, 2nd edn. Blackwell, Malden, MA

Bhattacharya A, Raith M, Hoernes S, Banerjee D (1998) Geochemical evolution of the massif-type Anorthosite complex at Bolangir in the Eastern Ghats Belt of India. J Petrol 39:1169–1195

Bizimis M, Sen G, Salters VJM, Keshav S (2005) Hf-Nd-Sr isotope systematics of garnet pyroxenites from Salt Lake Crater, Oahu, Hawaii: evidence for a depleted component in Hawaiian volcanism. Geochimica et Cosmochimica Acta 69:2629–2646

Bizimis M et al (2007) Ancient recycled mantle lithosphere in the Hawaiian plume: Osmium-Hafnium isotopic evidence from peridotite mantle xenoliths. Earth Planet Sci Lett 257:259–273

Blatt H, Tracy R, Owens B (2005) Petrology: igneous, sedimentary, and metamorphic, 3rd edn. W.H. Freeman, New York, NY

Blatt H, Tracy R, Owens B (2006) Petrology: igneous, sedimentary, and metamorphic rocks, 3rd edn. WH Freeman, New York, NY

Boggs S Jr (1992) Petrology of sedimentary rocks. McMillan, New York, NY

Bohlen J, Boettcher ALC (1981) Experimental investigations and geological application of orthopyroxene barometry. Am Mineral 19:951–964

G. Sen, *Petrology*, DOI 10.1007/978-3-642-38800-2,

Boles JR, Coombs DS (1977) Zeolite facies alteration of sandstones in the southland syncline, New Zealand. Am J Sci 277:982–1012
Bose K, Ganguly J (1995) Experimental and theoretical studies of the stabilities of talc, antigorite and phase A at high pressures with applications to subduction processes. Earth Planet Sci Lett 136:109–121
Bowen NL (1917) The problem of the anorthosites. J Geol 25:209–243
Bowen NL (1924) The evolution of the igneous rocks. Princeton University Press, Princeton, NJ
Boyd FR (1976) Infected and noninfected geotherm, vol 75. Carnegie Institution of Washington Yearbook, pp 521–523
Boyd FR (1989) Compositional distinction between oceanic and cratonic lithosphere. Earth Planet Sci Lett 96:15–26
Brandon AD, Goles GG (1988) A Miocene subcontinental plume in the Pacific Northwest: geochemical evidence. Earth Planet Sci Lett 88:273–283
Brooker RA, Kjarsgaard BA (2011) Silicate–carbonate liquid immiscibility and phase relations in the system SiO2–Na2O–Al2O3–CaO–CO2 at 0•1–2•5 GPa with applications to carbonatite genesis. J Petrol 52:1281–1305
Brownlow AH (1996) Geochemistry, 2nd edn. Prentice-Hall, Upper Saddle River, NJ
Bucher K, Frey M (1994) Petrogenesis of metamorphic rocks, 6th edn. of H. Winkler's textbook. Springer, New York, NY
Buddington AF (1959) Granite emplacement with special reference to North America. Geol Soc Am Bull 70:671–748
Burke K (2011) Plate tectonics, the Wilson cycle, and Mantle plumes: geodynamics from the top. Annu Rev Earth Planet Sci 39:1–29
Burke K, Steinberger B, Torsvik TH, Smethurst MA (2008) Plume generation zones at the margins of large low shear velocity provinces at the core-mantle boundary. Earth Planet Sci Lett 265:49–60
Cameron EN (1978) The lower zone of the eastern Bushveld complex in the Olifants River. J Petrol 19:437–462
Camp VE, Hanan BB (2008) A plume-triggered delamination origin for the Columbia River basalt group. Geosphere 4:480–495
Campbell IH (1996) Fluid dynamic processes in basaltic magma chambers. In: Cawthorn RG (ed) Layered intrusions, Developments in petrology. Elsevier, Amsterdam, pp 45–76
Campbell IH (2005) Large igneous provinces and the mantle plume hypothesis. Elements 1:265–269
Caprarelli G, Reidel SP (2004) Physical evolution of Grande Ronde basalt magmas, Columbia River basalt group, north-western USA. Miner Petrol 80:1–25
Caprarelli G, Reidel SP (2005) A clinopyroxene-basalt geothermobarometry perspective of Columbia Plateau (NW-USA) Miocene magmatism. Terra Nova 17:265–277
Carballo JD et al (1987) Holocene dolomitization of supratidal sediments by active tidal pumping, Sugerloaf Key, Florida. J Sediment Petrol 57:153–165
Carbotte SM et al (2006) Rift topography linked to magmatism at the intermediate spreading Juan de Fuca Ridge. Geology 34:209–212
Carlson WD (1986) Reversed phase equilibria in CaO-MgO-SiO2 at one atmosphere pressure. Contrib Mineral Petrol 92:242–252
Carlson RW, Hart WK (1988) Flood basalt volcanism in the northwestern United States. In: Macdougall JD (ed) Continental flood basalts. Kluwer Academic, Dordrecht, pp 35–61
Carlson WD, Swinea JA, Miser DE (1988) Stability of orthoenstatite at high temperature and low pressure. Am Mineral 73:1255–1263
Carmichael DM (1969) Intersecting isograds in the whetstone lake area, Ontario. J Petrol 11:147–181
Carmichael ISE, Turner FJ, Verhoogen J (1974) Igneous petrology. McGraw-Hill, New York, NY
Carslaw HS, Jaeger JC (1959) Conduction of heat in solids, 2nd edn. Oxford University Press, Oxford
Carstens H (1982) Spherulitic crystallization in lamprophyric magmas and the origin of ocelli. Nature 297:493–494
Carter JL (1970) Mineralogy and chemistry of the earth's upper mantle based on the partial fusion-partial crystallization model. Geol Soc Am Bull 81:2021–2034
Cashman KV, Marsh BD (1988) Crystal size distribution (CSD) in rocks and the kinetics and dynamics of crystallization. 2. Makaopuhi Lava Lake. Contrib Mineral Petrol 99:292–305
Cawthorn RG (ed) (1996) Layered intrusions, Developments in petrology. Elsevier Science Inc., New York, NY
Cawthorn RG (1999) Platinum-group element mineralization of the Bushveld complex—a critical reassessment of geochemical models. South Afr J Geol 102:268–281
Chakrabarti R et al (2011) Age and origin of Chilka anorthosites, Eastern Ghats, India: implications for Massif anorthosite petrogenesis and break-up of Rodinia. In: Ray J, Sen G, Ghosh B (eds) Topics in igneous petrology. Springer, New York, NY, pp 355–382
Chappell BW, White AJR (1974) Two contrasting magma types. Pacific Geol 8:173–174
Chatterjee N, Crowley JL, Ghose NC (2008) Geochronology of the 1.55 Ga Bengal anorthosite and Grenvillian metamorphism in the Chotanagpur Gneissic complex, eastern India. Precambrian Res 161:303–316
Chen C-H, Presnall DC (1975) The system Mg_2SiO_4 at pressures up to 25 kbar. Am Mineral 60:398–406
Chen JH, Wasserburg GJ (1983) The least radiogenic Pb in iron meteorites. In: 14th lunar and planetary science conference, abstracts, Pt. 1, pp 103–104
Chenet A-L, Quidelleur X, Fluteau F, Courtillot V, Bajpai S (2007) ^{40}K-^{40}Ar dating of the main Deccan large igneous province: further evidence of KTB age and short duration. Earth Planet Sci Lett 263:1–15
Chesley JT, Ruiz J (1998) Crust-mantle interaction in large igneous provinces: implications from the ReOs isotope systematics of the Columbia River flood basalts. Earth Planet Sci Lett 154:1–11
Chopin C (1984) Coesite and pure pyrope in high grade blueschists of the western Alps. Contrib Mineral Petrol 86:107–118
Christiansen RL, Foulger GR, Evans JR (2002) Upper mantle origin of the Yellowstone hotspot. Geol Soc Am Bull 114:1245–1256
Clague DA, Weber WS, Dixon JE (1991) Picritic glasses from Hawaii. Nature 353:553–556
Clague DA, Moore JG, Dixon JE, Friesen WB (1995) Petrology of submarine lavas from Kilauea's Puna Ridge, Hawaii. J Petrol 36:299–349
Clarke DB (1992) Granitoid rocks. Chapman and Hall, New York, NY
Class C, Goldstein S (1997) Plume-lithosphere interactions in the ocean basins: constraints from the source mineralogy. Earth Planet Sci Lett 150:245–260
Class C, Goldstein SL (2005) Evolution of helium isotopes in the Earth's mantle. Nature 436:1107–1112
Cloos M, Shreve R (1988) Subduction-channel model of prism accretion, melange formation, sediment subduction, and subduction erosion at convergent plate margins: 1. Background and description. Pure Appl Geophys 128:455–500
Coffin MF, Eldholm O (1994) Large igneous provinces: crustal structure, dimensions, and external consequences. Rev Geophys 32:1–36
Coleman RG, Wang X (1995) Ultrahigh-pressure metamorphism. Cambridge University Press, New York, NY
Condie KC, Sloan RE (1998) Origin and evolution of Earth. Prentice Hall, Upper Saddle River, NJ
Connolly JAD (2005) Computation of phase equilibria by linear programming: a tool for geodynamic modeling and its application to subduction zone decarbonation. Earth Planet Sci Lett 236: 524–541

Corti G (2009) Continental rift evolution: from rift initiation to incipient break-up in the main Ethiopian rift, east Africa. Earth Sci Rev 96:1–53

Courtillot V et al (2000) Cosmic markers, 40Ar/39Ar dating and paleomagnetism of the KT sections in the Anjar area of the Deccan large igneous province. Earth Planet Sci Lett 182:137–156

Cox KG, Bell JD, Pankhurst RJ (1979) The interpretation of igneous rocks. George Allen & Unwin, London

Daoud MA et al (2010) A LREE-depleted component in the afar plume: further evidence from quaternary Djibouti basalts. Lithos 114:327–336

Dasgupta R, Hirschmann MM (2006) Melting in the Earth's deep upper mantle caused by carbon dioxide. Nature 440:659–662

Davies PJ, Bubela B, Ferguson J (1978) The formation of ooids. Sedimentology 25:703–730

de Wit MJ et al (1992) Formation of Archaean continent. Nature 357:553–562

DePaolo DJ, Wasserburg GJ (1979) Petrogenetic mixing models and Nd-Sr isotopic patterns. Geochim Cosmochim Acta 43:615–627

DePaolo DJ (1981) Trace element and isotopic effects of combined wallrock assimilation and fractional crystallization. Earth Planet Sci Lett 53:189–202

DePaolo DJ (1988) Neodymium isotope geochemistry. Springer, New York, NY

Dickinson WR, Suczek CA (1979) Plate tectonics and sandstone compositions. AAPG Bull 63:2164–2182

Dodson A, Kennedy BM, DePaolo DJ (1997) Helium and neon isotopes in the imnaha basalt, Columbia River basalt group: evidence for a Yellowstone plume source. Earth Planet Sci Lett 150:443–451

Dott RH (1964) Wacke, greywacke and matrix-What approach to immature sandstone classification? J Sediment Petrol 34:625–632

Draper G (1986) Blueschists and associated rocks in eastern Jamaica and their significance for Cretaceous plate margin development in the northern Caribbean. Geol Soc Am Bull 87:48–60

Ducea MN (2001) Thick granitic batholiths, eclogitic residues, lithospheric- scale thrusting, and magmatic flare-ups. Geol Soc Am Today 11:4–10

Ducea MN (2002) Constraints on the bulk composition and root foundering rates of continental arcs: a California arc perspective. J Geophys Res 107:2304. doi:10.1029/2001JB000643

Ducea M, Saleeby JB (1998) A case for delamination of the deep batholithic crust beneath the Sierra Nevada, California. Int Geol Rev 40:78–93

Duncan RA, Richards MA (1991) Hot spots, matle plumes, flood basalts, and true polar wander. Rev Geophys 29:31–50

Dunham RJ (1962) Classification of carbonate rocks according to depositional texture. In: Ham WE (ed) Classification of carbonate rocks, vol 1. American Association of Petroleum Geologists Memoir, Tulsa, Oklahoma, pp 108–121

Durand SR, Sen G (2004) Preeruption history of the Grande Ronde formation lavas, Columbia River basalt group, American northwest: evidence from phenocrysts. Geology 32:293–296

Dzevanshir RD, Buryakovskiy LA, Chilingarian GV (1986) Simple quantitative evaluation of porosity of argillaceous sediments at various depths of burial. Sediment Geol 46:169–175

Edgar AD, Mitchell RH (1997) Ultra high pressure–temperature melting experiments on an SiO2-rich lamproite from smoky butte, Montana: derivation of siliceous lamproite magmas from enriched sources deep in the continental mantle. J Petrol 38:457–477

Ehlers EG (1972) The interpretation of geological phase diagrams. W.H. Freeman, San Francisco, CA

Elkins-Tanton LT, Burgess S, Yin Q-Z (2011) The lunar magma ocean: reconciling the solidification process with lunar petrology and geochronology. Earth Planet Sci Lett 304:326–336

Ellis DJ, Green DH (1979) An experimental study of the effect of Ca upon garnet-clinopyroxene Fe-Mg exchange equilibria. Contrib Mineral Petrol 71:13–22

Emslie RF, Hamilton MA, Thériault RJ (1994) Petrogenesis of a Mid-proterozoic anorthosite-mangerite-charnockite-granite (AMCG) complex: isotopic and chemical evidence from the Nain plutonic suite. J Geol 102:539–558

Enggist A, Chu L, Luth RW (2012) Phase relations of phlogopite with magnesite from 4 to 8 GPa. Contrib Mineral Petrol 163:467–481

Ernst WG (1976) Petrologic phase equilibria. W.H. Freeman, San Francisco, CA

Ernst WG (1988) Tectonic history of subduction zones: inferred from retrograde blueschists p-t paths. Geology 16:1081–1084

Ernst RE, Buchan KL (1997) Giant radiating dyke swarms: their use in identifying pre-Mesozoic large igneous provinces and mantle plumes. In: Mahoney J, Coffin M (eds) Large igneous provinces: continental, oceanic, and planetary volcanism, vol 100, Geophysical monograph series. American Geophysical Union, Washington, DC, pp 297–333

Eskola P (1920) The mineral facies of rocks. Norsk Geol Tidsskr 6:143–194

Falloon TJ, Danyushevsky LV, Green DH (2001) Peridotite melting at 1 GPa: reversal experiments on partial melt compositions produced by peridotite-basalt sandwich experiments. J Petrol 42:2363–2390

Faure F, Arndt NT, Libourel G (2006) Formation of spinifex texture in komatiite: an experimental study. J Petrol 47:1591–1610

Ferry JM, Spear FS (1978) Experimental calibration of the partitioning of Fe and Mg between biotite and garnet. Contrib Mineral Petrol 66:113–117

Field M, Stienfenhofer J, Robey J, Kurszlaukis S (2008) Kimberlite-hosted diamond deposits of southern Africa: a review. Ore Geol Rev 34:33–75

Flugel E (ed) (1982) Microfacies analysis of limestones. Springer, New York, NY

Folk RL (1959) Practical petrographic classification of limestones. Am Assoc Pet Geol Bull 43:1–38

Folk RL (1974) Petrology of sedimentary rocks. Hemphill, Austin, TX, p 182

Frey FA, Weis D, Borisova A, Xu G (2002) Involvement of continental crust in the formation of the Cretaceous Kerguelen Plateau: new perspectives from ODP Leg 120 sites. J Petrol 43:1207–1239

Frost BR et al (2001) A geochemical classification for granitic rocks. J Petrol 42:2033–2048

Fujii T, Bougault H (1983) Melting relations of a magnesian abyssal tholeiite and the origin of MORBs. Earth Planet Sci Lett 62:283–295

Fumagalli P, Poli S (2005) Experimentally determined phase relations in hydrous peridotites to 6-5 GPa and their consequences on the dynamics of subduction zones. J Petrol 46:555–578

Furman T, Bryce J, Rooney T, Hana B, Yirgu G, Ayalew D (2006) Heads and tails: 30 million years of the Afar plume. In: Yirgu G, Ebinger CJ, Maguire PKH (eds) The Afar volcanic province within the East African Rift System, vol 259. Special publication—Geological Society of London, pp 95–119

Garrels RM, Christ CL (1965) Solutions, minerals, and equilibria. Freeman, San Francisco, CA

Geist D, Richards M (1993) Origin of the Columbia Plateau and Snake River plain: deflection of the Yellowstone plume. Geology 21:789–792

Ghiorso MS, Sack RO (1995) Chemical mass transfer in magmatic processes. IV. A revised and internally consistent thermodynamic model for the interpolation and extrapolation of liquid-solid equilibria in magmatic systems at elevated temperatures and pressures. Contrib Mineral Petrol 119:197–212

Ghiorso MS et al (2002) The pMELTS: a revision of MELTS for improved calculation of phase relations and major element partitioning related to partial melting of the mantle to 3 GPa. Geochem Geophys Geosyst 3:1030. doi:10.1029/2001GC000217

Giese P, Scheuber R, Schilling F, Schmitz M, Wigger P (1999) Crustal thickening processes in the Central Andes and the different nature of the Moho-discontinuity. J South Am Earth Sci 12: 201–220

Glazner AF (2007) Thermal limitations on incorporation of wall rock into magma. Geology 35:319–322
Gonzaga RG et al (2010) Eclogites and garnet pyroxenites: similarities and differences. J Volcanol Geotherm Res 190:235–247
Green HW II, Burnley PC (1989) A low self-organizing mechanism for deep- focus earthquakes. Nature 341:737
Green DH, Hibberson WO, Kova'cs I, Rosenthal A (2010) Water and its influence on the lithosphere–asthenosphere boundary. Nature 467:448–451
Gromet LP, Silver LT (1987) REE variations across the peninsular ranges batholith: implications for batholithic petrogenesis and crustal growth in magmatic arcs. J Petrol 28:75–125
Grove TL, Baker MB (1984) Phase equilibrium controls on the tholeiitic versus calc-alkaline differentiation trends. J Geophys Res 89: 3253–3274
Grove TL, Donnelly-Nolan J (1986) The evolution of young silicic lavas at medicine lake volcano, California: implications for the origin of compositional gaps in calc-alkaline lava series. Contrib Mineral Petrol 92:281–302
Grove TL, Parman S (2004) Thermal evolution of the Earth as recorded by komatiites. Earth Planet Sci Lett 219:173–187
Grove TL, Gerlach DC, Sando TW (1982) Origin of calc-alkaline series lavas at Medicine Lake Volcano by fractionation, assimilation and mixing. Contrib Mineral Petrol 80:160–182
Grove TL, Till CB, Krawczynski MJ (2012) The role of H_2O in subduction zone magmatism. Annu Rev Earth Planet Sci 40: 413–439
Gudfinnsson GH, Presnall DC (2000) Melting behavior of model lherzolite in the system CaO–MgO–Al2O3–SiO2–FeO at 0.7–2.8 GPa. J Petrol 41:1241–1269
Gudfinnsson GH, Presnall DC (2005) Continuous gradations among primary carbonatitic, kimberlitic, melilititic, basaltic, picritic, and komatiitic melts in equilibrium with garnet lherzolite at 3-8 GPa. J Petrol 46:1645–1659
Guilbert JM, Park CF (1986) The geology of ore deposits. WH Freeman, New York, NY
Gust DA, Perfit MR (1987) Phase relations of a high-Mg basalt from the Aleutian island arc: implications for primary irland arc basalts and high-Al basalts. Contrib Mineral Petrol 97:7–18
Hacker BR, Peacock SM (1995) Creation, preservation and exhumation of UHPM rocks. In: Coleman RG, Wang X (eds) Ultrahigh pressure metamorphism. Cambridge University Press, Cambridge, pp 159–181
Hacker BR, Liou JG (1998) When continents collide: geodynamics and geochemistry of ultrahigh-pressure rocks. Kluwer, Boston, MA
Haggerty SE (1986) Diamond genesis in a multiply constrained model. Nature 320:34–48
Haggerty SE (1999) A diamond trilogy: superplumes, supercontinents, and supernovae. Science 285:851–860
Haggerty SE, Sautter V (1990) Ultradeep (greater than 300 km) ultramafic upper mantle xenoliths. Science 248:993–996
Hall A (1987) Igneous petrology. Wiley, New York, NY
Hames WE, Renne PR, Ruppel C (2000) New evidence for geologically instantaneous emplacement of the earliest Jurassic Central Atlantic Magmatic Province basalts on the North American margin. Geology 28:859–862
Hames W, McHone JG, Renne P, Ruppel C (eds) (2003) The central Atlantic magmatic province: insights from fragments of Pangea, vol 136, Geophysical monograph series. American Geophysical Union, Washington, DC, 267 pp
Hamilton DL, MacKenzie WS (1965) Phase equilibrium studies in the system NaAlSiO4-KAlSiO4-SiO2-H2O. Min Mag 34 (Tilley vol.):214
Harmer RE (1999) The petrogenetic association of carbonatite and alkaline magmatism: constraints from the Spitskop complex, South Africa. J Petrol 40:525–548
Hart SR, Hauri EH, Oschmann LA, Whitehead JA (1992) Mantle plumes and entrainment: isotopic evidence. Science 256:517–520
Hauri EH (1996) Major-elements variability in the Hawaiian mantle plume. Nature 382:415–419
Helz RT (2009) Processes active in mafic magma chambers: the example of Kilauea Iki Lava Lake, Hawaii. Lithos 111:37–46
Herz N (1969) Anorthosite belts, continental drift, and the anorthosite event. Science 164:944–947
Herzberg C (1992) Depth and degree of melting of komatiite. J Geophys Res 97:4521–4540
Herzberg CT, O'Hara MJ (1985) Origin of mantle peridotite and komatiite by partial melting. Geophys Res Lett 12:541–544
Herzberg C, Ohtani E (1988) Origin of komatiite at high pressures. Earth Planet Sci Lett 88:321–329
Herzberg C (2004) Partial crystallization of mid-ocean ridge basalts in the crust and mantle. J Petrol 45:2389–2405
Herzberg C, Asimow PD, Arndt N, Niu Y, Lesher CM, Fitton JG, Cheadle MJ, Saunders AD (2007) Temperatures in ambient mantle and plumes: constraints from basalts, picrites, and komatiites. Geochem Geophys Geosyst 8, Q02006. doi:10.1029/2006GC001390
Hess HH (1960) Stillwater Igneous complex, Montana. Geol Soc Am Mem 80:2
Hess PC (1989) Origins of igneous rocks. Harvard University Press, Cambridge, MA
Hibbard MJ (1995) Petrography to petrogenesis. Prentice-Hall, Englewood Cliffs, NJ
Hickey RL et al (1986) Multiple sources for basaltic arc rocks from the southern volcanic zone of the Andes: trace element and isotopic evidence for contributions from subducted oceanic crust, mantle and continental crust. J Geophys Res 91:5963–5983
Higgins MD (2006) Quantitative textural measurements in igneous and metamorphic petrology. Cambridge University Press, Cambridge, UK, 276 p
Hildreth W (1981) Gradients in silicic magma chambers: implications for lithospheric magmatism. J Geophys Res 86:10153–10192
Hildreth W, Moorbath S (1988) Crustal contributions to arc magmatism in the Andes of Central Chile. Contrib Mineral Petrol 98:455–489
Hildreth W, Wilson CJN (2007) Compositional zoning of the BishopTuff. J Petrol 48:951–999
Hirose K, Kushiro I (1993) Partial melting of dry peridotites at high pressure: determination of compositions of melts segregated from peridotites using aggregates of diamonds. Earth Planet Sci Lett 114:477–489
Hirschmann MM (2000) Mantle solidus: experimental constraints and the effects of peridotite composition. Geochem Geophys Geosyst 1, #2000GC000070
Hirschmann MM, Stolper EM (1996) A possible role for garnet pyroxenite in the origin of the 'garnet signature' in MORB. Contrib Mineral Petrol 124:185–208
Hirschmann MM, Kogiso T, Baker MB, Stolper EM (2003) Alkalic magmas generated by partial melting of garnetpyroxenite. Geology 31:481–484
Hofmann C, Courtillot V, Feraud G, Rouchett P, Yirgu G, Ketefo E, Pik R (1997) Timing of the Ethiopian flood basalt event and implications for plume birth and global change. Nature 389: 838–841
Hofmann C, Feraud G, Courtillot V (2000) 40Ar/39Ar dating of mineral separates from the western Ghats lava pile: further constraints on duration and age of the Deccan traps. Earth Planet Sci Lett 180:13–28
Hoke L, Hilton D, Lamb S, Hammerschmidt K, Friedrichson H (1994) 3He Evidence for a wide zone of active mantle melting beneath the Central Andes. Earth Planet Sci Lett 128:341–355
Hooper PR (1982) The Columbia River basalts. Science 215: 1463–1468

Hooper PR, Hawkesworth CJ (1993) Isotopic and geochemical constraints on the origin and evolution of the Columbia River basalt. J Petrol 34:1203–1246

Hooper PR et al (2002) Ages of the Steens and Columbia River flood basalts and their relationship to extension- related calc-alkalic volcanism in eastern Oregon. Geol Soc Am Bull 114:43–50

Hooper PR et al (2007) The origin of the Columbia River flood basalt province; plume versus nonplume models, vol 430. Special Paper-Geological Society of America, pp 635–668

Huerta AD, Nyblade AA, Reusch AM (2009) Mantle transition zone structure beneath Kenya and Tanzania: more evidence for a deep-seated thermal upwelling in the mantle. Geophys J Int 177: 1249–1255

Hunter RH, Sparks RSJ (1987) The differentiation of the Skaergaard intrusion. Contrib Mineral Petrol 95:451–461

Hunter RH, Sparks RSJ (1990) The differentiation of the Skaergaard intrusion, Replies to Morse SA, Brooks CK, Nielsen TFD, McBirney AR, Naslund HR, Contrib Mineral Petrol 104: 248–254

Huppert HE, Sparks RSJ (1985) Komatiites I: eruption and flow. J Petrol 26:694–725

Hyndman DW (1985) Petrology of igneous and metamorphic rocks, 2nd edn. McGraw-Hill, New York, NY

Ingram (1956) Terminology for stratification in sedimentary rocks. Geol Soc Am Bull 67:125–126

Irvine TN (1980) Magmatic infiltration metasomatism, double diffucive fractional crystallization, and adcumulus growth in the Muskox intrusion and other layered intrusions. In: Hargreaves RB (ed) Physics of magmatic processes. Princeton University Press, Princeton, NJ, pp 325–383

Ito E, Takahashi E (1987) Melting of peridotite at uppermost lower mantle condition. Nature 328:514–517

Jackson M, Carlson RW (2011) An ancient recipe for flood-basalt genesis. Nature 476:316–320

Jaques AL, Green DH (1980) Anhydrous memting of peridotite at 0–15 Kb pressure and the genesis of tholeiitic basalts. Contrib Mineral Petrol 73:287–310

Johannes W (1989) Melting of plagioclase-quartz assemblages at 2 kbar water pressure. Contrib Mineral Petrol 103:270–276

Johnson KTM, Dick HJB, Shimizu N (1990) Melting in the oceanic upper mantle: an ion microprobe study of diopsides in abyssal peridotites. J Geophys Res 95:2662–2678

Johannes W, Holtz F (1996) Petrogenesis and experimental petrology of granitic rocks. Springer, New York, NY

Johnson MC, Plank T (1999) Dehydration and melting experiments constrain the fate of subducted sediments. Geochem Geophys Geosyst 1(12):1007. doi:10.1029/1999GC000014

Kato T, Ringwood AE, Irifune T (1988) Experimental determination of element partitioning between silicate perovskites, garnets and liquids: constraints on early differentiation of the mantle. Earth Planet Sci Lett 89:123–145

Kawamoto T, Holloway JR (1997) Melting temperature and partial melt chemistry of H2O-saturated mantle peridotite to 11 gigapascals. Science 276:240–243

Kelemen PB (1990) Reaction between ultramafic wall rock and fractionating basaltic magma: part I, phase relations, the origin of calc-alkaline magma series, and the formation of discordant dunite. J Petrol 31:51–98

Kelemen P (1998) Melt extraction from the mantle beneath mid-ocean ridges. Oceanus 41:23–28

Kelemen PB, Shimizu N, Salters VJM (1995) Extraction of mid-ocean-ridge basalt from the upwelling mantle by focused flow of melt in dunite channels. Nature 375:747–753

Kelemen PB, Hart SR, Bernstein S (1998) Silica enrichment in the continental upper mantle via melt/rock reaction. Earth Planet Sci Lett 164:387–406

Kelemen PB, Rilling JL, Parmentier EM, Mehl L, Hacker BR (2003) Thermal structure due to solid-state flow in the mantle wedge beneath arcs. In: Eiler J (ed) Inside the subduction factory. American Geophysical Union, Washington, DC, pp 293–311

Keller RA, Fisk MR, White WM (2000) Isotopic evidence for Late Cretaceous plume-ridge interaction at the Hawaiian hotspot. Nature 405:673–676

Kellogg LH, Hager BH, van der Hilst RD (1999) Compositional stratification in the deep mantle. Science 283:1881–1884

Kennedy CS, Kennedy GC (1976) The equilibrium boundary between graphite and diamond. J Geophys Res 81:2467–2470

Keshav S, Sen G (2001) Majoritic garnets in Hawaiian Xenoliths: preliminary results. Geophys Res Lett 28(18):3509–3512

Keshav S, Gudfinnsson GH, Presnall DC (2011) Melting phase relations of simplified carbonated peridotite at 12-26 GPa in the systems CaO-MgO-SiO2-CO2 and CaO-MgO-Al2O3-SiO2-CO2: highly calcic magmas in the transition zone of the earth. J Petrol 52:2265–2291

Kimura J-I et al (2009) Arc basalt simulator version 2, a simulation for slab dehydration and fluid-fluxed mantle melting for arc basalts: modeling scheme and application. G-cubed 10(9), Q09004. doi:10.1029/2008GC002217

Kinzler RJ, Grove TL (1992) Primary magmas of mid-ocean ridge basalts 2. Applications. J Geophys Res 97:6907–6926

Kirby SH, Durham WB, Stern LA (1991) Mantle phase changer and deep earthquake faulting in subducting lithosphere. Science 252: 216–225

Kirby SH et al (1996a) Intermediate-depth intraslab earthquakes and arc volcanism as physical expressions of crustal and uppermost mantle metamorphism in subducting slabs. In: Bebout GE (ed) Subduction top to bottom, vol 96, Geophysical monograph. American Geophysical Union, Washington, DC, pp 195–214

Kirby SH et al (1996b) Metastable mantle phase transformations and deep earthquakes in subducting oceanic lithospher. Rev Geophys 34:261–306

Klein EM, Langmuir CH (1987) Global correlation of ocean ridge basalt chemistry with axial depth and crustal thickness. J Geophys Res 92:8089–8115

Kogiso T, Hirschmann MM, Frost DJ (2003) High-pressure partial melting of garnet pyroxenite: possible mafic lithologies in the source of ocean island basalt. Earth Planet Sci Lett 216:603–617

Kogiso T, Hirschmann MM, Petermann M (2004) High-pressure partial melting of mafic lithologies in the mantle. J Petrol 45: 2407–2422

Koppers AAP, Staudigel H (2005) Asynchronous bends in pacific seamount trails: a case for extensional volcanism? Science 307:904–907

Koziol AM, Newton RC (1978) Redetermination of the anorthite breakdown reaction and improvement of plagioclase-garnet-Al2SiO5-quartz barometer. Am Mineral 73:216–223

Krishnamurthy P, Gopalan K, Macdugall JD (2000) Olivine compositions in picrite basalts and the Deccan volcanic cycle. J Petrol 41:1057–1069

Krogh EJ (1988) The garnet-clinopyrxene Fe-Mg geothermometer- A reinterpretation of existing experimental data. Contrib Mineral Petrol 99:44–48

Krumbein WC, Garrels RM (1952) Origin and classification of chemical sediments in terms of Eh and oxidation-reduction potentials. J Geol 60:1–33

Kuehner SM, Edgar AD, Arima M (1981) Petrogenesis of the ultrapotassic rocks from the Leucite Hills, Wyoming. Am Mineral 66:663–677

Kushiro I (1969) The system forsterite-diopside-silica with and without water at high pressures. Am J Sci 267A:269–294

Kushiro I (1973) The system diopside-anorthite-albite: determination of compositions of coexisting phases, vol 72. Carnegie Institute of Washington Yearbook, pp 502–507

Kushiro I (1980) Viscosity, density, and structure of silicate melts at high pressures, and their petrological applications. In: Hargraves RB (ed) Physics of magmatic processes. Princeton University Press, Princeton, NJ, pp 93–120

Lallemand S, Heuret A, Boutelier D (2005) On the relationships between slab dip, back-arc stress, upper plate absolute motion, and crustal nature in subduction zones. Geochem Geophys Geosyst 6. doi:10.1029/2005GC000917

Lamb S, Hoke L, Kennan L, Dewey J (1997) Cenozoic evolution of the Central Andes in Bolivia and northern Chile. In: Burg J-P, Ford M (eds) Orogeny through time, Geological Society Special Publication No. 121, pp 237–264

Land LS (1973) Holocene meteoric dolomitization of Pliestocene limestones, North Jamaica. Sedimentology 20:411–424

Land L et al (1979) The ooids of Baffin Bay, Texas. J Sediment Petrol 49:1269–1278

Langmuir CH, Klein EM, Plank T (1992) Petrological systematics of mid-ocean ridge basalts: constraints on melt generation beneath ocean ridges. Geophys Monogr 71:183–280

Langmuir CE, Forsyth DW (2007) Oceanography, Special Issue 20: 78–89

Larsen RB, Tegner C (2006) Pressure conditions for the solidification of the Skaergaard intrusion: eruption of east Greenland flood basalts in less than 300,000 years. Lithos 92:181–197

Larson RL (1991) Latest pulse of the earth: evidence for a mid-Cretaceous superplume. Geology 19:547–550

Larson RL, Kincaid C (1996) Onset of mid-Cretaceous volcanism by elevation of the 670 km thermal boundary layer. Geology 24:551–554

Lassiter JC, Hauri EH (1998) Osmium-isotope variations in Hawaiian lavas: evidence for recycled oceanic lithosphere in the Hawaiian plume. Earth Planet Sci Lett 164:483–496

Lassiter JC, Hauri E, Reiners PW, Garcia MO (2000) Generation of Hawaiian post-erosional lavas by melting of a mixed lherzolite/pyroxenite source. Earth Planet Sci Lett 178:269–284

Lay T (1994) The fate of descending slabs. Annu Rev Earth Planet Sci 22:33–61

Lay T, Garnero EJ, Williams Q (2004) Partial melting in a thermo-chemical boundry layer at the base of the mantle. Phys Earth Planet Int 146:441–467

Le Fort PE (1981) Manaslu granite: a collision signature of the Himalaya. J Geophys Res 86:10545–10568

LeBas MJ, Streckeisen AL (1991) The IUGS systematics of igneous rocks. J Geol Soc Lond 148:825–833. doi:10.1144/gsjgs.148.5.0825

Lee CTA, Cheng X, Horodyskyj U (2006) The development and refinement of continental arcs by primary basaltic magmatism, garnet pyroxenite accumulation, basaltic recharge and delamination: insights from the Sierra Nevada. Contrib Mineral Petrol 151:222–242

Lee CTA, Luffi P, Plank T, Dalton HA, Leeman WP (2009) Constraints on the depths and temperatures of basaltic magma generation on Earth and other terrestrial planets using new thermobarometers for mafic magmas. Earth Planet Sci Lett 279:20–33

Leeman WP et al (2004) Petrologic constraints on the thermal structure of the Cascades arc. J Volcanol Geotherm Res 140:67–105

Leeman WP, Lewis JF, Evarts RC, Conrey RM, Streck MJ (2005) Petrologic constraints on the thermal structure of the Cascades. J Volcanol Geotherm Res 140:67–105

Leeman WP, Schutt DL, Hughes SS (2009) Thermal structure beneath the Snake River plain: implications for the Yellowstone hotspot. J Volcanol Geotherm Res 188:57–67

Lehman B et al (2010) Diamondiferous kimberlites in central India synchronous with Deccan flood basalts. Earth Planet Sci Lett. doi:10.1016/j.epsl.2009.12.014

Lei J, Zhao D (2006) A new insight into the Hawaiian plume. Earth Planet Sci Lett 241:438–453

LeMaitre RW et al (1989) A classification of igneous rocks and glossary of terms. Blackwell, Oxford

Lepp H, Goldich SS (1964) Origin of Precambrian iron formations. Econ Geol 59:1025–1060

Lesher CE, Cashman KV, Mayfield JD (1999) Kinetic controls on crystallization of Tertiary North Atlantic basalt and implications for the emplacement and cooling history of lava at site 989, southeast Greenland rifted margin. In: Larsen HC, Duncan RA, Allan JF, Brooks K (eds) Proceedings of the ocean drilling program, vol 163. Scientific Results, College Station, TX, pp 135–148

Li X et al (2000) Mapping the Hawaii plume conduit with receiver functions. Nature 405:938–941

Lindsley DH, Dixon SA (1976) Diopside-enstatite equilibria at 850 to 1400'C, 5 to 35 kbars. Am J Sci 276:1285–1301

Lindsley DH et al (2010) Petrology, geochemistry, and structure of the Chugwater anorthosite, Laramie anorthosite complex, southeastern Wyoming. Can Mineral 48:887–923

Liou JG (1971) P-T stabilities of laumontite, wairakite, lawsonite, and related minerals in the system CaAl2Si2O8–SiO2-H2O. J Petrol 12:379–411

Longhi J (2002) Some phase equilibrium systematics of lherzolite melting: I. Geochem Geophys Geosyst 3:1020. doi:10.1029/2001GC000204

Longhi J (2003) A new view of lunar anorthosites: postmagma ocean petrogenesis. J Geophys Res 108:5083

Longhi J, Boudreau AE (1980) The orthoenstatite liquidus field in the system forsterite-diopside-silica at one atmosphere. Am Mineral 65:563–573

Longhi J, Vander Auwera J, Fram M, Duchesne JC (1999) Some phase equilibrium constraints on the origin of Proterozoic (Massif) anorthosites and related rocks. J Petrol 40:339–362

Maaloe S (1985) Igneous petrology. Springer, New York, NY

Maaloe S (2004) The PT-phase relations of an MgO-rich Hawaiian tholeiite: the compositions of primary Hawaiian tholeiites. Contrib Mineral Petrol 148:236–246

Maaloe S, Abbott RN (2005) Tetrahedral plots of the phase relations for basalts. Math Geol 37:869–893

Macdonald KC (2001) Mid-ocean ridge tectonics, volcanism and geomorphology. In: Steele J, Thorpe S, Turekian K (eds) Encyclopedia of ocean sciences. Academic, London, pp 1798–1813

Mahoney J, Macdougall JD, Lugmair GW, Murali AV, Sankar Das M, Gopalan K (1982) Origin of the Deccan trap flows at Mahabaleshwar inferred from Nd and Sr isotopic and chemical evidence. Earth Planet Sci Lett 60:47–60

Marsh BD (1988a) Crystal capture, sorting, and retention in convecting magma. Geol Soc Am Bull 100:1720–1737

Marsh BD (1988b) Crystal size distribution (CSD) in rocks and the kinetics and dynamics of crystallization. 1. Theory. Contrib Mineral Petrol 99:277–291

Marsh BD (1989) On convective style and vigor in sheet like magma bodies. J Petrol 30:479–530

Marsh BD (1996) Solidification fronts and magmatic evolution. Mineral Mag 60:5–40

Marsh BD (1998) On the interpretation of crystal size distributions in magmatic systems. J Petrol 39:553–599

McBirney AR (1996) The Skaergaard intrusion. In: Cawthorn RG (ed) Layered intrusions. Elsevier, Amsterdam, pp 147–180

McBirney AR (2007) Igneous petrology, 3rd edn. Jones & Bartlett, Boston, MA, 550 p

McBirney AR, Hunter RH (1995) The cumulate paradigm reconsidered. J Geol 103:114–122

McBirney AR, Naslund HR (1990) The differentiation of the Skaergaard intrusion: a discussion of Hunter and Sparks. Contrib Mineral Petrol 104:235–247

McClean M (1995) Sedimentology. Oxford University Press, New York, NY

McKenzie D (1984) The generation and compaction of partially molten rock. J Petrol 25:713–765
McKenzie D, Bickle MJ (1988) The volume and composition of melt generated by extension of the lithosphere. J Petrol 29:625–679
McLelland JM et al (2004) Direct dating of Adirondack massif anorthosite by U-Pb SHRIMP analysis of igneous zircon: implications for AMCG complexes. Geol Soc Am Bull 116:1299–1317
McLelland JM, Selleck BW, Hamilton MA, Bickford ME (2010) Late- to post-tectonic setting of some major Proterozoic anorthosite-mangerite-charnockite-granite (AMCG) suites. Can Mineral 48:729–750
Miall AD (1990) Principles of sedimentary basin analysis, 2nd edn. Springer, New York, NY
Mibe K, Kanzaki M, Kawamoto T, Matsukage KN, Fei Y, Ono S (2007) Second critical endpoint in the peridotite-H2O system. J Geophys Res 112, Art no: B03201. doi:10.1029/2005JB004125
Milholland CS, Presnall DC (1998) Liquidus phase relations in the $CaO-MgO-Al_2O_3-SiO_2$ system at 3.0 GPa: the aluminous pyroxene thermal divide and high pressure fractionation of picritic and komatiitic magmas. J Petrol 39:3–27
Mitchell RH (1995) Kimberlites, orangeites, and related rocks. Plenum, New York, NY, 410 pp
Mitchell RH, Bergman SC (1991) Petrology of lamproites. Plenum, New York, NY, 447 pp
Mitchell RH, Dawson JB (2012) Carbonate–silicate immiscibility and extremely peralkaline silicate glasses from Nasira cone and recent eruptions at Oldoinyo Lengai Volcano, Tanzania. Lithos 152:40–46
Miyashiro A (1961) Evolution of metamorphic belt. J Petrol 2:277–311
Miyashiro A (1973) Metamorphism and metamorphic belts. Wiley, New York, NY
Miyashiro A et al (1977) Metamorphism in the Mid-Atlantic Ridge near 24° and 30°N. Philos Trans R Soc Lond A268:589–603
Moore KR, Wood BJ (1998) The transition from carbonate to silicate melts in the CaO–MgO–SiO2–CO2 system. J Petrol 39: 1943–1951
Morgan WJ (1971) Convection plumes in the lower mantle. Nature 230:42–43
Morse SA (1980) Basalts and phase diagrams. Springer, New York, NY
Naslund HR, McBirney AR (1996) Mechanisms of formation of igneous layering. In: Cawthorn RG (ed) Layered intrusions. Elsevier, Amsterdam, pp 1–43
Newhall CG, Self S (1982) The volcanic explosivity index (VEI): an estimate of explosive magnitude for historical volcanism. J Geophys Res 87:1231–1238
Niu Y, O'Hara MJ (2003) Origin of ocean island basalts: a new perspective from petrology, geochemistry, and mineral physics consideration. J Geophys Res 108(B4):2209. doi:10 1029/ 2002JB002048
Nixon PH (ed) (1987) Mantle xenoltihs. Wiley, New York, NY
Norman MD, Borg LE, Nyquist LE, Bogard DD (2003) Chronology, geochemistry, and petrology of a ferroan noritic anorthosite clast from Descartes breccia 67215: clues to the age, origin, structure, and impact history of the lunar crust. Meteorit Planet Sci 38: 645–661
O'Hara MJ (1965) Primary magmas and the origin of basalts. Scott J Geol 1:19–40
O'Hara MJ (1968b) The bearing of phase equilibria studies in synthetic and natural systems in the origin and evolution of basic and ultrabasic rocks. Earth Sci Rev 4:69–133
O'Hara MJ (1968a) The bearing of phase equilibria studies on the origin and evolution of basic and ultrabasic rocks. Earth Sci Rev 4:69–133
O'Hara MJ (1977) Geochemical evolution during fractional crystallisation of a periodically refilled magma chamber. Nature 266:503–507
O'Nions RK (1992) The continents. In: Brown GC, Hawkesworth CJ, Wilson ECL (eds) Understanding the earth: a new synthesis. Cambridge University Press, Cambridge, pp 145–163
Ohtani E et al (1995) Melting relations of peridotite and the density crossover in planetary mantles. Chem Geol 120:207–221
Osborn EF (1979) The reaction principle. In: Yoder HS Jr (ed) The evolution of igneous rocks fiftieth anniversary perspectives. Princeton University Press, Princeton, NJ, pp 133–170
Parman SW, Dann JC, Grove TL, de Wit MJ (1997) Emplacement conditions of komatiite magmas from the 3.49 Ga Komati formation, Barberton greenstone belt, South Africa. Earth Planet Sci Lett 150:303–323
Parman S, Grove TL, Dunn J (2001) The production of Barberton komatiites in an Archean subduction zone. Geophys Res Lett 28: 2513–2516
Patiño-Douce AE (1996) Effects of pressure and H2O contents on the compositions of primary crustal melts. Trans R Soc Edinb Earth Sci 87:11–21
Patiño-Douce A (1999) What do experiments tell us about the relative contributions of crust and mantle to the origin of granitic magmas? In: Castro A, Fernández C, Vigneresse JL (eds) Understanding granites: integrating new and classical techniques, vol 168., pp 55–75, Geol. Soc. London Special Publ
Patterson RJ, Kinsman DJJ (1982) Formation of diagenetic dolomite in coastal sabkha along Arabian (Persian) Gulf. AAPG Bull 66:28
Pattison D, Newton RC (1991) Reversed experimental calibration of the garnet-clinopyroixene Fe-Mg exchange theromometer. Contrib Mineral Petrol 101:87–103
Peacock SM, Wang K (1999) Seismic consequences of warm versus cool subduction metamorphism: examples from southwest and northeast Japan. Science 286:937–939
Pearce JA (1983) The role of the sub-continental Lithosphere in magma genesis at destructive plate boundaries. In: Hawkesworth CJ, Norry MJ (eds) Continental basalts and mantle xenoliths. Shiva, Nantwich, pp 230–249
Peng ZX, Mahoney JJ, Hooper P, Macdougall JD, Krishnamurthy P (1988) Basalts of the northeastern Deccan traps, India: isotopic and elemental geochemistry and relation to southwestern Deccan stratigraphy. J Geophys Res 103:29843–29865
Perfit MR (2001) Midocean ridge geochemistry and petrology, Encyclopedia of Ocean Science. Academic, San Diego, CA
Pertermann M, Hirschmann MM (2003) Anhydrous partial melting experiments on MORB-like eclogite: phase relations, phase compositions and mineral–melt partitioning of major elements at 2–3 GPa. J Petrol 44:2173–2201
Philpotts AR, Ague J (2009) Principles of igneous and metamorphic petrology, 2nd edn. Cambridge University Press, Cambridge
Phinney WC, Morrison DA, Maczuga DE (1988) Anorthosites and related megacrystic units in the evolution of Archean crust. J Petrol 29:1283–1323
Pik R, Deniel C, Coulon C, Yirgu G, Hoffmann C, Ayalew D (1998) The northwestern Ethiopian plateau flood basalts: classification and spatial distribution of magma types. J Volcanol Geoth Res 81:91–111
Pitcher WS (1993) The nature and origin of granite. Blackie, London
Polat A et al (2008) The origin and compositions of mesoarchean oceanic crust: evidence from the 3075 Ma Ivisaartoq greenstone belt, SW Greenland. Lithos 100:293–321
Polat A et al (2012) Geochemistry of ultramafic rocks and hornblendite veins in the Fiskenæsset layered anorthosite complex, SW Greenland: Evidence for hydrous upper mantle in the Archean. Precambrian Res 214–215:124–153. doi:10.1016/j.precamres.2011.11.013
Presnall DC (1969) The geometrical analysis of partial fusion. Am J Sci 267:1178–1194
Presnall DC, Dixon SA, Dixon J, O'Donnell TH, Brenner NL, Schrock RL, Dycus DW (1978) Liquidus phase relations on the join diopside-forsterite-anorthite from 1 atm to 20 kbar: their bearing on the

generation and crystallization of basaltic magma. Contrib Mineral Petrol 66:203–220
Presnall DC et al (1979) Generation of Midocean ridge tholeiites. J Petrol 20:3–35
Presnall DC, Weng Y-H, Milholland CS, Walter MJ (1998) Liquidus phase relations in the system MgO–$MgSiO_3$ at pressures up to 25 GPa—constraints on crystallization of a molten Hadean mantle. Phys Earth Planet Int 197:83–95
Presnall DC, Gudfinnsson GH (2011) Oceanicvolcanism from the low-velocity zone without mantle plumes. J Petrol 32:1533–1546. doi:10.1093/petrology/egq093
Price SE, Russell JK, Kopylova M (2000) Primitive magma from the Jericho Pipe, NWT, Canada: constraints on primary kimberlite melt chemistry. J Petrol 41:789–808
Priest GR (1990) Volcanic and tectonic evolution of the Cascades volcanic arc, central Oregon. J Geophys Res 95:19583–19599
Putirka KD (2005) Igneous thermometers and barometers based on plagioclase + liquid equilibria: tests of some existing models and new calibrations. Am Mineral 90:336–346
Putirka KD (2008) Thermometers and barometers for volcanic systems. In: Putirka KD, Tepley F (eds) Reviews in mineralogy and geochemistry, vol 69. The Mineralogical Society of America, Washington, DC, pp 61–120
Ramos VA (1999) Plate tectonic setting of the Andean Cordillera. Episodes 22:183–190
Ramos FC, Wolff JA, Tollstrup DL (2005) Sr isotope disequilibrium in Columbia River flood basalts: evidence for rapid shallow-level open-system processes. Geology 33:457–460
Rapp RP, Watson EB (1995) Dehydration melting of metabasalt at 8-32 kbar: implications for continental growth and crust-mantle recycling. J Petrol 36:891–931
Raymond L (2007) Petrology: the study of igneous, sedimentary, and metamorphic rocks, 2nd edn. Waveland, Long Grove, IL
Reid JB, Hamilton MA (1987) Origin of Sierra Nevada granite: evidence from small scale composite dikes. Contrib Mineral Petrol 96:441–454
Ren Z et al (2005) The chemical structure of the Hawaiian mantle plume. Nature 436:837–840
Reubi O, Blundy J (2009) A dearth of intermediate melts at subduction zone volcanoes and the petrogenesis of arc andesites. Nature 461:1269–1273
Ribe NM, Christensen UR (1999) The dynamical origin of Hawaiian volcanism. Earth Planet Sci Lett 171:517–531
Richards MA, Duncan RA, Courtillot VE (1989) Flood basalts and hot spot tracks: plume heads and tails. Science 246:103–107
Ringwood AE (1975) Composition and petrology of Earth's mantle. McGraw Hill, New York, NY
Ringwood AE (1979) Origin of the Earth and Moon. Springer, New York, NY
Ritsema J, van Heijst HJ, Woodhouse JH (1999) Complex shear wave velocity structure imaged beneath Africa and Iceland. Science 286:1925–1928
Robin-Popieul CCM, Arndt NT, Chauvel C, Byerly GR, Sobolev AV, Wilson A (2012) A New model for Barberton komatiites: deep critical melting with high melt retention. J Petrol. doi:10.1093/petrology/egs042
Rock NMS (1991) Lamprophyres. Van Nostrand Reinhold, New York, NY, p 285
Rodriguez S, Sen G (2013) Chapter 10: eruption of the Grande Ronde Formation Lavas, Columbia River Basalt Group: results of numerical modeling. In: Reidel SP et al. (ed) The Columbia river flood basalt province, vol 497. Geological Society of America Special Paper (due to be published in December 2013)
Rooney TO et al (2012) Upper mantle pollution during afar plume-continental rift interaction. J Petrol 53:365–389
Rudnick RL, McDonough WF, O'Connell RJ (1998) Thermal structure, thickness and composition of continental lithosphere. Chem Geol 145:395–411
Rushmer T (1991) Partial melting of two amphibolites: contrasting experimental results under fluid-absent conditions. Contrib Mineral Petrol 107:41–59
Rye R, Holland HD (1998) Paleosols and the evolution of atmospheric oxygen: a critical review. Am J Sci 298:668
Saleeby J, Ducea MN, Clemens-Knott D (2003) Production and loss of high-density batholithic root, southern Sierra Nevada, California. Tectonics 22. doi:10.1029/2002TC001374
Salters VJM, Stracke A (2004) Composition of the depleted mantle. G-cubed 6:Q05007. doi:10 1029/2004GC000824
Sawyer EW, Cesare B, Brown M (2011) When the continental crust melts. Elements 7:229–234
Saxena SK (1973) Thermodynamics of rock-forming crystalline solutions. Springer, New York, NY
Schmitz M et al (1999) The crustal structure beneath Central Andean forearc and magmatic arc as derived from seismic studies—the PISCO 94 experiment in northern Chile (21°˜-23°˜S). J South Am Earth Sci 12:237–260
Schulze DJ (2003) A classification scheme for mantle-derived garnets in kimberlite: a tool for investigating the mantle and exploring for diamonds. Lithos 71:195–213
Scoates JS (2002) The plagioclase—magma density paradox re-examined and the crystallization of Proterozoic anorthosites: a reply. J Petrol 43:1979–1983
Scoates JS, Mitchell JN (2000) The evolution of troctolitic and high Al basaltic magmas in proterozoic anorthosite plutonic suites and implications for the Voisey's Bay massive Ni-Cu sulfide deposit. Econ Geol 95:677–701
Scoates JS, Lindsley DH, Frost BR (2010) Magmatic and structural evolution of an anorthositic magma chamber: the Poe Mountain intrusion, Laramie anorthosite complex, Wyoming (USA). Can Mineral 48:851–885
Searle MP, Cox J (2002) Subduction zone metamorphism during formation and emplacement of the Semail ophiolite in the Oman Mountains. Geol Mag 139:241–255
Self S, Blake S (2008) Consequences of explosive supereruptions. Elements 4:41–46
Sen G (1983) A petrologic model for the constitution of the upper mantle and crust of the Koolau shield, Oahu, Hawaii, and Hawaiian magmatism. Earth Planet Sci Lett 62:215–228
Sen G (1988) Petrogenesis of spinel lherzolite and pyroxenite suite xenoliths from the koolau shield, Oahu, Hawaii: implications for petrology of the post.-eruptive lithosphere beneath Oahu. Contrib Mineral Petrol 100:61–91
Sen G (1995) A simple petrologic model for the generation of Deccan Trap magmas. Int Geol Rev 37:825–850
Sen G (2001) Generation of Deccan trap magmas. Proc Ind Acad Sci (Earth Planet Sci) 110:409–431
Sen G, Presnall D (1986) Petrogenesis of the Dunite xenoliths from the Koolau volcano, Oahu, Hawaii: implications for Hawaiian volcanism. J Petrol 27:197–217
Sen G, Keshav S, Bizimis M (2005) Hawaiian mantle xenoliths and magmas: composition and thermal character of the lithosphere. Am Mineral 90(5–6):871–887
Sen G, Chandrasekharam D et al (2011) Chapter 2: deccan traps flood basalt province: an evaluation of the thermochemical plume model. In: Ray J (ed) Topics in igneous petrology. Springer, New York, NY. doi:10.1007/978-90-481-9600-5_2
Sen G, Jones R (1989) Experimental equilibration of multicomponent pyroxenes in the spinel peridotite field: implication for practical thermometers and a possible barometer. J Geophys Res 94: 17871–17880

Sen G, Jones R (1990) Cumulate xenolith in Oahu, Hawaii: implications for deep magma chambers and Hawaiian volcanism. Science 249:1154–1157

Sen G, Presnall DC (1984) Liquidus phase relationships on the join anorthite-forsterite-quartz at 10 kbar with applications to basalt petrogenesis. Contrib Mineral Petrol 85:404–408

Sen G, Keshav S, Bizimis M (2005) Hawaiian mantle xenoliths and magmas: composition and thermal character of the lithosphere. Am Mineral 90:871–887

Sen G, Borges M, Marsh BD (2006) A case for short duration of Deccan trap eruption. EOS 87(20):197–204

Sen G, Bizimis M, Das R, Paul DK, Biswas S (2009) Deccan plume, lithosphere rifting, and volcanism in Kutch, India. Earth Planet Sci Lett 277:101–111

Serrano L, Ferrari L, Martinez ML, Petrone CM, Jaramillo C (2011) An integrative geologic, geochronologic and geochemical study of Gorgona Island, Colombia: implications for the formation of the Caribbean large igneous province. Earth Planet Sci Lett 309:324–336

Shand SJ (1947) Eruptive rocks. their genesis, composition, classification and their relation to ore deposits, 3rd edn. Wiley, New York, NY

Shen Y, Solomon SC, Bjarnason IT, Wolfe CJ (1998) Seismic evidence for a lower-mantle origin of the Iceland plume. Nature 395:62–65

Sheth H, Melluso L (2008) The Mount Pavagadh volcanic suite, Deccan traps: geochemical stratigraphy and magmatic evolution. J Asian Earth Sci 32:5–21

Sheth HC, Ray JS, Ray R, Vanderkluyse L, Mahoney JJ, Kumar A, Shukla AD, Das P (2009) Geology and geochemistry of Pachmarhi dykes and sills, Satpura Gondwana Basin, central India: problems of dyke-sill-flow correlations in the Deccan traps. Contrib Mineral Petrol 158:357–380. doi:10.1007/s00410-009-0387-4

Shirey SB et al (2003) Regional patterns in the paragenesis and age of inclusions in diamond, diamond composition, and the lithospheric seismic structure of Southern Africa. Lithos 71:243–258

Silver LT, Chappell BW (1988) The Peninsular Ranges batholith: an insight into the evolution of the Cordilleran batholiths of southwestern North America. Trans R Soc Edinb 79:105–121

Sinton JM, Detrick RS (1992) Mid-ocean ridge magma chambers. J Geophys Res 97:197–216

Sisson TW, Grove TL (1993) Experimental investigations of the role of H_2O in calc-alkaline differentiation and subduction zone magmatism. Contrib Mineral Petrol 113:143–166

Sobolev AV, Hofmann AW, Sobolev SV, Nikogosian IK (2005) An olivine-free mantle source of Hawaiian shield basalts. Nature 434:590–597

Sparks RSJ (1990) Crystal capture, sorting, and retention in convecting magma: discussion and reply. Geol Soc Am Bull 102:847–850

Sparks RSJ (1993) Magma generation in the Earth. In: Hawkesworth C, Wilson C (eds) Understanding the Earth. Cambridge University Press, Cambridge, pp 91–114

Spear FS (1993) Metamorphic phase equilibiria. Pressure-temperature-time paths. Monograph. Mineralogical Society of America, Washington, DC

Spear FS, Selverstone J (1983) Quantitative P-T paths from zoning in minerals: theory and some tectonic applications. Contrib Mineral Petrol 83:348–357

Spera FJ (1980) Aspects of magma transport, in: physics of magmatic processes. Princeton University Press, Princeton, NJ

Stachel T, Harris JW, Tappert R, Brey GP (2003) Peridotitic diamonds from the Slave and the Kaapvaal cratons—similarities and differences based on a preliminary data set. Lithos 71:489–503

Stern CR (1991) Comment on "Crustal contributions to arc magmatism in the Andes of Central Chile" by W. Hildreth and S. Moorbath. Contrib Mimeral Petrol 108:241–246

Stern RJ (1998) A subduction primer for instructors of introductory-geology courses and authors of introductory-geology textbooks. J Geosci Educ 46:221–228

Stern RJ (2002) Subduction zones. Rev Geophys 40(4):1012. doi:10.1029/2001RG000108

Stern CR (2004) Active Andean volcanism: its geologic and tectonic setting. Revista Geologica de Chile 31:161–206

Stern CR (2011) Subductionerosion: rates, mechanisms, and its role in arc magmatism and the evolution of the continental crust and mantle. Gondwana Res 20:284–308

Stern RJ, Fouch MJ, Klemperer S (2003) Overview of the Izu-Bonin-Marian subduction factory. Geophys monogr ser 138:175–222

Stern RJ et al (2012) To understand subduction initiation, study forearc crust: to understand forearc crust, study ophiolites. Lithosphere 4:469–483

Stolper EM (1980) A phase diagram for mid-ocean ridge basalts: preliminary results and implications for petrogenesis. Contrib Mineral Petrol 74:13–27

Stolper EM, Walker D (1980) Melt density and the average composition of basalt. Contrib Mineral Petrol 74:7–12

Suzuki A, Ohtani E (2003) Density of peridotite melts at high pressure. Phys Chem Miner 30:449–456. doi:10.1007/s00269-003-0322-6

Takahashi E (1986) Melting of dry perdotite KLB1 up to 14 GPa: implications on the origin of peridotite upper mantle. J Geophys Res 91:9367–9382

Takahashi E, Kushiro I (1983) Melting of a dry peridotite at high pressures and basalt magma genesis. Am Mineral 68:859–879

Takahashi E, Nakajima K, Wright TL (1998) Origin of the Columbia River basalts: melting model of a heterogeneous plume head. Earth Planet Sci Lett 162:63–80

Tatsumi Y et al (1983) Generation of arc basalt magmas and thermal structure of the mantle wedge in subduction zones. J Geophys Res 88:5815–5825

Tenner TJ, Hirschmann MM, Humayun M (2012) The effect of H2O on partial melting of garnet peridotite at 3.5 GPa. Geochem Geophys Geosyst 13:1–28. doi:10.1029/2011GC003942

Thompson JB Jr (1957) The graphical analysis of mineral assemblages in pelitic schist. Am Mineral 42:842–858

Thompson JB Jr (1982a) Composition space: an algebraic and geometric approach. Rev Mineral 10:1–31

Thompson JB Jr (1982b) Reaction space: an algebraic and geometric approach. Rev Mineral 10:33–51

Till CB, Grove TL, Withers AW (2012) The beginnings of hydrous mantle wedge melting. Contrib Mineral Petrol 163:669–688

Tirone M, Sen G, Morgan JP (2012) Petrological geodynamic modeling of mid-ocean ridges. Phys Earth Planet In 190–191 (2012):51–70

Torsvik TH, Smethurst MA, Burke K, Steinberger B (2006) Large igneous provinces generated from the margins of the large low-velocity provinces in the deep mantle. Geophys J Int 167:1447–1460

Torsvik TH, Steinberger B, Webb SJ, Ashwal LD (2010) Diamonds sampled by plumes from the core–mantle boundary. Nature 466:352–355

Turcotte DL, Schubert G (1982) Geodynamics: applications of continuum physics to geological problems. Wiley, New York, NY

Turner FJ (1968) Metamorphic petrology. McGraw Hill, New York, NY

Tuttle OF, Bowen NL (1958) Origin of granite in the light of experimental studies in the system $NaAlSi_3O8$—$KAlSi_3O_8$-SiO_2-H_2O. Geol Soc Am Mem 74:153p

Ulmer P (2001) Partial melting in the mantle wedge—the role of H2O in the genesis of mantle-derived arc related magmas. Phys Earth Planet Int 127:215–232

Ussler W III, Glazner AF (1992) Graphical analysis of enthalpy-composition relationships in mixed magmas. J Volcanol Geotherm Res 51:23–40

van der Hilst RD (1997) Evidence for deep mantle circulation from global tomography. Nature 386:578–584

Wager LR, Brown GM (1968) Layered igneous rocks. Oliver and Boyd, Ltd, London, 588 pp

Wager LR, Brown GM, Wadsworth WJ (1960) Types of igneous cumulates. J Petrol 1:73–85
Wagner TP, Grove TL (1998) Melt/harzburgite reaction in the petrogenesis of tholeiitic magma from Kilauea volcano, Hawaii. Contrib Mineral Petrol 131:1–12
Walker D (1986) Melting equilibria in multicomponent systems and liquidus/solidus convergence in mantle peridotite. Contrib Mineral Petrol 92:303–307
Walter MJ (1998) Melting of garnet peridotite and the origin of komatiite and depleted lithosphere. J Petrol 39:29–60
Wang Z, Gaetani G (2008) Partitioning of Ni between olivine and siliceous eclogite partial melt: experimental constraints on the mantle source of Hawaiian basalts. Contrib Mineral Petrol 156:661–678
Watson EB (1982) Melt infiltration and magma evolution. Geology 10:236–240
White WM (2013) Geochemistry. Wiley, Oxford
White WM (1985) Sources of oceanic basalts: radiogenic isotopic evidence. Geology 13:115–118
White R, McKenzie D (1989) Magmatism at Rift zones: the generation of volcanic continental margins and flood basalts. J Geophys Res 94:7685–7729
White RV, Saunders AD (2005) Volcanism, impact and mass extinctions: incredible or credible coincidences? Lithos 79:299–316
White JC et al (2012) Open System evolution of peralkaline trachyte and phonolite from the Suswa volcano, Kenya rift. Lithos 152:84–104
Whittington AG, Treloar PJ (2002) Crustal anatexis and its relation to the exhumation of collisional orogenic belts, with particular reference to the Himalaya. Mineral Mag 66:53–91
Wignall PB (2001) Large igneous provinces and mass extinctions. Earth Sci Rev 53:1–33
Wignall P (2005) The link between large igneous province eruptions and mass extinctions. Elements 1:293–297
Wilkinson BH (1979) Biomineralization, paleoceanography, and the evolution of calcareous marine organisms. Geology 7:524–527
Wilson JT (1963) A possible origin of the Hawaiian Islands. Can J Phys 41:863–870
Wilson M (1989) Igneous petrogenesis. Unwin Hyman, Boston, MA
Wilson AH (2012) A chill sequence to the Bushveld complex: insight into the first stage of emplacement and implications for the parental magmas. J Petrol 53:1123–1168
Wilson L, Head JW (2007) An integrated model of kimberlite ascent and eruption. Nature 447:53–57
Winter JD (2009) Principles of igneous and metamorphic petrology. Prentice-Hall, New York, NY
Wirth R, Rocholl A (2003) Nanocrystalline diamond from the Earth's mantle underneath Hawaii. Earth Planet Sci Lett 211:357–369
Wolfe CJ et al (2011) Mantle P-wave velocity structure beneath the Hawaiian hot spot. Earth Planet Sci Lett 303:267–280
Wolff JA, Ramos FC, Hart GL, Patterson JD, Brandon AD (2008) Columbia River flood basalts from a centralized crustal magmatic system. Nat Geosci 1:177–180
Wood BJ, Banno S (1973) Garnet-orthopyroxene and garnet-clinopyroxene relationships in simple and complex systems. Contrib Mineral Petrol 42:109–124
Wood BJ, Fraser DG (1976) Elementary thermodynamics for geologists. Oxford University Press, Oxford
Wood BJ, Fraser DG (1977) Elementary thermodynamics for geologists. Oxford University Press, Oxford
Wood BJ, Turner SP (2009) Origin of primitive high-Mg andesite: constraints from natural examples and experiments. Earth Planet Sci Lett 283:59–66. doi:10.1016/j.epsl.2009.03.032
Wyllie PJ (1978) Mantle fluid compositions buffered in peridotite–CO2–H2O by carbonates, amphibole, and phlogopite. J Geol 86:687–713
Yang HJ, Sen G, Shimizu N (1998) Mid-ocean ridge melting: constraints from lithospheric xenoliths at Oahu, Hawaii. J Petrol 39:277–295
Yaxley GM, Green DH (1998) Reactions between eclogite and peridotite: mantle refertilization by subduction of oceanic crust. Schweizerische Mineralogische und Petrographische Mitteilungen 78:243–255
Yoder HS, Tilley CE (1962) Origin of basalt magmas—an experimental study of natural and synthetic rock systems. J Petrol 3:342–582
Yoshida M, Santosh M (2011) Supercontinents, mantle dynamics and plate tectonics: a perspective based on conceptual vs. numerical models. Earth Sci Rev 105:1–24
Yuan H, Dueker K (2005) Teleseismic P-wave tomogram of the Yellowstone plume. Geophys Res Lett 32, L07304. doi:10.1029/2004GL022056
Zandt G, Gilbert H, Owens TJ, Ducea MN, Saleeby J, Jones C (2004) Active foundering of a continental arc root beneath the southern Sierra Nevada in California. Nature 431:41–46
Zhong S, Zhang N, Li ZX, Roberts JH (2007) Supercontinent cycles, true polar wander, and very long wavelength mantle convection. Earth Planet Sci Lett 261:551–564
Zieg MJ, Marsh BD (2002) Crystal size distributions and scaling laws in the quantification of igneous textures. J Petrol 43:85–101
Zindler A, Hart S (1986) Chemical geodynamics. Annu Rev Earth Planet Sci 14:493–571